AD-A243 383

(1)

Third International Conference on

Inverse Design Concepts and Optimization in Engineering Sciences

ICIDES-III

October 23-25, 1991

DTIC
ELECTE
C

Editors:
George S. Dulikravich

Unclassified

PROCEEDINGS

THIRD INTERNATIONAL CONFERENCE ON INVERSE DESIGN CONCEPTS AND OPTIMIZATION IN ENGINEERING SCIENCES ICIDES-III

October 23-25, 1991
Washington, D.C.

Sponsored by:

NASA HEADQUARTERS
Aeronautics Directorate
Aerodynamics Division
600 Independence Avenue, SW
Washington, D.C. 20546

NATIONAL SCIENCE FOUNDATION
Division of Electrical and Communications Systems
Communications & Computational Systems Program
1800 G Street, NW
Washington, D.C. 20550

OFFICE OF NAVAL RESEARCH
Department of the Navy
Mechanics Division
800 North Quincy Street
Arlington, VA 222171

PENN STATE UNIVERSITY
College of Engineering
Department of Aerospace Engineering
233 Hammond Building
University Park, PA 16802

Organized and edited by:

George S. Dulikravich

Accession For
NTIS GRA&I
DTIC TAB
Unannounced
Justification
By
Distribution/
Availability Codes
Dist | Avail and/or Special
A-1

QUALITY INSPECTED 4

FOREWORD

The need for organizing the ICIDES sequence of conferences arose in my mind almost a decade ago while noticing that there were no established forums for the exchange of conceptual ideas in the general field of inverse, semi-inverse, and direct design and optimization in engineering sciences. There were neither specialized technical journals nor textbooks available in this highly interdisciplinary field that rapidly grew with the availability of faster and larger computing machines. Consequently, there were no technical courses in engineering programs that would cover these design methodologies. The situation is starting to change, though, as a response to increased interest on the part of industry which feels the pressure from the competitive global market. ICIDES was envisioned as an open forum for experts and users alike to present their methodologies and discuss their concepts.

The ICIDES sequence has experienced a steady growth in attendance, the number of publications, and the international character of its audience, while maintaining high standards.

	Locations	Dates	Papers	Countries	Sponsors
ICIDES-I	*Univ. of Texas at Austin*	*Oct. 17-18, 1984*	*31*	*9*	*UT-Austin*
ICIDES-II	*Penn State University*	*Oct. 24-26, 1987*	*32*	*9*	*NSF,ONR,PSU*
ICIDES-III	*Washington, D.C.*	*Oct. 23-25, 1991*	*48*	*15*	*NSF,ONR,NASA,PSU*

Each contributed technical paper was reviewed by two colleagues without revealing to them the identities of the authors. Although unusual, this process has stimulated more substantial and constructive comments from the reviewers and has contributed to the improvements in the quality of the accepted technical papers. Invited lectures at ICIDES-III form a unique collection of survey articles that present a status report on the present state of the art worldwide.

ICIDES-III would not have been possible without financial support from NASA Headquarters (Ms. Pamela Richardson and Mr. Louis Williams), ONR-Mechanics Division (Dr. Philip Abraham and Dr. Spiridon Lekoudis), and NSF-Communications and Computational Systems Program (Dr. George Lea). I would also like to thank my student assistants, Mr. Branko Kosovic and Mr. Scott Sheffer for their help with the word processing of the conference announcements. Finally, I would like to thank the authors and reviewers of the technical papers and to the invited lecturers who contributed to the success of the ICIDES-III.

University Park, PA
September 1991

George S. Dulikravich

91-16423



91 1125 025

TABLE OF CONTENTS

	Page
Foreword George S. Dulikravich	ii
Partial contents:	
Review of Aerodynamic Design in the Netherlands (Invited) T. E. Labrujère, National Aerospace Lab. NLR, Anthony Fokkerweg 2, 1059 CM Amsterdam, THE NETHERLANDS	1
Aerodynamic Aircraft Design Methods and their Notable Applications -- Survey of the Activity in Japan (Invited) K. Fujii , Inst. of Space & Astro. Science, Yoshinodai 3-1-1, Sagamihara, Kanagawa, 229, JAPAN S. Takanashi, NAL, Jindaiji-Higashi 7-44-1, Chofu, Tokyo 182, JAPAN	31
On a Global Aerodynamic Optimization of a Civil Transport Aircraft G. Savu and O. Trifu, The Aviation Institute, Bd. Pacii 220, 77538 Bucharest, ROMANIA	45
Inverse Airfoil Design Procedure Using a Multigrid Navier-Stokes Method J.B. Malone and R.C. Swanson, Mail Stop 173, NASA Langley Research Center, Hampton, VA 23665-5225, USA	55
A Comparison of Two Closely-Related Approaches to Aerodynamic Design Optimization G. R. Shubin and P. D. Frank, Org. G-6412, M/S 7L-21, Boeing Computer Services, P.O. Box 24346, Seattle, WA 98124-0346, USA	67
Design of Thrust Vectoring Exhaust Nozzles for Real-Time Applications Using Neural Networks K. Prasanth, R. E. Markin and K.W. Whitaker, The University of Alabama, Dept. of Aerospace Engineering, Tuscaloosa, AL 35487-0280, USA	79
Finite Element Structural Redesign by Large Admissible Perturbations M.M. Bernitsas, E. Beyko, C.W. Rim and B. Alzahabi, Dept. of Naval Architecture and Marine Engineering, The University of Michigan-North Campus, Ann Arbor, MI 48109-2145, USA	87
Structural Damage Identification Using Mathematical Optimization Techniques M.H. H. Shen, Ohio State University, Dept. of Aero. & Astro. Eng., 2036 Neil Avenue Mall, Columbus, OH 43210-1276, USA	99
Electrical Impedance Imaging in Two-Phase, Gas-Liquid Flows; 1. Initial Investigation (over) J.T. Lin, L. Ovacik and O.C. Jones, Center for Multiphase Research, RPI, Troy, N.Y. 12180-3590, USA	111
Recent Progress in Inverse Methods in France (Invited) P. Bry ,SNECMA , Cincinnati, OH, USA and O. P. Jacquotte and M.-C. Le Pape, Aerodynamics Dept.,ONERA, BP 72, 92322 Chatillon, FRANCE	123

Research on Inverse, Hybrid and Optimization Problems in Engineering Sciences with Emphasis on Turbomachinery Aerodynamics: Review of Chinese Advances (Invited)
G.-L. Liu, Lab. for Turbomachinery Aerodynamics, Shanghai Institute of Mech. Eng., 516 Jun-Gong Road, Shanghai 200093, P. R. CHINA 145

The Turbomachine Blading Design Using S2-S1 Approach
T.S. Luu, L. Bencherif and B. Viney, LIMSI (CNRS), BP 133, F-91403 Orsay Cedex, FRANCE, and
J. M. Nguyen Duc, SEP, BP 802, F-27207 Vernon, FRANCE 165

A Proposed Through-Flow Inverse Method for the Design of a Mixed-Flow Pumps
J. E. B. T. Borges, Department of Mechanical Eng.,Instituto Superior Tecnico, Av. Rovisco Pais, 1096 Lisboa, PORTUGAL 177

An Inverse Inviscid Method for the Design of Quasi-Three Dimensional Rotating Turbomachinery Cascades
E. Bonataki, P. Chaviaropoulos and K.D. Papailiou, National Technical University of Athens, Dept. of Mechanical Eng., Lab. of Thermal Turbomachines, P.O. Box 64069, 15710 Athens, GREECE 189

A PC-Based Inverse Design Method for Radial and Mixed Flow Turbomachinery
I. H. Skoe, IA-T, Kristion Sonjugvei 20, 3600 Kongsberg, NORWAY 201

Optimal Design of Solidification Processes
J.A. Dantzig and D.A. Tortorelli, University of Illinois, Dept. of Mech. & Indust. Eng., 140 Mechanical Eng. Bld., MC-244, 1206 West Green Street, Urbana, Illinois 61801, USA 213

Numerical Identification of Boundary Conditions on Nonlinearly Radiating Inverse Heat Conduction Problems
D. A. Murio, Dept. of Math. Sciences, Old Chemistry Bldg. (ML 25), University of Cincinnati, Cincinnati, OH 45221-0025, USA 227

Comparison of Four Stable Numerical Methods for Abel's Integral Equation
D. A. Murio and C. E. Mejia, Dept. of Math. Sciences, Old Chemistry Bldg. (ML 25), University of Cincinnati, Cincinnati, OH 45221-0025, USA 239

Optimization of the Heating Surface Shape in the Contact Melting Problem
S.A. Fomin, Dept. of Appl. Math., Kazan State University, Kazan, 420008, USSR
S.-M. Cheng, Dept .of Power Eng., Huazhong University of Science and Technology, Wuhan 430074, P. R. CHINA 253

Design of 3-Dimensional Complex Airplane Configurations with Specified Pressure Distribution via Optimization (Invited)
K. Kubrynski, Tech. Univ. of Warsaw, Institute of Applied Mechanics and Aviation Technology, ul. Nowowiejska 24, 00-665 Warsaw, POLAND 263

Extended Mapping and Characteristics Techniques for Inverse Aerodynamic Design
H. Sobieczky, DLR-Inst. fuer Theoret. Stroemung., Bunsenstrasse 10, 3400 Goettingen, F. R. GERMANY
Y.-J. Qian, Beijing Univ. of Aero. & Astro., 37 Xue Yuan Road, Haidian District, Beijing 100083, P. R. CHINA 281

Supercritical Blade Design on Stream Surfaces of Revolution with an Inverse Method
E. Schmidt and H-D. Grein, Inst. fuer Aero. & Gas Dynamik, University of Stuttgart, Pfaffenwaldring 21, D-7000 Stuttgart 80, F. R. GERMANY 293

Applications of Direct Inverse Analogy Method (DIVA) and Viscous Design Optimization Techniques
E. Greff, D. Forbrich and H. Schwarten, Deutsche Airbus GmbH, Dept. of Aerodynamics, Postfach 107845, D-2800 Bremen 1, F. R. GERMANY 307

Blade Design and Analysis Using A Modified Euler Solver
O.Leonard and R.A. Van den Braembussche, von Karman Institute, Chaussée de Waterloo 72, 1640 Rhode-Saint-Genese, BELGIUM 325

Variational Formulation of Hybrid Problems for Fully 3-D Transonic Flow With Shocks in Rotor
G.-L. Liu , Lab. for Turbomachinery Aerodynamics, Shanghai Institute of Mech. Eng., 516 Jun-Gong Road, Shanghai 200093, P. R. CHINA 337

Aerodynamic Shape Optimization of Arbitrary Hypersonic Vehicles
G. S. Dulikravich and S. G. Sheffer, Dept. of Aerospace Eng., The Pennsylvania State University, University Park, PA 16802, USA 347

Analysis and Design of Transonic Airfoils Using Streamwise Coordinates
R. M. Barron and C.-F. An, Dept. of Mathematics and Statistics, University of Windsor, 401 Sunset, Windsor, Ontario N9B 3P4, CANADA 359

Research on Inverse Design Methods and Optimization in Italy (Invited)
F. Larocca, FIAT AVIO, Corso Ferruci 112, 10129 Torino, ITALY 371

Adjoint Operator Approach to Shape Design For Internal Incompressible Flows (Invited)
H. Cabuk, C.-H. Sung and V. Modi, Mech. Eng. Dept., 220 Mudd Hall, Columbia University, New York, NY, 10027, USA 391

An Inverse Method for the Aerodynamic Design of Three-Dimensional Aircraft Engine Nacelles
R.A. Bell and R.D. Cedar, G.E. Aircraft Engines, One Neuman Way, MD A317, Cincinnati, OH 45215-6301, USA 405

Vortex Generator Design for Aircraft Inlet Distortion as a Numerical Optimization Problem
B.H. Anderson, NASA Lewis Research Center, Mail Stop 5-11, 21000 Brookpark Road, Cleveland, OH. 44135, USA
R. Levy, Scientific Research Associates, Inc., 50 Nye Road, P.O. Box 1058, Glastonbury, CT 06033, USA 419

Airfoil Optimization With Efficient Gradient Calculations
T. Sorensen, MIT, Dept. of Aero. & Astro., 77 Massachusetts Ave, Room 37-350, Cambridge, MA 02139, USA 433

Design Optimization of Transonic Airfoils
C.-Y. Joh, B. Grossman and R.T. Haftka, VPI, Aero. & Ocean Eng.Dept., 214 Randolph Hall, Blacksburg, VA 24061, USA 445

Identification of Dynamic Characteristics of Flexible Rotors as a Dynamic Inverse Problem
W.P. Roisman and L.D. Vajingortin, Department of Applied Mechanics, Khmelnitsky Technological Institute, 11 Institutskaja Ulica, Khmelnitsky, 280016, USSR 457

On Designing for Quality
L.D. Vajingortin and W.P. Roisman, Department of Applied Mechanics, Khmelnitsky Technological Institute, 11 Institutskaja Ulica, Khmelnitsky, 280016, USSR 469

Optimal Interaction of Indenter With Inhomogeneous Plate
V. N. Aptukov, Lab. of Impulse Deformation of Bodies, Inst. of Continuous Media Mech., Acad. of Sci. of USSR, Koroleva Ulica 1, Perm, 614061, USSR 481

Analysis of the Optimal Laminated Target Made up of Discrete Set of Materials
V. N. Aptukov and V.L. Belousov, Laboratory of Impulse Deformation of Bodies, Institute of Continuous Media Mechanics, Academy of Sciences of USSR, Koroleva Ulica 1, Perm, 614061, USSR 489

Inverse Problems in the Design, Modeling and Testing of Engineering Systems (Invited)
O. M. Alifanov, College of Cosmonautics, Moscow Aviation Institute, 4,Volokolamskoe sh., Moscow, 125871, USSR 495

Inverse Problems and Optimal Experiment Design in Unsteady Heat Transfer Processes Identification (Invited)
E. A. Artyukhin, College of Cosmonautics, Moscow Aviation Institute, 4, Volokolamskoe sh., Moscow, 125871, USSR 513

A New Method of Optimal Design for a Two-Dimensional Diffuser by Using Dynamic Programming
C.-G. Gu, M.-J. Zhang, X. Chen and Y.-M. Miao, Department of Power Machinery Eng., Xi'an Jiaotong University, Xi'an 710049, Shaanxi Province, P. R. CHINA 531

Study of a New Airfoil Used in Reversible Axial Fans
C.-J. Li, B.-S Wei and C.-G. Gu , Department of Power Machinery Eng., Xi'an Jiaotong University, Xi'an, Shaanxi Province, P. R. CHINA 541

An Inverse Method With Regularity Condition for Transonic Airfoil Design
Z.-Q. Zhu, Z.-X. Xia and L.-Y.Wu, Beijing University of Aeronautics and Astronautics, 37 Xueyuan Road, Haidian District, Beijing 100083, P. R. CHINA 553

Inverse Problems in Diffraction
A. G. Mikheev and A.S. Shamaev, Institute for Problems in Mechanics, USSR Academy of Sciences, Pr. Vernadskogo 101, Moscow 117526, USSR 563

Optimization of Transistor Design Including Large Signal Device/Circuit Interaction at Extremely High Frequencies (20-100+ GHz)
R. Levy and H.L Grubin, Scientific Research Associates, Inc., 50 Nye Road, P.O. Box 1058, Glastonbury, CT 06033, USA 573

Design of Transonic Compressor Cascades Using Hodograph Method
Z.-Y. Chen and J.-R. Guo, Department of Thermal Engineering, Tsinghua University, Beijing, P. R. CHINA 593

The Research Progress on Hodograph Method of Aerodynamic Design at Tsinghua University
Z.-Y. Chen and J.-R. Guo, Department of Thermal Engineering, Tsinghua University, Beijing, P. R. CHINA 599

* * *

The following papers have been accepted for presentation at the ICIDES-III, but their final versions have not arrived in time to be included in the bound volume.

Numerical Optimization in Germany: A Non-Exhaustive Survey on Current Developments with Emphasis on Aeronautics (Invited)
L. Fornasier, DASA-MBB GmbH, Ottobrunn, F.R. GERMANY

A Design Algorithm for 2D Cascade Flow
H. Ye and R. M. Barron, Dept. of Mathematics and Statistics, University of Windsor, 401 Sunset, Windsor, Ontario N9B 3P4, CANADA

Third International Conference on Inverse Design Concepts and Optimization in Engineering Sciences (ICIDES-III). Editor: G.S. Dulikravich. Washington D.C. October 23-25, 1991.

REVIEW OF AERODYNAMIC DESIGN IN THE NETHERLANDS

by
Th.E.Labrujère

National Aerospace Laboratory NLR
Anthony Fokkerweg 2
1059 CM AMSTERDAM
THE NETHERLANDS

SUMMARY

A survey is given of aerodynamic design activities in The Netherlands, which take place mainly at Fokker, NLR and Delft University of Technology (TUD). The survey concentrates on the development of the Fokker 100 wing, glider design at TUD and research at NLR in the field of aerodynamic design. Results are shown to illustrate these activities.

1.INTRODUCTION

In the Netherlands, activities in the field of aerodynamic design take place at the aircraft factory Fokker, the aeronautical research institute NLR and the Technical University of Delft.

A well known product of these activities is the civil transport aircraft Fokker 100 (See fig.1.1). But no less successful is the ASW-24 glider designed by Boermans at the Low Speed Laboratory of TUD in collaboration with Alexander Segelflugzeugbau in Germany(See Fig.1.2).

Very often, new aircrafts result from modifying existing aircraft, aiming at e.g. improvement of performance, adaption to changed market requirements or improvement of economics in view of operating environment. In that way, the Fokker 100 has been derived from the Fokker F28 (see Fig.1.3) by means of sometimes drastic modifications. Also, the gliders designed at Delft are the result of continuous attempts to reach the limits of sailplane performance.

These developments would not have been possible without the help of computational tools which play an essential role in both the actual design process and the analysis of wind tunnel measurements and also at the interpretation of flight test data.

The present paper deals with the main aerodynamic design objectives pursued at the development of the transport aircraft Fokker 100 and the glider ASW-24 and the process followed to attain them. In conclusion, special attention will be paid to research activities at NLR in the field of computational fluid dynamics in support of design developments.

2.THE FOKKER 100.

The Fokker 100 design will be illustrated by considering two of the main design problems solved during development. A more complete and detailed account can be found in Refs. 1 and 2.

The Fokker 100 wing has been derived from the F-28 wing, which is determined by four wing sections connected with straight generators. The main objective for a new wing design was improvement of the Mach drag rise characteristics. The F-28 was originally designed for a lift coefficient of C_L=0.2 whereas the new design requirements lead to a C_L=0.4 to 0.5 at which condition the transonic drag increase of the F-28 wing is not negligible.

Third International Conference on Inverse Design Concepts and Optimization in Engineering Sciences (ICIDES-III), Editor: G.S. Dulikravich, Washington D.C., October 23-25, 1991.

Table I presents a survey of the most important modifications that have been implemented successively, thus defining a number of new wing shapes which have been analyzed by means of both computations and wind tunnel measurements.

The modifications applied to wing sections I and II in wing 4 resulted from a computational study with the help of a viscous transonic flow code, which predicted a significant improvement of the Mach drag rise characteristics as a consequence of these modifications (See Fig.2.1). This was fully confirmed by means of wind tunnel measurements, though it appeared necessary to improve the stalling characteristics of the outer wing.

Computational analysis led to the conclusion that the Mach drag rise characteristics could be improved by a further modification of section I. Moreover, by modifying section IV improvement of the outer wing stall behaviour was expected. Test results for the thus defined wings 5 and 6 are presented in Fig.2.2 indicating a further improvement when compared with wings 3 and 4.

As a preliminary final step wing 8 was defined, combining a rearward chord extension with rear camber. This modification led to a second improvement of the drag rise characteristics as illustrated by Fig.2.3 for section II.

At that time, however, it appeared necessary to adapt the design goals to market requirements in terms of an increase of take-off weight. This led to the definition of wing 10, which happened to exhibit a rather large drag rise at low lift coefficients cruising conditions. Subsequent reduction led to the definition of wing 11 (See Fig.2.4).

Modification of the lower leading edge of sections II and IV resulted in wing 11. The effect of this modification is shown in Figs. 2.4 and 2.5. And, finally, modification of section II leading to the definition of wing 12 took care of the design requirement with respect to the stalling behaviour.

In conclusion, a survey of the main modifications applied to the original F-28 wing is given by means of Fig.2.6 where a comparison is made between the definitive wing planform for the Fokker 100 and the F-28 wing planform and where also the basic wing sections are compared. This figure shows that a large part of the original F-28 wing has still been retained. The main differences are the span extension and leading as well as trailing edge modifications. However, as has been verified by means of wind tunnel measurements these modifications were sufficient for attaining amongst other things the design goals with respect to high- and low speed drag, buffet onset boundary and stalling behaviour.
Another important design problem was the improvement of the stub wing with respect to its drag characteristics. At the new cruising conditions the flow around the original F-28 stub wing contained regions with supersonic velocities, thus leading to undesirable wave drag. It appeared to be possible to reshape the stub wing such that the flow remained subcritical over the entire range of cruise lift coefficients.

Finally, some attention may be paid to the computer codes used during the design process. A major role has been played by two transonic flow analysis codes i.e. the 3D code XFLO-22 and a 2D viscous transonic flow code by means of which the effect of the various wing modifications was predicted. The wing modifications were based on earlier wing design computations, preceding the actual Fokker 100 wing design, by means of the constrained inverse code for the design of wings with a given pressure distribution in subsonic flow of Ref.3. More recently this code has been extended for application to supercritical flow conditions (Ref.4).

The wing design system is based on an inverse method of the residual correction type, combining a direct flow solver for transonic flow with simple geometric correction rules. In order to fulfil requirements from the structural engineer's point of view, geometric constraints are taken into account.

The transonic wing-body code XFLO-22 (Ref.6) is an extension of the non-conservative finite difference wing code FLO-22 (Ref.5) of Jameson and Caughey modified to simulate fuselage cross-flow effects. This simulation is achieved by replacing the boundary condition of zero normal velocity in the plane of symmetry in the original code by a condition of prescribed non-zero normal velocity, the latter being computed by means of the NLR panel method (Ref.7,8). By means of post-processing viscous effects may then be estimated using the 3-D laminar/turbulent boundary layer code BOLA (Ref.9).

An example of the usefulness of XFLO-22 is given in Fig.2.7 where a comparison is made between calculated and measured (wind tunnel and flight test) pressure distributions for two wing stations. It may be noted that a surprisingly good correlation is shown. Presumably the applied condition of taking the trailing edge flow tangential to the lower wing surface, when using a grid of 160 (chord) x 32 (span) x 28 (normal) points, compensates for the absence of viscous effects. The same kind of correlation is demonstrated in Fig. 2.8 where a comparison is made between measured and predicted buffet onset boundaries.

For the design problem associated with the stub wing with its strong interaction with the fuselage and the engine nacelle a design code was not available. The problem was solved by combining results of the 2D analogue of the wing design code with 3D panel method calculations (Ref.7). The success of this approach may be illustrated by means of Fig.2.9 where a comparison is made between calculated and measured stub wing pressures.

3.THE SAILPLANE ASW-24

The ASW-24 is a Standard Class Sailplane built by Alexander Schleicher Flugzeugbau in Germany. The aerodynamic design of this glider was performed in close cooperation between the manufacturer and the Low Speed Laboratory (LSL) of Delft University of Technology (TUD). Detailed account of aerodynamic as well as structural design is given in Ref.10.

When designing a glider, the main objectives are maximizing the glide ratio at the higher flight speeds and minimizing the rate of sink at the lower flight speeds. The higher flight speeds are applied when flying from one thermal to another, and the lower flight speeds are used when climbing in a thermal.

A typical glider flight performance polar is shown in Fig.3.1 for the ASW-24. It results from flight test measurements and computational analysis with respect to its component parts. From this figure it appears that the wing contributes considerably to the drag, at higher flight speeds especially in consequence of the profile drag. Accordingly, the history of glider design shows a continuous search for low drag wing profiles, mainly by attempting to maximize the laminar flow region on the airfoils.

When designing airfoils for laminar flow with a view to practical application the key problem is to avoid the appearance of laminar separation bubbles. These bubbles cause pressure drag and have a detrimental effect on the subsequent turbulent boundary layer such that a considerable drag increase results. Thus, the design should be such that transition to turbulent flow occurs before the laminar flow will separate.

Third International Conference on Inverse Design Concepts and Optimization in Engineering Sciences (ICIDES-III), Editor: G.S. Dulikravich, Washington D.C., October 23-25, 1991

There are a few alternatives to solve this problem. One of these is Wortmann's destabilizing region concept, the other is the application of some tripping device in order to provoke transition to turbulent flow.

When following the destabilizing region concept the airfoil is shaped such that in the region where laminar separation is expected to occur, a slightly adverse pressure gradient is induced. This adverse gradient destabilizes the laminar boundary layer causing transition and thus avoiding flow separation. Application of a tripping device amounts to disturbing the boundary layer by means of artificial roughness on the airfoil surface or by means of blowing.

Both alternatives have been used at the design of the airfoil DU84-158 applied in the ASW-24. The destabilizing region concept has been applied at the upper surface and a tripping device in the form of a so-called "zig-zag tape" has been applied at 77% chord position at the lower surface. The measured pressure distribution of Fig.3.2. shows a laminar separation bubble on the lower surface at about 85% chord and its removal due to application of the zig-zag tape. Transition to turbulent flow on the upper surface is triggered by the adverse gradient at about 59% chord.

The effectiveness of the zig-zag tape is also shown in Fig.3.3 where measured aerodynamic characteristics are given both for the clean airfoil and the taped airfoil. The maximum lift is hardly influenced by the roughness, the stalling behaviour is gentle and the drag reduction is considerable.

As is shown in Fig.3.1, at low speed climbing conditions, more than 50% of the total drag is due to induced drag. So, it will be clear that reduction of induced drag will be another major goal when designing sailplanes; wing planform and aspect ratio being the main parameters when optimizing for induced drag at a given wing loading.

In the present case the wing planform has been chosen with the help of numerical optimization studies based on lifting line theory with taper ratio and spanwise position of taper ratio change as design variables. The aspect ratio has been chosen in combination with the wing loading on the basis of cross country speed optimization studies, for details of which the reader is referred to ref.10.

A third aspect of wing design that may be considered here, is the effect of wing fuselage interaction. Applying the panel method of Ref.7 with the panel schematization of Fig.3.4 the pressure distribution on the wing-fuselage combination has been studied. Fig.3.5 shows the pressure distribution in a few wing sections for two different angles of attack.

The typical modern glider fuselage has been designed such that the forebody fits into the streamlines of the wing at higher lift coefficients in order to avoid the occurrence of high suction peaks in sections near the fuselage (Fig.3.5a). This has, however, as a consequence that at high speed conditions (lower lift coefficient) the cross flow effect is increased (Fig.3.5b), which causes the wing sections close to the fuselage to operate in non-optimal conditions. To improve the flow conditions at the junction of the ASW-24, a small fairing with 7% chord extension has been applied where the wing is lofted towards a wing root airfoil suitable for turbulent flow conditions. Nevertheless, improvement of the wing fuselage junction is still the subject of continuing study.

In the past decades considerable progress in glider design has been made. This may be illustrated by means of Fig.3.6, where the flight performance polar for the present design is shown in comparison with that of two predecessors. The difference in performance is a consequence of the improvement of the aerodynamic

characteristics as illustrated by Fig.3.7 which is mainly due to the wing profiles that have been applied.

In conclusion these profiles may be compared by means of Figs.3.8a,b,c , where calculated inviscid pressure distributions are shown. From these pressure distributions a rough estimate of the laminar flow region can be made, clearly showing the backward displacement of the transition point resulting in a decrease of the drag.

The DU84-158 airfoil has been designed with the help of the LSL computer program for airfoil analysis and design (Refs.12,13). This program is based on Timman's conformal mapping method for inviscid flow (Ref.14) in combination with Thwaites method for laminar and Green's method for turbulent boundary layer flow and the Van Ingen e^9-method for prediction of transition (Ref.15).

4.DEVELOPMENTS AT NLR

In support of aerodynamic aircraft design NLR has a continuing research program for the development of CFD codes both for analysis and design. Gradually, as will have become clear from the preceding sections the tools thus developed are incorporated in the actual design processes followed in the industry. In the present section, some attention will be paid to capabilities that have not yet been (fully) utilized for practical applications. Also, further contributions of NLR to improvement of airfoil- and wing design will be considered.

4.1 AIRFOILS

For analysis and design of airfoils in both subsonic and transonic flow taking viscous effects into account, the MAD computer program system has been developed. On the ICIDES conference of 1984 Slooff has given a global description of the system as it was available at that time (Ref.16).

Since then the system of Ref.17 has been extended by incorporating the transonic design method of Ref.25 in combination with the transonic analysis method of Refs.5 and 6. The general approach followed to solve the design problem has remained the same. It is of the residual correction type where the actual design problem is translated into an equivalent design problem of reduced complexity, thus enabling the application of relatively simple inverse methods and it leads to an iterative design process as depicted in Fig.4.1.
It is assumed that the design goal is formulated in terms of a target pressure distribution and that an initial guess of the airfoil shape will be given. A direct flow solver for either subsonic or transonic viscous flow is used for the determination of the pressure distribution on the given airfoil, and a constrained inverse method is used to determine the possibly required modification.

An example of application to a subsonic design problem is described in Refs.19 and 20.
It concerns the improvement with respect to drag behaviour of the wing-slat configuration of Fig.4.2. As becomes clear from Fig.4.3 it has been found in wind tunnel measurements that the flow around this airfoil shows early boundary layer separation on the main wing upper surface at the take-off condition lift coefficient $C_l \approx 2.1$.

With the aid of the method of Ref.18 for the determination of viscous subsonic flow around multi-element airfoils analysis calculations were made. From this analysis it was concluded that reduction of the drag should be attempted by

Third International Conference on Inverse Design Concepts and Optimization in Engineering Sciences
(ICIDES-III), Editor: G.S. Dulikravich, Washington D.C., October 23-25, 1991

reducing the extent of the separation region. This implied that the adverse pressure gradient on the wing upper surface had to be reduced.

As the basic airfoil geometry should not be altered when designing a wing-slat configuration, the sole possibility to reduce the pressure gradient is to lower the suction peak level on the wing nose, without however reducing the lift coefficient at the same time.

These considerations led to specification of the target as depicted in Fig.4.4, in terms of an equivalent potential flow pressure distribution. The main points of interest are :
(i) a decreased velocity peak on the main wing upper surface aiming at a delay of boundary layer separation,
(ii) increase of expansion around the wing nose aiming at an increase of the slat dumping velocity,
(iii) an increase of the slat dumping velocity aiming at increase of the slat lift contribution,
(iv) an increase of the slat lower surface pressure level aiming at increase of the slat lift and decrease of the slat drag.

Application of the design process depicted in Fig.4.1. led to the result depicted in Fig.4.5. The most striking geometry modification is the blunt nose of the main wing resulting in a rather thin slat trailing edge. Application of the viscous flow analysis method of Ref.18 to the new geometry produced the pressure distribution shown in Fig.4.6 in comparison with that on the original configuration.

Clearly two of the design goals have been attained according two these calculations. The suction peak on the main wing has been reduced and the dumping velocity on the slat has been increased. Hardly visible is a slightly rearward shift of the boundary layer separation point on the wing upper surface (it amounts to about 2% of the local chord) and the pressure level at the slat lower side has decreased instead of increased.

However, as the analysis method has not been developed for the treatment of separated flow regions, the quantitative value of these results is questionable. Moreover the results for the slat lower surface, modelled as shown in Fig.4.1 to simulate the existence of the separation bubble, are of course less reliable. Therefore it was concluded that the results were sufficiently encouraging in order to test the new slat geometry in the wind tunnel.

The measured C_l-α curves for both the original and new configuration are compared in Fig.4.7. Apparently $C_{l_{max}}$ has been retained and the increase of the C_l-α slope indicates reduced viscous losses. This is confirmed by the C_l-C_d curves shown in Fig.4.8 which also shows that at the present design condition ($C_l \approx 2.1$) a drag reduction of more than 30 % has been realized.

Another example of application of the MAD system will be presented in Ref.21. It concerns the design of a medium speed laminar flow airfoil. As a first step in the design process a target pressure distribution was specified. Here the goal was to choose a pressure distribution such that at the upper side the boundary layer would remain laminar over at least 60% of the chord.

The pressure distribution prescribed as target for the upper side of the airfoil is shown in Fig.4.9 together with calculated Re_θ (Reynolds number based on momentum loss thickness). Re_{θ_1} represents the Tollmien-Schlichting stability criterium and Re_{θ_t} is the transition criterium according to Granville. The

Third International Conference on Inverse Design Concepts and Optimization in Engineering Sciences
(ICIDES-III), Editor: G.S. Dulikravich, Washington D.C., October 23-25, 1991.

calculations predict instability of the boundary layer for x/c > .14, but a reasonable margin with respect to transition to turbulent flow is left until x/c=.6. As a result of applying the MAD system, an airfoil was obtained which produces the desired pressure distribution perfectly, as is shown in Fig.4.10.

From this example where, in connection with the laminar flow, special attention had to be paid to the nose shape, it has been learned once again, that care has to be given to the leading and trailing edge regions (adaptation of the target without adapting the design goals) in order to obtain convergence and in order to produce realistic airfoil shapes.

Notwithstanding these difficulties the design was successful as may be illustrated by means of Figs.4.11 and 4.12, where a comparison is made between pressure distributions and C_l-C_d curves as measured in the wind tunnel and as calculated by means of VGK, a 2D viscous transonic airfoil code (Ref.23,24), which is an extension of the semi-conservative finite difference method of Garabedian and Korn for inviscid transonic flow, weakly coupled with a boundary layer code based on Thwaites method for laminar and Green's lag-entrainment method for turbulent flow.

To conclude this subsection an application to wind turbine design may be considered (Ref.22). The objective was to design an airfoil with an increased maximum lift over drag ratio. Starting point was a blade based on the NACA 4421 airfoil of which the stall behaviour was considered appropriate for control by stall. Thus the airfoil design had to be done under the side condition that the stall behaviour should remain approximately the same. Moreover, from structural point of view, the thickness over chord ratio had to be at least 0.2.

An existing airfoil which could have been considered for application is the Wortmann FX 84-W-218 airfoil because of its favourable lift over drag ratio. It has, however, an unacceptable stall behaviour. Therefore it was concluded that an airfoil should be designed combining the advantages of both the NACA 4421 and the Wortmann airfoils.

Using CADOS (see section 4.3), a NACA 4421 pressure distribution has been modified in order to specify a target pressure distribution for the MAD system (see Fig.4.13). The target pressure distribution should lead to a flow with a laminar boundary layer in a larger region than at the NACA 4421 airfoil. On the other hand the target laminar flow region is smaller than at the Wortmann airfoil in order to avoid rash stall behaviour.

Application of the MAD system led to the NLR/VSH 8801 airfoil. This airfoil produces the desired pressure distribution as is shown in Fig.4.14. The geometry of the new airfoil is compared with those of the NACA airfoil and the Wortmann airfoil in Fig.4.15. A comparison of the aerodynamic characteristics is made in Fig. 4.16 which presents the calculated lift and moment coefficient as function of the angle of attack and in Fig.4.17 which presents the C_l-C_d curves.

The new airfoil has a somewhat larger lift coefficient than the NACA airfoil. The stall behaviour of both airfoils is approximately the same. For stall controlled wind turbines a lift curve such as that of the Wortmann airfoil with hardly any variation near stall is not useful. The maximum lift over drag ratio of the new airfoil is higher than those of the other airfoils. From these results it has been concluded that the design goal i.e. combination of the advantages of both reference airfoils has been met.

4.2 WINGS

Since the thin wing inverse panel method for design of wings in subsonic flow became available at NLR in 1974, further developments have gradually increased NLR's capabilities for wing design. To start with, the inverse method was incorporated in the design system (Ref.3) for wings in subsonic flow, using the inverse method for the determination of geometry corrections and the NLR panel method (Ref.7) for analysis of the modified wings. Subsequently, this system was extended for application to transonic flow using the XFLO-22 code of Ref.6 for analysis and applying a 3D analogue of the defect pressure splitting technique of Refs.25,26 for adaptation of the geometry correction procedure to transonic flow (Ref.27).

The practical applicability of the latter transonic wing design system may be demonstrated by means of a reconstruction example presented in Figs.4.18,4.19. Starting point is the well-known DFVLR-F4 wing for the present purpose attached to a simple cylindrical body. The target pressure distribution represented by the dashed line in Fig.4.19a is the pressure distribution as obtained by applying XFLO-22 to the original F4/body geometry of Fig.4.18. An "initial guess" of the geometry which is required at the start of the design process has been obtained by distorting the original geometry. The pressure distribution represented by the lines marked a is produced by this distorted configuration.

Application of the wing design system resulted after 6 iterations in the geometry shown in Fig.4.19b in comparison with the original F4 wing geometry (target). The corresponding pressure distribution is represented by the lines marked b in Fig.4.19a. The target pressure distribution is reproduced near the tip. In the other sections some deviations are still present, especially in the shock region. But the overall agreement between final- and target pressure distribution is satisfactory.

Fig.4.20 presents a functional breakdown of the algorithm. It follows the residual correction approach in which the basic idea is to apply a simple fast geometry correction procedure for determining estimates of the geometry to be designed and an accurate method for analysis of the flow around the current geometry.

In the present version of the design system flow analysis is performed by means of XFLO-22 (Ref.6), a program system based on a combination of Jameson's code FLO-22 (Ref.5) and the NLR panel method (Ref.7). With the aid of the latter method it has been attempted to remove the limitation of FLO-22 to wing-alone configurations. The usefulness of this method for engineering purposes has been demonstrated and validated by comparison with results of wind tunnel tests for a number of wing-body configurations (see Ref.6).

However, it was felt necessary to improve the accuracy of the design system by improving the accuracy of the analysis method , at the same time removing the limitation to wing-alone in a more fundamental way. Therefore, it was decided to develop a new code for transonic flow analysis. This Multi-component Aircraft Transonic Inviscid Computation System (MATRICS) is based on full potential theory applying discretizations according to the finite volume concept (Refs.28,29). It is applicable to wing-body configurations.

The next step in the development of a new analysis code will be the coupling of MATRICS to a boundary layer calculation method in a (strong) interactive way. The subsequent incorporation of that code in the wing design system will be one of the steps towards the development of a system (WINGDES) for the design of wings in viscous transonic flow.

Third International Conference on Inverse Design Concepts and Optimization in Engineering Sciences
(ICIDES-III), Editor: G.S. Dulikravich, Washington D.C., October 23-25, 1991

The geometry correction procedure, for which a functional breakdown is given in Fig.4.21, consists of two major steps. From the pressure defect i.e. the difference between the target and the current pressure distribution, an equivalent subsonic perturbation velocity distribution is derived using the splitting technique of Ref.25, whereupon by means of an inverse panel method geometry corrections are determined.

The pressure splitting technique applied to the pressure distribution in a wing section distinguishes between regions with a subsonic and regions with a supersonic flow behaviour. To this end a "critical" pressure coefficient is defined and the assumption is made that subsonic theory should be applied in regions where both target and current pressure distribution are "subcritical" and supersonic theory if both pressure distributions are "supercritical". (see Fig.4.22). Application of subsonic thin wing theory then translates the subsonic pressure defect into subsonic perturbation velocities. Application of supersonic wavy wall formulae leads to translation of the supersonic pressure defect into geometric slope corrections which however, for the sake of similarity in representation, are expressed in equivalent subsonic perturbation velocities by means of thin airfoil analysis.

Some details of the constrained inverse panel method which is applied for the derivation of the geometry corrections from the equivalent perturbation velocities, are given in Fig.4.23. It is essentially a linearized panel method which utilizes on the mean wing plane a distribution of x-doublets for representation of thickness effects and a distribution of vorticity for representation of camber effects and on the body surface constant source panels. Geometry constraints may be applied in the form of prescribed values of thickness and/or camber weighted in order to create a desired balance. The associated over-determined system of equations is solved in a least square error sense. By adding the squares of the residuals associated with the pressure defects and the constraints, each multiplied with their specified weight factors a functional is formed, from which by formal differentiation a new set of equations is derived that is solved by a block iteration procedure.

The geometry correction procedure thus described is very fast as a consequence of which the computing time needed for one iteration step is only slightly more than for one analysis run, however in the leading edge region the thin wing approximation to the real flow is not applicable and leads to difficulties when leading edge modifications are pursued.

4.3.TARGET PRESSURE DISTRIBUTIONS

Many design methods, amongst them the residual correction methods of NLR, are based on minimization of an object function formulated in terms of prescribed (target) pressure distributions. This leaves the user with the problem to translate his design goals in properly defined pressure distributions exhibiting the required aerodynamic characteristics.

Though skilful designers are capable of producing successful designs, as has been demonstrated in sections 2 and 3, the design efficiency can be improved by providing the designer with tools for target pressure specification. To this end two codes have been developed. SAMID (Ref.30) may be used for the selection of spanload distributions leading to minimum induced and viscous drag taking into account aerodynamic, flight-mechanical and structural constraints. CADOS (Ref.31) may be used for selection of appropriate chordwise pressure distributions. The latter code is an interactive optimization system for the solution of minimization (or maximization) problems defined by the user with respect to its object function, design variables and constraints.

SAMID is based on lifting line approximations using the conservation laws of momentum for determination of the induced drag. The viscous drag is approximated for given airfoil characteristics by deriving expressions for the sectional viscous drag in terms of the section lift coefficient using semi-empirical relations and thin airfoil theory. Through variational calculus a set of optimality equations is derived from the object function augmented with constraint terms using Lagrange multipliers. Application of appropriate discretization then leads to a system of linear equations for trailing edge vortex sheet strengths and Lagrange multipliers.

Propeller slipstream interaction with the lifting surfaces may be considered as well as long as it may be assumed that each propeller sheds a helical vortex sheet not influenced by the presence of the wing and confined to a cylindrical stream tube parallel to the free stream direction. The velocity distribution inside the slipstream is assumed to be known. As an example of such an application the results of Fig.4.25 are presented. This figure shows the optimal spanwise circulation distribution for the propeller induced velocity distribution presented in Fig.4.24. Clearly the optimal distribution differs greatly from the "clean wing" distribution. Application of this distribution would restore much of the loss associated with the slipstream swirl.

Using CADOS for chordwise pressure distribution specification implies the definition of a suitable object function and appropriate constraints reflecting the sense in which the target should be optimal. But first of all an appropriate pressure distribution representation should be chosen. Concentrating on transonic flow and pioneering with application of CADOS a number of relatively simple shape functions has been selected leading to a representation as schematically depicted in Fig.4.26. This representation involves a limited number of design variables in the form of coefficients and exponents.

As an example of the practical applicability of CADOS some results may be shown of case studies using the above representation and determining drag by means of boundary layer calculations based on Thwaites method for laminar and Green's lag-entrainment method for turbulent flow.
The first example is a demonstration of the capability to design high lift airfoils. The intention was to maximize lift by changing only the upper surface pressure distribution for a fixed arbitrarily chosen lower surface pressure distribution under the additional constraint that the flow had to remain attached and subsonic everywhere on the airfoil.

Keeping Liebeck's results for the so-called turbulent rooftop in mind, at the first optimization attempt the shape function coefficients were constrained to producing a Stratford type pressure recovery. This resulted in the rooftop solution of Fig.4.27 comparing reasonably well with Liebeck's solution as presented in Ref.32. Application of CADOS with the upper surface pressure distribution entirely free led to a solution with a slightly higher lift coefficient represented by the dashed line in Fig.4.27. To conclude this exercise the NLR airfoil design system of Ref.17 was applied to determine the corresponding geometries. The results are presented in Fig.4.27, showing that the second pressure distribution leads to a somewhat gentler airfoil shape.

The second example that may be presented here concerns transonic low drag design. At first, calculations were performed in order to check the suitability of the shape functions for representation of realistic transonic pressure distributions. To this end CADOS was used to determine the best fit to a pressure distribution calculated by means of the VGK code of Ref.24 for a given airfoil.The result is presented in Fig.4.28 . Apparently the discrepancies are largest in the shock region and at the nose.

Subsequently it was attempted to determine a new target pressure distribution aiming at a decrease of the drag with the "best fit" as starting point. Fig.4.29 shows the result, designated "new target". According to the CADOS boundary layer calculations this target should lead to a drag decrease of 5 counts.

Again the NLR airfoil design system was applied for determination of a new airfoil shape, upon which VGK was used for determination of the actual pressure distribution. The latter result is presented in Fig.4.30 in comparison with the original pressure distribution. The discrepancies between the shape function representation and the actual pressure distribution mentioned above may be responsible for the fact that here only 3 counts instead of 5 counts drag decrease is predicted. Nevertheless, the present example may be considered as illustrating the usefulness of CADOS in transonic airfoil design.

5.CONCLUDING REMARKS

A survey has been given of contemporary practice of aerodynamic design in The Netherlands, focusing on airfoil and wing design. It will have become clear that the application of analysis and design codes has become common practice in aerodynamic aircraft design procedures.

As has been mentioned before, work is in progress at NLR to extend the design system for wings in subsonic flow for application to wings of wing-body combinations in viscous transonic flow. A somewhat longer term development is the extension of this system to application for multi-point wing design. This work has been started within a BRITE/EURAM project sponsored by the European Community and aims at the development of a method for the design of wings in transonic flow, such that at a number of different flow conditions the wing (without changing the geometry) will operate according to preset requirements.

6.REFERENCES

1.Obert,E.:'The aerodynamic development of the Fokker 100',ICAS-88-1.6.2,1988

2.Voogt,N.,Mol,W.J.A.,Stout,J.,Volkers,D.F.:'CFD applications in design and analysis of the Fokker 50 and Fokker 100.',Validation of Computational Fluid Dynamics, Lissabon, 1988

3.Fray,J.M.J., Slooff,J.W.:'a constrained inverse method for the aerodynamic design of thick wings with given pressure distribution in subsonic flow',AGARD CP No.285,paper 16,1980

4.Slooff,J.W., Voogt,N.:'Aerodynamic design of thick,supercritical wings through the concept of equivalent subsonic pressure distribution',NLR MP 78011 U,1978

5.Jameson,A., Caughey,D.A.:'Numerical calculations of transonic flow past a swept wing',ERDA Report COO-3077-140, Courant Institute of Mathematical Sciences, New York University,1977

6.van der Vooren,J., van der Kolk,J.Th., Slooff,J.W.:'A system for the numerical simulation of sub- and transonic viscous attached flows around wing-body configurations',AIAA paper 82-0935,NLR MP 82019 U,1982

7.Labrujère,Th.E., Loeve,W., Slooff,J.W.:'An approximate method for the calculation of the pressure distribution on wing-body combinations at subcritical speeds',AGARD CP No.71,paper 11,NLR MP 70014 U,1970

8.Labrujère,Th.E., Sytsma,H.A.:'Aerodynamic interference between aircraft components ; illustration of the possibility for prediction',NLR MP 72020 U,1972

9.Lindhout,J.P ., de Boer,E., van den Berg,B.:'A method for the calculation of 3D boundary layers on practical wing configurations',NLR MP 79003 U,1979

10.Boermans,L.M.M., Waibel,G.:'Aerodynamic and structural design of the standard class sailplane ASW-24',ICAS-88-2.7.2,1988

11.Boermans,L.M.M.: Private communication, 1991

12.van Ingen,J.L.:'Advanced computer technology in aerodynamics: a program for airfoil section design utilizing computer graphics',AGARD Lecture Series no.37, 1970

13.van Ingen,J.L., Boermans,L.M.M., Blom,J.J.H.:'Low speed airfoil section research at Delft University of Technology',ICAS-80-10.1,1980

14.Timman,R.:'The direct and inverse problem of airfoil theory. A method to obtain numerical solutions', NLL-F16,1951

15.van Ingen,J.L.:'A suggested semi-empirical method for the calculation of the boundary layer transition region', Delft University of Technology, Faculty of Aerospace Engineering, VTH-74, 1956

16.Slooff,J.W.:' A survey of computational methods for subsonic and transonic aerodynamic design', NLR MP 84066 U, ICIDES ,1984

17.Labrujère,Th.E.:'MAD : A system for computer aided analysis and design of multi-element airfoils", NLR TR 83136 L, 1983

18.Oskam,B.:'A calculation method for the viscous flow around multi-component airfoils', NLR TR 79097 U, 1979

19.van Egmond,J.A., van den Berg,B., Labrujère,Th.E.:' Application of a constrained inverse method in the aerodynamic design of a low-speed wing-slat configuration', NLR TR 83123 L, 1983

20.van Egmond,J.A., van den Berg,B.:' Design of an airfoil leading edge slat using an inverse aerodynamic calculation method', AGARD CP-365 paper 6-1, 1984

21.Rozendal,D.:'Design of a thick natural laminar flow airfoil for a Mach number of .65', NLR Memorandum AX-91-004, 1991

22.Piers,W.J., van Egmond,J.A., Houwink,R.:'Aerodynamic design of the NLR/VSH 8801 airfoil for application in a wind turbine blade (in Dutch)', NLR TR 88070 C, 1988

23.Bauer,F., Garabedian,P., Korn,D.:'Supercritical wing sections',Lecture notes in economics and mathematical systems.Vol.66,Springer Verlag,Berlin,1972

24.Collyer,M.R.:'An extension to the method of Garabedian and Korn for the calculation of transonic flow past an airfoil to include the effects of a boundary layer and wake',RAE TR77104,1977

25.Fray,J.M.J, Slooff,J.W., Boerstoel,J.W., Kassies,A.:' Design of transonic airfoils with given pressure, subject to geometric constraints', NLR TR 84064, 1984

26.Fray,J.M.J, Slooff,J.W., Boerstoel,J.W., Kassies,A.:' Inverse method with geometry constraints for transonic airfoil design ', NLR MP 84069 U, ICIDES, 1984

27.Brandsma,F.J., Fray,J.M.J.:'A system for transonic wing design with geometric constraints based on an inverse method', NLR TP 89179 L, 1989

28.Van der Vooren,J., van der Wees,A.J., Meelker,J.H.:'MATRICS, Transonic potential flow calculations about transport aircraft', AGARD Conf.Proc. No. 412,1986

29.Van der Wees,A.J.:' FAS multigrid employing ILU-SIP smoothing: a robust fast solver for 3D transonic potential flow', NLR MP 85072 U, 1985, Lecture Notes in Mathematics 1228, Springer Berlin,1986

30.Van den Dam,R.F.:'Constrained spanload optimization for minimum drag of multi-lifting-surface configurations',AGARD CP No.463, Paper 16, 1989

31.Van Egmond,J.A.:'Numerical optimization of target pressure distributions for subsonic and transonic airfoil design',AGARD-CP No.463, Paper 1, 1989

32.Smith,A.M.O.:'High lift aerodynamics', AIAA paper No.74-939,1974

TABLE I : The Fokker 100 wing development (Ref.1)

Wing 1 : The basic F-28 wing, defined by four wing sections connected with straight generators
Wing 3 : Wing 1 with 0.75 m span extension (defining section V)
Wing 4 : Wing 1 modified with :
- forward extension of the chords of sections I,II and III
- modification of the front part of sections I and II
- 1.5 m span extension

Wing 5 : Wing 1 modified with :
- 1.5 % chord extension and modified front part of section IV
- straight leading edge at outer wing defined by section II and IV
- 5 % chord extension of section I
- 1.5 m span extension

Wing 6 : As wing 5 but with 9% chord extension of section I
Wing 8 : Wing 5 modified with rearward chord extension and rear camber
Wing 10: Wing 8 modified with :
- 0.75 m span extension
- straight leading edge between section III and V leading to kinks at sections II and III
- new front part of section IV

Wing 11: Wing 10 modified with :
- new lower leading edge of sections III and IV

Wing 12: Wing 11 modified with :
- new leading edge of section II

Third International Conference on Inverse Design Concepts and Optimization in Engineering Sciences (ICIDES-III), Editor: G.S. Dulikravich, Washington D.C., October 23-25, 1991

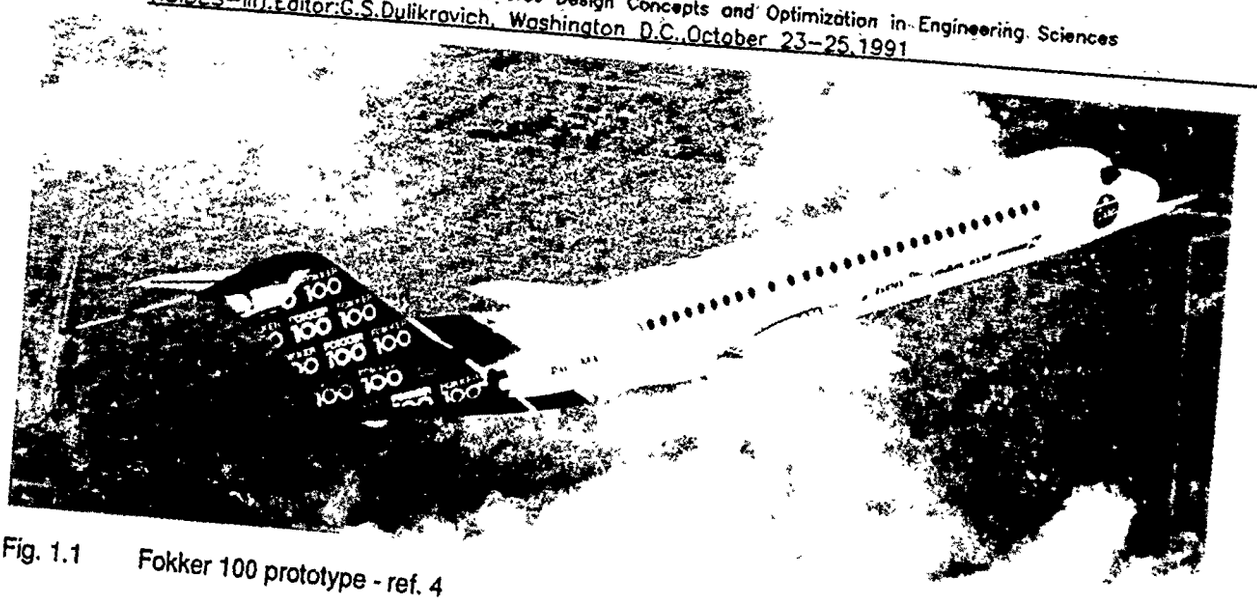


Fig. 1.1 Fokker 100 prototype - ref. 4

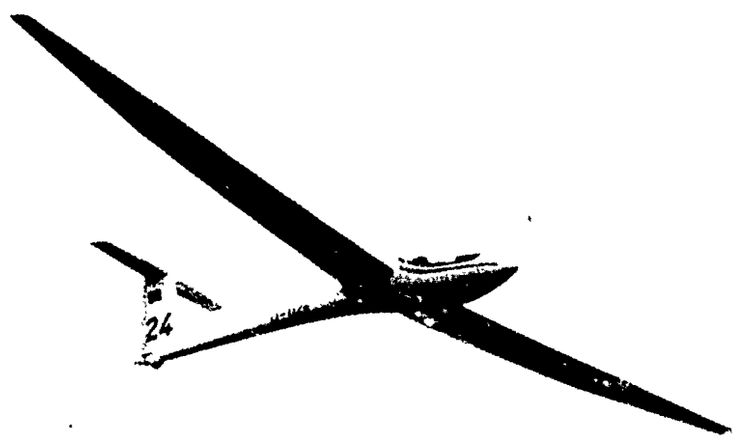


Fig. 1.2 ASW-24. ref. 11

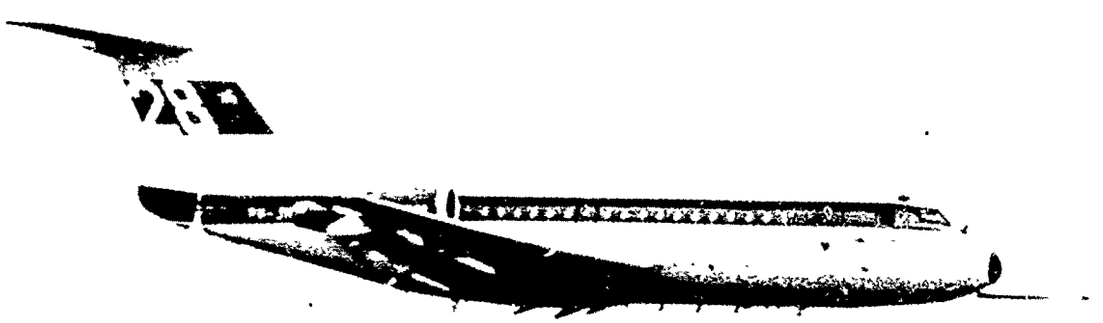


Fig. 1.3 Fokker F-28

Third International Conference on Inverse Design Concepts and Optimization in Engineering Sciences (ICIDES-III) Editor:G.S.Dulikravich, Washington D.C., October 23-25,199

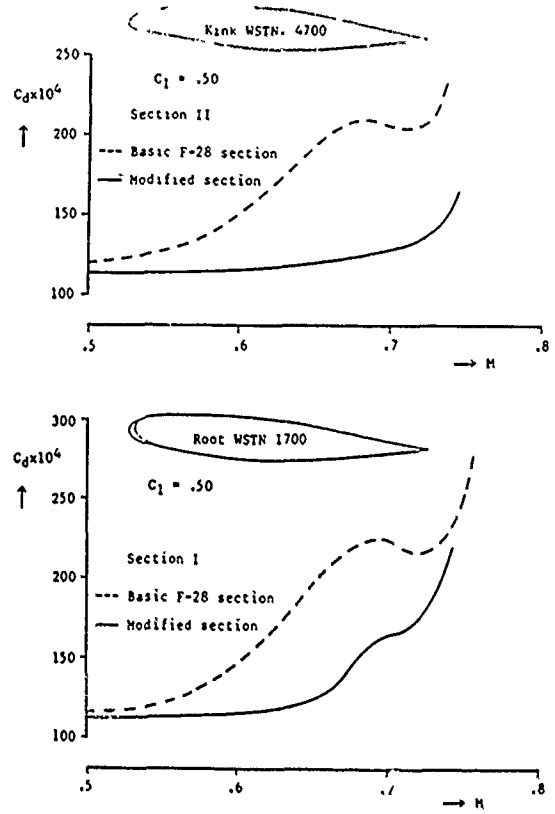


Fig. 2.1 Effect of modifications to root and kink sections of the F-28 wing. ref. 1

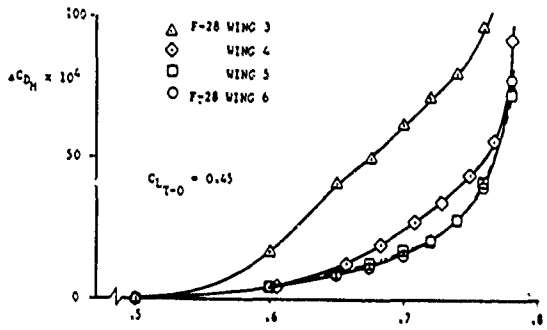


Fig. 2.2 Mach drag rise characteristics of wings 3, 4, 5 and 6 at CLT-O = 0.45. ref. 1

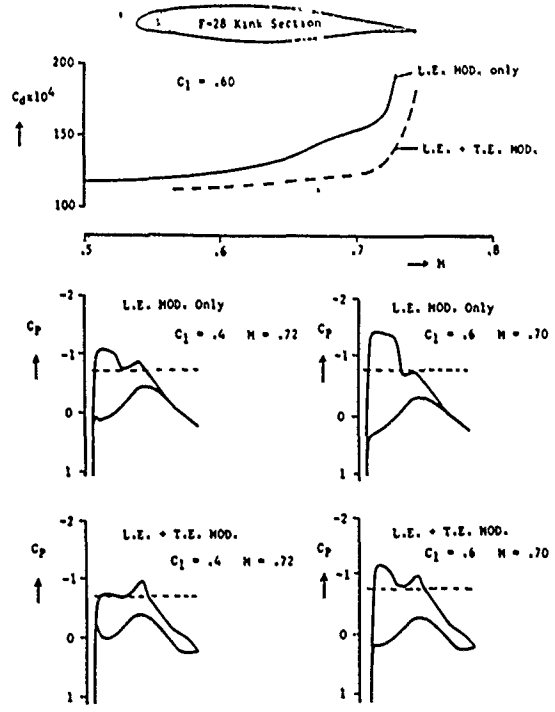


Fig. 2.3 Effect of trailing-edge modification on Mach-drag rise and pressure distribution. ref. 1

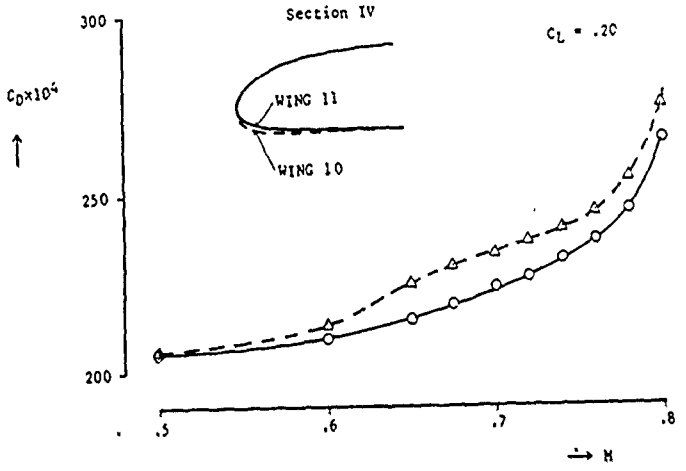


Fig. 2.4 Effect of blunt leading-edge on the Mach-drag rise at low lift coefficient. ref. 1

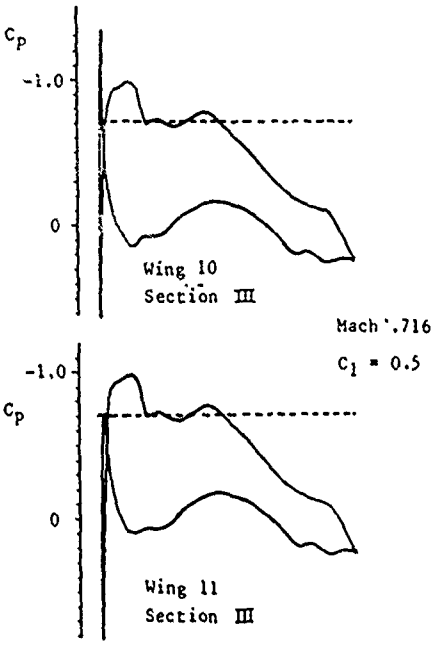


Fig. 2.5 Effect of blunt leading-edge on the lower-surface leading-edge suction peak. ref. 1

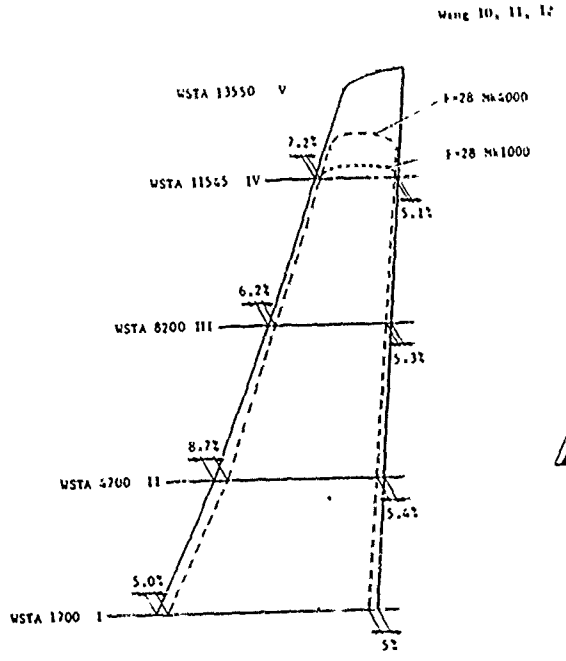


Fig. 2.6 a Comparison between F-28 and Fokker 100 wing geometry. ref. 1

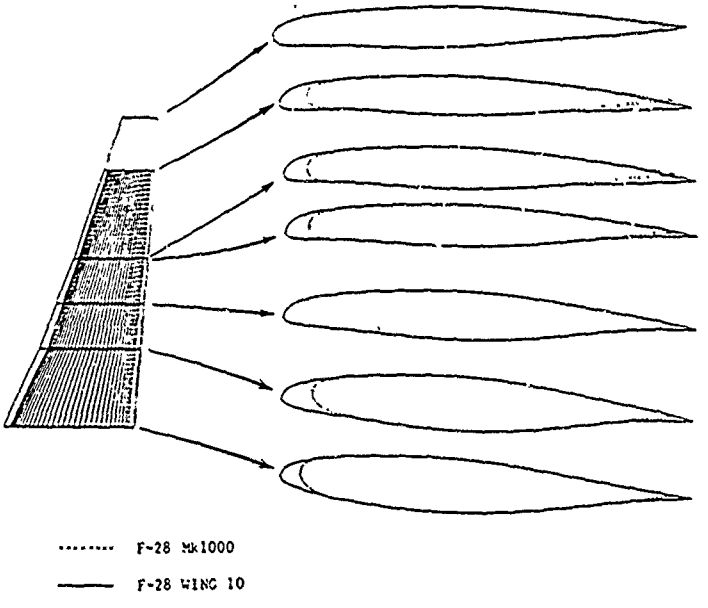


Fig. 2.6 b

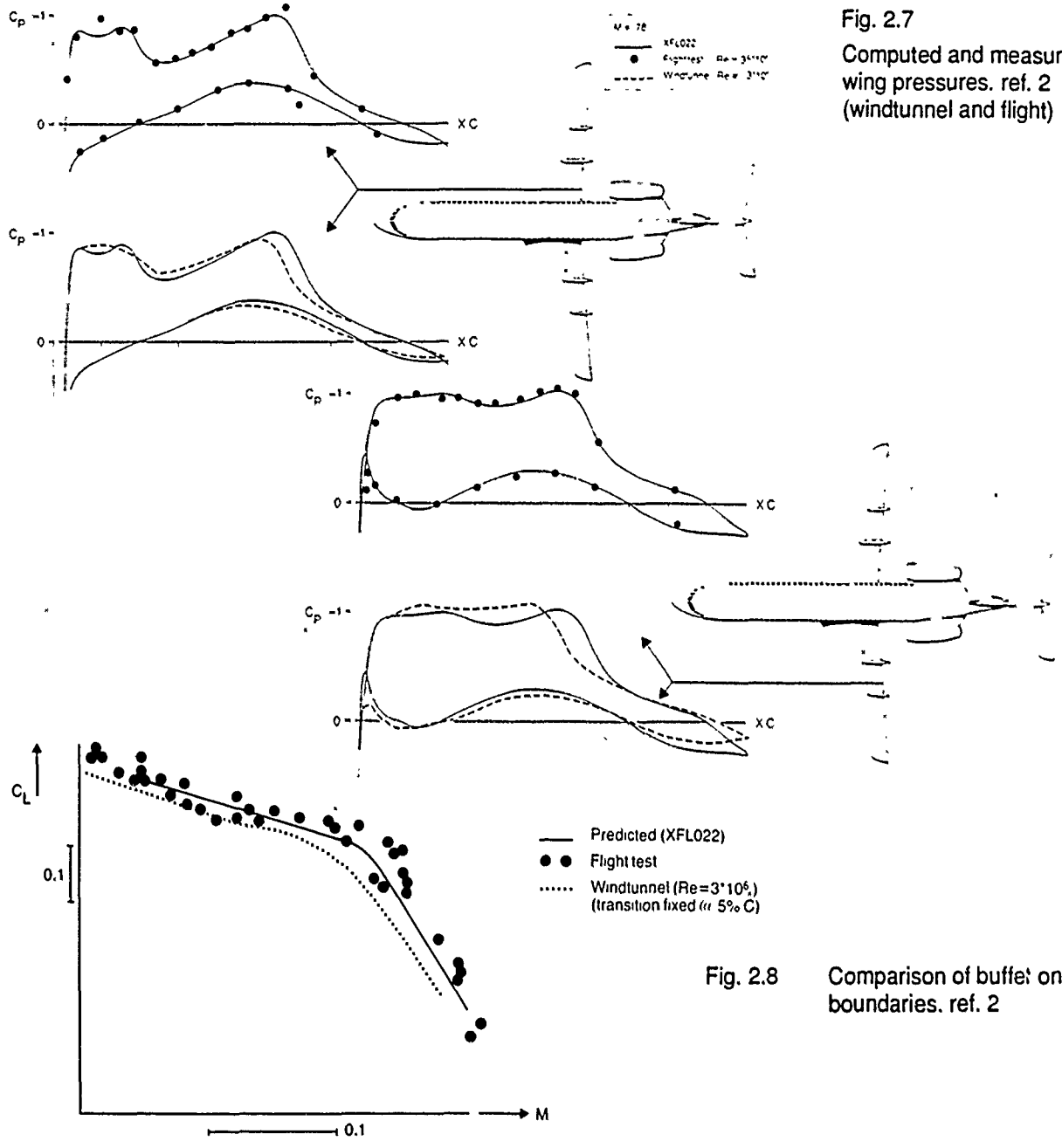


Fig. 2.7
Computed and measured wing pressures. ref. 2 (windtunnel and flight)

Fig. 2.8 Comparison of buffet onset boundaries. ref. 2

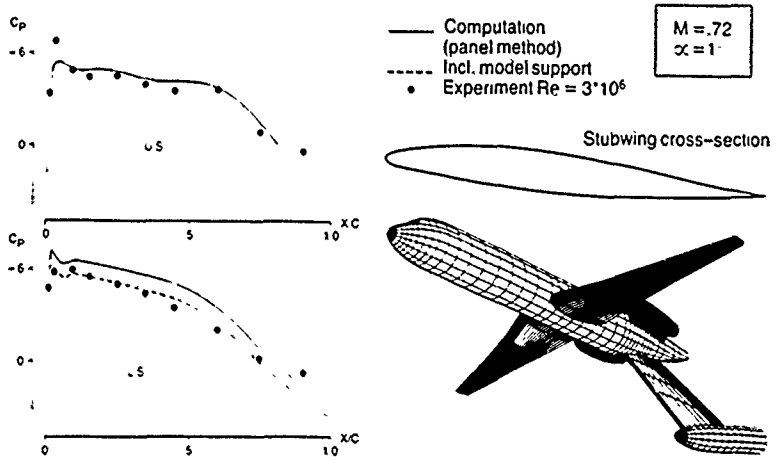


Fig. 2.9
Computed and measured stubwing pressures. ref. 2

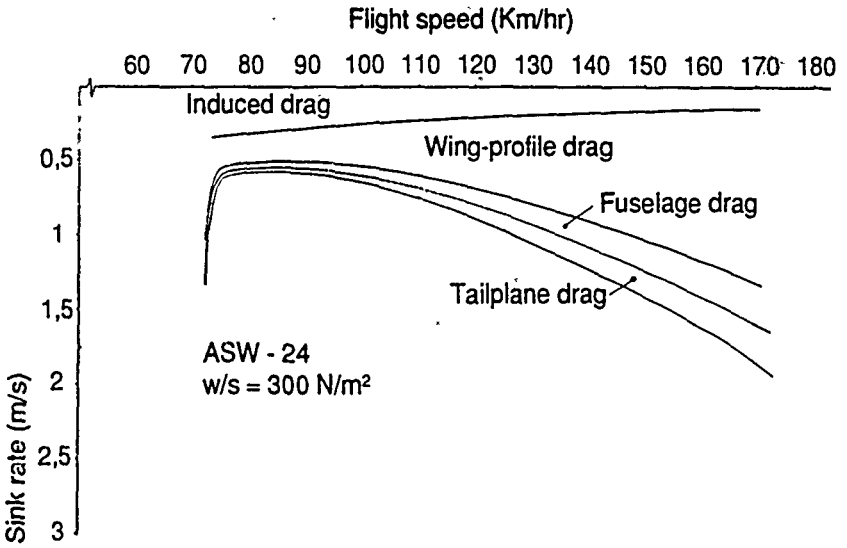


Fig. 3.1 Flight performance polar of ASW-24 ref. 11

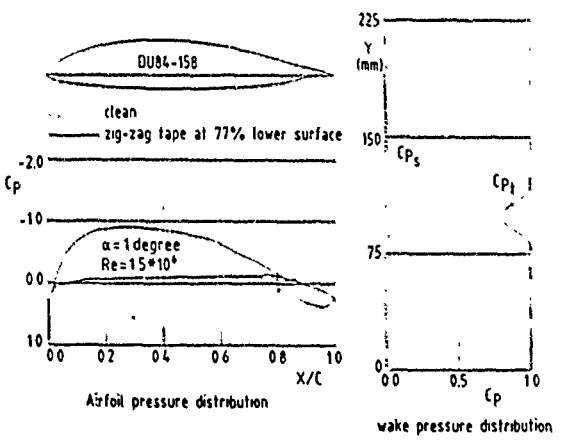


Fig. 3.2 Measured airfoil and wake pressure distributions. ref. 10

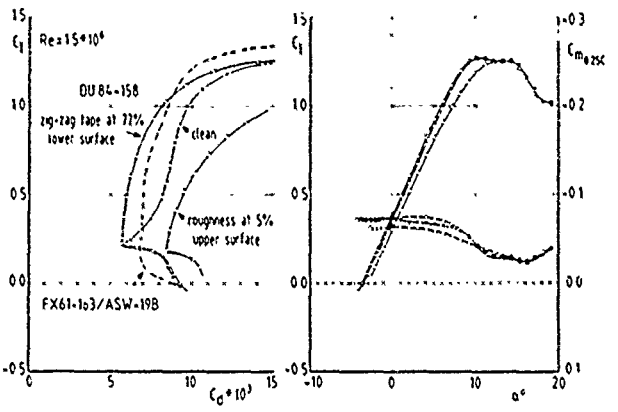


Fig. 3.3 Measured aerodynamic characteristics. ref. 10

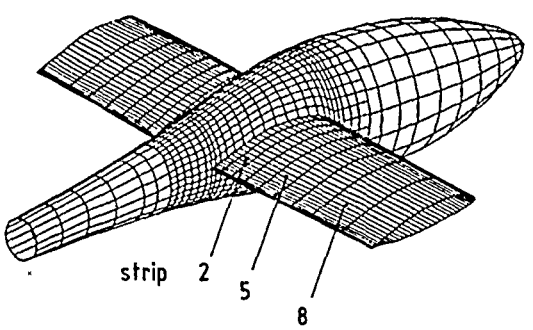


Fig. 3.4 Part of panel scheme of ASW-24 wing-fuselage combination. ref. 10

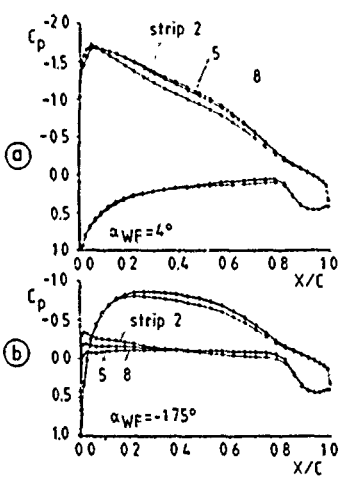


Fig. 3.5 Pressure distributions of wing strips in the wing root area. ref. 10

Third International Conference on Inverse Design Concepts and Optimization in Engineering Sciences
(ICIDES-III), Editor: G.S.Dulikravich, Washington D.C. October 23-25, 199

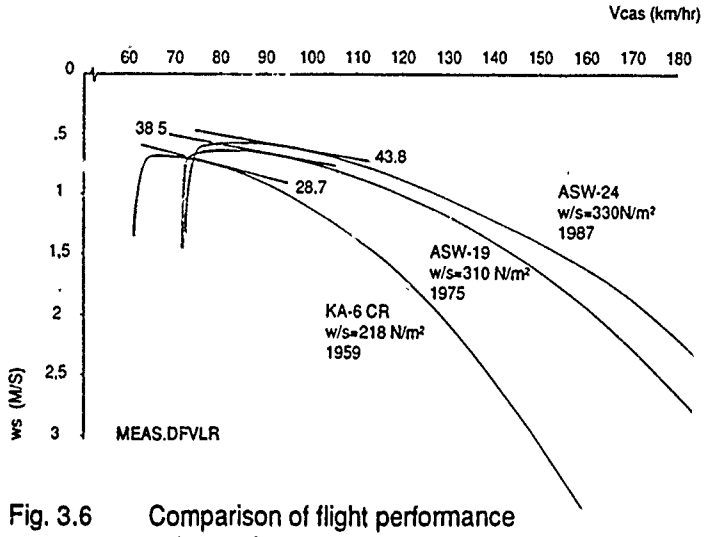


Fig. 3.6 Comparison of flight performance polars. ref. 11

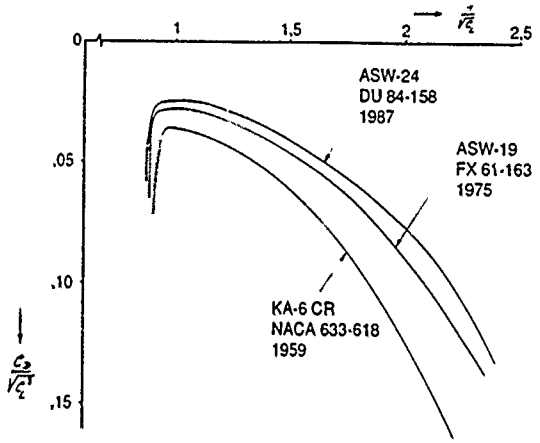


Fig. 3.7 Comparison of aerodynamic quality. ref. 11

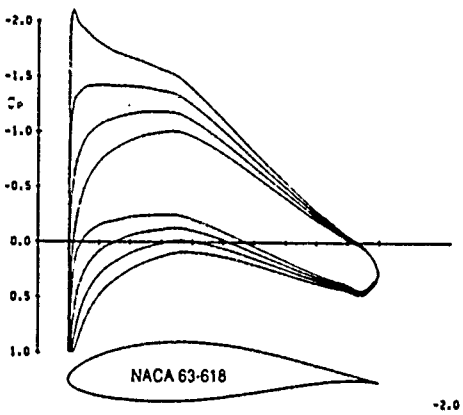


Fig. 3.8 a

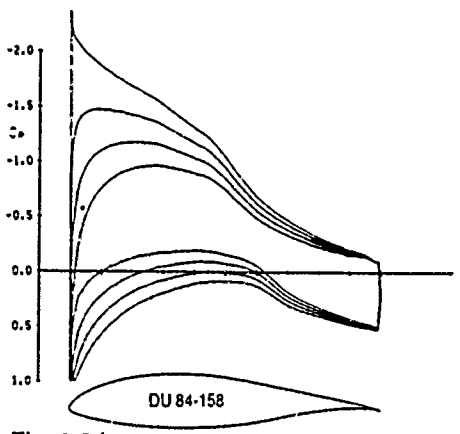


Fig. 3.8 b

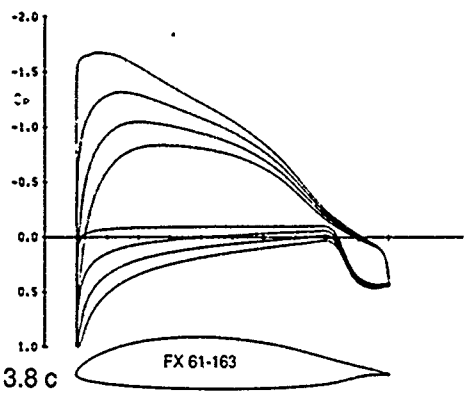


Fig. 3.8 c

Fig. 3.8 Comparison of pressure distribution ref. 11

Third International Conference on Inverse Design Concepts and Optimization in Engineering Sciences (ICIDES-III), Editor: G.S.Dulikravich, Washington D.C. October 23-25,1991

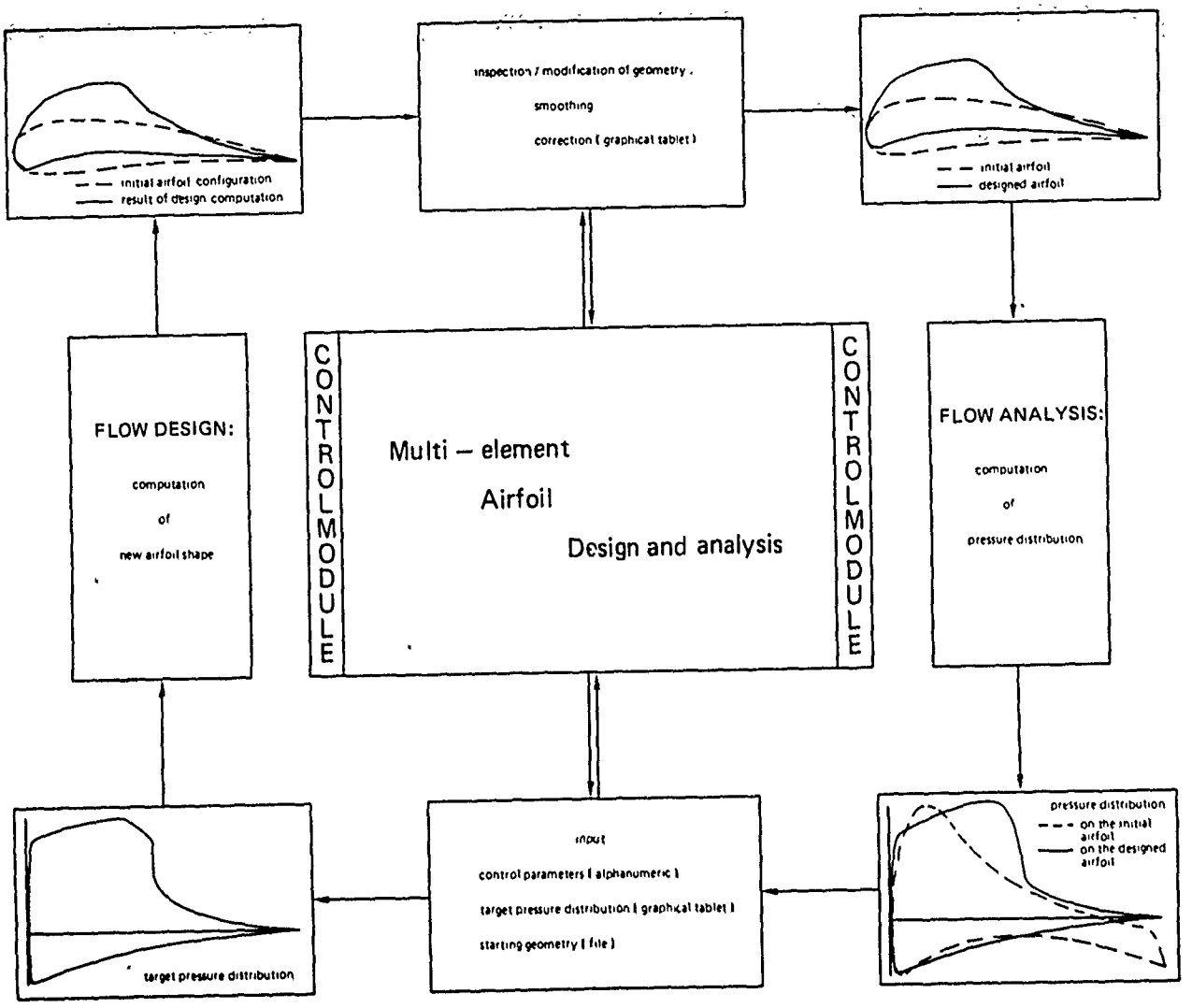
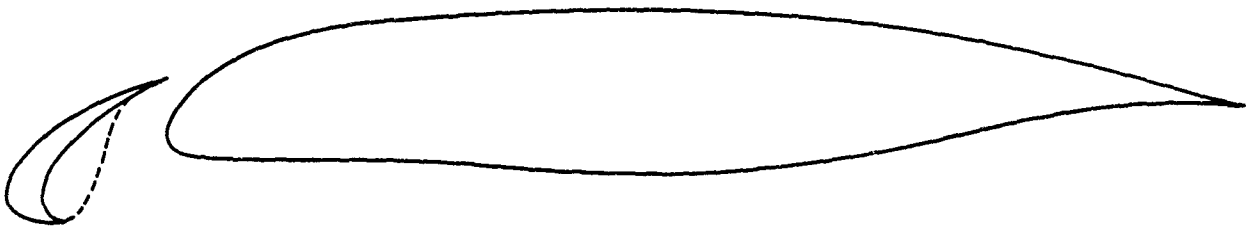


Fig. 4.1 ref. 17

Fig. 4.2 Sketch of the original wing-slat configuration. ref. 19



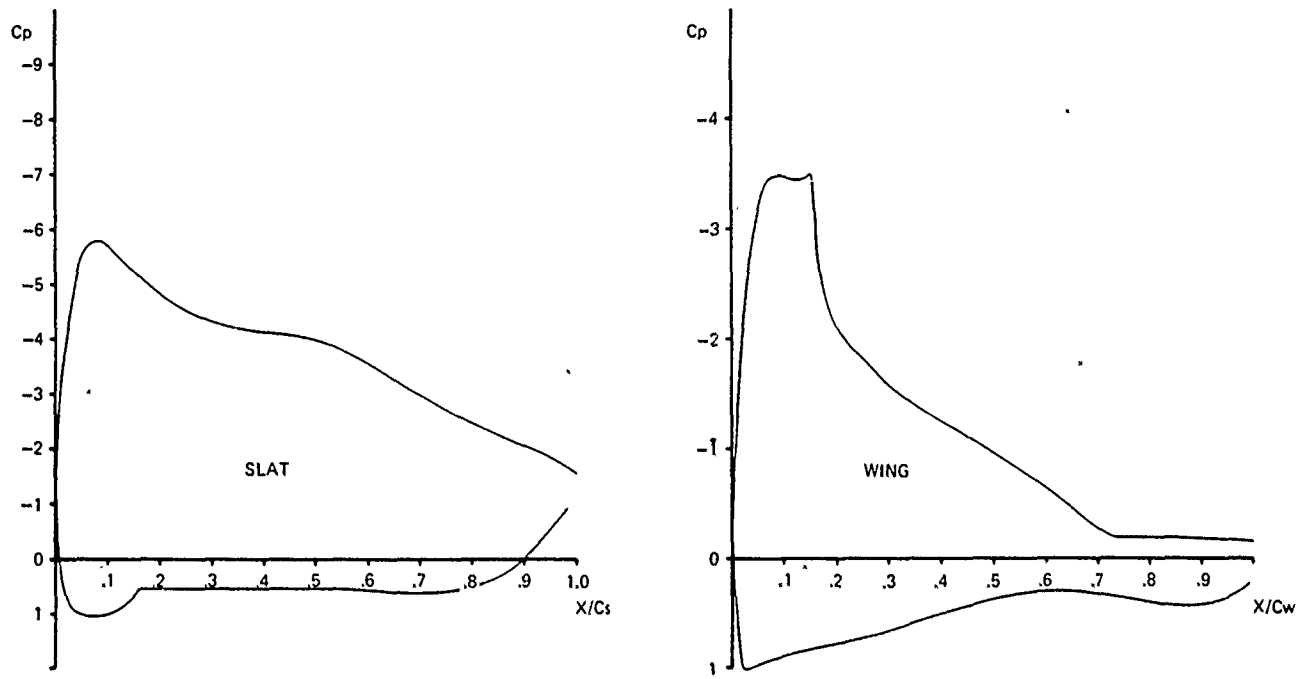
(SLAT POSITION : OV = 0
GA = 0.025
DS = 10°)

----- BUBBLE SIMULATION ; USED IN COMPUTATIONS

Third International Conference on Inverse Design Concepts and Optimization in Engineering Sciences
(ICIDES-III), Editor: G.S. Dulikravich, Washington D.C., October 23-25, 1991

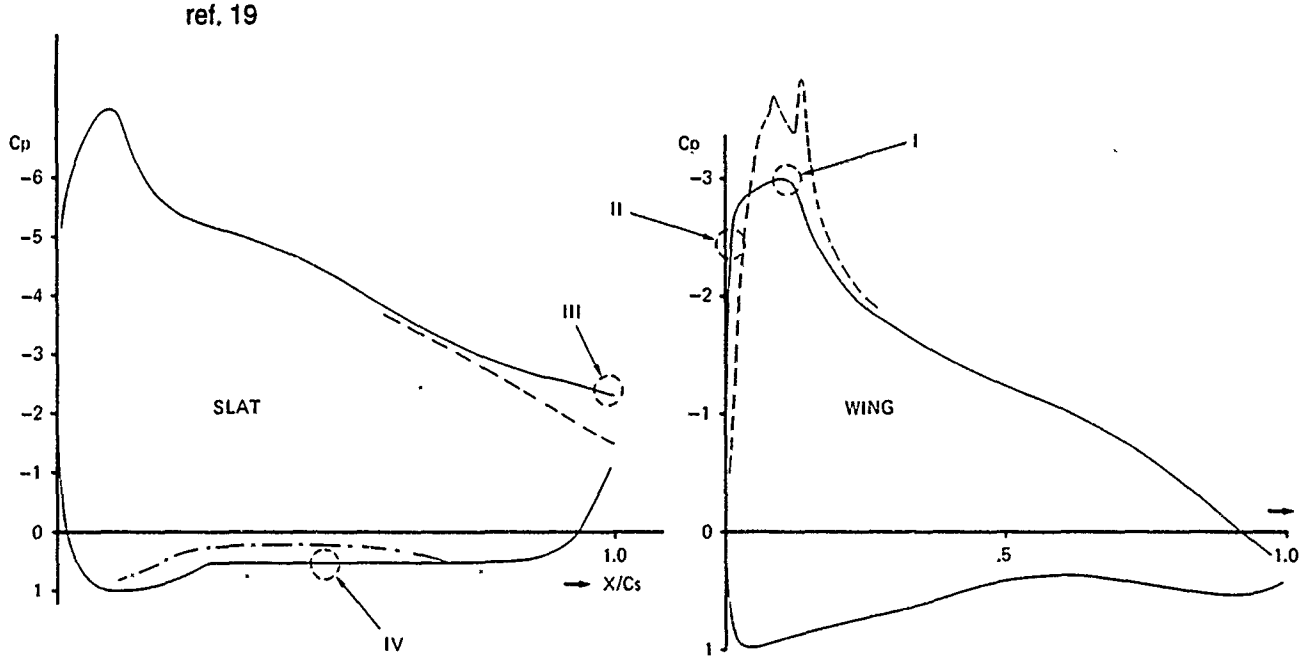
$\alpha = 20.16°$ $Rec = 3.1 \times 10^6$
$0V = 0$ $GA = 2.5\%$ $DS = 10°$

Fig. 4.3 Measured pressure distribution; original wing-slat configuration α=20.2 $C\ell$ =2.13. ref.19



TARGET PRESSURE DISTRIBUTION
ORIGINAL " "
EXPERIMENTAL PRESSURE DISTRIBUTION ON SLAT LOWER SURFACE
} POTENTIAL FLOW (MAD)

Fig. 4.4 Target pressure distribution for new wing-slat configuration α=17°. ref. 19



Third International Conference on Inverse Design Concepts and Optimization in Engineering Sciences (ICIDES–III) Editor: G.S. Dulikravich, Washington D.C. October 23–25, 1995

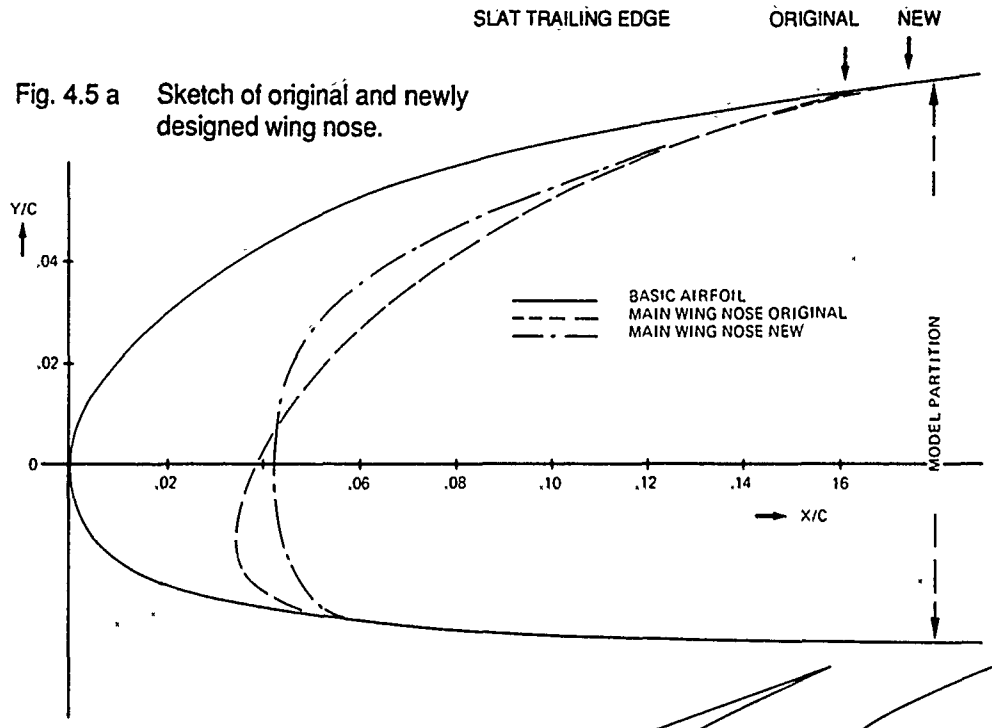


Fig. 4.5 a Sketch of original and newly designed wing nose.

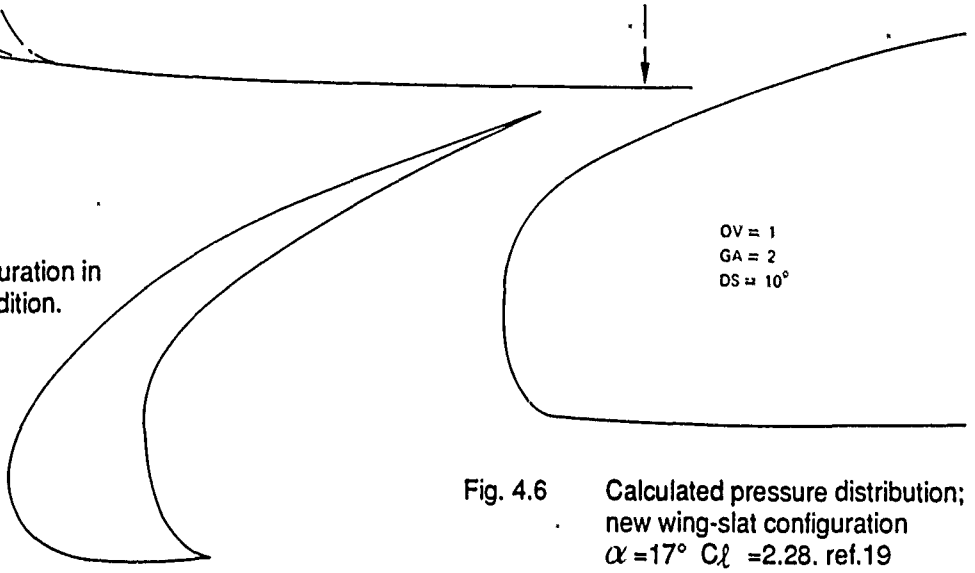
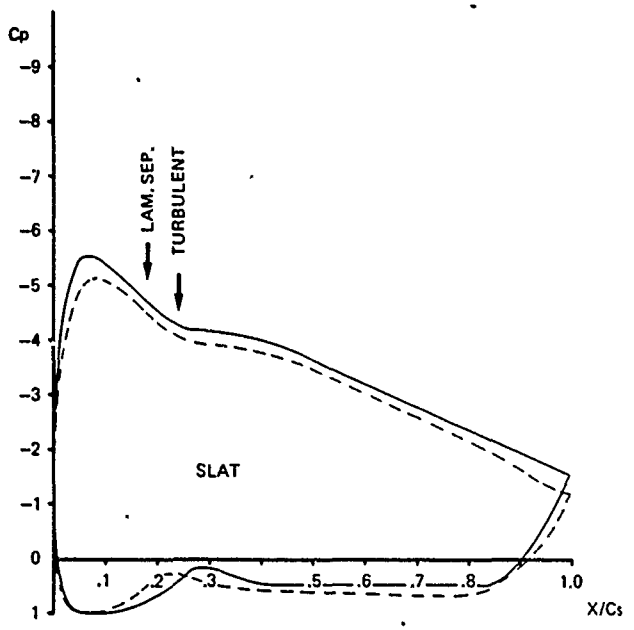
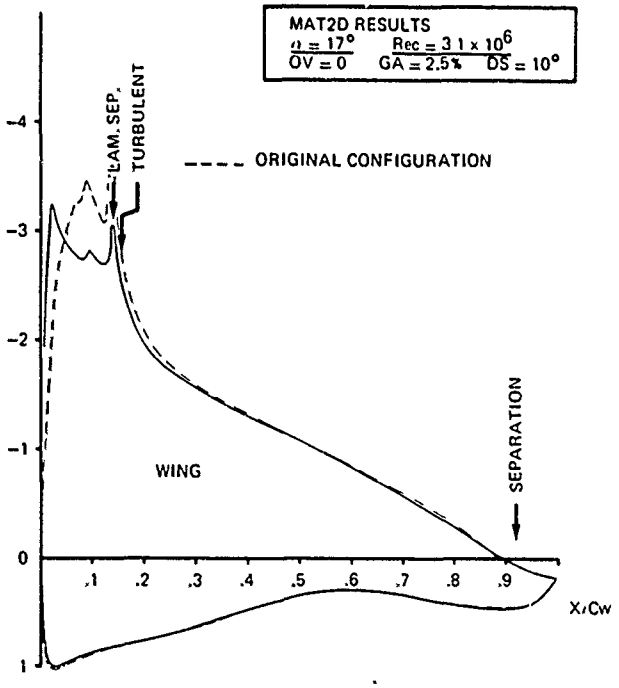


Fig. 4.5 b
Sketch of the new configuration in experimental design condition.

Fig. 4.6 Calculated pressure distribution; new wing-slat configuration $\alpha = 17°$ $C\ell = 2.28$. ref.19





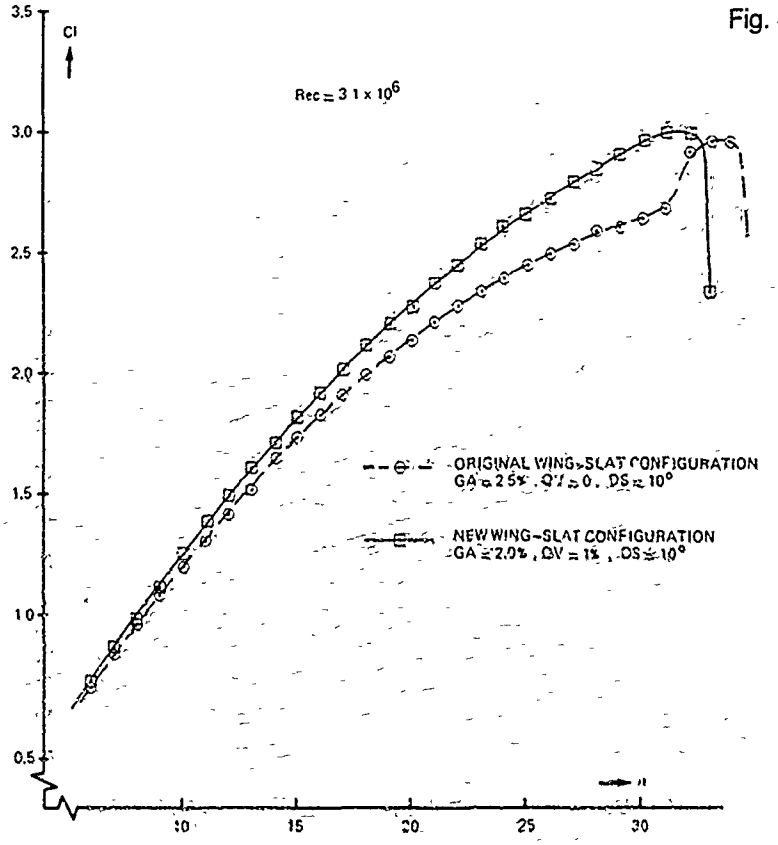
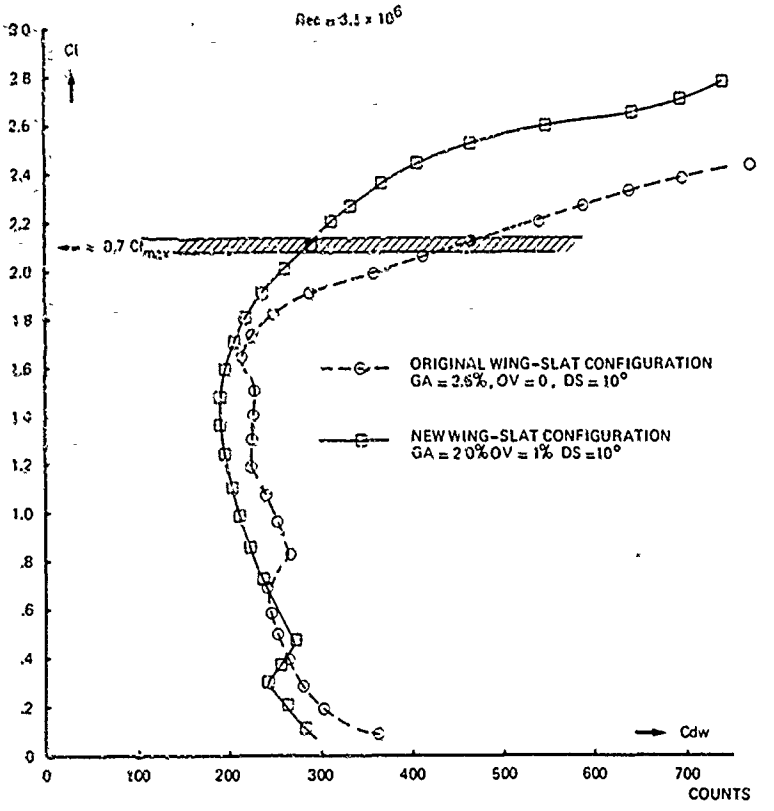


Fig. 4.7 Measured Cℓ - α curves for both wing-slat configurations. ref 19

Fig. 4.8 Measured Cℓ - Cd curves for both wing-slat configurations. ref. 19



Third International Conference on Inverse Design Concepts and Optimization in Engineering Sciences
(ICIDES-III) Editor: G.S. Dulikravich, Washington D.C. October 23-25 199

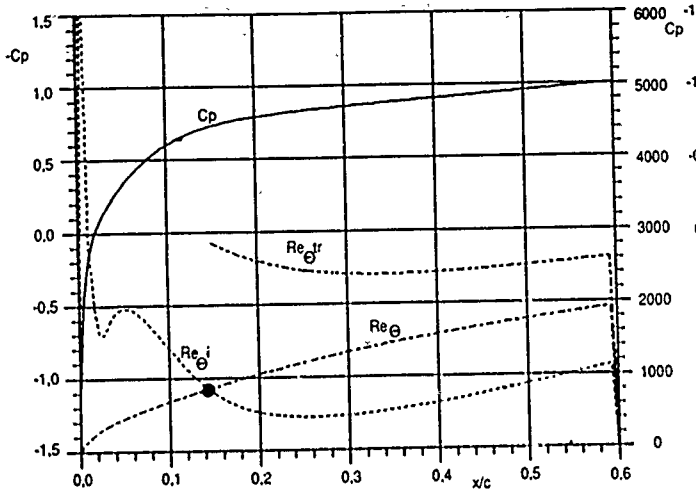


Fig. 4.9 Upper side target. ref.21

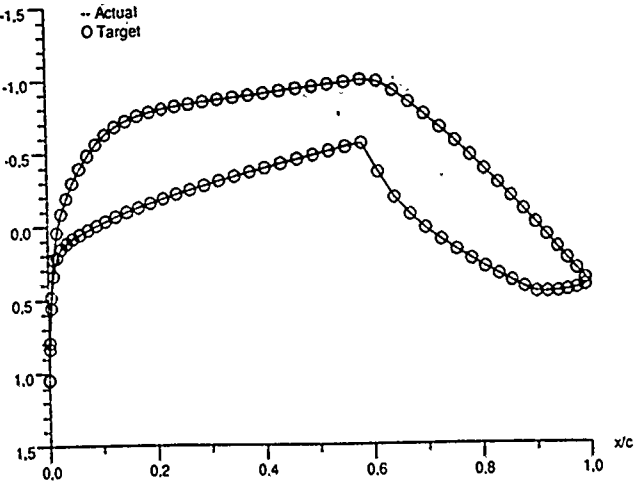


Fig. 4.10 Actual and target pressure distribution. ref. 21

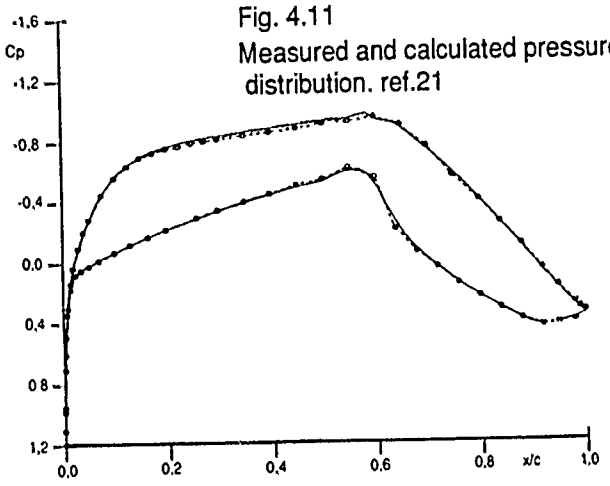


Fig. 4.11
Measured and calculated pressure distribution. ref.21

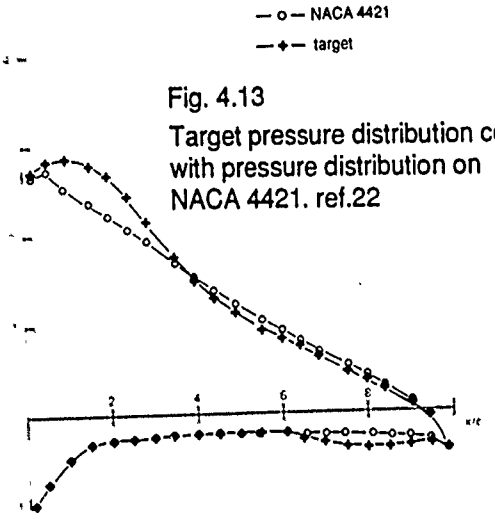


Fig. 4.13
Target pressure distribution compared with pressure distribution on NACA 4421. ref.22

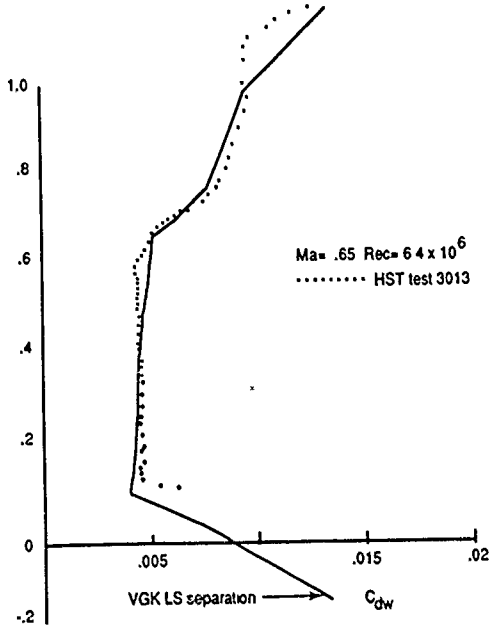


Fig. 4.12 Comparison of experimental and theoretical C_{ℓ} -Cd curves for the design Mach number. ref. 21

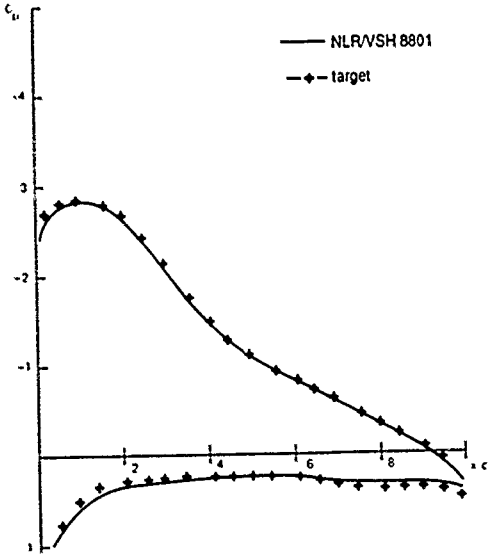


Fig. 4.14 Actual and target pressure distribution. ref. 22

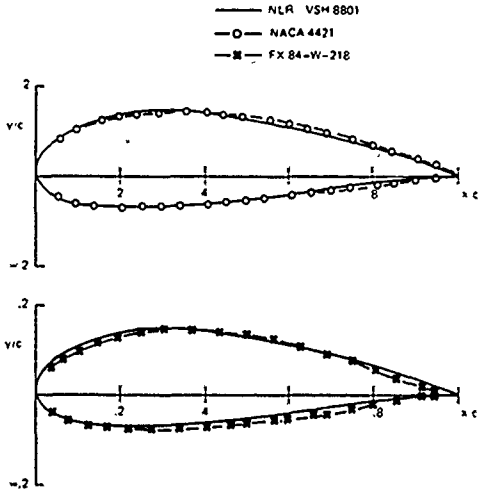


Fig. 4.15 Comparison of airfoil shapes. ref. 22

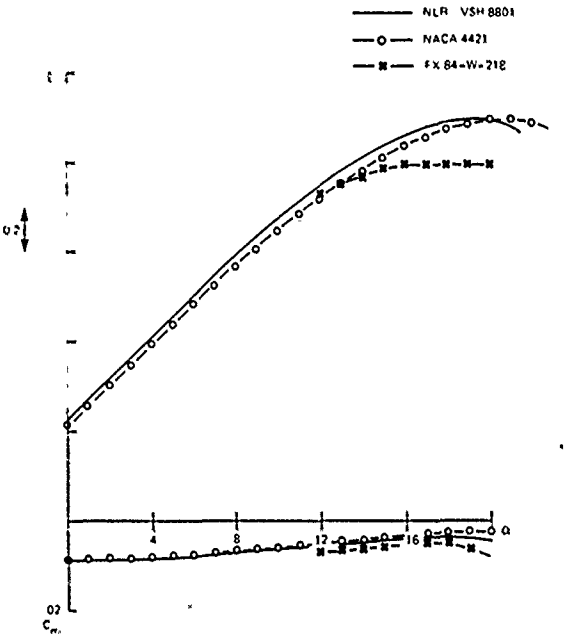


Fig. 4.16 : Calculated lift and moment coefficient ($Re=3 \times 10^6$). ref.22

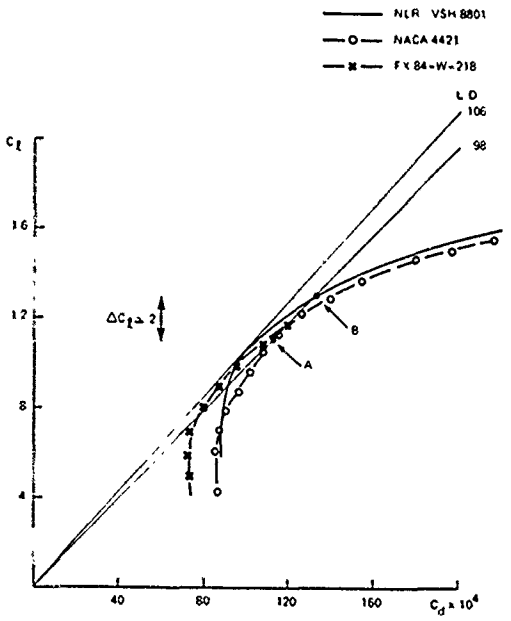
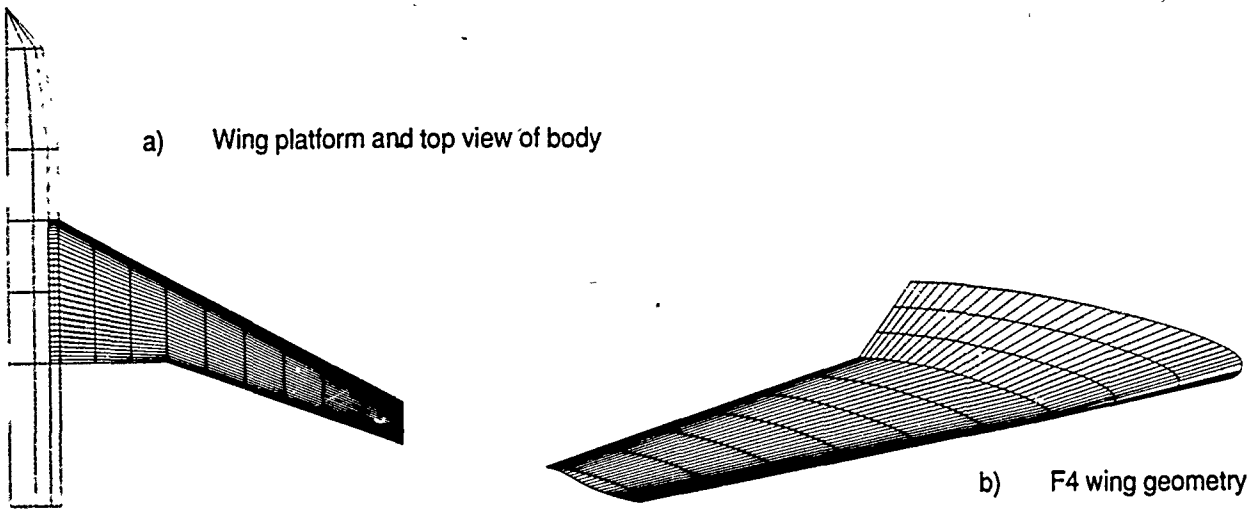


Fig. 4.17 Calculated C_ℓ -C d curves (Re = 3 x 10 6). ref. 22

Third International Conference on Inverse Design Concepts and Optimization in Engineering Sciences (ICIDES-III), Editor G.S.Dulikravich, Washington D.C. October 23-25,1991



a) Wing platform and top view of body

b) F4 wing geometry

Fig. 4.18 F4 wing attached to pencil shaped body used as an example. ref. 27

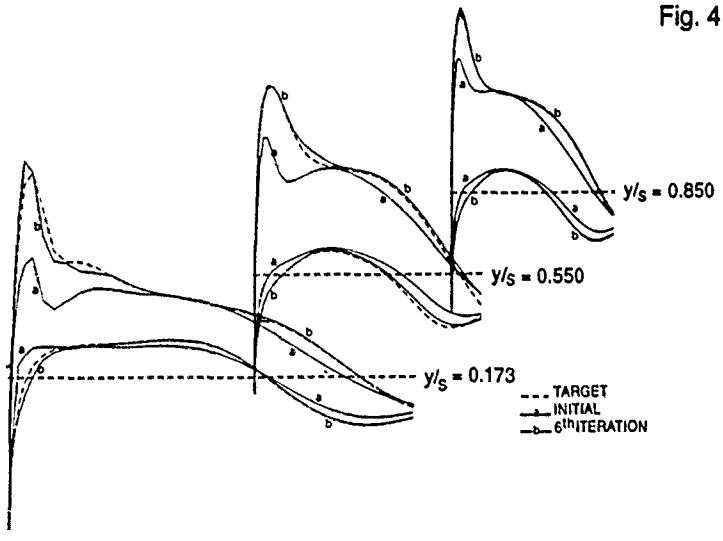
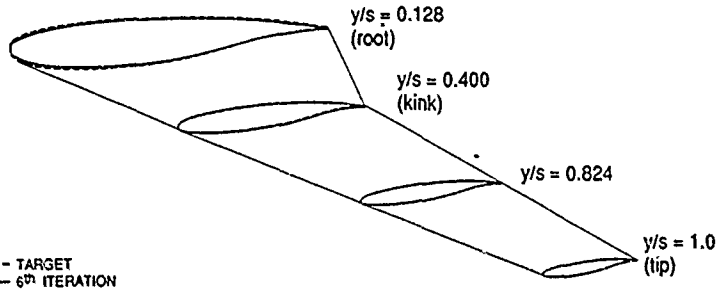


Fig. 4.19 Results of F4 wing reconstruction with influence of body for M=0.75 and 0°. (the target corresponds to the original geometry of fig. 4.18). ref. 27

a) Results for the pressure distribution at three spanwise stations (near root, near midspan near tip).



b) Results for the geometry at four spanwise stations

Third International Conference on Inverse Design Concepts and Optimization in Engineering Sciences (ICIDES-III), Editor: G.S. Dulikravich, Washington D.C., October 23-25, 1991

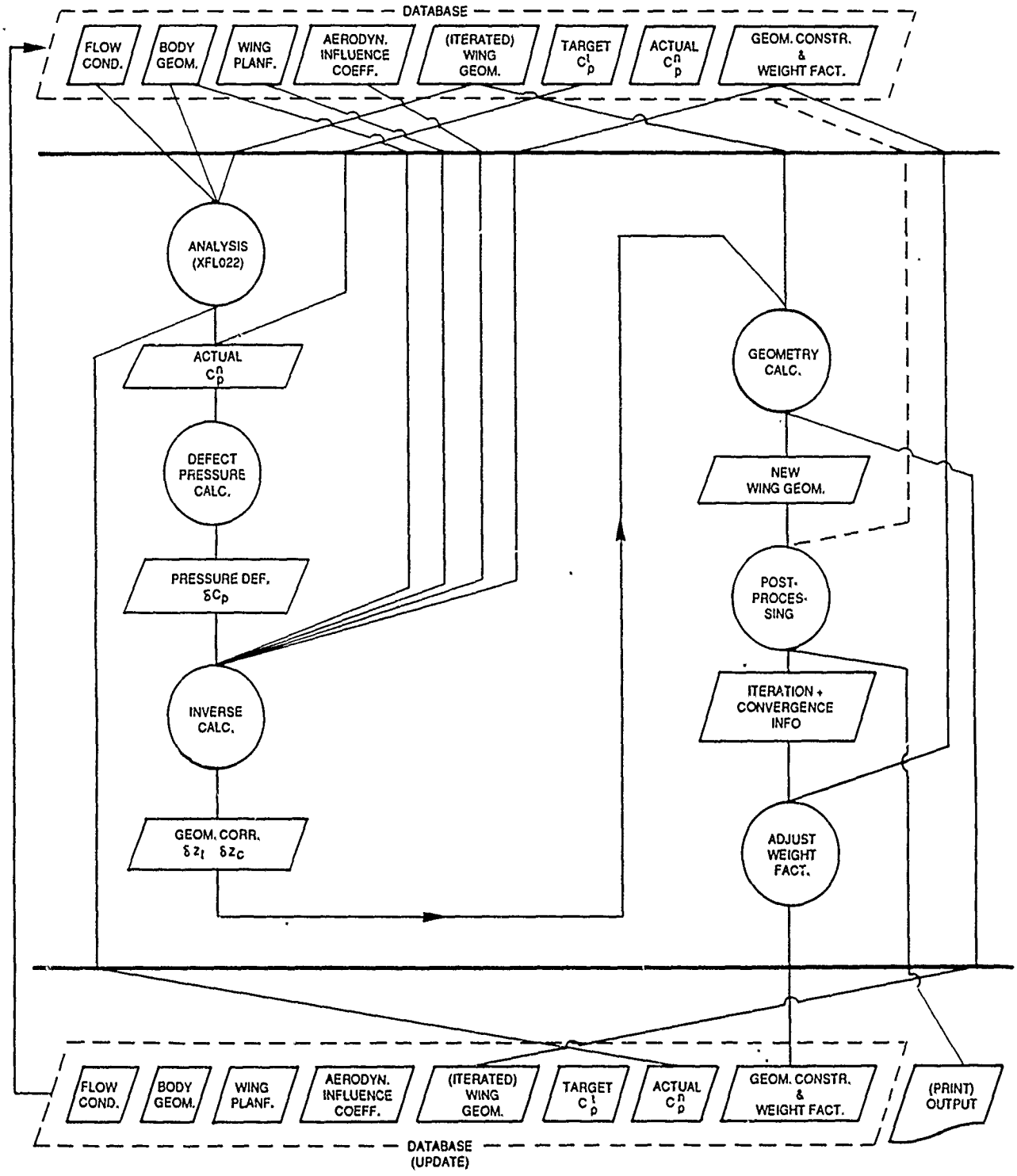


Fig. 4.20 Functional breakdown of the design procedure. ref. 27

Third International Conference on Inverse Design Concepts and Optimization in Engineering Sciences (ICIDES-III), Editor: G.S.Dulikravich, Washington, D.C., October 23-25, 1991

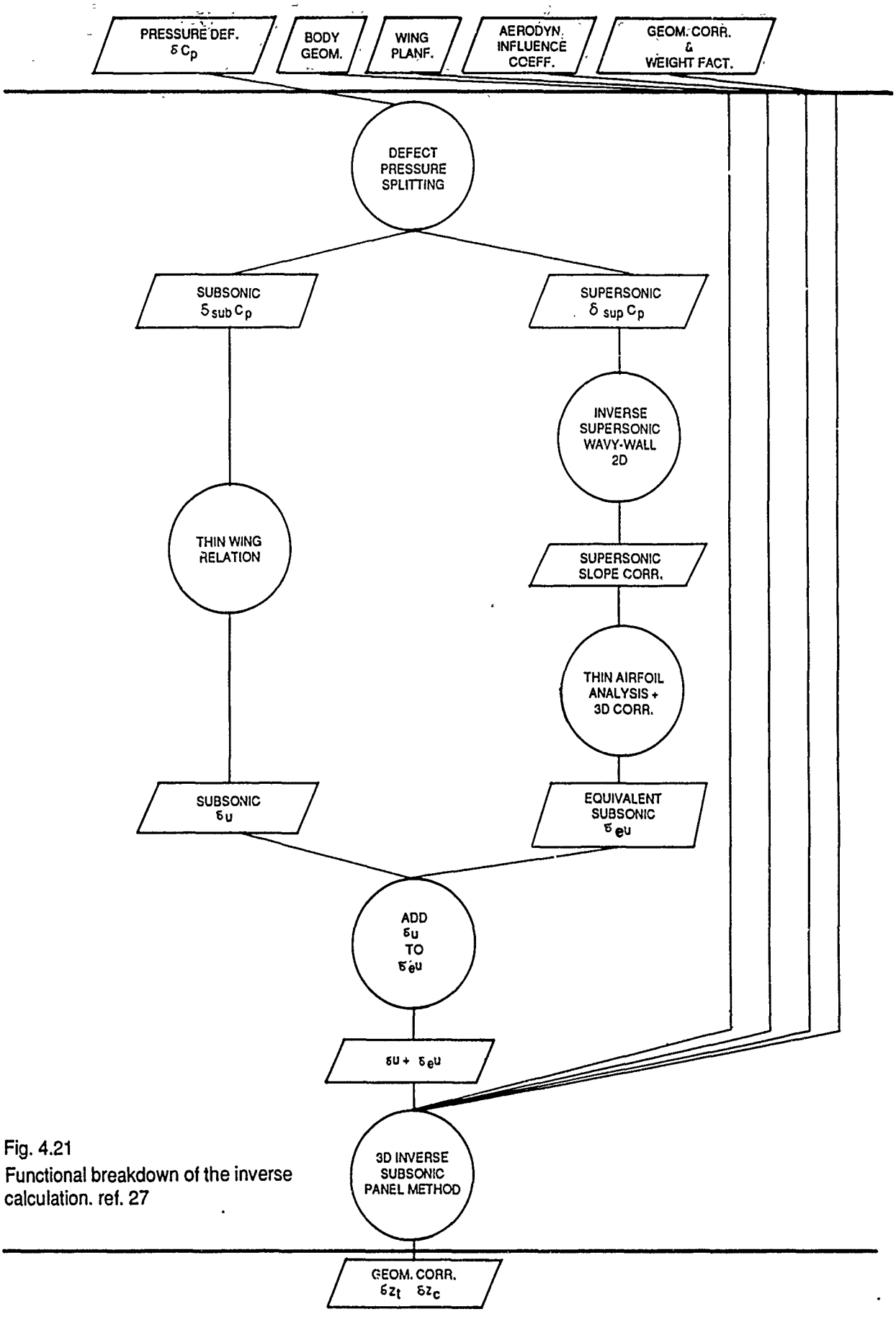
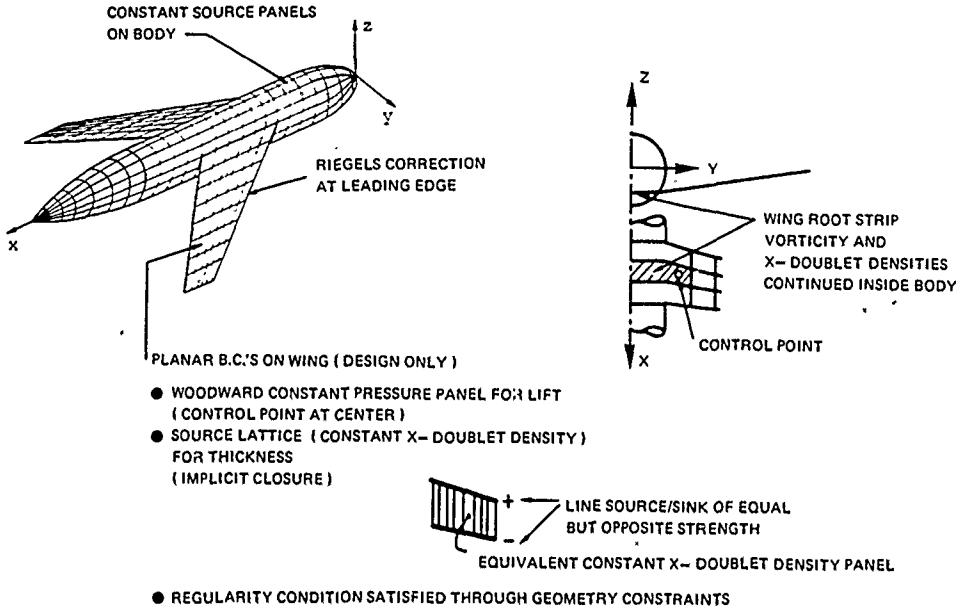


Fig. 4.21
Functional breakdown of the inverse calculation. ref. 27



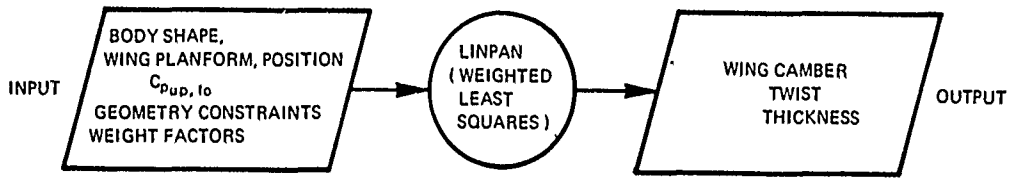


Fig. 4.23 NLR linear subsonic inverse code. ref. 30

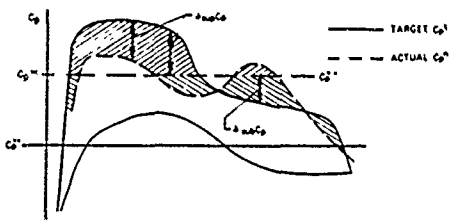
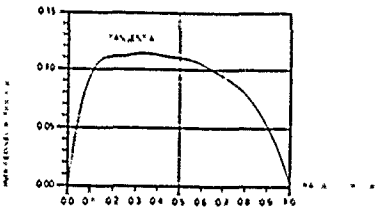
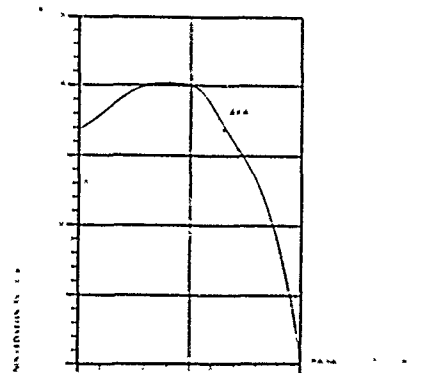


Fig. 4.22 Defect pressure split. ref. 27



(a) propeller-induced tangential velocity



b) Propellor-induced axial velocity.

Fig. 4.24 Propellor- induced velocities. ref 30

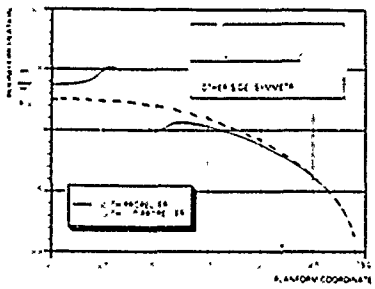


Fig. 4.25 Optimal bound circulation distribution for a wing with two up-inboard rotating propellors. ref. 30

Third International Conference on Inverse Design Concepts and Optimization in Engineering Sciences
(ICIDES–III), Editor: G.S.Dulikravich, Washington D.C. October 23–25 1991

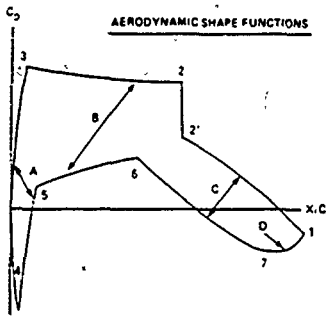


Fig. 4.26 Aerodynamic shape functions. ref. 31

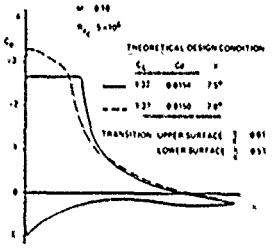
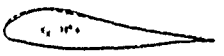


Fig. 4.27 High lift solutions. ref. 31



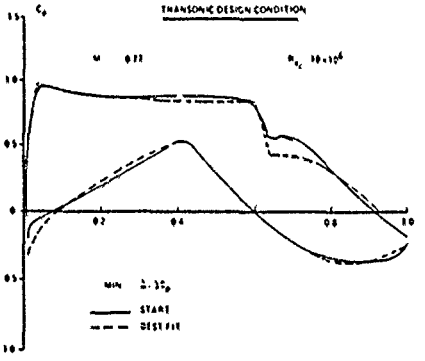


Fig. 4.28 Transonic design condition. ref. 31

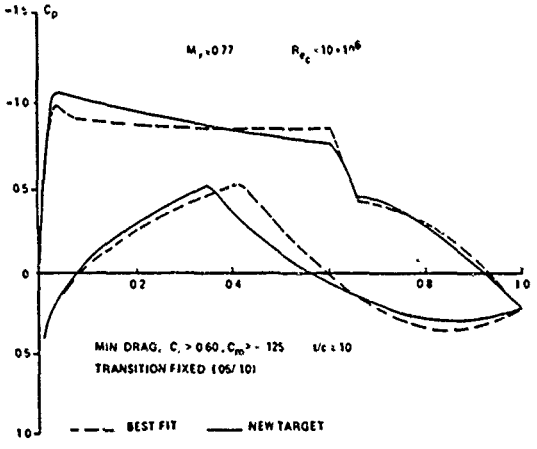


Fig. 4.29 Transonic design condition. ref 31

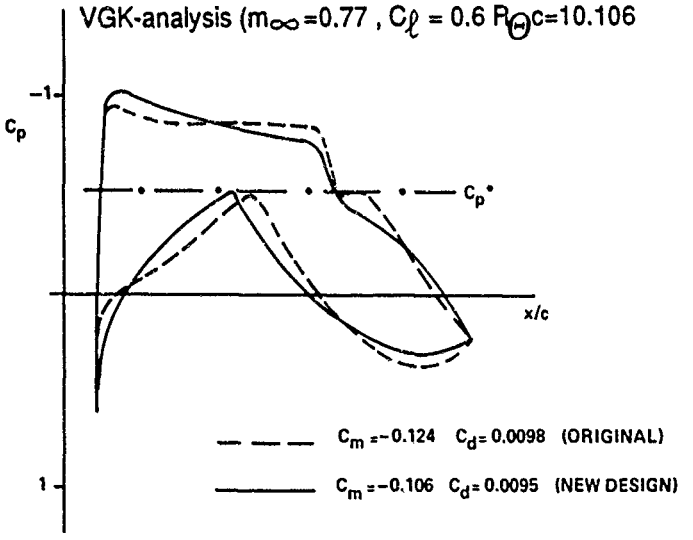


Fig. 4.30 Transonic design condition. ref. 31

Third International Conference on Inverse Design Concepts and Optimization in Engineering Sciences (ICIDES-III), Editor: G.S. Dulikravich, Washington D.C., October 23-25, 1991.

AERODYNAMIC AIRCRAFT DESIGN METHODS AND THEIR NOTABLE APPLICATIONS

— SURVEY OF THE ACTIVITY IN JAPAN —

Kozo Fujii
Institute of Space and Astronautical Science,
Yoshinodai 3-1-1, Sagamihara, Kanagawa, 229, JAPAN

and

Susumu Takanashi
National Aerospace Laboratory
Jindaiji-Higashi 7-44-1, Chofu, Tokyo, 182, JAPAN

ABSTRACT

In the present paper, an overview of the aerodynamic aircraft-design methods and their recent applications in Japan is presented. One of the design codes which was developed at the National Aerospace Laboratory (NAL) and widely used now is mainly discussed, and hence, most of the application examples are the results of the collaborative works between heavy industries and National Aerospace Laboratory. Wide variety of applications in transonic to supersonic flow regimes are presented. Although design of aircraft elements for external flows are the main focus, some of the internal flow applications are also presented. Recent applications of the design code using the Navier-Stokes and Euler equations in the analysis mode include the design of HOPE(space vehicle) and USB(upper surface blowing) aircraft configurations.

INTRODUCTION

With the advent of supercomputers having fast processors and large memories, CFD(computational Fluid Dynamics) is progressing at incredible speed. Three-dimensional Navier-Stokes simulations, which were very rare ten years ago even for relatively simple body configurations are now common at any conference on fluid dynamics[1,2,3]. Flow field simulations over complex body configuration are not difficult task once the geometry data is given. We can learn a lot of flow physics from the simulated results that may be helpful for re-designing the body configuration. Although such simulated results give us a lot of information about the flow field, they would not tell us how to modify the body configuration for the better design. One way to do it may be a trial-and-error type approach where conducting a large number of simulations is necessary, which is still not feasible even with advanced supercomputers. So-called design programs for determining the optimum geometry may be as useful as analysis programs simulating the given flow fields.

There has been a strong effort to develop both airfoil and wing design methods for many years. Unfortunately, the progress is not as remarkable as analysis methods.This is true in Japan as well as in the United States. CFD technology has been remarkably improved last several years, but on the other hand, no much progress was made for the design methods and code development. Only one remarkable progress in Japan was the design method developed by Takanashi at National Aerospace Laboratory in 1984. His method is "iterative correction method" based on the perturbation equations of potential flows. In this method, the geometry correction is made iteratively to reduce the difference between the target pressure distributions and the

Third International Conference on Inverse Design Concepts and Optimization in Engineering Sciences (ICIDES-III), Editor: G.S. Dulikravich, Washington D.C., October 23-25, 1991.

pressure distributions that is obtained by an analysis code. One of the advantages of this code is that any analysis code can be incorporated because analysis code is sort of black box for the geometry correction method. Analysis codes are not necessarily restricted to the potential codes. Even the Navier-Stokes codes can be used although the convergence is not guaranteed. Because of the flexibility and robustness of the code, it has been used for wide variety of applications. Now, most of the aircraft industries in Japan use this computer code and applied it to the practical problems.

In the present paper, Takanashi's design method and its applications are presented. Since this is a paper giving an overview of the Japanese activity, only the conceptual explanation is given about the method itself, and the focus is mainly laid on the demonstration of the applications to a wide variety of the flow fields.

DESIGN METHODOLOGY

Background

There are several approaches for the design problems. One way may be the numerical optimization using an analysis code. Wing design method was proposed by Hicks in 1976[4], and the research has been extensively conducted since then. In this optimization technique, a wing section with, for instance, minimal total drag under some constraints such as a specified lift and maximum thickness is sought by using the analysis code and the optimization code iteratively. Recently, Jameson[5] proposed an efficient method using a control theory. There exists so-called "inverse method" of wing design in which wing geometry is determined to realize the specified pressure distributions. This type of approach was used for wing design by Henne[6] and for wing-fuselage design by Shankar[7] for example. The approach used by Takanashi may be different from either of the approaches above. This is an iterative residual correction method similar to the works by Barger and Brooks[8], Davis[9], and McFadden[10] for the two-dimensional problems. The advantage of this approach is that only minimum effort in developing the geometry correction code is needed to decrease the pressure residual, while an analysis code is retained in its original form. In the next section, the formulation is briefly described.

Formulation of Inverse Problem and Iterative Procedure

Only a concept of the design method that was developed by Takanashi in 1984 is briefly described. More details can be found in his original and the following papers[11,12,13].

First, inverse problem is defined. Here the nonlinear full potential equations are taken as basic equations, and in the formulation process, small perturbations are assumed. Thus, the applicability is restricted to the flow field without shock waves or with weak shock waves. After some manipulations, integral equations that relate the geometry change and the surface pressure change are formulated. Iterative design procedure is formulated using the integral equations obtained above. Body (wing, wing-body complete aircraft etc.) surface is paneled into segments and the integral equations are discretized and numerically solved to find the necessary amount of geometry modification once the difference of required and calculated pressure difference is defined. Since we have the target pressure distributions which is required, we can define the difference using some analysis code.

The iteration process can be defined as follows. First, we assume initial body geometry, then calculate the surface pressure distributions using some analysis codes. Since we know the require pressure distributions, we can calculate the difference between the required an calculated

Third International Conference on Inverse Design Concepts and Optimization in Engineering Sciences
(ICIDES-III), Editor: G.S. Dulikravich, Washington D.C., October 23-25, 1991.

pressure distributions by a simple subtraction. Second, necessary body geometry change can be calculated using the integral equations which are discretized. Improved body geometry is now defined and the analysis code is once again used to calculate the pressure distribution in the second approximation. The iteration process is schematically shown in Fig. 1. One significant feature of this method is that analysis code is sort of "black box" and any type of analysis methods can be used. The Euler, Navier-Stokes, even the experimental measured data can be used to supply the pressure distribution data. They may be used so far as there occur no strong shock waves and the difference between the target and calculated pressure distributions is not large. Although there is no guarantee for the convergence in the case of some analysis code such as Euler and Navier-Stokes codes where perturbation between the geometry and surface pressure may not be uniquely defined because of the strong nonlinearity, many examples shown below indicate that the applicability of the present method is much wider than the theoretical prediction.

APPLICATION EXAMPLES

Transonic Wing Design

In Takanashi's original paper[11], applications to a couple of transonic wing design problems were presented. One of them is shown here. Figure 2 shows the original geometry data and the computed pressure distributions (dotted data). Also plotted is the target (specified) pressure distributions (solid lines). The freestream Mach number is 0.74 and the wing planform was fixed with 9.92 aspect ratio, 18.4 deg. sweep angle. The trailing-edge kink location is 30 % semispan. The target pressure distributions were determined to realize the same chordwise pressure distributions at any span station between the wing root and tip. Such pressure distributions are usually called "isobar pattern" because straight lines appear on the surface pressure contours over the entire wing surface. The chordwise pressure is determined by the two-dimensional airfoil design code, and its characteristics were investigated by airfoil analysis and wind-tunnel testings. Analysis code used in this example was "FLO22", nonlinear full potential code developed by Jameson. To avoid the monotonic increase of the thickness of the root section in the iteration process, the root section profile was fixed throughout the iteration process in this example.

Figure 3 shows the sectional wing geometry and the pressure distributions obtained after ten iterations. The target pressure distributions are almost realized. In Fig. 4, the pressure contours on the upper surface of the wing are plotted. Chordwise pressure distributions are almost the same for any spanwise station except close to the wing root section. Note that the computational time for the design mode is negligibly small compared to that of the analysis code in the iteration process.

To show that the design code can be combined with any analysis code, several computations for the design of transonic wings were carried out[12]. One of the computations using the analysis code[14] developed at the National Aerospace Laboratory is presented next. In this example, the boundary layer code also developed at the NAL[15] was incorporated. Only four iterations were necessary for the convergence. The isobar pattern is realized from the root section to the wing tip section in the computed result as is shown in Fig. 5. Mitsubishi Heavy Industries (MHI) used Takanashi's code and designed many practical wings for transonic transport aircraft[16]. As a design strategy, isobar pattern was required, and the final wing geometry was determined considering the off-design requirements about buffet, pitch-up and else. As an example, Fig. 6 shows the chordwise pressure distributions to be realized at each spanwise station. The Mach number on the design point was 0.77, and the CL was 0.65. The aspect ratio was 10, the sweep angle was 18 deg. and the tapered ratio 0.3 (see Fig. 7). The initial and the final pressure distributions along with the target pressure distributions are shown in Fig. 8, and the final wing geometry where thickness and the twisted angle are modified near the

Third International Conference on Inverse Design Concepts and Optimization in Engineering Sciences (ICIDES-III), Editor: G.S. Dulikravich, Washington D.C., October 23-25, 1991.

tip to satisfy the off-design requirements is shown in Fig. 9. The wind tunnel experiment was conducted to check the aerodynamic performance of the designed wing. The measured Cp distributions are presented in Fig. 10. Reasonable agreement is observed between the target and the measured pressure distributions. Figure 11 shows the comparison of the pressure contours on the upper surface of the wing. Here again, good agreement is obtained between the computed and measured contour plots even though small discrepancy is observed near the root and tip.

At the time of this design code development, there was a collaboration between JADC representing Japanese industries and Boeing company to develop a new transonic aircraft. The project was called 7J7 in the United States, and YXX in Japan. Although this project was retarted because of the market change, there left is a lot of technology accumulations for the Research and Development. Under this project, many wing configurations were designed by Mitsubishi Heavy Industries again using Takanashi's code. Some of the designed wings were used for the simulations using the Reynolds-averaged Navier-Stokes equations[17,18] and the computed results were compared with the corresponding experiments[19] to confirm the aerodynamic performance of the designed wings. These examples will be shown at the conference.

Airfoil Design Using Navier-Stokes Equations

As has been mentioned above, the analysis code is sort of a "black box" and it can use any analytical method even though the convergence is not necessarily guaranteed. Hirose et al. coupled Takanashi's design code with two-dimensional Reynolds-averaged Navier-Stokes code[20]. With specifying the same pressure distributions at each spanwise station for large aspect ratio wing, the three-dimensional design code was incorporated with the two-dimensional Navier-Stokes code for the design of two-dimensional airfoil. One of the application examples is shown here. Shockless supercritical pressure distributions at Cl= 0.6 was specified as a target and the initial geometry was set up to have strong shock wave. The freestream Mach number is 0.75 at the Reynolds number 13 million. The initial, target and computed Cp distributions along with the initial and final airfoil geometries are plotted in Fig. 12. The target Cp distributions are almost realized in ten iterations.

Two Dimensional Transonic Cascades

Takanashi reformulated his original design code and developed a two dimensional cascade design program in 1986. The analysis code in this case is a Euler code using explicit time integration. Even after 10 iterations, fully converged solution was not obtained. However, the pressure is becoming closer and closer to the target pressure on every iteration stages. The solution after 10 iterations is presented in Fig. 13 along with the cascade geometry. Takanashi insisted in his paper[13] that the convergence would be much improved by optimizing the parameters in the design process for cascade flows.

Additional Applications

Recently, with the rapid progress of supercomputers, the design code above was combined with three-dimensional Navier-Stokes codes and applied to more difficult cases. Both Mitsubishi (MHI) and Kawasaki (KHI) Heavy Industries applied it to the design of HOPE(H-II Rocket Orbiting Plane). The HOPE is a space vehicle that NASDA (National Space Development Agency) is currently developing. Both companies were interested in redesigning the tip fin of the configuration. MHI analysed the transonic flow at Mach number 0.9 with 5 degrees angles of attack and the Reynolds number 2 million[21]. They found by the Navier-Stokes simulations that the flow field surrounded by the fuselage, main wing and tip fin became almost channel flow and strong shock wave and associated flow separation occured. The Takanashi's design code was

Third International Conference on Inverse Design Concepts and Optimization in Engineering Sciences (ICIDES-III), Editor: G.S. Dulikravich, Washington D.C., October 23-25, 1991.

iteratively used with the three-dimensional Navier-Stokes code and the good improvement was obtained after five iterations. They used half a million of grid points for the Navier-Stokes analysis and the computer time required for each iteration step was 5 hours for the analysis mode and 0.2 hours for the design mode Thus, in total, 26 hours were necessary even with the Fujitsu VP400, one of the most advance supercomputers at that time. The initial body configuration is shown in Fig. 14 in terms of the computational grid. The initial and the final chordwise pressure distributions on the tip fin are presented in Fig. 15 with the corresponding sectional geometries. Although the target pressure is not precisely realized, there is obvious improvement such as disappearance of the suction peak. The close-up views of the near-surface streamlines obtained from the computed flow fields both for the initial and obtained configurations are presented in Fig. 16. Shock wave is weakened and the flow separation on the tip fin surface disappears in the final configuration.

Kawasaki Heavy Industries tried to modify the pressure distributions over the tip fin to satisfy the buffet boundary by re-designing the tip fin using Takanashi's design code with the Euler code[22]. About 200,000 grid points were used in the analysis mode and total computer time for five iterations was about 5 hours. In this example, the freesteam Mach number is 0.9 and the angle of attack is 6.5 degrees. The original and designed sectional geometries, and the initial and final Cp distributions along with the target Cp are presented in Fig. 17. Remarkable improvement is observed although the target Cp distributions are not realized also in this example.

Kawasaki Heavy Industries also applied the design code for the redesign of the USB (Upper Surface Blowing) wing configuration of the STOL[23]. The planform of the USB is shown in Fig. 18. In this example, Isobar pattern is the target, but the wing section is fixed near the nacelle and the tip to avoid resulted very thin wing section to weaken the shock wave. Figure 19 shows the sectional Cp distributions. The strong shock wave that appeared on the initial configuration is weakened and the target Cp distributions are almost realized.

Another aircraft company named Fuji Heavy Industries developed their own design code based on the Takanashi's method. They applied it to the design problem of wing-fuselage combination[24]. The analysis code was full potential code. The target pressure distributions were such that realize the isobar pattern on the wing surface and are the same as the initial ones on the fuselage. The initial and final Cp distributions and the surface pressure contours are plotted in Fig. 20. The computed Cp in the lower surface realizes the target Cp, but still some discrepancy exists on the upper surface. However, compared to the initial Cp distributions, improvement is obvious. The final configuration is shown in Fig. 21.

SUMMARY

An overveiw of the Aerodynamic aircraft-design methods and their recent applications in Japan was presented. One of the design codes developed at the National Aerospace Laboratory (NAL) is mainly discussed because of its popularity in Japan, and wide variety of applications were presented from transonic to supersonic flow regimes. This design method uses inverse design code and analysis code iteratively to realize the required pressure disbributions, and thus any anaysis code can be used. Some of the examples shown here used Euler and Navier-Stokes code as an analysis mode. These application examples indicated the capability and feasibility of the design code. The fact that many companies currently use this design code for practical problems and obtain successful results proves it.

This paper is written based on the results that the first author has noticed. There may be more activities in Japan that can not be included in the paper. Unfortunately many of the papers in the reference list are written in Japanese. However, some of the important papers such as

Third International Conference on Inverse Design Concepts and Optimization in Engineering Sciences (ICIDES-III), Editor: G.S. Dulikravich, Washington D.C., October 23-25, 1991.

Takanashi's original paper are written in English and the authors hope that the list of reference in this paper is useful for any researchers for the design problems.

ACKNOWLEDGEMENT

The first author of this paper only surveyed the development of the design methods in Japan, and did not contribute to the research at all. Many of the results shown in this paper are the contribution of many researchers in Japan. The authors would like to thank all of them that supplied computed results for this survey paper. Three aircraft companies, Fuji Heavy Industries, Kawasaki Heavy Industries and Mitsubishi Heavy Industries are greatly acknowledged for helping the authors to write this paper.

REFERENCES

1. Buning, P. G. et al., "Numerical Simulation of the Integrated Space Shuttle Vehicle in Ascent," AIAA Paper 88-4359, 1988.

2. Rizk, Y. M., Schiff, L. B., and Gee, K., "Numerical Simulation of the Viscous Flow Around Simplified F/A-18 at High Angle of Attack," AIAA Paper 90-2999, 1990.

3. Yeh, D. et al., "Numerical Study of the X-31 High Angle of Attack Characteristics," AIAA Paper 91-1630, 1991.

4. Hicks, R. M. et al., "Airfoil Section Drag Reduction at Transonic Speeds by Numerical Optimization," SAE Paper 760477, 1976.

5. Jameson, A., " Aerodynamic Design Via Control Theory," ICASE Report No. 88-64, 1988.

6. Henne, P. A., "Inverse Transonic Wing Design Method," J. Aircraft, Vol. 18, No.2, pp. 121-127, 1981.

7. Shankar, V., "A Full Potential Inverse Method Based on a Density Linearization Scheme for Wing Design," AIAA Paper 81-1234, 1981.

8. Barger, R. L. and Brooks, C. W., "A Streamwise Curvature Method for Design of Supercritical and Subcritical Airfoils," NASA TN D-7770, 1974.

9. Davis, W. H. Jr., "Technique for Developing Design Tools from the Analysis Methods of Computational Aerodynamics," AIAA Paper 79-1529, 1979.

10. McFadden, G. B., "An Artificial Viscosity Method for the Design of Supercritical Airfoils," Ph D. Thesis, New York Univ., 1979.

11. Takanashi, S., "Iterative Three-Dimensional Transonic Wing Design Using Integral Equations," J. Aircraft, Vol. 22, No. 8, pp. 655-660, 1985.

12. Takanashi, S., "Transonic Wing and Airfoil Design Using Inverse Code WINDES," Proc. 3rd NAL Symposium on Aircraft Computational Aerodynamics, NAL SP-5, 1985 (in Japanese).

13. Takanashi, S. et al., "Inverse Design Method for Two-Dimensional Transonic Cascades," Proc. 4th NAL Symposium on Aircraft Computational Aerodynamics, NAL SP-7, 1986 (in Japanese).

14. Ishiguro, T. et al., "Numerical Analysis of Inviscid Flows about Wing-Fuselage Combinations, III Calculation Based on the Euler Equations," NAL TR-896, 1985 (in Japanese).

15. Matsuno, K., "A Vector-Oriented Finite-Difference Scheme for Calculating Three-Dimensional Compressible Laminar and Turbulent Boundary Layers on Practical Configurations," AIAA Paper 81-1020, 1981.

16. Tanioka, T et al., "Wing Design Using Three-Dimensional Transonic Inverve Method," Proc. 22th Aircraft Symposium, 1984 (in Japanese).

17. Fujii, K. and Obayashi, S., "Navier-Stokes Simulations of Transonic Flows Over a Practical Wing Configuration," AIAA Journal, Vol. 25, No. 3, pp. 369-370, 1987.

18. Fujii, K. and Obayashi, S., "Navier-Stokes Simulations of Transonic Flows Over a Wing-Fuselage Combination," AIAA Journal, Vol. 25, No. 12, pp. 1587-1596, 1987.

19. Miyakawa, J, et al., "Searching the Horizon of Navier-Stokes Simulation of Transonic Aircraft," AIAA Paper 87-0524, 1987.

20. Hirose, N., et al., "Transonic Airfoil Design Based on Navier-Stokes Equation to Attain Arbitrary Specified Pressure Distribution -an Iterative Procedure, " AIAA Paper 85-1592, 1985.

21. Kaiden, T. et al., "Aerodynamic Design of Non-Planar Wing by Inverse Method with Navier-Stokes Equation," Proc. 8th NAL Symposium on Aircraft Computational Aerodynamics, " NAL SP-14, 1990 (in Japanese).

22. Sakai, K., "Wind Tunnel Experiments and Computational Fluid Dynamics at KHI," Proc. 9th NAL Symposium on Aircraft Computational Aerodynamics, " to be publised as NAL SP, 1991(in Japanese).

23. Takahashi, H. et al., "Wing Design of Small Transport Aircraft Using Three-Dimensional Inverse Method," Proc. 27th Aircraft Symposium, 1989 (in Japanese).

24. Tani, Y. et al., "Blended Wing-Body Configuration Design Using Transonic Inverse Code, " NAL SP-14, 1990 (in Japanese).

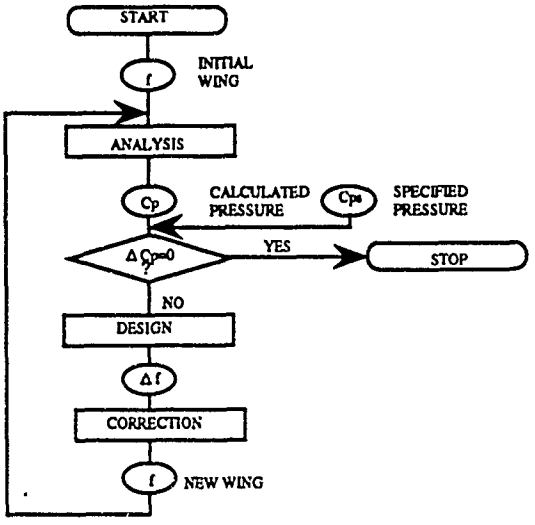


Fig. 1 Iteratvie design process.

Third International Conference on Inverse Design Concepts and Optimization in Engineering Sciences (ICIDES-III), Editor: G.S. Dulikravich, Washington D.C., October 23-25, 1991.

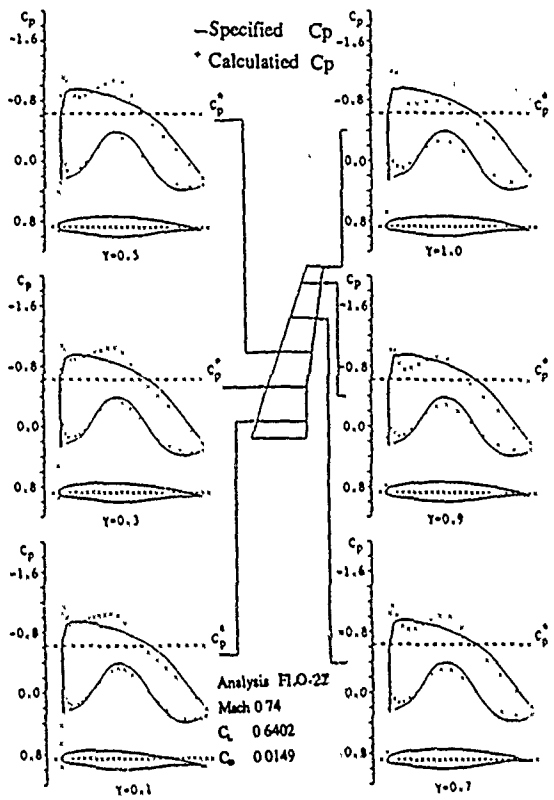


Fig. 2 Initial wing geometry with the plots of corresponding computed pressure distributions and the specified(target) pressure distributions[11].

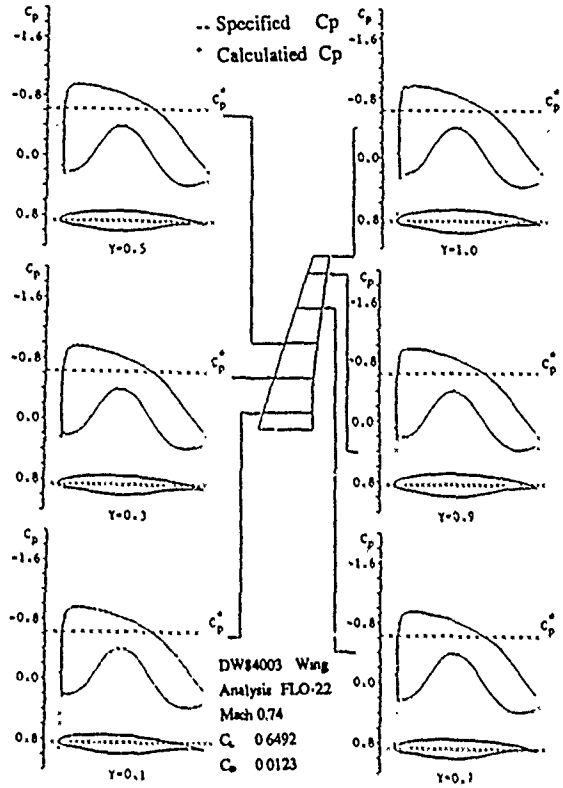


Fig. 3 Designed wing geometry and the pressure distributions[11].

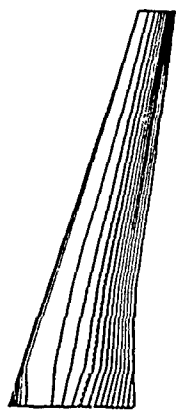


Fig. 4 Pressure contour plots on the upper surface of the designed wing[11].

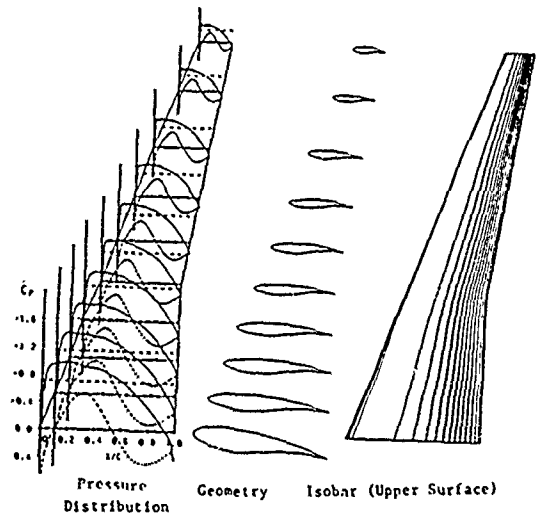


Fig. 5 Designed wing geometry with the plots of the pressure distributions and the upper surface pressure contour plots (potential code and the boundary code were used in the analysis mode)[12].

Third International Conference on Inverse Design Concepts and Optimization in Engineering Sciences (ICIDES-III), Editor: G.S. Dulikravich, Washington D.C., October 23-25, 1991.

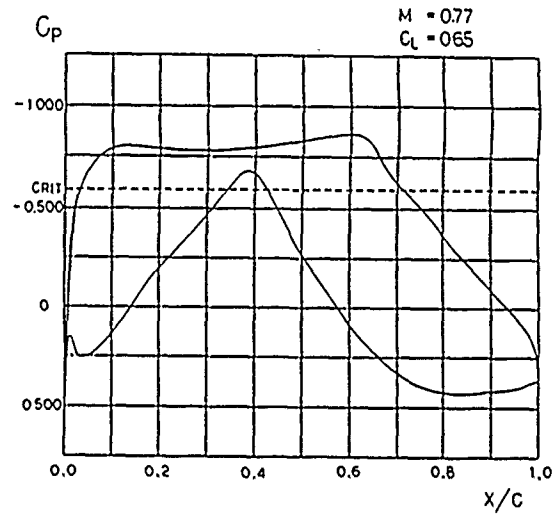


Fig. 6 Target chordwise pressure distributions at each span station[16].

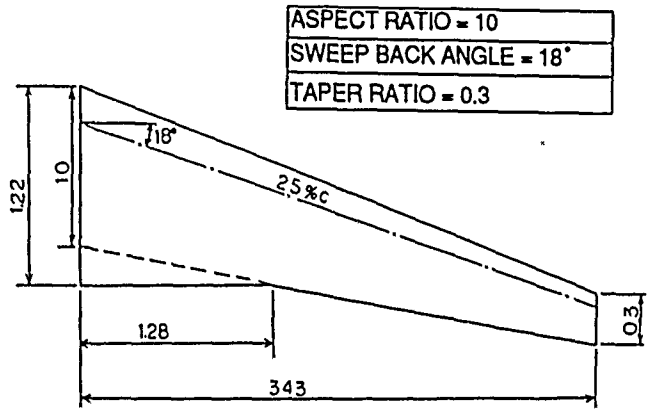


Fig. 7 Wing planform (fixed)[16].

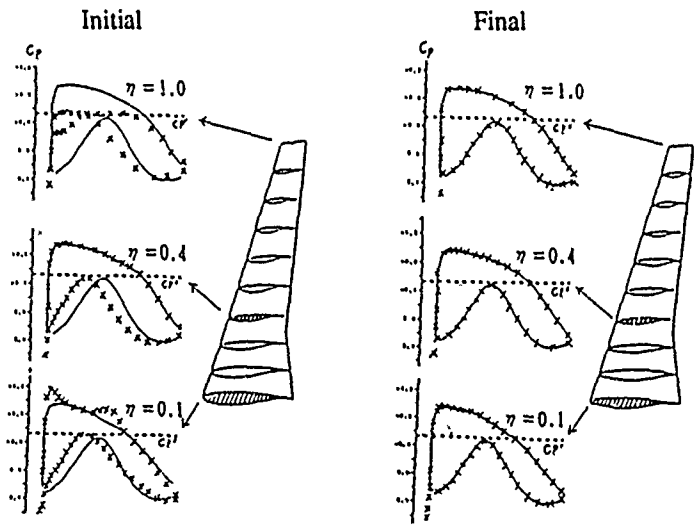


Fig. 8 Initial and final pressu distributions along with the target pressure distributions plotted with the wing geometries[16].

Third International Conference on Inverse Design Concepts and Optimization in Engineering Sciences (ICIDES-III), Editor: G.S. Dulikravich, Washington D.C., October 23-25, 1991.

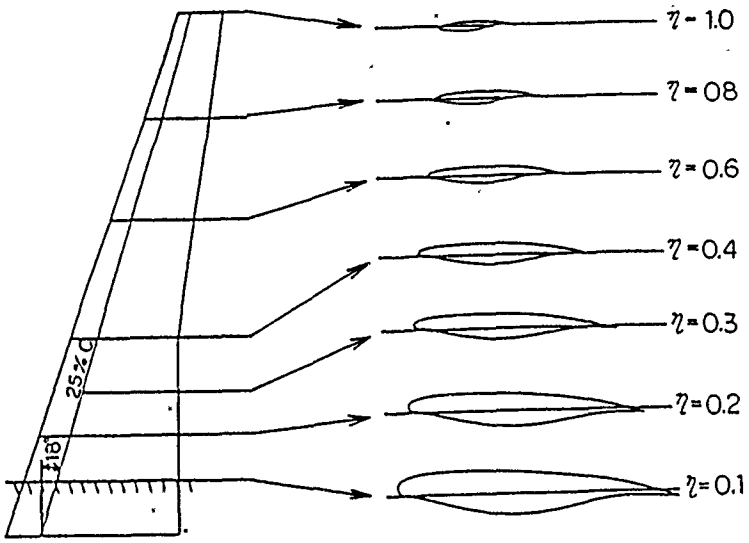


Fig. 9 Final wing geometry taking off-design requirements into account[16].

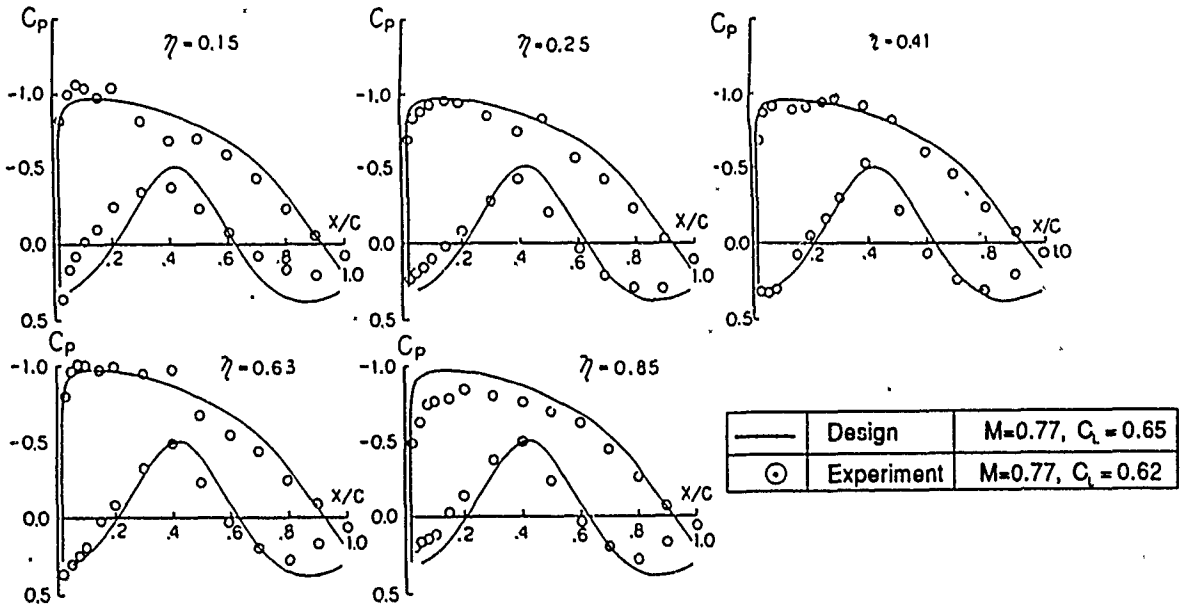


Fig. 10 Experimentally measured and designed pressure distributions[16].

Third International Conference on Inverse Design Concepts and Optimization in Engineering Sciences
(ICIDES-III), Editor: G.S. Dulikravich, Washington D.C., October 23-25, 1991.

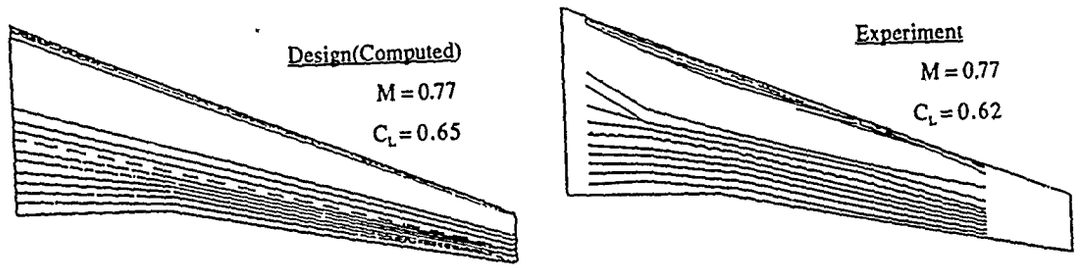


Fig. 11 Computed and experimentally measured pressure contour plots on the upper surface if the wing[16].

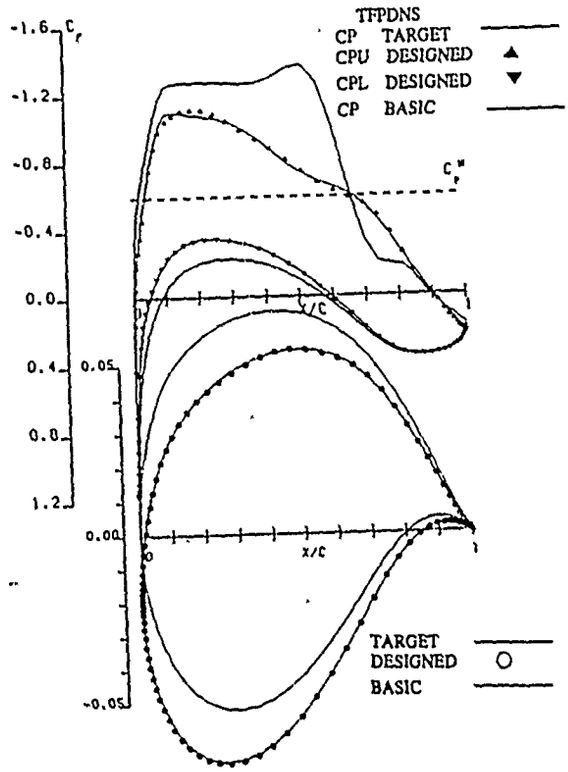


Fig. 12 Comparison of the initial, target and designed Cp distributions along with the initial and final airfoil geometries[20].

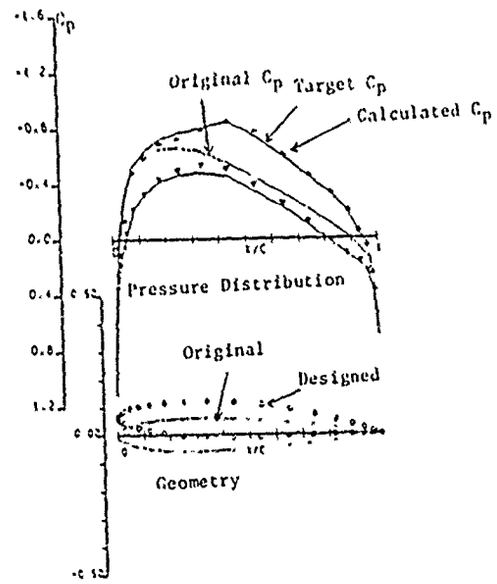


Fig. 13 Initial, target and designed Cp distributions with the initial and final cascade geometries[13].

Third International Conference on Inverse Design Concepts and Optimization in Engineering Sciences (ICIDES-III), Editor: G.S. Dulikravich, Washington D.C., October 23-25, 1991.

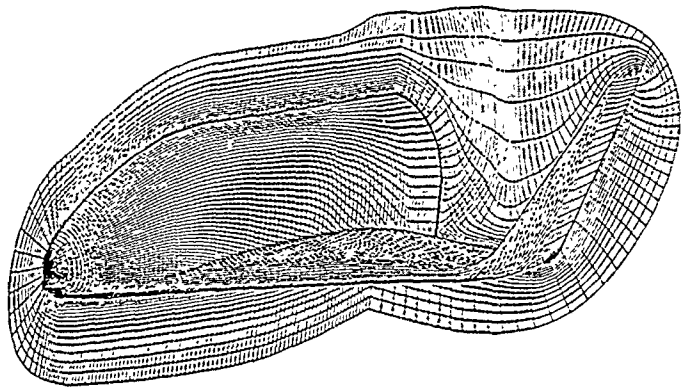


Fig. 14. Computational grid over a HOPE configuration[21].

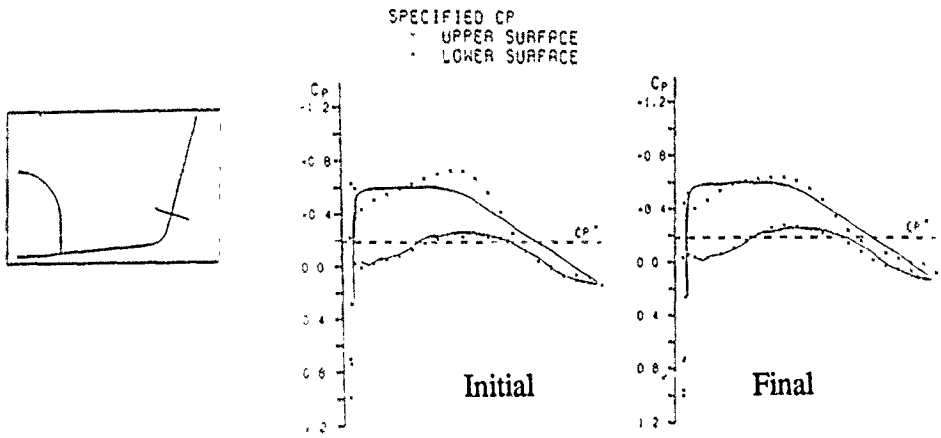
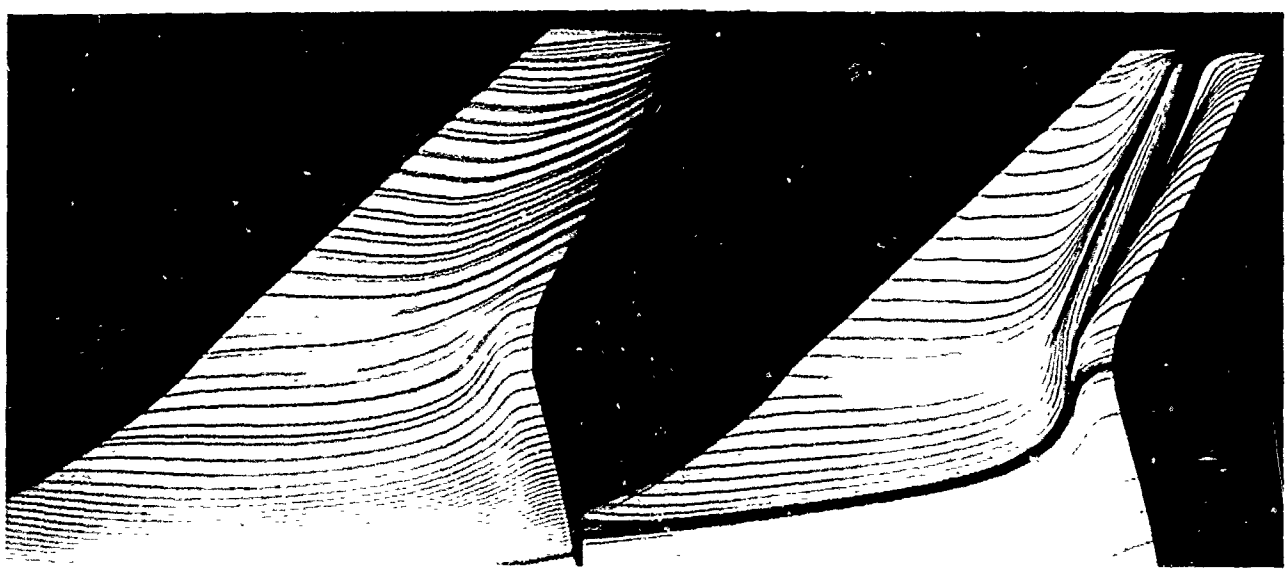


Fig. 15 Initial and final chordwise pressure distributions over the tip fin of the HOPE and their spanwise sections[21].



Final Initial

Fig. 16 Computed near-surface streamlines for the initial and final HOPE configurations[20].

Third International Conference on Inverse Design Concepts and Optimization in Engineering Sciences (ICIDES-III), Editor: G.S. Dulikravich, Washington D.C., October 23-25, 1991.

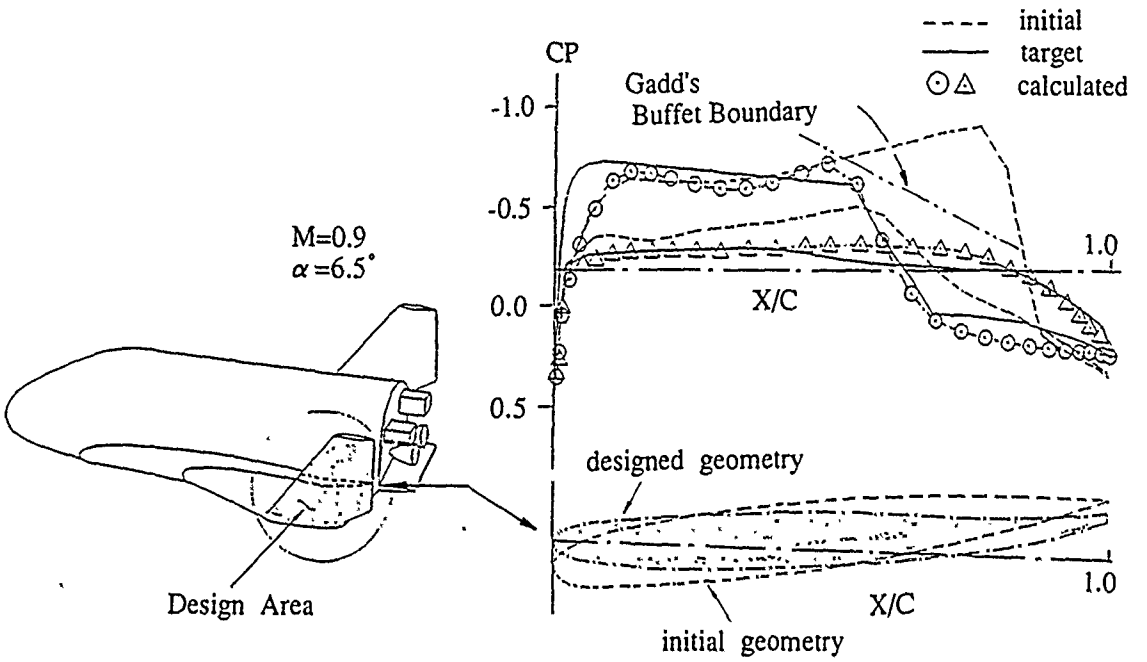


Fig. 17 Wing tip design of HOPE by KHI; initial and final chordwise pressure distributions over the tip fin and their spanwise sections[22].

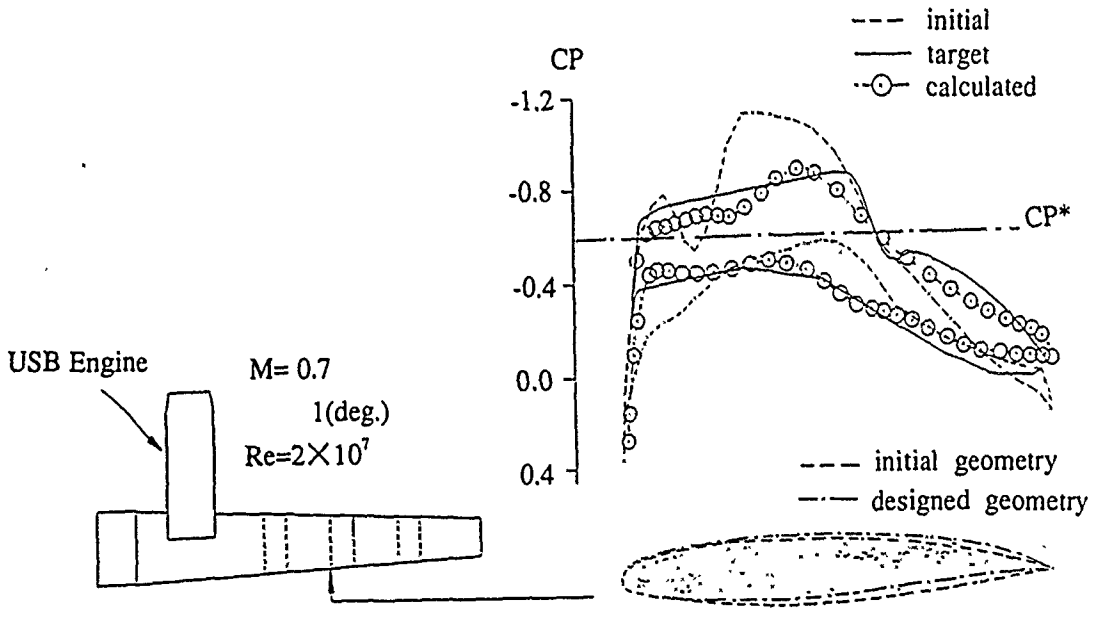


Fig. 18 USB wing planform[23].

Fig. 19 Sectional Cp distributions; initial and final Cp's and their geometries[23].

Third International Conference on Inverse Design Concepts and Optimization in Engineering Sciences (ICIDES-III), Editor: G.S. Dulikravich, Washington D.C., October 23-25, 1991.

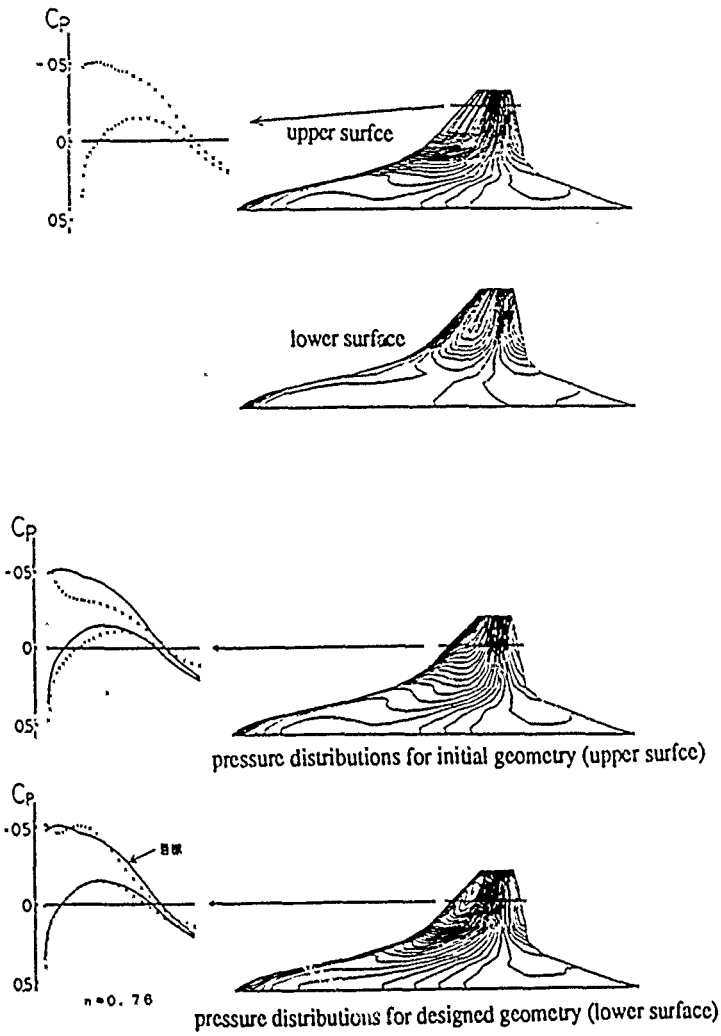


Fig. 20 Wing-body combination design by FHI; initial and final chordwise Cp distributions and surface pressure contour plots[24].

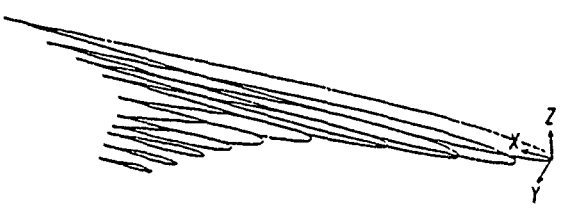


Fig. 21 Final designed wing-body combination[24].

Third International Conference on Inverse Design Concepts and Optimization in Engineering Sciences (ICIDES-III), Editor: G.S. Dulikravich, Washington D.C., October 23-25, 1991.

ON A GLOBAL AERODYNAMIC OPTIMIZATION OF A CIVIL TRANSPORT AIRCRAFT

G. Savu, O. Trifu
The Aviation Institute, Bd. Pacii 220,
77538 Bucharest, Romania

ABSTRACT

An aerodynamic optimization procedure, dedicated mainly to minimize the drag to lift ratio of a complete configuration: wing - body - tail, in the presence of some engineering and logical restrictions is described. An algorithm conceived to search the minimum of a hypersurface with 18 dimensions, which define an aircraft configuration, was developed, without using a gradient method. The obtained results, show that, at least, from the aerodynamic point of view, the optimal configuration is one of canard type, with a lifting fuselage.

I. INTRODUCTION

There are many arguments which plead for the using of a global and multicriterial optimzation procedure to design a transport aircraft. An usual practice, for the establishment of the aircraft's shape, adopted especially by the prudents, is the statistical processing of the data describing all the aircrafts of that class. Finally, after years of research, design, manufacture, testing and certifying, an out - of - date aircraft results, at least with two generations behind: one which was in service when the design of the new aircraft begun, and the second, which started at the same time, but has used the latest research results correctly forecasted.

To predict exactly the needs in the domain of passengers air transport, for the date when the new built aircraft will operate, taking into account all the economical, social and scientific conjunctures, a global and multicriterial optimization procedure is required. A new aircraft becomes competitive versus other aircrafts of its class, if the fuel consumption reduction is obtained not by affecting the passengers security and comfort and by adding laborious maintenance operations. Following these principial ideas, in the present paper we have tried to optimize, only from the aerodynamic standpoint, a short / medium - currier configuration aircraft for moderate subsonic speeds.

Here, by "optimal configuration" we understand the configuration which gives the best answer to a certain purpose. A more realistic objective function to be minimized in the presence of the engineering and airworthiness requirements, can lead to a competitive aircraft, providing benefits, both for passengers and companies.

Third International Conference on Inverse Design Concepts and Optimization in Engineering Sciences (ICIDES-III). Editor: G.S. Dulikravich, Washington D.C., October 23-25, 1991.

Another argument which demands the adoption of a global optimization procedure in the design process is the paradox, valid at least as far as our personal experience is concerned, that while aerodynamics, thermodynamics and stress analysis use the most sophisticated computing methods, their results are used mainly to decide whether a previously shaped by an "all experienced" project authority configuration is competitive, and not from to begining in the process of giving that configuration the best shape for a certain purpose.

II. THE AERODYNAMIC ANALYSIS

For the global aerodynamic characteristics (CL, CD, Cm) of a complete wing - body - tail configuration, a panel method [1] was used. Two rather hard approximations were adopted in order to ensure minimum CPU time for the analysis procedure:

a) Following the idea introduced in [2], the configuration is replaced by its horizontal projection (plane xOy "shadow"). The entire thin surface of this projection is divided into a number of triangular or quadrilateral panels, associated, each of them, to a horseshoe vortex filament.

b) For the friction drag, the flat plate assumption is adopted and consequently, on the wetted area the friction coefficient Cf is calculated as a function of the Reynolds number on each surface strip (without detachment).

The theoretical results obtained on the idealized configuration of Fig. 1.b. were compared with the experimental data measured in the Trisonic Wind Tunnel of the Aviation Institute of Bucharest, Romania, on a calibration model (Fig. 1.a).

The comparative diagrams CL, CD, Cm versus incidence (Fig.2) demonstrate that, in the domain of the small incidences, the analysis is in good agreement with the experiments. This meets our interest because the above - mentioned optimization will be performed at the cruise regime.

III. THE OPTIMIZATION PROCEDURE

Considering the results of the aerodynamic analysis as acceptable, the corresponding algorithm can be included into an optimization loop.

A generic aircraft configuration was defined by 18 geometrical parameters (Fig. 3) as follows:

x1 - the span of the surface I
x2 - the chord ratio of the surface I
x3 - the root chord of the surface I
x4 - the span of the surface II
x5 - the chord ratio of the surface II
x6 - the logitudinal position of wing apex
x7 - the logitudinal position of the horizontal tail apex

Third International Conference on Inverse Design Concepts and Optimization in Engineering Sciences (ICIDES-III), Editor: G.S. Dulikravich, Washington D.C., October 23-25, 1991.

x8 - the wing span
x9 - the wing chord ratio
x10 - the chord ratio of the horizontal tail
x11 - the span of the horizontal tail
x12 - the wing sweep angle
x13 - the horizontal tail sweep angle
x14 - the root chord of the horizontal tail
x15 - the incidence of the surface I
x16 - the incidence of the horizontal tail
x17 - the wing incidence
x18 - the root chord of the wing

The geometrical characteristics of the vertical tail and the dihedral angle of the wing were done as input data.

The incidence of the surface II was assumed equal to that of the surface I.

These 18 parameters are the 18 dimensions of a hypersurface, described by the objective function "F" which represents a sum of criteria of minimization.

Performing a statistical evaluation over a class of 30...50 passenger aircrafts, the overall mass of an aircraft was deduced to be estimated by:

$$G = 100*Npax + Ka*Sa + Kt*(Sht + Svt) + Kf*Sf + Goi \qquad (1)$$

where:

Npax - the number of the passengers
Sa - the effective wing area
Sht - the effective horizontal tail area
Svt - the effective vertical tail area
Sf - the xOy projected area of the fuselage
Goi - the inert mass of the aircraft (≅ 7700 daN for a 50 pax. and = 5500 daN for a 30 pax. aircraft)
Ka - the specific weight of the wing (≅ 58.3 daN/m)
Kt - the specific weight of the tails (≅ 33.8 daN/m)
Kf - the specific weight of the fuselage (≅ 40 daN/m)

In the present study the criterion of optimization was related to the minimizaton of the CD/CL ratio satisfying simultaneously the following constraints:

- the pitching moment My with respect to the gravity center must be zero or very close to this; the position of the gravity center is recalculated every time the configuration changes.

- the lifting force must be equal to the overall weight of the airplane in cruise flight.

- the position of the wing and tails apexes must be located within the fuselage length.

- because "in an aircraft, the main part of the structure's weight is given by the material which ensures the

Third International Conference on Inverse Design Concepts and Optimization in Engineering Sciences (ICIDES-III), Editor: G.S. Dulikravich, Washington D.C., October 23-25, 1991.

bending moment at the wing-body embeding" [3], an important restriction was to put a limitation on the bending moment at the wing-body junction. In the absence of this constraint the wing has the tendency to get a quite large aspect ratio, typical for sailplanes.

There are many objective functions Fi(X) for a class of aircrafts which can be minimized or maximized. For example, [4], with only four parameters (wing area, sweep angle, aspect ratio and the relative thickness of it's airfoil) a configuration was optimized with four objective functions:

F1(X) - ramp weight (minimize)
F2(X) - mission fuel (minimize)
F3(X) - lift to drag ratio at constant cruise Mach number (maximize)
F4(X) - range with fixed ramp weight (maximize)

or some combination of these objective functions.

Mathematically the optimization procedure means to search and find the minimum of the above-mentioned hypersurface in the presence of a number of given restrictions. The minimization problem with the restrictions "g(X)" is transformed into one without restrictions using "the penalty functions method" [5]. Each restriction is associated with a penalty function. If one restriction is violated, the corresponding penalty function is set to a great value; thus the objective function becomes greater (far from minimum). If the restriction is satisfied, the penalty function is set to zero: so it doesn't affect the value of the objective function F(X).

$$F(X) = CD/CL + \sum g_i(X) = \text{minimum} \qquad (2)$$

$$X = X(x1,.....,x18) \qquad (3)$$

For the effective searching of the minimum of the objective function F(X) the "one dimensional searching method" was adopted [5].

First, for the "starting configuration" (meaning the configuration determined by the initial values of the 18 optimization parameters) a first value of the objective function is calculated.

Than, one of the parameters is altered by a step "r", while all the others are kept constant:

$$x_i = x_i + r.x_i \qquad (4)$$

$$0 < r < 1$$

The aerodynamic analysis module is called and the value of the objective function F(X) is computed. If its value is smaller than the previous one the alteration of the parameter "x_i" is continued until the value of F(X) begins to rise. In that moment the parameter x_i is altered with $-r.x_i$ and the process of parameter x_{i+1} alteration is initiated (Fig.4). When the optimization loop, containing all the 18 parameters is ended, the procedure is repeated with

Third International Conference on Inverse Design Concepts and Optimization in Engineering Sciences (ICIDES-III), Editor: G.S. Dulikravich, Washington D.C., October 23-25, 1991.

a refined r, as long as r is superior to a selected error level.

The major disadvantage of this method is that a local minimum is usually reached by altering only some of the parameters and it is almost impossible to leave it. Besides of the parameters hierarcy, which is not so easy to establish, the procedure was modified in two different ways, in order to avoid the local minima:

a. At a certain value r the steps towards the minimum were limited at only two per parameter, even if the value of the objective function is still decreasing (Fig.5a).

b. For every parameter the sign of r is determined for which the objective function F(X) decreases. Then, all the parameters are simultaneously altered as long as F(X) decreases. When an increase in the value of F(X) is noticed the sign determination process is initiated again, followed by another phase of block alteration of all the parameters (Fig.5b). In this way, the aerodynamic analysis module is called once for a configuration resulted from the simultaneous alteration of all the parameters, thus saving computer running time. This modified version of the optimization procedure is somewhat similar to a gradient method but it doesn't need the calculation of the parameter's gradient vector.

IV. RESULTS AND DISCUSSION

The optimization procedure described above was transferred into a FORTRAN computer code and several tests were performed to certify its validity.

Among these tests, for example, the "FOKKER 27 - Friendship" airplane, quite repreentative for the 50 seats class, was adopted as a starting configuration in the idealized manner represented in Figure 6, by the lowest possible number of panels, to permit a fast aerodynamic analysis.

Denoting by "classic configuration" the wing-tail arrangement in which the wing is placed ahead of the tail and by "canard configuration" the well known tail in front of the wing arrangement, the optimzation computer code was applied and the results finally obtained are illustrated in Figures 7-9.

It can be noticed (Figure 7) that the aerodynamic (CL - CD) characteristics of the classic-optimized configuration are not much different from those classic - initial configuration, this proving that the F-27 airplane is aerodynamically well designed.

In the same time, the canard - optimized configuration has obviously superior aerodynamic characteristics, when compared to the initial (unoptimized) canard configuration (Fig. 8) and even compared to the classic - optimized configuration (Fig. 9).

During the optimization process an interesting fact was considered to be the tendency of the fuselage to widen its rear end, taking a shape somewhat similar to a small aspect ratio gothic delta wing, thus increasing its contribution to the global lift of the airplane.

We must stress that the aerodynamic analysis module and even the optimization algorithm used in the optimization procedure ex-

Third International Conference on Inverse Design Concepts and Optimization in Engineering Sciences (ICIDES-III), Editor: G.S. Dulikravich, Washington D.C., October 23-25, 1991.

empled here are, of course, not the best tools according to today's achievements, and any improvements in these directions could lead to better results at the end of an optimzation loop. Our choice was determined by the inherent limitations set by the presently available to us, computer equipment.

The CYBER 170/720 computer was used to perform the calculations which lead to the results presented here. A single call of the aerodynamic analysis module requires about 3 seconds CPU time for an idealized configuration of 40 panels (Fig. 6). To reach the optimum shape, at the moment when the relative error on "r" is less than 0.0001, some 260-300 calls of the aerodynamic analysis module are usually necessary.

The optimization code was used to define some of the principal features of the external shape for a few other short/medium range commuters.

Such an example, reffering an airplane with a 70 passengers capacity, flying at 650 km/h, 6000 m of altitude, is represented in Figures 10 a,b. The thickness was added to complete the shape of the idealized optimum configuration. Such a "thick" configuration is suitable for a much more accurate aerodynamic analysis, performed with better computer codes and even in the wind tunnel, in order to obtain a realistic final verdict on the optimization procedure and its results. The rear end wide fuselage is quite noticeable. Apart the aerodynamic gains, this type of fuselage can provide the passengers a better comfort, giving the opportunity for a cabin arrangement similar to that of a wide body airplane (Figure 11).

An indirect confirmation of these solutions, analysed since 1988, [6], was offered by a recently published paper [7], which reportss that studies are made to use an elliptical fuselage for a long range, high capacity airliner.

V. REFERENCES

[1] Trifu O. "A computer code for the calculation of the aerodynamic characteristics of a subsonic airplane", INCREST Computer Code Library, Bucharest, 1979.

[2] Belotserkovski S.M., Skripach B.K. "Aerodynamic derivatives of the flying machines" (in russian), Nauka Ed., Moskow, 1975.

[3] Sears W.R. "Flying wing could stealthy reappear", Aerospace America, July, 1987.

[4] Dovi A.R., Wrenn G.A. "Aircraft design for mission performance using nonlinear multiobjective optimization methods", J. of Aircraft, vol. 27, no. 12, 1990, pp. 1043 - 1049.

[5] Dancea I. "Optimzation methods", (in romanian), Ed. Dacia Cluj - Napoca, 1976.

[6] Savu G., Trifu O. "The estimation of the aerodynamic characteristics of some wing - body - tail configurations in sub sonic regime", The Aviation Institute - INCREST Report, N - 121, Bucharest, February, 1988.

[7] Moxon J. "Airbus aims for slice of "747" market", Flight International, 28 Nov. - 4 Dec. 1990, pp. 24 - 25.

Third International Conference on Inverse Design Concepts and Optimization in Engineering Sciences (ICIDES-III), Editor: G.S. Dulikravich, Washington D.C., October 23-25, 1991.

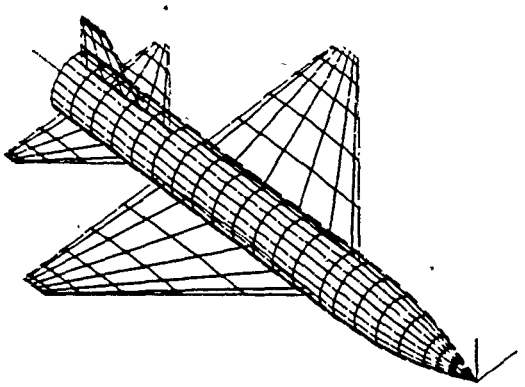


Fig.1.a. The calibration model for wind tunnel testing.

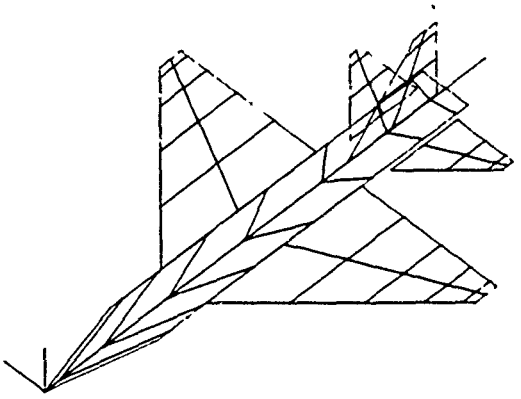


Fig.1.b. The idealized geometry for panel method calculation.

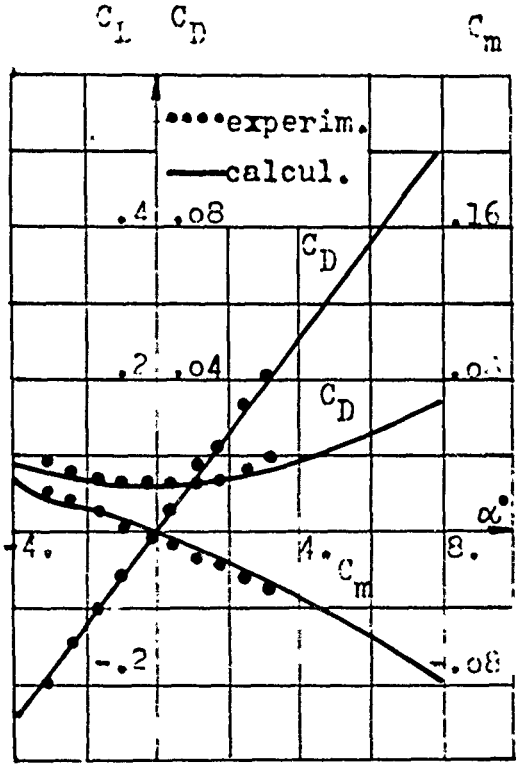


Fig.2. Comparison experiments-theory for test case 1.a. b. (Mach=0.304, MRe=4.26).

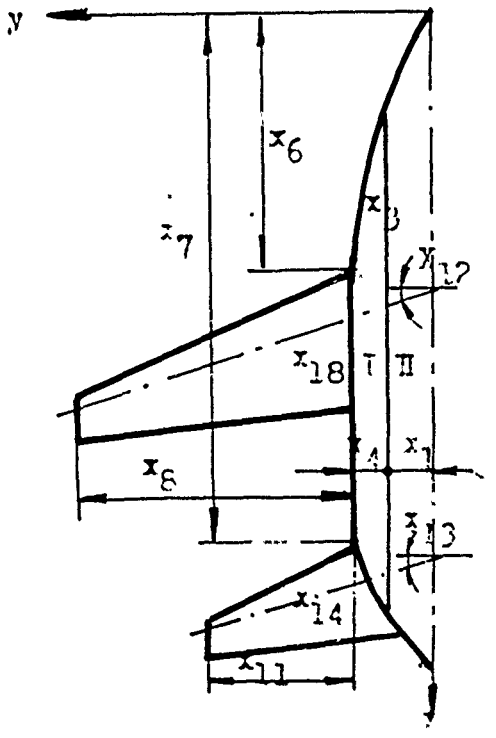


Fig.3. A generic configuration defined by 18 parameters.

Third International Conference on Inverse Design Concepts and Optimization in Engineering Sciences (ICIDES-III), Editor: G.S. Dulikravich, Washington D.C., October 23-25, 1991.

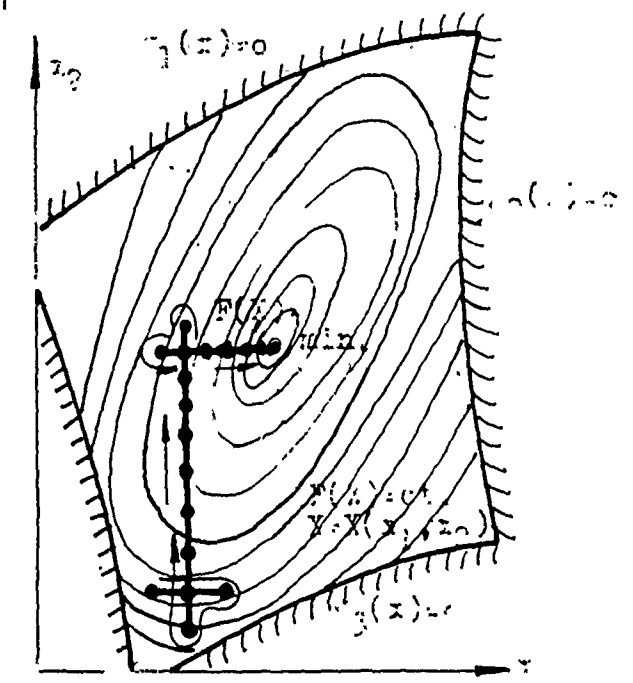


Fig.4. The "one-dimensional minimum searching"procedure with restrictions(2-D case)

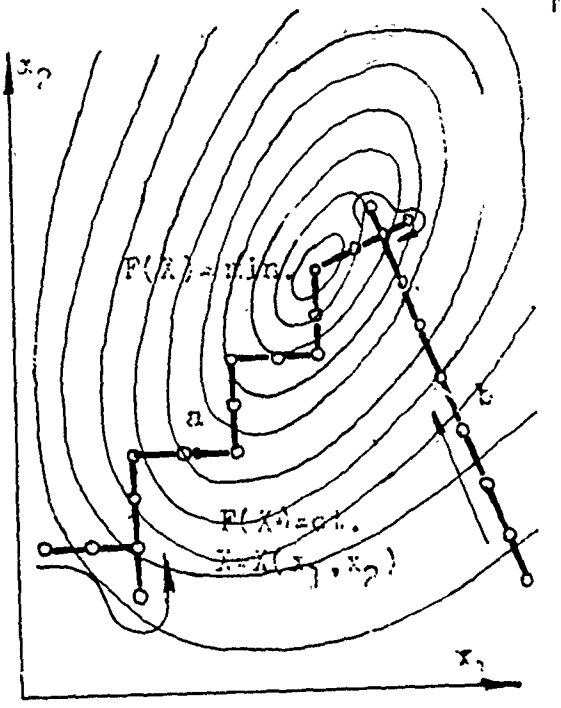


Fig.5. The modified (a,b) "one dimensional minimum searching" method (2-D case).

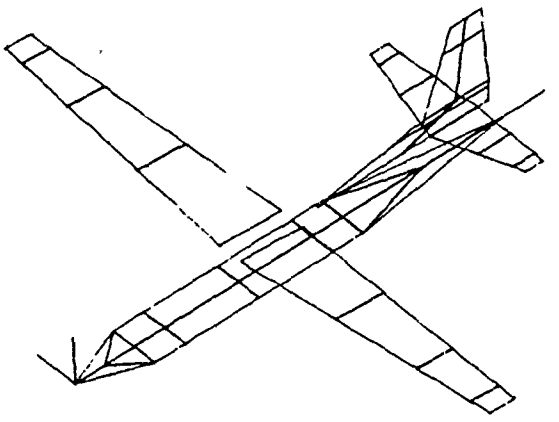


Fig.6. The "F-27" idealised configuration for the aerodynamic analysis.

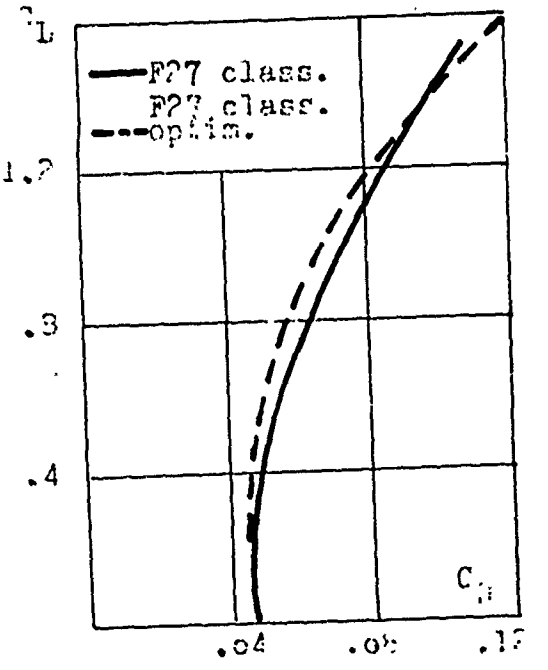


Fig.7.The comparative characteristics of "F-27"classic and "F-27"classic - optimized.

Third International Conference on Inverse Design Concepts and Optimization in Engineering Sciences (ICIDES-III), Editor: G.S. Dulikravich, Washington D.C., October 23-25, 1991.

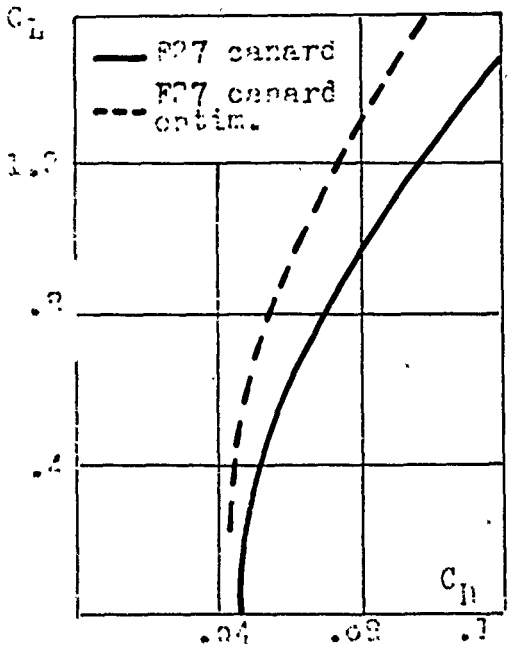


Fig.8. The comparative characteristics of "F-27" canard and "F-27" canard-optim.

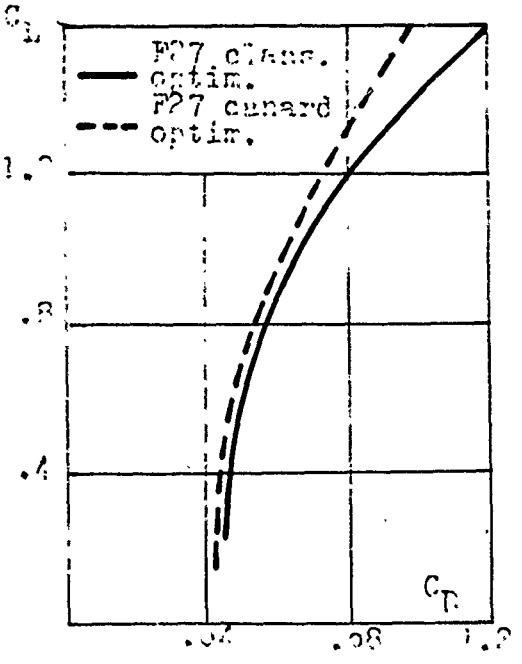


Fig.9. Comparison of "F-27" canard - optimized and "F-27" classic - optimized.

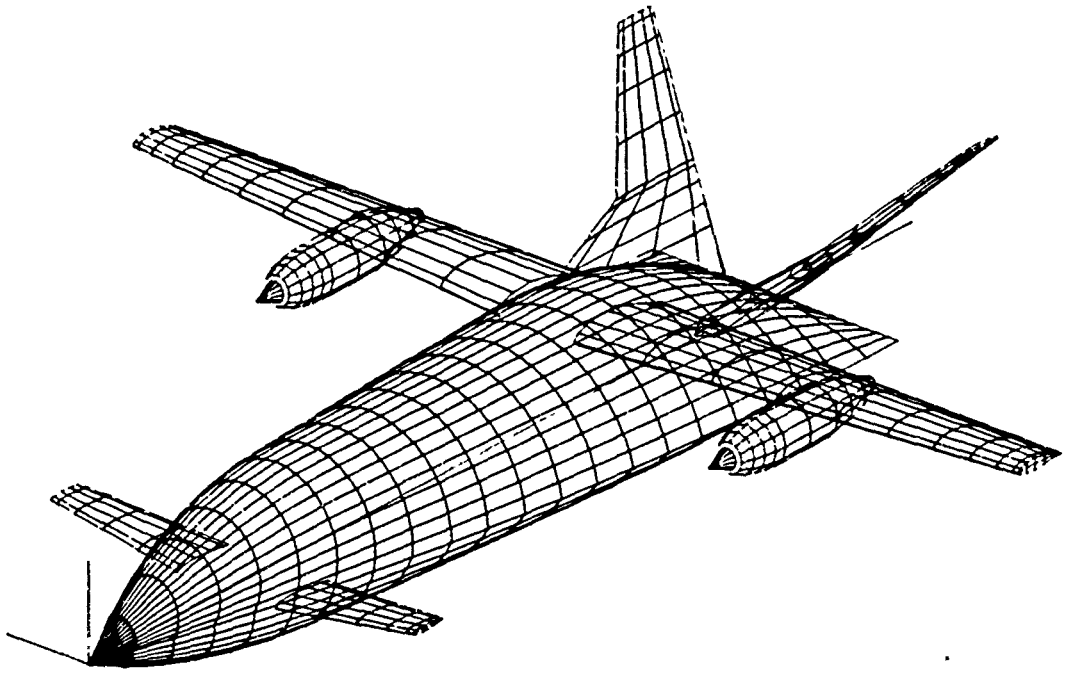


Fig.10. General view of an optimized short/medium currier (70 pax. capacity, V=650 km/h)

Third International Conference on Inverse Design Concepts and Optimization in Engineering Sciences (ICIDES-III), Editor: G.S. Dulikravich, Washington D.C., October 23-25, 1991.

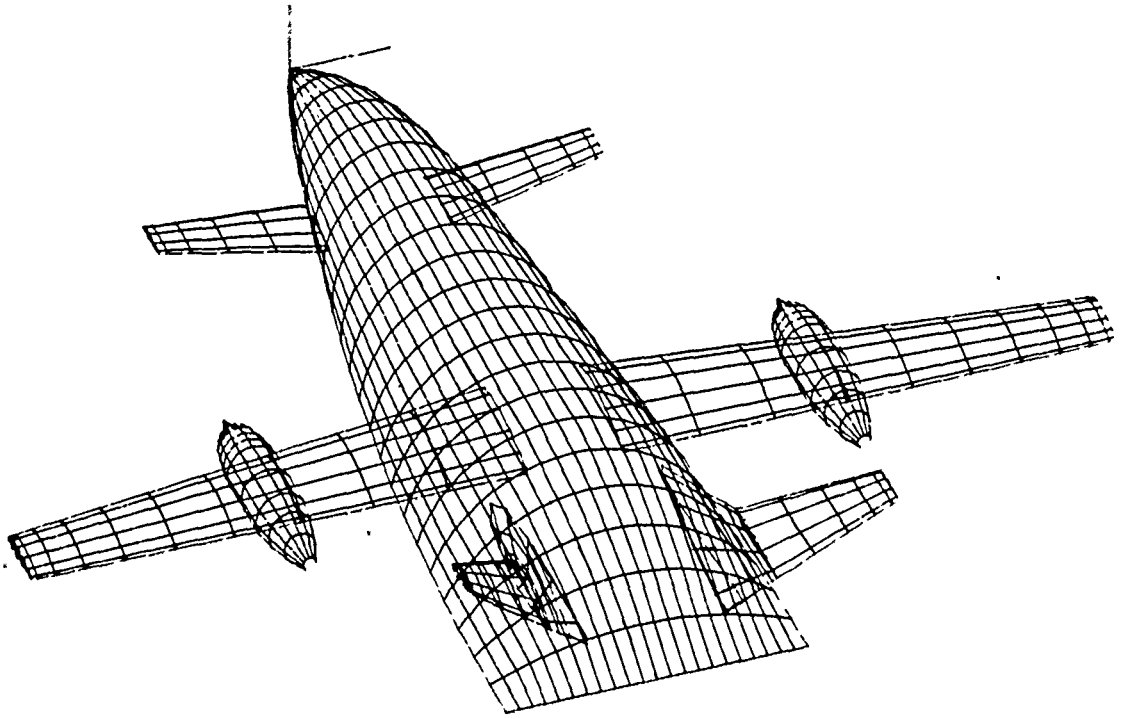


Fig. 10.b Another general view of the optimized configuration of Fig. 10.

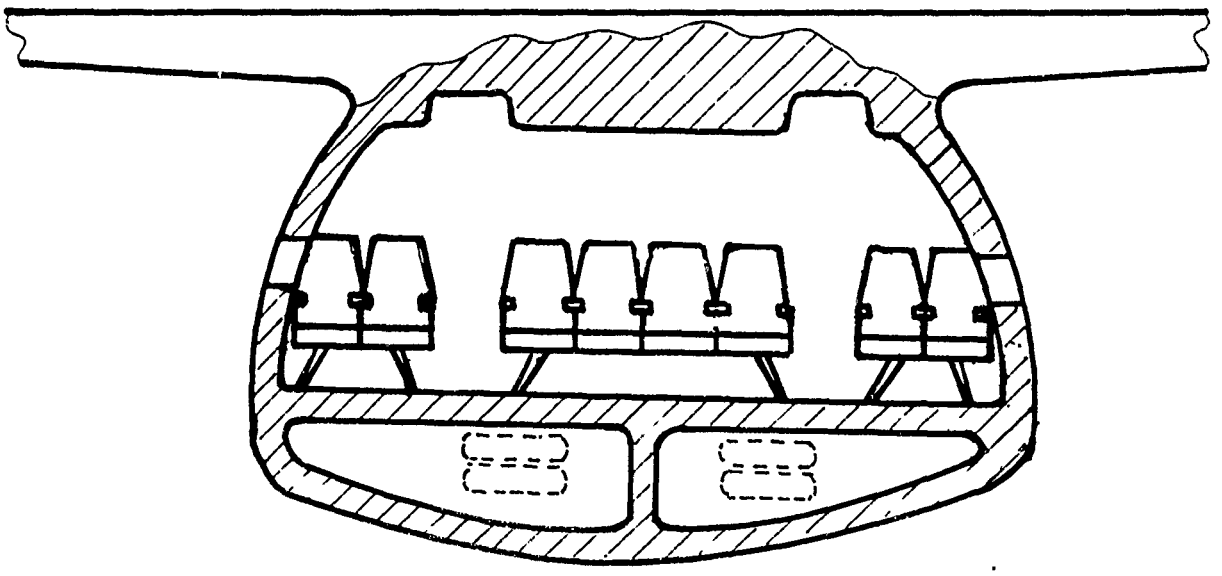


Fig.11. A possible seats arrangement in a cabin of an optimized short/medium currier airplane.

Third International Conference on Inverse Design Concepts and Optimization in Engineering Sciences (ICIDES-III), Editor: G.S. Dulikravich, Washington D.C., October 23-25, 1991.

INVERSE AIRFOIL DESIGN PROCEDURE USING A MULTIGRID NAVIER-STOKES METHOD

by

J. B. Malone
Unsteady Aerodynamics Branch
Structural Dynamics Division
NASA Langley Research Center
Hampton, Virgina 23665–5225

and

R. C. Swanson
Theoretical Flow Physics Branch
Fluid Mechanics Division
NASA Langley Research Center
Hampton, Virgina 23665–5225

ABSTRACT

The Modified Garabedian-McFadden (MGM) design procedure was incorporated into an existing 2D multigrid Navier-Stokes airfoil analysis method. The resulting design method is an iterative procedure based on a residual-correction algorithm and permits the automated design of airfoil sections with prescribed surface pressure distributions. The new design method, MG-MGM, is demonstrated for several different transonic pressure distributions obtained from both symmetric and cambered airfoil shapes. The airfoil profiles generated with the MG-MGM code are compared to the original configurations to assess the capabilities of the inverse design method.

INTRODUCTION

The aerodynamic design of aircraft components is often carried out by means of one of the following four approaches: a) cut-and-try analysis, b) indirect methods, c) optimization techniques, and d) inverse design techniques. Unlike the cut-and-try method, the latter three design techniques are far more automated, and can significantly reduce the overall engineering effort and calendar time required for developing aircraft components and configurations with improved aerodynamic performance or aerodynamic interference characteristics.

A common design approach is to specify, a priori, surface pressure distributions that have favorable aerodynamic characteristics at given freestream conditions. For example, an appropriately chosen pressure distribution can be used to achieve certain desired lift and moment coefficient goals, while a "weak-shock" or "shock-free" distribution can be used to minimize wave drag performance penalties. The automated design procedure is then used to generate, as efficiently as possible, the configuration geometry which will cause the specified pressures to exist on the

Third International Conference on Inverse Design Concepts and Optimization in Engineering Sciences (ICIDES-III), Editor: G.S. Dulikravich, Washington D.C., October 23-25, 1991.

designed component. Obviously, the use of these automated design methods requires that the aerodynamicist can specify, a priori, the desired pressure distributions for a particular application.

The most widely used aerodynamic design procedures for transonic-flow applications seem to be based upon potential-flow Computational Fluid Dynamics (CFD) methods.[1–5] This trend is most likely due to the relative low cost, in terms of computer-resource requirements, that is demonstrated by CFD methods based on the Transonic Small Disturbance (TSD) equation or the Full Potential equation (FPE). In the past decade, however, considerable interest has been demonstrated in the use of higher-order CFD methods such as the Euler equations and the Reynolds-averaged Navier-Stokes equations (RANS) for aerodynamic analyses in a variety of applications. Thus, there is now an increasing interest in also developing design procedures based on these higher-order CFD formulations.[6–10] If used during the design process, these higher-order CFD methods will help the aerodynamicist to account for the occurrence of fluid dynamic effects or phenomena which are not routinely predictable using potential flow methods.

In reference 11, Garabedian and McFadden described an inverse aerodynamic design procedure which they demonstrated using an existing FPE aerodynamics code. Their design method is based on a residual-correction algorithm, which we will refer to here as the GM method, and can be used to generate aerodynamic surfaces with prescribed surface pressure distributions. In reference 12, Malone, et al. presented a Modified Garabedian McFadden (MGM) design algorithm that removed some limitations of the original GM technique. These authors applied the new MGM design method, also using FPE aerodynamic analysis codes as a basis, to airfoil, axisymmetric nacelle inlet, and 3–D nacelle inlet design problems. Later, Hazarika[13] and Sankar used a FPE CFD method to apply the MGM procedure to the design of blended wing-body configurations. In a recent effort, Malone, et al.[14] described the first use of the MGM residual-correction design algorithm coupled with a 2–D Navier-Stokes solution procedure. Subsequently, a similar viscous-flow design procedure using MGM was presented by Birckelbaw[15], and new applications of MGM to multi-element airfoils using unstructured grids are under development.[16]

The objective of the present research was to develop an accurate design method for viscous, attached-flow, design problems which might be beyond the capability of potential-flow or Euler methods, even those using interactive boundary-layer theories. Because the aerodynamic designer normally seeks attached flow conditions, the method to be described is not expected to handle separated flow design problems. However, by virtue of the fact that a Navier-Stokes method forms the basis of the present procedure, the possible occurrence and extent of separated flow regions can be directly computed and noted by the designer during the design process.

The following sections of this paper will describe the multigrid Navier-Stokes computational procedure, the MGM design algorithm, implementation of the design procedure, and will also present the results of several sample airfoil design problems.

NAVIER-STOKES SOLUTION PROCEDURE

The two-dimensional Navier-Stokes procedure used in the present work was originally developed by Swanson and Turkel.[17] Their method solves the Reynolds-averaged form of the full Navier-Stokes equations (neglecting body forces and heat sources) on a body-fitted computational grid. The mathematical formulation in generalized coordinates consists of a non-dimensionalized

Third International Conference on Inverse Design Concepts and Optimization in Engineering Sciences (ICIDES-III), Editor: G.S. Dulikravich, Washington D.C., October 23-25, 1991.

set of equations cast in a strong conservative form:

$$Q_t + D_\xi + E_\eta = \sqrt{\gamma} M_\infty Re_c^{-1} (G_\xi + H_\eta) \tag{1}$$

In Eq. (1), Q is the vector of conserved flow variables, which are themselves combinations of the usual primitive variables, density (ρ), the components of fluid velocity (u, v), and the fluid total energy (e). The quantity M_∞ is the freestream Mach number and, Re_c is the Reynolds number. The vectors D and E are the inviscid flux vectors in the ξ and η coordinate directions, respectively. Also, the vectors G and H are the viscous flux terms in the corresponding coordinate directions. The techniques used to solve Eq. (1) are given in Refs. 17, 18, and 19. Here we present only a brief description of the Navier-Stokes solution procedure.

The spatial derivatives in the time-dependent Navier-Stokes equations are approximated with central differences. A cell-centered finite-volume technique is used to obtain the spatial discretization. For sufficiently smooth meshes the discretizations are second-order accurate. Adaptive numerical dissipation terms are appended to the resulting semidiscrete formulation. These terms, which are a blending of second and fourth differences, are included to provide shock capturing capability and to give the necessary background dissipation for convergence. In smooth regions of a flow field the dissipation terms are third order. The semidiscrete equations are integrated in time with a modified five stage explicit Runge-Kutta scheme. On the first, third, and fifth stages there is a weighted evaluation of the dissipation terms, which results in a good parabolic stability limit. The physical diffusion terms are evaluated only on the first stage and frozen for the remaining stages, without compromising stability. The decoupling of the temporal and spatial discretization makes the scheme amenable to convergence acceleration techniques, which are very beneficial in the computation of steady flows.

Three techniques are employed to accelerate convergence to steady state. The first one is local time-stepping, where the solution at any point in the domain is advanced at the maximum time step allowed by stability. This results in faster signal propagation, and thus, faster convergence. The second technique is variable coefficient implicit residual smoothing. It can be regarded as simply a mathematical step applied after each Runge-Kutta stage to extend the local stability range. The third technique is multigrid. A multigrid method involves the application of a sequence of meshes to a discrete problem to accelerate convergence of the time-stepping scheme. Successively coarser meshes can be generated by starting with the desired fine mesh and eliminating every other mesh line in each coordinate direction. An equivalent fine grid problem is defined on each coarse grid. Appropriate operators are introduced to transfer information between the meshes. In the method applied here a fixed W-type cycle is used to execute the multigrid strategy. The efficiency of the multigrid process depends strongly upon effective high frequency damping characteristics of the driving scheme. Such damping behavior is provided by the five stage Runge-Kutta scheme. The good smoothing of the highest frequencies on the coarser meshes allows rapid removal of the low frequency errors in the fine grid solution. There are two additional advantages of the multigrid method. First, less computational effort is required on the coarser meshes. Second, information is propagated faster on the coarser meshes due to larger allowable time steps.

Figure 1 presents typical computed lifts and moments for an NACA 0012 airfoil to demonstrate the capability of the multigrid algorithm for aerodynamic analysis applications. Turbulence closure was obtained with the Baldwin -Lomax model.

Third International Conference on Inverse Design Concepts and Optimization in Engineering Sciences (ICIDES-III), Editor: G.S. Dulikravich, Washington D.C., October 23-25, 1991.

MGM DESIGN PROCEDURE

The MGM design method can be classified as a residual-correction technique, in which the residuals are the difference between the desired speed distribution and the computed distribution. Over the past decade a number of residual-correction methods have been developed, such as the "wavy-wall" approach of Davis.[20] The methods differ primarily in the manner in which changes in residual are related to changes in surface shape. The MGM algorithm itself consists of an auxiliary PDE that is solved for incremental changes in surface coordinates during each design cycle. The final aerodynamic shape is approached in a stepwise fashion through a cyclical iteration between the flow solver and the MGM algorithm.

Mathematical Formulation

The MGM auxiliary PDE is heuristic in derivation and assumes that changes in surface pressures are proportional to changes in airfoil surface slopes and curvatures. For two-dimensional flow about an airfoil configuration, the auxiliary equation is given by

$$F_0 S_t + F_1 S_{xt} + F_2 S_{xxt} = R \tag{2}$$

where R is the residual, defined as $R = q_c^2 - q_t^2$. The quantities q_c and q_t are the computed and target speed distributions, the coordinate x is the usual cartesian coordinate taken here to lie along the airfoil chordline, and the coefficients F_0, F_1, and F_2 are constants chosen to provide a stable iterative process. Figure 2 shows how this auxiliary equation is typically incorporated into existing flow solution procedures. The computed surface velocities are normally obtained from partially converged numerical solutions to the flow equations under consideration at a given value of time, t. During the design process, as q_c approaches q_t, the right-hand side of Eq. (2) is reduced, and subsequent solutions of the auxiliary equation yield minimal changes in the airfoil surface coordinates.

Next, Eq. (2) is written in terms of a correction to the airfoil coordinates, ΔS, by using the temporal derivatives and choosing $\Delta t = 1$, so that Eq. (2) can then be written as:

$$F_0 \Delta S + F_1 (\Delta S)_x + F_2 (\Delta S)_{xx} = R \tag{3}$$

Numerical Solution Procedure

The auxiliary PDE is solved by writing finite-difference expressions for each term of Eq. (3). The computational grid used to solve this equation is the same grid used for the fluid-dynamic equations, which for the present Navier-Stokes solver, is an algebraically generated C-grid topology. Equation (3) is solved only along the airfoil surface, so that only the grid-line clustering in the x or streamwise direction is of importance.

Assuming that there are a total of N computational points on the airfoil surface, Eq. (3) is written for each of these points, i, where $1 \leq i \leq N$. A typical equation evaluated at the i th point on the surface is

$$A_i \Delta Y_{i+1} + B_i \Delta Y_i + C_i \Delta Y_{i-1} = R_i \tag{4}$$

Third International Conference on Inverse Design Concepts and Optimization in Engineering Sciences (ICIDES-III), Editor: G.S. Dulikravich, Washington D.C., October 23-25, 1991.

The coefficients A_i, B_i, and C_i are evaluated by means of standard finite difference expressions, and ΔY_i is the incremental change in surface coordinate, ΔS, at the i th computational point. Equation (4) is evaluated at each point, i, around the airfoil surface, leading to a system of equations with N unknowns, the ΔY_i values. At each point on the aerodynamic surface, ΔY_i is coupled to values at each neighboring point. The resulting algebraic equations form a tridiagonal system that is solved for values of ΔY_i using the Thomas algorithm.[21]

The design cycle is completed by updating the previous surface geometry using the new values of ΔY_i as follows:

$$Y_i^{new} = Y_i^{old} + \Delta Y_i, \; for\, i = 1 \; to \; N \tag{5}$$

Additional details of the MGM algorithm can be found in References 12 and 14.

Trailing-Edge Crossover

The present inverse procedure was developed to permit the design of complete airfoil surfaces, including the leading-edge and trailing-edge regions. However, a completely arbitrary choice for a target pressure distribution does not always result in a well-posed inverse design problem. For example, Volpe[4] has presented a technique to satisfy the three integral constraints relating target pressures and freestream conditions that are required to insure a well-posed problem in compressible flow. As a possible consequence of using unconstrained target pressures, any inverse procedure may produce an airfoil geometry which may exhibit trailing-edge crossover, or lead to other unrealistic configurations.

Therefore an artifice is used in the present work so that the trailing edge thickness can be controlled and so that any tendency of the airfoil to "fish-tail" is identified. If the geometry is driven to a "fish-tail" configuration (trailing-edge crossover), a linear wedge is added to the airfoil section so that the resulting trailing-edge thickness equals a predetermined value. It has been demonstrated that this wedge technique can give some measure of control over the potential manufacturability of airfoil configurations generated by automated design procedures.[22] It should be noted that if the above wedging technique is required continuously during the design process, the original target pressures should be examined for possible modification along the lines discussed by Volpe[4]. A technique such as this may be used to modify these pressure distributions in order to rigorously provide for a well posed inverse design problem.

RESULTS

The MGM design procedure has been incorporated into the 2–D Navier-Stokes code described previously. The resulting computer program is referred to here as the MG-MGM code. In this section, we present three sample problems to illustrate application of the design method. Target pressures are obtained from a known "target geometry", and the inverse design method is then used to "reproduce" the original "target" configuration. These test cases demonstrate that the starting geometry, or baseline configuration, used to start the design process does not have to be "close" in thickness or camber to the target geometry.

Third International Conference on Inverse Design Concepts and Optimization in Engineering Sciences (ICIDES-III), Editor: G.S. Dulikravich, Washington D.C., October 23-25, 1991.

Several parameters were held constant for each of the sample problems. A "W-type" multigrid cycle was used throughout, together with five successive levels of grid refinement. Also, five "W"multigrid cycles were used between all airfoil geometry updates (ie. one design cycle). The computational C-grid used consisted of 321 nodes in the wrap-around, or ξ-direction (33 of these in the wake region) and 64 nodes in the surface-normal, or η–direction, for a total of 20,544 grid points. The first η = constant grid line was clustered to within 0.0001 chord lengths from the airfoil surface. Since each point on the airfoil surface is allowed to move independently, each can be thought of as an independent variable in the context of an optimization problem. For the cases presented above, there were 257 such points around the airfoil surface.

For each case presented, a total of 160 design cycles (i.e. geometry updates) were specified. The program was executed on a Cray 2 and each airfoil design required approximately 16 minutes of CPU. Comparable Euler designs would require approximately 11 minutes on the same machine for a similarly dimensioned grid.

Design Case No. 1

For Case No. 1, the MG-MGM code was first used in the analysis mode to compute the surface pressures corresponding to an RAE 2822 airfoil at M_∞ = 0.8, an angle of attack, α, equal to zero degrees, and Re_c = 6,500,000, based on airfoil chord.

This calculated C_p distribution was then used as a target distribution for the MG-MGM code operated in the design mode. The baseline airfoil used to start the design was an NACA 0012 section. As shown in Fig. 3, this airfoil is significantly different in shape from the RAE 2822 airfoil used to produce the target pressure distribution. In this figure, as well as others depicting airfoil geometry, the vertical scale has been expanded.

Figure 4 compares the design and target airfoil pressures after 40 design cycles while Fig. 5 compares the design and target airfoil contours at this point in the design process. Figures 6 and 7 present the corresponding comparisons for pressure and geometry after 160 design cycles. Figure 8 shows the results of a separate analysis computation performed after the design was completed. This analysis started from uniform freestream conditions (impulsive start) and used the grid produced by the designed airfoil contour given in Fig. 7. The comparison between design and target pressures is actually better than that observed during the design process. This better correlation exists because the pressures obtained during the design process are generated with only a small number of multigrid cycles on the latest computational grid. The final design corresponds to 160 updates to the airfoil geometry and 160 grid-generation steps. The MGM design algorithm itself is not computationally intensive, and because a simple algebraic grid generation scheme is also used in the present application, the computational overhead represents only a small fractional increase over that which would be required to run the original CFD method in the analysis mode.

Design Case No. 2

For Case No. 2, the MG-MGM code was used in the analysis mode to compute the surface pressures corresponding to an NACA 0012 airfoil at M_∞ = 0.8, an angle of attack, α = 2.0 degrees, and Re_c = 6,500,000, based on airfoil chord.

This calculated C_p distribution was again used as a target distribution for the MG-MGM code operated in the design mode. This time the baseline airfoil was also an NACA 0012 section.

However, during the design process, the freestream angle of attack was kept at α = 0.0 degrees. This case was used to study the possible effects that a mismatch between specified pressures and angle of attack might have on the design process. Figure 9 compares the baseline and target airfoil pressures for this case. As would be expected for a transonic flight condition, the shock wave locations are significantly different for the α = 2.0 targets and the α = 0.0 baseline condition.

Figure 10 compares the design and target airfoil pressures after 40 design cycles, while Fig. 11 compares the design and target airfoil contours at this point in the design process. As can be seen in Fig. 11, after 40 design cycles the airfoil surface has already been rotated upwards to adjust to the target pressure. Figure 12 presents a comparison of the geometry after 160 design cycles. As in the previous case, a separate analysis run was performed to verify the airfoil design. Figure 13 shows the results of the separate analysis computation performed after the design was completed. This analysis started from uniform freestream conditions (impulsive start) and used the grid produced by the designed airfoil contour given in Fig. 12. Finally Fig. 14 shows a plot of the average Δq^2 versus multigrid work for the 800 multigrid cycles. This quantity drops approximately two orders of magnitude during the design process and is used to monitor the progress of the design algorithm.

Design Case No. 3

The final example problem, design Case No. 3, was chosen to demonstrate that large geometric changes can be achieved with the MGM design algorithm. For this application, the target pressures corresponded to an NACA 0012 airfoil at M_∞= 0.8, angle of attack, α = 0.0 degrees, and Re_c = 6,500,000, based on airfoil chord. The baseline configuration used was an NACA 0006 airfoil. A comparison of the target and final design airfoil shapes is shown in Fig. 15. A comparison of the target pressures, and those obtained from a separate analysis (impulsive start) of the final design configuration are shown in Fig. 16. In this example, an airfoil design was successfully accomplished which required a 100% increase in airfoil thickness over that of the baseline airfoil shape.

CONCLUDING REMARKS

The MGM design procedure has been incorporated into an existing multigrid Navier-Stokes code. The computational efficiency of the method indicates that it is a viable tool for the design process. The actual computational effort of this design method depends, of course, on the complexity of the target pressure distributions chosen. Normally, aerodynamicists would seek to eliminate shockwaves due to the impact of wave drag on performance. Previous experience with the MGM algorithm[14] indicates that shock-free design applications require about 50% less computational effort than for flows with shockwaves present. The transonic flow cases shown here were picked, in part, to demonstrate the design algorithm's robustness and ability to respond correctly to shockwaves in the flowfield. This feature is important because regions of sonic flow may be created locally near regions of high airfoil curvature even at relatively low freestream Mach numbers.

Because of the computer resource requirements, any Navier-Stokes based design method would likely be used in combination with other, lower-cost design methods. For example, an initial airfoil shape designed with a FPE method may prove to be an excellent starting configuration for

a higher-order design approach. Used in this manner, the present Navier-Stokes inverse design method should then be able to account for viscous flowfield phenomena that may not be detected or predicted accurately enough by other methods based on FPE or Euler solution procedures.

REFERENCES

1. Sloof, J. W.: Computational Methods for Subsonic and Transonic Aerodynamic Design, AGARD Report No. 712, 1983.

2. Lores, M. E.; and Smith, P. R.: Supercritical Wing Design Using Numerical Optimization and Comparisons with Experiment, AIAA Paper 79–0065, AIAA 17th Aerospace Sciences Meeting, New Orleans, LA, January 15–17, 1979.

3. Weed, R. A.; Anderson, W. K.; and Carlson, L. A.: A Direct-Inverse Three-Dimensional Transonic Wing Design Method for Vector Computers, AIAA Paper 84–2156, AIAA 2nd Applied Aerodynamics Conference, Seattle, WA, August 21–23, 1984.

4. Volpe, G: Inverse Design of Airfoil Contours: Constraints, Numerical Method, and Applications, Paper No. 2, AGARD Specialists Meeting on Computational Methods for Aerodynamic Design (Inverse) and Optimization, Loen, Norway, May 22–24, 1989.

5. Takanashi, S.: Iterative Three-Dimensional Transonic Wing Design Using Integral Equations, Journal of Aircraft, Vol. 22, No. 8, August 1985, pp. 655–660.

6. Mani, K. K.: Design Using Euler Equation, AIAA Paper 84–2166, AIAA 2nd Applied Aerodynamics Conference, Seattle, WA, August 21–23, 1984.

7. Giles, M. B.; and Drela, M.: Two-Dimensional Transonic Aerodynamic Design Method, AIAA Journal, Vol. 25, No. 9, September 1987, pp. 1199–1205.

8. Risk, M. H.: Applications of Single Cycle Optimization Approach to Aerodynamic Design, AIAA Paper 84–2165, AIAA 2nd Applied Aerodynamics Conference, Seattle, WA, August 21–23, 1984.

9. Hirose, N.; Takanashi, S.; and Kawai, N.: Transonic Airfoil Design Procedure Utilitizing a Navier-Stokes Analysis Code, AIAA Journal, Vol. 25, No. 3, March 1987, pp. 353–359.

10. Jameson, A.: Airfoil Design Via Control Theory, Paper No. 22, AGARD Specialists Meeting on Computational Methods for Aerodynamic Design (Inverse) and Optimization, Loen, Norway, May 22–24, 1989.

11. Garabedian, P.; and McFadden, G.: Design of Supercritical Swept Wings, AIAA Journal, Vol. 20, No. 3, March 1982, pp. 289–291.

12. Malone, J. B.; Vadyak, J.; and Sankar, L. N.: A Technique for the Inverse Aerodynamic Design of Nacelles and Wing Configurations, AIAA Paper 85–4096, Oct. 1985 (see also, Journal of Aircraft, Vol. 24, No. 1, January 1987, pp. 8–9.

13. Hazarika, N.: An Efficient Inverse Method for the Design of Blended Wing-Body Configurations, Ph.D. Thesis, Georgia Institute of Technology, June 1988.

14. Malone, J. B.; Narramore, J. C.; and Sankar, L. N.: An Efficient Airfoil Design Method Using the Navier-Stokes Equations, Paper No. 4, AGARD Specialists Meeting on Computational Methods for Aerodynamic Design (Inverse) and Optimization, Loen, Norway, May 22–24, 1989.

15. Birckelbaw, L.: Inverse Airfoil Design Using the Navier-Stokes Equations, AIAA Paper 89–2202, AIAA 7th Applied Aerodynamics Conference, Seattle, WA, July 31–August 2, 1989.

16. Jolly, B.: Private Communication, Wright Laboratories, WPAFB, January 1991.

17. Swanson, R. C.; and Turkel, E.: A Multistage Time-Stepping Scheme for the Navier-Stokes Equations, AIAA Paper 85–0035, AIAA 23rd Aerospace Sciences Meeting, Reno, NV, January 14–17, 1985.

18. Swanson, R. C.; and Turkel, E.: Artificial Dissipation and Central Difference Schemes for the Euler and Navier-Stokes Equations, AIAA Paper 87–1107, AIAA 8th Computational Fluid Dynamics Conference, Honolulu, HW, June 9–11, 1987.

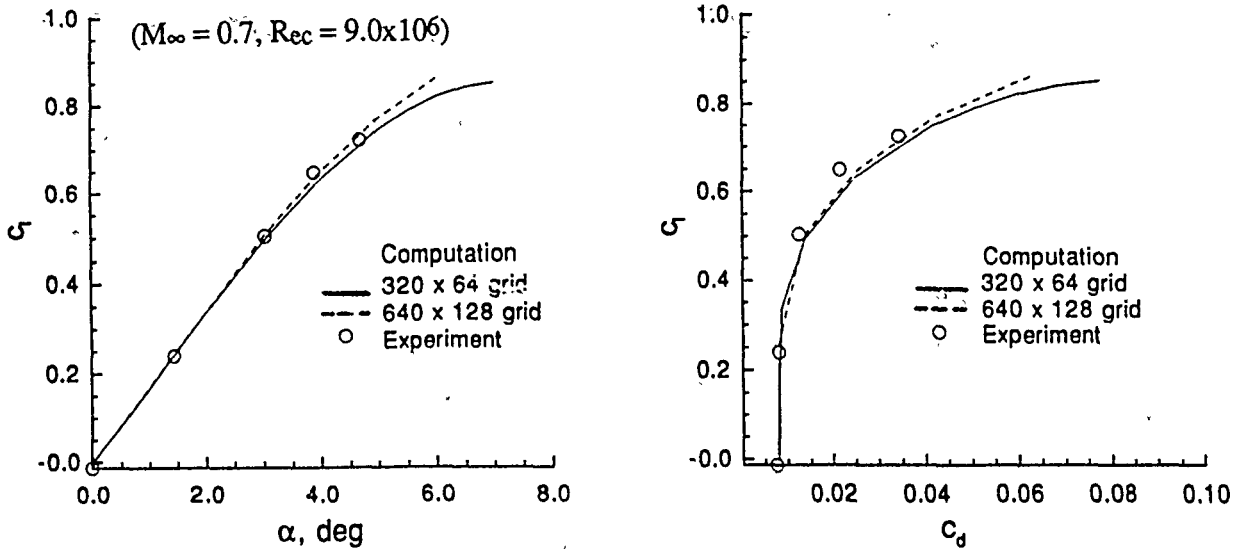
19. Swanson, R. C.; and Radespiel, R.: Cell Centered and Cell Vertex Multigrid Schemes for the Navier-Stokes Equations, AIAA Journal, Vol. 29, No. 5, May 1991, pp. 697–703..

20. Davis, W. H.: Technique for Developing Design Tools from Analysis Methods of Computational Aerodynamics, AIAA Paper 79–1529, AIAA 12th Fluid and Plasma Dynamics Conference, Williamsburg, VA, July 23–25, 1979.

21. Anderson, D. A.; Tannehill, J. C.; and Pletcher, R. H.: Computational Fluid Mechanics and Heat Transfer, McGraw-Hill Book Company, 1984.

22. Malone, J. B.: Subsonic Panel Method for Iterative Design of Complex Aircraft Configurations, Journal of Aircraft, Vol. 19, No. 10, October 1981, pp. 820–825.

Third International Conference on Inverse Design Concepts and Optimization in Engineering Sciences (ICIDES-III), Editor: G.S. Dulikravich, Washington D.C., October 23-25, 1991.



(a) Lift curve (b) Drag polar

Figure 1. Variation of lift and drag coefficients for NACA 0012 airfoil

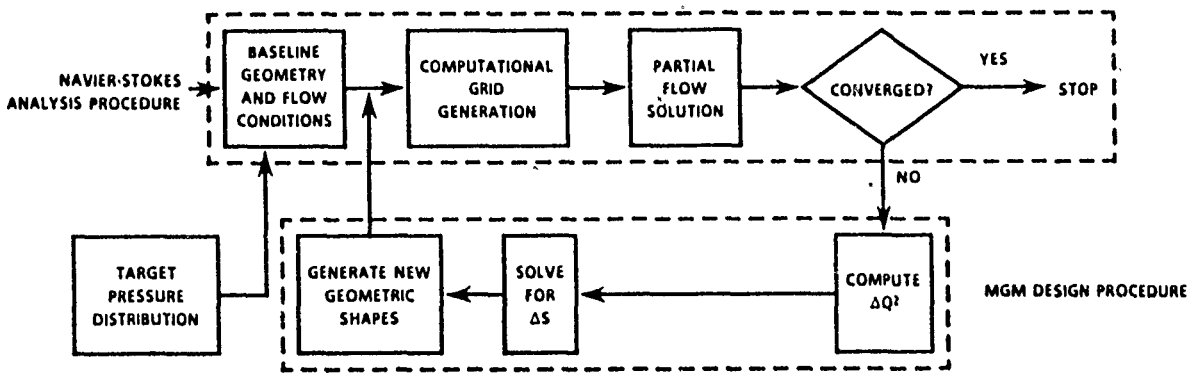


Figure 2. Implementation of the MGM Inverse Design Algorithm

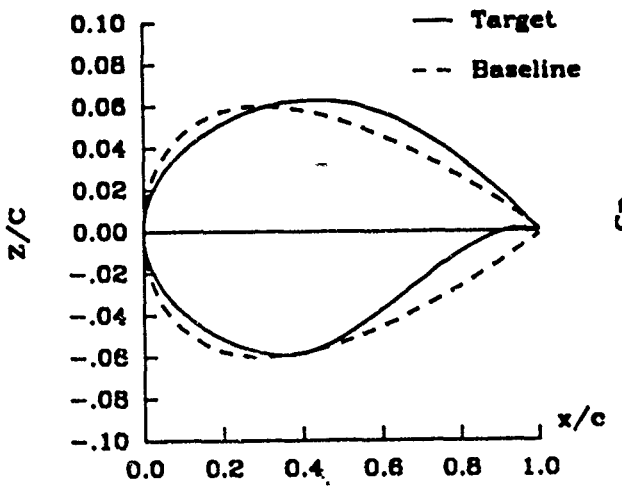


Figure 3. Comparison of target and baseline airfoil contours for case no. 1

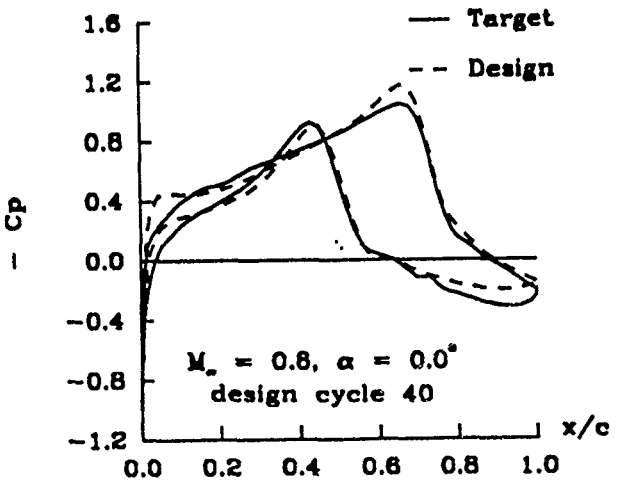


Figure 4. Comparison of target and inverse airfoil pressures for case no. 1

Third International Conference on Inverse Design Concepts and Optimization in Engineering Sciences
(ICIDES-III), Editor: G.S. Dulikravich, Washington D.C., October 23-25, 1991.

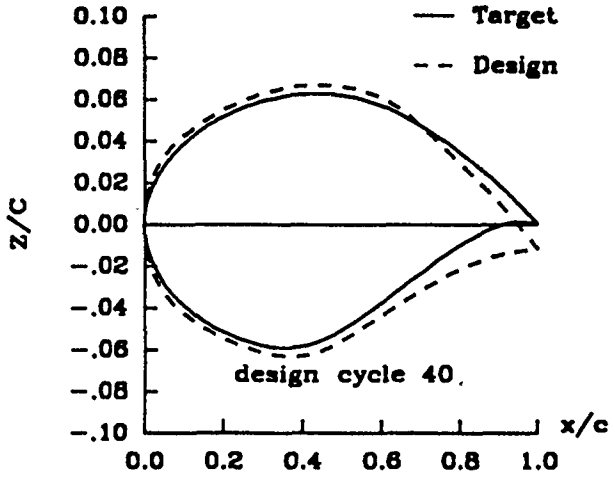


Figure 5. Comparison of target and inverse airfoil contours for case no. 1

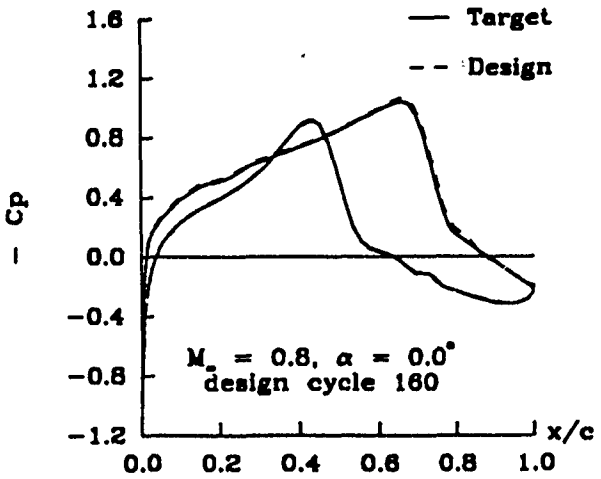


Figure 6. Comparison of target and inverse airfoil pressures for case no. 1

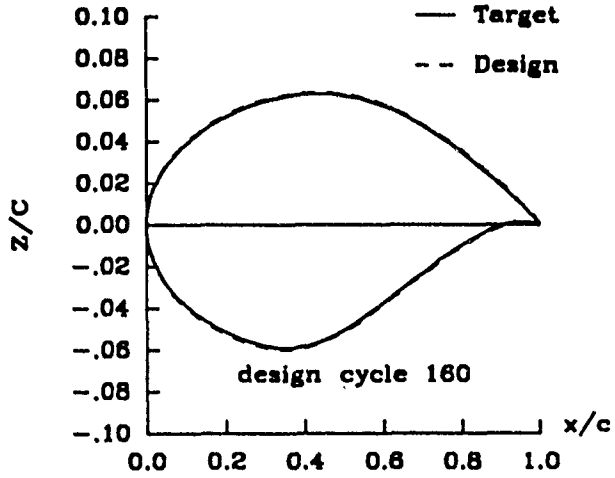


Figure 7. Comparison of target and inverse airfoil contours for case no. 1

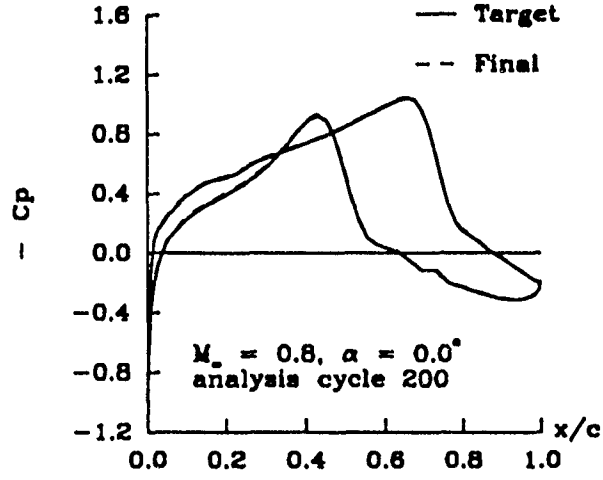


Figure 8. Comparison of target and final airfoil pressures for case no. 1

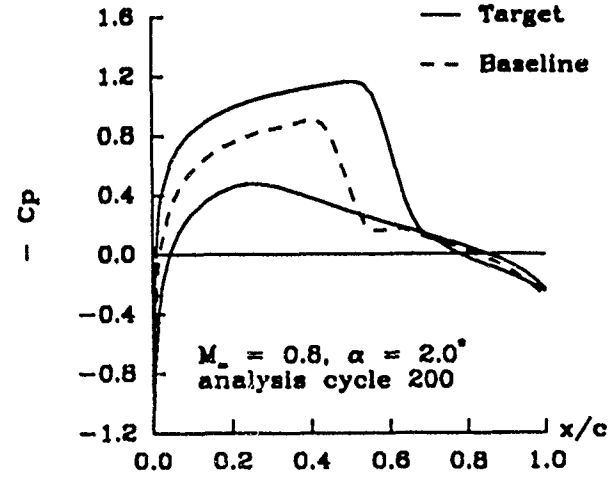


Figure 9. Comparison of target and baseline airfoil pressures for case no. 2

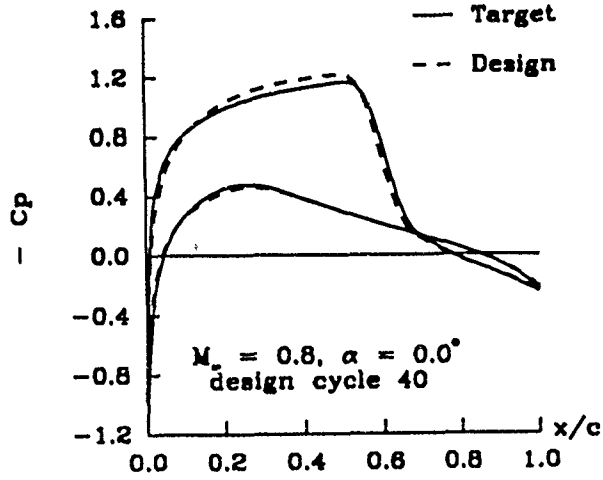


Figure 10. Comparison of target and inverse airfoil pressures for case no. 2

Third International Conference on Inverse Design Concepts and Optimization in Engineering Sciences (ICIDES-III), Editor: G.S. Dulikravich, Washington D.C., October 23-25, 1991.

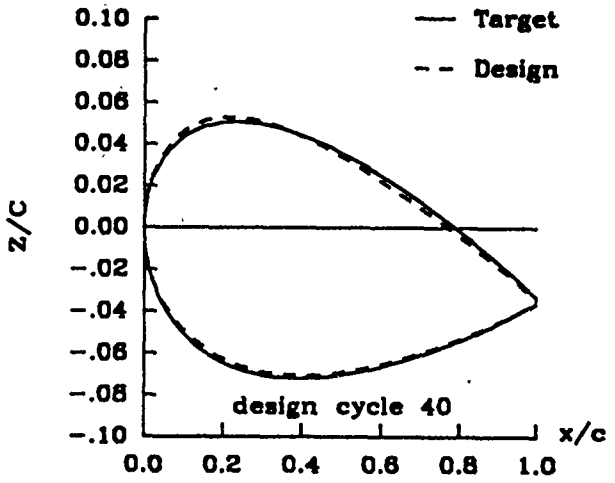


Figure 11. Comparison of target and inverse airfoil contours for case no. 2

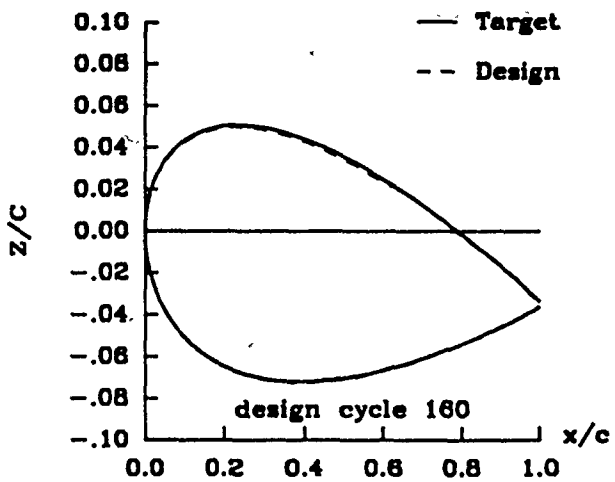


Figure 12. Comparison of target and inverse airfoil contours for case no. 2

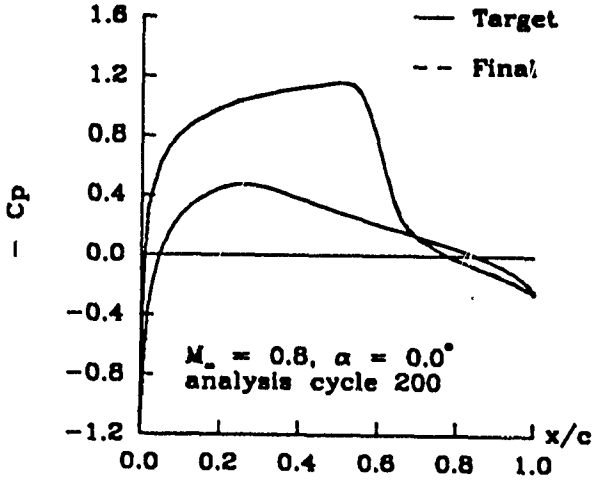


Figure 13. Comparison of target and final airfoil pressures for case no. 2

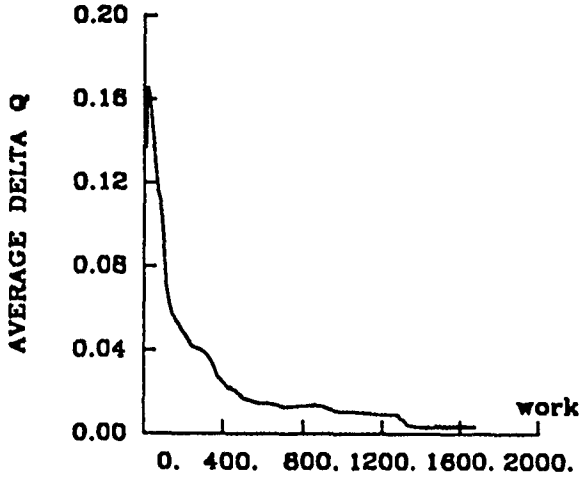


Figure 14. Average Δq^2 versus multigrid work performed for case no. 2

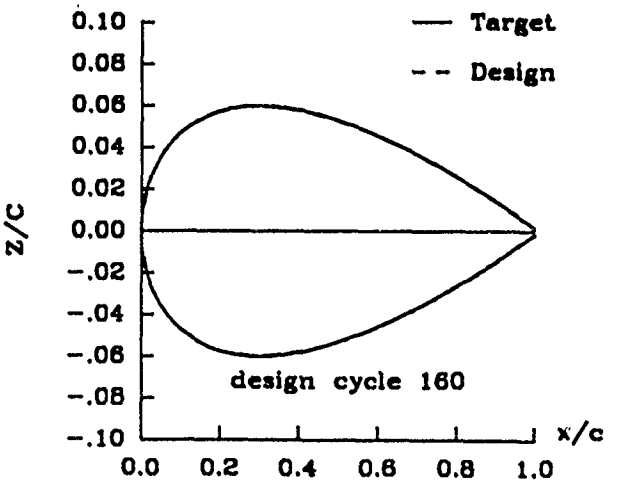


Figure 15. Comparison of target and inverse airfoil contours for case no. 3

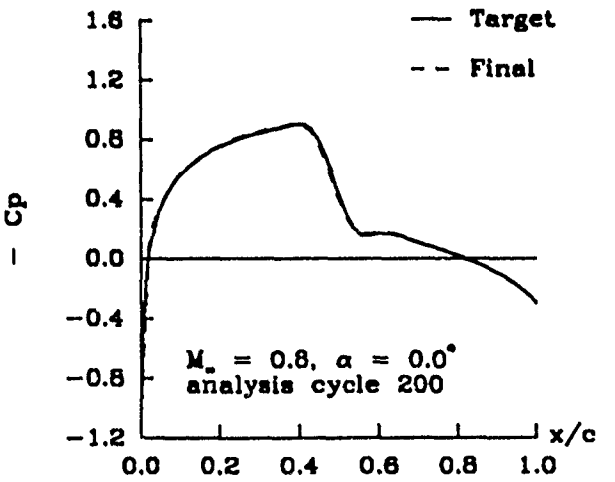


Figure 16. Comparison of target and final airfoil pressures for case no. 3

Third International Conference on Inverse Design Concepts and Optimization in Engineering Sciences (ICIDES-III), Editor: G.S. Dulikravich, Washington D.C., October 23-25, 1991.

A COMPARISON OF TWO CLOSELY-RELATED APPROACHES TO AERODYNAMIC DESIGN OPTIMIZATION

G. R. Shubin and P. D. Frank
Boeing Computer Services
P.O. Box 24346, Mail Stop 7L-21, Seattle, WA. 98124–0346

1. ABSTRACT

The objective of this paper is to compare two closely-related methods for aerodynamic design optimization. The methods, called the "implicit gradient" approach and the "variational" (or "optimal control") approach, both attempt to obtain gradients necessary for numerical optimization at a cost significantly less than that of the usual black-box approach that employs finite difference gradients. While the two methods are seemingly quite different, they are shown to differ (essentially) in that the order of discretizing the continuous problem, and of applying calculus, is interchanged. Under certain circumstances, the two methods turn out to be identical. We explore the relationship between these methods by applying them to a model problem for duct flow that has many features in common with transonic flow over an airfoil. We find that the gradients computed by the variational method can sometimes be sufficiently inaccurate to cause the optimization to fail.

2. INTRODUCTION

We first define what we mean by "analysis" and "design" in the context of computational aerodynamics. In the "analysis problem" we seek to determine the aerodynamic flow, given a description of the geometry of an airfoil or aircraft. In the "design problem" we seek to do the inverse; given the flow, find the geometry that will produce it. Here, we are concerned with methods for solving the design problem that are based on coupling solutions of the discretized analysis problem with numerical optimization procedures.

In a previous paper [4] we compared three optimization-based approaches for solving computational aerodynamics design problems. (Actually, the methods apply to many computational physics design optimization problems.) The optimization methods are (i) the common "black-box" method with finite difference gradients, (ii) a modification where the gradients are found by an algorithm based on the implicit function theorem (hereafter called the implicit gradient approach), and (iii) an "all-at-once" method where the flow and design variables are simultaneously altered. We also showed that the implicit gradient approach was very closely related to a particular "variational" or "optimal control" approach to design optimization that has recently attracted interest (e.g., [5]). The purpose of the present paper is to further explore this relationship. (We note that the close relationship between nonlinear optimization and optimal control has apparently been known for some time[2][6]. However, this relationship appears to be little-known among practitioners in applications disciplines utilizing these mathematical techniques.)

The finite difference approach to obtaining gradients is conceptually the simplest, but it is ordinarily prohibitively expensive for practical problems, since it requires at least one solution of an analysis problem for each design parameter. Both the implicit gradient approach and the variational approach have the objective of determining gradients needed in an optimization

procedure at a significantly reduced cost. Both approaches involve using "calculus-like" operations to derive the formulas employed in finding the gradients. As explained later, the procedures differ in that the order of applying calculus, and of discretizing the continuous problem, are interchanged. Because the implicit gradient approach applies to an already discretized analysis problem, it can be used to "retrofit" many analysis codes to produce inexpensive gradients for design optimization; see [7] for details.

3. MODEL PROBLEM

3.1 Continuous Analysis Problem

In [4] we showed how the steady flow of an inviscid fluid in a duct of variable cross-sectional area $A(\xi)$, governed by the Euler equations, can (under certain circumstances) be reduced to the single nonlinear ordinary differential equation

$$f_\xi + g = 0 \tag{1}$$

where

$$f(u) \equiv u + \bar{H}/u, \qquad g(u,\xi) \equiv \frac{A_\xi}{A}(\bar{\gamma}u - \bar{H}/u),$$

$u(\xi)$ is the fluid velocity, ξ is distance along the duct, and $\bar{\gamma}$ and $\bar{H}$ are given constants. Here, the subscript ξ means differentiation with respect to ξ. While a much more careful specification was given in [4], roughly speaking the continuous analysis problem is to find u, given a differentiable area function $A(\xi)$ and the specified boundary values $u(\xi = 0)$ and $u(\xi = 1)$. These boundary values are chosen so that the (weak) solution of (1) contains a shock.

3.2 Discrete Analysis Problem

Let the ξ-coordinate be discretized by a uniform, cell-centered grid with centers at $\xi_j = (j - 1/2)h$, $\Delta\xi = 1/J$, where J is the number of unknown grid values. Let U_j represent a piecewise constant approximation to u on each grid cell. Then, a conservative difference scheme for (1) is given by

$$W_j \equiv \frac{f_{j+1/2} - f_{j-1/2}}{\Delta\xi} + g_j = 0. \tag{2}$$

Here the source term $g_j = g(U_j, (A_\xi/A)_j)$ and we assume that the duct shape $A(\xi)$ is given by a piecewise cubic spline described in the B-spline basis with coefficients D_m for $m = 1, 2, \ldots, M$ and that $A(0)$ and $A(1)$ are fixed. $(A_\xi/A)_j$ is obtained by evaluating the spline and its derivative at ξ_j. The boundary conditions on U are $U_0 = u(\xi = 0)$ and $U_{J+1} = u(\xi = 1)$. The fluxes $f_{j+1/2}$, as functions of U_j and U_{j+1}, are chosen to correspond to the Godunov, Engquist-Osher, or Artificial Viscosity methods for numerically approximating hyperbolic conservation laws [4].

Once the discretization has been made, we are faced with solving a system of nonlinear algebraic equations. The system is

Given: D_m, $m = 1, \ldots, M$ (spline coefficients describing $A(\xi)$).
Find: U_j satisfying

$$W(U) = 0. \tag{3}$$

Third International Conference on Inverse Design Concepts and Optimization in Engineering Sciences (ICIDES-III), Editor: G.S. Dulikravich, Washington D.C., October 23-25, 1991.

Here W is the vector of discretized equations (2) for $j = 1, 2, \ldots, J$ and the boundary conditions on U.

3.3 Continuous Design Problem

We want to formulate the design problem as a minimization problem. It is:

Given: a desired (or goal) velocity $\hat{u}(\xi)$.
Let: $h(u) = \frac{1}{2}(u(\xi) - \hat{u}(\xi))^2, \mathfrak{f}(u) = \int_0^1 h(u)d\xi$.
Find: $A(\xi)$ such that $u(\xi)$ satisfies (1) and $\mathfrak{f}(u)$ is minimized.

3.4 Discrete Design Problem

We assume that a desired (or goal) velocity distribution $\hat{U}_j$ is given for each computational cell in the analysis problem. Then we have

Given: $\hat{U}_j, \quad j = 1, \ldots, J$.
Let: $H_j = \frac{1}{2}(U_j - \hat{U}_j)^2, F(U) = \sum_{j=1}^{J} H_j$.
Find: $D_m, \quad m = 1, 2, \ldots, M$ (spline coefficients describing $A(\xi)$) such that (3) is satisfied and $F(U)$ is minimized.

4. COMPARISON OF THE IMPLICIT GRADIENT APPROACH AND THE VARIATIONAL APPROACH

In this section, we compare two closely-related, optimization-based approaches to finding an approximate solution to the "Continuous Design Problem" posed above. In each case, function values needed in the optimization are obtained by solving a discrete analysis problem and evaluating a discrete form of the objective function (and constraints). The key question is how gradients needed in the optimization are computed:

1. **Implicit gradient approach.** Discretize the problem first to obtain the "Discrete Design Problem," then find a formula for the gradients by using the implicit function theorem.
2. **Variational (or control theory) approach.** Find a formula for the "gradients" for the continuous problem (i.e., in infinite dimensional space). This formula involves the solution of the analysis problem, and the solution of another differential equation called the adjoint problem. Discretize both the forward and adjoint problems, then evaluate the formula to get the gradient.

After the gradients are obtained, the function values and gradients are used in an optimization procedure to improve the current estimate of the design variables. As can be seen, these approaches differ, essentially, in that the order of discretizing, and of doing calculus-like operations, is interchanged.

4.1 Implicit Gradient Approach

The implicit gradient approach is a natural extension of the usual black-box method wherein gradients needed in the optimization are obtained by finite differences. We thus first introduce the black box method. We do so in a somewhat general setting, then specialize to the model problem.

We assume that the design problem has already been discretized. Let n_U and n_D be the number of flow variables U and design variables D, respectively. (In the duct flow model

Third International Conference on Inverse Design Concepts and Optimization in Engineering Sciences (ICIDES-III), Editor: G.S. Dulikravich, Washington D.C., October 23-25, 1991.

problem, the flow variables are the velocities, and the design variables are the spline coefficients describing the geometry.) Then we seek to solve

$$\begin{aligned} &\text{minimize } F(D) \ , \\ &D \in \mathbf{R}^{n_D} \\ &\text{subject to } C(D) \geq 0 \ , \end{aligned} \tag{4}$$

where $F(D)$ is the objective function and $C(D)$ is a vector of m_D constraint functions. In the black-box method, each evaluation of $F(D)$ requires a solution by the analysis code.

For simplicity, the unconstrained version of (4) is considered below. However, the results apply to the constrained problem as well.

As in our model problem, the function F will often be formulated in terms of the flow variables U. In this situation, F is dependent on the design variables D in an indirect manner. That is, the flow variables U are linked to the design variables D via the discretization of the differential equations, since the flow variables will change when the geometry is altered. In the general case, F will have both a direct dependence on D and an indirect dependence on D, due to the dependence of U on D. Thus, one could consider the objective function to be $F(U(D), D)$. The term $U(D)$ indicates that, given D, the value of U is obtained by solving an analysis problem.

Assume that the analysis problem has been discretized (as in Section 3.2) so that an analysis consists of solving a system of nonlinear equations. In this case function evaluations for the black-box method are computed as follows. Given a design specified by D, the analysis code solves $W(U) = 0$, where U is the vector of n_U flow variables and W is a vector of n_U nonlinear equations. Since the analysis problem is an implicit function of D it can be viewed as solving

$$W(U, D) = 0 \tag{5}$$

for U, given a design specified by D. When gradients are obtained by finite differences, each component of D is successively perturbed, and (5) is re-solved to get a perturbed value of U.

We now review how gradients can be obtained without recourse to finite differences. Suppose that U and D are considered as subsets of the $n_U + n_D$ vector X given by

$$X \equiv (\ U \ \mid D); \tag{6}$$

the Jacobian (first-derivative) matrix of (5) is then

$$J = \left[\begin{array}{c|c} & \\ J_U & J_D \\ & \end{array} \right] , \tag{7}$$

where J is $n_U \times (n_U + n_D)$, J_U is the $n_U \times n_U$ Jacobian with respect to the flow variables and J_D is the $n_U \times n_D$ Jacobian with respect to the design variables. (The partitioned view of the Jacobian implies $n_U \gg n_D$; this will usually be the case.) Note that J_U is sometimes available in analysis codes, especially those based on Newton's method and variants. J_D may, or may not, be easily obtainable. (The availability of J_U and J_D in computational aerodynamics codes is discussed in [7].)

Consider the function $\tilde{F}(U, D)$, where $\tilde{F}$ is the same as the black-box method objective function F, except that U and D are considered to be *independent* of each other. The function $\tilde{F}(U, D)$ is then equivalent to the black-box method objective function $F(U(D), D)$ only when

Third International Conference on Inverse Design Concepts and Optimization in Engineering Sciences (ICIDES-III), Editor: G.S. Dulikravich, Washington D.C., October 23-25, 1991.

(5) is satisfied. The gradients $\nabla_D \tilde{F}(X)$ and $\nabla_U \tilde{F}(X)$ are ordinarily "easy" to obtain because of the assumed independence.

However, the optimization code requires $\nabla_D F$, the gradient of the black-box objective function F with respect to the design variables D. As shown in [4], this gradient is given by

$$\nabla_D F(X) = \nabla_D \tilde{F}(X) - J_D^T J_U^{-T} \nabla_U \tilde{F}(X) . \tag{8}$$

Here, superscript T indicates transpose. The derivation of (8) assumes that we are at a solution of (5).

The following algorithm could be used for computing $\nabla_D F$ using (8):

i. Compute $\nabla_U \tilde{F}$ and $\nabla_D \tilde{F}$
ii. Solve $J_U^T \Lambda = -\nabla_U \tilde{F}$ for Λ
iii. Compute $\nabla_D F = \nabla_D \tilde{F} + J_D^T \Lambda$.

Note that the minus sign is associated with the second step of the algorithm to facilitate comparison with the variational approach later. Note also that, if it is difficult to solve linear systems with the matrix J_U^T, the linear algebra in (8) can be rearranged as $(J_U^{-1} J_D)^T \nabla_U \tilde{F}(X)$, requiring n_D solves with J_U. Observe that $J_U^{-1} J_D$ is the matrix of "sensitivities" of the solution U with respect to the design variables D.

We now apply this algorithm to the model problem and give a complete specification of one evaluation of a gradient during the optimization.

Implicit gradient algorithm for model problem:

1. Given the current estimate of the design variables D_m, solve the discrete analysis problem (3).
2. Compute $\nabla_U \tilde{F} = U - \hat{U}$ and $\nabla_D \tilde{F} = 0$.
3. Given the Jacobian J_U of the discretized flow equations with respect to the flow variables U, evaluated at the solution, solve $J_U^T \Lambda = -(U - \hat{U})$ for Λ
4. Given the Jacobian J_D of the discretized flow equations with respect to the design variables D, evaluated at the solution, compute the gradient $\nabla_D F = J_D^T \Lambda$

4.2 Variational Approach

In the variational approach, we deal first with the "Continuous Design Problem," and use calculus to derive an infinite dimensional "gradient." We then discretize the problem. Since it is somewhat cumbersome to present the methodology for a general case, we specialize to the model problem immediately.

For technical reasons that will become apparent later, it is desirable to augment the governing differential equation (1) with an artificial viscosity term $\epsilon u_{\xi\xi}$, giving

$$w(u, d) = -\epsilon u_{\xi\xi} + f_\xi + g(u, d) = 0. \tag{9}$$

Here, $d(\xi)$ is a function that controls A_ξ / A.

Recalling that $h(u) = \frac{1}{2}(u(\xi) - \hat{u}(\xi))^2$, the Lagrangian is

$$L = \int_0^1 h(u) d\xi + \int_0^1 \lambda(\xi) w(u, d) d\xi,$$

Third International Conference on Inverse Design Concepts and Optimization in Engineering Sciences (ICIDES-III), Editor: G.S. Dulikravich, Washington D.C., October 23-25, 1991.

and $\lambda(\xi)$ is an adjoint function that is the continuous analogue of Lagrange multipliers. Applying the calculus of variations, and doing the usual integration-by-parts, we find that the variation of the Lagrangian is

$$\delta L = [-\epsilon(\lambda \delta u_\xi - \lambda_\xi \delta u) + \delta(\lambda f)]_0^1$$

$$+ \int_0^1 (-\epsilon \lambda_{\xi\xi} - f_u \lambda_\xi + g_u \lambda + h_u)\delta u d\xi + \int_0^1 \lambda w_d (\delta d) d\xi.$$

(Note $w_d = g_d$.) The second term can be made to vanish by requiring that the adjoint equation

$$-\epsilon \lambda_{\xi\xi} - f_u \lambda_\xi + g_u \lambda = -h_u \tag{10}$$

be satisfied. In (10), f_u, g_u, and h_u are given functions of ξ, since they are evaluated at $u(\xi)$, the solution of (9). The integrated term $[\ ]_0^1$ vanishes since $\delta u(0) = \delta u(1) = 0$ and we choose $\lambda(0) = \lambda(1) = 0$ as the boundary conditions on the adjoint λ. Then, the "gradient" of the continuous design problem with respect to changes in the controlling function d is expressed by the variational formula

$$\delta \mathfrak{f} = \int_0^1 \lambda w_d (\delta d) d\xi. \tag{11}$$

We now need to discretize (9), (10), and (11). We assume that (9) is discretized by one of the methods described in Section 3.2. Thus, the discretization of the analysis problem is assumed here to be the same as for the implicit gradient approach. (In general, of course, this need not be so.) While those discretizations (the G-, EO, and AV-schemes) are designed to solve the inviscid ($\epsilon = 0$) equation, they in fact all incorporate some kind of artificial viscous effects, either by upwinding (G and EO) or by explicit artificial viscosity (AV). That is why we added the viscous term in (9): so it would appear in equation (10), and thus guide us to reasonable discretizations of the adjoint equation.

Let the computational grid be as described in Section 3.2, and Λ_j be the approximation to λ on the grid. Noting that $h_u = u - \hat{u}$, let us take the discretization of the (10) to be given by

$$B\Lambda = -(U - \hat{U}),$$

where the difference operator B remains to be specified. Note that this equation is linear in Λ since (10) is linear in λ.

Finally, to discretize (11) we could use any reasonable quadrature formula. However, we choose to use the rectangle rule, which gives for the k-th component of the gradient

$$(\nabla_D F)_k = \sum_{j=1}^{J} (W_j)_{D_k} \Lambda_j.$$

Here, $(W_j)_{D_k}$ is the derivative of the $j-$th discrete flow equation with respect to the $k-$th design variable. In matrix notation, this is none other than

$$\nabla_D F = J_D^T \Lambda,$$

so we have again deliberately chosen the discretization to agree with Step 4 of the implicit gradient algorithm.

Gathering these pieces together, a complete specification of one evaluation of a gradient in an optimization procedure is given below.

Variational algorithm for model problem:

1. Given the current estimate of the design variables D_m, solve the discrete analysis problem (3)
2. Compute $\nabla_U \tilde{F} = U - \hat{U}$ and $\nabla_D \tilde{F} = 0$.
3. Solve the discrete adjoint equation $B\Lambda = -(U - \hat{U})$ for Λ
4. Given the Jacobian J_D of the discretized flow equations with respect to the design variables D, evaluated at the solution, compute the gradient $\nabla_D F = J_D^T \Lambda$

As we have constructed this algorithm, it differs from the implicit gradient algorithm only in step 3. The two procedures are *identical* if we choose $B = J_U^T$, the transpose of the Jacobian of the analysis problem, evaluated at a solution of the analysis problem. Looked at another way, a particular choice of a discretization of the analysis problem, and the associated Jacobian J_U, suggests a specific choice of the discretization B of the adjoint problem, namely $B = J_U^T$. Pursuing this idea, let $(J_U)_G$,$(J_U)_{EO}$, and $(J_U)_{AV}$ denote the Jacobians associated with the G, EO, and AV schemes for the analysis problem, respectively. Then three possible discretizations of the adjoint are given by $B = (J_U)_G^T$,$B = (J_U)_{EO}^T$, and $B = (J_U)_{AV}^T$. We note that two of these, $(J_U)_G^T$ and $(J_U)_{EO}^T$, do not correspond to obvious discretizations of the adjoint equation (10). This is largely due to the careful treatment of "sonic points" (points where $f_u = 0$) and shocks in the G and EO schemes.

Let us call the discretizations of the forward and adjoint problems *incompatible* if $B \neq J_U^T$. This means that the discrete analysis problem and the discrete adjoint problem are *not discretely adjoint*. It is precisely the effect of such incompatibility that we want to test. Thus, to carry out such tests we may solve the forward problem with (say) the G-scheme, but choose the adjoint discretization to be $B = (J_U)_{EO}^T$. Such comparisons will be pursued in the Numerical Results section, below. There, we will use the notation $[G, (J_U)_{EO}^T]$ to refer to such a combination.

We may also look at (10) directly and ask "what is a good way to discretize this differential equation?" It turns out that, for our model and test cases, f_u changes sign once, and $g_u > 0$. For small ϵ, (10) is thus a singular perturbation, two-point boundary value problem with a turning-point. A good numerical method for such problems is the El-Mistakawy–Werle scheme; a complete specification of this scheme, and an analysis which applies directly to the cases tested below, is given in [1]. That analysis shows that, for our test cases, the adjoint function λ is "smooth" in the interior of the domain and has boundary layers at both ends. We will refer to this scheme for solving (10) as the EMW scheme. (In the results presented later, we took $\epsilon = 10^{-5}$ and used linear interpolation to move between the "point-centered" grid natural to the EMW scheme and the "cell-centered" grid used in the analysis solvers.)

4.3 What is the "correct" gradient?

When we use the variational formulation described above, and we choose B to be anything other than J_U^T, we will obtain a gradient different from the one obtained by the implicit gradient approach. This raises the issue of which gradient is "correct." There are two different philosophical points of view. The first holds that, since we are really computing an approximation to the continuous design problem, both gradients represent different approximations to the "continuous gradient," and hence neither is correct. The second holds that, irrespective of the continuous problem, our goal in computation is to solve the discrete design problem. We are more inclined to adopt the second point of view. Thus, we feel that (modulo finite precision arithmetic) the

Third International Conference on Inverse Design Concepts and Optimization in Engineering Sciences (ICIDES-III), Editor: G.S. Dulikravich, Washington D.C., October 23-25, 1991.

implicit gradient is the correct one, and that the variational formulation only yields the correct gradient when the particular discretization of the adjoint represented by $B = J_U^T$ is chosen.

5. NUMERICAL RESULTS

In this section we present numerical results obtained by solving the discrete design problem for duct flow described in Section 3, utilizing gradients computed by the implicit gradient and variational methods of Section 4. As constructed in Section 4, these methods differ only in step three of the algorithms, and they are identical if in step three of the variational algorithm we choose $B = J_U^T$, the transpose of the Jacobian of the discrete analysis problem with respect to the flow variables. The specific algorithm used below is thus specified by the choice of B. We will first outline the optimization methods and test cases used. Then we will report on some tests using controlled amounts of gradient error, and compare the implicit gradient and variational methods.

5.1 Optimization Methods

The basic optimization code used was NPSOL version 2.0, a product of the Systems Optimization Laboratory, Stanford University. NPSOL is an implementation of the Sequential Quadratic Programming (SQP) method. NPSOL 2.0 computes a secant approximation to the Hessian (2nd derivative) matrix and the user supplies first derivatives. Results obtained with an optimization method similar to steepest descent are not reported here, but may be found in [8].

5.2 Test Cases

For our tests, the design variables (called D in Section 4) were the B-spline coefficients describing the duct geometry $A(\xi)$. The two end values of A were fixed at $A(0) = 1.050$ and $A(1) = 1.745$. Velocities along the duct were the flow variables (called U in Section 4) for the duct design problem. We took $J = 40$ grid cells, so there were $n_U = 40$ flow variables; this gives resolution about equal to what might be expected in practical computations. The boundary conditions were $U_0 = 1.299$ and $U_{41} = 0.506$. In the optimization runs Newton's method was used to solve the analysis problem (3), and the analyses were "warm started." That is, the initial guesses for the flow velocities were taken to be the solutions from the preceding analysis. The initial velocity profile for the first analysis in an optimization run was a linear profile connecting the boundary conditions. The goal velocities $\hat{U}_j$ were the evaluations on the computational grid of the analytic solution for a goal duct shape with a cross-sectional area given by a sinusoidal perturbation of the linear duct. These area and velocity profiles are the curves marked (X) in Figure 1. No constraints were imposed in these tests. Without constraining the geometry, it is possible for the optimizer to generate designs that cannot be analyzed (the analysis problem has no solution). In this case, we assign a large function value and return to the optimizer. The optimizations were allowed a maximum of 70 major iterations, which is considerably more than would be tolerable in practical use. (This corresponds, *very* roughly, to a maximum amount of work equivalent to 1000 linear system solutions with the Jacobian of the analysis problem.)

The majority of the tests were conducted with $n_D = 2$ design variables. For these tests, three initial guesses for the design variables were selected. These three guesses yield solutions of the analysis problem shown in Figure 1. A contour plot showing the dependence of the objective function on the design variables is displayed in Figure 2. (This plot is for the AV-scheme; the plots for the other schemes are similar.) Also shown are the locations of the optimum and of the three initial guesses of D. The contour plot shows a narrow valley with steep sides and a

Third International Conference on Inverse Design Concepts and Optimization in Engineering Sciences (ICIDES-III), Editor: G.S. Dulikravich, Washington D.C., October 23-25, 1991.

relatively flat bottom. Descending the steep sides corresponds (roughly) to getting the shock in the correct location; this has the largest impact on reducing the objective function and is relatively easy for the optimizer. Moving along the valley bottom corresponds to getting the other details of the velocity profile right. This is much harder to do. Thus guess 1 corresponds to a relatively difficult problem, while guesses 2 and 3 correspond to problems that are somewhat easier.

5.3 Controlled gradient error tests.

Since we cannot directly control the gradient errors that are obtained when using incompatible discretizations of the forward and adjoint problems, we first conducted some controlled gradient error tests. In these tests we first obtained the correct gradient using the implicit gradient method, and then added controlled amounts of random error to the gradient. The quantitative results are given in [8]. We were surprised to find that the optimizations began to fail at fairly small amounts (a few percent) of gradient error.

The trust region methods for step size determination in optimization used in [3] apparently worked with a much higher level of relative error in the gradients. However, we found that trust region methods were not much better then line search methods (like in NPSOL) when applied to our model, which is apparently a "harder" problem than many standard optimization test cases.

5.4 Tests comparing the implicit gradient and variational approaches

We now proceed to compare results obtained with the implicit gradient and variational approaches.

The optimizations were run with the twelve combinations of analysis and adjoint solvers shown in Table 1. The discretizations of the analysis problem indicated by G, EO, and AV correspond to the Godunov, Engquist-Osher, and Artificial Viscosity schemes (described in Section 3.2), respectively. The discretizations of the adjoint problem are as described at the end of Section 4.2. Here, the notation $B = (J_U)^T_G$ means, for example, that the discretization of the adjoint differential equation in step 3 of the Variational Algorithm is given by the transpose of the Jacobian of the analysis problem when the Godunov scheme is used. The particular combinations $[G\ (J_U)^T_G]$, $[EO, (J_U)^T_{EO}]$, and $[AV, (J_U)^T_{AV}]$ mean that the forward and adjoint solvers are discretely adjoint, and thus that the implicit gradient method is being used. In all other cases, the analysis and adjoint solvers are incompatible (not discretely adjoint).

The qualitative results of Table 1 show that the only reliable combinations of forward and adjoint solvers are those corresponding to the implicit gradient method. There does not seem to be any other discernible pattern in the results. An examination of more quantitative data, like final value of the objective function and specific amounts of work used, also yield little additional useful information. An examination of the gradients obtained by the variational method (not discretely adjoint) shows that the relative error compared to the correct (implicit) gradient is often more than a few percent, and that the gradients are in error both in direction and magnitude [8].

We carried out many of the same tests with an optimizer more like steepest descent, and also with the objective function "smoothed" by a method suggested by Jameson [5]. Such smoothing should reduce the impact of getting the shock location correct on the objective function. (It broadens the valley of Figure 2.) The necessary modifications to the variational approach are described in [8]. Again, we were unable to discern any pattern in the results: sometimes the modifications helped, sometimes they hurt.

Additional test were carried out with $n_D = 10$ design variables, and the same conclusion was reached: the only reliable combinations of forward and adjoint solvers correspond to the implicit gradient method. That is, the forward and adjoint solvers should be discretely adjoint.

6. CONCLUSIONS

We have shown that two seemingly quite dissimilar approaches to design optimization can, under certain circumstances, be very closely related or even identical. The two approaches, the implicit gradient method and the variational method, both result in gradient calculations that are significantly cheaper than generating gradients by finite differences. The methods differ from each other (essentially) in that the order of discretizing the continuous problem, and of applying calculus, is interchanged. In the implicit gradient approach, the continuous problem is discretized first, and a formula for gradients needed in the optimization is derived by applying the implicit function theorem. In the variational method, calculus is applied first, and one then needs to solve two differential equation problems: the analysis (or forward) problem, and the adjoint problem. If the analysis problem is discretized the same way as for the implicit gradient approach, and if the adjoint is discretized by a method that corresponds to the transpose of the Jacobian of the forward discretization, then the methods are (modulo some details) the same. If the adjoint discretization is taken to be anything else, then the two methods generate different gradients and the variational method gradients are "in error." In our tests using a model for transonic duct flow, the gradient errors were generally small, but were nevertheless sufficient to cause the optimizations to slow down significantly or to fail altogether. For our model problem and optimization method, the only reliable combination of forward and adjoint discretizations is the one corresponding to the implicit gradient method.

7. REFERENCES

[1] Berger, A.E., Han, H., and Kellogg, R.B. A priori estimates and analysis of a numerical method for a turning point problem. *Mathematics of Computation*, 42:465–492, 1984.

[2] Canon, M.D., Cullum Jr., C.D., and Polak, E. *Theory of Optimal Control and Mathematical Programming*. McGraw Hill, 1970.

[3] Carter, R.G. Numerical experience with a class of algorithms for nonlinear optimization using inexact function and gradient information. Technical Report 89-46, ICASE, June, 1989.

[4] Frank, P.D. and Shubin, G.R. A comparison of optimization-based approaches for a model computational aerodynamics design problem. *Journal of Computational Physics*, to appear.

[5] Jameson, A. Aerodynamic design via control theory. Technical Report 88-64, ICASE, November, 1988.

[6] E. Polak. *Computational Methods in Optimization.* Academic Press, 1971.

[7] Shubin, G.R. Obtaining "cheap" optimization gradients from computational aerodynamics codes. Technical Report AMS-TR-164, Boeing Computer Services, June, 1991.

[8] Shubin, G.R. and Frank, P.D. A comparison of the implicit gradient approach and the variational approach to aerodynamic design optimization. Technical Report AMS-TR-163, Boeing Computer Services, April, 1991.

Third International Conference on Inverse Design Concepts and Optimization in Engineering Sciences
(ICIDES-III), Editor: G.S. Dulikravich, Washington D.C., October 23-25, 1991.

8. FIGURES AND TABLES

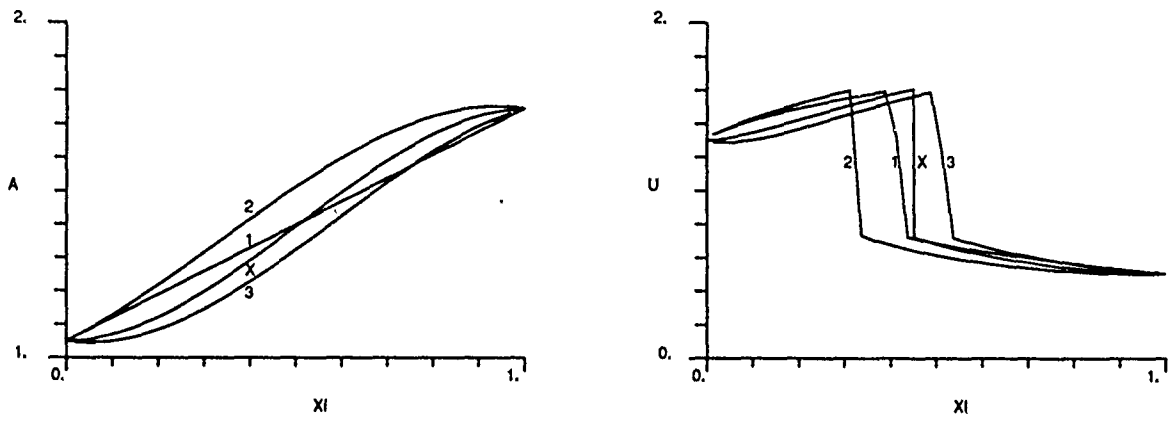


Figure 1: Area function A and corresponding velocity function U for Guesses 1, 2, 3, and optimal solution (X).

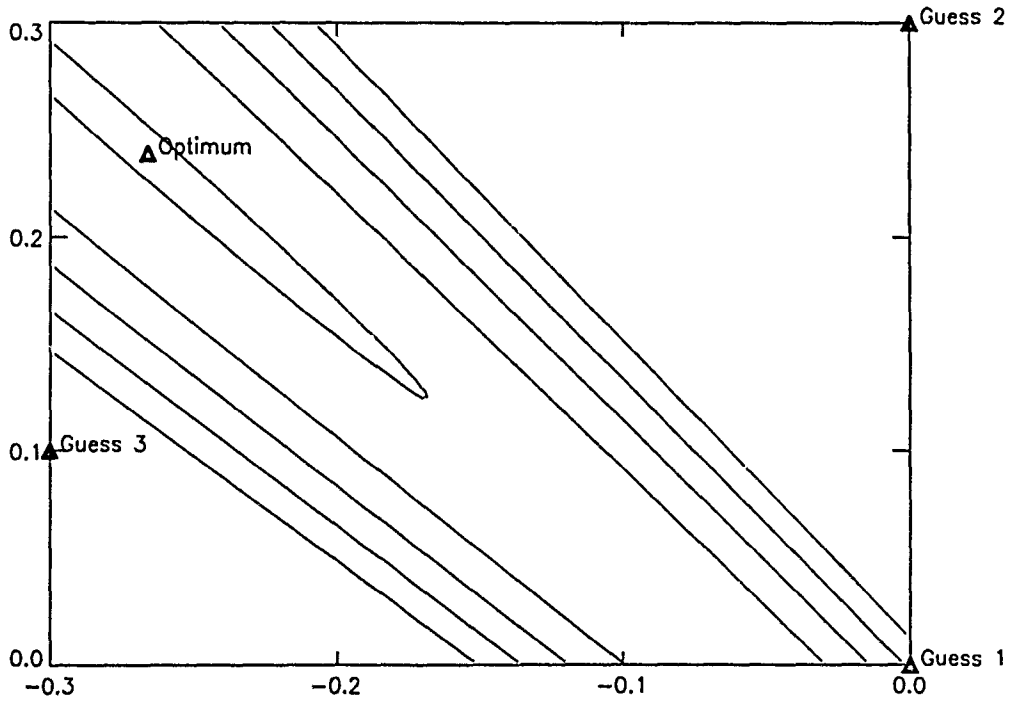


Figure 2: Contour plot of the objective function (for the AV-scheme) showing locations of Guesses 1, 2, 3, and the optimum. The two axes represent the two design variables (B-spline coefficients) describing the area function A

Third International Conference on Inverse Design Concepts and Optimization in Engineering Sciences (ICIDES-III), Editor: G.S. Dulikravich, Washington D.C., October 23-25, 1991.

Optimizer= NPSOL		Adjoint Discretization			
		$B = (J_U)^T_G$	$B = (J_U)^T_{EO}$	$B = (J_U)^T_{AV}$	$B = EMW$
Analysis Discretization	G	+	-	-	0
		+	-	-	-
		+	+	+	0
	EO	-	+	-	0
		-	+	0	0
		0	+	0	0
	AV	0	+	+	-
		-	+	+	0
		-	0	+	0

Table 1: Results obtained using NPSOL as the optimizer, for various combinations of forward and adjoint solvers. In each cell, the three entries correspond to initial guesses 1, 2, and 3 for the design variables. The designation (+) means that the optimization converged to the correct solution. The designation (o) means that the optimization got "close," but did not converge. The designation (-) means that the optimization did not succeed in getting close to the solution.

Third International Conference on Inverse Design Concepts and Optimization in Engineering Sciences (ICIDES-III), Editors: G.S. Dulikravich, Washington D.C., October 23-25, 1991

DESIGN OF THRUST VECTORING EXHAUST NOZZLES FOR REAL-TIME APPLICATIONS USING NEURAL NETWORKS

Ravi K. Prasanth, Research Assistant
Robert E. Markin, Research Assistant
Kevin W. Whitaker, Assistant Professor
Aerospace Engineering Department
The University of Alabama
Tuscaloosa, AL 35487

ABSTRACT

Thrust vectoring is continuing to become an important issue in future military aircraft system designs. A recently developed concept of vectoring aircraft thrust makes use of flexible exhaust nozzles. Subtle modifications in the nozzle wall contours produce a non-uniform flow field containing a complex pattern of shock and expansion waves. The end result, due to the asymmetric velocity and pressure distributions, is vectored thrust. Specification of the nozzle contours required for a desired thrust vector angle (an inverse design problem) has been achieved with genetic algorithms. However, this approach is computationally intensive preventing nozzles from being designed in real-time which is necessary for an operational aircraft system. An investigation was conducted into using genetic algorithms to train a neural network in an attempt to obtain, in real-time, two-dimensional nozzle contours. Results show that genetic algorithm trained neural networks provide a viable, real-time alternative for designing thrust vectoring nozzles contours. Thrust vector angles up to 20° were obtained within an average error of 0.0914°. The error surfaces encountered were highly degenerate and thus the robustness of genetic algorithms was well suited for minimizing global errors.

INTRODUCTION

Future military aircraft will rely heavily on two- and three-dimensional thrust vectoring engines to boost their maneuverability and provide enhanced performance spanning their large operating envelopes. Current new technology engines use post-exit vanes or large moveable surfaces to redirect engine exhaust to yield the desired thrust vectoring. Although this method has proven to be effective, penalties must be paid. For example, most thrust vectoring devices are heavy, primarily due to structural requirements involving the impinging exhaust flow. The devices must also be designed to withstand the extreme temperatures of the engine exhaust gases impinging on them. Control of the vectoring apparatus is complex and adds even more weight to the aircraft. Furthermore, the installation of typical thrust vectoring devices tend to mandate large clearance gaps to allow surface movement and there is little opportunity for aerodynamic fairing. These and other factors can combine to yield higher overall drag forces on the aircraft.

A novel concept of vectoring engine thrust which addresses these concerns has been developed and shown to be viable [1]. The concept makes use of flexible nozzles where engine exhaust gases are turned not by some post-exit apparatus, but by *subtle* changes in the contour of the nozzle walls. The contour modifications produce a complex shock and expansion wave pattern in the nozzle flow field and the end result is vectored engine thrust. Through judicious tailoring of the nozzle contour, a large range of thrust vector angles may be achieved. Theoretical pitch vectoring of ±20° has already been demonstrated with this concept. Full three-dimensional vectoring (pitch, yaw, and roll) is currently being investigated and could possibly eliminate the need for any tail control surfaces on future aircraft. This would result in a tremendous savings in weight and drag as well as a significant reduction in radar cross-section.

This novel approach to thrust vectoring is based entirely on modifying the contour of the exhaust nozzle. In order for the technique to be useful in an operational aircraft system, the nozzle contour must be alterable in real-time. Structural concerns aside, the challenge is to specify, on demand, a nozzle contour for a pilot-requested thrust vector angle. This suggests that modification of the nozzle contour would be tied to the flight control system of the aircraft. What is necessary for the success of such a thrust vectoring system is the real-time solution of an inverse design problem. Simply stated, for a requested thrust vector angle, what would be the required nozzle contour?

Existing Jacobian-based methods for solving an inverse problem of this type are fraught with numerical difficulties and usually require an intense computational effort. A non-Jacobian based method like genetic algorithms can be used to compute the required nozzle contour for a requested thrust vector angle as was proven in a recent study by King, et al. [2]. However, the specification of the nozzle contours still could not be accomplished in real-time using genetic algorithms due to the computational requirements. Genetic algorithms, although they can routinely solve the inverse nozzle design problem (a definite advantage over many Jacobian based methods), still require numerous flow field evaluations to do so.

The hypothesis of the work presented here was that the inverse design problem could be solved in real-time if a non-Jacobian based method (genetic algorithms) was coupled with a neural network. Neural networks are biologically inspired computing systems with the phenomenal ability to grasp topological invariances that underlie inverse transformations. Thus, a neural network has the potential to be trained by a genetic algorithm and then, after sufficient training, would be able to solve the inverse nozzle design problem in real-time. It is important to note that there is no intention to dismiss Jacobian methods; in fact the coupling of a Jacobian method with a neural network to design nozzles is currently under investigation by the authors. In this paper, however, it is demonstrated that by using genetic algorithms, neural networks can be designed to provide an alternative with remarkable dexterity and computational ease for the real-time specification of thrust vectoring exhaust nozzles.

GENETIC ALGORITHM OVERVIEW

Genetic algorithms are increasing in popularity as a search and optimization technique but are still unknown to a large portion of the scientific community. Thus a brief description is in order. Genetic algorithms (GAs) are search algorithms based on the mechanics of genetics; they use operations found in natural genetics to guide their trek through a search space. Their main strength lies in their ability to perform efficiently across a broad spectrum of search problems including problems that are large, noisy, and poorly behaved. Two empirical investigations in the early 1970's demonstrated the technique's efficiency in function optimization [3, 4]. Subsequent application of GA's to the search problems of pipeline engineering, VLSI (very large scale integration) microchip layout, structural optimization, job-shop scheduling, medical image processing, propulsion system component design, and machine learning adds considerable evidence to the claim that GAs are broadly based and robust.

GAs consider many points in a search space simultaneously and therefore have a reduced chance of converging to a local optimum. In most conventional search techniques a single point is considered based on some decision rule. These methods can be dangerous in multi-modal (many peaked) search spaces because they can converge to local optima. However, GAs generate entire populations of points, test each point independently, and then combine qualities from existing points to form a new population containing improved points. Aside from conducting a more global search, the GA's simultaneous consideration of many points makes it highly adaptable to parallel processors since the evaluation of each point is an independent process.

GAs require the natural parameter set of the problem to be coded as a finite length string of characters. This is actually true of all operations performed on a computer at the machine

level, however the GA requires this coding on the local level. The user must represent possible solutions to the search problem as character strings. This may at first seem like an imposing task but there have been a number of techniques developed for coding solutions to search problems [5]. Since GAs work directly with a coding of the parameter set and not the parameters themselves, they are difficult to fool because they are not dependent upon continuity of the parameter space. A GA only requires information concerning the quality of the solution produced by each parameter set (objective function values). This differs from many optimization methods which require derivative information or, worse yet, complete knowledge of the problem structure and parameters. Since GAs do not require such problem-specific information they are more flexible than most search methods.

Lastly, GAs differ from a number of search techniques in that they use random choice to guide their search. Although chance is used to define their decision rules, GAs are by no means "random walks" through the search space. They use random choice efficiently in their exploitation of prior knowledge to rapidly locate optimal solutions.

NEUROMORPHIC APPROACHES TO INVERSE PROBLEMS

Before presenting the results of the neural network designed thrust vectoring nozzles, it is necessary to discuss the justification for solving an inverse problem using a non-Jacobian, genetic algorithm trained neural network approach. Of fundamental importance in solving inverse problems is the classic Stone-Weierstrass theorem [6, 7]. Using the Stone-Weierstrass theorem it can be shown that under certain conditions non-linear operators, such as the one encountered in fluid flow problems, can be represented using the well known Volterra and Wiener series thereby allowing computation of an approximate solution to the inverse problem. The impressive theoretical works of Volterra, Wiener and Urysohn (see Ref. [6]) on the characterization and approximation of non-linear operators find their full expression in neuromorphic approaches to inverse problem solving.

Let f and θ be Lebesgue integrable functions representing the spatio-temporal evolution of nozzle geometry and temporal evolution of thrust vector angle, respectively. The complex cause-effect structure that relates nozzle geometry and thrust vector angle can be written as

$$\theta = \mathbf{T}(f) \tag{1}$$

where $\mathbf{T} : \mathbf{E} \rightarrow \mathbf{F}$ is a mapping between appropriately defined Banach spaces $\mathbf{E}$ and $\mathbf{F}$. The inverse problem is to determine the map $\mathbf{T}^{-1} : \mathbf{F} \rightarrow \mathbf{E}$ such that

$$f = \mathbf{T}^{-1}(\theta) \tag{2}$$

Except in certain cases of little practical interest, the precise nature of the operator $\mathbf{T}$ is usually not known. Thus, to solve the inverse problem, we must first characterize the class of Banach space operators to which $\mathbf{T}$ belongs. But, even when $\mathbf{T}$ is known to belong to a certain class, $\mathbf{T}^{-1}$ may not exist as a unique map resulting in an infinity of solutions to the inverse problem. Therefore, we must approximate $\mathbf{T}^{-1}$ using fairly *nice* operators that lie *close* to $\mathbf{T}$ in some sense. Commonly used notions of *closeness* usually involve L^p-norms defined on the terminal space $\mathbf{F}$:

$$L^2\ Norm:\ \|\theta\|_2 = \int_0^T |\theta|^2 dt$$

$$L^\infty\ Norm:\ \|\theta\|_\infty = ess\sup|\theta| \tag{3}$$

Several researchers have shown that infinite neural networks with a single hidden layer can approximate any Lebesgue measurable function [8, 9]. It has also been shown that L_2 (mean-square integrable) functions can be approximated by a three layer neural network [10]. These and other powerful results form the basis for applying neural networks to inverse problems. The canonical procedure for constructing a neuromorphic approximation to the inverse transformation is to capture topological invariances in the synaptic interconnections and weight structure using *a priori* generated training samples. Upon acquiring the invariances, a neural network can rapidly output a unique solution to any problem instance spanned by the training set.

To illustrate the advantages of a non-Jacobian method, consider a Jacobian based solution technique to a simple problem involving no unsteady effects. The goal is to find a static nozzle geometry f so as to minimize

$$\mathbf{J} = (\theta - \theta^*)^2 \tag{4}$$

subject to

$$\mathbf{T}f = \theta \tag{5}$$

where **J** represents the difference between the calculated and desired thrust vector angles. Under certain assumptions on **T**, variational calculus provides the necessary conditions for computing an *optimal* nozzle contour. In general, a numerical solution can then be found iteratively from

$$f_{new} = f_{old} + \mathbf{K}\,\nabla\mathbf{J} \tag{6}$$

where **K** is a gain and ∇**J** is the gradient of **J** evaluated at f_{old}. However, the disadvantages of this are:

1. Every time a thrust vector angle is demanded, the flow equations must be solved at every iteration until convergence in order to evaluate the gradient. This requires exceptional computing power for real-time applications.

2. The cost surface is highly degenerate and has a multitude of troughs. There is no guarantee that the iteration will converge to an acceptable solution.

3. Perhaps the most important limitation is that the *optimal* solution depends on the particular assumptions made regarding nozzle flow. The operator **T** that describes nozzle flow must be known explicitly for numerical implementation. Thus, experimental nozzle data cannot be used.

Consequently, the use of genetic algorithms for neural network design is justifiable. (As alluded to previously, a parallel research effort is currently underway at the University of Alabama to design a network using a Jacobian based back-propagation method and will be the subject of a future paper.)

NEURAL NETWORK DESIGN

Designing a feed forward neural network for real-time thrust vectoring involves two phases: a supervised training phase and a verification phase. Supervised training entails embedding the topological invariances in the synaptic weight space through repeated presentations of training samples that characterize the relationship between nozzle contour and thrust vector angle. Although a single network with a large number of synaptic interconnections can be designed to

span the wide range of in-flight thrust vector angle requirements (±20°), it is not ideally suited for real-time applications. Instead, designing several small neural networks with fewer real-time computations, each for a specified overlapping range of thrust vector angle, is more appropriate. Outputs from two neural networks that span the overlap containing the demanded thrust vector angle could be linearly interpolated to provide nozzle shapes. In addition to maintaining design simplicity, this approach has the significant advantage that the two neural networks can be run parallely, thereby reducing real-time computational requirements.

The feed forward neural network topology used in this study consists of a sigmoidal activation function, a single-node input layer, a four-node output layer, and two hidden layers each with four nodes. A schematic representation can be seen in Figure 1. Input to the neural network is the desired thrust vector angle θ; outputs from the network are polynomial coefficients $\{a_i,\ i = 1, 4\}$ that define the contour of the nozzle's upper wall as

$$f(x) = \sum_{i=1}^{4} a_i (x - x_0)^i (x - x_f)^i + g(x) \tag{7}$$

where x_0 and x_f are x-coordinates of the fixed ends of the baseline geometry $g(x)$. Only the upper nozzle wall was selected for modification to simplify this initial analysis. Thus, the neural network outputs define an incremental geometry referenced about the baseline.

The baseline nozzle developed for use in this study is shown in Figure 2. The nozzle type selected was a symmetric, dual expansion ramp nozzle with contourable walls. Concerns factored into the design were minimum length (to minimize weight) and reduced line of sight onto the engine hot-section to address observable characteristics. The baseline geometry was obtained after a number of iterations to insure the best performing nozzle was being used as a reference. The thrust vector angle of the baseline is zero degrees with a gross thrust coefficient of 0.983. In this study, a positive thrust vector angle corresponds to a vehicle nose-up pitching moment. It was assumed that the on-design conditions for the nozzle would be a nozzle pressure ratio of 10, a flight Mach number of 15, and a fluid specific heat ratio of 1.15. Being essentially a *proof-of-concept*, this study was also restricted to a two-dimensional (planar) nozzle to further simplify the analysis. However, except for an increase in the computational time required, no other technical challenges would be expected in the step from two to three dimensions.

Thrust vector angles corresponding to a large number of randomly generated, polynomial nozzle contours were computed using an analysis code based on the inverse method of characteristics [11]. This code, developed at the University of Alabama, allows for the analysis of supersonic flow fields internal to a nozzle as well as the supersonic exhaust plume. The code has been extensively validated with experimental data from NASA and industry. The network design procedure, however, does not depend on how the training samples are obtained and any method - numerical or experimental - can be used. Eight neural networks of identical topology were designed to span thrust vector angles between 5° and 20°. For each neural network design, 500 training samples that spanned the corresponding thrust vector angle range were presented to the network. Synaptic weights that minimized the ensemble error between neural network output $\{a_i,\ i = 1, 4\}$ and actual polynomial coefficients $\{c_i,\ i = 1, 4\}$ in the L^2 space were determined using a genetic algorithm. The set of weights displaying the minimum performance index over 25 generations was considered the optimal set of weights.

It must be noted that in an operational version of the neural network, inputs would be a function of time; whereas during the training phase, constant values of thrust vector angles constituted the training samples. This brings about a significant advantage of transforming what, in general, would be a dynamic optimization problem to a static network design problem. However, it is valid only upon neglecting unsteady fluid flow effects caused by dynamic changes in nozzle contour which is completely acceptable for aircraft thrust vectoring systems.

NEURAL NETWORK VERIFICATION

A Monte Carlo simulation was performed to verify the neural network design. 500 thrust vector angles between 5° and 20° were randomly generated. Each thrust vector angle was then presented to the neural network as an input. Polynomial coefficients obtained as outputs from the neural network were used to define a nozzle contour. Representative samples of nozzle contours obtained from the neural network can be seen in Figure 3. The MOC code was then run to find the actual thrust vector angle for each of the neural network specified contours. Figure 4 compares the requested thrust vector angle with the angle obtained from the MOC code. Figure 5 shows the error in the network achieved thrust vector angle. The performance of each of the eight networks used also can be clearly seen in Figure 5. Thrust vector angles of up to 20° were obtained within an average error of 0.0914° by affecting modifications to the upper nozzle wall only. Modifying both upper and lower walls would cause a very complex flow structure and could possibly expand the vectoring angle envelope. The maximum error in the thrust vector angle was 0.3791° which would be negligible in an operational aircraft system. Further improvements in vectoring performance can be expected to occur by using an L^{∞} type performance index and running the genetic algorithms in the training phase with an increased number of generations.

CONCLUSIONS

It has been have shown that neural networks provide a viable alternative to straight Jacobian based solution methods. They have significantly reduced real-time computations while maintaining accuracy and retaining design simplicity. In addition, although genetic algorithms may not be ideal for solving the inverse problem of thrust vectoring directly, their utility is demonstrated by their ability to train a neural network to do so.

The procedure presented here for designing neural networks and the subsequent design of thrust vectoring nozzles has advantages and disadvantages. Error surfaces encountered while designing thrust vectoring nozzles are highly degenerate and therefore a robust optimization scheme such as a genetic algorithm is required for global error minimization. But in problems of high dimensionality, there are numerical difficulties in using genetic algorithms, limiting the complexity of the simulated function and the size of the network that can be trained. Jacobian based back-propagation, for example, may reduce the training period significantly and would have no difficulty handling large dimensions. However, as with other gradient techniques, back-propagation is prone to converge to a local minimum, thereby converging to an incorrect network design or not converging at all. Further study is recommended to put these concerns to rest.

Finally, there are two competing aspects to neural network design - accuracy and generalizability - which need to be addressed. Accuracy has to do with how close is the approximation obtained using the neural network. Generalizability means that a neural network can interpolate and extrapolate beyond problem instances spanned by the training set. The performance indices used in this study do not reflect generalizability. It would be of considerable interest to develop performance indices that provide a balance between the two aspects and then redesign *adaptive* neural networks for thrust vectoring. In this study an off-line design method, wherein the entire training set is presented to the neural network at one time, was used; an on-line or adaptive neural network capable of learning while in operation would be better suited for practical applications.

REFERENCES

1. Whitaker, K. W., Gowadia, N. S., Fordyce, S. C., "Thrust Vectoring Using Non-Axisymmetric Nozzles With Flexible Contours," AIAA Paper No. 91-2368, 1991.

2. King, E. G., Freeman, L. M., Whitaker, K. W., and Karr, C. L., "Two-Dimensional Thrust Vectoring Nozzle Optimization Techniques," AIAA Paper No. 91-0473, 1991.

3. Holland, J. H., "Genetic Algorithms and the Optimal Allocations of Trials," *SIAM Journal of Computing*, Vol. 2, No. 2, p. 88, 1973.

4. Foo, N. Y. and Bosworth, J. L., "Algebraic, Geometric, and Stochastic Aspects of Genetic Operators," NASA CR-2099, 1972.

5. Goldberg, D. E., *Genetic Algorithms in Search, Optimization, and Machine Learning*, Addison-Wesley Publishing Company, Inc., 1989.

6. Zimmer, R. J., "Essential Results of Functional Analysis," *Chicago Lectures In Mathematics*, The University Of Chicago Press, Chicago, 1990.

7. Royden, H. L., *Real Analysis*, MacMillan Publishing Co., New York, 1988.

8. Cotter, N. E., "Stone-Weierstrass Theorem and its Application To Neural Networks," *IEEE Transactions On Neural Networks*, Vol. 1, No. 4, December, 1990.

9. Gallant, A. R., White, H., "There Exists a Neural Network That Does Not Make Avoidable Mistakes," *Proceedings of IEEE International Conference On Neural Networks*, Vol. 1, 1988.

10. Hecht-Nielsen, R., *Neurocomputing*, Addison-Wesley Publishing Co., New York, 1990.

11. Whitaker, K. W. and Cates, J. E., "A User-Friendly Exhaust Nozzle Design Program Based on the Method of Characteristics," AIAA Paper No. 90-2029, 1990.

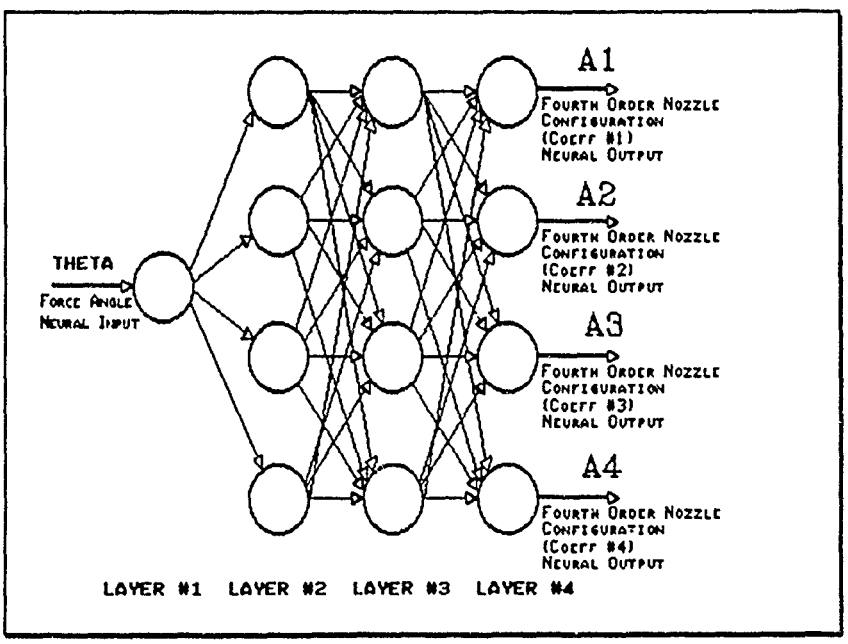


Figure 1. Schematic of Neural Network Used

Third International Conference on Inverse Design Concepts and Optimization in Engineering Sciences (ICIDES-III), Editor: G.S.Dulikravich, Washington D.C., October 23-25, 1991

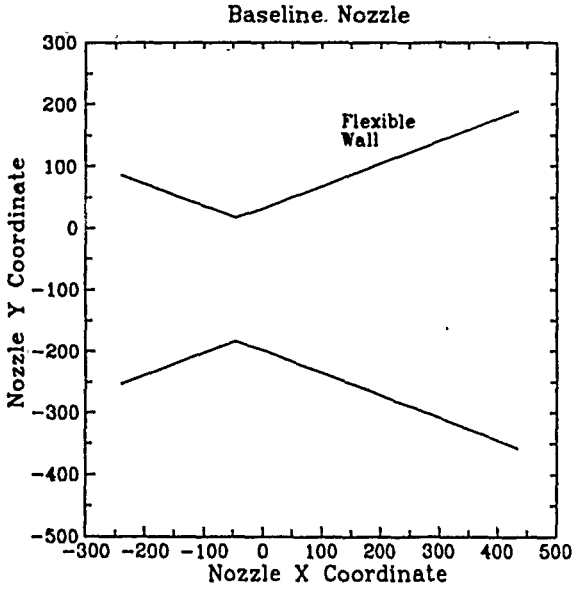


Figure 2. Baseline Nozzle Geometry

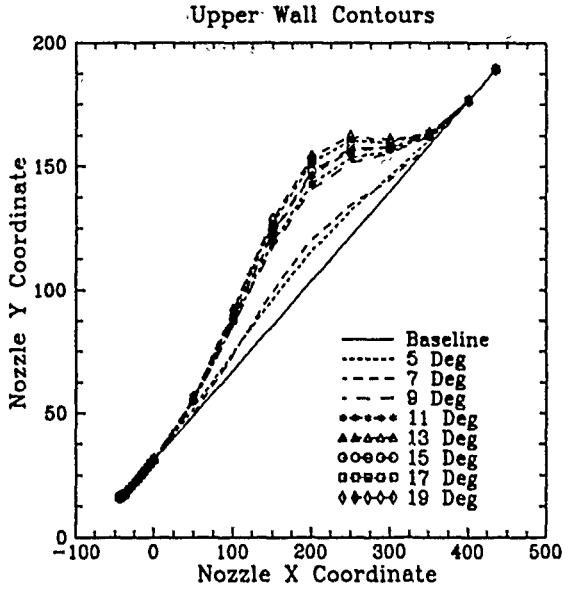


Figure 3. Representative Nozzle Contours Specified by Neural Network

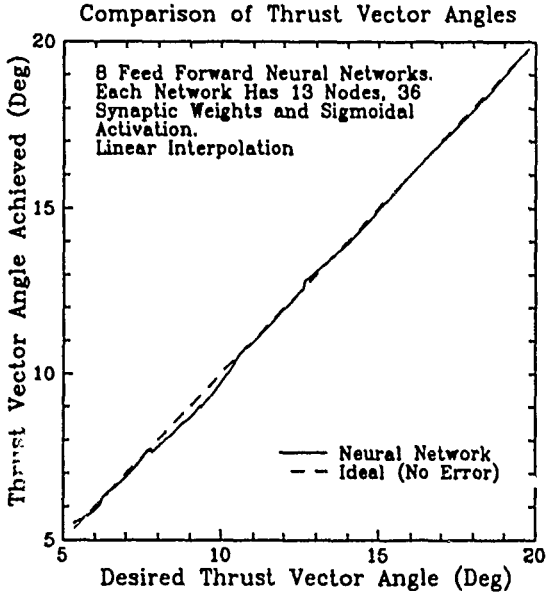


Figure 4. Comparison of Requested Angles with Angles Achieved

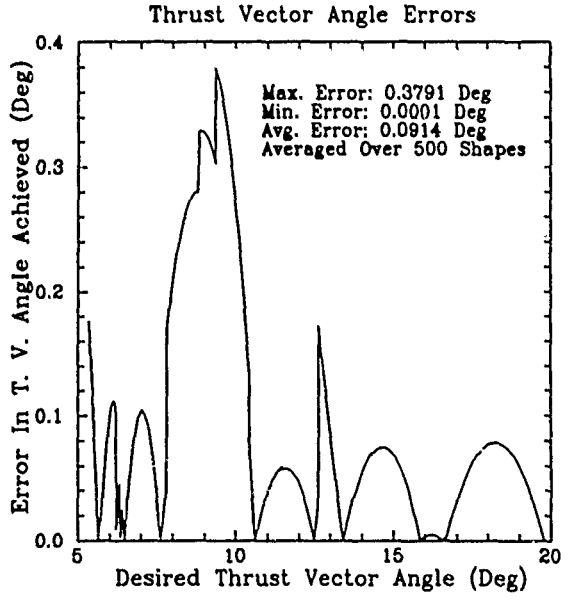


Figure 5. Error in Network Specified Angles

Third International Conference on Inverse Design Concepts and Optimization in Engineering Sciences (ICIDES-III), Editor: G.S. Dulikravich, Washington D.C., October 23-25, 1991.

FINITE ELEMENT STRUCTURAL REDESIGN BY LARGE ADMISSIBLE PERTURBATIONS

Michael M. Bernitsas, Professor
E. Beyko, C.W. Rim, B. Alzahabi, Research Assistants, Ph.D. Candidates

Department of Naval Architecture and Marine Engineering
The University of Michigan, Ann Arbor, Michigan 48109-2145

ABSTRACT

In structural redesign, two structural states are involved; the baseline (known) State S1 with unacceptable performance, and the objective (unknown) State S2 with given performance specifications. The difference between the two states in performance and design variables may be as high as 100% or more depending on the scale of the structure. A Perturbation Approach to Redesign (PAR) is presented to relate any two structural states S1 and S2 that are modeled by the same finite element model and represented by different values of the design variables. General perturbation equations are derived expressing implicitly the natural frequencies, dynamic modes, static deflections, static stresses, Euler buckling loads and buckling modes of the objective State S2 in terms of its performance specifications, and State S1 data and FEA results. LargE Admissible Perturbation (LEAP) algorithms are implemented in code RESTRUCT to define the objective State S2 incrementally without trial and error by postprocessing FEA results of State S1 with no additional FEAs. Systematic numerical applications in redesign of a 10-element 48-d.o.f. beam, a 104-element 192-d.o.f. offshore tower, a 64-element, 216-d.o.f. plate, and a 144 element 896-d.o.f. cylindrical shell show the accuracy, efficiency, and potential of PAR to find an objective state that may differ 100% or more from the baseline design.

I. INTRODUCTION

Several problems in analysis, design, and modification of a structure or a structural design can be stated as redesign problems. Those are two-state problems involving the baseline State S1 and the objective State S2. S1 is known and has been modeled and analyzed by FEM. In the event that the performance of State S1 is unacceptable, the objective State S2 must be defined to satisfy performance specifications. The Perturbation Approach to Redesign (PAR) developed in this work can relate any two structural states that can be modeled and analyzed by the same FE model. PAR has the potential to perform redesign in the sense of resizing, reshaping, and reconfiguration to satisfy any performance requirements that can be predicted by FEA including modal dynamics, static deflections and stresses, and global buckling. LEAP algorithms implemented in code RESTRUCT (REdesign of STRUCTures) [3] presently can handle resizing for natural frequencies, mode shapes and static deflections.

Figure 1 shows several two-state problems that appear in the analysis-design-redesign process following a basic FE analysis. In analysis, the following two-state problems are encountered: (P1) Model correlation [28], (P2) Derivation of global failure equations [1, 14], (P3) Failure point identification [14], (P4) Redundancy [14], (P5) Reliability, [4], (P6) Non-Destructive-Testing [24]. In design, the following two-state problems are encountered: (P7) Redesign for target performance [1, 2, 11, 12, 24, 26, 27], (P8) Redesign for target redundancy, (P9) Redesign for target reliability.

LEAP theory was developed during the past seven years from the linear perturbation techniques introduced by Stetson in 1975 [26, 27] and modified by Sandstrom et al [24]. They redesigned a structure for both natural frequency and mode shape objectives but allowed only small differences between the baseline and objective states. In that respect, linear perturbation methods are equivalent to design sensitivity methods. Nonlinear perturbation methods [11, 12] allow for large differences between the two states. The objective state is found by postprocessing

Third International Conference on Inverse Design Concepts and Optimization in Engineering Sciences (ICIDES-III), Editor: G.S. Dulikravich, Washington D.C., October 23-25, 1991.

data of the baseline structure only, using an incremental prediction correction scheme [1]. Presently, research efforts are directed towards two goals. The first one is to redesign larger scale structures as far away from the baseline structure as possible before a second FEA is needed. Large admissible perturbations [1] updating only cognate modes [2] in an incremental process are used towards that end. Substructuring is also investigated for that purpose, as well as for reshaping and reconfiguration. The second goal is to implement more and different objectives and derive the corresponding general perturbation equations. LEAP algorithms are under development for static stress, global buckling load, and buckling mode objectives.

The problem of redesign by large admissible perturbations is analyzed in Chapter II. Several two-state problems mentioned above are stated as redesign problems in Section II.1. The Perturbation Approach to Redesign (PAR) is presented in Section II.2 and LEAP theory for development of solution algorithms is summarized in Section II.3. Many numerical applications using four different structures are presented in Chapter III to assess the present status of code RESTRUCT, and the potential and limitations of PAR.

II. REDESIGN BY LARGE ADMISSIBLE PERTURBATIONS

A simple modeling-analysis-design-redesign process for structures using FEM is shown in Figure 1. Rectangular blocks indicate two-state problems which can be formulated as redesign problems using PAR and solved efficiently by a LEAP algorithm. Shaded blocks indicate problems already solved in some form by code RESTRUCT. Some of those problems are discussed below.

II.1. Redesign and Other Two-State Problems

The classical structural redesign problem appears in Figure 1 after analyzing either the original or the correlated FE model. Undesirable response – such as a natural frequency in the range of wave excitation, a dynamic mode with high amplitudes near the free surface where wave and current loads are maximum, or high stresses and deflections – makes redesign mandatory. The performance specifications of the objective design are desirable values of those response particulars.

After placing a structure in service, tests are performed to measure its performance and compare it to FEM predictions. In the modeling process, simplifying assumptions, uncertainty, and ignorance result in discrepancies between measurements and predictions particularly for marine structures which have large manufacturing tolerances. The process of finding a FE model of a physical structure that will correctly predict measured structural response is called model correlation. The initial FE model is the known State S1. The objective State S2 represents the unknown correlated FE model. The Perturbation Approach to Redesign presented in the following section preserves element connectivity and changes geometric properties so that the correlated model represents a real structure [2]. That is, PAR does not change simply numbers in the mass and stiffness matrices. PAR can also solve the problem of model correlation for geometry dependent hydrodynamic load [28].

The problem of failure point identification can also be formulated by PAR and solved by a LEAP algorithm. S1 represents the initial structural state and S2 the unknown failure point (design point in reliability terminology) on a limit surface [10, 20]. The advantage of PAR is that it can provide an implicit expression for a global failure criterion by relating State S2 to S1.

Related is the problem of reserve and residual redundancy. In the literature, several different aspects of redundancy are presented as definitions depending on the type of structure and analysis performed [5, 6, 21]. PAR remedies this lack of invariant and consistent redundancy definition by introducing a redundancy injective mapping [14] defining the difference between the initial intact or damaged structure and the design point.

Finally, a new methodology for reliability analysis and design of large scale structures is under development based on PAR [4]. The Perturbation Approach to Reliability provides an alternative to the systems approach [5, 21, 29] and the stochastic FEM [19, 30] which are the two most popular methods in structural reliability. PAR makes possible the introduction of advanced structural analysis in the reliability computations without simplifying the structure. PAR also

Third International Conference on Inverse Design Concepts and Optimization in Engineering Sciences (ICIDES-III), Editor: G.S. Dulikravich, Washington D.C., October 23-25, 1991.

allows randomness in geometry, material, and load. There is no limitation to the number of random variables used and the random load need not be applied incrementally until structural failure. The reliability analysis problem is a two-state problem where S1 is the initial structure and S2 the design point.

PAR can also address the very difficult problems of target redundancy and target reliability design. S1 is the initial structural design of inadequate redundancy or reliability and S2 is the objective structure of specified redundancy or reliability [4]. These are difficult design problems because redundancy and reliability are not computed by FEM. PAR can solve these problems because of the introduction of an injective mapping relating S1 to S2.

II.2. Perturbation Approach to Redesign (PAR)

The PAR methodology has been developed to solve the above two-state problems. It has five major steps: Step 1: A Structure (S1) is modeled and analyzed by a general purpose FE code; MSC/NASTRAN is used in our work. So far, four types of analysis have been considered in PAR and the governing equations are listed below. For modal dynamics the free vibration equations for S1 are

$$\left([k]-\omega_j^2[m]\right)\{\psi\}_j=\{0\} \quad \text{for } j=1,2,...,n \quad , \tag{1}$$

where the n eigenvalues ω_j, j=1,2,...,n satisfy equation $\det\left([k]-\omega_j^2[m]\right)=0$. In equation (1), damping may be included only in Rayleigh's form and added mass is included in [m] . For the static deflections and stresses of S1 we have

$$[k]\,\{u\} = \{f\} \tag{2}$$

and $$\{\sigma\} = [S]\,[k]^{-1}\,\{f\} \quad , \tag{3}$$ $$[S] = [G]\,[D]\,[N] \quad , \tag{4}$$

where [G], [D], [N] are the stress-strain, strain-displacement, and shape function matrices. The governing equation for global buckling in finite elements is

$$\left([k_o]+[k_\sigma]\right)\{\psi_b\}=\{0\} \quad , \tag{5}$$

where $[k_o]$ and $[k_\sigma]$ are the small displacement and initial geometric stiffness matrices.
Step 2: The following perturbation relations are introduced relating State S2 to S1:

$$[k']=[k]+[\Delta k] \quad , \tag{6}$$ $$[m']=[m]+[\Delta m] \quad , \tag{7}$$

$$\lceil\omega'^2\rfloor = \lceil\omega^2\rfloor + \lceil\Delta(\omega^2)\rfloor \quad , \tag{8}$$ $$[\phi'] = [\phi] + [\Delta\phi] \quad , \tag{9}$$

where unprimed and primed symbols refer to the baseline (S1) and the objective State S2, respectively, and prefix Δ indicates difference between counterpart quantities of states S1 and S2.

$[\phi]=\left[\{\psi\}_1, \{\psi\}_2, ...,\{\psi\}_n\right]$, is the matrix of eigenvectors of S1 and $\lceil\omega^2\rfloor$ is the diagonal matrix of the corresponding eigenvalues. Perturbation relations pertaining to equations (2) and (3) are

$$\{u'\} = \{u\} + \{\Delta u\} \quad , \tag{10}$$ $$\{f'\} = \{f\} + \{\Delta f\} \quad , \tag{11}$$

$$\{\sigma'\} = \{\sigma\} + \{\Delta\sigma\} \quad , \tag{12}$$ $$[S'] = [S] + [\Delta S] \quad . \tag{13}$$

For the global buckling eigenvalue problem we have

$$[k'_o]=[k_o]+[\Delta k_o] \quad , \tag{14}$$ $$[k'_\sigma]=[k_\sigma]+[\Delta k_\sigma] \quad , \tag{15}$$

Third International Conference on Inverse Design Concepts and Optimization in Engineering Sciences (ICIDES-III), Editor: G.S. Dulikravich, Washington D.C., October 23-25, 1991.

$$[P'_{cr}]=[P_{cr}]+[\Delta P_{cr}] \quad , \quad (16) \qquad [\phi'_b]=[\phi_b]+[\Delta\phi_b] \quad . \quad (17)$$

Further, in Step 2, desirable values of some response particulars of S2 such as natural frequencies, static deflections and mode shapes are specified. An incomplete set of mode shapes may be used and only some degrees of freedom may be defined in each mode.

Step 3: The differences in structural properties between S1 and S2 are expressed in terms of the fractional changes α_e,e=1,2,...,p of p properties of elements or groups of elements as:

$$[\Delta k]=\sum_{e=1}^{p}[\Delta k_e]=\sum_{e=1}^{p}[k_e]\alpha_e \quad , \quad (18) \qquad [\Delta m]=\sum_{e=1}^{p}[\Delta m_e]=\sum_{e=1}^{p}[m_e]\alpha_e \quad , \quad (19)$$

$$[\Delta S]=\sum_{e=1}^{p}[\Delta S_e]=\sum_{e=1}^{p}[S_e]\alpha_e \quad . \quad (20)$$

Several α_es may refer to the same element but different properties such as bending, torsion, and stretching. The unknowns in the process of defining S2 from its specifications and S1 are the fractional changes α_e. When the α_es are defined it is ensured that element connectivity in the FE model is preserved and S2 represents a real structure.

Step 4: The differences in structural response between states S1 and S2 are expressed implicitly in terms of the α_es by the general perturbation equations. For modal dynamics we have

$$\sum_{e=1}^{p}\left(\{\psi'\}_i^T[k_e]\{\psi'\}_i-\omega_i'^2\{\psi'\}_i^T[m_e]\{\psi'\}_i\right)\alpha_e=\omega_i'^2\{\psi'\}_i^T[m]\{\psi'\}_i-\{\psi'\}_i^T[k]\{\psi'\}_i \quad , \quad (21)$$

$$\sum_{e=1}^{p}\{\psi'\}_j^T[k_e]\{\psi'\}_i\alpha_e=-\{\psi'\}_j^T[k]\{\psi'\}_i \quad , \quad (22)$$

$$\sum_{e=1}^{p}\{\psi'\}_j^T[m_e]\{\psi'\}_i\alpha_e=-\{\psi'\}_j^T[m]\{\psi'\}_i \quad , \quad (23)$$

for $i=1,2,...,n$, $j=i+1, i+2,...,n$ [1, 2]. Equation (21) represents the n diagonal terms of the energy balance equation $[K']-[M'][\omega'^2]=0$ for S2, that is, the Rayleigh quotients for $\omega_i'^2$. Equations (22) and (23) represent the orthogonality conditions of modes $\{\psi'\}_i$ with respect to [k'] and [m']. Theoretically, orthogonality of modes with respect to one of [k'] or [m'] implies orthogonality with respect to the other. Numerically, however, both conditions must be forced if $\{\psi'\}_j$, j=1,2,...,n, are to represent modes of a real structure.

The general perturbation equations for static deflections are derived from the counterpart of equation (2) for structure S2 based on the modal dynamic expansion of $\{u'\}$ in terms of the unknown modes $\{\psi'\}_j$, j=1,2,...,n. Thus, inversion of matrix [k'] is avoided. Linearizing only the explicit dependence on the α_es, we have [1, 15]

$$u_i'=\sum_{m=1}^{n_r}\left(\frac{\phi'_{im}A_m}{B_m}\right)-\sum_{e=1}^{p}\left(\sum_{m=1}^{n_r}\frac{\phi'_{im}A_m}{B_m^2}C_{me}\right)\alpha_e \quad , \quad \text{where} \quad (24)$$

$$A_m=\sum_{j=1}^{n}\left(\phi'_{jm}f'_j\right) \quad , \quad B_m=\{\psi'\}_m^T[k]\{\psi'\}_m \quad , \quad C_{me}=\{\psi'\}_m^T[k_e]\{\psi'\} \quad .$$

The general perturbation equations for static stresses are derived in a similar manner [14]

$$\{\Delta\sigma\}=-\{\sigma\}+\left([S]+\sum_{e=1}^{p}[S_e]\alpha_e\right)\left[\sum_{m=1}^{n}\frac{\phi'_{im}A_m}{B_m}-\sum_{e=1}^{p}\left(\sum_{m=1}^{n}\frac{\phi'_{im}A_m}{B_m^2}C_{m_e}\right)\alpha_e\right] \quad . \quad (25)$$

For global buckling, the general perturbation equations are derived using the same method as in the case of the modal dynamics eigenvalue problem [14]

$$\sum_{e=1}^{p}\{\psi'_b\}_i^T\left([k_{c_e}]-P_i[k_{\sigma_{0e}}]\right)\{\psi'_b\}_i\alpha_e=\{\psi'_b\}_i^T\left(P_i[k_{\sigma_0}]-[k_c]\right)\{\psi'_b\}_i \quad , \tag{26}$$

$$\sum_{e=1}^{p}\{\psi'_b\}_j^T[k_{c_e}]\{\psi'_b\}_i\alpha_e=-\{\psi'_b\}_j^T[k_c]\{\psi'_b\}_i \quad , \tag{27}$$

$$\sum_{e=1}^{p}\{\psi'_b\}_j^T[k_{\sigma_{0e}}]\{\psi'_b\}_i\alpha_e=-\{\psi'_b\}_j^T[k_{\sigma_0}]\{\psi'_b\}_i \quad , \tag{28}$$

for i = 1,2,...,n , j=i + 1,i + 2,...,n , where $[k_c] = [k_o] - [k_{\sigma F}]$, $k_{\sigma F}$ includes the body force, and $[k_\sigma] = - P_i[k_{\sigma 0}] - [k_{\sigma F}]$.

Step 5: In this final step, the problem of finding State S2 based on its specifications and results of FEA for S1 is formulated and solved for the p unknown α_es using the LEAP algorithm presented in the next section. The problem formulation is as follows:

$$\text{Minimize} \quad \|\underset{\sim}{\alpha}\|_2 \in \Re^p \quad , \tag{29}$$

subject to n_ω natural frequency objectives $\omega_i'^2$, i = 1,2,...,n_ω ; n_ϕ normal mode objectives ϕ'_{ki} , number of (k, i) = n_ϕ ; n_u static deflection objectives u'_i , i=1,2,...,n_u ; n_σ static stress objectives σ'_i , i=1,2,...,n_σ ; n_b global buckling eigenvalues P'_i , i=1,2,...,n_b ; $n_{\phi b}$ buckling mode objectives $\phi'_{b_{ki}}$, number of (k,i) = $n_{\phi b}$; 2p lower and upper bounds on the redesign variables α_e , $-1 < \alpha_e^- \le \alpha_e \le \alpha_e^+$, e=1,2,...,p ; n_a admissibility constraints extracted from equations (22) and (23), where $n_a = 2\sum_{i=1}^{n_\omega}(n_r - i) = n_\omega[(2n_r - 1) - n_\omega]$; and n_{ab} admissibility constraints extracted from equations (27) and (28), where $n_{ab} = 2\sum_{i=1}^{n_b}(n_r - i) = n_b[(2n_r - 1) - n_b]$. All of the above redesign objectives are substituted in the appropriate general perturbation equations (21)-(28). The remaining unused general perturbation equations may be used to predict the unspecified performance particulars of the objective State S2. Accuracy of those predictions, however, it not as high as those of the redesign objectives. All the constraints of the above problem may result in an empty, non-empty, or countable feasible domain. In the first case, the redesign objectives cannot be achieved for the selected set of redesign variables, in which case a minimum error solution in satisfaction of the redesign objectives is achieved by a generalized inverse algorithm [1, 2, 11, 15]. In the second case, an optimum solution is achieved using an optimality criterion (29).

II.3. LargE Admissible Perturbation (LEAP) Algorithm

The redesign problem formulated by PAR in Section II.2 can be solved by a LEAP algorithm. Many LEAP algorithms have been developed to solve a variety of two-state problems [1, 2, 14, 15, 28] and have been documented in detail. Suffice to present here the basic steps and difficulties of the solution algorithm. The LEAP algorithm developed to solve the redesign problem is outlined in Figure 2. It starts from the baseline structure (S1) and reaches incrementally the

Third International Conference on Inverse Design Concepts and Optimization in Engineering Sciences (ICIDES-III), Editor: G.S. Dulikravich, Washington D.C., October 23-25, 1991.

objective S2 by prediction and correction. In the prediction phase of the algorithm, the small perturbation method [24, 26, 27] is used. The modal dynamics general perturbation equations are linearized. For that purpose, increments are limited to 7% differences between S2 specifications and the corresponding S1 properties. Predictions are small but inadmissible because admissibility conditions (22) and (23) are linearized. In the correction phase, perturbations are corrected by satisfying the nonlinear general perturbation equations and are forced back into the admissible space by satisfying the nonlinear admissibility conditions. The total CPU time for redesign may be reduced by a factor occasionally as high as 4 when in the first increment the space of cognate modes is identified and thereafter all computations are performed in that space. Such is the case for torsional redesign [2] of the offshore tower in Figure 5. Torsional modes (3, 18, 19) constitute one cognate subspace with very weak interaction with other modal subspaces such as those for bending and stretching.

In each increment, in both phases the resulting problem may be underdetermined or overdetermined depending on the relation between the number p of redesign variables α_e, the number of equality constraints (S2 specifications) $n = n_\omega + n_\phi + n_u + n_\sigma + n_b + n_{\phi b} + n_a + n_{ab}$, and the 2p bounds on the α_es. When the problem is overdetermined, a minimum error solution in satisfaction of the S2 specifications is produced by a generalized inverse algorithm. When the problem is undetermined, it is solved by optimization using the minimum change criterion in equation (29). To achieve this global objective, at each increment the following objective is minimized

$$\min \sum_{e=1}^{p} \left[(1+_\ell\alpha_e) \prod_{q=1}^{\ell-1} (1+_q\alpha_e) - 1 \right]^2 . \qquad (30)$$

The problem is solved by quadratic programming [8] or sequential quadratic programming [7] depending on whether the expression for $[\Delta k]$ is linear as in equation (18), or nonlinear as in the case of plate and shell redesign. In those cases, the plate or shell thickness is selected as redesign variable resulting in a cubic expression for $[\Delta k]$ in terms of the α_es. $[\Delta S]$ is always a nonlinear expression of the α_es because $[S_e]$ depends on the distance of the point where the stress is computed from the neutral axis. The LEAP algorithm is implemented in code RESTRUCT (REdesign of STRUCTures) [3]. It is 27,000 FORTRAN 77 commands and may serve as a postprocessor to any special or general purpose FE code. We presently use it to postprocess MSC/NASTRAN.V64 data on the secondary (UB) main frame computer (IBM-3090) of the University of Michigan.

The LEAP algorithm outlined above finds the optimum objective structure S2 without trial and error and with no additional FEAs. The [k] matrix inversion required in static deflection and stress redesign is avoided by using modal expansions as shown in equations (24) and (25). Thus, an accurate modal basis is mandatory even as S2 moves far away from S1. LEAP algorithms can surmount the following three difficulties as well. All general perturbation equations (which become equality constraints in the optimization problem) are strongly nonlinear implicit expressions of the redesign variables α_e. The static force vector $\{f'\}$ may depend on the structure's geometry (e.g. hydrodynamic loads) and consequently change in the redesign process. Finally, the set of specifications provided for S2 are usually incomplete and only some d.o.f.s of specified modes are defined.

III. NUMERICAL APPLICATIONS

A total of 42 numerical applications are presented in this section on optimal redesign of four different structures [22, 9, 31]. Results are summarized in Tables 1, 4, 5, 6 and show the accuracy of code RESTRUCT for applications with number of redesign variables ranging from 8 to 21; natural frequency and mode shape redesign objectives changing by a factor ranging from 0.3 to 2.0; degrees of freedom ranging from 48 to 896. For each redesign objective, Tables 1, 4, 5, 6 show the objective value, the value actually achieved as computed by reanalysis with MSC/NASTRAN and the corresponding relative error. CPU time and numbers of extracted modes n_r, admissibility conditions n_a, and redesign variables are also shown. The values of the redesign variables of the optimum solution are not shown. The optimal solution appears in the

Third International Conference on Inverse Design Concepts and Optimization in Engineering Sciences (ICIDES-III), Editor: G.S. Dulikravich, Washington D.C., October 23-25, 1991.

form of optimal Eucledian norm of the α_es in Tables 5 and 6; and in the form of the Hasover-Lind reliability index [10] in Tables 1 and 4.

10-element 48-d.o.f. beam: The clamped-hinged beam in Figure 4 is subjected to a uniform load in the y direction and a concentrated load applied at node 7 in the z direction. $\omega_1 = 183.092$ rad/sec, the horizontal and vertical deflections at node 7 are $v_7 = 12.151$ mm and $w_7 = 17.733$ mm as computed by MSC/NASTRAN. Redesign variables and structural groups are shown in Table 2. The accuracy of the redesign process is shown in Table 1 for one, two or three simultaneous redesign objectives. The problem of reliability analysis is studied assuming randomness in geometric properties, A (area), I_y, I_z (moments of inertia), and material properties E (Young's modulus) and ρ (density). The fractional changes α_e are assumed to be independent normal random variables of zero mean. Standard deviations are selected as $\sigma_{\alpha_{EI}} = 0.40$ for bending rigidities EI_y and EI_z, and $\sigma_{\alpha_{\rho A}} = 0.30$ for mass per unit length ρA. In order to compute the probability of failure to first (FORM) or second (SORM) order [20], computation of individual and joint design points and the corresponding Hasover-Lind reliability index β is required as shown in Figure 3. Computation of β is achieved by transforming the α_es to independent standard normal random variables through the Rosenblatt transformation [13]. These numerical applications as well as those following on the offshore tower show that large admissible perturbation methods can introduce sophisticated structural analysis in reliability without simplifying the structural model and without repeated FEAs [4].

104-element 192-d.o.f. offshore tower: The offshore tower shown in Figure 5 is 69.95 m high and operates in 45.72 m water depth. The tower at the base is square with a 38.10m side and tapers linearly to 22.86 m at the deck. The FE model of the tower is composed of 104 circular tubular beam elements and has 192 dofs. Loading on the tower is due to: (i) 240 tonnes deck load which is applied to the structure as uniformly distributed load at the deck nodal points. (ii) Wave hydrodynamic forces calculated for a design wave of 182.88 m length and 6.10 m height using Morison's equation. The wave propagates in the x-direction. (iii) Wind generated water current in the x-direction with linear velocity profile of 1.03 m/sec at the mean free surface waterline and zero at the sea bed. $\omega_1 = \omega_2 = 4.695$ rad/sec for the first bending modes in the XZ and the YZ planes. $\omega_3 = 5.353$ rad/sec for the first torsional mode with respect to axis Z. Redesign variables and structural groups are shown in Table 3.

Failure states are defined by deterioration factors in the first and third eigenvalues of 1.54 and 2.00. Geometric and material properties are random. The fractional changes α_es, shown in Table 3, are assumed to be independent normal random variables with zero mean. Standard deviations are selected as $\sigma_{\alpha_{EI}} = 0.40$ for bending rigidity EI and $\sigma_{\alpha_{\rho A}} = 0.30$ for mass per unit length ρA. Design points are again computed by postprocessing FE analysis results for the baseline design only. It should be noted that both in Tables 1 and 4 the computed β are very high because the external load is deterministic and limit states were pushed as far away from the baseline design as possible in order to demonstrate the accuracy and limitations of code RESTRUCT.

64-element 216-d.o.f. plate: The clamped-free-free-free plate in Figure 6 is subjected to a uniform load p and has the dimensions and properties shown in the figure. Its response is computed by MSC/NASTRAN and redesign is performed by RESTRUCT. The incremental optimization problem is nonlinear and solved by sequential quadratic programming [7] because $[\Delta k]$ is a cubic expression of the α_es which represent fractional changes of the plate thickness [17, 22]. The plate is subdivided into 8 structural groups each containing 8 finite elements. Results of redesign are summarized in Table 5 and show very high accuracy even for changes by a factor of 2 in eigenvalues and maximum deflection.

144-element 896-d.o.f. cylindrical shell: The simply supported shell shown in Figure 7 is subjected to hydrostatic pressure load p due to 286 meters submergence in salt water [23]. Dimensions [25] and properties are also shown in the figure. Its modal dynamic and static deflection response is computed by MSC/NASTRAN [16, 18]. The optimization problem in each increment is nonlinear and solved by sequential quadratic programming [7]. The cylindrical shell is subdivided into 5 structural groups and even though symmetry is not forced by linking

Third International Conference on Inverse Design Concepts and Optimization in Engineering Sciences (ICIDES-III), Editor: G.S. Dulikravich, Washington D.C., October 23-25, 1991.

symmetric groups (1 and 5, 2 and 4) as was done in the plate redesign problem, symmetry was preserved in the redesign process. Results of code RESTRUCT are summarized in Table 6 and show good accuracy even for changes by a factor of 2 in eigenvalues and deflection.

In all of the above applications, the LEAP algorithm in RESTRUCT can be pushed further by taking additional incremental steps if higher errors are considered acceptable. For higher accuracy, however, one more FE analysis may be used after about 10 increments.

CONCLUDING REMARKS

Several two-state problems in structural analysis, design, and redesign can be formulated by PAR (Perturbation Approach to Redesign) and solved by a LEAP (LargE Admissible Perturbation) algorithm. The objective structural design is found incrementally without trial and error or repeated FEAs for differences in response from the baseline design of the order of 100% or more. In structural reliability, PAR provides an attractive alternative to Stochastic Finite Elements and the Systems approach.

Computer code RESTRUCT which implements the large admissible perturbation methodology, is being developed since 1983, has been tested thoroughly and has generated confidence in its potential to solve two-state problems. Several theoretical and numerical developments are under way. New types of finite elements are being introduced; new structures are being redesigned, such as stiffened plates and shells; new two-state problems are studied, e.g. submarine acoustic noise reduction, redesign for buckling objectives, redesign for stress objectives; a perturbation approach to reliability analysis and design is being developed; larger scale structures are being redesigned by postprocessing FEA results by MSC/NASTRAN.V66 which has superelement capability. For that purpose, a supercomputer version of RESTRUCT running on the San Diego supercomputer has been developed.

ACKNOWLEDGEMENTS

Research support provided by the Office of Naval Research through Grant No. DOD-G-N00014-90-J-4081 is gratefully acknowledged.

REFERENCES

1. Bernitsas, M.M. and Kang, B.S., "Admissible Large Perturbations in Structural Redesign," AIAA Journal, Vol. 29, No. 1, January 1991, pp. 104-113.
2. Bernitsas, M.M. and Tawekal, R.L., "Structural Model Correlation Using Large Admissible Perturbations in Cognate Space," AIAA Journal, Vol. 29, No. 9, September 1991.
3. Bernitsas, M.M., Kang, B.S., and Tawekal, R., "RESTRUCT Version 3.0: A Program for REdesign of STRUCTures," Publication No. 312, Department of Naval Architecture and Marine Engineering, The University of Michigan, Ann Arbor, October 1989.
4. Beyko, E., "Development of a Large Admissible Perturbation Methodology for Reliability of Large Scale Structures," Ph.D. dissertation prospectus, Department of Naval Architecture and Marine Engineering, The University of Michigan, Ann Arbor, January 1991.
5. De, R.S., "Offshore Structural System Reliability: Wave-Load Modeling, System Behavior, and Analysis," Report No. RMS-6, Dept. of Civil Eng., Stanford Univ., March 1990.
6. D'Oliveira, J.G. and Zimmer, R.A., "Redundancy Considerations in the Structural Design of Floating Offshore Platforms," Proceedings of Design-Inspection-Redundancy Symposium, Williamsburg, Virginia, November 1983, pp. 13.1-13.31.
7. Gill, P.E., Murray, W., Saunders, M.A., Wright, M.H., "User's Guide for SOL/NPSOL: A Fortran Package for Nonlinear Programming," Department of Operations Research, Stanford University, 1983.
8. Gill, P.E., Murray, W., Saunders, M.A. and Wright, M.H., "User's Guide for SOL/QPSOL: A Fortran Package for Quadratic Programming," Department of Operations Research, Stanford University, 1983.
9. Haftka, R.T., Gürdal, Z. and Kamat, M.P., Elements of Structural Optimization, 2nd revision edition, Kluwer Academic Publishers, 1990.

10. Hasofer, A.M. and Lind, N.C., "Exact and Invariant Second-Moment Code Format," Journal of the Engineering Mechanics Division, ASCE, Vol. 100, 1974, pp. 111-121.
11. Hoff, C.J. and Bernitsas, M.M., "Dynamic Redesign of Marine Structures," Journal of Ship Research, Vol. 29, No. 4, December 1985, pp. 285-295.
12. Hoff, C.J., Bernitsas, M.M., Sandström, R.E., and Anderson, W.J., "Nonlinear Incremental Inverse Perturbation Method for Structural Redesign," AIAA Journal, Vol. 22, No. 9, September 1984, pp. 1304-1309.
13. Hohenbichler, M. and Rackwitz, R., "Non-normal Dependent Vectors in Structural Safety," Journal of Eng. Mechanics Div., ASCE, 107 (EM6), December 1981, pp. 1227-1238.
14. Kang, B.S., Beyko, E., and Bernitsas, M.M., "Invariant and Consistent Redundancy by Large Admissible Perturbations," Journal of Marine Structures (in press) 1991.
15. Kim, J.H. and Bernitsas, M.M., "Redesign of Marine Structures by Perturbation," Journal of Marine Structures, Vol. 1, No. 2, September 1988, pp. 139-183.
16. Koga, T., "Effects of Boundary Conditions on the Free Vibrations of Circular Cylindrical Shells," AIAA Journal, Vol. 26, No. 11, 1988. pp. 1387-1394.
17. Koski, J., Silvennoinen, R. and Lawo, M., "Multicriterion Plate Optimization," Structural Optimization, edited by Rosvany, G.I.N. and Karihaloo, B.L., Proceedings of the IUTAM Sym. on Structural Optimization, Melbourne Australia, Feb. 9-13, 1988, pp. 159-167.
18. Leissa, A., Vibration of Shells, NASA SP-288, Washington, D.C., 1973.
19. Liu, P.-L. and Der Kiureghian, A., "Finite Element Reliability of Two Dimensional Continua with Geometrical Nonlinearity," Proceedings, 5th Int. Conf. on Structural Safety and Reliability, ICOSSAR '89, Aug. 1989, San Francisco, pp. 1089-1096.
20. Madsen, H.O., Krenk, S., and Lind, N.C., Methods of Structural Safety, Prentice-Hall Inc., Englewood Cliffs, NJ, 1986.
21. Nordal, H., Cornell, C.A., and Karamchandani, A., "A Structural System Reliability Case Study of an Eight-Leg Steel Jacket Offshore Production Platform," Proceedings of Marine Structural Reliability Sym., SNAME, Arlington, VA, Oct. 5-6, 1987, pp. 193-216.
22. Prasad, B. and Haftka, R.T., "Optimal Structural Design with Plate Finite Elements," ASCE Journal of Structural Division, 105, pp. 2367-2382, 1979.
23. Ross, C.T., Pressure Vessels Under External Pressure: Statics and Dynamics, Elsevier Applied Science, 1990.
24. Sandström, R.E. and Anderson, W.J., "Modal Perturbation Methods for Marine Structures," SNAME Transactions, Vol. 90, 1982, pp. 41-54.
25. Simitses, G.J., Aswani, M., "Minimum-Weight Design of Stiffened Cylinders Under Hydrostatic Pressure," Journal of Ship Research, Vol. 21, No. 4, Dec. 1977, pp. 217-224.
26. Stetson, K.A., "Perturbation Method of Structural Design Relevant to Holographic Vibration Analysis," AIAA Journal, Vol. 13, No. 4, April 1975, pp. 457-459.
27. Stetson, K.A. and Harrison, I.R., "Redesign of Structural Vibration Modes by Finite-Element Inverse Perturbation," ASME Transactions, Journal of Engineering for Power, Vol. 103, No. 2, April 1981, pp. 319-325.
28. Tawekal, R.L. and Bernitsas, M.M., "Finite Element Model Correlation for Offshore Structures," Proceedings 10th International OMAE Conference, Norway, June 1991.
29. Thoft-Christensen, P. and Murotsu, Y., "Application of Structural Systems Reliability Theory," Springer-Verlag Berlin, Heidelberg, 1986.
30. Vanmarcke, E., Shinozuka, M., Nakagiri, S., Schueller, G.I. and Grigoriu, M., "Random Fields and Stochastic Finite Elements," Structural Safety, 3, 1986, pp. 143-166.
31. Yoshidao, N., Vanderplaats, G.N., "Structural Optimization Using Beam Elements," AIAA Journal, Vol. 26, No. 4, 1988, pp. 454-462.

Third International Conference on Inverse Design Concepts and Optimization in Engineering Sciences (ICIDES-III), Editor: G.S. Dulikravich, Washington D.C., October 23-25, 1991.

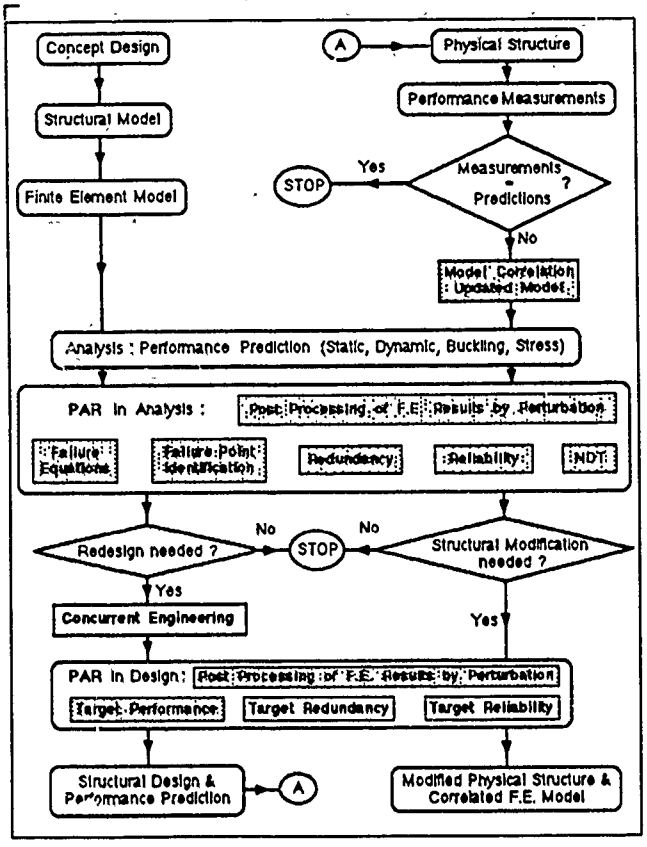


Figure 1. Structural analysis and design problems solved by PAR (rectangular blocks indicate problems that can be solved by LEAP theory; shaded blocks indicate problems already solved in some form)

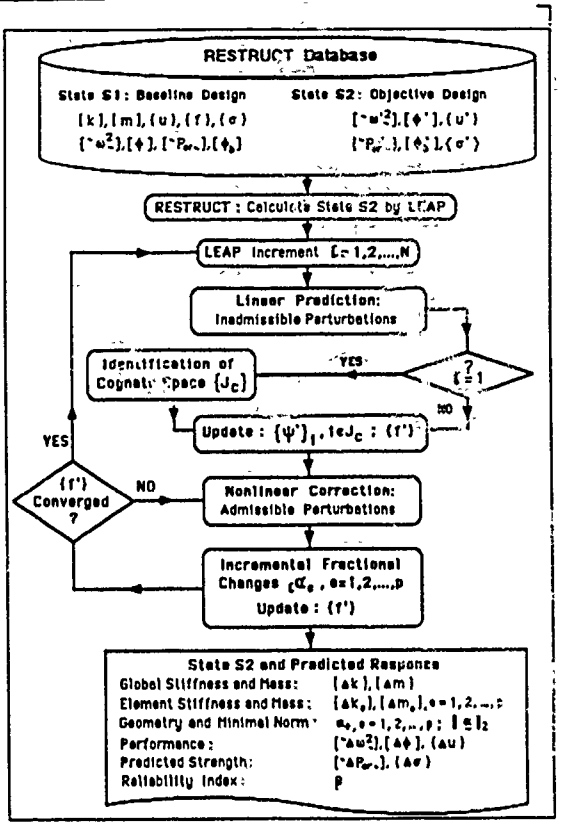


Figure 2. Implementation of LEAP (LargE Admissible Perturbation) algorithm in code RESTRUCT

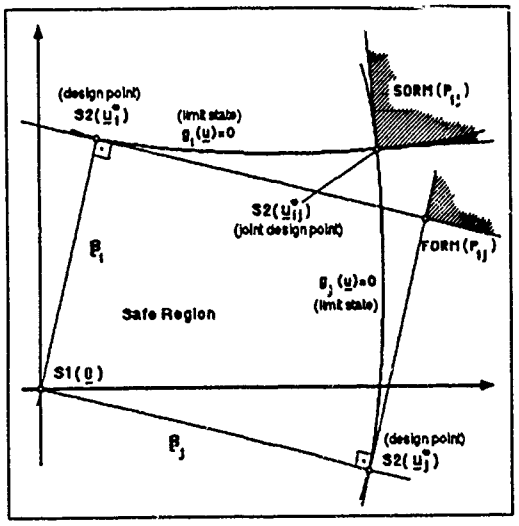


Figure 3. First and second order methods for reliability computations

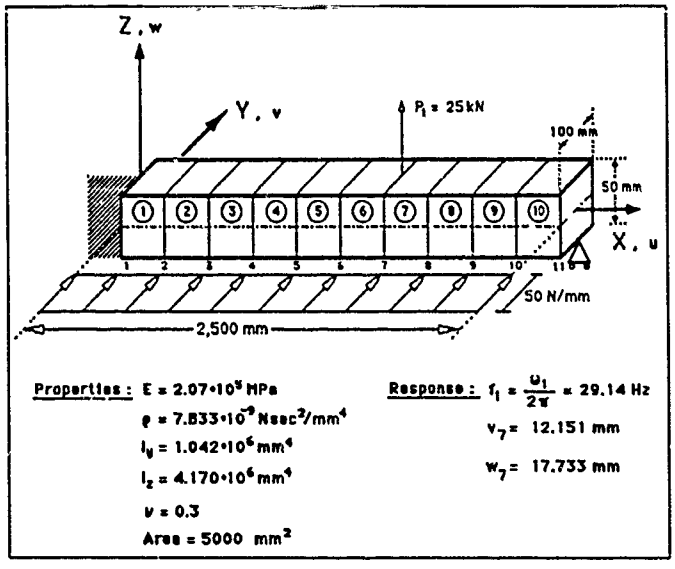


Figure 4. 10-element, 48-d.o.f. clamped hinged beam

Third International Conference on Inverse Design Concepts and Optimization in Engineering Sciences (ICIDES-III), Editor: G.S. Dulikravich, Washington D.C., October 23-25, 1991.

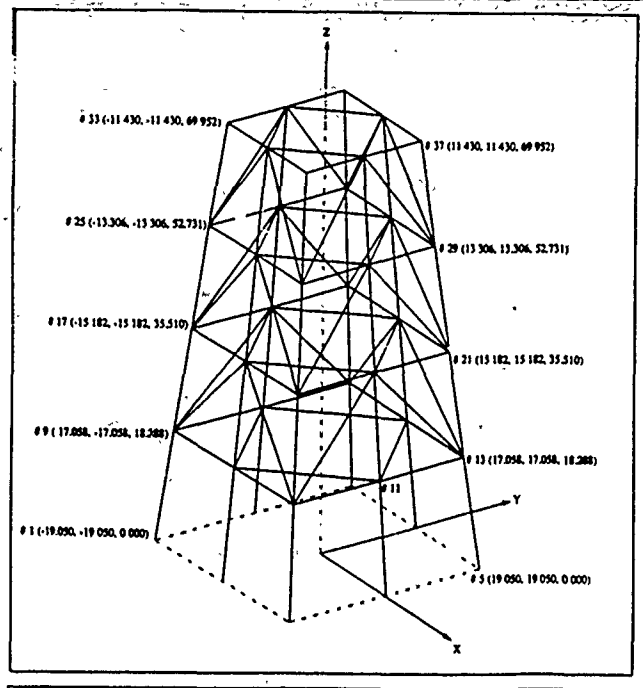
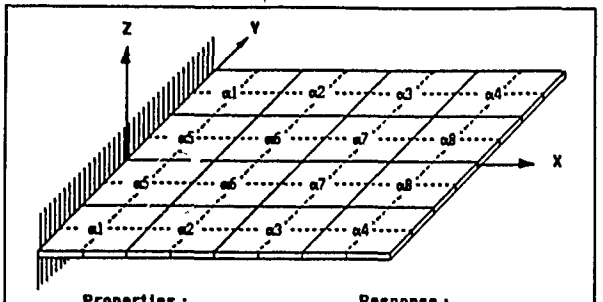


Figure 5. 104-element, 192-d.o.f. offshore tower



Properties :

$E = 2.07 \cdot 10^5$ MPa

$\rho = 7.833 \cdot 10^{-9}$ Nsec^2/mm^4

$\nu = 0.3$

Length = 1000 mm

Width = 1000 mm

Thickness = 10 mm

Uniform load $p = 1.6 \cdot 10^2$ MPa

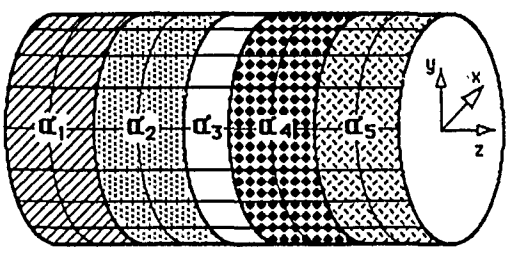
Response :

$f_1 = \frac{\omega_1}{2\pi} = 7.107$ Hz

$f_2 = \frac{\omega_2}{2\pi} = 17.21$ Hz

$U_{max} = 1.640$ mm

Figure 6. 64-element, 216-d.o.f. plate



Simply Supported Cylindrical Shell

Properties :

$E = 2.07 \cdot 10^5$ MPa

$\rho = 7.833 \cdot 10^{-9}$ Nsec^2/mm^4

$\nu = 0.3$

Length = 15.088 m

Radius = 5.029 m

Thickness = 5.08 cm

Hydrostatic pressure p = 2.967 MPa

Response :

$f_1 = f_2 = 13.0$ Hz

$f_3 = f_4 = 14.3$ Hz

$f_5 = f_6 = 17.5$ Hz

$U_{max} = 1.061$ cm

Figure 7. 144-element, 896-d.o.f. cylindrical shell

Table 1. Redesign and reliability of clamped-hinged beam

Case #	$\omega_1'^2/\omega_1^2$			v_7'/v_7			w_7'/w_7			β	CPU (msec)	n_r	n_a	p
	F.S.*	Reanalysis	Error(%)	F.S.*	Reanalysis	Error(%)	F.S.*	Reanalysis	Error(%)					
1	0.4588	0.4578	-0.205	—	—	—	—	—	—	7.65	31050	9	8	14
2	—	—	—	2.0358	2.0440	0.405	—	—	—	11.40	52620	10	12	14
3	—	—	—	—	—	—	2.0358	2.0458	0.489	7.39	48378	9	8	14
4	0.4588	0.4570	-0.401	2.0358	2.1124	3.762	—	—	—	20.83	75520	9	12	21
5	0.4588	0.4554	-0.736	—	—	—	2.0358	2.0568	1.033	7.36	68486	11	10	14
6	—	—	—	2.0358	2.1125	3.769	2.0358	2.0701	1.684	15.09	90435	9	9	14
7	0.4588	0.4545	-0.931	2.0358	2.1893	7.542	2.0358	2.0737	1.863	18.03	105928	10	12	21
11	0.3	0.2892	-3.586	—	—	—	—	—	—	13.02	81131	11	10	14
12	—	—	—	3.0	3.0122	0.407	—	—	—	19.52	80156	10	12	14
13	—	—	—	—	—	—	3.0	3.2152	7.173	11.31	108912	11	12	14
14	0.3	0.2959	-1.379	3.0	3.1554	5.179	—	—	—	39.65	116314	9	12	21
15	0.3	0.2841	-5.271	—	—	—	3.0	3.0997	3.325	15.63	99915	11	10	14
16	—	—	—	3.0	3.2042	6.801	3.0	3.2969	9.898	25.40	101394	7	5	14
17	0.3	0.2940	-2.002	3.0	3.3282	10.942	3.0	3.1003	3.342	33.59	167822	10	12	21

cases 4, 7, 13, 15, and 17 are solved by the generalized inverse algorithm. *F.S.= Failure State

Third International Conference on Inverse Design Concepts and Optimization in Engineering Sciences (ICIDES-III), Editor: G.S. Dulikravich, Washington D.C., October 23-25, 1991.

Table 2. 10-element , 48-d.o.f. clamped-hinged beam : structural groups and redesign variables

Structural Group #	Redesign Variables, α_e ; p = 21	Elements #
1	α_1 (α_{EI_y}) , α_2 (α_{EI_z}) , α_3 ($\alpha_{\rho A}$)	1, 2
2	α_4 (α_{EI_y}) , α_5 (α_{EI_z}) , α_6 ($\alpha_{\rho A}$)	3, 4
3	α_7 (α_{EI_y}) , α_8 (α_{EI_z}) , α_9 ($\alpha_{\rho A}$)	5
4	α_{10} (α_{EI_y}) , α_{11} (α_{EI_z}) , α_{12} ($\alpha_{\rho A}$)	6
5	α_{13} (α_{EI_y}) , α_{14} (α_{EI_z}) , α_{15} ($\alpha_{\rho A}$)	7
6	α_{16} (α_{EI_y}) , α_{17} (α_{EI_z}) , α_{18} ($\alpha_{\rho A}$)	8
7	α_{19} (α_{EI_y}) , α_{20} (α_{EI_z}) , α_{21} ($\alpha_{\rho A}$)	9, 10

Table 3. 104-element, 192-d.o.f. offshore tower : structural groups, redesign variables, and dimensions

Structural Group #	Redesign Variables α_e	Description	D_o (m)	D_i (m)	Number elements
1	α_1 (α_{EI}) α_2 ($\alpha_{\rho A}$)	Legs below first bracing	0.762	0.737	8
2	α_3 (α_{EI}) α_4 ($\alpha_{\rho A}$)	Legs between first and second bracing	0.610	0.584	8
3	α_5 (α_{EI}) α_6 ($\alpha_{\rho A}$)	Legs above second bracing	0.610	0.584	16
4	α_7 (α_{EI}) α_8 ($\alpha_{\rho A}$)	Horizontal bracing	0.483	0.464	32
5	α_9 (α_{EI}) α_{10} ($\alpha_{\rho A}$)	Horizontal cross bracing	0.508	0.489	16
6	α_{11} (α_{EI}) α_{12} ($\alpha_{\rho A}$)	Vertical cross bracing	0.610	0.591	24

Table 4. Redesign and reliability of offshore tower

Case #	$\omega_1'^2/\omega_1^2$			$\omega_3'^2/\omega_3^2$			β	CPU (msec)	n_r	n_a
	F.S.*	Reanalysis	Error(%)	F.S.*	Reanalysis	Error(%)				
1	0.6598	0.6531	-1.018	—	—	—	4.43	973814	18	8
2	—	—	—	0.6598	0.6530	-1.030	3.8	925711	19	8
3	0.6598	0.6547	-0.786	0.6598	0.6541	-0.871	9.37	985832	18	8
11	0.5000	0.4871	-2.572	—	—	—	8.03	1589439	18	8
12	—	—	—	0.5000	0.4844	-3.112	21.47	1529708	19	8
13	0.5000	0.4895	-2.100	0.5000	0.4877	-2.462	13.7	1617425	18	8

p = 12; cases 12 and 13 are solved by the generalized inverse algorithm. *F.S.= Failure State

Table 5. Redesign of 64-element 216-d.o.f. plate

Case #	$\omega_1'^2/\omega_1^2$			$\omega_2'^2/\omega_2^2$			u'_{max}/u_{max}			$\sum \alpha_e^2$	CPU (sec)
	Goal	Reanalysis	Error(%)	Goal	Reanalysis	Error(%)	Goal	Reanalysis	Error(%)		
1	1.2867	1.2844	-0.177	—	—	—	—	—	—	0.0267	263
2	2.0000	1.9818	-0.909	—	—	—	—	—	—	0.2354	713
3	—	—	—	—	—	—	0.7579	0.7633	0.718	0.0358	420
4	—	—	—	—	—	—	0.5000	0.5069	1.374	0.2794	1044
5	1.2867	1.2842	-0.195	—	—	—	0.7772	0.7818	0.594	0.0295	440
6	2.0000	1.9801	-0.997	—	—	—	0.5000	0.5064	1.289	0.2816	1199
7	1.2867	1.2848	-0.144	1.1589	1.1572	-0.140	—	—	—	0.0275	381
8	2.0000	1.9848	-0.760	1.5000	1.4875	-0.831	—	—	—	0.2407	1037
9	1.2867	1.2840	-0.204	1.2867	1.2788	-0.621	0.7772	0.7821	0.631	0.0549	562
10	2.0000	1.9747	-1.264	2.0000	1.9198	-4.011	0.5000	0.5077	1.531	0.4378	1532
11	1.3195	1.3157	-0.287	1.3195	1.3103	-0.697	0.6598	0.6649	0.787	0.1561	833
12	2.0000	1.9721	-1.395	2.0000	1.9341	-3.397	0.3536	0.3600	1.831	1.2394	2072
13	1.2867	1.2844	-0.173	1.1589	1.1574	-0.125	0.7772	0.7817	0.577	0.0297	562
14	2.0000	1.9806	-0.971	1.5000	1.4941	-0.395	0.5000	0.5063	1.259	0.2817	1528
15	1.3195	1.3093	-0.774	1.1761	1.1691	-0.591	0.6598	0.6678	1.224	0.1618	832
16	2.0000	1.9104	-4.479	1.5000	1.4408	-3.950	0.3536	0.3710	4.945	1.3025	2065

In all cases, $n_r = 7, n_a = 5, p = 8$.

Table 6. Redesign of Simply Supported Cylindrical Shell

Case #	$\omega_1'^2/\omega_1^2$			$\omega_2'^2/\omega_2^2$			u'_x/u_x			$\sum \alpha_e^2$	CPU (sec)
	Goal	Reanalysis	Error(%)	Goal	Reanalysis	Error(%)	Goal	Reanalysis	Error(%)		
1	1.3310	1.3200	-0.900	—	—	—	—	—	—	0.5867	549
2	1.5700	1.5300	-2.700	—	—	—	—	—	—	1.3300	715
3	1.9171	1.7800	-7.000	—	—	—	—	—	—	2.4800	1077
4	1.9171	1.7800	-7.000	1.6700	1.5000	-9.000	—	—	—	2.486	2031
5	1.331	1.3200	-0.900	—	—	—	0.6480	0.6610	2.000	0.5790	940
6	1.9171	1.7800	-7.000	—	—	—	0.648	0.646	0.00	2.486	2131

In all cases, $n_r = 5, n_a = 5$

Third International Conference on Inverse Design Concepts and Optimization in Engineering Sciences (ICIDES-III), Editor: G.S. Dulikravich, Washington D.C., October 23-25, 1991.

STRUCTURAL DAMAGE IDENTIFICATION USING MATHEMATICAL OPTIMIZATION TECHNIQUES

Mo-How Herman Shen
Department of Aeronautical and Astronautical Engineering
The Ohio State University

Abstract

An identification procedure is proposed to identify the damage characteristics (location and size of the damage) from dynamic measurements. This procedure was based on minimization of the 'mean-square' measure of difference between measurement data (natural frequencies and mode shapes) and the corresponding predictions obtained from the computational model. The procedure is tested for simulated damage in the form of stiffness changes in a simple fixed-free spring-mass system and symmetric cracks in a simply-supported Bernoulli-Euler beam. It is shown that when all the mode information were used in the identification procedure it is possible to uniquely determine the damage properties. Without knowing the complete set of modal information, a restricted region in the initial data space has been found for realistic and convergent solution from the identification process.

Introduction

There is a considerable body of research on identification problems, that is, the problem of identifying the engineering properties or reconstructing the structural configuration of a vibrating system from certain natural frequency spectra and/or corresponding mode shape. Such problems were considered by Barcilon [1, 2], McLaughlin [3, 4], Gladwell [5-7], and Gladwell *et al.* [8]. Most of these studies involve the determination of material properties from natural frequencies, and they emphasize the existence, uniqueness, and methods for determination of properties (termed 'reconstruction').

An detection procedure was developed by Shen and Taylor [9] to determine the crack characteristics (location xc and size cr of the crack) of Bernoulli-Euler beams from their dynamic response. The idea of this procedure was related to methods of structural optimization. Specifically, the structural damage was identified in a way to minimize one or another measure of the difference between a set of data (measurements) T_d, and the corresponding values for dynamic response M_d obtained by analysis of a model for the damaged beam. This may be expressed symbolically as the following optimization problem:

$$\min_{xc,cr} \; norm(T_d - M_d). \tag{1}$$

Naturally, the minimization represented here is constrained by the equations which model the physical system. Moreover, as indicated in the discussion by Shen and Pierre [10, 11], one can note that the more modal information used for crack detection, the more accurate and reliable the result that can be achieved. For practical purposes, the objective of Eq. (1) was formulated based on a certain set of specific modes; specifically the first three modes are considered in the inverse procedure.

In this study the corresponding to the mean-square measure of the norm, as shown in Eq. (1), is examined. The identification process is based on minimization of the 'mean-square' measure of difference between measurement data (natural frequencies and mode shapes) and the corresponding predictions obtained from the computational model. The identification procedure is tested for

Third International Conference on Inverse Design Concepts and Optimization in Engineering Sciences (ICIDES-III), Editor: G.S. Dulikravich, Washington D.C., October 23-25, 1991.

simulated damage in the form of a symmetric cracks in a simply-supported Bernoulli-Euler beam and a fixed-free spring-mass model. The uniqueness and reliability of the identification process is confirmed by solving several damage identification examples with specified damage positions.

Problem Statement

In this section, variational formulations for the identification of damaged one-dimensional structures are presented. The mean square differences between measured and modeled values of frequency and mode shape are employed as the objective function in one of the formulations. In other words, the inverse process seeks to determine the damage parameters, location xc and size cr, in the mathematical model to minimize the mean square difference between the test data and analytical predictions. The problem formulations are presented in forms of a cracked Bernoulli-Euler beam and a multi degrees of freedom (DOF) spring-mass system.

Cracked beam model

In the treatment of this problem, it is assumed that the testing information (data) is provided from certain test points distributed over the structure. This data is comprised of frequency and mode shape information associated with the lower several response modes.

For a simply-supported uniform beam containing one pair of symmetric cracks (see Fig. 1), the problem of optimization in crack detection can be expressed, in terms of comparisons between modeled response and test data, as

$$\min_{cr,xc} \; [norm(\omega_{t\alpha}^2 - \omega_\alpha^2, w_{t\alpha}(x_{tm}) - w_\alpha(x_{tm}))] \tag{2}$$

subject to constraints that define the beam response w_α (ie., the equations for free vibration), and which prescribe appropriate normalization of w_α and test data $w_{t\alpha}$.

Here $cr = \frac{d-h}{d}$ represents crack ratio (a measure of crack depth), and xc identifies crack position (see Fig. 1). Also, the objective function measure of differences between measured and modeled values of deflection and frequency in Eq. (2) is stated for present purposes in the form:

$$norm(\omega_{t\alpha}^2 - \omega_\alpha^2,\; w_{t\alpha} - w_\alpha) = (\sum_{\alpha=1}^{M}[(\omega_{t\alpha}^2 - \omega_\alpha^2)^2 + \sum_{m=1}^{T}(w_{t\alpha}(x_{tm}) - w_\alpha(x_{tm}))^2])^{\frac{1}{2}} \tag{3}$$

where ω_α, w_α represent the natural frequency and mode shape of αth bending free vibration mode, M is the number of modes for which test information is available, and, once again, the corresponding test data are symbolized by $\omega_{t\alpha}$ and $w_{t\alpha}$. Here x_{tm} $(m = 1, 2, ..., T)$ locates the m-th out of T measure stations, respectively. The measures $w_{t\alpha}$ and w_α that appear in the norm must be normalized on a common basis in order to facilitate comparison between the data and model values.

The symbol Φ is introduced to represent the square of the norm given in Eq. (3). The identification problem now can be stated:

$$\min_{cr,xc} \; \Phi \tag{4}$$

subject to:

$$\int_0^l \{EIQ(w_\alpha''(x))^2 - \omega_\alpha^2 \rho A \, w_\alpha^2(x)\} dx = 0 \tag{5}$$

$$\sum_{m=2}^{T-1}(w_\alpha(x_{tm}) w_\beta(x_{tm}))\Delta x_{tm} \; - \; \eta_{\alpha\beta} = 0 \tag{6}$$

$$(cr + \underline{a}\, xc) - R \leq 0 \tag{7}$$

$$\underline{cr} \leq cr \leq \overline{cr} \tag{8}$$

$$\underline{xc} \leq xc \leq \overline{xc} \tag{9}$$

where $\alpha,\beta=1,...,M$, $\underline{a}$ is a weighting factor on the cr and xc, R represents the upper bound on value $cr + \underline{a}xc$, and $\overline{xc}, \underline{xc}$, and $\overline{cr}, \underline{cr}$ represent the upper and lower bounds of the crack (damage) parameters xc and cr, respectively. (Note that both upper and lower bounds on the variables cr and xc are necessary in the present problem.) Since w_α comprise an orthonormal set, $\eta_{\alpha\beta}$ is defined as

$$\eta_{\alpha\alpha} = \sum_{m=2}^{T-1} w_\alpha^2 |_{x_{tm}} \Delta x_{tm}, \qquad \lim_{T\to\infty} \eta_{\alpha\beta} = 0 \quad \text{for} \quad \alpha \neq \beta \tag{10}$$

The effect of cracks on the structural properties of the beam is reflected by factor Q in Eq. (5), as described for symmetric surface cracks in Shen and Pierre [10]. In other words, the optimization parameters xc and cr cited in Eq. (4) enter the problem via Q.

According to the K-K-T (Kurash-Kuhn-Tucker) necessary conditions for the optimization problem Eqs. (4-9), there exist Lagrange multipliers λ_α, , $\Lambda_{\alpha\beta}$, and Γ_k which satisfy the following equations (the notation '$|_*$' refers to solution points):

$$\lambda_\alpha > 0$$

$$\Lambda_{\alpha\beta} > 0$$

$$\Gamma_1 [(cr + \underline{a}xc) - R] |_* = 0 \tag{11}$$

$$[\Gamma_2 (\underline{cr} - cr)] |_* = 0 \tag{12}$$

$$[\Gamma_3 (xc - \overline{xc})] |_* = 0 \tag{13}$$

$$[\Gamma_4 (\underline{xc} - xc)] |_* = 0 \tag{14}$$

$$[\Gamma_5 (cr - \overline{cr})] |_* = 0 \tag{15}$$

The solution must satisfy the following three equations as well:

$$[2(\omega_{t\alpha}^2 - \omega_\alpha^2) + \lambda_\alpha \rho A C_\alpha^2] |_* = 0 \tag{16}$$

$$[(EIQw_\alpha''(x))'' - \omega_\alpha^2 \rho A w_\alpha(x)] |_* = 0 \quad ; x_{tm} < x < x_{t(m+1)} \tag{17}$$

$$\sum_{m=2}^{T-1} \{-2(w_{t\alpha}(x) - w_\alpha(x)) + [2\Lambda_{\alpha\alpha} w_\alpha(x) + \sum_{\beta=1}^{\alpha-1} \Lambda_{\alpha\beta} w_\beta(x)$$

$$+ \sum_{\beta=\alpha+1}^{M} \Lambda_{\alpha\beta} w_\beta(x)] \Delta x_{tm} + 2\lambda_\alpha [(EIQw_\alpha''(x))'' - \omega_\alpha^2 \rho A w_\alpha(x)]\} \; |_{x=x_{tm}}|_* = 0 \tag{18}$$

Note that the above equation of motion (Eq. 17) is valid interval by interval over the span of the structure.

Finally, the conditions for stationarity of Φ w.r.t. the optimization variables cr and xc (ie., the optimality conditions) are:

$$[\sum_{\alpha=1}^{M} \lambda_\alpha (EI \int_0^l \frac{\partial Q}{\partial cr} (w_\alpha''(x))^2 dx) + \Gamma_1 - \Gamma_2 + \Gamma_5] |_* = 0 \tag{19}$$

$$[\sum_{\alpha=1}^{M} \lambda_\alpha (EI \int_0^l \frac{\partial Q}{\partial xc}(w''_\alpha(x))^2 dx) + \Gamma_1 \underline{a} + \Gamma_3 - \Gamma_4] \mid_* = 0 \tag{20}$$

• *The problem formulation for the numerical method-mean square criterion*

The purpose in this subsection is to re-state the inverse cracked beam problem with mean square criterion, Eqs. (4-9), in the following form that is more convenient for computational purposes. With the introduction of symbols ξ and Υ for convenience, the statement becomes:

$$\min_{\underline{x}_1} \sum_{\alpha=1}^{M} [(\xi_{t\alpha} - \xi_\alpha)^2 + \sum_{m=1}^{T} (w_{t\alpha}(x_{tm}) - w_\alpha(x_{tm}))^2] \tag{21}$$

subject to :

$$[\alpha^4 Q \sum_{m=1}^{T} (w_\alpha(x_{tm}))^2 - \xi_\alpha \sum_{m=1}^{T} (w_\alpha(x_{tm}))^2] \Delta x_{tm} - \Upsilon_\alpha = 0 \tag{22}$$

$$\sum_{m=2}^{T-1} (w_\alpha(x_{tm}) w_\beta(x_{tm})) \Delta x_{tm} - \eta_{\alpha\beta} = 0 \tag{23}$$

$$0 \leq cr \leq 1.0 \tag{24}$$

$$0 \leq xc \leq 1.0 \tag{25}$$

where $\alpha, \beta = 1,...,M$, variable vector $\underline{x}_1 = \{cr, xc, \xi_\alpha, w_\alpha(x_{tm})\}$,

$$\xi_\alpha = \frac{\omega_\alpha^2 l^4 \rho A}{EI\pi^4} \tag{26}$$

and

$$\Upsilon_\alpha = [\alpha^4 Q \sum_{m=1}^{T} (w_{t\alpha}(x_{tm}))^2 - \xi_\alpha \sum_{m=1}^{T} (w_{t\alpha}(x_{tm}))^2] \Delta x_{tm} \tag{27}$$

Spring-mass model

The spring-mass model to which the present identification procedure is applied is shown in Fig. 2. It consists of 3 masses connected by linear springs of stiffness defined by

$$k_i = k(1.0 - \frac{dm_i}{3})^3 \tag{28}$$

where dm_i is defined as a damage parameter at i-th spring. If dm_i is interpreted to represent the same physical meaning as cr does in the cracked beam model, the system's damage condition may be introduced by specifying a certain value to 'damage parameters'. For instance, according to Eq. (28), a damaged condition can be constructed in which stiffness drops 25% and 50% at the spring 2 and 3. This is accomplished by assigning the values dm_2 and dm_3 to be 0.2743 and 0.6189, respectively. In a sense, the spring-mass model can be viewed as a simple simulation analogy of the cracked beam, ie., both extent and location of damage can be represented in the model. The fundamental frequencies ω_i of axial vibrations are related to the mode shapes $\tilde{u}_i = (u_1, u_2, u_3)_i^T$, $i = 1,2,3$ through the equations:

$$\tilde{u}_i^T [K_s] \tilde{u}_i - \xi_i \tilde{u}_i^T [I] \tilde{u}_i = 0 \ ; i = 1,2,3 \tag{29}$$

where $\xi_i = \frac{m\omega_i^2}{k}$. Therefore, the present damage identification problem can be stated as

$$\min_{\underline{x}=dm_i,\xi_i,\tilde{u}_i} \sum_{i=1}^{3} [(\xi_{ti} - \xi_i)^2) + \sum_{j=1}^{3} (\tilde{u}_{tji} - \tilde{u}_{ji})^2] \tag{30}$$

Third International Conference on Inverse Design Concepts and Optimization in Engineering Sciences (ICIDES-III), Editor: G.S. Dulikravich, Washington D.C., October 23-25, 1991.

subject to:

$$\tilde{u}_i^T [K_s] \tilde{u}_i - \xi_i \tilde{u}_i^T \tilde{u}_i = 0 \quad ; i = 1,2,3 \tag{31}$$

$$\tilde{u}_i^T \tilde{u}_j - \delta_{ij} = 0 \quad ; i,j = 1,2,3 \tag{32}$$

$$0 \leq dm_i \leq 1.0 \tag{33}$$

Numerical Analysis

The numerical optimization technique set forth in this study for vibrating cracked beam identification problems is accomplished using the VMCON optimization package program (this implements a sequential quadratic programming method). The VMCON program uses Powell's algorithm which is an iterative scheme designed to converge to a point that satisfies the necessary conditions. Additional information regarding to VMCON is available in Ref. [12].

Cracked beam model

The cracked beam model to which the identification procedure is applied is shown in Fig. 1. It is a simply supported beam of length l equal to 18.11 of it's thickness $2d$, with uniform rectangular cross-section area A, and a pair of symmetric cracks of $cr = 0.5$ located at mid-span ($xc = 0.5$).

Unless otherwise stated, the damage properties (cr and xc) of the simply supported cracked beams are identified by direct solution of the optimalization problems described in the previous section. The sensitivity to chosen values for the initial crack position xc are discussed later in this section.

• *Examples with position of the crack (damage) specified*

Consider the first example for crack identification, the simply supported cracked beam, for which the crack position xc is known. In other words, only the crack ratio cr is to be identified; therefore, the variables in this problem are cr, $\xi's$, and mode shapes $w_\alpha(x)$ ($\underline{x}_1 = \{cr, \xi_\alpha, w_\alpha(x_{tm})\}, \underline{x}_2 = \{cr, \xi_\alpha, a_{\alpha i}\}$). This simplified example problem with the crack position specified ($xc = 0.5$) is presented to demonstrate the concept of the crack identification procedure described in the last section.

In this example, it is assumed that the dynamic measurements are collected at 9 test positions ($T = 9$) equally spaced over the span. The first and last test stations are located at the left and right supported end, respectively. Hence, the length of each test span $\Delta x_{tm}, m = 1,...,T-1$ is determined to be $\frac{36.22d}{T-1}$. In structural dynamic testing, ordinarily only a relatively small subset of the theoretically available eigenvalues and eigenvectors can be measured accurately, ie., realistic information on higher modes is difficult to obtain from the measurements at a limited set of test stations. Only information from the first three modes is to be used as test data in the present identification process. Furthermore, according to the observations in Shen and Pierre [10], the even modes of a simply supported beam are not sensitive to a mid-span crack; therefore, in effect only first and third mode ($\alpha = 1,3$) information is used to represent crack damage.

Once again, the crack identification problem presented by Eqs. 21-25 is solved here with a specified value $xc = 0.5$. For given initial values of $\underline{x}$, this optimization problem is solved to minimize the criterion F. The results of the cases with various initial conditions are shown in Table 1. In order to clearly compare the results, only the first three variables, ξ_1, ξ_3, cr, of variable vector $\underline{x}_1$ are listed in the Table 1.

In Table 1, the top row denotes the assumed crack ratio and corresponding first and third eigenfrequencies. The symbol * denotes the expected optimal solution through the identification process. The first two column entries, ξ_1, ξ_3, indicate the fundamental and the third frequencies corresponding to the initial crack ratio cr which is given in the next column. The last three columns give the final values corresponding to previous entry values. These final values are obtained at the

Third International Conference on Inverse Design Concepts and Optimization in Engineering Sciences (ICIDES-III), Editor: G.S. Dulikravich, Washington D.C., October 23-25, 1991.

stage where computation is terminated when the further optimal search obtains improvements for criterion F less than the specified tolerance ($10E-5$ was adopted in the present study). Recall that for an uncracked beam cr is identically zero. Therefore, in this example, it is decided to start with the case of the initial value $cr = 0.0$ and for each case thereafter the cr value is increased by 0.1.

From the results presented in the first case of Table 1, one sees that the parameters ξ_1, ξ_3, and cr were identified to be 0.84684, 70.1348, and 0.50033 from 1.0, 81.0, and 0.0, respectively. The mean square critera F was cut down from 118.13502 to 0.42440E-5. The maximum error is less than 0.5% of the test data for these parameters. The results are also quite impressive for mode shapes. In order to observe the global variance clearly, the initial, final, and testing mode shapes are plotted in Fig. 3. Three curves appear on each plot: the initial mode shape, the finial mode shape, and the mode shape from test response. The final mode shape on these plots agrees well with the test mode shape. This is expected and verified the accuracy observed from the results in Table 1. It can be clearly seen that accuracy of the mode shapes will worsen if higher mode results are to be predicted. Improvement can be obtained by an appropriate adjustment of the location of these test stations. However, a sensitivity analysis of the test stations with respect to the accuracy of the dynamic measurements is required. This is not considered further in the present study.

In Table 1, rows 5 to 11 present the results for cases with initial $cr = 0.1$ to 0.8. The corresponding final point values listed in the columns 4-6 show that these cases exhibit, as expected, similar solution characteristics and accuracy. This provides a physical understanding of the geometry of the solution set: for the inverse cracked beam problem with specified crack position, the mean square criterion of Eq. (21) is a convex function and it is bounded by the constraints of Eqs. (22-25). Hence, one may conclude that the convergence of the present optimization problem is obtained independent of the initial data chosen. In other words, as long as the initial data is selected within the problem's feasible domain, an accurate and unique solution through the identification process is expected.

Clearly the prediction of mode 3 shape shown in Fig. 3 fails to reproduce the expected sin curve. This is because the 3rd mode shape was plotted based on the deflections of the mode shape measured at only 9 test stations. While this reflects a limitation on how well mode shapes are portrayed, the quality of the final result for the identification problem is unaffected.

• *Simultaneous identification of crack position and depth*

The second numerical example deals with the crack identification of a simply supported cracked beam with unknown crack ratio and with crack position unknown. In this treatment, the variables in the optimization problem are cr, xc, $\xi's$, and mode shapes $w_\alpha(x)$ ($\underline{x}_1 = \{cr, xc, \xi_\alpha, w_\alpha(x_{tm})\}$). Due to the limitations of the VMCON program, the examples that concerning with the testing mode shapes w_t provided in the form of continuous functions are not shown in this subsection.

The formulation of the crack identification problem (Eqs. 21-25) is tested again with both crack position and depth are assumed unknown. In the first few cases, the simulated dynamic test measurements are assumed to be collected at 9 equally spaced test stations ($T = 9$). The first and last test positions are located at the left and right supported end, respectively. This example will be solved a second time using an increased number of test stations, to provide information on sensitivity of the procedure to the amount of test data.

In Table 2, the top row denotes the assumed crack ratio, crack position, and corresponding first and third eigenfrequencies. The symbol * denotes the expected optimal solution through the identification process. The first column entry T denotes the number of test stations used to collect dynamic measurements. The second and third column entries, ξ_1, ξ_3, indicate the fundamental and the third frequencies corresponding to the initial crack ratio cr and crack position xc, which are given in the next two columns. The last four columns provide the final values corresponding to

Third International Conference on Inverse Design Concepts and Optimization in Engineering Sciences
(ICIDES-III), Editor: G.S. Dulikravich, Washington D.C., October 23-25, 1991.

the previous entry values. These final values are obtained at the stage where the computation is terminated, when the optimal search obtains step-wise improvements of F less than a specified tolerance ($10E-5$ in the present study).

Table 2 shows that cases with T=9 have the final values of ξ close to ξ^*, but almost all of these cases have unacceptable final estimates of xc and cr. For instance, if the initial position is selected as $xc = 0.4$ and $cr = 0.4$, the values of xc and cr at the final iteration are 0.99789 and 0.36289 which are approximately 98% and 28% different than the given test data. In other words, evidently the configuration with $xc = 0.99789$ and $cr = 0.36289$ is able to provide another minimum value of the criterion (besides the one associated with the expected result). This cracked beam configuration is shown in the solid curve of Fig. 4 . The mis-match between final and test mode shapes can be clearly seen. This observation confirmed the unacceptable error previously obtained in the comparison of xc and cr between the final and test data. Except for the case with initial $cr = 0.4$ and $xc = 0.48$ which provides less than 1% estimation error, the rest of the cases in Table 2 with 9 test stations are also found to have similarly large estimation error. Therefore a dependable solution in crack identification is almost impossible to achieve on the basis of the 9 test stations simulated measurement information on first and third mode response. This confirmed the observations in Shen and Pierre [10, 11], ie., for a cracked beam with an unknown crack position, a unique solution is not to be expected.

However, by comparing the third mode shape in Figs. 3(b) and 4(b) to the mode shape in Fig. 11(c) of Ref. [10], it can be seen that an accurate third mode shape can not be approximated based on the displacements collected from 9 test stations only. This implies that the accuracy of the above computational identification might be improved if the third mode is approximated well. Therefore, the cases with more test stations should be examined since they would clearly provide better mode shape approximation. The largest number of test stations which can be accommodated in the identification procedure is 45, due to the limitations of the optimization program package. Once again, the test measurement points are equally spaced, and first and last stations are set located at the left and right supported end, respectively. The VMCON problem formulation is identical to the case of T=9; however, the variable vector $\underline{x}$ is expanded from 22 components to 94.

Rows 12 to 17 of Table 2 summarizes the results through the minimization process. As in the previous cases, the final values of frequency ξ are observed to be close to test values ξ^*. Acceptable final solution values for xc and cr are shown in the results of the cases in which initial xc and cr are selected within the range from $xc = 0.4, cr = 0.4$ to $xc = 0.6, cr = 0.6$. On the other hand, within this range, good agreement is also shown in mode shapes. Figures. 5 and 6 display the initial, final, and test mode shapes for cases with the initial $xc = 0.4, cr = 0.4$ and $xc = 0.6, cr = 0.6$. Excellent agreement is observed between the final and test mode shapes. Moreover, by comparing the final data curve in Figs. 5 and 6 with the mode shape in Fig. 11(c) of Ref. [10], a more accurate third mode is approximated. This indicates that more accurate information on mode shapes is required to obtain a satisfactory solution from the identification process in the case where both crack position and crack depth are unknown.

Questions arise concerning the conditions under which the identification procedure can provided an unique solution. As discussed in Shen and Pierre [10, 11] and concluded in the studies of Gladwell *et. al.* [8], if all the mode information is used in the identification procedure, then the system's properties can be identified uniquely. However, for practical reasons, in structural dynamic testing only a small subset of the eigenvalues and eigenvectors can be represented in the measurement data. Furthermore, even if substantially more modal information would be available, the minimization search may be prohibitive for such a large-dimensional feasible domain that would result. These comments are intended to point out certain limitations inherent in the identification procedures. These considerations is addressed with the presentation in the following, which

Third International Conference on Inverse Design Concepts and Optimization in Engineering Sciences (ICIDES-III), Editor: G.S. Dulikravich, Washington D.C., October 23-25, 1991.

describes sufficient conditions for the unique identification from the dynamic measurements of a multi DOF vibrating spring-mass system.

Spring-mass model

The following examples of damage identification problems were constructed by introducing the damage through the drop in the stiffness or, more conveniently, the value of each damage parameter to change the system's dynamics behaviour. These dynamic changes, taken as the test simulation of response data, are used to deduce the value of each damage parameter via the identification process.

The numerical optimization technique set forth in this study for vibrating cracked beam identification problems is accomplished using the VMCON optimization package program (this implements a sequential quadratic programming method). The damage properties ($dm_i, i = 1,2,3$) of the fixed-free spring-mass system are identified by direct solution of the optimalization problems described in the previous section.

The first example corresponds to the identification of a system's damage, $dm_1 = 0.0, dm_2 = 0.5, dm_3 = 0.25$, using first and second mode information. The first five variables, ξ_1, ξ_2, dm_1, dm_2, and dm_3 of each vector $\underline{x}$ are listed in Table 3. The top row denotes the assumed damage parameters and corresponding first and second eigenfrequencies and the symbol $*$ denotes the expected optimal solution through the identification process. The first and second column entries, ξ_1, ξ_2, indicate the fundamental and the second frequencies corresponding to the initial damage parameters, dm_1, dm_2, dm_3, which are given in the next three columns. The last five columns give the final values corresponding to previous entry values. These final values are obtained at the stage of the program is terminated when the further optimal search obtain improvements F less than a tolerance ($10E-5$ was adopted in the present study).

In Table 3, each case has the final values of ξ close to ξ^*, but almost all of them have the unacceptable final results for xc and cr. Only the case with initial $dm_2 = 0.48$ and $dm_3 = 0.24$ has less than a 1% estimation error. These results show performance of the present damage identification process is generally unacceptable if only first and second modes are used.

The first six variables, ξ_1, ξ_2, ξ_3, dm_1, dm_2, and dm_3 of each vector $\underline{x}$ are listed in Table 4 the top row denotes the assumed damage parameters and corresponding first and second eigenfrequencies and the symbol $*$ denotes the expected optimal solution through the identification process. In this example, all the modes are used to deduce the damage conditions. Satisfactory predictions are obtained in each case, in contrast to the results examined in Table 3. Even though starting point is located at boundary of the feasible set ($dm_1 = 0.0, dm_2 = 0.0, dm_3 = 0.0$), the agreement is still precise. These results confirm the expectation that a unique and accurate solution predictions are assured if all the modal information is included as data in the damage identification process.

Conclusions

A general method for damage identification of a simple beam and a spring-mass system is presented. The method may be useful as a component of an on-line nonintrusive damage detection technique for vibrating structures. A formulation is expressed as a direct minimization problem statement with a criteria of the mean square difference of natural frequencies and mode shapes between test measurements and corresponding model values. The damage identification problem is reduced to finding the damage parameters that will satisfy appropriate constraints and minimize the mean square difference.

The uniqueness and reliability of the identification process is confirmed by solving several damage identification examples with specified damage positions. Without knowing the damaged location, a restricted region in initial data space had been found for which there will be a realistic

Third International Conference on Inverse Design Concepts and Optimization in Engineering Sciences (ICIDES-III), Editor: G.S. Dulikravich, Washington D.C., October 23-25, 1991.

and convergent solution from the identification process. This region is small, and can be expanded if substantially more modal information would be available. However, the minimization search may be prohibitive for such a large-dimensional feasible domain that would result.

References

[1] V. Barcilon 1976 *Zeitschrift Fuer Angewandte Mathematik Und Physik* **27**, 346-358. Inverse Problem for a Vibrating Beam.

[2] V. Barcilon 1982 *Philosophical Transactions of the Royal Society of London* **304**, Ser. A, 211-252. Inverse Problems for the Vibrating Beam in the Free-Clamped Configuration.

[3] J. R. McLaughlin 1984 in Santosa, F., Symes, W. W., Pao, Y. H., and Holland, C., (Eds.), *Inverse Problems of Acoustic and Elastic Waves*, *SIAM*, 341-347. On Constructing Solutions to an Inverse Euler-Bernoulli Beam Problem.

[4] J. R. McLaughlin 1986 *SIAM Review* **28**, 53-72. Analytical Methods for Recovering Coefficients in Sturm-Liouville Equations.

[5] G. M. L. Gladwell 1984 *Proceeding of the Royal Society of London* **393**, Series A, 277-295. The Inverse Problem for the Vibrating Beam.

[6] G. M. L. Gladwell 1985 *Proceeding of the Royal Society of London* **401**, Series A, 299-315. Qualitative Properties of Vibrating Beam.

[7] G. M. L. Gladwell 1986 *Proceeding of the Royal Society of London*, **407**, Series A, 199-218. The Inverse Problem for the Euler-Bernoulli Beam.

[8] G. M. L. Gladwell, A. H. England, and D. Wang 1987 *Journal of Sound and Vibration* **119**, 81-94. Examples of Reconstruction of an Euler-Bernoulli Beam from Spectral Data.

[9] M. H. Shen and J. E. Taylor, *Journal of Sound and Vibration* **150**, NO.1, October 1991. An Identification Problem for Vibrating Cracked Beams.

[10] M. H. Shen and C. Pierre, 1990 *Journal of Sound and Vibration* Vol. 138, No. 1, pp. 115-134. Natural Modes of Bernoulli-Euler Beams with Symmetric Cracks.

[11] M. H. Shen and C. Pierre, *Journal of Sound and Vibration* submitted for publication, Free Vibrations of Beams with a Single-Edge Crack.

[12] R. L. Crane, K. E. Hillstrom, and M. Minkoff 1980, ANL-80-64, Argonne National Laboratory, Argonne, Illinois. Solution of The General Nonlinear Programming Problem With Subroutine VMCON.

Third International Conference on Inverse Design Concepts and Optimization in Engineering Sciences (ICIDES-III), Editor: G.S. Dulikravich, Washington D.C., October 23-25, 1991

Test Data: ξ_1^*=0.84703, ξ_3^*=70.1348, cr^*=0.5					
Initial Data			Final Data		
ξ_1	ξ_3	cr	ξ_1	ξ_3	cr
1.0	81.0	0.0	0.84684	70.1348	0.50033
0.98841	80.0769	0.1	0.84697	70.1346	0.50019
0.97217	78.8135	0.2	0.84704	70.1347	0.49998
0.94815	77.0062	0.3	0.84701	70.1348	0.50007
0.91032	74.3024	0.4	0.84694	70.1347	0.50024
0.73638	63.7848	0.6	0.84705	70.1348	0.49962
0.54574	55.0511	0.7	0.84703	70.1348	0.50034
0.27233	45.9316	0.8	0.84700	70.1347	0.50009

Table 1: Numerical results based on mean square problem statement of Eqs. (21-25) with the crack (damage) specified ($xc = 0.5$).

Test Data: ξ_1^*=0.84703, ξ_3^*=70.1348, cr^*=0.5, xc^*=0.5								
	Initial Data				Final Data			
T	ξ_1	ξ_3	cr	xc	ξ_1	ξ_3	cr	xc
9	0.91806	78.5161	0.4	0.4	0.69639	70.1359	0.99789	0.36289
9	0.91371	76.6365	0.4	0.42	0.70007	70.1362	0.99440	0.39620
9	0.91158	75.1335	0.4	0.46	0.84610	70.1347	0.91029	0.53775
9	0.91056	74.7464	0.4	0.47	0.84711	70.1347	0.67125	0.49033
9	0.91063	74.5157	0.4	0.48	0.84704	70.1348	0.50554	0.49972
9	0.73472	63.8062	0.6	0.51	0.84704	70.1348	0.60027	0.50526
9	0.73711	64.2643	0.6	0.52	0.84704	70.1348	0.60083	0.50531
9	0.73617	64.7619	0.6	0.53	0.84704	70.1348	0.60141	0.50534
9	0.73929	65.6727	0.6	0.54	0.84705	70.1348	0.60255	0.49459
9	0.73909	66.6112	0.6	0.55	0.84702	70.1348	0.99721	0.24709
9	0.75452	74.0109	0.6	0.6	0.70040	70.1363	0.99079	0.59307
45	0.97475	80.2193	0.2	0.4	0.90130	70.1347	0.94855	0.94404
45	0.91806	78.5161	0.4	0.4	0.84420	70.1345	0.53053	0.51586
45	0.91531	77.2676	0.4	0.42	0.84686	70.1347	0.50838	0.50198
45	0.96219	78.5819	0.25	0.45	0.84643	70.1348	0.51729	0.49389
45	0.75452	74.0109	0.6	0.6	0.84645	70.1348	0.51723	0.50609
45	0.64083	77.7173	0.7	0.7	0.89079	70.1347	0.58895	0.81817

Table 2: Numerical results based on mean square problem statement of Eqs. (21-25). The position of the damage xc is a variable.

Test Data: ξ_1^*=0.15296, ξ_2^*=1.2956, ξ_3^*=2.2494, dm_1^*=0.0, dm_2^*=0.5, dm_3^*=0.25									
Initial Data					Final Data				
ξ_1	ξ_2	dm_1	dm_2	dm_3	ξ_1	ξ_2	dm_1	dm_2	dm_3
0.19806	1.5549	0.0	0.0	0.0	0.15299	1.2956	0.21392	0.40077	0.10985
0.18986	1.4975	0.0	0.1	0.05	0.15294	1.2955	0.17532	0.41741	0.13265
0.18123	1.4429	0.0	0.2	0.1	0.15296	1.2956	0.13478	0.43493	0.15777
0.17218	1.3911	0.0	0.3	0.15	0.15297	1.2956	0.09222	0.45445	0.18530
0.16275	1.3420	0.0	0.4	0.2	0.15293	1.2955	0.04751	0.47535	0.21576
0.15846	1.3088	0.0	0.44	0.24	0.15294	1.2956	0.02043	0.48975	0.23502
0.15494	1.3047	0.0	0.48	0.24	0.15295	1.2956	0.00973	0.49511	0.24281

Table 3: Numerical results for spring-mass model using first and second mode information.

Third International Conference on Inverse Design Concepts and Optimization in Engineering Sciences
(ICIDES-III), Editor G.S. Dulikravich, Washington D.C., October 23-25, 1991

Test Data: ξ_1^*=0.15296, ξ_2^*=1.2956, ξ_3^*=2.2494, am_1^*=0.0, am_2^*=0.5, am_3^*=0.25											
Initial Data						Final Data					
ξ_1	ξ_2	ξ_3	am_1	am_2	am_3	ξ_1	ξ_2	ξ_3	am_1	am_2	am_3
0.19806	1.5549	3.2469	0.0	0.0	0.0	0.15294	1.2966	2.2494	0.0002	0.5001	0.2498
0.18986	1.4975	3.0209	0.0	0.1	0.05	0.15294	1.2955	2.2494	0.0002	0.5001	0.2498
0.18123	1.4429	2.8086	0.0	0.2	0.1	0.15242	1.2955	2.2494	0.0067	0.5026	0.2442
0.17218	1.3911	2.6095	0.0	0.3	0.15	0.15265	1.2955	2.2494	0.0039	0.5015	0.2494
0.16275	1.3420	2.4232	0.0	0.4	0.2	0.15280	1.2955	2.2494	0.0019	0.5008	0.2484
0.15848	1.3088	2.3329	0.0	0.44	0.24	0.15295	1.2956	2.2494	0.0000	0.5002	0.2499
0.15494	1.3046	2.2832	0.0	0.48	0.24	0.15292	1.2956	2.2494	0.0004	0.5002	0.2496

Table 4: Numerical results for spring-mass model using all three mode information.

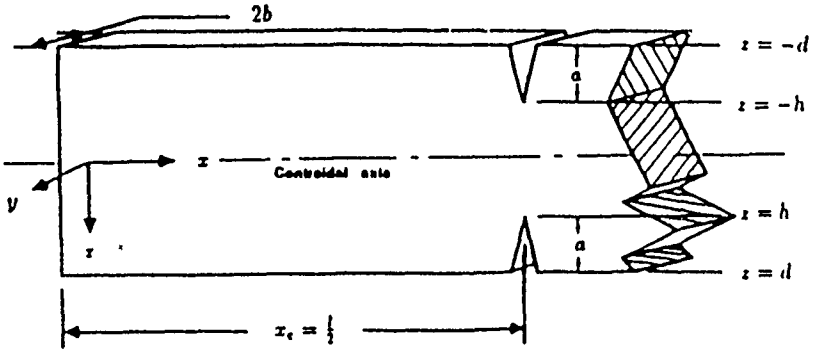


Figure 1. Geometry of a simply supported beam containing a pair of symmetric edge cracks at mid-span, $x_c = \frac{1}{2}$.

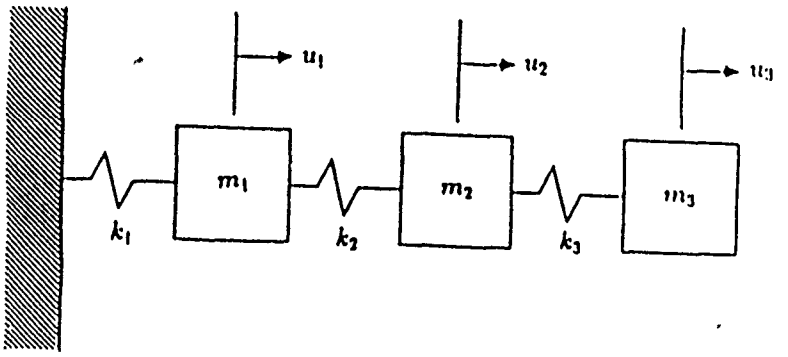


Figure 2. Geometry of a 3 DOF spring mass beam model

Third International Conference on Inverse Design Concepts and Optimization in Engineering Sciences (ICIDES-III), Editor: G.S. Dulikravich, Washington D.C., October 23-25, 1991

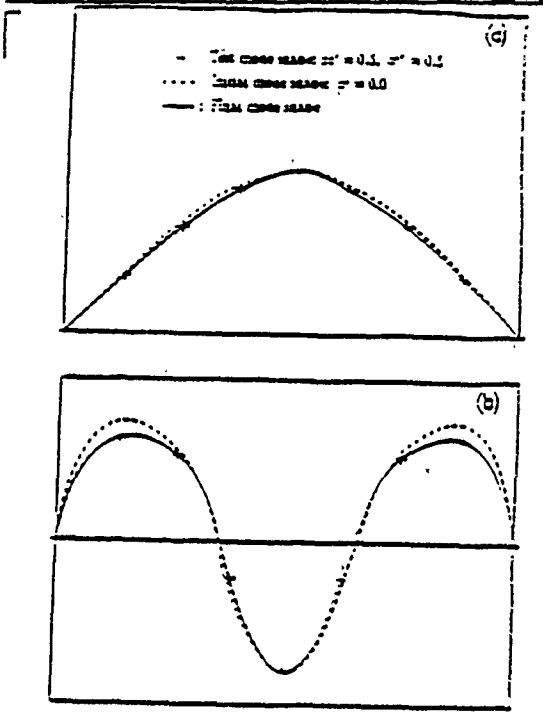


Figure 3. Comparison between the initial, final, and test mode shapes in the first mode (a) and third mode (b). The crack identification process is based on the mesa-square formulation with a specified crack position z_c and 9 test stations. The beam is simply supported with symmetric cracks at mid-span, for $c_r = \frac{1}{3}$. The initial data is selected at $c_r = 0.0$.

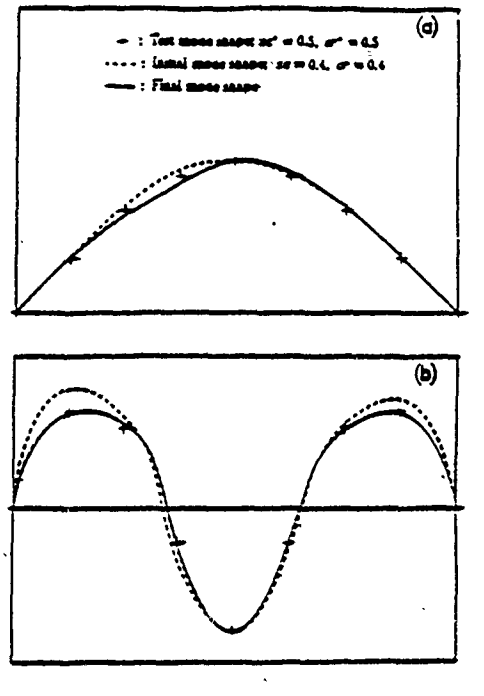


Figure 4. Comparison between the initial, final, and test mode shapes in the first mode (a) and third mode (b). The crack identification process is based on the mesa-square formulation, in which both crack position z_c and crack ratio c_r are unknown and 9 test stations. The beam is simply supported with symmetric cracks at mid-span, for $c_r = \frac{1}{3}$. The initial data is selected at $c_r = 0.4$, $z_c = 0.4$.

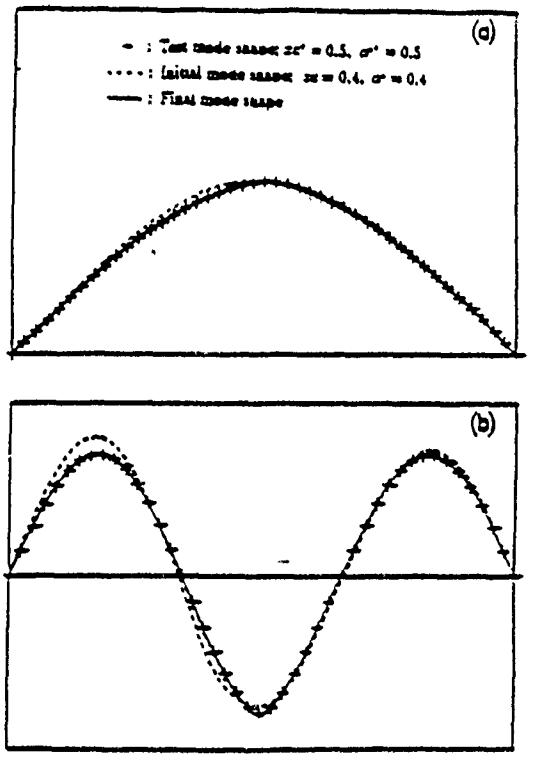


Figure 5. Comparison between the initial, final, and test mode shapes in the first mode (a) and third mode (b). The crack identification process is based on the mesa-square formulation in which both crack position z_c and crack ratio c_r are unknown and 45 test stations. The beam is simply supported with symmetric cracks at mid-span, for $c_r = \frac{1}{3}$. The initial data is selected at $c_r = 0.4$, $z_c = 0.4$.

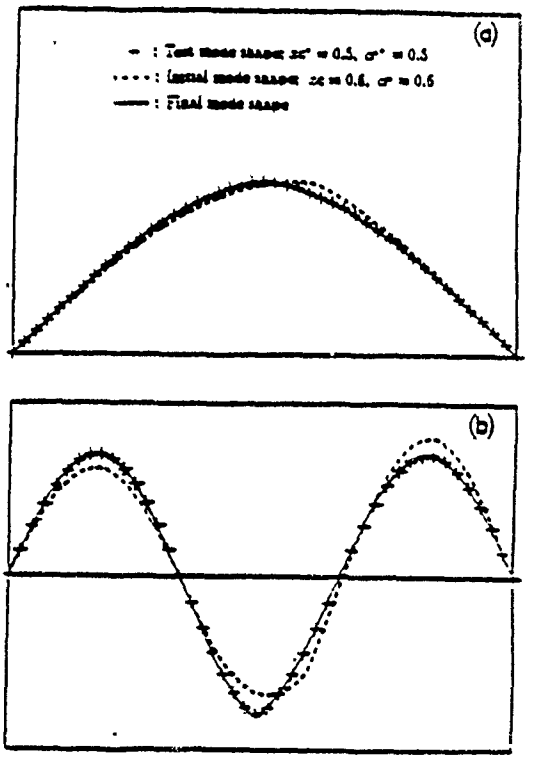


Figure 6. Comparison between the initial, final, and test mode shapes in the first mode (a) and third mode (b). The crack identification process is based on the mesa-square formulation in which both crack position z_c and crack ratio c_r are unknown and 45 test stations. The beam is simply supported with symmetric cracks at mid-span, for $c_r = \frac{1}{3}$. The initial data is selected at $c_r = 0.6$, $z_c = 0.6$.

Third International Conference on Inverse Design Concepts and Optimization in Engineering Sciences (ICIDES-III), Editor: G.S.Dulikravich, Washington D.C. October 23-25, 1991

Electrical Impedance Imaging in Two-Phase, Gas-Liquid Flows: 1. Initial Investigation

J.T. Lin[1], L. Ovacik[2], O.C. Jones[3]
Center for Multiphase Research, Rensselaer Polytechnic Institute
Troy, New York 12180-3590 U.S.A.

ABSTRACT

The determination of interfacial area density in two-phase, gas-liquid flows is one of the major elements impeding significant development of predictive tools based on the two-fluid model. Currently, these models require coupling of liquid and vapor at interfaces using constitutive equations which do not exist in any but the most rudimentary form. Work described herein represents the first step towards the development of electrical impedance computed tomography (EICT) for nonintrusive determination of interfacial structure and evolution in such flows.

INTRODUCTION

Description of interfacial structure and evolution, as well as the gradients which control transfer of mass, momentum, and energy at these phase boundaries is the single most important key element and the challenge for the future of two-phase flow analysis. Indeed, measurement and prediction of phase boundary structure and gradients at these boundaries is one of the major factors impeding development of true predictive capability for systems involving flows of liquid and vapor or gas mixtures.

There are no methods available today which allow determination of interfacial structure and evolution in any but the most simplistic cases. It is the purpose of this paper to describe a concept which appears to hold promise for determining the distribution and evolution of interfacial area density in two-phase, gas-liquid flows.

BACKGROUND

The concept of impedance imaging includes a body of unknown internal electrical field properties of conductivity and permittivity surrounded by electrodes on the bounding surface. These electrodes are excited electrically either in pairs or groups, and the response on the entire set of electrodes is determined. The excitation can be either applied current (AC) or applied voltage (AV), and the measured response can be similar. This is undertaken for all linearly independent combinations of excitation and response to provide numerous sets of data which can then be used to form an image. Maxwell's equations for the behavior of the electrical field are utilized to determine the internal distribution of electrical properties which minimizes (in the least squares sense) the difference between the computed boundary response (given the excitation) and the measured response. If there are N-electrodes, and all possible independent combinations of excitation and response are utilized, there are N(N-1)/2 independent measurements which allows the field to be broken into the same number of regions within which the conductivity and/or permittivity can be determined. The challenge is to develop an accurate and rapid tomography system coupled with accurate inverse computational methods which will allow clear images to be determined.

---

1. Post-Doctoral Research Associate
2. Graduate student
3. Professor of Nuclear Engineering and Engine
and Director--Center for Multiphase Research

Research in the development of electrical impedance computed tomography (EICT) has been undertaken in the geological area [c.f. Dynes and Lytle[1]] and in the biomedical field [c.f. Seagar, Barber, and Brown[2]]. Most methods have used the resistive field because the resistivities of relevant materials are low. To date, the best of applications applied to real systems produce a very fuzzy planar "picture" of resistivity or permittivity variations but the results are encouraging.

Most EICT methods can be classified by the number of poles used to make a single measurement, and the method of excitation. Two-pole methods use only two electrodes for both excitation and measurement whereas four-pole methods separate excitation electrodes from those used for measurement, the measurement generally being a potential difference. Some feel that the four-pole method eliminates errors due to contact resistance at excitation electrodes, but this is not clearly a benefit [Newell et al.[3,4]].

Price[5], although unsuccessful, appears to have been the first in the biomedical field to attempt obtaining impedance tomographs using the three-pole method but his reported work failed. His suggestion of the use of "guarding" methods was followed by others, all of whom were unsuccessful [Bates et al.[6], Schneider[7], Seagar et al.[2]]. Furthermore, in the three-pole method, small voltage differences are obtained by subtracting the measured voltages leading to substantial errors [Smith[8]].

Contact impedance was minimized by Barber et al.[9], using a two-pole method and high-impedance measurement methods, but results were quite blurred. Two-pole methods were also used with little success by Dynes and Lytle[1] and by Starzyk and Dai[10].

Seagar et al.[11] contend that the blurring of two-dimensional results in a continuously variable conservative field is due to nonzero effective wave number (infinite wave length) of the applied signal. They show, however, that successful reconstructions can be made for certain classes of piecewise constant media (similar to two-phase systems), and that the process is relatively simple when the discrete zones are circular in shape.

There can be orders of magnitude differences between the sensitivity of a given boundary measurement to a fixed size body depending on its location. Similar orders difference can thus occur in the eigenvalues of the solution matrix thereby making the inversion problem severely ill-posed and difficult to solve [Tarassenko and Rolph[12], Murai and Kagawa[13,14]]. In spite of ill conditioning, good results were obtained by Wexler[15] using a four-pole potential method with real domain reconstructions even where there were widely varying conductivities in an overall conducting medium--i.e., metal and plastic shapes in a conducting water field.

Isaacson and coworkers [Isaacson[16], Gisser, Isaacson, and Newell[17], Isaacson and Cheney[18]] described a method to estimate the conditions necessary to distinguish a homogeneous cylindrical body of one size, centered in a cylinder of a larger size with the region between the two also of homogeneous electrical field structure. This was followed by Fuks et al.[34] who also provided methods of estimating the degree of accuracy to be obtained with digital conversion of data. In general, they found that increasing the number of electrodes can improve the image only up to a point after which better imaging comes only by improving accuracy of measurement.

Barber and Brown[19,20] developed an iterative back-projection method based on linearization around a constant conductivity. This method was subsequently improved upon by Santosa and Vogelius[21] but with mixed results. Beck and his co-workers [Huang, et al.[22], Beck and Williams[23]] have also developed back-plane projection methods for analysis of gas-liquid pipe flows of gas and oil. A variational method developed by Kohn and Vogelius[24] is similar to that of Wexler et al.[15] but guaranteed to converge. It was shown by Kohn and McKenney,[25] however, to produce results no better than those of Wexler[15]. Murai and Kaga-

wa[13] used a "matrix regularization" method based on Akaike's information criterion and eliminated altogether the problem of ill-conditioning.

Yorkey, Webster, and Tompkins (YWT) followed a different approach using Marquardt's conditioning method which they stated to be better than Akaike's method. Their results appear singularly successful in inversion of two carefully-chosen numerical experiments [Yorkey[26], Yorkey and Webster[27], Yorkey, Webster, and Tompkins,[28-31]]. Finite element methods were used to obtain accurate reconstructions in four iterations. No reconstruction of real situations has yet been reported and Kohn and McKenney[25] indicate the YWT tests were "biased by the nature of the synthetic data."

Very slow transient results were obtained by Brown, Barber, and Seagar[32] when a dish of heated saline solution was reconstructed showing the thermal patterns of convection. From comparison of their results with Price's estimates of resistivity [Price[5]] it seems that changes of the order of 1.5-10 Ω-cm were easily resolved. These results also indicate that there is a good potential for application of EICT methods to natural convection studies.

Finite element methods seem to have been singularly useful in reconstruction tomography of electrical fields. Starting with the suggestions of Kim, Tompkins, and Webster[33], this work has been the basis for the most successful inversions reported on to date [Dynes and Lytle[1], Murai and Kagawa[13], and Yorkey[26-31]].

Yorkey et al.[31] examined several other methods including the perturbation method used by Kim et al.[33], the equipotential lines method used by Barber et al.[9] and by Barber and Brown[20], the iterative equipotential lines method (the original one proposed did not iterate), and the method used by Wexler et al., and similarly by Kohn and Vogelius[24] (referenced by YWT). Of the five methods tried, only the YWT method converged to zero error in overall resistivity, and seemed to obtain the correct result locally, in spite of the fact that they only utilized adjacent electrodes for excitation--a pattern guaranteed to produce the most difficult problems with sensitivity. Other methods either did not converge or converged with some error.

On a completely separate track, Newell, Gisser, and Isaacson and their coworkers at Rensselaer have been developing the multi-pole current distribution (MPCD) method. This method has resulted from mathematical analysis showing the "best" application of electrical current in a radially-symmetric system to be $\sin(k\theta)$ and $\cos(k\theta)$, $k=1...K$ where K is half the number of circumferential electrodes [Gisser et al.[17], Newell et al.[3,4], Fuks et al.[34], Isaacson and Cheney[18], Cheng et al.[35]]. This distribution is optimum in effect because at any instant all electrodes are simultaneously excited and the total input current is the sum of individual electrode-pair currents thereby increasing the sensitivity and decreasing the effects of noise in the system. Results on two-dimensional electrode arrays without iteration (Newton One Step Error Reconstruction, NOSER, method[36]) are quite fuzzy but are the equal of others described in the literature.

ANALYSIS

Reconstruction Method

The iterative method showing most rapid convergence (Yorkey's resistive network or YWT method) was extended to complex reactive networks. The computational logical includes two parts. The first part is the forward problem which is used to generate a voltage distribution using a given distribution of complex conductivity. The second part is the inverse problem which uses the calculated boundary voltages in comparison with the measured values to reconstruct the conductivity/permittivity distribution. The theoretical basis for the algorithm is given as follows. The steady-state governing equation for the voltage distribution within the inhomogeneous and isotropic field is given by the equation

$$\nabla \cdot (\sigma \nabla V) = 0. \tag{1}$$

where V is the voltage field and $\sigma = (c + j\omega\varepsilon)$, c being the conductivity, ε the permittivity, and ω the frequency. Finite element methods (FEM) are utilized where they are nodalized by quadrilateral elements then transformed to squares for computational purposes. It is known that this method converges to the exact solution where the element size becomes infinitesimal.

The FEM is defined for a reactive network as YV = C, such that the voltage field is given as

$$\mathbf{V}_{NxP} = \mathbf{Y}^{-1}_{NxN}\mathbf{C}_{NxP}. \tag{2}$$

where Y is the N x N indefinite admittance-matrix. The matrix-size parameters are defined as

N	= the number of nodes
P	= the number of current excitations
M	= the number of elements
E	= the number of external measurement electrodes

While V represents the voltages of the nodes both inside and on the periphery of the body, a transformation is made to extract the calculated boundary voltages from the calculated voltage matrix $\mathbf{V}_{NxP}$ to form a new vector $\mathbf{f}_{EPx1}$. The measured voltages on the E-electrodes with P-current excitations are collected to form the vector $\mathbf{V}_{0,EPx1}$.

There are differences between the calculated voltages $\mathbf{f}_{EPx1}$ and measured voltages $\mathbf{V}_{0,EPx1}$ on the electrodes. A scalar error function is defined as

$$\phi = \frac{1}{2}[\mathbf{f} - \mathbf{V}_0]^T[\mathbf{f} - \mathbf{V}_0]. \tag{3}$$

In order to get minimum error, the differential of ϕ relative to σ should vanish. Thus,

$$\phi' \equiv \frac{d\phi}{d\sigma} = [\mathbf{f}']^T[\mathbf{f} - \mathbf{V}_0] = 0 \tag{4}$$

where $\mathbf{f}' = d\mathbf{f}/d\sigma$. The quantity ϕ' can be expressed as a Taylor expansion

$$\phi' \cong \phi'(\sigma^K) + \phi''(\sigma^K)\nabla(\sigma^K) = 0. \tag{5}$$

Thus, since ϕ' vanishes, the gradient of the conductivity is given by

$$\nabla\sigma^K = -[\phi''(\sigma^K)]^{-1}\phi'(\sigma^K) \tag{6}$$

where

$$\phi' = [\mathbf{f}'(\sigma^K)]^T[\mathbf{f}(\sigma^K) - \mathbf{V}_0] \tag{7}$$

and where

$$\phi''(\sigma^K) \cong [\mathbf{f}'(\sigma^K)]^T\mathbf{f}'(\sigma^K). \tag{8}$$

The corrections to σ^K can be obtained after every iteration, until the convergence criteria is met.

A areasonable level of spatial resolution will need many current excitations and so the matrices required in the inversions can be very large. Since the forward computation of the field potential for a given complex resistivity pattern involves inversion of a sparse matrix, Gaussian elimination methods used are computationally expensive. Thus, the Jacobi conjugate gradient (JCG) method (similar to that described by Carey and Oden[45]) has been utilized for real domain inversions. Time savings was achieved by maintaining a constant Jacobian for several iterations.

In the case of a matrix having eigenvalues separated by orders of magnitude, preconditioning is obtained by pre-multiplying with the inverse of the diagonal or tridiagonal of the original matrix. The JCG

method is both extremely fast and absolutely convergent for positive definite matrices such as are anticipated in this problem. Since it is not necessary to calculate and store zeros in the matrix, the computational CPU time is decreased substantially.

The accuracy for both methods are similar. Hestenes and Stiefel[46] have shown that if the conjugate directions are chosen as the unit basis vectors, then the conjugate gradient will be equivalent to Gaussian Elimination method. Round-off error can also be corrected in the JCG algorithm.

Quadrilateral Mesh Scheme

All computations were undertaken in a dimensionless array of square elements. To easily model geometries having curved surfaces, a transformation from quadrilateral to square elements was included both for preprocessing and postprocessing of computed results.

The sketch in Fig. 1 shows the quadrilateral transformation scheme. Transformation was accomplished in the standard fashion. A shape function $N_i = N_i(\xi,\eta)$ is chosen with the values of ξ and η defined in the figure such that the mapping from the parent domain **R** into the square-element domain. An infinitely small area is transformed using the Jacobian with the following shape functions

$$\begin{aligned} N_1 &= (1/4)(1-\xi)(1-\eta) \\ N_2 &= (1/4)(1+\xi)(1-\eta) \\ N_3 &= (1/4)(1+\xi)(1+\eta) \\ N_4 &= (1/4)(1-\xi)(1+\eta) \end{aligned} \tag{9}$$

A bilinear expansion form is utilized such that

$$\begin{aligned} x(\xi,\eta) &= \alpha_0 + \alpha_1\xi + \alpha_2\eta + \alpha_3\xi\eta \\ y(\xi,\eta) &= \beta_0 + \beta_1\xi + \beta_2\eta + \beta_3\xi\eta \end{aligned} \tag{10}$$

where the α's and β's are determined by the transformation Jacobian

$$\mathbf{J} = \begin{bmatrix} \alpha_1 + \alpha_3\eta & \alpha_2 + \alpha_3\xi \\ \beta_1 + \beta_3\eta & \beta_2 + \beta_3\xi \end{bmatrix}. \tag{11}$$

Now the problem to be solved is Eq. (1). It is assumed that the conductivity is piecewise continuous being constant in each element such that Laplace's equation is solved element-by-element. Thus

$$V = \sum_{i=1}^{4} V_i N_i \quad \text{and} \quad \nabla V = \sum_{i=1}^{4} V_i \ \nabla N_i. \tag{12}$$

Solving Eq. (1) is equivalent to minimizing the functional

$$F = \frac{\sigma}{2} \int\int_{\mathbf{R}} |\nabla V|^2 dS \tag{13}$$

where **R** designates the region occupied by the individual elements for which Eq. (13) applies. Thus,

$$\frac{\partial F}{\partial V_i} = 0 \qquad \text{for} \qquad i = 1,4 \tag{14}$$

which, after minimizing, results identically in Eq. (2). The admittance elements are given by the transformation,

$$Y_{ij} = \sigma_R \int_{-1}^{1}\int_{-1}^{1} F_{ij}\,(\xi,\eta) d\xi d\eta \tag{15}$$

and where

$$F_{ij}(\xi,\eta) = \left(J_{11}^{-1}\frac{\partial N_i}{\partial \xi} + J_{12}^{-1}\frac{\partial N_i}{\partial \eta}\right)\left(J_{11}^{-1}\frac{\partial N_j}{\partial \xi} + J_{12}^{-1}\frac{\partial N_j}{\partial \eta}\right) + \left(J_{21}^{-1}\frac{\partial N_i}{\partial \xi} + J_{22}^{-1}\frac{\partial N_i}{\partial \eta}\right)\left(J_{21}^{-1}\frac{\partial N_j}{\partial \xi} + J_{22}^{-1}\frac{\partial N_j}{\partial \eta}\right) \quad (16)$$

RESULTS

Numerical

Square-element conductive arrays. Duplication of Yorkey's results required implementation of the method using square elements in the resistive mode only. Results obtained were identical to those found by Yorkey et al. Convergence is very rapid with the error function [Eq. (3)] for an 8 x 8 array converging to two significant figures within 4-5 iterations and within 1 part in 10^4 within 12 iterations where the contrast ratio is as large as 10,000:1. Aitken's method is also used to improve convergence speed more than a factor of 3.

Quadrilateral-element arrays. Both real and complex conductivity calculations have been undertaken; however, the real patterns converge much more readily than the complex. Varying Marquardt's constant and not recalculating the Jacobian matrix every iteration leads to nonuniform convergence.

Figure 2 shows two patterns with the number of iterations required for convergence with the fill pattern key between the two reconstructions. The original pattern is chosen to be uniform of high conductivity. Gauss elimination was used to perform matrix inversions. The ring pattern converges much more rapidly than the annular pattern because the zones requiring the greatest changes are nearer the boundary. Furthermore, the central region required no change whereas for the annular geometry, the central zones required maximum change.

Figure 3 shows the convergence sequence for a 64-element body with real-conductivity elements of 3:1 contrast ratio distributed in a relatively arbitrary pattern. The quantitative resistivity pattern definition is identical to that shown at the center of Fig. 2. It is seen that there is a relatively rapid convergence for elements near the boundary even though the change is from one extreme to the other. On the other hand, changes in the central region require significantly more computations for convergence due to the extreme lack of sensitivity of regions farthest from the boundaries. Global error for the three cases (arbitrary, ring, and annular) is shown in Fig. 4, confirming that the more complex the pattern, the larger the number of iterations required for convergence.

The question of noise and error generally pose real difficulties in the convergence of an inverse problem to its solution. In the case of the annular geometry, Gaussian noise was added to the "measured" voltages and the problems recomputed. As shown in Fig. 5, the global error generally decreases until the effects of the error become important and then become relatively constant. Figure 6 shows the variation in the local error for each of the four ring layers in the geometry showing increasing error with distance from the boundary. In the case of 1% Gaussian noise, the local error in the inner elements is above 30%. Even in this case, however, the noise has little effect on the visual recognition of the pattern (Fig 7).

Computation for these 8x8 reconstructions required approximately 3 minutes on the IBM 3090 computer. Of interest was the computational time required for a significantly larger problem, in addition to the interest in gaining better computational resolution. For this purpose, a 256-element pattern (16x16) was computed in two steps: starting with a uniform background pattern using an 8x8 mesh; switching to a 16x16 pattern when convergence ceased due to the effective noise in the system caused by nonalignment of pattern and mesh. Starting with an 8x8 pattern, and using a conjugate gradient method for matrix inversion, convergence is rapid at first, then slows as the effective noise becomes dominant. Switching to a grid

Third International Conference on Inverse Design Concepts and Optimization in Engineering Sciences (ICIDES-III) Editor: G.S. Dulikravich, Washington D.C., October 23-25, 1991

size of 16 x 16 results again in rapid convergence. Computation time in this case for a total of 30 iterations was 43 minutes on the IBM 3090 and convergence was not achieved, even though the global error was reduced to 0.00086. A 24 x 24-element problem required 54 minutes for a single iteration.

EXPERIMENTAL

An example of a electrical impedance tomographic image obtained using sinusoidal current excitation patterns at 15 kHz, and complex conductivity inversion is shown in Fig. 8 (NOSER method, Newell et al.[36]). The test geometry used is a rather shallow, two-dimensional bath 500-mm in diameter. Water filled the dish to a depth of approximately 12 mm except for an empty, 50-mm- diameter beaker placed in the center of the dish.

The NOSER method is a noniterative reconstruction which uses exact solution of the uniform field problem and exact computation of the first Taylor-series corrections in the iterative process. The results shown in Fig. 8 indicate the darker regions where higher impedances associated with air are calculated. In this case, the contrast associated with the central region is only approximate as, for air at 15 kHz excitation the impedance is virtually infinite in comparison with tap water where the resistivity is in the range of hundreds of ohm-cm. The results show that it is clearly possible to separately identify large separate regions of gas-phase surrounded by water in a large geometry, even without iteration.

CONCLUSIONS

A potentially useful method for electrical impedance imaging of two-phase fluid distributions methods has been discussed. The method solves the inverse problem where the internal conductivity field is piecewise approximated using iterative procedures which require computed boundary measurements converge to measured values which exist due to given boundary excitation. Convergence is undertaken in a manner which minimizes the least squares error between the computations and the measurements. Specific results of this work are:

1. The internal distribution of complex electrical impedance can be piecewise approximated within a body by using only boundary excitation and measurement.

2. Square-element FEM modeling of a resistive body allows iterative convergence to 1% within 4-5 iterations and within 0.01% within 12 iterations for all contrast ratios up to 10^5.

3. Quadrilateral-element, FEM modeling was slower to iterate and more sensitive to contrast ratio, perhaps due to the presence of highly acute or obtuse angles distorting the equivalent square-element conductivity. Local error in a given element was shown to be considerably slower to converge to a reasonable error. Elements farthest from the boundary showed slowest convergence, and more complex situations appear to require more iterations for convergence.

4. Complex contrast ratios as large as 10^2 were found to converge using Gauss elimination for matrix inversion. Situations with larger contrast diverged.

5. The computational methods utilized appear quite tolerant to Gaussian noise allowing inverse computations to be undertaken with as much as 1% rms noise in boundary "measurements." The global error is found to diverge from the no-noise case and arrive at a relatively constant value dependent on the noise. Even with relatively large local errors, visual discrimination of the patterns was easily possible.

6. Application to a practical, laboratory situation shows that even without iteration, reasonable results can be obtained for complex conductivity fluids.

ACKNOWLEDGEMENTS

This research was supported by the Energy Research Laboratory, Hitachi, Ltd., Hitachi-shi, Ibaraki-ken, Japan, and by the U.S. Department of Energy under contract number DE-FG07-90ER13032.

NOMENCLATURE

English

c	Conductivity
C	Current matrix
f	Calculated boundary voltage vector
J	Jacobian
N	Shape function for quadrilateral transformation
V	Voltage field
V	Voltage matrix
x	Cartesian coordinates
y	Cartesian coordinate
Y	Admittance matrix

Greek

α	Expansion coefficient
β	Expansion coefficient
ε	Permittivity
ϕ	Scalar error function
η	Transformed coordinate
ω	Radial frequency
σ	Complex conductivity ($c + j\omega\varepsilon$)
ξ	Transformed coordinate

Subscripts and Superscripts and Others

E	Number of measurement electrodes on boundary
i	Matrix element index
j	Matrix element index
K	Iteration number
M	Total number of elements
N	Total number of nodes
P	Number of current excitations
0	Measured

REFERENCES

1. Dynes, K.A., and Lytle, R.J., [1981] "Analysis of electrical conductivity imaging," **Geophysics, 46**, pg. 1025-1036.

2. Seagar, A.D., Barber, D.C., and Brown, B.H., [1987] "Electrical Impedance Imaging," **IEE Proc. 134, Pt. A**, No. 2, pg. 201-210.

3. Newell, J.C., Isaacson, D., and Gisser, D.G. [1989] "Rapid Assessment of Electrode Characteristics for Impedance Imaging," **IEEE-Trans., Biomed. Eng.**, in press.

4. Newell, J.C., Gisser, D.G., and Isaacson, D., [1988] "An Electric Current Tomograph," **IEEE-Trans. Biomed. Eng., 35** (10), pg. 828-833.

5. Price, L.R., [1979] "Electrical impedance computed tomography (ICT): a new CT imaging technique," **IEEE Trans. Nucl. Sci. (USA), NS-26, 2**, pg. 2736-2739.

6. Bates, R.H.T., Mckinnon, G.C., and Seager, A.D., [1980] "A limitation on systems for imaging electrical conductivity distributions," **IEEE Trans. Biomed. Eng., BME-27, 7**, pg. 418-420.

7. Shomberg, H., and Tasto, M., [1981] "Reconstruction of spatial resistivity distribution," Phillips GMDH, Hamburg, Germany (FRG), MS-H 2715/81.

8. Smith, D.N., [1985] "Determination of impedance using numerous simultaneous currents (DINSC) - system design and practical applications," **IEEE Conf. Publ. (Inst. Electr. Eng.)**, No. 257, pg. 69-73

9. Barber, D.C., Brown, B.H., and Freeston, I.L., [1983] "Imaging spatial distributions of resistivity using applied potential tomography," **Elec. Lett., 19**, pg. 933-935.

10. Starzyk, J.A., and Dai, H., [1985] "Element evaluation in the resistive networks," **Midwest Sym. Circuits Syst., 28**, pg. 178-181

11. Seagar, A.D., Yeo, T.S., and Bates, R.H.T., [1984] "Full wave computed tomography, part 2: Resolution limits," **Proc. IEE, part A, 131**, pg. 616-622.

12. Tarassenko, L., and Rolfe, P., [1984] "Imaging spatial distributions of resistivity - an alternative approach," **Electron. Lett., 20,** 14, pg. 574-576.

13. Murai, T., and Kagawa, Y., [1985] "Electrical impedance computed tomography based on a finite element model," **IEEE Trans. Biomed. Eng.,**

BME-32, 3, pg. 177-184.

14. Murai, T., and Kagawa, Y., [1986] "Boundary element iterative techniques for determining the interface boundary between two Laplace domains-a basic study of impedance plethysmography as an inverse problem," **Int. J. Numer. Methods Eng. (GB), 23**, 1, pg. 35-47

15. Wexler, A., Fry, B., and Neiman, M.R., [1985] "Impedance-computed tomography algorithm and system," **Appl. Opt., 24**, 23, pg. 3985-3992.

16. Isaacson, D., [1986] "Distinguishability of Conductivities by Electric Current Computed Tomography," **IEEE Med. Imaging MI-5**, 91-95.

17. Gisser, D.G., Isaacson, D., and Newell, J.C., [1987] "Current Topics in Impedance Imaging," **Clin. Phys. Physiol. Meas., 8**, Suppl. A, pg. 39-46.

18. Isaacson, D., and Cheney, M., [1990] "Current Problems in Impedance Imaging," in **Inverse Problems in Partial Differential Equations**, D. Colton, R. Ewing, and W. Rundell, Eds., SIAM, Philadelphia.

19. Barber, D.C., and Brown, B.H., [1984] "Applied Potential Tomography," **J. Phys. E: Sci. Instrum., 17**, pg. 723-733.

20. Barber, D.C., and Brown, B.H., [1985] "Recent developments in applied potential tomography--APT," in **Proc, 9th Int. Conf. Info. Proc. Med. Imaging**, Washington, D.C.

21. Santosa, F., and Vogelius, M., [1988] "A Backprojection Algorithm for Electrical Impedance Imaging," Institute for Physical Science & Technology, Univ. Maryland, Tech. Note BN-1081, July.

22. Huang, S.M., Plaskowski, A.B., Xie, C.C., and Beck, M.S., [1989] "Tomographic Imaging of Two-Component Flow using Capacitance Sensors," **J. Phys. E: Sci. Instrum., 22**, pg 173-177.

23. Beck, M., and Williams, R., [1990] "Looking into Process Plant," **The Chem. Engr., 26** July, pg. 14-15.

24. Kohn, R.V., and Vogelius, M., [1987] "Relaxation of a Variational Method for Impedance Computed Tomography," **Comm. Pure Appl. Math., 40**, pg. 745-777.

25. Kohn, R.V., and McKenney, A., [1989] "Numerical Implementation of a Variational Method for Electrical Impedance Tomography," Courant Institute of Mathematical Sciences, private communication.

26. Yorkey, T.J., [1986] **Comparing reconstruction methods for electrical impedance tomography**," Ph.D. Thesis, Dep. Elec. Comput. Eng., Univ. Wisc., Madison, WI 53706, August.

27. Yorkey, T.J., and Webster, J.G., [1987] "A comparison of impedance tomographic reconstruction algorithms," **Clin. Phys. Physiol. Meas., 8**, suppl. A, pg. 55-62.

28. Yorkey, T.J., Webster, J.B., and Tompkins, W.J., [1985] "Errors caused by contact impedance in impedance imaging," **Proc. Ann. Conf. IEEE Eng. Med. Biol. Soc., 7**, 1, pg. 632-637

29. Yorkey, T.J., Webster, J.G., and Tompkins, W.J., [1986] "An optimal impedance tomographic reconstruction algorithm," **Proc. Ann. Conf. IEEE Eng. Med. Biol. Soc., 8**, 1, pg. 339-342.

30. Yorkey, T.J., Webster, J.G., and Tompkins, W.J., [1987a] "An improved perturbation technique for electrical impedance imaging with some criticisms," **IEEE Trans. Biomed. Eng., 34**, 11, pg. 898-901.

31. Yorkey, T.J., Webster, J.G., and Tompkins, W.J., [1987b] "Comparing reconstruction algorithms for electrical impedance tomography," **IEEE Trans Biomed. Eng., 34**, PG. 843-852.

32. Brown, B.H., Barber, D.C., and Seagar, A.D., [1985] "Applied potential tomography - clinical applications," **IEEE Conf. Publ. (Inst. Electr. Eng.)**, No. 257, pg. 74-78.

33. Kim, Y., Webster, J.G., and Tompkins, W.J., [1983] "Electrical impedance imaging of the thorax," **J. Microwave Power, 18**, 3, pg. 245-257.

34. Fuks, L.F., Isaacson, D., Gisser, D.G., and Newell, J.C., [1989] "Tomographic Images of Dielectric Tissue Properties," **IEEE-Trans. Biomed. Eng.**, in review.

35. Cheng, K-S, Isaacson, D., Newell, J.C., and Gisser, D.G., [1989] "Electrode Models for Electric Current Computed Tomography," **IEEE-Trans. Biomed. Eng., 36**(9), pg. 918-924.

36. Cheney, M., Isaacson, D., Newell, J.C., Simske, S., and Goble, J., [1980] "NOSER: An algorithm for solving the inverse conductivity problem," **Int. J. Imaging. Systems and Tech., 2**, pg. 66-75.

37. Brown, B.H., and Barber, D.C., [1987] "Electrical impedance tomography; the construction and application to physiological measurement of electrical impedance images," **Medical Prog. Through Technology, 13**, pg. 69-75.

38. Brown, B.H., Karatzas, T., Nakielny, R., and Clarke, R.G., [1988] "Determination of upper arm muscle and fat areas using electrical impedance measurements," **Clin. Phys. Physiol. Meas. (UK), 9**, 1, pg. 47-55.

39. Gilbert, P., [1972] "Iterative methods for the reconstruction of three-dimensional objects from projections," **J. Theoret. Biol., 36**, pg. 105-117.

40. Griffiths, H., [1987] "The importance of phase measurement in electrical impedance tomography," **Phys. Med. Biol., 32**, 11, pg. 1435-1444.

41. Henderson, R.P., and Webster, J.G., [1978] "An impedance camera for spatially specific measurements of thorax," **IEEE Trans. Biomed. Eng., BME-25**, pg. 250-254.

42. Kagawa, Y., Murai, T., and Matsumoto, O., [1983] "Finite element iterative technique for determining the interface boundary between Laplace and Poisson domains--characteristic analysis of field effect transistor," **Int. J. Numer. Methods Eng., 19**, pg. 315-329.

43. Kardous, G., [1987] **Etude de la distribution de la sensibility d'un systeme circulaire multi-electrodes en vue de la reconstruction d'images d'impedance bio-electrique,** PhD Thesis, Institute National des Sciences Appliquees de Lyon, Villeirbanne, France.

44. Kim, Y., Tompkins, W.J., and Webster, J.G., [1982] "Medical body imaging using electrical impedance and nonlinear reconstruction," **Ann. Northwest Bioeng. Conf., 10**, pg. 298-303.

45. Carey, G.F., and Oden, J.T., [1984] **Finite Element Computational Aspects. Vol. 3**, Prentice-Hall, Englewood Cliffs, N.J.

46. Hestenes, M.R., and Stiefel, E., [1952] "Methods of Conjugate Gradients for Solving Linear Systems," **J. Res. NBS, 49**, 6, pg. 409-436.

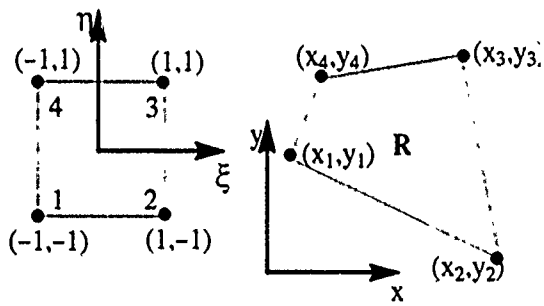


Figure 1. Quadrilateral element transformation geometry.

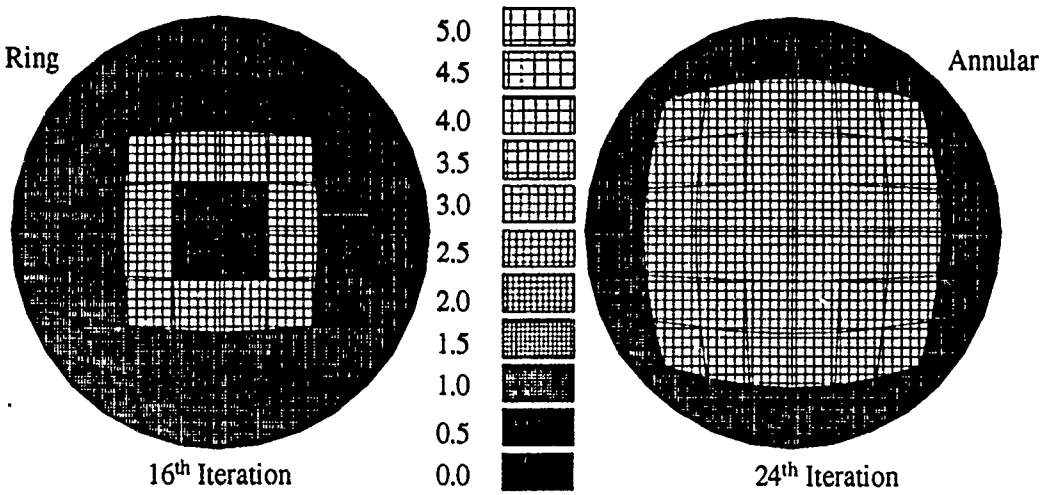


Figure 2. Converged patterns and resistivity index for both annular and ring geometries with zero permittivity. Contrast ratio: 3:1.

Third International Conference on Inverse Design Concepts and Optimization in Engineering Sciences (ICIDES–III) Editor: G.S. Dulikravich, Washington D.C. October 23–25, 199-

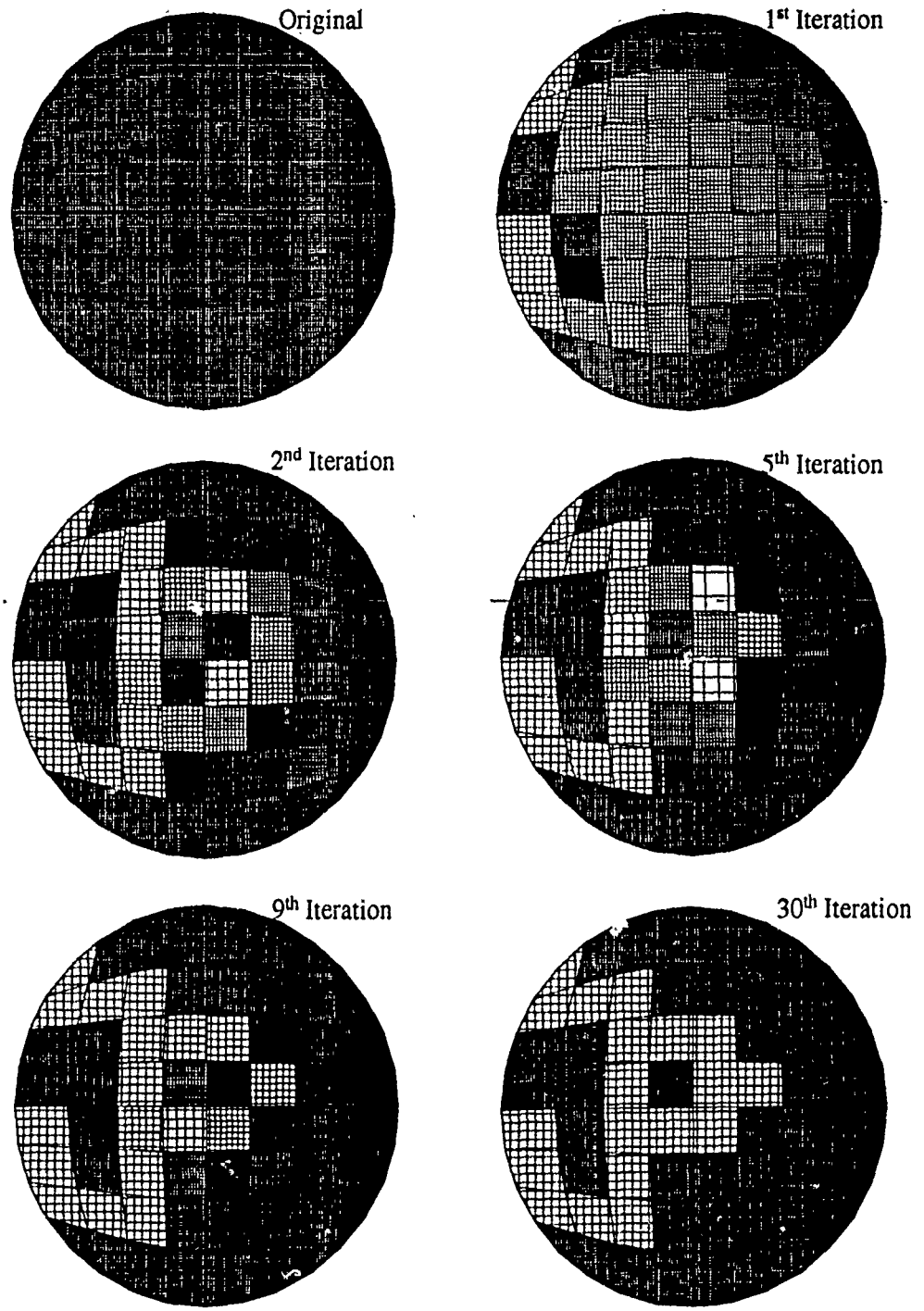


Figure 3. Typical convergence sequence for a 64 element array of quadrilateral elements with zero permittivity. Contrast ratio: 3:1.

Third International Conference on Inverse Design Concepts and Optimization in Engineering Sciences (ICIDES-III) Editor: G.S. Dulikravich, Washington D.C. October 23-25, 199[illegible]

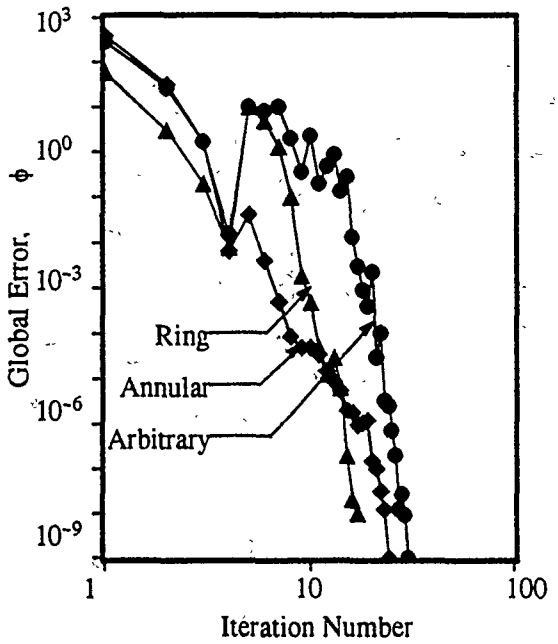


Figure 4. Global error for the three patterns tested.

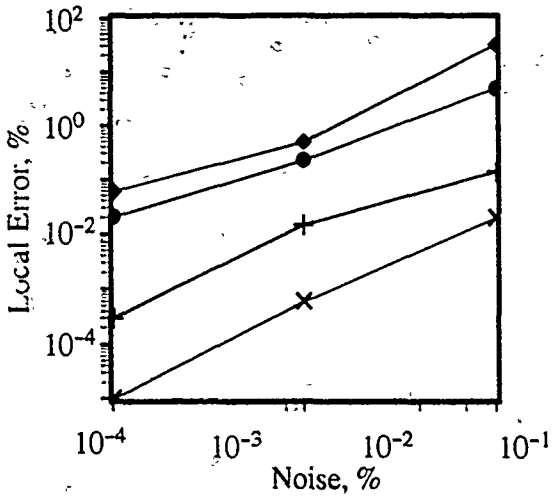


Figure 6. Local error for the annular-flow-like geometry. ♦ Inner Cells; • Inner Middle; + Outer Middle; x Outer Cells.

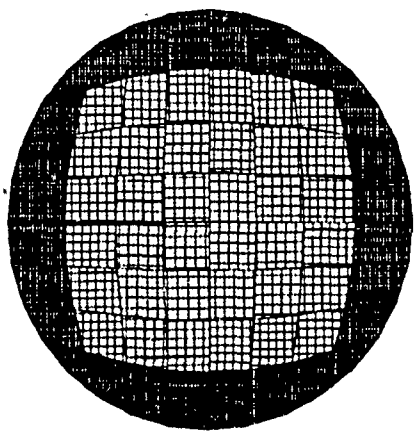


Figure 7. Converged annular pattern with 1% Gaussian noise.

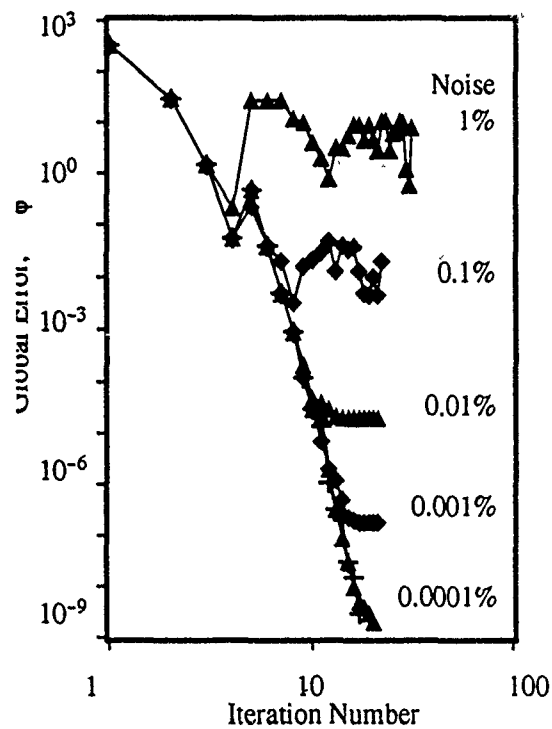


Figure 5. Effect of noise on convergence for the annular pattern.

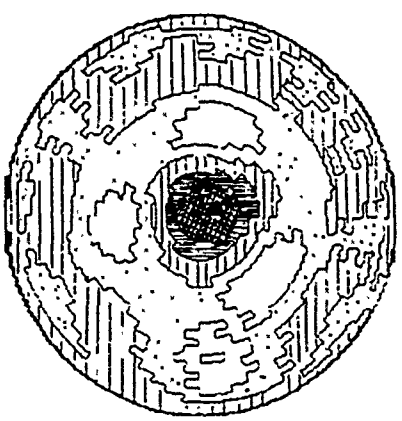


Figure 8. Example of electrical impedance reconstruction of an air-water system using the NOSER method.[36]

Third International Conference on Inverse Design Concepts and Opumization in Engineering Sciences
(ICIDES-III), Editor: G.S. Dulikravich, Washington D.C., October 23-25, 1991

"RECENT PROGRESS IN INVERSE METHODS IN FRANCE"

PIERRE-FRANÇOIS BRY (SNECMA)

Société Nationale d'Etude et de Construction
de Moteurs d'Aviation
(S.N.E.C.M.A.)
Cincinnati, Ohio, U.S.A.

OLIVIER-PIERRE JACQUOTTE
MARIE-CLAIRE LE PAPE

Office National d'Etudes et de Recherches Aérospatiales
(O.N.E.R.A.)
Aerodynamics Department
92322 CHATILLON FRANCE

ABSTRACT

Given the current level of jet engine performance, improvement of the various turbomachinery components requires the use of advanced methods in aerodynamics, heat transfer, aeromechanics as well as in other fields.
In particular, successful blading design can only be achieved via numerical design methods which make it possible to reach optimized solutions in a much shorter time than ever before. The present paper focuses on two design methods which are currently being used throughout the French turbomachinery industry to obtain optimized blading geometries. Examples are presented for compressor and turbine applications. The status of these methods as far as improvement and extension to new fields of applications is also reported on.

Third International Conference on Inverse Design Concepts and Optimization in Engineering Sciences
(ICIDES-III), Edited G.S. Dulikravich, Washington D.C., October 23-25, 1991

1. INTRODUCTION

The ever-increasing performance requirements for jet engines, together with the fast pace of development programs, have led designers to rely more than ever on computations when defining their products. The field of Fluid Mechanics has naturally been at the forefront of this evolution both in external and internal aerodynamics. A great deal of effort has been devoted to the development of powerful numerical tools which allow both the design and analysis of geometries with the obvious goal of obtaining optimized shapes that can enhance performance.

The present paper focuses on two design methods which are currently used throughout the French industry for turbomachinery applications. After a brief review of the general inverse problem in the turbomachinery field, examples of what can be achieved are presented both for compressor and turbine blading. In addition, the versatility of one of the methods is demonstrated by using the example of a jet engine inlet design.

2. A PROPER FORMULATION FOR THE INVERSE PROBLEM

The idea of inverse design methods is obviously not new. Once the blade or wing designers had the knowledge and the understanding of the flow around an airfoil, isolated or not, it was natural to try to define profiles not from the purely geometrical standpoint but rather by using this very knowledge of the fundamental profile aerodynamics. It was recognized early on that there was a direct relationship between the surface velocity distributions and overall performance. Hence the idea of defining the profile starting from the velocity distribution itself.

The inverse problem for isolated profiles in incompressible flows was first formulated by LIGHTHILL [1]. It consists in determining an airfoil that produces a given speed distribution prescribed on the unknown airfoil profile. It was shown that closed profiles could exist only if the prescribed velocity W^0 satisfies three integral constraints. In this early work, these were chosen as the upstream velocity W^∞ and two parameters related to the closure of the profile.

More recently, Volpe and Melnik [2] proposed several possible choices for the design of isolated profiles. In particular, they showed that it was possible to obtain closed profiles via introduction of two modification functions for the target velocity.

For turbomachinery applications, the problem is slightly different in the sense that 1) the flow is quasi-three dimensional (in first approximation) and 2) the profiles are entrapped between adjoining blade rows which partly determine the upstream and downstream boundary conditions. In particular, the upstream (or downstream) velocity as well as the upstream/downstream flow angles cannot be set as free parameters.

Third International Conference on Inverse Design Concepts and Optimization in Engineering Sciences
(ICIDES-III), Editor G.S. Dulikravich, Washington D.C., October 23-25, 1991

The prescribed velocity distribution is defined on the pressure and suction sides of the blade and is given by two separate functions of the arc lengths S (pressure) and S (suction). The relative lengths of the two sides or, equivalently, the position of the stagnation point, can therefore be considered as the first necessary parameter.
The second parameter is a direct consequence of the fact that, in general, a flow evolves (in basic approximation) on a quasi-three-dimensional surface throughout a blade row. Whereas it is possible to set free two parameters defining the trailing edge closure (Δx and Δy) for isolated 2-D profiles, it is obvious that a trailing edge cannot be reasonably defined if both suction and pressure side trailing edge points are not located at the same radius (the same m-coordinate in the standard (m-θ) quasi-three-dimensional blade-to-blade representation). Therefore, the remaining parameter pertaining to profile closure is the circumferential gap in the θ-direction at the trailing edge.
Finally, like in all turbomachinery problems, the solidity is a governing parameter, directly related to the circulation around the profile and the flow turning. It comes as no surprise that it is the third parameter to be computed by the algorithm since inlet/outlet angles as well as velocity distributions are given data for the design method.
Based on these general considerations, many methods were proposed in the past to deal with the problem of profile or blade design. It is not the purpose of this paper to review all these methods and we will instead refer the readers to overall summaries such as proposed by Sloof [3] or Meauzé [4].
A commonly used method for two-dimensional applications was proposed years ago by Stanitz [5] to determine analytically a profile from a given velocity distribution. It is still being used successfully for specific two-dimensional applications at a reasonably low Mach number. More recent developments by Cedar and Stow [6] in England and Jacquotte [7] in France allow the definition of high Mach number profiles within the quasi-three-dimensional and potential approximations. Finally Meauzé [8] in France and Leonard et al. [9] in Belgium have proposed solutions for the non-viscous quasi-three-dimensional problem solving the Euler equations that allow for the occurrence of strong shocks within the flow field.
In the following paragraphs, we will discuss the recent developments in France that concern both the potential design method by Jacquotte [7] and the Euler method by Meauzé [8].

3. FINITE ELEMENT INVERSE METHOD FOR POTENTIAL FLOW [7]

A thorough description of the method is given in [7] and [9]. We will therefore only give here a general outline while concentrating on concepts and applications.
The method was developed by Jacquotte in 1989. It makes use of the concept introduced in the previous paragraph pertaining to the constraints that must be taken into account in order to arrive at a solution.

3.1 Basic assumptions

Three very basic approximations are retained:

a) the flow is inviscid;
b) it is considered quasi-three-dimensional and computed on stream surfaces in the computational space (m,θ), where m is the arc length of the meridian line defining the stream surface, and θ is the polar angle around the axis 0z. It is therefore assumed that the characteristics of the through-flow are known and given by a function r (z) defining a stream surface and the stream tube thickness b(z);
c) third, the calculation is carried out within the potential flow approximation. Even though the entropy production through shocks cannot be taken into account, such a model is still valid for compressible transonic flows where strong shocks do not occur i.e., for relative Mach numbers that do not exceed 1.3 or 1.4. The advantage of using such a potential flow approach is to be found in the small CPU times necessary to obtain solutions. This turns out as a very strong point for a design method which can therefore be used on an interactive basis.

3.2 Computational domain and boundary conditions

In order to take advantage of the periodicity of the problem, the computation is of course restricted to a blade-to-blade channel. The profile is prolonged by a pseudo-wake, without lift and with a constant angular thickness equal to the trailing edge gap.
A C-topology is used to describe the computational domain since it is well adapted to profiles with relatively thick leading edges.

Upstream and downstream conditions are obtained from any standard through-flow computation; the upstream flow is prescribed via inlet angle and inlet relative Mach number while the downstream flow is defined only via the exit angle.
The other exit quantities are naturally obtained through the continuity equation. These boundary conditions are taken far enough upstream and downstream so that the flow can be considered as uniform.
The method can operate both in direct and inverse mode depending on the kind of boundary conditions which are applied on the profile: whereas a Neumann condition corresponding to a zero normal velocity is usually applied in direct calculations, a Dirichlet condition is imposed in the inverse method. This condition corresponds to the fact that the tangential velocity (to the profile) must be equal to a given W^0.

Third International Conference on Inverse Design Concepts and Optimization in Engineering Sciences
ICIDES-III, Editor: G.S. Dulikravich, Washington D.C., October 23-25, 1991

3.3 Profile modification

The goal here is to find the shape which satisfies both constraints:
a) zero normal velocity
b) tangential velocity equal to a given W^o.

The solution of the inverse problem leads to a flow that follows the prescribed tangential velocity W^o on the profile but does not necessarily satisfy the zero normal velocity condition. The non-zero normal velocity obtained from the algorithm is used to modify the profile via a transpiration model: the displacement of the blade surface is accounted for by injection of fluid through the original blade surface such that the new surface becomes a stream surface [6]. The displacement normal to the profile is then obtained simply by expressing the mass conservation between two elements of length ds on the profile (see figure 1).

3.4 Inverse design algorithm

The inverse method consists therefore of a sequence of the following three-step iterations:
a) computation of the potential on the profile by integration of the prescribed velocity;
b) computation of the potential in the domain by solution of the continuity equation with a Dirichlet boundary condition on the profile;
c) computation of the normal displacement of the blade surface as described above and modification of the profile.

While the first and third steps are simple one-dimensional integrations, the second step corresponds to the resolution of a two-dimensional, second order, non linear partial differential equation. The numerical method used to solve this equation is a finite-element method developed by Bredif [10] which will not be described here. Transonic flows can be handled by using a density upwinding also presented in [10].

3.5 Numerical results for turbomachinery applications

Starting from an initial profile, three modifications are generally needed in order to obtain good agreement between the prescribed velocity distribution and the one corresponding to the computed profile. The inverse computation is automatically followed by a direct calculation only to verify the convergence of the procedure. With a 10 x 117 point C-grid (used in most applications) the total computing time is about 15s on an IBM 3090 computer.

Third International Conference on Inverse Design Concepts and Optimization in Engineering Sciences
ICIDES-III, Editor G.S. Dulikravich, Washington D.C., October 23-25, 1991

Three examples are presented: one for a highly loaded compressor rotor hub section, one for the root section of a strongly quasi-three-dimensional turbine nozzle and the last one corresponding to a case where the robustness of the method is demonstrated.

Compressor rotor hub section

Figure 2 shows the compressor flow path. The stream tube thickness is obtained from a through-flow calculation which also provides all the input parameters:

- o inlet Mach number = 0.95
- o inlet flow angle = 61.7°
- o outlet flow angle = -2.5°

The initial geometry came from a previous calculation and the initial velocity distribution (see figure 3) was obtained by running the inverse code in its analysis mode.

The objective for the calculation was to reduce the peak Mach number on the suction side while retaining the same solidity and maximum thickness. Figure 3 shows the prescribed velocity distribution vs the original one as well as the new profile that was obtained after three successive modifications. The pitch angle and the thickness distribution have changed in a substantial manner.

Hub section of a turbine nozzle

The case considered here corresponds to a strongly quasi-three-dimensional section of a turbine nozzle with a large stream-wise variation of the stream tube thickness (outlet to inlet ratio of 1.3). Designing such blading with a two-dimensional inverse method results invariably in the occurrence of non-uniformities in the velocity distributions.

For the present computation, the inlet and exit flow angles are 31.4° and -61° respectively and the inlet Mach number is 0.424.

The velocity distribution on the initial blade and the target velocity distribution are shown in figure 4 together with the blade profiles. For this case, five blade modifications were necessary to reach convergence. The resulting profile remains very smooth.

Example with a poor initialization

The case in Figure 5 involves large changes in the profile from the initialization and demonstrates the robustness of the method. Starting with a geometry having a relative maximum thickness of 3% and a pitch

Third International Conference on Inverse Design Concepts and Optimization in Engineering Sciences
(ICIDES-III), Editor G.S. Dulikravich, Washington D.C., October 23-25, 1991

angle of 25°, the code is capable of converging to a new profile with a thickness of 7% and a pitch angle of 5°. After one iteration, a very large displacement is observed but nonetheless the calculation remains stable.

3.6 Extension of the method to the nacelle design

For the design of transonic blades presented up to now, the complete 3D blade is obtained by stacking a series of 2D profiles; this procedure leads to a reasonable blade if the input pressure (or velocity) distributions vary smoothly, and, most importantly, if the flow is essentially two dimensional, in the sense that there is a preferential direction where little happens in comparison to the other two directions. A complete 3D calculation using a more accurate model (Euler or Navier-Stokes) is the definite proof that the blade obtained by the inverse method possesses the desired features.
The flow around a commercial aircraft inlet (nacelle) demonstrates the "essentially 2D" quality mentioned above and therefore the stacking procedure can be used about its axis for the design of this type of geometry. The method has been extended with the following characteristics:

- basic assumptions:
a & c): same as in 3.1
b) the flow is considered to be axisymmetrical and the potential equation is written and discretized in the (z, r) plane.

- computational domain and boundary conditions:
a C-topology is used to describe the computational domain extending around the inlet from the compressor plane to the downstream plane behind the nacelle. The four boundaries and the conditions applied thereon are the following:

o the inlet profile and its continuation until the downstream plane; boundary condition: either no mass flow for the direct calculation, or Dirichlet condition on the profile in the inverse mode;
o the compressor plane, with a prescribed velocity distribution (varying Neumann condition);

- o a three-segment boundary, including the axis (no-mass-flow condition), the upstream plane (prescribed velocity) and a far field boundary (no-mass-flow condition);
- o the downstream plane, with a prescribed velocity computed from the mass balance equation between this boundary, the upstream plane and the compressor plane.
- the profile modification is carried out in the same way as before, using the transpiration model mentioned in 3.3 [6].
- the inverse design algorithm also remains the same as in 3.4

We will now present a result proving once again the robustness of the method with respect to arbitrary initializations. A velocity repartition (so-called "ideal velocity" on figures) is computed by direct calculation around a given profile ("ideal profile"); this profile is modified into the "initial profile" by thickening. The velocity distribution around this profile is represented in figure 6. It clearly shows an aspect different from that of the ideal velocity. The inverse method has been used in order to recover the ideal profile from this initialization. The convergence of the inverse algorithm is monitored by the decrease of the mass flow across the profile for each inverse calculation. The normal velocity distributions for the first three iterations are shown in Figure 7. After these iterations, the normal velocity is zero on most of the profile, except in the neighborhood of the leading edge. These initial iterations determine therefore the overall shape of the profile. The final iterations (there are four of them here) tend to precisely shape the leading edge of the profile.
The final geometry of the nacelle is compared to the initial one in Figure 8.
This example has been carried out around the H208 nacelle, (an Aerospatiale nacelle which was tested in a windtunnel at ONERA) in a subsonic case (Minf = 0.30). It required 7 profile modifications performed in one minute on an Alliant FX2800. Transonic cases have also been tested and have led to similar conclusions with a slight increase in CPU time.

To conclude this section, it may be stated that the method presented here is a powerful tool for the design of turbomachinery blading. It is currently being applied in the French industry for the definition of high performance turbomachinery.

Third International Conference on Inverse Design Concepts and Optimization in Engineering Sciences
ICIDES-III, Edited by G.S. Dulikravich, Washington D.C., October 23-25, 1991

Parallel research has been going on with the goal of opening a new field of application in the domain of engine inlet design for which the method has proven suitable. Improvements are still being worked on especially in the field of mesh definition for turbine applications. The method has naturally some limitations. One of these is the built-in potential approximation which in fact leads us to the next section devoted to the transonic inverse and semi-inverse method developed initially by Meauzé at ONERA.

4. TRANSONIC INVERSE AND SEMI-INVERSE METHOD [8]

Whereas the method described above solved the potential equation, the one under consideration here deals with the Euler equations which allow for the occurrence of shock waves within the flow field .
This method was first developed by Meauzé in the early eighties as a follow-up of the transonic blade-to-blade direct calculation developed at ONERA by Viviand and Veuillot [11].
These authors made a valuable contribution to the resolution of the Euler equations by using time-marching methods where time is only a computational parameter and the final asymptotic flow field is obtained as the steady solution of the equations.

4.1 Overall description and concepts

The basic features of these methods can be summarized as follows:

- the quasi-three-dimensional Euler equations are discretized in the physical plane;
- a McCormack type predictor-corrector numerical formulation is used;
- when strong pressure or velocity gradients occur, an artificial viscosity is used to smooth out numerical instabilities;
- boundary conditions (wall boundary conditions or inlet/outlet boundary conditions) are treated via compatibility relations which are derived from the theory of characteristics.

Using this framework, Meauzé developed an inverse method in which the standard zero normal velocity boundary condition on the profile can be completely or only partly replaced by a static pressure (or velocity) condition. Whatever the case, the boundary condition problem is always dealt with via the compatibility relations. When operating in inverse mode, the profile and consequently the grid system must be updated. This can be accomplished either through reconstruction of the blade surface by using the flow angle computed at each wall grid point or, more rigorously, via a transpiration model like in the previous method.

Third International Conference on Inverse Design Concepts and Optimization in Engineering Sciences
(ICIDES III), Edited by G.S. Dulikravich, Washington D.C., October 23-25, 1991

4.2 Inverse and semi-inverse methods

What makes the method especially attractive for the designers is the fact that not only does it allow the defining of blading in the transonic regime, but it can also operate in the semi-inverse mode. This makes it possible to apply a given boundary condition on one part of the profile - say a pressure distribution - while retaining for instance the initial geometry on another portion of the blade. Localized corrections of the geometry can therefore be implemented in order to improve the overall aerodynamics of the blade.

Of course, for such applications, special care must be taken at the junction between the direct and inverse calculations. This is especially true when the flow is locally subsonic; then a smooth transition from the prescribed to the computed pressure distribution is required.

On the other hand, for locally supersonic flows, jumps in static pressures are allowed which would correspond to crossing shock waves or expansions.

One interesting version of the code allows prescribing of the pressure distribution on only one blade surface - generally the suction surface - while the other surface is determined from purely geometrical considerations, such as a thickness distribution.

One may note that, in this case, the cascade solidity may be chosen in advance since the profile is automatically closed. However, one drawback is the lack of control over the velocity distribution on the surface for which the pressure distribution was not prescribed. Moreover, two solutions to the problem can exist. Numerical experiments have demonstrated that only solutions corresponding to small flow deflections are stable. Therefore, this method is really only suitable for compressor applications.

4.3 Numerical results

Three examples will be presented: the first corresponds to the definition of a high supersonic blading on the second stage of a rocket turbopump; the second one is devoted to the design of a high pressure ratio turbine cascade; finally, the third application deals with the definition of a supersonic compressor profile.

These three cases have been selected to give examples of the various modes of operation of the method and will demonstrate its versatility.

Third International Conference on Inverse Design Concepts and Optimization in Engineering Sciences
(ICIDES-III), Edited by G.S. Dulikravich, Washington D.C., October 23-25, 1991

High supersonic turbopump rotor

The case considered here corresponds to the redesign of the mean section of the high supersonic rotor of a rocket turbopump. For this configuration, the direct calculation on the original blade showed that the upstream flow was started, i.e., the inlet flow angle is fixed by the unique incidence phenomenon. An inlet relative Mach number of 1.22 was obtained for an inlet angle of 48.5°. The results of this direct blade-to-blade calculation are shown in Figure (9a). Strong shock waves are observed throughout the blade channel with a strong normal shock on the suction side.

An attempt was made to improve the situation with the inverse method operating in its semi-inverse mode. The pressure distributions were prescribed on the pressure and suction surfaces but only over part of the blade. In fact, for this case of supersonic inlet flow, the goal was to leave the inlet conditions undisturbed in order to guarantee adequate matching between the blade rows. The blade entrance region consists of a straight part on the suction side. The slope of this straight portion is chosen such as to obtain the specified unique incidence computed with the original blade. The pressure distribution is then prescribed downstream of this entrance region. Figure (10a) shows the selected distributions; on the pressure side, the flow becomes subsonic and the pressure gradient is chosen so as not to cause boundary layer separation. A smooth pressure distribution is prescribed on the suction side where the impingement of the shock has been deleted.

The resulting pressure field is presented in Figure (10b). An oblique shock is observed at the leading edge on the pressure side. On the suction side, a sharp change in the slope of the surface is observed which compensates for the impinging shock. The calculated relative inlet Mach number is 1.21 and the computed inlet angle 48.3°. These are in good agreement with the results of the direct blade-to-blade calculation on the original blade.

The result of the direct blade-to-blade calculation on the redesigned rotor profile is shown on Figure 11. Good agreement is likewise observed between the inverse and direct calculations.

High pressure ratio turbine cascade

Here again, the code is used in its standard semi-inverse mode for which the pressure distribution was prescribed on both blade surfaces but only downstream of certain points on the surfaces.

Upstream of these points, the initial geometry of the blade is retained and the method operates as a direct blade-to-blade computation. Figure (12a) shows, as broken lines, the initial pressure distributions with suction side non-uniformities. Also presented are the prescribed pressure distributions shown in solid lines. The blade shapes corresponding to these pressure distributions are shown in Figure (12b). Again, the solid line corresponds to the modified blade. Note that the solidity has changed, with a slight increase of the pitch.

Supersonic compressor cascade

This case is a typical example of the method described above where the blade is defined using a mixed type of aerodynamic and geometrical data. Here, the method is applied to the design of a supersonic compressor profile with an inlet Mach number of 1.2. Figure(13a) presents the initial pressure distribution where a shock at a peak Mach number of 1.6 occurs on the suction side near the trailing edge causing an increase in the loss and probable separation. The new blade is now obtained by tailoring the suction side pressure distribution so as not to exceed a peak Mach number of 1.42. The initial blade thickness distribution is retained.
Figure (13b) shows the new profile compared to the initial one. As can be seen, the difference between the two geometries is very small (which, by the way, ought to make us wonder what really happens in the machine when all manufacturing deviations have been taken into account).
The newly computed pressure distribution on the pressure side is also presented in Figure (13a). It exhibits a rather irregular shape especially in the trailing edge region. This is due to the evolutions of the pressure side curvature in this rear part of the blade which necessarily "follow" those of the suction side since the thickness distribution is prescribed.
This is one of the drawbacks of the method although a local correction of the blade on the pressure side can usually improve the situation without deteriorating the suction side pressure distribution.

4.4 Current developments

As stated earlier, this inverse Euler code must really be considered as a by-product of the direct blade-to-blade calculation. As a consequence, a major overhaul of the code is under way which reflects the improvement brought to the direct flow computation.

Third International Conference on Inverse Design Concepts and Optimization in Engineering Sciences
ICIDES-III, Edited by G.S. Dulikravich, Washington D.C., October 27-29, 1991

Most of these improvements have been obtained on the mesh itself where the standard H-grid has been replaced by an H-C or H-C-H one with a multi-domain approach (compatibility relations are used at the boundaries between the domains). The improvement is especially to be found in turbine applications where round leading edges can be properly modelled (see Figure 14).
In a parallel effort, the algorithm has been modified in such a way that the inverse mode and the profile modification procedures are now only applied after convergence has been achieved on a given intermediate geometry. Although this brings about some penalization of the computing time, this approach gives better quality solutions.

CONCLUSION

Two quasi-three-dimensional inverse methods have been described above. Taken as a whole, they allow the defining of turbomachinery blade profiles throughout the entire Mach number range of interest for jet engine (even rocket engine) rotating components. Examples have been presented for compressor and turbine profile designs.
Both methods are currently being used throughout the French industry. A parallel research effort is still under way to improve them and extend their fields of application. The next step will certainly include coupling with a boundary layer calculation in order to better predict viscous effects.
It is obvious, however, that even such improved methods will have their limitations. The next significant step in turbomachinery design will have to be found in optimization techniques similar to the ones developed for external aerodynamics. Although some progress has been observed in this domain in the recent past, it is still widely believed that a breakthrough in the field of fundamental mathematical analysis will be required in order to formulate this complex multi-parameter problem.

ACKNOWLEDGMENT

The authors wish to thank D. Nicoud and B. Petot from SNECMA and G. Meauzé from ONERA for their contributions to this paper.

References

[1] Lighthill, M.J., "A New Method of Two-Dimensional Aerodynamical Design," R. & M. No.2112, Aeronautical Research Council, London, 1945.

[2] Volpe, G. and Melnik, R.E., "The Role of Constraints in the Inverse Design Problem for Transonic Airfoils," AIAA Paper No.81-1233, AIAA 14th Fluid and Plasma Conf., 1981.

[3] Sloof, J.W., "A Survey of Computational Methods for Subsonic and Transonic Aerodynamic Design," Proceedings of the International Conference on Inverse Concepts in Engineering, Austin, TX, U.S.A., 1984.

[4] Meauzé G., "Overview of Blading Design Methods," Agard Lecture Series No. 167, Blading Design for Axial Turbomachines, June 1989.

[5] Stanitz, J.D., "Design of Two-Dimensional Channels with Prescribed Velocity Distributions along the Channel Walls," NACA, Rep 1115, 1952.

[6] Cedar, R.D., and Stow, P., "A Compatible Mixed Design and Analysis Finite Element Method for the Design of Turbomachinery Blades," International Journal for Numerical Methods in Fluids, Vol. 5, 1985, pp. 331-345.

[7] Jacquotte, O.P., "An Inverse Finite Element Method for the Design of Turbomachinery Blades," 7th Int'l Conference on Finite Element Methods in Flow Problems, Huntsville, U.S.A, April 1989.

[8] Meauzé, G., "An Inverse Time-Marching Method for the Definition of Cascade Geometry," Journal of Engineering for Power, Vol. 104, July 1982.

[9] Nicoud, C., Le Bloa, C., and Jacquotte, O.P., "A Finite Element Inverse Method for the Design of Turbomachinery Blades," ASME Paper 91-GT-80, Orlando, June 1991.

[10] Bredif, M., "A Fast Finite Element Method for Transonic Potential Flow Calculations," AIAA Paper 83-0507, AIAA 21st Aerospace Sciences Meeting, Renc, U.S.A 1983.

[11] Viviand H., and Veuillot, J-P., "Methodes Pseudo-Instationnaires pour le Calcul d'Ecoulements Transsoniques," Publications ONERA No. 1978-4. English Translation ESA TT 549.

Third International Conference on Inverse Design Concepts and Optimization in Engineering Sciences
(ICIDES-III), Editor G.S. Dulikravich, Washington D.C., October 23-25, 1991

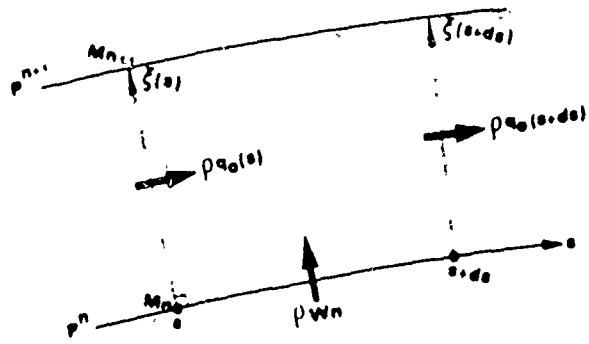


Fig.1 : Profile modification

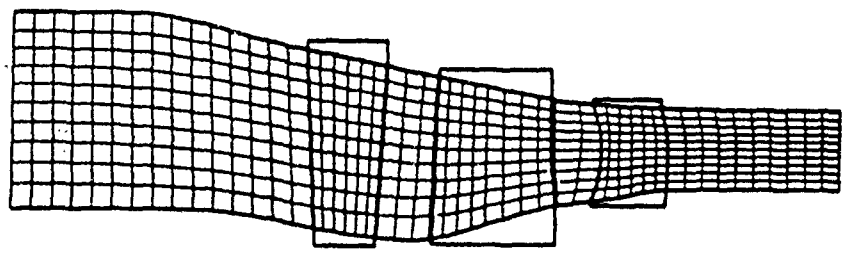


Fig.2 : Through-flow calculation

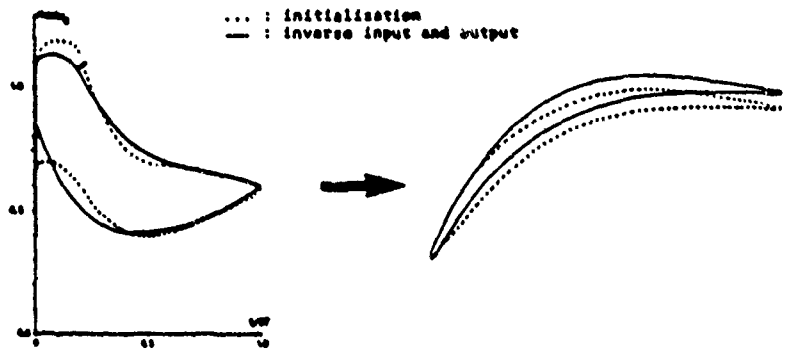


Fig.3 : Required Mach number distribution
and final profile after 3 modifications

Third International Conference on Inverse Design Concepts and Optimization in Engineering Sciences
ICIDES-III, Edwar G.S. Pulliam, Washington D.C., October 21-23, 1991

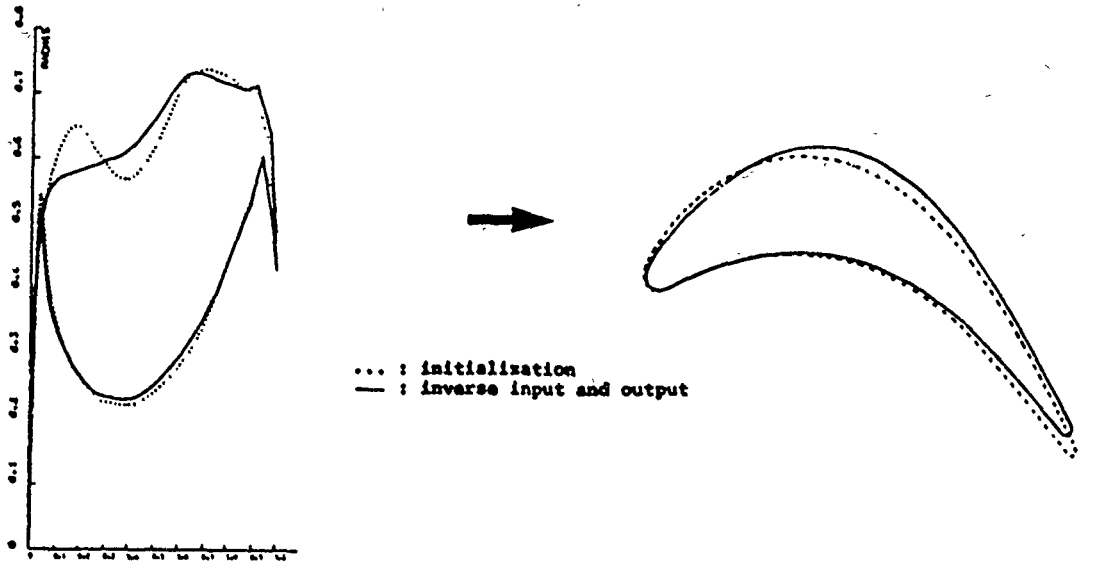


Fig.4: Required Mach number distribution and final profile after five modifications

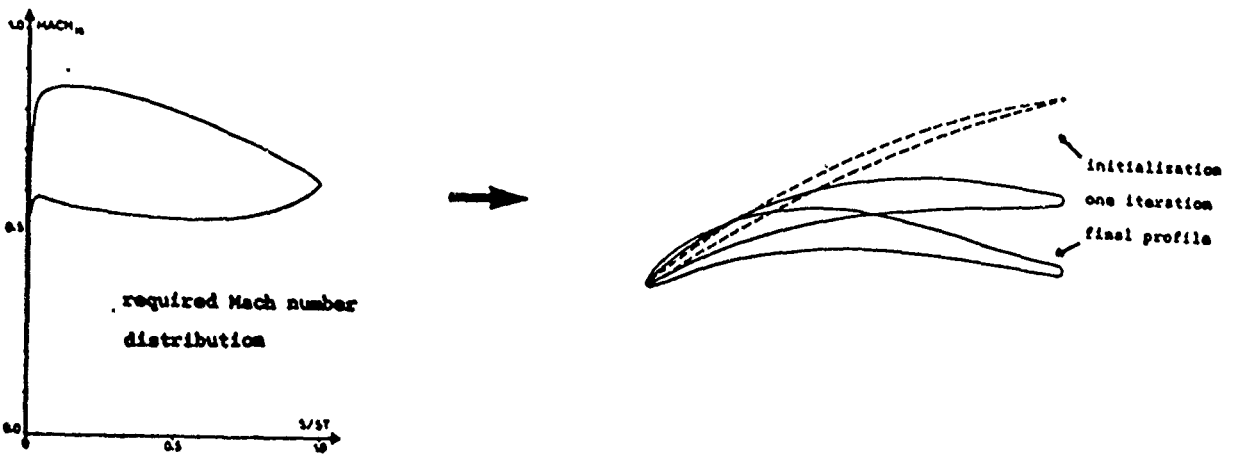


Fig.5: Subsonic example with a poor initialization

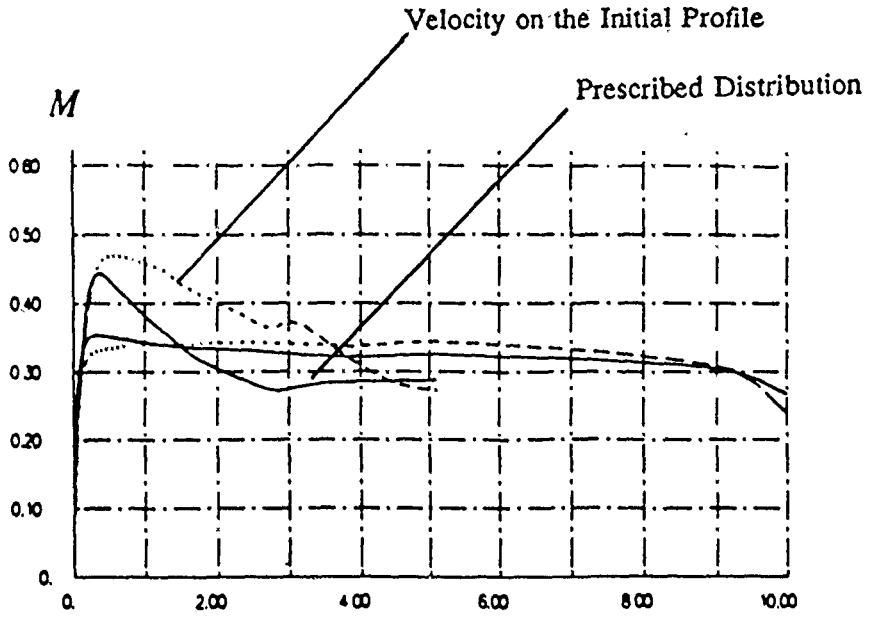
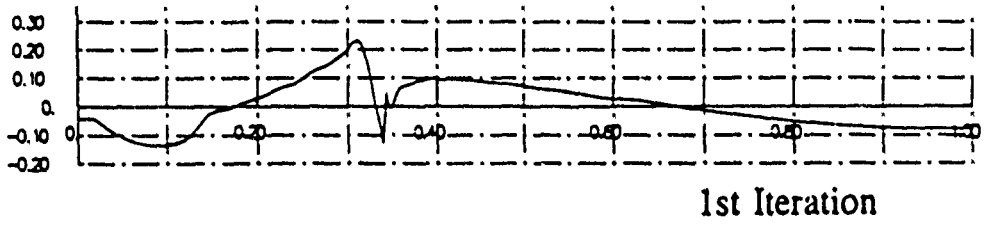
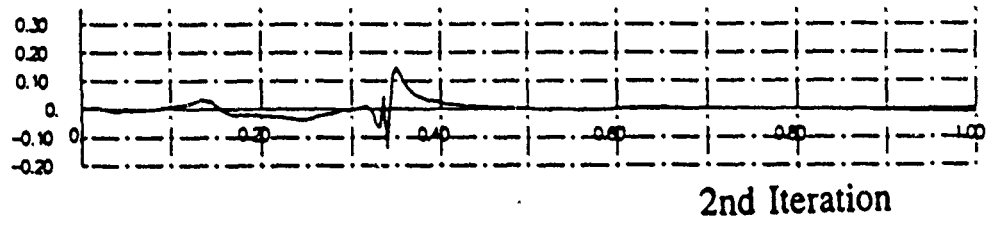


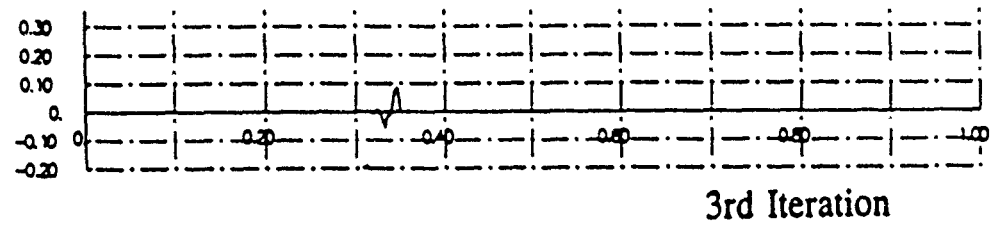
Fig.6 : Prescribed Velocity and Velocity around the Initial Profile



1st Iteration



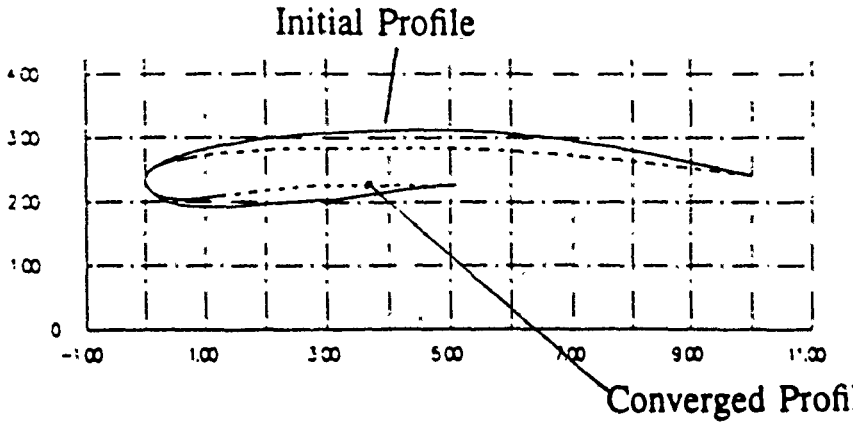
2nd Iteration



3rd Iteration

Fig. 7 : Velocity Normal to the Profile

Third International Conference on Inverse Design Concepts and Optimization in Engineering Sciences
(ICIDES-III), Editor: G.S. Dulikravich, Washington D.C., October 23-25, 1991



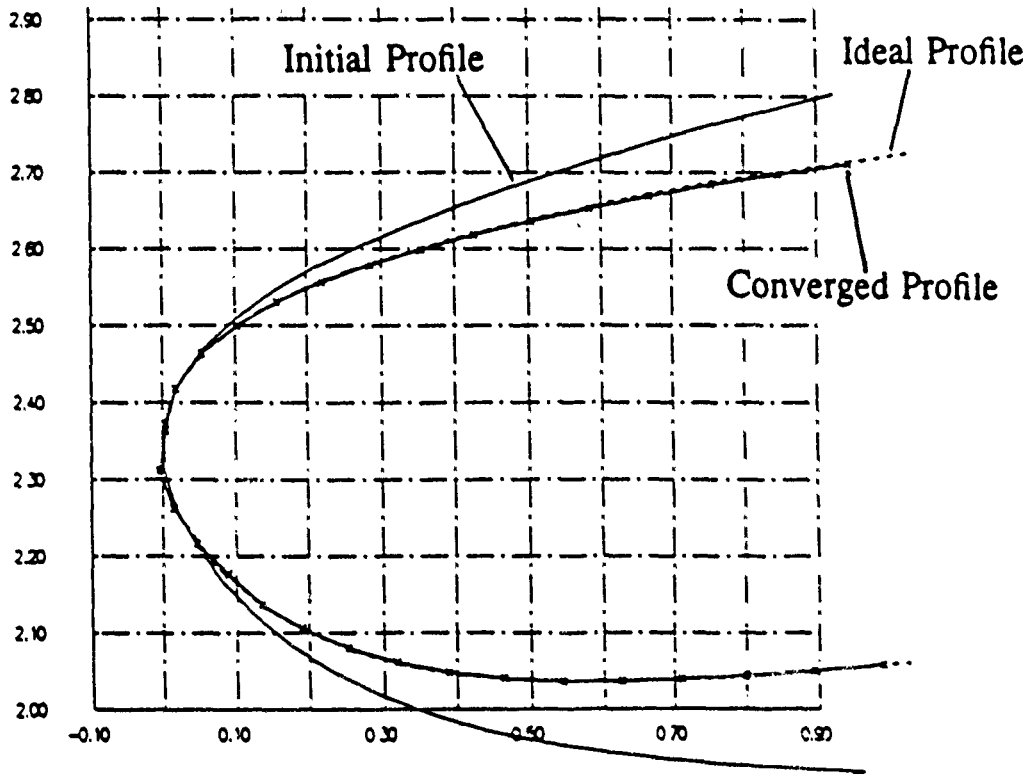


Fig.8 : Modification of the Profile

Third International Conference on Inverse Design Concepts and Optimization in Engineering Sciences
(ICIDES-III), Editor: G.S. Dulikravich, Washington D.C., October 23-25, 1991

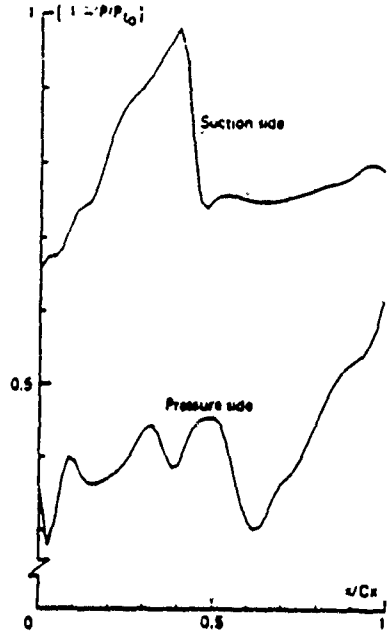


Fig.9a – *Mid span section of the second rotor : pressure distribution.*

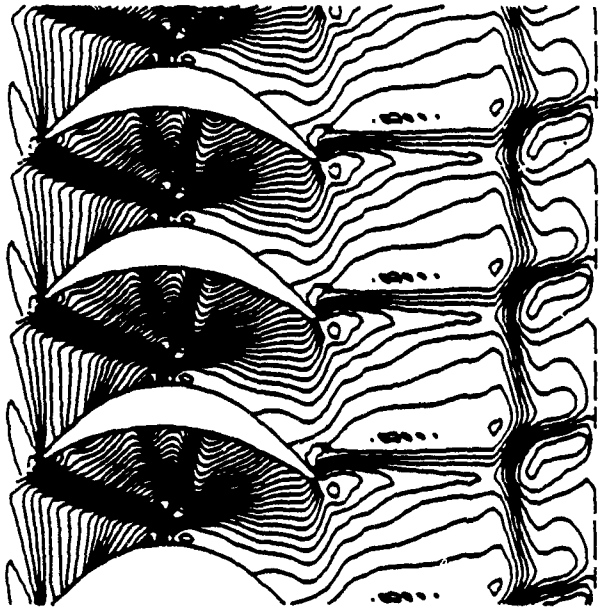


Fig.9b – *Mid span section of the second rotor : isobaric lines.*

Third International Conference on Inverse Design Concepts and Optimization in Engineering Sciences
(ICIDES-III), Editor: G.S. Dulikravich, Washington D.C., October 23-25, 1991

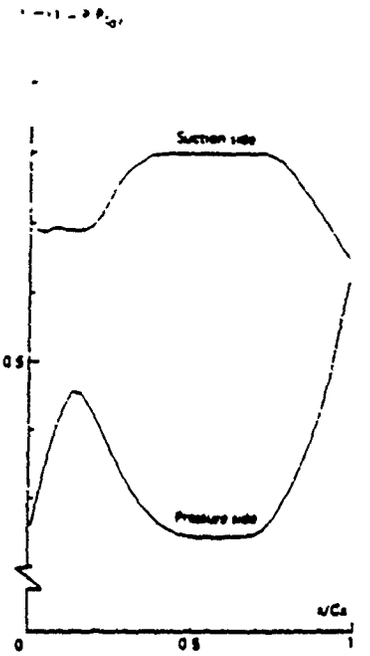


Fig.10a – *Second rotor design : pressure distribution (mid span section).*

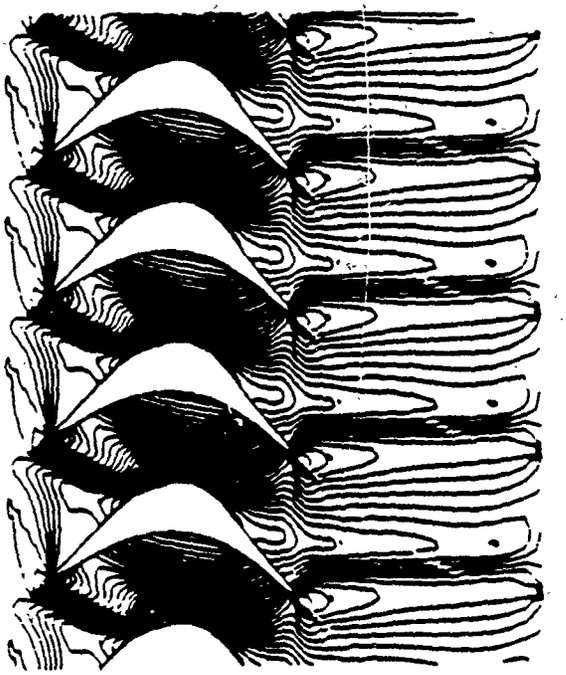


Fig.10b – *Second rotor design : isobaric lines. (mid span section).*

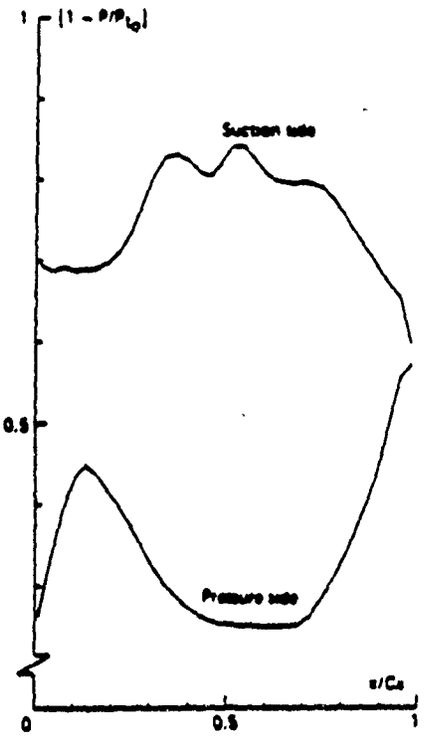


Fig.11 – *Second rotor design : pressure distribution (direct mode calculation).*

Third International Conference on Inverse Design Concepts and Opumization in Engineering Sciences
(ICIDES-III), Edwor G.S. Dulikravich, Washington D.C., Oriones 23-25, 1991

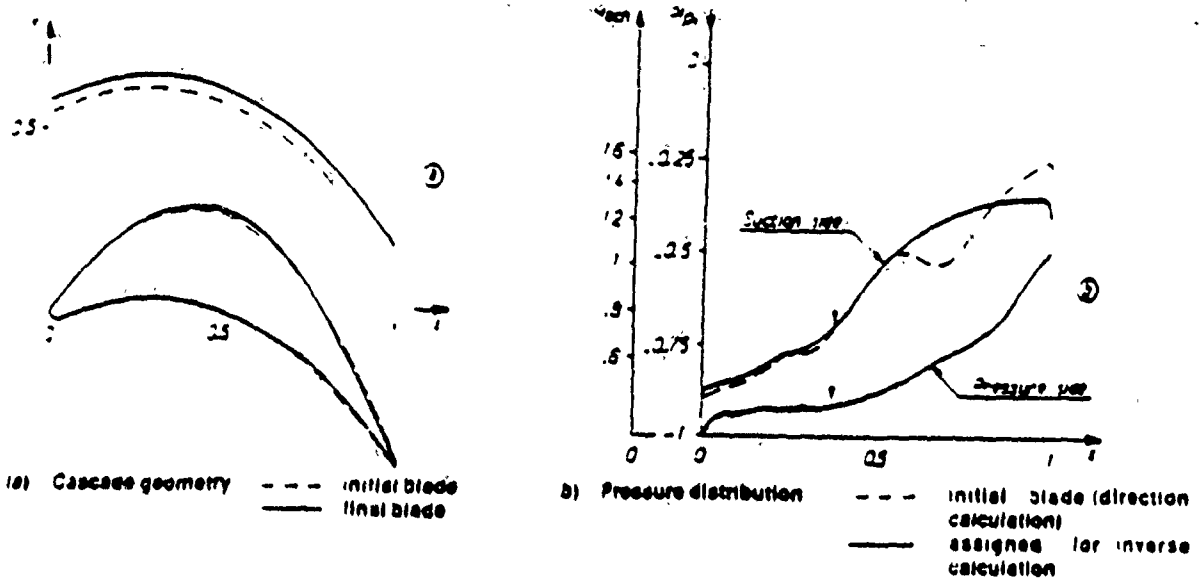


Fig.12 - Definition of a turbine blade and the cascade pitch, for pressure distributions assigned on the pressure and suction sides .

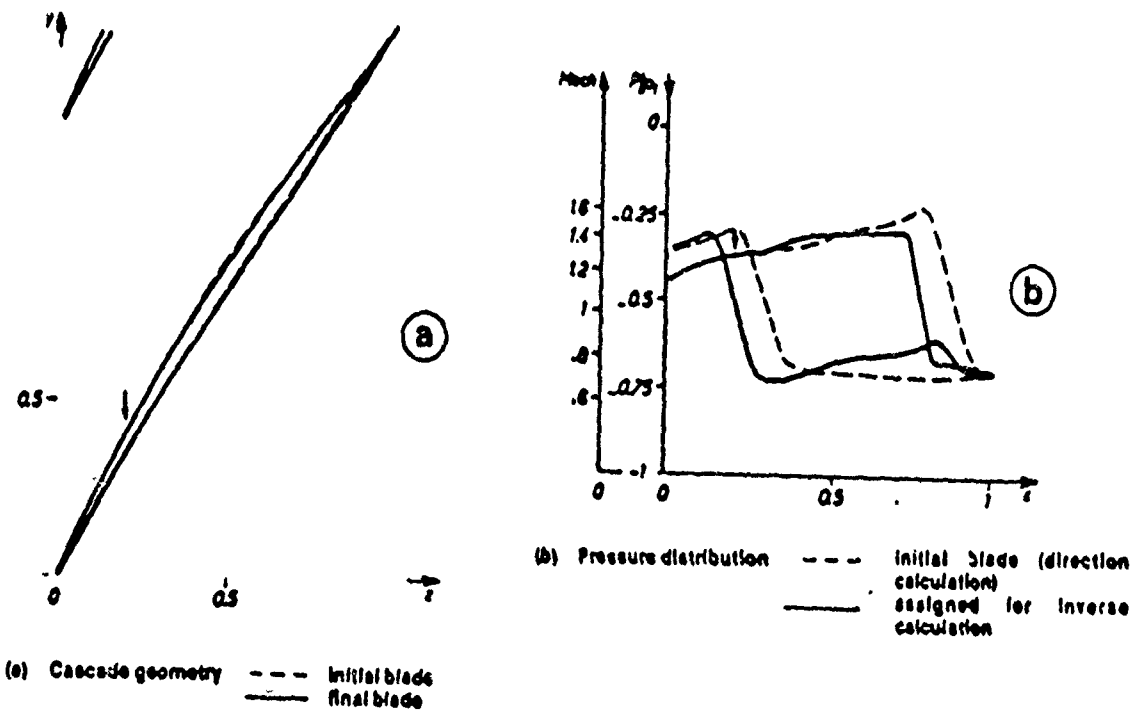


Fig.13 - Definition of a section of supersonic compressor

Third International Conference on Inverse Design Concepts and Optimization in Engineering Sciences
(ICIDES-III), Editor: G.S. Dulikravich, Washington D.C., October 23-25, 1991

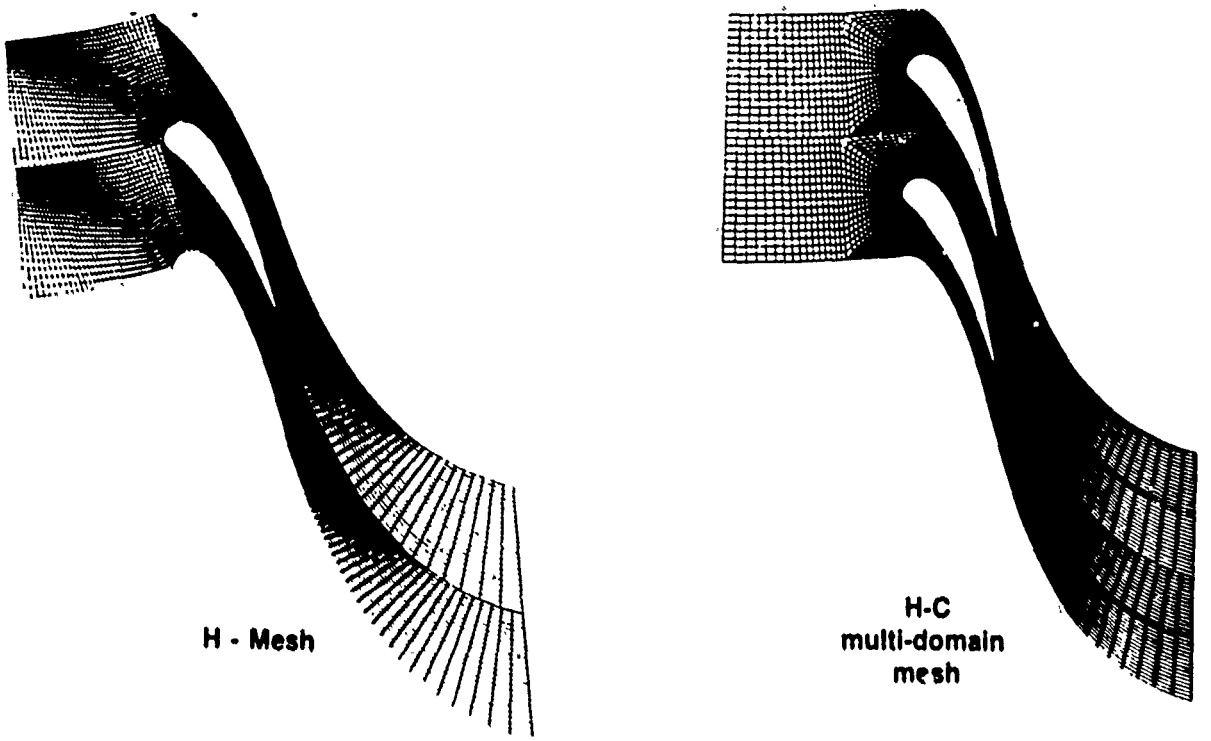


Fig.14 : Comparison of mesh types
for turbine applications

Third International Conference on Inverse Design Concepts and Optimization in Engineering Sciences (ICIDES-III), Editor: G.S. Dulikravich, Washington D.C., October 23-25, 1991.

RESEARCH ON INVERSE, HYBRID AND OPTIMIZATION PROBLEMS IN ENGINEERING SCIENCES WITH EMPHASIS ON TURBOMACHINE AERODYNAMICS: REVIEW OF CHINESE ADVANCES

Gao-Lian Liu, Professor
Laboratory of Turbomachinery Aerodynamics
Shanghai Institute of Mechanical Engineering
516 Jun-Gong Rd, Shanghai 200093, China

ABSTRACT

A brief review of advances in the inverse design and optimization theory in the following engineering fields in China is presented: I) Turbomachine aerodynamic inverse design: including mainly: (1) two original approaches——image-space approach and variational approach , (2) improved mean-streamline (stream surface) method, (3) optimization theory based on optimal control. II) Other engineering fields: inverse problem of heat conduction, free-surface flow, variational cogeneration of optimal grid and flow field, optimal meshing theory of gears.

I. INTRODUCTION

Up to now, most(over 95%) of the technical literature deals only with the direct (analysis) problem due to possibly the fact that the inverse(design) problem(finding the unknown boundary shape) is, in general, much more difficult to formulate as well as to solve than the direct one, though the inverse problem is more important for , and directly related to, practical design. As a result, for instance, almost all turbomachine bladings are still designed by repeated use of direct problem methods in a cut-and-try manner, which is of course not only inconvenient and time-consuming, but also incapable of providing very good results.So in the 1950's in China we have tried to apply the mean-streamline method for inverse problem of Wu & Brown[30] to cascade design and some improvements of this method were suggested[2]. In the 1960's a new image-plane approach to the inverse problem was proposed [5]. It was realized, however, that also the inverse problem can not be successfully used for practical blade design, because it often leads to blade configurations that are either unfeasible from consideration of stress, vibration, cooling and technology or even unrealizable(e.g. giving profiles unclosed or with negative thickness). Therefore the traditional direct and inverse problems can not keep up with the development of modern turbomachinery(TM) and it was suggested in Refs.[18,56] to extend the scope of aerodynamic problems and reclassify them into four categories: direct, inverse, hybrid and optimization problems. Then the image-plane approach was extended to hybrid problem in Refs.[6,56], and another new approach to inverse and hybrid problems based on variational principles (VPs) was also suggested in Refs. [18,21]. Since then, a lot of variants of the image-plane approach, the variational approach and the mean-streamline method have been developed in China and extended to 3-D case.

The Chinese research on the optimization problem of bladings started with the problem of optimal radial distribution of flow parameters in TM with long twisted blades in 1963[52]. Later, advances in this area are characterized and facilitated considerably by the introduction of modern optimal control theory.

Third International Conference on Inverse Design Concepts and Optimization in Engineering Sciences (ICIDES-III), Editor: G.S. Dulikravich, Washington D.C., October 23-25, 1991.

II. RECLASSIFICATION OF ENGINEERING PROBLEM SETTING

Generally speaking, any problem of engineering sciences can be posed in different ways, resulting in four problem categories: direct, inverse, hybrid and optimization problems. Specifically, for the aerodynamic problem of blade cascades these problems are defined conceptually in Table I. The aerodynamic problem for S_2-stream surface can be classified similarly as shown in Table II.

The hybrid problem is a unification as well as a generalization of the direct and inverse problems, encompasses a wide variety of types(see Table III for cascades on arbitrary streamsheet of revolution) and hence is very flexible and capable of meeting various design requirements. It provides design engineers with a series of new rational versatile ways for blade design. In addition, the inverse and hybrid problems also constitute an important ingredient of the optimization problem.

Table I. Problem Classification of Cascade Flow

	problem	Given	To be sought
1	Direct (D)	cascade geometry	velocity field
2	Inverse(I)	surface velocity distribution	cascade geometry
3	Hybrid (H)	'partly geometric conditions' & 'partly flow condition'	the remainding unknown geometry & flow field
4	Optimization (Opt)	1)objective functional 2)design inequality constraints	optimal cascade geometry & flow field

Table II. Problem Classification of S_2 -Flow

problem		Given	
		on S_2	on hub & casing
Direct	complete	Shape	geometry
	semi-		pressure distribution
Inverse	complete	$V_\varphi r$	pressure distribution
	semi-		geometry
Hybrid		Shape or $V_\varphi r$	'partly geometry'+ 'partly pressure distribution'
Optimization		1) objective function , 2) inequality design constraints	

Third International Conference on Inverse Design Concepts and Optimization in Engineering Sciences (ICIDES-III), Editor: G.S. Dulikravich, Washington D.C., October 23-25, 1991.

Table III. Hybrid Problem Types of Cascades

Types	Given conditions	
	geometric	aerodynamic
H_A	part of airfoil form	velocity distribution along the remainding part of profile contour
H_B	airfoil thickness distribution	blade loading distribution ($p_P - p_S$)
H_C	airfoil thickness distribution	velocity distribution along the suction surface
H_D	airfoil thickness distribution	distribution of velocity difference ($W_S - W_P$)

Since the hybrid problem of fully 3-D flow may have a wide variety of types, depending on the manner in which the boundary conditions (B.C.) on the blade surface are combined with those on the annuclar walls, it is necessary to employ some properly defined compound symbols to designate them as proposed in Refs. [46, 47]. For instance, the symbol ($I \times H_A$) designates such a hybrid problem type in which an inverse problem is posed on the blade surface, while a H_A-problem is posed on the annular walls(Fig. 1a). In other words, the symbol before 'X' characterizes the problem type on the blade surface, while the symbol behind 'X'---that on the annular walls. It is easy to see that the scope of possible hybrid problem types can be made even much broader by posing different problem types on different portions of the blade(and/or annular) walls (Fig. 1b).

III. INVERSE & HYBRID PROBLEMS OF BLADE-TO-BLADE FLOW IN TURBOMACHINES

The research on inverse and hybrid problems in China has been going basically along the following three lines: (i) universal approach based on image-plane concept; (ii) unified approach based on variational principles (VPs) and the related finite element method (FEM); (iii) improvement of the mean-streamline method and of other well-known methods.

1) Universal Approach Based on Image-Plane Concept

Two different image planes $\xi\psi$ and $\xi\eta$ have been introduced:

1-1. Methods based on image-plane $\xi\psi$.

The first universal image-plane method for solving the inverse problem of 2-D compressible cascade flow was suggested by Liu in 1964 [5] and extended to cascades on arbitrary streamsheet of revolution by Liu & Tao in 1967 [6] and to hybrid problem H_A by Liu & Tao in 1981 [6]. The main difficulty is the treatment of unknown boundary(blade surface) and was successfully overcome by introducing a nonorthogonal curvilinear(streamline) coordinate system (von-Mises coordinates) defined by (Fig. 2, where η should be replaced by ψ)

$$\left.\begin{aligned} \xi &= \ell \quad [\text{or: } \xi = f(\ell)] \\ \psi &= \psi(\ell, \varphi) \end{aligned}\right\} \tag{1}$$

where the stream function ψ is defined by

Third International Conference on Inverse Design Concepts and Optimization in Engineering Sciences (ICIDES-III). Editor: G.S. Dulikravich, Washington D.C., October 23-25, 1991.

$$\frac{\partial \psi}{\partial \ell} = -\tau \rho \Lambda_\varphi , \qquad \frac{\partial \psi}{\partial \varphi} = \tau r \rho \Lambda_\ell \tag{2}$$

It is expedient to regard Eq.(1) as a mapping, which transforms the original irregular periodic flow domain with some unknown boundary(AB in H_A-problem, Fig.2a) on the physical stream surface into a simple rectangular one with fully known boundary in the image plane (Fig.2b). Moreover, the following four alternative formulations were derived in Ref. [5,6]:

i) first-order partial differential equation (PDE) system
ii) second-order PDE
iii) integro-differential equation
iv) integral equation system,

of which only the integro-differential formulation for homentropic flow is given here for reference [6]:

$$\oint_{(\delta C)} \frac{1}{\tau \rho} \left\{ \left[1 + \left(r \frac{\partial \varphi}{\partial \xi} \right)^2 \right] \left(r \frac{\partial \varphi}{\partial \psi} \right)^{-1} d\xi + r \frac{\partial \varphi}{\partial \xi} d\psi \right\} = L_1 \tag{3}$$

where

$$\frac{\partial \varphi}{\partial \xi} = \Lambda_\varphi / (r \Lambda_\ell) , \qquad \frac{\partial \varphi}{\partial \psi} = 1 / \tau r \rho \Lambda_\ell \tag{4}$$

$$\rho = p^{1/\kappa} = \left\{ 1 - \frac{1}{2m} (\Lambda^2 - \Lambda_u^2) \right\}^m \tag{5}$$

$$L_1 = \frac{-2\omega B}{a_0} \iint_{(\delta A)} r \cdot \sin\sigma \frac{\partial \varphi}{\partial \psi} d\xi d\psi .$$

Here $\Lambda (= w/a_0)$ and $\Lambda_u (= \omega r / a_0)$ are dimensionless relative velocity and blade speed respectively; $m = (\kappa - 1)^{-1}$; a_0---reference speed of sound; ω---rotor angular speed; δC—the contour abcda of a finite area δA (Fig.2b).

A H_A-and an inverse problems of a cascade on a general streamsurface of revolution have been solved by this method by Chen et al. in Ref. [7].

This method was then improved considerably by Liu [8] via introducing a new moment function Ω defined by

$$\frac{\partial \Omega}{\partial \xi} = \tau r p / \kappa , \qquad \frac{\partial \Omega}{\partial \psi} = -(\Lambda_\varphi + \Lambda_u) r \tag{6}$$

The moment function has some special features, for instance: (i) its increment around any closed contour enclosing an airfoil $\Delta\Omega$ is just equal to the aerodynamic moment M_z exerted on airfoil:

$$\Delta\Omega = M_z = \Gamma \cdot \Delta\psi \tag{7}$$

This is just a generalization of the well-known Kutta's lift theorem for 2-D flow, showing that M_z is proportional to both absolute circulation around airfoil Γ and flow rate through an interblade channel $\Delta\psi$. (ii) the pressure p can be computed directly from Eq.(5), resulting in two advantages: first, no density ambiguity[80] appears; second, for the inverse problem the B.C.(i.e. the distribution of Ω) on the airfoil contour is of the Dirichlet's type and hence easy to deal with. Also in this case the four alternative formulations mentioned above are possible, of which only the second-order PDE formulation is given below:

Third International Conference on Inverse Design Concepts and Optimization in Engineering Sciences (ICIDES-III), Editor: G.S. Dulikravich, Washington D.C., October 23-25, 1991.

$$A\frac{\partial^2\Omega}{\partial\xi^2}+2B\frac{\partial^2\Omega}{\partial\xi\partial\psi}+C\frac{\partial^2\Omega}{\partial\psi^2}+D\frac{\partial\Omega}{\partial\xi}+E\left(\frac{\partial\Omega}{\partial\psi}\right)^2=F. \tag{8}$$

where A, B, C, D, E are functions of Mach number, ρ, τ and σ (Fig. 2); F is a function of the gradients of entropy and rothalpy. In Ref. [8] an inverse problem of a cascade on a conical streamsurface taken from Ref. [78] was solved and the result is given in Fig. 3.

Later, a number of methods using this image plane $\xi\psi$ have been also published in Refs [9-12], differing from one another, however, by different choice between the four above-mentioned formulations and by different iterative strategies. Thus, in contrast to Refs. [5, 6], Shen & Na [9] solved the H_A -and H_C -problems of 2-D transonic cascade flow by employing the 1st-order PDE formulation and Jameson's rotated difference scheme, while Chen & Zhang [10], using the second-order PDE formulation for the dependent variable $\varphi(\xi,\psi)$, presented a numerical method for solving direct, inverse and hybrid H_A -problems along with three numerical inverse problem examples, of which the one for a tandem cascade is given in Fig. 4. Some difference between the calculated and original profiles might be attributed to the use of the measured velocity distribution as input for the calculation. This method has been modified by Sun et al. in Ref. [11] by using a boundary-fitted coordinate η (see Eq. (9)) instead of φ. The numerical result of a supercritical cascade together with its modified design is shown in Figs. 5 & 6. In Ref. [12] a method similar to Ref. [10] for H_C - & I-problems was presented for rotational flow, and a method for removing the density ambiguity is also given. In addition, a rational cascade design procedure consisting of successive use of H_C -and I-problems is proposed.

1-2. Methods based on image-plane $\xi\eta$.

All methods using image-plane $\xi\psi$ suffer from the shortcoming that singularities appear in the vicinity of blunt leading and trailing edges due to local multivaluedness of the mapping Eq. (1). To circumvent this difficulty, another method for hybrid problems was suggested by Liu [13], where a new image-plane $\xi\eta$ defined by (Fig. 2)

$$\left.\begin{aligned}\xi&=\ell \quad [\text{or: } \xi=f(\ell)]\\ \eta&=\frac{\eta_p-\eta_s}{\varphi_p-\varphi_s}(\varphi-\varphi_s)+\eta_s\end{aligned}\right\} \tag{9}$$

was introduced, where η_p and η_s (the η-values on suction & pressure sides) are given constants. Also in this case four alternative formulations can be derived, but only the integro-differential formulation is given here for reference (Fig. 2b):

$$\oint_{(\delta c)}\frac{1}{\tau\rho}\left\{\left(tg\gamma\frac{\partial\psi}{\partial\xi}-\frac{\sec^2\gamma}{H_\eta}\frac{\partial\psi}{\partial\eta}\right)d\xi+\left(H_\eta\frac{\partial\psi}{\partial\xi}-tg\gamma\frac{\partial\psi}{\partial\eta}\right)d\eta\right\} =2\frac{\Lambda_u}{r}\Delta\eta\int_{(ab)}H_\eta\cdot\sin\sigma\cdot d\xi. \tag{10}$$

$$\frac{\partial\psi}{\partial\xi}=\tau\rho(\Lambda_\ell\cdot tg\gamma-\Lambda_\varphi), \qquad \frac{\partial\psi}{\partial\eta}=\tau\rho H_\eta\Lambda_\ell \tag{11}$$

$$\rho=\left[1-\frac{1}{2m}(\Lambda^2-\Lambda_u^2)\right]^m. \tag{12}$$

where $tg\gamma$ is the slope of the ξ-coordinate line; $H_\eta=r\cdot\delta\varphi/(\eta_p-\eta_s)$ is the scale factor of the coordinate η; $\delta\varphi=\varphi_p-\varphi_s$ is the angular width of the blade channel. We can see that this new image-plane method is particularly advantageous for solving those hybrid prob-

Third International Conference on Inverse Design Concepts and Optimization in Engineering Sciences (ICIDES-III), Editor: G.S. Dulikravich, Washington D.C., October 23-25, 1991.

lems with given airfoil thickness (and hence H_η is also known).

Other methods based on $\xi\eta$-image plane, using, however, the following second-order PDE formulation, have been presented by Chen et al. [14, 15] and Ge[16]:

$$A_1\frac{\partial^2\psi}{\partial\xi^2}+A_2\frac{\partial^2\psi}{\partial\xi\partial\eta}+A_3\frac{\partial^2\psi}{\partial\eta^2}+A_4\frac{\partial\psi}{\partial\xi}+A_5\frac{\partial\psi}{\partial\eta}=B_1 \tag{13}$$

where A_1, A_2, A_3, A_4, A_5 are functions of ρ and the metric tensor g_{22}, g_{23}; B_1 depends on the gradients of entropy and rothalpy, velocity, ω, σ and viscous forces. In Ref. [14] the H_A-problem of potential flow is solved and one of the numerical examples is given in Fig. 7. The figures 8 & 9 taken from the viscous inverse problem solutions of Refs. [15] & [16] respectively show that for the same inlet and outlet flow angles the airfoil in viscous flow is more strongly curved than that in inviscid flow.

2) Unified Approach Based on Variational Principles

Basically there have been developed two completely different variational approaches, following a systematic way suggested by Liu[17].

2-1. Approach based on VPs in the image plane $\xi\psi$(Fig. 2)

In Ref. [18] Liu established two families of VPs and generalized VPs in terms of the moment function Ω and angular function respectively for the H_A- and H_B-problems in the image plane $\xi\psi$, which were modified by Liu & Yao to give the VPs for the H_C-problem in Ref. [19]. Only one of these VPs is given below:

$$J_1(\Omega)=\iint_{(A)}\left\{\Lambda_u^2+2m\left[1-\left(\frac{\kappa}{\tau r}\frac{\partial\Omega}{\partial\xi}\right)^{\frac{1}{\kappa m}}\right]-\left(\frac{1}{r}\frac{\partial\Omega}{\partial\psi}+\Lambda_u\right)^2\right\}d\xi\,d\psi+L_\Omega \tag{14}$$

where the boundary integral term L_Ψ takes different form for different problem types. Based on these VPs involving Ω, some finite element (FE) solutions to H_A-and H_B-problems have been presented in Ref. [20] by Yao et al., from which Figs. 10 & 11 for a cascade on a conical stream surface [78] are taken.

2-2. Approach based on VPs with variable domain.

Making use of the functional variation with variable domain, Liu was able to establish three families of VPs and generalized VPs for H_A-, H_B-and H_C-problems in terms of the potential and stream functions Φ & Ψ for potential and rotational flows in Refs. [21, 22] and extended them to transonic flow with shocks in Ref. [24]. Moreover, variable-domain VPs using Clebsch variables have been also developed for 2-D transonic rotational channel flow by Liu[25].

Numerical solutions to H_A-and H_C-problems based on VPs of Refs. [21, 22] have been obtained by Yan & Liu[22, 23] by means of a new finite element with self-adjusting nodes for numerical realization of the functional variation with variable domain(Figs. 12 & 13).

Perhaps a very attractive merit of this variable-domain approach is that it can be straightforwardly extended to fully 3-D flow.

3) The Mean-Streamline Method (MSLM).

This method originally suggested by Wu & Brown[30] was improved in many aspects in China. A survey of this development before 1984 has been presented by Cai[2]. Recent research includes Cai's paper [3] and Wang's paper [4].

4) Miscellaneous Approaches.

Several known approaches to inverse design of cascades were improved or modified in China.

4-1. Iterative method based on direct problem solver.

Such a method is suggested by Wang in Ref. [26] to solve inverse and various hybrid problems(including H_A & H_C) and extended to viscous flow in Ref. [27] by incorporating a boundary layer solver of integral type. Based on this method, Wang et al. proposed a

Third International Conference on Inverse Design Concepts and Optimization in Engineering Sciences (ICIDES-III), Editor: G.S. Dulikravich, Washington D.C., October 23-25, 1991.

quasi-3-D design procedure for impellers[28,29].

4-2. Time-dependent method.

Starting from the integral form of aerodynamic equations, a finite-volume method for inverse cascade problem is given by Zhou & Zhu[31].

4-3. Hodograph method.

It was improved in the transonic region by incorporating some analytical nozzle solutions and generalized to cascade flow along general streamsheet of revolution independently by Chen[32] and Yao[33].

IV. INVERSE & HYBRID PROBLEMS OF S_2-FLOW IN TURBOMACHINES

Similarly to S_1-flow, the image-plane approach and the VP-based approach mentioned above can be applied to S_2-flow as well.

1) Unified VP-Based Approach.

Starting from the basic equations of Wu's S_2-flow model[1,79], first complete VPs and generalized VPs for the semi-inverse problem were established by Liu[34] and the corresponding FE solutions were obtained by Qin et al.[35]. Inverse and hybrid problems of S_2-flow were formulated in a unified manner by VPs with variable domain by Liu[36] and by VPs in an image-plane $\xi\psi$ by Cai & Liu[37], which have been generalized to flow of pure substance by Xu[38]. In Ref.[39] VPs for hybrid problems of axisymmetric channel flow were derived by Tao & Liu.

2) Universial Image-Plane Approach.

Using an image plane $\xi\psi$ and given a distribution of circulation $V_\varphi r$ on S_2-surface, Ge presented a method for solving the complete inverse problem and a hybrid problem(with unknown hub(or casing) wall, see Table II), thereby a second-order PDE for $r(\xi,\psi)$ was derived and solved [40].

V. INVERSE & HYBRID PROBLEMS OF FULLY 3-D ROTOR-FLOW

For these problems three approaches have been developed in China.

1) Method of Mean-Stream Surface.

It was originally suggested by Wu in 1952[1] by a Taylor-serise expansion of flow parameters in the azimuthal direction as an extension of MSLM[30, 2]. It was improved, numerically elaborated and applied to design by Zhao et al. in Refs.[41, 42], where an annular constraint condition is set up, which must be satisfied to ensure that the hub/casing walls are axisymmetric.

2) Universal Image-Space Approach.

In Ref.[43] Liu developed a universal image-space theory of hybrid problems for fully 3-D potential flow, which is a generalization of the image-plane approach of Ref.[13]. Applying tensor calculus and Stokes theorem, the basic flow equations are transformed into the following integro-differential equation system for the stream functions ψ_1 and ψ_2 in the image space $\xi^1\xi^2\xi^3$ (Fig.14b):

$$\oint_{(C)}\left(g_{ij}V^j+\Lambda_u r\frac{\partial\varphi}{\partial\xi^i}\right)d\xi^i=0 \tag{15}$$

$$\sqrt{g}\,\rho\{V^1,V^2,V^3\}=\left\{\frac{\partial(\psi_1,\psi_2)}{\partial(\xi^2,\xi^3)},\ \frac{\partial(\psi_1,\psi_2)}{\partial(\xi^3,\xi^1)},\ \frac{\partial(\psi_1,\psi_2)}{\partial(\xi^1,\xi^2)}\right\} \tag{16}$$

and Eq.(5), where V^i are the contravariant components of the velocity $\vec{A}$ in a body-fitted

Third International Conference on Inverse Design Concepts and Optimization in Engineering Sciences (ICIDES-III), Editor: G.S. Dulikravich, Washington D.C., October 23-25, 1991.

nonorthogonal curvilinear coordinate system ξ^i(Fig.16a). Similarly, a corresponding potential function formulation by integro-differential equations of this theory has been also presented by Liu et al.[44].

A similar method for solving 3-D hybrid problems was put forth by Chen et al.[45], using, however, a second-order PDE formulation:

$$\frac{\partial}{\partial \xi^i}\left(\sqrt{g}\,\rho g^{ij}\frac{\partial \Phi}{\partial \xi^j}\right)-\frac{\partial}{\partial \xi^2}\left(\sqrt{g/g^{22}}\;\rho \Lambda_u\right)=0 \tag{17}$$

This equation was solved numerically by the method AF2, the multigrid technique and the artificial density in the transonic region. To greatly simplify the numerical solution, the inverse problem is modified in such a way that the physical contravariant velocity components Λ^i(assuming that ξ^1-coordinate is the streamlike line) rather than the fully velocity Λ is prescribed on the blade surface. An axial compressor rotor was redesigned and improved by this method as shown in Figs.15 & 16.

3) Unified Variable-Domain Variational Approach

The variable-domain variational approach[21, 22] has been extended by Liu to hybrid problems for fully 3-D incompressible[46], compressible[47] and transonic[48] flows in rotors. Only one of the VPs is given below for reference:

$$J_2(\Phi, A_b^{**}, A_{2d})=\frac{1}{\kappa}\iiint_{(V)}\left\{1-\frac{1}{2m}\left[(\nabla\Phi)^2-\frac{2\Lambda_u}{r}\frac{\partial\Phi}{\partial\varphi}\right]\right\}^{\kappa m}\cdot dV+L. \tag{18}$$

where the boundary integral term L takes different form for different problem type. Note that the variable-domain variation of J_2 should be taken at the unknown boundaries A_b^{**} (blade surface)and A_{2d} (free trailing vortex sheet). Corresponding numerical solutions to incompressible(H_A×D)-problem of Mizuki's centrifugal compressor[51] and to compressible ([Hc+D]×D)-problem of an axial turbine stator have been obtained by a novel FE with self-adjusting nodes in Refs.[49] and [50] respectively and are shown partly in Figs.17 & 18.

VI. OPTIMIZATION OF AERODYNAMIC DESIGN OF BLADING.

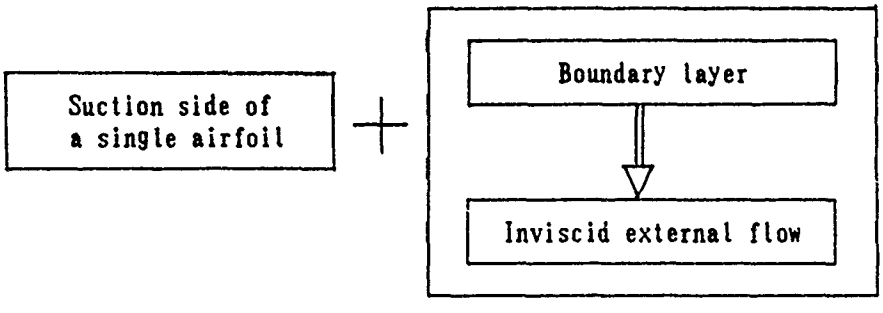
1) Optimization of S_2-Flow.

A basic and very important problem in this context is the optimal flow type(i.e. optimal radial distribution of flow) in bladings. This problem was first studided by a variational method by Liu[52] and later by Xue[53] and Lu[54]. Recently, this problem was treated by an optimal control method by Gu & Miao[55], so that various inequality design constraints can be accounted for.

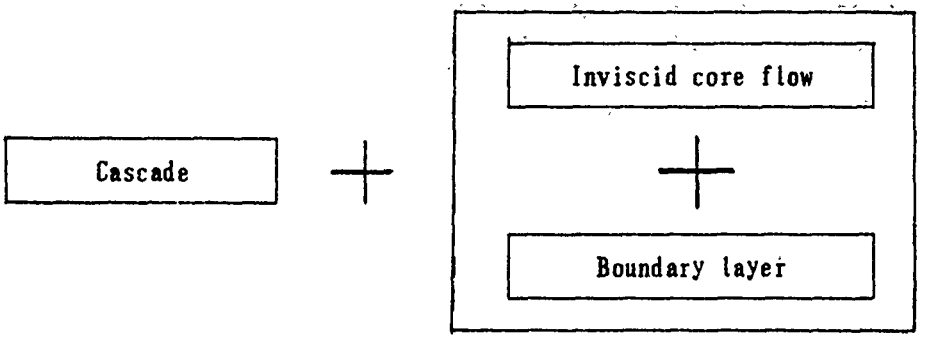
2) Optimization of 2-D Cascades.

Theory of optimization of cascade profile shape can be founded on the basis of one of the following flow models.

i) Simplified model(LeFoll, Citavy)



ii) Refined model (Liu[57-59])



Perhaps, a third, most accurate flow model based on Navier-Stokes equations incorporating some turbulence models should be also tried.

Two possible mathematical models(formulations) can be used here, namely: a) mathematical programing problem, b) optimal control problem.

2-1. Optimization based on the simplified flow model.

The problem of determining the optimal velocity distribution along the suction side was formulated as an optimal control problem with some inequality design constraints (e.g. separation-free, maximum or minimum velocity limit, etc) and solved by a heuristic grapho-analytical method by Liu[56,63]. This approach is followed by Wang[60] in the design of an axial ventilator. Having calculated the optimal velocity distribution along suction side and specified a reasonable airfoil thickness distribution, a Hc-problem was solved by the image-plane method given in Refs. [5,6] to yield the optimal airfoil shape. A similar method, with some modifications, for optimizing 2-D compressor cascade was presented by Hua & Chen[61], where a method for estimating the airfoil circulation was given and the optimal airfoil shape was obtained by MSLM[20,30].

The optimal velocity distribution along the suction side on a general streamsheet of revolution was obtained by Zou[62], using Mager's transformation of turbulent boundary layer.

In Ref. [63] some generalizations of the LeFoll's optimization theory of blades were given by Liu & Wu to accommodate different objective functionals with more general constraints.

2-2. Optimization based on refined model.

In Refs. [57,59] Liu suggested a new theory of optimal 2-D cascades based on the above-mentioned refined flow model, in which this problem has been formulated as an optimal control problem with multiple inequality design constraints on control-and phase-spaces. Two typical optimal control problems were considered: cascade with minimal losses and cascade with maximal loading (circulation), and a duality theorm between them has been proved theoretically, so that it is sufficient to study only the cascade with minimal losses. This theory has been generalized to 2-D compressible flow and to a 3-D axial-flow rotor by Liu[58]. The essential feature of this theory lies in its capability of handling a wide variety of practical design constraints(from stress, vibrational, cooling and technological considerations) in a unified manner so as to make the optimal solution surely feasible and suitable for use in practice.

2-3. Local optimization of transonic cascades

Jiang et al. suggested a numerical method for weakening shocks in transonic cascades by local optimization of airfoil shape[64]. The airfoil contour segment near the shock is represented by a cubic parabola with free coefficients a_1, a_2, a_3, a_4. Then the Mach number just before the shock Ms is minimized with respect to a_i.

3) Optimal Design of Diffusers.

The optimal design of 2-D diffusers was considered by Gu & Ji[66] using optimal

Third International Conference on Inverse Design Concepts and Optimization in Engineering Sciences (ICIDES-III), Editor: G.S. Dulikravich, Washington D.C., October 23-25, 1991.

control for searching optimal wall shape that maximizes the pressure recovery of diffuser. A more general optimization problem of diffuser was put forth by Liu et al. in Ref. [65], where not only the wall shape but also the wall suction distribution that maximize the pressure recovery without boundary layer separation are sought by optimal control method.

An 1-D optimal design method for turbine annular axial-radial exhaust diffuser was presented by Ling & Jin[67] based on an approximate loss model. The pressure recovery coefficient of an optimal diffuser designed in this way has been shown higher than the conventional one by 7% by expriment.

4) Other Optimization Problems.

Making use of the Parson's number and the concept of optimal reaction degree, Yao presented a method for optimizing aerothermodynamic parameters in one-and multi-stage steam turbine design. Some guidelines for optimal design of long twisted blades are given.

In Ref. [69], based on the diffusion factor and equivalent diffusion ratio, the optimal solidity problem of 2-D compressor cascades is formulated by Liu as nonlinear programing problems, whose analytical solution in form of simple formulae is very convenient for practical use.

A simple approximate method for determining the optimal relative azimuthal position of two blade rows in tandem cascades is suggested by Wu & Feng[70] using a simple total pressure loss model.

VII. MISCELLANEOUS INVERSE, HYBRID & OPTIMIZATION PROBLEMS IN ENGINEERING SCIENCES

In Ref. [71] the finite element method is generalized by Liu & Zhao via variable-domain variations in such a way that the nodes are movable. It allows both optimal grid and flow field to be cogenrated simultaneously and naturally using directly the VPs of aerodynamic problems.

The inverse problem of heat conduction with unknown boundary was handled by Liu & Zhang[72] using Ritz's and FEM based on Variable-domain VPs. An alternative method for solving this problem was suggested by Liu[73] by introducing an image plane $T\psi'$ (T and ψ' stand for transformed temperature and heat stream function respectively). An interesting invariance property of the nonlinear inverse problem solution with respect to variable conductivity is pointed out. An example is solved by FEM based on a pair of complementary extremum principles.

The inverse and hybrid problems of free surface flow under gravity over a dam are posed and handled by Liu via VPs in an image-plane $\xi\psi$ [74] and VPs with variable domain in the physical plane [75, 76].

In Ref. [77] Liu suggested a novel problem in gear theory---optimal meshing(i.e. optimal tooth profile) of spur gears and its variational theory. An analytical solution to the optimal meshing with minimal friction losses has been obtained and it has been revealed that the cycloidal gearing with radial tooth profile on the lower half tooth height used widely in watches and clocks can be regarded approximately as a practical gearing with maximal efficiency.

VIII. CONCLUDING REMARKS

Research on inverse, hybrid and optimization problems is of great theoretical as well as practical importance in engineering sciences. To our experiences, the three new approaches(image-space approach and VP-based approach, especially its variable-domain variational variat, for inverse and hybrid problems; optimization approach based on optimal control) suggested and intensively developed in China in the last two decades have proved to be efficient tools for inverse design and optimization not only in turbomachinery aerodynamics in particular but also in engineering sciences in general and deserve further development and application to practice. Design engineers and industry will surely benefit a lot from them, if a complete set of computer codes based on these

approaches can be finished and organized into a computerized automated interactive design system(something like that of Ref. [81].

REFERENCES

[1] Wu, Chung-Hua, A general theory of 3-D flow in subsonic and supersonic turbomachines of axial-, radial- and mixed-flow types, NACA TN 2604(1952)
[2] Cai, R., A summary of developments of the mean-streamline method in China, ASME J. Engrg for GT & Power, 106(1984) pp.300-305
[3] Cai, R., An engineering method for solving axial flow cascade inverse problem, ASME paper 87-GT-147(1987)
[4] Wang, Zhengming, A method for aerodynamic design of blades in quasi-3D calculation of turbomachines, ASME J. of Turbomachinery, 110, (1988) pp.181-186
[5] Liu, Gao-Lian, A universal computer method for solving inverse cascade flow problem with prescribed velocity distribution (in Chinese), Research Report, Institute of Mechanics of Chinese Academy of Sciences, Beijing, China, 1964.
[6] Liu, Gao-Lian & Tao, Cheng, A universal image-plane method for inverse & hybrid problems of compressible cascade flow on arbitrary streamsheet of revolution: Part I--Theory, Numerical Methods in Laminar & Turbulent Flow, Vol. 6, C. Taylor et al. (ed.), Pineridge Press, U.K., 1989, pp. 1343-1354. (or: Power Engrg (China), No. 2 (1981) pp. 20-29).
[7] Chen, Kang-min et al., A universal image-plane method for inverse and hybrid problems of compressible cascade flow on arbitrary streamsheet of revolution: Part II--Num. Solution. ibid, pp.1355-1366.
[8] Liu, Gao-Lian & Zhang, Dao-Fang, The moment function formulation of inverse & hybrid problems for blade-to-blade compressible viscous flow along axisymmetric streamsheet. Numerical Methods in Laminar & Turbulent Flow, Vol.6, C.Taylor et al.(ed.) Pineridge Press, U.K., 1989.pp.1289-1300. (or:Liu, Gao-Lian, Chinese J. of Engrg Thermophys. 3 (1982) pp.138-144 (in Chinese))
[9] Shen, M.Y. & Ma, Y.L., Direct-inverse problem of 2-D cascades in transonic flow (in Chinese), Acta Mechanica Sinica, 15, 1 (1983) pp.1-6.
[10] Chen, Naixing, Zhang Fengxian, A generalized numerical method for solving direct, inverse and hybrid problems of blade cascade flow by using streamline-coordinate equation, ASME Paper 87-GT-29(1987).
[11] Sun, X.Y. et al., A unified method for solving aerodynamic cascade design problems on an arbitrary surface of revolution, ASME Paper 88-GT-118(1988)
[12] Ge, Manchu.et al., A method for solving transonic S_1-Stream surface with a stream function equation(in Chinese), Chinese J. Engrg Thermophys. 8(1987) pp.31-38.
[13] Liu, Gao-Lian, A new approach to some hybrid aerodynamic problems of airfoil cascades on a general streamsheet of revolution(in Chinese), Chinese J.Engrg Thermophysics. 5. 1(1984) pp.27-32.
[14] Chen, Naixing & Li Weihong, A new method for solving aerodynamic hybrid problem of profile cascade on S stream surface of revolution by employing stream function equation expressed with non-orthogonal coordinate system. Int'l J. Num. Methods in Engrg, 22, (1986) pp.456-479.
[15] Chen, Naixing et al., A inverse problem solution method for the blade cascade flow on streamsurface of revolution, ASME Paper 86-GT-159(1986)
[16] Ge, Manchu et al., A method for solving subsonic and transonic viscous inverse problem of cascade with stream function equations(in Chinese), Chinese J. Engrg Thermophys, 8(1987) pp.243-245.
[17] Liu, Gao-Lian, A systematic approach to the search and transformation for VPs in fluid mechanics with emphasis on inverse and hybrid problems, Chinese J. Engrg Thermophysics (English ed.) 2, 4(1990), Allerton Press, New York.
[18] Liu, Gao-Lian, VPs and generalized VPs for the hybrid aerodynamic problem of airfoil

cascade on an arbitrary streamsheet of revolution: Part(I), Scientia Sinica, 23, 10 (1980) pp. 1339-1347; Part(II), Chinese J. of Engrg Thermophysics, 2, 4(1981) pp.335-342.

[19] Liu, Gao-Lian & Yao, Zheng., VPs & Generalized VPs for the hybrid aerodynamic problem of airfoil cascades on an arbitrary stream sheet of revolution: Part(III), Proc. 6th Int'l Symp. FEM in flow Problems, Antibes, France, June 1986, pp.137-142.

[20] Yao, Zheng et al., Variational FE calculation for hybrid aerodynamic problem of cascades on an arbitrary streamsheet of revolution, Comput'l Methods in Turbomachinery, IMechE, 1984, U.K. pp.237-245.

[21] Liu, Gao-Lian, VP families for hybrid problems of blade-to-blade flow along axisymmetric streamsheet: A unified variable-domain approach(in Chinese), Acta Aerodynamica Sinica, 3, 3(1985) pp.24-32.

[22] Liu, Gao-Lian & Yan, Shan, A unified variable-domain variational approach to hybrid problems of compressible blade-to-blade flow, ASME Paper 91-GT-169(1991)

[23] Yan, Shan & Liu, Gao-Lian, Variational FEM with variable domain for solving type 'A' hybrid problem of blade-to-blade compressible flow along an arbitrary streamsheet of revolution, Exper'l & Comput'l Aerothermodynamics of Internal Flow (Proc. 1st Int'l Symp., N.X.Chen & H.D.Jiang (ed.) World publ. Corp., Beijing, China, pp.457-463

[24] Liu, Gao-Lian, VPs for hybrid problems of transonic cascade flow along axisymmetric streamsheet: A unified variable-domain approach. Proc. 4th Int'l Symp. on Refined Flow Modeling and Turbulence Measurements, Sept. 1990, Wuhan, pp. 175-181.

[25] Liu, Gao-Lian, A variable-domain variational theory using Clebsch variables for hybrid problems of 2-D transonic rotational flow: Pt I ---Planar Channel design. Proc.Int'l Conf. on Fluid Mechanics, July 1977, Beijing, China, pp. 314-319.

[26] Wang, Zhengming, Inverse design calculations for transonic cascades, ASME Paper 85-GT-6 (1985)

[27] Wang, Zhengming, A numerical method for solving the inverse problem of cascade viscous flow, Proc. 1st ISAIF, July, 1990, Beijing, China, pp.482-488.

[28] Wang, Zhengming et al., An improved method for aerodynamic design of centrifugal impeller blades, ASME Paper 91-GT-76 (1991)

[29] Wang, Zhengming et al., A quasi-3D design method of transonic compressor blades with the function of improving velocity distribution. ISABE Paper 89-7089, the 9th Int'l Symp. on Air-Breathing Engines(1989).

[30] Wu, Chung-hua & Brown, C.A., A theory of the direct and inverse problems of compressible flow past cascade of arbitrary airfoils, J.A.S., 19, 3(1952).

[31] Zhou, Xinhai & Zhu Fangyuan, Finite volume method to solve the inverse problem for transonic flow in cascades(in Chinese), Chinese J. Engrg Thermophys., 6, 4 (1985) pp. 331-335.

[32] Chen, Zuoyi, The hodograph method for design of transonic turbine cascade in revolutionary surface(in Chinese), Chinese J. Engrg Thermophys. 3, 4 (1982) pp.353-356.

[33] Yao, Zheng, A hodograph-based FEM for 2-D transonic cascades and its generalization to cascades on arbitrary streamsheet of revolution (in Chinese). Master Thesis, Shanghai Inst. of Mech. Engrg, 1982.

[34] Liu, Gao-Lian, VPs and generalized VPs for semi-inverse problem of compressible flow along S2-stream surface in axial-flow Turbomachinery, J. Shanghai Institute of Mechanical Engrg, 3, 1 (1981)pp.1-14.

[35] Qin, Ren, et al., A new variational FE computation for the aerodynamic inverse problem in turbines with long blades, ASME J. Turbomachinery, 110, 4 (1988) pp.545-548.

[36] Liu, Gao-Lian, A unified variable-domain variational theory of hybrid problems for compressible S -flow in mixed-flow turbomachinery, Proc. 1987 Tokyo Int'l Gas Turbine Congress, Oct. 1987, Japan, Vol.II, pp. 259-264.(Paper 87-Tokyo-IGTC-34).

[37] Cai, Rong-Qian & Liu, Gao-Lian, Families of VPs for inverse & H hybrid problems of an S2 streamsheet in mixed-flow turbomachines, Int'l J.Heat and Fluid Flow, 9, 3(1988) pp.302-307.

[38] Xu, Hong-Yi, Families of VPs for semi-inverse and H hybrid problems on a S2-

streamsheet for fluids of pure substance (in Chinese). Acta Aerodynamics Sinica, 8, 1 (1990) pp.98-103.

[39] Tao, Cheng & Liu, Gao-Lian, VPs for hybrid problem of axisymmetric compressible channel flow using an image plane, Proc. 3rd Japan-China Joint Conf. on Fluid Machinery, April 1990, Osaka, Japan.

[40] Ge, Manchu et al., A new approach to the calculation of S2 stream surface with full inverse and hybrid methods for turbomachine. ASME Paper 88-GT-262(1988).

[41] Zhao, Xiao-lu et al., A simple method for solving 3-D inverse problems of turbomachine flow and the annular constraint condition, ASME J. of Engrg for Power, 107 (1985) pp.293-300.

[42] Zhao, Xiao-lu, Qin Li-Sen, An approximate 3-D aerodynamic design method for centrifugal impeller blades, ASME Paper 89-GT-73(1989).

[43] Liu, Gao-Lian, A general image-space theory of hybrid problems for fully 3-D compressible flow in turbo-rotors:(I) stream-function formulation, Comput'l Methods in Flow Analysis (Proc. of Int'l Conf., Okayama, Japan, Sept. 1988), H.Niki and M. Kawahara (ed.), Okayama univ. of Science, pp. 936-942. (or: Chinese J. Engrg Thermophysics, 6, 1(1985) pp.40-45)

[44] Liu, Gao-Lian et al., Ditto, Part (II) Axial-flow, potential function formulation(in Chinese), Chinese J.Engrg Thermophys., 9, 4(1988) pp. 331-333.

[45] Chen, Naixing et al., A numerical method for solving aerodynamic hybrid problem of fully 3-D flow in turbomachinery, Proc. 1st Int'l Symp. on Exper'l & Comput'l Aerothermodynamics of Internal Flows, July 1990, Beijing, China, pp. 441-448.

[46] Liu, Gao-Lian, A unified theory of hybrid problems for fully 3-D incompressible rotor flow based on VPs with variable domain, ASME J. Engrg for GT & Power, 108, 2(1986) pp.254-258.

[47] Liu, Gao-Lian, A variational theory of hybrid problems for fully 3-D compressible rotor-flow: A unified variable-domain approach, Comput'l Fluid Dynamics, G. d. V. Davis & C. Fletcher, (ed.), North-Holland, 1988, pp.473-480.

[48] Liu, Gao-Lian, Variational formulation of hybrid problems for fully 3-D transonic flow with shocks in rotor, Proc.3rd Int'l Conf. on Inverse Design Concepts and Optimization in Engrg Sciences, Oct.1991, Washington, D.C., USA.

[49] Yan, Shan & Liu, Gao-Lian, Variational FEM with variable domain for solving hybrid problems of 3-D incompressible rotor flow, Exper'l & Comput'l Aerothermodynamics of Internal Flow(Proc. 1st Int'l Symp.), Chen, N.X.& Jiang, H.D.(ed.), World Publ. Corp., Beijing, China, 1990, pp.449-456.

[50] Yan, Shan and Liu, Gao-Lian, Variable-domain FEM based on VPs for solving hybrid problems of fully 3-D compressible rotor-flow, Proc. 1991 Yokohama Int'l Gas Turbine Congress, Sept. 1991, Japan.

[51] Mizuki, S. et al., Investigation concerning the blade loading of centrifugal impeller, ASME Paper 74-GT-143(1974)

[52] Liu, Gao-Lian, On the optimal type of flow pattern in turbomachinery (in Chinese), Research Note, Institute of Mechanics of Chinese Academy of Sciences, Beijing, China, 1963.

[53] Xue, Ming-lun, Optimum aerodynamic design problem of axial turbomachines(in Chinese), Research Report, Institute of Mechanics of Chinese Academy of Sciences, Beijing, China, 1975.

[54] Lu, Wen-can, The theory and experiment of optimum flow distribution for low pressure axial fans, Proc. 2nd China-Japan Joint Conf. on Fluid Machinery, Oct. 1987, Xi'an China, pp.481-489.

[55] Gu, Chuan-Gong & Miao, Yong-Miao, Blade design of axial-flow compressors by the method of optimal control theory, ASME Pap. 86-GT-182, 86-GT-183(1986)

[56] Liu, Gao-Lian & Wang, Jiasheng, Fundamentals of Aerodynamic Theory of Turbomachinery (in Chinese), Machinery Press, Beijing, China, 1980.

[57] Liu, Gao-Lian, A new theory of 2-D cascades optimized aerodynamically via a generalized maximum principle: Pt(I) & Pt(II) (in Chinese), Acta Mechanica Sinica,

12, 4(1980) pp.337-346; 14, 2(1982) pp.122-128.

[58] Liu, Gao-Lian, Aerodynamic optimization theory of a 3-D axial-flow rotor-blading via optimal control. Proc. 6th Int'l Symp. on Air-Breathing Engines, June 1983, Paris, pp. 313-318 (AIAA Paper 83-7037)

[59] Liu, Gao-Lian, Aerodynamic theory of 2-D cascades optimized via optimal control, Numerical Methods in Laminar and Turbulent Flow, Vol.5, C.Taylor et al.(ed.), Pineridge Press, U.K. 1987. pp.1739-1749.

[60] Wang, Xue-Jin, Optimal design method for cascades in an axial ventilator(in Chinese), Master Thesis, North-East University of Technology, China, 1983.

[61] Hua, Yaonan & Chen Naixing, Optimization of the plane compressor blade aerodynamic design, Proc. 6th Int'l Symp. on Air-Breathing Engines, June 1983, Paris, pp.487-495.

[62] Zou, Zi-xiong, Method of calculation of optimal velocity distribution on arbitrary streamsurface of revolution for compressible flow in cascades of turbomachinery. Chinese J. Engrg Thermophysics, 1, 4(1980) pp.341-347.

[63] Wu, Bao-ren & Liu, Gao-Lian, Progress in aerodynamic optimization theory of turbomachine blading(in Chinese), Advances in Mechanics, 14, 2(1984) pp.161-174.

[64] Jiang, H.X. et al., A numerical method to weaken shocks in transonic cascades. Proc. 1983 Tokyo Int'l Gas Turbine Congress, Japan.

[65] Liu, Gao-Lian et al., Theory of optimum design of 2-D diffusers with optimal boundary layer control, Proc.6th Int'l Symp. FEM in Flow Problems, Antibes, France, June, 1986, pp.39-43.

[66] Gu, Chuan-gang, Ji Yong-ming, Theoretical analysis of the optimal shape for 2-D diffuser with incompressible flow. Proc. 2nd China-Japan Joint Conf. on Fluid Machinery, Oct. 1987, Xi'an, China, pp.416-422.

[67] Ling, Zhiguang & Jin Juanqian, Design optimization of turbine annular axial-radial exhaust diffuser and experimental verification(in Chinese), Chinese J. Engrg Thermophys., 6, 3 (1985) pp.245-248.

[68] Yao, F.S, Method of calculating optimal parameters of through-flow components in stream turbines(in Chinese), Chinese J. Mech. Engrg, (1979) No.2

[69] Liu, Gao-Lian, Simple formulae for optimal solidity of 2-D compressor cascades based on diffusion concept. ASME Paper 91-GT-308 (1991)

[70] Wu, GuoChuan & Feng, Qi, Optimization of the arrangement of the front & rear blade rows of a tandem blade cascade, Paper 87-Tokyo-IGTC-19(1987)

[71] Liu, Gao-Lian & Zhao, Yi-Hua, Generalized FEM via variable-domain variations: Cogeneration of optimal grid and flow field, Proc. 4th National Conf. on Fluid Mechanics, April 1989, Beijing, China.

[72] Liu, Gao-Lian & Zhang, Dao-Fang, Numerical methods for solving inverse problem of heat conduction with unknown boundary based on VPs with variable domain, Num.Methods in Thermal Problems, Vol. 5, R.W.Lewis et al.(ed.), Pineridge Press, U.K., 1987.

[73] Liu, Gao-Lian, A Novel variational formulation of inverse problem of heat conduction with free boundary on an image plane, Num. Methods in Thermal Problems, Vol.6, R.W. Lewis et al.(ed.), Pineridge press, U.K., 1989, pp.1712-1720.

[74] Liu, Gao-Lian, New VP families for direct, inverse and hybrid problems of free surface gravity flow over a spillway. Turbulence Measurements & Flow Modeling, C.J. Chen et al.(ed.), Hemisphere, Washington, 1987. pp.323-332.

[75] Liu, Gao-Lian, The hybrid problem of free-surface gravity spillway flow treated by VPs with variable domain: (I) Potential function formulation, Proc. 3rd Int'l Symp. Refined Flow Modeling & Turbulence Measurements, July 1988, Tokyo, Japan.

[76] Liu Gao-Lian, The hybrid problem of free-surface gravity spillway flow treated by VPs with variable domain: (II) Stream function formulation, Proc. 7th Int'l Conf. on FEM in FLow Problem, 1989, Alabama, USA.

[77] Liu, Gao-Lian, A variational theory of optimal meshing of spur gears (in Chinese), J.of Shanghai Institute of Mech. Engrg, 2, 2(1980) pp.25-42

[78] Wilkinson, D.H., Calculation of Blade-to-Blade flow in a turbomachinery by streamline curvature, ARC RM 3704 (1970)

Third International Conference on Inverse Design Concepts and Optimization in Engineering Sciences (ICIDES-III), Editor: G.S. Dulikravich, Washington D.C., October 23-25, 1991.

[79] Wu, Chung-Hua, 3-D turbomachine flow equations expressed with respect to nonorthogonal curvilinear coordinates and methods of solution, Proc, Third Int'l Symp. on Air-Breathing Engines, München, Germany, (1976) pp. 233-252.

[80] Hefez, M., Lovell, D., Numerical solution of transonic stream function equation, AIAA-J., 21 (1983) pp.327-335.

[81] Thomas, K.M. & Piendel, J.J., An automated interactive design system for advanced gas turbines, ASME, Paper 74-GT-82(1974).

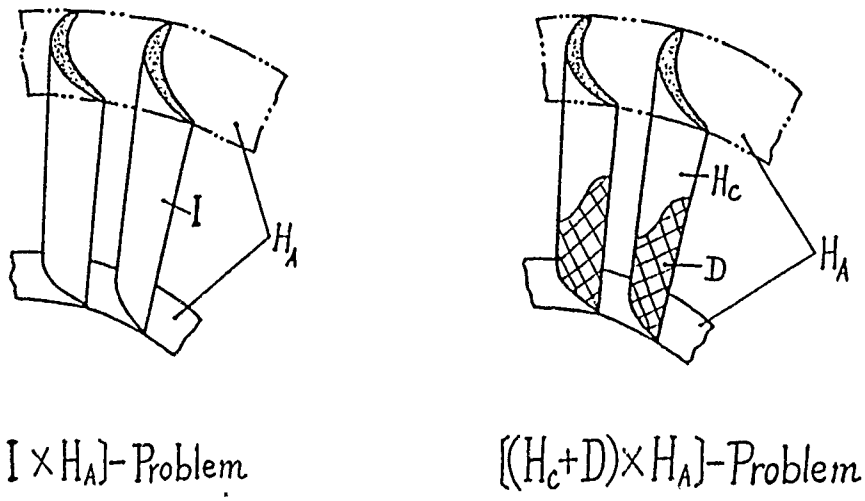
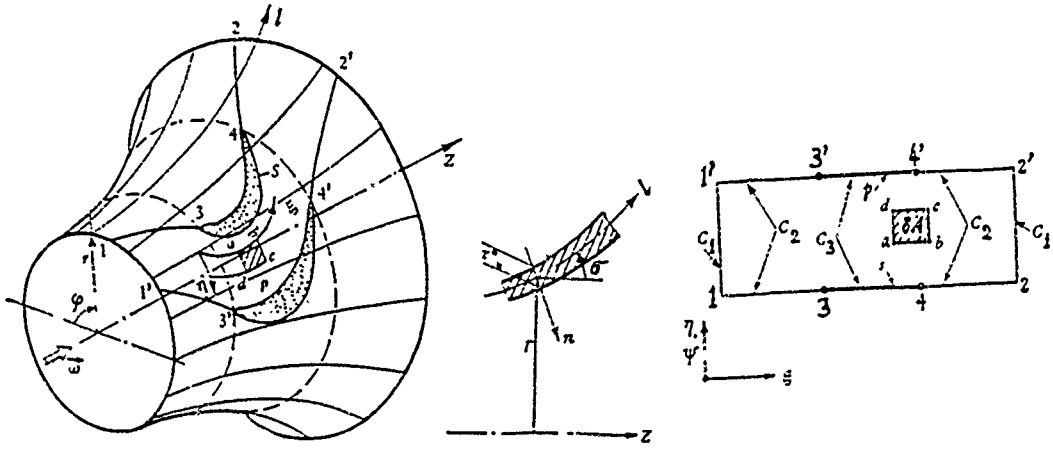


Fig.1 Definition of Symbols for fully 3-D hybrid problems



a) physical stream surface b) image-plane $\xi\psi$ (or $\xi\eta$)

Fig.2 Cascade flow and its image plane

Third International Conference on Inverse Design Concepts and Optimization in Engineering Sciences (ICIDES-III), Editor: G.S. Dulikravich, Washington D.C., October 23-25, 1991.

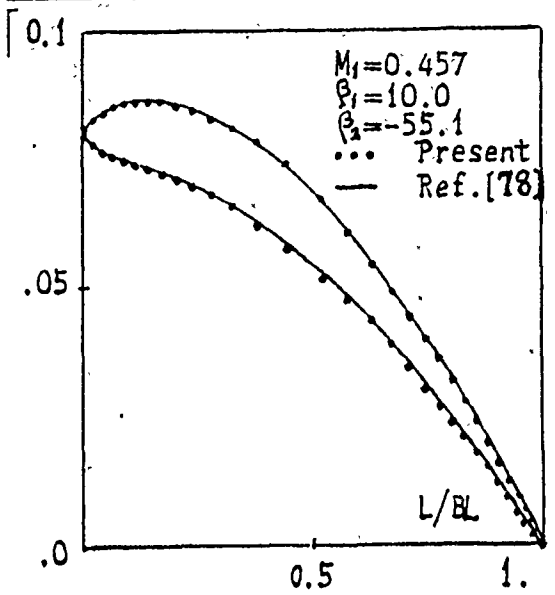


Fig.3 Image-plane solution by moment function

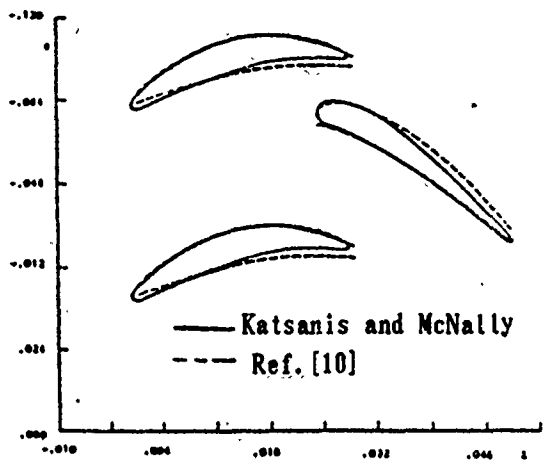


Fig.4 Tandem cascade profiles by an inverse solution

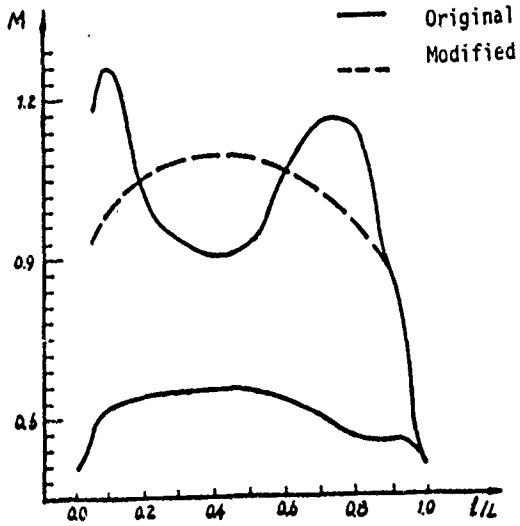


Fig.5 Modified distribution of Mach number

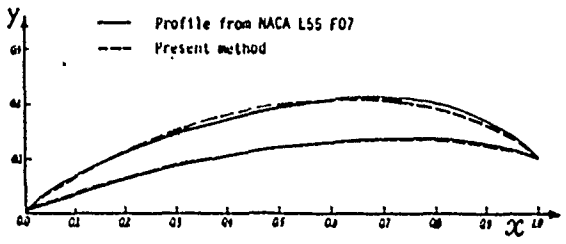


Fig.6 Comparison of profiles corresponding to Fig.5

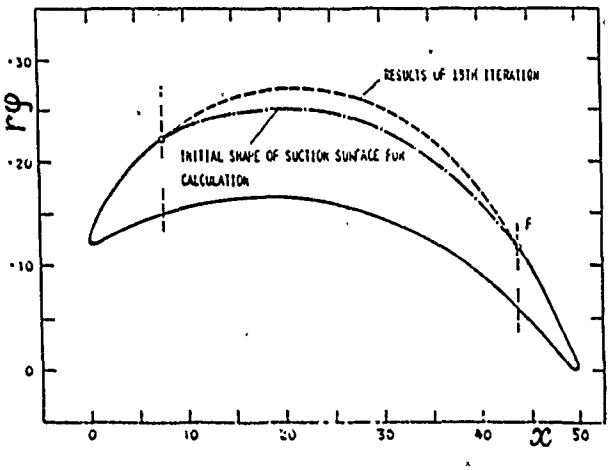


Fig.7 Cascade profile obtained by H_A-problem solution

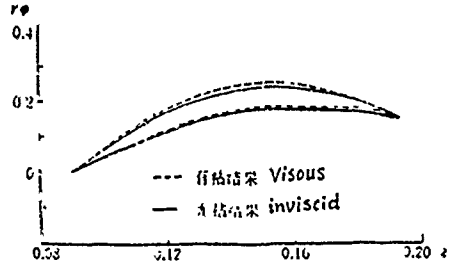


Fig.8 Viscous effect on airfoil shape

Third International Conference on Inverse Design Concepts and Optimization in Engineering Sciences (ICIDES-III), Editor: G.S. Dulikravich, Washington D.C., October 23-25, 1991.

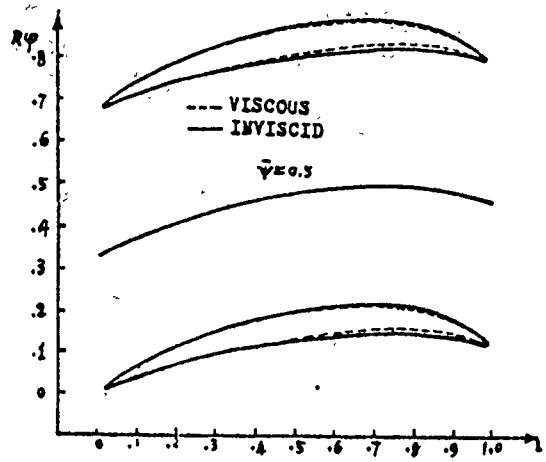


Fig.9 Viscous effect on airfoil shape

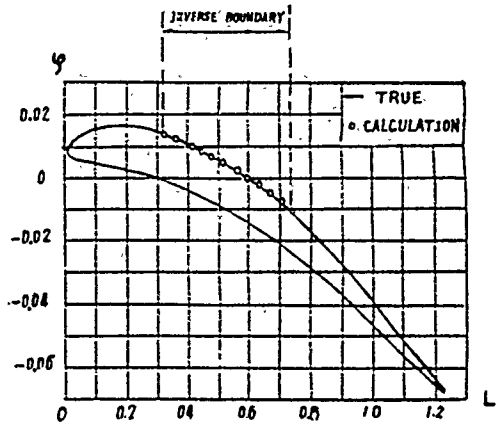
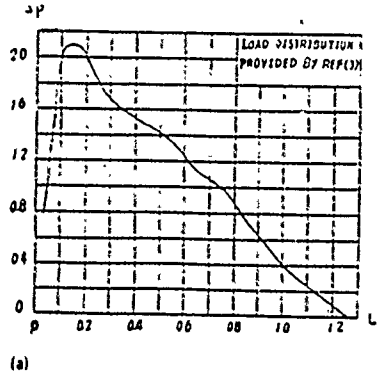
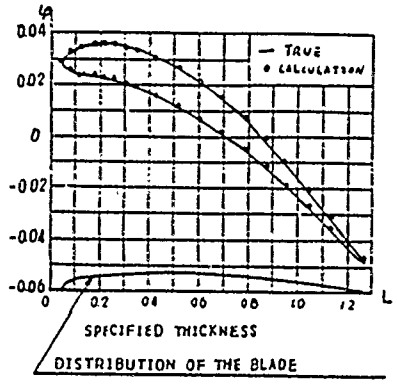


Fig.10 FE solution of H_A-problem



(a)



(b)

Fig.11 FE solution of H_B-problem

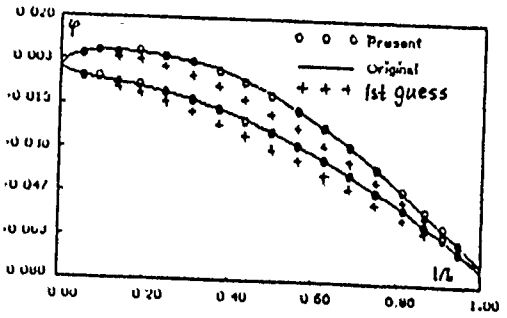


Fig.12 Airfoil shape by FE solution of a H_C-problem

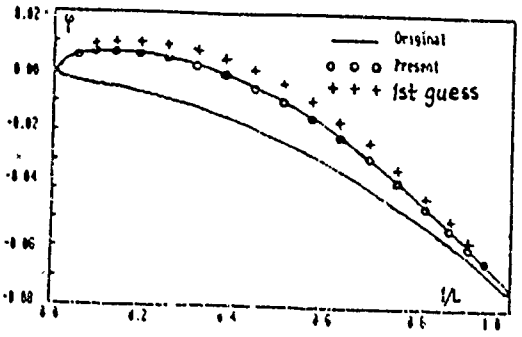
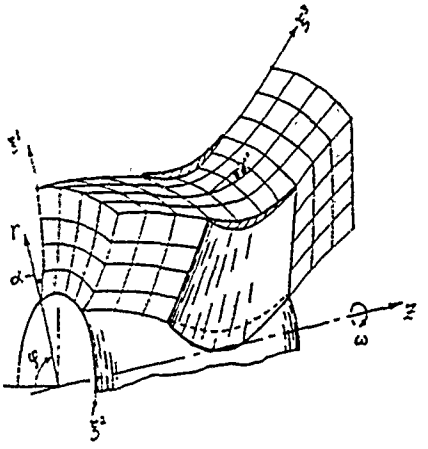
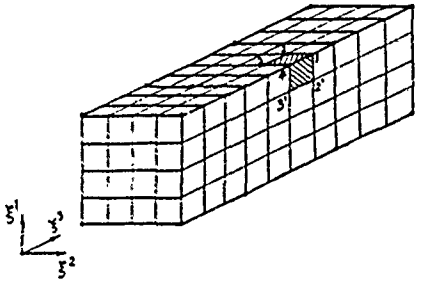


Fig.13 Airfoil shape by FE solution of a H_A-problem

Third International Conference on Inverse Design Concepts and Optimization in Engineering Sciences (ICIDES-III). Editor: G.S. Dulikravich, Washington D.C., October 23-25, 1991.

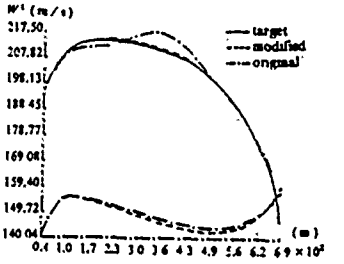


a) Physical space

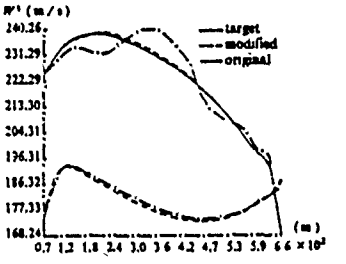


b) Image space

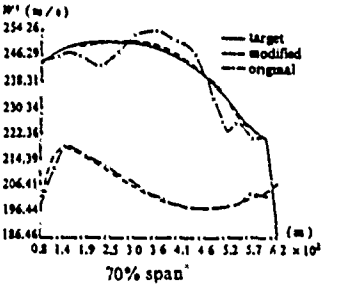
Fig.14 3-D rotor flow and its image space



20% span

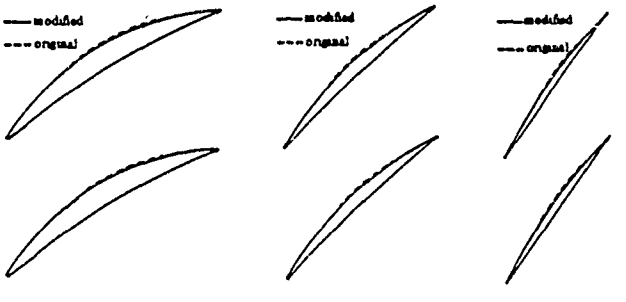


50% span



70% span

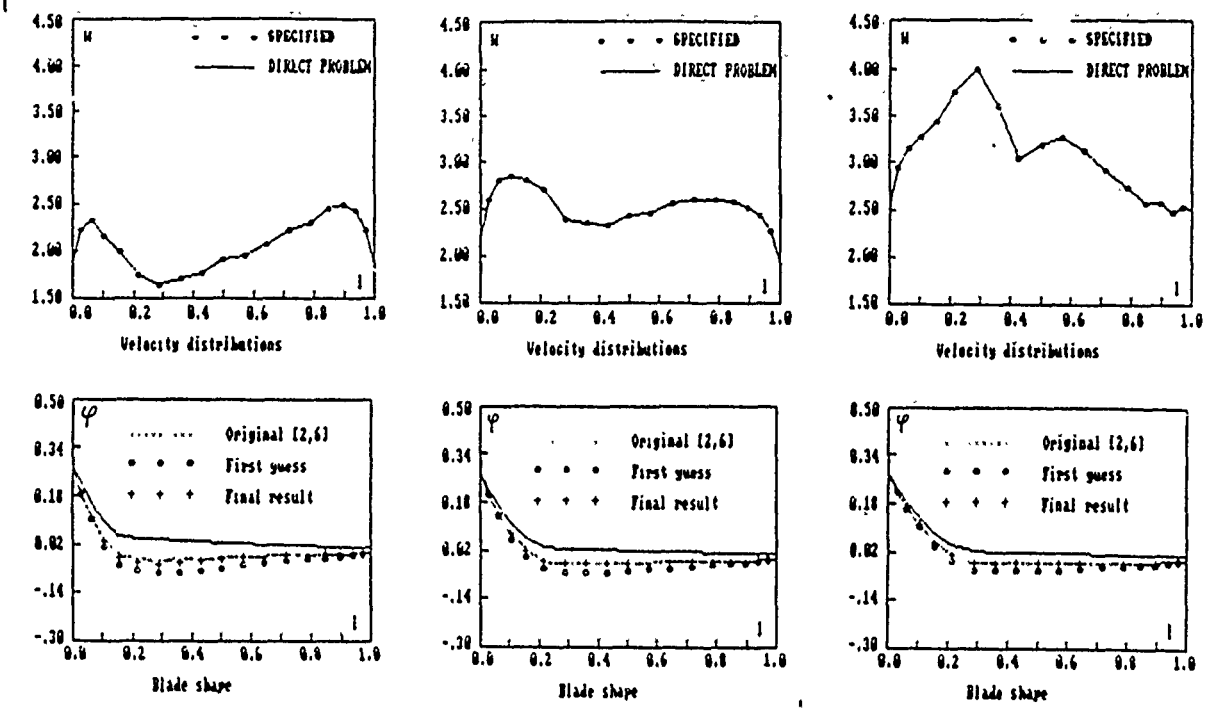
Fig.15 Distribution of A^1 over blade surface



20% span 40% span 70% span

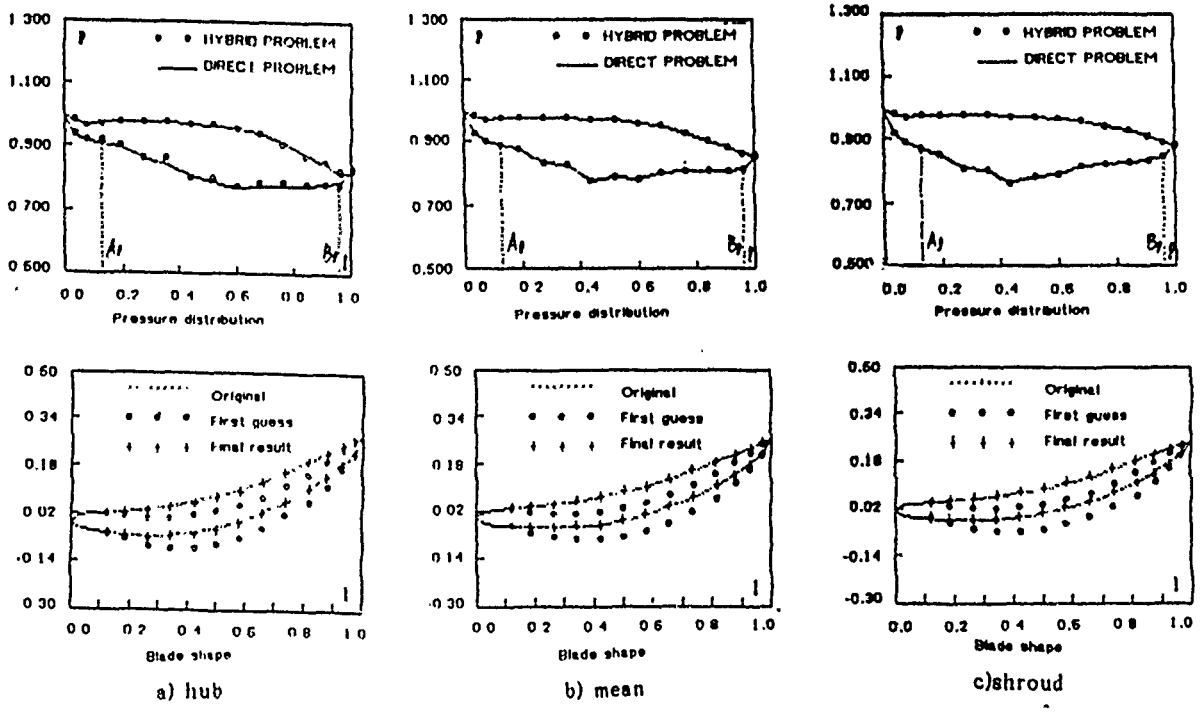
Fig.16 The shape of the blade after and before the modification

Third International Conference on Inverse Design Concepts and Optimization in Engineering Sciences
(ICIDES-III), Editor: G.S. Dulikravich, Washington D.C., October 23-25, 1991.



(a) hub (b) mean (c) shroud

Fig.17 FE solution of (H_A×D)-problem of a centrifugal compressor



a) hub b) mean c)shroud

Fig.18 FE solution of [(H_C+D)×D]-problem of an axial turbine stator

Third International Conference on Inverse Design Concepts and Optimization in Engineering Sciences (ICIDES-III), Editor: G.S. Dulikravich, Washington D.C., October 23-25, 1991.

THE TURBOMACHINE BLADING DESIGN USING $S2$-$S1$ APPROACH

T. S. LUU*, Dr., Senior Researcher
L. BENCHERIF*, Graduate student
B. VINEY*, Dr., Engineer
J.M. NGUYEN DUC**, Engineer

*LIMSI (CNRS), BP 133
F 91403 ORSAY CEDEX, FRANCE

**SEP, BP 802
F 27207 VERNON, FRANCE

SUMMARY

The boundary conditions corresponding to the design problem when the blades being simulated by the bound vorticity distribution are presented. The 3D flow is analyzed by the two steps $S2 - S1$ approach. In the first step, the number of blades is supposed to be infinite, the vortex distribution is transformed into an axisymmetric one, so that the flow field can be analyzed in a meridional plane. The thickness distribution of the blade producing the flow channel striction is taken into account by the modification of metric tensor in the continuity equation. Using the meridional stream function to define the flow field, the mass conservation is satisfied automatically. The governing equation is deduced from the relation between the azimuthal component of the vorticity and the meridional velocity. The value of the azimuthal component of the vorticity is provided by the hub to shroud equilibrium condition. This step leads to the determination of the axisymmetric stream sheets as well as the approximate camber surface of the blade. In the second step, the finite number of blades is taken into account, the inverse problem corresponding to the blade to blade flow confined in each stream sheet is analyzed. The momentum equation implies that the free vortex of the absolute velocity must be tangential to the stream sheet. The governing equation for the blade to blade flow stream function is deduced from this condition. At the beginning, the upper and the lower surfaces of the blades are created from the camber surface obtained from the first step with the assigned thickness distribution. The bound vorticity distribution and the penetrating flux conservation applied on the presumed blade surface constitute the boundary conditions of the inverse problem. The detection of this flux leads to the rectification of the geometry of the blades.

NOMENCLATURE

Γ	circulation
V_o	upstream velocity
h	pitch of the cascade
α	inlet angle
β	outlet angle
ϕ	potential function
ψ	stream function
$f(x)$, $f(m,\psi)$	bound vortex distribution function, or loading function
dl	tangential displacement
ϑ	camber line inclination angle with respect to the meridional plane
x, y	Cartesian coordinates
z, θ, r	cylindrical coordinates
ξ^1, ξ^2, ξ^3	body fitted curvilinear coordinates
g	determinant of the metric tensor
g_{ij}	metric tensor elements
N_b	number of blades in the rotor or stator
$r\delta\theta_e$	thickness of the blade measured in the azimuthal direction
$\tilde{g}_{22}$	modified g_{22} simulating flow channel striction
$\tilde{g}$	determinant of the modified metric tensor (flow channel striction)
ρ	density
U^1, U^2, U^3	contraviant components of the absolute or relative velocity
$\vec{V}$	absolute velocity
$\vec{W}$	relative velocity
V_θ	azimuthal component of the absolute velocity
m	meridional streamwise curvilinear abscissa

$\vec{\omega}$	angular velocity of the rotor
p	pressure
p_t	total pressure
H	stagnation enthalpy or p_t/ρ
I	rothalpy or $H+\omega(V_\theta)$
$\vec{F}_b$	blade force
$\vec{F}_d$	dissipative force
η	efficiency
x^1, x^2	transformed coordinates system in S1 approach
Subscripts	
le	leading edge
te	trailing edge
o	reference
t	tangentiel component
n	normal component
i,k	nodal point indices
Superscripts	
$+$	upper side of the blade
$-$	lower side of the blade

1. INTRODUCTION.

Most of the blading design procedures consider the velocity distribution on both sides of the blade as the initial data, the inverse problem becomes ill-posed and the designer loses the control of thickness distribution of the blade. To overcome this deficiency, this paper suggests an inverse method by representing the blades by a distribution of bound and free vortices which produce the desired swirl ($V_\theta r$) variation. By introduction of the notion of associated elements on both sides of the blade in respect of the thickness distribution, and by imposing a conservative flux penetration through each pair of the associated elements when the geometry of the blade is not yet well defined, we obtain the well-posedness of the inverse problem. The iterative rectification of the camber surface in order to cancel the flow penetration leads to the final geometry of the blade. Treating first the 2D cascade design, §2 is devoted to show how to get the well posed inverse problem with the appropriate boundary conditions applied on the presumed blade contour, and the procedure leading to the rectification of the camber line related to the penetrating flux of the fluid determined on both sides of the blade. To treat the quasi 3D design, the S2 and S1 approach as proposed by C.H. Wu [1] is adopted. The loading produced by the velocity difference between the two faces of the blade is directly related to the bound vorticity distribution that the blade has to generate. Assuming the number of blades infinite, the vortex distribution as well as the flow field become axisymmetric (S2 flow), §3 shows how the blade thickness distribution and the loading distribution can be taken into account in this scheme, and how to deduce the pressure distribution on the blades when their number is finite. An application to the case of the centrifugal impeller is presented. The loss scheme by the introduction of a plausible value of efficiency η for each streamline as suggested by J.H. Horlock [2] is used. This approach opens up possibilities for the elaboration of a design which maintains the assigned value of the total pressure gain in each stage by modifying the ($V_\theta r$) distribution in free space between blade rows. §4 is devoted to the blade to blade flow (S1) inverse problem, the boundary conditions for 2D inverse problem are transposed to this quasi-3D flow. The stream function is used to define the flow field and the finite volume method is used to solve the problem. Examples show the results concerning the design of centrifugal impeller.

2. INVERSE PROBLEM FOR THE 2D CASCADE.

Figure 1 shows the geometry of the blade characterized by its thickness distribution and the shape of its camber line. The arc elements taken respectively on the upper side and the lower side tangential to two inscribed circles centered on the camber line at $x - dx/2$ and $x + dx/2$ are called associated to the camber line element. The center of these associated elements are characterized by the abscissa x of the camber line element. Let V_o represent the upstream velocity, h the pitch of the cascade, α and β the inlet and outlet flow angles, the circulation Γ of the bound vortex generated by the blade is given by:

Third International Conference on Inverse Design Concepts and Optimization in Engineering Sciences (ICIDES-III), Editor: G.S. Dulikravich, Washington D.C., October 23-25, 1991.

$$\Gamma = V_o h(\sin\alpha - \cos\alpha \tan\beta)$$

The bound vortex distribution on the blade can be represented by the function $\Gamma f(x)$, where $f(x)$ has to be a monotonic increasing function of x for the inverse problem: $f(x_{le}) = 0$, $f(x_{te}) = 1$ and $df/dx \geq 0$ defines the local loading. Figure 2 shows the typical form of the function $f(x)$, $df/dx = 0$ must be imposed near the trailing edge in order to obtain the zero loading according to the Kutta-Joukowsky condition; when the zero loading condition is imposed near the leading edge, the design will give a blade with adapted leading edge. The flow field can be represented by the velocity potential ϕ or by the stream function ψ, the assignment of the bound vortex distribution leads respectively to the following boundary condition applied on the associated elements on both sides of the blade [3]:

$$[\phi]_-^+ = \Gamma f(x) \qquad \text{or} \qquad [\frac{\partial \psi}{\partial n} dl]_-^+ = \Gamma \frac{df}{dx} dx \tag{2.1}$$

As the boundary condition is imposed on the presumed contour of the blade, the penetration of the fluid must be admitted., In order that the boundary condition does not produce extra flux, the flux penetration through each pair of associated elements is to be conservative, this implies:

$$[\frac{\partial \phi}{\partial n} dl]_-^+ = 0 \qquad \text{or} \qquad [\psi]_-^+ = 0 \tag{2.2}$$

The solution of the inverse problem determines the flux penetrating through the associated boundary elements, the camber line inclination correction $\delta\vartheta$ is given by:

$$\delta\vartheta = 0.5[\tan^{-1}(\frac{V_n}{V_t})^+ + \tan^{-1}(\frac{V_n}{V_t})^-] \tag{2.3}$$

Using this, the camber line rectification is performed iteratively. For the 2D incompressible potential flow, the complex potential $\phi + i\psi$ is an analytical function of $x + iy$, the panel method using the multiform singularities distribution described in [4] was used firstly to solve the inverse problem with success, this confirms that the boundary problem is correctly formulated. Figure 3 shows the initial and the final shape of a blade designed with adapted leading edge and with an appropriate loading distribution to prevent the boundary layer separation.

3. MERIDIONAL FLOW, S2 APPROACH.

In the first step, the vortex distribution is transformed into an axisymmetric one by spreading it in the azimuthal direction, this situation is equivalent to the case where the number of blades in the rotor or in the stator is assumed to be ∞, the flow field becomes also axisymmetric and can be analyzed in a meridional plan. Let ξ^1, $\xi^2 = \theta$, and ξ^3 represent the body fitted curvilinear coordinates (Fig. 4), the meridional velocity is represented by: $\vec{U} = V^1\vec{e}_1 + V^3\vec{e}_3 = W^1\vec{e}_1 + W^3\vec{e}_3$, the continuity equation becomes:

$$\frac{1}{\sqrt{\tilde{g}}}[\frac{\partial \sqrt{\tilde{g}}\rho U^1}{\partial \xi^1} + \frac{\partial \sqrt{\tilde{g}}\rho U^3}{\partial \xi^3}] = 0 \tag{3.1}$$

where $\tilde{g}$ represents the determinant of the modified metric tensor due to the flow channel striction produced by the thickness of the blades. Indeed, $\sqrt{g}$ represents the volume of the elementary cube: $(\vec{e}_3 \times \vec{e}_1) \cdot \vec{e}_2$, in the free space $|\vec{e}_2| = \sqrt{g_{22}} = r$, and in the blade row space the thickness of the blade reduces the flow channel, if $r\delta\theta_e$ denotes the thickness measured in the peripheral direction, N_b the number of blades in the rotor or stator, the modified element $\tilde{g}_{22}$ of the metric tensor is determined by:

$$\tilde{g}_{22} = (1 - \frac{N_b \delta\theta_e}{2\pi})^2 r^2$$

$\sqrt{\tilde{g}}$ simulating the elementary volume with striction in (3.1) is evaluated with $\tilde{g}_{22}$. Using the stream function

Third International Conference on Inverse Design Concepts and Optimization in Engineering Sciences (ICIDES-III), Editor: G.S. Dulikravich, Washington D.C., October 23-25, 1991.

$\bar{\psi}$ to represent the flow field by imposing:

$$U^1 = \frac{1}{\sqrt{\rho \bar{g}}} \frac{\partial \psi}{\partial \xi^3} \quad \text{et} \quad U^3 = -\frac{1}{\sqrt{\rho \bar{g}}} \frac{\partial \psi}{\partial \xi^1} \tag{3.2}$$

the equation (3.1) is satisfied automatically. The governing equation for ψ is obtained by writing $\nabla \times \vec{U} = \Omega^2 \vec{e}_2$, where Ω^2 represents the axisymmetric component of $\nabla \times \vec{V}$, it is deduced from the hub to shroud equilibrium condition. Let

$$H = \frac{p}{\rho} + \frac{V^2}{2} = \frac{p_t}{\rho} \quad \text{and} \quad I = \frac{p}{\rho} + \frac{W^2}{2} - \frac{\omega^2 r^2}{2} = H + \omega (V_\theta r)$$

The momentum equation is:

$$\vec{\Omega} \times \begin{cases} \vec{V} \\ \vec{W} \end{cases} = \begin{cases} -\nabla H \\ -\nabla I \end{cases} + \frac{\vec{F}_b}{\rho} + \frac{\vec{F}_d}{\rho} \quad \begin{cases} \text{stator} \\ \text{rotor} \end{cases} \tag{3.3}$$

In fact, there is a pressure gradient in the axisymmetric direction in the flow space between blades, in the axial symmetric S2 flow where the number of blades is supposed infinite, this pressure gradient disappears and the volume force $\vec{F}_b/\rho$ due to the blades has to be added in the momentum equation. The loss scheme [2] related to the plausible value of efficiency η for each streamline of the stage is added, this scheme suggests that the dissipative force $\vec{F}_d/\rho$ is related to the variation de $V_\theta r$ via η:

$$\frac{\vec{F}_d}{\rho} = \begin{cases} (\eta - 1) \frac{\psi}{(\vec{V})^3} |\vec{V} \cdot \nabla (V_\theta r)| \vec{V} & \text{stator} \\ (1 - \eta) \frac{\psi}{(\vec{W})^3} |\vec{W} \cdot \nabla (V_\theta r)| \vec{W} & \text{rotor} \end{cases} \tag{3.4}$$

$\vec{F}_d = 0$ as well as $\vec{F}_b = 0$ are imposed in the free space. Figure 5 shows the relation between the kinetic moment distribution in the blade row space and the circulation of the bound vortices produced by the blades. Let Γ_ψ denote the circulation generated by the blade in the section cut by an axisymmetric stream surface $\psi = cte$, the kinetic moment $(V_\theta r)_{m,k}$ generated by the bound vortices located between the leading edge and the abscissa m can be represented by:

$$(V_\theta r)_{m,\psi} = (V_\theta r)_{le,\psi} + \frac{N_b}{2\pi} \Gamma_\psi f(m, \psi) \tag{3.5}$$

Using (3.4) and adopting that $\partial I / \partial \xi^2$ or $\partial H / \partial \xi^2$ being equal to $-(F_d)_2/\rho$ in the dissipative scheme, the azimuthal component of the momentum equation leads to:

$$\frac{(F_b)_2}{\rho} = \left[V^1 \frac{\partial (V_\theta r)}{\partial \xi^1} + V^3 \frac{\partial (V_\theta r)}{\partial \xi^3} \right] \tag{3.6}$$

where $W_2 = V_\theta r + \omega r^2$ and $V_2 = V_\theta r$. The coordinates system ξ^i is chosen so that the constant ξ^3 lines are iteratively replaced by the streamlines. The component following $\vec{e}^3$ of the momentum equation represents the hub to shroud equilibrium condition, which gives:

$$\sqrt{\bar{g}} \Omega^2 = \frac{1}{V^1} \left[\begin{cases} \frac{\partial I}{\partial \xi^3} + W^2 \sqrt{\bar{g}} \Omega^1 \\ \frac{\partial H}{\partial \xi^3} + V^2 \sqrt{\bar{g}} \Omega^1 \end{cases} - \frac{(F_b)_3}{\rho} - \frac{(F_d)_3}{\rho} \right] \quad \begin{cases} \text{rotor} \\ \text{stator} \end{cases} \tag{3.7}$$

Let $\vec{n}$ design the normal of the camber surface of the blade, we have:

$$\vec{n} = n_1 \vec{e}^1 + n_2 \vec{e}^2 + n_3 \vec{e}^3$$

As $\vec{W} \perp \vec{n}$ in the rotor and $\vec{V} \perp \vec{n}$ in the stator, we have:

$$W^2 \quad \text{or} \quad V^2 = -\left(\frac{n_1}{n_2} V^1 + \frac{n_3}{n_2} V^3 \right)$$

and $\vec{F}_b \parallel \vec{n}$, we have:

$$\frac{(F_b)_2}{n_2} = \frac{(F_b)_3}{n_3}$$

Third International Conference on Inverse Design Concepts and Optimization in Engineering Sciences (ICIDES-III), Editor: G.S. Dulikravich, Washington D.C., October 23-25, 1991

Using (3.4), (3.6) and the last 3 relations, (3.7) becomes:

$$\sqrt{g}\Omega^2 = \frac{1}{V^1}\left\{\begin{array}{l}\frac{\partial I}{\partial \xi^3}\\ \frac{\partial H}{\partial \xi^3}\end{array}\right. + \frac{n_1}{n_2}\frac{\partial (V_\theta r)}{\partial \xi^3} - \frac{n_3}{n_2}\frac{\partial (V_\theta r)}{\partial \xi^1}$$
$$- \left\{\begin{array}{l}(1-\eta)\frac{\omega}{(W)^2}\\ (\eta-1)\frac{\omega}{(V)^2}\end{array}\right. \frac{V_3}{V^1}\left[V^1\frac{\partial (V_\theta r)}{\partial \xi^1} + V^3\frac{\partial (V_\theta r)}{\partial \xi^3}\right] \qquad \left\{\begin{array}{l}\text{rotor}\\ \text{stator}\end{array}\right. \tag{3.8a}$$

In the free space, the component following $\vec{e}^3$ of the momentum equation leads directly to:

$$\text{free space} \qquad \sqrt{g}\Omega^2 = \frac{1}{V^1}\left\{\frac{\partial H}{\partial \xi^3} - \frac{(V_\theta r)}{r^2}\frac{\partial (V_\theta r)}{\partial \xi^3}\right\} \tag{3.8b}$$

The dot product of the momentum equation with $\vec{V}$ in the stator and in the free space or with $\vec{W}$ in the rotor leads to the following relations which serve to update the nodal values of H or I:

$$\left\{\begin{array}{ll}\text{free space} & \frac{\partial H}{\partial m} = \\ \text{stator} & \end{array}\right. \left\{\begin{array}{l}0\\ (\eta-1)\omega\frac{\partial (V_\theta r)}{\partial m}\end{array}\right. \tag{3.9a}$$

$$\text{rotor} \qquad \frac{\partial I}{\partial m} = (1-\eta)\omega\frac{\partial (V_\theta r)}{\partial m} \tag{3.9b}$$

where $\partial(\ )/\partial m$ denotes the meridional streamwise tangential derivative. Writing $\nabla \times \vec{U} = \Omega^2 \vec{e}_2$, we obtain the governing equation of ψ:

$$\frac{\partial}{\partial \xi^3}\left(\frac{g_{11}}{\rho\sqrt{g}}\frac{\partial \psi}{\partial \xi^3}\right) + \frac{\partial}{\partial \xi^1}\left(\frac{g_{33}}{\rho\sqrt{g}}\frac{\partial \psi}{\partial \xi^1}\right)$$
$$- \frac{\partial}{\partial \xi^3}\left(\frac{g_{13}}{\rho\sqrt{g}}\frac{\partial \psi}{\partial \xi^1}\right) - \frac{\partial}{\partial \xi^1}\left(\frac{g_{31}}{\rho\sqrt{g}}\frac{\partial \psi}{\partial \xi^3}\right) = \sqrt{g}\Omega^2 \tag{3.10}$$

For the inverse problem, the distribution of $V_\theta r$ is assigned, using (3.8), Ω^2 is updated iteratively. Let the camber surface of the blade be defined by $\theta = \xi^2(\xi^1, \xi^3) + cte$, if the coordinate lines $\xi^3 = cte$ are updated to the streamlines iteratively, ξ^2 can be computed using the slip condition:

$$\xi^2 = \xi^2_{i_e} + \int_{\xi^1_{i_e}}^{\xi^1} \frac{U^2}{U^1} d\xi^1 \tag{3.11}$$

Figure 5 shows the geometry of the blading of a multistage turbopump obtained by solving the inverse problem. The CPU time on IBM 3090 in scalar mode is about 1 minute for the entire turbopump. The grid used for the S2 computation is 300×16. Figure 6 shows the comparison of the centrifugal impellers designed with $\eta = 1$ and $\eta < 1$ having the same level of total pressure gain.

Blade surface pressure evaluation. – Usually the S2 approach leads to the determination of the mean velocity on both faces of the blade:

$$\left\{\begin{array}{ll}\text{rotor} & W\\ \text{stator} & V\end{array}\right. = \left[g_{11}V^1V^1 + 2g_{13}V^1V^3 + g_{33}V^3V^3 + \frac{g_{22}(V_\theta r + \omega r^2)^2}{g_{22}(V_\theta r)^2}\right]^{1/2} \tag{3.12}$$

Let ΔU denote the difference of the absolute velocities $(V^+ - V^-)$ or the relative velocity $(W^+ - W^-)$ on the two faces of the blade, when the number of blades is finite, this difference is related to the local density of bound vortex generated by the blade. In the S2 scheme, consider the blade section cut by a $\xi^3 = cte$ surface, the flux of bound vortices generated by the element $\delta\xi^1$ of the blade is determined by the flux of $\vec{\Omega}$ through the elementary surface $(\delta S)_3\vec{e}^3 = \sqrt{g}\delta\xi^1\delta\xi^2\vec{e}^3$, where $\delta\xi^2$ should be equal to $2\pi/N_b$. Using the Stokes relation that implies the circulation produced by ΔU is equal to the flux of the bound vortices we get the following relation:

$$(\Delta U)_{i,k} = \frac{2\pi}{N_b}\frac{cos\beta}{\sqrt{g_{11}}}\left|[V_\theta r]^{i+1/2,k}_{i-1/2,k}\right| \tag{3.13}$$

where β denotes the local angle of the blade section with respect to the meridional plane. (3.12) and (3.13) are used to compute surface velocity on both faces of the blades, then the pressure distribution by the S2 approach can be deduced. (Fig. 9)

4. BLADE TO BLADE FLOW, S1 APPROACH.

The blade to blade flow confined in each axisymmetric stream sheet is analyzed in order to define the final geometry for each section of the blade and to obtain the pressure distribution. At the beginning, the contour of the blade is created from the camber line obtained from the S2 step with the assigned thickness distribution. The conformal mapping $(m,\theta) \Longrightarrow (x^1,x^2)$:

$$\begin{cases} x^1 = r_o \int_{m_o}^{m} \dfrac{dm}{r} \\ x^2 = r_o(\theta - \theta_o) \end{cases} \tag{4.1}$$

transforms the blade to blade flow confined in an axisymmetric stream sheet into a 2D cascade flow in the (x^1,x^2) plane. The body fitted coordinate system constituted by the equipotential lines $\xi^1 = cte$ and the streamlines $\xi^2 = cte$ of a fictive 2D flow around the cascade is created using the panel method [4]. In this system, the continuity equation becomes:

$$\frac{1}{\sqrt{g}}\Big[\frac{\partial}{\partial \xi^1}(\rho\sqrt{g}U^1) + \frac{\partial}{\partial \xi^2}(\rho\sqrt{g}U^2)\Big] = 0 \tag{4.2}$$

where U^i represent the contravariant components of the absolute velocity $\vec{V}$ for the stator and relative velocity $\vec{W}$ for the rotor and

$$\sqrt{g} = \frac{D(x^1,x^2)}{D(\xi^1,\xi^2)}\Big(\frac{r}{r_o}\Big)^2 r$$

where $D(x^1,x^2)/D(\xi^1,\xi^2)$ denotes the Jacobian, r represents the local thickness of the stream sheet. Introducing the stream function ψ with

$$\begin{cases} U^1 = \dfrac{1}{\rho\sqrt{g}}\dfrac{\partial \psi}{\partial \xi^2} \\ U^2 = -\dfrac{1}{\rho\sqrt{g}}\dfrac{\partial \psi}{\partial \xi^1} \end{cases} \tag{4.3}$$

(4.2) is satisfied. From the momentum equation, we can show that the free vortex of the absolute velocity shedding from the preceeding blade row must be tangential to the axisymetric stream sheet, the governing equation of the blade to blade flow stream function is deduced from this condition: for the relative flow around the blades of the rotor, we have:

$$-\Big[\frac{\partial}{\partial \xi^1}\Big(\frac{g_{22}}{\rho\sqrt{g}}\frac{\partial \psi}{\partial \xi^1}\Big) + \frac{\partial}{\partial \xi^2}\Big(\frac{g_{11}}{\rho\sqrt{g}}\frac{\partial \psi}{\partial \xi^2}\Big)\Big] = - \frac{\partial g_{21}W^1}{\partial \xi^1} + \frac{\partial g_{12}W^2}{\partial \xi^2} + 2\sqrt{g}\frac{\omega r}{\tau}\frac{d\log r}{dm} \tag{4.4}$$

Boundary conditions for the inverse problem:

$$\begin{cases} \text{Flux conservation:} & [\psi]_-^+ = 0 \\ \text{Bound vorticity assigned:} & \big[W_1 d\xi^1 - \omega r^2 d\theta\big]_-^+ = \Gamma df \end{cases} \tag{4.5}$$

The solution of the inverse problem leads to the determination of flux penetration on the blade contour, the camber line inclination correction $\delta\vartheta$ is given by:

$$\delta\vartheta = 0.5\Big[\tan^{-1}\Big(\frac{\sqrt{g}}{r}\frac{W^2}{W_1}\Big)^+ + \tan^{-1}\Big(\frac{\sqrt{g}}{r}\frac{W^2}{W_1}\Big)^-\Big] \tag{4.6}$$

Figure 7 shows the network (ξ^1, ξ^2) around a blade row for an impeller. Figure 8 shows the comparison of the camber lines of the impeller obtained from the S2 approach and rectified by the S1 approach. Figure 9 shows the pressure distributions obtained from the S2 and S1 approaches. For the case of the turbopump, the loading is optimised to avoid the cavitation. The results from the S2 and S1 computations are similar, but not identical, the need of the S1 computation to obtain the final geometry definition of the blades is confirmed. For one stream sheet, the CPU time on a IBM workstation RISC 6000/320 is about 40 minutes, or about 5 minutes on IBM 3090 in scalar mode. The grid used is 150×16.

5. CONCLUSION.

The representation of the blades by the vortex distribution enables the formulation of the well-posed inverse problem, and which leads to design the blading of a turbomachine. The two steps S2 – S1 quasi-3D approach has been applied on different axial and radial geometries. Several kinds of loading function have been tried. The results show that the success of the blading design depends greatly on the meridional $(V_\theta r)$ distribution assignment associated with the loss distribution. To optimise the design in order to avoid the formation of the cavitation or the separation of the boundary layer in the design condition, when the loading is not too high, experiences show that an adequate modification of the bound vortices distribution function f may effectively lead to prevent the surface pressure to be lower than the cavitation level or to maintain the adverse pressure gradient below the boundary layer separation criterion. The inverse problem procedure has been elaborated to calculate the turbomachines in incompressible range, the research works are planning to extend this method to make the transonic designs.

ACKNOWLEDGEMENT

This work was supported by a research contract from the SEP (Société Européenne de Propulsion). The authors wish to thank them for their cooperation to this publication.

REFERENCE

1. Wu C.H., "A general theory of three dimensional flow in subsonic and supersonic turbomachines of axial, radial and mixed flow type. NACA TN 2604, 1952

2. Horlock J.H., "On Entropy Production in Adiabatic Flow in Turbomachines." Journal of Basic Engineering, Trans. ASME, Dec. 1971.

3. Luu T.S., and Viney B., "The Turbomachine Blading Design Achieved by Solving the Inverse Problem." ASME Paper No.87-GT-215.

4. Luu T.S., Coulmy G., and Viney B., "Design problem of the profile or cascade of profiles and construction of the orthogonal networks using the Riemann surface for the multiform singularities." Computational Mechanic (1989) 4, 309-317.

Third International Conference on Inverse Design Concepts and Optimization in Engineering Sciences
(ICIDES-III), Editor: G.S. Dulikravich, Washington D.C., October 23-25, 1991.

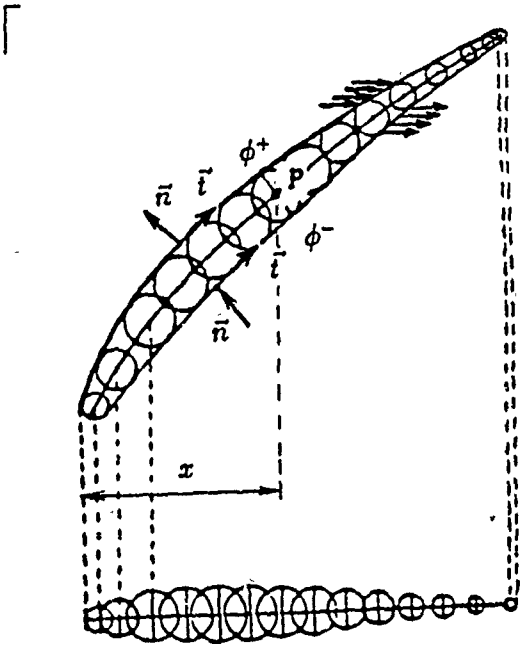


Fig. 1. Associated elements on both sides of the blade and on the camber line.

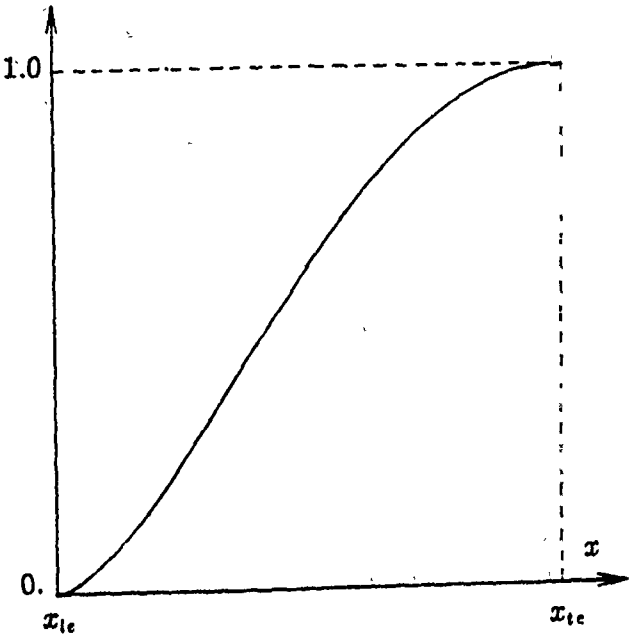


Fig. 2. Typical loading function $f(x)$.

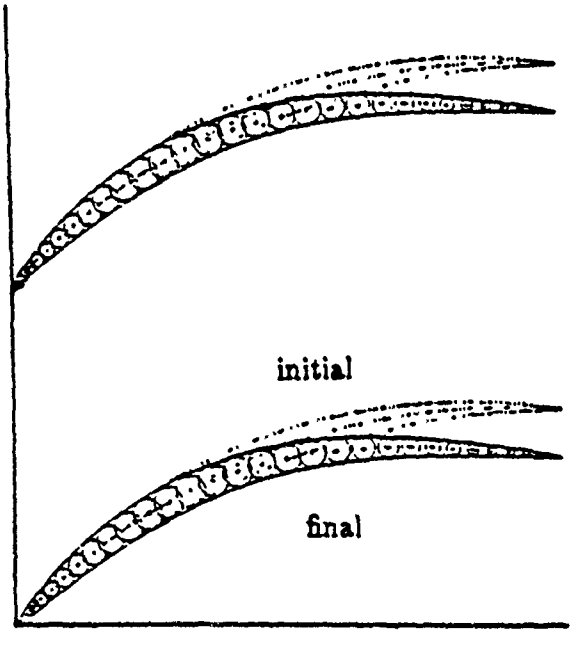


Fig. 3. Initial and final shape of the blade.

Third International Conference on Inverse Design Concepts and Optimization in Engineering Sciences (ICIDES-III), Editor: G.S. Dulikravich, Washington D.C., October 23-25, 1991.

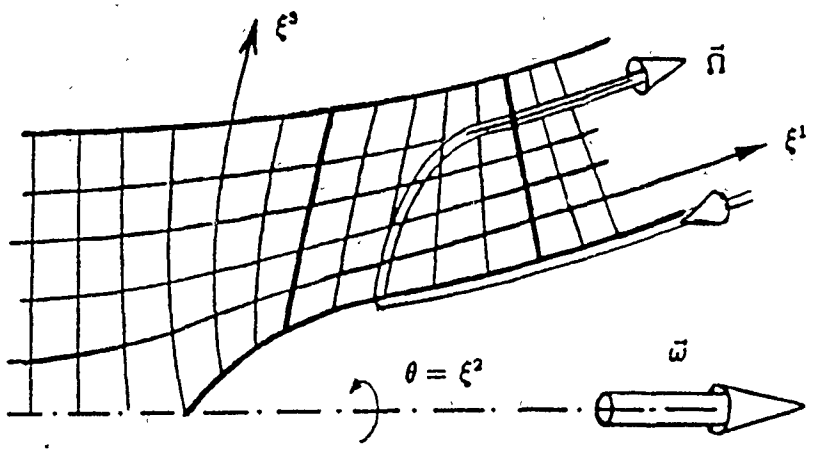
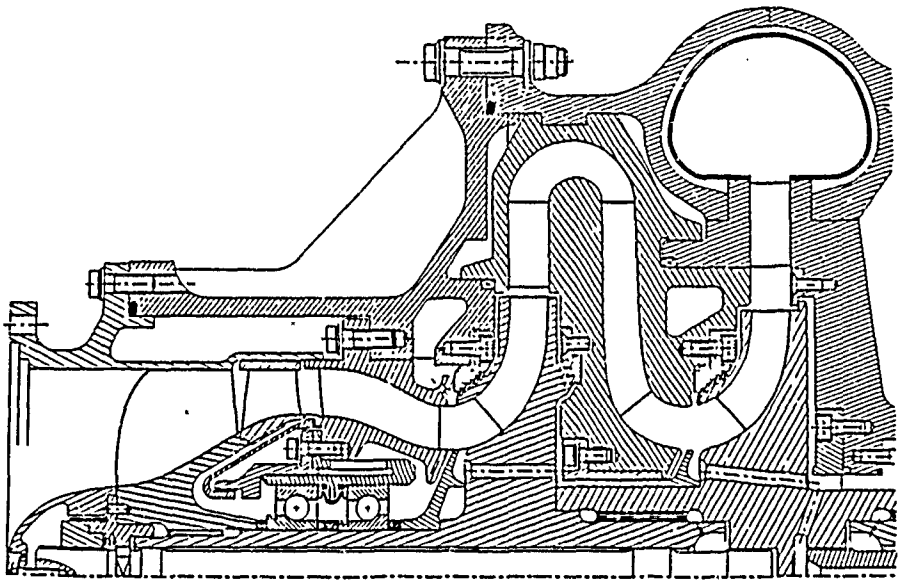
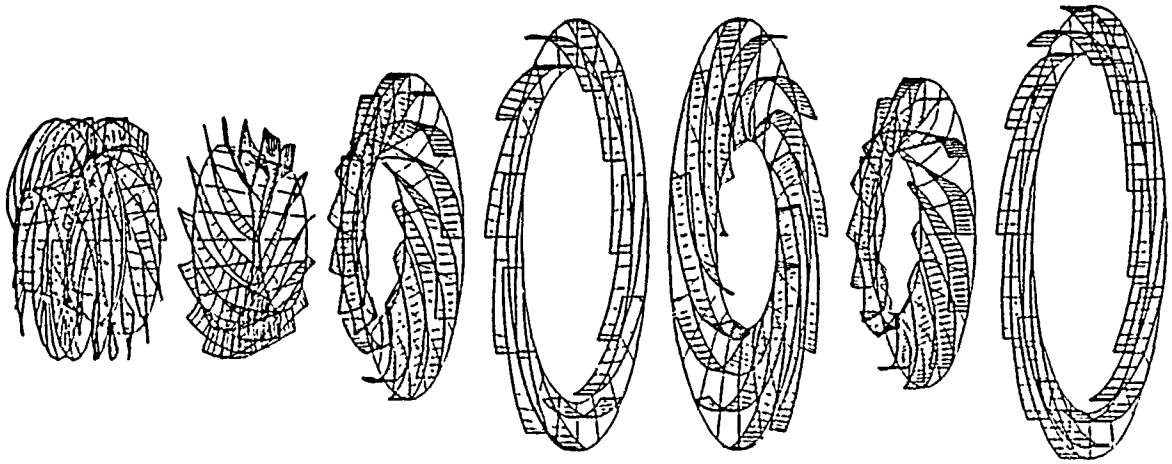


Fig. 4. Boby fitted coordinate system ξ^1, $\xi^2 = \theta$, ξ^3.



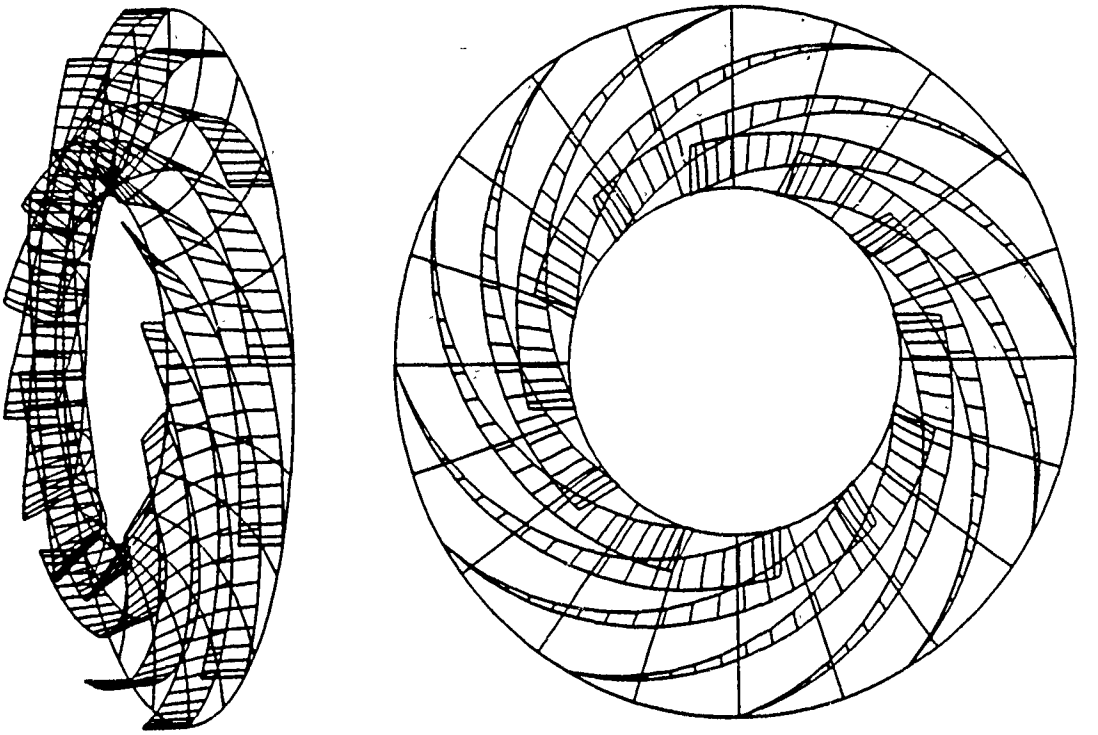
Meridional section of a multistage turbopump.



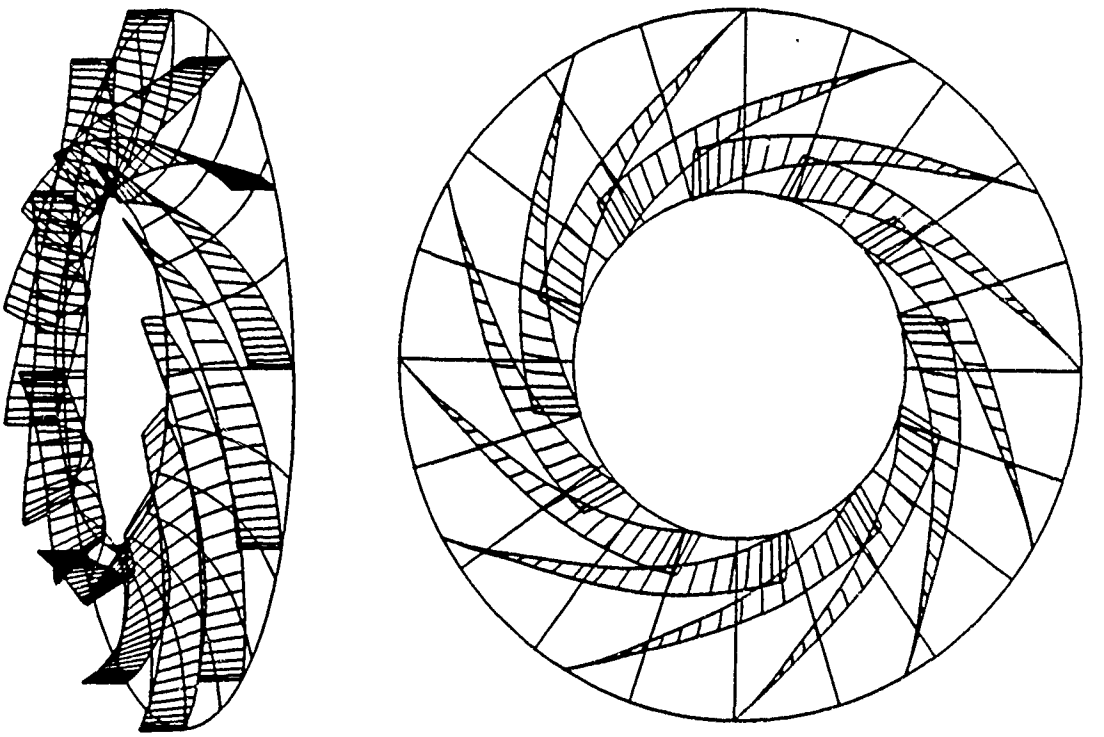
The blading obtained by the S2 inverse solution.

Fig. 5. The blading of a multistage turbopump.

Third International Conference on Inverse Design Concepts and Optimization in Engineering Sciences (ICIDES-III), Editor: G.S. Dulikravich, Washington D.C., October 23-25, 1991.



$\eta = 1$



$\eta = 0.7$

Fig. 6. Centrifugal impellers designed with $\eta = 1$ and $\eta < 1$ having the same level of total pressure gain.

Third International Conference on Inverse Design Concepts and Optimization in Engineering Sciences (ICIDES-III), Editor: G.S. Dulikravich, Washington D.C., October 23-25, 1991.

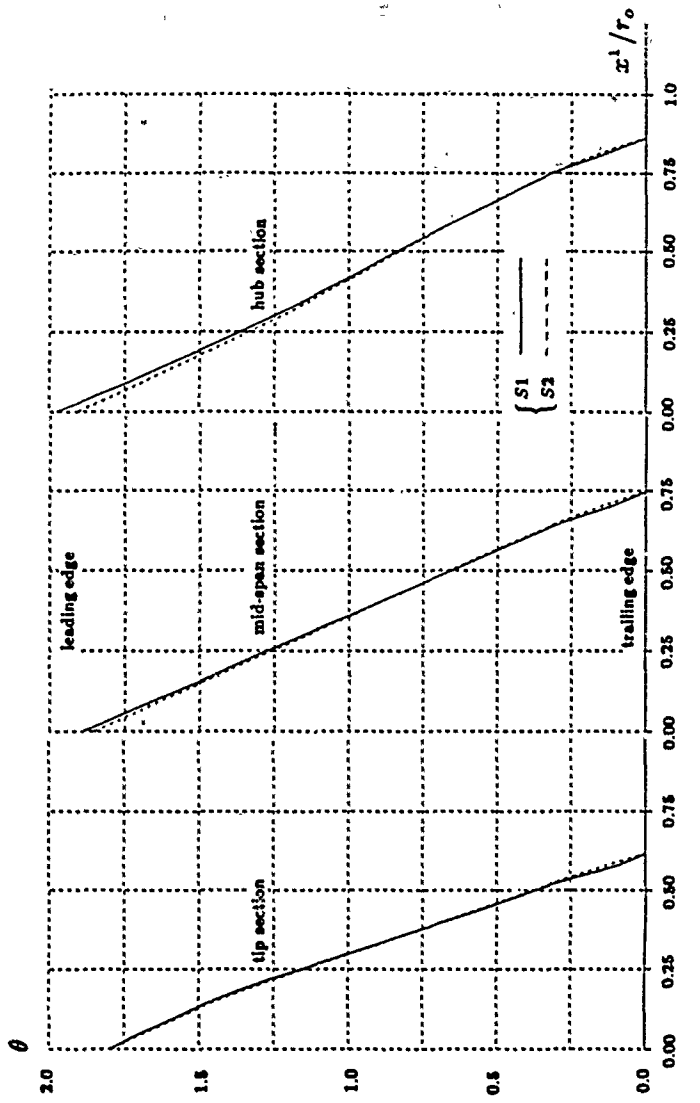


Fig. 6. Camber lines of the impeller obtained from S2-S1 approaches.

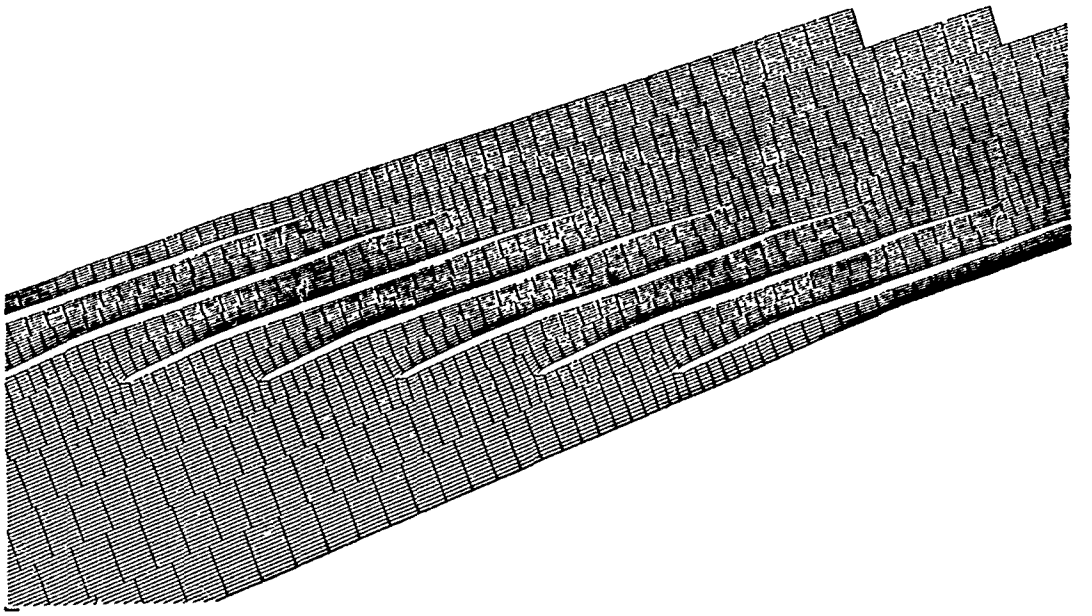


Fig. 7. Network (ξ^1, ξ^2) around a blade row in the (x^1, x^2) plane.

Third International Conference on Inverse Design Concepts and Optimization in Engineering Sciences (ICIDES-III), Editor: G.S. Dulikravich, Washington D.C., October 23-25, 1991.

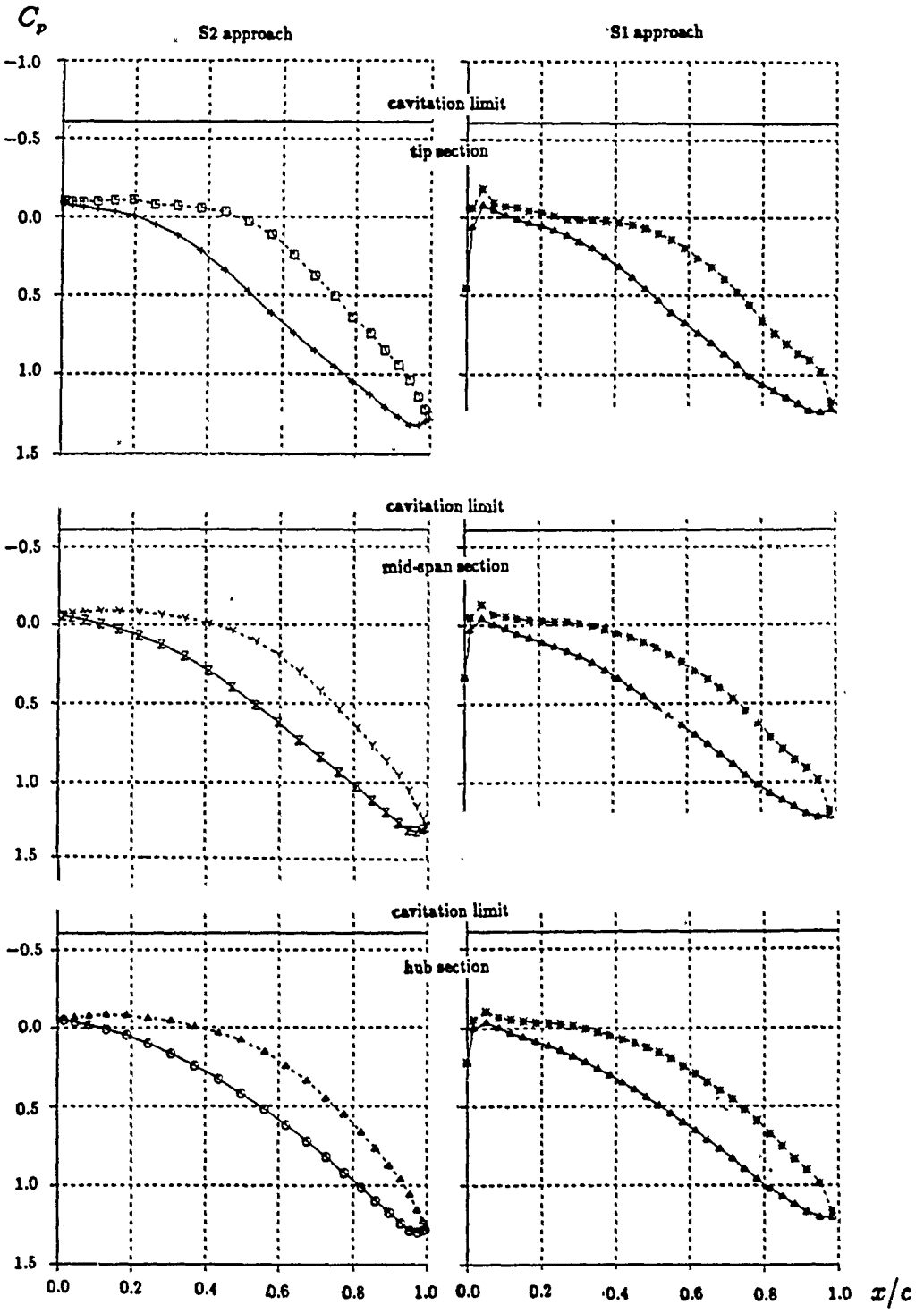


Fig. 9. Pressure distribution for 3 sections of the impeller from S2-S1 approaches.

Third International Conference on Inverse Design Concepts and Optimization in Engineering Sciences (ICIDES-III). Editor: G.S. Dulikravich. Washington D.C., October 23-25, 1991.

A PROPOSED THROUGH-FLOW INVERSE METHOD FOR THE DESIGN OF MIXED-FLOW PUMPS

João Eduardo Borges
Mechanical Engineering Dept.
Instituto Superior Técnico
Av. Rovisco Pais
1096 Lisboa Codex
PORTUGAL

ABSTRACT

A through-flow (hub-to-shroud) truly inverse method is proposed and described in this paper. It uses as a design initial specification an imposition of mean swirl, i.e., radius times mean tangential velocity, given throughout the meridional section of the turbomachine. In the present implementation, it is assumed that the fluid is inviscid, incompressible and irrotational at inlet and the blades are supposed to have zero thickness. Only blade rows that impart to the fluid a constant work along the span will be considered.

An application of this procedure to design the rotor of a mixed-flow pump will be described in detail. The strategy used to find a suitable mean swirl distribution and the other design inputs is also described. The final blade shape and pressure distributions on the blade surface are presented, showing that it is possible to obtain feasible designs using this technique. Another advantage of this technique is the fact that it does not require large amounts of CPU time.

1-INTRODUCTION AND LITERATURE SURVEY

The large majority of pumps is designed by using very simple and rudimentary one-dimensional considerations concerning the velocity triangles, considerations which allow the calculation of the evolution of the blade angle along the passage, see for example [1] and [2]. These methods are so easy that they can be carried out using only hand calculations and simple graphical processes.

Although some pumps are still being calculated using hand calculations, the above one-dimensional procedure can and has been programmed as computer codes which are being used by the most important pump manufacturers. The results obtained with these techniques are the better the more radial the blade passage is. However, for mixed-flow pumps, the velocity triangles vary appreciably along the span, so that the above methodology is not good enough. In order to take into account this effect in some way, designers usually split the flow passage in several parts, applying the above considerations to each one.

When the pump designs involve some responsibility, the above step is followed by a verification using a direct code which is run with the geometry arrived at previously. Before reaching the final design, several iterations following the above steps are usually required.

This complete process can be time consuming, so that one is left wondering whether it could be improved. One possible way to achieve this could be by using inverse methods, enabling the achievement of the blade row layout in a more direct form, in one single step. Among inverse methods, two-dimensional techniques are the most frequently used and the ones that require less CPU time. These two-dimensional inverse methods can be classified into two main groups, according to the approximations used when looking for the solution to the blade design. The first sort of approximations gives rise to blade-to-blade methods since the calculations are done in the blade-to-blade plane. This kind of methods is popular among designers of axial turbomachinery, but it did not attract much attention among designers of radial

Third International Conference on Inverse Design Concepts and Optimization in Engineering Sciences (ICIDES-III), Editor: G.S. Dulikravich, Washington D.C., October 23-25, 1991.

turbomachinery. The reason may be connected to the fact that the flow passages are more complicated and there are significant changes in radius.

The other way of tackling the solution consists in working in the hub-to-shroud plane (i.e., in the meridional plane), giving rise to what we could call hub-to-shroud (or through-flow) methods. In this sort of approach the flow is supposed axisymmetric, an approximation that can be interpreted as giving the mean flow through the turbomachine. This sort of approach seems more popular among radial turbomachinery designers. In fact, one can find examples of this kind of procedure as far back as 1955, when reference [3] described some work applied to the redesign of a centrifugal compressor, using a hub-to-shroud method. In this instance the blade shape was kept fixed and given as input, while the shroud contour was altered and evolved as a result of the calculations. The centrifugal compressors described in [3] were built and tested, the experimental results being presented in [4]. The experimental results show that this technique produced significant improvements in the overall efficiency and peak pressure ratio.

A different strategy was followed in reference [5] which, again, describes the application of an inverse technique to the design of centrifugal compressors. Contrary to the previous example the meridional geometry (hub and shroud contours) of the machine is supposed known and given as input. The other inputs consist of a suitable normal blade thickness and the desired velocity loading (difference in velocity across the blade) at hub, mid-span and shroud as a function of distance along the camberline. As a result of the calculations the blade shape was obtained. This paper presents some experimental evidence suggesting that the procedure gives reliable results when the flow is attached.

The method proposed in the present work has got some similarities to that of [5] in the sense that it is also a hub-to-shroud inverse technique that assumes as known the meridional geometry and calculates the blade shape that will satisfy some flow-field conditions, given as input to the procedure. The input design specification used here is a mean swirl (radius times mean tangential velocity, $r\overline{V_\theta}$) distribution given throughout the meridional section. This design specification is somewhat unusual, but a suggestion in this direction can already be found in the work of Wu (see [6]) and it is ideally suited to the design of radial turbomachinery as discussed in [7]. In fact, the work of [7], which presents a three-dimensional inverse method using a mean swirl specification, shows that the mean swirl specification is related to the way the work is imparted to the fluid as it passes through the blade row. In other words, the mean swirl can be related to the blade loading across the blades. Another reference that discusses the use of a mean swirl imposition is [8], where the equations to be used in the present work are derived. Nevertheless [8] does not present any practical examples of application of the equations.

2-DESCRIPTION OF THE DESIGN METHOD

Throughout this work we will use a right-handed cylindrical polar coordinate system defined by (r, Θ, z), where r is the radius, Θ the angular coordinate and z is the axial distance. In addition, we will use an auxiliary coordinate α, defined by:

$$\alpha = \Theta - f(r,z) \qquad (1)$$

where f(r,z) is the angular coordinate of a point on the blade camber surface. This variable α can be interpreted as a sort of helical angular coordinate aligned with the blade, so that when

$$\alpha = m\frac{2\pi}{B} \qquad (2)$$

Third International Conference on Inverse Design Concepts and Optimization in Engineering Sciences (ICIDES-III), Editor: G.S. Dulikravich, Washington D.C., October 23-25, 1991.

with m an integer (m = ...,-1, 0, 1, 2, 3,...) and B equal to the number of blades of the turbomachine, we are on a blade surface (eq. (2) describes the blade shape).

In the following we will use bold underlined characters for vectors and mean values will be denoted with an overbar.

2.1 Velocity Flow Field.

Since it was intended to apply this method to design pumps, it was assumed that the fluid was inviscid and incompressible and, for simplicity sake, the blade thickness is not considered in this procedure.

In agreement with the through-flow approximation, the flow through the turbomachine will be assumed axisymmetric even in the blade region. This mean velocity field will be calculated using the streamfunction concept and the value of the mean vorticity. Indeed, since the vorticity field is solenoidal, it can be written as the cross product of two gradients of scalar functions. One of these scalar functions may be α according to the fact that all the vorticity is confined to the blades. In fact, if we suppose the far upstream velocity is uniform (an approximation quite frequent), we can say the flow is irrotational at inlet. Concentrating in designs that execute constant work along the span, it is concluded that the flow must remain everywhere irrotational according to Kelvin's theorem. So, if there is any vorticity at all, it must be bound to the blade surfaces, justifying the statement just made. The other scalar function in the expression for the vorticity turns out to be the mean swirl as is shown in [7]. Therefore, the expression for the mean vorticity, $\underline{\overline{\Omega}}$ is:

$$\underline{\overline{\Omega}} = r\overline{V}_\theta \times \nabla\alpha \tag{3}$$

and now that the mean vorticity is known, the corresponding velocity field can easily be calculated. It is indeed known that the mean vorticity is the curl of the mean velocity $\underline{\overline{V}}$, or:

$$\underline{\overline{\Omega}} = \nabla \times \underline{\overline{V}} \tag{4}$$

Equating the θ-component of eqs. (3) and (4) the following equation is obtained:

$$\frac{\partial \overline{V}_r}{\partial z} - \frac{\partial \overline{V}_z}{\partial r} = \frac{\partial f}{\partial z}\frac{\partial r\overline{V}_\theta}{\partial r} - \frac{\partial f}{\partial r}\frac{\partial r\overline{V}_\theta}{\partial z} \tag{5}$$

relating the velocity field to the blade shape, f, and the mean swirl $r\overline{V}_\theta$. Besides this equation, the velocity field must satisfy the continuity equation. In order to achieve this we introduce the concept of a streamfunction defined by:

$$\overline{V}_r = -\frac{1}{r}\frac{\partial \psi}{\partial z} \tag{6a}$$

$$\overline{V}_z = \frac{1}{r}\frac{\partial \psi}{\partial r} \tag{6b}$$

Third International Conference on Inverse Design Concepts and Optimization in Engineering Sciences (ICIDES-III), Editor: G.S. Dulikravich, Washington D.C., October 23-25, 1991.

so that this definition satisfies identically the continuity equation for incompressible flow, i. e., $\nabla . \overline{V} = 0$. The actual value of ψ appearing in the definitions (6a) and (6b) is going to be determined substituting (6a) and (6b) in eq. (5). In this way we arrive at:

$$\frac{\partial^2\psi}{\partial r^2} - \frac{1}{r}\frac{\partial\psi}{\partial r} + \frac{\partial^2\psi}{\partial z^2} = -\,r\left(\frac{\partial f}{\partial z}\frac{\partial r\,\overline{V}_\theta}{\partial r} - \frac{\partial f}{\partial r}\frac{\partial r\,\overline{V}_\theta}{\partial z}\right) \tag{7}$$

For the resolution of this equation it is necessary to specify a complete set of boundary conditions. The boundary condition to use along the endwalls (hub and shroud) is the one that states that there is no flow through the solid walls. Using the streamfunction concept, this fact is expressed as:

$$\psi = \text{Const.} \tag{8}$$

or, in other words, the hub and shroud must be streamlines of the flow.

Far upstream we know the mean velocity vector, $\overline{V}_{-\infty}$, since it is given as input. Therefore we can write:

$$\frac{1}{r}\frac{\partial\psi}{\partial s} = \overline{V}_{-\infty} \cdot \underline{n} \tag{9}$$

where s is distance along the far upstream boundary and $\underline{n}$ is the unitary vector perpendicular to it. This expression enables us to calculate the values of ψ along the far upstream boundary, using a simple numerical integration. At the far downstream boundary a similar expression applies since the velocity there is uniform because the flow is irrotational at inlet and the blade row is supposed to execute constant work along the span. In this way the complete set of boundary conditions is obtained.

The partial differential equation (7) was solved using finite difference techniques. As a typical mixed-flow pump has a meridional section with complicated geometry bounded by curved boundaries (hub and shroud profiles) it was decided to use a transformation of coordinates to body-fitted curvilinear coordinates (see [9]). Since this coordinate system should be easy to generate and require little computational time, it was decided to use an algebraic transformation. For this kind of transformation of coordinates, mesh points are distributed along quasi-orthogonals and quasi- streamlines. Fig. 2 shows the grid used in the calculations to be discussed later on.

Eq. (7) was discretized using second-order accurate central difference formulae, obtaining a nine-point difference star. The resulting finite difference equations were solved by a relaxation method. In the present case, a Gauss-Seidel relaxation scheme was used, implemented in conjunction with a multi-grid technique in order to accelerate the convergence rate of the solution. A good description of multi-grid methods can be found in [10], and, in fact, the relaxation subroutines used in our program are a slightly modified version of the ones presented in [10].

2.2 Equation for the Determination of the Blade Shape.

After calculating the velocity field using the information presented in the previous subsection, it is necessary to evaluate the blade geometry. That is done by requiring the blade to be tangent to the velocity vector. This condition can be expressed as:

$$\overline{W} \cdot \nabla\alpha = 0 \tag{10}$$

Third International Conference on Inverse Design Concepts and Optimization in Engineering Sciences (ICIDES-III), Editor: G.S. Dulikravich, Washington D.C., October 23-25, 1991.

where $\underline{\overline{W}}$ is the local relative velocity, $\underline{\overline{W}} = \underline{\overline{V}} - \underline{U}$. Expanding eq. (10), the following expression is obtained:

$$\overline{V}_z \frac{\partial f}{\partial z} + \overline{V}_r \frac{\partial f}{\partial r} = \frac{r\overline{V}_\theta}{r^2} - \omega \qquad (11)$$

where f is the angular coordinate of the blade and ω is the rotational speed of the blade row. $\overline{V}_z$ and $\overline{V}_r$ are the mean axial and radial velocities, respectively.

Eq. (11) is a first-order partial differential equation with characteristic lines coincident with the meridional projection of the streamlines. In order to integrate this differential equation, some initial data must be specified along a line roughly perpendicular to these characteristic lines and extending from hub to shroud. This initial data on f will be called the stacking condition of the blade. In our method this stacking condition is implemented by giving, as input, the values of the blade coordinate f, along a quasi-orthogonal, for example, at the leading edge.

After the stacking condition is specified, we can integrate eq. (11), since all the velocities that appear in it are known from the previous iteration. The integration of eq. (11) was done using finite difference methods. More specifically, an Euler's modified method (see [11]) was used. This is an implicit numerical scheme that has a truncation error of second order in the mesh size and is consistent and stable.

2.3 Estimation of Blade Surface Pressures.

One result that is important in any design method is the values of pressure on the suction and pressure surfaces of the blade, for judging whether the pressure distribution is adequate or not. In order to estimate these values starting from the axisymmetric solution it is necessary to calculate the blade surface velocities using the mean values known. To do that we begin by determining the velocity jump across the blades ($\underline{W}^+ - \underline{W}^-$) which is given by (see [7]):

$$\underline{W}^+ - \underline{W}^- = \frac{2\pi}{B} \frac{(\nabla r\overline{V}_\theta \times \nabla\alpha) \times \nabla\alpha}{\nabla\alpha . \nabla\alpha} \qquad (12)$$

where, for a pump, $\underline{W}^+$ is the relative velocity at the pressure surface and $\underline{W}^-$ is the relative velocity at the suction surface. This expression is physically plausible as it gives a jump in velocity which lies on the blade since it is normal to $\nabla\alpha$ (a vector itself normal to the blade). In addition, we would expect the jump to be normal to the vorticity vector, $\frac{2\pi}{B}[\nabla r\overline{V}_\theta \times \nabla\alpha]$, lying in the blade. Knowing the velocity jump and assuming the velocity profile is linear between suction and pressure surfaces (a frequent approximation in hub-to-shroud methods, see [12]) it is possible to estimate the velocities at the suction and pressure surfaces. Indeed, their values are going to be equal to the mean velocity (solution of the axisymmetric problem) plus or minus one-half the velocity jump. Afterwards, using the fact that the flow is irrotational at inlet and applying Bernoulli's equation, the expression for the difference in pressure across the blades is obtained. The final expression is (see [7]):

$$p^+ - p^- = \frac{2\pi}{B} \rho \underline{\overline{W}} . \nabla r\overline{V}_\theta \qquad (13)$$

Third International Conference on Inverse Design Concepts and Optimization in Engineering Sciences (ICIDES-III), Editor: G.S. Dulikravich, Washington D.C., October 23-25, 1991.

where p^+ is the pressure at the pressure surface, p^- the pressure at the suction surface and ρ is the fluid density. $\overline{W}$ is known from the velocity field calculation so that all the terms in the right-hand side of eq. (13) are known, enabling the estimation of the pressure loading across the blades.

2.4 Flowchart.

To end section 2, we would like to draw the attention of the reader to the fact that the vorticity depends on the blade shape, f, which in its turn is an outcome of the calculations. So, the calculations must be iterated until convergence is obtained. This is done according to the following flowchart:

(i) input of initial data – specified values of $r\overline{V}_\theta$, definition of meridional section and body-fitted curvilinear coordinate system and all the relevant parameters;
(ii) estimation of a first guess for f, assuming that the mean velocity is uniform along the quasi-orthogonals;

(iii) using the input values of mean swirl, $r\overline{V}_\theta$, and the values of blade shape, f, from last iteration, calculate the mean velocity field (solution of eq. (7));
(iv) update the blade shape, f, by integration of eq. (11);
(v) if the solution is converged output the blade shape, f, and other relevant results. Otherwise go back to step (iii) and initiate a new iteration.

This flowchart was implemented as a FORTRAN computer code and applied to the design of the impeller of a mixed-flow pump.

3- DISCUSSION OF APPLICATION TO A MIXED-FLOW PUMP

In order to show the potentialities of the method, it was decided to apply it to the design of a mixed-flow pump. The chosen pump was based on a real machine which had as nominal conditions a value of 28 m for the head, H, a nominal volume flow, Q, of $600 m^3/h$ and a rotational speed of 1450 r.p.m.. These values give a nondimensional specific speed parameter equal to 0.919. The rotor has 8 blades and a tip diameter equal to 320 mm. This value will be used to non-dimensionalize all the linear dimensions and the velocities will be made nondimensional by using the transport blade tip velocity, ωr_{tip} (its value is 24.3 m/s).

The meridional geometry used in the calculations is based on an existing pump (with minor alterations), designed by a Portuguese pump manufacturer using hand calculations and graphical processes. The final meridional shape used is defined in Fig. 1. A grid formed by 145 quasi-orthogonals and 57 quasi-streamlines was fitted to this meridional section, there being in the blade region a total of 61x57 points. Fig. 2 shows every other line of the grid used. As can be seen, a region upstream and downstream of the blade zone was considered in the calculations.

An important input to the present inverse method is the specification of mean swirl, $r\overline{V}_\theta$. As it is supposed that the pump accepts the flow with no swirl, the value of $r\overline{V}_\theta$ along the entire leading edge is considered equal to zero. At the trailing edge the value was also considered constant in order to obtain a design that executes constant work along the span. The necessary value of $r\overline{V}_\theta$ at the trailing edge depends on the work per unit mass of fluid desired for the rotor, which is a value determined by the desired head and an assumed value of efficiency (in our case considered equal to 0.86). The value of $r\overline{V}_\theta$ used at the trailing edge is $0.5411\ \omega r^2_{tip}$.

Third International Conference on Inverse Design Concepts and Optimization in Engineering Sciences (ICIDES-III), Editor: G.S. Dulikravich, Washington D.C., October 23-25, 1991.

Another restriction was imposed on the derivatives of the mean swirl at the leading and trailing edges, namely, we forced there a zero derivative along the quasi-streamlines. This was done in order to obtain a zero pressure loading at the trailing edge (as is required by the Kutta-Joukowski condition), and at the leading edge. The equivalence between a zero derivative of the mean swirl and zero pressure loading can be seen from expression (13) which shows that the pressure loading depends on the gradient of mean swirl, being zero where the gradient of $r\overline{V}_\theta$ is zero, as it is the case at the leading and trailing edges.

This close equivalence between derivatives of mean swirl and pressure loading across the blade was one of the factors used when choosing the input mean swirl, $r\overline{V}_\theta$, along the entire meridional section, and whose contours are presented in Fig. 3. The other factor considered was the attempt to avoid a blade shape too twisted which would be difficult to manufacture. These two factors were exactly the same guidelines advanced and discussed in [7] when choosing the mean swirl for a completely different turbomachine, a radial inflow turbine.

Recalling briefly the arguments advanced in [7] and which are sufficiently general to apply to the present situation, it is evident from expression (13) that the pressure blade loading is proportional to the product of the modulus of the relative velocity and the value of the derivative of $r\overline{V}_\theta$ along the meridional projection of the flow streamlines, or:

$$p^+ - p^- = \frac{2\pi}{B} \rho \left| \overline{W} \right| \frac{\partial r\overline{V}_\theta}{\partial s} \qquad (14)$$

where s is distance along the meridional projection of the streamlines. In a well designed machine, $\left| \overline{W} \right|$ does not vary abruptly and the streamlines have a direction close to the quasi-streamlines. Therefore, eq. (14) implies that the pressure blade loading is mainly influenced by the value of the derivative of $r\overline{V}_\theta$ along the quasi-streamlines, which is a value known at the start of the calculations, and so can be controlled. In this way, if it is desired to design a blade with a big loading near the leading edge, then the derivatives of $r\overline{V}_\theta$ along the quasi-streamlines should have large values near the leading edge. In addition, if one wishes to obtain a pressure loading with a smooth evolution, then the derivatives of $r\overline{V}_\theta$ should be watched with special care, specifying them as smooth as possible and with a monotonic variation from the leading to the trailing edge. From the point of view of the pressure loading the most unfavourable situation is along the shroud, so that there the derivatives should have a smooth variation.

The other argument that one should bear in mind when choosing the input mean swirl schedule is the one connected with the amount of blade twist. In order to clearly understand this argument it is important to rewrite eq. (11) along a streamline, obtaining:

Third International Conference on Inverse Design Concepts and Optimization in Engineering Sciences (ICIDES-III), Editor: G.S. Dulikravich, Washington D.C., October 23-25, 1991.

$$f_a - f_b = \int_b^a \frac{\overline{W}_\theta}{r\overline{V}_m} dm = \int_b^a \frac{(\overline{V}_\theta - \omega r)}{r\overline{V}_m} dm \qquad (15)$$

where a and b are two arbitrary points on the same streamline, f is the angular coordinate of the blade, $\overline{V}_m$ is the mean velocity in the meridional plane and m is the distance along the meridional projection of the streamline. If one wishes to control the total variation in the angular coordinate of the blade, $f_a - f_b$, it is convenient to avoid high values for the expression under the integral sign in eq. (15). This can be achieved if one specifies the value of $r\overline{V}_\theta$ so that $\overline{W}_\theta$ has small values, or in other words, if one specifies $r\overline{V}_\theta$ so that the value of $\overline{V}_\theta$ closely follows the local value of the transport velocity, ωr. This is the more important, the lower is the value of radius and of the meridional velocity $\overline{V}_m$. From the point of view of highly twisted blades, the most critical streamsurface is the hub, not only because there the radius and meridional velocity take the lower values in the machine, but also because the meridional flow path is usually longer along the hub than anywhere else in the machine.

The next set of four figures is presented to demonstrate that the two above points were taken into consideration. Indeed, Fig. 4 gives the evolution of the input $r\overline{V}_\theta$ on the hub and the shroud. It is clearly seen that on the shroud the evolution of $r\overline{V}_\theta$ is quite gradual and smooth while at the hub the opposite happens.

Fig. 5 shows, on the same graph, the values of ωr and the specified values of $\overline{V}_\theta$ at the hub. Here it is evident that, on the hub, $\overline{V}_\theta$ has an evolution which is almost parallel to ωr, for most of the flow path and without much consideration in the direction of obtaining smooth derivatives. This was done so that $\overline{W}_\theta$ at the hub presented small and approximately constant values along most of the blade, leading to a reasonable overall change in the values of blade angular coordinate, f.

From the next figure, Fig. 6, it can be seen that the contrary happens on the shroud, where $\overline{V}_\theta$ was chosen to have a smooth variation rather than following the local value of blade speed, ωr. In fact, the main concern when specifying the mean swirl at the shroud was to obtain an adequate pressure distribution and not to control the overall variation in the blade angular coordinate, f.

The above ideas are corroborated by the next figure, Fig. 7, where the derivatives of $r\overline{V}_\theta$ along the quasi-streamlines for the hub and the shroud are presented. As can be clearly seen, the derivatives at the shroud present a smooth variation while the same does not apply at the hub, where a more abrupt change of the $r\overline{V}_\theta$ derivatives can be detected.

Using the close relationship between $r\overline{V}_\theta$ derivatives and pressure loading one can conclude that the present design presents a large loading near the leading edge at

Third International Conference on Inverse Design Concepts and Optimization in Engineering Sciences (ICIDES-III), Editor: G.S. Dulikravich, Washington D.C., October 23-25, 1991.

the shroud streamsurface, while at the hub streamsurface the blade loading is more evenly spread. However, one should point out that, at the hub, the derivative is zero for approximately the last 15% of the meridional flow path. This indicates that there will be a small pressure loading along the last portion of the blade at the hub, suggesting that perhaps one could use a shorter flow path there. This idea would entail an alteration of the trailing edge shape (using a trailing edge inclined to the axis, instead of parallel) and so, was not pursued further.

The inverse computer code was run, using the input described above together with a stacking condition imposed at the trailing edge and which consists of a linear variation of f between the value of 0.0 (at the hub) and 0.10 (at the shroud). As a result the blade shape described in the next figure was obtained. Since it is difficult to visualize the blade three-dimensional geometry, we decided to present the blade geometry in Fig. 8 as a view of two consecutive blades, as would be seen by an observer looking in the direction of the impeller axis. The blade obtained seems typical of a pump impeller and no particular problems are envisaged during its manufacture, since it is not a highly twisted blade.

In the next plot, Fig. 9, it is presented the estimated pressure distribution on hub and shroud, assuming a linear variation of the velocity from suction to pressure surfaces and using the procedure already discussed in subsection 2.3. The pressure coefficient, C_p , used in this plot is defined as:

$$C_p = \left(\frac{W}{W_{ref}}\right)^2 - 1 \qquad (16)$$

where W_{ref} is a reference relative velocity, which is equal to $0.311\omega r_{tip}$ in the present case. Notice that the loading has a behaviour quite similar to the evolution of the derivatives of $r\overline{V}_\theta$ along the quasi-streamlines, shown in Fig. 7, bearing out the comments made above, concerning the close relationship between derivatives of $r\overline{V}_\theta$ and pressure loading. For example, it is seen that, at the hub, the pressure loading varies more abruptly than at the shroud, and along the last 15% of the flow path at hub the pressure loading is zero as was already expected from the values of derivatives of mean swirl. It should also be remarked that the distribution of pressure on the blade surfaces at the hub is not ideal since its variation is not smooth and presents some decclerations. However, the optimization of the pressure distribution would entail changes in the meridional section of the machine, and so was not tried in this work.

One advantage of the present method lies in the fact that it is quite rapid, requiring small amounts of CPU time. In fact, the present run required 1m 39s of CPU time in a VAX 3400 computer. Since it is computationaly so cheap, several different input mean swirl distributions can be scanned quickly, enabling the choice of the most appropriate mean swirl schedule.

4- CONCLUSIONS

A through-flow (hub-to-shroud) inverse method was proposed and implemented as a computer code. In the present implementation the flow is assumed incompressible, irrotational at inlet and the blade thickness was not considered during the calculations. The necessary equations are presented and, as an example of a possible application, the inverse method was used to redesign the rotor of a mixed-flow pump.

The present method uses as an input specification the value of mean swirl, $r\overline{V}_\theta$. This input specification was chosen using a reasoning similar to that used in [7]. This is remarkable, since the turbomachine designed in [7] was a radial-inflow

turbine, and indicates that the strategy developed there is quite general, being able to cope with radically different machines. Briefly, this strategy consists in using the input mean swirl to control the pressure loading on the blades and the overall variation in the angular coordinate of the blade, f.

This work also shows that further research should be done in order to obtain reasonable pressure distributions on the blade surfaces. In fact, the design presented here has a pressure distribution on the hub which is not the ideal one. The optimization of the pressure distribution will probably involve some changes in the meridional section (hub and shroud contours).

One advantage of the present technique is the fact that it requires small amounts of CPU time. So it is a convenient tool to scan quickly and inexpensively several different input mean swirl distributions, in order to find the most appropriate one.

5. REFERENCES

[1] Lazarkiewicz, S. and Troskolanski, A.T., *Impeller Pumps*, Pergamon Press, Oxford, 1965.

[2] Lobanoff, V. S. and Ross, R. R., *Centrifugal Pumps: Design & Application*, Gulf Publishing Company, Houston, Texas, chapter 3, pp. 28-45, 1985.

[3] Smith, K. J. and Hamrick, J. T., *A Rapid Approximate Method for the Design of Hub Shroud Profiles of Centrifugal Impellers of Given Blade Shape*, NACA Technical Note 3399, 1955.

[4] Osborn, W. M.; Smith K. J. and Hamrick, J. T, , *Design and Test of Mixed-Flow Impellers* VIII- *Comparison of Experimental Results for Three Impellers with Shroud Redesigned by Rapid Approximate Method*, NACA Research Memorandum E56L07, 1957.

[5] Jansen, W, and Kirschner, A. M., *Impeller Blade Design Method for Centrifugal Compressors*, NASA SP304, Pt. 2, pp. 537-563, 1974.

[6] Wu, C.-H., *A General Theory of Three- Dimensional Flow in Subsonic and Supersonic Turbomachines of Axial-, Radial- and Mixed-Flow Types*, NACA Technical Note 2604, January 1952.

[7] Borges, J. E., *A Three-Dimensional Inverse Method for Turbomachinery: Part I- Theory*, Transactions of the ASME, Journal of Turbomachinery, Vol. 112, pp. 346-354, 1990.

[8] Hawthorne, W. R., *The Actuator Duct Representation of Turbomachinery Blade Rows*, CUED/A- Turbo/TR 119, 1983.

[9] Thompson, J. F.; Warsi, Z. U. A. and Mastin, C. W., *Boundary-Fitted Curvilinear Coordinate Systems for Solution of Partial Differential Equations – A Review*, Journal of Computational Physics, nº 47, pp. 1- 108, 1982.

[10] Brandt, A., *Multi-Level Adaptive Solutions to Boundary-Value Problems*, Mathematics of Computation, Vol. 31, nº 138, pp. 333-390, 1977.

[11] Roache, P. J., *Computational Fluid Dynamics*, Hermosa Publishers, Albuquerque, N.M., U.S.A., pp. 84-85, 1982.

[12] Stanitz, J. D. and Prian, V. D., *A Rapid Approximate Method for Determining Velocity Distribution on Impeller Blades of Centrifugal Compressors*, NACA Technical Note 2421, 1951.

Third International Conference on Inverse Design Concepts and Optimization in Engineering Sciences (ICIDES-III), Editor: G.S. Dulikravich, Washington D.C., October 23-25, 1991.

ACKNOWLEDGEMENTS

The work described here was financially supported by CTAMFUTL/INIC. The suggestions and help of the technical staff of EFACEC are also gratefully acknowledged.

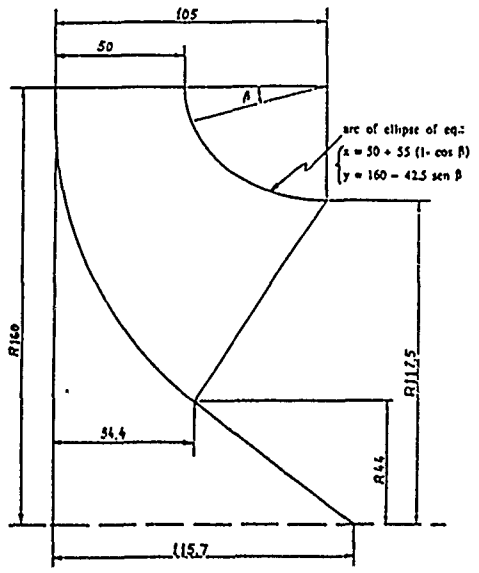


Fig. 1 Definition of meridional geometry

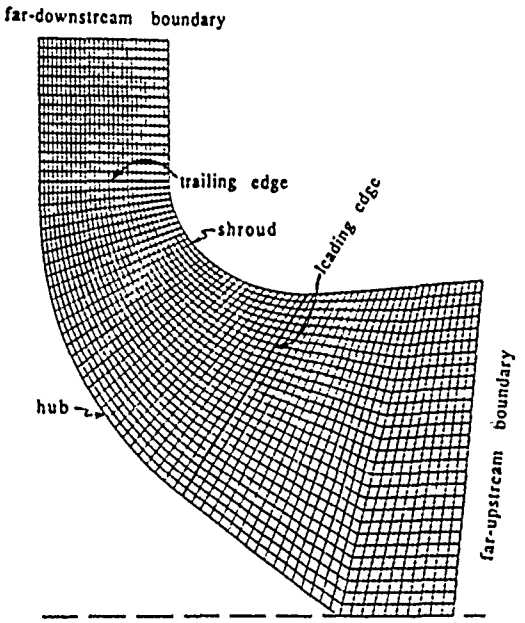


Fig. 2 Grid used in the meridional plane

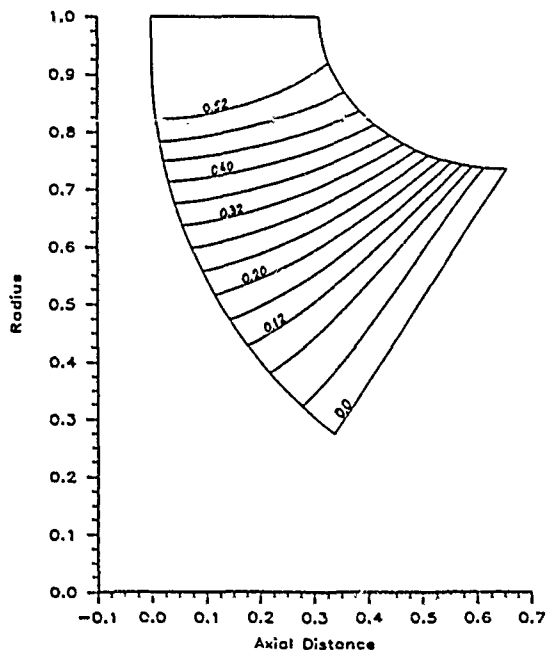


Fig. 3 Contours of the input mean swirl distribution (defined as $r\overline{V}_\theta / (r_{tip}\ U_{tip})$)

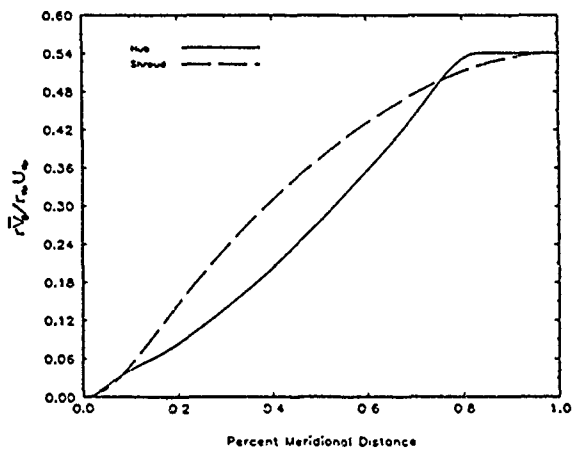


Fig. 4 Input mean swirl distribution at hub and shroud

Third International Conference on Inverse Design Concepts and Optimization in Engineering Sciences (ICIDES-III), Editor: G.S. Dulikravich, Washington D.C., October 23-25, 1991.

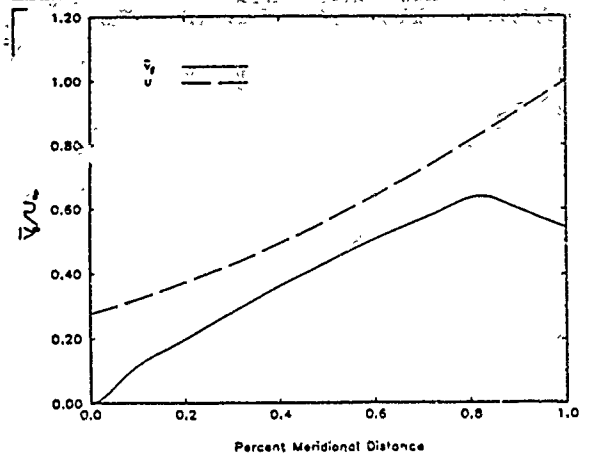


Fig. 5 Mean tangential velocity and blade speed at hub

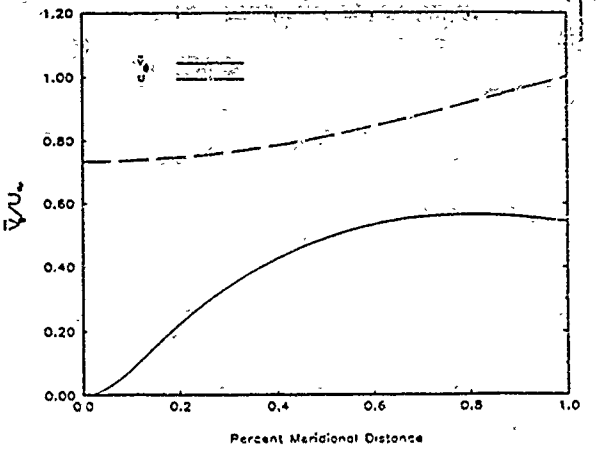


Fig. 6 Mean tangential velocity and blade speed at shroud

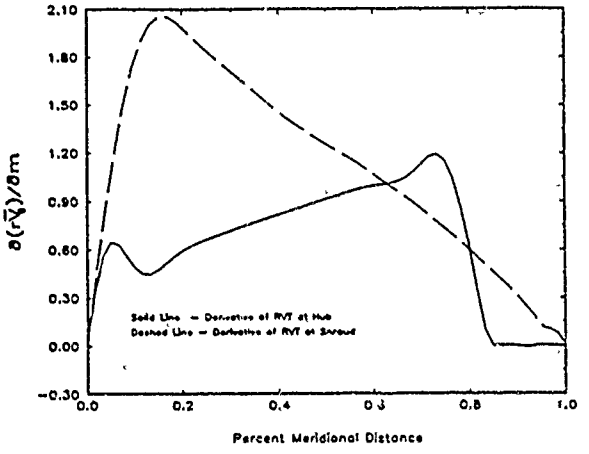


Fig. 7 Derivatives of the input mean swirl distribution

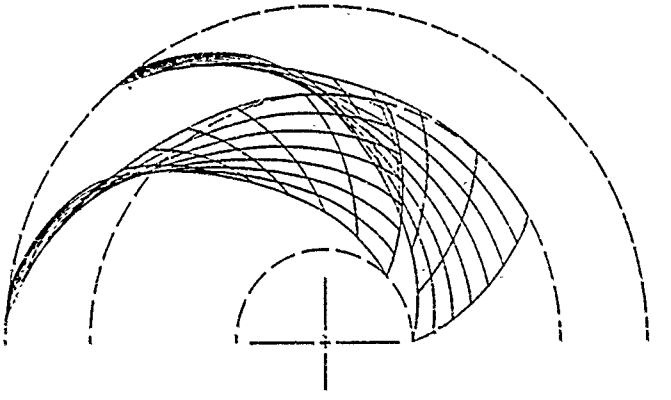


Fig. 8 Blade projection along the axis

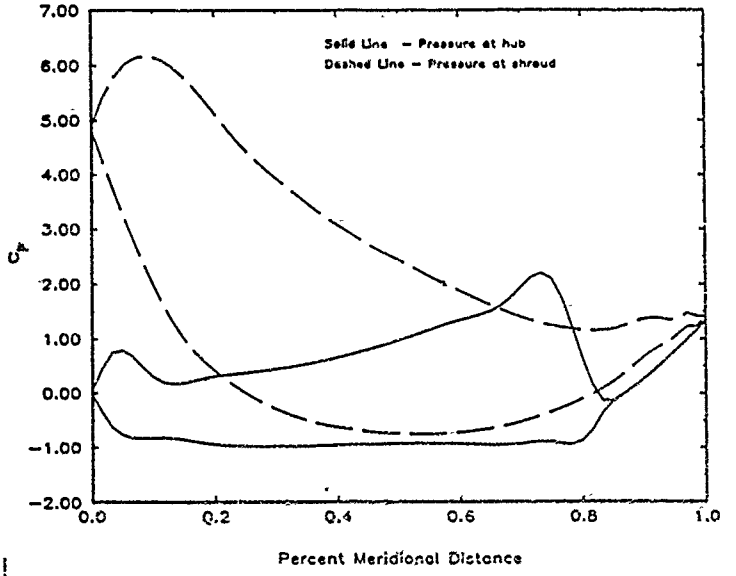


Fig. 9 Pressure distribution on hub and shroud

Third International Conference on Inverse Design Concepts and Optimization in Engineering Sciences (ICIDES-III), Editor: G.S. Dulikravich, Washington D.C., October 23-25, 1991.

AN INVERSE INVISCID METHOD FOR THE DESIGN OF QUASI-THREE DIMENSIONAL ROTATING TURBOMACHINERY CASCADES

BONATAKI, E. , Research Assistant
CHAVIAROPOULOS, P., Ph.D. Research Engineer
PAPAILIOU, K.D. , Professor

NATIONAL TECHNICAL UNIVERSITY OF ATHENS
Lab. of Thermal Turbomachines
P.O. Box 64069, 15710 Athens, Greece.

ABSTRACT

A new inverse inviscid method suitable for the design of rotating blade sections lying on an arbitrary axisymmetric stream-surface with varying streamtube width is presented.

Given are the geometry of the axisymmetric stream-surface and the streamtube width variation with meridional distance, the number of blades, the inlet flow conditions, the rotational speed and the suction and pressure side velocity distributions as functions of the normalized arc-length. The flow is considered irrotational in the absolute frame of reference and compressible. The output of the computation is the blade section that satisfies the above data.

The method solves the flow equations on a ($\Phi 1,\Psi$) potential function-streamfunction plane for the velocity modulus, W and the flow angle β; the blade section shape can then be obtained as part of the physical plane geometry by integrating the flow angle distribution along streamlines. The ($\Phi 1,\Psi$) plane is defined so that the monotonic behaviour of the potential function is guaranteed, even in cases with high peripheral velocities.

The method is validated on a rotating turbine case and used to design new blades. To obtain a closed blade a set of closure conditions has been developed and refered in the paper.

LIST OF SYMBOLS

A1...A9	differential equation coefficients	B	constant number
m	meridional distance	β	flow angle
$\vec{n}$	outward unit vector	(Δn)	streamtube thickness
R	radius	θ	peripheral distance
$\vec{U}$	peripheral velocity	$\Phi 1$	potential-type function
$\vec{W}$	relative velocity	Ψ	stream function

INTRODUCTION

The design method which is presented in this paper is developed in order to use the results of the meridional plane calculation and in particular the geometry of the axisymmetric flow streamtubes. The design method is, then, applied in order to specify the blade section shape lying on each axisymmetric stream-surface. The complete blade is constructed by stacking these blade section shapes in the span-wise sence, as desired.

Blade design methods have already been developed in the past, for both incompressible and compressible flows (refs [1]-[11]). However, most of them refer to plane cascade configurations only. During recent years the topic of developing blade design methodologies has received particular attention and important contributions have been published in this framework (refs [1]-[5]).

The aim of the present effort was to develop an inverse inviscid method supporting the blade optimization procedure described in reference [19] and capable to deal with the general case of an arbitrary rotating cascade. The method follows the work of Schmidt[9] and Zanneti[11] concerning the equations employed. However, it formulates the problem in a different way and employs different numerical techniques as well as closure conditions, for reasons explained below. A first

Third International Conference on Inverse Design Concepts and Optimization in Engineering Sciences (ICIDES-III), Editor: G.S. Dulikravich, Washington D.C., October 23-25, 1991.

version of the present method, using the classical potential function/stream-function definitions was presented in reference [12]. Nevertheless, problems occured, when the method was applied to high speed rotating cascades because of the non-monotonic behaviour of the potential function. Recently, a new version has been developed, capable of overcoming this problem. This improved version which makes use of a more appropriate definition of the potential function/stream-function plane (here refered as ($\Phi 1,\Psi$)) is presented in the present paper.

POSITION OF THE PROBLEM AND DEVELOPMENT OF THE EQUATIONS

A schematic representation of a peripheral cascade is given in figure 1. The aim is to compute a closed blade section, given the stream-surface geometry, the streamtube width variation with the meridional distance (m), the approximate number of blades (N), the inlet stagnation conditions (P_{T1},T_{T1}) and velocity vector ($\vec{W}_1$), the meridional position of the inlet stagnation point (m_1), the rotational speed (ω) and the derived outlet flow angle (β_2). Assumed given, as well, are the suction side velocity distribution and an approximate pressure side velocity distribution versus arc length. The number of blades and the pressure side velocity distribution will change during the computation, in order to obtain a closed profile, with the constraint to alter them as little as possible.

The flow is considered steady, inviscid, compressible subsonic and irrotational in the absolute frame of reference.

The physical plane is presented in figure 2a. The equations written on an axially symmetric system (m,θ), are:

a) the continuity equation

$$\frac{\partial}{\partial m}(\rho R (\Delta n) W_m) + \frac{\partial}{R\partial\theta}(\rho R (\Delta n) W_u) = 0 \tag{1}$$

b) the absolute irrotational flow equation

$$\frac{1}{R}\frac{\partial(R W_u + \omega R^2)}{\partial m} - \frac{\partial W_m}{R\partial\theta} = 0 \tag{2}$$

In the previous version of the method (ref.[12]) a transformation is performed to the (Φ,Ψ) plane defined as

$$\vec{n} \times \nabla_s \Psi = \rho (\Delta n) \vec{W} \tag{3}$$

$$\nabla_s \Phi = (\vec{W} + \vec{\omega} \times \vec{R}) \tag{4}$$

where ∇_s is the surface gradient operator and $\vec{n}$ the normal to the surface unit vector.

The difference $d\Phi$ along iso-Ψ lines is equal to

$$d\Phi = (\vec{W} + \vec{\omega} \times \vec{R})\, d\vec{s} = W ds + \omega R^2 d\theta \tag{5}$$

This difference, however, is not always positive since there may exist certain high peripheral speed cases for which $d\Phi$ locally takes negative values and, thus, Φ is non-monotonic along streamlines. This fact prohibits the mapping of the physical coordinate plane to the potential/stream-function plane (the Jacobian of the transformation becomes zero) and thus no arithmetical solution is possible. To overcome this inconveniency, a new transformed plane ($\Phi 1,\Psi$) is defined in the following way

$$\vec{n} \times \nabla s\, \Psi = \rho (\Delta n) \vec{W} \tag{6}$$

Third International Conference on Inverse Design Concepts and Optimization in Engineering Sciences (ICIDES-III), Editor: G.S. Dulikravich, Washington D.C., October 23-25, 1991.

$$\nabla s\,\Phi 1 = \vec{W} + \vec{U} - (\vec{B}/R) \tag{7}$$

where $\vec{B}$ is a vector parallel to the peripheral velocity $\vec{U}$ and its modulus B is constant. The difference $d\Phi 1$ along a streamline is, then, equal to

$$d\Phi 1 = (\vec{W}+\vec{\omega}x\vec{R}-\vec{B}/R)\cdot d\vec{s} = Wds+(\omega R^2-B)d\theta \tag{8}$$

It is obvious that B can be selected is such a way that guaranties the positivity of the Jacobian of the transformation from the physical to the $(\Phi 1,\Psi)$-plane.

On the $(\Phi 1,\Psi)$-plane the equations of continuity and absolute irrotational flow can be written in the form

$$A1(\ln W)_{\Phi 1\Phi 1} + A2(\ln W)_{\Phi 1}^{2} + A3(\ln W)_{\Phi 1} + A4(\ln W)_{\Psi\Psi} + A5(\ln W)_{\Psi}^{2} +$$

$$A6(\ln W)_{\Psi} + A7(\ln W)_{\Phi 1\Psi} + A8(\ln W)_{\Phi 1}(\ln W)_{\Psi} + A9 = 0 \tag{9}$$

$$\frac{\partial \beta}{\partial \Psi} = F1(W,\beta,R,(\Delta n)) \tag{10}$$

$$\frac{\partial \beta}{\partial \Phi 1} = F2(W,\beta,R,(\Delta n)) \tag{11}$$

The expressions for the coefficients A1 to A9 are given in the reference [15]. In the above equations $\Phi 1$ and Ψ are the independant variables, while the velocity modulus (W) and the flow angle (β) are the dependent ones. Equations (10) and (11) for the flow angle are equivalent so during the calculation one of them may be utilized.

THE BOUNDARY CONDITIONS ON THE $(\Phi 1,\Psi)$-PLANE

The transformed plane-$(\Phi 1,\Psi)$ is presented in figure 2b. The flow quantities are known at station (1), inlet, and the flow angle at station (2), outlet. The integral mass flux conservation equation, the energy conservation equation along a meridional streamline and the isentropic flow relations are used to calculate flow quantities at station (2). The integral mass flux equation is written in the form

$$\varrho_2 W_2 = \varrho_1 W_2 \frac{R_1 \cos\beta_1 (\Delta n)_1}{R_2 \cos\beta_2 (\Delta n)_2} \tag{12}$$

and the energy conservation equation along with the isentropic flow relations results to the following expression

$$\frac{\varrho_2}{\varrho_1} = \left(1 + \frac{W_1^2-U_1^2}{2c_pT_1} - \frac{W_2^2-U_2^2}{2c_pT_1}\right)^{1/\gamma-1} \tag{13}$$

From these two equations the flow quantities (ϱ_2,W_2) may be calculated for a known flow angle β_2.

The integral momentum equation can be written in the form

$$\Gamma = \oint_{\text{blade}} \vec{V}d\vec{s} = \oint_{\text{blade}} Wds + \Gamma_1 = \frac{2\pi}{N}(R_1V_{u1}-R_2V_{u2}) \tag{14}$$

Third International Conference on Inverse Design Concepts and Optimization in Engineering Sciences (ICIDES-III), Editor: G.S. Dulikravich, Washington D.C., October 23-25, 1991.

where

$$\Gamma_1 = \oint_{\text{blade}} \omega R^2 \, d\theta$$

This equation relates the flow conditions at the inlet and the outlet with the circulation Γ which depends on the velocity distributions along suction and pressure side, as well as, on the blade section geometry. Integral Γ_1, depending on the blade section geometry, is not a priori known. This explains one of the difficulties of the inverse methodology applied to arbitrary rotating cascades. Note that Γ_1 is zero only when the radius R is constant. During the computational procedure the integral Γ_1 is given an initial reasonable value and corrected accordingly, each time a blade section shape is computed. In any case the value of Γ must be compatible with the imposed value of the outlet flow angle β_2, so that, if the suction side velocity distribution (being most sensitive) must be maintained, the pressure side velocity distribution must be chosen to satisfy this value of Γ.

Considering, again, figure 2, periodic conditions are imposed along the ((AB),(EF)) and ((CD),(GH)) pairs of boundaries. W(Φ1) is specified along the suction and pressure side solid boundaries and the corresponding value of Φ1 is calculated from the following relation

$$d\Phi 1 = W ds + (\omega R^2 - B)\, d\theta \tag{15}$$

Consequently, differences in potential from a station ν to a station μ may be calculated as

$$\Delta\Phi 1 \Big|_{\nu}^{\mu} = \int_{\nu}^{\mu} W ds + \int_{\nu}^{\mu} (\omega R^2 - B)\, d\theta \tag{16}$$

Moreover, the way that the (Φ1,Ψ)-plane was built assures that

$$\Delta\Phi 1 \Big|_{A}^{B} = \Delta\Phi \Big|_{E}^{F} ; \Delta\Phi 1 \Big|_{B}^{C} + \Delta\Phi 1 \Big|_{G}^{F} = \Gamma ; \Delta\Phi 1 \Big|_{C}^{D} = \Delta\Phi 1 \Big|_{G}^{H} \tag{17}$$

During the computational procedure, the magnitudes of $\Delta\Phi \Big|_{A}^{B}$ and $\Delta\Phi \Big|_{C}^{D}$ are specified with the constraint to take them large enough in order to reach at AE and DH (see figure 2b) uniform conditions with sufficient accuracy. In this way, the position of the inlet and outlet of the calculation domain in the physical plane (positions of AE and DH in figure 2a) is not yet specified.However, using equation (4) along the peripheral direction one may get

$$d\Psi = \varrho(\Delta n) W \cos\beta R d\theta \tag{18}$$

so that the corresponding stream function differences are described by the following relation at the inlet and the outlet stations

$$\Delta\Psi \Big|_{\nu}^{\mu} = \int_{\nu}^{\mu} \varrho(\Delta n) W \cos\beta R d\theta \tag{19}$$

Along the inlet and outlet stations the flow is uniform with velocities and flow angles, W_1, W_2 and β_1, β_2, respectively. Consequently, if $\Psi_E = \Psi_F = \Psi_G = \Psi_H = 0$ is the streamfunction value characterizing the lower boundary, then the one characterizing the upper boundary, according to equation (19), is

$$\left[\Delta\Psi \Big|_{E}^{A} = \varrho_1 W_1 \cos\beta_1 \frac{2\pi R_1}{N} (\Delta n)_1 = \varrho_2 W_2 \cos\beta_2 \frac{2\pi R_2}{N} (\Delta n)_2 = \Delta\Psi \Big|_{H}^{D} \right] \qquad (20)$$

The upper boundary being a streamline, $\Psi_A=\Psi_B=\Psi_C=\Psi_D$.

THE NUMERICAL INTEGRATION OF THE EQUATIONS

Equations (9) and (10) or (11) are considered in the $(\Phi 1,\Psi)$-plane, which in general is non-orthogonal. If one considers suction and pressure side extensions of equal length in the periodic zones (to facilitate the application of the periodicity conditions), then the computational domain on the $(\Phi 1,\Psi)$-plane takes a trapezoidal form (see figure 2). A non uniform discretization of the $(\Phi 1,\Psi)$ boundary regions was found to be efficient, permitting the stretching of the grid lines in the near-leading and near-trailing edge regions of the blade section, where the velocity gradients are large. In view of the above, the resulting grid on the $(\Phi 1,\Psi)$-plane, composed only of straight lines, is generally skewed and stretched. In order to increase the generality of the solver and the accuracy of the solution, avoiding at the same time complexities (such as patched grid techniques), an additional body-fitted coordinate transformation is performed, which maps the $(\Phi 1,\Psi)$-plane to an orthogonal (ξ,η)-plane with square cells (see figure 2).

The resulting equation on W in the (ξ,η)-plane is discretized by use of second-order accurate finite-difference/ finite volume centered schemes. The discrete equation is, then, linearized, transfering all non-linear terms ($(\ln W)^2$, for example) to the right hand side (fixed point algorithm). The resulting system of algebraic equations, which has a 9-diagonal banded, non-symmetric characteristic matrix, is solved iteratively using the MSIP (refs [13],[14]) method (incomplete L-U approximate factorization procedure).

Once the velocity field is computed, the flow angle field is obtained integrating the ordinary differential equations (10) or (11), along the iso-$\Phi 1$ or the iso-Ψ lines. A fourth order Runge-Kutta method is used during this step. In practice, equation (11) is first integrated along the cascade mean streamline and the computed β-mean streamline values are used as boundary conditions for the integration of equation (10) along the iso-$\Phi 1$ lines. This procedure involves only a tangential derivation of the flow quantities along the blade and is, thus, more accurate. If a second order normal derivation along the blade is used, then quadratic extrapolation procedures would be required, decreasing the accuracy (mainly) in the sensitive leading edge region. The above procedure provides the complete $\beta(\Phi 1,\Psi)$ field and, consequently, the blade coordinates.

THE COMPUTATIONAL ALGORITHM

A computational algorithm was constructed, outlined by the following steps (without considering conditions for section closure, which will be examined later).

STEP 1 : The exit plane flow quantities are calculated through equations (12) and (13). A value for the integral Γ_1 is assumed and a velocity distribution for the pressure side compatible with the value of the circulation Γ issued from equation (14) is established. The value of constant B is defined so that $\Phi 1$ is monotonic along streamlines. The values of the potential differences $\Delta\Phi 1\,|_{A}^{B}$ and $\Delta\Phi 1\,|_{C}^{D}$ are specified.

STEP2 : A first approximation of the $(\Phi 1,\Psi)$-plane contour is considered and the boundary conditions for the velocity (through equations (16) and (19)) and the angle (utilizing plausible angle distributions), are specified. The interior grid points of the region (BCGF) are established using a simple linear procedure. In the upstream (ABFE) and downstream (CDHG) regions, the points on the boundaries are chosen and the grid is constructed, so that periodic conditions can be checked without interpolation. The complete velocity and flow angle fields are initialized making use of the values at the boundaries, through a linear interpolation. An initial estimate of (Δn) and R for each node is made, as well.

STEP 3 : The coefficients Ai(i=1,9) appearing in equation (9) are calculated.

STEP 4 : Equation (9) is solved for $W(\Phi 1,\Psi)$ using the numerical procedure and technique

Third International Conference on Inverse Design Concepts and Optimization in Engineering Sciences (ICIDES-III), Editor: G.S. Dulikravich, Washington D.C., October 23-25, 1991.

described in the previous section. At this point, an iterative procedure is performed involving the previous step, that is, updating the values of the coefficients Ai. This updating is performed, utilizing the values of the velocity field of the previous iteration.

At the end of the computational procedure involved in this step, the values of W at the periodic boundaries will have been updated along with the complete velocity field.

STEP 5 : The flow angle field $\beta(\Phi 1,\Psi)$ is computed after numerical integration of equations (10) and/or (11) in the manner described in the previous section. During this procedure, new angle values are computed at the boundaries, as well.

STEP 6 : The blade section shape $\theta=\theta(m)$ is computed using the following geometrical relations, valid along a streamline

$$m = \int \cos\beta ds = m(s) \tag{21}$$

$$\theta = \int \frac{\sin\beta}{R} ds = \theta(s) \tag{22}$$

Utilizing these relations, the values of m and θ are computed along streamlines for the whole flow field, as well. An interpolation procedure is used in order to estimate the new set of values R(m(s)) and $\Delta n(m(s))$, which will be used, along with the updated values of the angles.

The exit conditions are calculated at station (2), using the same procedure as in STEP1. The integral Γ_1 is then computed and its new value is used to update Γ. The pressure side velocity distribution is in turn modified in order to satisfy the new value of the circulation. The B constant value is modified for the new geometry and velocity distribution. The boundaries and associated conditions can then be established for a new $(\Phi 1,\Psi)$-plane. A new grid is thus generated on the $(\Phi 1,\Psi)$-plane, moving along Ψ-lines and computing each time the value of $\Phi 1$ corresponding to the previously updated values of the velocity field.

STEP 7 : STEPS 3 to 6 are repeated until convergence is achieved.

As observed before, the blade section shape obtained from the above described computational procedure is not necessarily closed.

RESULTS AND DISCUSSION

To validate the method stationary and rotating cascade reconstruction test cases were selected. Exact cases were prefered where possible, while a direct solver was used to calculate the "target", velocity distribution when the later was not analytically known. Inevitably, slight inaccuracies in the results of the direct calculation method resulted in inaccuracies of the computed blade shape by the inverse method. A complete outline of the test cases utilized for the validation of the method are reported by Bonataki[15]. Results for two analytical test cases and for a radial inflow turbine are presented below.

In figure 3 the Gostelow[16] exact case (incompressible flow, compressor cascade) and in figure 4 the Hobson[17] exact case (high Mach number, high turning angle, low pitch to chord ratio) are presented to demonstrate the accuracy of the method. A radial inflow turbine case[18] (strong variation of R(m), rotational, variation of $\Delta n(m)$) is presented in figure 5. In all three cases the presented results include the initial blade shape, the corresponding suction and pressure side velocity distribution and the blade shape provided by the inverse method. The typical number of grid points utilized for the above calculations was (78x15) and the computing time needed for the complete solution was 20 cpu seconds in an ALLIANT FX 80 computer.

As a next step the method was used for the design of new profiles. Starting from an arbitrary suction and pressure side velocity distribution, a procedure was developed which in few iterations provides a closed profile. This procedure is based on an extended investigation upon the parameters which influences the blade section shape[12],[15], an investigation which has pointed out that the ratio

Third International Conference on Inverse Design Concepts and Optimization in Engineering Sciences (ICIDES-III), Editor: G.S. Dulikravich, Washington D.C., October 23-25, 1991.

of pressure to suction side arc length and the pitch to chord ratio could control blade section closure. It was also observed that the velocity distribution near the blade section edges influences a small part of the blade shape near these edges, while the blade thickness is directly related to the mean value of the velocity distributions along both the pressure and suction sides[12]. Using the information provided by the above investigation new profiles were designed.

A rotating turbine cascade lying on a conical surface along with the "target" velocity distribution is presented in figure 6.

In figure 7 a turbine blade is presented, which was used as the starting point for the design of a thicker blade. This new blade was obtained by increasing the level of the suction and pressure side velocity distributions while retaining the same inlet and outlet flow conditions. This particular design is quite revealing, since the "target" velocity was obtained by modifying the original one in such a way, so that the maximum velocity along the blade surfaces was not increased.

The blade section shape of a radial inflow turbine with speed of rotation is presented in figure 8a along with the corresponding R(m) and $\Delta n(m)$ distributions (figures 8c,8d) and "target" velocity distribution (figure 8b). This is a typical case where the classical (Φ,Ψ) plane definition fails and this is demonstrated in figures 8e,8f where the $(\Phi 1,\Psi)$-plane is plotted for two different values of the B parameter, $B=0$ (the classical Φ definition) and $B=1.1$ (the modified definition). It is evident that the modified definition suits better to the specific case.

CONCLUSIONS

A new inverse inviscid method for designing stationary or rotating, plane or axisymmetric cascades was presented in this paper.

Compared with previous efforts, the new method may handle cascades rotating with high speed and provide closed blade shapes in few external iterations.

The formulation and the numerics of the corresponding inverse method were discussed, in order to distinguish it from similar methods and reveal its relative merits.

Finally, some calculation results were presented, to certify the accuracy and the capabilities of the present effort.

REFERENCES

1. International Conference on Inverse Design Concepts in Engineering Sciences (ICIDES-I), Aero. Eng. Dept., University of Texas, Austin, TX, Oct. 17-18, 1984.
2. International Conference on Inverse Design Concepts and Optimization in Engineering Sciences (ICIDES-II), Aero. Eng. Dept., Penn State Univ., University Part, Oct.26-28, 1987.
3. AGARD Specialist's Meeting on Computational Methods for Aerodynamic Design (Inverse) and Optimization, Loen, Norway, May 24-25, 1989.
4. AGARD Lecture Series 167, Blading Design for Axial Turbomachines,Lyon,France,19-20 June,1989.
5. AGARD VKI Special Course on Inverse Methods in Airfoil Design, Rhode-Saint-Genese, Belgium, 14-18 May, 1990.
6. STANITZ J.D., "Design of Two-Dimensional Channels with Prescribed Velocity Distributions along the Channel Walls", NACA report 1115,1953.
7. SCHMIDT E., "Computation of Supercritical Compressor and Turbine Cascades With a Design Method for Transonic Flows", Trans. of ASME, Jr. of Engg. for Power, Vol.102, pp.68-74, Jan.1980.
8. SCHMIDT E., BERGER P., "Inverse Design of Supercritical Nozzles and Cascades", Int. J. Num. Meth. Eng., Vol. 22, Feb. 1986, pp. 417-432.
9. SCHMIDT E., "Inverse Methods for Blade Design, Controlled Diffusion Blading for Supercritical Compressor Flow", VKI-LS 1988-03 Transonic Compressors.
10. SCHMIDT E., KLIMETZEK F., "Inverse Computation of Transonic Internal Flows With Application for Multi-Point-Design of Supercritical Compressor Blades", Presented at the Specialists Meeting on Computational Methods for Aerodynamic Design (Inverse) and

Optimization,Loen,Norway,May 1989.

11. ZANNETTI L., "A Natural Formulation for the Solution of Two-Dimensional or Axisymmetric Inverse Problems", Int. J. Num. Meth. Eng., Vol.22, Feb.1986, pp.451-463.
12. BONATAKI E., CHAVIAROPOULOS P., PAPAILIOU K.D., "An Inverse Inviscid Method for the Design of Quasi-Three Dimensional Turbomachinery Cascades", presented at the International Symposium on Numerical Simulations in Turbomachinery Joint ASME-JSME Fluids Engineering Meeting, Oregon, June 23-26, 1991.
13. ZEDAN M. SCHNEIDER G.E., "A Three-Dimensional Modified Strongly Implicit Procedure for Heat Conduction", AIAA Journal, Vol. 21, 1983.
14. CHAVIAROPOULOS P., GIANNAKOGLOU K., PAPAILIOU K.D., "Numerical Computation of Three-Dimensional Rotational Inviscid Subsonic Flows, Using the Decomposition of the Flow Field into a Potential and a Rotational Part", ASME paper 86-GT-169.
15. BONATAKI E., "Inviscid Subsonic Inverse Method for the Design of Blade Sections along Arbitrary Axisymmetric Stream Surfaces with Varying Stream Tube Width", Ph.D.Thesis, in preparation, NTUA, Greece.
16. GOSTELOW J.P., "Potential Flow Through Cascades -A Comparison Between Exact and Approximate Solutions", A.R.C., CP No 807, 1963.
17. JONES D.J., "Test Cases for Inviscid Flow Field Methods, Reference Test Cases and Contributors", AGARD AR-211.
18. KATSANIS T., "Fortran Program for Calculating Transonic Velocities on a Blade-to-Blade Stream Surface of a Turbomachine", NASA TN D-5427, 1969.
19. BOURAS B., KARAGIANNIS F., CHAVIAROPOULOS P., PAPAILIOU K.D., "Arbitrary Blade Section Design Based on Viscous Considerations. Blade Optimization", presented at the International Symposium on Numerical Simulations in Turbomachinery Joint ASME-JSME Fluids Engineering Meeting, Portland, Oregon, June 23-26, 1991.

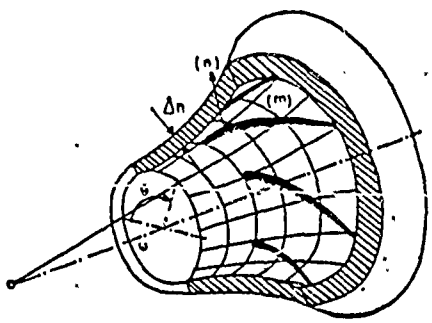
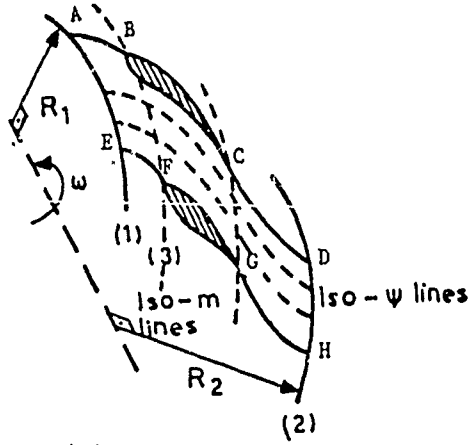
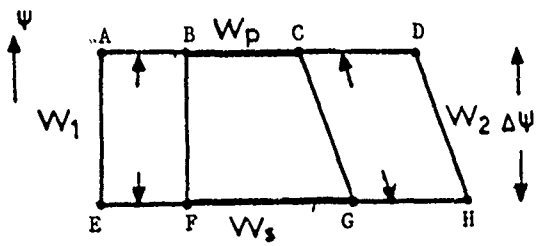


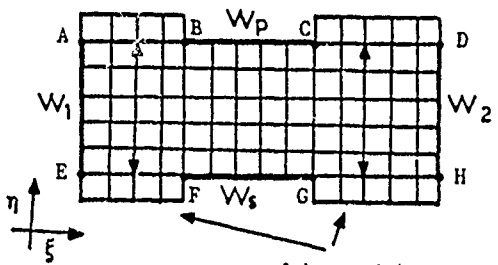
Fig.1 A schematic representation of a peripheral cascade



(a) The physical plane



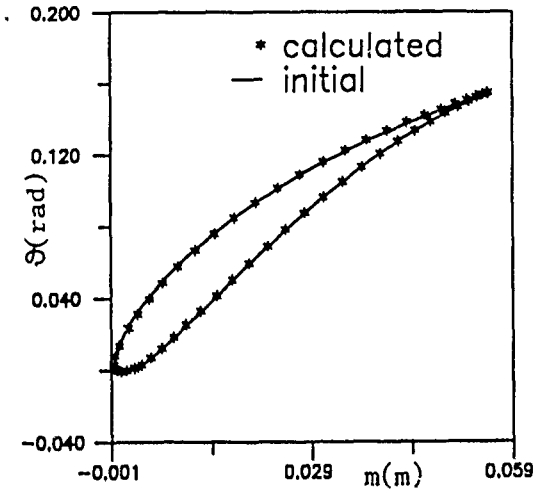
(b) The (Φ1,Ψ)- plane



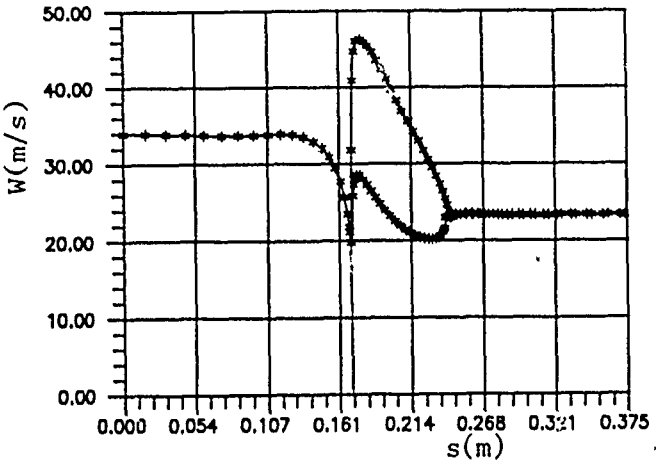
(c) The computational plane

Fig.2 The schematic representation of a blade passage of a peripheral cascade

Third International Conference on Inverse Design Concepts and Optimization in Engineering Sciences (ICIDES-III), Editor: G.S. Dulikravich, Washington D.C., October 23-25, 1991.

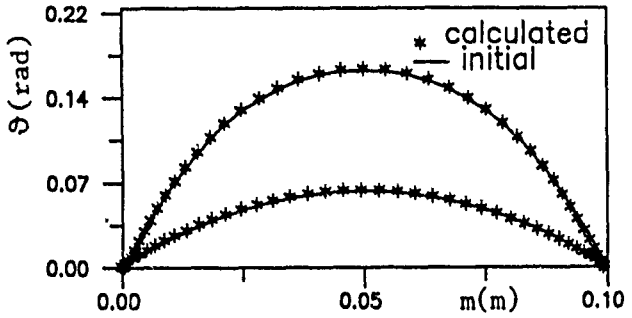


(a)The initial and recalculated blade shape

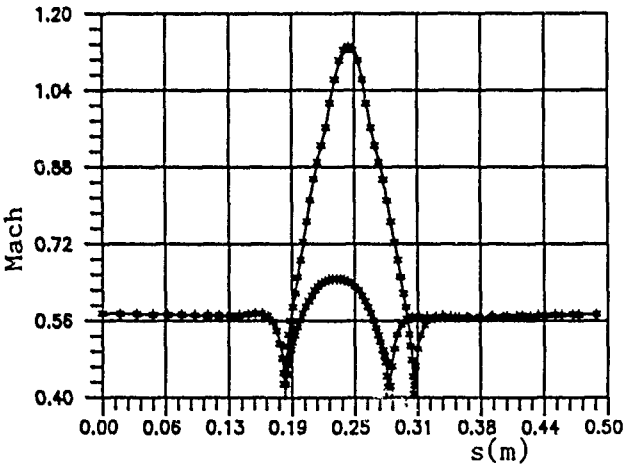


(b) The velocity distributions

Fig.3 The Gostelow cascade



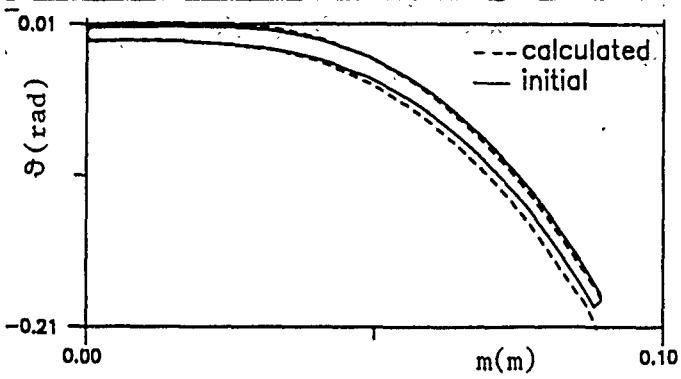
(a) The initial and recalculated blade shape



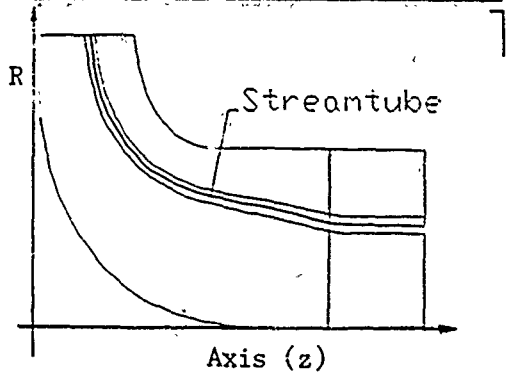
(b) The Mach number distributions

Fig.4 The Hobson cascade

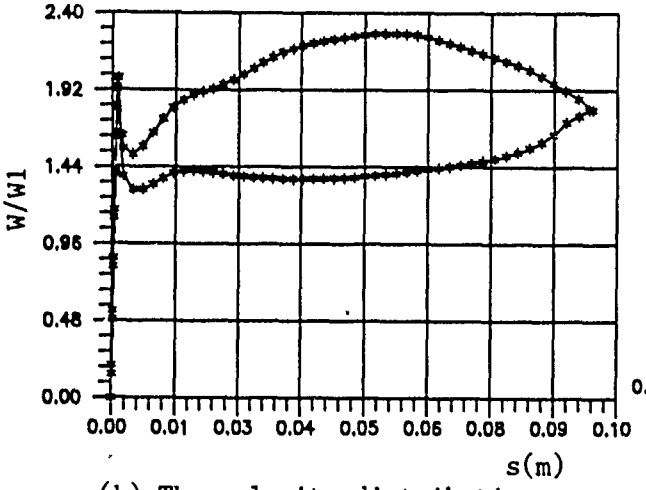
Third International Conference on Inverse Design Concepts and Optimization in Engineering Sciences (ICIDES-III), Editor: G.S. Dulikravich, Washington D.C., October 23-25, 1991



(a) The initial and recalculated blade shape

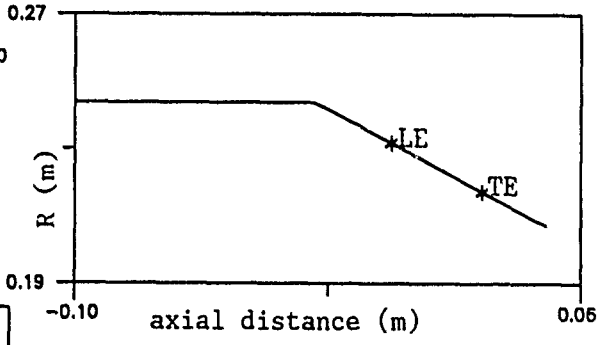


(c)The meridional plane and the streamtube variation

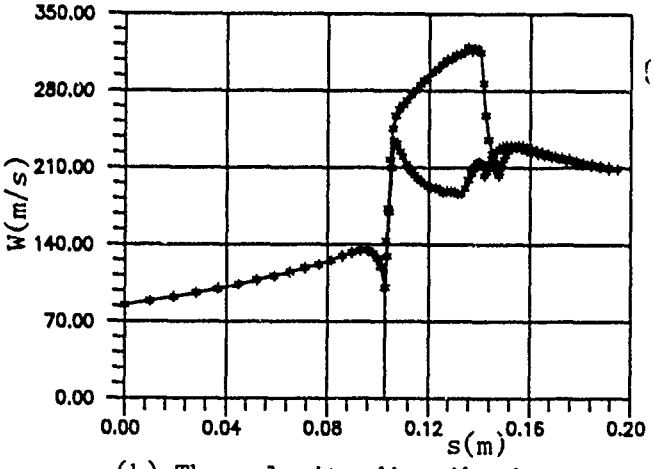


(b) The velocity distributions

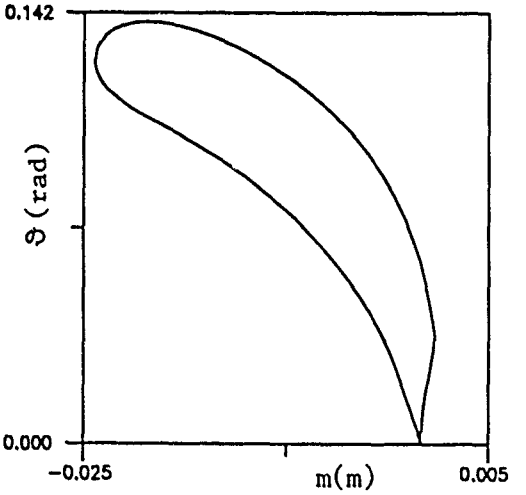
Fig.5 A rotating turbine case



(a) The generatrix of the axisymmetric streamsurface



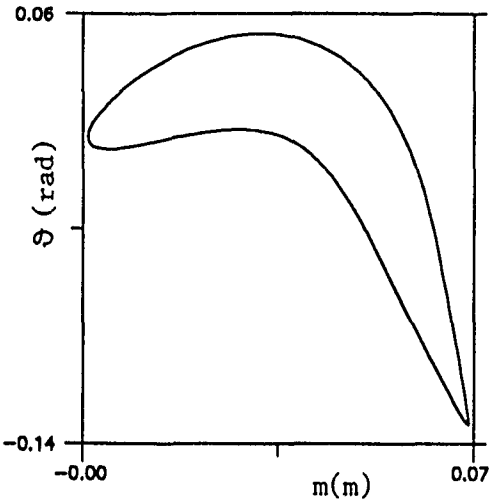
(b) The velocity distributions



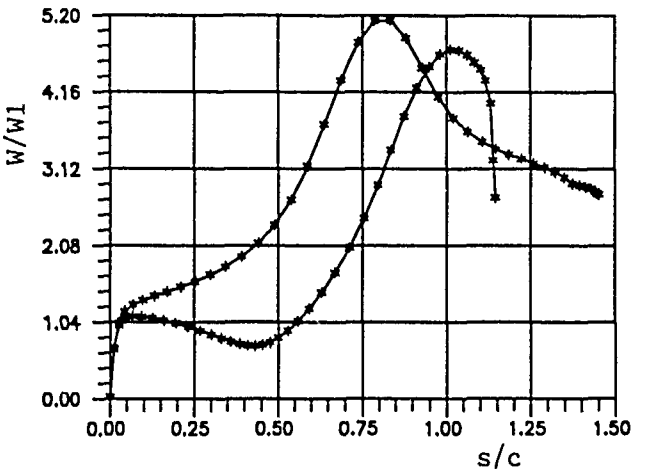
(c) The calculated profile

Fig.6 Design of a new rotating cascade

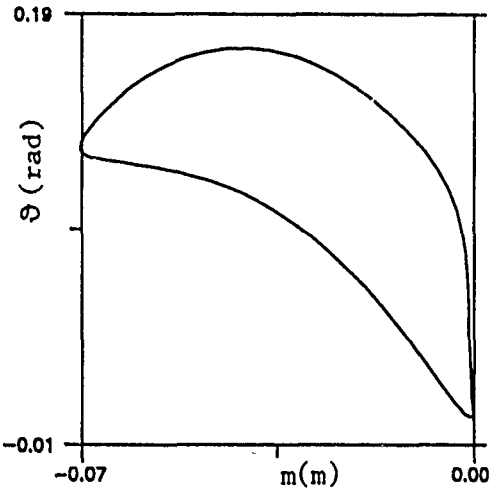
Third International Conference on Inverse Design Concepts and Optimization in Engineering Sciences
(ICIDES-III), Editor: G.S. Dulikravich, Washington D.C., October 23-25, 1991.



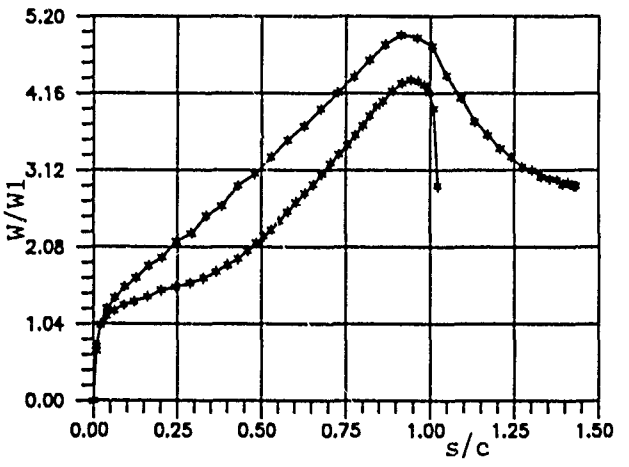
Starting profile



Velocity distributions of the starting profile



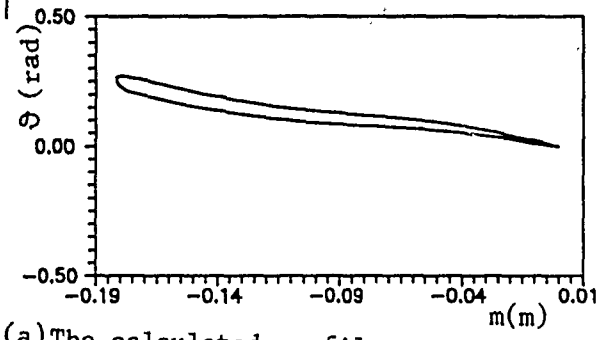
Calculated new profile



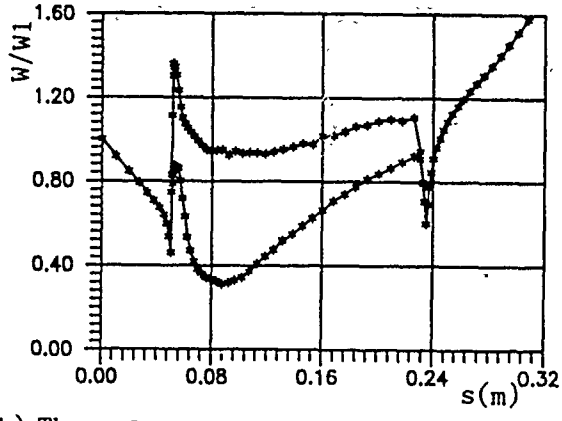
Velocity distributions of the new profile

Fig.7 Design of a thicker profile

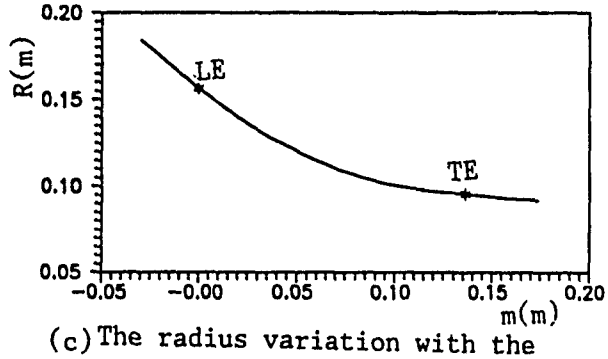
Third International Conference on Inverse Design Concepts and Optimization in Engineering Sciences (ICIDES-III), Editor: G.S. Dulikravich, Washington D.C., October 23-25, 1991.



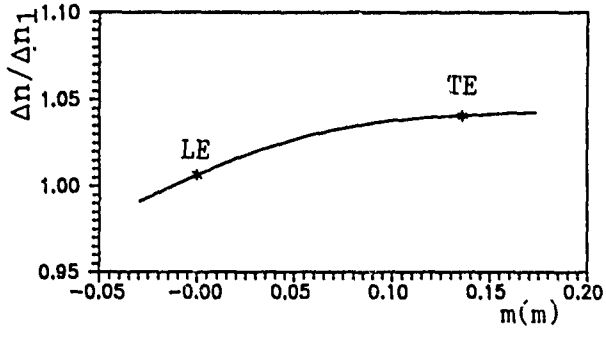
(a) The calculated profile



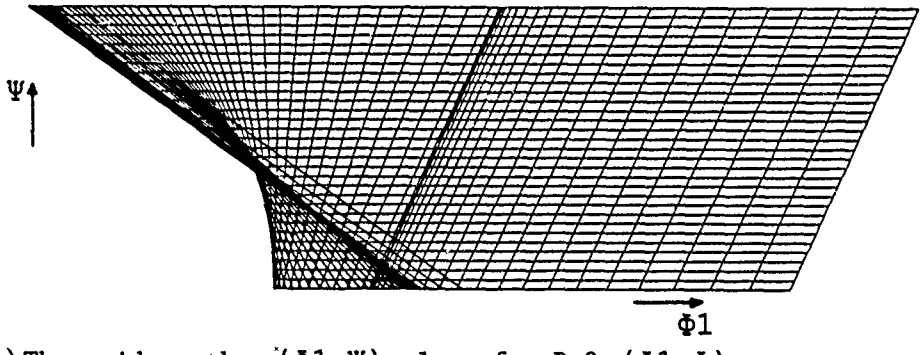
(b) The velocity distributions



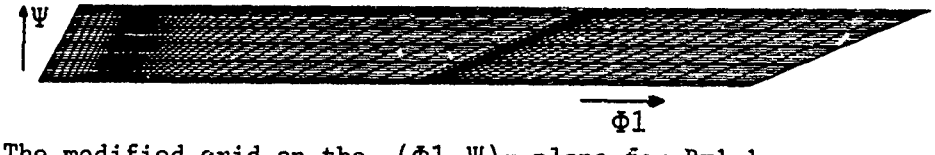
(c) The radius variation with the meridional distance



(d) The streamtube thickness variation with the meridional distance



(e) The grid on the (Φ1,Ψ)-plane for B=0 (Φ1=Φ)



(f) The modified grid on the (Φ1,Ψ)- plane for B=1.1

Fig.8 Design of a radial inflow turbine

Third International Conference on Inverse Design Concepts and Optimization in Engineering Sciences (ICIDES-III). Editor: G.S. Dulikravich, Washington D.C., October 23-25, 1991.

A PC-BASED INVERSE DESIGN METHOD FOR RADIAL AND MIXED FLOW TURBOMACHINERY

by
Ivar Helge Skoe
Kristion Sonjusvei 20
3600 Kongsberg,Norway

1. ABSTRACT

An Inverse Design Method suitable for radial and mixed flow turbomachinery is presented. The codes is based on the 'Streamline Curvature Concept' and is therefore applicable for current PC's from the 286/287- range.

In addition to the imposed aerodynamic constraints, mechanical constraints are imposed during the design process to ensure that the resulting geometry satisfies production considerations and that structural considerations are taken into account .

By the use of Bezier Curves in the geometric modelling, the same subroutine is used to prepare input for both aero & structural files since it is important to ensure that the geometric data is identical to both structural analysis and production.

To illustrate the method a Mixed Flow Turbine Design is shown.

CONTENTS

1 Abstract
2 Introduction
3 Analysis
- 3.1 Meridional flow
- 3.2. Blade to blade Flow
- 3.3. Implementation of the Inverse Procedure
  - 3.3.1. The aerodynamic part
  - 3.3.2. Structural Considerations
  - 3.3.3. Geometric Constraints due to Production

4 Results
- 4.1. A Mixed Flow Turbine
- 4.2. CPU times

5. References
6. Acknowledgements
7. Figures

2. INTRODUCTION

The objective of this paper is to present an inverse design method which can be used on ordinary PC's.

Since the conventional design process for centrifugal and mixed flow turbomachines is an iterative one, with successive changes to the input geometry subjected to the flow analysis , it is evident that the aero-design process takes considerable time. It can therefore be tempting to apply inverse design principles to ensure that , at the end of a computational task, the resulting geometry satisfies predetermined aero-restraints.

The method described is an 'engineering' approach to the inverse design problem where both aerodynamic and mechanical criteria are imposed.

Third International Conference on Inverse Design Concepts and Optimization in Engineering Sciences (ICIDES-III). Editor: G.S. Dulikravich, Washington D.C., October 23-25, 1991.

For rotors of radial and mixed flow design, the shroud line aerodynamics is considered the most critical aerodynamically. In the present method the shroud line aerodynamics are 'imposed' and the three-dimensional geometry is evaluated under mechanical constraints dictated by structural and production considerations.

A novel exducer geometry, featuring 'Balanced Work Extraction' is part of the design procedure for Radial/Mixed Flow Turbines.

The complete 3-D Geometry of the rotor is generated in the Inverse Design method. Through extensive use of 'Bezier Curves' in the geometric modelling the same subroutine performs the 'meshing' for the FEM-analysis and prepares the input files for the structural analysis in NASTRAN FEM-system, as well as the geometry definition for production.

3. ANALYSIS

The flow equations, in the form presented here, is a Quasi 3-D ,inviscid approach to the Navier Stokes Equations. The viscous effect, however is included in an approximate way by including the Entropy term in the equations. The spanwise and streamwise effect of losses are simulated by applying a Polytropic Efficiency, which is allowed to vary spanwise.

The basis of the quasi-three- dimensional flow analysis is the division of the flow field into two types of two-dimensional surfaces, as shown in Fig.1, from Ref. 1. The S2 surface, which describes an 'average' meridional flow is governed by the meridional flow equations is described below,while the S1, or blade to blade flow is handled in chapter 3.2.
The terminology is 'commonpractice' in turbomachinery, illustrated on Fig. 2 & 3.

3.1 THE MERIDIONAL FLOW

The meridional Equilibrium Equations has been applied to Hydraulic Francis Turbine Design since early in this century. Applied to Axial Flow Turbomachinery, the equations are termed The Radial Equilibrium Equations. These two forms of the Equations are treated in numerous reports from the last several decades, and for detailed information they are referred to the in Ref. 1,2 & 3 .

In the following chapter a short description of the equations is given, explaining how they are integrated into the procedure.

The meridional flow equation takes the following form

$$\frac{dV_m^2}{dl}+F*V_m^2+G=0 \qquad (1)$$

where the two terms F and G contain thermodynamic and geometric elements which are dependent on the flow solution itself. Hence an iterative solution is required.If the l-direction Fig. 2 is normal to the meridional streamline in a vaneless region the terms in Eq. (1) simplifies to:

$$F=\frac{2}{R_c}-\frac{1}{C_p}*\frac{dS}{dl} \qquad (2)$$

$$G=2*\frac{V_u}{R}*\frac{d(R*V_u)}{dl}-2*\frac{dH}{dl}+\frac{1}{C_p}*(2*H-V_u^2)*\frac{dS}{dl} \qquad (3)$$

Third International Conference on Inverse Design Concepts and Optimization in Engineering Sciences (ICIDES-III), Editor: G.S. Dulikravich, Washington D.C., October 23-25, 1991.

Since , in the general case, the meridional streamline location is unknown, it is convenient to fix most of the calculation 'stations' as 'quasiorthogonals' for the iterative flow calculation process, (Ref.3.) while for the rotor trailing edge the code is required to handle curved calculation station.

The solution of Eq. 1 is performed by Direct Integration

$$V_m^2=\exp-(\int F*dl)*[V_{m,hub}^2-\int G*\exp-(\int F*dl)*dl] \qquad (4\ ,a)$$

$$=\bar{V}_{m,hub}^2*e^{-\int F*dl}-e^{-\int F*dl}*\int G*e^{\int F*dl}*dl \qquad (4,b)$$

where the integration is performed from hub to the streamlin in question.
The constant of integration is set by the continuity equation:

$$\dot{W}=\int_{hub}^{shroud} 2*\pi*R*V_m*\cos(\delta)*\rho*\tau*C_d*dl \qquad (5)$$

where the angle (Fig.2)

$$\delta=\phi-\gamma \qquad (6)$$

the blade blockage (when inside bladerows)

$$\tau=2*\pi*R-Z_b*t_\theta \qquad (7)$$

and the Discharge Coefficient C_d is basically sized to take care of boundary layer displacements effects

3.2. BLADE TO BLADE FLOW

The aerodynamic blade loading can be derived by relating the change of moment of momentum for a flow-filament to the torque exerted by the pressure difference blade-to-blade (Fig.2)

$$dp*Z_b*dn*dm*R = d\dot{W}*\frac{d(R*V_u)}{dm}*dm \qquad (8)$$

The filament massflow can be expressed as

$$d\dot{W}=2*\pi*R*V_m*\rho*dn \qquad (9)$$

If the assumption (to be revised below) is made,that the flow is incompressible and linear blade-to-blade, the following expression relates the velocity difference to the pressure difference

$$dp_{stat}=\frac{1}{2}*\rho*(W_{ss}^2-W_{ps}^2)=2*\rho*\bar{W}*\Delta W \qquad (10)$$

By introducing this expression together with equation (9) into equation (8), an approximate expression for the suction side velocity can be formulated

$$W_{ss}=\bar{W}+\Delta W=\bar{W}+\frac{\pi}{Z_b}*\frac{V_m}{\bar{W}}*\frac{d(R*V_u)}{dm} \tag{11}$$

By means of the relative flow angle definition

$$\beta=\arccos(V_m/W) \tag{12}$$

equation (11) can be rearranged to give an approximate expression for the Suction Side Velocity

$$W_{ss}=\frac{V_m}{\cos(\beta)}(-/+)\frac{\pi}{Z_b}*\cos(\beta)*\frac{d(R*V_u)}{dm} \tag{13}$$

In our iterative design procedure we use the above mentioned linear approximation only in the first iteration. For the subsequent iterations

$$W=W_{ss}+A1*\theta^2_{Pitch}+B1*\theta_{Pitch} \tag{14}$$

and the two constants, A1 & B1, are evaluated so that, with compressibility Eq.(8)is satisfied. By integrating the massflow density blade-to-blade input for Eq. (5) is evaluated and the difference between the S1 flow surface, and the blade surface is determined.

The above formulation is similar to the SFC-concept (Stream-Function- Coordinate) method described by Professor G.S.Dulikavich in Ref.5, however, less ambiguous due to the intended use of a PC. For the blade to blade solution

there are three areas of major concern, namely the blade inlet, the blade exit, and splitter if present.

Blade Inlet

Since for radial and mixed flow turbomachinery we are normally dealing with high solidity blades in the rotors a 'channel flow' approach gives reasonable results (Ref. 1 & 4). For our Mixed flow turbine we selected an 'optimum' inlet blade angle by setting the 'slipfactor'=.85 in the following relation

$$\beta_{blade}=\arctan\left(1-\frac{1-\phi*\tan(\beta)}{\mu}\right) \tag{15}$$

where $\phi=\frac{v_m}{U}$ *is Flow Coefficient,* $\mu=$*'slippfactor'*

Blade Exit

In our mixed flow turbine rotor, where the flow is close to axial, the 'Cutta Condition' implies (when transonic effects are excluded) that the aerodynamic bladeloading is zero at the trailing edge, which is reflected by introducing zero gradient in the imposed ($R*V_u$) at the trailing edge. The difference between the S1 and blade average pitch must be corrected according to some deviation 'rules' based on experimental evidence.

Splitter blades

In our design method we must be capable of determining the position of rotor splitter blades for an imposed optimised suction side velocity.It should be evident from the above eqation (13) that

Third International Conference on Inverse Design Concepts and Optimization in Engineering Sciences
(ICIDES-III), Editor: G.S. Dulikravich, Washington D.C., October 23-25, 1991.

the splitter blade must be 'unloaded' to leave a smooth suction side velocity on the neighbouring 'mainblade'.

3.3. FORMULATION OF THE INVERSE DESIGN PROCEDURE.

A practical turbomachine design system must meet both
-aerodynamic
-structural (stress,vibration,cyclic load e.t.c)
-and geometric constraints imposed by the method of producing.
Since none of these requirements are secondary, they are handled in three different chapters.

3.3.1. THE AERO-PART OF THE INVERSE DESIGN.

In the aero-design of turbomachines the shroudline suction side relative velocity is considered the most critical part of the flowpath, regarding the boundary layer behaviour . This suction side velocity can be controlled by the distribution of the following parameters.
Since the suction side velocity cannot be 'dictated' for the whole 3-D geometry for a practical rotor

$$V_m, \beta, Z_b, \frac{d(R*V_u)}{dm}$$

design (Ref.6) the rest of the flowpath is defined from mechanical constraints. Also the Rotor Exit Flow Quality is imposed to enhance the suceeding diffusor performance.
Based on the anticipated gradient in efficiency from hub to shroud, the required temperature gradient at rotor exit is determined by Eq. (16)
With the assumption of Axisymetric Stream Surfaces (Chapter 3)

$$\frac{P_{Rotor\ Exit}}{P_{Rotor\ Inlet}} = \left[\frac{T_{Rotor\ Exit}}{T_{Rotor\ Inlet}}\right]^{\left(\frac{\kappa*\eta_p}{(\kappa-1)}\right)} \qquad (16)$$

the Euler turbomachinery equation is applied along the meridional streamline

$$T_{Rotor\ Exit} - T_{Rotor\ Inlet} = \omega * [R*V_{u,RotorExit} - R*V_{u,Rotor\ Inlet}] \qquad (17)$$

The novel exducer configuration with slanted trailing edge shown on Fig.3 & 8, allows controlled rotor exit bladeangles without violating structural considerations.
To ensure the performance (total-to-static) above conventional turbine designs a conical diffusor with 'centerbody' is required (Fig.5) since strong 'counterswirl' near hub results from the design.

The Inverse Design Procedure to be implemented consists of the following steps:
a) Define a 'first guess' meridional flowpath 'Grid'.
b) From estimated efficiency the streamwise distribution of ($R*V_u$) is determined including rotor exit (Equation (16)&(17).

Third International Conference on Inverse Design Concepts and Optimization in Engineering Sciences (ICIDES-III), Editor: G.S. Dulikravich, Washington D.C., October 23-25, 1991.

c) Impose a Smooth Meridional Velocity field in the grid. The value of the imposed meridional velocity along the shroud, together with the the ($R*V_u$) distribution, determine the 'Critical' shroudline suction side velocity according to Eq .(13)

d) Evaluate the F- and G- terms of equation 2 & 3.

e) Integrate equation (1) (Eq.(4)), with the constant of integration is set by the imposed shroud meridional velocity.

f) Integrate RHS of Equation (5) with the velocity resulting from e) above. Correct ,with a relaxation factor,the meridional streamline position according to the integrated massflow fraction. The lack of continuity dictates how the meridional flowpath is altered during the iterations. In other words, the rotor hub, (or shroud) is allowed to 'migrate' during the convergence to satisfy the continuity equation (ultimately).

g)Impose the 'Mechanical Constraints' (To be defined in section 3.3.2 & 3.3.3 below) .The characteristics of the blade depends on the S1 surface which is determined by integrating the relative flow angle:

$$\theta_{S1}=\int\frac{\tan\beta}{R}dm=\int\frac{\omega*R-V_u}{R*V_m}dm=\int(\frac{\omega}{V_m}-\frac{V_u}{R*V_m})dm \qquad (18)$$

The S1 surface /blade surface relations were mentioned under 3.2 above. The polar angle derivative along the integration path for Eq 1 is required to evaluate the Bladeforce Term.

h) Special attention is required for the rotor exit, where the air angle is dictated from the requirement of a prescribed ($R*V_u$) , according to Eq 16 & 17, due to the imposed total pressure. Depending on the mechanical restriction the trailing edge may have to 'migrate' during the design process.

i) With revised flowfield information the F- and G- terms in eq.1 is updated, and the computational procedure returns to e) above.

This process continues until some criterion of convergence is satisfied.

3.3.2. STRUCTURAL CONSIDERATIONS

The total structural life criteria cannot be analyzed during a PC- based inverse design procedure, since rather complex FEM- analysis is required.To ensure that the 'first guess' of the aero-defined blade respect some basic stress criteria (Creep e.t.c) a simple 2-D stress model can be performed during the inverse design. When second order terms are neglected the following equations applies for the maximum radial Stress near hub

$$\sigma_{Max}=\frac{1}{t_{\theta,Hub}}\int_{Hub}^{Shroud}\delta_{Cf}\,dr \quad +/- \quad \frac{M_{Hub}}{I_{x-x}}*\frac{1}{2}*t_{\theta,Hub} \qquad (19)$$

where the centrifugal force and bending to be integrated (Eq. 20 & 21) are

$$\delta_{Cf}=\rho_{Material}*t_\theta*\omega^2*R \qquad (20)$$

Third International Conference on Inverse Design Concepts and Optimization in Engineering Sciences (ICIDES-III). Editor: G.S. Dulikravich, Washington D.C., October 23-25, 1991.

$$M_{Hub} = \int_{Shroud}^{Hub} \delta_{Cf} * R * (\theta - \theta_{Hub}) * dR \tag{21}$$

and the second moment of inertia of the hub section (Eq. 22) is

$$I_{x,Hub} = \frac{1}{12} * t_{\theta,Hub}^{3} \tag{22}$$

This analysis require little additional code and can be performd during the inverse design procedure. For our Mixed Flow turbine rotor geometry,this integration was performed in 'Section B-B' and in 'Section A-A' to determine a tangential blade thickness ratio compatible with the materials creep life data . Equation (19) can be solved 'inversely' and the resulting 'constant creeplife blade' results in a 'Eifel Tower' blade shapes of the type seen in Fig.8. For critical designs like this radial turbine and centrifugal compressor of Ref.11, is vital that the structural analysis is performad with the same geometry as the geometry defined for production.The geometry definition of radial and mixed flow rotors is a typical case for 'special purpose' software , and it is logical that the aerodesigner prepare the complete geometry definition files for the FEM-program input, as illustrated on Fig.8. These geomtries are defined in the same subroutine with the constants determined in the designprosess. In subsequent structural analysis temperature, heat transfer cefficient e.t.c must be added.

3.3.3. GEOMETRIC CONSTRAINTS DUE TO PRODUCTION.

It is important that the 3-D blade geometry which is output of the inverse design is compatible with an available/economic production method. The two manufacturing methods which is common for radial and mixed flow turbomachines is Flank Milling and Casting.

For the Production of Castings, there is a close connection between the requested thickness distribution, material quality requirement and scrapprate. Due to this the relative thickness ratio for the tip vary with size .As a consequence the optimum bladenumber reduces, and the meridional flowpath length increase with reduced size to conserve the aerodynamic blade loading , Eq .8, 13, Fig. 9. Ref.14

The 'Cold Rig' version of the mixed Flow Turbine in question has been 'Flank milled' in a 5-Axis Controlled Milling Machine. Further 'Flank milling' is a candidate for the production of the forms for 'Lost Vax' casting process and it is a good method for high performance Centrifugal compressors with transonic inducers.

The 'Flank Milling' production process is illustrated on Fig. 3, where it can be shown that the production process will impose mechanical constraints on the blade geometry in the direction of the 'Cutter Centerline'.
The blade surface definition, and the machining process is illustrated on Fig.3,Section C-C, which is seen normal to the cutter centerline for one particular position along the 'Cutter Path'.

Since ,in the general case, a rotor blade is 'twisted' from hub to shroud, it is evident that the cutter direction (In woorkpice Coordinates) are different at shroud and 'near hub'. As a consequence, the contact line of the cutter spans an angle from hub to shroud and the blade surface are 'undercut' compared to the stright line a) to b). The deviation from this generatix half way from hub to shroud is close to

Third International Conference on Inverse Design Concepts and Optimization in Engineering Sciences (ICIDES-III), Editor, G.S. Dulikravich, Washington D.C., October 23-25, 1991.

$$\delta = R_{Cutter} * [1 - \cos(.5 * (\bar{\beta}_{Hub} - \bar{\beta}_{Shroud})] \quad (23)$$

where the bladeangles is taken in a plane normal to the Cutter Centerline.
For the Mixed flow Turbine, and for compressors as shown on Fig.9 & 10(Ref.11), undercutt can be comnpensated for when defining the blade for FEM-analysis by using a slightly different 'Cutter 'Path' for the geometry definition as compared to the 'Cutter Path' defined for machining.
The rather obvious requirement that a practical cutter has to pass between the blades to be machined does put restraints on the selectioon of number of blades and possition of splitters.

4. RESULT OF THE INVERSE DESIGN

4.1. A Mixed Flow Turbine

The presented design method has been utilized, during the development period, for several turbomachines from the Centrifugal Compressor for an 'Ultra Small Jet Engine' in 1988,Ref. 14, Fig 9, to the Radial Inflow Turbine currently in the design phase Fig.8.
The mixed flow turbine used to illustrate the inverse design method, Figs. 3 to 7, was designed for a Total to Static Pressure ratio of 2.05.
For the particular spool a high rpm was required due to the Compressor Efficiency , size, and cost. Applying typical 'turbocharger turbine geometry' would result in low total-to-static efficiency (Ref. 8 & 12), consequently a mixed flow turbine was designed for this application. Fig.5 shows the turbine rig which has been designed by ARTI in Praha, and Fig. 4 shows a photo of the turbine rig rotor , 'Flank Milled' at ARTI. The rig is currently in the manufacturing process and 'Cold Rig' tests are scheduled later this year.
Due to the combination of conical flowpath and 'almost' radial element blades, some freedom exist in the selection of rotor inlet tipspeed and 'Design Charts' for hydraulic Fransis Turbines could to a certain degree be utilized.
A design procedure as described in 3.3.1 with the restriction of 'Flank Milling' was performed with different combination of bladenumber and splitterlocation. The final design geometry shows the meridionalvelocity profiles in Fig 5.3 and the relative machnumbers in Fig 5.4. By imposing a 'kink' in the $R*V_u$ distribution in the splitter blade trailing edge region, a quite uniform suction side machnumber is obtainwd on the whole mainblade, and the deceleration near the trailing edge suction side should give low boundary layer growth (Ref.13).
Since both meridional curvature and aerodynamic blade loading are drastically lower than for High Pressure Ratio Radial Inflow Turbines the resulting 3-D effects, which is not taken care of in the quasi-3-D formulation, should be moderate. It is, however evident that a reliable design procedure for this type of turbines needs feedback from the 'real flow effect' regarding the deviation and loss characteristics. Since the basic Quasi 3-D procedure when properly 'calibrated' for efficiency and deviation, predict the static pressure along a compressor shroud as shown on Fig.11, the same procedure should apply for the lightly loaded turbine.

4.2. Computational Times:

The Computer code described has been used on computers ranging Homecomputer (Fig 1988) through 286/287 (for the Mixed Flow Turbine 90) to 486 type (Radial Inflow Turbine Fig .22 ,1991). It is difficult to give 'honest' figures for the performance of the code for several reasons :

-The code is seldom started from 'scratch'. Based on previous experience a tentative streamline pattern and a tentative meridional velocity level can be estimated as a 'first guess'. This reduces the time for obtaining satisfactory convergence drastically.
-The grid required varies with the type of task.
-The performance depends on how the computer is configured.
-An engineer seldom runs a program to the convergence level which a mathemathician would.

Comparison of several codes for turbomachinery flow analysis are given in Ref.1,b) Since both grid and computers vary a direct comparison is difficult. Since the basic characteristic of a streamline is that both the first and second derivative (Slope & Curvature) is included in the information it is logical that the grid can be quite coarsh for SC-procedure.

It would be a task for ICIDE to define a list of 2-D and 3-D turbomachinery geometries which could be used to evaluate different methods, since several factors in addition to relaxation , grid size and number of iterations affects the accuracy and time used.

For the 286/287 Mixed Flow Turbine Fig. 4 & 5,a total of 33 Meridional 'stations' vere used. The first 10 'stations' were used in the nozzles, which vere also inversly designed. In the rest of the flowpath, 23 additional 'stations' vere used , and 9 meridional streamlines vere used including hub & shroud. This task took typically 50 minutes on the 286/287 Laptop.

For the design of a axial/radial diffuser similar to that on Fig. 5 a smaller grid had to be used to include a simple boundary layer code (Ref. 13). For that design (not shown in this report) a optimum boundary layer shape factor vere the basis for the geometry definition.

Currently the code is running under the Microsoft Professional Development System 7.1.(QuickBASIC Extended, which is a very convenient development environment). This allows the DOS-barriere of 640 K to be broken by using EXTENDED or EXPANDED memory. In this case a simple 2-D boundary layer integration procedure (Ref.13) can be included in the present code together with a (35*9) meridional grid, at the 'cost' of a speed reduction of some 50% compared to the 486 '640K-DOS speed',and typical CPU is 12 minutes for a Turbine shown on Fig.8.

5. REFERENCES

1. Advanced Topics in Turbomachinery Technology, Concepts ETI,Inc. Norwich,Vt.USA.1986
   a) Chapter1: R.M.Hearsey:2Practical Compressor Aerodynamic Design2.
   b) Chapter 9: J.H.G. Howard:2Computational Methods for Quasi-Three-Dimensional and Three-Dimensional Flow analysis and Design of Radial Turbomachinery".
2. Novac,R. and Hearsy, R.M."A nearly 3-D intrablade computing system for turbomachinery" Tran. ASME, J. Fluid Eng. March 1977,P.154
3. Katsanis, T,H:"Use of arbitary quasi-orthogonals for calculating flow distribution in the meridional plane of a turbomachine"
   NASA TN- D-2546
4. Stanitz,J.D, and Prian,V.D,"A Rapid Approximation Method forvDetermining Velocity Distribution on Impeller Baldes of Centrifugal Compressors"NACA TN-2421,1951.
5. von Karman Institute (v.K.I) Short Course on Inverse Design Methods.
   Bruxelles ,May 1989
6. Zangeneh, M:"Therdimensional Design of a High Speed Radial Inflow Turbine by a Novel Design Method". ASME 90-GT-235

Third International Conference on Inverse Design Concepts and Optimization in Engineering Sciences.
(ICIDES-III), Editor: G.S. Dulikravich, Washington D.C., October 23-25, 1991.

7. Wood, H.J. "Current technology of radial-inflow turbines
for compressible fluids"
Tran. of ASME, J. of Engineering for Power, Jan 1963, pp72-83
8. Roelik, H.E. "Analyttical Determination of Radial Inflow
Turbine Design Geometry for Maximum Efficiency"
NASA THD-4384, 1978.
9. Rodgers,C:"High pressure ratio turbine design constraints"
vKI Lecture Series, Bruxelles 1987-7
10. OKAPU:"Mixed Flow Gas Generatore Turbine" vKI LS 1987-7,As above.
11. Mowill,R.J & Strom, S.,"An Advanced Radial-Component Industrial Turbine Engine"
ASME J of Eng. for Power.October 1983,Vol.105/947.
12. Whitfield, A.:"The Preliminary Design of Radial Inflow Turbines."
Tran. of ASME, Journal of Turbomachinery, Jan 1990.
13. Albring,W. "Angewandte Strømungslehre", Verlag Theodor Steinkopff.Dresden.GDR,1970
14. I.H.Skoe, "Design of a Centrifugal Compressor for an Ultra Small Jet Engine". Presentation
at the Norwegian Institute of Technology ,Trondheim, Norway,March 1989.

6. ACKNOVLEDGEMENT

The permission by R.J.Mowill/MOWILL TURBINMOTOR A/S to use the Mixed Flow Turbine to illustrate the use of the method is appreciated.
The enthusiastic Turbomachinery team at ARTI in Praha are acknovledged for the hardware efforts. (Ref. Figs. 4 & 5)

- and especially my vife Gerd, for her patience with my "inverse" sparetime activity
.-may the result be more sparetime !

7. FIGURES

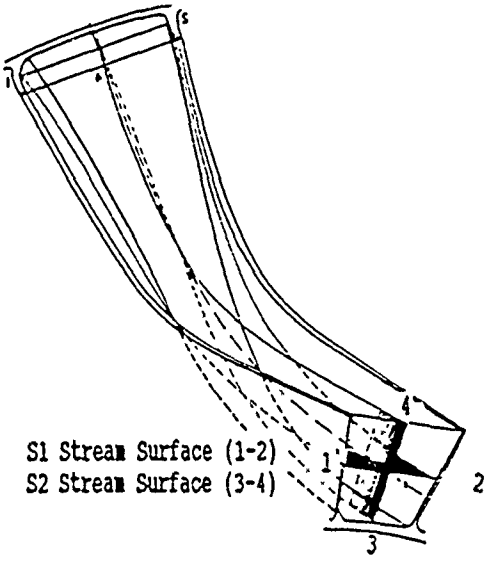


Figure 1. Stream Surfaces

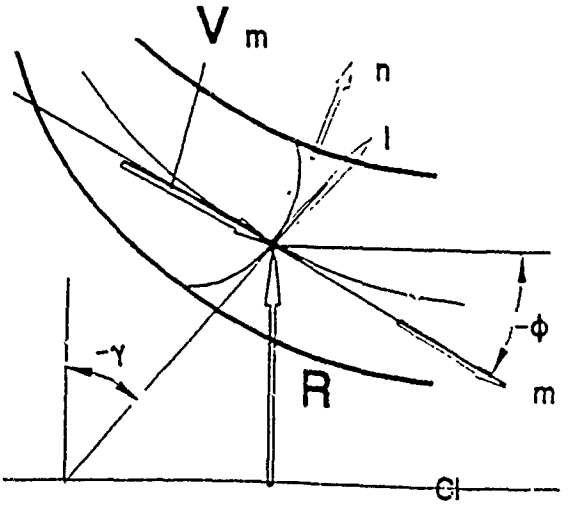


Figure 2. Coordinate System Definition

Third International Conference on Inverse Design Concepts and Optimization in Engineering Sciences
(ICIDES-III), Editor: G.S. Dulikravich, Washington D.C., October 23-25, 1991

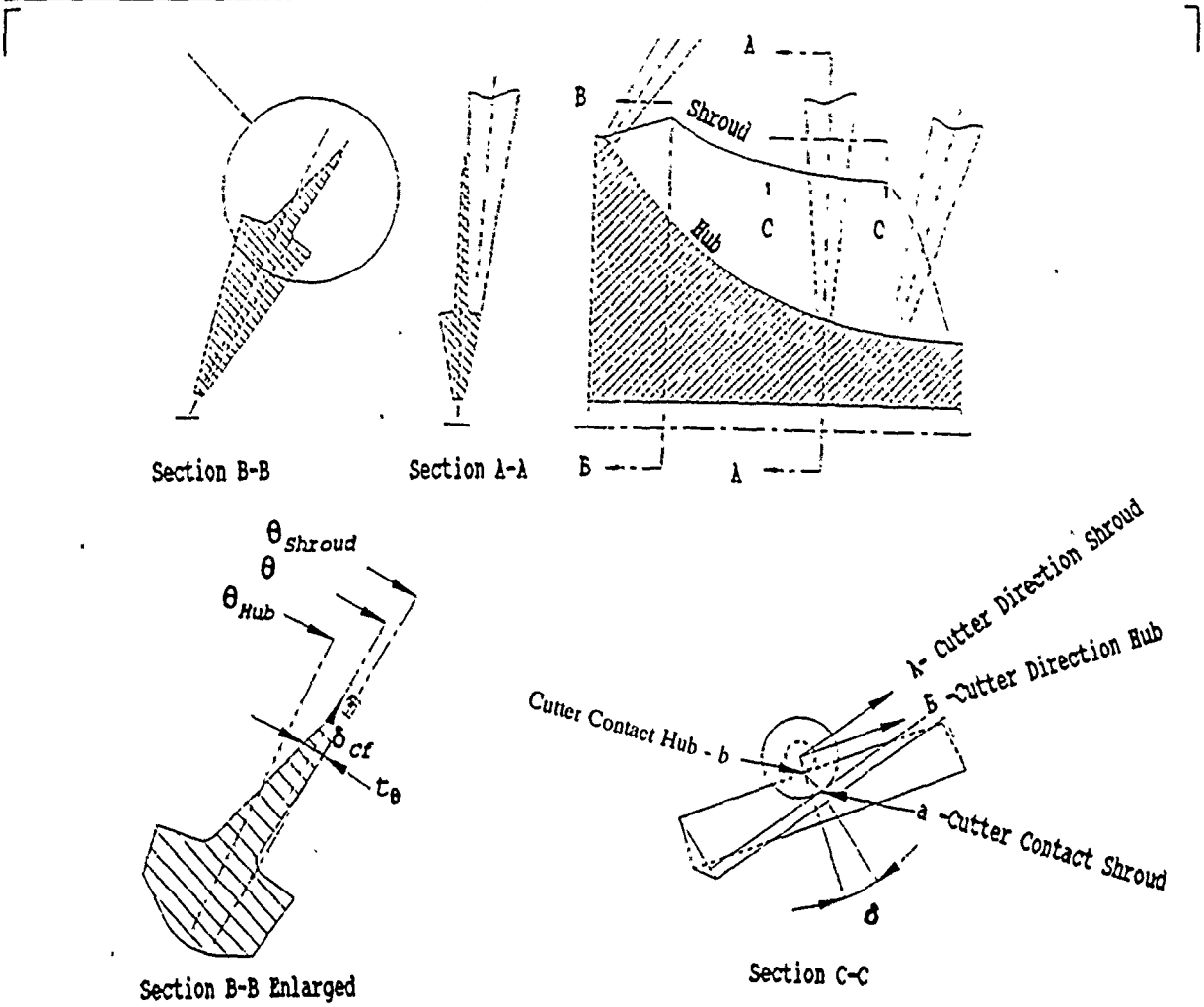


Figure 3. Geometric Constraints for 'Flank Milling'



Figure 4. Mixed Flow Turbine Rig Rotor
('Flank Milled')

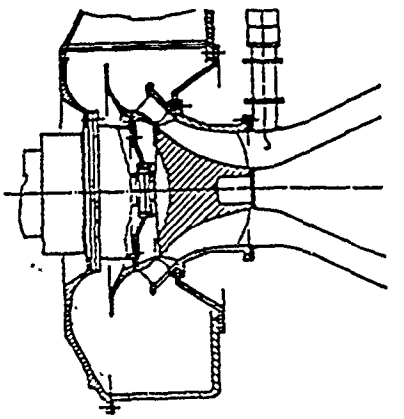


Figure 5. Turbine Rig
Meridional View

Third International Conference on Inverse Design Concepts and Optimization in Engineering Sciences (ICIDES-III), Editor: G.S. Dulikravich, Washington D.C., October 23-25, 1991

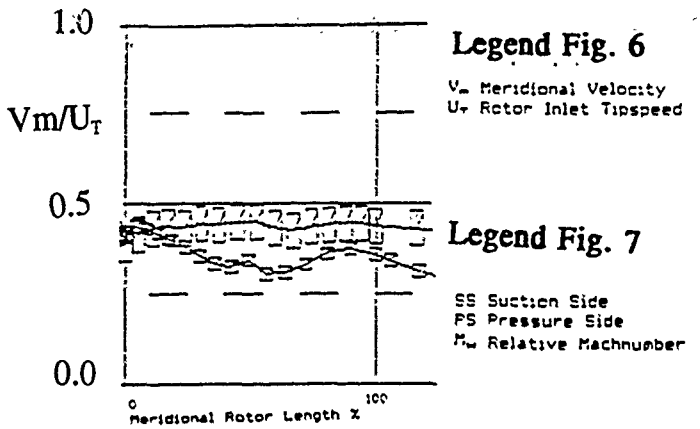


Figure 6. Meridional Velocity

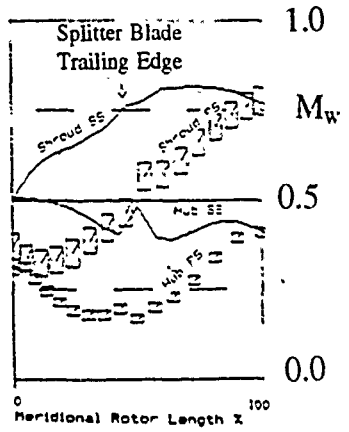


Figure 7. Relative Machnumbers

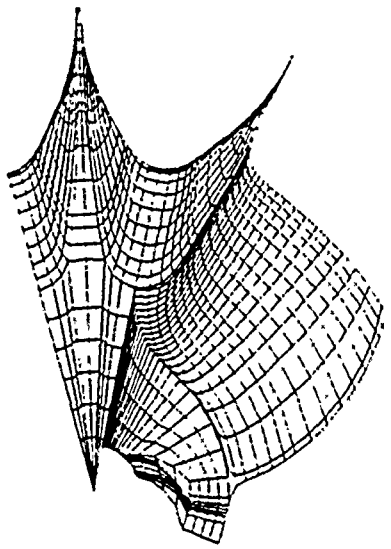


Figure 8. Radial Inflow Turbine (with Rotor FEM-Meshing)

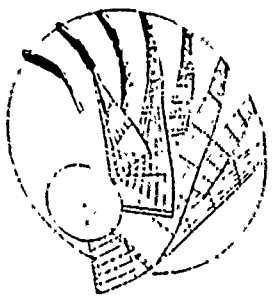


Figure 9. Centrifugal Compressor (Ref.14)



Figure 10.
High Pressure Ratio Compressor
(Reproduced from Ref. 11)

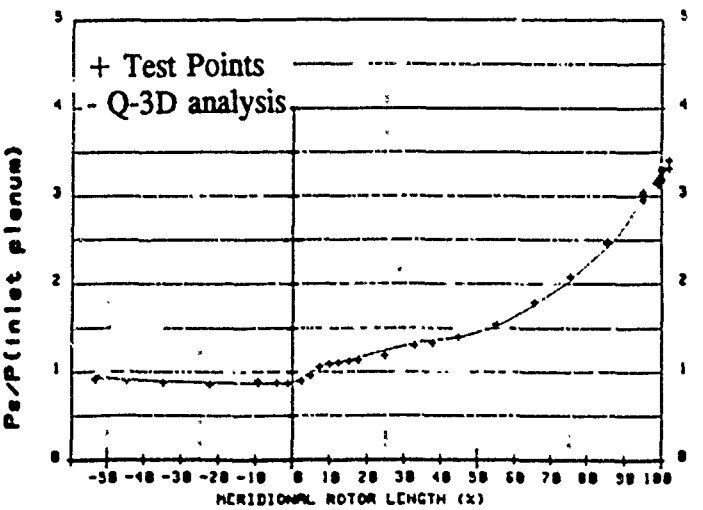


Figure 11. Comparison between Q-3D & Test (Compressor Static Pressure)

Third International Conference on Inverse Design Concepts and Optimization in Engineering Sciences (ICIDES-III), Editor: G.S. Dulikravich, Washington D.C., October 23-25, 1991.

OPTIMAL DESIGN OF SOLIDIFICATION PROCESSES

Jonathan A. Dantzig and Daniel A. Tortorelli

Department of Mechanical and Industrial Engineering, University of Illinois, Urbana, Illinois 61801 USA

1: INTRODUCTION

An optimal design algorithm is presented for the analysis of general solidification processes, and is demonstrated for the growth of GaAs crystals in a Bridgman furnace. The system is optimal in the sense that the prespecified temperature distribution in the solidifying materials is obtained to maximize product quality. The optimization uses traditional numerical programming techniques which require the evaluation of cost and constraint functions and their sensitivities. The finite element method is incorporated to analyze the crystal solidification problem, evaluate the cost and constraint functions, and compute the sensitivities. These techniques are demonstrated in the crystal growth application by determining an optimal furnace wall temperature distribution to obtain the desired temperature profile in the crystal, and hence to maximize the crystal's quality. A similar problem is investigated by Dantzig and Chao [1], however their approach does not utilize numerical optimization techniques.

Several numerical optimization algorithms are studied to determine the proper convergence criteria, effective one-dimensional search strategies, appropriate forms of the cost and constraint functions, etc. In particular, we incorporate the conjugate gradient and Quasi-Newton methods for unconstrained problems[2]. The efficiency and effectiveness of each algorithm is presented in the example problem.

We have chosen to adapt an existing commercially available finite element program, FIDAP [3], to compute of the sensitivities, rather than develop a new code. Thus, we are in position to investigate larger and more complicated problems in the future without significant code development. The explicit sensitivities are computed analytically by the adjoint technique[4], which has been applied to nonlinear transient conduction problems by Tortorelli *et. al.* [5]. Large computational savings and accurate calculations are realized by utilizing an explicit approach as opposed to the costly and sometimes unreliable finite difference method [5, 6].

In the following section, a brief outline of the conjugate gradient and quasi-Newton methods for unconstrained optimization are presented. In section 3, the adjoint sensitivity method is reviewed and presented in a specialized form appropriate to the processing problem. An example problem is presented in the last section.

Third International Conference on Inverse Design Concepts and Optimization in Engineering Sciences (ICIDES-III), Editor: G.S. Dulikravich, Washington D.C., October 23-25, 1991.

2: METHODS OF ANALYSIS

2.1 Optimization Algorithms

Vanderplaats [2] presents an excellent exposition of the algorithms which have been developed to resolve design optimization problems. The search method algorithms for unconstrained problems are characterized by sequential searches in the design space to reduce the value of the objective function, G. Beginning at a specified initial point in design space **b**, a line search is performed to find the minimum value of the objective in a search direction, **S**. Once the minimum is found in this direction, the present design is updated and a new search direction is chosen. This process is repeated until the design converges to its minimum objective function value. In this section we will briefly outline three search methods for unconstrained optimization. The methods are distinguished by the manner in which the sequence of search directions is determined.

Search methods which utilize derivatives of the objective function tend to be more efficient (*i. e.* will require fewer iterations) than zero-order methods. This is true because the gradients suggest the direction one should move in design space to reduce the value of the objective function. The sensitivity analyses, described in the next section, provide this gradient information at relatively little additional cost beyond that which is required to analyze the process and evaluate the objective function. Accordingly, the discussion here is limited to these first-order gradient-based methods, specifically, the methods of steepest decent, Fletcher- Reeves conjugate gradient, and the Quasi-Newton are described. The methods differ in the way that the search directions are determined.

Line searches are performed for all of the above-described algorithms. We are using a variant of Brent's Method for this purpose[7]. In this technique, the objective function is assumed to vary quadratically with the scalar α along the vector in design space given by $\mathbf{b} + \alpha\mathbf{S}$. Thus, the problem becomes one of finding the value of α corresponding to the minimum G. If G were truly quadratic in α, then a combination of three function evaluations or derivatives with respect to α would suffice to obtain the minimum. In practice, G is generally not quadratic in α, hence this technique requires repeated evaluations of G and its derivatives to determine the minimum. In some cases, the parabolic interpolation can diverge. To circumvent this problem, Brent's Method uses interval sectioning when divergence of the parabolic interpolation is detected.

Once the minimum for the given search direction is found, a new direction must be chosen. The most simplistic algorithm uses the gradient to determine the new search direction, *i. e.*

$$\mathbf{S} = -\nabla G \tag{1}$$

This "Method of Steepest Descent" has been shown to be inefficient [2]. Better algorithms utilize information about previously searched directions to construct the next search vector. In the Fletcher-Reeves conjugate gradient method, the new search direction is given by

$$\mathbf{S}^j = -\nabla G(\mathbf{b}^j) + \frac{|\nabla G(\mathbf{b}^j)|^2}{|\nabla G(\mathbf{b}^{j-1})|^2}\mathbf{S}^{j-1} \tag{2}$$

where $\mathbf{b}^j$ is the design vector at the beginning of the j^{th} line search. Such a selection of the S ensures that the search directions are Q-orthogonal. After several steps, it is possible that searching in direction $\mathbf{S}^j$ will not improve the objective, and the process is then re- initialized with Equation (1).

In the Quasi-Newton methods for unconstrained minimization, we consider a Taylor series expansion of G about the present design, $\mathbf{b}_0$.

$$G(\mathbf{b}) \approx G(\mathbf{b}_0) + \nabla G \cdot \delta\mathbf{b} + \frac{1}{2}\delta\mathbf{b}^T\mathbf{H} \cdot \delta\mathbf{b} \tag{3}$$

Third International Conference on Inverse Design Concepts and Optimization in Engineering Sciences (ICIDES-III), Editor: G.S. Dulikravich, Washington D.C., October 23-25, 1991.

where $\mathbf{H}$ is the Hessian matrix, and $\delta\mathbf{b} = \mathbf{b} - \mathbf{b}_0$ is the new search direction. Differentiating this equation with respect to the design variation and setting the result to zero (for the minimum) yields

$$\delta\mathbf{b} = -\mathbf{H}(\mathbf{b}_0)^{-1}\nabla G(\mathbf{b}_0) \tag{4}$$

Rather than compute the Hessian inverse, which is usually difficult because it contains second-order sensitivity information, we construct a series of approximations to $\mathbf{H}^{-1}$ from

$$\begin{aligned} \left(\mathbf{H}^{-1}\right)^1 &= \mathbf{I} \\ \left(\mathbf{H}^{-1}\right)^{j+1} &= \left(\mathbf{H}^{-1}\right)^j + \mathbf{D}^j \end{aligned} \tag{5}$$

where

$$\mathbf{D}^j = \frac{\delta\mathbf{b}\cdot\delta\mathbf{b}}{\delta\mathbf{b}\cdot\delta(\nabla G)} - \frac{\left(\mathbf{H}^{-1}\right)^j\left(\mathbf{H}^{-1}\right)^{jT}}{\delta(\nabla G)^T\left(\mathbf{H}^{-1}\right)^j\delta(\nabla G)} \tag{6}$$

This approximation to the Hessian inverse (Equation (5)) is then used with Equation (4) to determine the appropriate design increment.

A more detailed discussion of these algorithms is given in Reference [2]. Clearly, the use of these algorithms requires that the sensitivities be computed accurately, and because they are computed many times (once per design iteration), they must also be computed efficiently. In the next section, an efficient algorithm is described for obtaining the sensitivities after analyzing the original problem.

2.2 Explicit Design Sensitivity Analysis using an Adjoint Method

Tortorelli, *et al.*[5] described a Lagrange multiplier method for formulating the adjoint design sensitivities for nonlinear transient thermal systems. The variation of a general design functional may be expressed in explicit form with respect to variations in the prescribed boundary conditions. However, the design functional depends on these explicit quantities *and* implicitly on the temperature field. To obtain the explicit sensitivities, the implicit dependency on the temperature field must be resolved.

The design functional is expressed as

$$G(\mathbf{b}) = \int_B f(T)dV + \int_{\partial B} g(T,\mathbf{b})dA \tag{7}$$

where the temperature $T(\mathbf{x},\mathbf{b})$ represents the implicit response fields in G, $\mathbf{b}$ is the vector of design parameters, and the position vector is denoted by $\mathbf{x}$. The design vector will be used to define the boundary conditions, which ultimately control the values of all the response quantities and G. All quantities are defined in the region B or on the bounding surface ∂B (with outward unit normal vector $\mathbf{n}$), and are assumed to be smooth enough to justify the operations performed. Furthermore, differentiability of G with respect to the design is assumed.

The response quantities are implicitly defined by the design and the following mixed boundary value problem

$$\nabla\cdot\mathbf{q} + r = 0 \quad in\ B \tag{8}$$

with boundary conditions

$$\begin{aligned} T &= T^p \quad on\ A_T \\ q^s &= q^p(T,\mathbf{b}) \quad on\ A_q \\ q^s &= h(T,\mathbf{b})(T - T_\infty(\mathbf{b})) \quad on\ A_h \end{aligned} \tag{9}$$

Third International Conference on Inverse Design Concepts and Optimization in Engineering Sciences (ICIDES-III), Editor: G.S. Dulikravich, Washington D.C., October 23-25, 1991.

where $\mathbf{q}(\mathbf{x},\mathbf{b})$ is the heat flux vector, $r(T,\mathbf{g},\mathbf{x},\mathbf{b})$ represents the temperature– and temperature gradient–dependent internal heat generation, $\mathbf{g}(\mathbf{x},\mathbf{b}) \equiv \nabla T(\mathbf{x},\mathbf{b})$ is the temperature gradient, $q^s \equiv \mathbf{q}\cdot\mathbf{n}$ is the surface heat flux, and $h(T,\mathbf{b})$ is a convective transport coefficient between the surface of the domain and the ambient temperature, $T_\infty(\mathbf{b})$. A_T, A_q and A_h are complementary subsurfaces of ∂B and correspond to surfaces with prescribed temperature T^p, prescribed flux q^p, and prescribed convective boundary conditions, respectively. Note that the prescribed flux, heat transfer coefficient and ambient temperature distribution are all functions of the design vector, b, and the temperature to allow modeling of nonlinear heat flux and convective loads, as well as radiation. Note also that the internal heat generation term may be used to model convective transport terms when fluid flow is present. To complete the representation, a constitutive relation is introduced for the heat flux where $\hat{\mathbf{q}}$ is a general function of the position, temperature and temperature gradient,

$$\mathbf{q} = \hat{\mathbf{q}}(\mathbf{x},T,\mathbf{g}) \tag{10}$$

We will follow a finite element formulation, where Equation (8) is written in weak form and the boundary conditions in Equation (9) enter after integrating by parts and applying the divergence theorem.[8] First define the weighted residual, R, as

$$R(T,\mathbf{b},\lambda) \equiv -\int_B \{\nabla\lambda\cdot\mathbf{q} - \lambda r\}dV + \int_{A_q}\lambda q^p dA + \int_{A_h}\lambda h(T-T_\infty)dA \tag{11}$$

where λ is a weighting function which will described in more detail below. We use a *displacement* approach, in which the only dependent field is the temperature. Thus, Equations (9) and (10) are strictly enforced, and $\lambda = 0$ on A_T. When R is equal to zero (for all admissable λ) then Equation (8) is satisfied.

In general, the nonlinear nature of the problem will require that Newton-Raphson iteration be performed to find the zero of the residual. We introduce a truncated Taylor series expansion to update the temperature field from T^I at iteration I to T^{I+1} at iteration $I+1$:

$$R^{I+1} \approx R(T^I,\mathbf{b},\lambda) + \left\{\frac{\partial R(T^I,\mathbf{b},\lambda)}{\partial T}\right\}\Delta T = 0 \tag{12}$$

where $\Delta T \equiv T^{I+1} - T^I$ and

$$\begin{aligned}\frac{\partial R(T^I,\mathbf{b},\lambda)}{\partial T}\Delta T = -\int_B \left\{\nabla\lambda\cdot\frac{\partial\hat{\mathbf{q}}}{\partial T}(\Delta T) + \nabla\lambda\cdot\frac{\partial\hat{\mathbf{q}}}{\partial\mathbf{g}}\nabla(\Delta T) - \lambda\frac{\partial r}{\partial T}\Delta T - \lambda\frac{\partial r}{\partial\mathbf{g}}\nabla(\Delta T)\right\}dV + \\ \int_{A_q}\lambda\frac{\partial q^p}{\partial T}\Delta T dA + \int_{A_h}\lambda\left[\frac{\partial h}{\partial T}(T-T_\infty) + h\right]\Delta T dA\end{aligned} \tag{13}$$

In finite element analyses, R and $\frac{\partial R}{\partial T}$ form the residual vector and tangent stiffness matrix, respectively. The incremental problem given in Equation (12) is solved iteratively until the solution converges.

As we described earlier, changes in b affect the boundary conditions, which in turn affect the response quantities, which ultimately alter the value of the response functional G. The objective of sensitivity analysis then, is to derive an explicit expression for ∇G in which only variations of the design parameters $\delta\mathbf{b}$, are present.

In the Lagrange multiplier method for the adjoint sensitivity analysis, the residual is adjoined to G to define an augmented functional G^*,

$$G^* = \int_B f dV + \int_{\partial B} g dA - \int_B (\nabla\lambda\cdot\hat{\mathbf{q}} - r)\lambda dV + \int_{A_q}\lambda q^p dA + \int_{A_h}\lambda h(T-T_\infty)dA \tag{14}$$

This ensures that the governing equations are satisfied. In this equation, λ can be interpreted as a Lagrange multiplier, which will eventually be identified as the temperature field of a second, fictitious *adjoint* problem defined over B. Note that since the augmented term and its derivative are both identically zero, $G^* = G$ and $\nabla G^* = \nabla G$.

Formal differentiation of Equation (14) with respect to the design vector gives

$$\frac{dG}{d\mathrm{b}} = \int_B \frac{\partial f}{\partial T}\frac{\partial T}{\partial \mathrm{b}}dV + \int_{\partial B}\left(\frac{\partial g}{\partial \mathrm{b}} + \frac{\partial g}{\partial T}\frac{\partial T}{\partial \mathrm{b}}\right)dA - \int_B \left(\nabla\lambda\cdot\frac{\partial \mathbf{q}}{\partial T}\frac{\partial T}{\partial \mathrm{b}} + \nabla\lambda\cdot\frac{\partial \hat{\mathbf{q}}}{\partial \mathbf{g}}\frac{\partial \nabla T}{\partial \mathrm{b}} - \lambda\frac{\partial r}{\partial T}\frac{\partial T}{\partial \mathrm{b}} - \lambda\frac{\partial r}{\partial \mathbf{g}}\frac{\partial \nabla T}{\partial b}\right)dV + \int_{A_q}\lambda\left(\frac{\partial q^p}{\partial T}\frac{\partial T}{\partial \mathrm{b}} + \frac{\partial q^p}{\partial \mathrm{b}}\right)dA + \int_{A_h}\lambda\left(\left[\frac{\partial h}{\partial T}\frac{\partial T}{\partial \mathrm{b}} + \frac{\partial h}{\partial \mathrm{b}}\right](T - T_\infty) + h\left[\frac{\partial T}{\partial \mathrm{b}} - \frac{\partial T_\infty}{\partial \mathrm{b}}\right]\right)dA \tag{15}$$

With the exception of λ and the implicit terms involving the derivatives of T and ∇T with respect to b, all of the terms in Equation (15) are known once the original analysis problem is solved. In the sensitivity analysis, we will eliminate the implicit terms by a particular choice of the Lagrange multiplier λ.

To this end, we separate ∇G^* into terms which explicit quantities, ∇G^*_E, and those which are implicit quantities ∇G^*_I, where

$$\nabla G^*_E = \int_{\partial B}\frac{\partial g}{\partial \mathrm{b}}dA + \int_{A_q}\lambda\frac{\partial q^p}{\partial \mathrm{b}}dA + \int_{A_h}\lambda\left(\frac{\partial h}{\partial \mathrm{b}}(T - T_\infty) - h\frac{\partial T_\infty}{\partial \mathrm{b}}\right)dA \tag{16}$$

and

$$\nabla G^*_I = \overbrace{\left\{\int_B \frac{\partial f}{\partial T}\frac{\partial T}{\partial \mathrm{b}}dV + \int_{\partial B}\frac{\partial g}{\partial T}\frac{\partial T}{\partial \mathrm{b}}dA\right\}}^{\frac{\partial Q}{\partial T}\cdot\frac{\partial T}{\partial \mathrm{b}}} - \int_B \left(\nabla\lambda\cdot\frac{\partial \hat{\mathbf{q}}}{\partial T}\frac{\partial T}{\partial \mathrm{b}} + \nabla\lambda\cdot\frac{\partial \hat{\mathbf{q}}}{\partial \mathbf{g}}\frac{\partial \nabla T}{\partial \mathrm{b}} - \lambda\frac{\partial r}{\partial T}\frac{\partial T}{\partial \mathrm{b}} - \lambda\frac{\partial r}{\partial \mathbf{g}}\frac{\partial \nabla T}{\partial \mathrm{b}}\right)dV + \int_{A_q}\lambda\frac{\partial q^p}{\partial T}\frac{\partial T}{\partial \mathrm{b}}dA + \int_{A_h}\lambda\left(\frac{\partial h}{\partial T}\frac{\partial T}{\partial \mathrm{b}}(T - T_\infty) + h\frac{\partial T}{\partial \mathrm{b}}\right)dA \tag{17}$$

where $\frac{\partial T}{\partial \mathrm{b}} = 0$ on A_T. On examination of Equation (17) and Equations (8) and (9) we note that the implicit term can be annihilated by solving the following adjoint problem: Find that value of λ for which

$$-\frac{\partial G}{\partial T} = \frac{\partial R(T, \mathrm{b}, \lambda)}{\partial T}\frac{\partial T}{\partial \mathrm{b}} \tag{18}$$

for all admissible $\frac{\partial T}{\partial \mathrm{b}}$. Note that $\frac{\partial G}{\partial T}$ is the indicated quantity in Equation (17). This equation is linear in λ, and is the adjoint operator for the incremental problem (Equation (12)). This allows us to solve the adjoint problem efficiently when the finite element method is used.

Indeed, after solving the original problem with Newton-Raphson iteration, we next store the final decomposed tangent stiffness matrix. Then the adjoint load vector ($\frac{\partial G}{\partial T}$) is formed which corresponds to the following adjoint

Third International Conference on Inverse Design Concepts and Optimization in Engineering Sciences (ICIDES-III), Editor: G.S. Dulikravich, Washington D.C., October 23-25, 1991.

loads:

$$\begin{aligned} r_\lambda &= \frac{\partial f}{\partial T} \quad in\ B \\ \lambda &= 0 \quad on\ A_T \\ q^*_\lambda &= \frac{\partial g}{\partial T} \quad on\ A_q \\ q^*_\lambda &= \left(\frac{\partial h}{\partial T}(T - T_\infty) + h\right)\lambda + \frac{\partial g}{\partial T} \quad on\ A_h \end{aligned} \tag{19}$$

Finally, we perform a back substitution on the transpose (adjoint) of the decomposed stiffness matrix to evaluate λ. Once λ is determined, then $\nabla G^*_I \equiv 0$ and the sensitivities are obtained directly from Equation (16). The efficiency of this method lies in the fact that a single back-substitution into the already decomposed stiffness matrix, followed by substitution in Equation (16), yields all of the components of the sensitivity vector. In general, the solution of the primal problem requires several Newton-Raphson iterations. Hence, the added cost of evaluating the sensitivities is relatively small.

In the finite element evaluation of the adjoint load vector and ∇G^*_E, the same numerical quadrature is used as that used to evaluate G, the tangent stiffness matrix and residual. This ensures that consistent results are obtained. In the next section, these methods will be used in an example problem concerning Bridgman crystal growth.

3: APPLICATION TO A CRYSTAL GROWTH PROCESS

3.1 Bridgman Crystal Growth

When crystals for electronics applications are grown using the Bridgman process, the finished bulk crystals are sliced into thin wafers perpendicular to the growth direction. Electronic devices are then fabricated on these wafers. The properties of the devices are highly dependent on the degree of perfection and compositions of the wafer. Since these attributes are set during growth of the crystal, control of the growth process is vital. In particular, fluid flow in the melt during solidification can interact with the solute field near the crystal-melt interface to adversely affect the chemical composition of the crystal.[9] The primary means for controlling the convective flow is to control the shape of the crystal-melt interface, which may be accomplished by defining appropriate process parameters.

The latest generation of Bridgman furnaces are divided into several independent heating zones along their length, so that complex temperature distributions can be applied. While this gives these furnaces great flexibility, it also necessitates that detailed analyses be performed to relate the temperatures imposed on the furnace wall to the temperature distribution produced in the crystal.

Using the techniques described in the preceding sections, a model is presented for determining the optimal temperature distribution to impose on the furnace wall to produce the desired temperature distribution in the crystal. In particular, the desired temperature distribution in the crystal becomes the objective, and the temperatures on the furnace wall comprise the design parameters. In our example problem, the furnace to be examined is one that will be used in low gravity space processing.

A configuration proposed by researchers at GTE for growing GaAs crystals in space is illustrated in Figure 1.[10] In the proposed experiment, a round pyrolytic boron nitride crucible with graphite end plugs and a quartz bottom is used to contain a GaAs charge. The entire container is to be filled on earth, then sent into space, where it will be placed in a programmable gradient furnace, melted and resolidified in a controlled manner. The geometry

Third International Conference on Inverse Design Concepts and Optimization in Engineering Sciences (ICIDES-III), Editor: G.S. Dulikravich, Washington D.C., October 23-25, 1991.

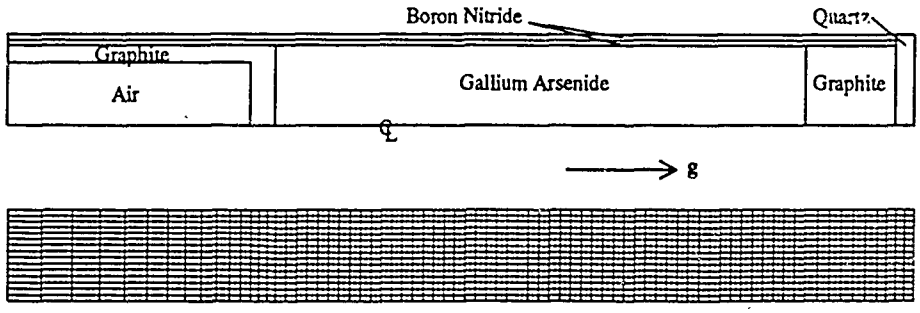


Fig. 1: Schematic view of the model for the proposed experiment to grow GaAs crystals, and corresponding finite element mesh containing 1216 nodes and 1230 elements.

of the experimental apparatus was exploited to describe the process using a two-dimensional axisymmetric finite element model. It will be assumed that the ampoule is maintained with its axis parallel to the gravity vector.

The commercial code FIDAP[3], with modifications to enable the design sensitivities to be calculated, was used for the analysis. The container and melt were modeled using four–noded linear isoparametric elements, whereas the presence of the furnace wall was represented by a specified temperature distribution exchanging heat by radiation with the exterior surface of the ampoule. Further details of the radiation calculation are given below.

The governing equations and boundary conditions for these types of problems are well established[11], and are reproduced here only to the extent necessary for the present discussion. In addition to the energy balance equation, we must consider the momentum balance equation to model buoyancy-driven convection in the crystal. The density was assumed to be constant, except for thermal expansion in the liquid phase, which is included by the Boussinesq approximation. With this assumption, the steady form of the momentum balance equation is

$$\rho_0(\mathbf{u}\cdot\nabla\mathbf{u}) = -\nabla p + \mu\nabla^2\mathbf{u} + \rho_0\mathbf{g}_o(1-\beta(T-T_{ref})) \tag{20}$$

where $\mathbf{u}$ is the velocity, p is the pressure, μ is the dynamic viscosity, $\mathbf{g}_o$ is the gravity vector, β is the volumetric thermal expansion coefficient, and T_{ref} is the temperature at which the density is ρ_0 (in this case, the melting temperature). Note that the presence of the buoyancy term couples the momentum balance equations to the energy balance equation. There is no slip of the liquid past the solid, so that the velocity of the fluid is zero at all of the boundaries of the melt.

The steady form of the energy balance equation, adopting Fourier's Law ($\hat{\mathbf{q}} = -k(\mathbf{x},T)\mathbf{g}$) for the constitutive relation for heat flux, is given by

$$\rho_0 c_p(\mathbf{u}\cdot\nabla T) = \nabla\cdot(k\nabla T) \tag{21}$$

where c_p is the specific heat and k is the temperature dependent thermal conductivity. The advection term on the left-hand side of this equation defines the internal heat generation term, r, noted above. Heat is conserved at the crystal-melt interface, requiring that

$$k_s\nabla T_s\cdot\mathbf{n} - k_l\nabla T_l\cdot\mathbf{n} = 0 \tag{22}$$

where $\mathbf{n}$ is a unit vector normal to the interface and the subscripts l and s refer to the liquid and solid phases, respectively. For very dilute alloys, the interface temperature can be assumed to be the melting temperature of the parent phase, denoted T_m.

Even though the problem is steady, latent heat can be convected by the fluid flow in the melt. Latent heat evolution was included in the model using an enthalpy-specific heat method.[12] This method requires that the enthalpy of solidification be spread over a range of temperatures, and in all of the simulations which follow, this interval was chosen to be 1K. The specific heat was computed from the gradients of enthalpy and temperature at each element integration point

$$c_p = \sqrt{\frac{\nabla H \cdot \nabla H}{\nabla T \cdot \nabla T}} \tag{23}$$

and assembled using a lumped mass matrix formulation. These formulations ensure that the entire heat content of the material is accounted for in a computationally efficient way.[12]

The ends of the ampoule were considered to be insulated. Heat was transferred between the ampoule and the furnace wall by radiation only. The ampoule was assumed to fit closely in the furnace, so that radiation exchange was limited to opposing faces in the furnace, *i.e.* no view factor calculations were required. The Stefan-Boltzmann law was factored, so that a nonlinear convection coefficient, h_{eff}, was defined for each integration point

$$\begin{aligned} q_{rad} &= \sigma\varepsilon\left(T^4 - T_{furnace}^4\right) \\ &= \underbrace{\sigma\varepsilon\left(T^2 + T_{furnace}^2\right)\left(T + T_{furnace}\right)}_{h_{eff}}\left(T - T_{furnace}\right) \end{aligned} \tag{24}$$

For all cases, the emissivity was taken to be constant at 0.7. The material properties used in the simulations are given in the Appendix.

Pressure was eliminated as a degree of freedom using a penalty method.[13] In this formulation, the continuity equation for an incompressible fluid is modified to allow an artificial compressibility, so that

$$\nabla \cdot \mathbf{u} = -\varepsilon_p p \tag{25}$$

where ε_p is a penalty parameter, taken to be $1\text{x}10^{-8}$ in all cases. The resulting coupled nonlinear equations for the velocities and temperatures were resolved at each time step by Newton-Raphson iteration or by successive substitution. Convergence was declared when both the rms change in each field variable and the residual errors in the finite element equations fell below $1\text{x}10^{-3}$.

The temperature distribution for a constant temperature gradient of 5 K/mm along the furnace wall was known to produce significant undesirable curvature of the crystal-melt interface.[1] The primary reason for is the variation in thermal conductivity between the liquid and solid. Thus, a constant temperature gradient results in unequal heat fluxes at the interface. (See Equation (22).) To alleviate this problem, the temperatures applied along the furnace wall will be adjusted to produce a specified temperature distribution within the crystal. The procedures developed in the previous sections were used for this purpose.

3.2 Implementation of Design Sensitivity Analysis

The commercial finite element code FIDAP[3] was modified to perform the adjoint load and sensitivity calculations described in the previous section. The sensitivity calculations neglected the fluid velocities and the coupling to the momentum equations. However, the optimization still converged in an acceptable number of iterations because the problem is dominated by the thermal aspects. A shell program was then written to coordinate

Third International Conference on Inverse Design Concepts and Optimization in Engineering Sciences (ICIDES-III), Editor: G.S. Dulikravich, Washington D.C., October 23-25, 1991.

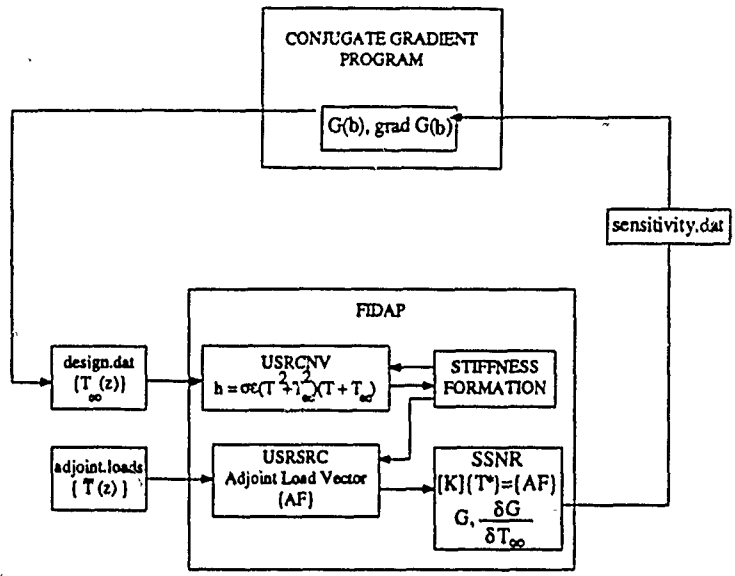


Fig. 2: Schematic of link between conjugate gradient search algorithm and FIDAP.

the nonlinear heat transfer analysis, the sensitivity analysis, and the numerical optimization. A schematic diagram showing the details of the interface between the shell program and FIDAP is shown in Figure 2.

The file *adjoint.loads* in Figure 2 contained the information describing the desired temperature profile, $\overline{T}(z)$, to be attained in the ampoule. This distribution was specified on both the center-line and the outer radius of the crystal (inner radius of the ampoule). The objective function was then defined as the error between the desired and computed temperatures at N discrete points

$$G = \sum_{i=1}^{N} \left(T_i - \overline{T}_i\right)^2 \tag{26}$$

Thus, G represents the function to be minimized.

The only design variables allowed in the problem were the furnace wall temperatures, $T_\infty(z)$. Note, however, that in view of Equation (24) there is an implicit dependence of the heat transfer coefficients on $T_\infty(z)$ which must be accounted for.

The progress of the optimization is illustrated in Figures 3 – 5. It is easy to see that the search through the design space converges quickly to the optimal solution. For this case, the ambient temperature at each position on the furnace wall opposite each surface node on the ampoule comprised the 76 design variables. The fact that there are so many design degrees of freedom leads to the unrealistic fluctuations seen in the furnace wall temperature profile.

This same case was then modeled using nine zones to span the entire length of the furnace. The ten specified wall temperatures represent the design parameters, and the intermediate wall temperatures were determined via linear interpolation. The results for this case are shown in Figure 6. It can be seen that equivalent results are obtained for the internal temperature. It is interesting to note, however, that the results for the latter case are not simply an average of the results from the former.

Notice that in all of these cases, the sudden changes in slope in the objective function led to sharp changes in the furnace wall temperature profile and that the ampoule temperature was unable to capture the sudden change. Accordingly, a new objective function was defined which maintained the discontinuity in slopes at the crystal-melt

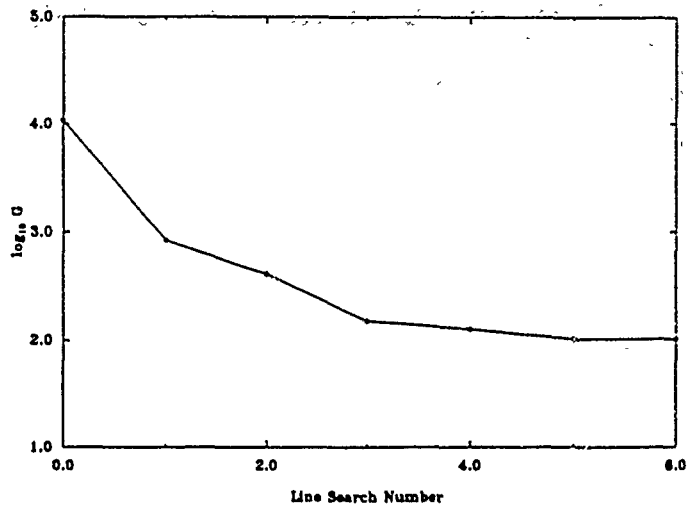


Fig. 3: Progress of the value of the objective function during the optimization

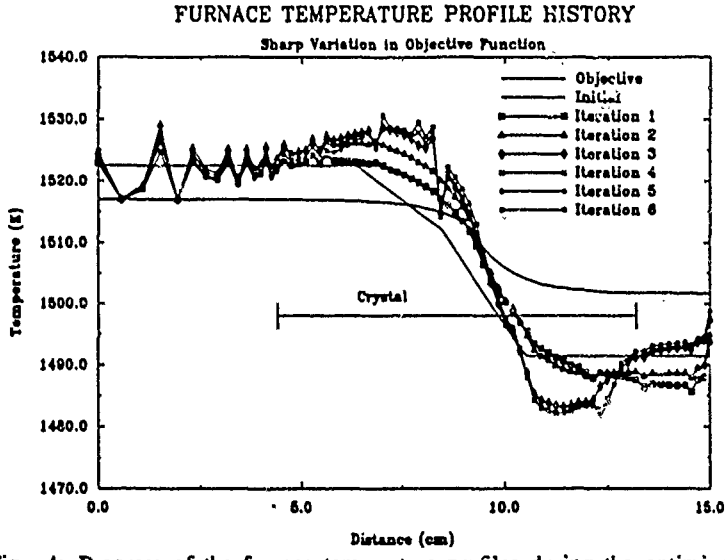


Fig. 4: Progress of the furnace temperature profiles during the optimization

interface, and rolled off exponentially with distance from the interface. The results, shown in Figure 7, illustrate that one may attain the final objective, if the physics of the problem allows it. This is the nature of optimization, where existence and uniqueness of solutions is not always guaranteed.

For each case, the progress through the numerical optimization was very similar. Five to ten line searches were required, with six to eight function evaluations along each line. This latter number was found to be very sensitive to the convergence tolerance for the parabolic interpolation. Setting the tolerance below 0.01 resulted in many more function evaluations with no improvement in the overall results. The problems ran to completion in about one hour on a Sun SPARCstation 1+.

A quasi-Newton method was also used, but for this problem the results were almost identical. The quasi-Newton procedure typically required one more line search than the conjugate gradient method, but there were not enough tests done to draw any definitive conclusions.

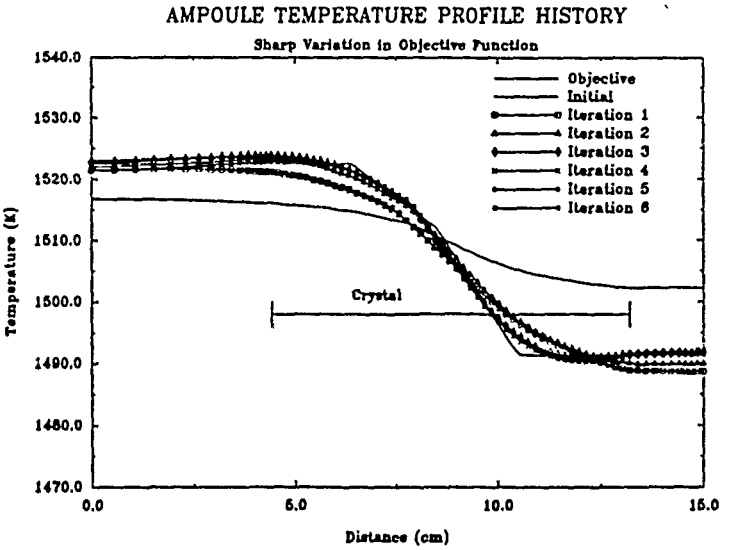


Fig. 5: Progress of the ampoule temperature profiles during the optimization

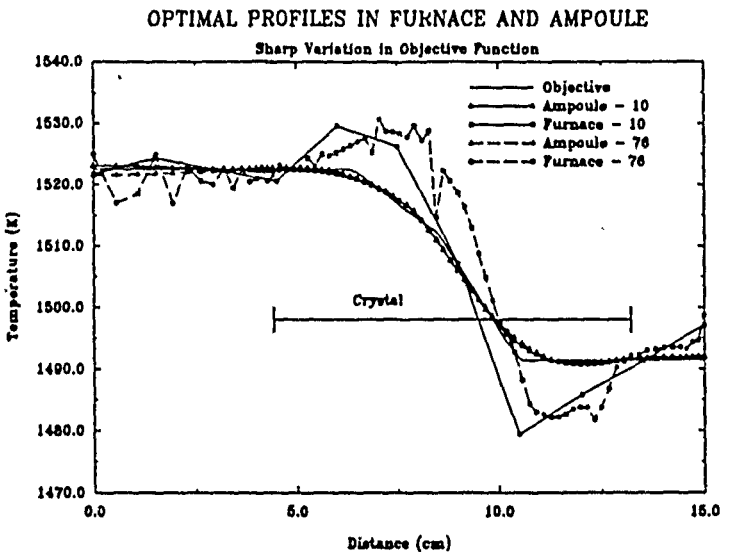


Fig. 6: Comparison of optimal solutions using 10 and 76 heating zones, respectively.

4: CONCLUSIONS

The results of the preceding section indicate the practicality of optimal process design and the utility of the sensitivity analysis for this class of problems. The optimal solution can be found with little user intervention. Indeed, the only work required beyond that for the normal analysis is the definition of the design variables and objective function.

In the future, we would like to extend this work to consider transient problems. However, the analysis becomes more complicated because the transient problem requires a convolution integral to be evaluated in the adjoint method. Other methods, such as direct differentiation, may prove to be more efficient for this class of problems.

The sensitivity formulation used for this work did not include the advective terms in the governing equations, and the fluid velocities were also not considered in evaluating the implicit variations of G. This will be important for advection-dominated flows, and this work is in progress.

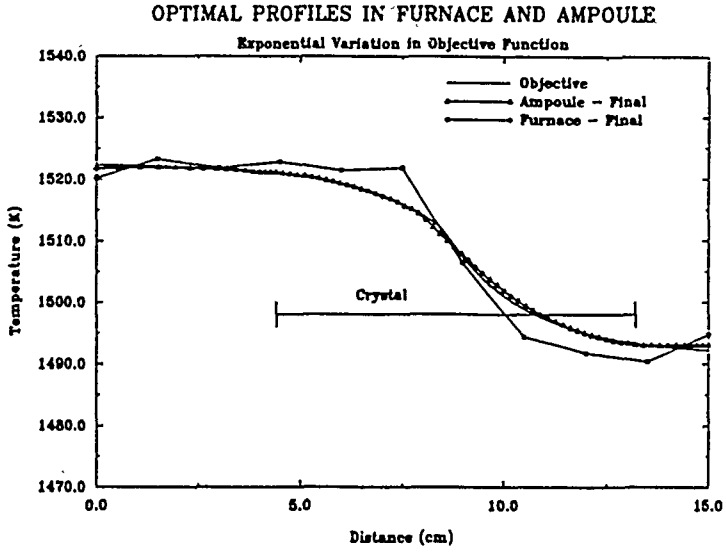


Fig. 7: Optimal furnace wall and ampoule temperature profiles for exponential variation in the objective function

5: ACKNOWLEDGMENT

The authors wish to thank NASA, which has supported this work under grant NASA NAGW-1683 and NAG3-1286, and the National Center for Supercomputing Applications for partial support of one of the investigators.

6: REFERENCES

[1] J. A. Dantzig and L. S. Chao. Interface shape control in bridgman crystal growth. In M. Rappaz and M. Ozgu, editors, *Modeling of Casting, Welding and Advanced Solidification Processes*, page in press, Warrendale, PA, 1991. TMS-AIME.

[2] G. N. Vanderplaats. *Numerical Optimization Techniques for Engineering Design: with Applications*. McGraw-Hill, New York, 1984.

[3] M. S. Engelman. *FIDAP Theoretical Manual*. Fluid Dynamics International, Evanston, IL, 1987.

[4] E. J. Haug, K. Choi, and V. Komkov. *Design Sensitivity Analysis of Elastic Mechanical Systems*. Academic Press, New York, 1986.

[5] D. A. Tortorelli, R. B. Haber, and S. C.-Y. Lu. Design Sensitivity Analysis for Nonlinear Transient Thermal Systems. *Computer Methods in Applied Mechanics and Engineering*, 75:61–78, 1990.

[6] D. Tortorelli. Sensitivity Analysis for Nonlinear Constrained Elastostatic Systems. In S. Saigal and S. Mukherjee, editors, *Sensitivity Analysis and Optimization with Numerical Methods, AMD Vol. 115*, pages 115–126, 1990.

[7] W. Press, B. Flannery, S. Teukolsky, and W. Vetterling. *Numerical Recipes*. Cambridge Universiy Press, Cambridge, 1986.

[8] R. D. Cook. *Concepts and Applications of Finite Element Analysis*. Wiley, New York, 1981.

[9] C. J. Chang and R. A. Brown. Radial segregation induced by natural convection and the melt/solid interface shape in vertical Bridgman growth. *J. Crystal Growth*, 63:343, 1983.

[10] J. A. Kafalas and A. H. Bellows. A comparative study of the influence of buoyancy driven fluid flow on gaas crystal growth. *Proc. AIAA Conference*, 1988.

Appendix A: Material Properties Used in the Simulations

Table I: Material properties used in the simulations

Material	Quartz	Air	Graphite	PBN - 1	PBN - 2	GaAs
Density (g/mm^3)						
	2.2×10^{-3}	2.35×10^{-7}	1.83×10^{-3}	1.9×10^{-3}	1.9×10^{-3}	5.71×10^{-3}
Thermal Conductivity (W/mmK)						
273 K	3.4×10^{-4}	1.15×10^{-5}	3.0×10^{-2}	2.50×10^{-2}	4.0×10^{-4}	1.7×10^{-3}
750 K	4.7×10^{-4}	1.43×10^{-5}	2.27×10^{-2}	1.70×10^{-2}	5.0×10^{-4}	1.7×10^{-3}
1060 K	6.6×10^{-4}	1.88×10^{-5}	1.78×10^{-2}	1.58×10^{-2}	5.6×10^{-4}	1.7×10^{-3}
1220 K	7.5×10^{-4}	2.02×10^{-5}	1.52×10^{-2}	1.51×10^{-2}	6.0×10^{-4}	1.7×10^{-3}
1511 K	7.5×10^{-4}	2.24×10^{-5}	1.29×10^{-2}	1.50×10^{-2}	6.0×10^{-4}	1.7×10^{-3}
1512 K	7.5×10^{-4}	2.24×10^{-5}	1.29×10^{-2}	1.50×10^{-2}	6.0×10^{-4}	3.5×10^{-3}
1600 K	7.5×10^{-4}	2.30×10^{-5}	1.24×10^{-2}	1.50×10^{-2}	6.0×10^{-4}	3.5×10^{-3}
Specific Heat (J/gK)						Enthalpy (J/g)
273 K	0.123	0.294	0.19	0.20	0.20	27.4
750 K	0.244	0.294	0.19	0.40	0.40	75.4
1060 K	0.278	0.294	0.19	0.44	0.44	106.5
1220 K	0.284	0.294	0.19	0.47	0.47	122.6
1511 K	0.299	0.294	0.19	0.47	0.47	151.8
1512 K	0.299	0.294	0.19	0.47	0.47	325.5
1600 K	0.299	0.294	0.19	0.47	0.47	575.5
Viscosity (g/mm s)						
<1511 K						1.0×10^{20}
>1512 K						1.7×10^{-3}

[11] M. E. Glicksman, S. R. Coriell, and G. B. McFadden. Interaction of Flows with the Crystal-Melt Interface. *Ann. Rev. Fluid Mech.*, 18:307–335, 1986.

[12] J. A. Dantzig. Modeling Liquid-Solid Phase Changes with Melt Convection. *International Journal of Numerical Methods in Engineering*, 28:1769–1785, 1989.

[13] M. Bercovier and M. S. Engelman. A Finite Element for Incompressible Fluid Flows. *J. Comp. Physics*, 30:181, 1979.

Third International Conference on Inverse Design Concepts and Optimization in Engineering Sciences (ICIDES-III), Editor: G.S. Dulikravich, Washington D.C., October 23-25, 1991.

NUMERICAL IDENTIFICATION OF BOUNDARY CONDITIONS ON NONLINEARLY RADIATING INVERSE HEAT CONDUCTION PROBLEMS*

by

Diego A. Murio

Department of Mathematical Sciences
University of Cincinnati
Cincinnati, OH 45221-0025
U.S.A.

ABSTRACT

An explicit and unconditionally stable finite difference method for the solution of the transient inverse heat conduction problem in a semi-infinite or finite slab mediums subject to nonlinear radiation boundary conditions is presented. After measuring two interior temperature histories, the mollification method is used to determine the surface transient heat source if the energy radiation law is known. Alternatively, if the active surface is heated by a source at a rate proportional to a given function, the nonlinear surface radiation law is then recovered as a function of the interface temperature when the problem is feasible. Two typical examples corresponding to Newton cooling law and Stefan -Boltzmann radiation law respectively are illustrated. In all cases, the method predicts the surface conditions with an accuracy suitable for many practical purposes.

* Partially supported by a W. Taft Fellowship.

Third International Conference on Inverse Design Concepts and Optimization in Engineering Sciences (ICIDES-III), Editor: G.S. Dulikravich, Washington D.C., October 23-25, 1991.

1. Introduction.

In this paper we investigate the numerical identification of surface transient heat sources in one-dimensional semi-infinite and finite slab mediums when the active surface radiates energy according to a known nonlinear law. Alternatively, if the active surface is heated by a source at a rate proportional to a given function, the nonlinear radiating boundary condition is then numerically identified as a function of the interface temperature if the problem is feasible.

These two tasks can be viewed as suitable generalizations of the classical problem of attempting to determine the interface temperature between a gas and a solid with a nonlinear heat transfer law. The existence and uniqueness of a strictly increasing solution of the semi-infinite body version of this problem has been considered by Mann and Wolf [Ref.7] for a monotone Lipschitz radiation law. Roberts and Mann [Ref.10] extended the previous result after removing the Lipschitz condition on the nonlinear heat transfer law. Keller and Olmstead [Ref.6] investigated the same problem in the presence of a positive integrable transient source and introduced a constructive proof for existence and uniqueness of the interface temperature by the method of lower and upper solutions. The numerical solution of the nonlinear Volterra integral equation characterizing the active surface temperature history was implemented by Chambré [Ref.1] using the method of succesive approximations and, more recently, by Groetsch [Ref.3] who succesfully combined Abel inversion formula with B-spline approximation and product integration. A natural extension of this technique to solve the same problem in the finite slab medium is discussed in Groetsch [Ref.4]. Also for the finite slab case, Villaseñor and Squire [Ref.12] have proposed a numerical procedure based on a generalized trapezoidal rule and Richardson extrapolation. More general problems of the same kind, combining the effects of convection and radiation at the interface, can be found in Friedman [Ref.2] and Saljnikov and Petrovic [Ref.11].

In all the works mentioned above, the nonlinear radiation law and the transient boundary source are supposed to be known in order to determine the interface temperature. Consequently, if the new task consists on the identification of the nonlinear radiation law or on the identification of the transient boundary source function, a different approach must be used.

It is possible to estimate the surface temperature and the surface heat flux in a body from measured temperature histories at fixed locations inside the body. However, this Inverse Heat Conduction Problem (IHCP) is an ill-posed problem because small errors in the data induce large errors in the computed surface heat flux history or in the computed temperature history solutions and, consequently, special methods are needed in order to restore continuity with respect to the data. In this paper we consider initially, the solution of a one-dimensional IHCP by a fully explicit and stable space marching finite difference implementation of the Mollification Method introduced by Murio [Ref.8] and Guo, Murio and Roth [Ref.5]. The procedure allows for a direct discretization of the differential equation and it is generated by automatically filtering the noisy data by discrete mollification against a suitable averaging kernel and then using finite differences, marching in space, to numerically solve the associated well-posed problem. Once the temperature and the heat flux transient functions have been approximately recovered at the interface, it is a simple task to numerically identify the transient heat source if the nonlinear radiation law is known. On the other hand, if the surface is heated by a source at a rate proportional to a given function, we proceed to approximately recover the nonlinear surface radiation law describing the physical conditions at the interface, provided that the range of temperatures at the interface contain sufficient information.

In Section 2, we define the new identification problems with data specified on a

Third International Conference on Inverse Design Concepts and Optimization in Engineering Sciences (ICIDES-III), Editor: G.S. Dulikravich, Washington D.C., October 23-25, 1991.

continuum of time and data errors measured in the L_2 norm and derive rigorous stability bounds. The efficiency of the method is demonstrated in Section 3, where together with a description of the numerical procedure, we present the results of several computational experiments with rapidly varying and discontinuous profiles, for both linear - Newton cooling law - and nonlinear - Stefan-Boltzmann law - models. In all cases, numerical stability and good accuracy are achieved even for small time steps and high levels of noise in the data. Section 4 includes a summary and some conclusions.

2. Description of the Problem.

We consider a one-dimensional IHCP in a semi-infinite or finite slab, in which the temperature and heat flux histories f(t) and q(t) on the left-hand surface (x = 0) are desired and unknown, and the temperature and heat flux at some interior point $x = x_0$ or at the right-hand surface x = a are approximately measurable. Note that, equivalently, the data temperature histories might be measured at two interior points. For the semi-infinite medium, $0 < x_0$ and for the finite slab, $0 < x_0 \le a$. We assume linear heat conduction with constant coefficients and normalize the problem by dimensionless quantities. Without loss of generality, we consider $x_0 = a = 1$ in all cases. The problem can be described mathematically as follows.

For the semi-infinite or finite slab, the unknown temperature u(x,t) satisfies respectively,

$$u_t(x,t) = u_{xx}(x,t), \qquad t > 0,\ 0 < x < \infty \text{ or } 0 < x < 1, \tag{1a}$$

$$u(1,t) = F(t), \qquad t > 0, \text{ with corresponding approximate data function } F_m(t), \tag{1b}$$

$$-u_x(1,t) = Q(t), \qquad t > 0, \text{ with corresponding approximate data function } Q_m(t), \tag{1c}$$

$$u(x,0) = u_0(x), \qquad 0 < x < \infty \text{ or } 0 < x < 1, \tag{1d}$$

$$u(0,t) = f(t). \qquad t > 0, \text{ the desired but unknown temperature function,} \tag{1e}$$

$$-u_x(0,t) = q(t) = E(u(0,t))-g(t), \qquad t > 0, \text{ the desired but unknown heat flux function.} \tag{1f}$$

The nonlinear boundary condition (1f), indicates that the active surface radiates energy at a rate proportional to E and is heated at a rate proportional to the function g. Our aim is to obtain more detailed information about the boundary condition at the interface x = 0. More precisely, we want to estimate the function E if g is known or, reciprocally, we want to identify the source function g if the radiation law E is given.

We also assume that all the functions involved are L_2 functions in any time interval of interest and use the corresponding L_2 norm, as defined below, to measure errors:

$$\|f\| = \left[\int_{t_1}^{t_2} |f(t)|^2 \, dt \right]^{1/2} .$$

In this setting, it is also natural to hypothesize that the exact data functions F(t) and Q(t) and the measured data functions $F_m(t)$ and $Q_m(t)$ satisfy the L_2 data error bounds

$$\|F-F_m\| \le \varepsilon \quad \text{and} \quad \|Q-Q_m\| \le \varepsilon.$$

Third International Conference on Inverse Design Concepts and Optimization in Engineering Sciences (ICIDES-III), Editor: G.S. Dulikravich, Washington D.C., October 23-25, 1991.

It is well known that solving for f(t) and q(t) from F(t) and Q(t) amplifies every Fourier frequency component of the error by the factor $\exp[w/2]^{1/2}$, $-\infty < w < \infty$. This shows that the inverse problem is highly ill-posed in the high frequency components. See Murio [Ref.8] and Guo, Murio and Roth [Ref.5] for further discussions.

Stabilized Problem.

The one-dimensional IHCP can be stabilized if instead of attempting to find the point values of the temperature function f(t) or the heat flux function q(t), we attempt to reconstruct the δ-mollification of the functions f and q, at time t, given by

$$J_\delta f(t) = (\rho_\delta * f)(t), \quad J_\delta q(t) = (\rho_\delta * q)(t),$$

where

$$\rho_\delta(t) = \frac{1}{\delta\, \pi^{1/2}} \exp[-t^2/\delta^2]$$

is the one-dimensional Gaussian kernel of radius $\delta > 0$. The mollifier $\rho_\delta(t)$ is always positive, falls to nearly zero outside the interval centered at the origin and radius 3δ and

$$(\rho_\delta * f)(t) = \int_{-\infty}^{\infty} \rho_\delta(\tau) f(t-\tau)\, d\tau$$

is the one-dimensional convolution of the functions ρ_δ and f. We notice that $J_\delta f(t)$ is a C^∞ (infinitely differentiable) function and that the mollifier has total integral 1. Mollifying system (1), we obtain the following associated problem: Attempt to find $J_\delta f_m(t) = J_\delta u(0,t)$ and $J_\delta q_m(t) = -J_\delta u_x(0,t)$ at some point t of interest and for some radius $\delta > 0$, given that $J_\delta u(x,t)$ satisfies for the semi-infinite or finite slab respectively,

$$\begin{aligned}
&(J_\delta u)_t = (J_\delta u)_{xx}, && t > 0,\ 0 < x < \infty \text{ or } 0 < x < 1,\\
&J_\delta u(1,t) = J_\delta F_m(t), && t > 0,\\
&-J_\delta u_x(1,t) = J_\delta Q_m(t), && t > 0,\\
&J_\delta u(x,0) = J_\delta u_0(x,0), && 0 < x < \infty \text{ or } 0 < x < 1,\\
&J_\delta u(0,t) = J_\delta f_m(t), && t > 0, \text{ unknown},\\
&-J_\delta u_x(0,t) = J_\delta q_m(t), && t > 0, \text{ unknown}.
\end{aligned} \tag{2}$$

This problem and its solutions satisfy the following:

Theorem 1. Suppose that $\|F-F_m\| \le \varepsilon$ and $\|Q-Q_m\| \le \varepsilon$. Then

(i) Problem (2) is a formally stable problem with respect to perturbations in the data.

(ii) If the exact boundary temperature function f(t) and the exact heat flux function q(t) have uniformly bounded first order derivatives on the bounded domain D = [0,T], then $J_\delta f_m$ and $J_\delta q_m$ verify

Third International Conference on Inverse Design Concepts and Optimization in Engineering Sciences (ICIDES-III), Editor: G.S. Dulikravich, Washington D.C., October 23-25, 1991.

$$\|f-J_\delta f_m\|_D \le O(\delta) + 3\varepsilon \exp[(2\delta)^{-2/3}] \tag{3}$$

and

$$\|q-J_\delta q_m\|_D \le O(\delta) + \frac{\varepsilon}{2}(1 + 3\exp[\delta^{-2/3}]). \tag{4}$$

The proof of this statement can be found in Guo, Murio and Roth [Ref.5].

Once the mollified temperature and mollified heat flux functions have been evaluated at the interface, it is feasible to attempt to identify the source function g or the radiation energy function E given in formula (1f).

Identification of the source function g.

Assuming that the radiation law at the active surface is known, according to (1f), the exact source function is given by

$$g(t) = E(f(t))-q(t). \tag{5}$$

The approximate source function, denoted $g_a(t)$, is defined by

$$g_a(t) = E(J_\delta f_m(t))-J_\delta q_m(t), \tag{6}$$

and in order to estimate the error, we suppose that the surface radiates energy at a rate proportional to $[f(t)]^p$. Here p is a positive integer, the value p = 1 corresponding to Newton's law of cooling and p = 4 to Stefan's radiation law.

The difference (5) - (6) gives

$$g(t) - g_a(t) = [f(t)]^p - [J_\delta f_m(t)]^p + q(t) - J_\delta q_m(t).$$

From the identity $a^n - b^n = (a-b)(a^{n-1}+a^{n-2}b +\ldots+ab^{n-2}+b^{n-1})$, taking norms and introducing $M = \max\{\|J_\delta f_m\|_{\infty,D}, \|f\|_{\infty,D}\}$, we get

$$\|g - g_a\|_D \le pM^{p-1} \|f - J_\delta f_m\|_D + \|q - J_\delta q_m\|_D.$$

Combining the last inequality with the upper bounds (3) and (4), we obtain the estimate

$$\|g - g_a\|_D \le (pM^{p-1} + 1)\{O(\delta) + 3\varepsilon \exp[\delta^{-2/3}]\}. \tag{7}$$

This shows that the identification of the source function g is stable with respect to errors in the data functions F and Q , for fixed p and $\delta > 0$.

Remarks:

1. Notice that the approximate source function g_a is actually a function of the radius of mollification δ, the amount of noise in the data ε and the exponent p in the radiation model E.
2. From a more theoretical point of view, inequality (7) can be used to show the convergence of g_a to g in the L_2 norm. In fact, setting $O(\delta) = C\,\delta$ for some constant $C > 0$, and choosing $\delta = [\ln(1/\varepsilon^{1/2})]^{-3/2}$, after replacing these quantities in (7), we obtain

$$\|g - g_a\|_D \le (pM^{p-1} + 1)(C[\ln(1/\varepsilon^{1/2})]^{-3/2} + 3\varepsilon^{1/2}).$$

This last inequality implies that, for the special selection of the radius of mollification indicated above, $\|g - g_a\|_D \to 0$ as $\varepsilon \to 0$, for any value of p.

Identification of the radiation law function E.

From equation (1f) it follows that the exact function E, assuming that the

Third International Conference on Inverse Design Concepts and Optimization in Engineering Sciences (ICIDES-III), Editor: G.S. Dulikravich, Washington D.C., October 23-25, 1991.

source function g is given, satisfies

$$E(u(0,t)) = E(f(t)) = g(t) + q(t). \tag{8}$$

The approximate function, denoted E_a, is defined by

$$E_a(J_\delta f_m(t)) = g(t) + J_\delta q_m(t). \tag{9}$$

Subtracting (8) from (9), taking norms and using inequality (4), we inmediately have

$$\|E - E_a\|_D \le O(\delta) + \frac{\varepsilon}{2}\,(1+ 3\,\exp[\delta^{-2/3}]). \tag{10}$$

This estimate also shows that the identification of the radiation law - as a function of time - is stable with respect to perturbations in the data functions F and Q, for a fixed $\delta > 0$, provided that the source function is known. However, this information is clearly not sufficient to identify the physical process at the interface. Nevertheless, since at each time t_i we know the ordered pairs $(t_i, J_\delta f_m(t_i))$ and $(t_i, E_a(t_i))$, it is possible to collect the coordinates $(J_\delta f_m(t_i), E_a(t_i))$ for t in a discrete subset of D and obtain a graph of the approximate funcional relationship between the radiation law and the temperature at the interface. This is certainly always the case if the cardinality of the range of temperatures $\{J_\delta f_m t(i)\}$ is sufficiently large. Similar remarks to the ones in the previous paragraph, about the parameter dependency of E_a and convergence in the L_2 norm of E_a to E as the quality of the data functions improve, $\varepsilon \to 0$, also apply here.

The computational details are presented in the next section.

3. Numerical Procedure.

With $v = J_\delta u$ and $z = -\partial v/\partial x$, system (2) is equivalent to

$$\begin{aligned}
&\frac{\partial v}{\partial t} = -\frac{\partial z}{\partial x}, && t > 0,\ 0 < x < \infty \text{ or } 0 < x < 1,\\
&z = -\frac{\partial v}{\partial x}, && t > 0,\ 0 < x < \infty \text{ or } 0 < x < 1,\\
&v(1,t) = J_\delta F_m(t), && t > 0,\\
&z(1,t) = J_\delta Q_m(t), && t > 0,\\
&v(x,0) = J_\delta u_0(x,0), && 0 < x < \infty \text{ or } 0 < x < 1,\\
&v(0,t) = J_\delta f_m(t), && t > 0, \text{ unknown},\\
&z(0,t) = J_\delta q_m(t), && t > 0, \text{ unknown}.
\end{aligned} \tag{11}$$

Without loss of generality, we will seek to reconstruct the unknown mollified boundary temperature function $J_\delta f_m$ and the mollified boundary heat flux function $J_\delta q_m$ in the unit interval I = [0,1] of the time axis (x = 0). Consider a uniform grid in the (x,t) space:{(x_i = ih, t_n = nk), i = 0,1,...,N, Nh = 1; n = 0,1,...,M, Mk = L}, where L depends on h and k in a way to be specified later, L > 1.
Let the grid functions V and W be defined by

$$V_i^n = v(x_i,t_n), \qquad W_i^n = z(x_i,t_n),\ 0 \le i \le N,\ 0 \le n \le M.$$

Notice that

Third International Conference on Inverse Design Concepts and Optimization in Engineering Sciences (ICIDES-III), Editor: G.S. Dulikravich, Washington D.C., October 23-25, 1991.

$$V_N^n = J_\delta F_m(t_n), \qquad W_N^n = J_\delta Q_m(t_n), \quad 0 \le n \le M,$$

and

$$V_i^0 = J_\delta u_0(x_i,0), \quad 0 \le i \le N.$$

We approximate the partial differential equation in system (11) with the consistent finite difference schemes

$$\begin{aligned} W_{i-1}^n &= W_i^n - \frac{h}{2k}(V_i^{n+1} - V_i^{n-1}), \\ V_{i-1}^n &= V_i^n - h\, W_{i-1}^n, \\ i &= N, N-1,\ldots,1; \quad n = 1,2,\ldots,M-1. \end{aligned} \tag{12}$$

Notice that, as we march backward in the x-direction, we must drop the estimation of the interior temperature from the highest previous point in time. Since we want to evaluate $\{V_0^n\}$ and $\{W_0^n\}$ at the grid points of the unit time interval $I = [0,1]$ after N iterations, the minimum initial length L of the data sample interval in the time axis ($x = 1$) needs to satisfy the condition $L = kM = 1 - k + k/h$.

Once the temperature $J_\delta f_m$ and the heat flux $J_\delta q_m$ have been reconstructed, we proceed with the approximate identification of the source function g_a or the radiation law function E_a as explained in Section 2.

Remarks:

1. The radius of mollification, δ, can be selected automatically as a function of the level of noise in the data. In fact, for a given $\varepsilon > 0$, there is a unique $\delta > 0$, such that

$$\|J_\delta F_m - F_m\|_D = \varepsilon. \tag{13}$$

For the proof of this assertion and some discussions on the numerical implementation of this practical selection criterion, see Murio [Ref.9].

2. For the proof of the unconditional stability of the finite difference scheme (12) and the analysis of the convergence of the numerical solution of the mollified problem (11), the reader should consult Guo, Murio and Roth [Ref.5].

Numerical Results.

In order to test the accuracy and the stability properties of our method, in Problem 1, the approximate reconstruction of a source function g(t) and a nonlinear radiation law E(u(0,t)) are investigated for a one-dimensional finite slab exposed to a heat flux data function at the free surface $x = 1$ given by $-u_x(1,t) = Q(t) = 0$, $t > 0$, and a temperature data function

$$u(1,t) = F(t) = \begin{cases} (t-0.2) - \dfrac{1}{6} - \dfrac{2}{\pi^2}\displaystyle\sum_{n=1}^{\infty}\frac{(-1)^n}{n^2}\exp\left[-n^2\pi^2(t-0.2)\right], & t > 0.2, \\ 0, & 0 < t \le 0.2. \end{cases}$$

The exact source solution to be approximately reconstructed at the interface $x = 0$ has equation $g(t) = E(u(0,t)) - q(t)$, where $E(u(0,t)) = [u(0,t)]^p$ and $q(t) = -u_x(0,t)$. We consider the values $p = 1$ and $p = 4$ corresponding to Newton's law of

Third International Conference on Inverse Design Concepts and Optimization in Engineering Sciences (ICIDES-III), Editor: G.S. Dulikravich, Washington D.C., October 23-25, 1991.

cooling and Stefan's radiation law respectively. The exact radiation law at the interface is given by $E(u(0,t)) = g(t) + q(t)$ and we only consider the nonlinear case $p = 4$. If the initial temperature distribution $u(x,0)$ is zero, the exact temperature and heat flux functions at the interface are given respectively by a function at the free surface $x = 1$ given by $-u_x(1,t) = Q(t) = 0$, $t > 0$, and a temperature data function

$$u(0,t) = f(t) = \begin{cases} (t-0.2) + \frac{1}{3} - \frac{2}{\pi^2}\sum_{n=1}^{\infty}\frac{1}{n^2}\exp\left[-n^2\pi^2(t-0.2)\right], & t > 0.2, \\ 0, & 0 < t \le 0.2. \end{cases}$$

and

$$-u_x(0,t) = q(t) = \begin{cases} 1, & t > 0.2, \\ 0, & 0 < t \le 0.2. \end{cases}$$

With this information we generate the exact functions $E(u(0,t))$ and $g(t)$ for our model problem.

In Problem 2, we attempt to approximately reconstruct the transient source function $g(t)$ for a semi-infinite body initially at zero temperature with data functions

$$u(1,t) = F(t) = \begin{cases} \operatorname{erfc}[(t-0.2)^{-1/2}/2], & t > 0.2, \\ 0, & 0 < t \le 0.2, \end{cases}$$

and

$$-u_x(1,t) = Q(t) = \begin{cases} [\pi(t-0.2)]^{-1/2}\exp(-[4)t-0.2)]^{-1}\}, & t > 0.2, \\ 0, & 0 < t \le 0.2. \end{cases}$$

The unique temperature solution at the interface is

$$u(0,t) = f(t) = \begin{cases} 1, & t > 0.2, \\ 0, & 0 < t \le 0.2. \end{cases}$$

and the corresponding heat flux at the interface is

$$-u_x(0,t) = q(t) = \begin{cases} [\pi(t-0.2)]^{-1/2}, & t > 0.2, \\ 0, & 0 < t \le 0.2. \end{cases}$$

In this case, we do not attempt the identification of the radiation law at the active boundary. The energy as a function of the interface temperature is either 0 or 1 for any value of p making its identification impossible. There is no enough information in the range of boundary temperatures which in this example is reduced to just two temperature values.

Since in practice only a discrete set of points is generally available, we shall assume that the data functions F_m and Q_m are discrete functions measured at equally spaced points in the time domain $I = [0,L]$, where $L = 1 - k + k/h$, $Nh = 1$, $h = \Delta x$ and $k = \Delta t$. In order to compute $J_\delta F_m(t_n)$ and $J_\delta Q_m(t_n)$ in I, we need to extend the data functions in such a way that F_m and Q_m decay smoothly to zero in the interval $I_{\delta max} = [-3\delta_{max}, L+3\delta_{max}]$ and both are zero in $R - I_{\delta_{max}}$. In what follows, we consider the extended discrete data functions F_m and Q_m defined at equally spaced sample points on any interval of interest in the time axis.

The selection of the radius of mollification is implemented by solving the

Third International Conference on Inverse Design Concepts and Optimization in Engineering Sciences (ICIDES-III), Editor: G.S. Dulikravich, Washington D.C., October 23-25, 1991.

discrete version of equation (13), using the bisection method.

Once the radii of mollification δ_F and δ_Q, associated with the data functions F_m and Q_m respectively, and the discrete filtered data functions $J_\delta F_m(t_n)=V_N^n$ and $J_\delta Q_m(t_n)=W_N^n$, $0\le n\le M$, are determined with $\delta = \max(\delta_F,\delta_Q)$, we apply the finite difference algorithm described previously in this section, marching backward in the x-direction. The values V_0^n and W_0^n, $0 \le n \le M-N$, so obtained, are then taken as the accepted approximations for the interface temperature and heat flux histories respectively at the different time locations at $x = 0$. Finally, we identify the approximate transient source function g_a or the approximate radiation law function E_a at the grid points of the time interval $I = [0,1]$ using equations (6) and (9).

In all cases, we use $h = \Delta x = 0.01$ and $k = \Delta t = 0.01$. Thus, $N = 100$, $L = 1.99$, $M = 200$, $\delta_{max}= 0.1$ and $I_{\delta_{max}} = [-0.3,2.29]$. The noisy data is obtained by adding a random error to the exact data at every grid point t_n in $I_{\delta_{max}}$:

$$F_m(t_n) = F(t_n) + \varepsilon_{n,1}$$
$$Q_m(t_n) = Q(t_n) + \varepsilon_{n,2},$$

where $\varepsilon_{n,1}$ and $\varepsilon_{n,2}$ are Gaussian variables of variance $\sigma^2 = \varepsilon^2$.

If the discretized computed transient source function component is denoted by g_a^n and the true component is $g^n = g(t_n)$, we use the sample root mean square norm to measure the error in the discretized interval $I = [0,1]$. The solution error is then given by

$$\|g_a - g\|_I = \left[\frac{1}{M-N} \sum_{n=1}^{M-N} (g_a^n - g^n)^2 \right]^{1/2}.$$

If the discretized computed radiation law function component is denoted by $E_a^n = E_a(t_n)$ and the true component is $E^n = E(t_n)$, after evaluating the ordered pairs (V_0^n,E_a^n), $0 \le n \le M-N$, we obtain a graph of the approximate functional relationship between the radiation law and the temperature at the interface. This plot is then compared with the exact graph corresponding to the values $(f(t_n),E(t_n))$ of the model problem.

Tables 1 and 2 show the results of our numerical experiments associated with Problems 1 and 2 respectively, when attempting to identify the transient source function at the interface. In all cases, the numerical stability of the method is confirmed. The uniformly smaller error norms in Problem 1 are expected since at time $t = 0.2$ the exact source solution has a finite jump discontinuity while in Problem 2 the exact source solution has an infinite jump at time $t = 0.2$. For this reason, we have added an extra column in Table 2 indicating the error norms in the time interval $[.3,1]$, after the discontinuity. It is clear that the method rapidly dissipates the effect of the singularity, a very desirable feature.

The qualitative behavior of the reconstructed transient source function for Problem 1 is illustrated in Figures 1 and 2 where the numerical solution for an average perturbation $\varepsilon = 0.005$ (full line) is plotted for $p = 1$ (Newton's cooling law) and $p = 4$ (Stefan's radiation law) respectively. In Figure 3 we show the graph associated with the reconstructed nonlinear radiation law as a function of the approximate temperature at the interface for $p = 4$ (full line) and the exact

boundary radiation law (star symbols). Figures 4 and 5 show the computed source functions (full lines) for p = 1 and p = 4 respectively, for Problem 2 and for the noise level $\varepsilon = 0.005$.

PROBLEM 1					
p = 1 (Newton)			p = 4 (Stefan)		
ε	δ	Error norm	ε	δ	Error norm
0.000	0.04	0.0866	0.000	0.04	0.0867
0.002	0.06	0.0921	0.002	0.06	0.0929
0.005	0.06	0.1014	0.005	0.06	0.1038

Table 1. Error norm as a function of the level of noise

PROBLEM 2					
p = 1 (Newon)			p = 4 (Stefan)		
ε	δ	Error norm [0,1]/[.3,1]	ε	δ	Error norm [0,1]/[.3,1]
0.000	0.04	.5208/.0183	0.000	0.04	.5135/.0373
0.002	0.06	.5560/.0631	0.002	0.06	.5673/.0675
0.005	0.06	.5879/.1108	0.005	0.06	.5935/.1375

Table 2. Error norm as a function of the level of noise

4. Conclusions.

An explicit and unconditionally stable space marching finite difference method for the solution of the one-dimensional transient inverse heat conduction problem has been implemented for the numerical identification of surface heat sources, if the energy radiation law at the active interface is known, and to the numerical identification of the nonlinear surface radiation law if the surface is heated by a source at a rate proportional to a given function and the interface temperature contains enough information.

The computational procedure is applied to two examples corresponding to Newton cooling law and to Stefan-Boltzmann radiation law. In both problems, the source functions to be identified have discontinuous histories and in one case an infinite jump. The algorithm restores stability with respect to the data, which is essential for the introduction of the inverse problem approach, and good accuracy is obtained, even for small time sample intervals and relative high noise levels in the data.

REFERENCES

[1] Chambré, P. L, "Nonlinear heat transfer problem", J. Applied Physics, Vol.10, No. 11, 1959, pp. 1683-1688.

[2] Friedman, A., "Generalized heat transfer between solid and gases under nonlinear boundary conditions", J. Math. Mech., Vol. 8, 1959, pp. 161-183.

[3] Groetsch, C. W., "Convergence of a numerical algorithm for a nonlinear heat

transfer problem", Z. angew. Math. Mech. Vol. 65, 1985, pp. 645.

[4] Groetsch, C. W., "A simple numerical model for nonlinear warming on a slab", to appear in J. Comp. Appl. Math.

[5] Guo, L., Murio, D. A. and Roth, C., "A mollified space marching finite difference algorithm for the inverse heat conduction problem with slab symmetry", Comp. Math. Applic., Vol. 19, No. 7, 1990, pp. 75-89.

[6] Keller, J. B. and Olmstead, W. E., "Temperature of a nonlinearly radiating semi-infinite solid", Quart. Appl. Math., Vol. 30, 1972, pp. 559-566.

[7] Mann, W. R. and Wolf, F., "Heat transfer between solids and gases under nonlinear boundary conditions", Quart. Appl. Math., Vol. 9, 1951, pp. 163-184.

[8] Murio, D. A., "The mollification method and the numerical solution of the inverse heat conduction problem by finite differences", Comp. Math. Applic., Vol. 17, 1989, pp. 1385-1396.

[9] Murio, D. A., "Parameter selection by discrete mollification and the numerical solution of the inverse heat conduction problem", J. Comp. Appl. Math., Vol. 22, 1988, pp. 25-34.

[10] Roberts, J. H. and Mann, W. R., "On a certain nonlinear integral equation of Volterra type", Pacific J. Math., Vol. 1, 1951, pp. 431-445.

[11] Saljnikov, V. and Petrovic, S., "Heating problem of a horizontal semi-infinite solid by natural convection", Z. angew. Math. Mech., Vol. 68, 1988, pp. 58-59.

[12] Villaseñor, R. and Squire, W., "Heat conduction in a slab with a general boundary condition: an integral equation approach", in Integral Methods in Science and Engineering (F. R. Payne, et al., eds.), Harper and Row, New York, 1986.

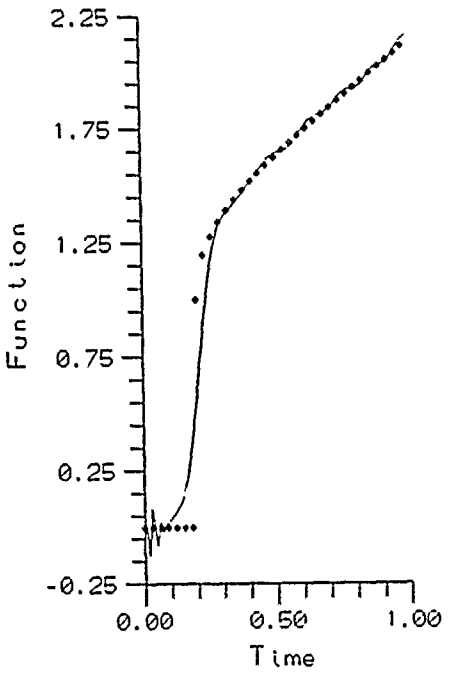


Fig.1 Source function for Newton Law
Problem 1, ε=0.005, δ=0.06, Δt=0.01
Exact: (* * *) ; Computed: (————)

Third International Conference on Inverse Design Concepts and Optimization in Engineering Sciences (ICIDES-III), Editor: G.S. Dulikravich, Washington D.C., October 23-25, 1991.

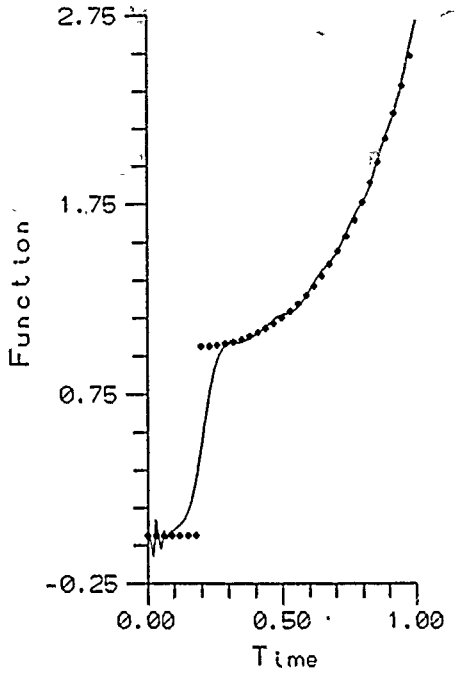


Fig.2 Source function for Stefan Law
Problem 1, ε=0.005, δ=0.06, Δt=0.01
Exact: (* * *) ; Computed: (————)

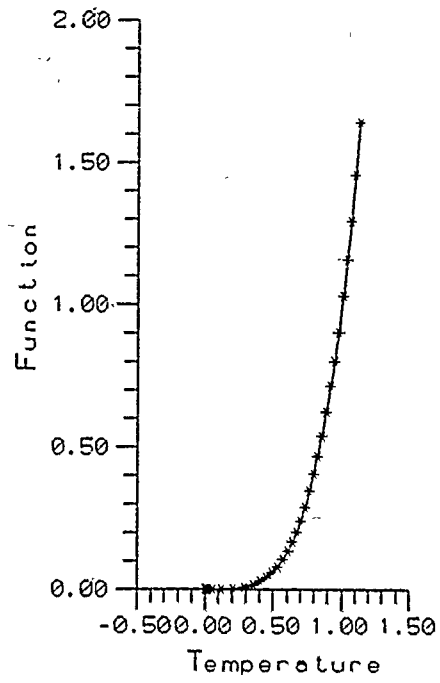


Fig.3 Reconstructed Stefan radiation Law
Problem 1, ε=0.005, δ=0.06, Δt=0.01
Exact: (* * *) ; Computed: (————)

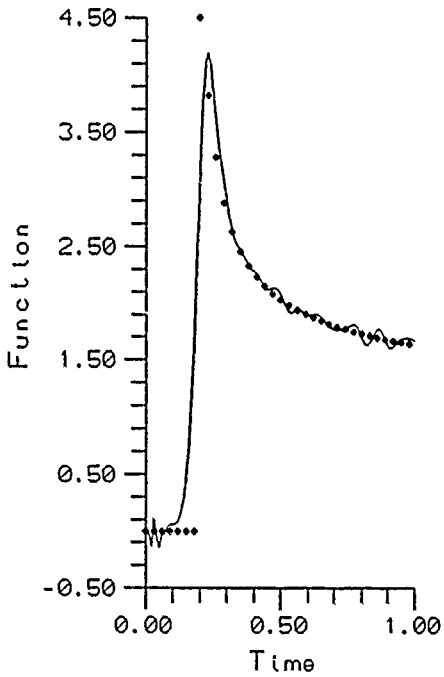


Fig.4 Source function for Newton Law
Problem 2, ε=0.005, δ=0.06, Δt=0.01
Exact: (* * *) ; Computed: (————)

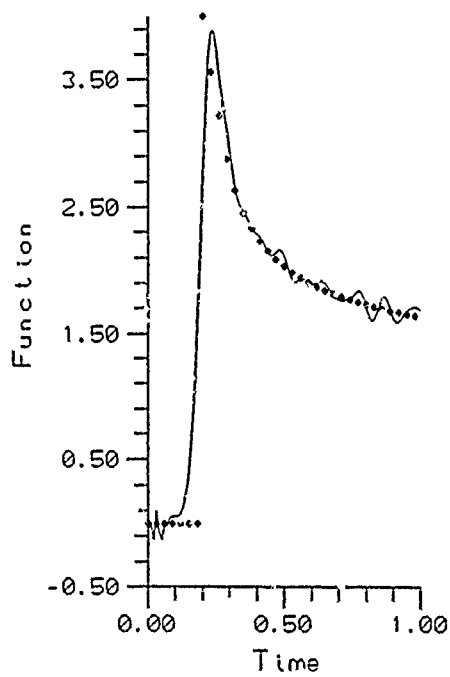


Fig.5 Source function for Stefan Law
Problem 2, ε=0.005, δ=0.06, Δt=0.01
Exact: (* * *) ; Computed: (————)

Third International Conference on Inverse Design Concepts and Optimization in Engineering Sciences (ICIDES-III), Editor: G.S. Dulikravich, Washington D.C., October 23-25, 1991.

COMPARISON OF FOUR STABLE NUMERICAL METHODS FOR ABEL'S INTEGRAL EQUATION

Diego A. Murio and Carlos E. Mejía

Department of Mathematical Sciences
University of Cincinnati
Cincinnati, OH 45221-0025
U.S.A.

ABSTRACT

The 3-D image reconstruction from cone-beam projections in computerized tomography leads naturally, in the case of radial symmetry, to the study of Abel-type integral equations. If the experimental information is obtained from measured data, on a discrete set of points, special methods are needed in order to restore continuity with respect to the data. A new combined Regularized-Adjoint-Conjugate Gradient algorithm (introduced in this work), together with two different implementations of the Mollification Method (one based on a data filtering technique and the other on the mollification of the kernel function) and a regularization by truncation method (initially proposed for 2-D ray sample schemes and more recently extended to 3-D cone-beam image reconstruction) are extensively tested and compared for accuracy and numerical stability as functions of the level of noise in the data.

1. INTRODUCTION.

The difficult problem of determining the structure of an object from its 3-D cone-beam data projections is currently receiving considerable attention (see B. D. Smith, Ref [16]). When the object is known to be radially symmetric, its structure can be determined by using the inverse Abel transform. If the object does not have radial symmetry, it can be reconstructed, in principle, by using the inverse Radon transform.

Abel's integral equation can be written as

$$f(x) = \int_0^x g(s)\,(x - s)^{-1/2}\,ds, \quad 0 \le x \le 1, \tag{1}$$

where the function $f(x)$ is the data function and $g(s)$ is the unknown function. The exact solution is given by

$$g(x) = \frac{1}{\pi} \int_0^x f'(s)\,(x - s)^{-1/2}\,ds, \quad 0 \le x \le 1, \tag{2}$$

provided the derivative exists and $f(0) = 0$. (See R. Gorenflo and S. Vessella, Ref [6]).

It is well-known (References [1], [2], [4] and [6]) that Abel's integral equation is somewhat ill-posed, that is, small errors in the data $f(x)$ might cause large errors in the computed solution $g(x)$. Consequently, the direct use of formula (2) is very limited and special methods are needed.

Third International Conference on Inverse Design Concepts and Optimization in Engineering Sciences (ICIDES-III), Editor: G.S. Dulikravich, Washington D.C., October 23-25, 1991.

This paper has two main purposes. First, we present and briefly analyze a new stable method for the numerical solution of Abel's integral equation, Method I, by weakly coupling the original problem with its adjoint formulation obtaining a regularized system of linear equations which is then successfully solved by the conjugate gradient method. Second, we test and compare the numerical stability and the accuracy of Method I and three other known algorithms on several benchmark examples as a function of the amount of noise in the data.

Method II in this paper (see D. A. Murio, Ref [12]), is obtained by initially filtering the noisy data by discrete convolution with a suitable averaging kernel instead of mollifying the kernel function in equation (2), Method III, as required by K. Miller (Refs [10] and [11]) in his reconstruction algorithm for 2-D ray-sampling schemes. Method IV has been implemented by D. A. Murio, D. Hinestroza and C. E. Mejía (Ref [13]) based on a regularization by truncation technique initially proposed by B. K. P. Horn (Ref [9]) and recently extended to 3-D image reconstruction methods from cone-beam projections by B. D. Smith (Ref [15]).

In Section 2 we introduce the new Method I, analyze the consistency and stability properties of the algorithm and obtain an upper bound for the error. In Section 3, we describe the other procedures and discuss in detail the numerical implementation of all the methods involved. Section 4 is devoted to the numerical testing of the four algorithms and the presentation of several useful comparisons involving Methods I, II, III and IV. Some conclusions are included in Section 5.

2. REGULARIZED-ADJOINT-CONJUGATE GRADIENT METHOD. (Method I).

In a more abstract setting, equation (1) can be written as

$$Ag = f,$$

where A represents the Abel integral operator. For suitable functions h and q, the adjoint operator A^* is defined by

$$A^*h(x) = q(x) \equiv \int_x^1 h(s)\,(s-x)^{-1/2}\,ds, \qquad 0 \le x \le 1,$$

and it is clear that the homogeneous equation $A^*h = 0$ has the unique solution $h(x) \equiv 0$, $0 \le x \le 1$. Hence, as a direct consequence of Fredholm alternative (see P. R. Garabedian, Ref [5]), solving the singular equation $Ag = f$ for smooth but otherwise arbitrary data functions f satisfying $f(0) = 0$, is equivalent to solve the uncoupled system of linear integral equations

$$\begin{cases} Ag = f \\ A^* h = 0. \end{cases} \tag{3}$$

In order to help stabilize the inverse problem, we propose to solve, instead of (3), the weakly coupled system of equations

$$\begin{cases} Au - \alpha v = f \\ A^*v + \alpha u = 0, \qquad 0 < \alpha << 1, \end{cases} \tag{4}$$

by successive approximations. This system is equivalent to

Third International Conference on Inverse Design Concepts and Optimization in Engineering Sciences (ICIDES-III), Editor: G.S. Dulikravich, Washington D.C., October 23-25, 1991.

$$\begin{cases} Au - \alpha v = f \\ \alpha\beta A^* v + \alpha^2\beta u - u + u = 0, \end{cases}$$

where β is any nonzero real number to be determined. We elect β to depend on the iteration and rewrite the previous system as

$$\begin{cases} Au_n - \alpha v_n = f \\ \alpha\beta_n A^* v_n + \alpha^2\beta_n u_n - u_n + u_{n+1} = 0, \end{cases}$$

to obtain

$$\begin{cases} \alpha v_n = Au_n - f \\ u_{n+1} = u_n - \beta_n[\alpha^2 u_n + A^*(\alpha v_n)], \qquad n = 0,1,2,\ldots, \end{cases} \tag{5}$$

u_0 arbitrary, usually 0.

Remarks:

1. Each iteration in (5) involves the solution of two "direct" problems: one corresponding to the original operator, Au_n, and the other associated with the adjoint operator, $A^*(\alpha v_n)$.

2. Elimination of v in system (4) leads to the set of normal equations, with I indicating the identity operator,

$$(A^*A + \alpha^2 I)u = A^* f, \tag{6}$$

which characterizes the minimum of the zero order Tikhonov functional (see C. W. Groetsch, Ref [7])

$$J(u) = \frac{1}{2}\left(\| Au - f \|^2 + \alpha^2 \| u \|^2 \right). \tag{7}$$

3. The gradient of the functional (7) is given by

$$\nabla J(u) = \alpha^2 u + A^*(Au - f)$$

and it is easily computed if the solution of the adjoint problem is known. In fact, taking into consideration (4), we can write $\nabla J(u) = \alpha^2 u + A^*(\alpha v)$, and for each iteration we get

$$\nabla J(u_n) = \alpha^2 u_n + A^*(\alpha v_n). \tag{8}$$

These considerations allow us to choose β_n, for each n, in such a manner that system (5) can now be solved by the Conjugate Gradient Method (W. M. Patterson, Ref [14]).

The complete abstract algorithm, after introducing the notations $(f,g) \equiv \int_0^1 f(x)g(x)\,dx$ and $\| f \| \equiv (f,f)^{1/2}$, corresponding to the inner product and

Third International Conference on Inverse Design Concepts and Optimization in Engineering Sciences (ICIDES-III), Editor: G.S. Dulikravich, Washington D.C., October 23-25, 1991.

norm respectively of square integrable functions on the interval [0,1], is as follows:

For n = 0;

0) Set $u_0 = 0$ and choose $\alpha > 0$.

1) Compute Au_0, i.e., solve the original direct problem.

2) Compute the residual $\alpha v_0 = Au_0 - f$.

3) Compute $A^*(\alpha v_0)$, i.e., solve the direct adjoint problem.

4) Evaluate the gradient $d_0 = \nabla J(u_0)$ using formula (8).

5) Set $r_0 = \dfrac{\| d_0 \|^2}{\alpha^2 \| d_0 \|^2 + \| Ad_0 \|^2}$.

6) Update: $u_1 = u_0 - r_0 d_0$.

For n = 1,2,...,

1') Solve the original direct problem Au_n.

2') Compute the residual $\alpha v_n = Au_n - f$.

3') Solve the direct adjoint problem $A^*(\alpha v_n)$.

4') Evaluate the gradient $\nabla J(u_n)$ using formula (8).

4'') Compute $d_n = \nabla J(u_n) + \dfrac{\| \nabla J(u_n) \|^2}{\| \nabla J(u_{n-1}) \|^2} d_{n-1}$.

5') Set $r_n = \dfrac{(\nabla J(u_n), d_n)}{\alpha^2 \| d_n \|^2 + \| Ad_n \|^2}$.

6') Update: $u_{n+1} = u_n - r_n d_n$.

Stability of Method I.

We consider now the more realistic situation when instead of the exact data function f, we only know some noisy data function f^ε satisfying

$$\| f - f^\varepsilon \| \le \varepsilon.$$

In this section the unique solution of system (4) will be denoted by u_α^ε to emphasize its dependency on the regularization parameter α and the level of noise in the data ε. Assuming that the ideal problem (1) for errorless data f has the unique solution $g = A^{-1}f$, since u_α^ε satisfies equation (6), with f replaced by f^ε, it follows from well-known estimates in the theory of Tikhonov regularization that

$$\| g - u_\alpha \| = C_0 \alpha^{1/2}, \quad \text{and} \quad \| u_\alpha - u_\alpha^\varepsilon \| \le \varepsilon \alpha^{-1/2},$$

for some constant $C_0 > 0$, independent of α; u_α denotes the regularized solution when $\varepsilon = 0$.

Combining these estimates, we obtain the error upper bound

Third International Conference on Inverse Design Concepts and Optimization in Engineering Sciences (ICIDES-III), Editor: G.S. Dulikravich, Washington D.C., October 23-25, 1991.

$$|| g - u_\alpha^\varepsilon || \le C_0 \alpha^{1/2} + \varepsilon \alpha^{-1/2}$$

and choosing $\alpha = C_1\varepsilon$ for some constant $C_1 > 0$, it follows that

$$|| g - u_\alpha^\varepsilon || \le (C_0 + C_1^{-1}) \alpha^{1/2} \tag{9}$$

which shows that, theoretically, as the quality of the data becomes better and better ($\varepsilon \to 0$), we get convergence with rate $\alpha^{1/2}$. See C. W. Groetsch (Ref [7]) for details.

The convergence of the sequence of iterates $u_{\alpha,n}^\varepsilon$ from system (5), with β_n as discussed above, to the unique solution u_α^ε of the canonical equations (6) as $n \to \infty$ is well documented, for instance, in the work of C. W. Groetsch, J. T. King and D. A. Murio (Ref [8]) and will not be pursued further here.

The finite dimensional version of the combined Regularized-Adjoint-Conjugate Gradient algorithm will be discussed in the next Section.

3. METHODS II, III AND IV. NUMERICAL IMPLEMENTATIONS.

Method II in this paper is based on attempting to reconstruct a mollified version of the solution g in equation (2). After introducing the δ-mollifier

$$p_\delta(x) = \frac{1}{\delta} \pi^{-1/2} \exp[-x^2/\delta^2] \tag{10}$$

of "blurring radius" δ and extending the data function f^ε to the interval $[-3\delta,1+3\delta]$ in such a way that it decays smoothly to zero on $[1,1+3\delta]$ and it is zero on $[-3\delta,0]$, an approximate solution is defined by

$$g_\delta^\varepsilon(x) = \frac{1}{\pi} \int_0^x (p_\delta * f^\varepsilon)'(s) \, (x - s)^{-1/2} \, ds, \qquad 0 \le x \le 1. \tag{11}$$

Here,

$$(p_\delta * f^\varepsilon)'(x) = \int_{-\infty}^{\infty} \frac{d}{dx} [p_\delta(x - s) \, f^\varepsilon(s)] \, ds \approx \int_{x-3\delta}^{x+3\delta} \frac{d}{dx} [p_\delta(x - s) \, f^\varepsilon(s)] \, ds,$$

showing that the main idea of the method consists on replacing the noisy data function f^ε by the filtered data function $p_\delta * f^\varepsilon$. It is important to notice that the radius of mollification, δ, can be uniquely and automatically determined as a function of the amount of noise in the data, ε, based in the fact that there is a unique value of the regularizing parameter δ for which

$$|| p_\delta * f^\varepsilon - f^\varepsilon || = \varepsilon. \tag{12}$$

Under very mild conditions, i.e., if f^ε is continuous and if the second derivative of the errorless data function f is uniformly bounded by M_2 in the

Third International Conference on Inverse Design Concepts and Optimization in Engineering Sciences (ICIDES-III), Editor: G.S. Dulikravich, Washington D.C., October 23-25, 1991.

sample interval (0,1), the following error estimate holds

$$|| g_\delta^\varepsilon - g || \le \frac{6}{\pi} (\delta M_2 + \varepsilon/\delta). \qquad (13)$$

The complete abstract algorithm is as follows:

1) Automatically determine the unique radius of mollification δ as a function of the level of noise ε.

2) Smoothly extend the noisy data function f^ε to $[-3\delta,1+3\delta]$.

3) Compute the derivative of the filtered data function $p_\delta * f^\varepsilon$.

4) Compute g_δ^ε using equation (11).

For more details and further discussions, the reader should consult D. A. Murio, Ref [12].

Method III is based on the Mollification Method as originally proposed by K. Miller (Refs [10] and [11]) for 2-D ray-sampling reconstruction geometries. First we notice that the exact formula (2) can be written

$$g(x) = \frac{1}{\pi} (k * f')(x), \qquad 0 \le x \le 1,$$

where $k(t) = t^{-1/2}$ represents the kernel function. The mollification of the last equation with the averaging kernel defined in (10) gives

$$(p_\delta * g)(x) = \frac{1}{\pi} (p_\delta * k * f')(x).$$

In Method II, we associated the right-hand side of this equation as $k * (p_\delta * f') = k * (p_\delta * f)'$; for Miller's idea we associate as $(p_\delta * k) * f' = (p_\delta * k)' * f$ and obtain the approximate reconstruction solution

$$g_\delta^\varepsilon(x) = \frac{1}{\pi} \int_0^x (p_\delta * k)'(x - s) f^\varepsilon(s)\, ds, \qquad 0 \le x \le 1. \qquad (14)$$

Mathematically, formulae (11), for Method II, and (14), for Method III, are identical. Consequently, the theoretical error bound (13) derived for Method II also applies for Method III.

The complete abstract algorithm for Method III is given by:

1) Choose $\delta > 0$.

2) Compute the mollified kernel $p_\delta * k$.

3) Evaluate the derivative of the mollified kernel $p_\delta * k$.

4) Compute g_δ^ε using equation (14).

Remarks:

1. In Method III, the mollified kernel is computed only once and is used repeatedly for different data functions.

Third International Conference on Inverse Design Concepts and Optimization in Engineering Sciences (ICIDES-III), Editor: G.S. Dulikravich, Washington D.C., October 23-25, 1991.

2. Method II requires a filtering of each data function and the corresponding parameter is automatically selected according to the quality of the measured data.
3. The selection of the mollification parameter in Method III requires further consideration.

Method IV is based on a reconstruction technique initially proposed by B. K. P. Horn (Ref [9]) for arbitrary 2-D ray schemes and more recently extended to 3-D image reconstruction methods from cone-beam projections by B. D. Smith (Ref [15]).

Integrating by parts equation (2), we obtain the equivalent expression

$$g(x) = \frac{1}{\pi} \lim_{\gamma \to 0} \left\{ \gamma^{-3/2} \int_{x-\gamma}^{x} f(s)\, ds - \frac{1}{2} \int_{0}^{x-\gamma} f(s)(x-s)^{-3/2} ds \right\}, \qquad 0 \le x \le 1.$$

The approximate inverse Abel transform is now obtained by eliminating the limit procedure in the last expression, i.e.,

$$g_\gamma^\varepsilon(x) = \frac{1}{\pi} \left\{ \gamma^{-3/2} \int_{x-\gamma}^{x} f^\varepsilon(s)\, ds - \frac{1}{2} \int_{0}^{x-\gamma} f^\varepsilon(s)\, (x - s)^{-3/2}\, ds \right\}, \qquad 0 \le x \le 1. \quad (15)$$

By requiring the second derivative of the errorless data function f and the measured data function f^ε to be continuous, we obtain the following error estimate

$$\| g_\gamma^\varepsilon - g \| \le \frac{5}{2} \frac{\gamma^{1/2}}{\pi} M_1 + \frac{2}{\pi} \varepsilon\, \gamma^{-1/2} + O(\gamma^{3/2}), \quad (16)$$

where M_1 is a uniform bound for f' on the interval (0,1). For a proof of this assertion and a complete analysis of Method IV, see D. A. Murio, D. Hinestroza and C. E. Mejía (Ref [13]).

The complete abstract algorithm for Method IV is reduced to
1) Choose $\gamma > 0$.
2) Compute g_γ^ε using formula (15).

Remark:

The error estimates (9), (13) and (16) show that all the methods are consistent and stable with respect to perturbations in the data, in the L_2 norm, for a fixed choice of the several regularization parameters α, δ or γ.

Numerical Implementations.

Since in practice only a discrete set of data points is generally available, we assume that the data function f^ε is a discrete function measured at equally spaced sample points on the interval [0,1]. For $h > 0$ and $Nh = 1$, we let $x_j = jh$ and denote $f^\varepsilon(x_j) = f_j^\varepsilon$, $j = 0,1,\ldots,N$, with $f_0^\varepsilon = 0$.

Method I:

Discretization leads to a finite dimensional version of the combined Regularized-Adjoint-Conjugate Gradient algorithm of Section 2. The operators A and A^* are represented now by a matrix A and its transpose A^T, respectively. The

Third International Conference on Inverse Design Concepts and Optimization in Engineering Sciences (ICIDES-III), Editor: G.S. Dulikravich, Washington D.C., October 23-25, 1991.

approximate discrete solution $u^{\varepsilon}_{m,\alpha}$, obtained after m iterations, the gradient $\nabla J(u_m)$, d_m, r_m, u_0 and the residual αv_m are now N-dimensional real vectors. From equation (1), a simple discretization gives the lower triangular system of linear equations

$$h \sum_{l=1}^{j} a_{j+1-l}(u^{\varepsilon}_{m,\alpha})_l = f^{\varepsilon}_j ,$$

where

$$a_j = (jh)^{-1/2}, \qquad j = 1,2,\ldots,N,$$

indicates the (j-1) subdiagonal of the N x N matrix A.

The discrete algorithm for the Conjugate Gradient method (see P. G. Ciarlet, Ref [3]) follows exactly the steps described previously in Section 2, and we only have to add the necessary stopping criteria, given by

$$|| u^{\varepsilon}_{m,\alpha} - u^{\varepsilon}_{m-1,\alpha} ||_2 \le TOL \, || u^{\varepsilon}_{m,\alpha} ||_2,$$

where TOL is a small positive tolerance parameter entered by the user and

$$|| f ||_2 = \left\{ \frac{1}{N} \sum_{j=0}^{N} [f_j]^2 \right\}^{1/2} \tag{17}$$

is the discrete l_2 norm on [0,1].

Method II:

To numerically approximate $g^{\varepsilon}_{\delta}(x)$, a quadrature formula for the convolution equation (11) is required. The objective is to introduce a simple approximation and avoid any artificial smoothing in the process.

Given x_j, $j = 0,1,\ldots,N$, we define

$$q^{\varepsilon}(x) = \sum_{l=0}^{j} f^{\varepsilon}_l \phi_l(x), \qquad 0 \le x \le x_j,$$

a piecewise constant interpolation of $f^{\varepsilon}(x)$ at the grid points x_j. Here,

$$\phi_0(x) = \begin{cases} 1, & 0 \le x \le h/2 \\ 0, & \text{otherwise} \end{cases}, \qquad \phi_j(x) = \begin{cases} 1, & x_j - h/2 \le x \le x_j \\ 0, & \text{otherwise} \end{cases}$$

and

$$\phi_i(x) = \begin{cases} 1, & x_i - h/2 \le x \le x_i + h/2 \\ 0, & \text{otherwise} \end{cases}, \quad i = 1,2,\ldots,j-1.$$

The computational algorithm is as follows:

After smoothly extending the discrete data function to any interval of interest containing the sample interval [0,1], we determine the radius of mollification δ as

Third International Conference on Inverse Design Concepts and Optimization in Engineering Sciences (ICIDES-III), Editor: G.S. Dulikravich, Washington D.C., October 23-25, 1991.

a function of the amount of noise in the data ε by solving the discrete version of equation (12) using the bisection method. Next, we substitute f^ε by its interpolation q^ε and compute the approximation to $p_\delta * f^\varepsilon$ given by the discrete convolution

$$(p_\delta * q^\varepsilon)(x) = \sum_k f_k^\varepsilon (p_\delta * \phi_k)(x_j) = \sum_k f_k^\varepsilon \, m_j^\delta,$$

where the weights m_j^δ are evaluated exactly. A discrete version of the derivative of the discrete filtered data function is obtained using centered finite differences. Finally, the discrete approximation to g_δ^ε is calculated by discretely convolving the computed derivative approximation against the sampled data function (see equation (11)). For a detailed analysis of this algorithm, the reader is referred to D. A. Murio (Ref [12]).

Method III:

The convolution $p_\delta * k$ requires an extension of the singular kernel k for values of x less or equal to zero. In our implementation we use the following symmetric extension:

$$k(0) = 2h^{-1/2}, \quad k(-x) = k(x), \; x > 0.$$

The discrete approximation is now straightforward:
With $s_j = (p_\delta * k)(x_j)$, $j = 0,1,\ldots,N$, the discrete convolution formula corresponding to equation (14) is

$$g_{h,\delta}^\varepsilon(0) = 0,$$

$$g_{h,\delta}^\varepsilon(x_j) = \frac{1}{\pi} \sum_{k=1}^{j} s_{j-k}(f_{k+1}^\varepsilon - f_{k-1}^\varepsilon)/2, \qquad j = 1,2,..,N-1$$

and

$$g_{h,\delta}^\varepsilon(1) = g_{h,\delta}^\varepsilon(x_{N-1}) + \frac{1}{\pi} s_0(f_N^\varepsilon - f_{N-1}^\varepsilon),$$

where $g_{h,\delta}^\varepsilon$ is the approximate inverse Abel transform at the grid points.

Method IV:

In this case, we first construct a piecewise linear interpolation of $f^\varepsilon(x)$ at the grid points x_j, given by

$$q^\varepsilon(x) = \sum_{i=0}^{j} f_j^\varepsilon \, \phi_i(x), \qquad 0 \le x \le x_j,$$

where the functions $\phi_i(x)$, $i = 0,1,\ldots,N$ are given by

$$\phi_0(x) = \begin{cases} 1-x/h, & 0 \le x \le h \\ 0 & \text{otherwise,} \end{cases} \qquad \phi_j(x) = \begin{cases} 1+(x-x_j)/h, & x_{j-1} \le x \le x_j \\ 0 & \text{otherwise,} \end{cases}$$

and

$$\phi_i(x) = \begin{cases} 1+(x-x_i)/h, & x_{i-1} \le x \le x_i \\ 1-(x-x_i)/h, & x_i \le x \le x_{i+1} \\ 0 \text{ otherwise,} & \end{cases} \qquad i = 1,2,\ldots,j.$$

We notice that the approximate solution $g_\gamma^\varepsilon(x)$ of formula (15) can also be written as

$$g_\gamma^\varepsilon(x) = \frac{1}{\pi} (H_\gamma * f^\varepsilon)(x), \quad 0 \le x \le 1, \tag{18}$$

where the kernel H_γ is defined by

$$H_\gamma(t) = \begin{cases} \gamma^{-3/2}, & 0 \le t < \gamma \\ \dfrac{1}{2}\, t^{-3/2}, & \gamma \le t. \end{cases}$$

The quadrature formula for equation (18) is obtained by directly convolving the kernel function H_γ with q^ε as indicated below. Thus, the computed solution at the grid points is given by

$$g_{\gamma,h}^\varepsilon(x_j) = \frac{1}{\pi} (H_\gamma * q^\varepsilon)(x_j) = \frac{1}{\pi} \sum_{i=0}^{j} f_i^\varepsilon \, b_i^\gamma(x_j),$$

where the weights

$$b_i^\gamma(x_j) = \int_0^{x_j} H_\gamma(x_j - s)\, \phi_i(s)\, ds$$

are evaluated exactly for $i = 0,1,\ldots,j$. The readers interested in further details should consult D. A. Murio, D. Hinestroza and C. E. Mejía (Ref [13]).

4. NUMERICAL RESULTS AND COMPARISON.

In this section we describe the tests that have been implemented in order to compare the performance of the methods introduced in previous sections.

We tested the methods on three examples. In all of them, the exact data function is denoted $f(x)$ and the noisy data function $f^\varepsilon(x)$ is obtained by adding an ε random error to $f(x)$, that is, $f^\varepsilon(x_j) = f(x_j) + \varepsilon\sigma_j$, where $x_j = jh$, $j = 0,1,\ldots,N$; $Nh = 1$ and σ_j is a uniform random variable with values in $[-1,1]$ such that

$$\max_{0 \le j \le N} \left| f^\varepsilon(x_j) - f(x_j) \right| \le \varepsilon.$$

The exact inverse Abel transform is denoted $g(x)$ and its approximation given by

Third International Conference on Inverse Design Concepts and Optimization in Engineering Sciences (ICIDES-III), Editor: G.S. Dulikravich, Washington D.C., October 23-25, 1991.

any of the methods is denoted $g^{\varepsilon}_{p,h}(x)$, where p represents the regularization parameter of the particular method.

Example 1:

As a first example we consider the data function $f(x) = x$ with exact inverse Abel transform $g(x) = \frac{2}{\pi} x^{1/2}$. This data function satisfies all the necessary hypotheses for convergence estimates of Sections 2 and 3.

Example 2:

The data function

$$f(x) = \begin{cases} 2x^2, & 0 \le x < 1/2 \\ 1-2(1-x)^2, & 1/2 \le x \le 1, \end{cases}$$

is only once continuously differentiable on [0,1], partially violating the required conditions for the theoretical error analysis of Sections 2 and 3. In this example, the exact inverse Abel transform is given by

$$g(x) = \begin{cases} (16/3\pi)x^{3/2}, & 0 \le x \ 1/2 \\ (16/3\pi)x^{3/2} + (16/3\pi)\,(x-1/2)^{3/2} - (8/\pi)(x-1/2)^{1/2}(2x-1), \\ \qquad 1/2 < x \le 1. \end{cases}$$

Example 3:

The data function is defined as follows:

$$f(x) = \begin{cases} 0, & 0 \le x < 0.2, \\ 2(x-0.2)^{1/2}, & 0.2 \le x \le 0.6, \\ 2(x-0.2)^{1/2} - 2(x-0.6)^{1/2} & 0.6 < x \le 1. \end{cases}$$

Its first derivative is not continuous on [0,1], strongly violating the necessary hypotheses for the convergence estimates of Sections 2 and 3. The exact inverse Abel transform is given by

$$g(x) = \begin{cases} 1, & 0.2 \le x \le 0.6, \\ 0, & \text{otherwise.} \end{cases}$$

The four methods were tested for three different values of N, N = 200, 500 and 1000, three different values of ε, ε = 0.0, 0.005 and 0.01, and several values of the corresponding regularization parameters. The algorithms were extensively used and we numerically determined appropriate values for the regularization parameters for each method, except for Method II where the radius of mollification was selected automatically. These quasi-optimal parameter values are used in the tables and figures below.

Third International Conference on Inverse Design Concepts and Optimization in Engineering Sciences (ICIDES-III), Editor: G.S. Dulikravich, Washington D.C., October 23-25, 1991.

Different values of ε provide a crucial test for stability. Tables 1, 2 and 3 illustrate this point. The error norms in the tables are computed as $\| g - g^{\varepsilon}_{p,h} \|_2$ according to definition (17). In the tables, each row corresponds to one of the methods with a fixed regularization parameter, and shows the change in the error norm due to changes in the level of noise in the data. The presented numerical results indicate stability. The columns in the tables allow us to compare the performance of the methods under similar conditions.

Figures 1 to 4 show the reconstructions of the step function of Example 3 provided by the four methods for the same number of sample data points, N = 500, the same noise level, ε = 0.01, and quasi-optimal regularization parameters. The qualitative behavior is quite good taken into consideration the high amount of noise in the data.

5. CONCLUSIONS

The following are some conclusions based on the implementations of the methods presented in this paper:

Consistency and stability of the four methods is clearly confirmed throughout experimentation and very weak dependency on the parameter N is observed.

Method II provides an automatic mechanism to select the radius of mollification as a function of the level of noise in the data. Furthermore, as a consequence of the stability of the four methods, it is easy to find, by numerical experimentation,lower and upper bounds for quasi-optimal regularization parameters.

An advantage of method III over method II is that the mollification of the kernel is computed only once and can be used for different data functions. Methods II applies mollification to each data set.

All the results are very competitive. However, mollification solutions are slightly better in terms of accuracy and method IV, the easiest to implement, seems to be more sensitive to perturbations in the data.

REFERENCES

1. Baker, C.T.H., The Numerical Treatment of Integral Equations, Clarendon Press, Oxford, 1977.

2. Baker, C.T.H., An Introduction to the numerical treatment of Volterra and Abel-type integral equations. Lecture Notes in Mathematics 965, Springer-Verlag, 1982, 1-38.

3. Ciarlet, P.G,, Introduction to Numerical Linear Algebra and Optimisation, Cambridge University Press, Cambridge, 1989.

4. Delves, L.M. and J. Walsh, editors. Numerical solution of Integral Equations, Clarendon Press, Oxford, 1974.

5. Garabedian, P. R., Partial Differential Equations, John Wiley and Sons, New York, 1964.

6. Gorenflo, R. and S. Vessella, Abel Integral Equations; Analysis and Applications, Lecture Notes in Mathematics 1461, Springer-Verlag, 1991.

7. Groetsch, C. W., The theory of Tikhonov regularization for Fredholm equations of the first kind, Pitman, 1984.

8. Groetsch, C. W., J. T. King and D. A. Murio, Asymptotic Analysis of a Finite Element Method for Fredholm equations of the first kind, in Treatment of Integral Equations by Numerical Methods. C. T. H. Baker and G. F. Miller, editors. Academic Press, 1982, 1-11.

9. Horn, B. K. P., Density reconstruction using arbitrary ray-sampling schemes, Proc. IEEE, Vol. 66, No. 5, 1978, pp. 551-562.

10. Miller, K., An optimal method for the x-ray reconstruction problem, preliminary report, Amer. Math. Soc. Notices, January, 1978, A-161.

11. Miller, K., New results on reconstruction methods from x-ray projections, Lecture Notes (unpublished), Department of Mathematics, University of Firenze, December, 1978, available from the author.

12. Murio, D. A., Stable numerical inversion of Abel's integral equation by discrete mollification, to appear in SIAM Proceedings on Design Theory, Great Lakes Section, Wright-Patterson Air Force Base, Dayton, Ohio, April 1990.

13. Murio, D. A., Hinestroza, D. and Mejía, C. E., New stable numerical inversion of Abel's integral equation, to appear in Proceedings Third International Symposium of Numerical Analysis, Madrid, Spain, May 1990.

14. Patterson, W. M., Iterative Methods for the Solution of Linear Operator Equations in Hilbert Spaces, Lecture Notes in Mathematics 394,Springer-Verlag, 1974.

15. Smith, B. D., Image reconstruction from cone-beam projections: Necessary and sufficient conditions and reconstruction methods, IEEE Trans. Med. Imaging, Vol. MI-4, No. 1, 1985, pp. 14-25.

16. Smith, B. D., Cone-beam tomography: recent advances and a tutorial review, Optical Engineering Journal, Vol. 29, May 1990, pp. 524-534.

Method	Parameter	$\varepsilon = 0.0$	$\varepsilon = 0.005$	$\varepsilon = 0.01$
I	$\alpha = 0.08$	0.0279	0.0294	0.0359
II	$\delta = 0.008$	0.0000	0.0048	0.0096
III	$\delta = 0.008$	0.0005	0.0137	0.0274
IV	$\gamma = 0.004$	0.0302	0.0315	0.0349

Table 1. Error Norms as functions of ε in Example 1 with N = 500

Method	Parameter	$\varepsilon = 0.0$	$\varepsilon = 0.005$	$\varepsilon = 0.01$
I	$\alpha = 0.08$	0.0275	0.0293	0.0365
II	$\delta = 0.008$	0.0001	0.0048	0.0096
III	$\delta = 0.008$	0.0005	0.0136	0.0273
IV	$\gamma = 0.001$	0.0174	0.0263	0.0431

Table 2. Error Norms as functions of ε in Example 2 with N = 500

Method	Parameter	$\varepsilon = 0.0$	$\varepsilon = 0.005$	$\varepsilon = 0.01$
I	$\alpha = 0.08$	0.0615	0.0618	0.0641
II	$\delta = 0.008$	0.0052	0.0052	0.0053
III	$\delta = 0.008$	0.0295	0.0330	0.0411
IV	$\gamma = 0.001$	0.0648	0.0678	0.0760

Table 3. Error Norms as functions of ε in Example 3 with N = 500

Third International Conference on Inverse Design Concepts and Optimization in Engineering Sciences (ICIDES-III), Editor: G.S. Dulikravich, Washington D.C., October 23-25, 1991

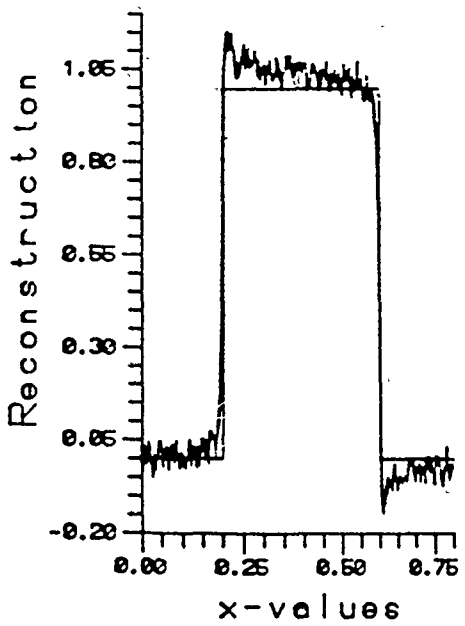


Fig. 1 Reconstruction with Method I
ε = 0.01, α = 0.08, N = 500

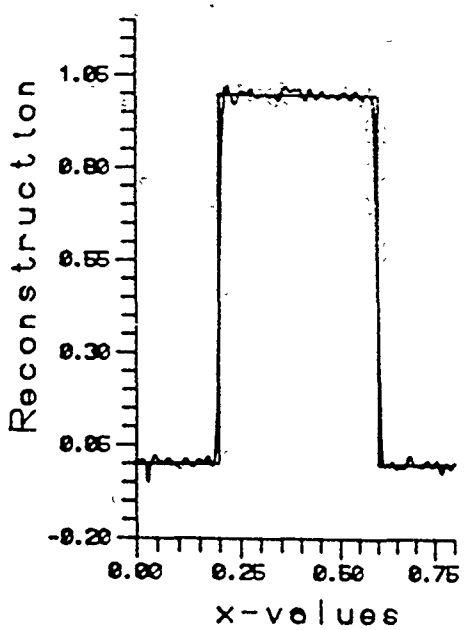


Fig. 2 Reconstruction with Method II
ε = 0.01, δ = 0.008, N = 500

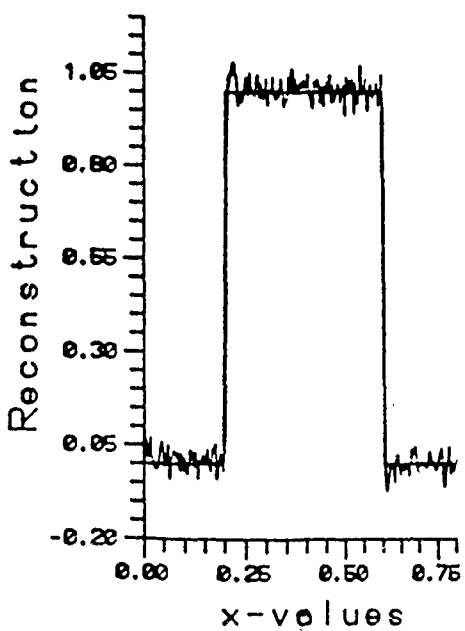


Fig. 3 Reconstruction with Method III
ε = 0.01, δ = 0.008, N = 500

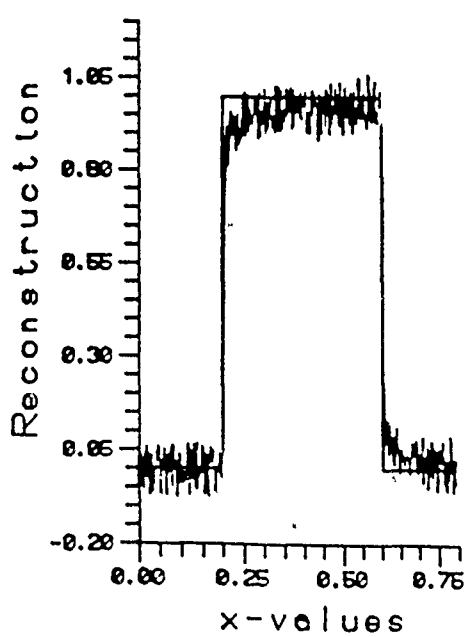


Fig. 4 Reconstruction with Method IV
ε = 0.001, γ = 0.001, N = 500

Third International Conference on Inverse Design Concepts and Optimization in Engineering Sciences (ICIDES-III), Editor: G.S. Dulikravich, Washington D.C., October 23-25, 1991.

OPTIMIZATION OF THE HEATING SURFACE SHAPE IN THE CONTACT MELTING PROBLEM

Sergei A. Fomin

Department of Appplied mathematics, Kazan State University, Kazan, 420008, USSR

and

Shangmo Cheng

Department of Power Engineering, Huazhong University of Science and Technology, Wuhan, 430074, China

ABSTRACT

The work is devoted to the theoretical analysis of contact melting by the migrating heat source with an arbitrary shaped isothermal heating surface.After the substantiated simplification the governing equations are transformed to the convenient for engineering calculations relationships. Analytical solutions are used for numerical prediction of optimal shape of the heating surface. Problem is investigeted for the constant and for temperature dependent physical properties of the melt.

1. INTRODUCTION

Melting of solids by contact with a heating surface takes place in numerous natural and technological processes. These processes are enumerated in the previous works [2, 4, 12–14, 22] devoted to contact melting problem and are divided into two groups. In one group the melting material lies on the heating surface and pressed against it by some external force (for instance, the force of the weight of the melting material). This situation arises when an unfixed solid melts in an enclosure [1, 16, 22] and in other contact melting devices used in industry [8]. Another group of applications involves a moving heat source melting its way through the surrounding solid. This situation arises in such fields as welding [21], geology [3], nuclear technology [9, 10] thermal drilling of rocks [4, 6, 18, 20] and glaciers [11, 17, 19]. Thermal drilling is commonly recognized now as the most effective method of boring glaciers. Boring rocks, sands and soil by thermopenetrators is a relatively new method in mining engineering. It has some advantages in comparison with traditional rotary drilling. The most considerable advantage of thermodrilling is that three major facts of excavation (rock fracturing, debris removal and wall stabilization) are accomplished in a single integrated operation.

This work is devoted to the theoretical analysis of the contact melting process by the moving heating source with an arbitrary shaped isothermal heating surface.

2. ANALYSIS

2.1. The physical model and governing equations.

Obviously every technological process where contact melting occurs has its own specific character. In particular case of thermodrilling, it is contact melting with a great specific load and heat energy, with arbitrary shaped heating surface. Thermopenetrators are radially symmetric and in some cases ring–shaped,

Third International Conference on Inverse Design Concepts and Optimization in Engineering Sciences
(ICIDES-III), Editor: G.S. Dulikravich, Washington D.C., October 23-25, 1991.

or toroidal, with a large central hole for forming and extracting the core sample [6]. A schematic diagram of the contact melting for the thermodrilling conditions is shown in Fig.1. Axisymmetric heater –1 is penetrating into the melting solid –2 with the velocity V under the effect of applied external force F. The thermopenetrator is separated from the solid with a layer of melt –3, flowing along the thin channel between the heating surface $\sum_h$ and solid–liquid interface $\sum_m$. It is assumed that the solid–liquid interface is a sharply defined surface and melting occurs precisely at temperature t_m, melt flow is laminar and two–dimensional. Molten layer is assumed to be incompressible Newtonian liquid with a temperature dependent physical properties (except density). Experimental results [6, 15] indicated that the heat source velocity attains its quasi–steady, constant value V soon after initiation of melting. This fact justifies the next assumption of quasi–steady heat and mass transfer in the contact melting problem.

According to the physical model and assumptions enumerated above the governing differential equations of heat and mass transfer in the molten layer can be written as follows:

$$\begin{aligned} &\mathrm{div}\bar{v} = 0 \\ &\rho_L(\bar{v}\cdot\nabla)\bar{v} = \bar{G} - \rho_L\nabla p + \mathrm{div}T \\ &C_L\rho_L(\bar{v}\cdot\nabla t_L) = \mathrm{div}(\lambda_L\nabla t_L) + \Phi \end{aligned} \qquad (1)$$

where T is the deviator part of the tensor of internal stresses; $\bar{v}$, p, t_L are the liquids velocity, pressure and temperature respectively; Φ represents the dissipative terms in heat transfer equation; C_L, ρ_L, λ_L liquid properties defined in Nomenclature; the rest of the symbols are standard.

It is convenient for further analysis to use two systems of coordinates fixed to the heating surface: cylindrical coordinates (r, z) and local orthogonal boundary layer coordinates S and ξ are indicated in Fig. 1.

Transforming (1) to non–dimensional form and using the similarity method in a preliminary analysis the main dimensionless parameters and numbers are generated [7]:

$$\mathrm{Pe} = \frac{Vd}{a_s},\quad \mathrm{Ste} = \frac{C_s(t_m - t_\infty)}{L},\quad K_h = \left(\frac{\rho_s\mu_L^m V}{\rho_L W d}\right)^{1/3},\quad K_c = \frac{C_s}{C_L^m},\quad \mathrm{Re} = V\rho_s d/\mu_L^m \quad K_h,$$

$$\mathrm{Br} = \frac{W\bar{P}_c}{C_L^m\rho_L(t_m - t_\infty)},\quad \bar{\mathrm{Pe}} = \frac{\mathrm{Pe}K_\lambda K_h}{K_c},\quad K_\lambda = \frac{\lambda_s}{\lambda_L^m},\quad K_g = \rho_L g d/W \qquad (2)$$

All the quantities here are defined in the Nomenclature. Each of the dimensionless numbers (2) has an exact obvious physical meaning. In order to substantiate the simplification of the governing equations (1), the analysis of the values of these non–dimensional numbers for the concrete conditions of thermal drilling of ice and rock was carried out. Dimensionless parameter $K_h \sim 10^{-3}$—10^{-1} physically represents the ratio of characteristic thickness of the molten layer and characteristic size of the heating surface d; criterion $K_g \sim 10^{-3}$ is the ratio of the characteristic mass force of the melt and external force; Reynolds number $\mathrm{Re} \sim 10^{-6}$—10^{-4}; Brinkman number $\mathrm{Br} \sim 10^{-5}$—10^{-4} represents the viscous dissipation of heat in the molten layer, Pecklet number $\mathrm{Pe} \sim 10$—100; Stefan number $\mathrm{Ste} \sim 1$—10; K_λ, $K_c \sim 1$.

After neglecting terms of $0(K_h, K_g, \mathrm{Re}, \mathrm{Br})$ the governing nondimensional equations of heat and mass transfer in the molten layer will take the following form:

$$\frac{1}{R^\nu}\frac{\partial}{\partial s}(R^\nu H u_s) + \frac{\partial u_\eta}{\partial \eta} = 0 \qquad (3)$$

$$H^2\frac{dp}{ds} = \frac{\partial}{\partial \eta}\left(\mu\frac{\partial u_s}{\partial \eta}\right) \qquad (4)$$

Third International Conference on Inverse Design Concepts and Optimization in Engineering Sciences (ICIDES-III), Editor: G.S. Dulikravich, Washington D.C., October 23-25, 1991.

$$PeCH(Hu_s\frac{\partial\theta}{\partial s}+u_\eta\frac{\partial\theta}{\partial\eta})=\frac{\partial}{\partial\eta}(\lambda\frac{\partial\theta}{\partial\eta}) \tag{5}$$

where $\eta=\frac{\xi}{h}$, $P=p/w$, $S=s/d$, $H=h/K_h d$, $\mu=\mu_L/\mu_L^m$, $C=C_L/C_L^m$, $\lambda=\lambda_L/\lambda_L^m$, $R=r/d$, $u_s=\frac{v_s\rho_L}{V\rho_s}$, $u_\rho=\frac{v_\eta\rho_L}{V\rho_s}$, $\theta=\frac{t_L-t_m}{\bar{t}_h-t_m}$, $R=R(s)$–equation of generating line Γ_h of heating surface $\sum_h$; $h=h(s)$ –thickness of the molten layer mersured along the internal normal to Γ_h; v_s, v_η –longitude and transverse velocities in the molten layer; all the physical properties of liquid C_L, λ_L, μ_L are nondimensionalized by their values C_L^m, λ_L^m, μ_L^m at temperature t_m; reference temperature ($\bar{t}_h-t_m$) is determined after nondimensionalization of Stefans condition,

$$\bar{t}_h-t_m=\bar{P}eK_c(t_m-t_\infty) \tag{6}$$

Here t_∞ is initial temperature of melting material. In the equation (3) $\nu=0$ corresponds to the ring–shaped penetrator with a large central hole. In this case since the thickness of the liquid film is of $0(K_h)$ it is possible to ignore the axially symmetric behaviour of heat and mass transfer and to consider (r, z) as the Cartesian coordinates; $\nu=1$ corresponds to the continuous heating surface without hole.

The boundary conditions in dimensionless form are following

At the heating surface $\sum_h(\eta=0)$

$$u_s=u_\eta=0;\quad \theta=\theta_h; \tag{7}$$

$\theta_h=(t_h-t_m)/(\bar{t}_h-t_m)$; t_h is the unknown temperature on $\sum_h$

At the solid–liquid interface $\sum_m(\eta=1)$

$$u_s=0;\quad u_\eta=-\frac{dR}{ds};\quad \theta=0 \tag{8}$$

$$-\frac{1}{H}\frac{\partial\theta}{\partial\eta}\Big|_{\eta=1}=[\frac{Q}{Pe}+(\frac{dR}{ds})/Ste\ ];\quad Q=(-\frac{\partial\theta_s}{\partial n})|_{\sum_m}; \tag{9}$$

where $\theta_s=(t_s-t_\infty/(t_m-t_\infty)$, t_s is a temperature of the solid material, n is an external relatively tomolten layer normal to $\sum_m$.

For the pressure in the exit points of the molten layer $s=s_1$ and $s=s_2$

$$P(s_1)=P(s_2)=0 \tag{10}$$

Since when $\nu=1$ it is only one exit point $s=s_2$ then in this case $s_1=0$ is the critical point where $u_s=0$ $dP/ds=0$.

The assumption of quasi–stationary heat and mass transfer couses the equality of external force F and the force of internal stresses in the molten layer. This condition with the defined accuracy of $0(K_h)$ in non–dimensional form is [4]

$$1=\frac{2}{R_2^2-R_1^2}\int_{R_1}^{R_2}RPdR \tag{11}$$

The function Q in Stefan condition (9) is the non–dimensional density of heat flux to the solid from surface $\sum_m$ It's value depends on the temperature distribution in the solid and is obtained from the solution of the heat transfer problem which is the same as the problem of temperature distribution in the surrounding weldpool material [21]:

Third International Conference on Inverse Design Concepts and Optimization in Engineering Sciences (ICIDES-III), Editor: G.S. Dulikravich, Washington D.C., October 23-25, 1991.

$$-\mathrm{Pe}\frac{\partial\theta_s}{\partial Z}+\frac{\partial^2\theta_s}{\partial Z^2}+\frac{1}{R^\nu}\frac{\partial}{\partial R}\left(R^\nu\frac{\partial\theta_s}{\partial R}\right)=0;\quad \nu=0,1; \tag{12}$$

$$\theta_s|_{\Sigma_m}=1;\quad \lim_{R^2+Z^2\to\infty}\theta_s=0;\quad \theta_s|_{\Sigma_f}=\theta_f;\quad (R,Z)=(r,z)/d; \tag{13}$$

θ_f – is temperature distribution on surface $\sum_f$, formed after melting (Fig.1). Problem (12) (13) was solved in [4, 18] numerically by the boundary element method.

2.2. Analytical solutions

In [4] it was proved that boundary value problem (12), (13) admits an analytical solution as a function of one independent variable when and only when the generating curve Γ_m of $\sum_m$ is parabola. In parabolic coordinates σ and τ related to the coordinates R and Z by $R=\tau\sigma$, $Z=0.5(\sigma^2-\tau^2)$ with boundary conditions on $\sum_m$; $\tau=\tau_m, \theta_s=1$, in infinity: $\tau\to\infty$, $\theta_s\to 0$, equasion (12) has the following solution

$$\theta_s=\begin{cases}\mathrm{Ei}\left(-\frac{\mathrm{Pe}}{2}\tau^2\right)/\mathrm{Ei}\left(\frac{-\mathrm{Pe}}{2}\tau_m^2\right), & \nu=1\\ \mathrm{erfc}\left(\sqrt{\frac{\mathrm{Pe}}{2}}\tau\right)/\mathrm{erfc}\left(\sqrt{\frac{\mathrm{Pe}}{2}}\tau_m\right), & \nu=0\end{cases} \tag{14}$$

where $\mathrm{erfc}(x)=\frac{2}{\sqrt{\pi}}\int_x^\infty \exp(-u^2)du$, $\mathrm{Ei}(-x)=\int_1^\infty\frac{\exp(-xu)}{u}du \quad x>0$

According the formulae (9) and (14) the heat flux distribution on $\sum_m$ is

$$Q=\frac{\mathrm{Pe}\ c^{-\alpha^2}\tau_m}{\sqrt{\tau_m^2+\sigma^2}}\Big/\begin{cases}\alpha^2\mathrm{Ei}(-\alpha^2), & \nu=1\\ \sqrt{\pi}\,\alpha\,\mathrm{erfc}(\alpha), & \nu=0\end{cases} \tag{15}$$

where $\alpha^2=\mathrm{Pe}\tau_m/2$ Taking into account the fact that the distance between $\sum_h$ and $\sum_m$ is the value of $0(K_h)$ we can rewrite (15) with the accuracy of $0(K_h)$

$$Q=\mathrm{Pe}\cdot c^{-\alpha^2}\frac{dR}{ds}\Big/\begin{cases}\alpha^2\mathrm{Ei}(-\alpha^2), & \nu=1\\ \sqrt{\sigma}\,\alpha\,\mathrm{erfc}(\alpha), & \nu=0\end{cases} \tag{16}$$

After simple transformation of equations (3) and (4) with invoked boundary conditions (7), (8) and (10) the velocities and pressure distribution in the molten Layer are obtained

$$u_s=\frac{R^{\nu+1}-R_*^{\nu+1}}{(\nu+1)HDR^\nu}\int_0^\eta\frac{\eta_0-\eta}{\mu}d\eta \tag{17}$$

$$u_\eta=-\frac{1}{(\nu+1)R^\nu}\frac{\partial}{\partial s}\left[\frac{(R^{\nu+1}-R_*^{\nu+1})}{D}\varphi\right] \tag{18}$$

$$P=\frac{1}{\nu+1}\int_s^{s_2}\frac{R^{\nu+1}-R_*^{\nu+1}}{R^\nu H^3 D}ds \tag{19}$$

where $D=\int_0^1\frac{(\eta-\eta_0)}{\mu}\eta d\eta$, $\eta_0=\int_0^1\frac{\eta d\eta}{\mu}\Big/\int_0^1\frac{d\eta}{\mu}$

$$\varphi=\eta\int_0^\eta\frac{\eta_0-\eta}{\mu}d\eta-\int_0^\eta\frac{\eta_0-\eta}{\mu}\eta d\eta$$

R_* is a critical point which is determined by (19) and the boundary coudition $P(s_1)=0$

Third International Conference on Inverse Design Concepts and Optimization in Engineering Sciences (ICIDES-III), Editor: G.S. Dulikravich, Washington D.C., October 23-25, 1991.

$$R_*^{\nu+1} = \int_{s_1}^{s_2} \frac{Rds}{H^3 D} \Big/ \int_{s_1}^{s_2} \frac{ds}{R^\nu H^3 D} \tag{20}$$

when $\nu = 1$ it is supposed that $R_* = 0$

According the assumption $\theta_h = \text{const}$ the temperature distribution in the molten layer is sought as a function of one independent variable η

$$\theta = \theta(\eta) \tag{21}$$

As follows from interfacial condition (9) in this case

$$H\frac{dR}{ds} = \overline{H} = \text{const.} \tag{22}$$

Last formulae (22) and (21) simplify equalities (18), (19)

$$u_\eta = -\frac{1}{D}\frac{dR}{ds}\varphi(\eta) \tag{23}$$

$$P = \frac{1}{(\nu+1)D}\int_{s_1}^{s_2} \frac{R^{\nu+1} - R_*^{\nu+1}}{H^3 R^\nu} ds \tag{24}$$

and heat transfer equation in the molten layer

$$-\frac{\overline{Pe}\overline{H}\varphi(\eta)}{D}\frac{d\theta}{d\eta} = \frac{d}{d\eta}\left(\lambda\frac{d\theta}{d\eta}\right) \tag{25}$$

Integration of this equation with the associated boundary conditions

$$\theta|_{\eta=1} = 0; \quad -\frac{d\theta}{d\eta}\Big|_{\eta=1} = \overline{H}E; \quad E = \frac{Q}{Pe\frac{dR}{ds}} + \frac{1}{Ste} \tag{26}$$

reduce to the following relationship

$$\theta(\eta) = E\overline{H}\int_\eta^1 \frac{1}{\lambda}\exp\left(\frac{\overline{PeH}}{D}\int_\eta^1 \frac{\varphi C}{\lambda} d\eta\right)d\eta \tag{27}$$

puting in (27) $\eta = 0$ the temperature of the heating surface is determined

$$\theta_h = E\overline{H}\int_0^1 \frac{1}{\lambda}\exp\left(\frac{\overline{PeH}}{D}\int_\eta^1 \frac{\varphi C}{\lambda} d\eta\right)d\eta \tag{28}$$

In order to simplify further computations assume that Γ_h is specified by the equation $Z = A(R-R_*)^2$. In this case heat flux distribution Q is determined by the equality (16), where

$$\frac{dR}{ds} = \frac{1}{\sqrt{1+4A^2(R-R_*)^2}}$$

P(s) introduction into (11) yields

$$\overline{H}^3 = \frac{1}{(R_2^2 - R_1^2)(\nu+1)^2 D}\int_{R_1}^{R_2} \frac{R(R^{\nu+1} - R_*^{\nu+1})}{1+4A^2(R-R_*)^2} dR \tag{29}$$

where $R_1 = R_* = 0$ if $\nu = 1$

One of the most important characteristics of contact melting is the heat energy removal from the heating surface to the melt. Combining heat energy definition in non-dimensional form

$$N = 2\pi\int_{R_1}^{R_2} \frac{R}{\overline{H}}\left(-\lambda\frac{d\theta}{d\eta}\right)\Big|_{\eta=0} dR$$

with the equation (27) we have

Third International Conference on Inverse Design Concepts and Optimization in Engineering Sciences (ICIDES-III), Editor: G.S. Dulikravich, Washington D.C., October 23-25, 1991.

$$N = \pi(R_2^2 - R_1^2)E\exp\left(\frac{\overline{Pe}\overline{H}}{D}\int_0^1 \frac{c\varphi}{\lambda}d\eta\right) \tag{30}$$

The quantity of heat energy calculated according (30) excesses the minimum heat power N_0 which is necessary to sustain the chosen melting velocity V. In non-dimensional form

$$N_0 = \pi(R_2^2 - R_1^2)(1 + 1/Ste)$$

Here N_0 in comparison with N does not contain the energy rate for heating melt and useless heat dissipation in the surrounding thermopenetrator solid material.

The main scope of present paper is to elucidate the influence of the heating surface shape upon the effectivety of the contact melting process. Defining efficiency of the heating surface as a ratio $\beta = N_0/N$ we'll have

$$\beta = \frac{1 + \frac{1}{Ste}}{E}\exp\left(-\overline{Pe}\overline{H}/D \int_0^1 \frac{c\varphi}{\lambda}d\eta\right) \tag{31}$$

Equations (23), (24), (27)–(31) simulate heat and mass transfer processes in contact melting problem with the accuracy of $0(K_h)$. They are convenient for prediction of contact melting process for materials with variable physical properties such as different kinds of rocks and sands.

When the physical properties of melt are constant (for example in the case of ice melting) equations (17), (23), (24), (27), (28), (30), (31). allows the considerable simplification.

$$u_s = \frac{6(R^{\nu+1} - R_*^{\nu+1})}{(\nu+1)R^{\nu}H}\eta(1-\eta) \tag{32}$$

$$u_\eta = -\frac{dR}{ds}\eta^2(3-2\eta) \tag{33}$$

$$P = \frac{12}{\nu+1}\int_s^{s^2} \frac{R^{\nu+1} - R_*^{\nu+1}}{H^3 R^{\nu}}ds \tag{34}$$

$$\theta = E\overline{H}\exp(\overline{Pe}\overline{H}/2 \int_\eta^1 \exp[\overline{Pe}\overline{H}\eta^3(1-0.5\eta)]d\eta \tag{35}$$

$$N = \pi(R_2^2 - R_1^2)E\exp\left(\frac{\overline{Pe}\overline{H}}{2}\right) \tag{36}$$

$$\beta = \frac{(1 + \frac{1}{Ste})}{E}\exp\left(-\frac{\overline{Pe}\overline{H}}{2}\right) \tag{37}$$

3. RESULTS

Numerical prediction of u_s, u_η, P, H, θ, β and other quantities of interest is carried out for ice and rock thermodrilling conditions. All the calculations of rock melting are based on equations (23), (24), (27)—(31). Relatively complete description of basalt physical properties at high temperature is available in [5, 6]. Non-linear equation (27) is solved numerically by the iteration procedure. After this other quantities are obtained automatically in a view of equations (23), (24), (28)—(31). As the initial estimate of iterative process solution (35) is chosen. When the ice boring process is investigated formulae (29), (32)—(37) are used. The values of ice physical properties one can find for example in [4, 17, 19]. Effectiveness of the heating surface is estimated by the value of parameter β. It is shown in previous works [4, 17] that in com-

Third International Conference on Inverse Design Concepts and Optimization in Engineering Sciences (ICIDES-III), Editor: G.S. Dulikravich, Washington D.C., October 23-25, 1991.

parison with the other (cone–shaped, sphere–shaped, etc.) thermopenetrators of the same power output the parabolic shaped penetrator attains the highest melting velocity, Therefore present paper is devoted to more detail analysis of contact melting with parabolic heating surface. The elongation of the surface is characterized by the value of shape parameter A. The results of numerically predicted efficiency as a function of A for different conditions of ice and rock melting are plotted in Fig. 2. Numerical results indicates that for slow melting when heat transfer in the molten layer is of minor significance and in the contrary the heat dissipation increases the flat heating surface ($A < 1$) is more effective. Vice versa for high speed melting the heat energy rate in the melt is dominating in comparison with the dissipation in surrounding solid material. So in this case the elongate form of heating surface is preferable. According the calculations presented in Fig.2 there is the interval for melting velocities when the definition of the optimal shape is not trivial. For toroidal penetrator ($\nu = 0$)and ice melting conditions $20 < Pe < 55$; for non–coring penetrator ($\nu = 1$) and rock melting conditions $40 < Pe < 75$. In order to find the maximum of β and the corresponding value of A, the derivative of β with respect to A is calculated. When the problem is non–linear and the physical properties of the melt depend on temperature the derivative is calculated numerically; when μ, c, λ are constants it is feasible to calculate β'_A analytically. In a view of relationship (37) the equation $\beta'_A = 0$ for computation of the optimal A can be written as follows: $-\overline{Pe}\,\overline{H}'_A E - E'_A = 0$.

This simple equation is solved by dividing segment in half method.

NOMENCLATURE

A – shape parameter of the heating surface;
a – thermal diffusivity;
c – specific heat;
d – characteristic size of heating device;
F – external force;
G – mass force;
g – acceleration;
h – melt layer thickness;
L – latent melting heat;
P – pressure;
Q – heat flux density;
r, z – cylindrical coordinates defined in Fig.1;
r_1 – internal radius of the heating device;
r_2 – external radius of the heating surface;
s_1, s_2 – coordinates of the end points of generating curve of the heating surface;
t – temperature; $\bar{v}$ – velocity of the molten layer;
v_s, v_η – longitude and transverse velocities in the molten layer;
V – melting velocity;
s, ξ – longitudinal and transverse local coordinates in the molten layer defined in Fig. 1;
W – specific axial load from heating device side ($W = \dfrac{F}{\pi(r_2^2 - r_1^2)}$)
β – efficiency;
Γ – generating curve of surface Σ;
λ – thermal conductivity;
μ – dynamic viscosity coefficient;
ρ – density;
σ, τ – parabolic coordinates.

Indices:

L – liquid phase;
s – solid phase;
* – critical point;
h – heating surface;
m – melting surface;
∞ – value in infinite point.

All the non–dimensional parameters, numbers and functions are determined in the text: (2), (5), etc.

REFERENCES

[1] Bareis, M. and Beer, H. (1984). "An analytical solution of the heat transfer process during melting of unfixed solid phase change material inside a horizontal tube", Int. J. Heat Mass Trasfer, v.27, pp.739–746.

[2] Bejan, A. and Litsek, P. A. (1989), "The contact heating and lubricating flow of a body of glass", Int. J. Heat Mass Transfer, v.32, No4, pp.751–760.

[3] Birth, F. S. (1975), "Conduction heat flow anomalies over a hot spot in moving medium", J. of Geophysical Research, v.80, pp.4825–4827

[4] Chistyakov, V. K., Fomin, S.A. and Chugunov, V.A. (1984), "Heat mass Tansfer in contact melting", Kazan State Univ. Press, Kazan (in Russian).

[5] Filatoff, N., Lasek, A, (1989), "On variable viscosity magma flow", Int. J. Heat Mass Transfer, v.32, No. 12, pp.2485–2495.

[6] Fisher, N. (1976), "Thermal analysis of some subterrene penetrators", J. Heat Transfer, v.98, No. 3, pp.485–490.

[7] Fomin, S. A. (1988), "Mathematical modeling of heat and mass transfer in contact melting", Issled po priklad. Matem, v.16 pp.105–122 (in Russian).

[8] Griffin, O. M. (1970), "On the melting solid to non–Newtonian fluids", Chem. Eng. Science, v. 25, No.1, pp.109–117.

[9] Jansen, G. and Stepnewski, D. D. (1973), "Fast reactor fuel interactions with floer material after a hypothetical core meltdown", Nuclear technology, v. 17, pp.85–96.

[10] Logan, S. E. (1974), "Deep self–burial of radiative waste by rock melting capcules", Nuclear Technology. v.21 pp.111–124.

[11] Mellor, M. and Sellman, P. V. (1974), "General considerations for drill system design, Ice–core drilling", Proc. of Symp. Univ. of Nebraska, Lincoln, 28–30 August, pp. 77–111.

[12] Moallemi, M. K. and Viskanta, R. A. (1986), "Analysis of close contact melting heat transfer", Int. J. Heat Mass Transfer, v.29, No.6, pp.855–867.

[13] Moallemi, M. K. and Viskanta, R.A. (1986), "Analysis of melting around a moving heat source", Int. J. Heat Mass Transfer, v.29, No.8, pp.1271–1282.

[14] Moallemi, M. k. and Viskanta, R. A. (1985), "Melting around a migrating heat source", J. Heat Transfer, v.107, No.2, 451–458.

[15] Moallemi, M. K. and Viskanta, R. (1985), "Experiments of fluid flow induced by melting around a migrating heat source", J. Fluid Mech; v.157, pp.35–51.

[16] Moore, F.E and Bayzitoglu, Y. (1982), "Melting within a spherical enclosure", J. Heat Transfer, v.104, pp.19–23.

[17] Pudovcin, M. A., Salamatin, A. N., Fomin, S. A, and Chistyakov, V. K. (1988), "Effect of a thermal drill on hot–point ice boring performance", Journal of Soviet Mathematics, v.43, No. 3, pp.2496–2505.

[18] Salamatin, A. N., Fomin, S. A., Chistyakov, V. K. and Chugunov, V. A. (1984), "A mathematical description and calculation of contact melting", J. of Engineering Physics, v.XLVII, No. 3, pp.439–446.

[19] Shreve, R. L. (1962), "Theory of performance of isothermal solidnose hot points boring in temperate ice", J. of Glaciology, v.4, No.32, pp.151–160.

[20] The subterrene program. Mini–review 75–2 (1975), Los Alamos scientific laboratory, Los Alamos, New Mexico, USA.

[21] Thompson, M. E. and Szekely, J. (1989), "The transient behavior of weldpools with the deformed free surface", Int. J. Heat Mass Transfer, v.32, NO.6, pp.1007–1019.

[22] Webb, B. W., Moallemi, M. K and Viskanta, R. A. (1987), "Experiments of meltig unfixed ice in a horizontal cylindrical capsule". J. Heat Transfer, v.109, pp.454–459.

Third International Conference on Inverse Design Concepts and Optimization in Engineering Sciences (ICIDES-III), Editor: G.S. Dulikravich, Washington D.C., October 23-25, 1991.

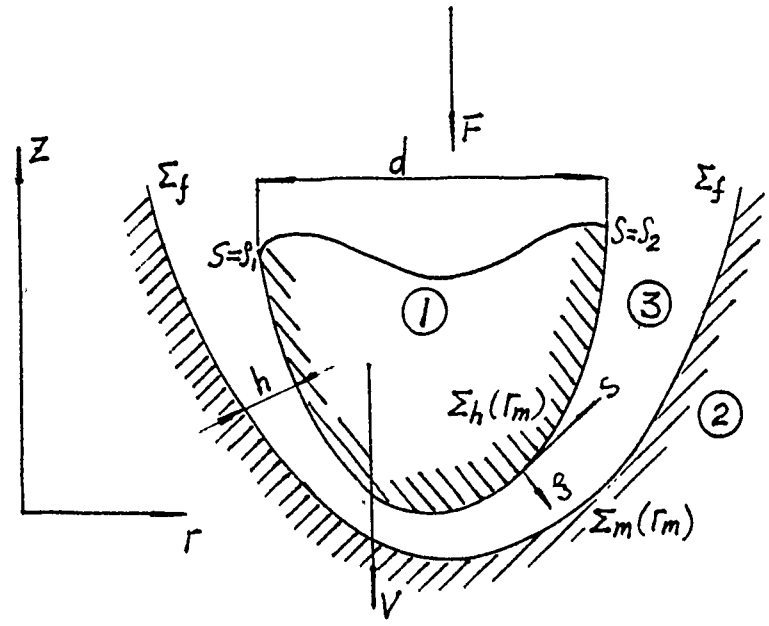


Fig. 1. Schematic representation of the contact melting process:1–heating device, 2–melting solid, 3–molten layer.

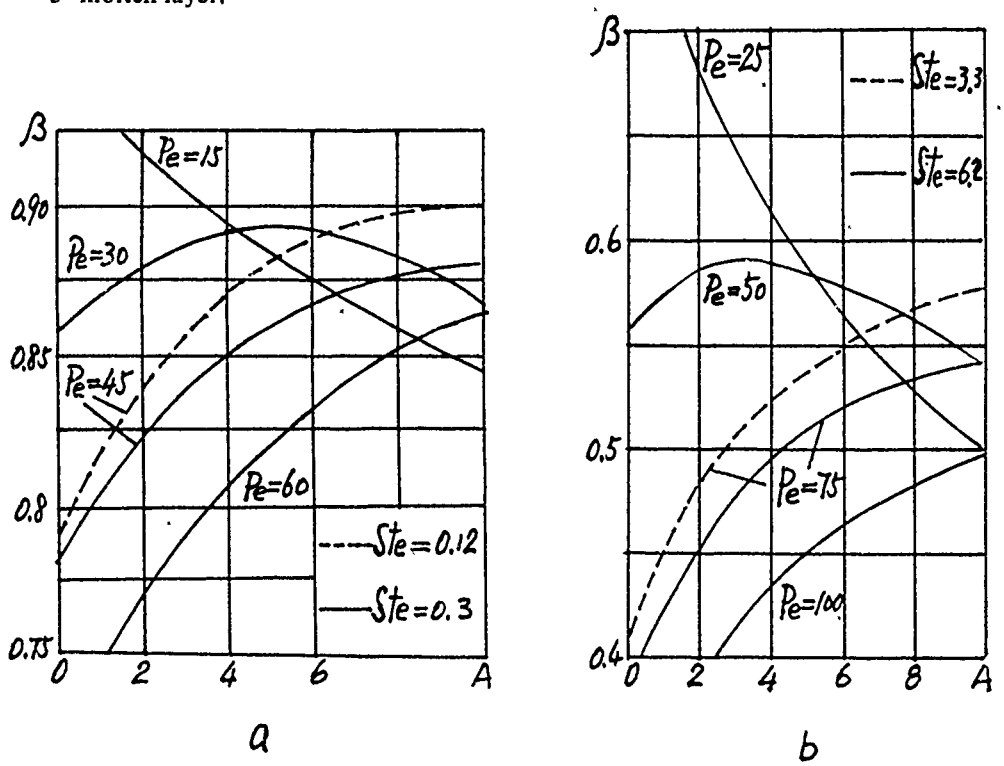


Fig. 2. Efficiency β as a function of shape parameter A.

a) Ice boring conditions; $v=0$, $R_* = 3.2$ (ring shaped penetrator)

b) Rock boring conditions; $v=1$, $R_* = R_1 = 0$ (non–coring penetrator)

Third International Conference on Inverse Design Concepts and Optimization in Engineering Sciences
(ICIDES-III).Editor:G.S.Dulikravich, Washington D.C.,October 23-25,1991

DESIGN OF 3-DIMENSIONAL COMPLEX AIRPLANE CONFIGURATIONS WITH SPECIFIED PRESSURE DISTRIBUTION VIA OPTIMIZATION

Krzysztof Kubrynski
Technical University of Warsaw
Institute of Applied Mechanics
and Aviation Technology
ul. Nowowiejska 24
00-665 Warsaw - POLAND

ABSTRACT: A subcritical panel method applied to flow analysis and aerodynamic design of complex aircraft configurations is presented. The analysis method is based on linearized, compressible, subsonic flow equations and indirect Dirichlet boundary conditions. Quadratic dipol and linear source distribution on flat panels are applied.
In the case of aerodynamic design the geometry which minimizes differences between design and actual pressure distribution is found iteratively using numerical optimization technique. Geometry modifications are modelled by surface transpiration concept. Constraints in respect to resulting geometry can be specified. A number of complex 3-dimensional design examples are presented. The software is adopted to personal computers, and as result an unexpected low cost of computations is obtained.

INTRODUCTION

One of the most important task in aerodynamic design is such airplane shape definition which fulfills the following requirements: low CD, high MA_{DD} and CL_{MAX}, appropriate boundary layer stability and stall progression, elimination of shock waves etc. This, however, depends on appropriate pressure distribution on the surface. It is extremely difficult to fulfill all these requirements for complex, 3-dimensional airplane configurations where strong interference effects occur between aerodynamically close coupled elements. Optimal design of each element does not lead to optimum of configuration because of adverse interference effects. But in principle it is possible to design such configurations with neutral or even favorable interference, where interaction between airplane components gives benefits and leads to better global characteristics then those of separated elements. It is impossible to realize such a configuration only on the ground of experimental technique. Computational methods of aerodynamics, which have developed quickly during last 30 years enable, in connection with the aerodynamic concepts worked out at this time ("roof-top", "peaky" etc.), to realize many interesting designs. The problem can be illustrated by wing-nacelle-pylon configuration. In the past the nacelles were shaped as axisymmetrical body and mounted to swept wing by plane pylons. A strong adverse interference occurs leading to loss in

isobar sweep, higher local Mach numbers and shock waves, losses in lift coefficient at design angle of attack etc., creating the lower aerodynamic efficiency. Later the method of designing for neutral interference was worked out, where nacelle and pylon were shaped along stream lines of isolated wing in order to minimize interference. It is difficult however, even now, to design such configurations with favorable interference.

Slightly simplifying the problem we can consider three kinds of design treatments in aerodynamics using computational methods:

1. Design by trial and error method
2. Direct optimization method
3. Inverse design method

The first is direct transformation of the wind-tunnel technique on the computational ground, where wind-tunnel is replaced by computational system and the process of "aerodynamic model manufacture" and "testing" is significantly cheaper and faster. Experienced aerodynamicist analyses results, specifies the needed modifications and the process is repeated until satisfactory computational results are obtained.

In the second method geometry which minimizes aerodynamic object function (such as drag) and fulfills additional constraints is found directly without external detailed considerations about flow properties. This method, conceptually very attractive and fully automated, can not be actually performed in the case of complex configurations because of very high cost and many times too low accuracy of up-to the date flow analysis methods which lead to so called "numerical noise" and make impossible to find real solution.

The third method is actually the most effective and refined method acceptable in practice. It consists of two steps. First is such a pressure distribution specification which fulfills aerodynamic requirements. In the second step the geometry corresponding to this pressure is calculated using inverse method. It is obvious that the possession of the appropriate inverse method is worthy. The method presented in the paper is actually probably the most general inverse method applied to subsonic flow region, which allows to design of real complex configurations even via interference effects.

FLOW ANALYSIS

The method is based on linearized theory of compressible flow [1].

The Prandtl-Glauert equation

$$\beta^2\varphi_{xx} + \varphi_{yy} + \varphi_{zz} = 0 \; ; \quad \beta^2=(1-Ma_\infty^2) \tag{1}$$

Third International Conference on Inverse Design Concepts and Optimization in Engineering Sciences (ICIDES-III).Editor:G.S.Dulikravich, Washington D.C.,October 23-25,1991

is assumed to govern the perturbation velocity potential in the flowfield. The linearized mass flux boundary conditions on external surface are applied

$$\mathbf{W}\cdot\mathbf{n} = (\mathbf{V}_\infty + \mathbf{w})\cdot\mathbf{n} = \dot{m}_s/\rho_\infty \tag{2}$$

and express the intensity of mass outflow through the surface.
$\mathbf{w}$ is the perturbation mass flux vector defined by

$$\mathbf{w} = (\beta^2\varphi_x, \varphi_y, \varphi_z) \tag{3}$$

The second order pressure formula [assuming $\mathbf{V}_\infty = (1,0,0)$]

$$Cp_2 = -2\varphi_x - (\beta^2\varphi_x^2 + \varphi_y^2 + \varphi_z^2) \tag{4}$$

is applied to find aerodynamic forces and moments, and isentropic formula is used to express pressure distribution on the surface:

$$Cp = \frac{2}{kM_\infty^2}\left\{\left[1 + \frac{k-1}{2}M_\infty^2\left(1 - \mathbf{V}.\mathbf{V}\right)^{k/k-1}\right] - 1\right\} \tag{5}$$

Applying Greens Theorem to the flowfield the perturbation velocity potential on the surface can be expressed as:

$$E_P\varphi_P = \frac{1}{4\pi}\iint_{Sb}\left[\frac{-(\dot{m}_s/\rho_\infty - \mathbf{V}_\infty.\mathbf{n}_Q)}{r_\beta} + \varphi_Q\beta^2\frac{\mathbf{r}_{QP}.\mathbf{n}_Q}{r_\beta^3}\right]dS_Q + \frac{1}{4\pi}\iint_{Sw}\langle\varphi\rangle_Q\beta^2\frac{\mathbf{r}_{QP}.\mathbf{n}_Q}{r_\beta^3}dS_Q \tag{6}$$

where $\langle\varphi\rangle$ is the jump of potential across the wake and E is function of position (respectively: 1, 1/2 and 0 for P in the flowfield, on the surface and outside the flowfield). Equation (6) is solved by panel method based on quadratic dipol and linear source distribution on flat panels and indirect Dirichlet boundary conditions (zero perturbation potential is specified on the internal side of surface). Control points and unknown singularity parameters are located in panel center of gravity. Jump of potential across the wake is determined by Kutta condition: flow behind the trailing edge of lifting surface must be tangent to trailing edge bisector. Finally the integral equation (6) is replaced by system of linear equations of the form:

$$[A]\left\{\begin{matrix}\varphi\\ \hline \langle\varphi\rangle\end{matrix}\right\} = -\left\{\begin{matrix}0\\ \hline V\infty\circ N_K\end{matrix}\right\} - [B]\left\{\dot{m}_s/\rho_\infty - \mathbf{V}_\infty.\mathbf{n}_Q\right\} \tag{7}$$

Third International Conference on Inverse Design Concepts and Optimization in Engineering Sciences (ICIDES-III).Editor:G.S.Dulikravich, Washington D.C.,October 23-25,1991

which is solved to obtain the perturbation potential on the surface and jump of potential across the wake. Velocity distribution on the surface is obtained by numerical differentiation of perturbation potential and adding the free-stream contribution. In the local panel coordinate system:

$$\begin{aligned} V_t &= \partial\varphi/\partial t + \mathbf{V}_\infty.\mathbf{t} \\ V_s &= \partial\varphi/\partial s + \mathbf{V}_\infty.\mathbf{s} \end{aligned} \tag{8}$$

INVERSE METHOD

The inverse problem is solved in the present method via optimization. The method is extension of the previous design method of the author. The requested geometry of configuration is searched in a form of sum of the initial geometry and linear combination of basic design shapes:

$$\text{GEOMETRY} = \text{INITIAL GEOMETRY} + \sum_{i=1}^{ND} X_i \circ (\text{i-th BASIC SHAPE}) \tag{9}$$

Coefficients X_i are found from the condition of minimizing the error in pressure distribution:

$$E = \sum_{j=1}^{NP} W_j \circ (Cp_j - Cp_j^D)^2 \tag{10}$$

where: W_j - weight function of j-th point

Cp_j^D - design pressure coefficient

Cp_j - its actual value

using numerical optimization technique.

Direct application of panel method to find the object function brings the high cost of computations. In the presented method the basic design shapes are modelled by surface transpiration. The mass flux through the surface which shift the stream surface with the distance *h* normal to the initial surface is given by:

$$W_{TR} = \frac{1}{\rho_\infty}\left[\frac{\partial(\rho U h)}{\partial\xi} + \frac{\partial(\rho V h)}{\partial\eta}\right] \tag{11}$$

The mean value of the transpiration over the panel is obtained by mass flux balance in the volume enclosed by body surface and modelled stream surface.

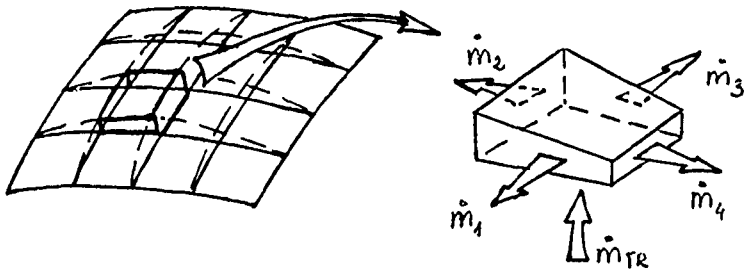


Fig.1 Mass balance over panel area

The incremental potential distribution due to surface transpiration (i-th basic shape) is calculated from linear equations system similar to (7):

$$\left[A\right]\left\{\begin{matrix}\delta\varphi \\ --- \\ \delta\langle\varphi\rangle\end{matrix}\right\}_i = -\left[B\right]\left\{W_{TR}\right\}_i \qquad (12)$$

Potential on the new geometry is expressed as the sum of initial potential distribution and linear combination of incremental potential distribution due to basic shapes. The new velocity distribution is calculated using eq. (7) with new potential value and unit tangent vectors taken from the new geometry. Geometry redefinition is performed directly using eq. (9). The optimization is performed by quadratic programing method. Additionally geometrical constraints are introduced via penalty function. Gradient and Hessian of object and penalty functions are calculated analytically which lead to high accuracy and low cost. Because of nonlinear nature of the design problem it is solved iteratively using geometry obtained after actual design iteration as initial in the next one. Block diagram of the method is shown on the Fig. 2.

COMPUTER CODE

The method described above was coded in FORTRAN 77 language and implemented on PC-Computers. Because of hardware limitations it is performed as a package of programs. All basic parts of the method are performed by separate computer program, which are sequentially started from batch file. The software package consists of 13 programs including two methods of solution of linear equations system (iterative and block Crout decomposition) and post-processing program. The iterative method of solution performs matrix modification and makes possible to use this method even when other iterative methods do not provide the convergence.
It is possible to use up to 1200 body panels, 500 wake panels, 80 Kutta points, 1280 unknown singularity parameters (plus symmetry condition), and

Third International Conference on Inverse Design Concepts and Optimization in Engineering Sciences
(ICIDES-III), Editor: G.S. Dulikravich, Washington D.C., October 23-25, 1991

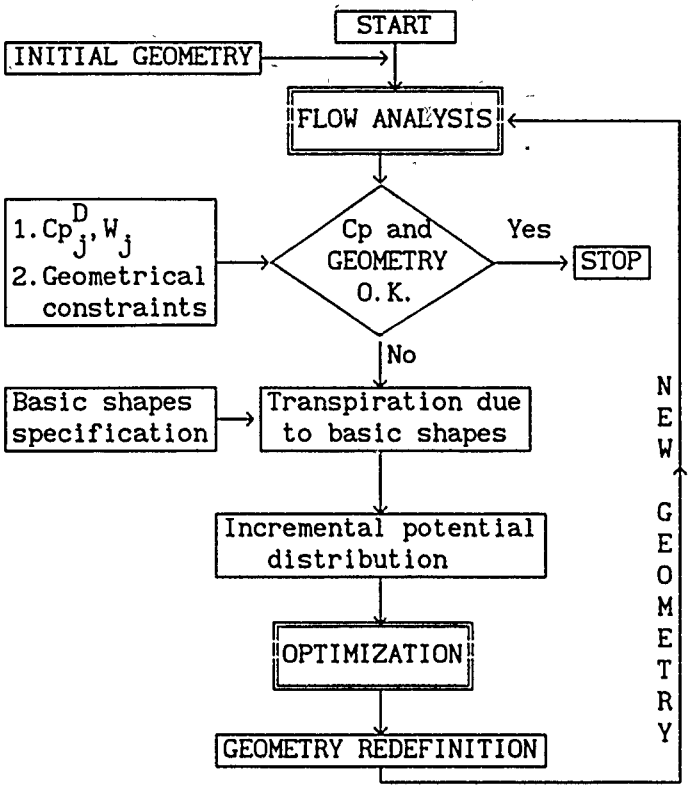


Fig.2 Block diagram of the design method

63 basic design shapes. Flow analysis for PC-386/25MHz and 1000 panels (plus symmetry) took about 25'-40' if using iterative method of solution and about 60' if Crout decomposition method is used. Design process took about 12' for 40 basic design shapes using Crout method. Using computer 486 computing time is about 50% shorter. Cost of such computations is unexpectedly low.

RESULTS

Flow analysis. To show efficiency and accuracy of the method results of analysis of test cases from AGARD AG-241 are shown on Fig. 4 and 5. Results for RAE WING and STRAKED WING with NACA 0002 profile is compared with Datum Results of Rubbert and Roberts.

560 panels were used (40x14) for RAE WING and 640 (40x16) for STRAKED WING. Computing time on PC-386/25MHz respectively 10' (iter)/16.5' (Crout) and 14'/23'. It is seen excellent agreement with compared methods.

Full aircraft configuration design. It consists of wing, body, tail and rear mounted nacelle and pylon. The geometry of the configuration is shown on Fig.6. A new pressure distribution (of "roof-top" type) is specified on the wing upper surface. At all points of pylon where initial negative pressure exceeds Cp = -0.5 this value was specified as design one.

Third International Conference on Inverse Design Concepts and Optimization in Engineering Sciences (ICIDES-III),Editor:G.S.Dulikravich, Washington D.C.,October 23-25,1991

38 basic design shapes of spline-support type were specified. The idea of this type of shapes is shown on Fig. 3. Node lines on the surface in both directions are specified and movement of the node of such network in specified direction corresponds to the desired shape function. To find movement of other points of the surface the interpolation spline is used. The shape functions used correspond to:

-changes of upper surface section of the wing at four control stations (wing-body-junction, η = 0.3, 0.5 and 1.0) corresponding to vertical displacement of points with max. laying at 75%, 55%, 40%, 25%, 15%, 9% and 4% of arc length (measured from leading edge to trailing edge)

-changes of wing twist at wing-body-junction, η = 0.5 and 1.0

-changes of fuselage width in the pylon region with max. at four stations

-changes of nacelle width in the pylon region with max. at three stations

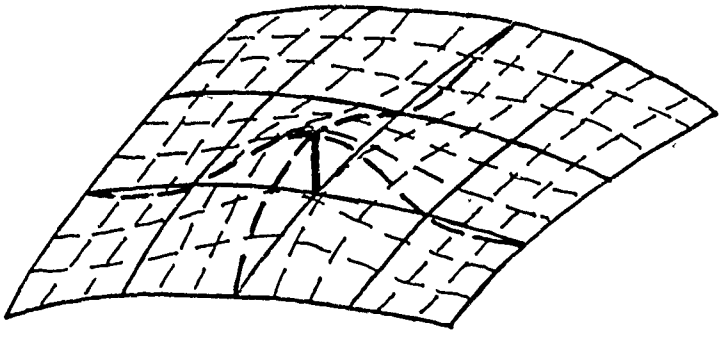


Fig.3 The idea of spline support basic shapes

Geometrical constraints used:

-distance between network points near the trailing edge (for control the trailing angle)

-distance between network points near the max thickness (for control the thickness)

-distance between network points near the leading edge (for control the leading edge radius)

-distance (in vertical direction) between leading edge and trailing edge (for control twist) at three control stations

-distance between points of pylon (at pylon-fuselage intersection) and symmetry plane (for control fuselage shape) at three stations

-distance between points of pylon (at pylon-nacelle intersection) and symmetry plane (for control pylon shape) at three stations.

1042 body panels, 72 wake panels and 1068 unknown singularity parameters for half geometry were used. Computing time using PC-386/25: analysis 78', design cycle 14'. Isobar pattern on the initial geometry and after four design

Third International Conference on Inverse Design Concepts and Optimization in Engineering Sciences (ICIDES-III), Editor: G.S. Dulikravich, Washington D.C., October 23-25, 1991

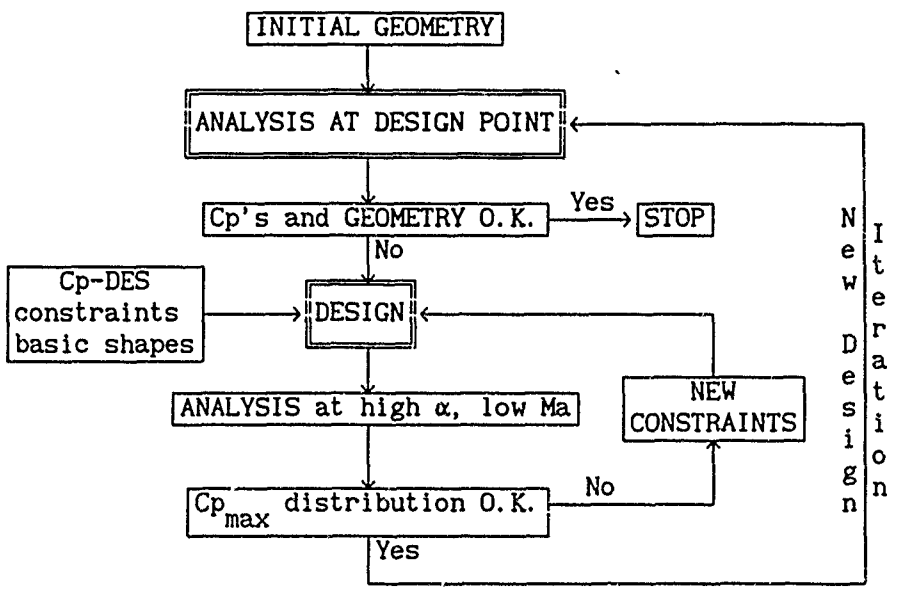
iterations are shown on Fig.7. Pressure distribution at four wing sections before and after designing are presented on Fig.8 and pressure distribution on the pylon on Fig.9. The shape of body-nacelle region and isobar pattern is shown on Fig. 10. The region of higher negative pressure occurs on the fuselage and nacelle in front of pylon. Adding two shape functions modifying fuselage in front of the pylon and specifying additional points with design pressure, the result (after 4 iterations) as on Fig.11 can be obtained. The convergence history of the design process is shown on Fig.12.

Wing-body-underwing nacelle configuration. The geometry of the configuration and details of nacelle region are shown on Fig.13. 1160 body panels, 104 wake panels and 1183 unknowns were used. The pressure on the wing-body alone configuration was calculated. Results are shown on Fig.14a (lower and upper surface respectively). Pressure distribution obtained for this configuration is used as design pressure for wing-body-nacelle. Adding plane pylon and axisymmetrical nacelle the new pressure distribution and isobar pattern are obtained: Fig.14b. Isobar pattern on the wing after four design iterations is shown on Fig.14c, shape of pylon and nacelle on Fig.15 and pressure at subsequent wing sections before and after designing on Fig.16. Shape of pylon section before and after designing is seen on Fig.17. 38 basic design shapes of spline-support type were used. Wing was changed at three control stations: η = 0.4, 0.5 and 0.6. Four points on upper surface (x/c=0.03, 0.11, 0.27 and 0.50) five points on lower surface (x/c = 0.06, 0.17, 0.33, 0.50 and 0.72) and twist at each of this stations can vary. Additionally four points of upper nacelle contour (x/L = 0.38, 0.50, 0.63 and 0.81) and four points of pylon mean line (x/c = 0.25, 0.50 0.75 and 1.00) were changed. The constraints, in respect to wing thickness and twist, nacelle shape and pylon modification, were specified. It should be noted that despite the constraints used are not very restrictive some of them are active. As result, for example, pylon has nonzero side force (it had tendency to bend more). Convergence history is shown on Fig.18. It is of value to show some aerodynamic coefficient for the configuration:

	Cl_{wing}	$Cl_{nac-pyl}$	Cl_{total}	Cm_{total}
wing-body alone	0.5098	-	0.506	-0.1463
initial	0.4772	0.0051	0.575	-0.1482
designed	0.5096	-0.0008	0.605	-0.1439

Computing time using PC-386/25: flow analysis 84', inverse cycle 15'.

Design of transonic wing. The research wing for jet-trainer type aircraft was designed via subcritical equivalent pressure distribution concept [3] by the author as a part of research investigations on supercritical wing performed at Aviation Institute in Warsaw (unpublished Report of Aviation Institute in Warsaw). The supercritical wing section (of slightly peaky-type pressure distribution) was designed using finite-difference method. Equivalent subcritical pressure distribution for swept wing (sweep angle of leading edge 20.7°, at 25% chord 17.3°) was calculated and used as design pressure on the upper surface of the wing. The originality of the method consist in including the off-design characteristics. By modifying constraints it was forced max. pressure peak at high angle of attack and low Mach number at about $\eta = 0.4$, which suggest separation first at this station. If max negative pressure was too high at the station under consideration, the higher leading edge radius was enforced by constraints (worsening, of course, the pressure distribution) and vice versa. 28 basic design shapes were used: five kinds of changes of thickness distribution along the chord at five control stations along the span and twist at three stations. The geometrical constraints in respect to max thickness, trailing edge angle, leading edge radius and twist are utilized.
480 body panels, 24 wake panels and 492 unknown singularity parameters were used. The block diagram of the design process can be introduced as follow:



Computing time (386/25): analysis 9' (Crout), 5' (Iter). In each design iteration the flow, at high α, was calculated about 3 times. Resulting isobar

Third International Conference on Inverse Design Concepts and Optimization in Engineering Sciences (ICIDES-III).Editor:G.S.Dulikravich, Washington D.C.,October 23-25,1991

pattern and pressure distribution at three wing sections are presented on Fig.19. Geometrical parameters of the resulting wing are shown on Fig.20. Quite unexpected for swept wing R_{LE} distribution along the span is seen. Max of the leading edge radius occurs at 80% of semispan. Max of pressure peak ($\alpha=12^{\circ}$, Ma=0.2) occurs at $\eta = 0.40$. The drag divergence Mach number obtained in wind tunnel tests is shown on Fig.22 and beginning of separation on Fig.23 (unpublished Report of Aviation Institute in Warsaw). It is seen good agreement with expectation.

CONCLUDING REMARKS

The method presented above shows great versatility in the case of design of real, complex configurations. It has nearly no restrictions in respect to the complexity of the geometry. The major limitation is the lack of possibility to take into account modification of planform of the wing and necessity to fix leading edge point (twist can be changed only by moving vertically trailing edge point). It is possible to take into account interference effects in designing, that allows to obtain specified pressure distribution on one element by changing geometry of the other.
Recently the method has been extended to the case of multi-point optimization: the pressure distribution on different parts of the surface can be specified for different angles of attack and the design process is performed at once. The method is exceptionally cheap and efficient because of implementation on PC-computers. The possibility to take into accounts some characteristics at off-design conditions via constrains was shown also.

REFERENCES

1. Ward G.N. - "Linearized Theory of Steady High-Speed Flow" - Cambridge University Press 1955
2. Kubrynski K. - "A Subsonic Panel Method for Design of 3-Dimensional Complex Configurations with Specified Pressure Distribution" - Proceedings of the III GAMM-Seminar in Kiel - Vieweg 1988
3. Slooff J.W. - "Application of Computational Procedures in Aerodynamic Design" - AGARD R-712 1983.

Third International Conference on Inverse Design Concepts and Optimization in Engineering Sciences (ICIDES-III).Editor:G.S.Dulikravich, Washington D.C.,October 23-25,1991

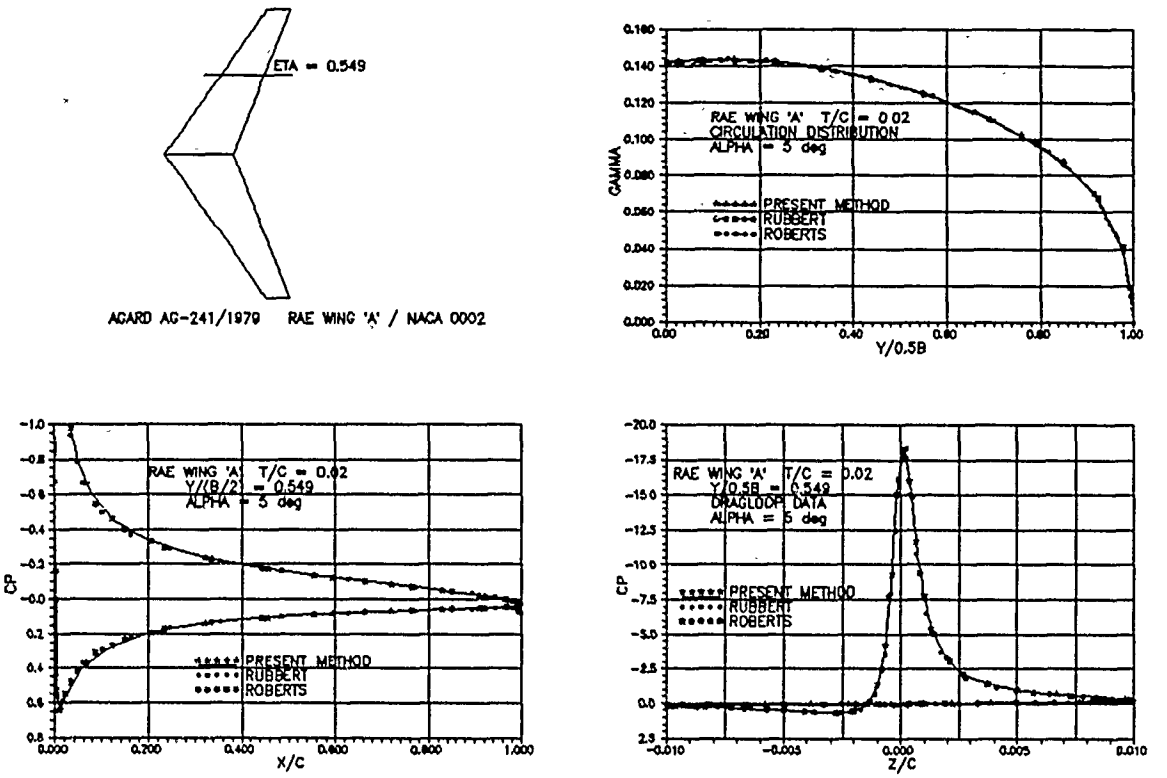


Fig. 4 RAE-WING 'A'/NACA 0002 : comparison of results

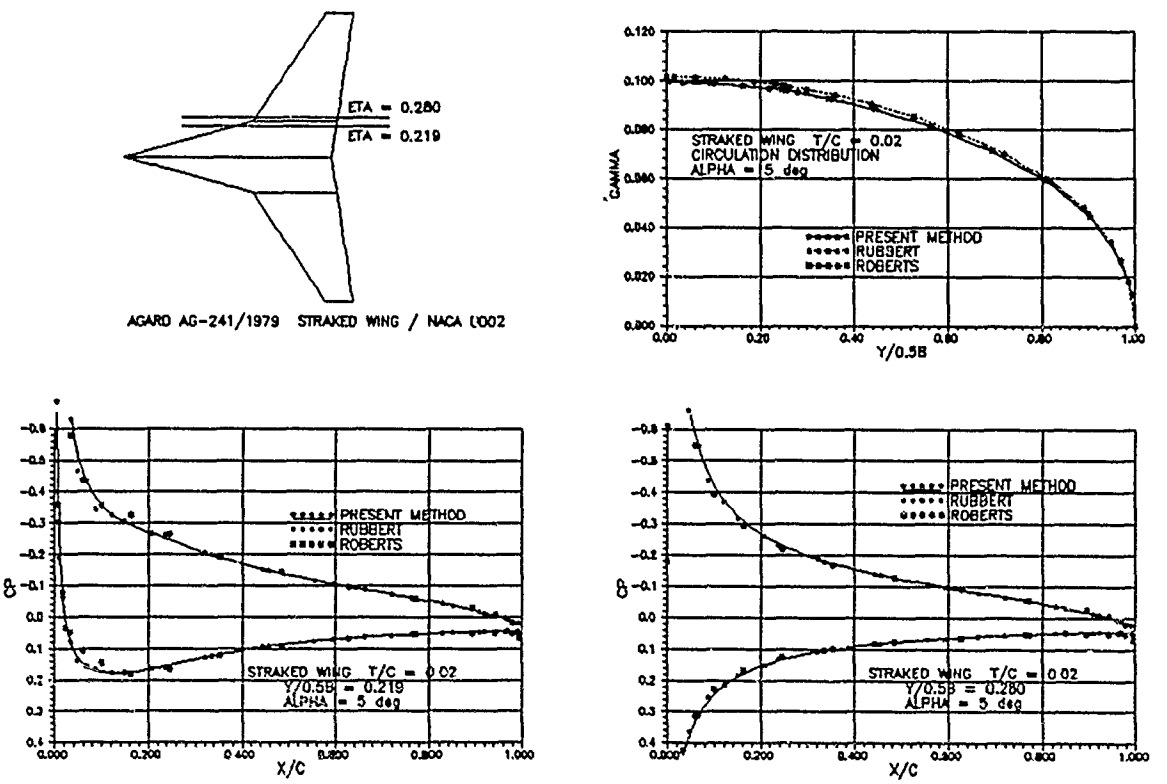


Fig. 5 STRAKED-WING/NACA 0002 : comparison of results

Third International Conference on Inverse Design Concepts and Optimization in Engineering Sciences (ICIDES-III).Editor:G.S.Dulikravich, Washington D.C.,October 23-25,1991

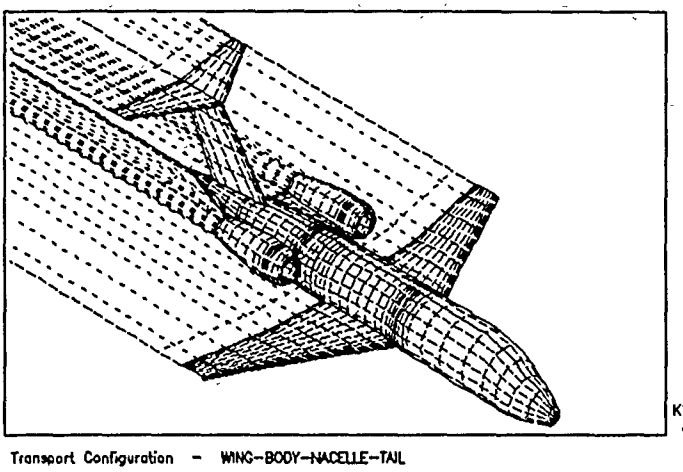


Fig. 6
Network geometry of the entire aircraft configuration

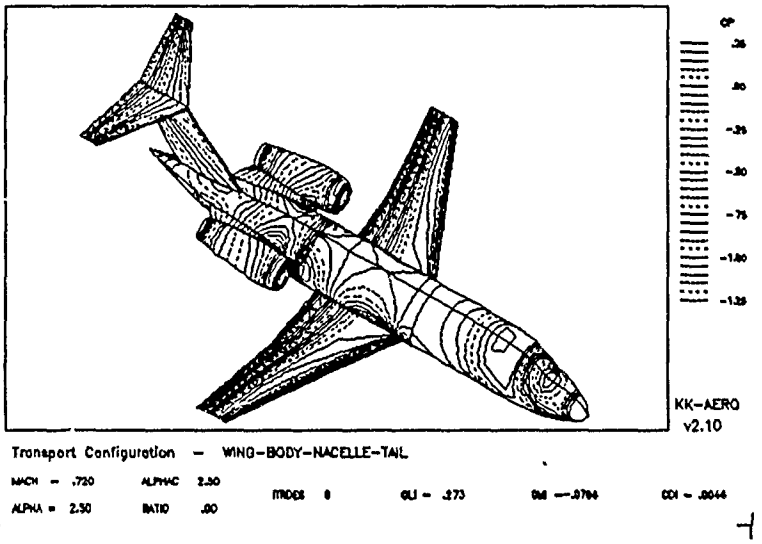


Fig. 7
Isobar pattern on the surface of the initial configuration

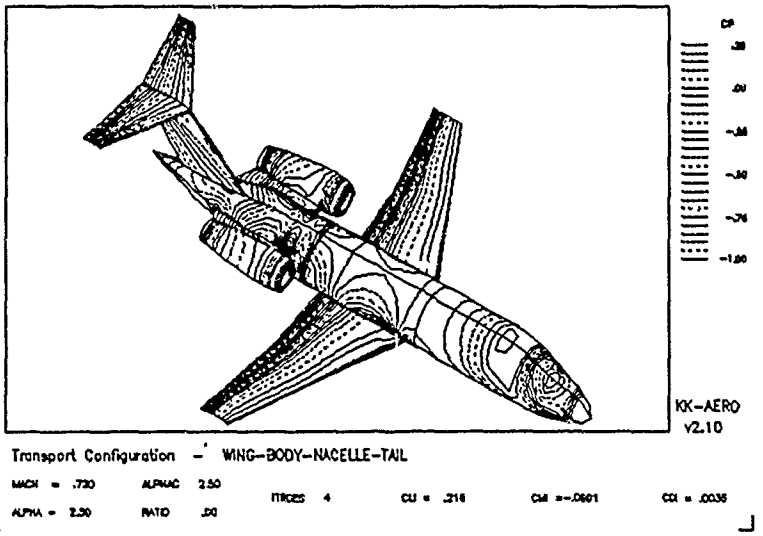


Fig. 8
Isobar pattern on the surface after 4 design iterations

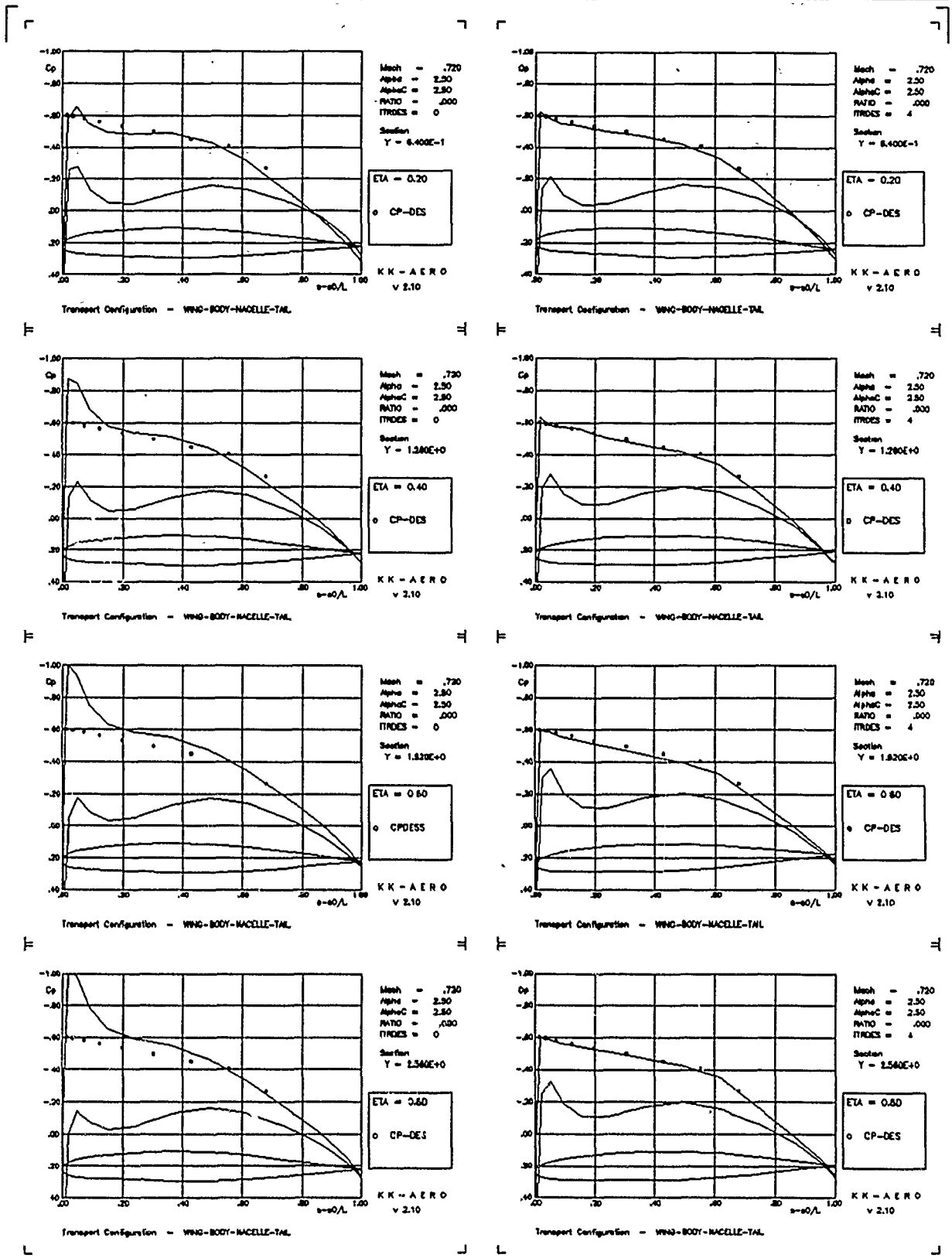


Fig. 8 Pressure distribution on the wing before (left) and after designing (right)

Third International Conference on Inverse Design Concepts and Optimization in Engineering Sciences (ICIDES–III), Editor: G.S. Dulikravich, Washington D.C., October 23–25, 1991

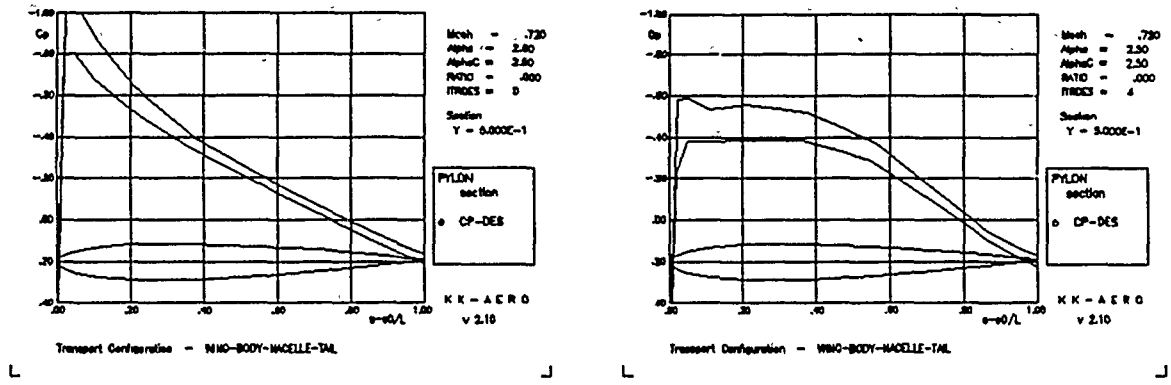


Fig. 9 Pressure distribution on the pylon before and after designing (Cp = −0.5 specified at all points where this value is exceeded)

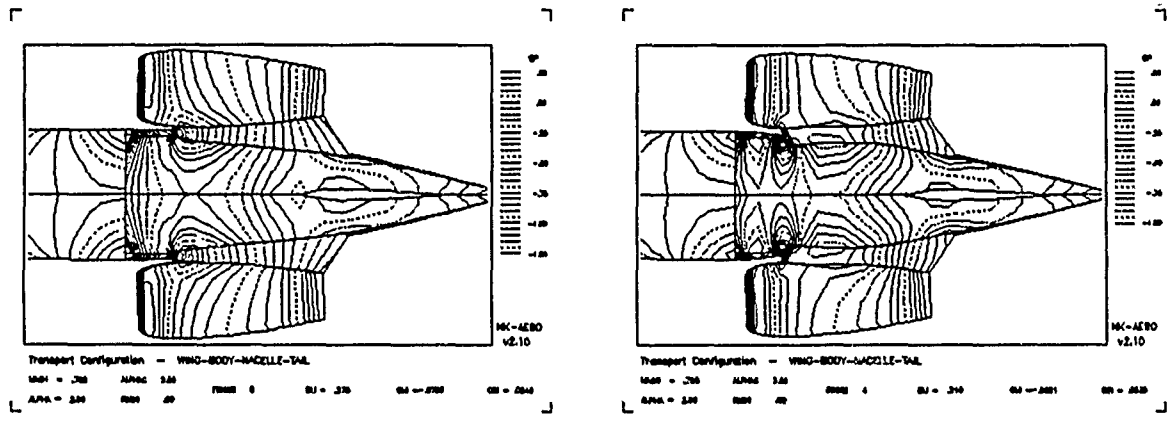


Fig. 10 Fuselage–pylon–nacelle region before and after designing

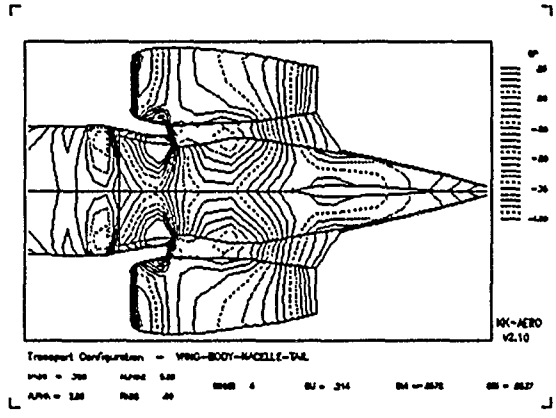


Fig. 11 Fuselage–pylon–nacelle region after designing with additional shape function modyfing fuselage in front of the pylon

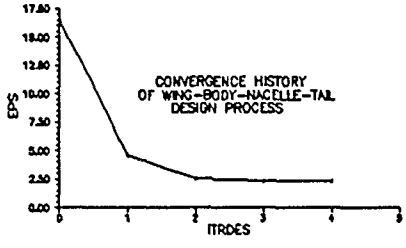


Fig. 12 Convergence of the design process

Third International Conference on Inverse Design Concepts and Optimization in Engineering Sciences
(ICIDES–III),Editor:G.S.Dulikravich, Washington D.C.,October 23–25,1991

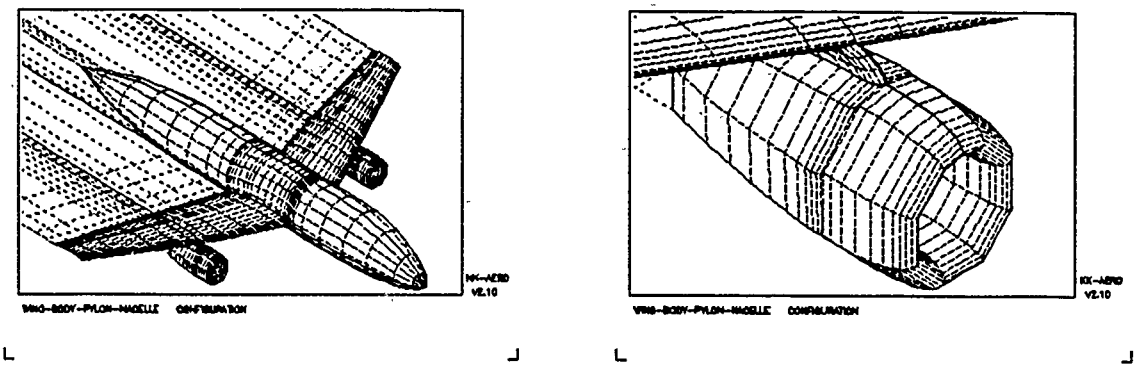


Fig. 13 Geometry of the configuration and details of wing–pylon region

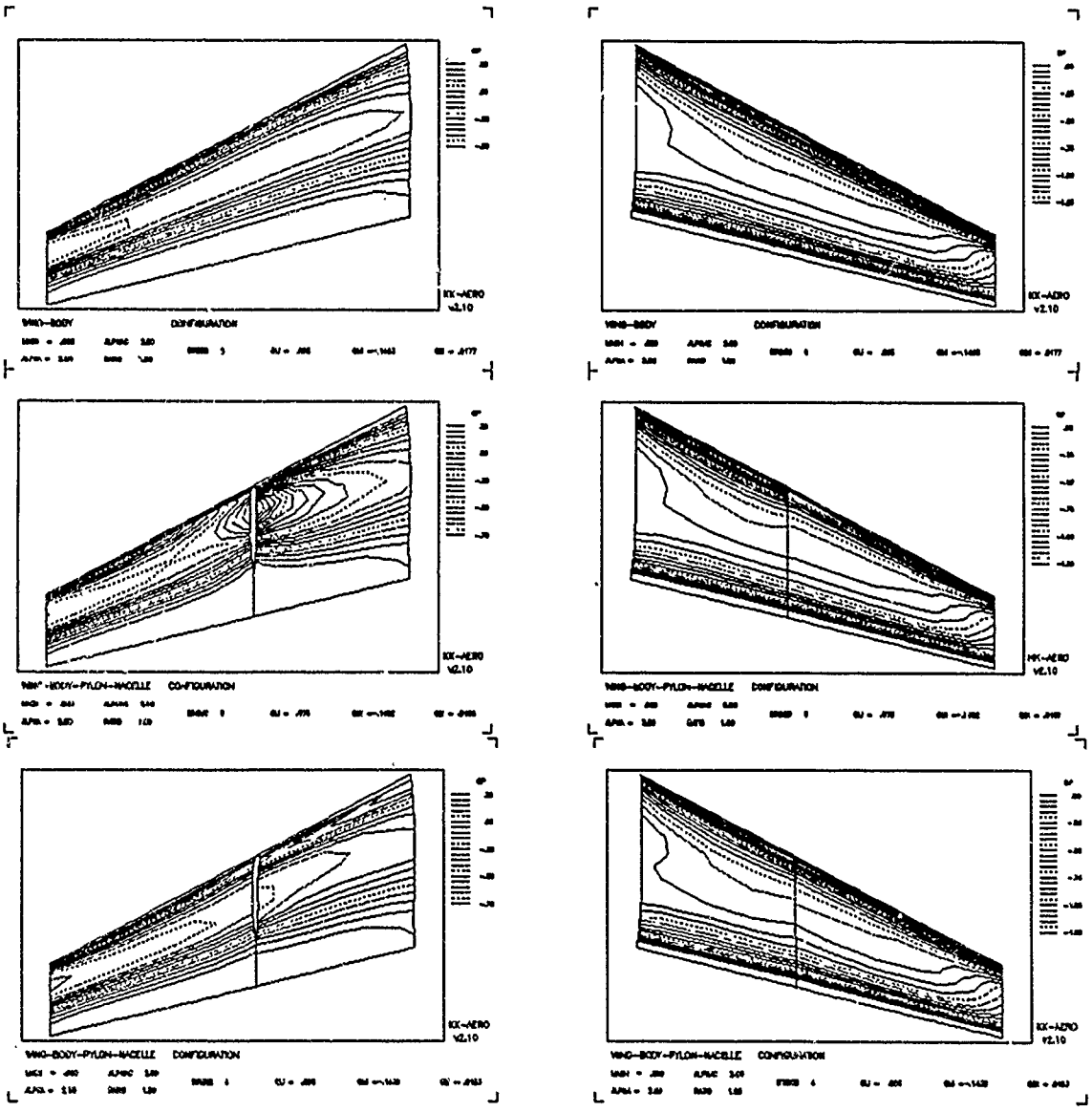


Fig. 14 Isobar pattern on the lower (left) and upper (right) surfaces of the wing: a) without nacelle b) initial geometry c) designed configuration

Third International Conference on Inverse Design Concepts and Optimization in Engineering Sciences (ICIDES-III), Editor: G.S. Dulikravich, Washington D.C., October 23-25, 1991

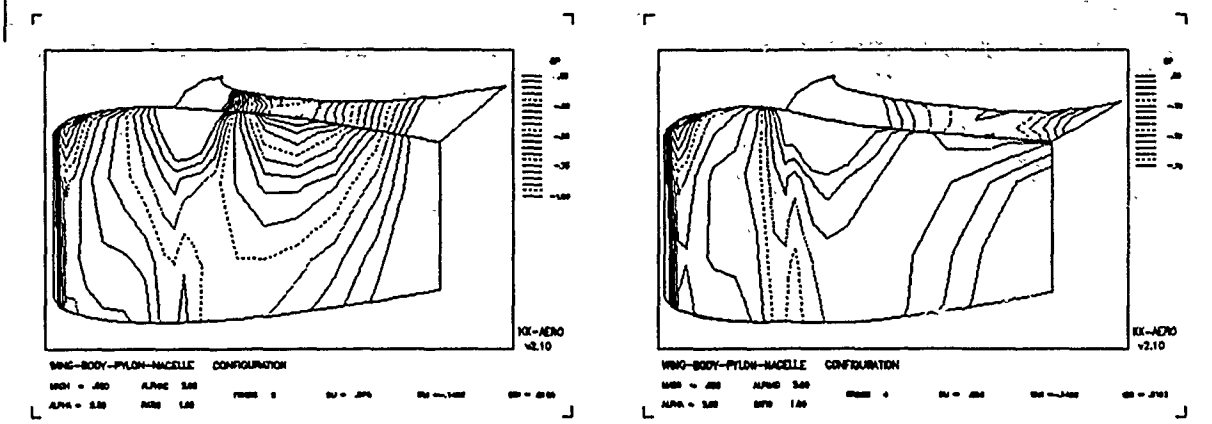


Fig. 15 Contour of the nacelle and pylon before and after design process

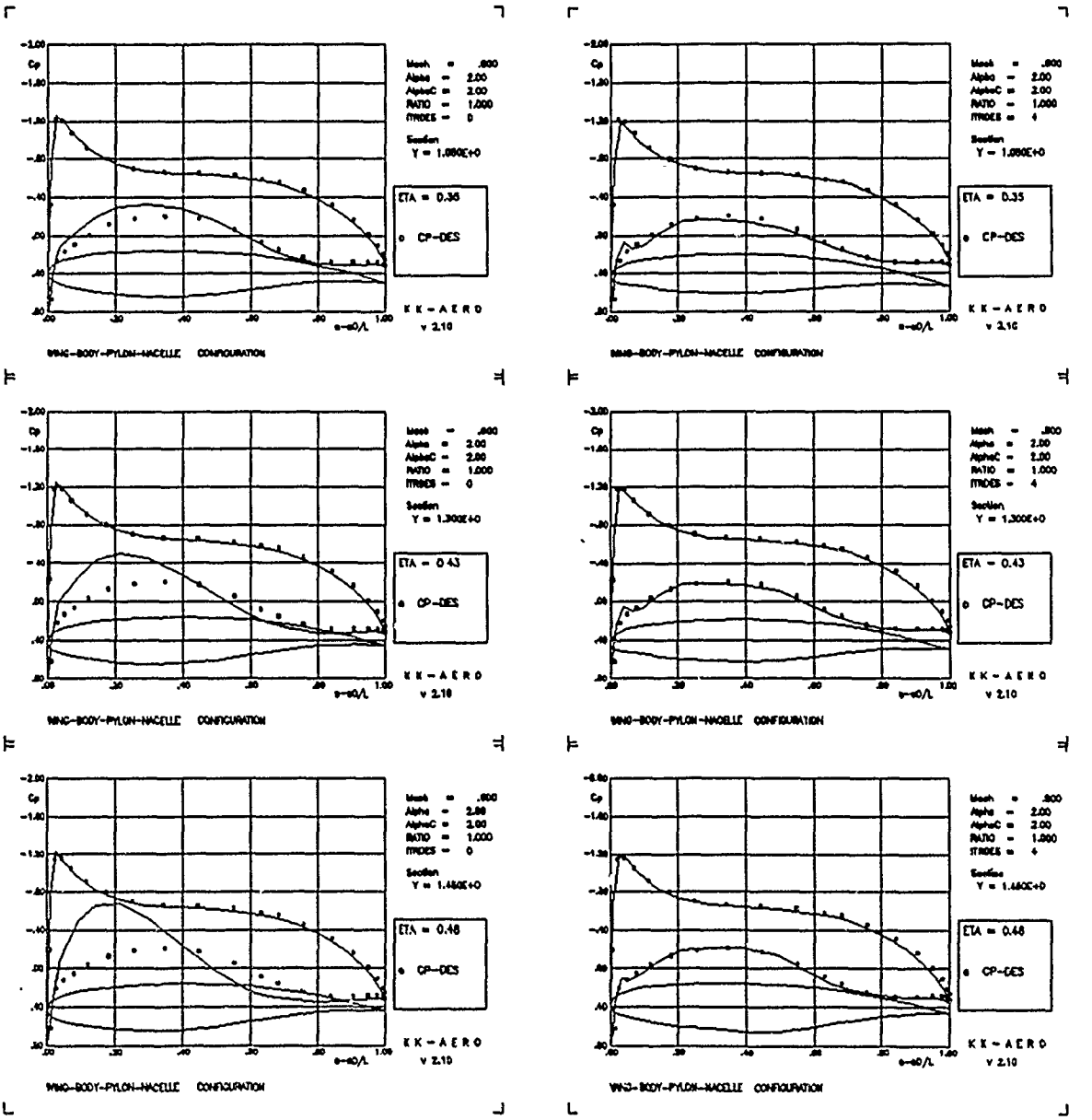


Fig. 16 Pressure distribution on the wing before and after four design iterations

Third International Conference on Inverse Design Concepts and Optimization in Engineering Sciences
(ICIDES-III).Editor:G.S.Dulikravich, Washington D.C.,October 23-25,1991

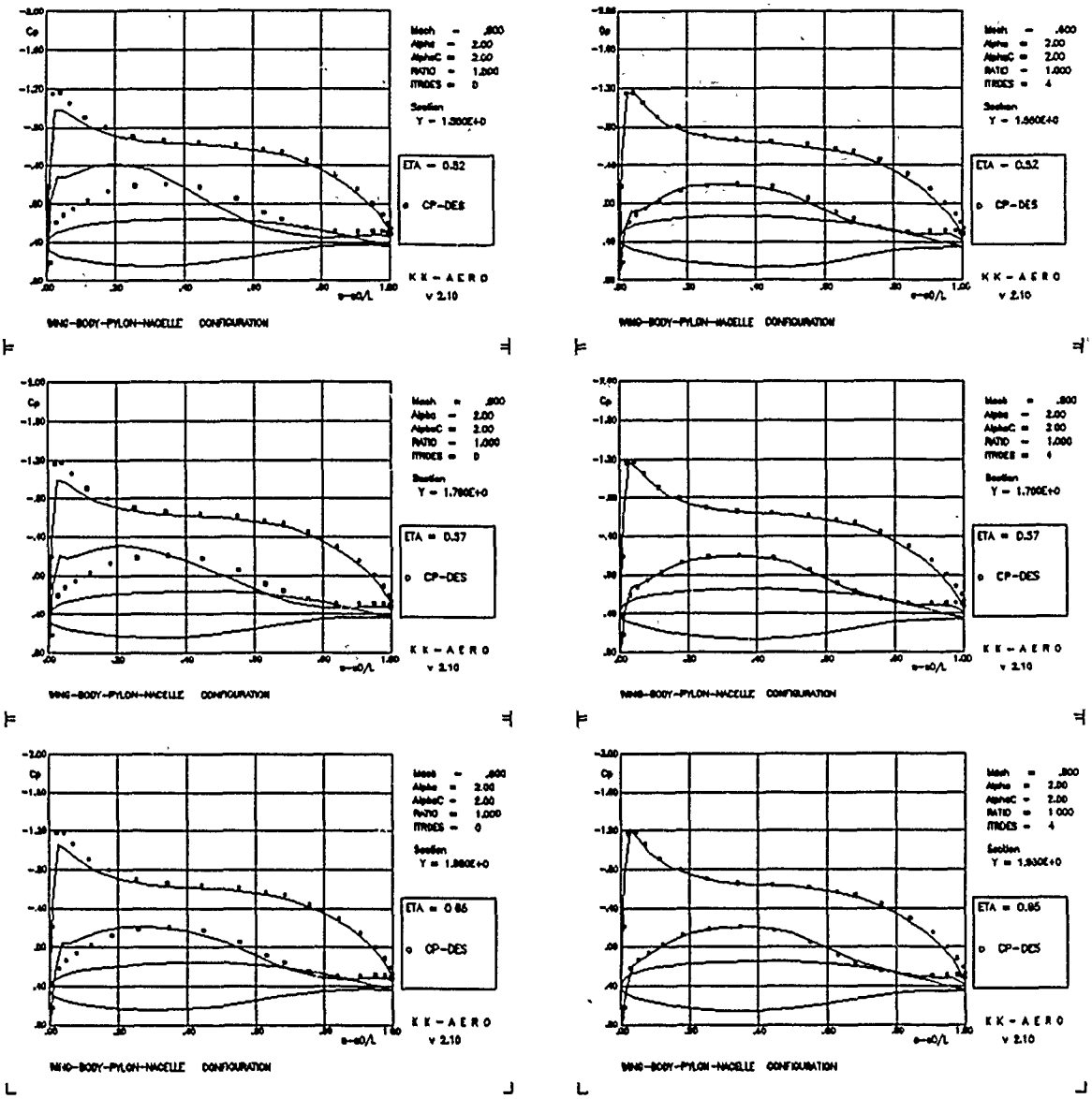


Fig. 16 Pressure distribution on the wing – continued

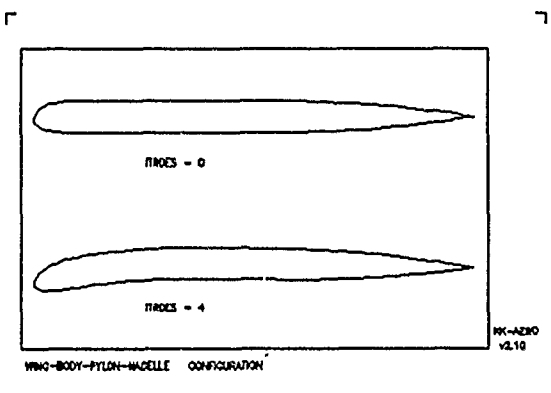


Fig. 17 Cross section of the pylon

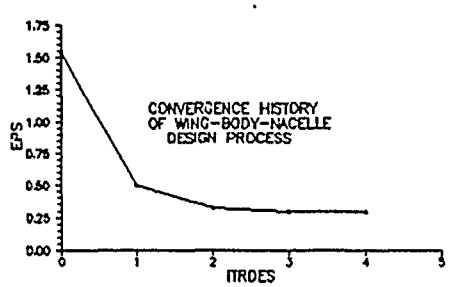


Fig. 18 Convergence of the design process

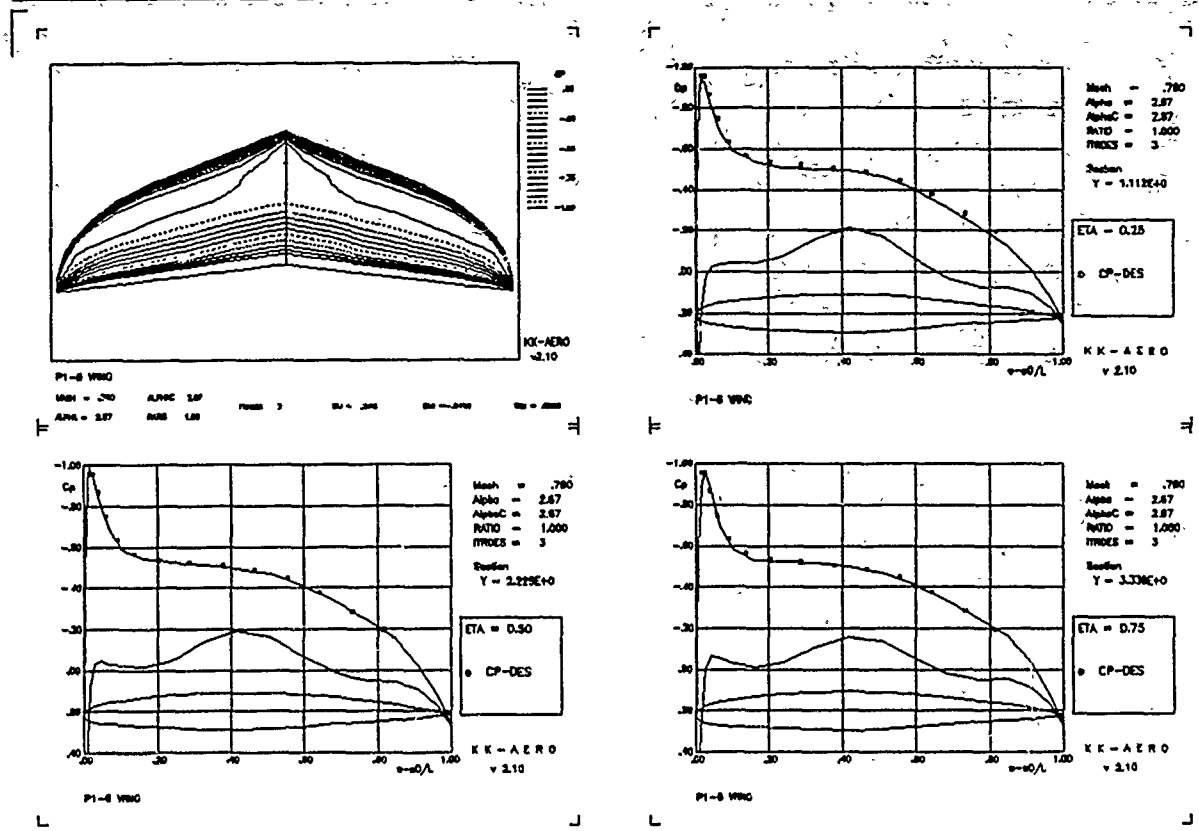


Fig. 19 Planform, isobar pattern and pressure distribution on the designed wing

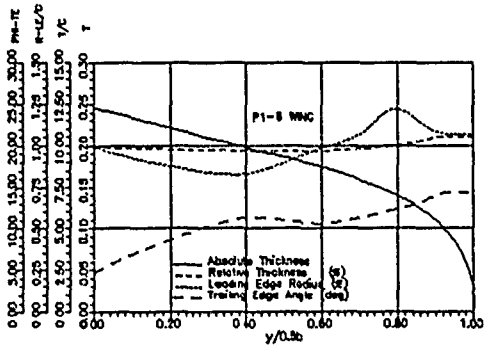


Fig. 20 Geometrical parameters of the designed wing sections

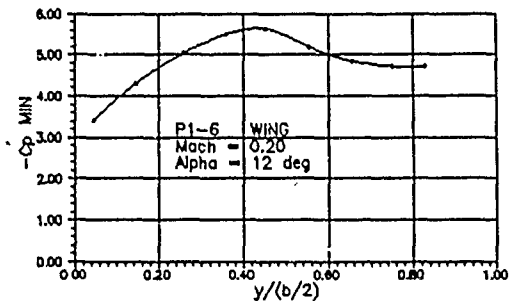


Fig. 21 Peak pressure distribution

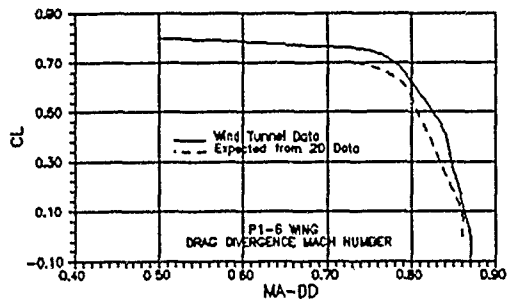


Fig. 22 The drag divergence Mach number

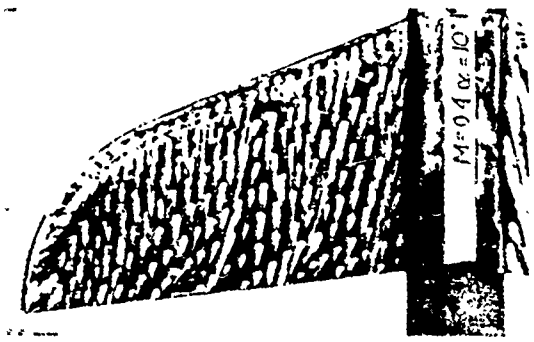


Fig. 23 Begining of separation

Third International Conference on Inverse Design Concepts and Optimization in Engineering Sciences (ICIDES-III), Editor: G.S.Dulikravich, Washington D.C. October 23-25, 1991

Extended Mapping and Characteristics Techniques for Inverse Aerodynamic Design

H. Sobieczky*, Y. J. Qian**
DLR German Aerospace Research Establishment
Inst. Theoret. Fluid Mechanics
Bunsenstr. 10, D-3400 Göttingen
Germany

Abstract
Some ideas for using hodograph theory, mapping techniques and method of characteristics to formulate typical aerodynamic design boundary value problems are developed. Inverse method of characteristics is shown to be a fast tool for design of transonic flow elements as well as supersonic flows with given shock waves.

Introduction

This paper is intended to illustrate a revitalization of classical tools of theoretical aerodynamics for use on modern graphic workstation computers presently available to the design engineer:

The theoretical methods have their origins in the time before large scale numerical computing became the standard approach for analyzing aerodynamic performance, about two decades ago these tools were already operational for practical aerodynamic tasks. Transonic flows then posed challenging problems and analytical mathematical modelling was used to gain insight into various theoretical and applied questions resulting from nonlinear model equations. The "Hodograph Method" gave answers to many of such type problems. Similarly, the "Method of Characteristics" yielded practical results. Combination of both methods, more recently, has permitted inverse - or at least indirect - formulation and solution of aerodynamic design problems.

Later, numerical methods became more important because of their general applicability but frequently they give only poor insight into a mathematical model underlying a described phenomenon. The previous hodograph approach was somewhat complicated because of mapping procedures, but results still serve as test cases for numerical methods.

Nowadays, while most of the successful analytical methods are used only for educational purposes, we witness another type of tool emerging from developments in computer technology: Graphic Workstations and even PC's provide powerful computation, illustration and documentation of results to the model equations for fast aero analysis and design. Interactive methods are being developed to provide a strong coupling of computer power and speed with the design engineer's experience and strategies to obtain his design goals: For many applications we seem to have the knowledge base and computer hardware to develop a variety of what may be called "Aerodynamic Expert Systems".

---

*) Senior Research Scientist. **) Visiting Professor, Permanent Address: 北京航空航天大学
Beijing University of Aeronautics and Astronautics, Beijing, China

In this situation we may want to recall classical "pre-CFD" methods because, if implemented to those fast graphical desktop computers, they might be modernized and improved to easily give fast first steps for aerodynamic design and optimization, and last not least to serve as educational tools.

In the present paper we illustrate the idea of combining fast classical aero methods with most recent computer and software technology by using hodograph formulations and characteristics to obtain some well known and some new plane and axisymmetric transonic and supersonic flow elements. The fast computation and powerful graphic evaluation of results invite experimenting with conceptual extensions: Here the hodograph method is extended to axisymmetric flows and a method of characteristics for axisymmetric rotational flows will be presented and proposed for use of designing more general three-dimensional flows.

Hodograph-based methods for transonic flows

The following review of an extended hodograph method is focused on transonic applications. For two-dimensional isentropic flow this approach is wellknown in the literature, here the illustration is carried out for plane flow and extended to small perturbation axisymmetric transonic flow - an option widely unknown because the main purpose of the hodograph, linearity, obviously cannot be obtained for axisymmetric flow.

Potential flow models

Isentropic flow assumptions result in a system of PDEs for potential Φ and streamfunction Ψ with D and Q suitably dimensionless density and velocity, and flow angle ϑ and velocity Q independent variables:

$$\Phi_Q = \frac{1}{DQ}(M^2-1)\Psi_\vartheta$$
$$\Phi_\vartheta = \frac{Q}{D}\Psi_Q \qquad (1)$$

Rheograph transformation: Beltrami equations

Here we use a modification of the hodograph variables: System (1) is transformed by using the Prandtl - Meyer angle

$$\nu = \int_{(Q=1)}^{Q} \sqrt{|M^2-1|}\frac{dQ}{Q} \qquad (2)$$

as one independent variable instead of the velocity Q. The basic PDEs become

$$\Phi_\nu = jK\Psi_\vartheta$$

$$\Phi_\vartheta = K\Psi_\nu \tag{3}$$

with j = -1 representing subsonic flow (where $\nu < 0$) and j = 1 for supersonic flow (where $\nu > 0$). The coefficient

$$K = \frac{\sqrt{|M^2 - 1|}}{D} \tag{4}$$

is, for isoenergetic flow and with (2), a function of ν only. So far any hodograph problem formulation is just a matter of stretching from a (Q, ϑ) - plane to a (ν, ϑ) - plane.

The technique stressed here involves further elliptic or hyperbolic mapping of the variables (ν, ϑ)

$$\nu_s = \vartheta_t$$

$$\nu_t = j\vartheta_s \tag{5}$$

which results in a transformation of (3) to become

$$\Phi_s = jK\Psi_t$$

$$\Phi_t = K\Psi_s \tag{6}$$

Both (3) and (6), and also the Cauchy-Riemann or wave equations (5) are more generally named Beltrami equations. With K now a function of s and t this system of PDEs is linear. The first author has made extensive use of it for transonic airfoil design [1, 2].

For the purpose of illustrating a generalization to axisymmetric flow, we use here the small perturbation version of (5) and (6), with a notation

$$\nu \sim U$$

$$\vartheta \sim VY^{-p_1}$$

$$\Phi \sim X \tag{7}$$

$$\Psi \sim Y^{1+p_1}$$

where for plane 2D flow $p_1 = 0$. Replacing the coefficient K by its leading term near sonic conditions,

$$jK \sim v^{p_2} \tag{8}$$

with $p_2 = 1/3$ results in the near sonic version of the systems (5) and (6), the compatibility relations

$$V_s = jY^{p_1}U_t$$
$$V_t = Y^{p_1}U_s \tag{9}$$

and characteristic equations

$$X_s = U^{p_2}Y_t$$
$$X_t = jU^{p_2}Y_s \tag{10}$$

Now we see an elegant symmetry of these two coupled pairs of equations, each modeling a generalized axially symmetric potential, [3]. We can distinguish between various types of flow, depending on the parameters j, p_1 and p_2. Linear subsonic (j = -1) or supersonic (j = 1) flow is described by $p_2 = 0$, while transonic flow requires $p_2 = 1/3$, with j both -1 and +1 for mixed type flow. With $p_1 = 0$ or 1 we have plane 2D or axisymmetric flow, respectively. Mapping in various aero or fluid dynamics case studies can so be reduced to one generalized system of basic equations [4, 5]. Any one of p_1 or p_2 being equal to zero yields linear equations, but for near-sonic axisymmetric flow a weak nonlinearity persists, which seems to be the reason why this formulation has not been used for aerodynamic problems, except in the one work by Hassan [6].

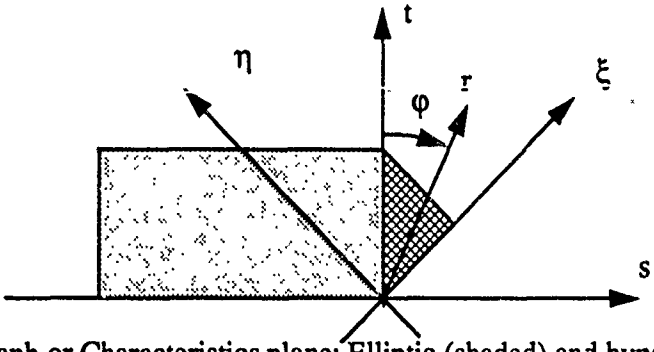


Fig. 1: Rheograph or Characteristics plane: Elliptic (shaded) and hyperbolic (cross-hatched) domain for mixed type model equations

Self-similar solutions

We see the relation of Beltrami equations to conformal and characteristic mapping: singular solutions in classical hydromechanics have helped to understand many aerodynamic phenomena, so we wish to use the system for axisymmetric near-sonic flow also for solving some of its typical features.

Figure 1 illustrates the working plane (s, t): neither physical plane (X, Y) nor hodograph plane (U, V), it is suited for a definition of boundary and initial value problems which require a parametric formulation. In transonic flows, the mixed elliptic/hyperbolic type subdomains require contact along the

mapped sonic line, here suitably fixed at s = 0. Earlier applications and illustrations [5] explain the use of the name "Rheograph" and "Characteristics Plane".

Some classical and many new phenomena may be modeled from the general harmonic set of self-similar solutions in polar coordinates

$$U = r^n \cdot h(\varphi)$$

$$V = r^{n+p_1 \cdot b} \cdot k(\varphi) \qquad (11)$$

$$X = r^{b+p_2 \cdot n} \cdot f(\varphi)$$

$$Y = r^b \cdot g(\varphi)$$

which require only solving a set of four coupled ODEs for the generalized harmonic functions h, k, f and g, with two free parameters n and b.

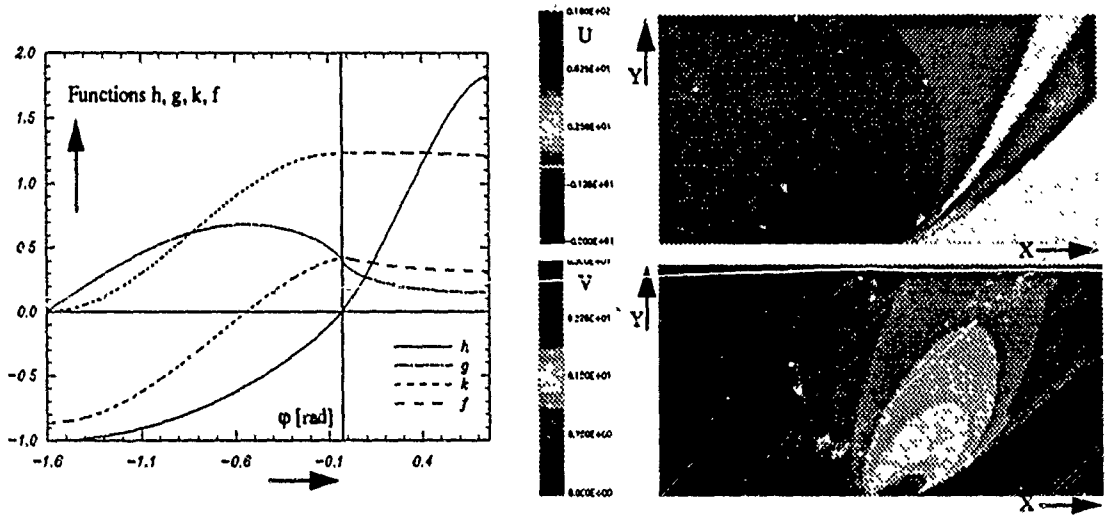


Fig. 2: Quasi-harmonic functions for far-field singularity U,V(X,Y) modeling flow past a body of revolution in sonic free-stream Mach = 1

Example: Guderley's far-field singularity of an axisymmetric body in sonic flow

M. Klein [7] has investigated these coupled potential flow problems calculating some plane and axi-symmetric cases with different exponents n, b. This was done prior to using some gained knowledge for setting up more general boundary/initial value problems for numerical solution of (9) and (10) with a Poisson solver and the method of characteristics on a graphic workstation. One case studied in detail is the solution for simulating the flow past a body of revolution in sonic free-stream. This is a classical transonic problem first solved by Guderley 1954 [8] and elegantly confirmed by Müller & Matschat 1964 [9]. Their work suggests use of (11) with a ratio of the exponents b/n = - 7/9. In fact, it is just this ratio which yields a physically reasonable solution.

Figure 2 illustrates the result: Graphic CFD postprocessing software is used to show the U and V distribution in the physical meridional plane (X, Y). This example may be used to illustrate the use of working in the Rheograph plane, to understand flow details with nonlinear model equations better and to have more freedom to suitably model boundary values. In transonic flow, meaningful solutions frequently can only be obtained by formulating boundary conditions in an indirect, inverse way, - this is the basic reason why some practical design problems are easier solved in inverse mode.

For the following transonic 2D example ($p_1 = 0$) we return to the systems (5) and (6), the Rheograph equivalent of the 2D full potential equation.

Example: 2D transonic nozzle exit

Equations (5) and (6) for supersonic flow j = 1 transform into compatibility relations

$$\left.\frac{d\vartheta}{d\nu}\right|_{\eta = const} = 1 \qquad \left.\frac{d\vartheta}{d\nu}\right|_{\xi = const} = -1 \tag{12}$$

and characteristic equations

$$\left.\frac{d\Psi}{d\Phi}\right|_{\eta = const} = \frac{1}{K} \qquad \left.\frac{d\Psi}{d\Phi}\right|_{\xi = const} = -\frac{1}{K} \tag{13}$$

which are the basis for a rapid linear method of characteristics. Implemented on a graphic workstation, solutions may be obtained and visualized extremely fast, we use the method to set up a knowledge base for interactive transonic design expert systems with advanced graphic pre- and postprocessing. Flexible geometry input for boundary conditions was used by Gentner [10] to define a 2D sonic throat and the downstream accelerated exit flow. With initial data for Mach number, flow angle and physical coordinates along the t-axis (Fig. 1) a first calculation determines the solution of (12) and with $K(\nu(\xi,\eta))$ available, the second step is the solution of (13).

Figure3 once more stresses the difference between hodograph and Rheograph or Characteristics plane: The flow structure may map into a multivalued hodograph, while the Rheograph may be controlled to show a single-valued characteristics grid.

The result with a non-symmetrical exit contour designed by prescribing velocity distribution along the nozzle axis is depicted in Figure 4. The idea here was the combination of (known and well-developed) potential flow modeling with mapping transformations based on hodograph theory (also known but considered complicated), and the use of powerful workstations (helping with rapid computation and graphic visualization). The above isentropic model equations are either linear or weakly nonlinear. In the following, design problems involving non-isentropic flow will also be solved by the method of characteristics.

Third International Conference on Inverse Design Concepts and Optimization in Engineering Sciences (ICIDES–III), Editor: G.S.Dulikravich, Washington, D.C., October, 23–25, 199*

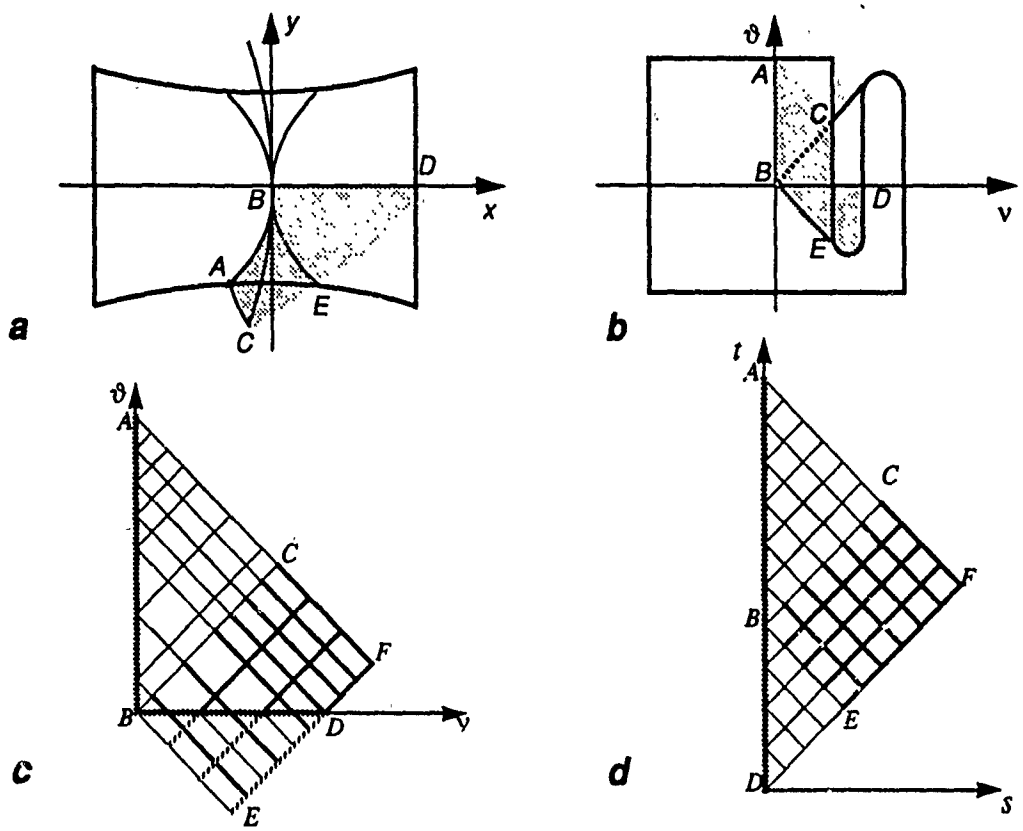


Fig. 3: Unfolding the multi-valued mapping of a Laval-nozzle (a) supersonic hodograph (b, c) to single-valued triangular domains (c) in the Rheograph plane

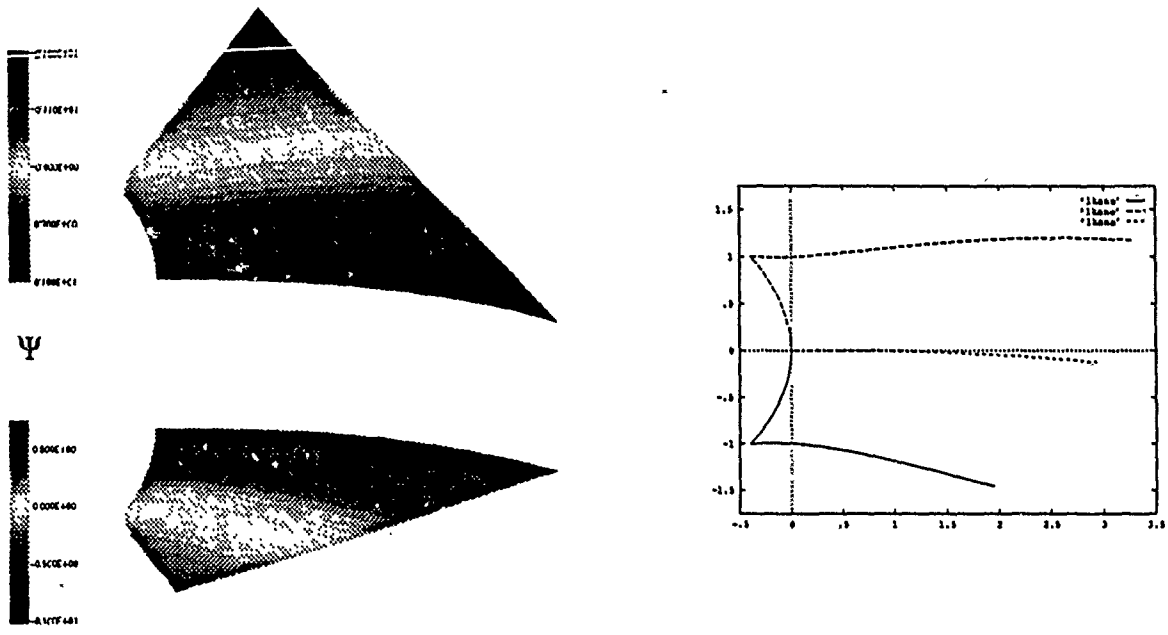


Fig. 4: Laval nozzle exit designed from sonic line Cauchy data and velocity distribution (Mach, flow angle) along a curved axis. Color graphics illustrate stream function / contour .

Supersonic flows with controlled shock waves

Before we apply the method of characteristics to a problem involving oblique shocks, it should be illustrated that given initial data in the Rheograph working plane directly relate to Cauchy data in the physical plane, the marching direction starting from AB and progressing towards C runs approximately normal to the resulting local flow direction, Fig. 5. We call this and related numerical approaches to compute the flow field "Cross - (stream) Marching". This will be useful for supersonic design applications where we seek to control the shape and strength of occurring shock waves.

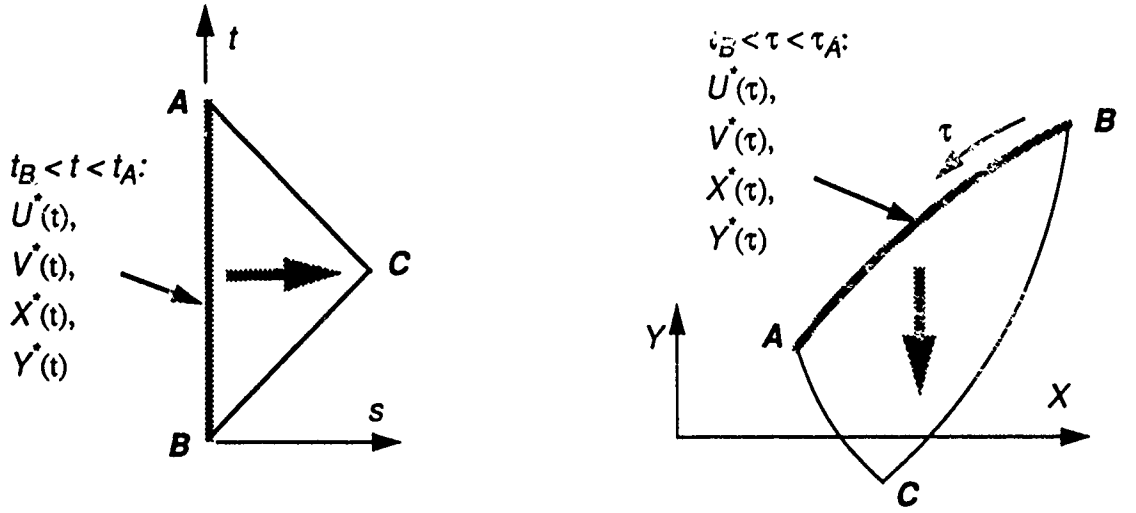


Fig. 5: Cauchy Initial data in characteristics plane (s, t) and in physical plane (X, Y)

Cross-Marching from given shock waves

As can easily be seen from a flow field with an oblique shock wave and its supersonic post-shock characteristics, there is only the possibility of Cross-Marching since the initial data do not allow for marching downstream, Fig. 6. A portion AB of oblique shock wave determines a flow field ABC and a limited portion AD of the contour compatible with the given shock wave. A larger region of dependence ABEF and contour ADG are obtained if also the flow at a segment BE at the axial exit station is prescribed, see [11] for some remarks about numerical consequences of such given input.

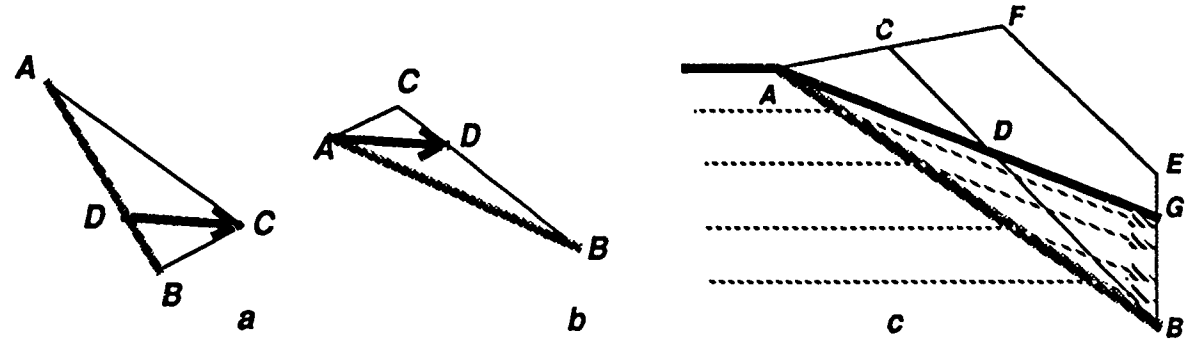


Fig. 6: Basic steps of downstream marching (a) and Cross-Marching (b), depending on initial data curve AB. Computing the flow behind oblique shocks (c) requires Cross-Marching.

Third International Conference on Inverse Design Concepts and Optimization in Engineering Sciences
(ICIDES-III), Editor: G.S.Dulikravich, Washington D.C., October 23-25, 1991

Numerical methods of characteristics have been developed for plane and axisymmetric , for isentropic and rotational flows. Prescribing arbitrary shock waves results in rotational flow because of shock curvature. Cauchy initial data for flow field computation therefore require coordinates, velocity components and entropy distribution along the prescribed shock geometry. For Cross-Marching (Fig. 6b), the iterative calculation of entropy convection along the streamlines requires an extrapolation of data BD→C, while for the usual downstream marching (Fig. 6a) an interpolation of data A→D←B is needed.

The following two examples were obtained with a new numerical Cross-Marching method of characteristics for axisymmetric isentropic or rotational flow by the second author [12]. A flexible input geometry generator and workstation implementation lay ground for further extensions and use for aerodynamic design tasks.

Example: Segment of a conical flow field

As a first example for the new method of characteristics a part of the flow field past a circular cone is computed. Input data are the upstream Mach number, a set of coordinates of and post-shock conditions behind the given conical shock wave with given angle. Fig. 7 illustrates the characteristic grid, a selected integrated streamline and reveals a limit line singularity along a ray through the cone vertex, well within the solid cone which is compatible with the shock cone and Mach number. The case is well-suited for checking the accuracy in comparison with the solution of the Taylor-Maccoll ODE; graphic visualization of the Mach number and flow angle distribution must show constant values along rays through the cone vertex, though its location is not part of the input data.

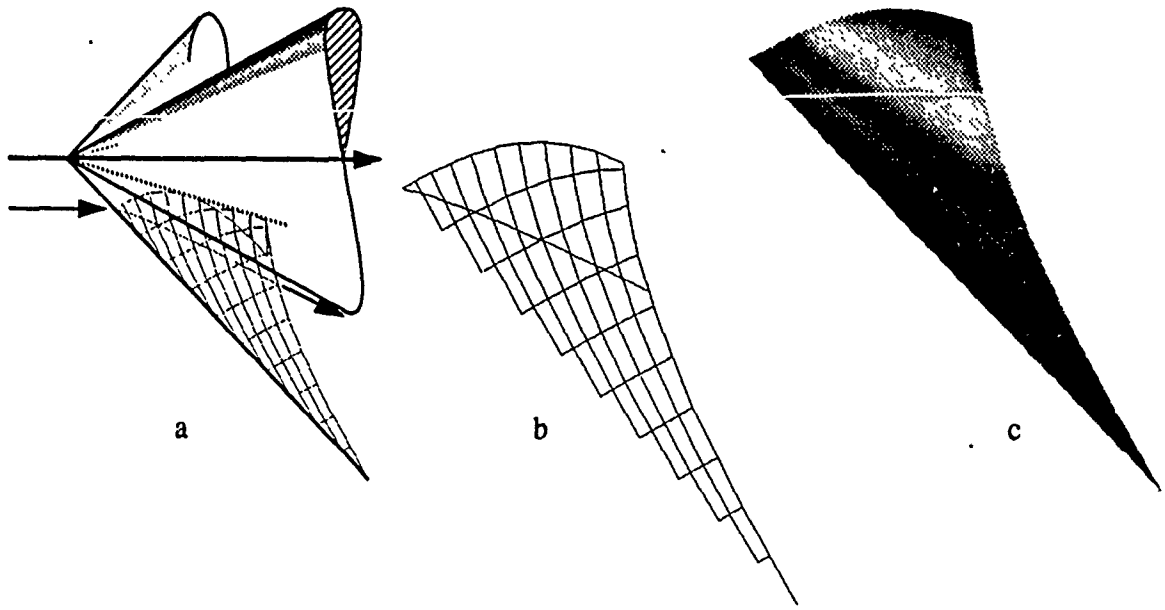


Fig. 7: Ideal gas ($\gamma = 1.4$) flow past a circular cone. Given Mach = 2, shock angle = 45^0 (compatible with a solid cone of 27.32^0). Choice of shock segment size relative to axial distance: Characteristics grid (a) with or (b) without limit cone of ~16.3^0. Every third grid line shown. Color graphics (iso - Mach) for flow field conicity check (c).

Computation time on a Sun Sparc Station: 6 seconds.

Example: Segment of a flow field downstream of a curved shock

A slight variation of the input shock segment geometry brings rotation to the flow field downstream of the shock. Color graphic visualization of the velocity and pressure distribution shows a strong deviation from conical structure, Fig. 8.

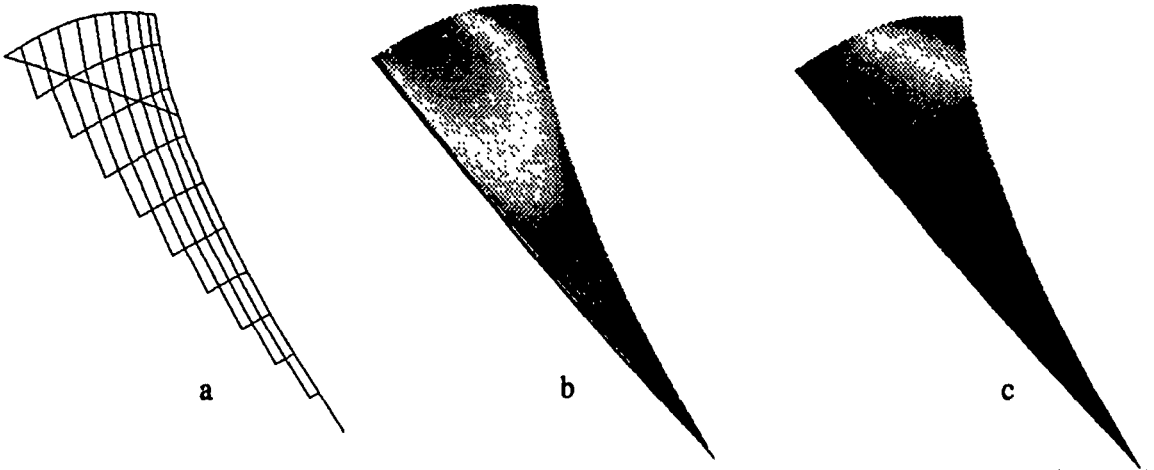


Fig. 8: Flow with a curved shock wave. Given Mach = 2, shock angle varies from 50^0 to 45^0. Characteristics grid, surface streamline (a). Color graphics for iso-Mach (b) and iso-flow angle (c)

Design of three-dimensional flow fields

The exploitation of plane and axisymmetric inviscid flow fields for the definition of flow patterns generated by three-dimensional bodies in supersonic flow has been used since about three decades when Nonweiler [13] created the first "waveriders". In recent years renewed interest originated in such configurations for generic lifting aerospace transport vehicles and supersonic inlet shapes [14]. The first author recently contributed an idea to this research which is aimed in generalizations of waverider shape definition by applying conical flow solutions with constant shock strength but axial distance of the shock segments varying along span [11]. The idea is based on the assumption of a local axisymmetry in every 3D flow, which is well defined in an"osculating plane" if the shock wave is known, Fig. 9. The method to generate three-dimensional configurations requires little more effort than evaluating one Taylor-Maccoll conical flow solution. Only the Mach number, shock angle, leading edge and shock profile in the exit plane need to be prescribed. Based on this method a very rapid interactive design code was developed by Center et al [15]. Numerical analysis with an Euler code shows a striking agreement of the numerically captured shock location with the design solution, which makes it worthwhile to further develop such techniques.

The method of characteristics with Cross-Marching developed here may be used for such further development, with the possibility of exploiting also rotational flow fields to find 3D body contours. This method is then equivalent to solve the 3D Euler equations in an inverse design mode, rapidly carried out in an interactive fashion on the workstation.

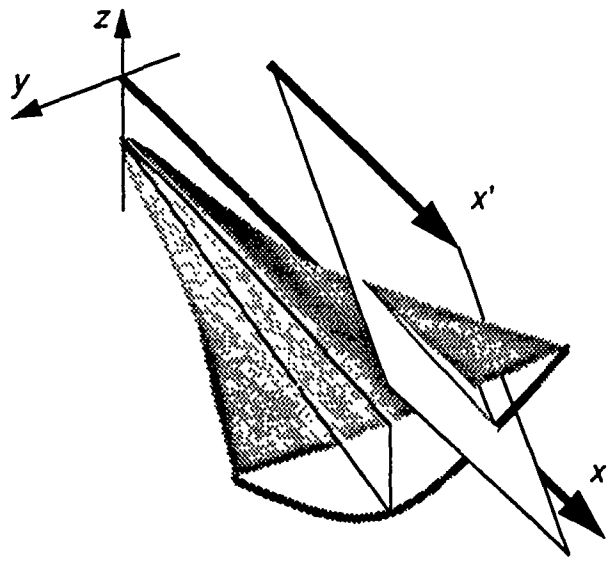


Fig. 9: Local conicity in osculating plane of a flow behind given rule surface shock wave: Design of generalized super/hypersonic waveriders.

Conclusion

We have tried to illustrate some ideas to extend classical theoretical methods for the aerodynamics of inviscid, compressible flows. The purpose is an implementation of these tools to develop software on fast modern workstation computers which enables the design aerodynamicist to perform rapid early stage design studies with aerodynamic expert systems, but also to develop these techniques toward convincing educational programs for students. Transonic and supersonic aerodynamics require inverse problem formulations if flow properties should be used optimally for design goals. This was shown using the method of characteristics for inverse applications.

Acknowledgement
Numerical codes were written or adapted to interactive workstation versions and combined with CFD color graphics postprocessing at DLR Göttingen by Birgit Seitz, Thomas Gentner and Michael Klein.

References

1. Sobieczky, H.: Related Analytical, Anolog and Numerical Methods in Transonic Airfoil Design. AIAA paper 79-1556 (1980)

2. Sobieczky, H.: Verfahren für die Entwurfsaerodynamik moderner Transportflugzeuge. DFVLR-FB 85-08 (1985), ESA-Technical Translation TT 923 (1985)

3. Weinstein, A.: Generalized Axially Symmetric Potential Theory. Bull. Amer. Math. Soc. **59** (1953), p. 20 - 38

4. Sobieczky, H.: Indirekte Methode zur Berechnung von schallnahen achsensymmetrischen Strömungen. DFVLR-IB 251 - 74 A 13 (1974)

5. Sobieczky, H.: Transonic Fluid Mechanics, Lecture Notes.
University of Arizona Report EES TFD 77-01 (1978)

6. Hassan, A. A.: A Method for the Design of Shock-free Slender Bodies of Revolution
AIAA Journal **24**, No. 5, (1986)

7. Klein, M.: Berechnung Schallnaher Strömungen auf modernen Arbeitsplatzrechnern,
Diplomarbeit Universität Göttingen, (1991)

8. Guderley, K. G.: Theorie Schallnaher Strömungen. Berlin, Göttingen, Heidelberg: Springer (1957)

9. Müller, E. A., Matschat, K.: Ähnlichkeitslösungen der transsonischen Gleichungen bei der Anström-Machzahl 1.
Proc. 11th Int. Congress Appl. Mech., Berlin, Heidelberg, New York: Springer (1964)

10. Gentner, T.: Inverses Charakteristikenverfahren zur Berechnung lokaler Überschallgebiete in Transsonischer Strömung.
Diplomarbeit Universität Karlsruhe (1991)

11. Sobieczky, H., Dougherty, F. C., Jones, K. D.: Hypersonic Waverider Design from Given Shock Waves. Proc. First Int. Hypersonic Waverider Symposium, University of Maryland, (1990)

12. Qian, Y. J., Sobieczky, H.,: Inverse Method of Characteristics for Axisymmetric Flow
DLR IB 221 - 90 A 10, to be published (1991)

13. Nonweiler, T. R. F.: Delta Wings of Shape Amenable to Exact Shock Wave Theory.
J. Royal Aero. Soc., **67**, 1963, p. 39

14. Anderson, J. D. (Ed.): Proc. First Int. Hypersonic Waverider Symposium, University of Maryland (1990)

15. Center, K., B., Dougherty, F. C., Sobieczky, H.: Interactive Design of Hypersonic Waverider Geometries. AIAA-91-1697, (1991).

Third International Conference on Inverse Design Concepts and Optimization in Engineering Sciences (ICIDES-III), Editor: G.S. Dulikravich, Washington D.C., October 23-25, 199?

SUPERCRITICAL BLADE DESIGN ON STREAM SURFACES OF REVOLUTION WITH AN INVERSE METHOD

E. Schmidt, H.-D. Grein

Institut für Aerodynamik
und Gasdynamik
Universität Stuttgart
Pfaffenwaldring 21
D-7000 Stuttgart 80
FRG

Abstract

The described method solves the inverse problem for supercritical blade-to-blade flow on stream surfaces of revolution with variable radius and variable stream surface thickness in a relative system. Some aspects of shockless design and of leading edge resolution in the numerical procedure are depicted. Some supercritical compressor cascades were designed and their complete flow field results were compared with computations of two different analysis methods.

Nomenclature

A	area
BN	blade number
La	Laval number
R	radius of stream surface
W	magnitude of velocity vector
d	profile thickness
h	stream surface thickness
l	profile chord length
m	meridional coordinate
s	arc length
t	cascade pitch
$\vec{w}$	velocity vector
x	chord coordinate
z	axial coordinate
Γ	circulation
Ω	axial velocity density ratio
θ	circumferential angle
β	flow angle
ε	inclination angle of stream surface
ρ	density
φ	potential function
ψ	stream function
ω	angular velocity

Subscripts:

1	upstream
2	downstream
BW	blade wake
SW	side wall
ax	axial
m	meridional
u	circumferential
Um	Transition

Third International Conference on Inverse Design Concepts and Optimization in Engineering Sciences
(ICIDES-III) Editor: G.S.Dulikravich, Washington D.C. October 23-25,1991

INTRODUCTION

Increasing requirements on turbomachines concerning efficiency, compact construction and density of power lead to aerodynamically highly loaded blades. The admissible blade load and the profile losses are determined by the boundary layer development. High pressure ratios per stage and high turning of the flow increase the risk of boundary layer separation with the result of strongly growing losses. This problem is intensified by the risk of arising compression shocks. They are caused by the supercritical through-flow (with local supersonic regions), which is necessary for high mass flow density.

In regions with pressure rise, boundary layer separation can only be avoided by careful blade profiling for flow with minimum loss. In the past, turbomachinery bladings have mostly been designed with the aid of profile families. But in this way, depending on the plurality of parameters, a loss minimization is not possible. Especially in the transonic velocity region this procedure is insufficient since shockfree solutions can be found with only poor chances by iterative contour variation. In this region of maximum mass flow density very small variations of the geometry are connected with very high changes in the flow velocity. Therefore, it is convenient to prescribe the physical quantity, where the great changes appear, and to calculate the small but important variations of the geometry.

This alternative is given by inverse design: Starting from a prescribed shockfree velocity distribution, the corresponding profile contour is calculated numerically. By this means a perfect tailoring of the blade to the required turning problem is possible.

Up to now a perfect three-dimensional inverse design of flow fields in turbomachines is not executed since this problem is quite overdetermined. At present a standard procedure is to start a quasi three-dimensional computation by calculating the flow on meridional planes (S_2) by an analysis code (duct- or through-flow) to get the starting values of the calculation on several blade-to-blade planes (S_1) distributed along the blade height.

This multi-section design of the blade can be realized by inverse computation. The following inverse computation method is an extension of the former cylindrical version [1,2] to the design on stream surfaces of revolution with variable radius and variable stream surface thickness in a relative system. This development is a further step to approximate the real physical behaviour of the flow. The method is applied to the multi-section design of a three-stage research compressor which is now in construction. Computations for comparison were carried out with two different analysis codes.

Third International Conference on Inverse Design Concepts and Optimization in Engineering Sciences (ICIDES-III), Editor: G.S.Dulikravich, Washington D.C., October 23-25,1991

FUNDAMENTAL EQUATIONS OF THE METHOD

Since inverse design strives for low loss flow without shocks and boundary layer separation, Prandtl's concept of distinct potential flow and boundary layer calculation is applied. In Fig. 1 the fundamental process of the method is sketched. The method computes the steady compressible potential flow in the passage between two blades of unknown shape from far upstream to far downstream on a stream surface of revolution. Besides the upstream and downstream velocity vector, the velocity distributions are prescribed along the arc length of the stagnation streamlines with their periodic parts in the upstream and downstream regions and along the blade suction and pressure sides. In this way velocity gradients can be prescribed, which is important for the boundary layer development and a prerequisite for loss minimization. Moreover, radius and thickness of the stream surface of revolution are prescribed along the axial coordinate. These boundary conditions are transformed by integration into the computation plane with stream function coordinates and their normals. The computation grid is rectangular in this plane and contour adapted in the physical plane. Therefore, no interpolations are necessary on the boundaries.

The equations of continuity and motion for steady, isentropic flow on a stream surface of revolution are

$$\frac{\partial\left[\rho\ h\ W_u\right]}{\partial\theta} + \frac{\partial\left[\rho\ h\ R\ W_m\right]}{\partial m} = 0 \qquad (1)$$

$$\frac{\partial W_m}{\partial\theta} - \frac{\partial\left[R\ W_u\right]}{\partial m} = 2\ \omega\ R\ \frac{\partial R}{\partial m} \qquad (2)$$

with the isentropic relation

$$\rho = f\ (W,\ \omega,\ R) \qquad (3)$$

The appearance of a variable stream surface radius in the fundamental equations requires a different treatment of rotor and stator flows since in the relative system of the rotor an energy alteration is connected with a radius alteration. So the relative velocity W can no longer be prescribed by a potential. In the absolute system (following Vavra [3]) an equivalent potential φ_A can be defined by

$$\nabla\cdot\varphi_A = \vec{v}_A = \vec{w} + \vec{i}_1\,\omega\,R \qquad \text{and } \nabla\times\vec{v}_A = 0 \quad . \qquad (4)$$

But the contour velocity distribution has to be prescribed in the relative system, thus one coordinate direction is given by the streamlines in the relative system. Together with the potential lines normal to the absolute velocity an oblique-angled coordinate system results, Fig. 2.

At velocities $W \ll \omega R$ and flow angles $\delta \approx \pi/2$ (e.g. in the stagnation point region) the angle α approaches zero so that both coordinate directions coincide. Following from numerical reasons this system consisting of an absolute potential and relative stream function is inconvenient for use as a computational grid.

The potential-streamfunction-plane is the computation plane of the inverse design method. Furthermore, for using it in the rotor the equation of motion is reduced to $\nabla \times \vec{w} = 0$. The consideration of the rotational character of the flow occurs by variation of the total quantities dependent on the stream surface radius. (Another consideration by definition of a transformed potential is published in [4,5].)

Since the critical sonic velocity is no longer constant, because of the variation of the total temperature, it is no longer applicable for normalization of the velocity like in the stator case. Hence, the upstream velocity W_1 is now applied for this purpose. The decision which difference operator for consideration of the type-dependence of the differential equation system has to be applied is taken by the magnitude of the local Mach number.

By transformation of the fundamental equations into the potential-streamfunction-plane and elimination of the flow angle the full potential equation follows [6]:

$$C_1 \cdot \frac{\partial^2 \ln W^*}{\partial \varphi^2} + C_2 \cdot \frac{\partial^2 \ln W^*}{\partial \psi^2} + C_3 \cdot \left(\frac{\partial \ln W^*}{\partial \varphi}\right)^2 + C_4 \cdot \left(\frac{\partial \ln W^*}{\partial \psi}\right)^2 + C_5 \cdot \frac{\partial \ln W^*}{\partial \varphi} + C_6 \cdot \frac{\partial \ln W^*}{\partial \psi} + C_7 = 0$$

$$\text{with} \quad C_1 \ldots C_7 = f\,(W^*,\ \omega,\ R,\ h) \qquad (5)$$

$$\text{and} \quad W^* = W/W_1 \quad \text{for the rotor}$$
$$= La \quad \text{for the stator}$$

The flow field is computed by the solution of the corresponding difference equation system applying relaxation combined with multi-grid. The change of type (elliptic-hyperbolic) from subsonic to supersonic flow regions depending on the sign of the coefficient C_1 is considered by modified difference equations. The transformation of the solution back into the physical plane is performed by integration of the equations of continuity and motion. It yields the field boundaries, i.e. the blade profiles and the cascade geometry.

For solving eq.(5) the dependence of the radius on the potential and stream function $R = f(\varphi, \psi)$ is necessary. Since only the axial development $R = f(z)$ is known by the prescription, this relation can only be discovered by an additional iteration in the course of the solution process. The radius distribution has to fulfill the

condition of constant values in circumferential direction. Normally the same is true for the stream surface thickness. Moreover, the desired values of turning angle, pitch-chord ratio or blade thickness distributions are attainable by iterative variations of the prescribed boundary values (which are selfacting included in the code). The whole geometry of the problem is always the *result* of the computation and therefore completely unknown at the beginning.

CIRCULATION, LEADING EDGE RESOLUTION, SHOCKLESS DESIGN

The profile circulation necessary for the desired turning, follows from (s. Fig. 3):

$$\Gamma_P = \oint \vec{w}\cdot d\vec{s} - W_1\cdot\cos\beta_1\cdot\frac{2\pi R_1}{BN} + W_2\cdot\cos\beta_2\cdot\frac{2\pi R_2}{BN\cdot\Omega_{BW}} \qquad (6)$$

The line integral of the velocity along the computation grid boundary can be converted by the law of Stokes into an area integral

$$\oint \vec{w}\cdot d\vec{s} = -2\int \vec{\omega}\cdot d\vec{A} \quad . \qquad (7)$$

The rotational vector $\vec{\omega}$ indicates in axial direction, $d\vec{A}$ is perpendicular to the through-flowed area. For the stator ($\omega \equiv 0$) and for a rotor with constant radius ($\vec{\omega} \parallel d\vec{A}$) the value of the line integral equals zero. Because of the reduction of the equation of motion this is also true for rotor flow with varying radius. The additionally existing circulation inside the computation grid is thereby neglected.

$$\oint \vec{w}\cdot d\vec{s} = 0 \qquad (8)$$

The profile circulation which is necessary for the actual turning problem and which should be rendered by the prescribed velocity distribution at the beginning of the design process is

$$\Gamma_P = \frac{2\pi\cdot R_1}{BN}\cdot\left[W_2\cdot\cos\beta_2\cdot\frac{R_2}{R_1}\cdot\frac{1}{\Omega_{BW}} - W_1\cdot\cos\beta_1\right] \qquad (9)$$

The circulation inside the computation grid neglected in the rotor case with varying radius can be estimated in maximum if the flow conus area divided by the blade number (i.e. vanishing profile area) is assumed as upper limit for the integration area:

$$\oint \vec{w}\cdot d\vec{s} = \frac{4\pi^2 n}{BN}\cdot\left(R_2^2 - R_1^2 \right) \qquad (10)$$

The relative deviation (refered to the circulation of the reduced equation of motion) is

$$\Delta\Gamma = \frac{-2\cdot\pi\cdot n\cdot R_1\cdot\left[\left(\frac{R_2}{R_1}\right)^2 - 1\right]}{W_1\cdot\left[-\cos\beta_1 + \cos\beta_2\cdot\frac{W_2}{W_1}\cdot\frac{R_2}{R_1}\cdot\frac{1}{\Omega_{BW}}\right]} \qquad (11)$$

In the case of compressor cascades ($\beta_1 \geq 90°$) the reduced equation of motion yields lower circulation for increasing stream surface ($R_2/R_1 > 1$) and higher circulation for decreasing stream surface. In standard cases the deviation amounts to less than 5 percent according to a turning angle deviation of less than 1 degree.

The leading edge region of a profile has special requirements for the numerical aspects of a computer program for calculation of the flow around an airfoil. In the design method this difficulty becomes especially clear since even the prescription data - the velocity distribution on the boundaries of the flow field to be computed - show the strong gradients in the stagnation point region (Fig. 4). This area can be recorded only insufficiently in an equidistant divided computation grid.

For appropriate resolution of the blade nose region it was found that the number of points on the flow field boundaries should be up to 2^4 or 2^5 times higher than that of the normal grid. Thereby local grid refinement is provided for the regions with steep gradients. For smaller point distances the possibility of emboxing of refinements was established. In a corresponding fitted arrangement a gradual transition of the mesh size follows. This is especially favourable for the accuracy of the solution. For even higher accuracy, a feedback calculation can be performed which uses the results of the fine grid for recalculation in the coarse grid in an iterative way with overlapping boundaries of both regions.

In case of velocity prescriptions on the boundaries of local supersonic regions an "ill-posed problem" is treated, i.e. no physical solution may exist. Numerically this often leads to the formation of oscillating shocks in the flow field, shown in Fig. 5. If they are weak enough, a provision for cancellation of these shocks is given in Fig. 6: Following the plotted characteristic directions in the supersonic region from the concerned region to the corresponding boundary values, these values can be modified for generation of additional expansion waves to remove the shocks [7].

RESULTS

The first example is a cascade for a compressor stator hub section with supercritical flow (local supersonic region on the suction side), Fig. 7. The high subsonic velocity $La_1 = 0.90$ is decelerated to the downstream value $La_2 = 0.593$ by a turning angle of 25 degrees and a relatively high pitch-chord ratio of $t/l_{ax} = 1.0$.

The stream surface radius R increases by 30 percent from upstream to downstream and the stream surface thickness h decreases by 25 percent in the same direction. Their prescribed slopes dependent on the axial length z are given in Fig. 8. The curves of the inner and outer radius of the stream surface of revolution consist of cosine slopes, the maximum angle of inclination of the stream surface is ε = 25 degrees. In the cascade region the stream surface thickness distribution follows a cubic parabola, in the upstream and downstream region it is calculated by constant flow area.

In the upper part of Fig. 7 the full line shows the prescribed velocity distribution on the blade suction and pressure side. This roof top distribution with maximum Mach number of 1.19 (La = 1.15) was chosen for separation-free flow with high loading. On the suction side transition takes place at the beginning of the pressure rise at 31 percent of chord length (at $Re = 4.7 \cdot 10^5$ and Tu = 4%).

In the lower part of Fig. 7 the computed profile shape is plotted. The dashed line marks the contour of the potential flow computation from which the manufacturing contour (full line) is derived by subtraction of the boundary layer displacement thickness (computed by Rotta's integral method [8]). The complete cascade geometry and the flow field characterized by the (full) lines of constant velocity (with the sonic line La = 1.0) are shown in Fig. 9. The cascade geometry data were used as input for the analysis code of Lücking [9]. The results, the contour velocity distribution (crosses in Fig. 7) and the velocity distributions in the flow field (dashed lines in Fig. 9) agree well with the distributions of the inverse code, even in the supersonic region.

Moreover, in Fig. 10 the course of the lines of constant radius (dashed-dotted), which can only be calculated iteratively (see above), coincide well with the demanded circumferential direction.

In Fig. 11 the prescribed velocity distribution of a rotor tip section (n = 3600 rpm) is plotted together with the resulting profile shape (both full lines). Despite of the low turning of 6 degrees, due to the high upstream velocity of La = 0.866 and the high pitch-chord ratio of t/l_{ax} = 1,761 the loading is high enough to require local supersonic flow on the suction side. In Fig. 12 the cascade geometry and the flow field consisting of lines of constant velocity is drawn, showing the great stagger of this design. The geometry of this result was again used to compute the velocity distributions for comparison by the finite volume method originating in P.W. McDonald [10]. The crosses in Fig. 11 and the dashed lines in Fig. 12 exhibit satisfying agreement with the design computation (full lines).

The velocity distribution of the rotor hub section (Fig. 13) belonging to the preceding rotor tip section was mainly influenced by a desired maximum thickness of the profile (in consideration of structural reasons). Therefore, high velocities appear on the suction and pressure side without high aerodynamic loading. The design on stream surface with radius increase of 14 percent (full line) is compared with plane flow design for equal upstream and downstream velocity vectors. It is to be seen that in the plane

flow case higher circulation is needed for the same turning problem but a thinner profile results compared to the design on increasing radius. In Fig. 14 the cascade geometry is demonstrated and the isolines of the velocity are compared with the results of the finite-volume method [10]. In the front part of the flow channel including the local supersonic region the velocity field compares well. In the rear part, refering to a local aft-acceleration behind the supersonic patch the coincidence of the isolines is somewhat disturbed.

CONCLUSION

The present extended inverse method seems to be an effective procedure to design highly loaded axial compressor cascades on stream surfaces of revolution. It produces accurate results compared with complete flow field results of other methods and was successfully applied to cascade and multi-section compressor blade design.

[1] Schmidt, E.: Computation of Supercritical Compressor and Turbine Cascades with a Design Method for Transonic Flows. Trans. ASME, J. Eng. Power, Vol. 102, Jan. 1980, pp. 68-74

[2] Schmidt, E., Berger, P.: Inverse Design of Supercritical Nozzles and Cascades. Int.J.Num.Meth.Eng., Vol. 22, No. 2, Feb. 1986, pp. 417-432

[3] Vavra, M.H.: Aero-Thermodynamics and Flow in Turbomachines. Wiley, New York, 1960

[4] Klimetzek, F., Schmidt, E.: Transonic Blade Design on Rotational Stream Surfaces. AGARD Conf. Proc. No.421, May 1987

[5] Schmidt, E., Klimetzek, F.: Inverse Computation of Transonic Internal Flows with Application for Multi-Point Design of Supercritical Compressor Blades. AGARD Specialist's Meeting Computational Methods for Aerodynamic Design (Inverse) and Optimization, Loen, Norway, May 22-23, 1989

[6] Grein, H.-D., Schmidt, E.: Ein Berechnungsverfahren für die Auslegung von Verdichterbeschaufelungen. MTZ Motortechnische Zeitschrift 51, Juni 1990, pp. 248-255

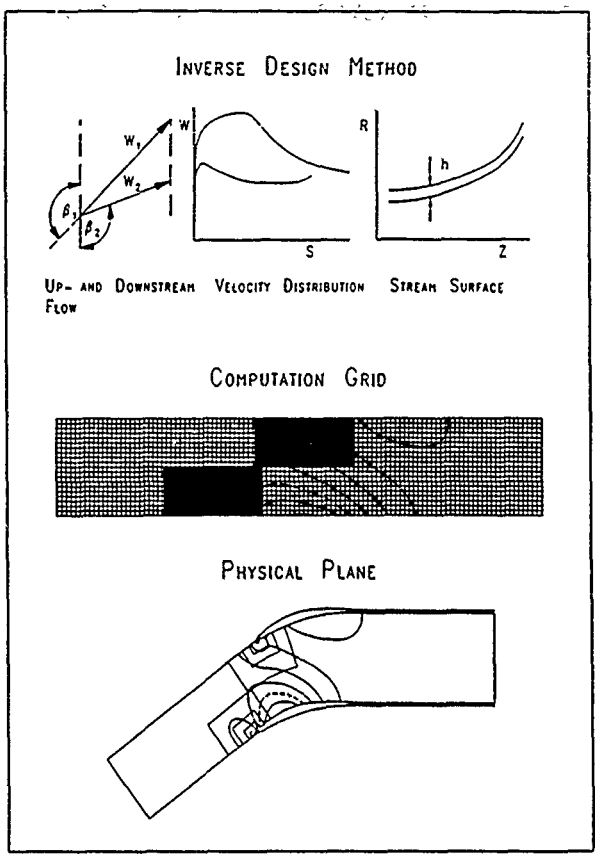
[7] Schmidt, E.: Inverse Methods for Blade Design, Controlled Diffusion Blading for Supercritical Compressor Flow. VKI-LS Transonic Compressors, Brussels 1988-03

[8] Rotta, J.-C.: FORTRAN IV-Rechenprogramm für Grenzschichten bei kompressiblen, ebenen und achsensymmetrischen Strömungen. DLR FB 71-51, Göttingen, 1971

[9] Lücking, P.: Numerische Berechnung der dreidimensionalen reibungsfreien und reibungsbehafteten Strömung durch Turbomaschinen. Dissertation, RWTH Aachen, 1982

[10] Happel, H.W.: Anwendung neuer Entwurfskonzepte auf Profile für axiale Turbomaschinen. MTU Techn. Bericht 78/54A, München, 1978

Third International Conference on Inverse Design Concepts and Optimization in Engineering Sciences (ICIDES-III), Editor: G.S. Dulikravich, Washington D.C., October 23-25, 1991.



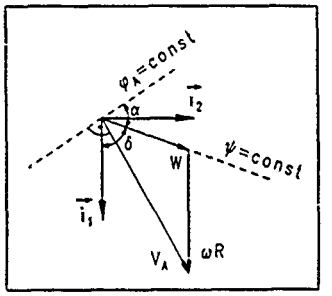


Fig. 2: Velocities and coordinate directions in an absolute potential/relative stream function system.

Fig. 1: Solution process of the inverse design method.

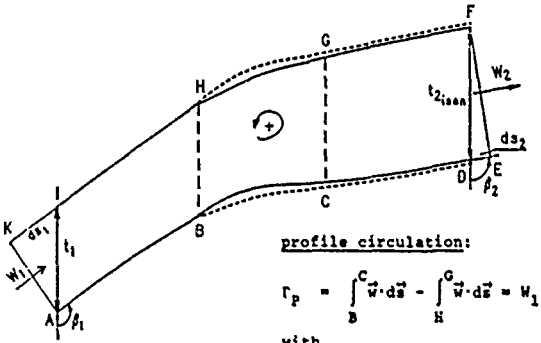
Calculation of Profile Circulation

circulation inside computation grid:

$$\Gamma = \int (\nabla \times \vec{W}) \cdot d\vec{A} = \oint \vec{W} \cdot d\vec{s}$$

stator, rotor with reduced equation of motion:

$$\nabla \times \vec{W} = 0 \quad \Rightarrow \quad \oint \vec{W} \cdot d\vec{s} = 0$$



profile circulation:

$$\Gamma_P = \int_B^C \vec{W} \cdot d\vec{s} - \int_H^G \vec{W} \cdot d\vec{s} = W_1 \cdot t_1 \cdot \sin(\beta_1 - 90) + W_2 \cdot t_{2_{isen}} \cdot \sin(90 - \beta_2)$$

with

$$t = \frac{2\pi R}{BN}, \quad \frac{t_2}{t_{2_{isen}}} = o_{BW}, \quad \sin(\beta - 90) = -\cos\beta :$$

$$\Gamma_P = \frac{2\pi R_1}{BN} \cdot W_1 \cdot \left[\frac{W_2}{W_1} \cdot \cos\beta_2 \cdot \frac{R_2}{R_1} \cdot \frac{1}{o_{BW}} - \cos\beta_1 \right]$$

Fig. 3: Calculation of the profile circulation.

Third International Conference on Inverse Design Concepts and Optimization in Engineering Sciences (ICIDES-III), Editor: G.S. Dulikravich, Washington D.C., October 23-25, 1991.

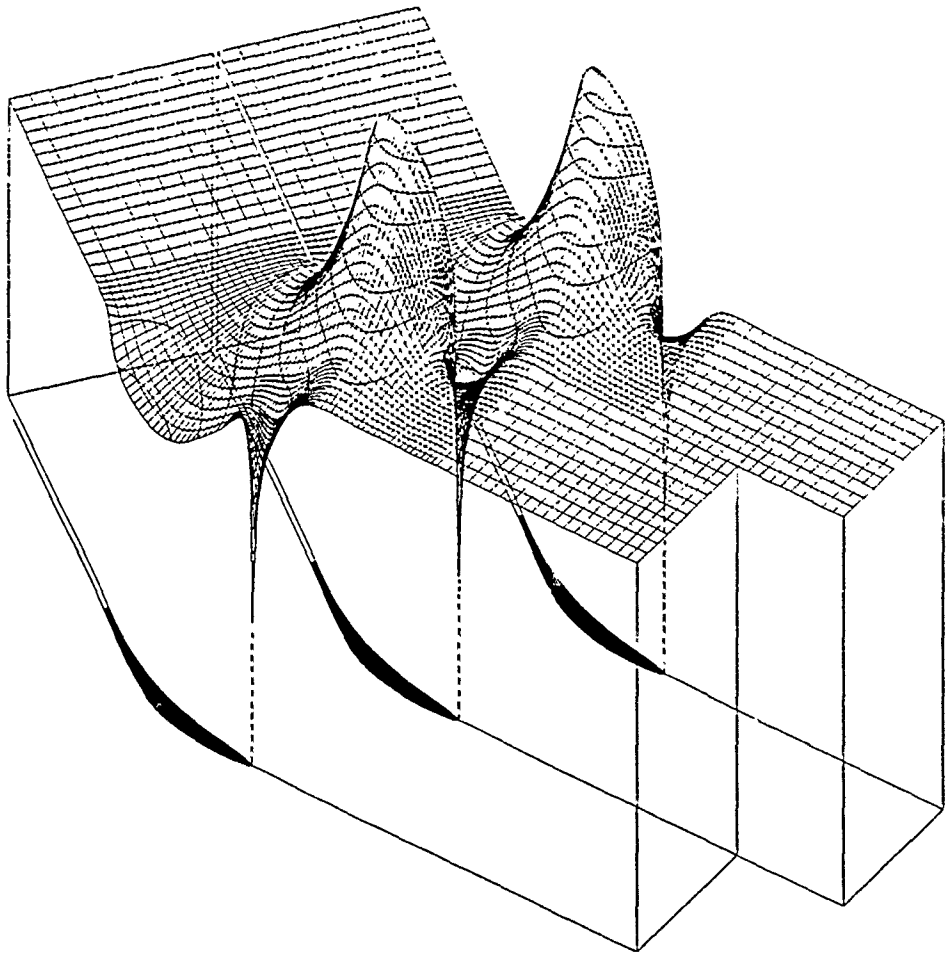


Fig. 4: Computation grid of a compressor cascade in the flow plane with velocity as height coordinate, demonstrating the resolution of of steep gradients in the stagnation point region.

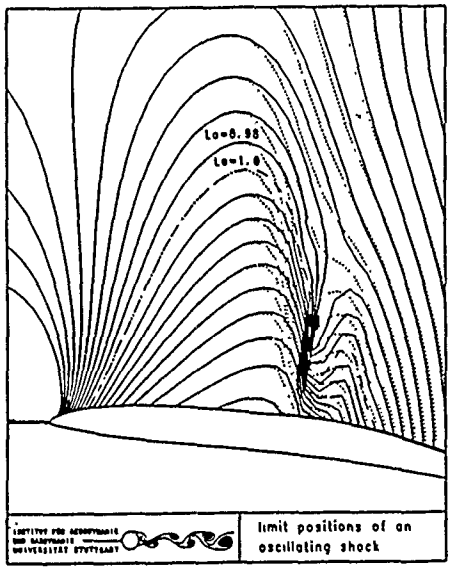


Fig. 5: Velocity fields and profile contours of a design with a shock for the limit positions of the oscillating shock.

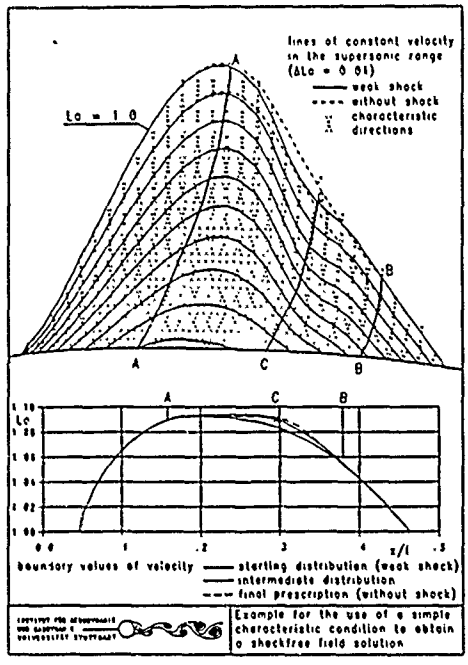


Fig. 6: Procedure for shockfree design.

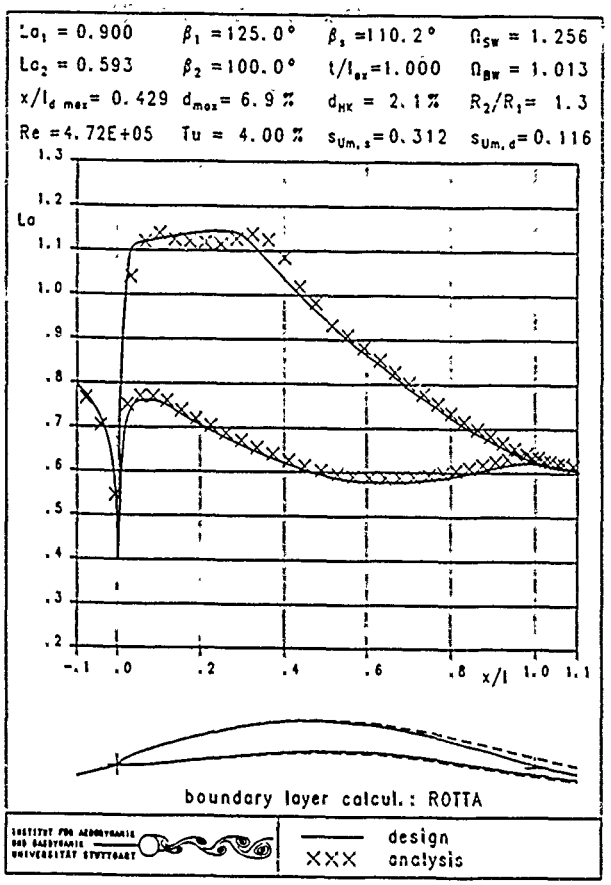


Fig. 7:

Comparison of Laval number distributions on the blade between design and analysis calculation on stream surfaces of revolution for the stator hub section. Additionally the potential flow contour (dashed line) and the metal section contour (full line) are indicated.

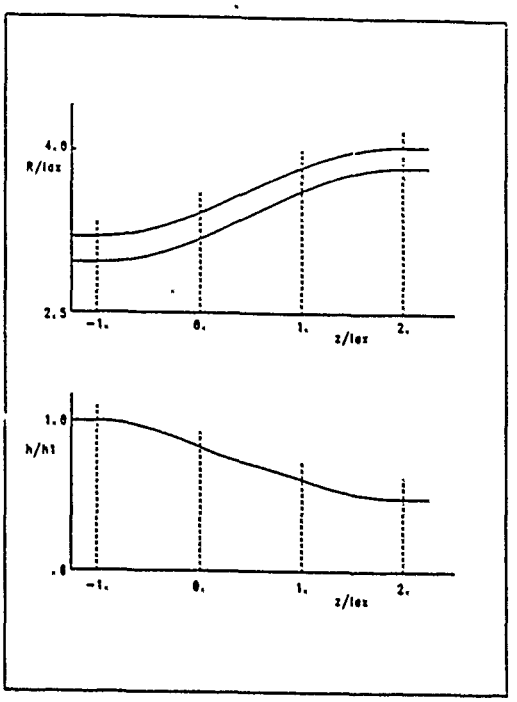


Fig. 8:

Slopes of inner and outer radius of the stream surface (top) and stream surface thickness (bottom) for the stator hub section.

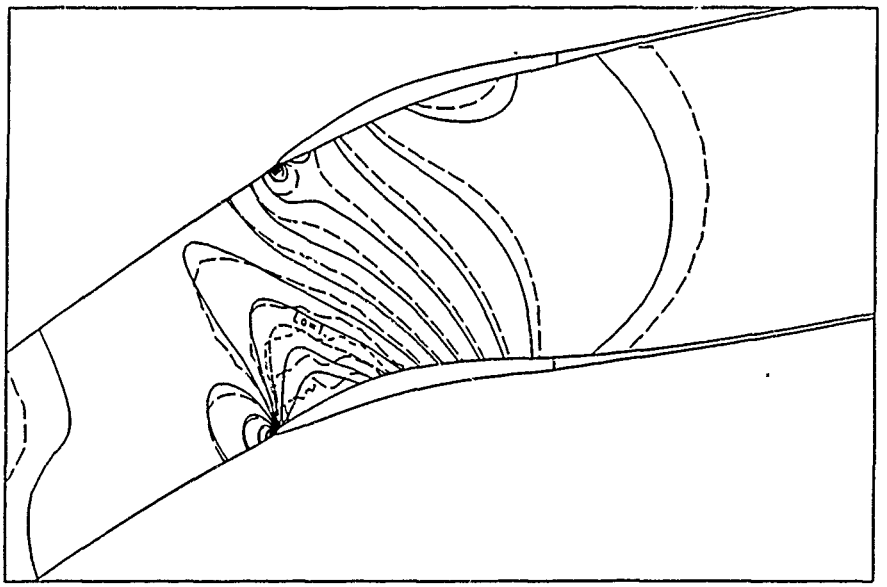


Fig. 9: Comparison of field distributions of Laval numbers between design (full line) and analysis calculation (dashed line) on stream surfaces of revolution for the stator hub section (increment ΔLa = 0.05, sonic line La = 1.).

Third International Conference on Inverse Design Concepts and Optimization in Engineering Sciences (ICIDES-III), Editor: G.S. Dulikravich, Washington D.C., October 23-25, 1991.

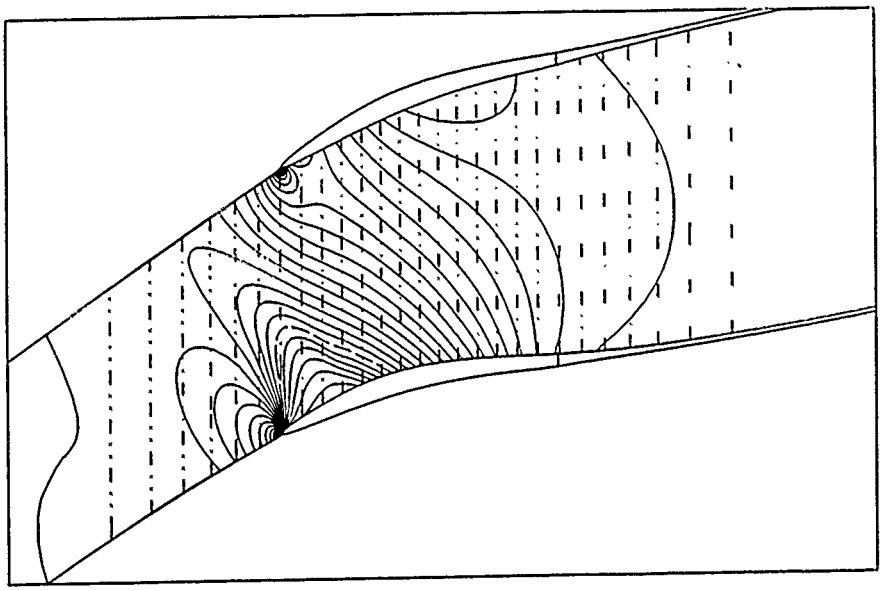


Fig. 10: Field distribution of Laval number (sonic line dashed, increment ΔLa = 0.025) and lines of constant stream surface radius (dashed-dotted) for the stator hub section.

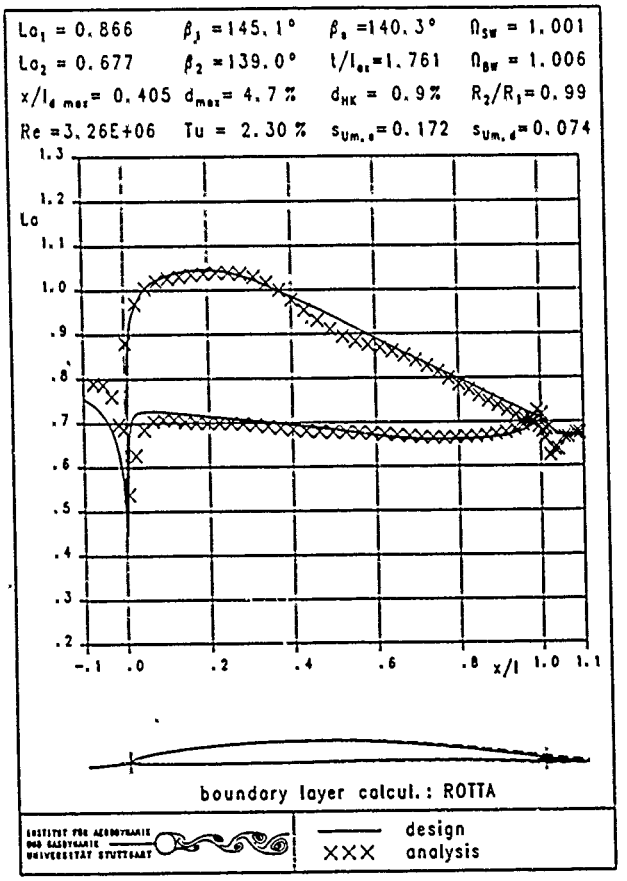


Fig. 11:
Comparison of Laval number distributions on the blade between design and analysis calculation on stream surfaces of revolution for the rotor tip section.

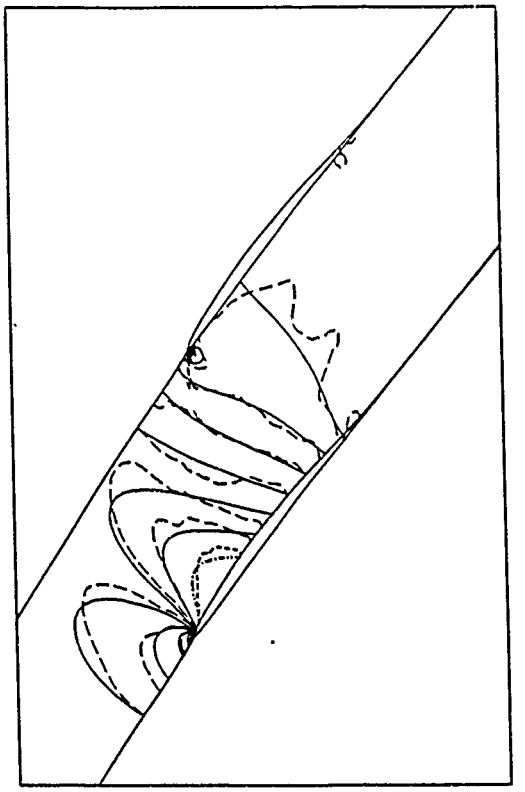


Fig. 12:
Field distributions of Laval number of design calculation (full line, sonic line dashed-dotted) and analysis calculation (dashed line, sonic line short dashed) for the rotor tip section (increment ΔLa = 0.5).

Third International Conference on Inverse Design Concepts and Optimization in Engineering Sciences (ICIDES-III), Editor: G.S. Dulikravich, Washington D.C., October 23-25, 1991.

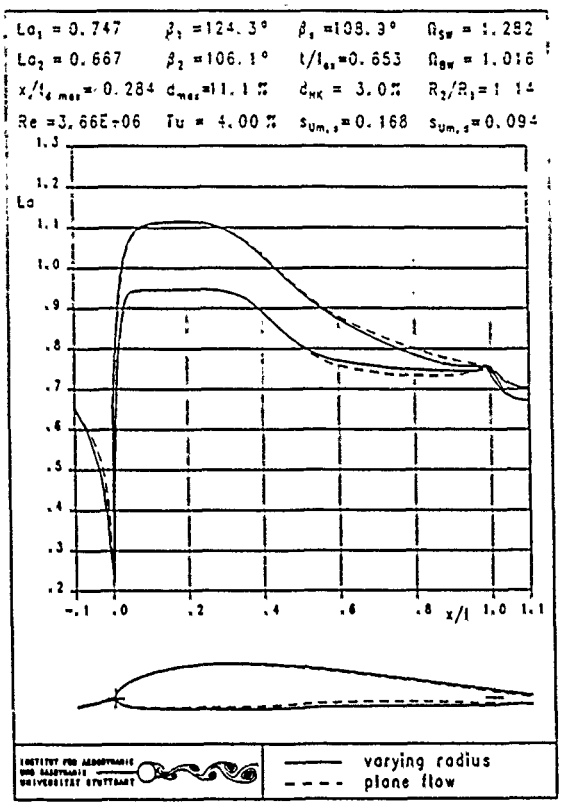


Fig. 13: Comparison of Laval number distributions on the blade and of blade contours between design of rotor hub section on plane stream surface (dashed line) and on stream surface of revolution (full line).

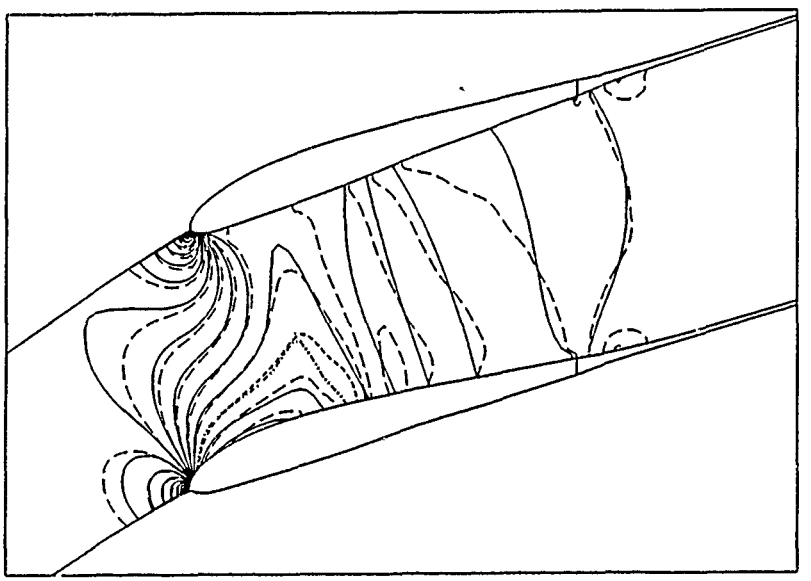


Fig. 14: Comparison of field distributions of Laval numbers between design (full line, sonic line dashed-dotted) and analysis calculation (dashed line, sonic line short dashed) on stream surfaces of revolution for the rotor hub section (increment ΔLa = 0.05).

Third International Conference on Inverse Design Concepts and Optimization in Engineering Sciences (ICIDES-III). Editor: G.S. Dulikravich. Washington D.C., October 23-25, 1991.

APPLICATION OF DIRECT INVERSE ANALOGY METHOD (DIVA) AND VISCOUS DESIGN OPTIMIZATION TECHNIQUES

E. Greff[+], D. Forbrich* and H. Schwarten**
Deutsche Airbus GmbH, Dept. of Aerodynamics, Bremen F.R.G.

ABSTRACT

A direct-inverse approach to the transonic design problem was presented in its initial state at ICIDES I. This paper reports further applications of the DIVA-method to the design of airfoils and incremental wing improvements and the verification in experiment. First results of a new viscous design code also from the residual correction type with semi-inverse boundary-layer coupling are compared with DIVA which may enhance the accuracy of trailing-edge design for highly loaded airfoils.
Finally the capabilities of an optimization routine coupled with the two viscous full potential solvers are investigated in comparison to the inverse method. The designer with expertise in specifying pressures can usually sort through certain design philosophies and off-design criteria more efficiently than an optimizer up to now.

I. INTRODUCTION

The application of CFD methods for analysis and design has been progressively increased in the past decade[1,2,3] but when it comes down to the global forces lift, drag and moment for transonic wings, let alone more complex configurations with pod interference, the general accuracy of wind tunnels remains unmatched. As cruise performance is the main driver for a transport aircraft design and the current designs in service already represent a high standard the designer has to meet very tight performance targets at a guarantee margin of 1-2% in drag.

This has to be achieved at limited budget and within a time frame of ~2.5 years during the definition phase through extensive iterations and repeated wind tunnel test loops. Increased quality requirements and complexity of the models, however, reduced the number of possible wing steps to 4-6. Hence greater emphasis was placed on inverse design concepts at DA based on a combination of a direct-inverse transonic design code with measured pressure distributions on complete configurations in order to derive incremental design improvements and performance estimates of high accuracy. Previous design codes in the 1970's have either worked with the hodograph equations[4,5], used direct optimization techniques[6] or tried the inverse approach for the full potential equation[7-10]. Hodograph methods are extremely difficult to use and limited to shock-free flows which in practice reveal adverse drag in off-design cases. Inverse methods that solve the Dirichlet problem need special treatment of the trailing-edge closure, which used to be a problem with earlier codes[9]. A variation of the nose shape[8] or tangential speed distribution along the a priori unknown arc length[11,12] can force closed profiles but in several cases the resulting pressure distribution is far off the desired one.

[+] Head of Aerodynamic Design Department
* Research Engineer, Aerodynamic Design
** Research Engineer, Theoretical Aerodynamics

Third International Conference on Inverse Design Concepts and Optimization in Engineering Sciences (ICIDES-III), Editor: G.S. Dulikravich, Washington D.C., October 23-25, 1991.

A direct-inverse approach turns out to be more flexible in practical design, as it merely needs a specified pressure distribution and a starting geometry. Due to the modular structure of the computing concept - the residual between actual and specified pressures is determined by the use of an analysis code and the geometry corrected to minimize the residual - the transonic analysis code is exchangeable and flows with shocks and viscous interaction can be treated in the design cycle.

At ICIDES I the DIVA-method was presented in its initial state[13] and applied to several successful designs for airfoils and wings[14]. Further approaches to the viscous direct-inverse design were reported recently by Campbell[15] and Carlson[16] where even separated flows can be treated.

Higher order analysis codes that solve the Euler equations are already in use as to mention the ISES-Code by Drela[17] which is based on a coupling with an integral boundary layer formulation with a lag-dissipation closure. This code is very accurate in the analysis mode, the design modi available so far do not solve for an arbitrary pressure distribution. A starting geometry close to the desired one is necessary as the speed distribution on the leading edge is prescribed - a major disadvantage. Even Navier-Stokes-Codes are already offered as an analysis code in residual-correction design mode.

Efficient full-potential solvers coupled with semi-inverse boundary layer integral methods simulating wake curvature and thickness effects have demonstrated their accuracy with respect to pressure distribution and drag which is in the tolerance of different 2D windtunnels[18-21]. Three-dimensional analysis with full-potential or Euler solvers has experienced significant progress and even complex configurations with engine/jet-effects are being treated worldwide. Viscous effects however are mostly omitted or inaccurately modelled so far. Moreover the inverse formulation is an ill-posed problem.

For design purposes we therefore rely upon 2D-methods which can be used more rapidly and allow the designer to focus on key design parameters and quickly sort out different design philosophies. Some ingenuity is needed for the transfer to three-dimensional design, but this can be done by using an analogy method based on pressure distributions of a datum wing quite accurately.

II. THE DIRECT-INVERSE ANALOGY-METHOD (DIVA)

The two-dimensional transonic direct-inverse design method was presented in[13,14]. The DIVA uses an improved stream function method - based upon the work of Oellers[22] and Ormsbee and Chen[23] - to design an airfoil for a specified subsonic pressure distribution. The airfoil surface is replaced by a vortex sheet with linear variation of singularity strength between the surface node points (fig. 1), whereas the Ormsbee method used a constant strength.

The sum of a stream function for a parallel flow and the perturbation stream function of the vortex sheet is a constant on the airfoil surface. This is expressed in the following integral equation:

$$\psi_b + \frac{1}{2\pi} \oint_b \gamma(s) \ln r \, ds = Z \cdot U_\infty \cdot \cos \alpha - X \cdot U_\infty \cdot \sin \alpha \qquad (1)$$

Third International Conference on Inverse Design Concepts and Optimization in Engineering Sciences (ICIDES-III), Editor: G.S. Dulikravich, Washington D.C., October 23-25, 1991.

where ψ_b is the unknown constant on the body's surface. In order to solve the equation for the vorticity strength $\gamma(s)$ and ψ_b, the integral is approximated by a quadrature. The airfoil is divided into N-1 segments, where N is the odd number of panel node points. The singularity strength varies linear in between two node points. This yields a system of N simultaneous linear equations

$$\frac{1}{2\pi} \sum_{j=1}^{N} K_{ij} \cdot \gamma_j + \psi_b = Z_i \cdot U_\infty \cdot \cos \alpha - X_i \cdot U_\infty \cdot \sin \alpha \qquad (2)$$

i = control point.

The Kutta condition is

$$\gamma_1 + \gamma_N = 0 \qquad (3)$$

The influence of the wake is simulated by continuing the vortex sheet with constant γ downstream. It starts aligned with the bisector and turns slightly downstream into the direction of the oncoming flow.

A specified pressure distribution can be achieved by successive iteration of the ordinates Z_i, while the abscissae X_i remain constant. The ordinates Z_i^m of the mth iteration are determined by replacing the singularities of the (m-1)th iteration by the prescribed values γ_p:

$$Z_i^{(m)} = \frac{1}{\cos \alpha} \left(X_i \cdot \sin \alpha + \psi_b^{(m-1)} + \sum_{J=1}^{N-1} K_{ij}^{(m-1)} \cdot \gamma_p \right) \qquad (4)$$

The iteration ends if either the condition

$$\max_i \{\Delta Z_i\} = \max_i \{|Z_i^{(m)} - Z_i^{(m-1)}|\}$$

or

$$\max_1 \{\Delta C_{Pi}\} = \max_1 \{|C_{Pi}^{(m)} - C_{Pi}^{(m-1)}|\} \qquad (5)$$

is met.

As a first step for transonic design, the subsonic pressure distribution for a starting geometry is computed for M = 0 (M = Mach number). This wing section is then analysed in the high-speed region with the BGKJ program[24] coupled with a semi-inverse boundary layer method[18]. The target pressure distribution at transonic speed is compared with the BGKJ result and the differences (fig. 2) are scaled down to the subsonic regime according to a modified Kármán-Tsien rule. A new inverse step follows after modifying the subsonic pressure distribution. This iteration loop usually converges within 5-10 design cycles.

Sample design cases for inviscid and viscous design were reported[13] as well as applications to three-dimensional design. The purpose of this paper is to show successful applications and comparison with experiments for designs derived with the code and to present an improved viscous design code.

Third International Conference on Inverse Design Concepts and Optimization in Engineering Sciences (ICIDES-III), Editor: G.S. Dulikravich, Washington D.C., October 23-25, 1991.

III. APPLICATIONS OF DIVA-2D AND COMPARISON WITH EXPERIMENT

A typical task for a design engineer is to increase speed flexibility and for this purpose we tried to transpose the known characteristics of a datum airfoil designed for Cl = 0.565/M = 0.73 to M = 0.75 at constant lift and moment for a given thickness. Fig. 3 shows the computed result of the datum airfoil as well as the target which was slightly modified to keep local Mach numbers below 1.2. The required thickness was 11.5%, whereas the datum airfoil had 11.93%.

The measured pressures at off-design demonstrate the successful design. At this lift the new design shows nearly the same drag, whereas at lower lifts a significant improvement is demonstrated which is 5 drag counts (1 d.c. = 0.0001) better than the pure thickness effect. As the shock-strength at higher lifts turned out to be higher than expected, a geometry check was performed.

Whereas the maximum deviations in curvature are concentrated on the lower side and the nose region, the slope change on the upper surface seemed to be small (fig. 4). The computed iso-Mach contours however revealed a bucket in the sonic line. This is due to the coalescence of the compression waves reflected by the surface changing from convex to concave curvature. Such a coalescence results in the earlier formation of shock waves which was confirmed by Schlieren-pictures (fig. 5).

The new airfoil served as a fixed camber reference for a variable camber (VC) airfoil - a concept which was reported for example in[25]. A scheme of a system solution is given in fig. 6 using the existing high-lift system. The camber variation is achieved by small fowler motions, where the wheels of the flap carriage are guided by two individual tracks in such a way, that in VC-operation the flap body slides underneath the spoiler trailing edge. The control track and the flap upper surface have to be shaped such, that camber variation is performed with minor discontinuities in surface curvature.

As a consequence to this proposal - which allows only positive camber deflections - the design point is shifted to lower lifts where the wing is optimized with respect to minimum drag with relaxed off-design constraints. This will be the setting at low altitudes, low weight (medium range mission) and towards the end of cruise. At start of cruise, step climbs to higher altitudes or increased weight the lift demand is satisfied by discrete camber/fowler settings resulting in the envelope in fig. 6.

A first VC-airfoil was developed in reference to the fixed camber optimum airfoil mentioned above. For the design of the VC-airfoil criteria for a "VC-suited" pressure distribution were concluded which are illustrated in fig. 7. At the design point (Cl ≈ 0.45)

- the supersonic region should be confined to X/C ≈ 0.4 and terminated with a weak shock;
- the region close to Cp* should exhibit small gradients in order to guarantee a stable shock position in off-design conditions;
- the subsonic recompression gradients should not be larger than dCp/dx=3;
- the trailing edge recompression gradient should be degressive (Stratford-Type), which is benefical for the turbulence structure and hence reduces the friction drag;
- the balance of front loading and rear loading at the lower surface should be altered towards front loading to reduce the adverse effect of pitching moment.

Third International Conference on Inverse Design Concepts and Optimization in Engineering Sciences (ICIDES-III), Editor: G.S. Dulikravich, Washington D.C., October 23-25, 1991.

According to these criteria the airfoil was designed by DIVA.

A wind tunnel model with three VC-flap settings was tested. For each level of efficiency M*L/D the VC-airfoil demonstrated a greater flexibility in the Cl-M-plane and the maximum efficiency was increased by 12% (fig. 8). A calculation of the pressure distribution according to the VC-control law for four settings adjusted to the lift demand (fig. 9) incorporated the surface imperfections due to the discrete variation. The effects in pressure and drag are negligible which was confirmed by experiment.

In the framework of the national research program ZKP-TLFI natural laminar flow (NLF) investigations were performed. In comparison to a conventional airfoil the typical NLF design features are depicted in fig. 10. Laminar flow runs of 60% and 80% of the exposed wing area were assumed resulting in some 10% of aircraft cruise drag reduction. The required continuous acceleration imposes the problem of increased recompression gradients with potential separation and shock-wave boundary layer interaction upon the designer. In off-design conditions laminarity loss due to pronounced suction peaks and corresponding Tollmien-Schlichting instability or cross-flow instability with changing gradients versus lift may occur. A tool to shift the laminar bucket with increasing lift demand is available by the VC concept.

A first NLF-airfoil was designed with DIVA for a lift of 0.4 and M = 0.73 and tested. Fig. 11 shows a comparison of measurement and computation. The transition free drag is ~40% of the turbulent level and even the turbulent level turned out to be competitive to a conventional airfoil of same thickness.

Finally the survey of 2D-designs is concluded by an example for hybrid laminar flow control (HLFC). An arbitrary starting geometry was chosen (NACA 0008) and the result was established after 20 iterations (fig. 12, 13), a further proof of the versatility of the DIVA method.

IV. SAMPLE DESIGN CASE FOR 3D-DERIVATIVE DESIGN

In view of the difficulties of producing a design method for airfoils it is not surprising that no completely successful solutions for the three-dimensional transonic case are available. A combination of wind tunnel results of a datum aircraft with a direct-inverse design method seemed to be more promising though not satisfying from the scientists' viewpoint. Subsonic pressure distributions (up to M = 0.6) are used to design a zeroth iteration geometry by means of the subsonic inverse code. These sections include the subsonic cross-flow and viscous effects. If a transonic pressure distribution is then prescribed as target distribution, the DIVA method can design an airfoil representing the measured three-dimensional distribution when analysed with a two-dimensional direct code. This airfoil deviates from the actual section profile: it is an analogous numerically adapted profile.

Starting from this state, a redesigning of the wing is possible by improving the target pressure distributions in selected spanwise stations. The result is a new set of analogous profiles. The differences between the two sets of profiles have to be added to the datum wing sections and the new wing is defined. This may sound artificial, but is a quite reliable way to incorporate interference aspects in the design of a new wing. In[13] already two applications of this DIVA-3D were reported.

Third International Conference on Inverse Design Concepts and Optimization in Engineering Sciences (ICIDES-III), Editor: G.S. Dulikravich, Washington D.C., October 23-25, 1991.

A recent successful application was the validation of a trailing-edge modification on the Airbus A340 (fig. 14). A 3.75% chord extension combined with a camber increase was designed at the outboard engine position. The effect of the modification is a reduction of the lift break due to the engine and hence a gain in induced drag as well as a pressure drag improvement (fig. 15). The estimate in fig. 15 is in surprisingly good correlation with the subsequent test result.

V. AN IMPROVED DIRECT-DESIGN CODE WITH A HIGH ACCURACY VISCOUS TRANSONIC ANALYSIS CODE

The high accuracy of the viscous transonic analysis code SGW[19-21] was coupled with a new direct design method called REPAN, a name, which is an abbreviation of reverse panel method. The basic principle is the formulation as a minimization problem, which is adapted in the form

$$E = \sum_{i=1}^{M} \sigma_i [C_{pi}(\vec{a}) - C_{pi}^{target}]^2 \stackrel{!}{=} \text{Min} \qquad (6)$$

Thus we look for a profile, which fits best to the target-Cp-distribution at M discrete stations. The minimum of the merit function E is done with an algorithm due to Levenberg and Marquardt[26]. The geometry to be designed is given in terms of a set of design parameters $\vec{a}$, which specify the location and shape of the profile. Starting from an initial geometry the minimization is done by variing these parameters. To perform a minimization step, a matrix, relating pressure changes and parameter changes, has to be computed. This matrix is just the Jacobian of the transformation from parameters to pressures (= analysis code!). It is computed numerically.

The set of parameters, which specify the actual geometry, splits into two groups: global and local ones. The former include the chord angle and translation vector components between profiles for multi-element cases (fig. 16). They specify the location of the profiles without altering the shape. The profile shape is defined - separately for lower and upper side - by Bezier splines.

This technique uses a set of points $\vec{r}_i^B = (x_i^B, z_i^B), i = 1...n$ ('Bezier-knots', fig. 16) to define a curve with position vector $\vec{r}(t) = (x(t), z(t))$ by the parametric equation

$$\vec{r}(t) = \sum_{i=0}^{n} \vec{r}_i^B B_{n,i}(t) \qquad (7)$$

with

$$B_{n,i}(t) = \binom{n}{i} t^i (1-t)^{n-i} \quad , \quad 0 \leq t \leq 1 \qquad (8)$$

$\binom{n}{i}$ is the i^{th} binomial coefficient of order n.

The curve defined in this way has the following properties:

(i) The curve passes through the first and last Bezier knot for parameter values t = 0 resp. t = 1. This follows immediately from the definition, because we have

Third International Conference on Inverse Design Concepts and Optimization in Engineering Sciences (ICIDES-III). Editor: G.S. Dulikravich, Washington D.C., October 23-25, 1991.

$$B_{n,i}(0) = \begin{cases} 1 & i = 0 \\ 0 & i \neq 0 \end{cases}, \quad B_{n,i}(1) = \begin{cases} 0 & i \neq n \\ 1 & i = n \end{cases} \tag{9}$$

and the above sum reduces to

$$\vec{r}(0) = \vec{r}_0^B \; ; \; \vec{r}(1) = \vec{r}_n^B \tag{10}$$

(ii) Taking the derivative at t = 0 it follows, that

$$\dot{\vec{r}}(0) = n(\vec{r}_1^B - \vec{r}_0^B) \tag{11}$$

which is equivalent to

$$\left.\frac{dz}{dx}\right|_{t=0} = \frac{\dot{z}(0)}{\dot{x}(0)} = \frac{z_1^B - z_0^B}{x_1^B - x_0^B} \tag{12}$$

The derivative of the curve at the beginning is therefore given by the tangent of the first Bezier segment. An analogous result is valid at the endpoint t = 1.

These properties can be used to impose simple constraints on airfoil geometry. For airfoil design, $\vec{r}(t)$ represents a lower or upper side and t = 0|1 corresponds to the leading/trailing edge. The $\{x_i\}$ coordinates of the points of the initial airfoil are used to establish a corresponding set of parameters $\{t_i\}$; the Bezier ordinates - excluding the first and last one - z_i^B, i = 1, ...n-1 are the local design variables mentioned above. These will be determined in such a way, that the sum of squared pressure deviations is minimized.

As the airfoil is composed of two parts, some restrictions on Bezier knots have to be imposed to insure continuity of values, first and second derivative at the connection point i.e. the leading edge:

- The first Bezier knot is placed at the leading edge and held rigid.
- The second one has the same x-value as the first one: $x_1^B = x_0^B$. This serves for a normal tangent at the leading edge (see fig. 16).
- The ordinate z_1^B of the second Bezier knot is related to the curvature at the leading edge. This fact can be used in two ways: (1) relating the ordinates of the first Bezier Knots on the lower and upper side serves for continuous curvature with a value, determined by the design process, or (2) we can do a design with specified leading edge radius just by fixing the ordinates to their appropriate values. The design in fig. 19 is done with continuous but variable leading edge radius.

Similar conditions hold at the trailing edge. The last Bezier knot is placed at the last point of the lower resp. upper side and held rigid thereby keeping the trailing edge thickness constant. Additionally we could prescribe the tangent of the last Bezier segment thus performing a design with specified trailing edge angle.

The minimization of the sum of squared pressure deviations is done with an algorithm after LEVENBERG and MARQUARDT. It is an elegant method that combines the inverse Hessian method and the steepest descent method by introducing a factor ("Marquardt-factor"), which switches smoothly between these extremes.

Third International Conference on Inverse Design Concepts and Optimization in Engineering Sciences (ICIDES-III), Editor: G.S. Dulikravich, Washington D.C., October 23-25, 1991.

Far from the minimum (large factor) steepest descent steps are performed whereas approaching the minimum this factor is reduced automatically thus switching to inverse Hessian steps.

This method works very well in practice and has become the standard of nonlinear least squares routines. Details of the method may be found in[26]. Fig. 17 shows a simplified flow chart of the REPAN-design procedure.

In the past authors used the least squares method for solving the profile design. Labrujere[27] prescribes tangential velocities and uses Legendre polynomials for the shape description. He did not include global parameters. Bristow[28] used panel direction angles as design variables. He had to do additional Cp-control to achieve smooth profiles.

To formulate the inverse problem as a minimization problem has several advantages:

(1) As the inverse step is purely algebraic, each analysis code can be run in the reverse direction. The present method is optimized for coupling with panel codes - concerning calculation time - but any given code, even large scale ones as used in our test case two, can be used as well. But it should be mentioned, that additional code dependent research is required, to obtain solutions in reasonable time. Calculation time is the crucial point of this approach.

(2) The geometry definition includes the possibility of geometrical constraints, such as fixed trailing edge thickness, normal tangent at the leading edge, prescribed trailing edge angle. Curvature control during design process is possible by additional control of the turn-around angles at the Bezier-knots (fig. 16). This option is needed in critical cases only.

(3) From a practical point of view, flexibility in cases of partly unphysically specified target pressures, is the most important feature. Although we know, that constraint conditions are to be fulfilled by the Cp-target values[29], there are two situations, in which unproperly specified Cp's are unavoidable: measured Cp-distributions (because of measurement errors) and 2D-Cp-cuts from 3D-configurations (because of missing stagnation point). In such ill-posed cases we solve for the "nearest" profile in the least square sense. Additionally, if we have a guess of some unphysical target pressures, they can be "switched off" by setting the corresponding σ equal to zero. For small regions of the profile - where "small" means small with respect to the distance of Bezier-knots - we are allowed to do that, because the variation of a local parameter affects a reasonable part of the profile (in fact, the whole side, because Bezier-splines are nonlocal) and therefore the geometry is determined by the influence of nearby pressures, which are assumed to be correct. This has been proven to be helpful in the vicinity of the stagnation point and the trailing-edge region.

As a first validation example test case 2 from ref.[13] was chosen, which shows the design potential of a typical supercritical airfoil with rear loading. By means of a calculation with the BGKJ code including semi-inverse boundary-layer coupling, the pressure distribution in fig. 18 was obtained. Considerations concerning a reduction of rear loading led to the modified target distribution also depicted in fig. 18.

In the case of DIVA a liquid surface is designed where the displacement thickness has to be subtracted whereas the REPAN code solves directly for the solid geometry by applying viscous iteration in the analysis. The geometry modifications delivered from both codes are given in fig. 19 as well as a comparison of

Third International Conference on Inverse Design Concepts and Optimization in Engineering Sciences (ICIDES-III), Editor: G.S. Dulikravich, Washington D.C., October 23-25, 1991.

the last REPAN iteration with respect to the target pressures which is satisfactorily matched. The redesigned airfoils are quite similar at first sight but the REPAN airfoil does not meet the required thickness (12.55% instead of 12.93%) and a significant deviation of the trailing-edge camber can be noticed. This corresponds to not properly specified trailing-edge thickness. As mentioned above this quantity is held fixed during design process. Cp-control is done everywhere except at three stations near stagnation point.

In order to compare the two different designs, the airfoils were calculated for the same lift and Machnumber with the BGKJ code incl. boundary layer iteration. While the agreement with the target distribution (fig. 20) for the DIVA airfoil is still quite good the REPAN airfoil shows a larger deviation. This is due to the local change at the trailing-edge and corresponding higher angle of attack for a given lift. At the design point the DIVA airfoil shows 1.5 d.c. less drag and a 43% reduction in pitching moment with respect to the datum airfoil. The REPAN airfoil however exhibits 2.5 d.c. excess drag despite the reduced thickness. If the thickness is scaled to the target value additional 2 d.c. have to be added; i.e. that the improvement at lower lifts in fig. 20 is diminished. Hence it can be concluded that at the present state further investigations devoted to the accuracy of the trailing-edge region seem to be necessary in order to enhance the viscous design modus.

VI. Application of a Numerical Optimization Routine

The design methods described so far require an experienced designer with physical insight into the trade-offs of the pressure distribution he specifies. But what is the ideal pressure distribution with respect to different objectives under practical constraints? A further class of design methods using optimization routines may give an answer to this.

Coupling of a gradient method with two transonic aerodynamic analysis codes
In an optimization process a so-called 'objective function' $F(\bar{X})$ is to be minimized (or maximized) subject to a set of (m) given constraints $G_j(\bar{X}) \leq 0$, $j = 1,m$ with $\bar{X}$ being the vector of the design variables.

Relating to the design of an airfoil the variables would have to define the airfoil shape while the objective function would be a characteristic of this airfoil, for example the drag coefficient Cd, at a given design point. To keep the design inside certain boundaries and allow the optimization code to converge faster some constraints on other airfoil characteristics such as lift, pitching moment etc. or geometrical constraints like the thickness, camber, trailing edge thickness should be imposed.

Though a lot of different optimization techniques can be applied to approach this design problem it is evident that, among the existing nonlinear minimization routines, the Vanderplaats gradient method[6,30,31,35] is the most widely used[32,33,34,36].

This optimization code called CONMIN (Constrained Function Minimization) is part of COPES, a Control Program for Engineering Synthesis. In this code the strategy, one-dimensional search direction and optimizer can be chosen by the user and adapted to a certain problem.

Fig. 21 shows the principle of the design process. The optimization direction finding process of COPES is illustrated for the two-variable case. First each

Third International Conference on Inverse Design Concepts and Optimization in Engineering Sciences (ICIDES-III), Editor: G.S. Dulikravich, Washington D.C., October 23-25, 1991.

component of the design variable vector $\bar{X}$ is varied starting from $\bar{X}^\circ$ (initial design variables) and leading to a gradient $\nabla F(\bar{X}^\circ)$. This could be taken as the search direction $\bar{S}$ but because of convergence problems for nonlinear functions the "method for conjugate directions" is being prefered. In this case $\bar{S}$ is calculated from the gradient and the last search direction by

$$\bar{S}^q = -\nabla F^q + |\nabla F^q|^2 \,/\, |\nabla F^{q-1}|^2 \cdot \bar{S}^{q-1} \qquad (13)$$

If the design comes in contact with a constrained region the search direction $\bar{S}$ is found taking the gradient ∇G_j of the active constraint and ∇F of the objective function. In addition a "push off factor" is used to direct the search vector in the region where the feasible sector (allowed designs) and the usable sector (designs with improved objective function) overlap. This region is called the usable feasible sector. Since every iteration step needs n+3 analysis, i.e. about 10n+30 calculations for one design, which has to be done by a precise, time consuming (therefore expensive) aerodynamic analysis code, COPES offers another design mode to approach these problems. Here the objective function and the constraints are developed as second order Taylor series expansions :

$$F(\bar{X}) = F^\circ + \Delta\bar{X}^T\nabla F + 1/2\Delta\bar{X}^T[H]\,\Delta\bar{X}$$

$$G_j(\bar{X}) = G_j^\circ + \Delta\bar{X}^T\nabla G_j + 1/2\Delta\bar{X}^T[H]_j\Delta\bar{X}$$

with
$\Delta\bar{X} = \bar{X}-\bar{X}^\circ$
$F = F(\bar{X})$ at $\bar{X}^\circ$
$[H]$ = Hessian Matrix
∇F = vector of first partial derivatives (14)

Using this mode of the code assures accelerated convergence because data calculated in one iteration step are still known in another step, which is not the case for the standard design mode. Also only one exact analysis is needed for every iteration, whereas the first Taylor series expansion requires 1+n+n*(n+1)/2 additional analysis in this approximation mode. So the method should be used for less than twenty design variables to be more efficient than the standard finite difference mode. Through the Taylor series the user is also able to prescribe a solution and accelerate the convergence of the code even more if he has some good designs to start from. In fig. 21 the approximation mode is depicted.

An airfoil shape can be described by the design variables either in the form of an analytical function or a function of aerodynamic origin, i.e. an airfoil library (fig. 21) or so-called aerofunctions. The analytical functions describe an airfoil by polynomials of higher order, which leads to a large number of design variables or problems of fitting the polynomials together if the airfoil is divided into different sections. Also some unrealistic shapes may occur because the solutions are purely mathematical.

In order to start the process the analytical functions are fitted on an initial shape and coefficients are obtained. These coefficients together with the Mach-number, the angle of attack (or the lift coefficient) and the given set of constraints are needed by the program to optimize the objective function. The coefficients are the design variables being perturbed by the optimizer to reach an optimal design. A new shape is prescribed by the linear combination

$$\bar{Y} = \bar{X}_0 + X_1\bar{F}_1 + X_2\bar{F}_2 + \ldots + X_n\bar{F}_n \qquad (15)$$

with $(X_j,\ j = 0,n)$ design variables (shape coefficients)
$(F_j,\ j = 1,n)$ vector with analytical shape functions

Third International Conference on Inverse Design Concepts and Optimization in Engineering Sciences (ICIDES-III), Editor: G.S. Dulikravich, Washington D.C., October 23-25, 1991.

With respect to the orders of the analytical function n, a compromise has to be found between a large number of variables and a good approximation of an airfoil shape. The last also depends on the type of function that will be used, since some functions tend to reveal oscillations even at higher polynomial orders. Generally the order should not exceed twenty on the whole airfoil because the analysis especially with a viscous code will be too expensive.

Similar to the preceding definition functions of aerodynamic origin are applied by superposition of different airfoil shapes from an airfoil library with a linear combination (see fig. 23). In this case the Y-coordinates (shape functions) are defined numerically and not by analytical functions. By adding special airfoils to the library that fulfil some desired constraints it is possible to impose these constraints on the optimized shape without giving this information to the optimization code. Therefore these constraints do not have to be evaluated and checked for their influence on the objective function during every design loop, which means saving time.

Another type of functions with aerodynamic origin are quoted as "aerofunctions" in some references[32,36]. Here pressure distribution shape functions are superimposed on an initial pressure distribution and the perturbations are related to different airfoil shapes. This also promises to provide some realistic shapes as optimum solutions. In the present design task an airfoil library is used to define the shape but later the program should be expanded with regard to analytical functions.

The viscous BGKJ-code[18,24] and the SGW-code[19-21] are both coupled with COPES. Especially the latter provides a high accuracy analysis tool to calculate coefficients describing the characteristics of an airfoil at the design point. This is needed to make the direct design competitive against the inverse design methods.

Test cases

To validate the successful coupling a testcase from Vanderplaats[31,35] is being calculated with the BGKJ-code as analyser. With a given set of four NACA airfoils and two basic shapes to impose geometric conditions an airfoil with maximum lift for $M_\infty = 0.1$ and $\alpha = 6°$ should be found that satisfies the constraints mentioned in fig. 22.

In this figure the initial airfoil, the reference airfoil and the optimized airfoil after 42 iterations without and 17 iterations with Taylor series expansion are compared. Despite the different analyser the result differs only slightly from the reference, whereas the result without Taylor series expansion is still not converged.

For the second test case a library of six transonic airfoils is given to redesign the VA2 airfoil at $M_\infty = .73$, $Cl = .552$ for minimum drag. Since the design was already performed by the DIVA-code with the BGKJ-code as analyser the role of constraints and the influence of the library on the design should be investigated.

Fig. 23 illustrates the set of airfoils and constraints for which the converged solution after 30 iterations does not give a realistic shape comparable with the one designed by DIVA. This is also the case if the constraints are relaxed or a pressure gradient is prescribed. Only if the Cm-constraint is omitted the optimizer converges after 25 iterations showing an airfoil that resembles more the VA2 type, especially concerning the rear loading. The pressure distribution

Third International Conference on Inverse Design Concepts and Optimization in Engineering Sciences (ICIDES-III), Editor: G.S. Dulikravich, Washington D.C., October 23-25, 1991.

emphasizes this circumstance. A solution close to the DIVA optimized airfoil however can be found if this airfoil is included in the library. Therefore it can be concluded that for the given task the airfoil library is not sufficient to design an airfoil as good as the DIVA airfoil, for which off design aspects are also considered.

For the third test case COPES is coupled with the SGW-code to redesign the VA7 airfoil. This basic VC-airfoil should be optimized with respect to minimum drag at the design point M = 0.74, Cl = 0.45 and constant thickness. The optimization result after 19 iterations is depicted in fig. 24. Though the changes are only moderate a drag reduction of one count is reached. Again the library of four airfoils (see fig. 24) does not allow a better result starting from the VC-airfoil with only small changes in the shape for every design iteration.

Nevertheless this combination of COPES and SGW as analyser promises to work more efficient if analytical functions are used to describe the airfoil.

VII. Conclusion

Applications of the direct-inverse analogy-method (DIVA) for the design of supercritical airfoils and wing modifications have been presented and verified by experiment.

The method yields results with high accuracy even for flows with strong shocks. It is as simple as possible from the user's point of view and merely needs a pressure distribution as input. The influence of the starting geometry (i.e. nose shape) is negligible.

An application to three-dimensional design is possible, provided an initial wing shape and pressure measurements are available. Incremental improvements of wing performance may be assessed with an accuracy less than 1 per cent.

Due to the modular structure of the computing concept, the transonic code is exchangeable, and improved codes can be implemented. So the DIVA method is a comprehensive tool for practical wing design. Future applications by using 3D-Euler results including viscous corrections instead of measurements are planned in order to obtain further refinements of the design before testing it.

A new residual correction design code with complete semi-inverse boundary layer iteration in the design cycle was presented which may enhance the accuracy of trailing-edge design for highly loaded airfoils. Further work in this field is envisaged.

Finally applications of a numerical optimization routine coupled with two viscous full potential solvers were discussed. A significant dependence of the results upon the airfoil library to be composed was found. A more general geometry description seems of paramount interest. However the designer with expertise in specifying pressures may win hands down in this competition.

VIII. REFERENCES

1. L.R. Miranda, **'Application of computational aerodynamics to airplane design'**, J. Aircraft, **21** (6)(1984).
2. P. Rubbert and M. Goldhammer, **'CFD in design: An airframe perspective'**, AIAA paper No. 89-0092 (1989).
3. R.C. Lock, **'Aerodynamic design methods for transonic wings'**, Aeron. Journal, Jan. 1990, 1-16.
4. G.Y. Nieuwland, **'Transonic potential flow around a family of quasi-elliptical aerofoil sections'**, NLR-TR-T.172, National Lucht- en Ruimtevaart Laboratorium, Amsterdam (1967).
5. F. Bauer, P. Garabedian and D. Korn, **'A Theory of Supercritical Wing section, with Computer Programs and Examples'**, Springer- Verlag, 1972.
6. R.M. Hicks, E.M. Murman and G.N. Vanderplaats, **'An assessment of airfoil design by numerical optimization'**, NASA TM X-3092 (July 1974).
7. L. Carlson, **'Transonic airfoil design using cartesian coordinates'**, NASA-CR 2578 (April 1976).
8. T.L. Tranen, **'A rapid computer aided transonic airfoil design method'**, A.I.A.A. Paper No. 74-501 (June 1974).
9. G.B. Mc Fadden, **'An artificial viscosity method for the design of supercritical airfoils'**, NASA-CR-158840 (1979).
10. H. Sobieczky, **'Supercritical airfoil and wing design'**, Ann. Rev. Fluid Mech., **16**, 337-363 (1984).
11. G. Volpe, **'The inverse design of closed airfoils in transonic flow'**, A.I.A.A. paper 83-0504.
12. G. Volpe and R.E. Melnik, **'Method for designing closed airfoils for arbitrary speed distributions'**, J. Aircraft, 1986, **23**, (10), 775-782.
13. E. Greff and J. Mantel, **'An Engineering Approach to the inverse transonic wing design problem'**, Comm. in Appl. Num. Meth., Vol. 2, (1986), 47-56.
14. H. Sobieczky, **'Research on inverse design and optimization in Germany'**, Proc. of the 2. Int. Conf. on Inv. Design Concepts in Eng. Sciences, Oct. 26-28, 1987, Penn-State-University, Pennsylvania
15. R.L. Campbell and L.A. Smith, **'Design of transonic airfoils and wings using a hybrid design algorithm'**, SAE-paper No. 871756, (1987).
16. L.A. Carlson, **'A direct-inverse method for transonic and separated flows about airfoils'**, NASA CR-4270, Jan. 1990.
17. M. Drela and M.B. Giles, **'ISES - a two-dimensional viscous aerodynamic design and analysis code'**, AIAA-paper No. 86-0424, (1987).
18. P. Thiede, G. Dargel and E. Elsholz, **'Viscid-inviscid interaction analysis on aerofoils with an inverse boundary layer approach'**, in Recent Contribution to Fluid Mechanics (Ed. W. Haase), Springer-Verlag, 1982.
19. G. Dargel and P. Thiede, **'Viscous transonic airfoil flow simulation by an efficient viscous-inviscid interaction method'**, AIAA paper 87-0412, Jan. 1987.
20. T. Holst, **'Viscous Transonic Airfoil Workshop'**, AIAA paper 87- 1460, June 1987, Honolulu.
21. J. Mertens, K.D. Klevenhusen and H. Jakob, **'Accurate transonic wave drag prediction using simple physical models'**, AIAA Journal, **25**(6)(June 1987), 799-805.
22. H.J. Oellers, **'Die inkompressible Potentialströmung in der ebenen Gitterstufe'**, WGL Jahrbuch, 1962.
23. A.I. Ormsbee, **'Multiple element airfoils optimized for maximum lift coefficient'**, J. Aircraft, **10**(12)(Dec. 1972).

24. F. Bauer, P. Garabedian, D. Korn and A. Jameson, **'Supercritical wing sections I, II, III'**, Lecture Notes in Economics and Mathematical Systems, **66**(1972), **108**(1975), **150**(1977), Springer- Verlag, Berlin/Heidelberg/New York.
25. E. Greff, **'Aerodynamic Design and Integration of a Variable Camber Wing for a New Generation Long/Medium Range Aircraft'**, ICAS-88-2.2.4, Jerusalem/Israel.
26. P.E. Gill, W. Murray and M.H. Wright, **'Practical optimization'**, Academic Press, Inc., 1981.
27. Th.E. Labrujere, **'Multi-element airfoil design by optimization'**, ICAS Proceedings, Volume 1978, 305-312.
28. D.R. Bristow, **'A new surface singularity method for multi-element airfoil analysis and design'**, AIAA-paper No. 76-20,(1976), 14th Aerospace science meeting.
29. G. Volpe and R.E. Melnik, **'Role of constraints in inverse design for transonic airfoils'**, AIAA Journal, **22**(12), (Dec. 1984), 1770-1778.
30. G.N. Vanderplaats, **'CONMIN-A Fortran Program for Constrained Function Minimisation'**, NASA TM X-62, 282, August 1973.
31. G.N. Vanderplaats and R.M. Hicks, **'Numerical airfoil optimization using a reduced number of design coordinates'**, NASA TM X-73, 151, July 1976.
32. J. Reneaux and J.J. Thibert, **'The use of numerical optimization for airfoil design'**, AIAA-paper No. 85-5026, (1985).
33. P. Krantz, S.G. Hedman, **'Airfoil Optimization'**, J. Aircraft, 1986, **23**(5), 355-335.
34. K.-W. Bock, **'Aerodynamic Optimization'**, ICAS-88-4.4.1, Jerusalem/Israel.
35. G.N. Vanderplaats, **'Efficient Algorithm for numerical airfoil optimization'**, J. Aircraft, **16**(12), (Dec. 1979).
36. P.V. Aidala, W.H. Davis, W.H. Mason. **'Smart aerodynamic optimization'**, AIAA-paper No. 83-1863, (1983).

Third International Conference on Inverse Design Concepts and Optimization in Engineering Sciences (ICIDES-III), Editor: G.S. Dulikravich, Washington D.C., October 23-25, 1991.

IX. FIGURES

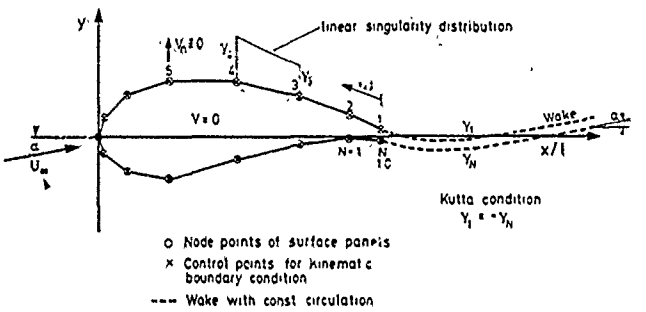


Fig. 1 Singularity Distribution for Subsonic Inverse Code

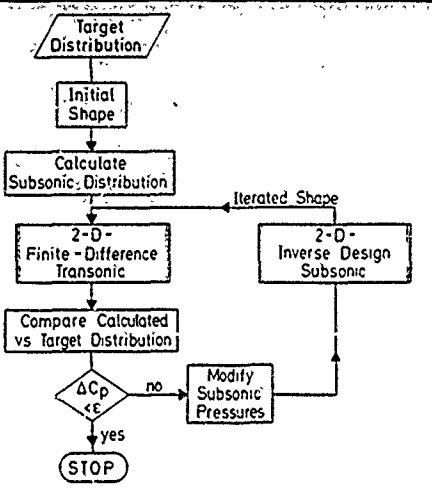


Fig. 2 Direct Inverse Analogy (DIVA) Method

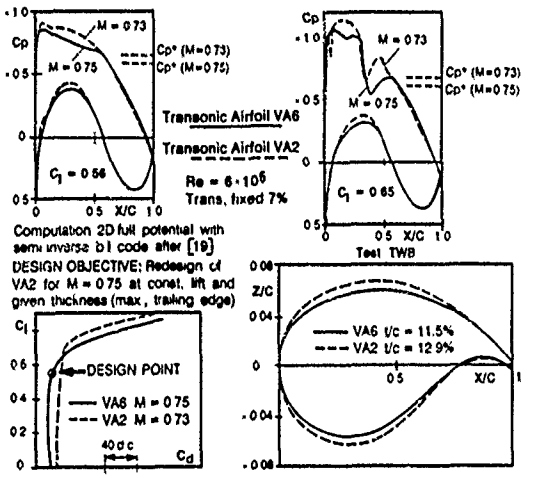


Fig. 3 Redesign of VA2 Airfoil at Increased Speed

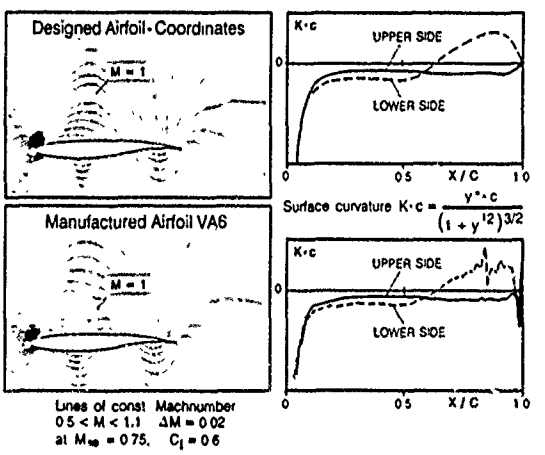


Fig. 4 Effect of Manufacture Tolerances



Fig. 5 Schlieren-Picture Showing Coalescence of Compression Waves at M = 0.75; C_l = 0.602

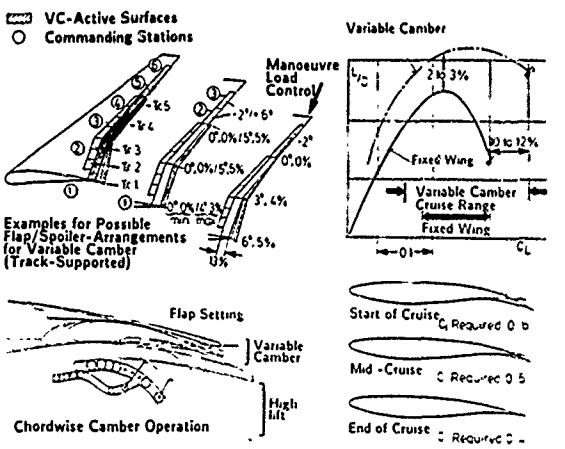


Fig. 6 Principle of Variable Camber Operation

Third International Conference on Inverse Design Concepts and Optimization in Engineering Sciences (ICIDES-III), Editor: G.S. Dulikravich, Washington D.C., October 23-25, 1991.

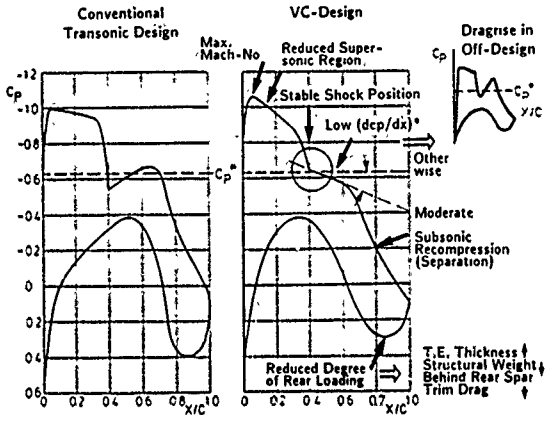


Fig. 7 Considerations on Properly Prescribed Pressure Distributions for Variable Camber Airfoil

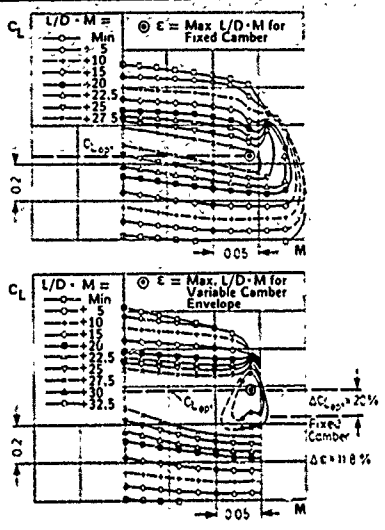


Fig. 8 Aerodynamic Efficiency of the VC - Airfoil in Reference to the Fixed Camber Design VA6

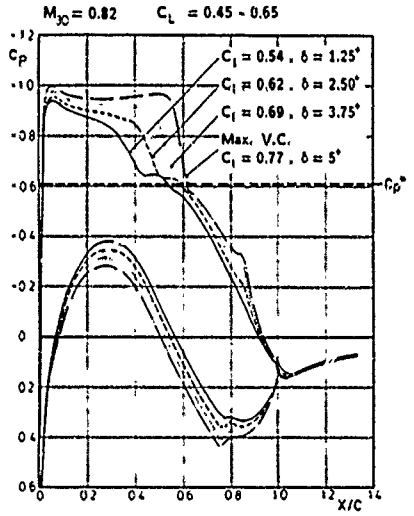


Fig. 9 Pressure Distribution of VC - Airfoil with Increasing Lift

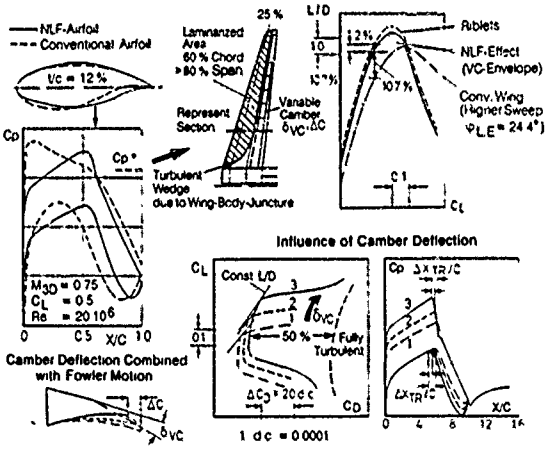


Fig. 10 Principle and Potential of NLF - Technology

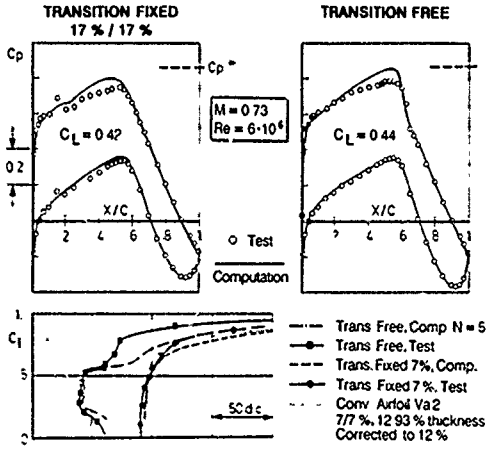


Fig. 11 Comparison of Experiment / Theory for NLF - Airfoil

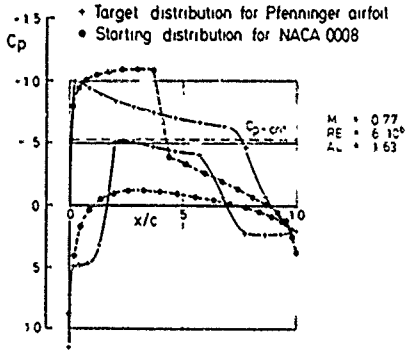


Fig. 12 Design of HLFC - Airfoil Target Distribution

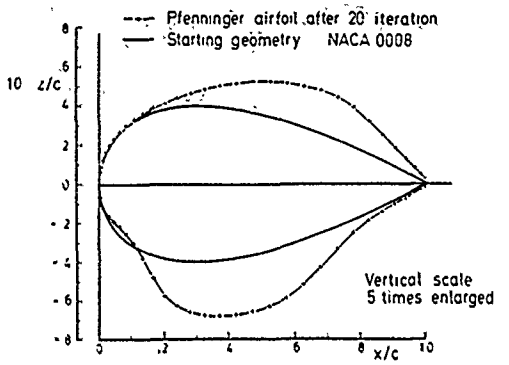


Fig. 13 Design of HLFC - Airfoil
Comparison of Iterated Shape With Starting Shape

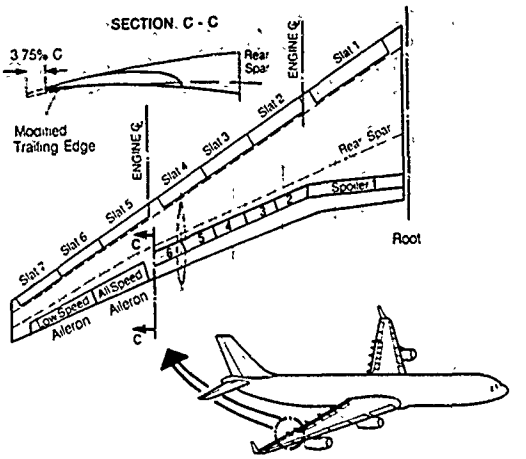


Fig. 14 Trailing Edge Extension on Airbus A 340

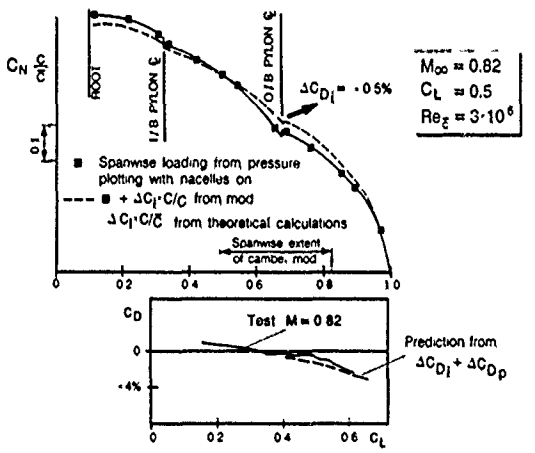


Fig. 15 Efficiency of Drag Prediction Using DIVA - 3D

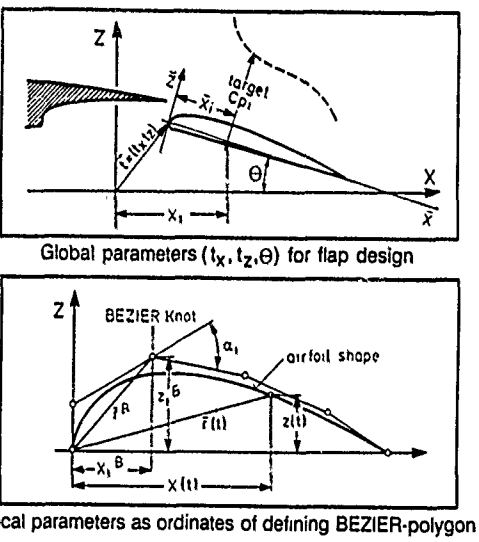


Fig. 16 Local and Global Parameters of Defining BEZIER Polygon

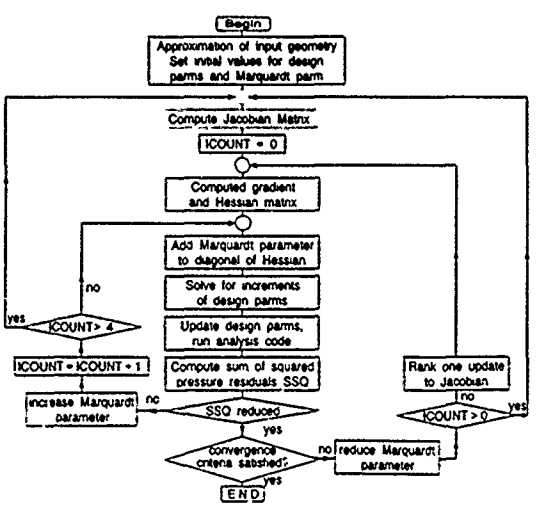


Fig. 17 REPAN Flow Chart

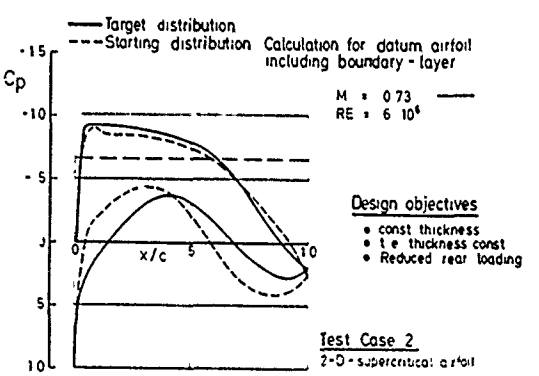


Fig. 18 Testcase 2 for 2D - Viscous Design

Third International Conference on Inverse Design Concepts and Optimization in Engineering Sciences (ICIDES-III), Editor: G.S. Dulikravich, Washington D.C., October 23-25, 1991

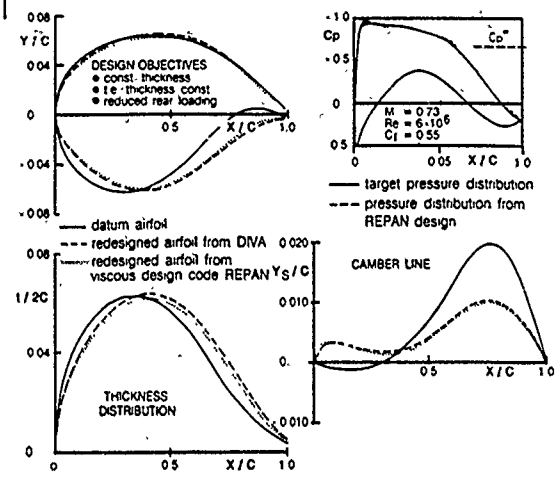


Fig. 19 Geometry Modifications on a Supercritical Airfoil

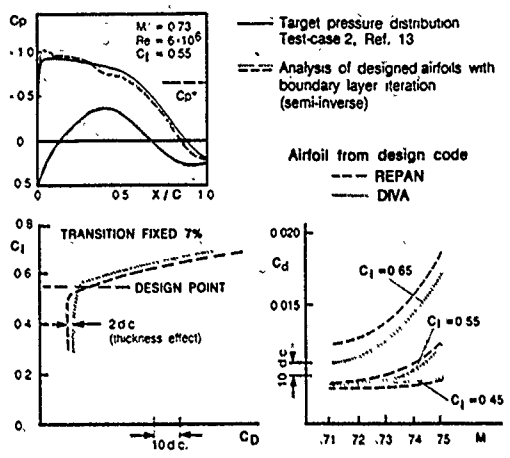


Fig. 20 Accuracy of 2D - Viscous Design

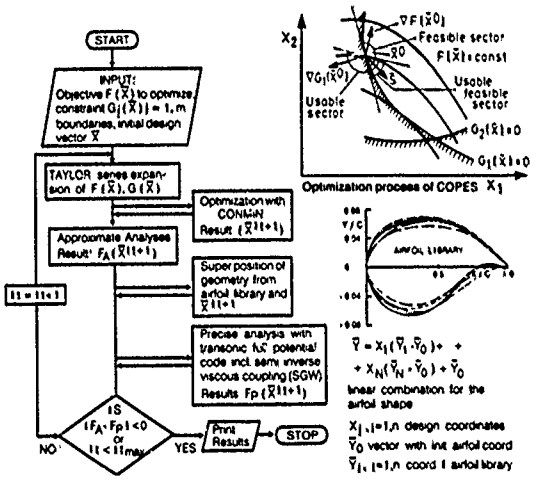


Fig. 21 Principle Flowchart of the Optimization Process with COPES

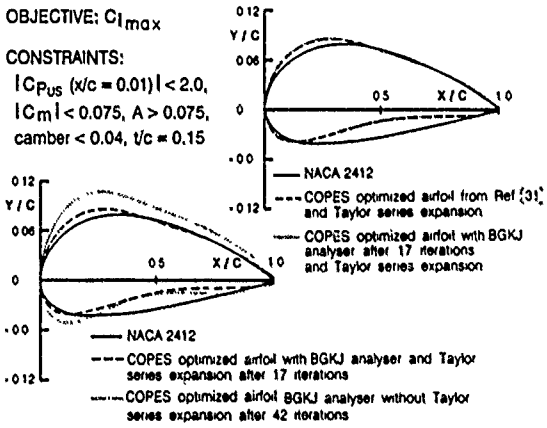


Fig. 22 Verification of the COPES - BGKJ - Coupling with a Testcase from Ref. 35

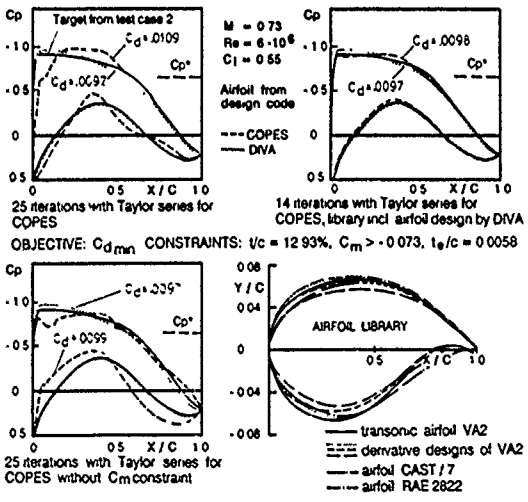


Fig. 23 Role of Constraints and Airfoil Library

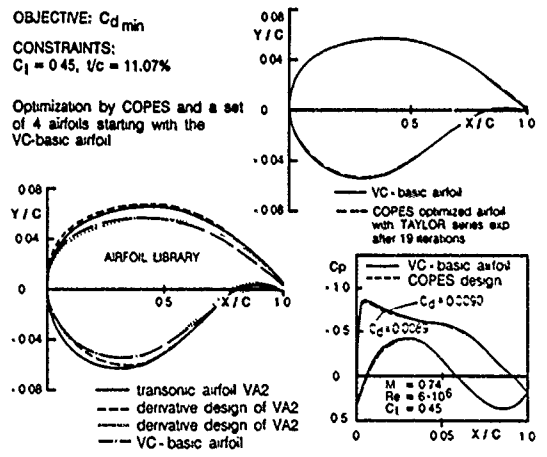


Fig. 24 Application of COPES for Optimization of a VC - Airfoil

Third International Conference on Inverse Design Concepts and Optimization in Engineering Sciences (ICIDES-III), Editor: G.S. Dulikravich, Washington D.C., October 23-25, 1991

BLADE DESIGN AND ANALYSIS USING A MODIFIED EULER SOLVER

O. Léonard and R. A. Van den Braembussche

von Karman Institute
Chaussée de Waterloo 72
1640 Rhode-Saint-Genèse
Belgium

ABSTRACT

An iterative method for blade design based on an Euler solver and described in an earlier paper is used to design compressor and turbine blades providing shock free transonic flows. The method shows a rapid convergence, and indicates how much the flow is sensitive to small modifications of the blade geometry, that the classical iterative use of analysis methods might not be able to define.

The relationship between the required Mach number distribution and the resulting geometry is discussed. Examples show how geometrical constraints imposed upon the blade shape can be respected by using free geometrical parameters or by relaxing the required Mach number distribution.

The same code is used both for the design of the required geometry and for the off-design calculations. Examples illustrate the difficulty of designing blade shapes with optimal performance also outside of the design point.

SYMBOLS

a	speed of sound
M	isentropic Mach number
$\vec{n}$	normal vector
p^0	total pressure
p	static pressure
t	time
T^0	total temperature
$\vec{V}$	velocity vector
β	flow angle (with resp. axial)
σ	cascade solidity

subscripts

n	normal component
t	tangential component
1	cascade inlet
2	cascade outlet

Third International Conference on Inverse Design Concepts and Optimization in Engineering Sciences (ICIDES-III), Editor: G.S. Dulikravich, Washington D.C., October 23-25, 1991.

INTRODUCTION

The design of new compressor and turbine blades is in most cases still done by successive direct analysis of the flow field around a given blade shape and modifications of the blade geometry, according to some empirical criteria and/or the designer's own experience. This approach makes it easier to respect geometrical and mechanical constraints imposed to the designer, such as thickness distribution, inertia momentum, stagger angle, pitch-to-chord ratio, etc.

New aerodynamic design tools have been developed, that have shown the ability to provide conclusive improvements of the aerodynamic performance when compared to existing blades. These improvements result from a specified controlled diffusion along the blade surface or a shock-free transonic flow. It is unlikely that they can be obtained by a traditional design procedure, namely by a series of flow analysis and empirical blade modifications. The design of transonic shock-free blades by means of an inverse method is one of the main topics discussed in this paper.

Analytical design methods developed in the past, using conformal mapping (Lighthill, 1945, Woods, 1955), permitted to build a complete theory of the inverse design of airfoils and blades, and provided the conditions required for the existence of a solution. However, they have a limited application due to the restrictive assumptions needed to allow an analytical formulation of the problem. As the blade shape results from the calculation, it is also more difficult to satisfy the mechanical constraints that one may wish to impose on the blade shape.

Numerical inverse methods have been developed for potential flows, using singularities for incompressible cases (Murugesan and Railly, 1969, Ubaldi, 1984, Van den Braembussche et al., 1989) and the odograph plane (Bauer et al., 1972, Sanz, 1984) or the potential-stream function plane (Stanitz, 1953, Schmidt, 1980) for the compressible cases. The last methods are not very accurate in the stagnation point region and are unable to predict shocks. It is therefore questionable whether blades designed in this way for shock-free transonic flows are shock-free in reality.

Non potential flow fields require solving the Euler equations. Such methods are capable of treating shocks correctly and are therefore suited to verify shock-free designs. They are mostly used in iterative procedures and require a first guess of the blade shape. This initial geometry is modified from the results of a flow analysis until the imposed pressure or velocity distribution is reached. The blade modifications can be calculated in a pure mathematical way, in order to minimize an error function, eg. depending on the difference between the calculated pressure distribution and the target (Vanderplaats, 1979, Hicks, 1981). Although these methods have the capability to respect geometrical constraints, they are still very expensive in terms of CPU time, because many iterations and flow analyses are required.

The blade modification can be determined in a more physical way, resulting in decrease in CPU time. The present method imposes the required Mach number distribution as a boundary condition on the blade wall and uses the concept of a permeable wall to define the modification of the geometry. This approach allows a reduction of the number of blade modifications, and consequently of the number of mesh generations. The method has proven to be very efficient in subsonic and transonic applications (Léonard, 1990, Léonard and Van den Braembussche, 1991). As shown in this paper, the iterative procedure makes it easier to meet geometrical and mechanical constraints imposed in industrial applications, and to find out whether a realistic

Third International Conference on Inverse Design Concepts and Optimization in Engineering Sciences (ICIDES-III), Editor: G.S. Dulikravich, Washington D.C., October 23-25, 1991.

blade shape corresponds to the required Mach number distribution. Another advantage of the present method is the possibility of using the same code for the blade design procedure as well as for the off-design analysis.

THE EULER SOLVER

The system of Euler equations for unsteady flows is solved using a time marching procedure and a finite volume approach. The numerical domain is discretized using C grids, for a good description of the leading edge geometry (fig.1). The unknowns are located at the vertices of the mesh cells, in such a way to avoid extrapolation towards the blade wall. The code can handle open trailing edges, in order to allow additional degrees of freedom in the geometrical definition of the blades. This makes the problem of solution existence easier to solve and allows a sufficient blade thickness to contain the boundary layer.

The equations are integrated in time using a Runge-Kutta first order accurate scheme, with local time-stepping, enthalpy damping and implicit residual averaging to accelerate the convergence. A detailed description of the solver may be found in Léonard (1990).

CALCULATION OF THE UNKNOWNS ON THE BLADE WALL

The method developed by the authors is an "iterative inverse method", in which the final geometry is the result of the flow calculation, imposing the required Mach number distribution on the blade wall. It has to be iterative since the location of this boundary is part of the solution, approximated at the beginning of the design procedure by any convenient initial geometry. There is no reason that the flow remains tangent to this geometry during the calculation, except in two cases, when the blade "is" the solution of the problem or when the blade wall is modified in order to respect the slip condition, as the time marching procedure iterates to the steady state.

Methods based on the second case have been proposed by Meauzé (1982), Giles and Drela (1987), and Zannetti et al. (1984). This approach has not been considered here since a minimum of successive blade modifications and corresponding mesh generations is desired. The blade wall must therefore be treated as permeable to the flow field. After convergence of the time marching procedure, the flow calculation results in a distribution of a normal velocity component on the blade wall that is used to modify the geometry.

The calculation of the unknowns at a boundary is dominated by the mathematical nature and the physical properties of the system of equations. As the Euler unsteady equations are hyperbolic, the solution can be constructed, at any location in the calculation domain (including the boundaries) using the information propagating in directions perpendicular to characteristic surfaces. The eigenvalues of the Jacobian matrices of the Euler system, projected in a considered direction $\vec{n}$, are $\overline{V}\overline{n}$, $\overline{V}\overline{n}$, $\overline{V}\overline{n}+a$ and $\overline{V}\overline{n}-a$, and define the propagation speeds in that direction. If the vector $\vec{n}$ is chosen perpendicular and entering the blade wall, a positive speed means that the information is propagated on the wave front, in the $\vec{n}$ direction, from the inside of the calculation domain to the outside, and is therefore available to calculate the value of the unknowns at this point of the blade wall. On the other hand, a negative speed means that the information comes from the outside of the numerical domain and propagates towards the inside. This entering information has to be provided by a boundary condition at the boundary point.

Third International Conference on Inverse Design Concepts and Optimization in Engineering Sciences (ICIDES-III), Editor: G.S. Dulikravich, Washington D.C., October 23-25, 1991.

If the slip condition is imposed on the blade wall ($\overline{V}\overline{n} = 0$) only the speed $\overline{V}\overline{n} - a$ is negative and therefore only one boundary condition must be imposed, i.e. the velocity direction at that point. This shows that the slip condition can not be imposed together with the Mach number value, at least for a fixed blade wall.

On the other hand, if the static pressure p (or the Mach number) is imposed on the blade, a velocity component normal to the blade can appear and, depending on its sign, 1 or 3 eigenvalues will be negative and 0 or 2 additional conditions must be imposed. The sign of this normal velocity component can be determined as a function of the imposed static pressure, using the compatibility relation corresponding to the only eigenvalue which is always positive ($V_n + a$).

If the normal velocity is positive, one boundary condition (the required static pressure) must be imposed, since only one eigenvalue ($V_n - a$) is negative. The additional information necessary to calculate all the unknowns at the boundary can be provided by the two compatibility relations corresponding to V_n and V_n since they are positive.

If the normal velocity is negative, two additional boundary conditions must be imposed. The best results have been obtained by imposing the total pressure and total temperature at that point. Imposing the latter does not give any special problem, since in a blade-to-blade calculation it is supposed to remain equal to the total temperature at the inlet. Imposing the total pressure is not so straightforward because of numerical dissipation. This problem is solved by imposing the value of the total pressure from the previous time level in such a way that the total pressure can adapt to the new flow field. This is important when a shock-free design is performed starting from a blade for which a shock was present in the original flow field, since in this case the initial and final total pressure distributions on the blade wall can be very different from each other. A detailed derivation of the compatibility relations can be found in Léonard (1990).

MODIFICATION OF THE GEOMETRY

A new geometry must be found since the initial shape no longer corresponds to a streamline. The modification algorithm is based on a transpiration model and calculates the position of the new streamlines using the velocity component normal to the initial blade (Léonard, 1990) The modification starts at the stagnation point, and is performed separately for the pressure side and the suction side. The new suction and pressure sides are defined as streamlines of the flow satisfying the Euler equations, and therefore can not cross each other. This guarantees a blade with positive thickness if the numerical integration procedure and the normal velocity calculation are sufficiently accurate.

RESULTS

The first example illustrates the accuracy of the method for shock-free transonic flows by applying it to the supercritical compressor blade designed by Sanz (1984) with an odograph method, and proposed as a test case for inviscid calculation methods in AGARD-AR-275 (fig. 2a). Analysis of the flow with the present method shows discrepancies on the suction side Mach number distribution (fig. 2b) similar to the ones observed by Denton (1983).

The geometry calculated by Sanz has been redesigned using the present method in order

Third International Conference on Inverse Design Concepts and Optimization in Engineering Sciences (ICIDES-III), Editor: G.S. Dulikravich, Washington D.C., October 23-25, 1991.

to obtain the shock-free Mach number distribution imposed by Sanz as the input data of his design (fig. 2c). Only one modification of the geometry has been necessary to obtain good agreement (fig. 2d). The difference between the initial geometry designed by Sanz and the one designed with the present method is very small. This example suggests that the original geometry defined by Sanz may not be shock-free, and illustrates how supersonic flows are very sensitive to geometry changes.

A second example illustrates the design of a shock-free compressor blade, using a NACA-65 $(12A_2I_{8b})10$ as an initial geometry. This blade is not suited to transonic flows, and a strong shock is present in the flow field. Therefore large geometry modifications are expected. The flow conditions are: $M_1 \simeq 0.8$, p_1^0 =1.33 bar, $T_1^0 = 341.5$ K, $\beta_1 = 45$ deg, $M_2 = 0.5$. The cascade geometry is defined by a stagger angle of 31 deg and a solidity of 1.

In a first design, only the suction side Mach number distribution has been modified. The initial distribution is compared to the shock-free required distribution in figure 3a. Good agreement between the calculated and the imposed Mach number distributions is obtained after 4 blade modifications (fig. 3b). The final blade is compared to the NACA-65 blade in figure 3c. One observes a thick leading edge, due to the velocity peak in the pressure side leading edge region. This is not desirable because it leads to strong diffusion and subsequent flow separation along the pressure side, as predicted by a boundary layer calculation.

A second design has been performed, starting also from the NACA-65 blade, but by modifying both the pressure and suction side Mach number distributions (fig. 4a). Decreasing the pressure side velocity in the leading edge region results in a lower average velocity, and in a smaller leading edge thickness because continuity requires a smaller blade blockage. Convergence to the required distribution is obtained after 3 modifications of the geometry (fig. 4b). The initial and final geometries are compared in figure 4c. One can observe a thinner leading edge and a shift of the maximum thickness location towards the middle of the blade.

Blade shapes designed by inviscid methods include the boundary layer blockage on the pressure and suction sides. The physical blade geometry can be obtained by subtracting the boundary layer displacement thickness from the so-called "inviscid" geometry. The minimum thickness of the "inviscid" blade, required to contain the boundary layer, can be calculated as a function of the target velocity distribution before the design procedure is started.

The analysis of the boundary layer for the prescribed Mach number distribution shown on figure 4b indicates that the boundary layer thickness at the trailing edge is of the order of 5% of the chord length, which is larger than the total trailing edge thickness of the blade shown on figure 4c and makes this blade unphysical. Increasing the trailing edge thickness is possible by increasing both the suction and pressure side Mach number distributions in the trailing edge region by the same amount (fig. 5a). The circulation is unchanged, resulting in the same turning of the flow, but the bade thickness must increase to satisfy continuity. The redesigned geometry is compared to the previous design in figure 5b and shows a larger trailing edge thickness capable of enclosing the boundary layer and the mechanical thickness.

An off-design analysis of the second blade has been performed with the same solver, changing the incidence by $\pm$ 2 degrees (fig. 6a and 6b). One can observe that the shock reappears. Although the flow field is no longer shock-free, the off-design behaviour of the new blade is better than that of the initial geometry.

Third International Conference on Inverse Design Concepts and Optimization in Engineering Sciences
(ICIDES-III), Editor: G.S. Dulikravich, Washington D.C., October 23-25, 1991.

The third example illustrates the redesign of a transonic turbine blade. The starting geometry is taken from the workshop VKI-LS 82-05 (Arts, 1982). The flow conditions are: $p_1^0 = 1$ bar, $T_1^0 = 278$ K, $\beta_1 = 0$ deg, $M_2 = 1.1$. The cascade geometry is defined by a stagger angle of -60 deg and a solidity of 1.25.

The imposed shock-free Mach number distribution assures a monotonically increasing velocity on the suction side (fig. 7a). Two modifications of the blade geometry are sufficient to give good agreement between the calculated and the required Mach number distributions (fig. 7b). The original and final geometries are compared in figure (7c). Off-design distributions are shown in figures 7d for an exit Mach number of 1.05 and 1.15 instead of 1.1.

The number of grid nodes used in the above examples ranges from 161×15 to 199×15. The typical amount of CPU time for one blade modification is 15 minutes on an ALLIANT FX/8 computer with 5 processors.

CONCLUSIONS

The present method has been successfully used to design shock-free transonic blades. It provides in few iterations results that could not be achieved using traditional direct methods and empirical blade modifications.

The method combines the advantages of a pure inverse method, since the Mach number distribution can be imposed on the blade wall, and the advantages of a direct method, allowing good control of the geometrical parameters.

It has been shown how modifications of the required Mach number distribution influence the blade geometry. Special attention was given to design trailing edges of sufficient thickness to enclose the boundary layer blockage.

Off design analysis of designed geometries illustrate the difficulty of optimizing for more than one operating point.

REFERENCES

ARTS, T., 1982, "Numerical methods for flow in turbomachine bladings", *Workshop on 2D and 3D flow calculations in turbine bladings*, VKI LS 1982-05.

BAUER, F., GARABEDIAN, P. and KORN, D., 1972, *Supercritical Wing Sections*, Vol. I, New York: Springer-Verlag.

DENTON, J.D., 1983, "An Improved Time-Marching Method for Turbomachinery Flow Calculation", ASME Journal of Engineering for Power, Vol. 105, No. 3, pp 514-524.

GILES, M.B. and DRELA, M., 1987, "Two-Dimensional Transonic Aerodynamic Design Method", *AIAA Journal*, Vol. 25, No. 9, pp 1199-1206.

HICKS, R.M., 1981, "Transonic Wing Design Using Potential Flow Codes - Successes and Failures", SAE Paper 810565.

JAMESON, A., SCHMIDT, W. and TURKEL, E., 1981, "Numerical Solutions of the Euler Equations by Finite Volume Methods Using Runge-Kutta Time Stepping Schemes", AIAA Paper 81-1259.

LEONARD, O., 1990, "Subsonic and Transonic Cascade Design", AGARD-R-780.

LEONARD, O., and VAN DEN BRAEMBUSSCHE, R., 1991, "Design Method for Subsonic and Transonic Cascade with Prescribed Mach Number Distribution", ASME Paper 91-GT-18.

LIGHTHILL, J.M., 1945, "A New Method of Two-Dimensional Aerodynamic Design", ARC R&M 2112.

MEAUZE, G., 1982, "An Inverse Time Marching Method for the Definition of Cascade Geometry", *Journal of Engineering for Power*, Vol. 104, pp 650-656.

MURUGESAN, K. and RAILLY, J.W., 1969, "Pure Design Method for Airfoils in Cascade", *Journal Mechanical Engineering Science*, Vol. 11, No. 5, pp 454-465.

SANZ, J.M., 1984, "Improved Design of Subcritical and Supercritical Cascades Using Complex Characteristics and Boundary-Layer Correction", *AIAA Journal*, Vol. 22, No. 7.

SCHMIDT, E., 1980, "Computation of Supercritical Compressor and Turbine Cascades with a Design Method for Transonic Flows", *Journal of Engineering and Power*, Vol. 102, pp 68-74.

STANITZ, J.D., 1953, "Design of Two-Dimensional Channels with Prescribed Velocity Distributions along the Channel Walls", NACA R-1115.

UBALDI, M., 1984, "Un metodo di progretto per profili in schiera basato sulla teoria delle equizioni integrali", AIMETA, VII Congr. Nazionale, Trieste.

VAN DEN BRAEMBUSSCHE, R., LEONARD, O. and NEKMOUCHE, L., 1989, "Subsonic and Transonic Blade Design By Means of Analysis Codes", AGARD-CP-463.

VANDERPLAATS, G.N., 1979, "Approximation Concepts for Numerical Airfoils Optimization", NASA TP-1370.

ZANNETTI, L. and PANDOLFI, M., 1984, "Inverse Design Technique for Cascades", NASA CR-3836.

WOODS, L.C., 1955, "The design of two-dimensional airfoils with mixed boundary conditions", *Quaterly of Applied Mathematics*, Vol. 13, pp. 139-146.

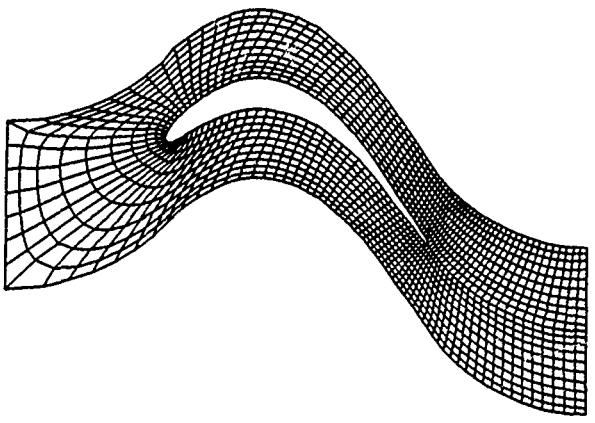


Fig. 1 C-grid discretization for a turbine blade

Third International Conference on Inverse Design Concepts and Optimization in Engineering Sciences (ICIDES-III), Editor: G.S. Dulikravich, Washington D.C., October 23-25, 1991.

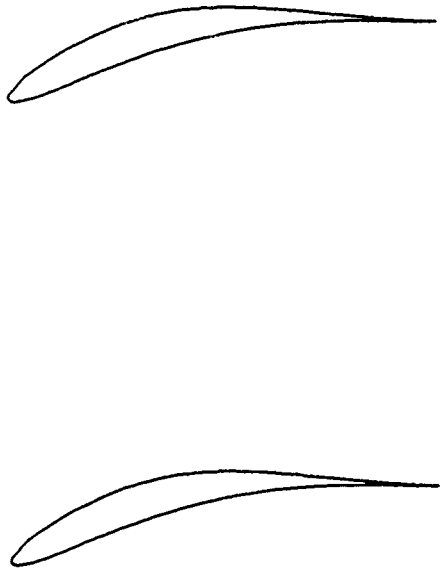


Fig. 2a Sanz supercritical compressor blade

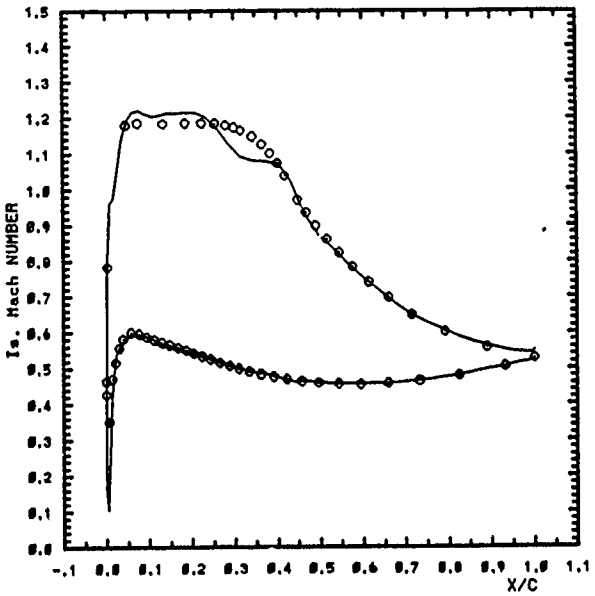


Fig. 2b Analytical (○) and calculated (full line) Mach number distributions

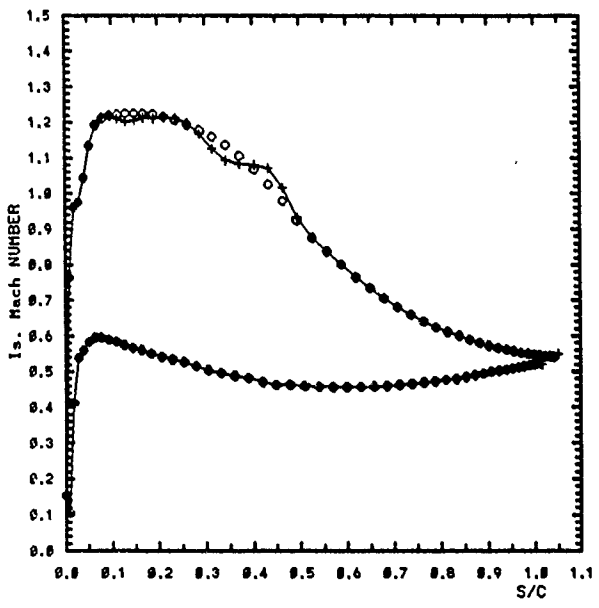


Fig. 2c Initial (+) and required (○) Mach number distributions

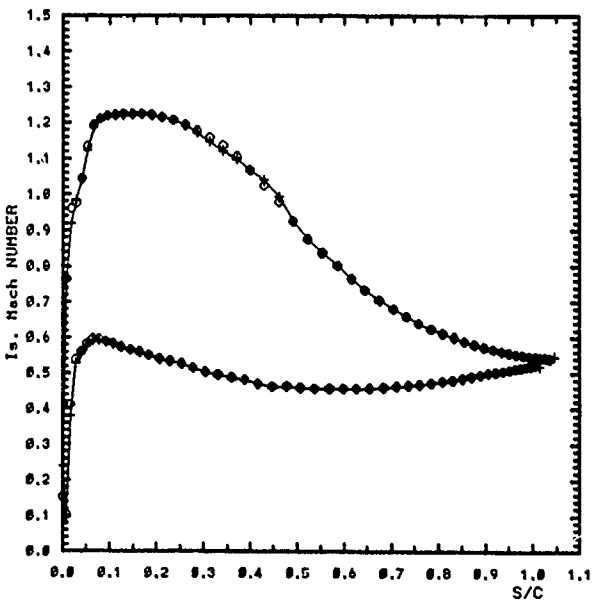


Fig. 2d Calculated (+) and required (○) Mach number distributions after 1 modification

Third International Conference on Inverse Design Concepts and Optimization in Engineering Sciences (ICIDES-III), Editor: G.S. Dulikravich, Washington D.C., October 23-25, 1991.

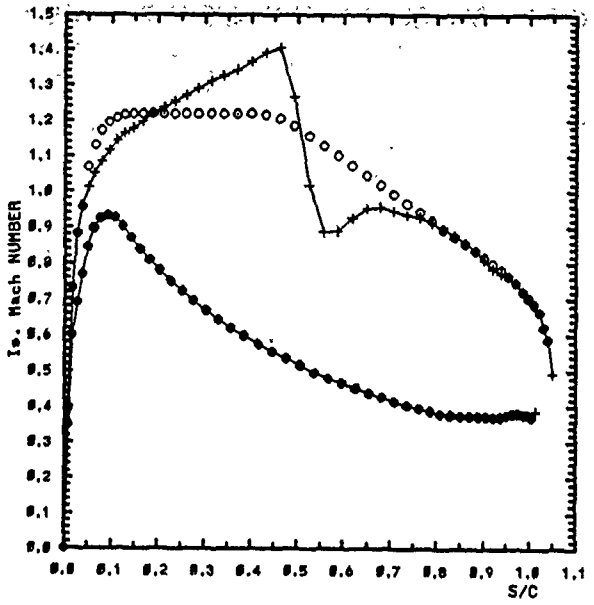


Fig. 3a Initial (+) and required (○) Mach number distributions

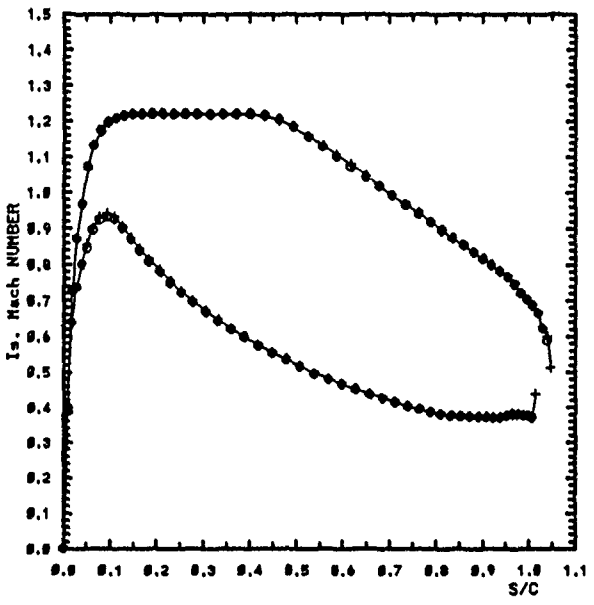


Fig. 3b Calculated (+) and required (○) Mach number distributions after 3 modifications

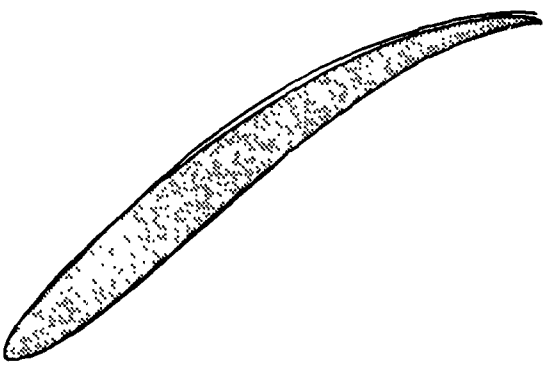


Fig. 3c Original and final geometries

Third International Conference on Inverse Design Concepts and Optimization in Engineering Sciences (ICIDES-III), Editor: G.S. Dulikravich, Washington D.C., October 23-25, 1991.

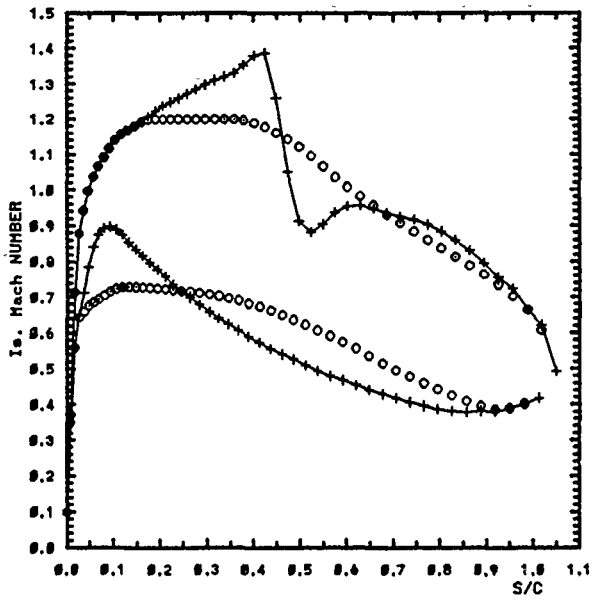


Fig. 4a Initial (+) and required (○) Mach number distributions

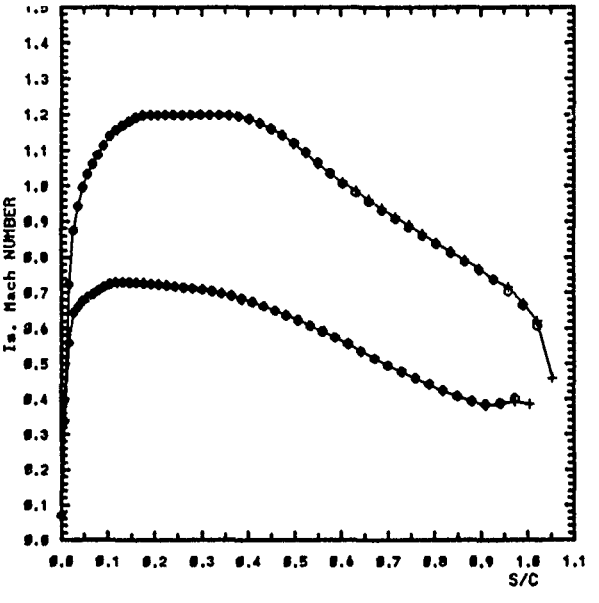


Fig. 4b Calculated (+) and required (○) Mach number distributions after 3 modifications

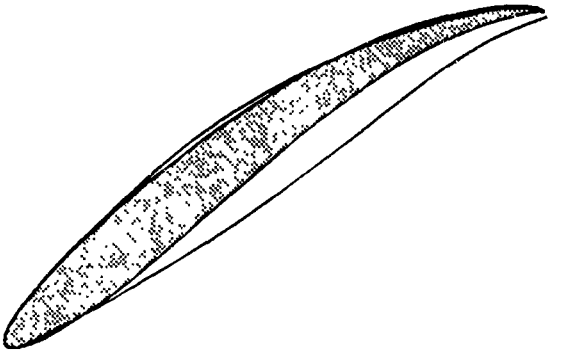


Fig. 4c Original and final geometries

Third International Conference on Inverse Design Concepts and Optimization in Engineering Sciences (ICIDES-III) Editor: G.S. Dulikravich, Washington D.C., October 23-25, 1991

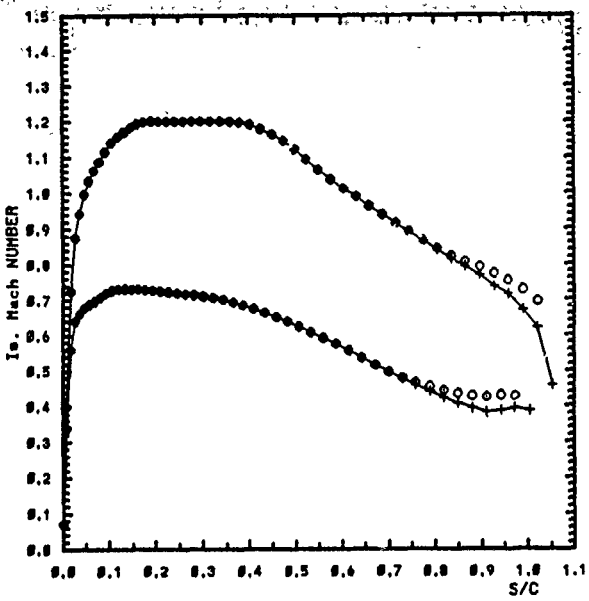


Fig. 5a Initial (+) and required (○) Mach number distributions for increased blade thickness

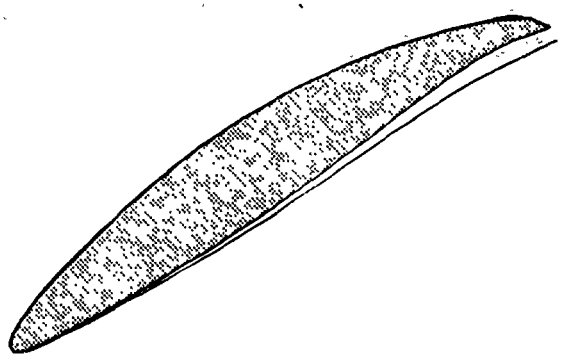


Fig. 5b Original and thicker geometries

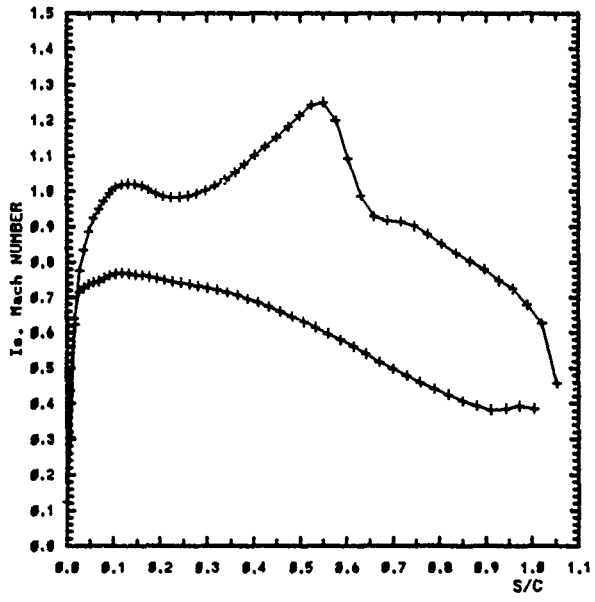


Fig. 6a Off design (-2 deg incidence)

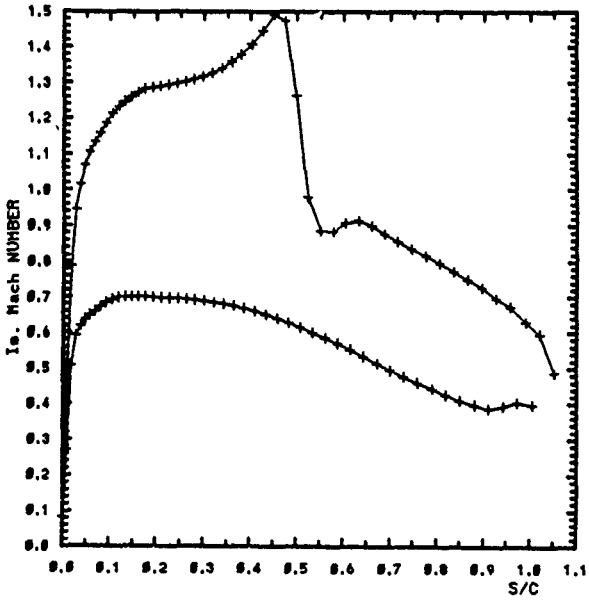


Fig. 6b Off design (+2 deg incidence)

Third International Conference on Inverse Design Concepts and Optimization in Engineering Sciences (ICIDES-III), Editor: G.S. Dulikravich, Washington D.C., October 23-25, 1991.

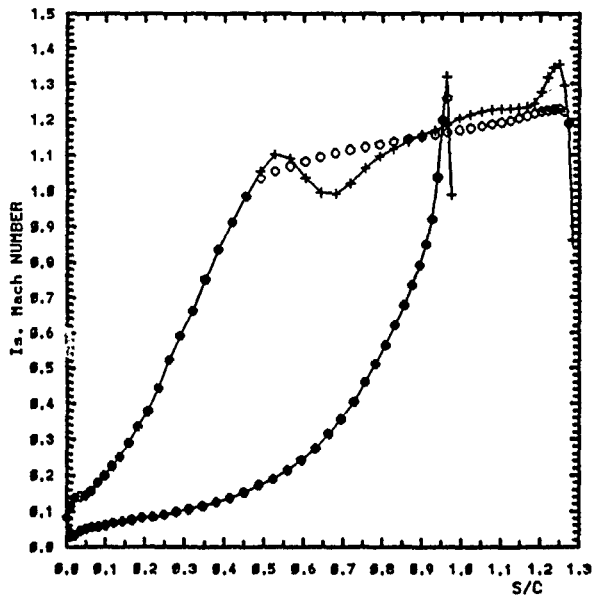


Fig. 7a Initial (+) and required (○) Mach number distributions

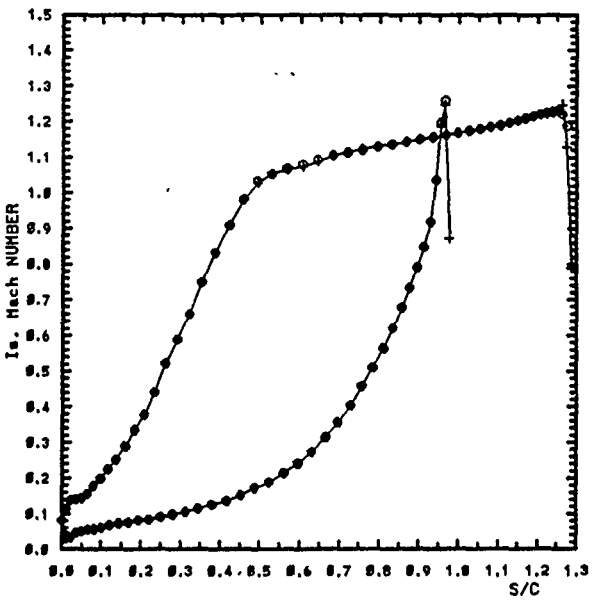


Fig. 7b Calculated (+) and required (○) Mach number distributions after 2 modifications

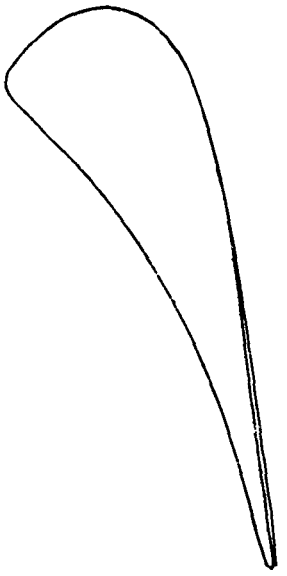


Fig. 7c Original and final geometries

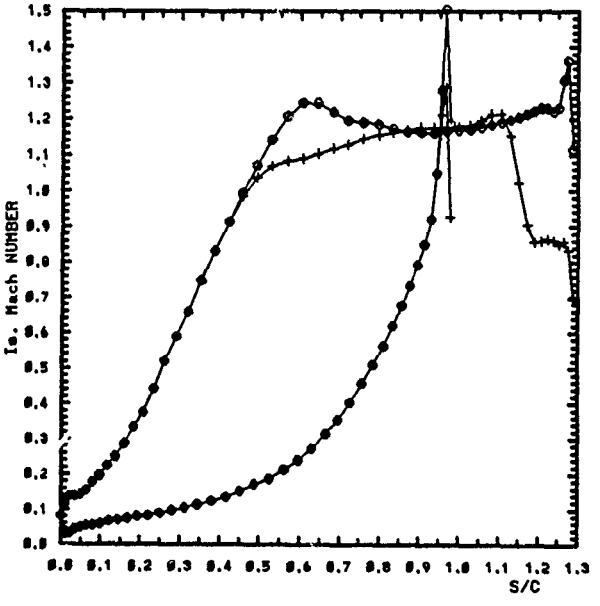


Fig. 7d Off design for $M_2 = 1.05$ (+) and $M_2 = 1.15$ (○)

Third International Conference on Inverse Design Concepts and Optimization in Engineering Sciences (ICIDES-III), Editor: G.S. Dulikravich, Washington D.C., October 23-25, 1991.

VARIATIONAL FORMULATION OF HYBRID PROBLEMS FOR FULLY 3-D TRANSONIC FLOW WITH SHOCKS IN ROTOR

Gao-Lian Liu, Professor & Director
Laboratory of Turbomachinery Aerodynamics
Shanghai Institute of Mechanical Engineering
516 Jun-Gong Rd, Shanghai 200093, China

ABSTRACT:

Based on Refs [3,4], the unified variable-domain variational theory of hybrid problems for rotor-flow [1,2] is extended to fully 3-D transonic rotor-flow with shocks, unifying and generalizing the direct and inverse problems. Three variational principle (VP) families have been established. All unknown boundaries and flow discontinuities (such as shocks, free trailing vortex sheets) are successfully handled via functional variations with variable domain, converting almost all boundary and interface conditions, including the Rankine-Hugoniot shock relations, into natural ones. This theory provides a series of novel ways for blade design or modification and a rigorous theoretical basis for finite element applications and also constitutes an important part of the optimal design theory of rotor-bladings [6]. Numerical solutions to subsonic flow by finite elements with self-adapting nodes given in Refs[16,19,22] show good agreement with experimental results.

NOMENCLATURE:

A	total area of boundary surfaces.
A_1	inlet & outlet surfaces (Fig.1).
A_2	periodic boundary surfaces (Fig.1): $A_2=A_{2u}UA_{2d}$, $A_{2u}=A'_{2u}UA''_{2u}$, $A_{2d}=A'_{2d}UA''_{2d}$.
A_{2d}	free trailing vortex sheets.
A_3	all solid boundary walls: $A_3=A_aUA_b=A_3^*UA_3^{**}$.
A_a	hub- & casing annular walls: $A_a=A_a^*UA_a^{**}$.
A_b	blade surfaces: $A_b=A_b^*UA_b^{**}$.
$dA_{r,\varphi,z}$	components of elementary area $d\vec{A}$ in r-, φ-, z- directions respectively, $d\vec{A}=dA\cdot\vec{n}$.
A_S	shock surfaces.
a	sound speed.
$\vec{C},\vec{W}$	absolute, relative flow velocity respectively.
κ,m	specific heat ratio C_p/C_v and $m=(\kappa-1)^{-1}$
M	relative Mach number.
$\vec{n}$	outward normal unit vector.
p	dimensionless pressure
q	mass flux ρA.

Third International Conference on Inverse Design Concepts and Optimization in Engineering Sciences (ICIDES-III), Editor: G.S. Dulikravich, Washington D.C., October 23-25, 1991.

r,φ,z and $\vec{i}_r,\vec{i}_\varphi,\vec{i}_z$, cylindric coordinates fixed on rotor and the corresponding unit vectors.

$\mathfrak{R},S$ rothalpy & entropy.

$\vec{s},\delta\vec{s}$ boundary position vector & its variation.

$\vec{U}$ $\vec{U}=\vec{\omega}\times\vec{r}$.

dv elementary volume $dv=rd\varphi drdz$.

Φ potential function

$\vec{\omega}$ angular speed of the rotor.

$\vec{\Lambda}_c,\vec{\Lambda},\vec{\Lambda}_u$ demensionless forms of $\vec{C},\vec{W},\vec{U}$ respectively.

ρ dimensionless density.

Subscripts:

a,b annular and blade walls respectively.
d,u downstream and upstream respectively.
m circumferentially averaged value.
n,τ normal & tangential components.
pr prescribed.
r,φ,z radial, azimuthal and axial components respectively.
p pressure blade surface.
s suction blade surface.
', " parameters on (Λ'_{2u} , Λ'_{2d}) and (Λ''_{2u} , Λ''_{2d}) respectively.
-,+ parameters just before & behind the interface or shock respectively.

Superscripts:

o restricted variation [10].
*,** known and unknown portions of the boundary respectively.

1. INTRODUCTION

Nowadays the design of advanced turbomachinery would be impossible without using advanced aerodynamic theory and thereupeon based computational methods. During the last decade much progress has been made in this field and a detailed state-of-the-art review is given in Ref.[5], which reveals that with few exceptions, e.g. Refs [1,2,11-17], most of work done to date, however, are concerned with the direct (analysis) problem, quasi-3-D flow model and mainly finite difference, finite volume and streamline curvature methods. Owing to the lack of exact (classical) variational principles (VPs) for rotor-flow finite element methods (FEM) used so far are exclusively based either on Galerkin approach or on approximate VPs for the linearized problem. It is the great progress and the widespread and fruitful applications of the FEM in solid mechanics that motivated the present author in the mid 1970's to start a systematic search for VPs in fluid mechanics in general [17,18] and in 3-D turbomachine flow theory in particular [1-4,8,11,12] with special emphasis on inverse and hybrid problems in order to provide both a new rigorous, sound theoretical foundation for FEM in computational aerodynamics of turbomachinery and a number of novel rational versatile ways for new blade design or old blade modification. The hybrid problem is the one which, being a unification as well as generalization of the traditional direct and inverse problems, is capable of combining the merits of the two, while eliminating their shortcomings [1,2,11]. As a result, a lot of VP families have been established first for the direct problem [8] and the hybrid problem [11-13,16] of quasi-3-D cascade flow. In extending them to

Third International Conference on Inverse Design Concepts and Optimization in Engineering Sciences (ICIDES-III), Editor: G.S. Dulikravich, Washington D.C., October 23-25, 1991.

fuly 3-D flow the major difficulties encountered were how to capture all possible unknown flow discontinuities, such as shock waves, free trailing vortex sheets and the unknown portions of the blade- and/or annular walls in inverse and hybrid problems. Subsequently, a series of VPs in terms of potential or stream functions for the direct problem of fully 3-D transonic potential and rotational flows with shocks in rotors have been developed in Refs [3,4], and furthermore, a unified variational theory of various hybrid problems for fully 3-D incompressible rotor flow has been presented in Ref.[1] and extended to compressible flow in Ref.[2], thereby a very powerful mathematical apparatus "the functional variation with variable domain" being used to full advantage for handling abovementioned flow discontinuities. Successful numerical validations of such a theory have been carried out in Refs[16,19,22] by using a new finite element with self-adapting nodes.

In the present paper, based on Refs [3,4], the unified variable-domain variational theory of hybrid problems for rotor-flow of Refs [1,2,16] is extended to fully 3-D transonic flow with shock waves in rotors of axial, radial- and mixed-flow types.

2. BASIC AEROTHERMODYNAMIC EQUATIONS

Consider the fully 3-D subsonic and transonic potential, steady relative flow of an inviscid fluid past a rotating blading with constant angular speed $\vec{\omega}$ (Fig.1).

For such potential flows the nondimensional governing aerodynamic equations have the following form [3,4,7]:
Continuity equation:

$$\nabla\cdot(\rho\vec{\Lambda})=\frac{1}{r}\left\{\frac{\partial(\rho r\Lambda_r)}{\partial r}+\frac{\partial(\rho\Lambda_\varphi)}{\partial\varphi}+\frac{\partial(\rho r\Lambda_z)}{\partial z}\right\}=0 \tag{1}$$

Irrotationality of the absolute flow:

$$\left\{\frac{\partial\Phi}{\partial r},\ \frac{1}{r}\cdot\frac{\partial\Phi}{\partial\varphi},\ \frac{\partial\Phi}{\partial z}\right\}=\left\{\Lambda_r,\ (\Lambda_\varphi+\Lambda_u),\ \Lambda_z\right\} \tag{2}$$

First law of thermodynamics:

$$\frac{p}{\rho}+\frac{1}{2m}(\Lambda^2-\Lambda_u^2)=1 \tag{3}$$

Homentropic equation:

$$p=\rho^\kappa \tag{4}$$

Eliminating p in Eq.(3) via Eq.(4) yields:

$$\rho=\left\{1-\frac{1}{2m}(\Lambda^2-\Lambda_u^2)\right\}^m \tag{3'}$$

Using Eqs. (2) & (3'), a full potential equation can be obtained from Eq.(1) [2,3,4,7]:

$$(1-M_r^2)\frac{\partial^2\Phi}{\partial r^2}+\frac{1-M_\varphi^2}{r^2}\cdot\frac{\partial^2\Phi}{\partial\varphi^2}+(1-M_z^2)\frac{\partial^2\Phi}{\partial z^2}-\frac{2M_rM_\varphi}{r}\cdot\frac{\partial^2\Phi}{\partial r\partial\varphi}$$

$$-\frac{2M_zM_\varphi}{r}\cdot\frac{\partial^2\Phi}{\partial z\partial\varphi}-2M_rM_z\frac{\partial^2\Phi}{\partial r\partial z}+\frac{1+(M_\varphi+M_u)^2}{r}\cdot\frac{\partial\Phi}{\partial r}=0 \tag{5}$$

where

$$\rho^{1/m}=1-\frac{1}{2m}[(\frac{\partial\Phi}{\partial r})^2+(\frac{1}{r}\cdot\frac{\partial\Phi}{\partial\varphi}-\Lambda_u)^2+(\frac{\partial\Phi}{\partial z})^2-\Lambda_u^2], \tag{3''}$$

Third International Conference on Inverse Design Concepts and Optimization in Engineering Sciences. (ICIDES-III). Editor: G.S. Dulikravich, Washington D.C., October 23-25, 1991.

$$M_r=W_r/a=\frac{\partial\Phi}{\partial r}/\rho^{1/2m},$$

$$M_\varphi=W_\varphi/a=(\frac{1}{r}\cdot\frac{\partial\Phi}{\partial\varphi}-\Lambda_u)/\rho^{1/2m},$$

$$M_z=W_z/a=\frac{\partial\Phi}{\partial z}/\rho^{1/2m},$$

$$M_u=\omega r/a=\Lambda_u/\rho^{1/2m}.$$

In the present paper, just as in Refs [1,2], the following three types of 3-D hybrid problems (H_A×H_A), (H_B×H_A) & (H_C×H_A) are studied in detail, where, as defined in Refs [1,2], e.g. (H_C×H_A) denotes such a hybrid problem in which a hybrid problem of type C (H_C) is posed on the blade surface, while a hybrid problem of type A (H_A) is posed on the annular walls (Fig.2a). In other words, the first symbol characterizes the problem type on the blade surface, while the second symbol ----- that on the annular wall. As for the hybrid problems H_A, H_B,...., they are defined in Table I for 2-D cascades [11,12,16], for the annular walls they are defined similarly [1,2].

Table I. Problem Classification (for the Blade Surface)

Types	Given conditions	
	Geometric	Aerodynamic
H_A	Part of airfoil form	Pressure distribution along remaining part
H_B	Airfoil thickness distribution	Blade loading distribution (p_p -- p_s)
H_C		Pressure distribution along suction surface
H_D		Velocity difference distribution ($\Lambda_s-\Lambda_p$)
D	All cascade geometry	none
I	none	Pressure distribution along airfoil contour

Of course, the abovementioned three 3-D hybrid-problem types are only some typical ones taken as examples for consideration herein. Generally speaking, 3-D hybrid problems encompass a much wider variaty of types. They provides the designer with a series of novel design tools, which enable him to choose the most suited problem types or their combinations for meeting various practical design conditions at hand (e.g. aerodynamics, cooling, strength-vibrational and technological requiements etc). As pointed out in Ref.[1], the three hybrid problems studied herein per se embrace also very comprehensive special cases, which, to a large extent, are capable of fulfilling various practical requirements of blade design and which can be made even much broader by posing different problem types on different portions of the blade (or annular) wall (Fig.2b).

3. VP FAMILY FOR THE (H_A×H_A)-PROBLEM

In the development to follow, starting from the VPs for the direct problem given in Refs [3,4] and employing the functional variation with variable domain

Third International Conference on Inverse Design Concepts and Optimization in Engineering Sciences (ICIDES-III), Editor: G.S. Dulikravich, Washington D.C., October 23-25, 1991.

[1,4], we present a unified variational theory of hybrid problems for fully 3-D subsonic and transonic flows with shocks.

Proceeding similarly to Ref.[1] leads to the following results without going into details.

VP I: The solution to the (H_A)-(H_A)-problem of 3-D sub- and transonic rotor-flow makes the functional J_I stationary: $\delta J_I=0$, where Φ, A_3^{**}, Λ_{2d}, Λ_S should be varied independently.

$$J_I(\Phi,A_3^{**},\Lambda_{2d},\Lambda_S)=I_I+L+L^{AA}, \tag{6}$$

where

$$\kappa I_I=\iiint_{(V)} p\,dv=\iiint_{(V)}\left\{1-\frac{1}{2m}\left[\left(\frac{\partial\Phi}{\partial r}\right)^2+\left(\frac{1}{r}\frac{\partial\Phi}{\partial\varphi}\right)^2+\left(\frac{\partial\Phi}{\partial z}\right)^2-\frac{2\Lambda_u}{r}\cdot\frac{\partial\Phi}{\partial\varphi}\right]\right\}^{\kappa m}dv$$

$$L=\iint_{(A_1)}(q_n)_{pr}\Phi\,dA-\iint_{(A_{2u}')}(\Phi''-\Phi'-\Delta\Phi_u)(\rho\Lambda_n)'dA$$

$$-L^{AA}=\iint_{(A_a^{**})}\left(\frac{p_m}{\kappa}\right)_{pr}\vec{s}\cdot d\vec{A}+\iint_{(A_b^{**})}\left(\frac{p}{\kappa}\right)_{pr}\vec{s}\cdot d\vec{A}.$$

With all unknown boundaries or interface A_3^{**}, Λ_S and Λ_{2d} treated by the method of functionnal variations with variable domain [1,4] the following set of stationarity conditions for J_I can be derived from $\delta J_I=0$:

Euler's eq.: Eq.(5)

Natural boundary conditions (B.C.):

on Λ_1: $\rho\Lambda_n=(q_n)_{pr}$,

on Λ_{2u}: $(\rho\Lambda_n)'=(\rho\Lambda_n)''$, $\Phi''-\Phi'=\Delta\Phi_u$,
leading to the circumferential periodicity of all flow parameters.

on Λ_{2d}: $(\rho\Lambda_n)'=(\rho\Lambda_n)''=0$, $p'=p''$,
They are just the interface conditions on the free trailing vortex sheets.

on Λ_S: Using $\Phi_-=\Phi_+$ as an essential (enforced) interface condition, we have $(\partial\Phi/\partial\tau)_-=(\partial\Phi/\partial\tau)_+$, that is, the tangential velocity components at both sides of the shock are equal:

$$(\vec{\Lambda_\tau})_-=(\vec{\Lambda_\tau})_+ \tag{7a}$$

So we obtain the following natural interface conditions:

$$(\rho\Lambda_n)_-=(\rho\Lambda_n)_+ \tag{7b}$$

$$(p/\kappa+\rho\Lambda_n^2)_-=(p/\kappa+\rho\Lambda_n^2)_+ \tag{7c}$$

In addition, from Eq.(3) we can write

$$\mathfrak{R}_-=\mathfrak{R}_+ \tag{7d}$$

Obviously, Eq-s (7a)-(7d) are none other than the well-known Rankine-Hugoniot shock relations [3,4].

on Λ_3^*: $\rho\Lambda_n=0$.

on Λ_a^{**}: $\rho\Lambda_n=0$, and $p_m=(p_m)_{pr}$.

on A_b^{**}: $\rho\Lambda_n=0$, and $p=p_{pr}$.

Thus, it has been shown that from this VP I actually the full potential

Third International Conference on Inverse Design Concepts and Optimization in Engineering Sciences (ICIDES-III), Editor: G.S. Dulikravich, Washington D.C., October 23-25, 1991.

equation (5) together with almost all boundary conditions for the 3-D $(H_A \times H_A)$-problem can be derived naturally, and all unknown surface (e.g. shocks, free trailing vortex sheets and unknown walls) can be determined using e.g. FEM.

Applying a constraint-removing transformation [17], the above VP I can be extended to the following generalized VP(GVP).

GVP II: The solution to the above 3-D $(H_A \times H_A)$-problem makes the following functional J_{II} stationary: $\delta J_{II}=0$, with independent variations of Φ, $\vec{A}$, p, ρ, A_3^{**}, A_s and A_{2d}.

$$J_{II}(\Phi,\vec{A},p,\rho,A_3^{**},A_s,A_{2d})=I_{II}+I.+L^{AA}, \tag{8}$$

where

$$-I_{II}=\iiint_{(V)}\left\{\rho[\vec{A}\cdot\nabla\Phi-\frac{1}{2}(A^2+A_u^2+2A_uA_\varphi)]+\frac{mp}{K}[1-\ln(p/\rho^K)]-m\rho\right\}dv$$

In a way similar to the above one it can be shown that from $\delta J_{II}=0$ the following set of natural conditions results:

Eular's equations: Eqs (1)-(4).

Natural B.C.: All the same as those of VP I.

Subgeneralized VPs (SGVPs):

Via a constraint-recovering transformation [17], from GVP II a family of subgeneralized VPs can be derived, one of which is the foregoing VP I.

4. VP FAMILY FOR THE $(H_B \times H_A)$-PROBLEM

In this case the B.C. on the annular walls remain the same as those of the $(H_A \times H_A)$-problem, while the B.C. on the blade surface become:

(i) Blade thickness distribution given by

$$\varphi_p-\varphi_s=g_\varphi(r,z); \tag{9A}$$

(ii) blade-loading distribution given by

$$\frac{p_p-p_s}{K}=g_p(r,z) \tag{9B}$$

where $g_\varphi(r,z)$ and $g_p(r,z)$ are prescribed functions.

Proceeding in just the same way as in the foregoing section, we can establish the following VP family for the $(H_B \times H_A)$-problem, which differs from that for the $(H_A \times H_A)$-problem only in that the boundary integral term L^{AA} now should be replaced by the following L^{BA}:

$$L^{BA}=-\iint_{(A_3^{**})}(\frac{p_m}{K})_p\vec{s}\cdot d\vec{A}+\iint_{(A_b)_s}g_p\,\vec{s}\cdot d\vec{A}, \tag{10}$$

imposing Eq.(9A) as an essential B.C.. In Eq.(10) the symbol $(A_b)_s$ stands for the suction blade surface. In this way we obtain the following VP family.

VP III: The solution to the $(H_B \times H_A)$-problem of 3-D sub- and transonic rotor-flows makes the functions J_{III} stationary: $\delta J_{III}=0$, thereby Φ, A_3^{**}, A_s, A_b and A_{2d} should be varied independently.

$$J_{III}(\Phi,A_3^{**},A_b,A_s,A_{2d})=I_I+L+L^{BA}, \tag{11}$$

It is easy to verify that from $\delta J_{III}=0$ the same Euler's equation and natural B.C. set as those of VP I can be derived with the only exception that the natural

B.C. on the blade surface A_b has now become Eq.(9B).

GVP IV: The solution to the above 3-D $(H_B \times H_A)$-problem makes the following functional J_{IV} stationary: $\delta J_{IV}=0$ with independent variations of Φ, $\vec{A}$, p, ρ, A_a^{**}, A_b, A_s and A_{2d}.

$$J_{IV}(\Phi,\vec{A},p,\rho,A_a^{**},A_b,A_s,A_{2d})=I_{II}+L+L^{BA}, \tag{12}$$

From $\delta J_{IV}=0$ the same Euler's equations and natural B.C. set as those in GVP II follow except only that the natural B.C. on the blade surface has become Eq. (9B).

SGVP Family: By means of a constraint-recovering transformation [17] a family of SGVPs can be derived from the GVP IV, including also the VP III.

5. VP FAMILY FOR THE $(H_C \times H_A)$-PROBLEM

Here the B.C. on the annular walls still remain unchanged as before, while the B.C. on the blade surface are now given as follows:
(i) blade thickness distribution given by Eq.(9A):
(ii) pressure distribution along the suction blade surface:

$$p_s=[p_s(r,z)]_{pr} \tag{13}$$

To establish the VP family for the $(H_C \times H_A)$-problem, we proceed similarly as above. It turns out that this VP family differs from that for the $(H_A \times H_A)$-problem only in that the boundary integral term L^{AA} should be replaced by the following L^{CA}:

$$L^{CA}=-\int_{(A_a^{**})}\int (\frac{p_T}{K})_{pr}\vec{s}\cdot d\vec{A}+\int_{(A_b)_S}\int (\frac{p_T^{o}-p_s}{K})\vec{s}\cdot d\vec{A}, \tag{14}$$

while the Eq.(9A) should be treated as an enforced B.C.. In Eq.(14) the superscript 'o' denotes that the 'restricted variation' [10] should be taken. Thus, we have:

VP V: For the $(H_C \times H_A)$-problem $\delta J_V=0$ with independent variations of Φ, A_a^{**}, A_b, A_s and A_{2d} holds, and

$$J_V(\Phi,A_a^{**},A_b,A_s,A_{2d})=I_I+L+L^{CA}, \tag{15}$$

VP VI: For the $(H_C \times H_A)$-problem $\delta J_{VI}=0$ with independent variations of Φ, $\vec{A}$, p, ρ, A_a^{**}, A_b, A_s and A_{2d} holds, and

$$J_{VI}(\Phi,\vec{A},p,\rho,A_a^{**},A_b,A_s,A_{2d})=I_{II}+L+L^{CA}, \tag{16}$$

SGVP Family: Applying the constraint-recovering transformation [17], we can derive a SGVP family for the $(H_C \times H_A)$-problem from GVP VI, including also the VP V.

It can be shown similarly as in previous sections that the Euler's equations and the naturall B.C. sets of the VP V, GVP VI and its derived SGVP family are the same as those of the VP I, GVP II and its derived SGVP family respectively, except that the natural B.C. on the blade surface now has become Eq.(13).

6. SOME GENERAL REMARKS

1) It is easy to see that the traditional direct problem (D×D) [3,4] and inverse

Third International Conference on Inverse Design Concepts and Optimization in Engineering Sciences (ICIDES-III), Editor: G.S. Dulikravich, Washington D.C., October 23-25, 1991.

problem (I×I) are simply two special cases of the (H_A×H_A)-problem, corresponding to $A_3^{**}=0$ and $A_3^{*}=0$ respectively. Accordingly, by setting $A_3^{**}=0$ all VPs developed herein reduce to those presented previously in Refs [3,4].

2) If, alternatively, the B.C. on the upstream periodic boundary A_{2u} (namely $\Phi''=\Phi'+\Delta\Phi_u$) is imposed as essential B.C., the boundary integral terms on A_{2u}^{*} involved in L of all VPs should be dropped accordingly.

3) An alternatve approach to handling free trailing vortex sheets A_{2d} is also possible by taking formally no variation of A_{2d}, though A_{2d} is unknown, but the interface conditions on A_{2d} (namely $\Lambda_n'=\Lambda_n''=0$, $p'=p''$) are enforced as essential ones [21].

4) As stressed in Ref.[1], sufficient attention should be paid to a rational choice of the position-variation $\delta\vec{s}$ of the unknown boundaries A_3^{**} and A_{2d} for facilitating the practical computation of $(\delta\vec{s}\cdot d\vec{A})$ & δJ_i (i=I~VI). Some recommendations on this point are available in Ref.[1] and, of course, also valid for the present case.

For better shock-capturing a special finite element with self-adaptive build-in discontinuities is very promising and is now being under development.

The numerical solutions to the problems [(H_B+D)×D] & [(H_C+D)×D] obtained for subsonic flow by finite elements in Refs.[19,22] show good agreement with experimental results.

8. CONCLUSIONS

The unified theory of 3-D hybrid problems of Refs [1,2] has been extended to transonic flow with shocks. This theory is primarly aimed at providing, firstly, a new rigorous theoretical basis of blade design for use in FEM and other direct variational methods (e.g. Ritz's method, Kantorovich's method) and, secondly, a wide variety of new rational versatile ways for new blade design and old blade modification. It also constitutes an important ingredient of the optimal design theory of 3-D rotor-bladings [6]. Based on the VPs for the direct problem of 3-D rotational flow [3,4], the present theory can be extended also to 3-D rotational flow. This will be presented in a companion paper.

ACKNOWLEGEMENT:

This research is supported by the National Natural Science Foundation of China.

REFERENCES

[1] Liu, G.L.: A unified theory of hybrid problems for fully 3-D incompressible rotor-flow based on variational principles (VPs) with variable domain, ASME J.Engrg for GT & Power, Vol. 108, 2 (1986), 254-258.

[2] Liu, G.L.: A variational theory of hybrid problems for fully 3-D compressible rotor flow: A unified variable-domain approach, Comput'l Fluid Dynamics, G.d.V. Davis & C. Fletcher, ed., North-Holland, (1988)473-480

[3] Liu, G.L.: VPs & generalized VPs for fully 3-D transonic rotor-flow with shocks, Proc. of the 6th Int. Symp. on FEM in Flow Problems, June 1986, Antibes, France, 125-130.

[4] Liu, G.L.: VPs and generalized VPs for 3-D transonic flow with shock waves in a rotating turbo-impeller, to appear in Acta Mechanica.

[5] McNally, W.D. & Sockol, P.M.: Review-----Computational methods for internal flows with emphasis on turbomachinery, ASME J. Fluids Engng, Vol.107,

1(1985), 6-22.

[6] Liu, G.L.: Aerodynamic optimization theory of a 3-D axial-flow rotor-blading via optimal control. Proc. 6th Int. Symp. Air-Breathing Engines, June 1983, Paris (AIAA Paper 83-7037).

[7] Wu, C.H.: A general theory of 3-D flow in sub- & supersonic turbomachines of axial-, radial- and mixed-flow types. NACA TN 2604 (1952).

[8] Liu, G.L.: VP families for direct aerodynamic problem of multi-row airfoil cascades on an arbitrary streamsheet of revolution, Proc. Int. Conf. on FEM, Aug. 1982, Shanghai, China, Gordon & Breach Sci. Publishers, New York, 520-523.

[9] Serrin, J.: Mathematical principles of classical fluid mechanics, Handbuch der Physik, Vol. VIII-1, Springer-Verlag (1959).

[10] Finlayson, B.A.: The method of weighted residuals & VPs. Acad. Press, New York(1972).

[11] Liu, G.L.: VPs & generalized VPs for hybrid aerodynamic problem of cascades on an arbitrary stream sheet of revolution: Pt(I), Scientia Sinica, Vol.23, 10(1980) 1339-1347; Pt(II), J. Engng. Thermophysics, Vol.2, 4(1981),335-342.

[12] Liu, G.L. & Yao, Z.: Ditto, Pt (III), Proc. 6th Int. Symp. on FEM in Flow Problems, June 1986, Antibes, France, 137-142

[13] Yao, Z. et al.: Variational FE calculation for hybrid aerodynamic problem of cascades on an arbitrary streamsheet of revolution, IMechE Paper C69/84, 237-245(1984).

[14] Meauze, G.: An inverse time-marching method for the difinition of cascade geometry. ASME J. Engng for Power, Vol.104, 3(1982), 650-656.

[15] Thompkins, W.T.Jr. & S.S. Tong: Inverse or design calculation for non-potential flow in turbomachinery blade passages. Ibid, Vol.104, 2(1982), 282-285.

[16] Liu, G.L. & Yan, S.: A unified varable-domain variational approach to hybrid problems of compressible blade-to-blade flow, ASME paper 91-GT-169(1991).

[17] Liu, G.L.: A systematic approach to the search and transformation for VPs in fluid mechanics with emphasis on inverse and hybrid problems, Chinese J. of Engrg Thermophysics (English edition), Vol.2, 4(1990), Allerton Press, New York.

[18] Liu, G.L.: New VP families for direct-, inverse- & hybrid- problems of free surface gravity flow over a spillway, Turbulence Measurements and Flow Modelling, edited by C.J.Chen et al., Hemisphere, New York, (1987)323-332.

[19] Yan, S. and Liu, G.L.: Variable-domain FEM based on VPs for solving hybrid problems of 3-D compressible rotor-flow, presented at the 1991 Yokohama International Gas Turbine Congress. Japan.

[20] Eeer, A. & H.U. Akay: A FE formulation of Euler's equations for the solution of steady transonic flows. AIAA-J. Vol.21, 3(1983), 343-350.

[21] Liu, G.L. & Zhang D.F.: Numerical methods for solving inverse problem of heat conduction with unknown boundary based on VPs with variable domain, Num. Methods for Thermal Problems, edited by R.W. Lewis et al.,Vol.5, Pineridge Press, UK, 1987.

[22] Yan,S. and Liu, G.L.: Variational FEM with variable domain for solving hybrid problems of 3-D incompressible rotor-flow, Experim'l & Comput'l Aerothermodynamics of Internal Flow, N.X.Chen & H.D. Jiang, ed., World Publ. Corp., Beijing, China, (1990)449-456.

Third International Conference on Inverse Design Concepts and Optimization in Engineering Sciences
(ICIDES-III), Editor: G.S. Dulikravich, Washington D.C., October 23-25, 1991.

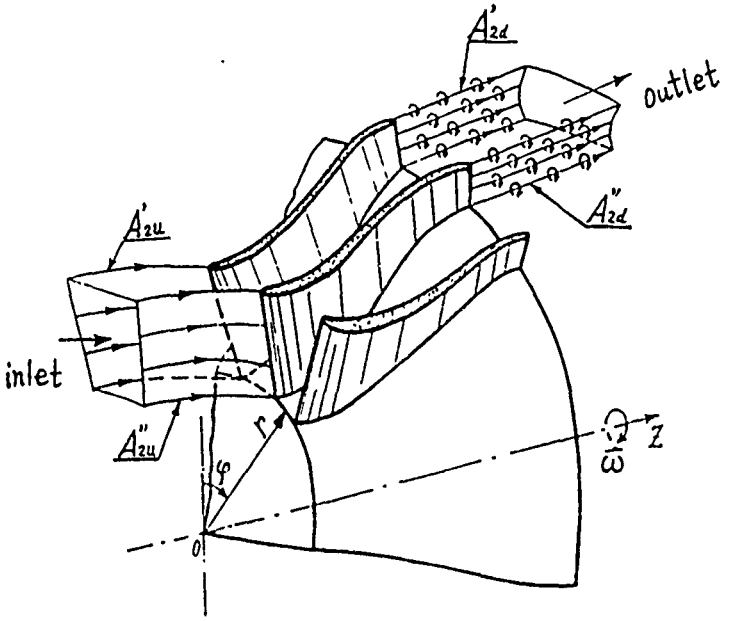


Fig.1 Fully 3-D rotor flow

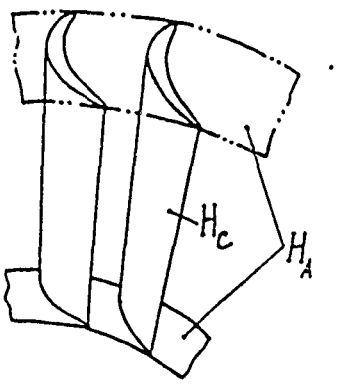


Fig.2a $(H_C > H_A)$-problem

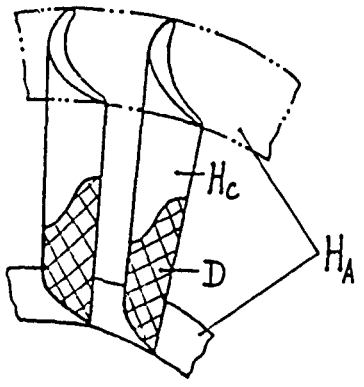


Fig.2b $[(H_C + D) > H_A]$-problem

Third International Conference on Inverse Design Concepts and Optimization in Engineering Sciences (ICIDES-III), Editor: G.S.Dulikravich, Washington, D.C., October 23-25, 1991

Aerodynamic Shape Optimization of Arbitrary Hypersonic Vehicles

George S. Dulikravich and Scott G. Sheffer
Department of Aerospace Engineering
The Pennsylvania State University
University Park, PA 16802, USA

Abstract

A new method has been developed to optimize, in terms of aerodynamic wave drag minimization, arbitrary (nonaxisymmetric) hypersonic vehicles in modified Newtonian flow, while maintaining the initial volume and length of the vehicle. This new method utilized either a surface fitted Fourier series to represent the vehicle's geometry or an independent point-motion algorithm. In either case, the coefficients of the Fourier series or the spatial locations of the points defining each cross section were varied and a numerical optimization algorithm based on a quasi-Newton gradient search concept was used to determine the new optimal configuration. Results indicate a significant decrease in aerodynamic wave drag for simple and complex geometries at relatively low CPU costs. In the case of a cone, the results agreed well with known analytical optimum ogive shapes. The procedure is capable of accepting more complex flow field analysis codes.

Nomenclature

C_p	= surface pressure coefficient
C_{po}	= stagnation pressure coefficient
p	= static pressure at a point
p_∞	= free stream static pressure
M_∞	= free stream Mach number
θ_n	= angle between free stream and normal to the surface of a vehicle
A_m, B_m	= coefficients of Fourier trigonometric series for coordinates at cross section i
x	= Cartesian coordinate along the axis of the body
y, z	= Cartesian coordinates of a contour point at cross section i
s	= body cross section contour-following coordinate
$\bar{s}$	= normalized body cross section contour-following coordinate
γ	= specific heat ratio of the gas
A	= area of a panel on the body surface
$\bar{F}$	= aerodynamic force applied to a panel
$\hat{n}$	= unit normal to the body surface
M	= number of terms in the Fourier trigonometric series
S	= least squares summation
FAC	= percentage change in design variable

Subscripts

i	= i^{th} cross section of the vehicle
j	= j^{th} point of a cross section contour
m	= m^{th} coefficient of a Fourier trigonometric series
n	= angle between free stream and local body surface normal
∞	= free stream value

Introduction

Although optimization of axisymmetric hypersonic bcdies has been accomplished in the past [1,2], the aerodynamic drag minimization of an arbitrary hypersonic vehicle has not been attempted [3]. The objective of this paper is to present an optimization procedure for arbitrarily shaped hypersonic vehicles. While there are certainly some limitations in this paper, including the choice of flow field solver and non-convergence for some shapes, it demonstrates that optimization of numerous variables can indeed be done and that this can be applied to complex configurations.

In hypersonic flow ($M_\infty > 5.0$), the flow around an object may be modeled using an impact theory. In this theory, oncoming particles strike, or impact, the surface of the object and impart the normal component of their momentum to that body. Classical Newtonian theory has been shown to approach reality when the free stream Mach number approaches infinity and the value of the ratio of specific heats approaches $\gamma = 1$ [4]. In the case of lower hypersonic Mach numbers, modified Newtonian theory has been shown to be quite satisfactory for predicting the aerodynamic forces and moments on a body [5]. Modified Newtonian theory has the main advantage of being extremely simple, accurate [6], and fast when faced with the thousands of flow field calculations needed in an optimization problem of this scope. Because of the use of modified Newtonian theory, it was implicitly assumed that the flow field was inviscid.

In this study, modified Newtonian impact flow theory was used with a modified Newtonian constrained search optimization routine [7] to obtain vehicle shapes which had significantly lower wave drag in inviscid hypersonic flow. In the first part of the study, cross section coordinates of the body were represented with curve-fitted Fourier series. Curve-fitted Chebyshev series [8] were initially considered, but it was found that the Fourier series represented complex shapes, such as a Space Shuttle configuration, better than the Chebyshev series. The coefficients of the Fourier series, one set representing the y coordinate and one set for the z coordinate (Fig. 1), then became the design variables that were fed to the optimization routine. The optimization routine sequentially perturbed each of the coefficients by a small amount and determined the new shape that reduced wave drag while keeping the volume and length of the vehicle constant. In the second part of the study, the y and z coordinates of the vehicle's cross section were used as the design variables directly. Again, the optimization routine perturbed separately each of the coordinates at each of the cross section contour points. Then, it combined the changes into a new shape with lower wave drag while still honoring the constraints of constant volume and constant length of the vehicle.

Numerical Models

The first part of this investigation used a least squares Fourier series curve fit to represent the y and z coordinates of each half cross section, i , that is,

$$y_{ij} = \sum_{m=1}^{M} A_{mi} \cos[(m-1)\pi \bar{s}_{i,j}] \qquad (1)$$

Third International Conference on Inverse Design Concepts and Optimization in Engineering Sciences (ICIDES-III), Editor: G.S.Dulikravich, Washington D.C. October 23-25,1991

$$z_{ij} = \sum_{m=1}^{M} B_{mi} \sin[m\pi \bar{s}_{i,j}] \tag{2}$$

where $\bar{s}_{i,j}$ is a normalized contour-following coordinate (Fig. 1) such that

$$s_{i,j} = s_{i,j-1} + \sqrt{(y_{i,j}-y_{i,j-1})^2 + (z_{i,j}-z_{i,j-1})^2} \quad \text{and} \quad \bar{s}_{i,j} = \frac{s_{i,j}}{s_{i,jmax}} \tag{3}$$

and A_{mi} is determined from the least squares fit of the Fourier series

$$S_i = \sum_{j=1}^{jmax} (\sum_{m=1}^{M} (A_{mi} \cos[(m-1)\pi \bar{s}_{i,j}]) - y_{i,j})^2 \quad \text{and} \quad \frac{\partial S_i}{\partial A_{mi}} = 0. \tag{4}$$

The coefficients B_{mi} are determined in a similar way. Since it was assumed that the vehicle had a vertical plane of symmetry, the z-coordinates of the first (j=1) and the last (j=jmax) point of each half cross section were always zero thus ensuring symmetry across the y-axis.

The local surface pressure coefficient, $C_{p,ij}$, was calculated by the use of modified Newtonian impact flow theory, which states that

$$C_{p,ij} = C_{po} \cos^2\theta_{n,ij} \tag{5}$$

where $\theta_{n,ij}$ is the angle between the free stream and the normal to the surface. The stagnation pressure coefficient, C_{po}, is given by

$$C_{po} = \frac{2}{\gamma M_\infty^2}\left[\left(\frac{\gamma+1}{2\gamma M_\infty^2 - \gamma + 1}\right)^{\frac{1}{\gamma-1}} \left(\frac{\gamma+1}{2} M_\infty^2\right)^{\frac{\gamma}{\gamma-1}} - 1\right]. \tag{6}$$

The pressure on a given segment of the body may then be calculated from the rearranged formula for $C_{p,ij}$, that is

$$p_{ij} = p_\infty + \frac{1}{2} C_{p,ij} \gamma p_\infty M_\infty^2 \tag{7}$$

The aerodynamic force on each surface panel is found by

$$\bar{F}_{ij} = - p_{ij} A_{ij} \hat{n}_{ij} . \tag{8}$$

so that the resultant force is obtained by summing up all of the panel forces

$$\bar{F}_{total} = \sum_{ij} \bar{F}_{ij} \tag{9}$$

Aerodynamic wave drag was then the x-component of the resultant aerodynamic force.

The optimization algorithm perturbed each of the Fourier coefficients to obtain a slightly different shape. After perturbing all of the coefficients and analyzing these new perturbed shapes, the optimization algorithm combined the changes into a new shape that met the constraints of constant volume and constant length, but which had a reduced aerodynamic wave drag.

The second part of the study was exactly the same as the first except that instead of working with the Fourier series coefficients we worked with the y and z coordinates of the cross sections' points directly.

Results

Four test cases were run for each part of this study. They consisted of a straight cone having circular cross section shapes, a straight cone having a four pointed star as a cross section, a stubby-wing shaped body and a Space Shuttle-like configuration. All cases were run at an angle of attack of 0°, a specific heat ratio of $\gamma = 1.4$ and a free stream Mach number of $M_\infty = 10$. Notice that the values for γ and M_∞ appear in C_{p0} which may be factored out of the pressure coefficient ratio. They affect the numerical amount of drag, but not the qualitative amount of drag. The x-axis for each case was chosen to coincide with the long axis of the body. The y and z-axes were then mutually perpendicular to the x-axis.

Fourier Series Algorithm: For the initial part of the study, twenty terms in a Fourier series for y and z coordinates were used for seven cross sections. Twenty terms were chosen because of the constraints of computational facilities (an IBM 3090 was used) and because twenty terms were able to represent the geometries of all four test cases, including the complex Space Shuttle shape. Only six of the cross sections were allowed to deform; the nose cross section was kept constant to serve as a tip. Thus there were 6 x 20 x 2 = 240 design variables. Twenty-five points were used per cross section; thus, the half body was discretized into 6 x 24 = 144 panels. FAC, the percent perturbation of A_{mi} and B_{mi} in the optimization algortihm, was set equal to 5%.

For the case of a right circular cone (Fig. 2), after a total of 43 iterations, the program converged to an ogive configuration that had 47.96% less wave drag than the original conical configuration. Note that horizontal and vertical symmetry were maintained.

The next shape tested was a four pointed star configuration (Fig. 3). The aerodynamic wave drag of this shape was reduced by 39.16% after 43 iterations. This case did not converge due to "fishtailing" of the fins and was terminated just before such fishtailing occurred. Note the streaking near the nose and the thinning of the points on the last cross section. Also, notice that vertical and horizontal symmetry was maintained and the fins gave an ogiving contour.

The third shape optimized was that of a "stubby wing" configuration (Fig. 4). The wave drag was reduced by 64.62% when the algorithm converged after 53 iterations while preserving the cross-axis symmetry. Again, note the streaking toward the nose and the smooth appearance of four small fins along the wing tip line.

The fourth test case was that of a Space Shuttle configuration (Fig. 5). After 22 iterations, the wing surface crossed itself and the process was terminated. Aerodynamic wave drag was reduced by 18.52%. With careful scrutiny, one can notice that the centerbody has become ogived, the wing thickness has been reduced, the wing roots have become filleted, and the underside of the fuselage has been reduced in size.

The convergence histories (Fig. 6) indicate that the general trend is a monotonic decrease in drag. This trend can also be seen from the drag plot (Fig. 7) which shows the percentage of original drag remaining at a given iteration number (Table 1).

Point-Motion Algorithm: For the point-motion algorithm, 21 points per half cross section were used. Only six cross sections were analyzed due to computer storage limitations. With only five cross sections being active, this yielded 2 x 5 x 21 = 210 design variables and 5 x 20 =100 surface panels per half cross section. FAC for this algorithm was set to 0.1%.

Third International Conference on Inverse Design Concepts and Optimization in Engineering Sciences (ICIDES-III), Editor: G.S.Dulikravich, Washington D.C., October 23-25, 1991

Numerical optimization of a straight circular cone resulted in an ogive shape with axisymmetry successfully maintained. After 49 iterations, the shape converged to that of Fig. 8 with a corresponding decrease in drag of 45.37%.

The second shape was the four pointed star. With the point-motion algorithm, the shape converged after 35 iterations to that pictured in Fig. 8. There was a reduction of drag of 34.65%. As in the case of the circular cone, symmetry was maintained across both the y and z-axes. The resulting shape is very similar to that obtained by the coefficient algorithm. Considerably less streaking can be seen near the nose of the star, while the fin planforms exibited significant ogiving.

The next shape optimized was the "stubby wing". The fin tips, after 24 iterations, crossed themselves and the process was terminated. However, a decrease of 40.58% of the original wave drag was achieved just before the shape cross-over. Note the development of the fins along the side of the vehicle (Fig. 8) and streaks near the nose, somewhat similar to those developed when using the coefficient algorithm. Once again, symmetry was maintained.

The final case for the point motion algorithm was the Space Shuttle vehicle (Fig. 8). Similar to the case in the coefficient algorithm, the wing eventually crossed itself and the run was terminated. A decrease in drag of 27.38% was found after 16 iterations preceding the cross-over.

For the point-motion algorithm, the convergence histories (Fig. 9) indicate monotonic decrease in wave drag for all four test configurations. Figure 10 demonstrates the total reduction in wave drag for the four test configurations when using the point-motion algorithm (Table 2).

A comparison (Figs. 11 and 12) of the numerically optimized ogive shapes with analytically optimal ogives obtained by Sears and Haack and by von Karman [9] demonstrates the reliability and accuracy of the numerical optimization algorithms.

Conclusions

Two procedures, a coefficient algorithm and a point-motion algorithm, for aerodynamically optimizing aribitrarily shaped hypersonic vehicles have been shown to significantly reduce aerodynamic wave drag while keeping the vehicle's volume and length constant. Both formulations are very fast only because a modified Newtonian flow theory was used as the flow field analysis algorithm. These formulations would be very effective as preliminary design tools for unconventional hypersonic vehicles. The point motion algorithm can be used to keep parts of the original vehicle fixed, such as cabin size or wing thickness, during the optimization. More sophisticated flow field solvers that include viscosity and the effects of heat transfer could be substituted in place of the modified Newtonian theory during the final stages of the optimization.

Acknowledgments

The second author would like to thank Penn State's Propulsion Engineering Research Center, the Penn State CFD Studies Program and the ICIDES project for financial support. Many thanks are due to Mr. Florian Sobieczky for his invaluable assistance in producing the graphics for this paper. The authors would like to thank Apple Computer, Inc. for their donated equipment.

References

1. Dulikravich, G. S, Buss, R. N., Strang, E. J. and Lee, S., "Aerodynamic Shape Optimization of Hypersonic Missiles", AIAA Paper 90-3073, Proceedings of the AIAA 8th Applied Aerodynamics Conference, Portland, OR, August 20-22, 1990.
2. Lee, J. and Mason, W. H., "Development of an Efficient Inverse Method for Supersonic and Hypersonic Body Design", AIAA Paper 91-0395, 29th Aerospace Sciences Meeting, Reno, Nevada, January 7-10, 1991.
3. Blankson, I., "Hypersonic Waveriders: State of the Concept", AIAA Paper 91-0529, Reno, NV , Jan. 7-10, 1991.

4. Anderson, J. D. Jr., Hypersonic and High Temperature Gas Dynamics, McGraw-Hill, New York, 1989.
5. Cox, R.N. and Crabtree, L.F., Elements of Hypersonic Aerodynamics, Academic Press, New York, 1965.
6. Geiger, R. E., "Experimental Lift and Drag of a Series of Glide Configurations at Mach Numbers 12.6 and 17.5," Journal of Aerospace Sciences, April 1962, pp. 410-419.
7. Pshenichny, B. N and Danilin, Y. M., Numerical Methods in Extremal Problems, MIR Publishers, Moscow, 1969.
8. Kuo, S. S., Computer Applications of Numerical Methods, Addison-Wesley Publishing Company, Inc., Philippines, 1972.
9. Ashley, H. and Landahl, M., Aerodynamics of Wings and Bodies, Addison-Wesley Publishing Company, Inc., Reading, Massachusetts, 1965.

Coefficient Test Case	Drag Reduction (%)	# of Optimization Cycles	# of Analysis Calls
Cone	47.96	43	10493
Star	39.16	43	10493
Stubby wing	64.62	53	12689
Space Shuttle	18.52	22	5125

Table 1. Drag reduction, number of optimization cycles and analysis calls for the coefficient test cases that uses Fourier series representation.

Point-Motion Test Case	Drag Reduction (%)	# of Optimization Cycles	# of Analysis Calls
Cone	45.37%	49	10273
Star	34.65	35	7277
Stubby wing	40.58	24	4923
Space Shuttle	27.38	16	3211

Table 2. Drag reduction, number of optimization cycles and analysis calls for the point-motion test cases.

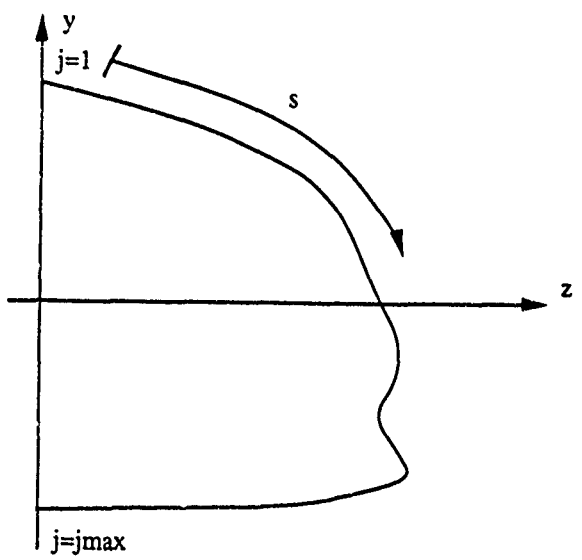
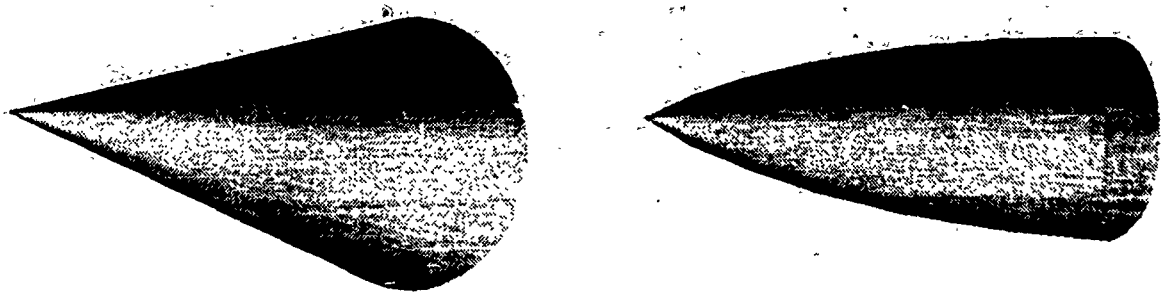


Figure 1. Cross section contour-following coordinate system.

Third International Conference on Inverse Design Concepts and Optimization in Engineering Sciences
(ICIDES-III), Editor: G.S. Dulikravich, Washington D.C. October 23-25, 199



a) initial b) final

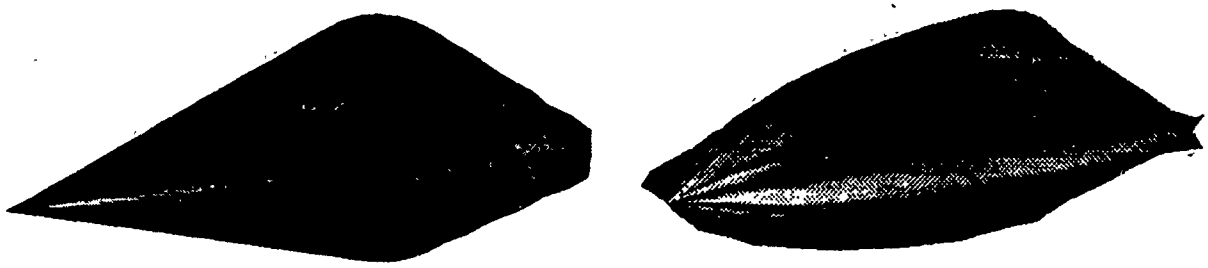
Figure 2. Straight circular cone shape; coefficient algorithm: a) initial shape, b) final shape.



a) initial b) final

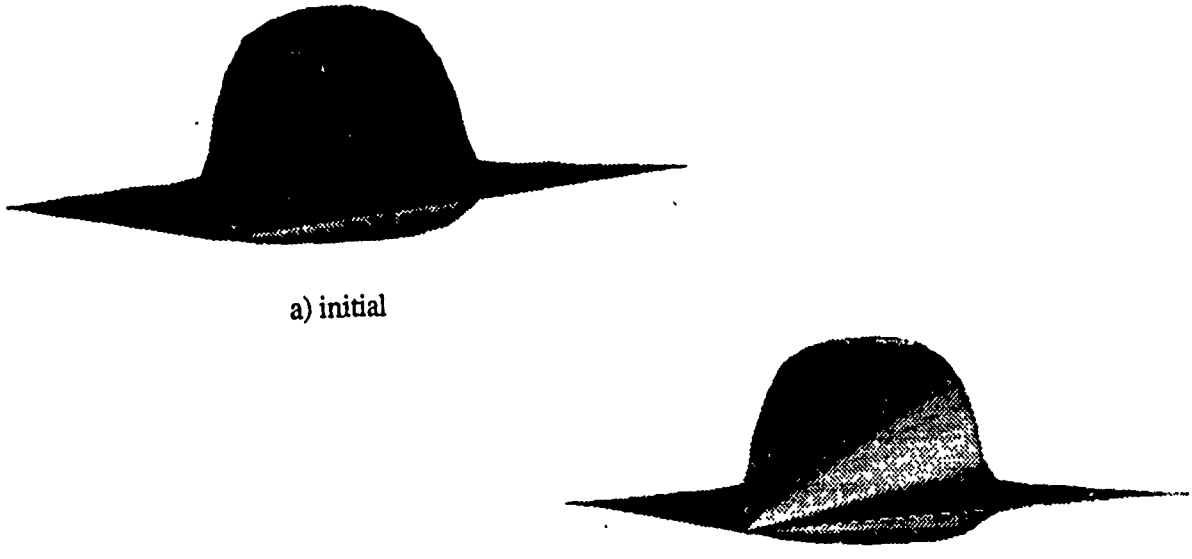
Figure 3. Four pointed star shape; coefficient algorithm: a) initial shape, b) final shape.

Third International Conference on Inverse Design Concepts and Optimization in Engineering Sciences (ICIDES-III), Editor: G.S. Dulikravich, Washington D.C., October 23-25, 1991



a) initial b) final

Figure 4. Stubby wing shape; coefficient algorithm: a) initial shape, b) final shape.



a) initial

b) final

Figure 5. Space Shuttle-like shape; coefficient algorithm: a) initial shape, b) final shape.

Third International Conference on Inverse Design Concepts and Optimization in Engineering Sciences (ICIDES-III), Editor: G.S. Dulikravich, Washington D.C., October 23-25, 1991

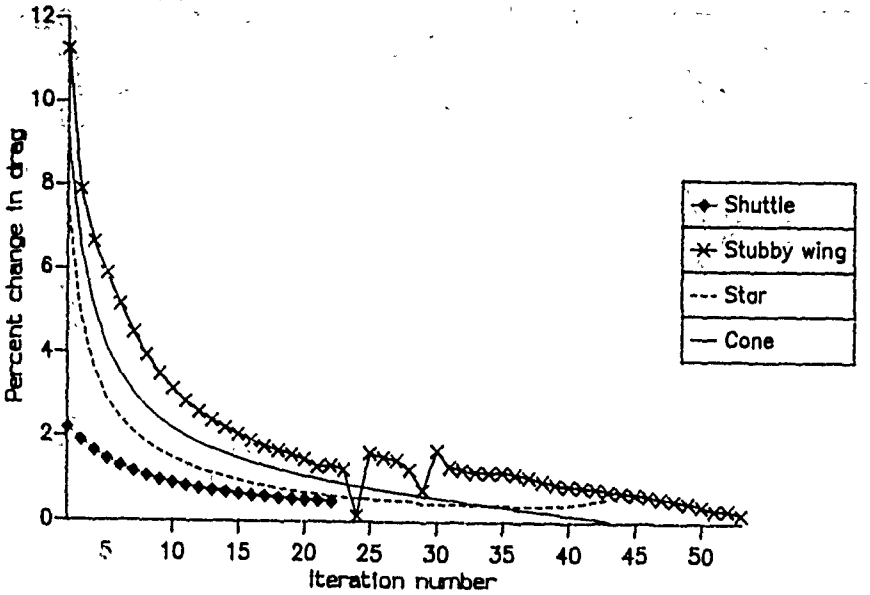


Figure 6. Convergence histories for four test shapes when using coefficient algorithm; percentage change in wave drag per iteration.

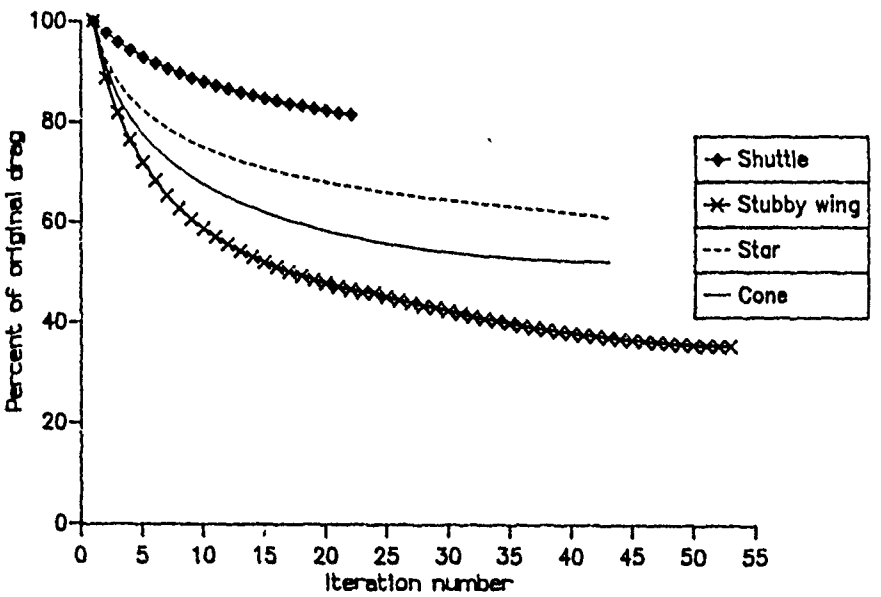


Figure 7. Convergence histories for four test shapes when using coefficient algorithm; total change in wave drag per iteration.

Third International Conference on Inverse Design Concepts and Optimization in Engineering Sciences
(ICIDES-III), Editor: G.S. Dulikravich, Washington D.C. October 23-25, 1991

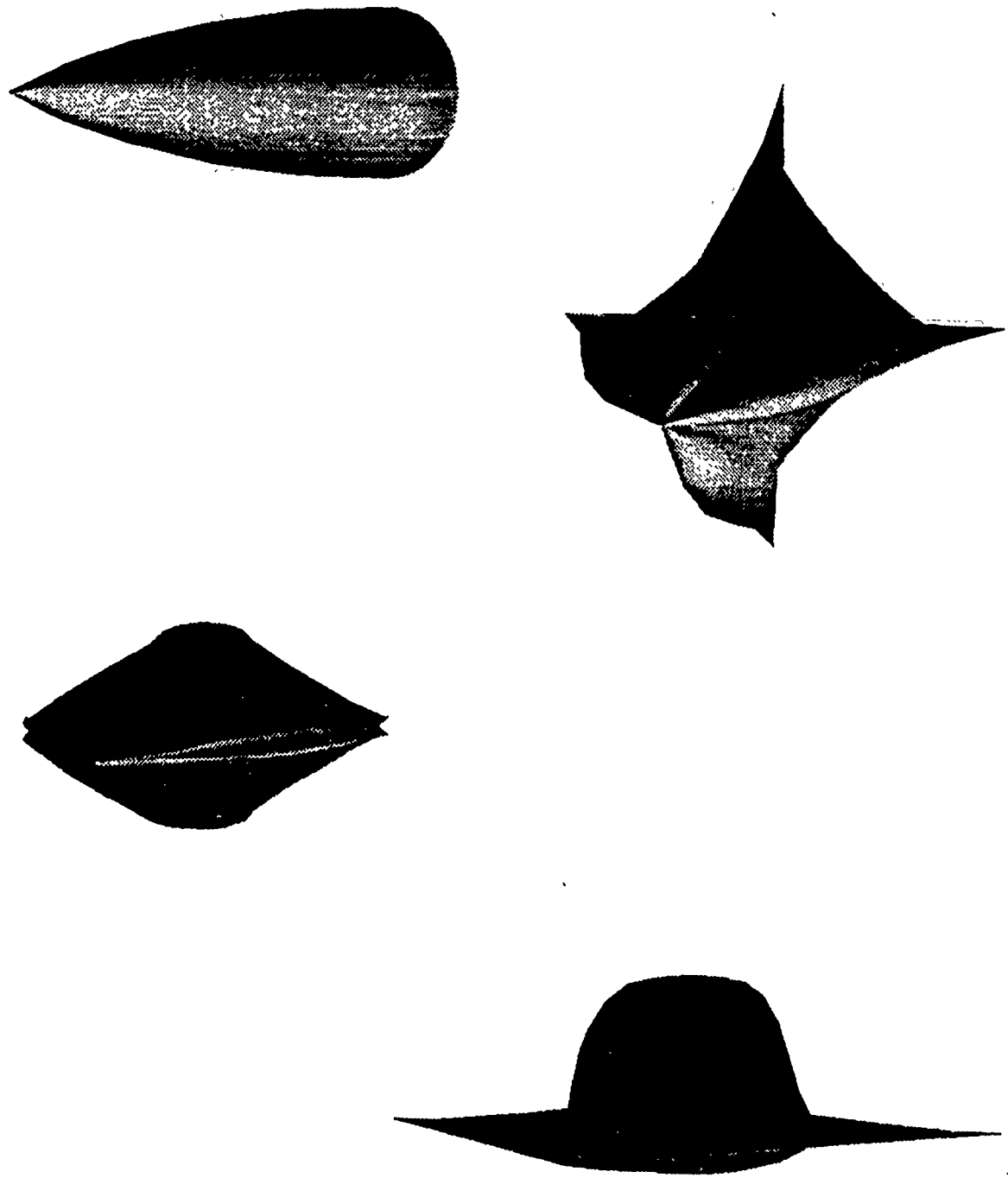


Figure 8. Optimized shapes obtained with the point-motion algorithm.

Third International Conference on Inverse Design Concepts and Optimization in Engineering Sciences (ICIDES-III), Editor: G.S.Dulikravich, Washington D.C. October 23-25, 1991

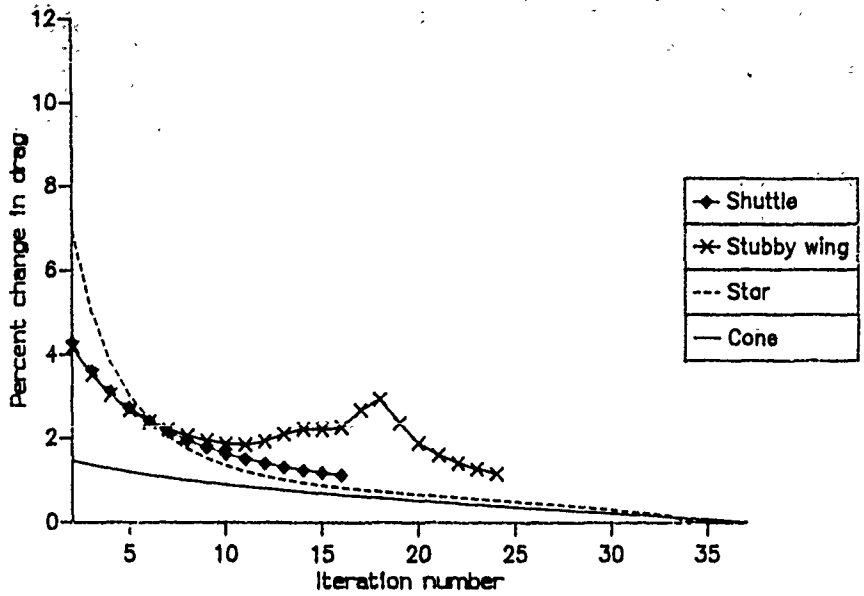


Figure 9. Convergence histories for four test shapes when using point-motion algorithm; percentage change in wave drag per iteration.

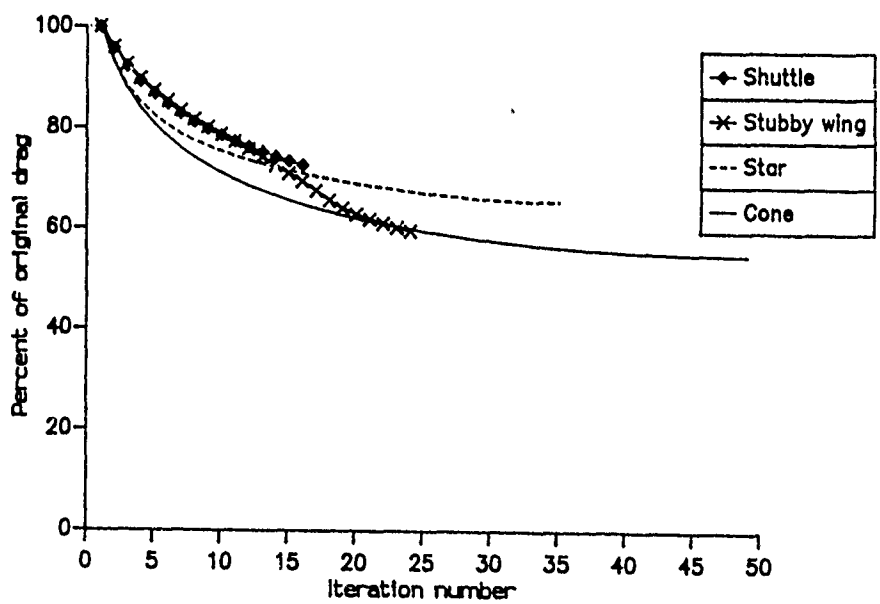


Figure 10. Convergence histories for four test shapes when using point-motion algorithm; total change in wave drag per iteration.

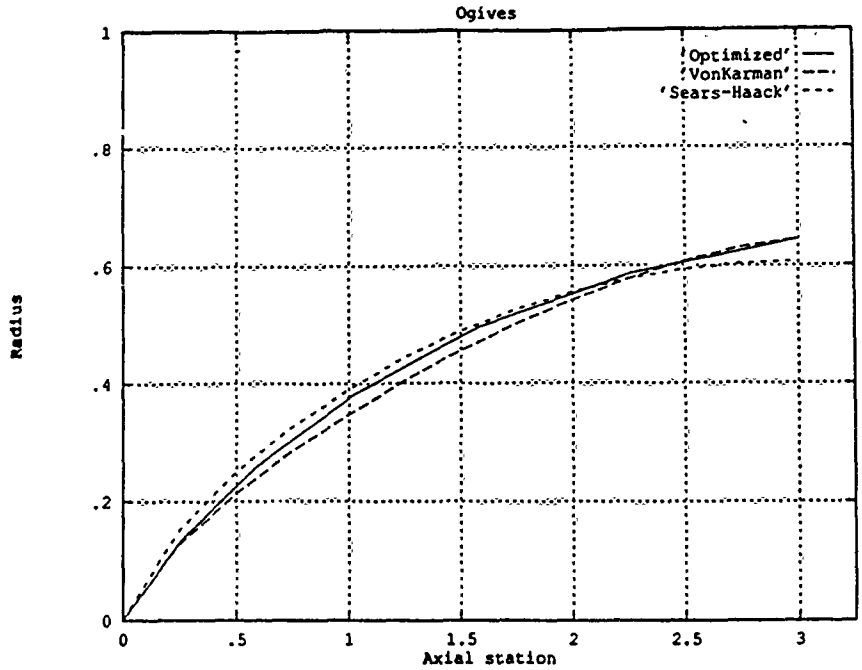


Figure 11. Comparison of analytically optimized ogives and a numerically optimized ogive using coefficient algorithm.

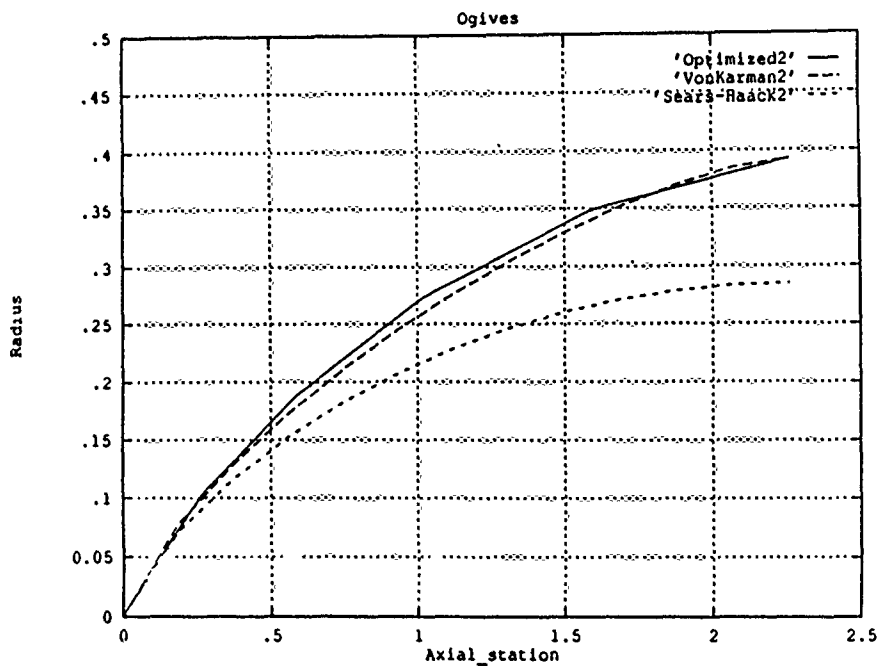


Figure 12. Comparison of analytically optimized ogives and a numerically optimized ogive using point-motion algorithm.

Third International Conference on Inverse Design Concepts and Optimization in Engineering Sciences (ICIDES-III), Editor: G.S. Dulikravich, Washington D.C., October 23-25, 1991

ANALYSIS AND DESIGN OF TRANSONIC AIRFOILS USING STREAMWISE COORDINATES

R.M. BARRON AND C.-F. AN

Department of Mathematics and Statistics
and Fluid Dynamics Research Institute
University of Windsor
Windsor, Ontario, Canada N9B 3P4

Abstract. In this work, a new approach is developed for analysis and design of transonic airfoils. A set of full-potential-equivalent equations in von Mises coordinates is formulated from the Euler equations under the irrotationality and isentropic assumptions. This set is composed of a main equation for the main variable y, and a secondary equation for the secondary variable R. The main equation is solved by type-dependent differencing combined with a shock point operator. The secondary equation is solved by marching from a non-characteristic boundary. Sample computations on NACA 0012 and biconvex airfoils show that, for the analysis problem, the present approach achieves good agreement with experimental C_p distributions. For the design problem, the approach leads to a simple numerical algorithm in which the airfoil contour is calculated as a part of the flow field solution.

1. Introduction

Transonic flow is a widely encountered phenomenon in aeronautics and astronautics but is not easy to calculate because the flow field, and the governing equations as well, are mixed type. Therefore, transonic computation had little progress until 1971 when Murman and Cole developed a type-dependent difference scheme and successfully solved the transonic small disturbance (TSD) equation[1]. Since then, transonic computation has become one of the most upsurging topics for computational fluid dynamicists[2-8]. In 1974, Jameson extended transonic flow computation to the full potential (FP) stage by constructing a rotated difference scheme[4]. Afterwards, papers were published on transonic computation by solving Euler equations[5,6] and their equivalent streamfunction-vorticity formulation[7,8]. Nevertheless, in spite of the recent active efforts on Euler solvers, the full potential calculation is still attractive due to its simplicity, efficiency and sufficient accuracy.

The von Mises transformation is a type of streamline-based transformation which generates a streamwise coordinate system. The von Mises formulation has a number of advantages when applied in CFD. For example, one can resolve the problem of body-fitting coordinates without performing any grid generation. This is because the governing equation (flow physics) and grid generation equation (flow geometry) are combined together in this formulation. Furthermore, the boundary condition on the airfoil for the analysis problem is Dirichlet, and a non-iterative design technique

Third International Conference on Inverse Design Concepts and Optimization in Engineering Sciences (ICIDES-III), Editor: G.S. Dulikravich, Washington D.C., October 23-25, 1991.

can be developed for the inverse problem, leading to simplified numerical algorithms and a saving of computer time. Therefore, since Barron[9] connected the von Mises transformation with Martin's approach[10] and solved incompressible 2-D symmetric flow, numerical simulations based on the von Mises transformation have been considerably extended, such as to incompressible lifting[11], axisymmetric[12] and design[13] problems, and to transonic flow[14,15]. In addition, Greywall[16] and Dulikravich[17] obtained a similar formulation for incompressible and compressible flows, respectively.

However, when extending Barron's approach[9] to transonic flow, several problems appear. For compressible flow, apart from the von Mises variable y, another variable, the density ρ, must be updated in each iteration. But in the transonic range, the classical difficulty of double value density-massflux relation still exists. Besides, shock waves are not easy to handle in von Mises coordinates either by the artificial density technique or by type-dependent differencing. Recently, the authors[18] developed a new approach to overcome these difficulties by solving so-called full-potential-equivalent equations in von Mises coordinates. The principal advances over the previous transonic work[14,15] are as follows: 1) To update density, instead of solving the non-linear algebraic Bernoulli equation, a first order partial differential equation is solved, thereby avoiding the double density problem; 2) To handle shock waves properly, a shock point operator in von Mises coordinates is proposed and combined with the type-dependent difference scheme so that shock waves can be captured correctly; 3) Introducing a concept of generalized density linearizes the density equation.

In the next section, an outline of the mathematical formulation is given. The numerical algorithms for analysis and design problems are constructed in sections 3 and 4. In section 5, sample computations are performed to test the approach, and conclusions are given in section 6.

2. Flow Equations in Streamwise Coordinates

Two dimensional, steady, inviscid fluid flows are governed by the Euler equations

$$\begin{pmatrix} \rho u \\ \rho u^2 + p \\ \rho uv \\ \rho uH \end{pmatrix}_x + \begin{pmatrix} \rho v \\ \rho uv \\ \rho v^2 + p \\ \rho vH \end{pmatrix}_y = 0 \qquad (2\text{-}1)$$

where ρ is density, u and v are velocity components in Cartesian coordinates, p is pressure, $H = \frac{\gamma}{\gamma-1} p/\rho + (u^2+v^2)/2$ is total enthalpy and γ is the ratio of specific heats. ρ, u, v and p are normalized by free stream density ρ_∞, speed q_∞ and dynamic pressure head $\rho_\infty q_\infty^2$ while x and y are scaled by the airfoil chord length.

Introducing streamfunction ψ, such that $\psi_y = \rho u, \psi_x = -\rho v$ and substituting

Third International Conference on Inverse Design Concepts and Optimization in Engineering Sciences (ICIDES-III), Editor: G.S. Dulikravich, Washington D.C., October 23-25, 1991.

into equation $(2-1)$, one gets

$$\begin{pmatrix} \psi_y^2/\rho + p \\ -\psi_x\psi_y/\rho \\ \psi_y H \end{pmatrix}_x + \begin{pmatrix} -\psi_x\psi_y/\rho \\ \psi_x^2/\rho + p \\ -\psi_x H \end{pmatrix}_y = 0. \tag{2-2}$$

Streamfunction $\psi = \psi(x,y)$ can be rewritten in an implicit form, $F(x,y,\psi) = 0$, or in an explicit form, $y = y(x,\psi)$. This process is equivalent to introducing von Mises transformation: $x \equiv \phi, y = y(\phi,\psi)$. If the Jacobian $J = \partial(x,y)/\partial(\phi,\psi) \neq 0, \infty$, then the transformation is single-valued and $(2-2)$ becomes

$$\begin{pmatrix} 1/(\rho y_\psi) + p y_\psi \\ y_\phi/(\rho y_\psi) \\ H \end{pmatrix}_\phi + \begin{pmatrix} -p y_\phi \\ p \\ 0 \end{pmatrix}_\psi = 0 \tag{2-3}$$

where the total enthalpy $H = \frac{\gamma}{\gamma-1}p/\rho + (1+y_\phi^2)/(2\rho^2 y_\psi^2)$. The streamline ordinate y, called von Mises variable, is viewed as a function of ϕ and ψ. The velocity components can be easily calculated from $u = 1/(\rho y_\psi), v = y_\phi/(\rho y_\psi)$, after y and ρ are solved.

It is known that the entropy increase across a shock wave is of third order of the shock strength. So, if the shock is not strong, transonic flow can be assumed isentropic and irrotational. Replacing the energy equation in (2–3) by the isentropic relation and keeping in mind that $\phi \equiv x$, we reduce $(2-3)$ to

$$(\frac{1}{\rho y_\psi} + p y_\psi)_x - (p y_x)_\psi = 0, \tag{2-4a}$$

$$(\frac{y_x}{\rho y_\psi})_x + p_\psi = 0, \tag{2-4b}$$

$$p = \frac{\rho^\gamma}{\gamma M_\infty^2}, \tag{2-4c}$$

$$(\frac{y_x}{\rho})_x - (\frac{1+y_x^2}{\rho y_\psi})_\psi = 0 \tag{2-4d}$$

where M_∞ is free stream Mach number and the last equation is the irrotationality condition, $\omega = 0$, expressed in von Mises coordinates. Substituting $(2-4c)$ into $(2-4a)$ and $(2-4b)$ and expanding $(2-4d)$, we get

$$-y_{x\psi} + y_\psi(y_\psi^2 \frac{\rho^{\gamma+1}}{M_\infty^2} - 1)\frac{\rho_x}{\rho} - y_x y_\psi^2 \frac{\rho^{\gamma+1}}{M_\infty^2}\frac{\rho_\psi}{\rho} = 0, \tag{2-5a}$$

$$y_\psi y_{xx} - y_x y_{x\psi} - y_x y_\psi \frac{\rho_x}{\rho} + y_\psi^2 \frac{\rho^{\gamma+1}}{M_\infty^2}\frac{\rho_\psi}{\rho} = 0, \tag{2-5b}$$

Third International Conference on Inverse Design Concepts and Optimization in Engineering Sciences (ICIDES-III), Editor: G.S. Dulikravich, Washington D.C., October 23-25, 1991.

$$y_\psi^2 y_{xx} - 2y_x y_\psi y_{x\psi} + (1+y_x^2)y_{\psi\psi} - y_x y_\psi^2 \frac{\rho_x}{\rho} + y_\psi(1+y_x^2)\frac{\rho_\psi}{\rho} = 0. \qquad (2\text{-}5c)$$

Properly manipulating the above three equations can produce several sets of equations. Each set has two independent equations for two variables. To make the formulation more compact, define generalized density $R = \rho^{\gamma+1}$ as an alternative to density ρ. Solving for ρ_x/ρ and ρ_ψ/ρ from $(2-5a)$and $(2-5b)$, and substituting into $(2-5c)$, one gets

$$(y_\psi^2 - \frac{M_\infty^2}{R})y_{xx} - 2y_x y_\psi y_{x\psi} + (1+y_x^2)y_{\psi\psi} = 0. \qquad (2\text{-}6a)$$

Eliminating $y_{x\psi}$ from $(2-5a)$ and $(2-5b)$ gives

$$y_x y_\psi^2 R_x - y_\psi(1+y_x^2)R_\psi = (\gamma+1)M_\infty^2 y_{xx}. \qquad (2\text{-}6b)$$

Equation $(2-5a)$ can be rewritten as

$$y_\psi(y_\psi^2 - \frac{M_\infty^2}{R})R_x - y_x y_\psi^2 R_\psi = (\gamma+1)M_\infty^2 y_{x\psi}. \qquad (2\text{-}6c)$$

Substituting the above $y_{xx}, y_{x\psi}$ into $(2-5c)$ and replacing ρ by R, one obtains

$$y_x(y_\psi^2 - \frac{M_\infty^2}{R})R_x + y_\psi(1 - y_x^2 - \frac{M_\infty^2}{R}\frac{1+y_x^2}{y_\psi^2})R_\psi = (\gamma+1)M_\infty^2 \frac{1+y_x^2}{y_\psi^2} y_{\psi\psi}. \qquad (2\text{-}6d)$$

It is important to note that $(2-6b)$ is linear after introducing the new variable R. The term M_∞^2/R is usually called compressibility factor.

In principle, any two of the above four equations could be combined as a set of equations to solve for y and R. But, in practice, equation $(2-6a)$ is always selected to solve for y and one of the remaining three equations is selected to solve for R. Equation $(2-6a)$ is a second order, non-linear, partial differential equation of mixed type depending on the local flow property. If the flow is subsonic/supersonic, then $(2-6a)$ is elliptic/hyperbolic. In other words, the mathematical classification of the equation is consistent with the physical nature of the local flow. Therefore, $(2-6a)$ is named the main equation for the corresponding main variable y. Equations $(2-6b)-(2-6d)$ are called secondary equations for the secondary variable R. Among the three secondary equations, $(2-6b)$ appears simpler because it is linear and hence priority is given to it to accompany the main equation. The main equation $(2-6a)$ and one of the secondary equations $(2-6b)-(2-6d)$ constitute a set of so-called full-potential-equivalent equations. They are coupled with each other and solved in an alternating and iterative manner. More details and other forms of full-potential-equivalent equations can be found in [18].

Third International Conference on Inverse Design Concepts and Optimization in Engineering Sciences (ICIDES-III), Editor: G.S. Dulikravich, Washington D.C., October 23-25, 1991.

3. Analysis Problem

For a symmetric airfoil placed in a transonic stream at zero angle of attack, the governing equations $(2-6a)$ and $(2-6b)$ can be rewritten as

$$A_1 y_{xx} + A_2 y_{x\psi} + A_3 y_{\psi\psi} = 0, \tag{3-1}$$

$$B_1 R_x + B_2 R_\psi = B_3 \tag{3-2}$$

where $A_1 = y_\psi^2 - M_\infty^2/R, A_2 = -2y_x y_\psi, A_3 = 1 + y_x^2, B_1 = y_x y_\psi^2, B_2 = -y_\psi(1 + y_x^2), B_3 = (\gamma+1)M_\infty^2 y_{xx}$. The boundary conditions on y are Dirichlet: $y = f(x)$ on the airfoil, $y = \psi$ at infinity, $y = 0$ on the symmetry line and $R = 1$ at infinity, where $f(x)$ is the airfoil shape function. The computational domain and boundary conditions are shown in Fig.1.

Since the mathematical character of $(3-1)$ depends on the local flow property, it is necessary to apply Murman and Cole's type-dependent scheme[1] to solve for y. Applying the type-dependent difference scheme to $(3-1)$ gives

$$Ay_{i,j-1} + By_{i,j} + Cy_{i,j+1} = RHS \tag{3-3}$$

where $A = \beta^2 A_3 - \frac{1-\nu}{2}\beta A_2, B = -2\beta^2 A_3 + (1-3\nu)A_1, C = \beta^2 A_3 + \frac{1-\nu}{2}\beta A_2,$

$$\begin{aligned} RHS = &-\nu A_1(y_{i+1,j} + y_{i-1,j}) + (1-\nu)A_1(2y_{i-1,j} - y_{i-2,j}) \\ &- \nu\beta A_2(y_{i+1,j+1} - y_{i+1,j-1} - y_{i-1,j+1} + y_{i-1,j-1})/4 \\ &+ (1-\nu)\beta A_2(y_{i-1,j+1} - y_{i-1,j-1})/2, \end{aligned}$$

and $\beta = \Delta x/\Delta\psi$, for $i = 2,3,...,I_{max}-1, j = 2,3,...,J_{max}-1$. The switch parameter $\nu = 1$ for a subsonic point, $\nu = 0$ for a supersonic point. The resulting system of difference equations $(3-3)$ has a tridiagonal coefficient matrix so that SLOR can be applied by relaxing along vertical lines, sweeping from left to right and iterating up to convergence. (see Fig.1)

After $y(x,\psi)$ is solved from the main equation $(3-1)$ and y_x, y_ψ, y_{xx} are properly differenced, the secondary equation $(3-2)$ can be solved for $R(x,\psi)$ by marching from an initial line other than its characteristic curve. The slope of its characteristic curve is $d\psi/dx = -(1+y_x^2)/(y_x y_\psi)$. At infinity, $d\psi/dx = \infty$. Thus, left and right far field boundaries are characteristic curves and hence cannot serve as initial lines. Fortunately, the horizontal boundary is not a characteristic and we can march equation $(3-2)$ from the top boundary to the airfoil using the condition $R = 1$ at infinity.

The Crank-Nicolson scheme for $(3-2)$ gives

$$\tilde{A}R_{i-1,j} + \tilde{B}R_{i,j} + \tilde{C}R_{i+1,j} = \widetilde{RHS} \tag{3-4}$$

Third International Conference on Inverse Design Concepts and Optimization in Engineering Sciences (ICIDES-III), Editor: G.S. Dulikravich, Washington D.C., October 23-25, 1991.

where $\widetilde{RHS} = \widetilde{C}R_{i-1,j+1} + \widetilde{B}R_{i,j+1} + \widetilde{A}R_{i+1,j+1} + 4\Delta x B_3, \widetilde{A} = -B_1, \widetilde{B} = -4\beta B_2,$ $\widetilde{C} = B_1, \beta = \Delta x/\Delta\psi$ for $j = J_{max} - 1, ..., 3, 2, 1, i = 2, 3, ..., I_{max} - 1$. The system of difference equations $(3-4)$ can be solved row by row from the horizontal far field to the airfoil using SLOR, but no iteration is needed because $(3-2)$ is linear. After R is solved, the pressure coefficient is calculated from

$$C_p = \frac{2}{\gamma M_\infty^2}(R^{\frac{\gamma}{\gamma+1}} - 1). \tag{3-5}$$

However, it has been found after numerical tests that this procedure is efficient only for flow in which the shock is weak. For flow with a stronger shock, the iterations fail to converge. To overcome this difficulty, a special treatment of the shock wave is proposed following the ideas of Murman's shock structure analysis[2,3]. For usual transonic flows, the shock wave is approximately normal and the shock jump conditions are given by

$$[\frac{y_x}{\rho}] = 0, \qquad [y_\psi] = 0. \tag{3-6}$$

where [...] represents a jump across the shock. Based on this analysis, the difference quotient approximations to $y_{xx}, y_{x\psi}$ at a shock point, i.e. grid point just behind the shock, are constructed as below:

$$(y_{xx})_{i,j} = \frac{1}{\Delta x^2}(y_{i+1,j} - y_{i,j} - \alpha_j y_{i-1,j} + \alpha_j y_{i-2,j}) \tag{3-7a}$$

$$\begin{aligned}(y_{x\psi})_{i,j} = \frac{1}{4\Delta x\Delta\psi}(&y_{i+1,j+1} - y_{i+1,j-1} + y_{i,j+1} - y_{i,j-1} \\ &- 3y_{i-1,j+1} + 3y_{i-1,j-1} + y_{i-2,j+1} - y_{i-2,j-1}).\end{aligned} \tag{3-7b}$$

where α_j is the density jump factor on j^{th} streamline and given by the Rankine-Hugoniot relation of a normal shock. $(3-7a)$ and $(3-7b)$ are called shock point operator (SPO) in von Mises coordinates. The difference equations $(3-3)$ for y and $(3-4)$ for R are modified using SPO. Numerical experimentation has shown that SPO must be applied in the $y_{xx}, y_{x\psi}$ terms of the main equation $(3-1)$ and in the B_3 term of the secondary equation $(3-2)$. SPO is a crucial tool to capture shock waves in supercritical transonic flows.

4. Design Problem

Similar to the analysis problem, the main equation $(2-6a)$ and secondary equations $(2-6b)$ or $(2-6c)$ can be solved for y and R alternatively:

$$A_1 y_{xx} + A_2 y_{x\psi} + A_3 y_{\psi\psi} = 0, \tag{4-1a}$$

Third International Conference on Inverse Design Concepts and Optimization in Engineering Sciences (ICIDES-III), Editor: G.S. Dulikravich, Washington D.C., October 23-25, 1991.

$$B_1 R_x + B_2 R_\psi = B_3, \tag{4-1b}$$

$$D_1 R_x + D_2 R_\psi = D_3 \tag{4-1c}$$

where $A_1 = y_\psi^2 - M_\infty^2/R, A_2 = -2y_x y_\psi, A_3 = 1 + y_x^2, B_1 = y_x y_\psi^2, B_2 = -y_\psi(1 + y_x^2), B_3 = (\gamma+1)M_\infty^2 y_{xx}, D_1 = y_\psi(y_\psi^2 - M_\infty^2/R), D_2 = -y_x y_\psi^2, D_3 = (\gamma+1)M_\infty^2 y_{x\psi}$. The boundary conditions are the same as in the analysis problem, except on the airfoil, which is unknown. There, the pressure coefficient C_{p_s} is specified, hence, the generalized density is also specified:

$$R_s = (1 + \gamma M_\infty^2 C_{p_s}/2)^{(\gamma+1)/\gamma} \tag{4-2}$$

On the airfoil surface, the Bernoulli equation in von Mises coordinates leads to

$$F(x)y_\psi^2 - y_x^2 = 1 \tag{4-3}$$

where

$$F(x) = \frac{2}{(\gamma-1)M_\infty^2}[(1 + \frac{\gamma-1}{2}M_\infty^2)R_s^{\frac{2}{\gamma+1}} - R_s].$$

This is a Neumann boundary condition on the airfoil when solving $(4-1a)$ for y. $(4-2)$ is a Dirichlet boundary condition on the airfiol when solving $(4-1c)$ for R. In addition, on a symmetry line off the airfoil, $R_\psi = 0$.

If streamlines do not intesect each other on the airfoil, then $y_\psi > 0$, and if, furthermore, $F(x) \neq 0$ on the airfoil, then equation $(4-3)$ gives $y_\psi = \sqrt{(1 + y_x^2)/F(x)}$. For most practical transonic flows the required conditions are easily satisfied as long as C_{p_s} is reasonably specified. Differencing y_ψ, we get

$$y_{i,1} = [4y_{i,2} - y_{i,3} - 2G(x_i)]/3 \tag{4-4}$$

where $G(x_i) = \Delta\psi\sqrt{[1 + (y_x^2)_{i,1}]/F(x_i)}$. Considering this new boundary condition, we modify system $(3-3)$ as follows:

For $j = 2$, equation $(3-3)$ reads $Ay_{i,1} + By_{i,2} + Cy_{i,3} = RHS$. Substituting $(4-4)$ into it, we have

$$(B + 4A/3)y_{i,2} + (C - A/3)y_{i,3} = RHS + 2AG(x_i)/3 \tag{4-5}$$

Replacing the first equation in system $(3-3)$ by $(4-5)$, solving the resulting system and applying $(4-4)$, we can obtain the desired airfoil contour $f(x_i) = y_{i,1}$ without further iteration of the airfoil shape. The computational domain and boundary conditions are shown in Fig. 2.

To solve for the secondary variable R, two secondary equations $(4-1b)$ and $(4-1c)$ are available. For equation $(4-1b)$, the marching procedure is the same as in the analysis problem, while for equation $(4-1c)$, the marching procedure is

different. The slope of its characteristic curve is $d\psi/dx = -(y_x y_\psi)/(y_\psi^2 - M_\infty^2/R)$. At infinity, $d\psi/dx = 0$. So, the horizontal far field boundary is a characteristic curve, but the vertical boundaries are not. Therefore, the marching process can be carried out from left to right.

Crank-Nicolson scheme for $(4-1c)$ gives

$$\bar{A}R_{i,j-1} + \bar{B}R_{i,j} + \bar{C}R_{i,j+1} = R\bar{H}S \tag{4-6}$$

where $R\bar{H}S = \bar{C}R_{i-1,j-1} + \bar{B}R_{i-1,j} + \bar{A}R_{i-1,j+1} + 4\Delta x D_3, \bar{A} = -\beta D_2, \bar{B} = 4D_1$, $\bar{C} = \beta D_2, \beta = \Delta x/\Delta\psi$, for $i = 2,3,...,I_{max}-1, j = 2,3,...,J_{max}-1$.

For the first equation in system $(4-6)$, the boundary conditions $R_{i,1} = R_s(x_i)$ on the airfoil and $R_{i,1} = R_{i,2}$ on symmetry line should be imposed. It is noted that $y_{x\psi}$ in D_3 should be type-dependent differenced with SPO to keep consistency with the main equation.

Both $(4-1b)$ and $(4-1c)$ have been coupled with $(4-1a)$. Numerical experiments have shown that $(4-1c)$ gives better accuracy than $(4-1b)$. This is reasonable because the boundary condition on the airfoil is considered not only in the main equation $(4-1a)$, but also in the secondary equation $(4-1c)$, while it is not suitably considered in the secondary equation $(4-1b)$. However, the price to pay is more iterations because $(4-1c)$ is non-linear.

5. Sample Computations

The approach developed here is applied to calculated transonic flows for both analysis and design problems. Only symmetric airfoils at zero angle of attack are considered, but both subcritical and supercritical Mach numbers are included. In the computational domain, a 65x33 uniform mesh covers $-2 \le x \le 3, 0 \le \psi \le 2.5$ and the airfoil is placed between 0 and 1. For higher Mach numbers, a 80x31 mesh has been used. The computational domain and boundary conditions are shown in Figures 1 and 2.

Figures 3 and 4 are comparisons of calculated C_p distributions of NACA 0012 with experimental data at NAE[19] for $M_\infty = 0.490$ and at ONERA[19] for $M_\infty = 0.803$. Figure 5 indicates the calculated C_p distribution of a 6 percent biconvex airfoil at $M_\infty = 0.909$ compared with experimental data at NASA[20]. From these plots we can see that the present approach is able to accurately predict C_p distributions on airfoils in transonic flows. The agreement between computed pressure and available experimental data is quite satisfactory. For supercritical transonic flows, the shock wave can be captured by the presently proposed type-dependent scheme with SPO.

Figure 6 shows the designed contour of a 6 percent biconvex airfoil compared with the exact shape[21]. The specified C_p distribution on the airfoil comes from experiments at NASA[20] for $M_\infty = 0.909$. Figures 7 and 8 give designed NACA 0012 contours compared with the exact shape[21]. The specified C_p is from NAE[19] for $M_\infty = 0.490$ and ONERA[19] for $M_\infty = 0.803$. Here, we can see that the present approach is capable of designing airfoil contours with satisfactory accuracy.

Third International Conference on Inverse Design Concepts and Optimization in Engineering Sciences (ICIDES-III), Editor: G.S. Dulikravich, Washington D.C., October 23-25, 1991.

6. Conclusions

1) The newly developed approach based on the full-potential-equivalent equations in von Mises coordinates is able to solve transonic flows for both analysis and design problems.

2) The full-potential-equivalent equations are composed of a main equation for the corresponding main variable, streamline ordinate y, and a secondary equation for the related secondary variable, generalized density R.

3) The type-dependent difference scheme with shock point operator is effective to solve the main equation for y and the shock point operator is crucial to capture shock waves in supercritical transonic flows.

4) The secondary equation can be solved for R by marching from a certain non-characteristic, density-specified boundary. Crank-Nicolson scheme proves to be useful to march such a equation.

5) For analysis problems, the boundary condition on the airfoil is Dirichlet, which is easy to implement.

6) For design problems, the airfoil contour can be obtained in a non-iterative manner because it is a part of the solution of the main equation.

References

1. E. M. Murman and J. D. Cole, Calculation of Plane Steady Transonic Flows, AIAA J., Vol.9, 114-121 (1971)

2. E. M. Murman and J. A. Krupp, Solution of the Transonic Potential Equation Using a Mixed Finite Difference System, Lecture Notes in Physics, Vol.8, pp199-206, Springer-Verlag, Berlin, 1974

3. E. M. Murman, Analysis of Embedded Shock Waves Calculated by Relaxation Methods, AIAA J., Vol.12, 626-633 (1974)

4. A. Jameson, Iterative Solution of Transonic Flows over Airfoils and Wings, Including Flows at Mach 1, Communications on Pure and Applied Mathematics, Vol.27, 283-309 (1974)

5. R. M. Beam and R. F. Warming, An Implicit Finite Differnce Algorithm for Hyperbolic System in Conservation Law Form, J.of Comp. Phys., Vol.22, 87-110 (1976)

6. J. C. Steger, Implicit Finite Difference Simulation of Flow around Arbitrary Two Dimensional Geometries, AIAA J., Vol.16, 676-686 (1978)

7. M. Hafez and D. Lovell, Numerical Solution of Transonic Stream Function Equation, AIAA J., Vol.21, 327-335 (1983)

8. H. L. Atkins and H. A. Hassan, A New Stream Function Formulation for the Steady Euler Equations, AIAA J., Vol.23, 701-706 (1985)

9. R. M. Barron, Computation of Incompressible Potential Flow Using von Mises Coordinates, J. of Math. and Comp. in Simulation, Vol.31, 177-188 (1989)

Third International Conference on Inverse Design Concepts and Optimization in Engineering Sciences (ICIDES-III), Editor: G.S. Dulikravich, Washington D.C., October 23-25, 1991.

10. M. H. Martin, The Flow of a Viscous Fluid I, Archives for Rational Mechanics and Analysis, Vol.41, 266-286 (1971)

11. R. K. Naeem and R. M. Barron, Lifting Airfoil Calculations Using von Mises Variables, Communications in Applied Numerical Methods, Vol. 5, 203-210(1989)

12. R. M. Barron, S. Zhang, A. Chandna and N. Rudraiah, Axisymmetric Potential Flow Calculations, Part 1: Analysis Mode, Communications in Applied Numerical Methods, Vol. 6, 437-445(1990)

13. R. M. Barron, A Non-Iterative Technique for Design of Aerofoils in Incompressible Potential Flow, Communications in Applied Numerical Methods, Vol. 6, 557-564(1990)

14. R. M. Barron and R. K. Naeem, Numerical Solution of Transonic Flows on a Streamfunction Coordinate System, Intl. J. for Num. Methods in Fluids, Vol.9, 1183-1193 (1989)

15. R. K. Naeem and R. M. Barron, Transonic Computations on a Natural Grid, AIAA J., Vol.28, 1836-1838(1990)

16. M. S. Greywall, Streamwise Computation of 2-D Incompressible Potential Flows, J. of Comp. Phys., Vol.59, 224-231 (1985)

17. G. S. Dulikravich, A Stream-Function-Coordinate (SFC) Concept in Aerodynamic Shape Design, AGARD VKI Lecture Series, May 14-18, 1990

18. C.-F. An and R. M. Barron, Numerical Solution of Transonic Full-Potential-Equivalent Equations in von Mises Coordinates, to appear

19. J. J. Thibert, M. Grandjacques and L. H. Ohman, Experimental Data Base for Computer Program Assessment, AGARD AR-138, pp.A1-1 — A1-36, 1979

20. E. D. Knetchtel, Experimental Investigation at Transonic Speeds of Pressure Distributions over Wedge and Circular-Arc-Airfoil Sections and Evaluation of Perforated Wall Interferance, NASA TN D-15, 1959

21. I. Abbott and A. E. von Doenhoff, Theory of Airfoil Section, Dover Publ. Inc., N.Y., 1959

Third International Conference on Inverse Design Concepts and Optimization in Engineering Sciences (ICIDES-III), Editor: G.S. Dulikravich, Washington D.C., October 23-25, 1991.

FIG.1 ANALYSIS PROBLEM
Computational Domain
and Boundary Conditions

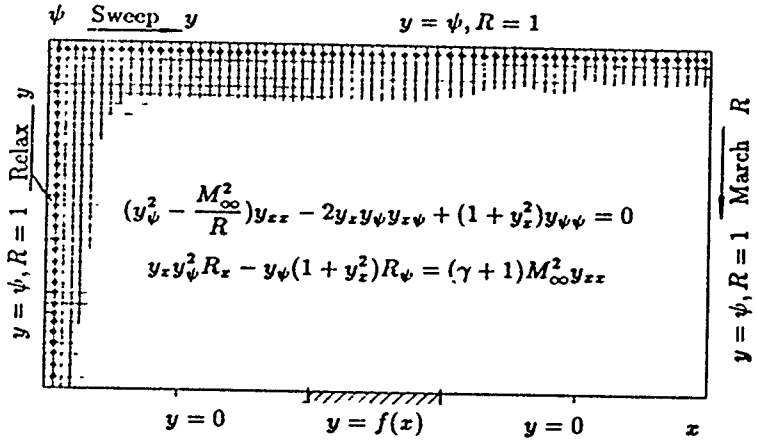


FIG.2 DESIGN PROBLEM
Computational Domain
and Boundary Conditions

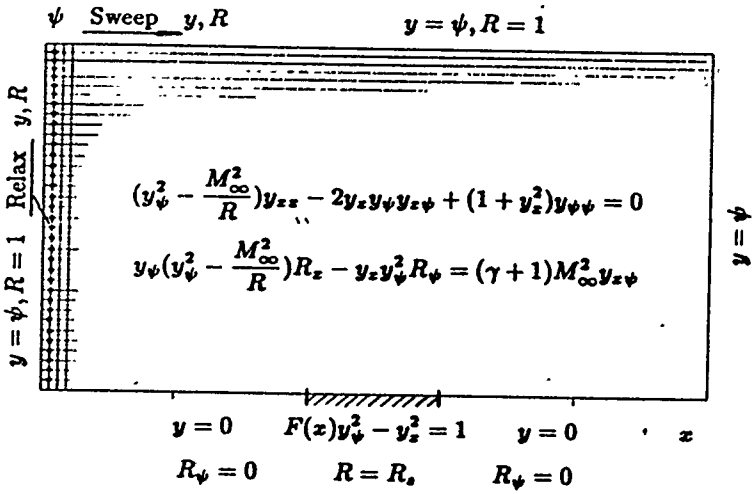


FIG.3 COMPARISON OF Cp DISTRIBUTION
NACA 0012, Mach=0.490

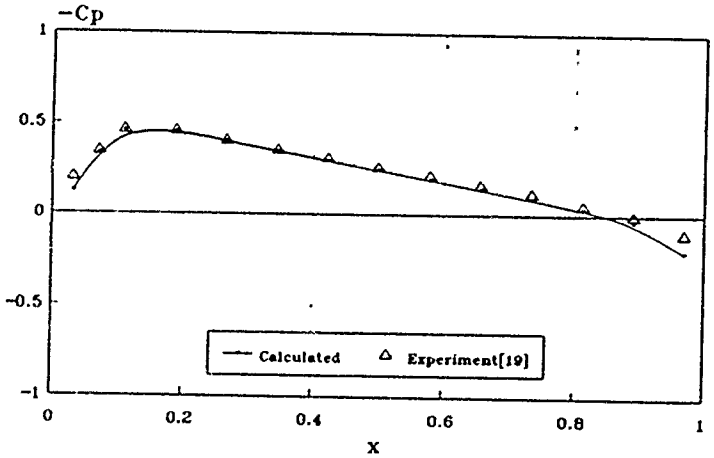
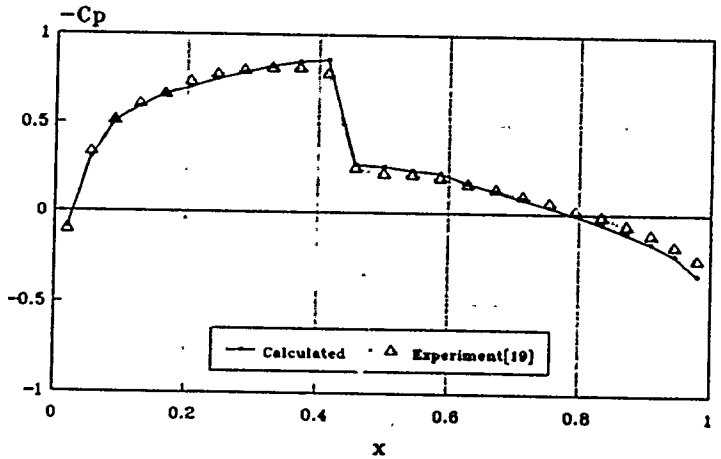


FIG.4 COMPARISON OF Cp DISTRIBUTION
NACA 0012, Mach=0.803



Third International Conference on Liverse Design Concepts and Optimization in Engineering Sciences
(ICIDES-III), Editor: G.S. Dulikravich, Washington D.C., October 23-25, 1991.

FIG.5 COMPARISON OF Cp DISTRIBUTION
Biconvex(6%) Airfoil, Mach=0.909

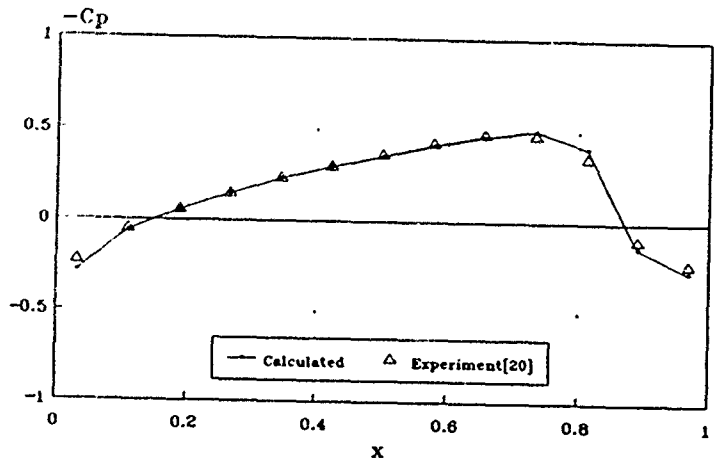


FIG.6 DESIGNED BICONVEX(6%) AIRFOIL
Mach=0.909

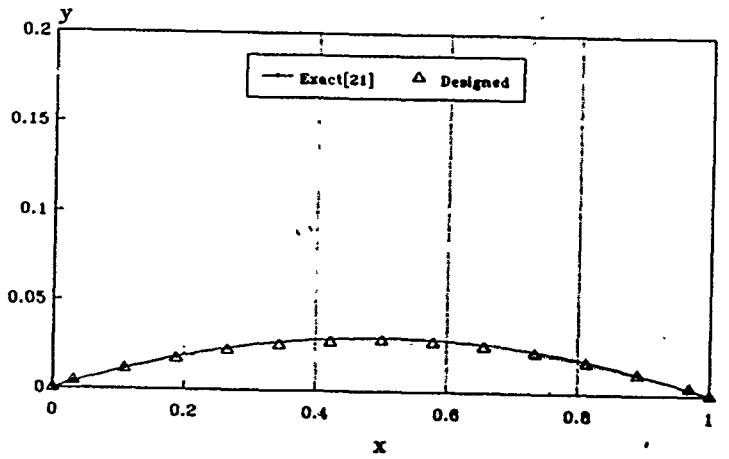


FIG.7 DESIGNED NACA 0012 AIRFOIL
Mach=0.490

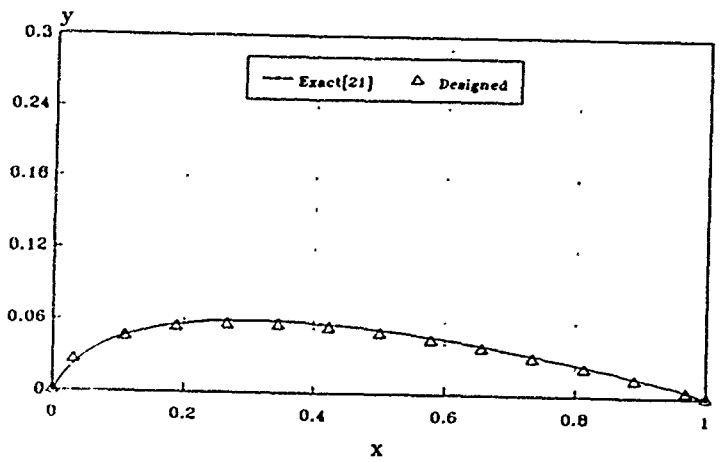
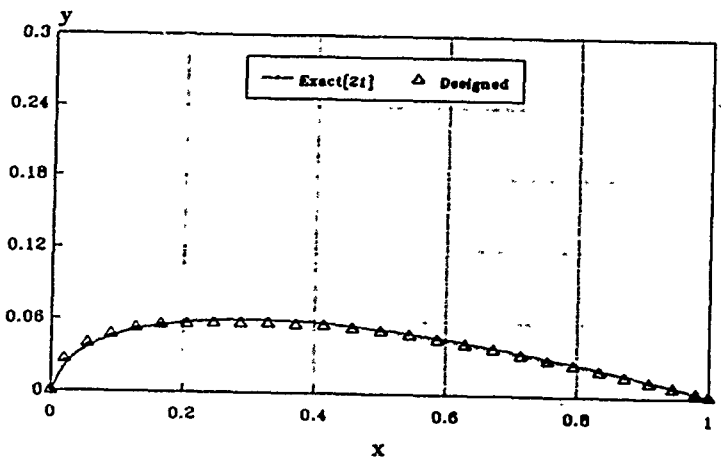


FIG.8 DESIGNED NACA 0012 AIRFOIL
Mach=0.803



Third International Conference on Inverse Design Concepts and Optimization in Engineering Sciences (ICIDES-III), Editor: G.S. Dulikravich, Washington D.C., October 23-25, 1991.

RESEARCH ON INVERSE METHODS AND OPTIMIZATION IN ITALY

Francesco Larocca
FIAT AVIO, Corso Ferrucci 112, 10129, Turin Italy

1 Introduction

The paper deals with the research activities in Italy on inverse design and optimization. The review is focused on aerodynamic aspects in turbomachinery and wing sections design.

Inverse design of blade rows and ducts of turbomachinery in subsonic and transonic regime are illustrated here by the contributions of "Politecnico di Torino" and turbomachinery industry (FIAT AVIO).
As far as turbomachinery design is concerned, the development of an optimization technique is shown by the contributions of the "Universita' di Genova".

Contributions from the " Universita' di Bari " illustrate recent progress in aerfoils design in the field of subsonic flow.

2 Turbomachinery Components

2.1 Design of cascade and ducts in transonic flow

A methodology to solve inverse design problems for channels and blade rows, assuming the flow to be multidimensional and the fluid inviscid, compressible and ideal, is described in [1]. The methodology is based on the procedures described in [2] for the solution of inverse problems in 2D channels, in [3] for 2D inverse cascade problems, in [5] for 3D inverse blade rows problems. An updated version of the methodology is described in [6] for both 2D and 3D inverse problems in channels and blade rows.
The basic idea is described in [2]. Briefly, a time-dependent computation is performed in a duct, where a distribution of pressure is prescribed on a wall, the geometry of which is unknown and has to be determined. Such a wall is a boundary of the flow field and it is assumed as a flexible and impermeable surface. Some initial configuration is guessed for the shape of the wall and for the internal flowfield. During the following transient the flexible wall move in a wavy fashion and, at the end, it will assume the steady shape required by the prescribed pressure on it and in agreement with the steady internal flow.
A coordinate transformation is used in order to map the physical region, whose shape depends on time, into a computational domain, whose shape is independent of time. The Euler equations are integrated in time by a finite difference method on the time-dependent, body fitted, grid defined by the mapping.
In order to show the way the solution is gained in time, we report here one of the examples of [2]. The Ringleb flow [8] was taken as benchmark case. A set of streamlines $\psi = const$ of the Ringleb flow are plotted in fig. 1. Once two streamlines are selected, they may be regarded as the solid walls of a channel, and, from the point of view of an inverse problem, the theoretical pressure acting on these may be taken as the design input datum. The chosen channel is in the transonic region, and is confined by the streamlines $\psi = 0.8$, $\psi = 1.0$ and by the radial coordinate lines $\theta = 40^o$, $\theta = 90^o$.
Fig. 2 shows the shapes of the walls during the transient (solid lines), from the initial guessed configuration ($K = 0$) to the final one ($K = 500$). The dots denote the theoretical location of the streamlines. The maximum relative error of the location of the wall points is less than 0.6%, while the maximum relative error of the computed Mach number in the whole flow field is less than 0.4%

Since [2] was published, several improvements have been done. Upwind numerical schemes have been adopted to attain consistency with the wave propagation phenomena described by the Euler equations, as a consequence the computation at the boundaries has been improved; the extension to 3D problems has been shown feasible; different formulations have been attempted. The path of the evolution runs from [2] to [6].

2.1.1 The cascade problem

For a 2D cascade of airfoils, the inverse problem consists of finding the geometry of a cascade producing a flow of which some parameters are prescribed. There is a certain freedom in the formulation of the problem. We confine the discussion in the present report to problem for the 2D and 3D cases, where, in addition to suitable condition at infinity one may prescribe the distribution of thickness and load along the chord of a profile, and inquire for the geometry of the camber line.
In [2] - [6], the problems are solved by using the technique briefly outlined in the previous section: a time-dependent computation is performed, in which the boundary conditions are imposed according to the formulation of the inverse problem, until a steady state is reached asymptotically. The contours of the blades are considered as impermeable but perfectly deformable. An initial geometry is assumed. Since such a geometry is incompatible with a steady motion, consistent with the prescribed conditions, a transient is generated. During the transient, the walls of the blades change in shape, in order to satisfy the condition of impenetrability. The solution of the inverse problem is given by a geometry obtained asymptotically.
The reader may refer to Ref.[3] and Ref.[7] for the discussion of the 2D different problem formulations.

We proceed now to describe the process, in particular the boundary conditions, that have been chosen to generate the solution, confining ourself to the physical viewpoint.
Figs. 3a) and 3b) show typical initial and final configurations. The flow is assumed to be confined between two consecutive blades, the arcs BC, and two parallel lines issuing from the leading edge and the trealing edge of the blades. The lines in front of the blades are denoted by AB. The lines behind the blades are denoted by CD. Such boundaries are assumed to be impermeable and perfectly deformable: therefore, we can think in terms of a flow within a channel, the geometry of which may change in time, although its width (measured parallel to the y-axis) is independent of time. The channel is confined by the permeable boundaries AA and DD, upstream and downstream, respectively. The inlet boundary AA is considered fixed in time, whereas the exit boundary DD can slide upwards and downwards, maintaining a constant pitch. A time-dependent computational grid, which fits the boundaries, is defined inside the channel.
The design data are prescribed, according to problem formulation, by giving the distribution of thickness $\tau(x)$ and pressure jump between the two sides of the blades, $\Delta p(x)$. Since the flow is periodic, the upper and lower boundaries of figs. 3 can be reduced to a single boundary for a single blade, as in fig. 4. Note that the upper part of the ABCD line in figs.3 is the lower boundary in fig.4, and viceversa.
The arcs, AB and CD are deformable and impermeable interfaces, across which the pressure is continuous but the tangential velocity component may be discontinuous. In formulating the boundary conditions, the whole ABCD arc can be treated homogeneously. The interfaces can be considered as surfaces of blades for which a vanishing thickness and a vanishing pressure jump are prescribed. With this convention in mind, we procede to describe the technique for any blade surface.
In fig. 5 we show two grid points on two different sides of the blade, at the same abscissa. The velocity vector is decomposed along the tangent and the normal to the blade at each point. Since the blade is impermeable, the two flow velocities and the blade velocity must have the same normal component. Moreover, by imposing the pressure jump $\Delta p(x)$ to be constant in time, the boundary conditions that allow the geometry and the the flow to be updated at each computational step, are obtained.
At the inlet boundary AA (figs.3) we prescribe the total pressure, the total temperature and the flow angle, if the flow is subsonic, whereas all the flow quantities are prescribed if the flow is axially supersonic.
At the exit boundary DD no boundary conditions are needed if the flow is axially supersonic, while in the case of subsonic flow, the kind of boundary conditions to be enforced has to be selected carefully, in fact, as it is discussed in [1] and [3], the inverse problem has not an uniquely defined solution. The kind of boundary conditions that is used selects one solution among the possible ones.

The numerical process used approximates the governing equations written in quasi-linear form, as a consequence it is not conservative and weak solutions are not captured spontaneusly, but they need some special

treatment. This shortcoming is the price to be paid for the main advantage that our numerical process offers: the capability of computing the boundaries in a way consistent with domain of dependence due to the hyperbolic nature of the governing equations, avoiding the need for spurious additional numerical boundary conditions. This point is crucial for the success of method,in fact the computation in a domain whose physical shape depends on the solution is very sensitive to the way the boundary condition are enforced and any mistreatment may produce catastrophic instabilities.
Moreover, the inverse problems that generally one asks to be solved are shockless and the need for shock-capturing capability is rare; if this capability is requested, the scheme can be easily converted in a conservative Flux Vector Splitting scheme, as described in [12].

In the early formulation [3]-[5], a numerical procedure to solve inverse problems has been developed according to the *lambda*-scheme [9] and [10]. Briefly, the wave system affecting a given point in an unsteady flow field is described by four orthogonal waves. The λ-scheme uses one-sided differences to approximate the compatibility equations relative to the four waves, according to their direction of propagation and, as a consequence, satisfying the domain of dependence. The computations of a transonic shockless compression comes quite accurate and, besides that, the computation at the boundaries is simple and naturally suited for this kind of numerical scheme based on compatibility equations, avoiding almost completely the need for numerical additional boundary conditions.

Two numerical examples are here presented according to the selected formulation and prescribing the static pressure p_e as exit boundary condition. Further examples are shown in Ref. [3].
Fig. 6 shows the initial configuration and fig. 7 the steady solution to the inverse problem for the case corresponding to

$$\tau = .025\,[1-\cos(2\pi x)] \qquad \Delta p = c\,[1-\cos(2\pi x)] \qquad (0 < x < 1)$$

The ratio p_e/p^o between downstream pressure and total pressure is 0.8, the upstream flow angle σ_i is 20^o, and the upstream nondimensional total temperature Θ^o is 1, while $c = .1$. Both this case and the following one have been computed using 40 intervals in x and 10 in y.
A check on the accuracy of the computation is shown in fig. 8, where the theoretical behavior of the y-momentum is compared with the numerical result. The maximum error is less then 1%.
The case of fig. 9 has the same τ, σ_i, and Θ^o as in the preceding case, but $c = 0.15$ and $p_e/p^o = 0.71$.
The resulting cascade is supercritical but unchoked and shockless. It can be seen from the isoMach lines of fig. 9 that a supersonic bubble appears on the upper side of the blade, but the lower side is entirely subsonic. The pressure cannot be discontinuous on the subsonic side; therefore, it must be continuous on the supersonic side as well, since Δp is prescribed as a continuous function of x.

A further example is presented in fig. 10. It refers to the axial cascade with supersonic inlet Mach number, but having subsonic axial component. In this case the regime of unique incidence is established and it requires a boundary condition at inlet wich does not violate the simple wave region upstream of the cascade. This is obtained by imposing, at the inlet boundary, besides the total pressure and total temperature, the compatibilty relationship between Mach number and flow direction along a Mach line for steady supersonic flow. In fig. 10 the isomach contours are presented; the inlet Mach number is equal to 1.19, while th exit flow is subsonic and the cascade is shockless. In fig. 11, as a check, in the odograph plane the upstream flow field is presented. The simple wave region is well described, as it can be seen by the points belonging to a unique epicycloid.

In Ref. [4] a different formulation of the 2-D inverse problem is attempted: instead of looking for the shape of the walls, which in turn define the grid, it is looked for a whole orthogonal grid which adapts itself to the solution of the inverse problem. the Euler equations are written by assuming a set of indipendent variable that, at the steady state, coincide with the stream function and with a curvilinear co-ordinate along the lines orthogonal to the streamlines. The Euler equation so written are integrated in time according to the λ-scheme, the numerical process turns out very simple and quite accurate. The main drawback of method presented in [4], is that such method has not a straighforward extension to 3-D problems.

The success of a computational method aiming to solve multidimensional problems governed by the time-

dependent Euler equations lies mainly and obviously on the integration scheme and on the treatment of the boundaries. The λ-formulation shows good qualities in both respects, it does not violate the domains of dependence and it allows the boundaries to be treated in a way consistent with the wave phenomena approximated in the inner flow field. Nevertheless, the upwind schemes to approximate multidimensional wave phenomena have a sort of weakness being necessarily based on the approximation of waves propagating along a finite number of directions, while the possible directions along which actual waves propagate are infinite. The problem is addressed in Ref. [10], and, more recently, in Ref. [11]

Following Ref. [11], the 3D time-dependent Euler equations written in tensor notations, can be rearranged in a form suitable for upwind discretization by decomposing the 3D unsteady motion as due to waves fronts parallel to the coordinate surfaces; the resulting set of equations prompts an upwind discretization that preserves the 3D nature of the actual flow and that is particularly convenient from the point of view of the treatment of the boundaries.
The resulting scheme is very close to the λ-scheme, coinciding with it for orthogonal grids; moreover, the boundaries can be treated avoiding completely the need for local frames of references and additional boundary conditions, even in the case of non orthogonal grid. Details on this matter can be found in [11].

2.1.2 Examples

Here three numerical results are presented: the first one refers to the design of a 3D rotational, transonic, convergent-divergent nozzle, while the other two refer to the design of turbomachinery bladings. In order to test the capabilities of the present inverse technique, in Ref. [1] the authors choose an example with a distorted geometry, quite far from the guessed initial one. Fig. 12a) shows the 3D view of the initial configuration and Fig.12b) the final one that solves the inverse problem. The solid walls are planes. The design pressure distribution on the lower moveable wall is

$$p_d = .8 - .7x^3$$

on the upper wall:

$$p_e = .8 - .35[1 - \cos(\pi x^3)]$$

On the inlet boundary the total temperature is kept uniform and constant in time $\Theta^0 = 1$, the flow velocity has the direction of the x^3 coordinate lines and the total pressure obeys the law:

$$p^0 = 1 - \Delta p^0 (y^1 - y_c^1)/(y_b^1 - y_c^1); \qquad \Delta p^0 = .1$$

The resulting flow is rotational and non homoentropic.
Figg.13a), 13b) show the isoMach lines over the left and right solid walls, Figg. 14a), 14b) over the upper and the lower moveable walls and Figg. 15a), 15b) over the inlet and exit surfaces, respectively. Figg. 16a), 16b) show the constant-entropy lines on the inlet and exit surfaces, respectively.
The second example refers to the design of the blades of a stator. Figg. 17a), 17b), show the initial and final 3D view, respectively. The tip and hub solid annulus walls are cylindrical with $r_t/r_h = 1.5$.
The design thickness and the design loading are, respectively:

$$\tau = .07 \sin\left[\pi \frac{y^3 - y_l^3}{y_t^3 - y_l^3}\right] \qquad \Delta p = .08 \sin\left[\pi \frac{y^3 - y_l^3}{y_t^3 - y_l^3}\right]$$

with $y_t^3 - y_l^3$ =axial chord.
At the inlet boundary the flow is axial. The total temperature is kept constant $\Theta^0 = 1$, while the tototal pressure is distorted:

$$p^0 = g\sqrt{y^1} + h$$

with $g = .1/(\sqrt{r_t} - \sqrt{r_h})$, $h = 1. - g\sqrt{r_t}$.
At the exit surface, a distribution of pressure, in agreement with an approximate solution based on the radial equilibrium theory, is given as boundary condition, with $p_h = .7$ at hub radius.
Figg. 18a), 18b) show the isoMach lines on the blade to blade surfaces at the hub and tip radii, Figg. 19a), 19b) on the pressure and suction sides of the blades, respectively. Figg. 20a) and 20b) show the constant entropy lines at the inlet and exit surfaces.

The constant entropy surfaces coincide with stream-surfaces; as it has been pointed out in Ref. [5], looking at Figg. 20a) and 20b) one would expect to see the typical rotation of such surfaces as consequence of the secondary flows generated in 3D rotational flow. Actually, a streamwise component of the vorticity is correctly generated, it does not reveal itself as a rotation of the streamtubes, but rather as a peculiar twisting of the blades: the loading is prescribed as design datum and it cannot be decreased as a consequence of secondary flows, but the lower is the total pressure (and density) the higher the deflection to provide such loading.
Finally, two integral checks have been done on the continuity and angular momentum of the computed flow field: Fig. 21 shows the mass flow computed on cross sections along the blade to blade channel; Fig. 22 compares the angular momentum evaluated on cross sections along the channel with the corrisponding theoretical torque due to the design loading.
In the third example the annulus walls form a conical surface at hub radius, and a cylindrical surface at tip radius. The flow at entry is assumed to have axial direction, with constant total temperature and a parabolic distribution of total pressure, the smallest being at hub radius. A certain distribution of thickness and pressure jump as functions of the radial and axial coordinates are assumed, $\tau = g(y^1, y^3)$, $\Delta p = f(y^1, y^3)$. At the exit surface, a distribution of pressure, in agreement with an approximate solution based on the radial equilibrium theory, is given as boundary condition, as well as in the previous example.
The initial configuration of the blade row is shown in fig. 23a). The blades are without camber and twist. Fig. 23b) shows the final configuration of the blade row. Figg. 24 and 25 represent the isoMach lines of the initial and final configuration of blade to blade section at hub radius, respectively. Figg. 26-28 represent the final configurations of the intermediate and tip blade to blade sections. The threedimensional nature of the flow field and the twisting of blades is shown in these results.
The flow is transonic, in fact a supersonic bubble extends from hub to tip on the section side. Figg. 29 and 30 show the isoMach lines on the projection on the meridional plane of the suction and pressure sides of the blades, respectively. Finally, figg. 31a) and 31b) show constant entropy lines on the sections normal to the axis, corresponding to the trailing edges and the exit of the streamtube.
The constant entropy surfaces coincide with stream-surfaces. Figg. 31a) and 31b) show the absence of the typical rotation of such surfaces and the peculiar twisting of the blade to blade channel, as well as in the previous example.

2.2 Design optimization of axial compressor

The aerothermodynamic design of turbomachines requires a number of indipendent parameters which results in a multiplicity of possible design configurations.
In order to have an optimized design of turbomachinery components, the choice of many design parameters requires an optimization problem to be solved in an early stage in the design cycle. The objective function in a general optimization problem represents a basis for the choice between various equally acceptable designs.

A computational procedure for design and optimization of axial turbomachines has been presented in [15]. The geometrical and fluid dynamic optimized quantities are obtained by coupling non linear minimization algorithms with methods for flow analysis and design. In the early formulation [16], the optimized design methodology uses the fluid dynamic analysis at mean diameter for axial turbine/compressors stages.
The optimization procedure presented in [15] and [16], is based on a constrained non linear minimization problem and is obtained by using three different methods: *Monte Carlo, Simplex* and *Gradient*. The numerical optimization strategies used in [16], based on a combination of the previous methods, has shown that the best results are obtained in general by enforcing the three methods sequentially.

In the work presented in [17], the authors used objective functions that are composed not only of a single variable, but of a combination of variables. This is done in order to avoid the improvement of a single quantity (e.g. efficiency), to the detriment of other important compressor characteristics. Moreover, multivariable objective function is used so that the optimum design of an aerospace or industrial compressor can be found using the same numerical procedure and ascribing suitable importance to the efficiency (η_{TT}), stall margin (identified by a coefficient C_h) and weight of the machine (identified by a specif area A_{sp}), whose linear combination represents an appropriate objective function.

For the design of an axial flow compressor stage, the following parameters are taken as the design variables:

Third International Conference on Inverse Design Concepts and Optimization in Engineering Sciences (ICIDES-III), Editor: G.S. Dulikravich, Washington D.C., October 23-25, 1991.

X_1 = stage enthalpy drop (ψ)
X_2 = inlet flow coefficient (ϕ)
X_3 = stator outlet absolute flow angle (α_3)
X_4 = mean diameter of the stage (D_m)
X_5 = rotor axial velocity ratio (AVR_R)
X_6 = stator axial velocity ratio (AVR_S)
X_7 = stator solidity (σ_S)
X_8 = rotor solidity (σ_R)
X_9 = rotor blade chord to mean diameter ratio (C_R/D_m)
X_{10} = stator blade chord to mean diameter ratio (C_S/D_m)
X_{11} = stator max thickness to chord ratio $(t_m/C)_S$
X_{12} = rotor max thickness to chord ratio $(t_m/C)_R$

The design process is shown in fig. 32. For given design specifications, the design parameters, defined at mean diameter, are guessed at the beginning of the computation and they define a first rough design wich is modified during the analysis design procedure in order to minimize the objective function. The evaluation of the efficiency is performed by using performance analysis of the stage defined by the actual values of the indipendent variables, while the stall margin is computed by using some simple correlation [19] suited for preliminary design studies.

The constraints of the optimization design method could be of two kinds. That is, rectangular constraints wich are directly applied on the design variables and they come from the field of the possible applicability of the correlations used in the objective function evaluation. However, a diret constraining of any single design variable does not ensure that, in a particular combination of them, some of the mechanical or fluid dynamic variables could exceed the usual limits. For these reasons, non-rectangular constraints have been chosen: they are related to the aerodynamic loading, flow instabilities, limiting flow rate through a flow path element, aeroelastic aspect of compressor blade rows, and noise generation. In order to take into account these non-rectangular constraints of the problem it is necessary to introduce in the optimization procedure the penalty function technique. The optimization problem is stated as a non linear programming problem as follows: find X that minimizes

$$f(X) = G_\eta(1-\eta_{TT}) + G_A(1-A_{Sep}) + G_C(1-C_h) \tag{1}$$

subject to the constraints

$$X_i^l < X_i < X^u \qquad i=1,m \qquad g_j(X) \qquad j=1,n \tag{2}$$

where G_η, G_A and G_C are coefficients.Details of the method are given in Ref. [18].

In the following examples, the complete optimization method was first used with a single objective function coincident with η_{TT} and then with a multivariable function (η_{TT}, C_h, A_{sp}).
From [17], the design of a stage of a small axial compressor (4 kg/s) with a high pressure ratio ($\beta_{TT} = 1.65$) is presented. The design variables are shown in Tab. 1, while Tab. 2 presents the numerical values of the constraints. The optimization has been performed with a single variable objective funcion, the total-to-total stage efficiency.
The initial stage efficiency value of 0.875 grows up to 0.927, with the absolute exit flow angle $\alpha_3 < 20°$.
The optimized results shown in Tab 1 have been obtained by imposing different limits to the stage (α_3). As shown, the design variables, ϕ, ψ, AVR and σ seem to be particularly sensitive to the α_3 limits. The optimization procedure has carried out a reduction of the relative Mach number (to which shock losses are related) allowing for a remarkable reduction in the rotor losses ($\omega_{Ri} = 0.114$ and $\omega_{Ro} = 0.0675$).
Additional calculations have been performed by modifying the inlet flow algle (α_1), simulating in this way the presence of an IGV or of a stage upstream. As an example, Tab. 3 shows the results obtained for $\alpha_1 = 0; 10; 20°$.
In the previous examples it can be seen that, whereas η_{TT} increases, the other significant design variables (C_h,A_{sp}) are drammatically reduced. This points out the necessety to operate with mixed objective function.

Third International Conference on Inverse Design Concepts and Optimization in Engineering Sciences
(ICIDES-III), Editor: G.S. Dulikravich, Washington D.C., October 23-25, 1991.

A design optimization has been performed using a multivariable objective function with different values of the coefficients G_η,G_A and G_C, ranging from 0.0 to 1.0.
Table 4 shows the initial values of η_{TT}, C_h and A_{sp}, and the final ones after the optimization process. From Tab. 4 it is evident that if $G_\eta = 0$, the values of η_{TT} are absolutely unsatisfactory, especially in the case where G_A and G_C are unity. For this reason, the efficiency should always be present in the objective function. In the case where $G_\eta = 1$ and $G_C = 0$, a high reduction results in the stall margin (especially if $G_A = 1$).
If $G_\eta = G_A = G_C = 1$, the dominant effect of G_A leads to a large increase in the specific area and also a corresponding decrease in the starting value of efficiency (from 0.87 to 0.78).
Finally, the analysis of the optimization with the multivariable objective function has been performed varying G_A from 0 to 1, with G_C as parameter and $G_\eta = 1$. The optimum efficiency, plotted in fig. 33, decreases greatly with G_A. The same trend, even if reduced in effects, is shown by G_C. Fig. 34 shows the stall margin coefficient; the influence of G_A is negligible for high values of G_C, while if $G_C = 0$ the increase in G_A is positive for the stall margin.

The one dimensional design procedure at mean diameter is simple and is justified by the need for an immediate definition of the global geometry of the machine and by the possibility of a preliminary design choice, but it does not provides any informations about the hub-to-tip geometry.
The one-D procedure has then been extended in [15],[18], by coupling the numerical optimization strategies with 2-D flow computation in the meridional plane (through-flow analysis) in order to have an optimized radial distribution of geometrical and aerodynamic quantities. This makes possible to optimize the radial distribution of the main geometrical and fluid dynamic parameters of the stage. Nevertheless, the method solves non linear equations by an iterative technique and therefore their introduction in the optimization procedure could be quite expensive as far as the computational time is considered due, also, to the high number of iterations required by the minimization.

Some difficulties is rappresented by the choice of the design variables. In a previous work [20], the authors chose to deal with three radial sections - root,mean and tip - for a total of ten design variables for each single row, considering fixed the geometry of the meridional section. The results obtained demonstrates the need for a better definition of the design variables and, therefore of the row geometry. In ref. [18], the coefficients of suitable polynomial that represents the 3-dimensional geometry of the row to be optimized were chosen as design variables.
The design variables -13 for each row- are all geometric, as opposed to the procedure presented in the preliminary design. This is due to the assumption that the optimization criteria will be applied to a machine of which the design is known, even if only in a preliminary way.
The evaluation of the objective function is obtained with a through-flow calculation by using a matrix method [21]. The code, furthermore, permits the calculation of the annulus wall boundary layer with an integral type solution [22] and the computation of the secondary deviation angle [23].

The general scheme is illustrated in fig. 35. Starting from initial data (P_0,T_0,β_{TT},m) and from the mean diameter design variables (X_i), and working with a multivariable objective function, the mean diameter optimum geometry is obtained. From here, by considering a law of radial geometry distribution (e. g. the free vortex), the values of the the initial data of the through-flow calculation (D_h,D_t,n) and the new design variables (polynomial coefficients a_i) are obtained. Using the same algorithm of constrained minimization as in the previous case, the procedure continues until the objective is reached.
The optimization problem uses only one objective function coincident with the stage efficiency.

The procedure has been applied to solve two kinds of problems. In the first one the process is used to redesign an existing isolated transonic rotor. The one described in [24] is selected to verify the optimization process. The initial geometrical data of the rotor, which coincide with the polinomial functions to be optimized, are shown in figg. 36,37 and 38, respectively. The root chord is equal to 0.0388 m and is constant along the blade span. The calculation is carried out for the design conditions: $m = 96.18 kg/s$ and $n = 8870 rpm$. The initial efficiency (original geometry) is equal to 0.897, while the value obtained at the end of the optimization process is 0.943, greater than a 4 percent increase. Fig. 39 illustraes the objective function history during the optimization. In figg. 36, 37 and 38 in addition to the initial radial distributions, the optimized values are

also given; it is possible to note how the angle β_{1b} has undergone slight variation, with the maximum variation at the root (4°). The angle β_{2b} shows the maximum shift with respect to the initial value at meadspan of the blade (6°). This involves an increase of the blade curvature in the central zone with slight reduction in the root and tip regions. The solidity is reduced along nearly all the span, while at tip it change from 1.30 to 1.41. The maximum thickness/chord ratio has, at the end of the optimization, a more uniform radial distribution. The optimization operates in the sense of a reduction of the diffusion factor in the $R < 0.4$ region (fig. 40), while in the upper zone D_f increases. For $R < 0.6$, the loss reduction is significant as shown in fig. 41; in the tip region, where a great deal of the losses is due to the shock, although a reduction occurs (from 0.062 to 0.049), it appears to be more contained.

The second example is relative to the use of both procedures (pitchline and throughflow) in order to design a stage working from the following informations: mass flow rate= 4kg/s; pressure ratio $\beta_{TT} = 1.60$; $P_{01} = 101.3kPa$; $T_{01} = 300K$. The initial optimization procedure is carried out with an objective function having the following weights: $G_\eta = 1$, $G_C = 0.0$, $G_A = 0.0$, and with a higher constraint for α_3 of 10°.
The meridional section optimized with such a procedure is illustrated in fig. 42. The rotational speed is 39,500 rpm; optimized efficiency is equal to 0.91, the stall margin is $C_h = 0.50$ and the specific inlet area is $A_{sp} = 170$.
The radial distribution of geometrical characteristics of the blade, from which the new design variables a are obtained, was aquired by considering the free vortex law for the rotor and inlet section of the stator. For the stator outlet section, the angle α_{3b} was chosen in a different way (fig. 43). Optimization results are shown and compared with starting values in the above mentioned figures.
As far as efficiency is concerned, it must be pointed out that the value calculated with pitchline analysis differs from the initial finding obtained with the through-flow calculations. This latter, however, changes with the second optimization process from 0.844 to 0.905, showing at the same time a sufficiently rapid increase.

The previous examples have shown that the optimization technique allows a design of turbomachinery components with high degree of efficiency not only in one-dimensional approach, but also in an integrated analysis in the meridional plane where an optimal radial distribution is obtained for geometrical and aerodynamic quantities.
The same procedure has been applied by the authors to solve optimization problems for multistage axial flow turbines ([25]).

3 Inverse wing section design

From a fluid dynamic point of view the design of an airfoils looks for a geometry wich satisfy the equation of motion, given some boundary conditions. Two kinds of methodology can be used: the first one imposes some parameters (such as pressure, Mach number distribution, etc...) on the surfaces, while the second one prescribes some global properties to the flow field, such as minimum drag, shock-free, minimum entropy generation, etc... Both of them require some constraints in order to obtain a final airfoil shape with physical meaning.
As far as a design technique of the first type is conceived, and in the light of the well-posedness of the problem, the distribution of the flow parametes must satisfy some constraints in order to have the solution of the inverse problem for incompressible flow.
A methodology for solving inverse problem for airfoils by prescribing a pressure or velocity distribution is presented in ref. [26]. The inverse technique there presented is based on conformal mapping (ref. [27], [28]) for inviscid incompressible flow and it has been extended to the compressible subsonic flow case by applying the Karman-Tsien transformation. The assumption of inviscid flow is sufficiently approximated unless low Reynolds numbers are considered, when the boundary layer thickness can change significantly the resulting geometry. In this case the model is still valid, but the new surface is obtained by the displacement thickness given by the imposed pressure distribution.
The method outlined in ref. [26], consists in mapping the phisical domain $z(x, y)$, external to the closed line, in a seminfinity strip on the computational domain $\zeta(\xi, \eta)$ with $\eta > 0$ and $-\pi/4 \leq \xi \leq \pi/4$ (fig. 44).
The airfoils is approximated by rectilinear elements, and the mapping function, valid for poligonal contours

Third International Conference on Inverse Design Concepts and Optimization in Engineering Sciences
(ICIDES-III), Editor: G.S. Dulikravich, Washington D.C., October 23-25, 1991.

(ref. [26]), can be written in general form:

$$\frac{\partial z}{\partial \zeta} = f(M, \zeta, a_m, \alpha_m, g_m, C_m) \quad m = 1, N \tag{3}$$

where M is a scale factor, a_m represents the abscissa in the computaional domain of the nodal points of the elements, g_m are function of ζ and the position of the m_{th} element on the computational domain, and, finally, C_m depend on the change of the tangent to the airfoil along the element m_{th} as function of a_m. The C_m values, which are known in a direct analysis because the geometry is given, in the inverse design they rapresent the unknowns of the problem.

In order to evaluate the C_m, the complex potential is imposed on the central point of the N-2 elements, where the modulus of the velocity is known. The resulting system with $C_m (m = 1, N + 1)$ unknowns is closed by giving the velocity and incidence at infinity, by imposing the Kutta condition, two geometrical constraints at the trailing edge in order to have a closed profile, and, finally, by imposing the tangent at leading edge to be perpendicular to the chord. Moreover, if the compressible flow is considered, the Karman-Tsien relationship is used to trasform the compressible distribution on a fictitious incompressible distributions.

Since the coefficient of system of equations are function of the position of nodal points in the computational domain which are unknown, an iterative procedure is followed:

1. An initial guessed distribution of nodal points is assumed in the computational domain
2. The system equation is solved by Gauss-Siedel method
3. The equation 3 is integrated by assuming a value of M; the airfoil is obtained in the phisycal plane and then M is scaled in order to have a computed chord equal to the prescribed one
4. If the position of the nodal points does not coincide with the previous values, the abscissa of these points are updated
5. The iterative process restarts from point 2 by using the new values of C_m

The method has been applied to the design of airfoils for wich the incompressible solution is known. Fig. 45 shows the incompressible velocity distribution associated to the symmetrical Karman-Treffez airfoil without incidence, wich is prescribed to solve inverse problem.

The resulting airfoil is shown in fig. 46. Here different solutions, obtained with 16 (triangles), 32 (circles) and 64 (plus) elements, are compared with the exact one. For the 64 elements, tab. 5 shows the abscissa of nodal points, the exact values Y_E and the computed Y_N coordinate, and the error with respect to the maximum thickness.

A further example relative to the Karman-Treffez airfoil with camber and 5^o incidence, with the prescibed velocity distribution given in fig. 47, is shown in fig. 48.

The method, which seems to be very accurate in the incompressible case, has been extended to the design problem by considering compressible subsonic flow. In this case also airfoils from catalogue have been selected as test cases. For the NACA0012 airfoils with $M_\infty = 0.72$, $\alpha_\infty = 0^o$; and $M_\infty = 0.5$, $\alpha_\infty = 3^o$, by prescribing the pressure coefficient reported in figs. 49 and 50, respectively, the results obtained by using 32 elements are shown in figs. 51,52.

Also for the compressible case the method seems to be very accurate, even when the Mach number is very close to one on the airfoils.

References

[1] L. Zannetti, F. Larocca, *Inverse Methods for 3-D Internal Flows*, VKI Lecture Series 1990-8, Bruxelles, 14-18 May, 1990.

[2] L. Zannetti, *Time Dependent Method to Solve Inverse Problems for Internal Flows*, AIAA J., 18 July 1980, pp. 754-758.

[3] L. Zannetti, M. Pandolfi, *Inverse Design Techinque for Cascades*. NASA CR 3836, Nov. 1984.

[4] L. Zannetti, *A Natural Formulation for the Solution of 2D or Axisymmetric Inverse Problems*, Int. J. Num. Meth. in Eng., Vol. 22, Feb. 1986, pp. 451-463.

[5] L. Zannetti, T. T. Ayele, *Time Dependent computation of the Euler Equations for Designing Fully 3D Turbomachinary Blade Rows, Including the Case of Transonic Shock Free Design*, AIAA 25th Aerospace Sciences Meeting, Reno, Nevada, Jan. 1987, AIAA-87-0007.

[6] L. Zannetti, F. Larocca, *Time Dependent Solution of Multidimensional Inverse Problems*, 2nd Int. Conf. on Inverse Design Concept Optimization in Engineering Sciences, University Park, Pen. Oct. 1988.

[7] G. Meauze, *An Inverse Time Marching Method for the Definition of Cascade Geometry*, ASME Paper 81-GT-167.

[8] F. Ringleb, *Exacte Losungen der Differentialk-gleichungen einer adiabatischen Gasstromung*, ZAMM, Vol. 20, N. 4, 1940, pp. 785-798.

[9] G. Moretti, *The lambda-scheme*, Comput. Fluids, 7, 191-205 (1979).

[10] G. Moretti, L. Zannetti, *A New, Improved Computational Technique for Two-dimensional Unsteady Flow*, AIAA J., 22 June, 1984, pp 758-765

[11] L. Zannetti, B. Favini, *About the numerical modelling of multidimensional unsteady compressible flow*,Comput. Fluids, 17 289-299 (1989).

[12] L. Zannetti, B. Favini, *A difference scheme for weak solution of gasdynamic equations*, AIAA Paper 87-0537.

[13] G. Moretti, M. Pandolfi, *Critical study of calculations of subsonic flow in ducts*, AIAA Jou , 19 April 1981, pp. 449-457.

[14] M. Pandolfi, L. Zannetti, *Some permeable boundaries in multidimensional flows*, 6th Int. Conf. on Num. Meth. in Fluid Dyn., Tbilisi 1978, Lecture Notes in Physics N. 90, Springer-Verlag, pp. 439-446.

[15] A. Massardo, A. Satta, *Procedura di ottimizzazione per il Progetto dei Compressori Assiali*, VIII AIMETA 1986, Torino, Italy, 29 Sept-3 Oct, 1986.

[16] A. Massardo, C. Serrati, *Codice di Ottimizzazione del Progetto di Turbomacchine Assiali*, DINE-SMF, Genova, Italy, Jan 1985.

[17] A. Massardo, A. Satta, *Axial Flow Compressor Design Optimization: Part I - Pitchline Analysis and Multivariable Objective Funcion Influence*, ASME J. of Turbomachinery, Vol. 112, July 1990, pp 399-404.

[18] A. Massardo, A. Satta, M. Marini, *Axial Flow Compressor Design Optimization: Part II - Throughflow Analysis*, ASME J. of Turbomachinery, Vol. 112, July 1990, pp 405-410.

[19] C. C. Kock, *Stalling Pressure Rise Capability of Axial Flow Compressor Stages*, ASME J. Engineering for Power, Vol. 103, 1981, pp 645-656.

[20] A. Massardo, A. Satta, *The Use of Optimization Technique and Through-flow Analysis for the Design of Axial Compressor Stages*, Proceedings 8th Turbomachinery Conference, Budapest, Hungary, 1987.

[21] D. Breschi, A. Massardo, *Metodo Matriciale per il Calcolo Meridiano di un compressore assiale pluristadio*, 37th ATI Confernce, Padova, Italy, 1982.

[22] H. Perkins, J. Horlock, *Annulus Wall Boundary Layer in Turbomachines*, AGARDOGRAPH.

[23] A. Massardo, A. Satta, *A Correlation for the Secondary Deviation Angle*, ASME paper No. 85-GT-36.

[24] D. R. Seyler, J. P. Gostelow, *Single Stage Experimental Evaluation of High Mach Number Compressor Rotor Blading, Part 2. Performance of Rotor 1-B*, NASA CR-582.

[25] A. Massardo, A. Satta, *Industrial Design Optimization of Small and Large Size Axial Turbines*, ASME paper No. 90-GT-220.

[26] B. Fortunato, A. Lippolis, *Progetto di Profili Aerodinamici Mediante Trasformazione Conforme*, Atti dell' Ist. di Macchine ed Energetica dell' Universita' di Bari, Italy, Sept, 1990.

[27] A. Lippolis, *A Grid Generation Technique Based on a Conformal transformation*, Atti dell' Ist. di Macchine ed Energetica dell' Universita' di Bari, Italy, Oct, 1990.

[28] L. C. Woods, *The Theory of Subsonic Plane Flow*, Cambridge, University Press, 1961.

Third International Conference on Inverse Design Concepts and Optimization in Engineering Sciences (ICIDES-III), Editor: G.S. Dulikravich, Washington D.C., October 23-25, 1991.

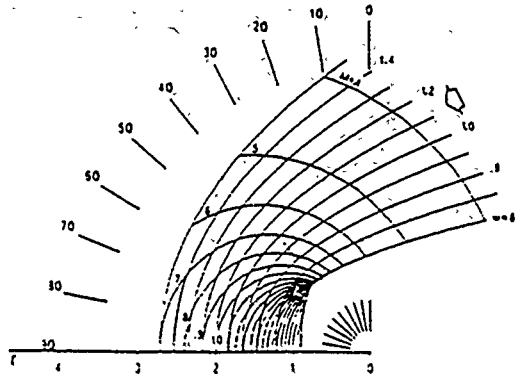


Figure 1: Ringleb flow

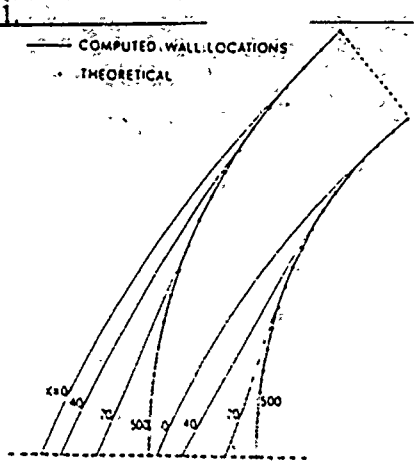


Figure 2: time evolution of the movable walls

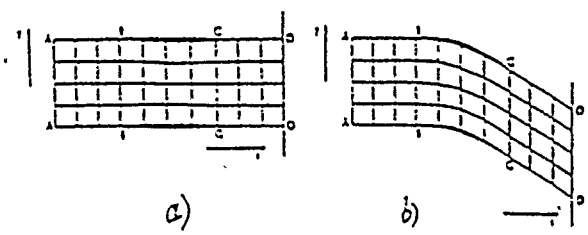


Figure 3:

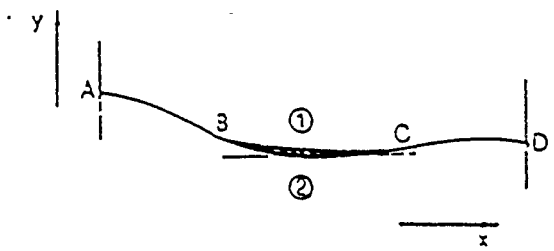


Figure 4:

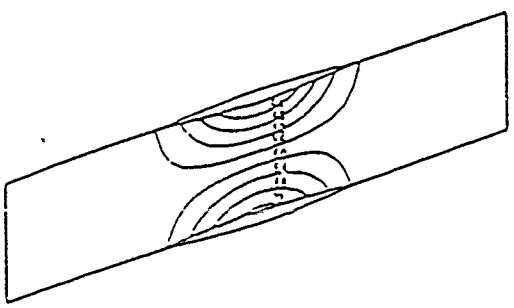


Figure 6:

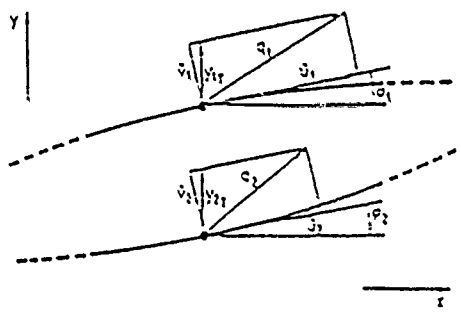


Figure 5:

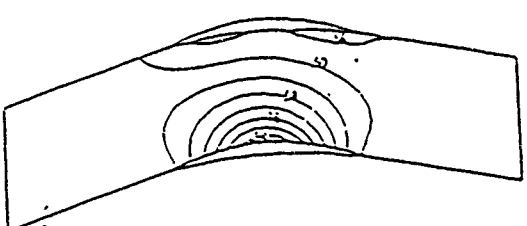


Figure 7:

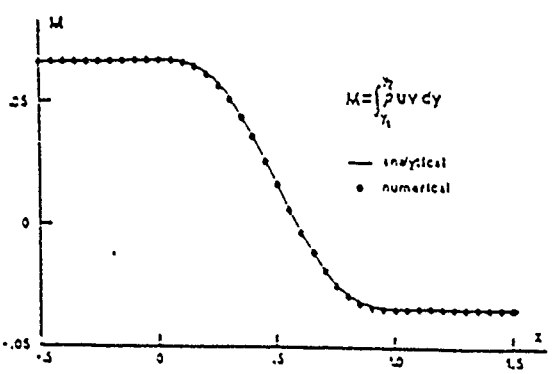


Figure 8:

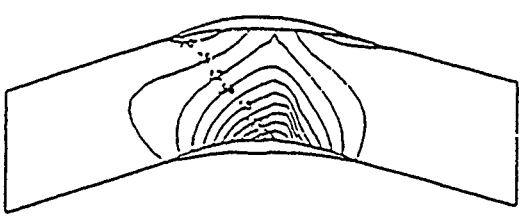


Figure 9:

Third International Conference on Inverse Design Concepts and Optimization in Engineering Sciences (ICIDES-III), Editor: G.S. Dulikravich, Washington D.C., October 23-25, 1991

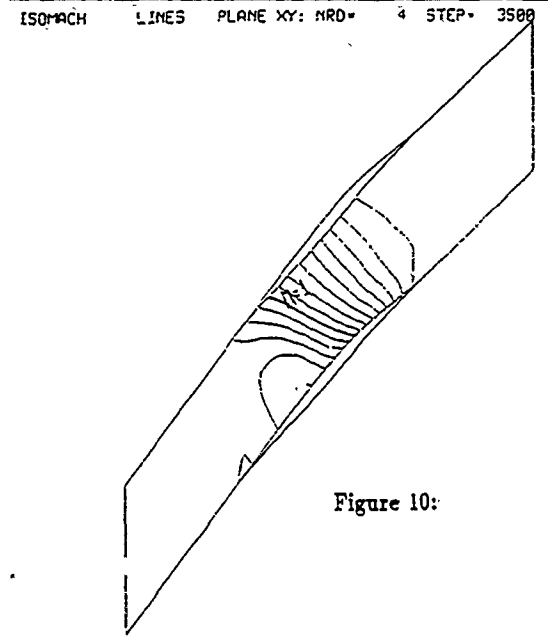


Figure 10:

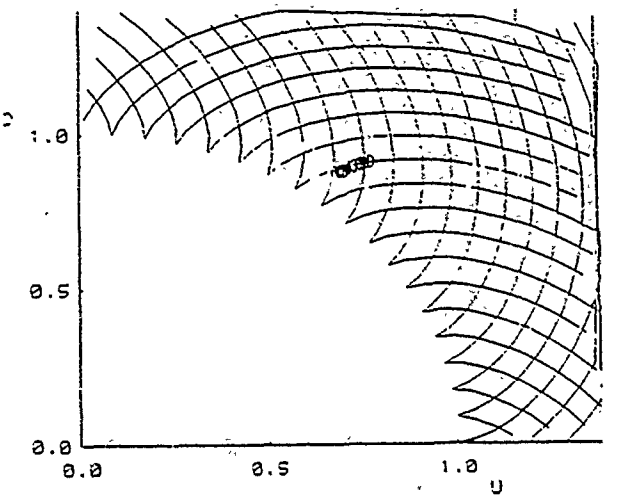


Figure 11:

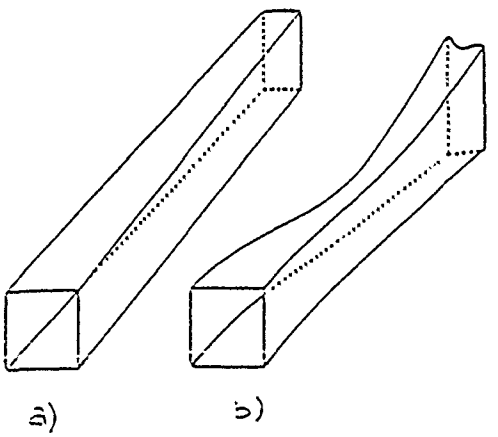


Figure 12:

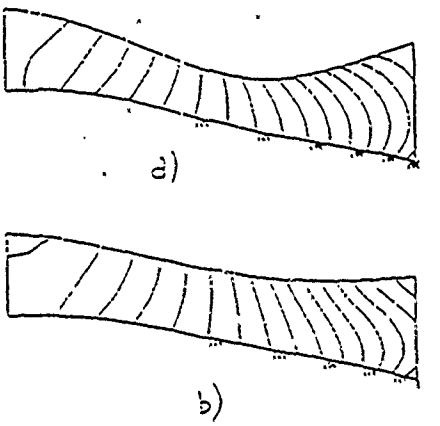


Figure 13:

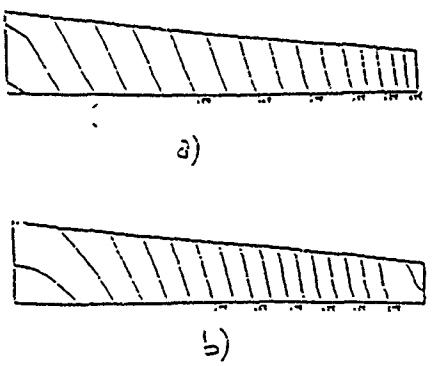


Figure 14:

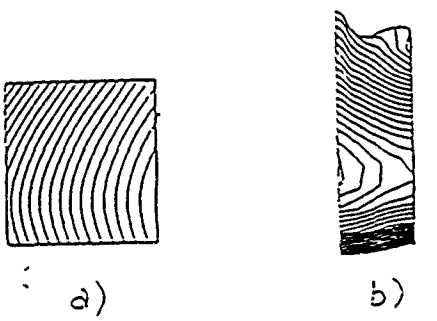


Figure 15:

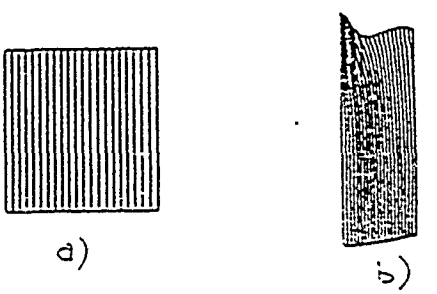


Figure 16:

Third International Conference on Inverse Design Concepts and Optimization in Engineering Sciences (ICIDES-III), Editor: G.S. Dulikravich, Washington D.C., October 23-25, 1991.

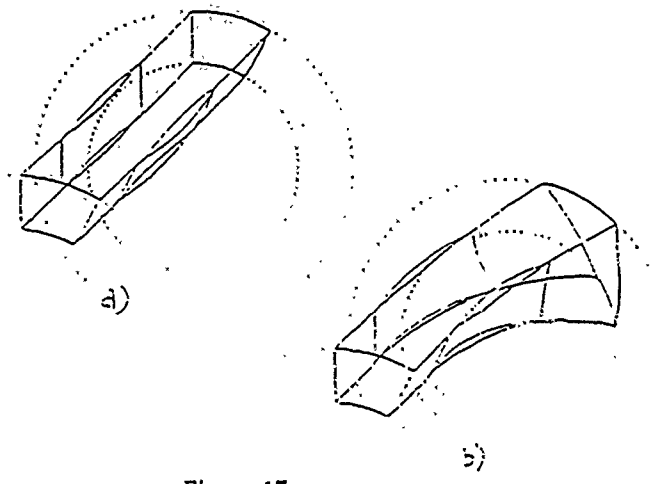


Figure 17:

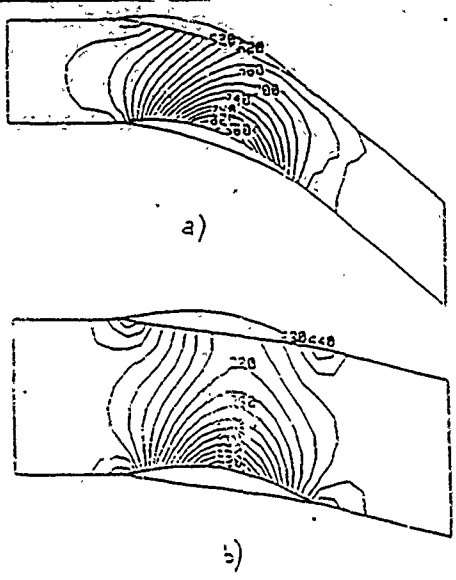


Figure 18:

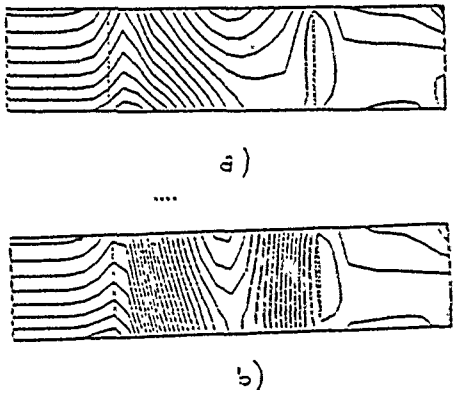


Figure 19:

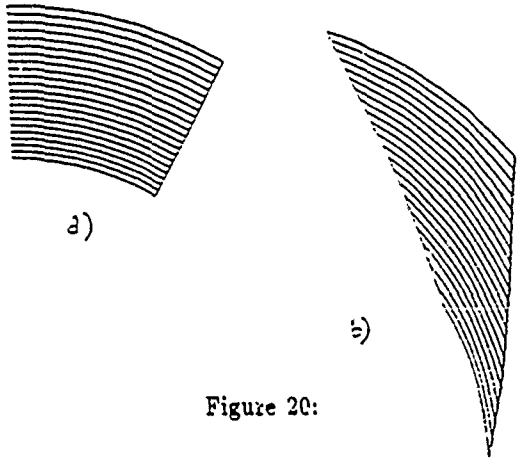


Figure 20:

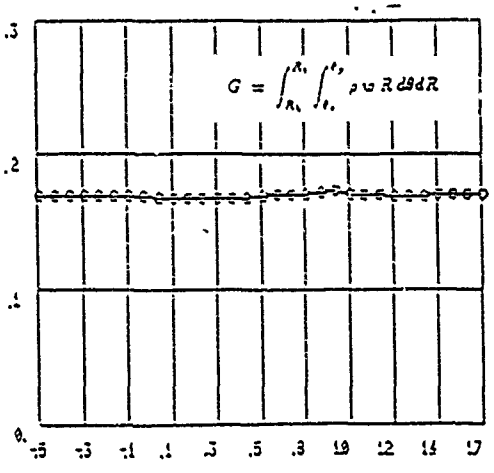


Figure 21:

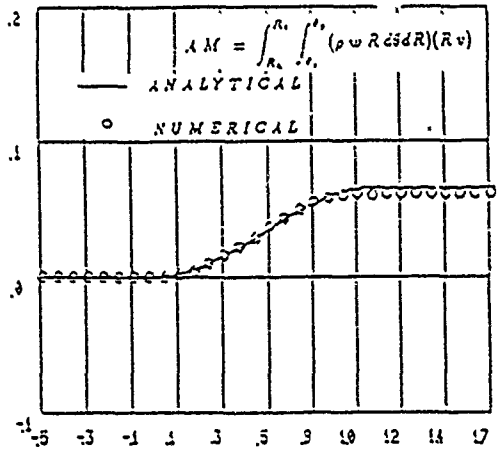


Figure 22:

Third International Conference on Inverse Design Concepts and Optimization in Engineering Sciences (ICIDES-III), Editor: G.S. Dulikravich, Washington D.C., October 23-25, 1991.

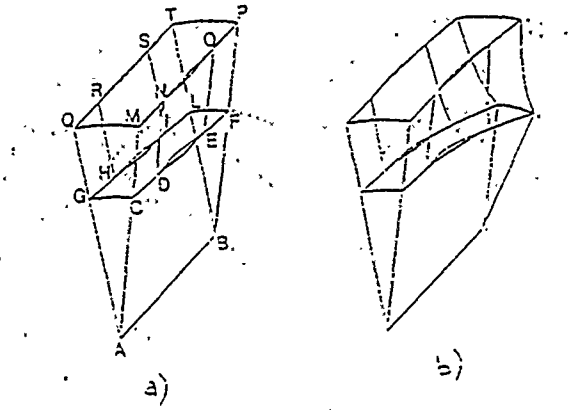


Figure 23:

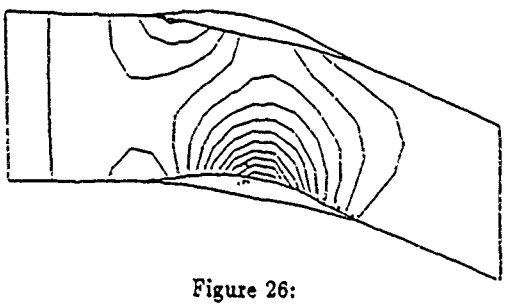


Figure 26:

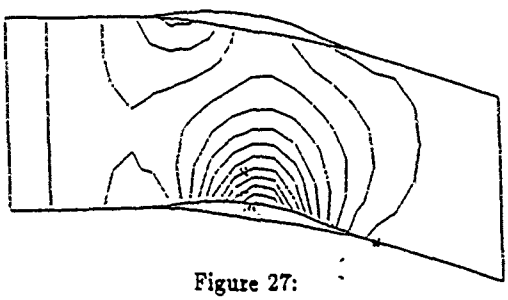


Figure 27:

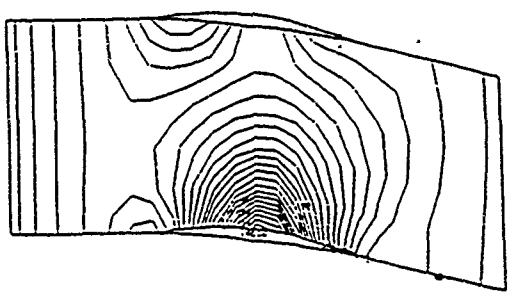


Figure 28:

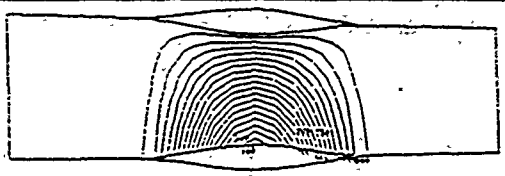


Figure 24:

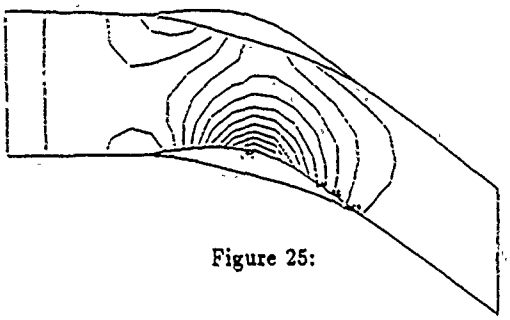


Figure 25:

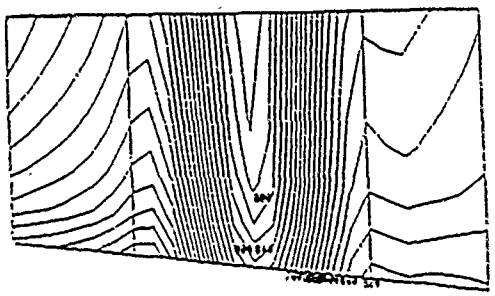


Figure 29:

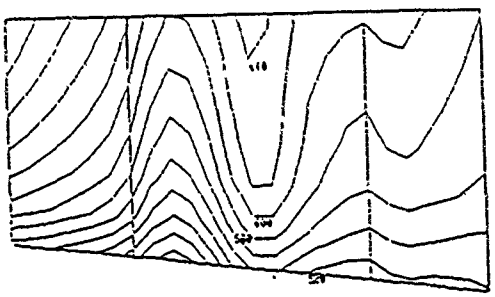


Figure 30:

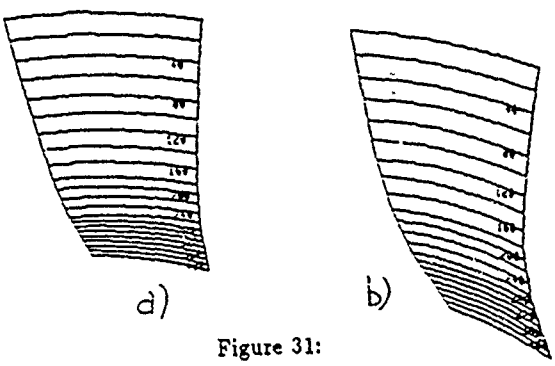


Figure 31:

Third International Conference on Inverse Design Concepts and Optimization in Engineering Sciences (ICIDES-III). Editor: G.S. Dulikravich. Washington D.C., October 23-25, 1991.

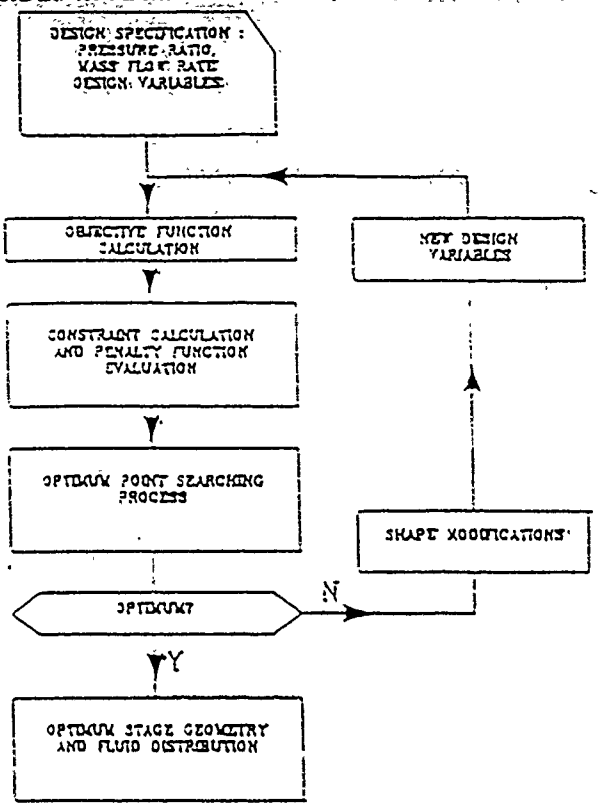


Figure 32: General optimization flow chart

DESIGN VARIABLES	STARTING VALUE	OPTIMUM VALUE		
		$\alpha_3 \leq 20°$	$\alpha_3 \leq 10°$	$\alpha_3 \leq 0°$
ψ	0.4	0.496	0.462	0.438
φ	0.45	0.465	0.471	0.464
α_3(°)	0.9 (0.0)	19.99	9.19	0.0
D_m(m)	0.170	0.163	0.159	0.158
AVR_R	1.15	1.04	1.00	1.00
AVR_S	1.20	1.32	1.40	1.48
σ_S	1.9	1.50	1.50	1.74
σ_R	1.3	1.25	1.26	1.27
C_R/D_m	0.333	0.200	0.200	0.222
C_S/D_m	0.140	0.128	0.13	0.122
t_m/C_R	0.050	0.0518	0.0487	0.0447
t_m/C_S	0.050	0.0498	0.0502	0.0745
$OBJ=(1-\eta_{TT})$	0.875	0.927	0.920	0.917

$\dot{m}$ = 4 kg/s ; β_{TT} = 1.65 ; P_{01} = 101300 Pa ; T_{01} = 300 K ; α_1 = 0°.

Table 1 Optimization results for three different limits imposed a $X_3 = \alpha_3$

	α_1 = 0°		α_1 = 10°		α_1 = 20°	
	i	o	i	o	i	o
η_{TT}	0.870	0.914	0.884	0.914	0.883	0.910
A_{SD}	180	166	178	178	176	177
C_n	0.541	0.516	0.534	0.512	0.526	0.531
ω_R	0.128	0.082	0.103	0.076	0.088	0.075
ω_S	0.061	0.047	0.069	0.051	0.089	0.063
M_{rlm}	1.224	1.081	1.134	1.089	1.052	1.049
M_{s3}	0.569	0.546	0.564	0.705	0.826	0.780

Table 3 Influence of α_1 value on the optimization (OBJ = $1-\eta_{TT}$; α_3 = 20 deg; DCA blade; β_{TT} = 1.75; i = initial; o = optimum)

$0.03 < H_1/D_m < 0.3$	$0.03 < H_2/D_m < 0.3$	$0.03 < H_3/D_m < 0.3$
$150 < U < 450$ (m/s)	$0.5 < (H_1/C_R) < 3$	$0.5 < (H_2/C_S) < 3$
$0.1 < M_{a1} < 0.7$	$0.1 < M_{a2} < 0.8$	$0.1 < M_{a3} < 0.9$
0.1 (mm) $< \tau < 1$ (mm)	$0.001 < \tau/H_1 < 0.01$	$\sigma_{stress} < \sigma_{all}$
$15 < Z_R < 50$	$20 < Z_S < 100$	$M_{rlm} < 2.0$
$0.35 < C_{mR}$	$0.35 < C_{mS}$	$140 < A_{SD}$
$0.75 < \eta_{TT}$	$1. < H_2/H_1 < 2.5$	$1. < H_2/H_3 < 1.5$
$0.2 < \varphi < 0.60$	$0.15 < \psi < 0.5$	$2° < \alpha_3 < 20°$
$0.15 < D_m < 0.3$ m	$0.8 < AVRR < 1.5$	$1.0 < AVRS < 1.5$
$1.0 < \sigma_S < 2.0$	$0.8 < \sigma_R < 2.0$	$0.2 < (C_R/D_m) < 0.5$
$0.1 < (C_S/D_m) < 0.5$	$0.025 < t_m/C_R < 0.2$	$0.025 < t_m/C_S < 0.2$

Table 2 Design constraints

G_η	G_A	G_C	η_{TT}	A_{SD}	C_m
-	-	-	0.875	171.98	0.535
1	0	0	0.921	158.88	0.481
0	1	0	0.600	225.74	0.539
0	0	1	0.415	145.72	0.598
1	1	1	0.786	208.95	0.572
1	0	1	0.888	162.04	0.553
1	1	0	0.854	208.60	0.478
0	1	1	0.730	213.90	0.572
1	0.5	1	0.891	187.63	0.577

Table 4 Influence of the different coefficient values in the multivariable objective function (C – sense; m = 4 kg/s; $\alpha_3 \leq 20$ deg; β_{TT} = 1.65)

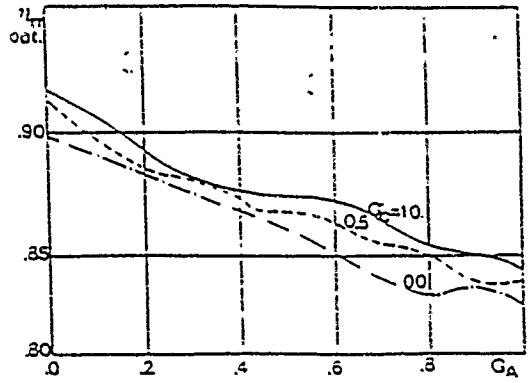


Figure 33: Efficiency diagram versus G_A and G_C

Third International Conference on Inverse Design Concepts and Optimization in Engineering Sciences (ICIDES-III), Editor: G.S. Dulikravich, Washington D.C., October 23-25, 1991.

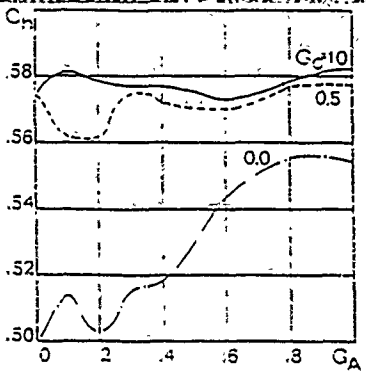


Figure 34: Influence of G_A and G_C on stall margin

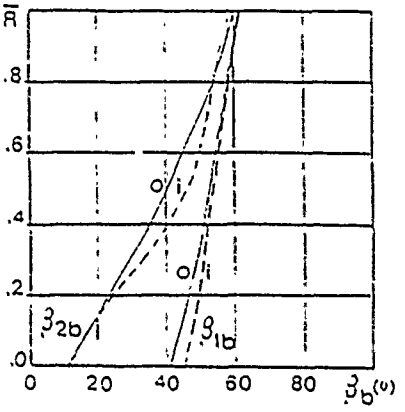


Figure 36: Radial distribution of blade anlgles (i=initial; o=optimum)

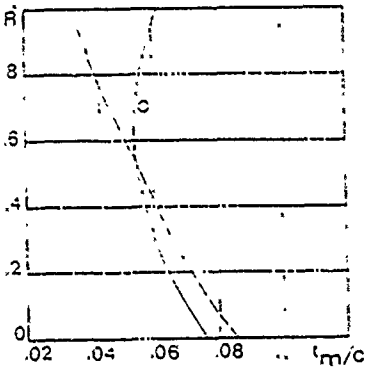


Figure 37: Radial distribution of max blade thickness

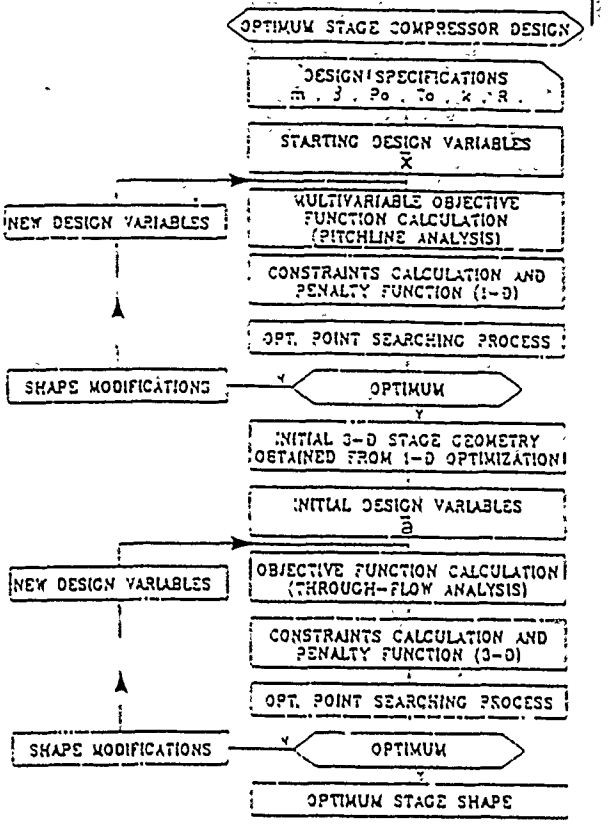


Figure 35: Optimum complete stage design

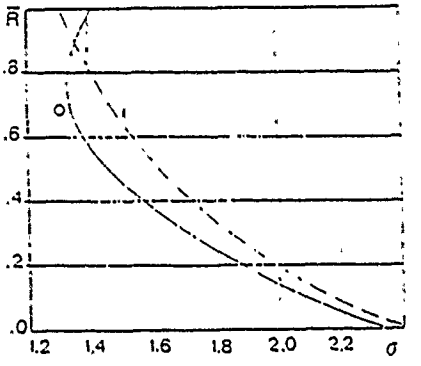


Figure 38: Radial distribution of solidity

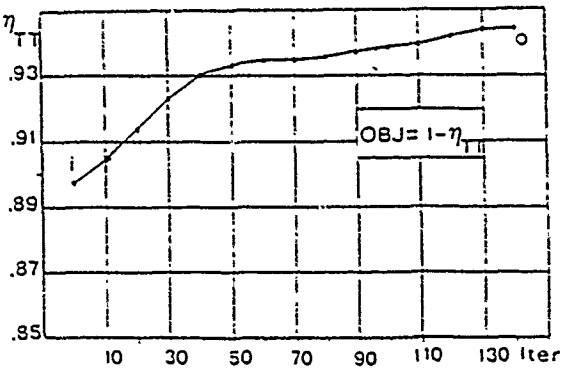


Figure 39: Optimization history of rotor total-to-total efficiency

Third International Conference on Inverse Design Concepts and Optimization in Engineering Sciences (ICIDES-III), Editor: G.S. Dulikravich, Washington D.C., October 23-25, 1991.

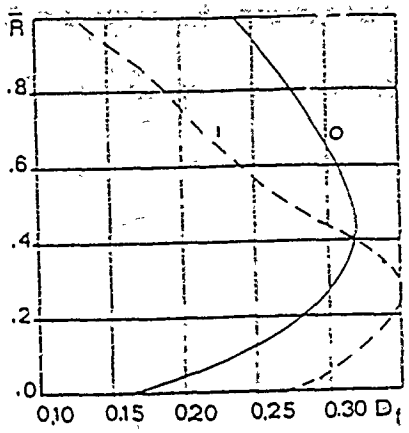


Figure 40: Radial distribution of diffusion factor

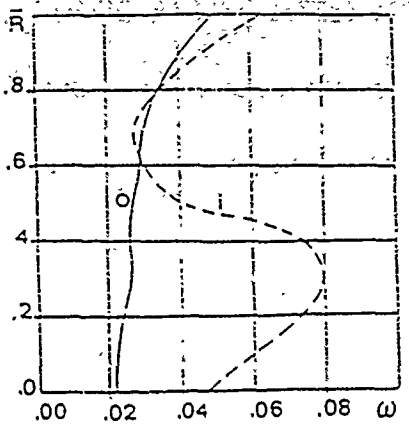


Figure 41: Radial distribution of total pressure loss

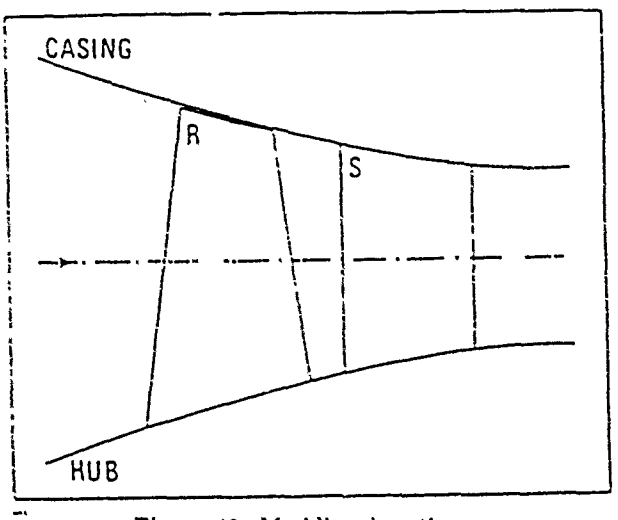


Figure 42: Meridional section

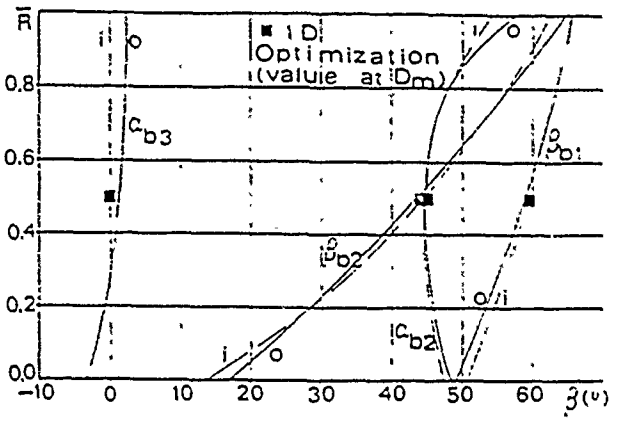


Figure 43: Stator and rotor angles

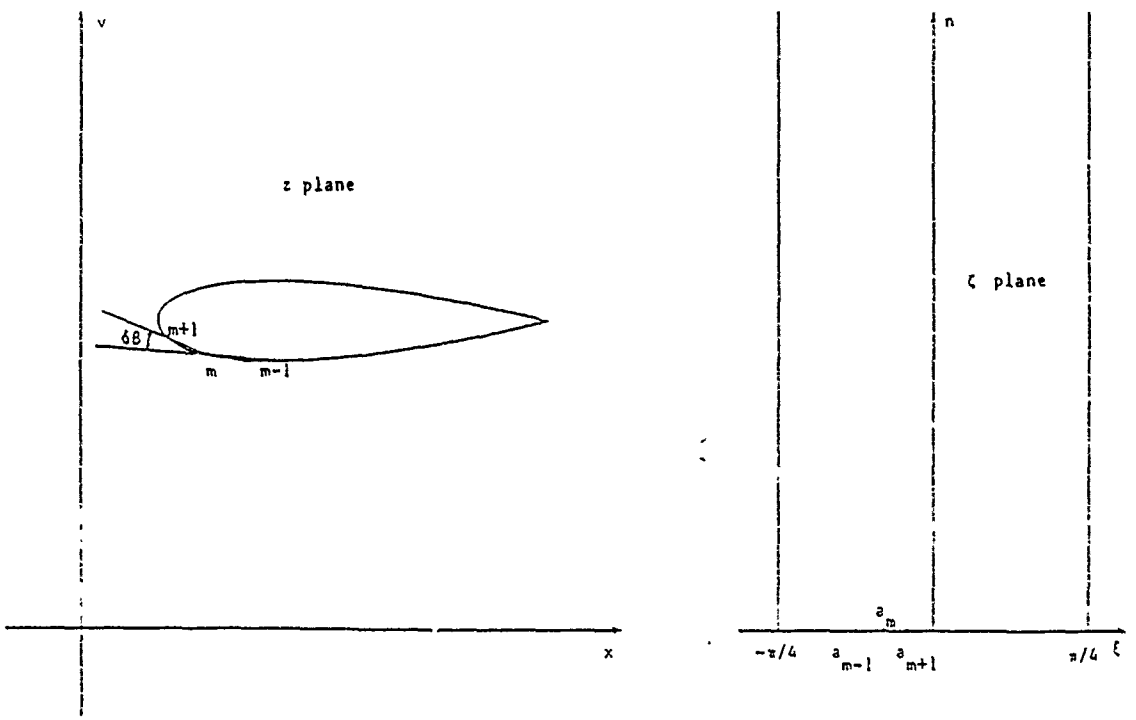


Figure 44: Physical and computational domain

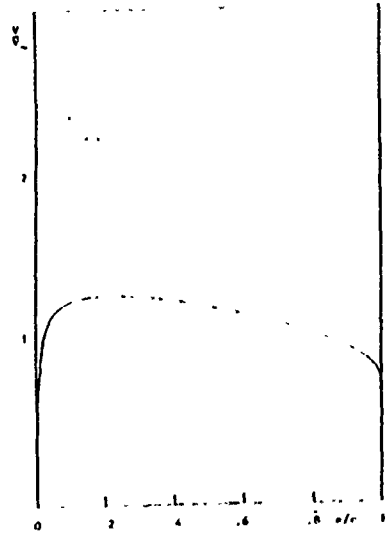


Figure 45: Karman-Treffez airfoil: velocity distribution

Tab 5 KARMAN-TREFFTZ $\alpha = 0°$

x	Y_E	Y_H	ϵz
.00000	.000000	.000000	.00
.00241	.011094	.011737	.34
.00961	.022164	.022873	.37
.02153	.033113	.033607	.26
.03806	.043774	.044191	.22
.05904	.053944	.054310	.19
.08427	.063411	.063740	.17
.11349	.071966	.072266	.16
.14645	.079420	.079695	.14
.18280	.085607	.085861	.13
.22221	.090393	.090628	.12
.26430	.093683	.093900	.11
.30866	.095420	.095621	.11
.35486	.095593	.095779	.10
.40245	.094232	.094405	.09
.45099	.091412	.091571	.08
.50000	.087252	.087397	.08
.54901	.081906	.082039	.07
.59754	.075562	.075683	.06
.64514	.068437	.068546	.06
.69134	.060764	.060862	.05
.73570	.052789	.052876	.05
.77778	.044759	.044835	.04
.81720	.036911	.036977	.03
.85355	.029468	.029523	.03
.88650	.022624	.022669	.02
.91573	.016542	.016577	.02
.94096	.011345	.011372	.01
.96194	.007117	.007134	.01
.97847	.003894	.003903	.00
.99039	.001671	.001672	.00
.99759	.000400	.000397	.00
1.00000	.000000	.000000	.00

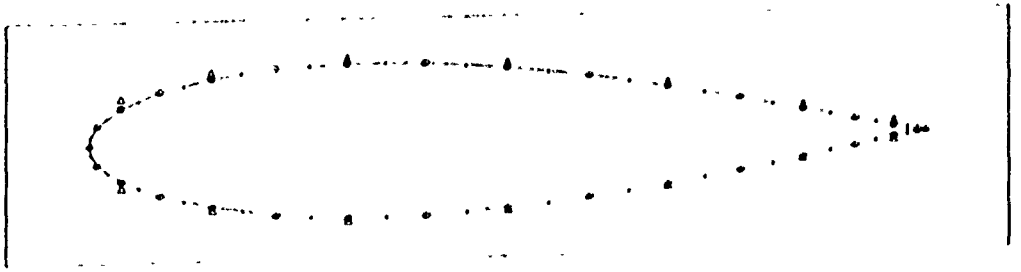


Figure 46: Karman-Treffez airfoil: exact and numerical solution $\alpha = 0$

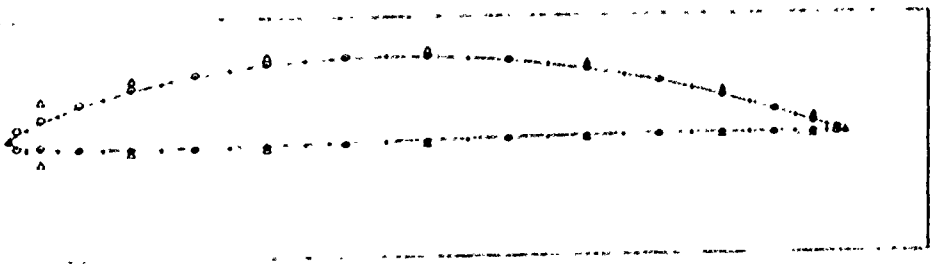


Figure 48: Karman-Treffez airfoil with camber and 5° incidence

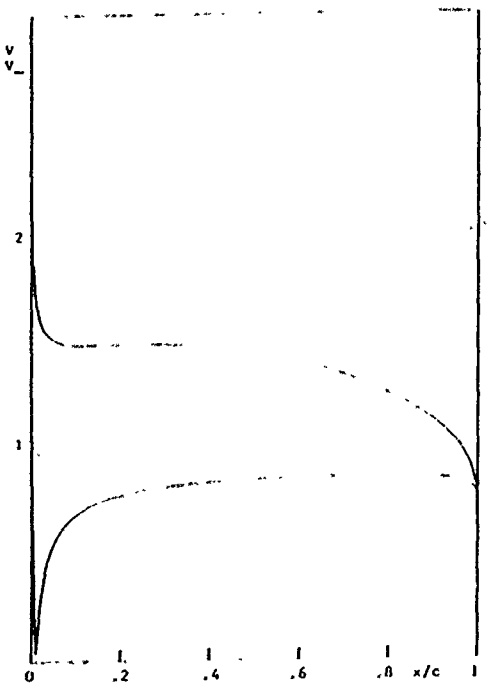


Figure 47: Karman-Treffez airfoil: velocity distribution

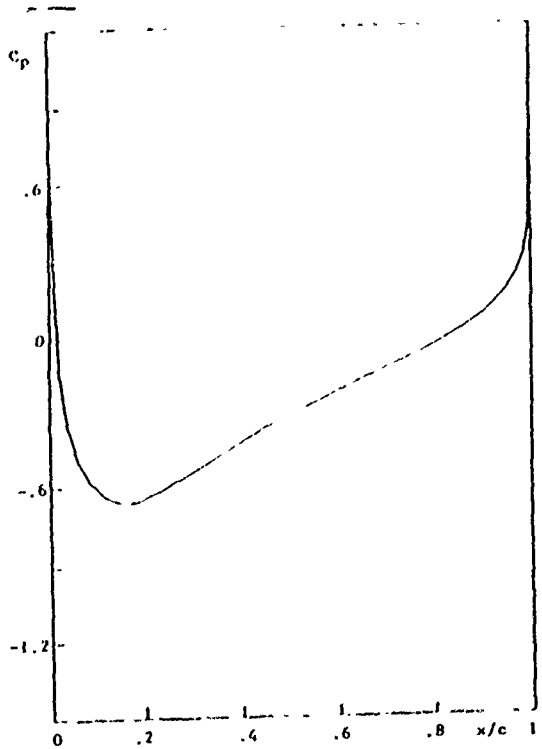


Figure 49: NACA0012 $M_\infty = 0.72$, $\alpha_\infty = 0^o$

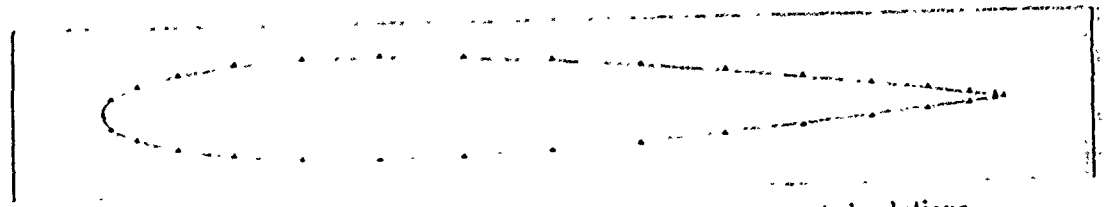


Figure 52: NACA0012 $M_\infty = 0.5$, $\alpha_\infty = 3^o$: exact and computed solutions

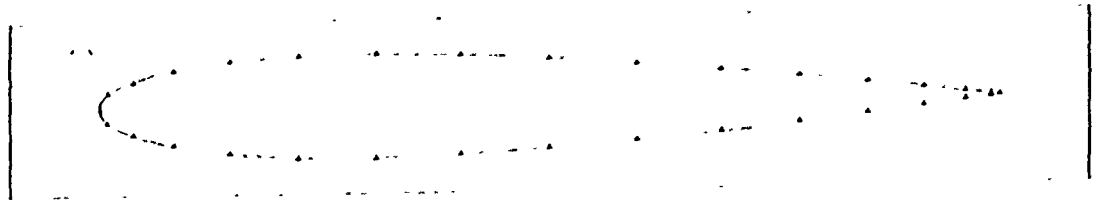


Figure 50: NACA0012 $M_\infty = 0.5$, $\alpha_\infty = 3^o$: exact and computed solutions

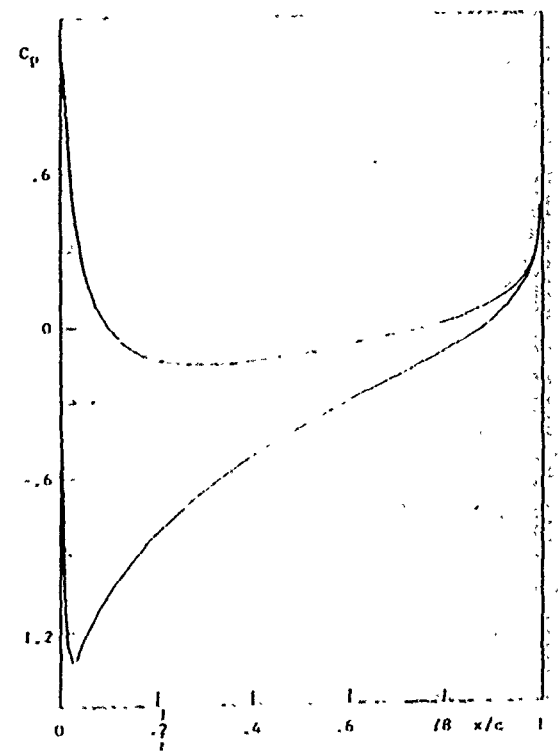


Figure 51: NACA0012 $M_\infty = 0.5$, $\alpha_\infty = 3^o$

Third International Conference on Inverse Design and Optimization in Engineering Sciences
(ICIDES-III) Editor: G.S.Dulikravich, Washington D.C. October 23-25, 1991.

ADJOINT OPERATOR APPROACH TO SHAPE DESIGN FOR INTERNAL INCOMPRESSIBLE FLOWS

H. Cabuk, C.-H. Sung*, and V. Modi,

Department of Mechanical Engineering,
Columbia University,
New York, New York 10027

* David Taylor Research Center
Bethesda, Maryland 20084

The problem of determining the profile of a channel or duct (given its upstream cross-section and length) that provides the maximum static pressure rise is solved. Incompressible, laminar flow governed by the steady-state Navier-Stokes equations is assumed. Recent advances in computational resources and algorithms have made it possible to solve the "direct" problem of determining such a flow through a body of known geometry. It is possible to obtain a set of "adjoint" equations, the solution to which permits the calculation of the direction and relative magnitude of change in the diffuser profile that leads to a higher pressure rise. The solution to the adjoint problem can be shown to represent an artificially constructed flow. This interpretation provides a means to construct numerical solutions to the adjoint equations that do not compromise the fully viscous nature of the problem. This paper addresses the algorithmic and computational aspects of solving the adjoint equations. The form of these set of equations is similar but not identical to the Navier-Stokes equations. In particular some issues related to boundary conditions and stability are discussed. The use of numerical solvers is validated by solving the problem of optimum design of a plane diffuser. The direct as well as the adjoint set of partial differential equations are discretized using a finite-volume formulation. Each of the resulting set of algebraic equations are then solved numerically to obtain a change in profile that will ensure an increase in the static pressure rise. Upon successive applications of this procedure, an "optimum" profile is obtained beginning with an initial guess of a diffuser profile. Such optimum diffuser profiles are obtained at Reynolds numbers varying from 10 to 2000. The optimality condition, that the shear stress all along the wall must vanish for the optimum diffuser, is also recovered from the analysis. It is shown that numerical solutions obtained in this fashion do satisfy the optimality condition.

1. INTRODUCTION

A shape optimization problem is one in which an objective function defined on a domain and/or on its boundary through the solution of a boundary value problem, is minimized (or maximized) with respect to the variation of the domain. One problem of this nature is "What is the shape of a body (of given volume) which has minimum drag when moved at constant speed in a viscous fluid?". Pironneau (1973) addressed this problem in Stokes flow for a three-dimensional unit-volume body. It was shown that at optimality the normal derivative of the velocity is constant along the boundary of the body. In addition it was also shown that the general shape of the body is similar to a prolate spheroid including a conical front end and rear ends of angle 120 degrees. However, due to the lack of a numerical Stokes flow solver, a complete body profile could not be obtained.

In a subsequent study, Pironneau (1974) derived the change in energy dissipation due to a small hump on a body in uniform, steady, laminar flow. Using the above result in conjunction with variational methods of optimal control "necessary optimality conditions" for four minimum-drag problems were obtained. These conditions lead to a set of equations for an additional set of variables called the "co-state" or the "adjoint" variables as opposed to the "direct" variables which are the unknown velocities. At the time Pironneau (1974) was unable to carry out such a numerical integration. Instead, however using a boundary layer assumption he was able to prove that a two-dimensional unit-area body with the smallest drag has a wedge-shaped

Third International Conference on Inverse Design and Optimization in Engineering Sciences
(ICIDES-III) Editor: G.S.Dulikravich, Washington D.C. October 23-25, 1991.

front end. In a subsequent work Glowinski and Pironneau (1975) presented numerical computations of the minimum-drag profile of a two-dimensional body in laminar flow, although with a Reynolds number large enough (between 1,000 to 100,000) to permit a boundary layer approximation. The present study belongs to this class in its theoretical approach with particular emphasis on computation of optimum profiles in the absence of simplifying assumptions such as Stokes flow or thin boundary layers.

Another related class of optimum design problems is the question of determining the profile of a two-dimensional body that will attain a desired surface pressure distribution. The body is assumed to be in otherwise uniform flow. The designer usually has a better understanding of how the performance is related to the the pressure distribution than the relationship between the profile and the performance. In recent survey paper, Jameson (1988) suggests that the design problem be treated as a control problem in which the control is the profile of the boundary. He also provides a comprehensive summary of the earlier related studies in this direction. In a significant step towards addressing real flows Giles et. al. (1985) addressed the problem of shape design for flows governed by the two-dimensional Euler equations. They write the two-dimensional Euler equations in a streamline coordinate system and for fixed pressure distribution obtain a Newton solution for the unknown surface coordinates.

In the present study optimum design of an internal flow component such as a diffuser in laminar flow is considered. The problem of determining the profile of a plane diffuser (of say, given upstream width and length) that provides the maximum static pressure rise is formulated using a variational method derived from optimal control theory. Careful consideration of the numerical stability of the adjoint equations we have been able to demonstrate the feasibility of optimum design in the context of laminar Navier-Stokes equations without the additional boundary layer assumption.

2. STATEMENT OF THE PROBLEM

Consider a plane diffuser as shown in figure 1 of given upstream width W_1 and given length L with incompressible, laminar flow through it. The flow is governed by the incompressible, steady forms of the Navier-Stokes and continuity equations. These are:

$$\begin{aligned} u_{i,i} &= 0 \\ u_j u_{i,j} &= -p^*_{,i} + \nu u_{i,jj} \end{aligned} \tag{1}$$

where $p^* = p/\rho$. Here u_i, p, ρ, and ν are the velocity components, pressure, density and kinematic viscosity respectively.

A no slip condition is imposed on the bounding wall. Dirichlet type boundary conditions are assumed at the entrance and exit, specifically, it is assumed that the streamwise velocity component at the entrance and exit is specified and the transverse velocity component at the entrance and exit is assumed to be zero. Symmetry conditions are assumed at the centerline. All velocities and lengths are scaled using the average entrance velocity, V, and the diffuser entrance width W_1 throughout the paper. Hence the Reynolds number for the flow through the diffuser is defined as $Re = (V \cdot W_1)/\nu$.

It is desired that the optimum diffuser profile be such as to maximize the value of this parameter for a given upstream width and length. Since pressure may vary across the diffuser inlet and exit regions it was decided to choose the change in the flow weighted integral (over the exit and inlet cross-sectional areas) of the static pressure rise as the objective function. This quantity is given by:

$$J(\Gamma_M) = \int_{\Gamma_I} p^* u_i n_i ds + \int_{\Gamma_O} p^* u_i n_i ds \tag{2}$$

where n_i is the i^{th} component of the unit normal vector and Γ_M is the portion of the diffuser wall that is to be shaped. The goal then is to determine the diffuser profile that maximizes the above function. The normalized diffuser length, L/W_1, (henceforth simply called the length) is kept constant. The normalized exit width W_2/W_1, (henceforth simply called the exit width) is left arbitrary, and its actual value for the optimum diffuser is part of the solution to the problem and is determined along with the rest of the profile. Since the only mechanism for total pressure drop in the diffuser is viscous dissipation, the optimum profile is also the profile for which the viscous dissipation is a minimum.

Third International Conference on Inverse Design and Optimization in Engineering Sciences (IDES-III) Editor: G.S.Dulikravich, Washington D.C. October 23-25, 1991.

3. MATHEMATICAL FORMULATION

In this section, the variation of the objective function with respect to the variation of the boundary is obtained by means of a perturbation type of analysis. This analysis follows from arguments not unlike those used for optimum design in potential flow, in an earlier paper by Çabuk and Modi (1990).

First the variation of the solution of the direct problem due to boundary variation is obtained. Let $\rho(s)$ be an arbitrary function of arclength s, defined on Γ_M, and let ϵ be a positive number. Here Γ_M is part of the boundary that is to be shaped. The whole boundary, including the wall of the diffuser, the centerline and the inlet and exit areas, is denoted by Γ and the domain enclosed by Γ is denoted by Ω. Let each point on Γ_M be moved by $\epsilon\rho(s)$ along the outer normal direction. The curve constructed in this way is denoted by $\Gamma_{M,\epsilon}$ and the new domain is denoted by Ω_ϵ as shown in figure 1. Let $(u_i^\epsilon, p^\epsilon)$ be the solution of (1) in the new domain Ω_ϵ. Let (ϕ_i, π) be defined as follows.

$$\begin{aligned} \phi_i &= \lim_{\epsilon\to 0} \epsilon^{-1}[u_i^\epsilon - u_i] \qquad \in \Omega, \\ \pi &= \lim_{\epsilon\to 0} \epsilon^{-1}[p^\epsilon - p^*] \qquad \in \Omega. \end{aligned} \tag{3}$$

Then $(u_i^\epsilon, p^\epsilon)$ can be written as:

$$\begin{aligned} u_i^\epsilon &= u_i + \epsilon\phi_i \\ p^\epsilon &= p^* + \epsilon\pi \end{aligned} \tag{4}$$

Since both $(u_i^\epsilon, p^\epsilon)$ and (u_i, p^*) satisfy the Navier-Stokes equations, it can be shown that (ϕ_i, π) satisfy the following set of equations:

$$\begin{aligned} \phi_{i,i} &= 0 \\ u_j\phi_{i,j} + \phi_j u_{i,j} &= -\pi_{,i} + \nu\phi_{i,jj} \end{aligned} \tag{5}$$

In a similar way it can be shown that on the fixed portions of the boundary

$$\phi_i = 0 \qquad \text{on } (\Gamma - \Gamma_M) \tag{6}$$

since both u_i^ϵ and u_i satisfy the same boundary conditions.

The next step is to derive the conditions satisfied by ϕ_i on Γ_M. Consider a point P on Γ_M, and a corresponding point P_ϵ on $\Gamma_{M,\epsilon}$ such that P_ϵ lies on the outward normal $\vec{n}$, as shown in figure 1. Assume that $\epsilon\rho(s)$ is positive. A Taylor's series expansion of u_i^ϵ about the point P, evaluated at $\bar{x} = \bar{x}|_{P_\epsilon}$, along the normal direction $\vec{n}$ is

$$\begin{aligned} u_i^\epsilon|_{P_\epsilon} &= u_i^\epsilon|_P + \epsilon\rho\left(\frac{\partial u_i^\epsilon}{\partial n}\right)_P + O(\epsilon^2) \\ &= u_i|_P + \epsilon\phi_i|_P + \epsilon\rho\left(\frac{\partial u_i}{\partial n}\right)_P + O(\epsilon^2) \end{aligned} \tag{7}$$

Since the velocities satisfy the no slip condition on Γ_M, (i.e. $u_i^\epsilon|_{P_\epsilon} = u_i|_P = 0$);

$$\phi_i = -\rho\left(\frac{\partial u_i}{\partial n}\right) \qquad \text{on } \Gamma_M. \tag{8}$$

The first variation of the objective function is obtained next. The value of the objective function for the new domain is given by,

$$J(\Gamma_{M,\epsilon}) = \int_{\Gamma_I} p^\epsilon u_i^\epsilon n_i ds + \int_{\Gamma_O} p^\epsilon u_i^\epsilon n_i ds \tag{9}$$

The first variation of the objective function, δJ, is defined by the relation

$$J(\Gamma_{M_\epsilon}) - J(\Gamma_M) = \epsilon\delta J + O(\epsilon^2). \tag{10}$$

The first variation of the objective function can be shown to be:

$$\delta J = \int_{\Gamma_I} \pi u_i n_i ds + \int_{\Gamma_O} \pi u_i n_i ds\ , \tag{11}$$

Third International Conference on Inverse Design and Optimization in Engineering Sciences (ICIDES-III) Editor: G.S.Dulikravich, Washington D.C. October 23-25, 1991.

which is an integral expression over the entrance and exit boundaries. The next step is the transformation of this integral from one that is over Γ_I and Γ_O to one that is over Γ_M. This is achieved through the introduction of an adjoint variable problem. The inner product of the perturbation equations (5) and the adjoint variables, (z_i, r), integrated over the domain, and added to (11), and after using the divergence theorem gives

$$\begin{aligned}\delta J = &\oint \pi\,(u_i - z_i)\,n_i ds + \nu \oint \left(z_i \frac{\partial \phi_i}{\partial n} - \phi \frac{\partial z_i}{\partial n}\right) ds \\ &+ \oint \left(r\phi_i n_i - \phi_i z_i u_j n_j - u_i z_i \phi_j n_j\right) ds + \iint \pi z_{i,i} dA \\ &+ \iint \phi_i \left(\nu z_{i,jj} + u_j z_{i,j} + u_j z_{j,i} - r_{,i}\right) dA\,.\end{aligned} \tag{12}$$

The adjoint problem has to be defined such that the domain integrals in (15) vanish identically. The choice of boundary conditions for these equations is made such that the only nonzero terms are those that are integrals over Γ_M, the wall that is to be shaped. Let us define the following adjoint problem

$$\begin{aligned} z_{i,i} &= 0 && \text{in } \Omega \\ \nu z_{i,jj} + u_j(z_{i,j} + z_{j,i}) - r_{,i} &= 0 && \text{in } \Omega \\ z_i &= u_i && \text{on } \Gamma. \end{aligned} \tag{13}$$

Using (6), (8), and (13), equation (12) can be written as

$$\delta J = \nu \int_{\Gamma_M} \rho(s) \left(\frac{\partial u_i}{\partial n}\right) \left(\frac{\partial z_i}{\partial n}\right) ds\,. \tag{14}$$

In the above equation, the integration is over the boundary that is to be shaped. We can choose $\rho(s)$ as:

$$\rho(s) = \omega(s) \left(\frac{\partial u_i}{\partial n}\right) \left(\frac{\partial z_i}{\partial n}\right) \tag{15}$$

since that would ensure a positive change in the objective function, J, for a sufficiently small non-negative weighting function, $\omega(s)$. The function $\rho(s)$ provides the boundary movement for a positive change in J. To evaluate $\rho(s)$ we need to solve the direct problem (i.e. Navier-Stokes equations) given by (1) and the adjoint problem in z_i given by (13). Note that the optimality condition is satisfied when either the shear stress, $\partial u_i/\partial n$, or the adjoint shear stress, $\partial z_i/\partial n$, on the walls vanishes. The former criterion for optimum diffuser profiles was also pointed out by Chang(1976).

It will be shown that the above formulation is equivalent to the earlier work of Glowinski and Pironneau (1975). By a change of variable, the adjoint problem can be transformed into the following form:

$$\begin{aligned} w_{i,i} &= 0 && \text{in } \Omega \\ \nu w_{i,jj} + u_j w_{i,j} + w_j u_{j,i} - q_{,i} &= -u_j u_{i,j} && \text{in } \Omega \\ w_i &= 0 && \text{on } \Gamma. \end{aligned} \tag{16}$$

where $2w_i = (z_i - u_i)$ and $2q = \left(r - p^* + (1/2)u_j^2 - 2u_j w_j\right)$. The first variation of the objective function then becomes

$$\delta J = \nu \int_{\Gamma_M} \rho \left(\frac{\partial u_i}{\partial n}\right) \left(\frac{\partial u_i}{\partial n} + 2\frac{\partial w_i}{\partial n}\right) ds\,. \tag{17}$$

The form of the adjoint variable problem defined by (16) is identical to that derived by Glowinski and Pironneau (1975). Either one of the above adjoint problems can be solved numerically to obtain the next shape. However upon examination of (16), it becomes evident that the $w_j u_{j,i}$ term may lead to a numerically unstable scheme. This is because the approach to steady state would be attained via an iterative "time evolution" like scheme that would then be of the form $dw/dt = w(\text{const}) + \cdots$. This form is likely to result in the exponential growth of the inevitable roundoff and truncation errors present at any iterative step. Also

Third International Conference on Inverse Design and Optimization in Engineering Sciences
(ICIDES-III) Editor: G.S.Dulikravich, Washington D.C. October 23-25, 1991.

the presence of the inhomogeneous term, $-u_j u_{i,j}$, in the above equations may lead to a linear growth of the roundoff and truncation errors in the numerical computations. It is expected that these numerical difficulties will be absent in the (z_i, r) formulation of the adjoint variable problem obtained in this paper and given by (13). Hence this is the set of equations for which the algorithm for the numerical solution of the adjoint problem is developed.

As pointed out by Pironneau (1974), the adjoint equations do not seem to arise from any identifiable physical phenomenon. It is however possible to demonstrate that the adjoint variable problem is associated with a certain artificially constructed flow. A change of variables leads to the following form.

$$\begin{aligned} z'_{i,i} &= 0 && \text{in } \Omega \\ \nu z'_{i,jj} - u'_j \left(z'_{i,j} + z'_{j,i}\right) - r'_{,i} &= 0 \quad \text{in } \Omega \\ z'_i = u'_i &= -u_i && \text{on } \Gamma. \end{aligned} \tag{18}$$

where $z'_i = -z_i$, $u'_i = -u_i$, and $r' = -r$. The first equation in (18) is identical to the continuity equation. Compare the second equation in (18) with the Navier-Stokes equation written here in a slightly different form.

$$\nu u_{i,jj} - u_j \left(u_{i,j} + u_{j,i}\right) - \tilde{p}_{,i} = 0 \tag{19}$$

where $\tilde{p} = p^* - (1/2)u_k^2$. Observe that the problem in adjoint variable z'_i is analogous to the the Navier-Stokes problem in variable u_i with the following exception: the convective velocities in the adjoint problem are specified rendering the problem linear and are obtained from the direct problem. These convective velocities, u'_i, are identical in magnitude but opposite in direction to those of the "direct" problem. The boundary conditions for the adjoint variables are $z'_i = -u_i$ on Γ. Hence on the walls they imply a no slip condition as in the direct problem. But at the inflow and outflow boundaries, "adjoint" flow is found entering at the domain exit Γ_O and leaving at the domain entrance Γ_I, thus suggesting an "adjoint" flow in the direction opposite to that of the actual flow.

The above interpretation of the adjoint variable problem will be useful in constructing a modified problem whose solution will provide numerical values, albeit approximate, for the shear stress, $\partial u_i/\partial n$, and the adjoint shear stress, $\partial z_i/\partial n$, in (15). It is found that a shape optimization algorithm that obtains its boundary movement from these approximate numerical solutions does indeed lead to diffuser shapes that satisfy the optimality condition.

4. NUMERICAL ASPECTS

The boundary conditions chosen for the diffuser in the above formulation are of Dirichlet type. A parallel flow of arbitrary distribution is assumed to exist at the diffuser entrance and exit. These boundary conditions are clearly unrealistic both from a practical as well as computational standpoint. However this is the only set of boundary conditions for which we have been able to derive the adjoint variable problem. Given this limitation it was decided to verify whether the boundary movement suggested by (15) would continue to provide a means to obtain optimum shapes even if some of the Dirichlet conditions were replaced with computationally suitable Neumann conditions.

Boundary Conditions for Navier-Stokes Equations

A parallel flow assumption at the upstream boundary implies Dirichlet boundary conditions for both the velocity components. Instead a computationally desirable Neumann condition for the transverse velocity component ($\partial u_2/\partial n = 0$ on Γ_I) is substituted while retaining a Dirichlet condition for the streamwise component. A parabolic profile corresponding to a fully developed laminar flow is specified for this component. At the downstream boundary the parallel flow assumption is replaced with computationally desirable Neumann conditions for both the velocity components ($\partial u_1/\partial n = \partial u_2/\partial n = 0$ on Γ_O). Similar approximations will be made in the solution of the adjoint variable problem, keeping in mind the reversal of the role of entrance and exit boundaries. At the solid wall, a boundary whose profile is to be determined, a no slip condition is enforced. At the diffuser centerline the usual symmetry conditions are used since the flow is assumed to be symmetric. At the entrance, exit, and wall, pressure has been extrapolated from the within the domain by assuming that the second derivative of the pressure vanishes on the domain boundary. At the centerline symmetry condition is imposed for the pressure.

Third International Conference on Inverse Design and Optimization in Engineering Sciences (ICIDES-III) Editor: G.S.Dulikravich, Washington D.C. October 23-25, 1991.

Boundary Conditions for Adjoint Equations

The role of entrance and exit are reversed for the adjoint equations. Therefore, at the exit boundary a Dirichlet type condition is used only for the streamwise component of the co-state vector. Therefore we set $z_1 = u_1$ on Γ_O, with u_1 taken from the solution of the Navier-Stokes equations. For the remaining component z_2 of the co-state vector at exit and for both components of the co-state vector at entrance, Neumann conditions are employed instead. At the wall where all velocity components vanish and therefore, z_i, the co-state vector that is analogous to the velocity is set to zero. The adjoint variable, r^*, is analogous to the pressure term in the Navier-Stokes equations and hence no analytical boundary condition is available for this variable. However, a computational boundary condition is implemented for this variable. The value of r^* is extrapolated to the boundary from values at interior points assuming that the streamwise second derivative vanishes at the boundary. This is done at all boundaries except at the centerline where a symmetry condition is enforced.

5. NUMERICAL SOLVERS

Navier-Stokes Equations Solver

The primitive variable form of the incompressible steady Navier-Stokes equations is solved using an artificial compressibility formulation due to Chorin(1967). In this formulation, the continuity equation is modified using the time derivative of the pressure term. The steady-state solution of the Navier-Stokes equations is then obtained as the large time solution of the unsteady momentum equations with the perturbed divergence equation. These unsteady equations are:

$$\begin{aligned} p_t^* + \beta^2 u_{i,i} &= 0 \\ u_{i,t} + (u_j u_i)_{,j} &= -p_{,i}^* + \nu u_{i,jj} \end{aligned} \tag{20}$$

where β is analogous to the speed of sound. Note that these equations do not represent any transient physical phenomenon and hence the transient solution has no physical meaning until steady state is attained. This is indicated by the vanishing of the time derivative terms in the numerical solution.

The equations are normalized using the velocity and length scales V and W_1 defined earlier. In addition time and pressure are normalized using the ratio W_1/V and ρV^2 respectively. The Reynolds number of the flow through the diffuser is then given by $Re = (V \cdot W_1)/\nu$.

The equations are discretized in space using a finite volume formulation. The spatial discretization is performed on the conservative form of the governing equations using a central difference scheme.

An explicit one-step multistage Runge-Kutta stepping scheme is used for integration in time. Since transient behavior is not an issue and a larger time step is desirable, a four-stage Runge-Kutta scheme with first order accuracy in time and a relatively high Courant-Friedrichs-Lewy (CFL) number has been chosen. In order to improve the convergence rate, a local time step is computed for each cell at each elapsed time level. These time steps have been estimated from a stability analysis of the algorithm. A fourth order linear artificial dissipation term is introduced to damp the high-frequency oscillations associated with the so-called sawtooth or plus-minus waves, i.e. waves associated with the shortest wavelengths. Implicit residual smoothing is performed at each iteration to enhance the stability region of the technique. A more complete discussion of the finite volume formulation, stability considerations, local time stepping, artificial dissipation, implicit residual smoothing and the computational boundary conditions is provided in Cabuk, Sung and Modi (1991).

The computational grid is generated by solving a set of elliptic partial differential equations similar to those suggested by Thompson et al. (1974). The set of algebraic equations thus obtained is solved by successive over-relaxation (SOR). A typical grid is shown in figure 2. Grids generated by this method were nearly orthogonal and the cell dimensions in each direction are approximately equal.

Adjoint Equation Solver

The solution to the adjoint set of equations is obtained as the steady state solution to the following set of equations:

$$\begin{aligned} r_t^* &= -\beta^2 z_{i,i} \\ z_{i,t} &= \nu z_{i,jj} + u_j(z_{i,j} + z_{j,i}) - \frac{1}{2}(z_k z_k)_{,i} - r_{,i}^* \end{aligned} \tag{21}$$

Third International Conference on Inverse Design and Optimization in Engineering Sciences
(ICIDES-III) Editor: G.S.Dulikravich, Washington D.C. October 23-25, 1991.

where $r^* = r - z_k z_{k,i}$. A nonlinear term $\frac{1}{2}(z_k z_k)_{,i}$ is introduced in the above equation to enhance the rate of convergence. The utility of this term was established by means of preliminary calculations performed on a straight duct geometry where an exact solution of the Navier-Stokes solution is known for fully developed laminar flow.

The equations are normalized following a procedure similar to that utilized for the Navier-Stokes equations. The nondimensional form of the above equation is identical to the equations above with the exception of the first term on the right hand side of (21) where the kinematic viscosity, ν, is replaced by the reciprocal of the Reynolds number.

The numerical algorithm for the solution of the adjoint set of equations is essentially similar to the algorithm for the Navier-Stokes equations. Some subtle but important differences do exist since the equations solved are after all not the same. A discussion of the numerical algorithm is presented here, since this solution to the best of our knowledge represents the first successful numerical solution of the adjoint set of equations in the absence of either a thin boundary layer or a Stokes flow assumption. Spatial discretization is carried out by centered-difference finite volume formulation. The term, $u_j(z_{i,j} + z_{j,i})$, on the right hand side of (21) is not in a divergence form. In the treatment of this term the velocities, u_j, which have already been obtained by the Navier-Stokes solver, are treated as known quantities and are assumed constant inside each cell. Hence the volume integral over the cell is performed by applying the divergence theorem to the remaining part of this term, i.e. $(z_{i,j} + z_{j,i})$.

The other terms in (21) are treated in the same fashion as the finite volume formulation of the Navier-Stokes equations. A fourth order linear artificial dissipation term is introduced to damp high-frequency oscillations. Time integration is carried out by a Runge-Kutta scheme with local time stepping. The discrete form of the equations for the adjoint problem are:

$$\Delta V \frac{dq}{dt} - (A\delta_I + B\delta_J + C\delta_K)q = E\frac{Re^{-1}}{\Delta V}(SI\delta_I^2 + SJ\delta_J^2 + SK\delta_K^2)q - \epsilon K(\delta_I^4 + \delta_J^4 + \delta_K^4)q \qquad (22)$$

where

$$A = \begin{bmatrix} 0 & \beta^2 SIX & \beta^2 SIY & \beta^2 SIZ \\ SIX & U + (u_1 - z_1)\,SIX & (u_1 - z_1)\,SIY & (u_1 - z_1)\,SIZ \\ SIY & (u_2 - z_3)\,SIX & U + (u_2 - z_2)\,SIY & (u_2 - z_2)\,SIZ \\ SIZ & (u_3 - z_3)\,SIX & (u_3 - z_3)\,SIY & U + (u_3 - z_3)\,SIZ \end{bmatrix}$$

$$B = \begin{bmatrix} 0 & \beta^2 SJX & \beta^2 SJY & \beta^2 SJZ \\ SJX & V + (u_1 - z_1)\,SJX & (u_1 - z_1)\,SJY & (u_1 - z_1)\,SJZ \\ SJY & (u_2 - z_3)\,SJX & V + (u_2 - z_2)\,SJY & (u_2 - z_2)\,SJZ \\ SJZ & (u_3 - z_3)\,SJX & (u_3 - z_3)\,SJY & V + (u_3 - z_3)\,SJZ \end{bmatrix}$$

$$C = \begin{bmatrix} 0 & \beta^2 SKX & \beta^2 SKY & \beta^2 SKZ \\ SKX & W + (u_1 - z_1)\,SKX & (u_1 - z_1)\,SKY & (u_1 - z_1)\,SKZ \\ SKY & (u_2 - z_3)\,SKX & W + (u_2 - z_2)\,SKY & (u_2 - z_2)\,SKZ \\ SKZ & (u_3 - z_3)\,SKX & (u_3 - z_3)\,SKY & W + (u_3 - z_3)\,SKZ \end{bmatrix}$$

$$E = \begin{bmatrix} 0 & 0 & 0 & 0 \\ 0 & 1 & 0 & 0 \\ 0 & 0 & 1 & 0 \\ 0 & 0 & 0 & 1 \end{bmatrix}$$

and

$$q = [r^*, z_1, z_2, z_3]^T$$

with

$$U = u_1 SIX + u_2 SIY + u_3 SIZ, \qquad SI = SIX^2 + SIY^2 + SIZ^2,$$
$$V = u_1 SJX + u_2 SJY + u_3 SJZ, \qquad SJ = SJX^2 + SJY^2 + SJZ^2,$$
$$W = u_1 SKX + u_2 SKY + u_3 SKZ, \qquad SK = SKX^2 + SKY^2 + SKZ^2$$

Third International Conference on Inverse Design and Optimization in Engineering Sciences
(ICIDES-III) Editor: G.S.Dulikravich, Washington D.C. October 23-25, 1991.

The volume of the cell is ΔV and (SIX, SIY, SIZ), (SJX, SJY, SJZ) and (SKX, SKY, SKZ) are the surface-area vectors normal to the I, J and K cell surfaces, respectively. SI, SJ and SK are the squares of the surface areas of I, J and K cell surfaces, respectively. The first, second and fourth order centered differences are defined in the same fashion as in Sung(1987). The maximum local time step permitted for stability is obtained by neglecting both the viscous and the artificial dissipation terms in the adjoint problem and is given by

$$\Delta t \leq CFL\left(\frac{\Delta V}{\lambda_0}\right) \tag{23}$$

The maximum eigenvalue, λ_0, in the above equation is estimated as

$$\lambda_0 = \frac{1}{2}\left[\hat{U} + \sqrt{\hat{U}^2 + \beta^2 C^2}\right] \tag{24}$$

where

$$\begin{aligned}\hat{U} = &|U| + |SIX\,(u_1 - z_1)| + |SIY\,(u_2 - z_2)| + |SIZ\,(u_3 - z_3)| \\ &+ |V| + |SJX\,(u_1 - z_1)| + |SJY\,(u_2 - z_2)| + |SJZ\,(u_3 - z_3)| \\ &+ |W| + |SKX\,(u_1 - z_1)| + |SKY\,(u_2 - z_2)| + |SKZ\,(u_3 - z_3)|\end{aligned}$$

and

$$\begin{aligned}C^2 = &(|SIX| + |SIY| + |SIZ|)^2 \\ &+(|SJX| + |SJY| + |SJZ|)^2 \\ &+(|SKX| + |SKY| + |SKZ|)^2.\end{aligned}$$

The maximum eigenvalue of the resulting matrix system, including both the viscous terms and the artificial dissipation term has been estimated as

$$\begin{aligned}\lambda_0 = &\sqrt{\lambda_I^2 + (4Re^{-1}SI/\Delta V + 16\epsilon K)^2} \\ &+\sqrt{\lambda_J^2 + (4Re^{-1}SJ/\Delta V + 16\epsilon K)^2} \\ &+\sqrt{\lambda_K^2 + (4Re^{-1}SK/\Delta V + 16\epsilon K)^2}\end{aligned} \tag{25}$$

where

$$\lambda_I = \frac{1}{2}\left[\hat{U}_I + \sqrt{\hat{U}_I^2 + \beta^2 SI}\right]$$

$$\lambda_J = \frac{1}{2}\left[\hat{U}_J + \sqrt{\hat{U}_J^2 + \beta^2 SJ}\right]$$

$$\lambda_K = \frac{1}{2}\left[\hat{U}_K + \sqrt{\hat{U}_K^2 + \beta^2 SK}\right]$$

and

$$\begin{aligned}\hat{U}_I =&|U| + |SIX\,(u_1 - z_1)| + |SIY\,(u_2 - z_2)| + |SIZ\,(u_3 - z_3)| \\ \hat{U}_J =&|V| + |SJX\,(u_1 - z_1)| + |SJY\,(u_2 - z_2)| + |SJZ\,(u_3 - z_3)| \\ \hat{U}_K =&|W| + |SKX\,(u_1 - z_1)| + |SKY\,(u_2 - z_2)| + |SKZ\,(u_3 - z_3)|\end{aligned}$$

Then the local time step has been computed from (23) with the maximum eigenvalue given by (25).

Profile Modification Algorithm

The principal steps of the optimization procedure are;

a) Choose an initial diffuser profile.
b) Generate a computational grid that conforms to the diffuser wall.
c) Obtain the steady state solution to the direct problem.

Third International Conference on Inverse Design and Optimization in Engineering Sciences
(ICIDES-III) Editor: G.S.Dulikravich, Washington D.C. October 23-25, 1991.

d) Obtain the steady state solution to the adjoint problem, by treating the required velocities as known from step (c).
e) Compute $\partial u_i/\partial n$ and $\partial z_i/\partial n$ from the solutions in steps (c) and (d) respectively. Choose a non-negative weighting function $\omega(s)$ and hence obtain $\rho(s)$ from (15).
f) Move nodes on the diffuser wall to be profiled along the outer normal direction by $\rho(s)$. The curve connecting the nodes after this movement represents the new diffuser profile.
g) Go to step (b) unless the change in diffuser pressure rise obtained from step (c) is smaller than a desired convergence parameter.

The iterative profile modification process is continued until the change in pressure rise is a small fraction of the total pressure rise. An alternate method is to continue the process until the value of $\rho(s)$ everywhere along the wall is less than a critical value. In step (e), the weighting function, $\omega(s)$, is chosen to be proportional to the arclength, s, along the diffuser wall measured from the diffuser entrance. This ensures that the entrance width is maintained constant but the exit width may vary with the diffuser profile. When shifting the diffuser wall to a new curve obtained from step (f) some care must be exercised since the curve is being redefined using only a finite number of discretely spaced points. Checks are performed on the location of points on the new curve to ensure that boundary nodes do not conglomerate or coalesce after their movement to a new position. Heuristic measures are also adopted to ensure that the appearance of small amplitude wiggles in the new profile are damped to some extent so as to prevent the growth and built up of numerical errors in the subsequent calculation

RESULTS AND DISCUSSION

Using the numerical solvers and the profile modification algorithm described above, optimum diffuser profiles have been obtained for a single diffuser length $L/W_1 = 3$ at Reynolds numbers Re=50, 100, 200 and 500. A sound speed, β^2, of 2 for the Navier-Stokes equations and 2.5 for the adjoint equations was used at all Reynolds numbers. The calculation at Re=200 (henceforth called the reference case) has been examined in particular detail to establish issues of convergence and accuracy.

The reference case was first examined for convergence of the profile modification algorithm. For this purpose, a computational grid of 61 nodes in the x and 31 nodes in the y directions is employed, both for the Navier-Stokes as well as the adjoint variable problem. Beginning with an initial shape the diffuser profile was obtained after each application of the shape modification algorithm. The initial profile and some of the intermediate profiles are shown in figure 3. The change in the profile shape is observed to be small between the fourth and the ninth iteration and the change was found to be insignificant after nine iterations. Hence the iterative process is stopped at the ninth iteration providing a reasonably converged optimum shape. The question of computational accuracy of the solvers and hence the accuracy of the optimum profile is addressed next.

The precise error due to a finite grid size on the optimum profile is difficult to determine since the actual optimum curve is not known apriori, nor are any other calculations or experimental data available. However one way to estimate the effects of the unavoidable truncation errors in a numerical calculation is to obtain the optimum diffuser profile using progressively finer grids until the there is no change with grid size. Once again the reference case of Re=200 was examined for this purpose using grids of 31 by 16, 61 by 31 and finally 121 by 61. The optimum profiles obtained using the three grids are shown in figure 4. The results show that the difference between the shapes is negligibly small, providing some evidence that at these grids the contribution of the truncation errors may not be significant. In view of this observation, a grid size of 61 by 31 is found to be a suitable compromise between accuracy and computational work for the results presented here.

In an earlier section we proposed that it was computationally desirable to replace some of the Dirichlet-type boundary conditions with Neumann-type conditions in both the Navier-Stokes and the adjoint equation solvers. To justify at least partially the validity of solving the modified numerical problem we must verify whether the optimum shapes obtained in this fashion do indeed satisfy the optimality condition, i.e. vanishing shear stress on the wall, arising from the analysis.

In figure 5 the wall shear stress normalized by the corresponding value for a straight duct, is shown for the optimum shape as well as at several intermediate stages of iteration. The wall shear stress for the optimum shape is found to be vanishingly small for all but 10 percent of the wall at the upstream end.

Third International Conference on Inverse Design and Optimization in Engineering Sciences (ICIDES-III) Editor: G.S.Dulikravich, Washington D.C. October 23-25, 1991.

The shear stress distributions at intermediate iterations demonstrate a monotonous decrease towards the optimum values. Closer examination of the shear stress for the optimum and intermediate shapes at other Reynolds numbers confirm the same behavior as well. Hence the results obtained do provide some aposteriori justification for the boundary condition approximations made in the modified numerical problem.

Further justification is sought by examining the behavior of the objective function for the reference diffuser. The velocity averaged static pressure rise (i.e. the objective function defined by equation 2) is shown in figure 6 at successive iterations of the shape modification process. The objective function for this modified numerical problem is indeed found to increase with each application of the boundary movement suggested by equation (15). The area averaged static pressure rise through the reference diffuser also increases with with shape modification as seen in figure 6. These observations are found to be valid at calculations at other Reynolds numbers in the present study as well.

In addition to the reference case, calculation of the optimum diffuser profile was carried out at three other Reynolds numbers, Re= 50, 100 and 500. In figure 7, these profiles are shown for a diffuser of $L/W_1 = 3$ for a grid of 61 by 31. At lower Reynolds numbers the optimum diffuser profile permits a larger exit area to inlet area ratio as one would expect higher viscous effects to support greater diffusion without separation. The angle at which the diffuser profile departs at the upstream corner is difficult to compute accurately since the flow in that corner may not be accurately resolved. Nevertheless, the approximate angle decreases from 56 degrees to 19 degrees as the Reynolds number increases from 50 to 500. For the Reynolds number range in which numerical solutions are presented here, further refinement of the grid did not lead to any significant change in the optimum profile. This was not found to be true of computations at Reynolds numbers higher than 500.

To evaluate the performance of the optimum diffuser, a pressure recovery coefficient, C_p, is defined, which is the ratio of the static pressure rise of the optimum diffuser to the static pressure rise for an ideal diffuser (in potential flow) with the same W_2/W_1 ratio as the optimum diffuser. Note that the denominator of this ratio is independent of the actual profile between the upstream and downstream cross-sections of the diffuser. Using C_p as a parameter, the performance of the optimum diffuser is now compared with that of a straight walled diffuser with the same W_2/W_1 ratio at several different Reynolds numbers in the laminar regime. The C_p values of straight diffusers are found numerically using the Navier-Stokes solver on the straight walled geometry without any shape modification steps. As seen from figure 8, the C_p values for the optimum diffusers are always higher than those for straight diffusers.

In conclusion, the feasibility of shape optimization for incompressible laminar flows has been demonstrated. This approach may also be adopted to other domain optimization problems where the performance depends on the geometry of the component, and flow is governed by the viscous laminar flow (either compressible or incompressible) equations. It may also be possible to consider variations of the objective functions depending upon the design criterion of interest. All computational results presented in this paper were carried out either on an Intel 30386 33MHz microprocessor based machine or on a microVAX II workstation. The CPU times for these calculations are of the order of several hours. The theoretical framework as well as numerical solution code for the extension of the method to three-dimensional flow now exist and such flows are the subject of study by the authors at present.

The research reported in this paper is based upon work supported by the National Science Foundation under Grant No. CBT-87-10561.

BIBLIOGRAPHY

1. Cabuk, H. and Modi, V., "Shape Optimization Analysis: First- and Second-Order Necessary Conditions', *Optimal Control,- Applications and Methods*, **11**, 173–190 (1990).
2. Cabuk, H., Sung, C.-H. and Modi, V., "An Explicit Runge-Kutta Method for 3-D Internal Incompressible Flows", Submitted to AIAA J. (1991).
3. Chang, P. K., *Control of Flow Separation*, McGraw Hill Book Company, New York, 1976.
4. Chorin, A. J., "A Numerical Method for Solving Incompressible Viscous Flow Problems", *J. Comput. Physics* **2**, 12–26 (1967).
5. Giles, M., Drela, M. and Thompkins, W. T., "Newton Solution of Direct and Inverse Transonic Euler Equations", AIAA Paper 85-1530, Proc. AIAA 7th Computational Fluid Dynamics Conference,

Cincinnati, pp. 394-402 (1985).

6. Glowinski, R. and Pironneau, O., "On the Numerical Computation of the Minimum Drag Profile in Laminar Flow", *J. Fluid Mech.* **72**, 385-389 (1975).
7. Jameson, A., Schmidt, W. and Turkel, E., "Numerical Solutions of the Euler Equations by Finite Volume Methods Using Runge-Kutta Time-Stepping Schemes", AIAA Paper 81-1259, (June 1981).
8. Jameson, A.,"Aerodynamic Design via Control Theory", NASA ICASE Report 88-64, (November 1988).
9. Pironneau, O., "On Optimum Profiles in Stokes Flow", *J. Fluid Mech.* **59**, 117-128 (1973).
10. Pironneau, O., "On Optimum Design in Fluid Mechanics", *J. Fluid Mech.* **64**, 97-110 (1974).
11. Rizzi, A. and Eriksson, L.-E.,"Computation of Inviscid Incompressible Flow with Rotation", *J. Fluid Mech.* **153**, pp. 275-312 (1985).
12. Sung, C.-H., "An Explicit Runge-Kutta Method for 3D Turbulent Incompressible Flows", David W. Taylor Naval Ship Research and Development Center, Ship Hydromechanics Department Report DTNSRDC/SHD-1244-01, (July 1987).
13. Swanson, R. C. and Turkel, E., "A Multistage Time-Stepping Scheme for the Navier-Stokes Equations", AIAA Paper 85-35, (January 1985).
14. Thompson, J. F., Thames, F. C. and Mastin, C. W., "Automatic Numerical Generation of Body-Fitted Curvilinear Coordinate System for Field Containing any Number of Arbitrary Two-dimensional Bodies", *J. Comp. Phys.*, **15**, pp. 299-319 (1974).

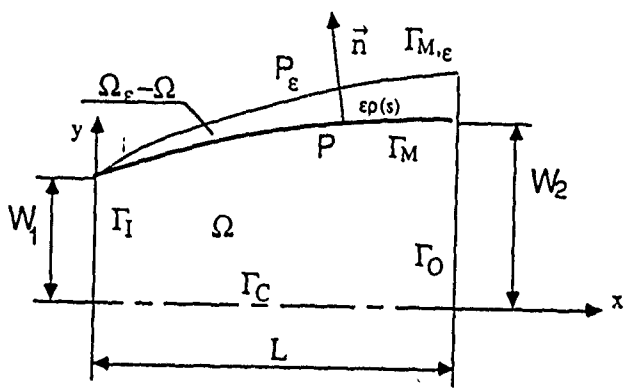


Figure (1) Schematic diagram of a plane diffuser. Flow enters at upstream boundary Γ_I and exits at the downstream boundary Γ_O. The wall to be shaped is Γ_M and symmetry line is Γ_C.

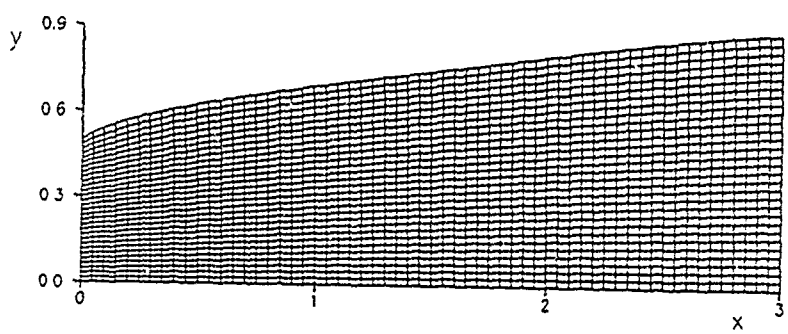


Figure (2) A typical computational grid for a plane diffuser obtained using the grid generation program. Grid size is 61 by 31. This was the domain for the optimum diffuser at Re=200 and $L/W_1 = 3$.

Third International Conference on Inverse Design and Optimization in Engineering Sciences (ICIDES-III) Editor: G.S.Dulikravich, Washington D.C. October 23-25, 1991.

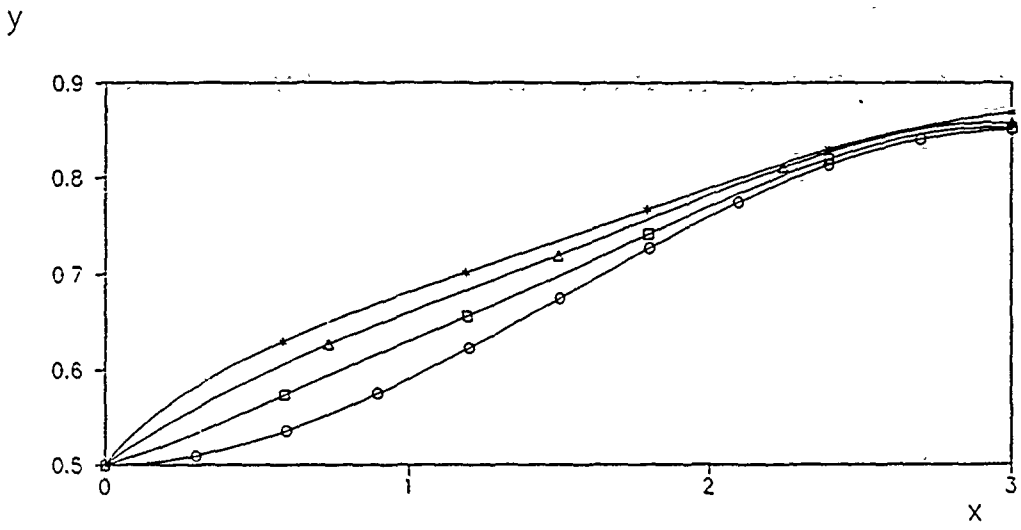


Figure (3) Profiles of a reference diffuser at successive iterations. The grid size is 61 by 31. ○ : Initial shape, □ : First iteration, △ : Fourth iteration, * : Ninth iteration.

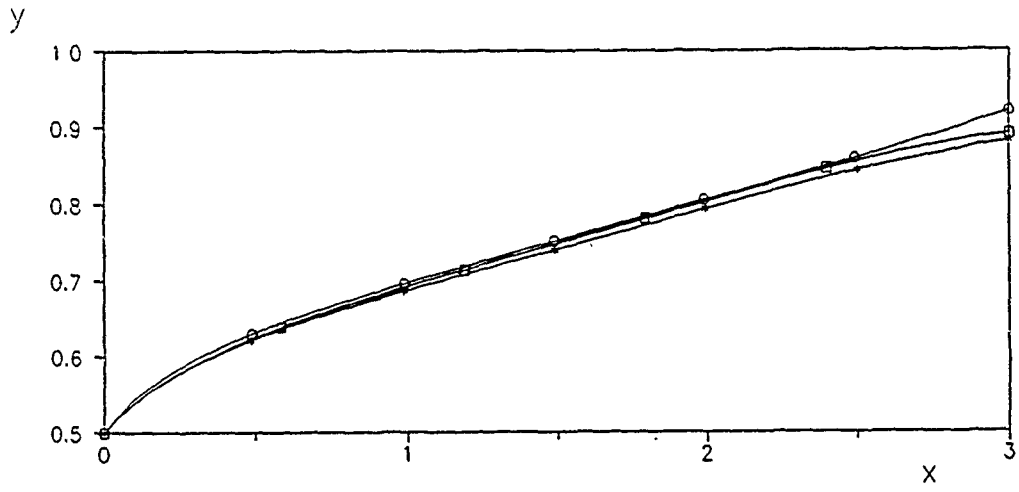


Figure (4) Effect of grid size on optimum profile of a reference diffuser. ○ : 31 by 16, ⊓ : 61 by 31, * : 121 by 61.

Third International Conference on Inverse Design and Optimization in Engineering Sciences
(ICIDES-III)-Editor: G.S.Dulikravich, Washington D.C. October 23-25, 1991.

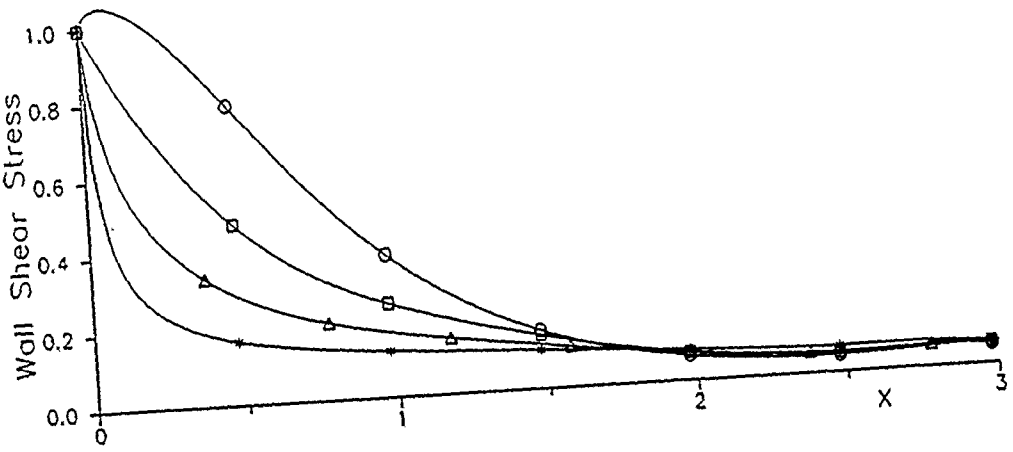


Figure (5) Normalized wall shear stress at successive iterations for a reference diffuser. The grid size is 61 by 31. ○ : Starting shape, □ : First iteration, △ : Fourth iteration, * : Ninth iteration.

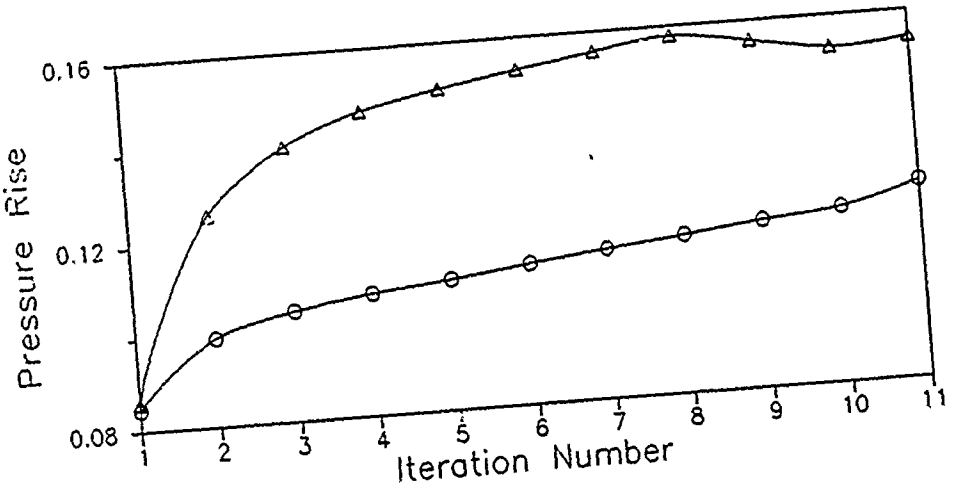


Figure (6) Static pressure rise through the reference diffuser at successive iterations. The grid size is 61 by 31. ○ : Area-averaged pressure rise, △ : Velocity-averaged pressure rise.

Third International Conference on Inverse Design and Optimization in Engineering Sciences
(ICIDES-III) Editor: G.S.Dulikravich, Washington D.C. October 23-25, 1991.

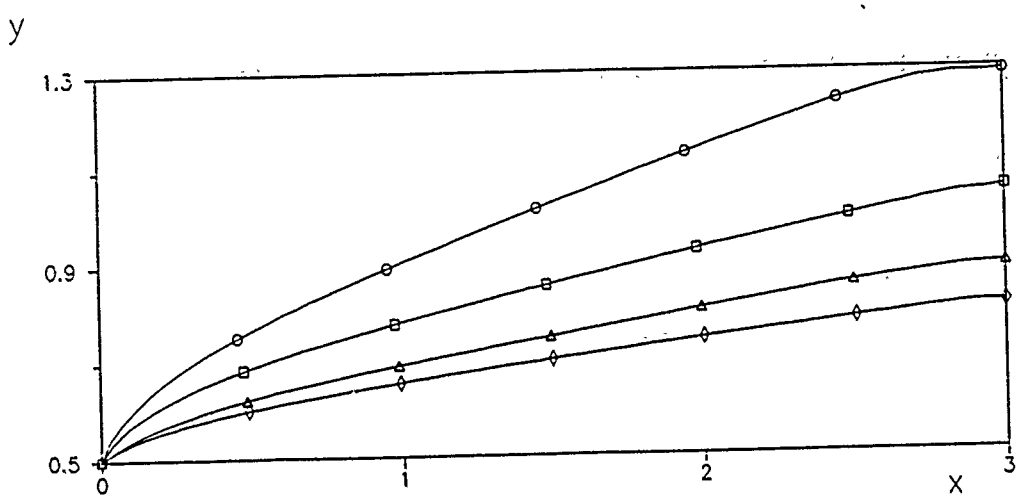


Figure (7) Optimum diffuser profiles at different Reynolds numbers for $L/W_1 = 3$. Grid size is 61 by 31. ○ : Re=50, □ : Re=100, △ : Re=200, ◇ : Re=500.

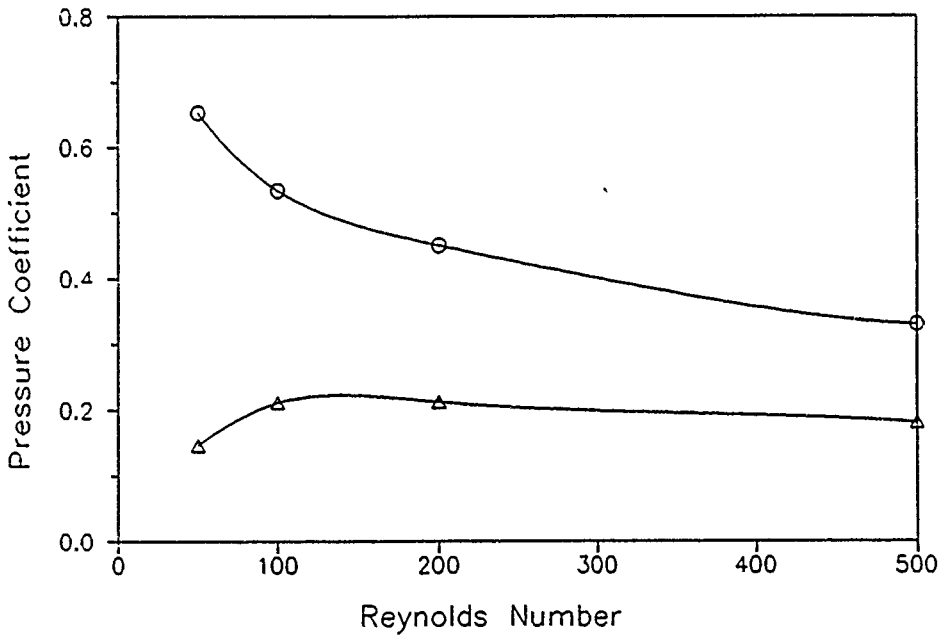


Figure (8) Variation of the pressure coefficient, C_p with Reynolds number for $L/W_1 = 3$. ○ : Optimal diffusers, △ : Straight diverging diffusers.

Third International Conference on Inverse Design Concepts and Optimization in Engineering Sciences (ICIDES-III), Editor: G.S. Dulikravich, Washington D.C., October 23-25, 1991.

An Inverse Method For The Aerodynamic Design of Three-Dimensional Aircraft Engine Nacelles

R. A. Bell R. D. Cedar

GE Aircraft Engines
One Neumann Way
Cincinnati, OH 45215

Abstract

A fast, efficient and user-friendly inverse design system for three-dimensional nacelles has been developed. The system is a product of a two-dimensional inverse design method originally developed at NASA Langley Research Center (LaRC) and the CFL3D analysis code which was also developed at NASA LaRC and modified at GEAE for nacelle analysis. The design system uses a predictor/corrector design approach in which an analysis code is used to calculate the flow field for an initial geometry, the geometry is then modified based on the difference between the calculated and target pressures. A detailed discussion of the design method, the process of linking it to the modified CFL3D solver and its extension to three-dimensions is presented in this paper. This is followed by a number of examples of the use of the design system for the design of both axisymmetric and three-dimensional nacelles.

Third International Conference on Inverse Design Concepts and Optimization in Engineering Sciences (ICIDES-III), Editor: G.S. Dulikravich, Washington D.C., October 23-25, 1991.

Introduction

The purpose of a nacelle, on a high bypass ratio turbofan engine is to supply the airflow required by the engine efficiently with low distortion levels, provide a low drag aerodynamic enclosure for the engine hardware, and expand the exhaust gasses from the engine through an exhaust system with maximum efficiency. The nacelle has three major components, the inlet, the fan cowl and the exhaust system (Figure 1). The nacelle's crown, side and keel cuts are also shown in Figure 1. In this paper a three-dimensional inverse design technique is presented for the aerodynamic design of the fan cowl of the nacelle. In this inverse design method, the designer analyzes an initial geometry and then interactively modifies the resulting pressure distribution to remove any undesirable features. The method then determines the nacelle geometry that will give the desired pressure distribution.

A diverse variety of inverse methods have been developed for airfoils and wing design. An overview of these methods can be found in review papers by Slooff [1] and Dulikravich [2]. Many of these methods, however, are often only suited to specific applications and are not easily extendible to meet the requirements of nacelle design. Examples of this are the Hodograph method of Bauer, Garabedian and Korn [3], which is limited to two-dimensional airfoil and turbomachinery flows and the fictitious gas method [4] which is only suitable for the design of transonic shock free flows.

Unfortunately, modern high bypass ratio turbofan engine nacelles are far from axisymmetric and to obtain a meaningful solution a fully three-dimensional analysis has to be performed. There are also geometric constraints imposed on the design process that the inverse method must be able to handle. In an aero engine, the fan nozzle acts as the throttle controlling the engine operating characteristics; therefore the fan nozzle area, and thus the radius of the trailing edge of the fan cowl, must remain fixed in the design process. Similar constraints apply to the nacelle inlet area, so that the radius of the leading edge of the fan cowl must also remain fixed during the design process. The aerodynamic designer, therefore has to design a surface between two fixed endpoints. In reality, the situation can be further constrained. The trend in the aero engine industry has been to produce derivative families of engines. When designing the nacelle of a derivative engine there can be large economic incentives to keep as much of the hardware common between the members of an engine family. This is especially true for complex components that have high initial tooling costs such as the inlet anti-icing system and the thrust reverser. In these cases, the aerodynamic designer may be limited to changes in the geometry between about 5% and 60% of the fan cowl length. The new surface having to blend smoothly with the existing hardware.

In this paper an inverse design technique is described that meets the needs of the fan cowl designer in that it is three-dimensional and allows either all or a portion of the fan cowl to be modified. The method incorporates the CFL3D [5] analysis code and the inverse design technique of Campbell and Smith [6,7].

Aerodynamic Code

CFL3D was developed by the Computational Fluid Dynamics Laboratory at NASA Langley Research Center [5] and modified at General Electric Aircraft Engines (GEAE) for nacelle analysis [8]. The modified code solves the Euler equations by using a finite volume discretization method. Solutions are advanced in time with a spacially-split three-factor approximate factorization method in diagonalized form. The flux quantities are represented using the flux-vector-splitting approach of Van-Leer with third-order spacial accuracy. Special features include multigrid convergence acceleration and the

Third International Conference on Inverse Design Concepts and Optimization in Engineering Sciences (ICIDES-III), Editor: G.S. Dulikravich, Washington D.C., October 23-25, 1991.

ability to handle multiple grid blocks with a variety of block interfaces and boundary conditions.

The Euler equations express the conservation of mass, momentum, and energy for an inviscid, non-conducting gas in the absence of external forces. The conservation form of the equations in generalized coordinates is:

$$\frac{\delta \hat{Q}}{\delta t} + \frac{\delta \hat{F}}{\delta \xi} + \frac{\delta \hat{G}}{\delta \eta} + \frac{\delta \hat{H}}{\delta \zeta} = 0$$

where

$$\hat{Q} = \frac{Q}{J} = \frac{1}{J} \begin{bmatrix} \rho \\ \rho u \\ \rho v \\ \rho w \\ e \end{bmatrix}$$

$$\hat{F} = \frac{1}{J} \begin{bmatrix} \rho U \\ \rho U u + \xi_x P \\ \rho U v + \xi_y P \\ \rho U w + \xi_z P \\ (e+P)U \end{bmatrix}$$

$$\hat{G} = \frac{1}{J} \begin{bmatrix} \rho V \\ \rho V u + \eta_x P \\ \rho V v + \eta_y P \\ \rho V w + \eta_z P \\ (e+P)V \end{bmatrix}$$

$$\hat{H} = \frac{1}{J} \begin{bmatrix} \rho W \\ \rho W u + \zeta_x P \\ \rho W v + \zeta_y P \\ \rho W w + \zeta_z P \\ (e+P)W \end{bmatrix}$$

The equations are non-dimensionalized in terms of the reference density ρ_∞ and the speed of sound a_∞. The cartesian velocity components are u,v,w in the x,y and z cartesian directions. The pressure, P, is related to the conserved variables, Q, through the ideal gas law:

$$P = \frac{(\gamma - 1)}{2} \left[e - \rho \left(u^2 + v^2 + w^2 \right) \right]$$

where γ is the ratio of specific heats ($\gamma = 1.4$). U, V, and W are the contavariant velocity components in the ξ, η, and ζ directions respectively. J is the Jacobian of the transformation and e represents the internal energy.

The boundary conditions used consist of far-field, solid surface and fan face boundary conditions. The farfield boundary condition is based on Riemann invariants for a one-dimensional flow. On the solid surface of the nacelle and spinner, the velocity normal to the wall is set to zero and a slip condition is imposed. In order to simulate the exhaust plume, the fan cowl is extended downstream of the fan nozzle as a solid body. A full description of how this is achieved is given in reference 8. The intake flow rate is controlled by setting the fan face boundary condition (static pressure). The fan face static pressure required for a given flow rate is calculated using a one-dimensional flow equation. Since the pressure does not account for the three-dimensional effects and loss in the flowfield it is readjusted based on results from the one dimensional analysis. A symmetry boundary condition is also placed at the nacelles's vertical plane of symmetry when cross-wind or yaw requirements are not

Third International Conference on Inverse Design Concepts and Optimization in Engineering Sciences (ICIDES-III), Editor: G.S. Dulikravich, Washington D.C., October 23-25, 1991.

imposed. For these cases a 180 degree grid is used for the analysis. For flow conditions involving cross-wind or yaw, a full 360 degree grid is used with a continuous boundary condition specified at the vertical plane of geometric symmetry (Figure 2). An option is also available to analyze axisymmetric configurations that only requires one computational cell in the circumferential direction. This code has been validated against test data for a large range of nacelle designs and operating conditions. For further details on the modified version of CFL3D for three-dimensional nacelle analysis see reference 8.

Design Method

The predictor/corrector approach used by this design method is illustrated in Figure 3. A target pressure distribution is specified by the designer that has desirable characteristics such as no shocks, no steep diffusions or favorable pressure gradients for natural laminar flow. The aerodynamic analysis code (CFL3D) is used to determine the pressure distribution on an initial geometry. The nacelle surface pressure coefficients are compared with the target pressure distributions in the design module. The initial geometry is then modified based on the pressure differences. The grid is then perturbed and the new geometry is analyzed in the analysis code to determine its pressure distribution. This process continues until the convergence criteria specified by the designer is reached.

Design Algorithm

The design method, described in reference 6, uses two design algorithms, one for subsonic flow and the other for supersonic flow. The supersonic algorithm is blended with the subsonic algorithm to design regions of transonic flow. Both algorithms assume that ΔC_p is proportional to the change in geometry.

The subsonic algorithm is based on the assumption that changes in curvature are directly proportional to changes in pressure coefficient. The relationship used to express the change in curvature as a function of change in pressure coefficient is:

$$\Delta C = \Delta C_p A (1 + C^2)^B$$

where

C is the curvature
C_p is the pressure coefficient
A = +1 for the upper surface, -1 for the lower surface
B = input constant ranging from 0.0 to 0.5

The derivation of this equation is given in reference [6]. The change in curvature is converted to a change in r'' by using the formula

$$\Delta r'' = \Delta C \left[1 + (r')^2\right]^{1.5}$$

where

r is the surface radius
r' is the surface slope
r'' is the second derivative of surface radius

This equation assumes that the changes in the surface slope are small.

The supersonic algorithm is based on supersonic thin airfoil theory. Based on relations between the pressure coefficients and surface slope the expression

$$\Delta r' = K \Delta C_p$$

can be derived [6]. Differentiating this expression gives the following relationship between r'' and ΔC_p.

$$\Delta r'' = K \frac{d(\Delta C_p)}{dx}$$

The value for the constant K is 0.05 and is used to under relax the changes in the geometry during each design iteration.

Using these equations the required change in r'' is calculated at each point along the fan cowl. To change the magnitude of r'' at point I without changing r'' at other locations, points I+1 through N are rotated through a given angle. Figure 4 shows the result of this process.

Closure of the Design Range

It is clear from Figure 4 that in general the last point in the design range will not remain fixed and therefore a method of closing the geometry is required. The method suggested in reference 6 was to rotate the newly designed section about the most forward point of the design range so that the end of the design range closes. This process, however, leaves a surface slope discontinuity at the beginning of the design range. If the beginning of the design range was the nacelle's leading edge, then an option would be to blend a new leading edge geometry into the modified nacelle. This was felt to be undesirable as a nacelle's off-design (takeoff, climb etc.) performance is critically dependent on the leading edge shape. An alternative would have been to smooth the geometry in the region of the slope discontinuity but there is no guarantee that the resulting pressure distribution in this region will be smooth.

A solution of this problem was found in a paper by Lin etal. [9] where they advocate modifying the target pressure distribution to ensure that the end point of the design range remains fixed. In this method a sine function is added to the target pressure with the maximum modification at the center of the design region, and zero at the ends (Figure 5). The amplitude of the sine function is iteratively determined by using the secant method. Figure 6 shows the logic used to close the geometry by modifying the target pressure distribution. This process is performed at each design update and it has been found that this scheme normally converges in three iterations.

Coupling the Design to the Analysis Code

For ease of use, the design algorithm has been incorporated as a module in a modified version of the CFL3D analysis code. The information that is passed from the design module to CFL3D is an updated computational grid that reflects the changes in surface geometry calculated by the design algorithm. Rather than regridding the complete configuration every design calculation, a grid perturbation scheme has been developed. In this scheme the grid lines along the fan cowl surface are moved radially to account for the change in surface geometry. This is repeated for the grid line away from the nacelle surface but the change in radius is reduced linearly with the local radius, so that the outer boundary does not move.

Third International Conference on Inverse Design Concepts and Optimization in Engineering Sciences (ICIDES-III), Editor: G.S. Dulikravich, Washington D.C., October 23-25, 1991.

The normal procedure for designing a nacelle is that the designer analyzes a first guess at the nacelle geometry using the CFL3D code. An interactive graphic program has been written that presents the designer with the nacelle surface Mach number distribution and allows the designer to specify the portion of the surface to be modified. The designer can interactively alter the Mach number distribution in order to obtain the desired characteristics for the target pressure distribution. CFL3D is then run with the design option active. The converged solution from the initial nacelle geometry can be used as the starting solution. The difference between this solution and the required target pressure distribution is used by the design module to calculate a new geometry. The grid is perturbed and the geometry is re-analyzed. Numerical studies have shown that after each pass through the design module the analysis does not have to be fully converged. It has been found that only 40 iterations of CFL3D are needed, where as, 250 iterations would be required for full convergence. About 20 passes through the design calculation are needed to obtain a pressure distribution that matches the modified target pressure distribution to engineering accuracy for a typical design. Convergence is slowed if the original geometry has large supersonic patches with strong shocks or if the designer is making large changes to the pressure distribution.

Axisymmetric Results

Because the design method does not account for three-dimensional (circumferential) effects, the first test cases that were run were purely axisymmetric. The results of two of these runs are presented in Figures 7 and 8. The design range for both of these cases is the complete length of the fan cowl. In the first test case the the inverse design method was used to eliminate a shock on the fan cowl as shown in Figure 7a. A comparison of the final pressure distribution and the initial and modified target pressure distributions are shown in Figure 7b. The final pressure distribution matches the modified target distribution almost perfectly. As shown, the difference between the initial and modified target pressure distributions, is quite small. Figure 7c shows a comparison of the initial and final geometry.

The same geometry is used in the second test case (Figure 8) but larger changes are being made to the pressure distribution. In this case a significant change in the target pressure distribution is required to close the geometry but the characteristics of the final pressure distribution are still similar to the designers intent. Figure 8b shows that the final pressure distribution matches the modified target distribution quite well. At the trailing edge, however, there is a small difference because the geometry downstream of trailing edge is fixed during the design, resulting in a discontinuity in surface slope and curvature. This highlights the problem of how one specifies a pressure distribution that ensures that the geometry at the end points of the design range match and the pressure distribution remains smooth.

Three-Dimensional Extension

Having shown that the axisymmetric inverse design code works well, the next stage was to extend it to the design of three-dimensional nacelles. In the axisymmetric version only one radial cut is considered. For three-dimensional nacelles, the radius varies from crown to keel and so a number of circumferential cuts must be taken into account during the design process.

Three options were considered for the three-dimensional version. The first option requires the designer to specify the target pressure distribution at each circumferential cut of the grid (typically 13 cuts are used on a 180-degree sector). The problem with this approach is that there is no guarantee of a

Third International Conference on Inverse Design Concepts and Optimization in Engineering Sciences (ICIDES-III), Editor: G.S. Dulikravich, Washington D.C., October 23-25, 1991.

smooth geometry in the circumferential direction (Figure 9). Thus, the designer would have to know how to distribute the pressure distribution circumferentially to ensure a smooth geometry. It was felt that this would be difficult to achieve, and therefore this option was rejected.

The second option requires the designer to specify the target pressure distribution on only three cuts (crown, side and keel). The design procedure would be used on only these cuts and the remaining cuts would be designed by parabolically interpolating the new radii circumferentially. The problem with this method is that the original cross-sectional geometric shape of the nacelle is not preserved during the design. As shown in Figure 10, the elliptic shape of the original nacelle cross-section is altered to a parabola by the interpolation scheme.

The third option considered was very similar to the second one. With this option the designer specifies the target pressure distribution on the crown, side and keel cuts but the remaining cuts are designed by parabolically interpolating the changes in the radii from these three cuts (Figure 11). With this approach the essence of the original cross-sectional shape of the nacelle is preserved and some degree of smoothness in the circumferential direction is ensured.

The third option was chosen to be used in the three-dimensional version of the inverse design method. As stated before, the designer specifies the target pressure distribution on the crown, side and keel cuts, of the nacelle. At each design iteration all three cuts are redesigned using the same design method as had been used in the axisymmetric version. No attempt has been made to extend the relationship between change in C_p and change in geometry to account for three-dimensional (circumferential) effects. The changes in geometry from the three cuts are then interpolated for the other radial cuts and the grid is perturbed in a similar manner to the axisymmetric version. Experimentation has shown that although changes made in the crown cut, for instance, do effect the flow at the side cut and to a lesser extent the keel cut, these effects do not cause instabilities in the design scheme.

Three-Dimensional Results

The results for a three-dimensional test case are shown in Figures 12 through 14. In this case the design range started at the nacelle leading edge and ended 10 inches upstream of the nacelle trailing edge. The Mach number distributions along the crown, side and keel cuts of the original nacelle as well as the desired target Mach number distribution are shown in Figure 12. Figure 13 shows the Mach number distribution achieved after 40 design iterations and the initial and final target Mach number distributions. The resulting modifications to the geometry is shown in Figure 14. It should be noted that the vertical scale has been expanded so that the change in geometry can be clearly seen.

Summary

A predictor corrector design method originally developed by Campbell and Smith has been coupled to a modified version of the CFL3D analysis code and extended to allow the design of three-dimensional nacelles. A designer can interactively modify the Mach number distribution of the crown, side and keel cuts of a fan cowl and the required geometry is automatically calculated. The method is capable of designing any local region of the fan cowl, the remainder being fixed, although further work is required in determining how to specify the pressure distribution so that both the geometry and pressure distribution are smooth at the end points of the design range.

Third International Conference on Inverse Design Concepts and Optimization in Engineering Sciences (ICIDES-III), Editor: G.S. Dulikravich, Washington D.C., October 23-25, 1991.

Further work is being pursued to try and reduce the computational time required by the method. The aim is to reduce the cost of an inverse design calculation from the present value of about four times that of an analysis calculation to about twice. Future work on the choice of an optimum pressure distribution that meets both geometric constraints and off-design performance criteria is also being considered.

Acknowledgements

The authors would like to thank R L Campbell of NASA LaRC for providing GEAE with the DISC code and his valuable help and suggestions. They would also like to express their appreciation for the excellent technical support for the CFL3D code provided by NASA LaRC researchers Sheri Krist and Jim Thomas. Thanks are also extended to our colleagues at GEAE, especially K Uenishi, D A Dietrich, and M S Pearson for their assitance thoughout this project.

References

1. Sloof, J. W., "Computational Methods for Subsonic and Transonic Aerodynamic Design", Proceedings of ICIDES-I, ed G. S. Dulikravich, Univ. of Texas, Austin, TX, Oct 17-18, 1984, pp. 1-68.

2. Dulikravich G. S., "Aerodynamic Shape Design and Optimization", AIAA 91-0476, 29th Aerospace Sciences Meeting, Jan 7-10, 1991, Reno, Nevada.

3. Bauer, F., Garabedian, P., Korn, D. and Jameson, A., "Supercritical Wing Sections 1,2,3", Lecture Notes in Econ., Math. Syst., No 66, 108, 150, Springer Verlag, Berlin, 1972, 1975, 1977.

4. Sobieczki, H., Yu, N. J., Fung, K. Y., and Seebass, A. R., "New Method for Designing Shock-Free Transonic Configurations", AIAA Journal, Vol. 17, No. 7, July 1979, pp. 722-729.

5. Thomas, J. L., Van Leer, B., and Walters R. W., "Implicit Flux-Split Schemes for the Euler Equations", AIAA 85-1680.

6. Campbell, R. L., and Smith, L. A., "A Hybrid Algorithm for Transonic Airfoil and Wing Design", AIAA 87-2552-CP, August, 1987.

7. Campbell, R. L., and Smith, L. A., "Design of Transonic Airfoils and Wings Using a Hybrid Design Algorithm", SAE 871756, October, 1987.

8. Uenishi, K., Pearson, M. S., Lehnig, T. R., Leon, R. M., "CFD Based 3D Turbofan Nacelle Design System", AIAA 90-3081, 1991.

9. Lin, W. F., Chen, A. W., and Tinoco, E.N., "3D Transonic Nacelle and Winglet Design", AIAA 90-3064-CP 1990.

Third International Conference on Inverse Design Concepts and Optimization in Engineering Sciences (ICIDES-III), Editor; G.S. Dulikravich, Washington D.C., October 23-25, 1991.

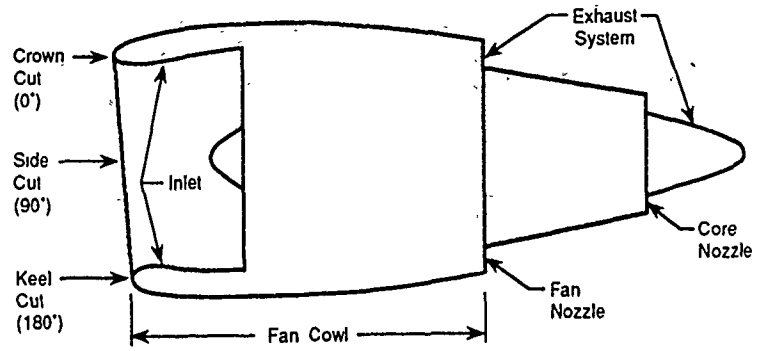


Figure 1. The Aerodynamic Components of a Nacelle.

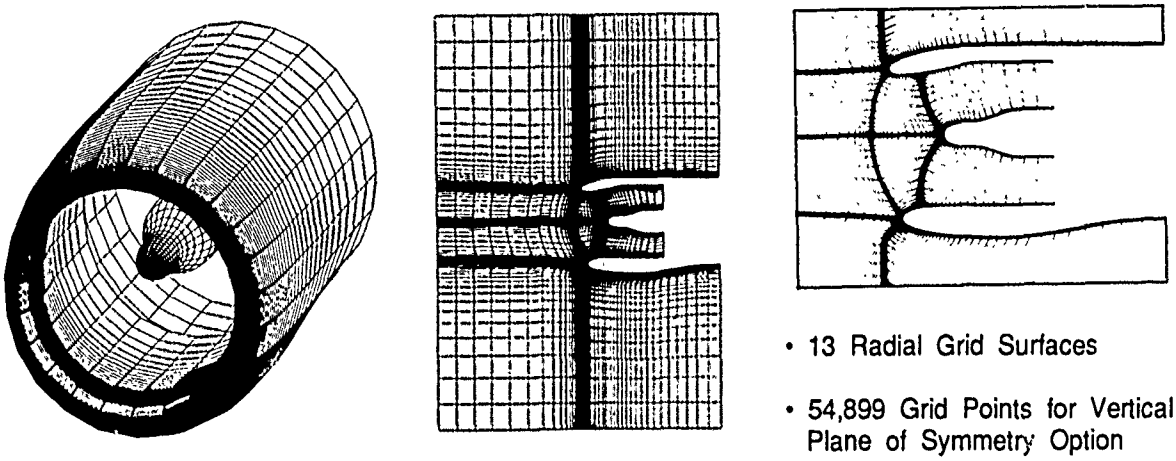


Figure 2. Typical Computational Grid for Nacelle Design.

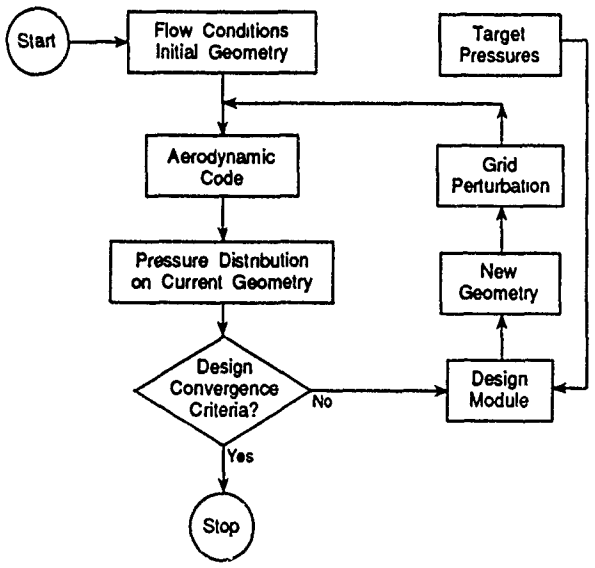


Figure 3. Flow Diagram of Automated Predictor/Corrector Design Method.

Third International Conference on Inverse Design Concepts and Optimization in Engineering Sciences (ICIDES-III), Editor; G.S. Dulikravich, Washington D.C., October 23-25, 1991.

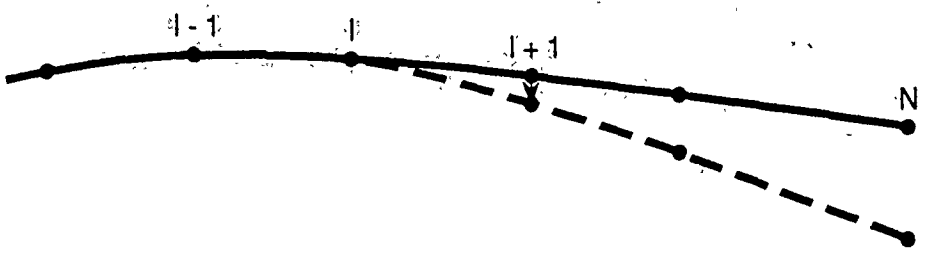


Figure 4. Method of Changing Curvature at One Point Only.

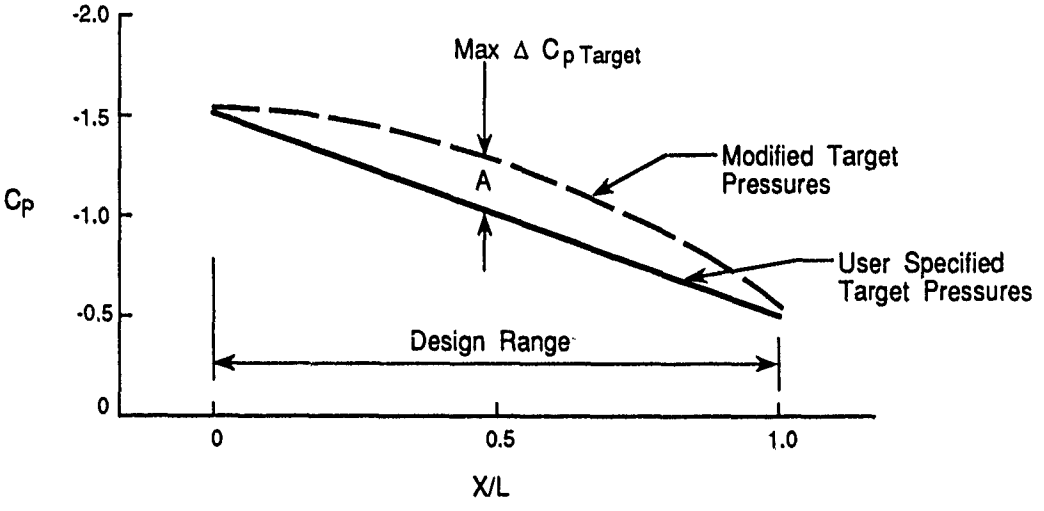


Figure 5. Modification of Target Pressure Distribution by a Sine Function.

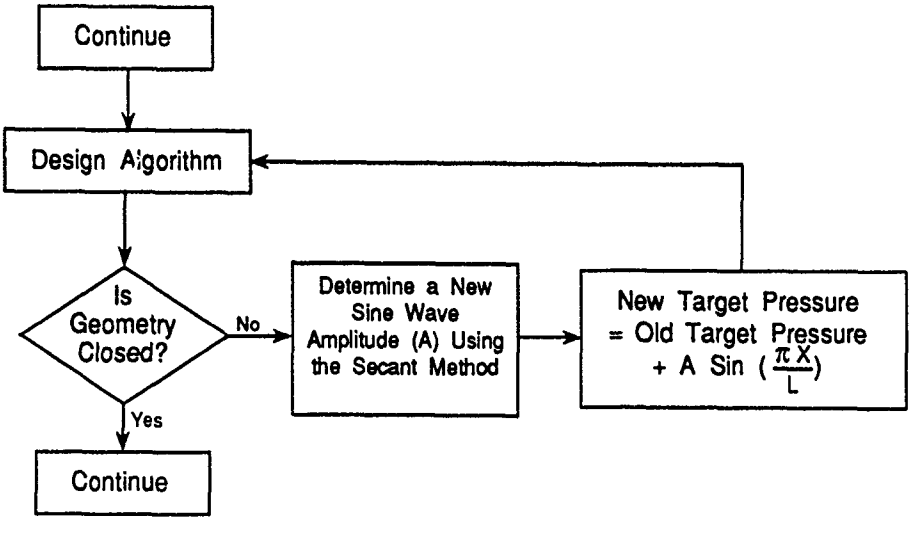


Figure 6. Logic Used to Close the Geometry by Modifying the Target Pressure Distribution.

Third International Conference on Inverse Design Concepts and Optimization in Engineering Sciences (ICIDES-III), Editor; G.S. Dulikravich, Washington D.C., October 23-25, 1991.

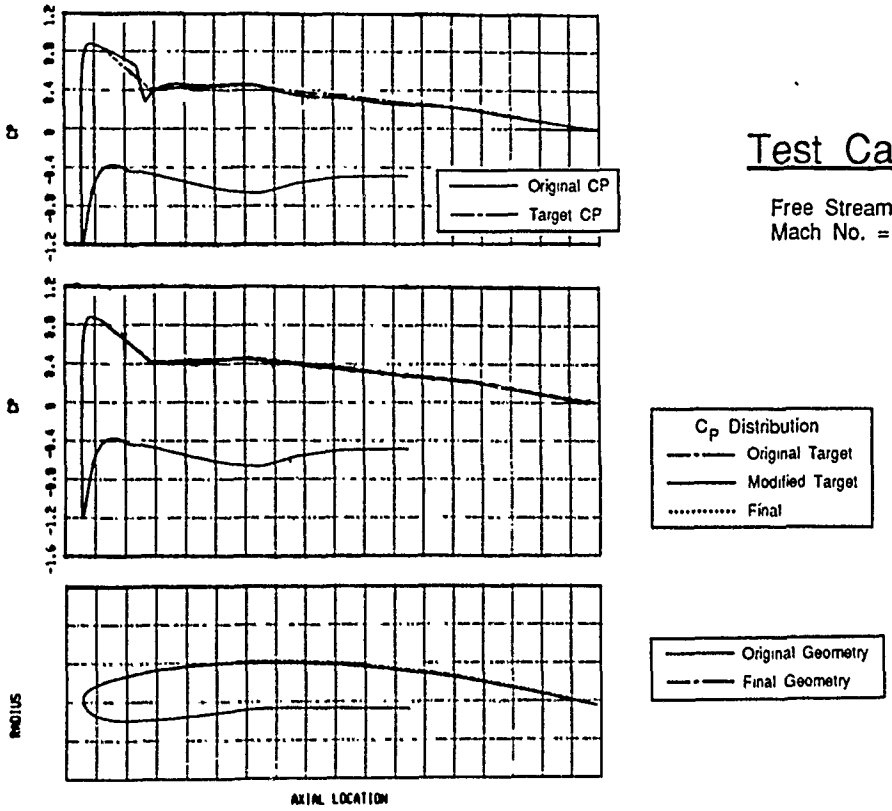


Figure 7. Results for Axisymmetric Test Case 1.

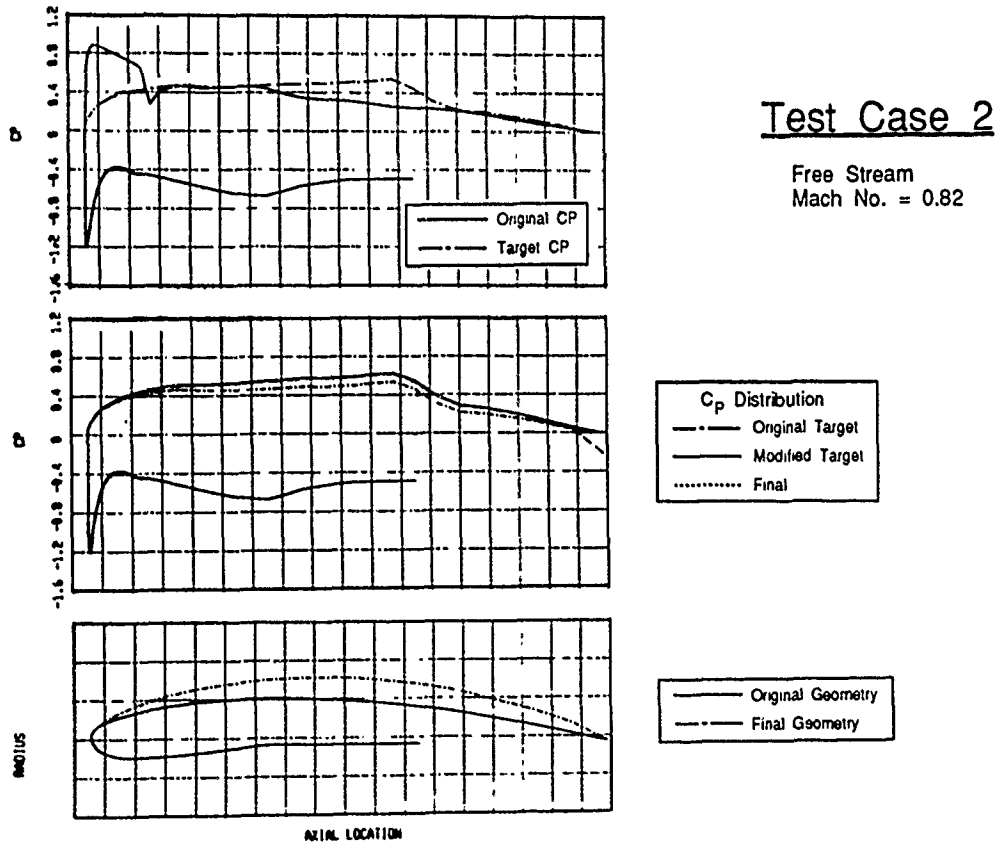


Figure 8. Results for Axisymmetric Test Case 2.

Third International Conference on Inverse Design Concepts and Optimization in Engineering Sciences (ICIDES-III), Editor: G.S. Dulikravich, Washington D.C., October 23-25, 1991.

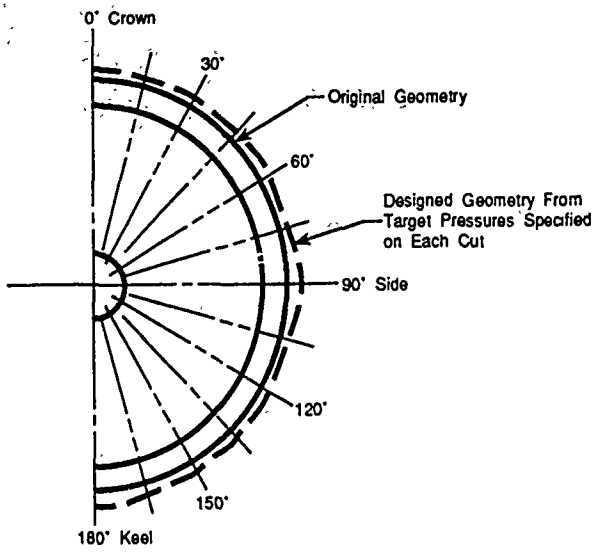


Figure 9. Three-Dimensional Inverse Design Option 1.

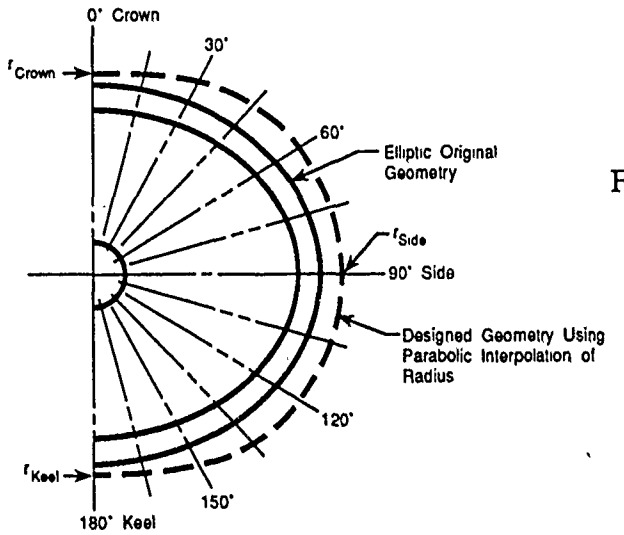


Figure 10. Three-Dimensional Inverse Design Option 2.

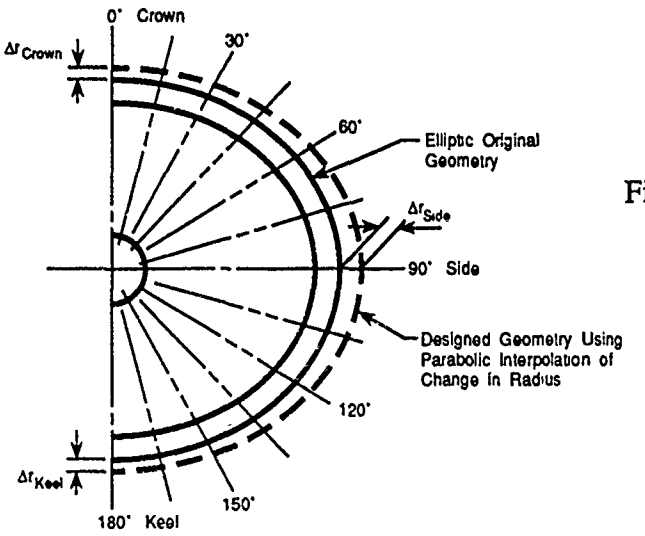


Figure 11. Three-Dimensional Inverse Design Option 3.

Third International Conference on Inverse Design Concepts and Optimization in Engineering Sciences (ICIDES-III), Editor; G.S. Dulikravich, Washington D.C., October 23-25, 1991.

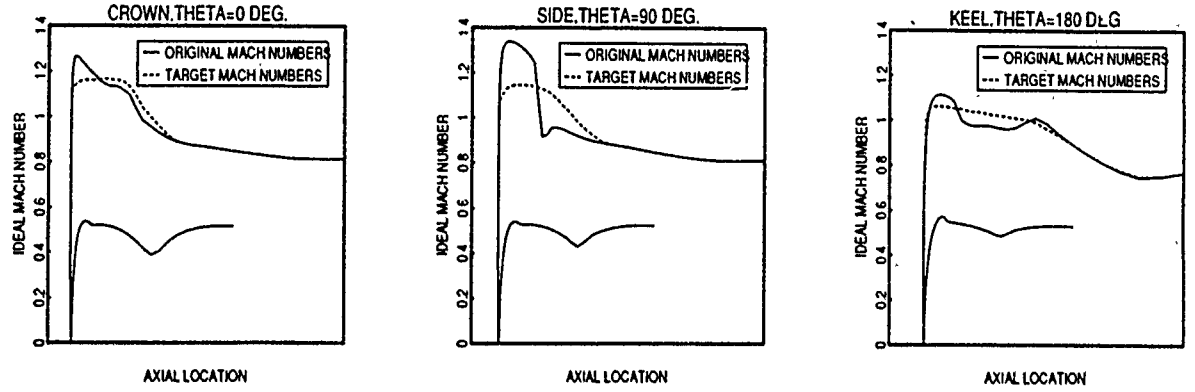


Figure 12. Original and Target Mach Number Distributions for the Three-Dimensional Test Case.

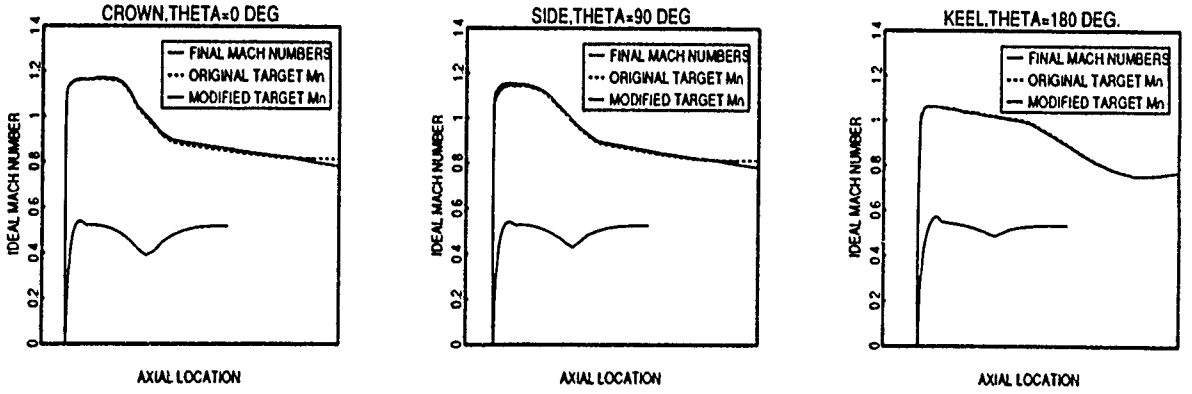


Figure 13. Final Mach Number Distributions and Original and Final Target Mach Number Distributions for the Three-Dimensional Test Case.

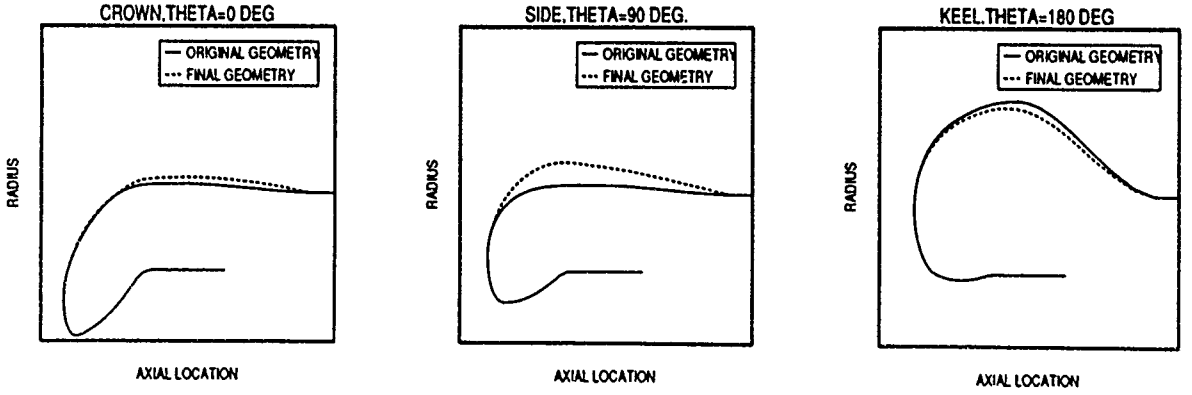


Figure 14. Original and Final Geometries for the Three-Dimensional Test Case.

Third International Conference on Inverse Design Concepts and Optimization in Engineering Sciences (ICIDES-III), Editor: G.S. Dulikravich, Washington D.C., October 23-25, 1991.

VORTEX GENERATOR DESIGN FOR AIRCRAFT INLET DISTORTION AS A NUMERICAL OPTIMIZATION PROBLEM

by

Bernhard H. Anderson
NASA Lewis Research Center
Cleveland, OH 44135

and

Ralph Levy
Scientific Research Associates, Inc.
Glastonbury, CT 06033

INTRODUCTION

Aerodynamic compatibility of aircraft/inlet/engine systems is a difficult design problem for aircraft that must operate in many different flight regimes. Take-off, subsonic cruise, supersonic cruise, transonic maneuvering and high altitude loiter each place different constraints on inlet design. Vortex generators, small wing-like sections mounted on the inside surfaces of the inlet duct, are used to control flow separation and engine face distortion. This paper attempts to define the design of vortex generator installations in an inlet as a problem addressable by numerical optimization techniques. A performance parameter is suggested to account for both inlet distortion and total pressure loss at a series of design flight conditions. The resulting optimization problem is difficult since some of the design parameters take on integer values. If numerical procedures could be used to reduce multi-million dollar development test programs to a small set of verification tests, numerical optimization could have a significant impact on both cost and elapsed time to design new aircraft.

Inlet flow distortion is one of the most troublesome and least understood problems for designers of modern inlet engine systems (Refs. 1 and 2). One issue is that there are numerous sources of flow field distortion that are ingested by the inlet or are generated within the inlet duct itself. Among these sources are (a) flow separation at the cowl lip during maneuvering flight, (b) flow separation on compression surfaces due to shock-wave boundary layer interactions, (c) spillage of fuselage boundary layer into the inlet duct, (d) ingestion of aircraft vortices and wakes emanating from upstream disturbances, and (e) secondary flow and flow separation within the inlet duct itself. Most developing aircraft have experienced one or more of these types of problems, particularly at high Mach numbers and/or extreme maneuver conditions, such that flow distortion at the engine face exceeded allowable limits. Such compatibility problems were encountered in the early versions of the B70, the F-111, the F-14, the MIG-25, the Tornado and the Airbus A300, to name a few examples.

The effect of inlet distortion, be it pressure or temperature, steady or transient, is that the power available is reduced along the engine compressor surge margin (i.e. the difference between the operating line and the surge line). Aeromechanical effects such as rotor-blade forced response and distortion effects on flutter boundaries have received less attention, so that a

consensus on importance and state-of-the-art methodology has yet to emerge. Stability characteristics of current high performance turbofan engines are adversely affected by both spatial as well as temporal distortion.

PROBLEM DEFINITION

One of the most commonly used methods to control local boundary layer separation is with the placement of vortex generators upstream of the problem area. Vortex generators in use today are small wing sections mounted on the inside surface of the inlet duct or wing surface, inclined at an angle to the oncoming flow to generate a shed vortex. The generators are usually sized to local boundary layer height to allow for the best interaction between the shed vortex and boundary layer itself, and are usually place in groups of two or more upstream of the problem area. The principle of boundary layer control by vortex generators relies on induced mixing between the external or core stream and the boundary layer region. This mixing is promoted by vortices trailing longitudinally over the duct surface adjacent to the edge of the boundary layer. Fluid particles with high momentum in the streamwise direction are swept along helical paths toward the duct surface to energize, and to some extent to replace, the low momentum boundary layer flow. This is a continuous process that provides a source of re-energization to counter the natural boundary layer growth caused by friction, adverse pressure gradients, and low energy secondary flow accumulation.

There are two basic configurations of vortex generators. In one configuration, all the vortex generators are inclined at the same angle with respect to the oncoming flow direction. These are called co-rotating configurations because the shed vortices rotate in the same direction. In the other configuration, the vortex generators are grouped in pairs one at a positive angle of attack and one at a negative angle of attack, such that pairs of counter-rotating shed vortices are generated. Co-rotating vortex generators are very effective in reducing flow separation if the generators are properly selected and located. The main advantage of co-rotating type vortex generators is their downstream effectiveness resulting in more effective usage of the vortex energy within the affected boundary layer. This type of vortex generator has a few special advantages when used within S-duct inlet configurations, namely: (1) the induced vortices will remain close to the wall resulting in a "cleaner" core flow, and (2) the induced vortices will counteract the natural and often strong secondary flow which develops.

Counter-rotating, equal strength vortex generators have been used in a number of aircraft inlet ducts, such as the F/A-18 and the center inlet duct on the production 727 aircraft. This type of vortex generator is very effective in reducing flow separation if the vortex generators are placed slightly upstream of the region of separation. The disadvantages of these types of generators, as compared to co-rotating generators, are: (1) the induced vortices tend to lift off the duct surface, thus reducing their effectiveness, (2) higher loss in inlet total pressure recovery, and (3) higher total pressure distortion at the compressor face.

It was not until the confirmation test for the refanned JT3D engine on the 727 center duct inlet in 1973 by Kaldschmidt, Syltebo, and Ting, Ref. 3, that an attempt was made to use vortex generators to restructure the development of secondary flow in order to improve the engine face distortion level. Thus, a very important shift in strategy on the use of vortex generators had occurred. The perspective had moved from a local two-dimensional boundary layer approach aimed at eliminating local flow separation to a global three-dimensional vortex-secondary flow

Third International Conference on Inverse Design Concepts and Optimization in Engineering Sciences (ICIDES-III), Editor: G.S. Dulikravich, Washington D.C., October 23-25, 1991.

interaction concept, where the design goal was now to control the development of three-dimensional secondary flow itself, by introducing discrete sources of vorticity at selected locations throughout the inlet duct.

In order to accomplish this new objective for internal flow control, the design strategy must shift from an experimental based methodology to an approach based on analysis. This paper represents one in a series of studies on the design issues associated with inlet-engine compatibility problems, and in particular, engine face distortion and its control. These studies center on the development of CFD tools and techniques which look promising within an analysis-design environment, and the application of these new analysis approaches to understand and control inlet-engine distortion. The first paper in this series by Anderson (Ref. 4) deals with the aerodynamic characteristics of vortex interaction within the F/A-18 inlet duct, where the vortex interaction arises as a result of a vortex ingestion. Later studies will involve the effect of vortex ingestion on the engine face flow field itself. In the second paper in this series, by Anderson and Levy (Ref. 5), it was demonstrated that an installation of co-rotating vortex generators could be constructed to tailor the development of secondary flow to reduce engine face distortion. Of importance is the conclusion that there exists an optimum axial location for the installation of co-rotating vortex generators, and within this configuration there exists a maximum spacing of generators above which the engine face distortion rapidly increases. This study also showed that the vortex strength, generator scale, and secondary flow field structure have a complicated and interrelated influence on the engine face distortion, over and above the influence of the initial arrangement of generators. These are the only three-dimensional calculations of inlets with vortex generators known to the authors.

ANALYSIS

With these computational tools in place the present paper attempts to pose the design of low distortion inlets through the use of vortex generators as a numerical optimization problem. To be a valid optimization problem a quantitative measure of goodness must be defined. Although inlet distortion is caused in the inlet, its effect is meaningful in the response of the engine to the distorted airflow. Inlet distortion can reduce surge margin and limit aircraft maneuverability. Aircraft and engine manufacturers have developed measures of inlet distortions that characterize the inlet flow, although they must be recalibrated for each airframe, engine and flight profile.

It is impractical to measure anything at the engine face when the engine is installed and operating; consequently, the engine and inlet designers agreed upon an Aerodynamic Interface Plane which is forward of the compressor face but sufficiently close to the engine face to have a similar flow field. Current U.S. practice uses forty or forty-eight transducer probes arranged in eight rakes with five or six rings. The radius of each ring is set such that all probes are at the centroid of equal areas. All distortion descriptors, whether they quantify steady state or transient distortion conditions, are always calculated relative to the standard rake located at the Aerodynamic Interface Plane.

The most widespread quantitative distortion descriptor available in the literature, because of its use in the earliest measurements on inlet ducts in the late 1950's, is simply:

$$DT = \left[Pt_{max} - Pt_{min}\right] / Pt_{ave} \qquad (1)$$

where Pt_{max} is the maximum rake total pressure, Pt_{min} is the minimum rake total pressure, and Pt_{ave} is the area weighted average rake total pressure. In experimental data reduction, it is assumed that both the static pressure and temperature are constant and steady across the Aerodynamic Interface Plane; thus both the velocity and Mach number can be considered functions only of total pressure and the distribution of this quantity is the only measurement that needs to be made. This parameter is always useful to determine for comparison purposes and to describe the 'general health' of inlet ducts irrespective of the type of power plant that may be used.

The effect of circumferential distortion on compressor surge margin is essentially to drop the maximum pressure ratio of a constant corrected speed line. One descriptor for circumferential distortion is from Rolls Royce and is defined as

$$DC_{theta} = [Pt_{ave} - Pt_{min}] / q_{ave} \qquad (2)$$

where Pt_{ave} and q_{ave} are the average total and dynamic pressure at the engine face or aerodynamic interface plane and Pt_{min} is the minimum total pressure in any section of extent theta. Significant theta values can vary with engine design and commonly are 60°, 90° and 120°. For bypass engines, a circumferential distortion descriptor $DC_{theta\text{-}GG}$ is often used, where GG indicates that the index is taken over the area of the gas generator.

More advanced distortion descriptors, introduced in the late 1960's and 1970's, take into account the Dt distortion of each ring of total pressure measurements. Thus, the radial distortion Dt_r is defined as

$$Dt_r = [[Pt_{max} - Pt_{ave}] / Pt_{max}]_{ring} \qquad (3)$$

where Pt_{ave} is the average total pressure for a given ring radius and Pt_{max} is the maximum local ring total pressure. The circumferential distortion Dt_{theta} is defined as:

$$Dt_{theta} = [[Pt_{ave} - Pt_{min}] / Pt_{ave}]_{ring} \qquad (4)$$

where Pt_{min} is the lowest total pressure in any theta segment, usually 60° or 180° of arc for a given ring radius having an average ring total pressure Pt_{ave}.

Whatever distortion parameter is selected, there are a large number of design parameters to be optimized. Figures 1, 2 and 3 define many of the geometric parameters which may vary from vortex generator to vortex generator in a single inlet, although in this study all vortex generators in each inlet were of the same size, shape and spacing. The effects of several parameters on inlet distortion are now presented. Note in the following examples that the parameters are highly coupled, i.e. the Hessian matrix is not well approximated as a diagonal matrix.

Vortex Generator Design Parameters

The 727/JT8D-100 center inlet duct geometry was used for illustrative purposes in this study. Other inlets, such as in the F-18 aircraft [4] can have significantly different distortion

characteristics and different responses of inlet distortion to variations in vortex generation design parameters. The computations were made at an inlet entrance Mach number of 0.6, and Reynolds numbers that ranged from 4.0×10^6 to 16.0×10^6 based on hydraulic inlet diameter (D_i), and inflow conditions that correspond to a shear layer thickness $\delta/D_i = 0.005$.

The geometry of the co-rotating vortex generators used in this study, along with the nomenclature used in positioning the individual blades are presented in Figs. 1, 2 and 3. The important geometric design parameters include: (1) the vortex generator blade height (h/R_i), (2) the blade chord length (c/R_i), and (3) the vane angle of attack (β_{vg}). For all the calculations within this study, the vortex generator blade height (h/R_i) was set at 0.075, the ratio of generator height to chord length (h/c) was fixed at 0.5, and the vane angle of attack (β_{vg}) was set at 16.0°. Instead of the usual spacing parameter (d/R_i), i.e., the distance between adjacent blades, the positioning of the vortex generator blades was described in terms of spacing angle (α_{vg}) and a sector angle over which the blades were positioned (θ_s).

Shown in Fig. 4 is the axial location of the vortex generator sector region (X_{vg}/R_i) covered in this study. These sector regions were located between $X_{vg}/R_i = 1.0$ and $X_{vg}/R_i = 7.0$, and cover a sector angle (θ_s) up to 157.5° as measured counter-clockwise relative to an azimuthal angle of 180° with respect to the vertical axis of the duct.

Installed Vortex Generator Performance Characteristics

The effect of Reynolds number on engine face peak 60°-sector circumferential pressure ring distortion is presented in Fig. 5 for the baseline inlet duct, i.e., without vortex generators. There is a significant increase in maximum circumferential pressure ring distortion, from 0.045 to 0.087, over the Reynolds number range from 16.0×10^6.

Presented in Fig. 6 is the influence of Reynolds number on engine face distortion for the vortex generator installation composed of 9 generators located at an axial location $X_{vg} = 5.0$. For this installation of vortex generators, the maximum 60°-sector circumferential pressure ring distortion index remains reasonably level between the Reynolds numbers of 16.0×10^6 and 8×10^6. For Reynolds numbers less than 8.0×10^6 the flow at the engine face "breaks" down and the distortion increases very rapidly. The systematic and continuous nature of the flow field breakdown can be seen in the engine face total pressure recovery maps presented in Fig. 5. Installed vortex generator performance, as measured by engine face circumferential distortion descriptors, is sensitive to Reynolds number and thereby the generator scale, i.e., the ratio of generator blade height to local boundary layer thickness. Installations of co-rotating vortex generators work well in terms of minimizing engine face distortion within a limited range of generator scales. This means that the design of vortex generator installation is a point design, and all other conditions are off-design.

The relative engine face distortion levels at different flight conditions is important since inlets must be designed to operate with low distortion over the flight envelop. Trades between what is needed at one flight condition, such as takeoff, and what is needed at other conditions, such as transonic maneuvering at low altitudes or cruise, must be made. Reynolds number, Mach number, inlet mass flow and engine tolerance to distortion can all change from one operating condition to another. The different shapes of curves in Figs. 4 and 5 represent different relationships between distortion levels at key aircraft operating conditions.

Third International Conference on Inverse Design Concepts and Optimization in Engineering Sciences
(ICIDES-III), Editor: G.S. Dulikravich, Washington D.C., October 23-25, 1991.

The relative engine face distortion at different flight conditions is important since inlets must be designed to operate with sufficiently low distortion at all critical flight conditions. Trade-offs between what is needed at one flight condition (e.g., take-off) and what is need at other flight conditions (e.g. transonic maneuvering at low altitudes or high Mach number cruise at high altitude) must be made. Reynolds number, Mach number, inlet mass flow and engine tolerance to distortion can all change from one operating point to another. The different shapes of curves in Figures 5 and 6 represent different relationships between distortion levels at key aircraft operating conditions.

Figures 7 and 8 show the change in distortion with the number of vortex generators. Vortex sector angle increases as the number of vortex generators is increased because of constant spacing between generators causing a decrease in engine face distortion. The vortex generators are at x/R = 3 in Figure 7 and at x/R = 5 in Figure 8 where the distortion levels are lower. The effect of axial location is shown in Figure 9 showing an optimum in this case at x/R between 5 and 6. The effect of spacing between vortex generators is shown in Figure 10 for a 127.5° sector angle at x/R = 5 indicates that generating strong vorticity at the correct location can significantly reduce distortion. Parameters such as vortex generator height, length and angle of attack have not yet been systematically studied in other than simple model problems.

NUMERICAL OPTIMIZATION PROBLEM

Design of complex systems by numerical optimization techniques is becoming an accepted, and in some cases even a standard approach. Vortex generator design for aircraft inlets can be cast in a form to bring the large body of optimization tools to bear on this problem. Comments will now be made on the choice of design variables, the performance parameters and requirements for a numerical optimization method.

The design variables include the geometric variables of each vortex generator, i.e., length, height, and geometric angle of attack. They also include the relationship between vortex generators such as their circumferential separation, α, and their axial location, x. These variables are continuous. However, the number of vortex generators used is also a design variable which must take integer values. In addition, the geometric angle of attack of a particular vortex generator has local optima at both positive and negative values. These correspond to the co-rotating and counter-rotating cases described above.

Selection of a performance parameter is a particularly difficult task for three reasons. First, the required distortion level can be different at each important flight condition. Second, distortions worse than the requirement are unacceptable whereas distortion levels better than the requirement are of limited value. Third, use of vortex generators can cause loss of total pressure which implies loss of thrust.

At each flight condition, i, a performance parameters could have the form:

$$P_i = f_p\left[D_i^* - D_i\right] * \left[\Delta P_i^0 \; g_i \; m_i^f\right] \qquad (5)$$

Third International Conference on Inverse Design Concepts and Optimization in Engineering Sciences (ICIDES-III). Editor: G.S. Dulikravich, Washington D.C., October 23-25, 1991.

where D_i is the distortion at the flight condition, D_i^* is the allowed distortion, f_p is either a penalty function or a barrier function. As a penalty function it is adverse when the argument is negative and constant or only moderately improving when the argument is positive. As a barrier function it gets increasingly adverse as the argument approaches zero. ΔP_i^o is the pressure loss in the inlet including the effect of vortex generators, m_i^f is the rated fuel burned at this flight condition and g_i is the gross-to-net thrust ratio. This performance parameter sums the contribution of performance parameters at several flight conditions. The contribution from each flight condition is weighted by the amount of fuel burned in that segment of the flight by the second term in (5). Consequently this term heavily weights the design to good cruise performance. The first term in (5) requires that an acceptable level of distortion be achieved at all flight conditions. The barrier or penalty function must be designed to prohibit unacceptable distortion levels since this can result in engine damage or worse. The weighted summation of performance at each flight condition is analogous to techniques presently used for component design in aircraft systems. Using the discrete penalty function:

$$f_\delta(a) \quad \begin{cases} = 1 & a \geq 0 \\ = \infty & a < 0 \end{cases} \tag{6}$$

in Equation (5) results in a statement of the engineering problem that may preclude the use of differential methods.

Evaluation of the performance parameter for each set of design variables requires solution to a set of four partial differential equations at 250,000 to 500,000 node points. Each evaluation uses 6 to 12 minutes of CPU time on a Cray X-MP or Y-MP. At commercial Cray computer cost of $200 per hour, performance parameter evaluations are not excessively expensive compared to multi-million dollar model tests in a wind tunnel. Evaluation on an engineering workstation at 1/10 the Cray speed and a purchase price on the order of $15,000 allows a trade of evaluation cost versus time.

Two computational strategies are suggested. The first is based on gradient methods and uses the barrier function. First order "steepest descent" methods are not expected to be useful because of the strong interaction among the variables. In particular, consider terms of the form

$$\frac{\partial^2 P}{\partial x_i \partial x_j} \tag{7}$$

where x_i and x_j are design variables and P is the performance parameter. Successful solution by first order gradient techniques can be inhibited by large values of (7) for $i \neq j$ compared to terms where $i = j$. In these cases higher order methods are required. A full second order method requires many evaluations of the performance parameter, which can be costly. Quasi-Newton techniques approximate the matrix terms, Eq. (7), by a positive definite matrix. The approximation improves with successive 1-D searches.

Since the number of vortex generators is not a continuous variable and since co-rotating and counter-rotating vortex generators form two classes of solutions, a series of optimization problems need to be solved. The most favorable of the separate cases would be selected as the favored design.

Rather than solve the entire problem *de novo*, aspects of a design could be improved by numerical optimization strategies. For example, vortex generator height, length and angle of attack could be held constant. Then for a predetermined number of co-rotating vortex generators, their location and spacing could be optimized using traditional optimization techniques.

A second strategy is discrete and uses the discrete penalty function, Eq. (6). The resulting optimization problem is a mixed discrete-continuous design variable problem with a discontinuous performance parameter. Discrete optimization techniques, such as simulated annealing, may be adapted to this hybrid problem. Such techniques can require a large number of evaluations of the performance parameter, so careful strategies must be adopted. Such strategies are areas for further research.

CONCLUSIONS

Vortex generator design for aircraft inlets has played an important role in solving inlet distortion problems in the last 20 years. Present design procedures are based on expensive and therefore limited model tests. With the ability to compute inlet flows with vortex generators comes the ability to apply numerical optimization techniques to the design problem, at least in a limited sense.

A performance parameter is suggested to account for both inlet distortion and total pressure loss at a series of design flight conditions. The resulting optimization problem is difficult since some of the design parameters take on integer values. If numerical procedures could be used to reduce development test programs to a small set of verification tests, numerical optimization could have a significant impact on both cost and elapsed time to design new aircraft.

REFERENCES

1. Advisory Group for Aerospace Research and Development (AGARD), "Engine Response to Distorted Inflow Conditions," AGARD CP-400, Sept. 1986.

2. Bowditch, D.N. and Coltrin, R.E., "A Survey of Inlet/Engine Distortion Compatibility," AIAA-83-1166, June 1983.

3. Kaldschmidt, G., Syltedo, B.E. and Ting, C.T., "727 Airplane Center Duct Inlet Low-Speed Performance Confirmation Model Test for Refanned JT8D Engines - Phase II," NASA CR-134534, Nov. 1973.

4. Anderson, Bernhard, H., "The Aerodynamic Characteristics of Vortex Ingestion for the F/A-18 Inlet Duct," AIAA Paper No. 91-0130, AIAA 28th Aerospace Sciences Meetings, Jan. 1991.

5. Anderson, Bernhard, H. and Levy, Ralph, "A Design Strategy for the Use of Vortex Generators to Manage Inlet-Engine Distortion Using Computational Fluid Dynamics," AIAA/ASME/SAE 27th Joint Propulsion Conference, Sacramento, CA, June 1991.

Third International Conference on Inverse Design Concepts and Opumization in Engineering Sciences (ICIDES-III), Editor: G.S. Dulikravich, Washington D.C., October 23-25, 1991.

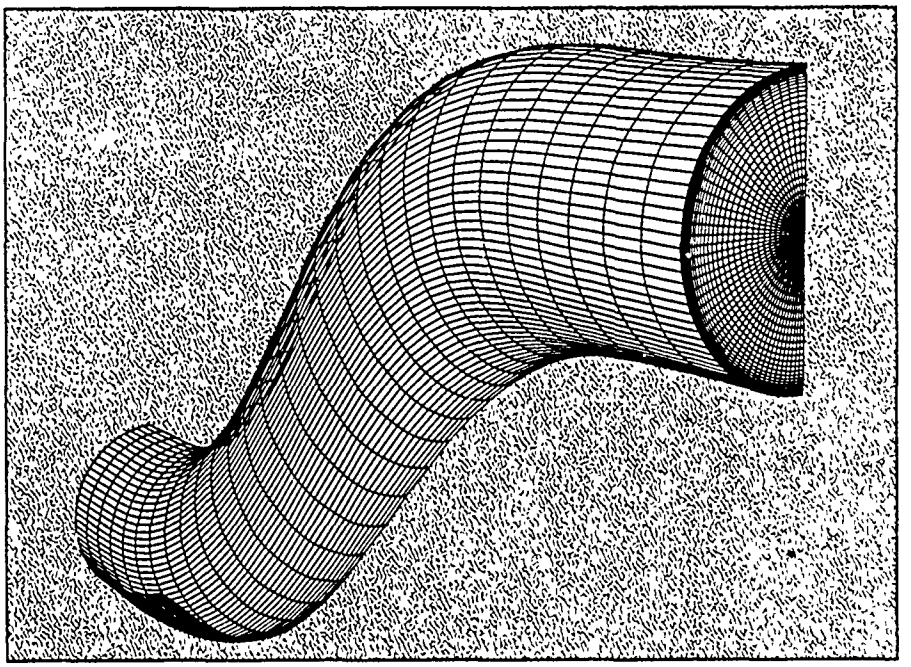


Figure (1) - Geometry definition for the 727/JT8D-100 center inlet.

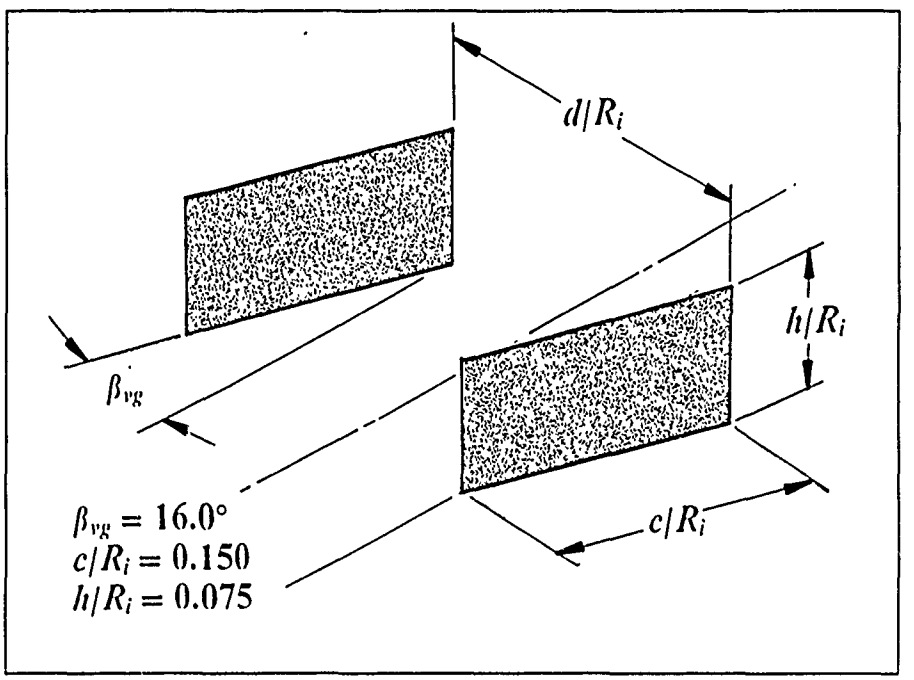


Figure (2) - Geometry definition of co-rotating vortex generators.

Third International Conference on Inverse Design Concepts and Optimization in Engineering Sciences (ICIDES-III), Editor: G.S. Dulikravich, Washington D.C., October 23-25, 1991.

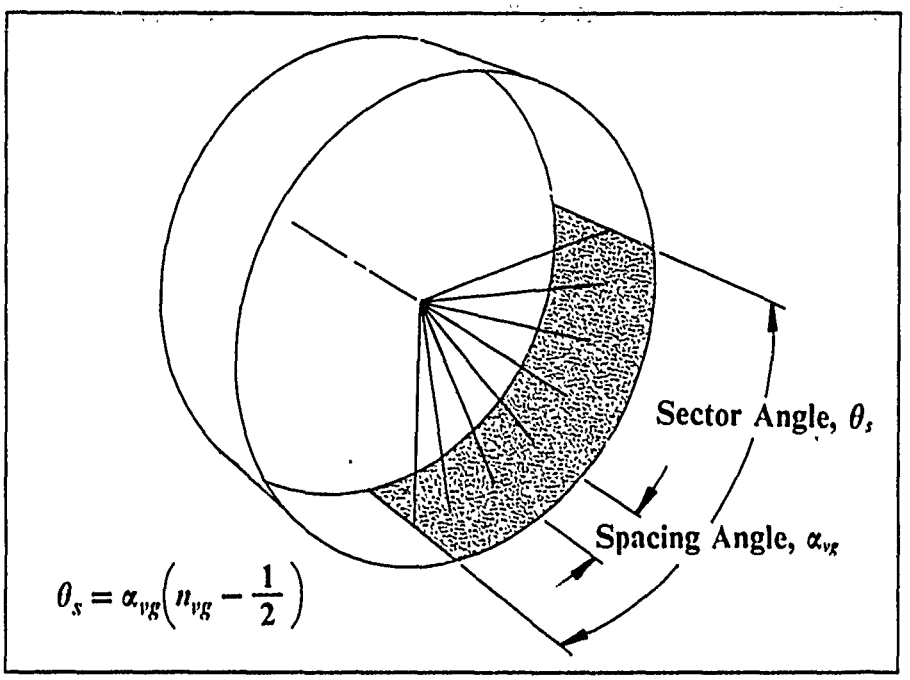


Figure (3) - Nomenclature used for vortex generator positioning.

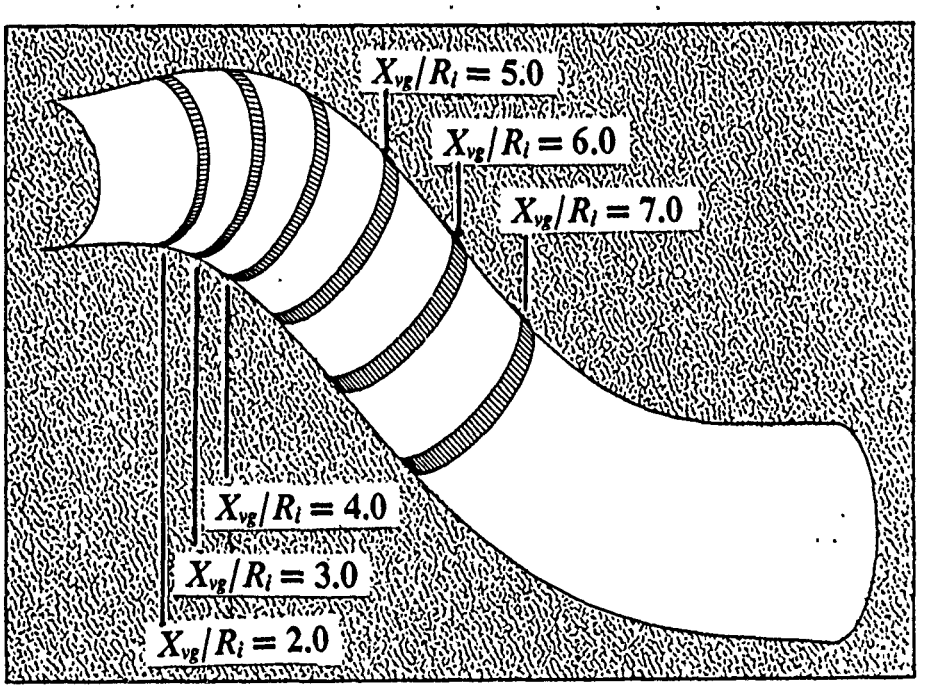


Figure (4) - Axial locations of the vortex generator sector regions.

Third International Conference on Inverse Design Concepts and Optimization in Engineering Sciences
(ICIDES-III), Editor: G.S. Dulikravich, Washington D.C., October 23-25, 1991.

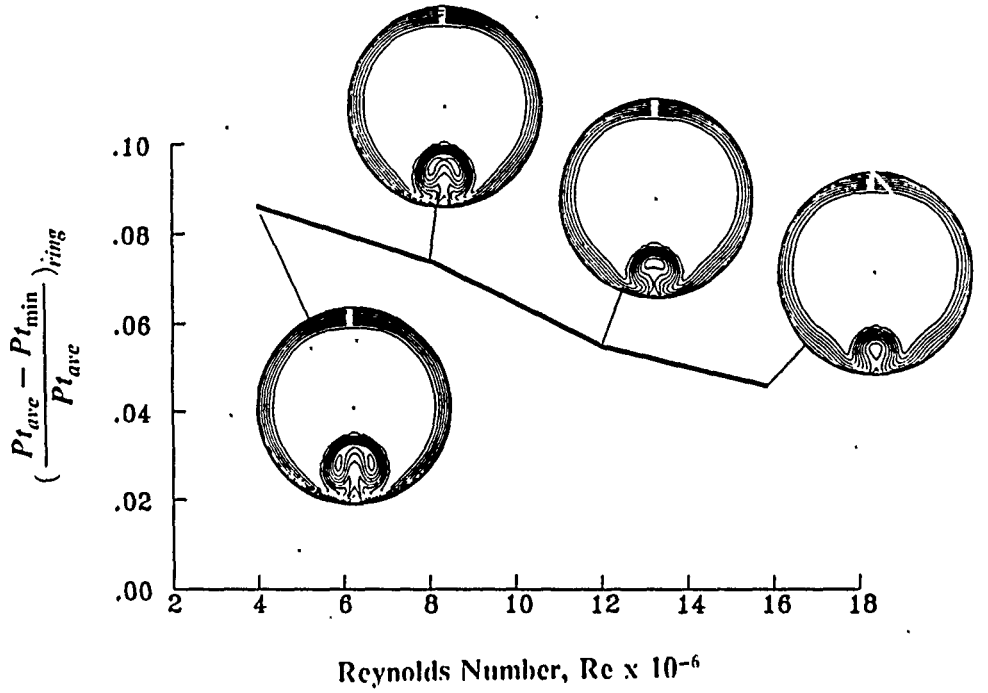


Figure (5) - Effect of Reynolds number on the maximum 60°-sector circumferential pressure ring distortion without vortex flow control.

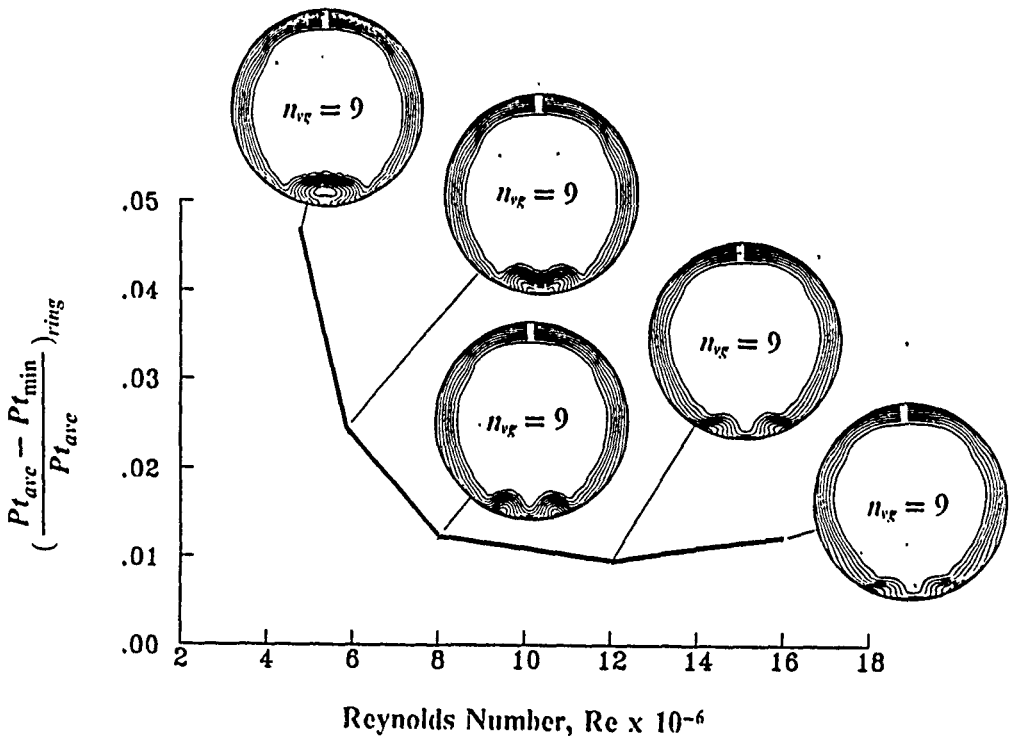


Figure (6) - Effect of Reynolds number on the maximum 60°-sector circumferential pressure ring distortion at $X_{vg}/R_i = 5.0$

Third International Conference on Inverse Design Concepts and Optimization in Engineering Sciences (ICIDES-III), Editor: G.S. Dulikravich, Washington D.C., October 23-25, 1991.

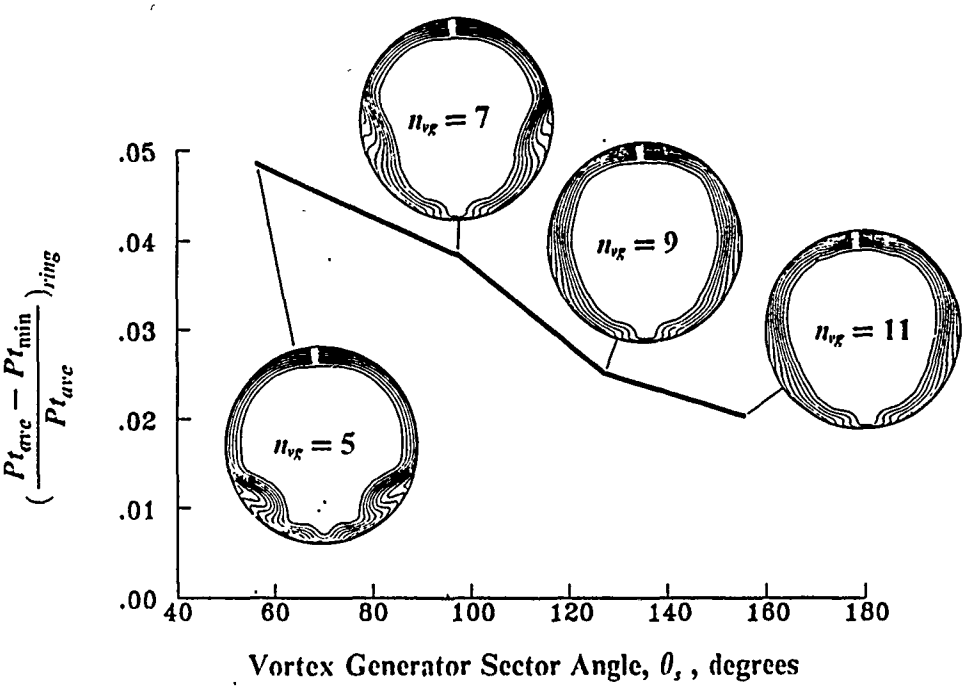


Figure (7) - Effect of vortex generator sector angle (θ_s) on the maximum 60°-sector circumferential pressure ring distortion at $X_{vg}/R_i = 3.0$.

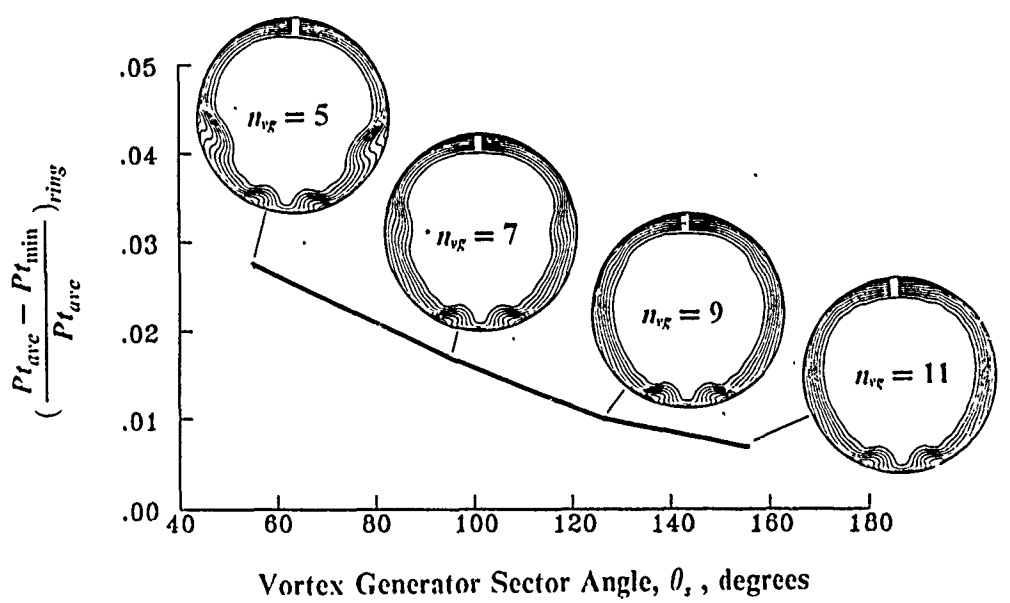


Figure (8) - Effect of vortex generator sector angle (θ_s) on the maximum 60°-sector circumferential pressure ring distortion at $X_{vg}/R_i = 5.0$.

Third International Conference on Inverse Design Concepts and Optimization in Engineering Sciences (ICIDES-III), Editor: G.S. Dulikravich, Washington D.C., October 23-25, 1991.

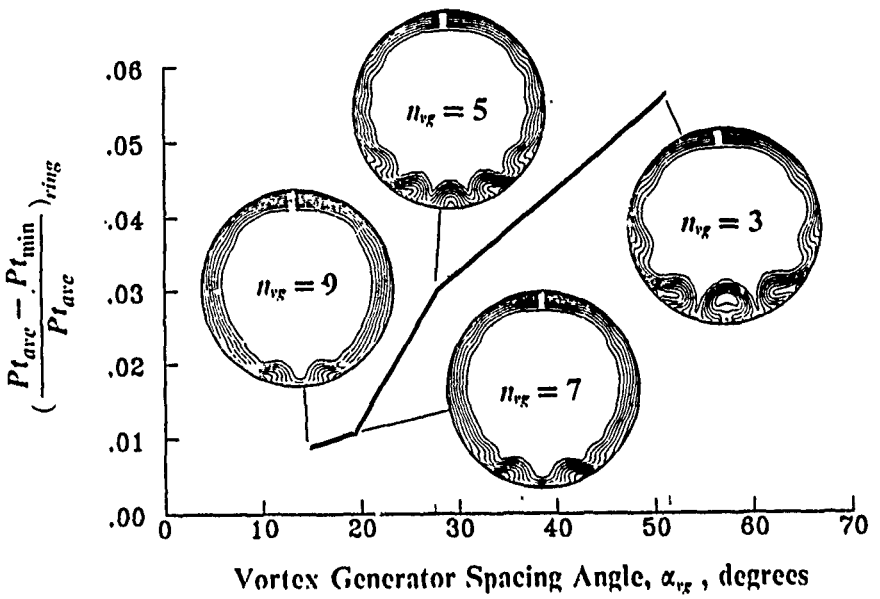


Figure (9) - Effect of vortex generator spacing angle (α_{vg}) on the maximum 60°-sector circumferential pressure ring distortion.

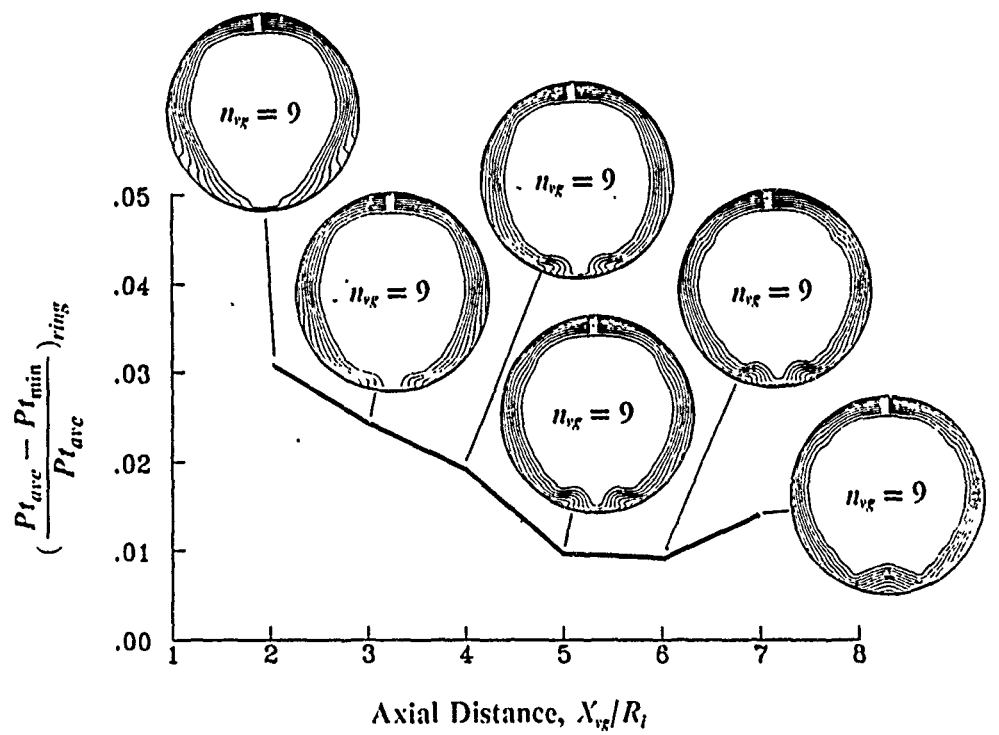


Figure (10) - Effect of vortex generator sector location (X_{vg}/R_t) on the maximum 60°-sector circumferential pressure ring distortion.

Third International Conference on Inverse Design Concepts and Optimization in Engineering Sciences (ICIDES-III), Editor: G.S. Dulikravich, Washington D.C., October 23-25, 1991.

AIRFOIL OPTIMIZATION WITH EFFICIENT GRADIENT CALCULATIONS

Thomas Sorensen
Department of Aeronautics and Astronautics
Massachusetts Institute of Technology
77 Massachusetts Avenue
Room 37-350
Cambridge, MA 02139

1 ABSTRACT

The viscous airfoil design/analysis code XFOIL was extended to allow optimization using conformal mapping coefficients as design variables. The optimization technique employed was the Steepest Descent method applied to a Penalty Function. The gradients of the aerodynamic variables with respect to the design variables were cheaply calculated as by-products of XFOIL's integral boundary layer Newton solver. The speed of the optimization process was further increased by updating the Newton system boundary layer variables after each optimization step using the available gradient information. Two examples are presented.

2 INTRODUCTION

Airfoil design can be broken into two schools of thought. The more recent of the two involves the use of inverse design methods whereby the airfoil geometry is generated to match a specified pressure distribution. The drawback is in determining what makes a good pressure distribution. Many examples of inverse design techniques exist in the literature [1, 2, 3]. The older design practice uses trial and error geometry guessing. Each new geometry is evaluated using an airfoil analysis method and is compared to previous designs. This is continued until an acceptable design is iteratively converged upon. This is a time consuming process, but, it does lend itself to numerical optimization techniques. Many methods have been tried for inviscid airfoils, several examples of which are given by Vanderplaats [4, 5]. Optimization can be computationally intensive, so to be a viable design tool the optimization method employed must be efficient. Optimization efficiency can be increased by the use of gradient information but calculation of this information adds to the computational burden. One method of obtaining the gradient information is to perform finite difference calculations, however, this can be extremely expensive.

The object of the present research was to modify an existing 2D airfoil design/analysis code to calculate gradient information during the analysis procedure, with a minimum of excess work, such that this information can be used in an optimization process. The optimizer written for the design code was simple and robust, but not necessarily the most efficient since the emphasis was on developing the ingredients for the optimization: design variables and gradient information. The code used was Drela's XFOIL code [6]. XFOIL has several design routines, and includes both viscous and inviscid analysis routines. Principles from both the design and viscous analysis routines were combined to allow viscous optimizations.

The outline for the remainder of this paper is to first present the governing equations, the choice of design variables, and how these variables allow efficient gradient calculations. These same gradients can also be used to further speed the optimization process which will be presented next. Two design examples will be given at the end.

Third International Conference on Inverse Design Concepts and Optimization in Engineering Sciences (ICIDES-III), Editor: G.S. Dulikravich, Washington D.C., October 23-25, 1991.

3 ANALYSIS

3.1 Governing Equations

The optimization scheme utilized in XFOIL was an iterative 'Steepest Descent'-type. In order to use this technique the Objective Function and constraints were combined into a Penalty Function such that the constrained airfoil optimization problem is converted into an unconstrained problem. A constrained airfoil optimization problem can be stated in Penalty Function form as

$$Minimize: P(\mathbf{x}) = F(\mathbf{x}) + \frac{1}{2}\sum_{j=1}^{m} K_j \left(g_j(\mathbf{x})\right)^2, \tag{1}$$

where,

$$g_j(\mathbf{x}) \geq 0 \qquad for \;\; j = 1, m \tag{2}$$

are the constraints that the airfoil is subject to, and

$$K_j = \begin{cases} 0 & g_j(\mathbf{x}) \geq 0 \\ \kappa & g_j(\mathbf{x}) < 0 \end{cases}, \tag{3}$$

are the switches that turn the constraints on and off. The cost parameter, κ, is a large positive quantity used to control the influence of the constraint on the optimization process [5]. The Objective Function, $F(\mathbf{x})$, is the function that the optimizer will drive to the lowest possible value, subject to the stated constraints, using the design variables $\mathbf{x}$. For airfoil optimization the Objective Function could be simply the drag coefficient or a combination of several airfoil characteristics such as the negative of the range parameter, $-MC_l/C_d$.

3.2 Design Variables

The unit circle in the ζ-plane can be mapped to an airfoil in the z-plane by the transformation [3]

$$\frac{\partial z}{\partial \zeta} = (1 - \frac{1}{\zeta})^{(1-\epsilon_{te})} \exp\left\{\sum_{n=0}^{\infty}(A_n + iB_n)\zeta^{-n}\right\}, \qquad n = 0, 1, 2, \cdots \tag{4}$$

where, $\pi\epsilon_{te}$ is the trailing edge angle. The design variables employed in XFOIL's optimizer are a finite number of the real and imaginary parts of the complex coefficients of Eq. 4:

$$\mathbf{x} = \{A_2,\ A_3, \cdots A_{N_A},\ \ B_2,\ B_3, \cdots B_{N_B}\}^T. \tag{5}$$

Using the above notation, there are a total of $(N_A - 2) + (N_B - 2)$ design variables. Each design variable corresponds to a single design mode such that the optimal airfoil is constructed by a sum of these design modes. A particular convenience of these design variables is that the A_n's control the thickness distribution of the airfoil and the B_n's the camber distribution. Due to this distinction the A_n's and B_n's will be referred to, respectively, as the symmetric modes and the anti-symmetric modes. The first 3 symmetric and anti-symmetric design modes are shown in Fig. 1. The solid lines for the symmetric modes indicate the airfoil surface for one value of A_n. The dashed lines show how the surface (i.e. the thickness) changes as another value of A_n is used. For the anti-symmetric modes, the lines are not the airfoil surface, but the camber lines. The first usable design modes are A_2 and B_2 since A_0, A_1, B_0, and B_1 are constrained by Lighthill's constraints [2] and therefore are not available as design variables.

Third International Conference on Inverse Design Concepts and Optimization in Engineering Sciences (ICIDES-III), Editor: G.S. Dulikravich, Washington D.C., October 23-25, 1991.

The A_n and B_n coefficients completely control the airfoil geometry with the exception of the trailing edge angle and gap. For a typical airfoil only the first twenty or so C_n's are required to define the airfoil. The value of the design variables for a DAE11 airfoil are plotted in Fig. 2 as an indication of their magnitudes for a typical airfoil. The higher frequency modes quickly become unimportant. In both cases, only approximately the first 15 modes are important. The DAE11 geometry is shown in Fig. 3 for reference. The higher modes, however, become important for airfoils with small leading edge radii.

3.3 Aerodynamic Quantities

For optimization efficiency it is imperative that gradient information be calculated and calculated cheaply. The gradient information will also prove useful in making XFOIL's viscous analysis procedure run faster as will be shown shortly.

In its unmodified configuration XFOIL solves a viscous flow around an airfoil by constructing 3 linearized boundary layer (BL) equations at each airfoil and wake node (N airfoil nodes, N_w wake nodes) and solving the resulting system using a Newton solver. For a viscous airfoil analysis all aerodynamic quantities of interest are functions of the five BL variables: C_τ, θ, $m \equiv u_e\delta^*$, u_e, and δ^*. In this text C_τ will represent two quantities: in laminar regions it will be the amplitude of the most-amplified Tollmien-Schlichting wave, and in turbulent regions it will be the maximum shear coefficient. The Newton system only solves for three of these variables, C_τ, θ, and m, since u_e and δ^* are related to the first three variables. For more details of XFOIL, see Drela [6].

To calculate the required BL variable gradients, consider the Newton System used in XFOIL

$$[J]\{\delta\} = -\{R\}. \tag{6}$$

This equation is a block matrix equation where the i^{th}-row, j^{th}-column block of the Jacobian Matrix is

$$[J_{i,j}] = \begin{bmatrix} \frac{\partial f_i}{\partial C_{\tau_j}} & \frac{\partial f_i}{\partial \theta_j} & \frac{\partial f_i}{\partial m_j} \\ \frac{\partial g_i}{\partial C_{\tau_j}} & \frac{\partial g_i}{\partial \theta_j} & \frac{\partial g_i}{\partial m_j} \\ \frac{\partial h_i}{\partial C_{\tau_j}} & \frac{\partial h_i}{\partial \theta_j} & \frac{\partial h_i}{\partial m_j} \end{bmatrix}. \tag{7}$$

The corresponding i^{th}-row block of the vectors are

$$\{\delta_i\} = \begin{Bmatrix} \delta C_{\tau_i} \\ \delta\theta_i \\ \delta m_i \end{Bmatrix}, \qquad \{R_i\} = \begin{Bmatrix} f_i \\ g_i \\ h_i \end{Bmatrix}. \tag{8}$$

Many of the terms in the Jacobian Matrix are zero, but the detailed structure is not important here.

Equation (6) is constructed using 3 BL equations at each node all with the functional form

$$R_i = R_i(C_{\tau_{i-1}},\ C_{\tau_i},\ \theta_{i-1},\ \theta_i,\ m_1,\ m_2, \cdots,\ m_{N+N_W}), \tag{9}$$

where, R_i can be f_i, g_i, or h_i and the subscripts indicate which node is being considered. The edge velocity, u_e, is composed of an inviscid and a viscous source contribution,

Third International Conference on Inverse Design Concepts and Optimization in Engineering Sciences (ICIDES-III), Editor: G.S. Dulikravich, Washington D.C., October 23-25, 1991.

$$u_{e_k} = q_k + \sum_j d_{kj} m_j, \tag{10}$$

where, the inviscid part q_k depends on the airfoil geometry and hence A_n and B_n. The mass defect, m, therefore also depends on A_n and B_n, and so does the viscous residual R_i in Eq. (9). Consequently, a new Newton system is obtained in the form

$$[J \mid A] \left\{ \frac{\delta}{\Delta} \right\} = -\{R\}. \tag{11}$$

The i^{th}-row block of the Jacobian addition, $[A]$, is

$$[A_i] = \begin{bmatrix} \frac{\partial f_i}{\partial A_2} & \frac{\partial f_i}{\partial A_3} & \cdots & \frac{\partial f_i}{\partial A_{N_A}} & \frac{\partial f_i}{\partial B_2} & \frac{\partial f_i}{\partial B_3} & \cdots & \frac{\partial f_i}{\partial B_{N_B}} \\ \frac{\partial g_i}{\partial A_2} & \frac{\partial g_i}{\partial A_3} & \cdots & \frac{\partial g_i}{\partial A_{N_A}} & \frac{\partial g_i}{\partial B_2} & \frac{\partial g_i}{\partial B_3} & \cdots & \frac{\partial g_i}{\partial B_{N_B}} \\ \frac{\partial h_i}{\partial A_2} & \frac{\partial h_i}{\partial A_3} & \cdots & \frac{\partial h_i}{\partial A_{N_A}} & \frac{\partial h_i}{\partial B_2} & \frac{\partial h_i}{\partial B_3} & \cdots & \frac{\partial h_i}{\partial B_{N_B}} \end{bmatrix}. \tag{12}$$

The added vector term contains the changes in the design variables

$$\{\Delta\} = \left\{ \Delta A_2, \ \Delta A_3, \ \cdots \ \Delta A_{N_A}, \quad \Delta B_2, \ \Delta B_3, \ \cdots \ \Delta B_{N_B} \right\}^T, \tag{13}$$

where, $\Delta(\ )$ implies a change in the design variables between the current optimization step and the next optimization step. The modified Jacobian matrix, $[J \mid A]$, is no longer square, but during normal viscous calculations the geometry is fixed and thus the ΔA_n and ΔB_n's are known (i.e. they are zero). Therefore, rewriting Eq. (11) with all knowns on the right hand side and then pre-multiplying both sides by $[J]^{-1}$ the system reduces to

$$\{\delta\} = -[J]^{-1}\{R\} + [D]\{\Delta\}, \tag{14}$$

where,

$$[D] = -[J]^{-1}[A]. \tag{15}$$

The viscous solution is obtained when the residual, $\{R\}$, is zero. Thus, at convergence Eq. (14) will have the same form as a first order Taylor series expansion of the 3 BL equations in terms of the design variables. For example, the Taylor expansion for C_τ, θ, and m at the i^{th} node is

$$\begin{Bmatrix} \delta C_{\tau_i} \\ \delta\theta_i \\ \delta m_i \end{Bmatrix} = \sum_{n=2}^{N_A} \Delta A_n \begin{Bmatrix} \frac{\partial C_{\tau_i}}{\partial A_n} \\ \frac{\partial \theta_i}{\partial A_n} \\ \frac{\partial m_i}{\partial A_n} \end{Bmatrix} + \sum_{n=2}^{N_B} \Delta B_n \begin{Bmatrix} \frac{\partial C_{\tau_i}}{\partial B_n} \\ \frac{\partial \theta_i}{\partial B_n} \\ \frac{\partial m_i}{\partial B_n} \end{Bmatrix}. \tag{16}$$

The Taylor coefficients are the BL variable derivatives being sought and after close examination it can be seen that they are the columns of $[D]$. For example, the i^{th}-row block of $[D]$ is

Third International Conference on Inverse Design Concepts and Optimization in Engineering Sciences (ICIDES-III), Editor: G.S. Dulikravich, Washington D.C., October 23-25, 1991.

$$[D_i] = \begin{bmatrix} \frac{\partial C_{r_i}}{\partial A_2} & \frac{\partial C_{r_i}}{\partial A_3} & \cdots & \frac{\partial C_{r_i}}{\partial A_{N_A}} & \frac{\partial C_{r_i}}{\partial B_2} & \frac{\partial C_{r_i}}{\partial B_3} & \cdots & \frac{\partial C_{r_i}}{\partial B_{N_B}} \\ \frac{\partial \theta_i}{\partial A_2} & \frac{\partial \theta_i}{\partial A_3} & \cdots & \frac{\partial \theta_i}{\partial A_{N_A}} & \frac{\partial \theta_i}{\partial B_2} & \frac{\partial \theta_i}{\partial B_3} & \cdots & \frac{\partial \theta_i}{\partial B_{N_B}} \\ \frac{\partial m_i}{\partial A_2} & \frac{\partial m_i}{\partial A_3} & \cdots & \frac{\partial m_i}{\partial A_{N_A}} & \frac{\partial m_i}{\partial B_2} & \frac{\partial m_i}{\partial B_3} & \cdots & \frac{\partial m_i}{\partial B_{N_B}} \end{bmatrix}. \tag{17}$$

The elements of this matrix are found not by carrying out the matrix multiplication as indicated in Eq. (15) but by solving the original Newton system with the columns of $[A]$ added as extra right hand sides. Since a direct matrix solver is used, very little extra work is needed to calculate the required sensitivities. In addition, the extra right hand sides only have to be included *after* convergence of the system, not *every* time the system is solved.

The above derivation presents a scheme to compute the BL variable gradients if the gradients of the BL equations, Eqs. (9), are known (i.e. if the terms of $[A]$ are known). The terms in $[A]$ are found by use of the chain rule and are included here without derivation

$$\frac{\partial R_i}{\partial A_n} = \left(\frac{\partial R_i}{\partial q_{i-1}}\right)\left(\frac{\partial q_{i-1}}{\partial A_n}\right) + \left(\frac{\partial R_i}{\partial q_i}\right)\left(\frac{\partial q_i}{\partial A_n}\right), \tag{18}$$

where,

$$\frac{\partial R_i}{\partial q_{i-1}} = \frac{\partial R_i}{\partial u_{e_{i-1}}} - \frac{\partial R_i}{\partial \delta^*_{i-1}} \frac{m_{i-1}}{u^2_{e_{i-1}}}, \tag{19}$$

is found using Eq. (10) and the definition of the mass defect, $m = u_e \delta^*$. Similarly for the B_n derivatives. In the above four equations R_i can be f_i, g_i, or h_i. At node i the derivatives depend only on the information at that node and the upstream node $i-1$. All the terms in Eq. (19) are already available once XFOIL constructs the Newton system. Further details of the above equations can be found in the author's Master's Thesis [7].

The only remaining unknown sensitivities in Eq. (18) are the derivatives of q. These can be calculated analytically from the expression for q obtained after the complex potential is mapped from the circle-plane to the airfoil-plane. At any point, ζ, in the circle-plane, the physical speed is

$$q = \exp\left\{\Re\left[\ln\left(\left(1-\frac{1}{\zeta}\right)^{\epsilon_{te}}\left(e^{-i\alpha} + e^{i\alpha}\zeta^{-1}\right)\right) - \sum_{n=0}^{\infty}(A_n + iB_n)\zeta^{-n}\right]\right\}. \tag{20}$$

The derivatives of this equation are remarkably easy and cheap to compute:

$$\frac{\partial q}{\partial A_n} = -q\Re\left(\frac{1}{\zeta^n}\right), \tag{21}$$

$$\frac{\partial q}{\partial B_n} = +q\Im\left(\frac{1}{\zeta^n}\right). \tag{22}$$

3.4 Geometry Gradient

Now, all aerodynamic variables that depend on the flow solution have been differentiated, and only one further piece of gradient information is necessary; the geometry sensitivity. This can be found analytically using the integrated form of Eq. (4), however, in practice there is a complication. The difficulty arises due to the need for the geometry gradient for the unit chord

Third International Conference on Inverse Design Concepts and Optimization in Engineering Sciences (ICIDES-III), Editor: G.S. Dulikravich, Washington D.C., October 23-25, 1991.

airfoil. Equation (4), when integrated, does not produce a unit chord airfoil and therefore its gradient will not be for a unit chord. The geometry is subsequently normalized, however this is not completely satisfactory for the gradient due to movement of the leading edge. This is not a concern for symmetric airfoils and is a relatively small effect for cambered airfoils. Therefore, the movement of the leading edge point was ignored in calculations for the gradient of z.

3.5 Updating BL Variables

The Newton system of XFOIL uses the BL variables of the previous solution as the starting point of the new solution, therefore, the speed of the optimization can be increased by simply approximating the BL variables of the new airfoil. This can be done by adding the following perturbations to the BL variables at the old optimization step at those nodes not affected by the transition point:

$$\{\delta\} = [D]\{\Delta\}. \tag{23}$$

The ΔA_n's and ΔB_n's in the $\{\Delta\}$ vector of Eq. (23) are the changes in the design variables between the current and new optimization steps, and are calculated from Steepest Descent Equation. The remaining two perturbations, δu_e and $\delta\delta^*$, can be found using

$$\delta u_e = \sum_{n=2}^{N_A} \frac{\partial u_e}{\partial A_n}\Delta A_n + \sum_{n=2}^{N_B} \frac{\partial u_e}{\partial B_n}\Delta B_n, \tag{24}$$

and

$$\delta\delta^* = \sum_{n=2}^{N_A} \frac{\partial \delta^*}{\partial A_n}\Delta A_n + \sum_{n=2}^{N_B} \frac{\partial \delta^*}{\partial B_n}\Delta B_n. \tag{25}$$

For a reasonable optimization step size this linear extrapolation will give a good approximation to the new BL variables. Thus, the Newton system constructed during the analysis of the new design point will converge faster than if no updating were done since it will have a better initial condition.

Movement of the upper and lower surface transition points from one panel to another will cause such severe changes in the BL variables that this linear extrapolation will not work near the transition points. If not considered separately, the poor transition point approximations would be enough to negate the gains in efficiency promised by the updating. The new location of the transition points is approximated and then the BL variables at each panel the transition points have passed over are 'fudged' . This 'fudging' process will only affect the rate at which the Newton system converges, it will not affect the converged solution. For C_τ, θ, and u_e the approximation across the transition point shift is a linear extrapolation from the previous two approximated points, i.e.

$$C_{\tau_i} = 2C_{\tau_{i-1}} - C_{\tau_{i-2}}, \tag{26}$$

where i is a BL node the transition point has passed over. The equations for θ and u_e are similar. For the remaining two BL variables, m and δ^*, it was found to be a better approximation is to set $m_i = m_{i-1}$ and $\delta_i^* = \delta_{i-1}^*$. All that remains to be able to use these transition point approximations is to determine how far the transition point has shifted. This is done using

$$\delta x_{tran} = \frac{\partial x_{tran}}{\partial C_\tau}\delta C_\tau + \frac{\partial x_{tran}}{\partial \theta}\delta\theta + \frac{\partial x_{tran}}{\partial \delta^*}\delta\delta^* + \frac{\partial x_{tran}}{\partial u_e}\delta u_e. \tag{27}$$

Third International Conference on Inverse Design Concepts and Optimization in Engineering Sciences (ICIDES-III), Editor: G.S. Dulikravich, Washington D.C., October 23-25, 1991.

All the derivative terms in the above are already calculated in XFOIL to construct the Newton system, so the derivation is complete.

The convergence histories for a simple test case with and without updating the BL variables are shown in Fig. 4. The number of iterations for the Newton solver to convergence is plotted versus the optimization step number. The amount of time saved is not extensive, but the low cost of updating makes it worthwhile. As the optimization continues the savings will be smaller since the step sizes are small.

4 RESULTS

The two examples presented in this section were run on a DecStation 5000. These examples were chosen to show the various properties of XFOIL's optimizer, they are not designed to be realistic design problems.

5 Example 1 - C_d minimization, $M = 0$, $\alpha = 0°$

The first test case was designed as a simple example to build faith in the optimization code. A NACA 0015 airfoil was used as the seed airfoil with C_d used as the Objective Function. The only constraint was to keep the angle of attack constant at 0°. The Reynolds Number based on the chord was 10^6. The two design variables used were A_2 and A_3. Using only two design variables will allow a pictorial representation of the optimization path to be constructed.

Figure 5 portrays the optimization space for this test case. The contours are of constant C_d and a local minimum is located in the upper left corner. The seed airfoil is located out of the picture in the lower right corner and the path taken by the optimizer is marked by the crosses. Convergence took 24 iterations and approximately 12 minutes. Figure 5 clearly shows the larger step sizes in the first five steps, i.e. in the region of large slope. The step directions are perpendicular to the contours, as they should be, where the gradients are large. As the optimum is neared the step directions start to parallel the contours. This is due to the approximations made in the gradient calculations. This is not a detriment since the exact mathematical optimum is relatively unimportant.

From Fig. 6 it is obvious that the largest drag reductions are produced in the first few iterations. This is a recurrent observation. Figure 7 compares the optimal airfoil to the seed airfoil. Because only two design modes were utilized, the possible change in the airfoil is small. However, large changes were made in C_d by modifying the airfoil such that the transition points were moved further aft.

5.1 Example 2 - C_d minimization, $M = 0$, $C_l = 0.5$

The second example optimized the C_d of an airfoil using 7 symmetric and 5 anti-symmetric design modes. The seed airfoil was an NACA 3412 and was constrained for a constant lift coefficient and a minimum allowed thickness at 95% of the chord. This constraint was necessary to prevent negative thickness airfoils. The cost parameter and the Reynolds number were $\kappa = 100$ and $Re = 5 \times 10^6$.

This example was stopped after a viscous Newton system was unconverged at the 38^{th} optimization iteration. The Penalty Function is shown in Fig. 8. The drag reduction slows slightly after 20 iterations but is definitely still headed down when the optimizer was stopped. The optimizer was restarted using the last airfoil generated before the Newton system failed as

Third International Conference on Inverse Design Concepts and Optimization in Engineering Sciences (ICIDES-III), Editor: G.S. Dulikravich, Washington D.C., October 23-25, 1991.

the new seed airfoil. Optimization convergence was achieved after an additional 15 iterations. The optimization required approximately 30 minutes. The drag was further lowered from $C_d = 0.00389$ to $C_d = 0.00380$. The reason for the unconverged Newton system is unexplained but it does not invalidate the results of the optimizer.

The pressure plots of the seed and optimized airfoils are shown in Figs. 9 and 10, respectively. The dashed lines in the C_p curves are the inviscid solutions and the solid lines the viscous solutions. The waviness apparent in the C_p curve of the optimized airfoil is due to the fact that higher design modes were not used during the optimization.

Modification of an airfoil design code to use mapping coefficients as the design variables was successfully implemented. Gradient information was calculated within the analysis portion of the code with a minimum of extra effort. The gradient information was shown to be accurate

When used in the proper way, the XFOIL optimizer can become a valuable design tool The optimizer should not be used as a 'black box' to create perfect airfoils but as a designer's tool that will free the designer to become more creative and productive by reducing the time spent in iterative design modifications. The 'optimal' airfoils obtained should be used to give the designer ideas for what characteristics the real airfoil should have.

There were also several areas in which the XFOIL optimizer did not live up to expectations. The first is the limited number of design variables that could be utilized. It was found that the optimizer should be restricted to $N_A \leq 12$ and $N_B \leq 12$ because the higher mode derivatives became inaccurate. This does not allow the generation of completely general airfoils with the chosen design variables. This is a disappointment, however the cheap gradient calculations made possible by using the mapping coefficients as design variables make up for this deficiency. Another disappointment was the temperamental nature of XFOIL's Viscous Newton solver. This does not destroy the promise of the optimizer it only enforces that some care needs to be exercised when using the optimizer.

Another area for future research is the development of design variables that can also control the trailing edge angle and gap, and if possible, be completely general.

6 ACKNOWLEDGMENTS

This research was supported by MIT's Department of Aeronautics and Astronautics' Fellowship and the National Science Foundation's PYI Program.

7 NOMENCLATURE

F	Objective function
$\mathbf{x}$	General design variables
g_j	Constraints
m	Number of constraints
A_n	XFOIL thickness design variables (symmetric)
B_n	XFOIL camber design variables (anti-symmetric)
N_A	Last symmetric design mode used in optimization
N_B	Last anti-symmetric design mode used in optimization
$[J]$	Newton system Jacobian matrix
$[A]$	Addition to Jacobian matrix
$\{\delta\}$	Newton system unknown vector
$\{\Delta\}$	Addition to unknown vector

Third International Conference on Inverse Design Concepts and Optimization in Engineering Sciences (ICIDES-III), Editor: G.S. Dulikravich, Washington D.C., October 23-25, 1991.

$\{R\}$	Residual vector
$[D]$	Aerodynamic variables derivative matrix
C_l	Coefficient of lift
C_d	Coefficient of drag
M	Mach number
Re	Reynolds number based on airfoil chord
N	Number of airfoil nodes
N_w	Number of wake nodes
f_i, g_i, h_i	Node i boundary layer equations
C_τ, θ, m, d_{kj}, u_e, δ^*	Boundary layer variables
x_{tran}	Transition point location
ϵ_{te}	Trailing edge angle parameter
α	Angle of attack
q	Inviscid surface speed
$\zeta = re^{i\omega}$	Complex circle-plane coordinate
Δ	Difference operator
$\delta(\ )$	Newton system perturbation
$\Re(\ )$	Real part of the quantity in the parenthesis
$\Im(\ )$	Imaginary part of the quantity in the parenthesis

References

[1] R. Eppler and D. M. Somers. A computer program for the design and analysis of low-speed airfoils. NASA TM 80210, Aug 1980.

[2] M. S. Selig and M. D. Maughmer. A multi-point inverse airfoil design method based on conformal mapping. In *29th Aerospace Sciences Meeting*, Reno, Nevada, Jan 1991.

[3] J. L. Van Ingen. A program for airfoil section design utilizing computer graphics. In *AGARD-VKI Short Course on High Reynolds Number Subsonic Aerodynamics*, AGARD LS-37-70, April 1969.

[4] G. N. Vanderplaats. Efficient algorithm for numerical airfoil optimization. *Journal of Aircraft*, 16(12), Dec 1979.

[5] G. N. Vanderplaats. *Numerical Optimization Techniques for Engineering Design: with Applications*. McGraw-Hill, New York, 1984.

[6] M. Drela. XFOIL: An analysis and design system for low Reynolds number airfoils. In T.J. Mueller, editor, *Low Reynolds Number Aerodynamics*. Springer-Verlag, Jun 1989. Lecture Notes in Engineering, No. 54.

[7] T.M. Sorensen. Viscous airfoil optimization using conformal mapping coefficients as design variables. Master's thesis, Massachusetts Institute of Technology, Jun 1989.

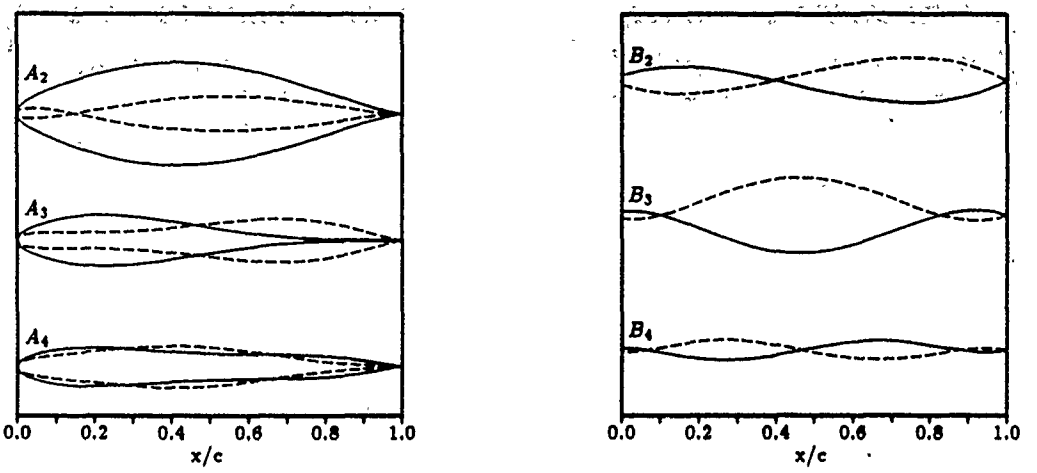


Figure 1: First Three Symmetric and Anti-Symmetric Design Modes

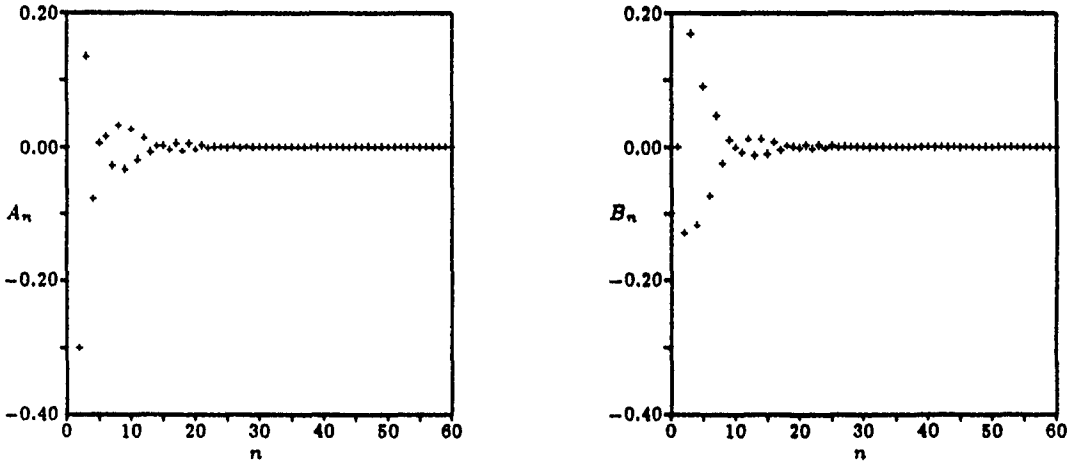


Figure 2: A_n and B_n Distributions for a DAE11 Airfoil

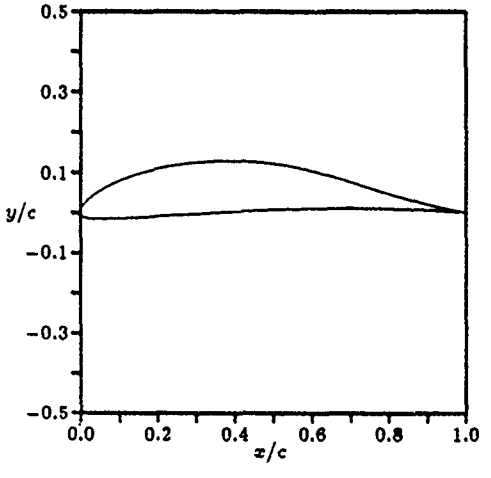


Figure 3: DAE11 Airfoil Geometry

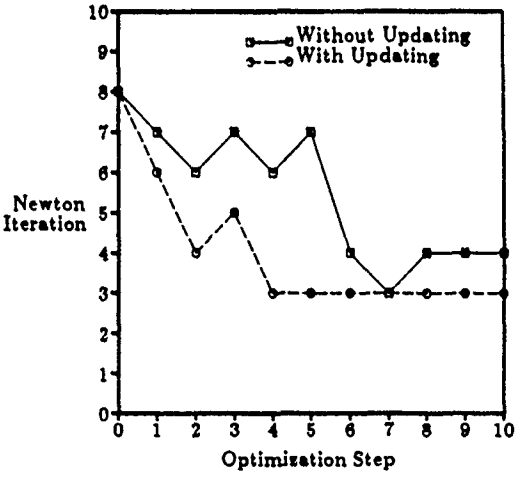


Figure 4: Convergence History With and Without Updating

Third International Conference on Inverse Design Concepts and Optimization in Engineering Sciences
(ICIDES-III), Editor: G.S. Dulikravich, Washington D.C., October 23-25, 1991.

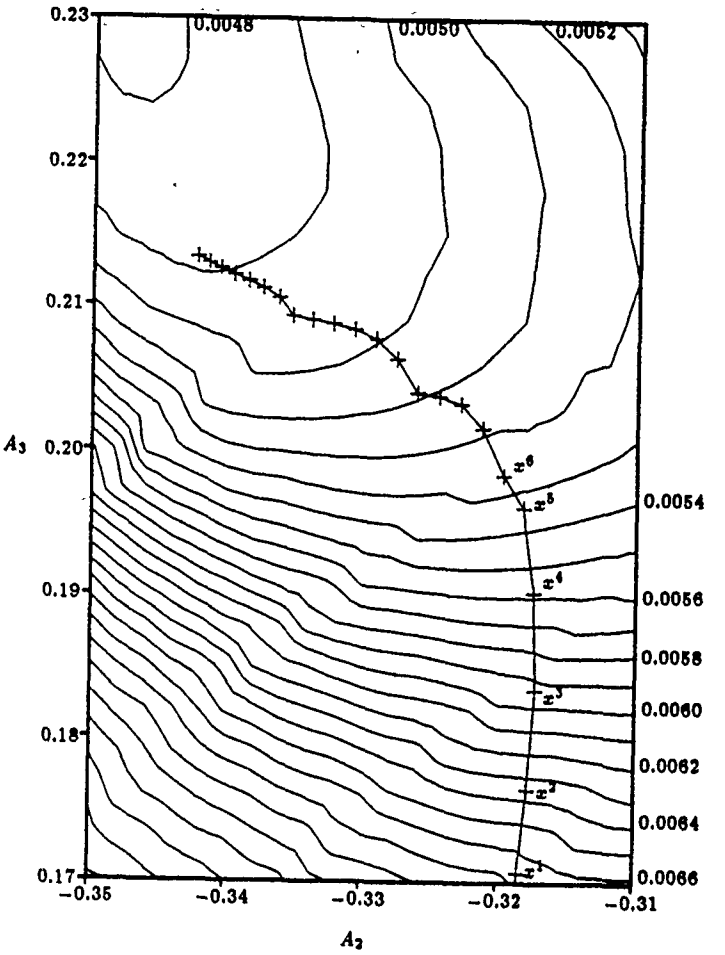


Figure 5: Example 1 - Optimization Path

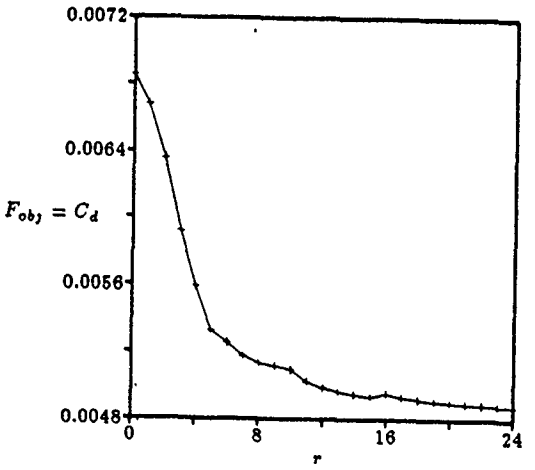


Figure 6: Example 1 - Optimization History

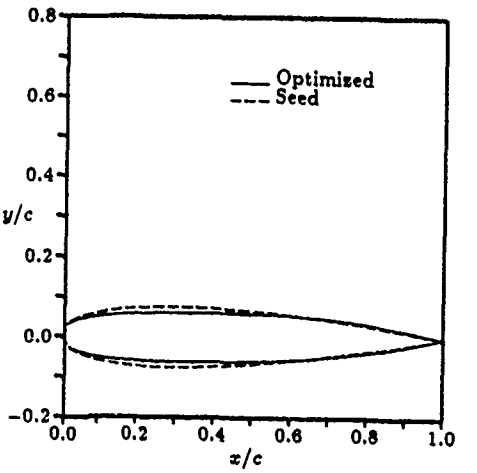


Figure 7: Example 1 - Airfoil Comparisons

Third International Conference on Inverse Design Concepts and Optimization in Engineering Sciences (ICIDES-III), Editor: G.S. Dulikravich, Washington D.C., October 23-25, 1991.

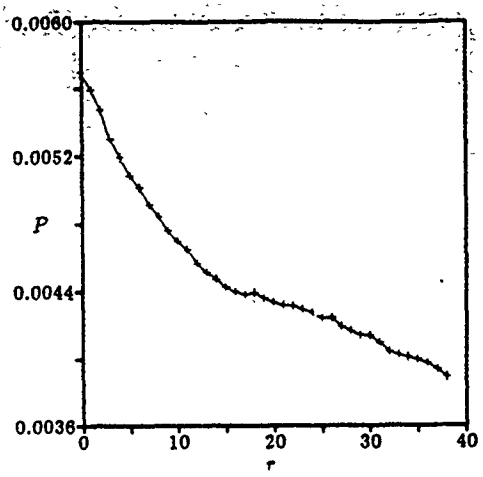


Figure 8: Example 2 - Optimization History

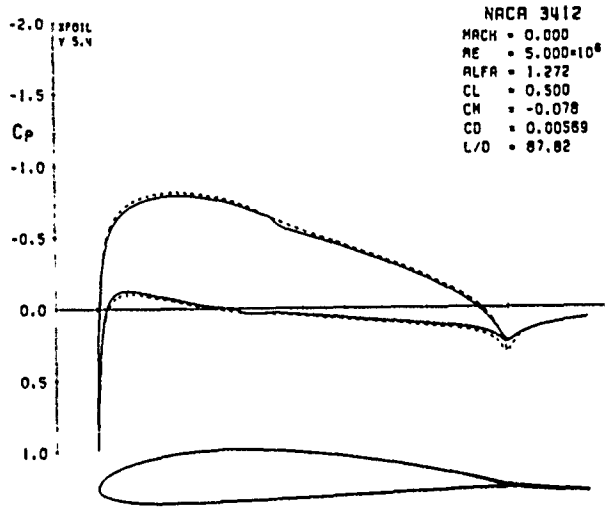


Figure 9: Example 2 - NACA 3412 C_p Plot

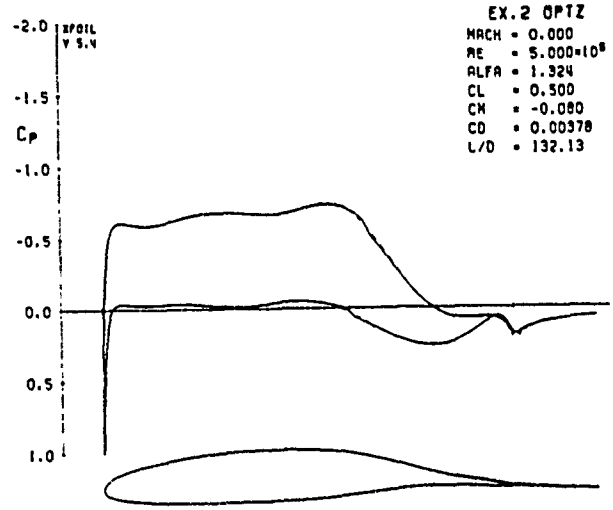


Figure 10: Example 2 - Optimized Airfoil C_p Plot

Third International Conference on Inverse Design Concepts and Optimization in Engineering Sciences (ICIDES-III), Editor: G.S. Dulikravich, Washington D.C., October 23-25, 1991.

DESIGN OPTIMIZATION OF TRANSONIC AIRFOILS

C.-Y. Joh, B. Grossman, and R.T. Haftka
Department of Aerospace and Ocean Engineering
Virginia Polytechnic Institute and State University
Blacksburg, Virginia 24061

ABSTRACT

Numerical optimization procedures have been considered for the design of airfoils in transonic flow based on the transonic small-disturbance (TSD) and Euler equations. A sequential approximation optimization technique was implemented with an accurate approximation of the wave drag based on the Nixon's coordinate straining approach. A modification of the Euler surface boundary conditions was implemented in order to efficiently compute design sensitivities without remeshing the grid. Two effective design procedures producing converged designs in approximately 10 global iterations were developed: interchanging the role of the objective function and constraint and the direct lift maximization with move limits which were fixed absolute values of the design variables.

INTRODUCTION

Current aerodynamic design methods can be broadly categorized as inverse methods, *e.g.*, Volpe and Melnik[1], and numerical optimization methods, *e.g.*, Vanderplaats and Hicks[2]. In general, inverse methods have been widely used as design tools primarily due to their computational efficiency. They do have a weakness associated with the *closure problem*, which generally requires considerable design experience. Also inverse methods, initially developed for potential flows, have been successfully applied to rotational flows based on the Euler equations, *e.g.*, Giles, Drela and Thompkins[3] and the Navier-Stokes equations, *e.g.*, Malone, Narramore and Sankar[4].

Numerical optimization methods have not been widely used in practical airfoil designs primarily due to the large amounts of computational resources needed. Nevertheless, the methods will continue to be developed since they have many advantages such as automated design capability, ability to handle multi-point design and varieties of constraints along with a capability of inclusion into multi-disciplinary design of complete vehicles. A major reason for the large computational effort of numerical optimization methods is the very large number of transonic analyses needed to develop converged designs. Some improvements to the efficiency of numerical optimization methods have been obtained through the implementation of the shape functions, by Vanderplaats and Hicks[2] and Aidala, Davis, and Mason[5], and through the use of efficient optimization procedures, Vanderplaats[6], Joh, Grossman and Haftka[7] and Joh[8].

The motivation for the present work stems from plans to incorporate transonic airfoil designs within an integrated aerodynamic/structural design of an aircraft wing, *e.g.*, Grossman *et al.*[9]. Thus, our objective is to develop efficient numerical optimization procedures for the design of two-dimensional airfoils at transonic speeds, using as few complete transonic analyses as possible.

A preliminary study for this effort is reported in Ref. 7, where some special treatments were developed for design optimization based upon the transonic small-disturbance (TSD) equations. In this paper, we will amplify and improve these ideas and examine in detail the applicability of the methods to the more accurate Euler equation analysis.

DESIGN FORMULATION

Design Problem

The design problem considered can be stated as:

$$\begin{aligned} &\textit{maximize} \quad C_l(\bar{X}) \\ &\textit{such that} \quad C_d(\bar{X}) \le C_{d_l}, \\ &\qquad\qquad A(\bar{X}) \ge A_{min}, \end{aligned} \tag{1}$$

where $\bar{X}$ is the vector of design parameters $\bar{X} = (X_1, X_2, \ldots, X_N)^T$ specifying the airfoil geometry, C_d is the drag coefficient due to wave drag, C_{d_l} is the prescribed upper limit on wave drag, A is

Third International Conference on Inverse Design Concepts and Optimization in Engineering Sciences (ICIDES-III), Editor: G.S. Dulikravich, Washington D.C., October 23-25, 1991.

ANALYTICAL FORMULATION

TSD Analysis

The first approach taken is based on a TSD formulation. This approach is based on an asymptotic expansion of the perturbation potential in the limits of airfoil thickness $(t/c) \to 0$ and free-stream Mach number $M_\infty \to 1$, *e.g.*, Ref. 12. The governing equation may be written as

$$\left[(1-M_\infty^2)\phi_x - \frac{(\gamma+1)}{2}M_\infty^2\phi_x^2\right]_x + \phi_{yy} = 0\,, \tag{3}$$

with the surface boundary condition on the airfoil surface, $y = Y(x)$ expanded to be

$$\frac{\partial\phi}{\partial y}(x,0) = \frac{dY}{dx}, \qquad 0 \le x/c \le 1\,. \tag{4}$$

It may be noted that the governing equation retains the important non-linear effects of transonic flows but does not include the effects of entropy change across shock waves. Also, since the airfoil surface boundary condition is applied along the axis and not on the actual surface of the airfoil, the calculation can be performed on a simple Cartesian grid. This is useful in the design problem, since we can efficiently utilize a fixed grid even with changing airfoil geometries. The specific analysis code used for our TSD calculations is TSFOIL described in Ref. 13.

Euler Analysis

In order to evaluate whether the design procedures developed using the approximate TSD analysis are valid for more accurate flow field methods, we have investigated the airfoil design with the Euler equations. We utilize the complete set of governing equations for an inviscid, non-heat conducting, adiabatic flow with negligible body forces. The equations may be written in conservation-law form in Cartesian coordinates as

$$\frac{\partial Q}{\partial t} + \frac{\partial F}{\partial x} + \frac{\partial G}{\partial y} = 0, \tag{5}$$

where

$$Q = \begin{pmatrix} \rho \\ \rho u \\ \rho v \\ \rho e_0 \end{pmatrix}, \quad F = \begin{pmatrix} \rho u \\ \rho u^2 + p \\ \rho uv \\ (\rho e_0 + p)u \end{pmatrix}, \quad G = \begin{pmatrix} \rho v \\ \rho uv \\ \rho v^2 + p \\ (\rho e_0 + p)v \end{pmatrix}, \tag{6}$$

with velocity components u, v, density ρ, total energy per unit mass $e_0 = e + (u^2+v^2)/2$, with e being the internal energy per unit mass and pressure p, which for a perfect gas may be expressed as $p = (\gamma-1)[\rho e_0 - \rho(u^2+v^2)/2]$. The surface boundary conditions for the Euler equations, representing no flow through the solid surface may be expressed as

$$v(x, Y) = Y'(x)\,u(x, Y)\,, \qquad 0 \le x/c \le 1\,, \tag{7}$$

where a prime denotes differentiation with respect to x. Thus we see that the boundary conditions must be applied on the actual airfoil geometry, requiring a new mesh to be generated at each stage of the design process. We partially alleviate the computational burden of re-creating the grid for each geometry by assuming that design changes proceed slowly, and for a specified number of cycles consider the grid to be fixed to a baseline airfoil geometry. Then the surface boundary condition must be altered to allow a small amount of mass transpiration through the surface to approximately account for the changing geometry. This procedure fits in well with the sequential approximate optimization algorithm used in the design process, which imposes move limits on the design. For each optimization cycle a baseline geometry will define the grid and the grid will be kept fixed throughout the approximate optimization cycle. This greatly reduces the computational effort for the Euler designs.

Let the subscript b refer to the body surface of the new airfoil and the subscript b_0 refer to the body surface of the baseline airfoil. The exact surface boundary condition on the new airfoil surface is the vanishing of the normal velocity $\vec{V}_b \cdot \hat{n}_b = 0$ or, as in Eq. (7)

$$v_b = Y' u_b\,. \tag{8}$$

Third International Conference on Inverse Design Concepts and Optimization in Engineering Sciences
(ICIDES-III), Editor: G.S. Dulikravich, Washington D.C., October 23-25, 1991.

the airfoil cross-sectional area, non-dimensionalized by c^2, with c the airfoil chord and A_{min} is the minimum required area. The design is performed at a free-stream Mach number of $M_\infty = 0.75$ and zero angle of attack, $\alpha = 0$.

This type of problem has been solved first by Vanderplaats and Hicks[2] with a full potential code, requiring 70 exact analyses. In Ref. 6, the same problem required 44 exact analyses with a sequential optimization technique and data base approach where all the previous design information is stored and reused for constructing higher-order approximations.

Here, we will examine the effects of utilizing two different codes, one a more approximate transonic small-disturbance (TSD) analysis and the second, a more exact inviscid Euler analysis. However, due to the different approximations in the two analyses, particularly the neglect of entropy jumps across the shock waves, the wave drag values are found to be different, with the TSD result at a lower level. In order to develop somewhat similar designs between the Euler and TSD methods it was found necessary to utilize a larger value of C_{d_t} in Eq. (1) for the Euler designs.

Shape functions and Design Variables

We have chosen to design the airfoil using shape functions following the successful implementation of Vanderplaats and Hicks[2]:

$$Y = \sum_{i=1}^{N+2} X_i Y_i \left(\frac{x}{c}\right), \tag{2}$$

where $Y \equiv y/c$ with y being the airfoil ordinate and c the airfoil chord length. The specified shape functions Y_i are functions of the non-dimensional abscissa x/c and the parameters X_i are the design variables. For the shape functions here, we selected four existing airfoils ($N = 4$), namely, $NACA\ 2412$, $NACA\ 64_1-412$, $NACA\ 65_2-415$ and $NACA\ 64_2A215$. There are two additional shape functions for imposing the boundary conditions at the trailing edge of the airfoil. These are $Y_{N+1} = +x/c$ on the upper surface and zero on the lower surface, and $Y_{N+2} = -x/c$ on the lower surface and zero on the upper surface. Usually with TSD analyses an open trailing edge is considered; here we specify this thickness to be .0025c. For Euler analyses a closed trailing edge is utilized. This fixes the values of the coefficients X_{N+1} and X_{N+2} in terms of $X_1, \ldots, X_N$.

Approximate Optimization

When a design optimization is coupled with expensive numerical analysis code, most of the cost of the optimization is associated with the exact analyses and sensitivity calculations. Even with the most efficient transonic flow analysis code, the cost of the design process may be prohibitive if the analysis code and an optimization algorithm are linked together directly, so that full analyses are made for all the function evaluations during the design process. Instead we utilize a sequential approximate optimization algorithm[10]. This approach replaces the original objective function and constraints with approximations based upon nominal values and derivatives at an initial point. Additionally, move limits are used to prevent the design from moving outside the bound of validity of the approximations. Each approximate optimization problem is solved until an optimum is found, and then a new approximation is constructed there, and the design optimization process is repeated until convergence is achieved. An approximate optimization is typically referred to as an optimization cycle, and this is also the terminology used here. A key part of implementing a sequential approximation algorithm involves the approximation of the objective function and constraints. We have found that these approximations play a crucial role in the design process. The procedures that we have developed for approximating the lift and drag appear in detail later in this paper.

The specific optimizer used for our study is the general purpose optimization program NEWSUMT-A[11] which is based on a quadratic extended interior penalty function and Newton method for unconstrained minimization. The program provides the user with several approximation-switching and move limit strategies.

Third International Conference on Inverse Design Concepts and Optimization in Engineering Sciences (ICIDES-III), Editor: G.S. Dulikravich, Washington D.C., October 23-25, 1991.

Now we utilize the grid system which was generated for the baseline airfoil to analyze the flow over the new airfoil. Thus it is necessary to evaluate the new normal and tangential velocities on the baseline airfoil surface Y_0. (The normal velocity on the baseline airfoil $\vec{V}_{b_0} \cdot \hat{n}_{b_0}$ will not be zero). This can be achieved by expanding the Cartesian velocity components at the baseline airfoil surface in terms of the coordinates of the new airfoil surface as

$$v_{b_0} = v_b + (\frac{\partial v}{\partial y})_b (Y - Y_0) + \ldots = v_b + \mathcal{O}(\Delta Y), \tag{9.a}$$

$$u_{b_0} = u_b + (\frac{\partial u}{\partial y})_b (Y - Y_0) + \ldots = u_b + \mathcal{O}(\Delta Y), \tag{9.b}$$

where $\Delta Y = Y - Y_0$. Thus using the boundary condition (8) we have $v_{b_0} = u_b Y' + \mathcal{O}(\Delta Y)$ and $u_{b_0} = u_b + \mathcal{O}(\Delta Y)$. We can write these in terms of normal and tangential velocity components to the baseline geometry as

$$V_{n_{b_0}} = \frac{v_{b_0} - u_{b_0} Y_0'}{\sqrt{1 + Y_0'^2}}, \tag{10}$$

$$V_{t_{b_0}} = \frac{u_{b_0} - v_{b_0} Y_0'}{\sqrt{1 + Y_0'^2}}. \tag{11}$$

Using Eqs. (8)-(11), we can write an expression for $V_{n_{b_0}}$ in terms of $V_{t_{b_0}}$ which takes into account the vanishing of the normal velocity at the new airfoil surface, $V_{n_b} = 0$, as

$$V_{n_{b_0}} = \frac{V_{t_{b_0}}}{1 + Y' Y_0'} (Y' - Y_0'), \tag{12}$$

where terms of $\mathcal{O}(\Delta Y)$ have been neglected.

The boundary conditions for the Euler calculation may be evaluated by extrapolating from the field points to the surface $y = Y_0$ values of ρ_{b_0}, p_{b_0} and u_{b_0} and v_{b_0}. The tangential velocity $V_{t_{b_0}}$ is computed from Eq. (11) and the normal velocity $V_{n_{b_0}}$ from Eq. (12). Values of the total energy are computed from

$$(\rho e_0)_{b_0} = \left[\frac{p_{b_0}}{\gamma - 1} + \frac{\rho_{b_0} (V_{n_{b_0}}^2 + V_{t_{b_0}}^2)}{2} \right]. \tag{13}$$

The specific analysis code used for our Euler calculations is FLOMG which is based on Jameson's time-stepping[14] and multigrid algorithms[15]. Although the code was developed by Swanson and Turkel[16] for solving the Navier-Stokes equations, we will utilize it only in the inviscid, Euler solver mode.

LIFT AND DRAG APPROXIMATIONS

We first considered simple linear approximations for the lift and wave drag, as:

$$f = f^0 + \sum_{i=1}^{4} \frac{\partial f}{\partial X_i} (X_i - X_i^0), \tag{14}$$

where f is either the lift or the wave drag and f^0 is evaluated with the initial design parameters $X_1^0, \ldots, X_4^0$. The sensitivity derivatives, $\partial f / \partial X_i$ are evaluated using one-sided finite-difference expressions. The effectiveness of the lift approximation is indicated in Tables 1a and 1b for both TSD and Euler analysis methods. We see that when the design variables are changed by as much as 2%, the linear approximation of the lift coefficient remains within a 2% accuracy, compared to the exact analysis, for the TSD solutions and to within 0.5% for the Euler solutions. However, this situation is not repeated for the drag approximation. As seen in Tables 1a and 1b the linear approximation for the wave drag does not correlate closely with the exact results, with errors of 25% for the TSD solutions and 15% for the Euler solutions, when the design variables change by 2%. This result

Third International Conference on Inverse Design Concepts and Optimization in Engineering Sciences (ICIDES-III), Editor: G.S. Dulikravich, Washington D.C., October 23-25, 1991.

was not unexpected since transonic flows are very nonlinear and shock-wave movement must play an important role in the wave-drag approximation.

In order to better approximate the wave drag, we considered the method of strained coordinates for perturbations of transonic flows with shock waves, introduced by Nixon[17]. This method has been applied for airfoil approximations by Stahara[18]. In this method, the perturbations are made in a *strained* coordinated system where the shock remains fixed. Coordinate straining uses the axial position of the shock wave on the airfoil, x_s and the height of the tip of the shock wave above the airfoil, y_t. When x_s changes by Δx_s and y_t changes by Δy_t, the coordinates (x, y) of each point in the flow field are changed by Δx and Δy given by

$$\Delta x = s(x)\,\Delta x_s\,, \qquad \Delta y = \frac{y}{y_t}\,\Delta y_t\,. \tag{15a,b}$$

For the TSD analysis, following Ref. 17, the straining function $s(x)$ is taken as

$$s(x) = \frac{x(c-x)}{x_s(c-x_s)}\,, \tag{16}$$

which is valid for $0 \le x \le c$ and is equal to zero otherwise.

For the TSD analysis, the strained coordinates are used first in the process of calculating finite-difference sensitivity derivatives according to the following steps:

1. The i-th design variable is perturbed by ΔX_i and the corresponding Δx_s and Δy_t are calculated from a new solution of the flow field and used to approximate the shock sensitivities

$$\frac{\partial x_s}{\partial X_i} \simeq \frac{\Delta x_s}{\Delta X_i}\,, \qquad \frac{\partial y_t}{\partial X_i} \simeq \frac{\Delta y_t}{\Delta X_i}\,. \tag{17a,b}$$

2. The flow-field sensitivities are approximated, using Δx and Δy from Eqs. (15a,b), in terms of the axial velocity for the nominal design u^0 and the axial velocity for the perturbed flow field u as

$$\frac{\partial u}{\partial X_i}(x,y) = \frac{1}{\Delta X_i}[u(x+\Delta x, y+\Delta y) - u^0(x,y)]\,. \tag{18}$$

The strained coordinates are used again in approximating the flow at a new design point $\tilde{X}$ as follows: First the new shock location and shock-tip position are calculated by a linear approximation

$$\Delta x_s = \sum_{i=1}^{4} \frac{\partial x_s}{\partial X_i}(X_i - X_i^0)\,, \qquad \Delta y_t = \sum_{i=1}^{4} \frac{\partial y_t}{\partial X_i}(X_i - X_i^0)\,. \tag{19a,b}$$

Values of Δx and Δy are calculated from Eqs. (15a,b) and then the axial velocity u is estimated from

$$u(x+\Delta x, y+\Delta y) = u^0(x,y) + \sum_{i=1}^{4} \frac{\partial u(x,y)}{\partial X_i}(X_i - X_i^0)\,. \tag{20}$$

The wave drag coefficient is determined from a contour integral of the jump in pressure across the shock, which may be written as[13]:

$$C_d = -\delta^{5/3} M_\infty^{-3/4} \frac{(\gamma+1)}{\gamma} \int_{shock} [u]^3\, dy\,, \tag{21}$$

where M_∞ is the free-stream Mach number, δ is the nominal airfoil thickness, γ is the ratio of specific heats and $[u]$ is the *jump* in u across the shock.

For the Euler analysis a different implementation of the method of the strained coordinates is utilized. First, since the wave drag is calculated by integrating surface pressures, only the solution at the body surface needs to be approximated. The coordinate straining in y direction is not necessary. Furthermore, accurate solutions for the Euler wave drag were obtained by approximating the surface

Third International Conference on Inverse Design Concepts and Optimization in Engineering Sciences (ICIDES-III), Editor: G.S. Dulikravich, Washington D.C., October 23-25, 1991.

pressures directly, rather than computing from the flow field. Thus the surface pressure sensitivity and approximation, respectively were calculated as

$$\frac{\partial p}{\partial X_i}[x, Y_0(x)] = \frac{1}{\Delta X_i}\left(p[x+\Delta x, Y_0(x+\Delta x)] - p^0[x, Y_0(x)]\right), \tag{22}$$

$$p[x+\Delta x, Y_0(x+\Delta x)] = p^0[x, Y_0(x)] + \sum_{i=1}^{4} \frac{\partial p[x, Y_0(x)]}{\partial X_i}(X_i - X_i^0), \tag{23}$$

where Δx is the amount of coordinate straining and the superscript 0 corresponds to the value for the nominal design. The pressure on the perturbed geometry can be approximated by using Taylor series expansion about this pressure on the baseline geometry and then the wave drag coefficient is determined from the integration of the approximate surface pressure force in x-direction.

The non-uniqueness of the straining function has been discussed in Refs. 17 and 18. Here, several tests were made to select the best straining function in terms of approximation accuracy for the Euler analysis. The linear piecewise continuous straining appeared to be most accurate and well-behaved. This has been also pointed out with the full potential method in Ref. 18. The linear piecewise continuous function is given by

$$s(x) = \begin{cases} x/x_s & ; 0 \le x \le x_s, \\ (c-x)/(c-x_s) & ; x_s \le x \le c, \end{cases} \tag{24}$$

was used, where x_s is the location of shock wave.

The results of Nixon's coordinate-straining approximation on the drag coefficient are tabulated in Tables 1a and 1b. It is seen to significantly improve the wave drag approximation, with the errors reducing to less than 3% for the TSD solutions and 7% for the Euler solutions, when the design variables change by 2%. The effect of this approximation on the airfoil pressure distributions is shown in Figs. 1a and 1b.

DESIGN RESULTS

In this section we consider several optimization strategies for the transonic airfoil design problem of maximizing lift with constraints on wave-drag and airfoil cross-sectional area as given by Eq. (1). The minimum non-dimensional area is taken to be $A_{min} = 0.075$. The wave drag constraint is taken to be $C_{d_l} = 0.004$ for the TSD designs and $C_{d_l} = 0.010$ for the Euler designs.

Designs based on the TSD analysis

Strategy A: Approximate Optimization with Tight Move Limits - The first optimization strategy that we employed consisted of imposing tight move limits in the approximate optimization procedure. The results of applying this strategy with two different initial designs are tabulated in Tables 2a and 2b. In the first case, we imposed 5% move limits in order to keep the error in the drag approximation to within 10%. The solution ceased to improve after 27 iterations and the move limits were tightened to 2.5%. At 60 iterations the move limits were further reduced to 1.25% and the solution was considered to be converged. However, in the second case, corresponding to different initial conditions, employing a similar strategy resulted in a completely different design, as can be seen in Table 2b.

In order to examine whether these solutions were local maxima we considered the following: denoting the first converged solution as $\bar{X}^1$ and the second as $\bar{X}^2$, we defined an intermediate design state

$$\bar{X} = \bar{X}^2 + \xi(\bar{X}^1 - \bar{X}^2), \tag{25}$$

where the parameter ξ may be considered the proportional distance of the intermediate design between $\bar{X}^2$ and $\bar{X}^1$. We computed both approximate and exact value for the lift and wave-drag coefficients for intermediate designs with $0 \le \xi \le 1$. The results are plotted in Fig. 2. From the upper chart in Fig. 2 we see that the lift coefficient is well-behaved between design state 2 and state 1, exhibiting no local maxima or minima. In the lower chart, we see that the culprit is the drag-coefficient constraint, which exhibits a very *wavy* behavior about $C_d = 0.0040$. Thus we can see that if we are a design state 2, the optimizer would prevent you from moving toward state 1, since that would be a direction of increasing drag.

Third International Conference on Inverse Design Concepts and Opumization in Engineering Sciences
(ICIDES-III), Editor: G.S. Dulikravich, Washington D.C., October 23-25, 1991.

Strategy B: Drag Minimization followed by Lift Maximization - The strategy that we found to be useful to avoid the problems associated with the drag constraint consisted of interchanging the role of the drag constraint with the lift objective function: We had noticed that design problems of minimizing drag with a constraint on the lift were well behaved. In order to solve the design problem formulated in this paper, we adopted the following strategy: first the wave-drag coefficient was minimized with a constraint on the lift coefficient of $C_l \geq 0.5$ and cross-sectional area ratio $A \geq 0.075$; then, when C_d was below 0.004 we reverted back to the original design formulation of maximizing C_l with constraints of $C_d \leq 0.004$ and $A \geq 0.075$.

The results of this strategy were very good. We found that during the drag minimization phase, very large move limits, as large as 500% could be used without any adverse effects. During the lift maximization phase, move limits of 20% were imposed. This strategy seemed to be robust, and the solutions did not depend upon the initial data. The design history for the first case, starting from $\bar{X}^0 = (1.0,\ 0.0,\ 0.0,\ 0.0)^T$ is tabulated in Table 3a. The design results for four different initial designs are summarized in Table 3b. In all cases convergence to nearly the same design result was obtained in 8–13 design cycles. The pressure coefficient and corresponding airfoil shape of the initial and final designs tabulated in Table 3a, are shown in Fig. 3. The design appears to be physically reasonable, with a weakened shock wave and lift increased through aft camber.

Strategy C: Approximate Optimization with Absolute Move Limits - After we obtained successful design results using the strategy B, we carefully investigated the TSD solutions to determine the cause of the noisy drag calculation. We found that the spline interpolation routine in the TSFOIL program generated an irregular airfoil leading-edge geometry. Although this should not be important in the TSD solutions, which lose their validity at the leading edge, it clearly affected wave drag calculations and generated noise. We replaced the original routine with a more effective interpolation based on the approximate arc-length of the airfoil with a periodic boundary condition and consequently was able to generate fairly smooth and round noses.

Next, we attempted to directly maximize the lift with tight move limits using the new geometry interpolations. The design process behaved much better due to the considerably reduced noise in the wave drag, even though the noise was not removed completely. We felt that we should increase the move limits in order to get faster convergence. We also found that we could produce reasonably efficient designs using move limits which were fixed absolute values rather than percentages of the design variables. By several tests, we found that initially 0.5 could be used without any adverse effect and then it was reduced by half when the design did not make any improvement. The design results using this procedure are tabulated in Tables 4a and 4b. We experienced some convergence difficulties with TSFOIL using this approach. We will examine this strategy in more detail with the Euler analysis method.

For the TSD designs, each exact airfoil analysis using the program TSFOIL required 10–15 CPU seconds on the IBM 3090 at V. P. I. & S. U., with N+1(5) analyses needed per design cycle. The approximate optimization using the program NEWSUMT-A required 10–12 CPU seconds on the same computer.

Designs based on the Euler analysis

On the basis of the TSD design experience, we applied the two successful design strategies, B and C to the same design problem with the Euler analysis. Recall that the wave-drag constraint value was changed to 0.01 for the Euler design due to the differences in wave drag prediction between the TSD and Euler methods. The original value of 0.004 was found to be too stringent for the design problem with the Euler analysis.

Strategy B: Drag Minimization followed by Lift Maximization - Table 5a represents the complete design history for the first case, starting from $\bar{X}^0 = (1.0,\ 0.0,\ 0.0,\ 0.0)^T$. In the lift maximization phase, initially 50% move limits were utilized, which yielded a large improvement in the lift coefficient to a value of $C_l = 0.7136$ for the first 8 iterations. After that we reduced move limits by half twice and then finally we imposed very tight move limits of 2% which after 25 iterations resulted in $C_l = 0.7144$. For the purposes of this study, we consider the design achieved after 8 iterations, corresponding to the 50% move limits to be acceptable as a final design. The equivalent value of C_l in the table is the relevant estimated lift coefficient when all of the violated constraints are brought to be critical.

Third International Conference on Inverse Design Concepts and Optimization in Engineering Sciences (ICIDES-III), Editor: G.S. Dulikravich, Washington D.C., October 23-25, 1991.

Lagrange multipliers are used to estimate these equivalent lift coefficients since they represent the amount of change in the objective function due to the unit change in a constraint at an optimum. This provides us information whether the design makes true improvement or not. We found that this strategy was as robust and efficient for the design based on the Euler method as it was for the TSD method. As shown in Table 5b, four different initial conditions yielded nearly the same final design in 10–12 design cycles. The pressure distributions and corresponding airfoil shapes of the initial and final designs are shown in Fig. 4.

Strategy C: Lift Maximization with Absolute Move Limits - The complete design history for the first case with strategy C is tabulated in Table 6a. Here also, we consider the design achieved after 9 iterations, corresponding to the 0.5 move limits to be acceptable as a final design. Table 6b represents the summary of the design results for four different cases. All cases did converge to approximately the same design result in 8–10 global iterations.

For the Euler designs, each exact airfoil analysis using the program FLOMG required approximately 40 CPU seconds on the CRAY 2S at NASA Langley. The approximate optimization using the program NEWSUMT-A required 40–60 CPU seconds on the IBM 3090 at V. P. I. & S. U. The additional computer time associated with the approximate optimization of the Euler design is partly related to the more complicated wave drag calculation compared to that used for the TSD design.

Error Magnification during Optimization

Table 7 compares the lift/wave drag ratios predicted by TSD and Euler methods for the four airfoils used in the shape definition and the optimum TSD airfoil. It is seen that the agreement between TSD and Euler is much poorer for the optimized airfoil. This indicates that there may be a risk associated with optimization based on an approximate method. The optimization procedure may "improve" the design by exploiting the weaknesses of the approximation.

CONCLUSIONS

We have considered numerical optimization procedures for the design of transonic airfoils based on the transonic small-disturbance (TSD) and Euler equations. A sequential approximate optimization procedure was implemented with accurate approximation of the wave drag based on the Nixon's coordinate straining technique. A modification of the surface boundary conditions was utilized in order to efficiently compute sensitivity derivatives without remeshing the grid with the Euler analysis.

The airfoil design problem which we considered consisted of maximizing the lift with constraints on the wave drag and area. We found that when the computed drag did not vary smoothly with the design parameters, the optimization process produced local extrema. A procedure interchanging the role of the objective function and constraint, initially minimizing drag with a constraint on the lift was found to be effective in producing converged designs. This procedure was also proven to be robust and efficient for cases where the drag varied smoothly, such as with the Euler solutions. The direct lift maximization with move limits which were fixed absolute values of the design variables, was also found to be a reliable and efficient procedure for designs based upon the Euler equations.

ACKNOWLEDGEMENT

We wish to thank Dr. R. C. Swanson of NASA Langley Research Center for providing us with access to FLOMG, and consulting with us on the use of the code. We also thank Dr. W. H. Mason of V. P. I. & S. U. for his helpful comments. This research was supported by NSF grant DMC-8615336.

REFERENCES

1. Volpe, G. and Melnik, R. M., "The Design of Transonic Airfoils by a Well-posed Inverse Method", *Int'l. Journal for Numerical Methods in Engineering*, **22**, 1986, pp. 341–361.
2. Vanderplaats, G. N. and Hicks, R. M., "Numerical Airfoil Optimization Using a Reduced Number of Design Coordinates", NASA TM X-73151, July 1976.
3. Giles, M., Drela, M. and Tompkins, W. T. Jr., "Newton Solution of Direct and Inverse Transonic Euler Equations", AIAA Paper No. 85-1530, Jan. 1985.

Third International Conference on Inverse Design Concepts and Optimization in Engineering Sciences (ICIDES-III), Editor: G.S. Dulikravich, Washington D.C., October 23-25, 1991.

4. Malone, J. B., Narramore, J. C. and Sankar, L. N., "An Efficient Airfoil Design Method Using the Navier-Stokes Equations", in *Computational Methods for Aerodynamic Design (Inverse) and Optimization*, AGARD CP-463, 1990, pp. 5.1–5.18.
5. Aidala, P. V., Davis, W. H. Jr. and Mason, W. H., "Smart Aerodynamic Optimization", AIAA Paper No. 83–1863, July 1983.
6. Vanderplaats, G. N., "Approximation Concepts for Numerical Airfoil Optimization", NASA TP 1370, 1979.
7. Joh, C.-Y., Grossman, B. and Haftka, R. T., "Efficient Optimization Procedures for Transonic Airfoil Design", proceedings ASME Winter Annual Meeting, AD–**16**, *Computational Structural Mechanics and Multidisciplinary Optimization*, editors: Grandhi, Stroud and Venkayya, Book No. H00534, Dec. 1989, pp. 67–76.
8. Joh, C.-Y., "Efficient and Robust Design Optimization of Transonic Airfoils", Ph.D. dissertation, Aerospace and Ocean Engineering, Virginia Polytechnic Inst. & State Univ., May 1991.
9. Grossman, B., Haftka, R. T., Kao, P.-J., Polen, D. M., Rais-Rohani, M. and Sobieszczanski-Sobieski, J. "Integrated Aerodynamic-Structural Design of a Transport Wing", *J. Aircraft*, **27**, No. 12, 1990, pp. 1050–1056.
10. Schmit, L. A. and Farshi, B., "Some Approximation Concepts for Structural Synthesis", *AIAA J.*, **12**, No. 7, 1974, pp. 692–699.
11. Grandhi, R.V., Thareja, R. and Haftka, R.T., "NEWSUMT-A: A General Purpose Program for Constrained Optimization using Constraint Approximations," *ASME Journal of Mechanisms, Transmissions and Automation in Design*, **107**, 1985, pp. 94–99.
12. Spreiter, J. R., "Transonic Aerodynamics–History and Statement of the Problem", Chapter 1 in *Transonic Aerodynamics*, **81**, Progress in Astronautics and Aeronautics, D. Nixon, Ed., AIAA, New York, 1982, pp. 3–66.
13. Murman, E. M., Bailey, F. R., and Johnson, M. H., "TSFOIL - A Computer Code for 2-D Transonic Calculations, Including Wind-Tunnel Wall Effects and Wave-Drag Evaluation", in NASA SP-347, Part II, 1975, pp. 769–788.
14. Jameson, A., Schmidt, W. and Turkel, E., "Numerical Solution of the Euler Equations by Finite Volume Methods Using Runge-Kutta Time Stepping Schemes", AIAA Paper No. 81-1259, June 1981.
15. Jameson, A., "Solution of the Euler Equations for Two Dimensional Transonic Flow by a Multigrid Method", *Applied Mathematics and Computation*, **13**, 1983, pp. 327–355.
16. Swanson, R. C. and Turkel, E., "A Multistage Time-Stepping Scheme for the Navier-Stokes Equations", AIAA Paper No. 85-0035, Jan. 1985.
17. Nixon, D., "Perturbation of a Discontinuous Transonic Flow", *AIAA Journal*, **16**, No. 1, 1978, pp. 47–52.
18. Stahara, S. S., "A Rapid Approximation Procedure for Nonlinear Solutions: Application to Aerodynamic Flows and Design/Optimization Problems", Chapter 18 in *Transonic Aerodynamics*, **81**, Progress in Astronautics and Aeronautics, D. Nixon, Ed., AIAA, New York, 1982.

change*	Lift Coeff.		Drag Coeff.		
%	Linear	Exact	Linear	Coord-St.	Exact
0.0		0.5341			0.00511
0.5	0.5472	0 5471	0 00584	0 00579	0.00585
-0.5	0.5210	0.5216	0.00439	0.00447	0.00436
1 0	0.5602	0.5614	0.00656	0.00654	0.00657
-1.0	0.5080	0 5098	0.00367	0.00396	0.00400
1.5	0.5733	0 5762	0 00728	0.00736	0.00755
-1.5	0 4949	0.4987	0.00295	0.00346	0.00342
2.0	0.5864	0 5918	0.00800	0.00827	0.00845
-2.0	0.4818	0.4881	0.00223	0 00302	0.00295

* Design variables increased by specified percentage from $(0.5, 0.5, -0\,5, 0.5)^T$

Table 1a. Lift and Drag Approximations - TSD.

change*	Lift Coeff.		Drag Coeff.		
%	Linear	Exact	Linear	Coord-St.	Exact
0 0		0.4878			0.00787
0 5	0.4948	0 4942	0.00866	0.00870	0.00854
-0.5	0 4809	0 4813	0.00708	0 00718	0.00724
1.0	0.5016	0.5006	0.00946	0 00957	0.00923
-1.0	0.4737	0 4749	0.00628	0.00652	0.00664
1.5	0.5086	0 5070	0.01029	0.01049	0.00996
-1 5	0 4667	0 4685	0.00549	0.00590	0 00607
2.0	0 5153	0 5135	0 01104	0.01149	0 01072
-2 0	0.4598	0 4621	0.00470	0.00533	0 00553

* Design variables increased by specified percentage from $(0.5, 0.5, -0.5, 0.5)^T$.

Table 1b. Lift and Drag Approximations - Euler.

Third International Conference on Inverse Design Concepts and Optimization in Engineering Sciences (ICIDES-III), Editor: G.S. Dulikravich, Washington D.C., October 23-25, 1991.

Design cycle	Design Parameters				C_l	C_d	A
	X_1	X_2	X_3	X_4			
0	0.5	0.5	-0.5	0.5	0.5296	0.0059	0.0805
1	0.510	0.498	-0.524	0.490	0.4954	0.0040	0.0779
-	—	—	—	—	—	—	—
27	0.400	0.750	-0.649	0.481	0.5385	0.0040	0.0750
-	—	—	—	—	—	—	—
60	0.301	0.891	-0.763	0.565	0.5542	0.0040	0.0750
-	—	—	—	—	—	—	—
71	0.280	0.934	-0.805	0.591	0.5592	0.0040	0.0750

Table 2a. TSD Design Strategy A : Approximate Optimization with Tight Move Limits – initial condition 1.

Design cycle	Design Parameters				C_l	C_d	A
	X_1	X_2	X_3	X_4			
0	0.8	-0.4	0.7	-0.3	0.4418	0.0061	0.0739
1	0.837	-0.426	0.659	-0.281	0.4081	0.0038	0.0729
-	—	—	—	—	—	—	—
9	1.093	-0.483	0.504	-0.273	0.4061	0.0041	0.0750
-	—	—	—	—	—	—	—
11	1.114	-0.487	0.491	-0.275	0.4049	0.0040	0.0750
-	—	—	—	—	—	—	—
15	1.122	-0.487	0.487	-0.277	0.4055	0.0040	0.0750

Table 2b. TSD Design Strategy A : Approximate Optimization with Tight Move Limits – initial condition 2.

Design cycle	Design Parameters				C_l	C_d	A
	X_1	X_2	X_3	X_4			
0	1.0	0.0	0.0	0.0	0.5656	0.0103	0.0822
1	1.024	0.100	-0.075	-0.096	0.5195	0.0054	0.0750
2	0.773	0.280	-0.244	0.137	0.5041	0.0038	0.0750
3	0.631	0.417	-0.393	0.295	0.4999	0.0032	0.0750
4	0.504	0.516	-0.476	0.404	0.4989	0.0028	0.0750
5	0.418	0.650	-0.648	0.542	0.5005	0.0025	0.0750
6	0.071	1.038	-1.072	0.945	0.5080	0.0017	0.0750
7	0.080	1.308	-1.614	1.261	0.5124	0.0011	0.0750
8	0.001	1.475	-1.938	1.516	0.5049	0.0006	0.0750
*9	0.001	1.770	-1.863	1.215	0.6696	0.0034	0.0750
10	0.001	1.876	-1.940	1.209	0.7078	0.0041	0.0750

* begin lift maximization.

Table 3a. TSD Design Strategy B : Drag Minimization followed by Lift Maximization – initial condition 1.

case	Design Parameters				C_l	C_d	A	design cycles
	X_1	X_2	X_3	X_4				
1	1.0	0.0	0.0	0.0	0.5656	0.0103	0.0822	
	0.001	1.876	-1.940	1.209	0.7078	0.0041	0.0750	10
2	0.0	1.0	0.0	0.0	1.0676	0.0459	0.0771	
	-0.025	1.878	-1.889	1.179	0.7149	0.0042	0.0750	8
3	0.0	0.0	0.8	0.0	0.6491	0.0297	0.0786	
	0.043	1.904	-2.068	1.279	0.7034	0.0041	0.0750	13
4	0.0	0.0	0.0	1.0	0.5534	0.0242	0.0996	
	-0.006	1.923	-2.033	1.270	0.7091	0.0040	0.0750	10

Table 3b. TSD Design Strategy B : Drag Minimization followed by Lift Maximization – summary of designs with various initial conditions.

Design cycle	Design Parameters				C_l	C_d	A
	X_1	X_2	X_3	X_4			
0	1.0	0.0	0.0	0.0	0.5656	0.0103	0.0822
1	1.123	0.347	-0.491	0.041	0.5594	0.0061	0.0750
2	0.640	0.524	-0.452	0.263	0.5450	0.0043	0.0750
3	0.518	0.881	-0.844	0.473	0.5966	0.0045	0.0750
4	0.032	1.257	-1.000	0.737	0.6407	0.0044	0.0750
5	0.155	1.381	-1.249	0.785	0.6649	0.0046	0.0750
6	-0.006	1.524	-1.374	0.929	0.6672	0.0041	0.0750
7	-0.099	1.667	-1.504	1.024	0.6853	0.0041	0.0750
8	-0.224	1.916	-1.752	1.179	0.7218	0.0041	0.0750

Table 4a. TSD Design Strategy C : Approximate Optimization with Absolute Move Limits – initial condition 1.

case	Design Parameters				C_l	C_d	A	design cycles
	X_1	X_2	X_3	X_4				
1	1.0	0.0	0.0	0.0	0.5656	0.0103	0.0822	
	-0.224	1.916	-1.752	1.179	0.7218	0.0041	0.0750	8
2	0.0	1.0	0.0	0.0	1.0676	0.0459	0.0771	
	-0.332	2.035	-1.841	1.264	0.7360	0.0040	0.0750	8
3	0.0	0.0	0.8	0.0	0.6491	0.0297	0.0786	
	-0.539	2.340	-2.069	1.423	0.7922	0.0041	0.0753	8
4	0.0	0.0	0.0	1.0	0.5534	0.0242	0.0996	
	-0.434	2.077	-1.749	1.224	0.7638	0.0042	0.0750	5

Table 4b. TSD Design Strategy C : Approximate Optimization with Absolute Move limits – summary of designs with various initial conditions.

Third International Conference on Inverse Design Concepts and Optimization in Engineering Sciences (ICIDES-III), Editor: G.S. Dulikravich, Washington D.C., October 23-25, 1991.

Move Limits	Design cycle	Design Parameters X_1	X_2	X_3	X_4	C_l	C_d	A	** $C_{l_{eqv}}$
500%	0	1.0	0 0	0.0	0 0	.48912	.011768	0.0810	
	1	0.827	0.100	0.094	-0.088	.49602	.009069	0.0750	
	2	0.555	0.331	-0.108	0.157	.49838	.007961	0.0750	
	3	0.325	0 558	-0.346	0.405	.49742	.006879	0.0750	
	4	-0.313	1 150	-0.923	1.040	.49438	.005745	0.0750	
50%	*5	-0.270	1.645	-1.231	0.927	65665	.009951	0.0750	
	6	-0 375	1.924	-1.549	1.110	.68561	.009783	0.0750	
	7	-0.480	2.067	-1.665	1.200	.70255	.010024	0.0750	
	Δ8	-0.632	2.218	-1.777	1.319	.71358	.010223	0.0750	.70617
	9	-0.721	2.277	-1 822	1.390	.71068	.010204	0 0750	.70358
25%	10	-0.679	2.252	-1 822	1.375	.70759	.010026	0.0750	.70669
	Δ11	-0 729	2.303	-1.870	1.425	.70838	.010026	0 0750	.70746
	12	-0 792	2.350	-1 905	1 474	.70806	.010084	0.0750	.70484
12.5%	13	-0.729	2.295	-1 860	1.421	70698	.010019	0.0750	70660
	14	-0.721	2.302	-1.877	1.426	.70759	.009973	0 0750	.70864
	15	-0.717	2.307	-1.885	1.426	70899	.009979	0 0750	70980
		-	-	-	-	-	-	-	-
	22	-0.719	2.344	-1.931	1.446	.71384	.009999	0 0750	.71388
	23	-0.725	2.351	-1.939	1.452	.71404	.010001	0.0750	.71402
	24	-0 736	2.365	-1 954	1 465	.71427	009998	0 0750	71435
	25	-0.736	2.365	-1.953	1.465	.71439	.010002	0.0750	.71432

* begin lift maximization.
Δ starting point for reduced move limits.
** $C_{l_{eqv.}}$: Equivalent Value of C_l.

Table 5a. Euler Design Strategy B : Drag Minimization followed by Lift Maximization - initial condition 1.

case	Design Parameters X_1	X_2	X_3	X_4	C_l	C_d	A	design cycles
	1.0	0.0	0.0	0.0	0.4891	0.0118	0.0810	
1	-0.670	2.266	-1.837	1.371	0.7129	0.0101	0.0750	11
	0.0	1.0	0.0	0.0	0.6977	0.0266	0.0759	
2	-0.640	2.233	-1.801	1.337	0.7127	0.0101	0.0750	11
	0.0	0.0	1.0	0.0	0.5050	0.0467	0.0967	
3	-0.649	2.237	-1.803	1.344	0.7121	0.0101	0.0750	12
	0.0	0.0	0.0	1.0	0.3558	0.0165	0.0984	
4	-0.630	2.206	-1.772	1.322	0.7090	0.0101	0.0750	10

Table 5b. Euler Design Strategy B : Drag Minimization followed by Lift maximiation - summary of designs with various initial conditions.

case	Design Parameters X_1	X_2	X_3	X_4	C_l	C_d	A	design cycles
	1.0	0.0	0.0	0.0	0.4891	0.0118	0.0810	
1	-0.605	2.159	-1.722	1.288	0.7051	0.0101	0.0750	9
	0.0	1.0	0.0	0.0	0.6977	0.0266	0.0759	
2	-0.636	2.194	-1 759	0.323	0.7055	0.0101	0.0750	8
	0.0	0.0	1.0	0.0	0.5050	0.0467	0.0967	
3	-0.650	2.208	-1.774	1.339	0.7049	0.0100	0.0750	10
	0.0	0.0	0.0	1.0	0.3558	0.0165	0.0984	
4	-0 664	2.255	-1.833	1.372	0.7090	0.0101	0.0750	9

Table 6b. Euler Design Strategy C . Approximate Optimization with Absolute Move limits - summary of designs with various initial conditions.

Move Limits	Design cycle	Design Parameters X_1	X_2	X_3	X_4	C_l	C_d	A	** $C_{l_{eqv}}$
0.5	0	1.0	0 0	0 0	0.0	.48912	.011768	0 0810	
	1	0 652	0.500	-0.220	0.057	.56529	.010919	0.0750	
	2	0.239	1.000	-0.672	0 455	.60127	.010031	0.0750	
	3	0.071	1.267	-0.923	0.634	62789	.009978	0.0750	
	4	-0 078	1.470	-1.098	0.772	64813	.010042	0 0750	
	5	-0.227	1 635	-1.227	0.894	.66244	.010129	0.0750	
	6	-0.341	1.792	-1.380	1.018	67371	.009992	0.0750	
	7	-0.434	1.956	-1 553	1.137	.68770	009898	0.0750	
	8	-0.514	2.082	-1.675	1.226	69950	009951	0 0750	
	Δ9	-0 605	2.159	-1.722	1.288	70507	010117	0 0750	70143
	10	-0 677	2.199	-1 749	1 342	70144	010089	0 0750	69855
0.25	11	-0 665	2 232	-1.805	1 362	70542	009989	0 0750	70581
	12	-0 721	2.292	-1 858	1.415	70795	010031	0 0750	70684
	Δ13	-0 768	2.340	-1 907	1.465	70768	010012	0 0750	.70723
	14	-0.811	2.367	-1.924	1 495	70710	010064	0 0750	70464
0.125	Δ15	-0.784	2.360	-1.931	1 486	70734	.009989	0.0750	.70776
	16	-0.810	2.379	-1.942	1.504	70790	010040	0.0750	.70632
0.02	17	-0 778	2 365	-1 942	1 488	70809	009970	0.0750	.70932
		-	-	-	-	-	-	-	-
	29	-0 790	2.415	-2.005	1.521	71310	009997	0 0750	71323
		-	-	-	-	-	-	-	-
	35	-0.804	2.435	-2.028	1.540	.71336	.009998	0.0750	.71345
	36	-0.807	2.438	-2.032	1.543	.71343	.010000	0.0750	.71339

Δ starting point for reduced move limits.
** $C_{l_{eqv.}}$: Equivalent Value of C_l.

Table 6a. Euler Design Strategy C : Approximate Optimization with Absolute Move Limits - initial condition 1.

Airfoils	$C_l/C_{d_{wave}}$	
	TSD Anaysis	Euler Analysis
Airfoil 1	54.9	41.4
Airfoil 2	23.3	26.2
Airfoil 3	21.9	23.9
Airfoil 4	22.9	21.6
Optimized, TSD	171.0	83.4

Table 7. Error Maginification during Optimization.

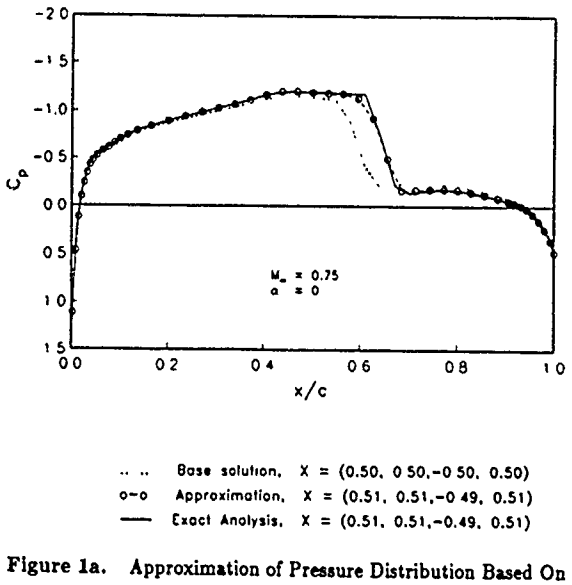
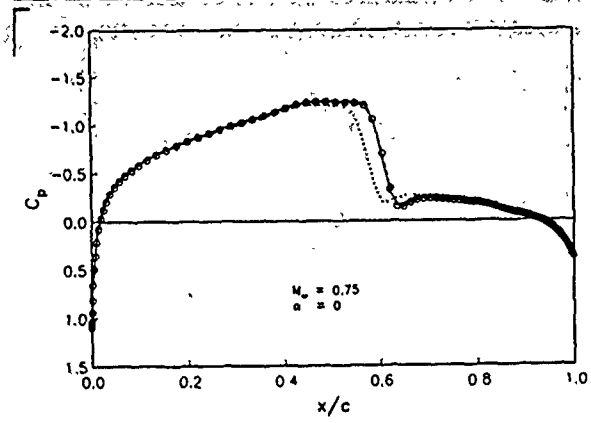


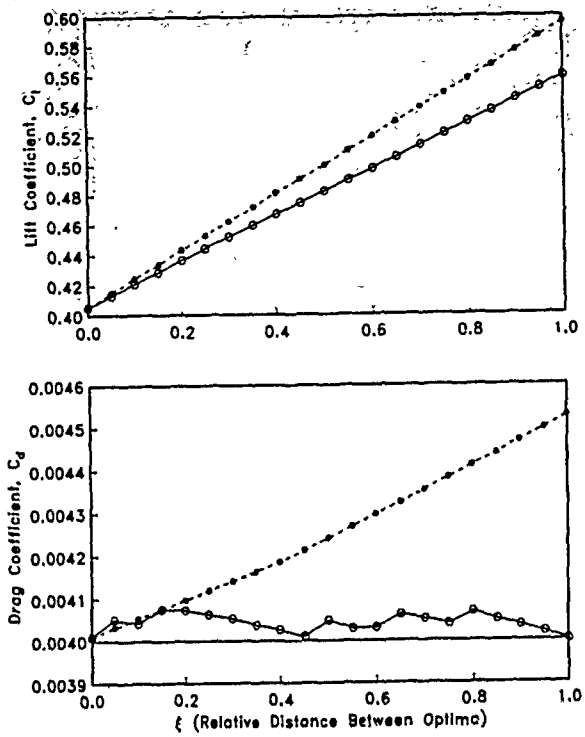
Figure 1a. Approximation of Pressure Distribution Based On the Method of Strained Coordinates - TSD.

Third International Conference on Inverse Design Concepts and Optimization in Engineering Sciences (ICIDES-III), Editor: G.S. Dulikravich, Washington D.C., October 23-25, 1991.



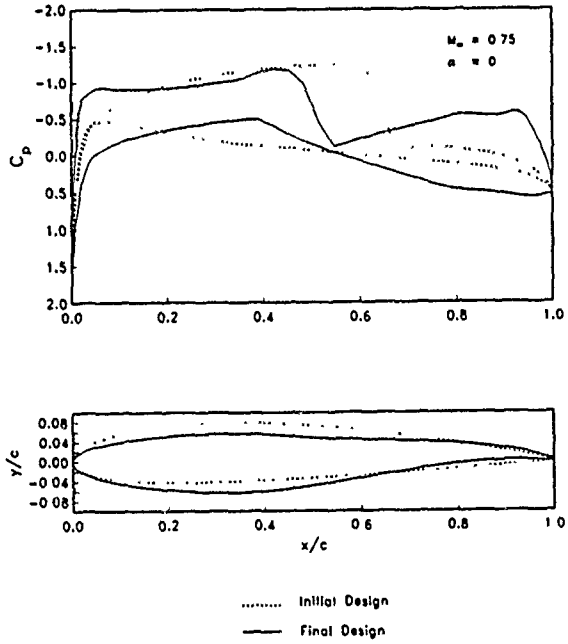
..... Base solution, X = (0.50, 0.50,-0.50, 0.50)
o-o Approximation, X = (0.51, 0.51,-0.49, 0.51)
—— Exact Analysis, X = (0.51, 0.51,-0.49, 0.51)

Figure 1b. Approximation of Pressure Distribution Based On the Method of Strained Coordinates – Euler.



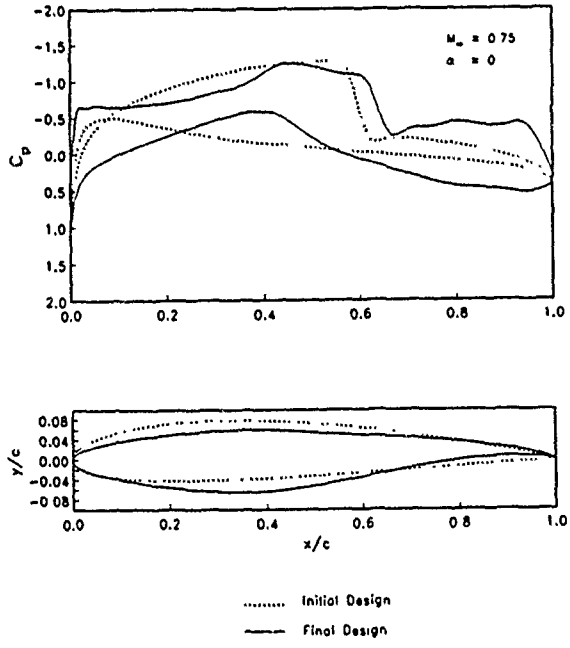
—o— Exact Value
--•-- Approximate Value

Figure 2. Objective Function and Constraint Behavior for Two TSD Local Optima.



..... Initial Design
—— Final Design

Figure 3. TSD Design Results



..... Initial Design
—— Final Design

Figure 4. Euler Design Results

Third International Conference on Inverse Design Concepts and Optimization in Engineering Sciences (ICIDES-III), Editor: G.S. Dulikravich, Washington D.C., October 23-25, 1991.

IDENTIFICATION OF DYNAMIC CHARACTERISTICS OF FLEXIBLE ROTORS AS DYNAMIC INVERSE PROBLEM

W.P.Roisman, L.D.Vajingortin
Khmelnitsky Technological Institute, USSR.

In this work the problem of dynamic and balancing of flexible rotors were considered, wich problems were set and solved as the problem of the identification of flexible rotor systems, or which is the same, the inverse problem of the oscillation theory dealing with the task of the identifying the outside influences and system parameters on the basis of the law of motion known. This approach to the problem allows to disclose the picture of disbalances throughout the rotor-under-test (something that traditional method of flexible rotor balancing, based on natural oscillations, could not provide), and identify dynamic characteristics of the system, which correspond to a selected mathematical model. Eventually, various methods of balancing were developed depending on the special features of the machines as their design, technology and operation specifications. Also, theoretical and practical methods are given for the flexible rotor balancing at far-from-critical rotation frequences, which methods do not necessarily require to know forms of oscillation, dissipation and elasticity-and-inertia characteristics, and to use testing masses.

1. INTRODUCTION

The universal trend of reducing weight and gabarits of flying device engines along with high power requirements has paved way for the wide-spread application of flexible rotors and non-rigid supports. For these types of rotors, dynamics problem dealing, whith the elimination of dangerous resonance states in the area of operating rotation frequences of the machine, becomes vital. For machines under development, which do not have any well-proven analogs it is hardly possible to evaluate in terms of quantity such characteristics as inertia, rigidity and damping capability judging only by the drawing of the machine, for every one of construction elements comes simultaneously as a mass and rigidity, a source of both exiting and extinguishing vibrations, and the assumption of rotor non-deformity is no more valid. This brings us to the point where principally new balancing, technique and dynamic research are required. Now, a good deal of experimental methods are known, which allow to more precisely evaluate the elasticity-and-inertia parameters, deflection curves and rotation frequences while finishing the machine. However, these methods can not always take into account the diversity of influencing factors and dynamic model of the system. In the meanwhile, it is the task of a vital importance to find accurate values of the said parameters, corresponding to the selected mathematical model, thus making this model more effective. Finding values of these parameters for subsequent ascertaining the deflection curve forms and rotation frequences is an extremely important stage of realization of the most balancing methods.

It is well known that now close attention has been given to the problem of development of mathematical or dynamic models of higher accuracy, which models have to reflect real objects, and as many of their real features as possible. However, no calculation scheme can fully reflect the set of properties of the real object (through the vast number of these properties), but it is possible to make them close to reality. Any mathematical models are under risk of being compromized, whatever close they might be to reality, if precisely dynamic characteristics of the machine are unknown. Therefore, identification methods are required, allowing to determine dissipation and elasticity-and-inertia characteristics of the machine on the basis of appropriate experiments, the sought-for parameters being calculated with regard for all more or less

Third International Conference on Inverse Design Concepts and Optimization in Engineering Sciences (ICIDES-III), Editor: G.S. Dulikravich, Washington D.C., October 23-25, 1991.

important peculiarities of the machine. By practicing these methods we can escape the necessity for particularizing and analyzing every one of the machine's characteristics. Parameters thus identified are all the more valuable due to the fact that they were defined with regard to the selected idealization of the real object, that is the said parameters were reduced to the selected dynamic model describing the real system. Whether the selected dynamic model is adequate to the real model and whether identified parameters are sufficiently accurate, one can judge by how much measurred parameters of the real object differ from those calculated in accord with the identified parameters. Critical rotation frequences, deflection curve forms, peaks of vibration et cetera can serve as those criterion parameters. Plus, methods of identification can be used to set the distribution of unbalances along the rotor axis. As the rotor eccentricities are included in the equations for disturbed motion of the rotor, it is possible to create identification algorithms of elasticity-and-inertia and dissipation characteristics along with the rotor eccentricities at the same time. The theory of flexible rotor balancing pays much attention to the problem of computing the values of discrete correcting masses for rotors with pre-set unbalanse, while the angular and linear values of the unbalance itself were half-neglected. In the meanwhile, it is obvious that one has to know the unbalance before getting to the task of finding solution to the set of problems dealing with dynamic strength.

2. METHODS OF BALANCING AND IDENTIFICATION OF DYNAMIC CHARACTERISTICS OF FLEXIBLE ROTORS

Taking into account rotor flexibility allows to state and solve very important (although more complicated) problems which were beyond the rigid rotor method possibilities, and first of all it allows to find eccentricities of any masses placed along the rotor axis. But unbalance is not the value to be directly measured, instead it has to be calculated through some other directly measured magnitudes connected with the former one by unknown operators. Hence, it is evident that the only way to find the flexible rotor unbalances lies through their identification on the results of operating testing of the machine or any emulating testing. It is noteworthy that along with unbalances, elasticity-and-inertia and dissipation characteristics as well as all other characteristics of the identification algorithm can be identified. As practice demonstrated, complex structure rotors being tested at critical frequences get deformed in three-dimensional manner rather than in two-dimensional one, so that the orthogonality conditions are not valid for them. Therefore, it is necessary to develop balancing methods on the basis of real deformations at critical frequences. But, as the critical frequency operation is not safe and it can affect the strength and life of the construction, it is desirable to develop balancing methods on natural curve form of the rotor, but at non-critical friquences and with the restricted number of start-ups. There are sertain types of machines which require balancing only under operation mode with unchanging frequency value, while others have to be balanced over the full frequency range. For each case, individual and economically effective balancing methods and approaches can be employed. Far from all structures would permit the attaching of testing masses. For such types of machines it is necessary to employ balancing methods free from testing unbalances. As it is connected with considerable difficulties to obtain complex object's natural oscillation forms, one should permanently search for the balancing methods not requiring the said oscillation forms.

Certain types of designs allow deflection measuring, while other reject the possibility absolutly. Therefore, balancing methods are needed, resting on the deflection measuring and support reactions, housing vibrations et cetera.

Finally, in a number of cases a method is necessary which combines all above-mentioned methods, that is when there is no need to know curve forms and

Third International Conference on Inverse Design Concepts and Optimization in Engineering Sciences (ICIDES-III), Editor: G.S. Dulikravich, Washington D.C., October 23-25, 1991.

oscillation frequences or to work at critical frequences of rotor rotation, or to use testing masses and additional start-ups, or even to know riqidity, mass or demping parameters of the rotor - one has only to measure general weight and external geometric dimensions.

The above-stated material proves a necessity for variuos methods of flexible rotor balancing depended on specific designing, productive, operating, economic and other features.

Identification algorithms of rotor characteristics of mass and reqidity as well as their eccentricities were attained on the basis of solutions for the differential and integral equations of the oscillations, such as Fredholm's equations of the 2-nd kind [1], giving a description of non-balanced rotor motion, the rotor having an arbitrary mass-and-rigidity distribution law.

$$y(z)=\omega^2\cdot\int_0^L m(s)\cdot\alpha(z,s)\cdot(y(s)+e(s))ds-\omega^2\cdot\int_0^L I(s)\cdot B(z,s)\cdot(y'(s)+\varepsilon(s))ds, \qquad (1)$$

$$y'(z)=\omega^2\cdot\int_0^L m(s)\cdot\gamma(z,s)\cdot(y(s)+e(s))ds-\omega^2\cdot\int_0^L I(s)\cdot\delta(z,s)\cdot(y'(s)+\varepsilon(s))ds,$$

where $y(z)$, $y'(z)$ - is, respectively, deflection and turning angle of coordinate z cross-section of the rotor, $y(s)$, $y'(s)$, $m(s)$, $I(s)$, $e(s)$, $\varepsilon(s)$ is, recpectively, deflection and angle of turning, linear mass, moment of inertia, radial and angular eccentricities of the coordinate s cross-section of rotor $L,\omega,\alpha,B,\gamma,\delta$ - respectively, the length, anqular speed, and influence functions.

Two ways are suggested in respect of the search for solution to these equations. The first one is to approximize the equations with a system of linear equations, which are convenient for decription of the motion of rotors with discrete parameters, while the second way is excellent for description of rotors with distributed parameters using Gilbert-Shmidt theorem for accomplishing expansion in a series witn respect to deflection forms of some parameters. Both ways of finding the solution would lead you to the balancing methods resting on natural form of deflection at critical rotation frequences. The difference between them is that the second way is usable after some restrictions being imposed upon the distribution function,making the said expansion possible, while the first way is free from these restrictions, and therefore it covers a wider range of rotor types.

2.1. TESTING MASS BALANCING

There exists more general solution. Taking into account that a defection at any rotation frequences can be represented by the sum of deflections (which deflections are multiplyed by some constant factors), it is possible to employ the method of balancing on natural deflection forms at any other rotation frequency at which the rotor deflection can be detected; and doing this you can use a single testing mass system whith a singe start-up of the machine.

Really, carring out the rotor deflection measurments at far-from-critical frequences (first measurment is made on the rotor with initial unbalance, the second one-on the rotor with testing unbalances system whose eccentricities are similar to the measured elasticity line of the rotor) and accomplishing the expansion of these deflections and eccentricities in series, you can find the components of eccentricities of the counterbalances, and the whole system e(z). As balancing frequences are subjected to no restrictions except for as indicators of the rotor deformity, this common method when particularized by critical frequences, turns into well-known balancing method at critical frequences.

In those cases when natural deflection forms of a rotor are not known, the received information can be processed by means of expansion in series related to

Third International Conference on Inverse Design Concepts and Optimization in Engineering Sciences (ICIDES-III). Editor: G.S. Dulikravich. Washington D.C. October 23-25, 1991.

any orthonormal system of fuctions such as sine series as shown below:

$$y(z)=\frac{A_0}{2}+\sum_{k=1}^{n}A_k\cdot\sin\frac{\pi kz}{L}, \tag{2}$$

$$h(z)=\frac{B_0}{2}+\sum_{k=1}^{n}B_k\cdot\sin\frac{\pi kz}{L}, \tag{3}$$

$$y^{*}(z)=\frac{D_0}{2}+\sum_{k=1}^{n}D_k\cdot\sin\frac{\pi kz}{L}, \tag{4}$$

$$e(z)=\frac{F_0}{2}+\sum_{k=1}^{n}F_k\cdot\sin\frac{\pi kz}{L}, \tag{5}$$

where $y(z)$ and $y^{*}(z)$ - is the deflection caused by the initial unbalance, and the deflection appeared after attaching the testing unbalance system on the rotor, respectively; $h(z)$ and $e(z)$ - are the systems of testing and initial eccentricities, respectively; A_i, B_i, D_i, F_i - coefficients of the expansions.

Assuming the unbalance-to-deflection ratio for similar expansion members to be linear, we can obtain:

$$F_i=A_iB_i/(D_i-A_i).$$

After the curves of eccentricity projection on the two inter-perpendicular planes have been determined their vector sum can be found, which allows to obtain the form of the curve depicting the distribution of the initial eccentricities.

It is noteworthy that you can use not only deflections functions to implement these methods, but also their derivatives such as cross-section turning angles, mechanical tensions, and relative deformation; note that the highest form of unbalance reveals itself in a more apparent manner with the deflection derivatives $y^{(i)}$ that with the deflection itself, as can be seen from the expression

$$y^{(i)}=\frac{\pi^i}{L^i}\cdot\sum_{k=1}^{\infty}A_k\cdot k^i\cdot\sin\frac{\pi kz}{L}, \qquad i=1,2,3,4.$$

2.2. BALANCING WITHOUT TESTING MASSES

This group of methods ensues from the first method of finding solution for Fredholm equation and suggests the eccentricity identification on basis of static coefficients of influence. The coefficient of influence is the value of deflection (or turning angle) of the i-cross-section caused by unity force (or bending moment) applied to the k-cross-section. The main idea of the method is like the following: deflections and turning angles or one of these parameters are measured at noncritical rotation frequencies and their projections on two inter-perpendicular planes are substituted into equations (6); equations (6) are solved for unknown projections of eccentricities.

$$y_i=\sum_{k=1}^{n}m_k\cdot\alpha_{ik}\cdot\omega^2\cdot(y_k+e_{yk})-\sum_{k=1}^{n}I_k\cdot B_{ik}\cdot\omega^2\cdot(y'_k+\varepsilon_{yk}), \tag{6}$$

Third International Conference on Inverse Design Concepts and Optimization in Engineering Sciences (ICIDES-III), Editor: G.S. Dulikravich, Washington D.C., October 23-25, 1991.

$$y'_i = \sum_{k=1}^{n} m_k \cdot \gamma_{ik} \cdot \omega^2 \cdot (y_{yk} + e_{yk}) - \sum_{k=1}^{n} I_k \cdot \varepsilon_{ik} \cdot \omega^2 \cdot (y'_{yk} + \varepsilon_{yk}),$$

Similar equations may be written and solved for the second projection of deflections.

This group of methods gave birth to some methods, that can be distinguished by the parameters to be measured such as deflections, turning angles, support reactions, and vibrations.

2.3. PARAMETRIC IDENTIFICATION OF FLEXIBLE ROTORS

In order to escape the procedures of obtaining static coefficient of influence as well, a group of identification algorithms was suggested allowing to find the unknown elasticity-and-inertia characteristics related to the mathematical model depicting the real rotor.

Let's consider the universally known dependences of the deflection theory:

$$M''_{zz}(z,\omega) = q(z,\omega) = m(z) \cdot \omega^2 \cdot (y(z,\omega) + e_y(z)), \qquad (7)$$

where bending moment $M(z,\omega)$ at the rotation frequance ω is equal to

$$M(z,\omega) = K(z,\omega) \cdot EI(z), \qquad (8)$$

The rotor axis curvature is determined from the expression

$$K = y'' / (1 + (y')^2)^{3/2}, \qquad (9)$$

and $q(z,\omega)$ - is inertial load, E - is Young's modulus.

Taking into account the resistance forces we can obtain (denoting the total moment of these forces through $f(z,\omega)$):

$$f(z,\omega) + M(z,\omega) = K(z,\omega) \cdot EI(z).$$

Using relations (7-9) we can obtain after some manipulations:

$$\frac{1}{m(z)} \cdot f''_{zz}(z,\omega) + \alpha_0(z) \cdot K''_{zz}(z,\omega) + 2\alpha_1(z) \cdot K'_z(z,\omega) +$$

$$+ \alpha_2(z) \cdot K(z,\omega) - \omega^2 \cdot e_y(z) = \omega^2 \cdot y(z,\omega),$$

where $$\alpha_i(z) = \frac{1}{m(z)} \cdot \frac{d^i}{dz^i}[EI(z)], \quad i=0,1,2.$$

Let's reprezent the function $-f''_{zz}(z,\omega)/m(z)$ as expanded in the series on z. Setting a finite number for members of the series we assume that the sum of the abolished members would not violate the pre-set deflection measuring accuracy. Hence,

Third International Conference on Inverse Design Concepts and Optimization in Engineering Sciences (ICIDES-III), Editor: G.S. Dulikravich, Washington D.C., October 23-25, 1991.

$$\sum_{k=0}^{n} \delta_k(z)\cdot\omega^k + \alpha_o(z)\cdot K''_{zz}(z,\omega) + 2\alpha_1(z)\cdot K'_z(z,\omega) + \alpha_2(z)\cdot K(z,\omega) -$$

$$-\omega^2\cdot e_y(z) = \omega^2\cdot y(z,\omega).$$

The objective of consequent manipulations is to find the value of fuctions $\delta_k(z)$, $k=0,1,\ldots,n$; $e_y(z)$; $\alpha_i(z)$, $i=0,1,2$ for some fixed point $z=a$. Thus we have n+5 unknown values requiring for their determination the same number of equations.

Then, we obtain the sought-for system of n+5 equations with the same number of unknown values, putting down the previous equation for each value of ω_j at the point $z=a$.

$$\sum_{k=0}^{n} \delta_k(a)\cdot\omega_j^k + \alpha_o(a)\cdot K''_{zz}(z,\omega_j)\Big|_{z=a} + 2\alpha_1(a)\cdot K'_z(z,\omega_j)\Big|_{z=a} +$$

$$+\alpha_2(a)\cdot K(a,\omega_j) - e_y(a)\omega_j^2 = \omega_j^2\cdot y(a,\omega_j), \qquad j=1,2,\ldots n+5. \tag{10}$$

When we find the solution for this system we'll be able to determine the unknown values at the pre-set point. Keeping in mind that this point $z=a$ was selected arbitrary we create the similar system for any other point z, obtaining thus the sought-for values at this point.

In this manner we obtain functions $e_y(z)$ and $\alpha_i(z)$ $(i=0,1,2)$.

Carring out the similar manipulations for $e_x(z)$ we obtain the value of the unbalance vector:

$$D(z)=M(z)\cdot\sqrt{e_x^2(z) + e_y^2(z)},$$

as well as the angle formed by this vector and OY-axis.

$$\operatorname{tg}\gamma = e_x(z)/e_y(z).$$

Finding the solution for the system of equations gives us not only the eccentricity value but also $\alpha_i(z)$, $i=0,1,2$ and $\delta_k(z)$, $k=0,1,\ldots,n$

The known values of $\delta_k(z)$ allow to determine a total moment of resistance, while α_i give reduced masses and regidities of the rotor

$$m(z)=M\cdot\exp\Big(\int_0^z (\alpha_1/\alpha_o)\,dz\Big)\Big/\Big(\alpha_o(z)\cdot\int_o^L \exp\Big(\int_o^z (\alpha_1/\alpha_o)\,du\Big)dz/\alpha_o(z)\Big),$$

$$EI(z) = \alpha_o(z)\cdot m(z),$$

Third International Conference on Inverse Design Concepts and Optimization in Engineering Sciences (ICIDES-III), Editor: G.S. Dulikravich, Washington D.C., October 23-25, 1991.

where M - is the mass of the rotor.

In the most general case, a number of equations required for determining all unknown values and the same number of rotation frequences at which deflection values are measured, is equal to n+5. In practice, things are more simple.

If you know the law under which the resistance forces are changing, you need 4 equations; if this law is accompanied by a law of rigidity changing you need only 3 equations; with uniform shaft - 2 equations are enough; and if you know elasticity-and-inertia characteristics you'll need only one equation.

When you find it convenient to use a certain method such as, for example, the electric strain-gauging for relative deformation measuring and (or) parameter stability tracking during the operating period, there are parametric identification algorithms for eccentricities and flexural rigidity (or eccentricities only) based on the relative deformation being measured, and then the transition is made to the values of curvature, tension, bending moments, turning angles and deflections.

2.4. PARAMETRIC IDENTIFICATION ON RELATIVE DEFORMATIONS

Let us use Hocke's law $\sigma = \varepsilon \cdot E$ and linear differential equation for curve axis of the rotor

$$M_z = EI \cdot y''_{zz} = EI \cdot \varepsilon / t, \tag{11}$$

where M_z - is a bending moment, ε - is a relative deformation, t-is the distance from the neutral axis to the fibres for which the ε - measurment is taken.

For multidisk rotor which can to any degree of accuracy approximate (by means of adjusting a number of disks) a rotor with an arbitary mass distribution, nonbalanced forces are equal to

$$P_i = m_i \cdot (e_i + y_i) \cdot \omega^2, \tag{12}$$

where y_i can be determined by double integration of y".

Bending moment for an arbitrary cross-section of the rotor is equal to the sum of all moments of external forces (including the support reactions) applied to a single side (left or right) from the section examined

$$M_{zi} = \sum_{k=1}^{n} b_{ik} \cdot p_k, \tag{13}$$

where b_{ik} - coefficients depending on the distances from the unbalanced forces to the supports and cross-section being examined; b_{ik} are calculated in advance.

Accomplishing the ε - measurments at some non-critical frequences for n sections we can determine the values of bending moments for these sections using (11); then unbalanced forces can be found from (12). If these forces would now be compensated with the appropriate counterbalances, the balancing would be correct only for the anqular speed ω.

To carry out the balancing over the full speed range, you have to determine eccentricities e_i using (12). But you can choose another way of searching for the solution.

$$\sigma_i = \varepsilon_i \cdot E = M_{zi} / W_i = \sum_{k=1}^{n} b_{ik} \cdot P_k / W_i, \tag{14}$$

Third International Conference on Inverse Design Concepts and Optimization in Engineering Sciences (ICIDES-III). Editor: G.S. Dulikravich. Washington D.C., October 23-25, 1991.

where $W_i = \frac{I_i}{R_i}$ - is an axial moment of resistance for section i;

Ri - radius of the rotor's cross-section.

The same can be written down differently

$$\varepsilon_i \cdot EI_i / t_i = \sum_{k=1}^{n} b_{ik} \cdot (y_k + e_k)\omega^2, \quad i=1,2,\ldots,n \tag{15}$$

Now, if the e_k and EI_i values are considered unknown, you have to get two times equations then was represented by system (15); this can be obtained by measuring the values of ε for all sections at some other non-critical angular speed ω_2. It can be shown that equations of the (15) type are independent.

2.5. STABILITY OF IDENTIFICATION ALGORITHMS

Thus, all balancing methods requiring no testing masses, are based on the identification of unbalances within the framework of inverse problems of dynamics. In this connection, the stability of identification algorithms was researched on the static influence factors known. The whole research is published in works [4] and [5]. These works also hold all major results. Fredhom's equation in the matrix form looks like the following (gyroscopic moments neglected):

$$\bar{y} = A(\bar{y} + \bar{e}) \cdot \omega^2 \tag{16}$$

where $\bar{y}$ and $\bar{e}$ are vectors of n-dimension; A-square matrix of nxn dimension, whose elements are the products of the static unfluence coefficients by the masses of corresponding disks.

This model can be practically applied in cases when small measuring errors of the values in equetion (16) (the values are measured experimentally) cause similarly small eccentricity calculation errors.

Taking into account the measuring errors we can represent system (16) in following form:

$$\bar{y} + \Delta\bar{y} = (\omega^2 + \Delta\omega^2) \cdot (A+\Delta A)\ (\bar{y} + \Delta\bar{y} + \bar{e} + \Delta\bar{e}),$$

where Δ - are the measuring errors.

In process of evaluating the relative error of the eccentricity identification we can see from the following expression

$$\frac{\|\Delta\bar{e}\|}{\|\bar{e}\|} \leq C(A) \cdot C\left(\frac{E}{\omega^2} - A\right) \cdot \frac{\|\Delta\bar{y}\|}{\|\bar{y}\|} + \frac{1}{\omega^2}[C(A)]^2 \cdot \frac{C((E/\omega^2)-A)}{\|(E/\omega^2)-A\|} \cdot \frac{\|\Delta A\|}{\|A\|} +$$

$$+ \frac{1}{\omega^2} \cdot C(A) \frac{C((E/\omega^2)-A)}{\|(E/\omega^2)-A\|} \cdot \frac{|\Delta\omega|^2}{\omega^2}$$

(where C-is the stipulation number of any square matrix B, which number is equal to the product of the straight matrix norm by the norm of invers matrix, that is, $C(B) = \|B\| \cdot \|B^{-1}\| \geq 1$, E - is the unit matrix), that the selected model is

Third International Conference on Inverse Design Concepts and Optimization in Engineering Sciences (ICIDES-III), Editor: G.S. Dulikravich, Washington D.C., October 23-25, 1991.

theoretocally stable, but as in reality we can not assume that measurment errors are likely to be less than any pre-set values, this problem is reduced to the task of evaluating the solution accuracy, which is defined by the stipulation numbers of the matreces involved.

We succeded in trying to disclose the physical sense of the matrix A stipulation number. It can be evaluated initially by the ratio of squared maximum and minimum natural rotation frequences for given discrete model. At this point, a descrepancy has came over: on the one side, trying to approximate the real rotor by increasing a number of masses, we bring the dynamic model still closer to the real structure; on the other side we increase the calculation error due to the growth of the stipulation number. Gyroscopic moments (when included in the scheme) also contribute to the growth of the calculation errors.

This is the sourse for obtaining quantitative relations between balancing accuracy on the one hand and measuring devices and a number of masses approximating the real rotor on the other hand. These relations allow to determine the third factor on the two others. For example, you can select measuring devices of required accuracy knowing the balancing accuracy and the planes of correction.

To get the required accuracy under a high stipulation number you can use the possibility to pass from the one identification algorithm to another one, for example, from system of equations of the fourth special case of the method described in section 2.3, with only one equation suggested.

3. EXAMPLE

We are going to analyse the results of the research and balancing of aero-engine compressor rotor on static influence coefficients. The disk-and-drum type compressor rotor (Fig.1) consists of ten separate disks bearing operating fan blades on their rims. Factory balancing was carried out in usual way in the "rigid rotor" mode for the two correction planes on a balancing machine at 800 rpm with operating frequences within 10000...12500 rpm.

In the process of exploitation some defects emerged such as deformation of the rear shaft, pin joint breakage, unpermissibly high resonance vibration level of the whole aero-engine.

Varios calculating techniques for natural oscillation frequences did not bring any reliable results due to the absence of precise data on the local rigidities of rotor as well as on the support pliabilities.

To increase the calculating scheme effectiveness, static tests of a number of rotors of this type were carried out, and precise values of static influence coefficients were determined over all ten stages. The first critical rotation frequency for this rotor fixed supports (the frequency was calculated on static influence coefficients) turned out to be 11000 rpm. Practically this value coincides with the third peak of vibration of the amplitude-and-frequency characteristic of the rotor (Fig.2). Peaks of vibration in the region of 4200 rpm and 8300 rpm are connected with resonance oscillation of "rigid" rotor on pliable supports.

To check whether the precise values of the elasticity-and-inertia characteristics (reduced to the selected model) were used effectively, natural oscillation frequency of this very rotor was calculated, but the calculation scheme assumed only one general mass-that of the whole rotor (M=115,4 kg) with the static influence coefficient in the centre-of-mass cross-section. The schematization error of the calculation of the first natural oscillation frequency turned out to be not more than 1,5%.

Therefore, we decided to use the said single-mass model for balancing in the region of the first critical rotation frequency, due to difficulties connected with attaching correction masses to all stages of the rotor. Maximum deflection (y=0,15 mm) value of the eighth stage was assumed for the eccentri-

Third International Conference on Inverse Design Concepts and Optimization in Engineering Sciences (ICIDES-III). Editor: G.S. Dulikravich, Washington D.C., October 23-25, 1991.

city identification at 10500 rpm. $e=0,17\cdot10^{-7}$ m was found from the expression $y=\omega^2\cdot m(y+e)\alpha$. Correcting mass was brought into on the score of the eighth stage fan blade, which was replaced. Balancing results are shown on Fig.2.

The carried out research allowed to improve the design and balancing technology of the rotor and to eleminate the indicated defects.

Eccentricity identification based on measured deflections of the rotor using static influence coefficients was also carried out by Bradjko A.I. [6] employing a computerized imitation model, laboratory physical model and a natural rotor of compressor on an accelarating vacuum stand.

Table 1 holds data on mass of stages, static influence coefficients and deflections of the 5-mass rotor, which he balanced.

For $\omega=0,274\cdot10^{6}$ $1/c^2$ the following values of eccentricities were obtained:

$e_1=77,4\cdot10^{-6}$ m; $e_2=89,9\cdot10^{-6}$ m; $e_3=105\cdot10^{-6}$ m;

$e_4=79\cdot10^{-6}$ m; $e_5=59,5\cdot10^{-6}$ m.

Correcting masses were attached to all of the five stages.

As a result of the balancing that was carried out, the maximum rotor deflections were diminished almost by 4 times, and housing vibration were diminished by 2,5 times.

CONCLUSIONS

The problem studying dynamics and high-frequency balancing of flexible rotor systems can be set and solved as the task of identification of elasticity-and-inertia characteristics and eccentricities corresponding to a selected calculating model within the framework of the inverse problem of the oscilation theory.

On the basis parametric identification of the flexible rotor systems on the measured vibration parameters of products was developed, providing simultaneous determining of the mass, rigidity, and demping characteristics of the rotor and its eccentricities as well.

The identification algorithms obtained on measured parameters of products allowed to develop three groups of flexible rotor balancing, which don't require knowing rotor oscillation forms or operating at critical angular speeds:

- with emploing only system of testing masses and a single testing start-up;
- without employing testing masses and start-ups, grounding known and unknown elasticity-and-inertia characteristics.

The accomlished research on stability and accuracy of the suggested identification algorithms allows to have optimal relations between the required balancing accuracy, measuring instruments and dynamic model of the system.

The obtained results were used for research of dynamic and high-frequency balancing of a turbopump assembly unit, a turbogenerator, rotors of gas turbine engine compressors, and they allowed to considerably lower the vibration level, deflections and tensions in the parts of flexible rotor systems, thus increasing life and reliability of products.

Third International Conference on Inverse Design Concepts and Optimization in Engineering Sciences
(ICIDES-III), Editor: G.S. Dulikravich, Washington D.C., October 23-25, 1991.

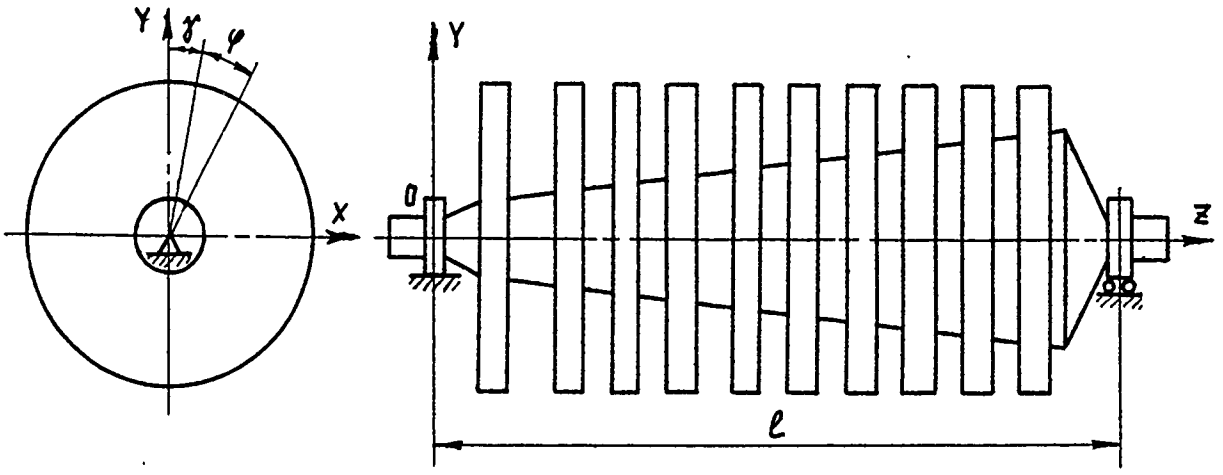


Fig.1. The rotor scheme.

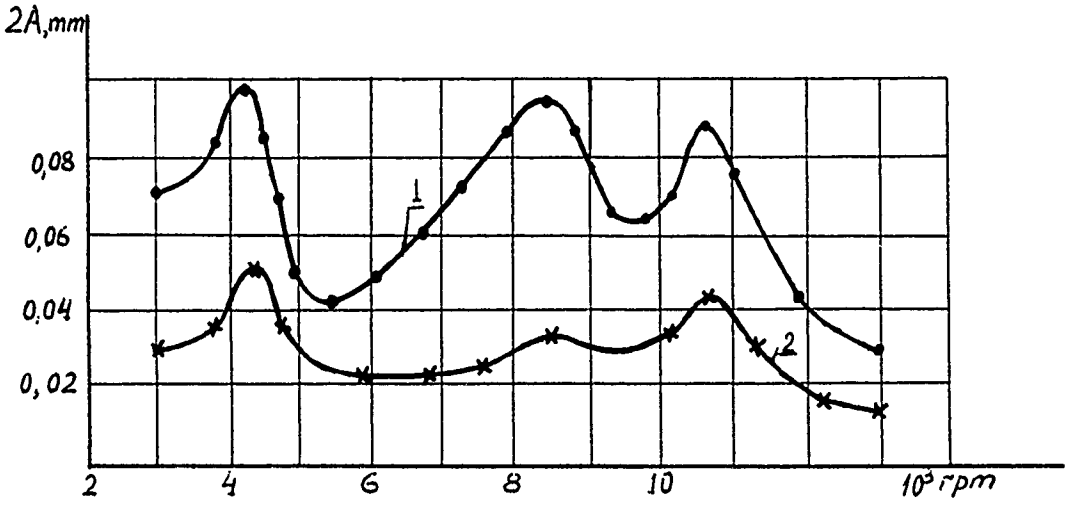


Fig.2. Amplitude-and-frequency characteristics of the rotor.
1 - before the balancing; 2 - after the balancing

Third International Conference on Inverse Design Concepts and Optimization in Engineering Sciences (ICIDES-III), Editor: G.S. Dulikravich, Washington D.C., October 23-25, 1991.

Table 1

Data for identification of eccentricities of a five-masses rotor

N	masses m_i, kg	deflections $y_i \cdot 10^{-5}$ m	static coefficients of influence $\alpha_{ik} \cdot 10^{-9}$, m/N				
			1	2	3	4	5
1.	9,03	7,87	9,2	7,4	6,23	4,8	2,77
2.	9,96	11,38	7,45	9,0	8,95	7,3	5,25
3.	12,32	11,16	5,3	7,85	9,88	8,5	6,8
4.	12,53	11,37	4,2	7,0	8,62	9,7	8,98
5.	17,6	10,35	2,62	4,67	7,6	9,43	10,8

REFERENCE LIST

1. Lovitt U.V. Linear integral equations. -NTI-publishers, Moscow, 1933.
2. Levit M.E., Roizman W.P. Vibration and balancing of the aero-engines rotors. -Mashinostroyeniye Publishers, Moscow, 1970.
3. Roizman W.P., Vajingortin L.D. Invention certificates # 1921852 and # 1961887. The discription of the inventions.
4. Roizman W.P., Vajingortin L.D. Selected problems of the theory of flexible rotor balancing. Part of the book: Elastic and hydroelastic oscillations of assembly parts and whole structures, Nauka Publishers, Moscow, 1979, p. 55-63.
5. Roizman W.P., Vajigortin L.D., Guditch R.V. Statictic identification algorythms of objects and processes. Mashinovedenie, N5, Nauka, Moscow, 1984, p.43-45.
6. Bradjko A.I., Roizman W.P. Computer-assisted balancing of the rotors of hydro-turbine engines. Selected works collection titled: Theory and practical of balancing technique, Mashinostroyeniye Publishers, Moscow, 1973, p.137-145.

Third International Conference on Inverse Design Concepts and Optimization in Engineering Sciences (ICIDES-III), Editor: G.S. Dulikravich, Washington D.C., October 23-25, 1991.

ON DESIGNING FOR QUALITY

L.D.Vajingortin, W.P.Roisman
Khmelnitsky Technological Institute, USSR

The problem to ensure the required quality level of products and (or) technological processes often becomes more difficult due to that there is no general theory for determining the optimal sets of values of the primary factors, that is, of the output parameters of the parts and units comprising an object and ensuring the correspondance of the object's parameters to the quality requirements. This is the main reason for a number of years being spent for finishing complex articles of vital importance.

To create this theory, one has to overcome a number of difficulties and to solve the following tasks : creating reliable and stable mathematic models showing the influence of the primary factors on the output parameters; finding of accurate solutions when mathematical models are poorly stipulated; creating new technique of assigning tolerances for primary factors with regard to economical, technological and other criteria, the technique being grounded on the solution of the main problem; well-reasoned assignment of nominal values for primary factors which serve as the basic for creating tolerances. Each of the above listed tasks is of independent importance. The present work is an attempt to give solution for this problems. The foregoing problem dealing with quality ensuring in mathematically formalized aspect has been called the multiple inverse problem.

1. INTRODUCTION

When creating any new machine, mechanism, technological, medical and other systems and processes one has to start with presenting the original technical specifications of output parameters.

The above-mentioned technical conditions are normaly represented as rated values and tolerances of output parameters. Then, creators face the problem of designing, manufacturing and finishing up the object so that it could carry out predetermined functions while preserving the output parameters within the range specified by the technical conditions, thus providing the required level of quality.

The values of complex object's output parameters depend on the rated values and tolerances of great number of parts and units, which form the object and provide its functional purposes. These units' and components' parameters are further called as basic parameters or primary factors.

It is well known, that finishing up the object is a long and hard task, especially for a new one that has no analogues. Of course, it would be mostly desirable to get quick solutions for the following problems : does the scheme or construction created meet the specifiend requirements under the suggested technology; if not, which construction and which technology would satisfy the objectives?

We have no possibility to analyse the solutions accomplished in diffirent period. But we have to note, that the steady developtment of sciences and technique makes this problem up continuosly change, making it more complex but all the time up-to-date. Its solution is defined by the level of modern scientific achievements. The formalized description of the problem as well as possible method of its solution are described below.

2. THE STATEMENT OF THE PROBLEM

Let the quality of each object is rated by values of its control output parameters represented by the vector

$$\bar{Y} = \{ Y_1, Y_2, \ldots, Y_m \}.$$

Third International Conference on Inverse Design Concepts and Optimization in Engineering Sciences (ICIDES-III), Editor: G.S. Dulikravich, Washington D.C., October 23-25, 1991.

To provide the required level of quality the following relations should be valid

$$[y_i] < Y_i < [Y_i], \quad i=1,2,...,m, \tag{1}$$

where $[y_i]$ and $[Y_i]$ are lower and upper limits of the parameter Y_i, correspondingly. They are represented by initial technical conditions.

We've going to look for the solution of this problem as a set of values of the primary factors, which can be represented by following inequalities:

$$[x_i] < X_i < [X_i], \quad i=1,2,...,n. \tag{2}$$

The belonging of the vector to this set has to provide the fulfiling of the restrictions (1), which are imposed on the output parameters.

We've call the problem, which has just been formulated as the multiple inverse problem. This term emphasizes that the solution of the problem suggests the determination of the set of points (region) in the n-dimensional space of the primary factors. This circumstance differs it from the point inverse problems, which are traditionally solved in many technical bronches. In the point inverse problem only one vector of the primary factors and (or) one collection of model's parameters have to be determined, if the vector $\bar{Y}$ is set beforehand.

3. THE REDUCTION TO THE PROBLEM OF THE OPTIMIZATION

The above mentioned vector $\bar{Y}$ is completely defined by the vector of the primary factors $\bar{X}=(X_1, X_2, ..., X_n)$ and the operator

$$\bar{Y} = \bar{f}(X_1, X_2, ..., X_n; B_1, B_2, ..., B_k), \tag{3}$$

which carries out connectioh between the said vectors. The structure of $\bar{f}$ and the vector of parameters of the mathematical model $B_1, B_2, ..., B_k$ corresponds to the phisical nature of the object and its functional destination.

As a rule, the industrial, physical, economical and other considerations allow to indicate the widest bounderies of the set of the possible values of the primary factors. Then, the relations (3) enriched with these new bounderies can be presented as a system

$$\begin{cases} Y_i = f_i(X_1, X_2, ..., X_n; B_1, B_2, ..., B_k), \ i=1,2,...,m, \\ C_i < X_i < D_i, \quad i=1,2,...,n, \end{cases} \tag{4}$$

keeping in mind the co-ordinate form of the operator (3).

It should be noted, that the structure of the functions and the sets of the primary factors' values may be various. For example, one of the primary factors X_i can have the descrete or even finite set of values. Then, this fact must be reflected in (4) by such relations as $X_i = 1,2,...,N$.

The system (4) defermines some curved region in the n-dimensional space of the primary factors. In geometrical sense, if you'd find some sets in the form of (2), you would inscribe n-dimensional parallelepiped in the said curved region.

This problem has more than one solution due to the fact that countless set

Third International Conference on Inverse Design Concepts and Optimization in Engineering Sciences (ICIDES-III), Editor: G.S. Dulikravich, Washington D.C., October 23-25, 1991.

of this kind of parallelepipeds may be inscribed into the above-mentioned region. Every one of them can be entirely determined by two conditions. The first one comprises the point $\bar{X} = \{X_{10}, X_{20}, \ldots, X_{no}\}$ which is known to belong to the region and corresponds to one of the object's basic version with these nominal inner characteristics. The second condition is represented by set of lower δ_i and upper Ω_i deviations of the primary factors from their basic values corresponding to the boundaries of the tolerance zones of the primary factors, that is to the technology chosen.

The following relations are evident here:

$$X_{io} - \delta_i < X_i < X_{io} + \Omega_i, \quad i=1,2,\ldots,n. \tag{5}$$

But not every solution (5) of the problem formulated above can be realized in practice because of various constructive, technological, economical and other considerations. The high cost of production or the absense of the necessary equipment, components, materials, performers of required qualification, peculiarities of the object can serve the sourses of the troubles.

These considerations can be analytically formulated by the criteria expressed through the deviations of the primary factors from their basic values

$$F_i = F_i(\delta_1, \delta_2, \ldots, \delta_n, \Omega_1, \Omega_2, \ldots, \Omega_n), \quad i=1,2,\ldots,L. \tag{6}$$

It is evident that of the above mentioned parallelepipeds the most acceptable for the practical implementation are those, in which the criteria (6) or some of them are optimized and another of the criteria are added to the restrictions in (4).

Various criteria of the tolerances optimization are possible. The cost function is the most important. Sinse this functional dependence on the current tolerance values is usually unknown, it might be possible to replace it by in some sense equivalent criteria. For example, it might be possible to demand the maximizing of every or some tolerances.

Then the criteria (6) will look like following

$$\max_i (\delta_1, \delta_2, \ldots, \delta_n, \Omega_1, \Omega_2, \ldots, \Omega_n) \rightarrow \max.$$

Thus, the problem of providing the pre-determined level of the object's quality is drawn to the multicriteria optimization problem with the certain restrictions. The deviations δ_i and Ω_i are to be determined in this problem so that the restrictions (1) are valid for the region (5).

4. NECESSARY POINTS OF THE SOLUTION

The way to the solution of the formulated problem is connected with some difficulties. The overcoming of these difficulties has to be the necessary points of the solution.

4.1. MATHEMATICAL MODELLING

In practice there are cases, when the model required for writing down the functional part of the restrictions (1) is known. But as a rule, complicated objects can have either unknown (inaccurate) parameters or unknown structure or both. Therefore it is necessary to develop an easy-operated approach to the task of setting functional dependences of primary factors and output parameters having reliable coefficients reduced to the object model.

The algorithm-creating technique for urgent mathematical modelling can be ground on the active-controlled influence on the object.

Let the calculated model of the experimental sample be represented as

Third International Conference on Inverse Design Concepts and Optimization in Engineering Sciences (ICIDES-III), Editor: G.S. Dulikravich, Washington D.C., October 23-25, 1991.

$$\begin{cases} Y_i = f_i(X_1, X_2, \ldots, X_n; B_1, B_2, \ldots, B_k), \\ i = 1,2,\ldots,L. \end{cases} \qquad (7)$$

At the beginning we suppose that the structures of the functions f_i as known, but parameters B_i are not.

If the output parameters' values and some primary factors are substituted in (7) then k of unknown values of primary factors and j of coefficients of the model should satisfy (7) together with the substituted values. As a rule, the system (7) is not completely defermined (that is $k+j>L$) and admits of countless set of solutions. However, keeping in mind that the object operates and really exists, it would be natural to find the solution fully responsive to the given object. Hence, it is necessary to complete the problem by means of some additional experiments. The method of test parameters suggested here is bound to provide the afore mentioned completion.

To put it into practice, $k+j-L$ additional components should be employed or varied in the object under examination, or the object should be exposed to the same number of the test modes of functioning, the modes belonging to the set of modes specified by initial technical conditions. Thus, the operation of the object is regulated in active manner. The influence of the said test components (or modes) in accord with components whose parameters are being identified, allow the measuring of missing values of the output parameters make the system (7) complete, and identify the missing factors and coefficients of the model, that is to find the solution of the inverse point problem.

In case the structure of functions f_i is unknown we recommend to disintegrate them by series according to any complete system of functions, for example, the series

$$\begin{cases} Y_i = B_{io} + \sum_j B_{ij} \cdot X_j + \sum_{j,k} B_{ijk} \cdot X_j \cdot X_k + \ldots, \\ i = 1,2,\ldots,L \end{cases} \qquad (8)$$

and to identify coefficients by several sequential stages. At the beginning, we suggest to determine the coefficients of linear approximation using required quantity of test parameters. Then, after employing additional test parameters, the functions Yi are selected which are adequate to the object. For the rest of Yi functions the square and higher appoximation are considered. It is easy to show that the process is converging and the number of stages usually does not exceed two or three.

Putting the method into practice one has to start with considering the output parameters of large units as primary factors and to sort out those vitally influencing the functioning of the object. Then, the functional dependence of sorted out characteristics on the smaller units is ascertained in similar manner and so on. This approach based on the principle of hierarchy allows to operatively adjust the model to the object under examination with regard to the degree of its idealization and functioning conditions, and eliminates the necessity of the registration and analysis of the inessential primary factors.

However, the hierarchical principle of modelling can be employed only if the output parameters of separate units can be measured at every cascade. If this possibility is not provided by the design the method of multy-cascade modelling can be used. Let us assume that the interconnection exists between separate units (cascade) and an output parameter, that is we know the function $Y = f(\varphi_1, \varphi_2, \ldots, \varphi_s)$, where $\varphi_i = \varphi_i(X_{i1}, X_{i2}, \ldots, X_{it})$ - output parameter of

Third International Conference on Inverse Design Concepts and Optimization in Engineering Sciences (ICIDES-III), Editor: G.S. Dulikravich, Washington D.C., October 23-25, 1991.

i unit. Then, fixing the values of the primary factors of all cascades but one, and measuring the output parameter Y, we can create the model of every cascade and combine them into the common model of the object capable to varying parameters of all units [1].

We would like to emphasize that this manner of mathematical modelling is in itself a particular case of the inverse problem solution.

4.2. PROVIDING THE MODEL STABILITY

However models are practically important only if the faults of the experimental input information are not likely to cause intolerably large faults of the values being determined, that is the models should be stable. In [2] it is shown how the stability of the model should be determined with regard to all or some factors, as well as the necessary proof is placed to estimate the relative fault of parameters identified with the help of linear model:

$$\| \Delta\bar{X} \| / \| \bar{X} \| \leqslant C(A) \cdot \| \Delta\bar{Y} \| / \| \bar{Y} \| + [C(A)]^2 \cdot \| \Delta A \| / \| A \| . \qquad (9)$$

This estimation, thus, is represented by the number of stipulation C(A) and the faults of characteristics and elements A being measured. Estimation (9) allows to explain the decreasing stability of the model while the degree of A is growing. In other words, it states the necessity to search the compromize between the desire to give thorough description of the object using large number of factors and ensuring the stability of the model. The estimation (9) showes that the model can be regularized not only by way of influencing the A operator, which in real production environments can not always be available for the various reasons. Not less efficient regularization can be achieved by way of influencing the Y vector of parameters being measured, which method is based on the statistical nature of the vector. To achieve this, you have to carry out a great number of Y measurments, insert the value of the vector into the calculated model and count the realization of every one of identified parameters. Mathematical expectations of parameters values calculated on the base of these realizations are assumed as true values of these parameters. The estimation of the number of realizations sufficient to ensure the accuracy of the method

$$n \geqslant t^2 \cdot (C(A) \cdot \sigma_1^2 / \| \bar{Y} \|^2 + C^2(A) \cdot \sigma_2^2 / \| A \|^2) / \delta^2 \qquad (10)$$

(where σ_1, σ_2 - mean root squere deviations of the vector components and matrex A correspondingly, t - Student's coefficient) shows that the described method of statistical solution is efficient when coupled with methods of influencing the A operator [2].

Estimation (9) places interest in pure practical aspect, since it states the functional interdependence of economical factors (accuracy of the method and accuracy of measuring facilities), thus making it possible to choose one of these requirements to provide the two others set apriory.

5. PROBLEMS, CONNECTED WITH OPTIMIZATION

The concrete optimizing method can be chosen from the sufficiently wide collection of the detailly developed optimizing algorithms. It is evident that the results of the criteria optimization depends on the basic version chosen, i.e. on the point X_0. Here we offer some recommendations connected with it.

5.1. CONSTRUCTING THE REGIONS

We suggest that the algorithm is implemented through making proper regions spreading from basic point with step-by-step checking the validity of the restrictions (1). This basic point often can be determined out of physical or practical considerations. But there are cases when this point is uknown, and the problem of the seeking becomes very difficult one.

5.2. ON CHOISE OF THE BASIC POINTS

Because of great number of random and unpredictable situations that may occur during the manufacturing and exploiting of the object, and due to non-

Third International Conference on Inverse Design Concepts and Optimization in Engineering Sciences (ICIDES-III). Editor: G.S. Dulikravich. Washington D.C., October 23-25, 1991.

stability of properties of construction materials, the characteristics of the object may be treated as random values. Then we can estimate the true values using the method of confidential intervals [3], provided that the law of distribution is known.

For a long time, the normal distribution law or its modification was considered the best approximation for which the majority of statistical criteria and estimations can be applied. However, a lot of practical problems have turned up lately which give strong evidences that the normal distribution law is not so universal as it was thought. The situations emerging during the study of real process bear evidences that a good deal of the object's parameters' distributions deviate from the normal distribution, moreover they often have more than one summit of the probabilities' function densities. Therefore the physical essence and new technical schemes of the processes of this sort are disclosed in [4]. The schemes are based on the method of representation of each random value selection in the form of the set of subselections, combined by some dominant causes for diversity of values of the quantity under examination. Here some examples of such kind of situations are illustraited and it is shown that more often than not the situations of this type can be depicted by Gauss functions' linear combinations with some weight coefficients Pi assigned to estimate the contribution of each subselection to total selection of the realized random values.

$$f(X; a_1, a_2, \ldots a_n; S_1, S_2, \ldots, S_n; P_1, P_2, \ldots P_n) =$$

$$= \sum_i P_i S_i^{-1} \cdot (2\Pi)^{-0,5} \cdot \exp\left(-(X-a_i)^2/2S_i^2\right). \qquad (11)$$

In [4], various methods for finding the unknown parameters of the function (11) are described, depended on the required accuracy of calculation and the selected criterion of approximation histograms. The values thus determited define the integral function which in turn makes it possible to write down the equations for locating the permissible [X] value:

$$W = P\{X < [X]\} = \sum_i P_i S_i^{-1} \cdot (2\Pi)^{-0,5} \cdot \int_{-\infty}^{[x]} \exp(-(X - a_i)^2/2S_i^2)\,dX. \qquad (12)$$

When processing the experimental data one has employ well-founded technique for compiling histograms to prevent, on the one hand, the probability of missing considerable part of the distribution by too large spacing intervals, or having to deal with unimportant subselections which may turn up under too small spacing intervals, on the other hand. It is good idea to start making a histogram with the smallest possible spacing interval which can be compared with the measuring accuracy, and to approximize the histogram using function (11) having the number of additieves equal to the number of spacing intervals. The already known weight parts which turned out to be less than pre-set probability $\alpha = 1 - W$ give you an indication of unimportant subselections joined with the contiguous subselections. Then, the spacing interval tends to gradually increase, and the whole procedure is carried out over again untill each weight part is made comparable with α.

And now the recommendation on the selection of the basic point rest on the following ideas.As basic point we can select the point belonging to the space of primary factors and having one of the mathematical expectation as the first co-ordinate, the mathematical expectation being that of random value depicting the distribution of the first primary factor. Analogically, the second co-ordinate will be connected in the similar way with the second primary factor, and so on.

Third International Conference on Inverse Design Concepts and Optimization in Engineering Sciences (ICIDES-III). Editor: G.S. Dulikravich. Washington D.C. October 23-25, 1991.

5.3. CHECKING THE VALIDITY OF THE RESTRICTIONS

When making regions spreading from basic point checking the validity of the restrictions (1) during each step of the optimization can be accomplished on the set of uniformly distributed points belonging to the created region of points. But in some practical situations this checking technique can be simplified. For example, when partial derivatives of the functions (3) have invarriable signs then the checking may be accomplished only for the tops of the region.

5.4. CHOOSING THE OPTIMAL BASIC VERSION

As the number of the basic points can be more than one it is natural to realise the optimizing algorithm for each of the possible basic versions separately, and to choose the most optimal of them as regards to criteria (6).

6. POSSIBLE APPLICATIONS

This approach which generally formalizes the problem of optimal ensuring of technical conditions requirements for output parameters of the article or technological process allows, in the first place, to ascertain the interlinkage of problems connected with selection of the object's basic version determined by rated values of its primary factors, with the problem of setting disigning and technological tolerances for them depended on the restrictions of the technical conditions for the object output parameters. This practicularly provides for the study of various selection possibilities concerning the already known and finished units, processes and technological decisions which might be utilized in the article or technological process being created.

Thus we are granted the possibility of formulating and solving the problem of synthesizing some of the design versions of articles, having optimal sensetivity towards manufacturing and operational deviations of their primary factors, that is we can directly link the selection of the object basic version to specific features of its practical implementation.

Secondly, this approach allows of formalizing a great quantity of important promiscuous special problems of design, manufacturing and testing procedures regardless of the technical branch of application.

The same conditions are capable of procuring recommendations for setting tolerances for both primary factors of the article as a whole and its separate units during design, manufacturing and finishing procedures. It allows also of carrying out the selective machine assembly by way of sorting out the object's components and materials by real values of their parameters which are sure to create the most favourable combinations.

When it comes to serial production it is possible by means of multiple inverse problem with regard to statistical origin of parameters, to effect diagnostics dealing with the yield (or the percentage of waste articles) and allowing of setting conditions providing the technical conditions requirements.

The same approach is effective when solving other types of problems. For instance, we can check the possibility of attaining the desired values of all or some output parameters under given design or technological conditions, which stands for finding a solution of a relative multiple inverse problem. If the solution doesn't exist or it's out of reasonable limits in designer's or productive engineer's point of view, that means that the given object fails to meet the requirements if technical conditions therefore it is necessary to take to searching for completely new designing or technological decisions based on different principles.

This approach is also good to cover not only the article as a whole but its components as well.

Thus the approach under examination is a natural reflection of the set of real situations emerging at the stage of design, manufactoring and finishing articles.

7. EXAMPLE

To check up the versatality of the above described theory multiple inverse

Third International Conference on Inverse Design Concepts and Optimization in Engineering Sciences (ICIDES-III), Editor: G.S. Dulikravich, Washington D.C., October 23-25, 1991.

problem was formuleted and solved, the problem being applied to various branches of technical engineering including:

- providing the strength and air-water proof quality for radioelectronic elements [5];
- enhancing the stability of the output parameters of the articles of the secondary radiodetection (airplane answering devices) [1];
- lowering to preset level of vibrating activity of gas-turbine engines and turbopump assembly unites [2,6-8,11];
- assigning of well-reasoned tolerances for the residual unbalance during balansing and assembling of rotors [4,9];
- developing of balancing technique for flexible rotors [10].

Each of the above-listed applications is complex enough in itself, and it would take more time and space than we have,to give their full description here. Therefore, the present work is an attempt to throw light upon general ways of finding solutions to multiple inverse problem, and the new approach to the problem is illustrated by brief example showing the way to lower vibrating activity of a turbopump assembly unit. We also supplyed the example with necessary references to the sources containing more detailed description of the statements placed here.

Turbopump assembly units with high-speed rotors are widely used in varius branches of industry including rocket production, aircraft building, chemical industry and so on. As it has been found out that the device-under-test had enhanced vibration caused by rotor unbalance, the task was to lower the vibration and the rotor deformation; to put the rotor bearings load within the threshold of 300 N, in particular, by way of assigning the appropriate residual values of eccentricity for the most massive parts attached to the rotor shaft.

7.1. GETTING AN EFFECTIVE MATHEMATICAL MODEL

The turbopump assembly unit shaft, rotating in two supporting bearings, carries two compressor impellers and axial turbine disk. These are very points of heavy masses fraught with possible unbalance; which consideration served a basic reason for choosing the "three-masses" calculation scheme shown on Fig.1.

To make the mathematical model of the rotor oscillations, corresponding to this scheme, more effective, we have accomplished the identification of the rotor parameters including stiffness, and mass and inertia characteristics, using the method of testing parameters which in our case, are four different values of the speed of rotation ω_j, where j = 1,2,3,4.

The rotation of the rotor is described with the help of the integral-and-differential equations of the bending theory [10]. The resulting equations for the three cross-sections of the rotor link the unknown values of stiffness EI, mass m and eccentricity e with the rotor deflection y (the equations being created for the two inter-perpendicular planes).

$$\alpha_0 \cdot K''_{zz}(z,\omega_j) + 2\alpha_1 \cdot K'_z(z,\omega_j) + \alpha_2 \cdot K(z,\omega_j) - e \cdot \omega_j^2 = \omega_j^2 \cdot y, \quad j = 1,2,3,4, \quad (13)$$

where

$$\alpha_i = \alpha_i(z) = \frac{1}{m} \cdot \frac{d^{(i)}(EI)}{dz^i}, \quad i = 0,1,2, \quad (14)$$

$K(z,\omega) = y''/(1+(y')^2)^{3/2}$ - is the curvature of the rotor elastic curve,
z - is the axial co-ordinate of a cross-section.

Then, we accomplished the measurments of the diflection values at the above

Third International Conference on Inverse Design Concepts and Optimization in Engineering Sciences (ICIDES-III). Editor: G.S. Dulikravich. Washington D.C. October 23-25, 1991.

mentioned points for the whole range of the rotation frequency (in our case 0-18000 rpm), and selected four specific values - 14100,15000,15600, and 16000 rpm.

After that, two components of the defections at each of the points (each component being a projection to one of the said inter-perpendicular planes) were substituted to the two systems of equations (13).

7.2. CHECKING UP THE STIPULATION AND PROVIDING THE ACCURACY OF SOLUTIONS

Before dealing with the system of equations (13) we calculated their stipulation numbers, which numbers turned out to be within the range of 3,2...6,7.

Consequently, [13] the expected error of the solution might be as high as 134% provided that the 15% measuring devices accuracy is achieved. To rise the accuracy of calculation we employed our statistical method for ensuring stability of mathematical models [2]. In our example, the measuring operation was carried out over 50 times, the result being that we found the mathematical expectations of the values and phases of the deflections. The averaged values were substituted to the equations (13). The solution brought us the following results:

For the first cross- section:

$$e_x = -5\cdot10^{-6}\ m;\ e_y = 5{,}84\cdot10^{-6}\ m;\ \alpha_0 = 185{,}65\ m^4/s^2;$$

$$\alpha_1 = 270{,}37\ m^3/s^2.$$

For the second cross-section:

$$e_x = -9{,}0\cdot10^{-6}\ m;\ e_y = 1{,}7\cdot10^{-6}\ m;\ \alpha_0 = 710{,}67\ m^4/s^2;$$

$$\alpha_1 = -247{,}18\ m^3/s^2.$$

For the third cross-section:

$$e_x = -6{,}2\cdot10^{-6}\ m;\ e_y = 30\cdot10^{-6}\ m;\ \alpha_0 = 280{,}83\ m^4/s^2;$$

$$\alpha_1 = 680\ m^3/s^2.$$

The values of α_0 and α_1, thus found for each of the cross-sections, made it possible to determine the values of the rotor reduced mass and stiffness according to the formulae

$$m = M\cdot\exp\left(\int_0^z \alpha_1/\alpha_0\, dz\right) \Big/ \left(\alpha_0 \cdot \int_0^L \exp\left(\int_0^z (\alpha_1/\alpha_0)\, du\right) dz/\alpha_0\right),\quad EI = \alpha_0 \cdot m,$$

where M is the rotor mass.

For the first cross-section:

$$EI_1 = 4147\ N/m^2;\ m_1 = 0{,}22\cdot10^{-2}\ kg/m;\ M_1 = 4{,}05\ kg.$$

Third International Conference on Inverse Design Concepts and Optimization in Engineering Sciences (ICIDES-III). Editor: G.S. Dulikravich. Washington D.C., October 23-25, 1991.

For the second cross-section:

$EI_2 = 15954$ N/m ; $m_2 = 0{,}2 \cdot 10^{-2}$ kg/m; $M_2 = 2{,}74$ kg.

For the third cross-section:

$EI_3 = 23988$ N/m ; $m_3 = 0{,}83 \cdot 10^{-2}$ kg/m; $M_3 = 11$ kg.

These values of EI and m in their turn, allowed us to calculate the critical frequences of the rotor oscillations for the first and second forms correspondingly:

$n_1 = 16600$ rpm, $n_2 = 25080$ rpm.

Experimentally measured value was 16100 rpm, which means that the calculation error did not exceed 3%.

7.3. FINDING PERMISSABLE VALUES FOR ACCENTRICITIES OF THE IMPELLERS AND THE TURBINE DISK

Let us denote $\bar{\Delta} = \{\Delta_1, \Delta_2, \ldots, \Delta_n\}$ - vector, whose coordinates are represented with the product of disk masses by their residual eccentricities.

The vector of residual deflection values should satisfy the equation

$$\bar{y} = \omega^2 \cdot A\bar{y} + \omega^2 \cdot A'\bar{\Delta} ,$$

where A' - matrix of pliabilities α_{ik}, created by means of the Mohr method [12] on the basis of already known values of stiffness EI, A - matrix composed of the products $\alpha_{ik} \cdot M_k$, where M_k - mass of the disks.

Hence,

$$\bar{y} = \omega^2 \cdot (E - \omega^2 \cdot A)^{-1} \cdot A'\bar{\Delta} ,$$

where E is unit matrix.

Now, the equation for the support reactions looks like

$$R_i = \sum_k b_{ik} \cdot (M \cdot y_i + \Delta_i)\omega^2, \quad i = 1,2.$$

where b_{ik} - are known values represented through distances from the disks fitting planes to the corresponding support plane. The following inequalities serve here as conditions of the (1) type:

$$|R_i| < 300 \text{ N}, \quad i = 1,2. \qquad (15)$$

The acceptable value of defections is limited to 0,1 mm value.

The criteria of optimization are

$$\Delta_i \rightarrow \max, \quad i = 1,2,3.$$

It is easy to understand that the basic point $\bar{\Delta}_0$ represents the ideal situation, that is when rated values of the eccentricity equals to 0 ($\bar{\Delta}_0 = \{0; 0; 0\}$).

When trying to create the three-measured expansions around this point it is

Third International Conference on Inverse Design Concepts and Optimization in Engineering Sciences (ICIDES-III), Editor: G.S. Dulikravich, Washington D.C., October 23-25, 1991.

quite satisfactory to check the conditions (15) for rotation frequences in the region of critical value 16000 rpm.

We accomplished all calculations resting on the algorithm set forth in [13], and found out that the residual eccentricity values should not exceed 0,0008 mm.

Considering that it would be extremely difficult to put this condition into practice, and costly too (plus loss of balancing during operation possible), it has been decided that with given construction of the assembly unit the above-formulated problem has no practical solution and some other method should be used for lowering vibrating activity of the unit.

Particularly, we suggested and realized the high-frequency balancing technique comprising the rotor eccentricities identification on the basis of deflections measured at the three sections, and compensation of the deflections by counterbalances.

While so doing we determined the values of unbalances Di for rotor under-test using already known values of the eccentricity projections

$$D_i = M_i \cdot \sqrt{e_{xi}^2 + e_{yi}^2} \, .$$

Also, orientation of the vectors in relation to a projection plane is represented by angles

$$\varphi_i = \operatorname{arctg} (e_{yi} / e_{xi})$$

It's turn out that $D_1 = 273$ g.cm, $\varphi_1 = 95^0$;

$D_2 = 2{,}48$ g.cm, $\varphi_2 = 170^0$; $D_3 = 30{,}6$ g.cm, $\varphi_3 = 102{,}3^0$.

Fig.2. represents values of the rotor deflection for the section III experimentally measured in initial state and after applying three correcting counterbalances used as compensators, whose values have just been calculated.

In general, the balancing procedure gave the following results: the rotor deflections, withing the range of frequences 2000-18000 rpm. lowerd by 6 times, vibration amplitude of supports lowered by 4 times, support reactions lowered by 4,5 times, the rotor shaft static strains fell by 3,5 times, while dynamic strains-by 3,5 times.

8. SUMMARY

The results of the accomplished are characterized with a concrete tendency for industrial application and can be used for: chosing optimal basic versions of objects, components and parts; assigning optimal, and economically and technologically reasonable tolerances for functional parameters of parts and units being produced; assigning optimal operating conditions for assembling and adjusting technological processes; accomplishing diagnostic of technical condition of objects and their components; identifying real values of the parameters of objects, and the distribution laws for the errors of creating of parameters. Finding solutions to this problem allows to cut investments and save time for finishing objects and controlling their quality in the process of manufacturing, and on the basis of pre-set criteria, to rate the output parameters (quality characteristics) of the object as a whole and its components and parts as well.

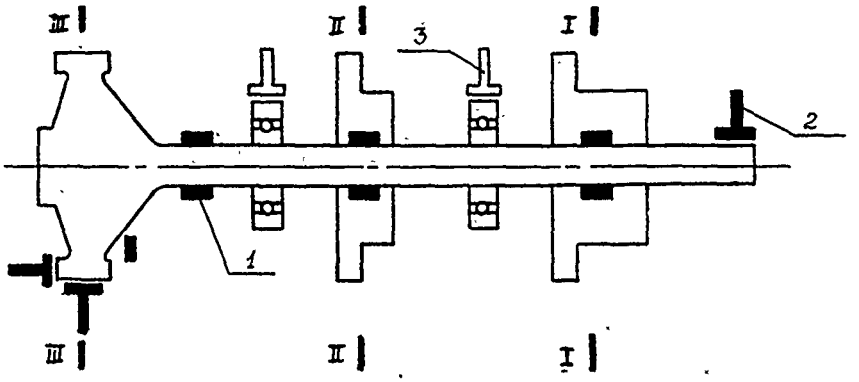


Fig.1. The scheme of the rotor preparation
1. strain resistors, 2. sensors of movements, 3. vibration sensors

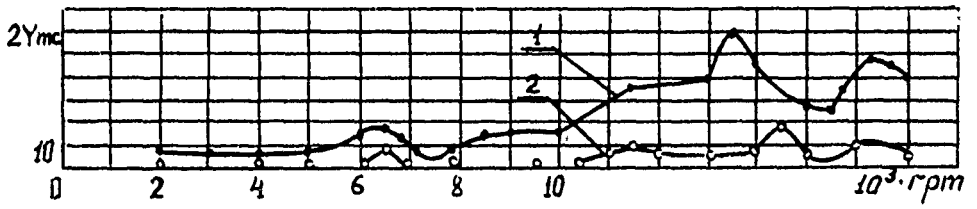


Fig.2. The dependence of the rotor deflections on motion frequency (III cross-section). 1 - before balancing, 2 - after balancing

REFERENCE LIST

1. Харкевич Н.А., Вайнгортин Л.Д., Яновицкий А.К. Метод создания статистически-детермированных моделей многокаскадных радиотехнических систем - Изв.Вузов СССР, Радиоэлектроника, 1981, т. XXIV, N7,с.76-78.
2. Ройзман В.П., Вайнгортин Л.Д., Гудич Р.В. Статистические алгоритмы идентификаций объектов и процессов. Машиноведение, 1984, с.43-46.
3. Румшинский Л.З. Элементы теории вероятностей. М: Наука, 1970.
4. Ройзман В.П., Вайнгортин Л.Д. О представлении статистических функций, не подчиняющихся нормальным законам распределения.- В сб.:Упругие и гидроупругие колебания машин и конструкций. М: Наука, 1979, с.50-55.
5. Ройзман В.П., Вайнгортин Л.Д., Хавкин М.И. Идентификация физико-механических характеристик полимерных электроизоляционных материалов. - В сб.: Работоспособность полимерных материалов для низковольтной изоляции. М: МДНТП., 1985, с.110-116.
6. Ройзман В.П., Вайнгортин Л.Д. А.с.МКИ GOI M I/24. Способ определения дисбалансов гибких роторов. - N 484425, Бюл. N 15, 1975.
7. Ройзман В.П., Вайнгортин Л.Д. А.с. МКИ GOI M I/24. Способ определения упруго-инерционных характеристик гибких роторов. - N 517822. Бюл. N 22, 1976.
8. Ройзман В.П., Вайнгортин Л.Д. А.с. МКИ GOI M I/24. Способ определения динамических характеристик гибких роторов. - N 729457. Бюл. N 15, 1980.
9. Системы классов точности балансировки. - ГОСТ СССР. 22061-76. М: Изд. стандартов, 1977, с.19-22, 126-128.
10. Основы балансировочной техники /Под ред.Щепетильникова В.А., т.20. М: Машиностроение, 1975, с.179-252.
11. Левит М.Е., Ройзман В.П. Вибрация и уравновешивание роторов авиадвигателей. М: Машиностроение, 1970.
12. Феодосьев В.И. Сопротивление материалов. М: Наука, 1972.
13. Калинин И.Н. К исследованию и сравнению алгоритмов оптимизации. - Кибернетика, 1984, N 1, с.77-80.

Third International Conference on Inverse Design Concepts and Optimization in Engineering Sciences (ICIDES-III). Editor: G.S. Dulikravich. Washington D.C., October 23-25, 1991.

OPTIMAL INTERACTION OF INDENTER WITH INHOMOGENEOUS PLATE

Valery N. Aptukov

Institute of Continuous Media Mechanics
UB of the Academy of Sciences USSR,
Koroleva st., 1, Perm, 614061, USSR

ABSTRACT

Consideration is given to a new class of problems dealing with an optimal design of inhomogeneous plate during dynamic penetration of the rigid indenter. The quality criterion of the process is defined by the specific mass of the target, which absorbs the given kinetic energy of the indenter. Parameters of control are expressed in terms of mechanical characteristics, i.e. distribution of density ρ and the related hardness H across the plate thickness. The maximum principle of Pontryagin are used to search for piece-wise continuous control function. With consideration of impact conditions and characteristics for a given class of material an optimal target structure criterion has been estimated for engineering application.

INTRODUCTION

The problem of searching for mechanical characteristics of inhomogeneous plate subject to impact of a rigid body has been stated first in [1] in the framework of theory of optimal control. This study employs Pontryagin principle of maximum [2] to obtain an optimal structure for a plate with minimal thickness and prescribed specific mass. At present a considerable attention is focused on the problem of structure optimization as applied to the case of inhomogeneous plate of a minimal specific mass using both linear $H(\rho) = A\rho + B$ [3] and nonlinear $H(\rho) = \varphi(\rho)$ [4] relations. An approximate approach to the analysis of penetration process, based on the empirical relation [5] allows to obtain rather simple criteria for structure optimizatcn.

ANALYSIS

1. Formulation of the problem.

According to the applied theory of the plate specific resistance p, penetration of the rigid indenter can be expressed [5] as

$$p = H + k\rho v^2 \qquad (1.1)$$

where H is dynamic hardness; k is the shape factor of the indenter head (in case of a tapered head $k=\sin^2\alpha$, α is a half angle of the cone opening); v is the current penetration rate.

The equation of motion for indenter is given as [3]

$$(1/2)M\, d(v^2)/dL = -2\pi \int_0^L p(x,L)\, r(\xi)\, \partial r(\xi)/\partial\xi \, d\xi, \qquad (1.2)$$

where L is the current penetration depth; $r(\xi)$ is the expression for generating line of axisymmetrical indenter; $\xi = L-x$ is the

Third International Conference on Inverse Design Concepts and Optimization in Engineering Sciences (ICIDES-III). Editor: G.S. Dulikravich, Washington D.C., October 23-25, 1991.

coordinate relative to the tip of the indenter (fig.1).

Distributions of density and hardness are assumed to meet the following requirements

$$\rho \subseteq \Omega, \quad \Omega = \{ \rho(x): \rho_1 \le \rho(x) \le \rho_2, \ (x \subseteq [0, L_k]) \} ,$$

$$H \subseteq \mathcal{H}, \quad \mathcal{H} = \{ H(x): H_1 \le H(x) \le H_2, \ (x \subseteq [0, L_k]) \} \qquad (1.3)$$

We shall restrict ourselves to a class of materials for which there exists a one-to-one mapping φ of the set Ω in the set $\mathcal{H}$: $H = \varphi(\rho)$, $\rho_1 \Rightarrow H_1$, $\rho_2 \Rightarrow H_2$ with $\partial\varphi/\partial\rho > 0$. According to the quality criterion stated below, materials inconsistent with the latter conditions are considered inadequate. Further it is assumed that each of the materials is plastic enough and impact velocities lie within the range, in which application of the relation (1.2) proved to be valid.

The boundary conditions for (1.2) imply that the indenter moves with the initial penetration rate $v(h=0) = v_0$ and reaches some unknown finite penetration depth L_k for which $v(L_k) = 0$. We shall concentrate on the case with the plate thickness being equal to the finite penetration depth $b = L_k$.

Specific mass of such target is taken as the principle criterion of quality

$$J = \min_{\rho \subseteq \Omega} \left\{ \int_0^{L_k} \rho(x)\, dx \right\} \qquad (1.4)$$

2. *Conical indenter. Linear relation $H = \varphi(\rho)$.*

Let us consider the technique of applying the maximum principle [2] to a number of particular problems. Within the framework of theory of optimal control the problem may be expressed in the form of ($(y^1 \equiv v^2, y^2, y^3)$ is the vector of phase coordinates, $t \equiv L$ is the time analog)

$$dy^1/dt = -E\,[(1/2)\,t^2 + (A + ky^1)y^2],$$
$$dy^2/dt = y^3, \quad dy^3/dt = \rho, \qquad (2.1)$$

where $E = (4\pi/M)\,(\mathrm{tg}\alpha)^2$.

In the following it is reasonable to introduce additional phase coordinates y^2, y^3, since the right side of the equation of motion involves an explicit form of functional (1.3), leading to condition $d\psi_0/dt = -\partial h/\partial y^0 \neq 0$.

The mapping $H = \varphi(\rho)$ is assumed in the form of linear approximation

$$H(\rho) = A\rho(x) + B,$$
$$A = (H_2 - H_1)/(\rho_2 - \rho_1), \quad B = (H_1\rho_2 - H_2\rho_1)/(\rho_2 - \rho_1), \qquad (2.2)$$

At the initial moment of time the vector of phase coordinates remains fixed $t = 0$: $y^1 \equiv y^1_0$, $y^2 = y^3 = 0$. The finite vector value $\bar{y}_k$ belongs to a smooth, two-dimensional variety S_k Euclidean space with dimension $n = 3$

$$S_k : F_k(y^1_k, y^2_k, y^3_k) \equiv y^1_k = 0 \qquad (2.3)$$

The condition of transversality for the vector of conjugate variables ψ yields two relations

Third International Conference on Inverse Design Concepts and Optimization in Engineering Sciences (ICIDES-III), Editor: G.S. Dulikravich, Washington D.C., October 23-25, 1991.

$$t = t_k \ : \ \psi_2 = 0, \quad \psi_3 = 0 \qquad (2.4)$$

The equation for the conjugate variables takes the form

$$d\psi_1/dt = Eky^2\psi_1, \quad d\psi_2/dt = E(A + ky^1)\psi_1, \quad d\psi_3/dt = -\psi_2 \qquad (2.5)$$

Optimization of the process $\rho^0, \bar{y}^0$ requires the existence of such nontrivial constant $\psi_0 \le 0$ and vector-function $\psi(t)$ with will allow to meet the maximum condition [2]

$$\max_{\rho \le \Omega} h(\bar{\psi}(t), y(t), t, \rho) = h(\bar{\psi}(t), \bar{y}(t), t, \rho^0) \qquad (2.6)$$

and transversality condition

$$h(\bar{\psi}(t_k), \bar{y}(t_k), t_k, \rho^0(t_k)) = \sum_n \psi_n(t_k) q^n \qquad (2.7)$$

where $\bar{q} = \left\{0, \ dy^2/dt, \ dy^3/dt \right\}\Big|_{t=t_k}$.

According to (2.4) the right-hand side of (2.7) is equal to zero.

Hamiltonian operator is expressed as

$$h = (\psi_0 + \psi_3)\rho - \psi_1 E\left[(1/2)Bt^2 + (A + ky^1)y^2\right] + \psi_2 y^3 \qquad (2.8)$$

Integration of the system (2.5) combined with conditions (2.4), (2.7) enables one to define behavior of Hamiltonian h in terms of linear function of ρ with coefficient $\Phi = \psi_0 + \psi_3$.

3. Cylindrical indenter with a conic head of the height δ. Linear relation $H = \varphi(\rho)$.

The system of differential equations describing the process is divided into two parts:

$$dy^1/dt = \begin{cases} -E\left[(1/2)B\, t^2 + (A + ky^1)y^2\right], & t < \delta \\ -E\left[(1/2)B\, \delta^2 + (A + ky^1)y^2\right], & t \ge \delta \end{cases}, \qquad (3.1)$$

$$dy^2/dt = \begin{cases} y^3, & t < \delta \\ y^3 - \delta\rho(t-\delta), & t \ge \delta \end{cases}, \quad dy^3/dt = \begin{cases} \rho(t), & t < \delta \\ \rho(t) - \rho(t-\delta), & t \ge \delta, \end{cases}$$

Hamiltonian operator takes the form

$$h = (\psi_0 + \psi_3)\rho(t) - \psi_1 E\left[(1/2)Bt^2 + (A + ky^1)y^2\right] + \psi_2 y^3, \text{ for } t < \delta;$$

$$h = (\psi_0 + \psi_3)\rho(t) - (\delta\psi_2 - \psi_3)\rho(t-\delta) + \psi_2 y^3 - \qquad (3.2)$$

$$- \psi_1 E\left[(1/2)B\delta^2 + (A + ky^1)y^2\right], \text{ for } t \ge \delta$$

The equations for the conjugate variables is expressed as (2.5) $\forall t \in [0, t_k]$. It is assumed that the value y_0^1 is such that

Third International Conference on Inverse Design Concepts and Optimization in Engineering Sciences (ICIDES-III), Editor: G.S. Dulikravich, Washington D.C., October 23-25, 1991.

condition $L_k > \delta$ is satisfied automatically.

4. Cylindrical indenter with a flat end-face. Nonlinear relation $H = \varphi(\rho)$.

The equation of motion for indenter and Hamiltonian are written, respectively as

$$dy^1/dt = -E\,[\varphi(\rho) + \rho y^1], \tag{4.1}$$

$$h = \psi_0 \rho - \psi_1 E[\varphi(\rho) + \rho y^1] \tag{4.2}$$

Using differential equation for conjugate variables and transversality condition gives:

$$h = \rho\Phi_1 + \varphi(\rho)\Phi_2 \tag{4.3}$$

$$\Phi_1 = 1 + y^1 fZ, \quad \Phi_2 = fZ, \quad Z = \exp\left(-E\int_t^{t_k} \rho d\tau\right) \tag{4.4}$$

For a piecewise-linear relation $\varphi(\rho)$ (see fig.2) Hamiltonian is transformed to a piecewise-linear function ρ with the slope Φ

$$\Phi = \begin{cases} -1 + (Z\rho_k/(B+A\rho_k))(A+y^1), & \rho\in[\rho_1, \rho_*] \\ -1 + (Z\rho_k/(B_1+D\rho_k))(D+y^1), & \rho\in(\rho_*, \rho_2] \end{cases} \tag{4.5}$$

For nonlinear relation $\varphi(\rho)=B+A\rho^n$ $(A>0, n>0)$ Hamiltonian reduces to

$$h = \rho\Phi(\rho) + B\Phi_2, \quad \Phi = 1 + f_n Z(y^1 + A\rho^{n-1}), \quad f_n = \rho_k/(B+A\rho_k^n) \tag{4.6}$$

The conditions assumed for existence of continuous solutions may be expressed as

$$(\partial h/\partial\rho)\Big|_{\rho=\rho^\circ} = \Phi_1 + A_n\Phi_2(\rho^\circ)^{n-1} = 0 \tag{4.7}$$

$$(\partial^2 h/\partial\rho^2)\Big|_{\rho=\rho^\circ} = A_n n(n-1)\Phi_2(\rho^\circ)^{n-2} < 0 \tag{4.8}$$

Following (4.7) one gets:

$$\rho^\circ = \left[-\Phi_1/(A_n\Phi_2)\right]^m, \quad m = 1/(n-1) \tag{4.9}$$

Differentiation of (4.9), using (4.1) gives

$$\partial\rho^\circ/\partial t = -G(\rho^\circ)^2\left[1 + B/(A(1-n))\,(\rho^\circ)^{-n}\right], \quad G = E/n \tag{4.10}$$

RESULTS

Without going into details we shall examine some qualitative results obtained for a number of special cases.

1. Linear relation $H = \varphi(\rho)$.

From the analysis of the system (2.1),(2.5),(2.8) we can draw the following qualitative conclusions :

(i) There is an interval $(t_*, t_k]$ in which the optimal functi-

Third International Conference on Inverse Design Concepts and Optimization in Engineering Sciences (ICIDES-III). Editor: G.S. Dulikravich. Washington D.C., October 23-25, 1991.

on has the form of $\rho^0 = \rho_1$, i.e. the rear layer should be made of more light and less hardness materials;

(ii) The function $\rho^0 = \rho_1$ is optimal within the entire interval $(t_0, t_k]$, if $B \geq 0$;

(iii) In the case of $B < 0$ the structure of target should be double layer with the front lay being made of hard and heavy material. In this case a relay-type control is realized.

Similar results have been obtained for the case (3.1),(3.2). A general phase diagram of the optimal structure is shown in fig.3.

Here v_1 is the velocity at which $L_k = \delta$, where δ the height of the indenter head. It is seen that the structure largely depends on the parameter B. If the specific hardness $Q = H/\rho$ is assumed the measure of material quality, then, according to (2.2), the condition $B<0$ identifies the maximum quality of heavy material (ρ_2, H_2). In this case a double layer plate is an optimal structure for a target. Contrary, when $v_1 > v_0$ an optimal structure may be represented by a homogeneous plate made from a light material.

2. Nonlinear relation $H = \varphi(\rho)$.

(i) For a piece-wise linear function $H(\rho)$ as plotted in fig.2 the problem is solved for three different materials. The "phase-diagram" of the optimal structure is shown in fig.4, where $\alpha = -(\rho_1/\rho_2)(\rho_2-\rho_*)/(\rho_*-\rho_1)$, $X = (L_k/\delta)^2-1$. As it follows from the observable scale effect, the optimal structure for a given set of materials (B, B_1) depends on the relation L_k/δ.

(ii) For nonlinear dependence $H(\rho)$ the function of the optimal control may not include discontinuities. Inequality (4.8) is valid for $n < 1$ in the neighborhood of $(t_*, t_k]$, $0<t_*<t_k$. The procedure of qualitative estimating the type of solution to the equation (4.10) may be as follows. The first approximation (the expression in square brackets in (4.10) is constant) follows from $\partial\rho^0/\partial t = -G(\rho^0)^2$ as $(\rho^0)^{-1} = \rho_2^{-1} + G(t-t_*)$. This solution is found to be exact for $B = 0$. The second approximation has a more complicated form. The results are shown in fig.5. The position (coordinate) of the point t_* is calculated numerically and may coincide with the starting point of the process.

The results of present investigation allow to make a prompt qualitative estimation of the optimal target structure. The best ratio of layers in a double-layer target may be calculated numerically by solving the equation of motion for indenter.

REFERENCES

1. Aptukov, V.N., Pozdeev, A.A. (1982) "Some minimax problems of technology and strength of structures", Izv. AN. USSR. Tech. cybernetics, 1, 47-55 (in russian).

2. Pontryagin, L.L., Boltyanski, V.G. etc. (1969), *Mathematical*

Third International Conference on Inverse Design Concepts and Optimization in Engineering Sciences (ICIDES-III). Editor: G.S. Dulikravich. Washington D.C., October 23-25, 1991.

theory for optimal processes, Nauka, Moscow (in russian).
3. Aptukov,V.N., Petruhin,G.I., Pozdeev,A.A. (1985) "Optimal braking of rigid body by the inhomogeneous plate under normal impact", Izv.AN.USSR. Mech.Solids, 1, 165-170 (in russian).
4. Aptukov,V.N. (1985) "Optimal structure of inhomogeneous plate with continuous properties distribution over section", Izv.AN.USSR. Mech.Solids, 3, 149-152 (in russian).
5. Vitman,F.F., Stepanov,V.A.(1958), *Some problems of the strength of solids*, Acad.Sci., Moscow, (in russian).

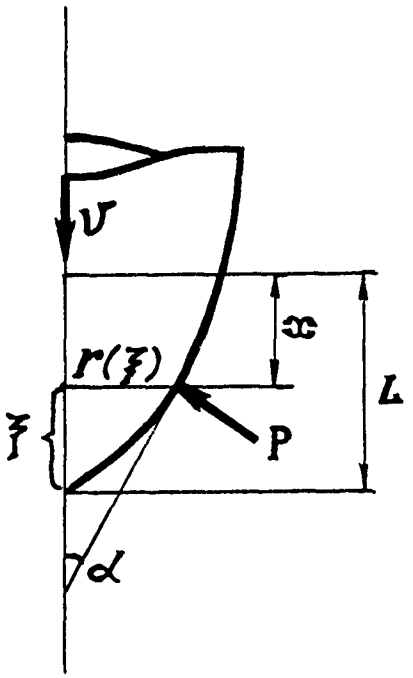


Fig. 1.

Third International Conference on Inverse Design Concepts and Optimization in Engineering Sciences (ICIDES-III), Editor: G.S. Dulikravich, Washington D.C., October 23-25, 1991.

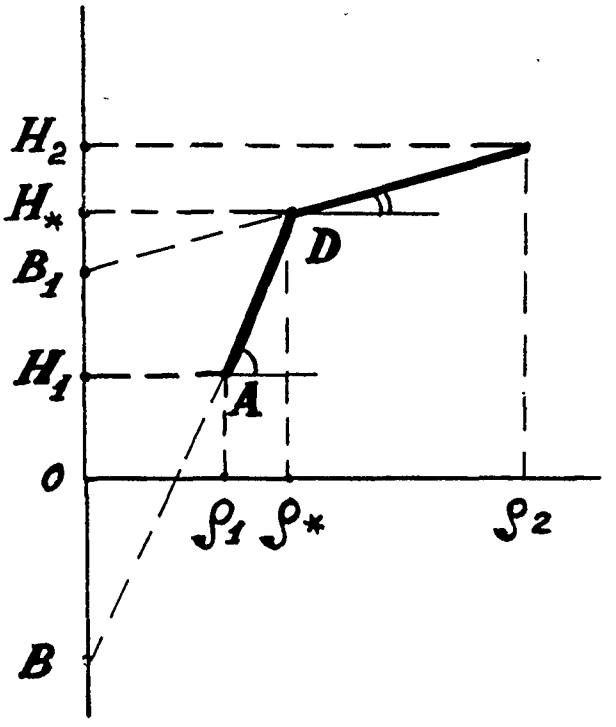


Fig. 2.

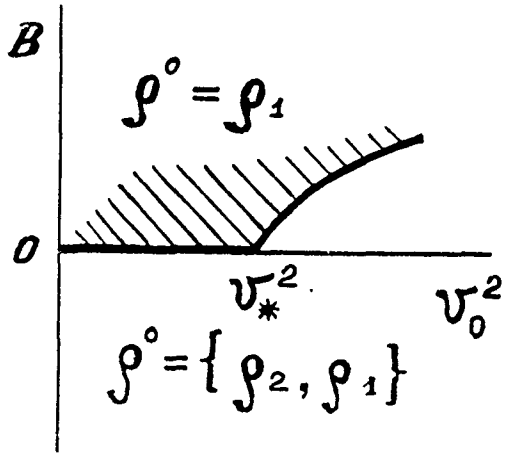


Fig. 3.

Third International Conference on Inverse Design Concepts and Optimization in Engineering Sciences (ICIDES-III), Editor: G.S. Dulikravich, Washington D.C., October 23-25, 1991.

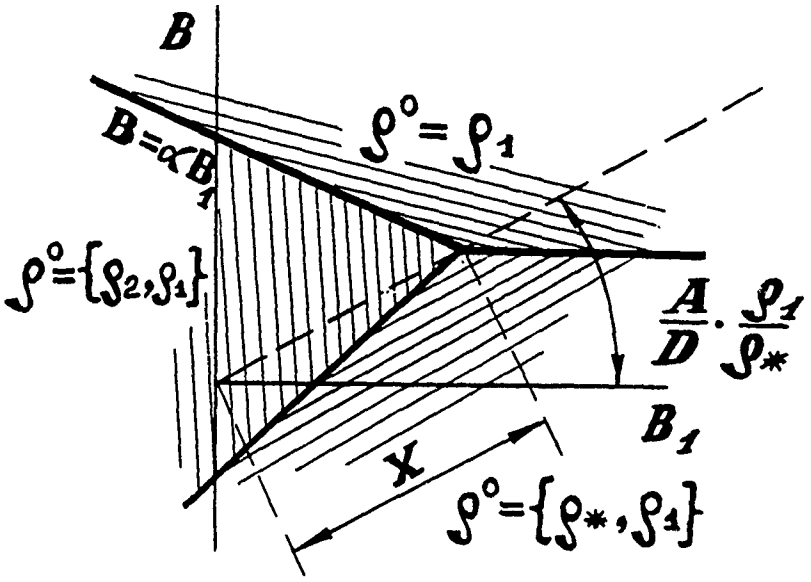


Fig. 4.

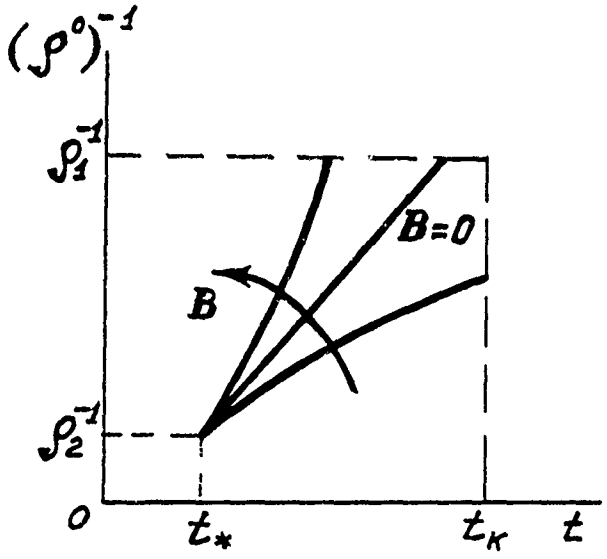


Fig. 5.

Third International Conference on Inverse Design Concepts and Optimization in Engineering Sciences (ICIDES-III), Editor: G.S. Dulikravich, Washington D.C., October 23-25, 1991.

ANALYSIS OF THE OPTIMAL LAMINATED TARGET MADE UP OF DISCRETE SET OF MATERIALS

Valery N. Aptukov, Valentin L. Belousov

Institute of Continuous Media Mechanics
UB of the Academy of Sciences USSR,
Koroleva st., 1, Perm, 614061, USSR

ABSTRACT

A new class of problems has been analyzed to estimate an optimal structure of laminated targets, fabricated from the specified finite set of homogeneous materials. An approximate description of perforation process is based on the model of radial hole extension. The problem is solved by using the needle-type variation technique. The desired optimization conditions and quantitative/qualitative estimations of optimal targets have been obtained and discussed using specific examples.

INTRODUCTION

The problem of optimizing strength properties of inhomogeneous targets under impact of tapered conical indenter was first considered in the study [1]. The qualitative criteria of optimal target structure, developed in this and the following studies (for example [2]), were based on Pontryagin maximum principle [3]. In the previous research an assumption was made about existence of analytical relation between material hardness and density - a class of so called control functions.

In the present investigation the range of control functions belongs to some finite discrete set. This suggests using technique of needle variations [4] when estimating the necessary optimization conditions and constructing computational algorithm.

An approximate analysis of penetration is based on the model of radial hole extension [5].

ANALYSIS

1. Penetration model.

The model of radial hole extension is based on the assumption of radial displacement of material particles under the plane axially-symmetric deformation, caused by penetration of the tapered indenter.

According to [5], the pressure acting on the indenter within the distance $\zeta = x-\xi$ from the front plate surface can be written as

$$p = (1/2)\rho v^2\left\{(\partial r/\partial\xi)^2\left[\theta(\varepsilon)-\varepsilon/(1+\varepsilon)\right] + r\partial^2 r/\partial\xi^2\right\} + \\ + (1/2)\rho\dot{v}\,\theta(\varepsilon)r\partial r/\partial\xi + (1/2)\sigma_s\left[1 + \theta(\varepsilon)\right] \qquad (1.1)$$

Third International Conference on Inverse Design Concepts and Optimization in Engineering Sciences (ICIDES-III), Editor: G.S. Dulikravich, Washington D.C., October 23-25, 1991.

where $r = r(\xi)$ is the expression for the generating line of the axisymmetric indenter, ρ is the density, $\theta(\varepsilon) = \ln(1+\varepsilon)$, $\varepsilon = E/[\sigma_s(1+\nu)]$, v is the indenter current velocity, σ_s is the yield stress, ν is Poisson ratio, E is Young's modulus.

The equation of motion for the indenter of mass M has the form

$$(1/2)Md(v^2)/dx = -2\pi \int_0^x p(\zeta)r(\xi)(\partial r/\partial \xi)d\xi \qquad (1.2)$$

with the initial condition $v(0) = v_o$.

2. Optimization problem.

It is convenient to represent the penetration process as a system of differential equations relative to a vector of phase coordinates y with u as a control function

$$dy/dx = f(y,u), \quad y(0) = y_o \qquad (2.1)$$

and to define Freshet's differentiable functionals by

$$F_0[u(.),b] = \int_0^b \rho(x)dx, \qquad (2.2)$$

$$F_1[u(.),b] = y^1(b) = 0 \qquad (2.3)$$

Insertion of additional phase coordinates and use of (1.1) and (1.2) reduces (2.1) to

$$dy^1/dx = -2(y^1 y^2 + d_1 y^3)/(d_2 + y^4), \quad dy^2/dx = y^5 - A(x-h)\cdot h,$$

$$dy^3/dx = y^6 - B(x-h)\cdot h, \quad dy^7/dx = 2y^7 - C(x-h)\cdot h^2, \quad dy^5/dx = A(x) - A(x-h),$$

$$dy^6/dx = B(x) - B(x-h), \quad dy^7/dx = y^8 - C(x-h)\cdot h, \quad dy^8/dx = C(x) - C(x-h),$$

$$y^1(0) = v_o^2, \quad y^i(0) = 0, \quad (i = 2,3,\ldots 8), \qquad (2.4)$$

where $d_1 = (\mathrm{tg}\ \alpha)^{-2}$, $d_2 = M d_1^2/\pi$, $y^1 \equiv v^2$,

$$A(x) = 0 \ (if\ x<0), \ \rho(x)\left[\theta(\varepsilon(x)) - \varepsilon(x)/(1+\varepsilon(x))\right] \ (if\ x\geq 0),$$

$$B(x) = 0 \ (if\ x<0), \ \sigma_s(x)\left[1+\theta(\varepsilon(x))\right] \ (if\ x\geq 0),$$

$$C(x) = 0 \ (if\ x<0), \ \rho(x)\,\theta(\varepsilon(x)) \ (if\ x\geq 0),$$

The size, number and class of materials to be used in the target layers are specified by a distribution of material properties

$$u(x) = \{u_s : x\in[x_s, x_{s+1}), \ s=\overline{1,n}\}, \quad x_1 = 0, \quad x_{n+1} = b,$$

where n is the number of layers. The value of u_s belongs to a finite set U which corresponds to a given set of materials $u \subseteq U = \{U_1, U_2 \ldots U_q\}$. Here u_s is the material in the s^{th} layer, U_i is the material number and q is the material quantity.

Third International Conference on Inverse Design Concepts and Optimization in Engineering Sciences (ICIDES-III), Editor: G.S. Dulikravich, Washington D.C., October 23-25, 1991.

The stated optimization problem suggests that from all piecewise continuous functions $u(x) \subseteq U$ and numbers $b > 0$ one should choose a control $\{u^\circ(x), b^\circ\}$ which will provide minimum for the functional (2.2) under the limiting conditions (2.1), (2.3). The quality criterion may be refered to as a specific plate mass (2.2) subject to $v(b) = 0$ (under the requirement of arrested indenter).

3. Necessary conditions of optimization.

A discrete character of the control function range doesn't allow to generate small variations in the norm $\|\delta u\| = \max_{x \subseteq [0,b]} |\delta u|$. The disturbed control may be written in the form

$$u(x) = \begin{cases} w, & x \subseteq m, \ w \subseteq U \\ u^\circ, & x \notin m, \end{cases} \qquad (3.1)$$

where $m \subseteq [0, b^\circ]$ is the set of measure zero.

An equation for the system (2.1) is expressed in terms of variations and the main terms of functional increments (2.2), (2.3) are given by

$$\delta(d\bar{y}/dx) - \partial\bar{f}/\partial\bar{y}\ \delta\bar{y} = \bar{f}(\bar{y}, u) - \bar{f}(\bar{y}, u^\circ),$$

$$\delta F_0 = \int_m [\rho(w) - \rho(u^\circ)]dx + \rho[u^\circ(b^\circ)]\delta b^\circ, \qquad (3.2)$$

$$\delta F_1 = \delta y'(b^\circ) + \bar{f}[\bar{y}(b^\circ), u^\circ]\delta b^\circ$$

Using the Lagrange identity and desired limiting conditions for the disturbed trajectory one finds an expression for δb°

$$\delta b^\circ = \left[1/f_1[\bar{y}(b^\circ), u^\circ]\right] \int_0^{b^\circ} \bar{\psi}[\bar{f}[\bar{y}, w) - \bar{f}[\bar{y}, u^\circ)]dx \qquad (3.3)$$

where the conjugate vector-function $\bar{\psi}$ satisfies

$$d\bar{\psi}/dx = -\partial\bar{f}/\partial\bar{y}\ \bar{\psi} \qquad (3.4)$$

Variation of the minimized functional is written as

$$\delta F_0[u(.), b] = \int_m [H(\bar{y}, \bar{\psi}, u^\circ) - H(\bar{y}, \bar{\psi}, w)]dx \qquad (3.5)$$

In order to make the control function optimal it is necessary to follow the principle of maximum

$$H(\bar{y}, \bar{\psi}, u^\circ) = \max_{w \subseteq U} H(\bar{y}, \bar{\psi}, w) \qquad (3.6)$$

An expression for H is given as

$$H = D\left[\psi_5(x)A(w) + \psi_6(x)B(w) + \psi_8(x)C(w)\right] - \rho(w), \ m \subseteq [b^\circ - h, b^\circ],$$

$$H = \left\{\left[\psi_5(x) - \psi_2(x+h)h - \psi_5(x+h)\right]A(w) + \left[\psi_6(x) - \psi_6(x+h)h - \psi_3(x+h)\right]B(w)\ldots\right.$$

$$\left. + \left[\psi_8(x) - \psi_8(x+h) - \psi_7(x+h)h - \psi_4(x+h)h^2\right]\right\} - \rho(w), \quad m \subseteq [0, b^\circ - h], \qquad (3.7)$$

Third International Conference on Inverse Design Concepts and Optimization in Engineering Sciences (ICIDES-III), Editor: G.S. Dulikravich, Washington D.C., October 23-25, 1991.

where $D = \rho[u^0(b^0)]/f\,[\bar{y}(b^0), u^0]$, $x \subseteq m$.

4. Geometrical interpretation and qualitative conclusions [6].

(i) Function H can be expressed as $H = \sum_1^n \mu_i(\bar{y}, \bar{\psi})\varphi_i(w)$, φ_i are continuous functions of x. The function H given in φ_i is refered to as a hyperplane of support to a vector-gradient, which defines direction of increase grad $H = (\mu_1, \mu_2, \ldots, \mu_n)$. From this follows that H approaches maximum at one of the vertices of convex polyhedron Q, which represents a convex shell of the point set $\varphi_i(w_s)$, $w_s \subseteq U$, $s = \overline{1,q}$. The remaining materials of the set U can be excluded from a further discussion.

(ii) The continuity of $\mu_i(x)$ implies that at any vertex of the polyhedron Q there is a hypercone K the interior of which may contain grad H at slight variation in $x \subseteq (x^*, x^{**}) \subseteq [0, b]$ and allow to satisfy the maximum condition. Thus, the optimal plate structure includes the finite number of layers of finite thickness.

(iii) Substitution of materials is expected to take place at the contact points x^* of the hypercone K and one of the polyhedron edges. It is to be noted here that the immediately adjacent materials may be only there which match the adjoining vertices of the polyhedron.

(iv) It can be shown that from the entire set of materials assumed in the vicinity of the rear surface the preference should be given to material with minimal density.

5. Numerical algorithm.

Numerical procedure requires insertion of some admissible control function $u(x) \subseteq U$ and a small parameter χ which describes the set of measure zero. Computational algorithm involves the uniform mesh x_i having the mesh spacing χ. The values of $\bar{y}$ and ψ are calculated at points $x_s + \chi/2$ and assumed constant for the segment $[x_s, x_{s+1}]$.

Solution includes the following steps:

(i) The system (2.4) is integrated and $\bar{y}(x)$ and b are defined at mesh nodes.

(ii) Boundary conditions for conjugate functions are prescribed at the point $x = b$ and the system (3.4) is solved.

(iii) A new value of u_s^* on the segment m_s is derived from condition $H(.,.,u_s^*) = \max_{w \subseteq U} H(.,.,w)$; if $u_s^* = u(x_s + \chi/2)$ this step is repeated for $s = s+1$; otherwise, a new control function is assumed $u^* = u_s^*$ (*if* $x \subseteq m_s$), $u(x)$ (*if* $x \notin m_s$) and calculation returns

Third International Conference on Inverse Design Concepts and Optimization in Engineering Sciences (ICIDES-III), Editor: G.S. Dulikravich, Washington D.C., October 23-25, 1991.

to step (i).

The procedure of improving control function proceeds like this up to the terminal point on the right of the interval. The process is completed as soon as $u(x)$ remains constant at any s.

RESULTS

A set of materials contain annealed aluminum (a), aluminum alloy B-95 (b), annealed titanium (c), titanium alloy BT-6 (d), steel Ст.6 (e), steel 12Х2Н4А (f). Material properties are given in Table 1.

Table 1.

Material	Density ρ, g/sm^3	Young's modulus E, GPa	Yield stress σ_s, GPa	Poisson ratio, ν
a	2.8	70	0.06	0.33
b	2.8	70	0.45	0.32
c	4.5	110	0.08	0.30
d	4.5	120	0.83	0.32
e	7.8	200	0.21	0.28
f	7.8	200	0.11	0.30

For the case of dynamic penetration of tapered cylinder the optimal plate will consist of two materials (d)+(b). The relative front layer thickness of the optimal plate increases with the increase in a half-angle of the cylinder opening α and initial impact velocity v_o.

Fig. 1 shows the decreased mass optimally $\bar{F}_o$ of homogeneous plates made up of (*b*), (*d*) and (*f*) -materials as compared to the optimal one. Disadvantage of heavy materials (*d*) and (*f*) decreases with the increase of v_o, since their fraction in the optimal plate is growing high. At $v_o < 600$ m/s the preference is given to a homogeneous material (*b*) rather then (*d*), while at $v_o > 600$ m/s the prefered material is of *d*- type.

The results of present investigation agree qualitatively and quantitatively with data reported in [2]. If instead of material (f) one uses steel with the yield stress 1.5 GPa an optimal plate will consist of three layers. In case of a large choice of materials an optimal target structure will be multilayer. However, the main qualitative characteristic - a decrease of density and hardness with a distance from the upper to lower surfaces of the target - remains uncharged.

It is to be noted here, that the usefulness of a soft rear layer in a target has been already justified but only in context of fracture behavior of material. From mechanical point of view the optimality of target structure predicted in [2] and in present investigation implies its high resistance to penetration while preserving the same ductile type of cratering.

REFERENCES

1. Aptukov,V.N. (1981) "Interaction between indenter and target as a game situation", Proc.V Congr.Theor.Appl.Mech., Alma-Ata, 29 (in russian).
2. Aptukov,V.N. (1991) "Optimal Interaction of Indenter With Inhomogeneous Plate" (paper in this book).
3. Pontryagin,L.L., Boltyanski,V.G. (1969) *Mathematical Theory for Optimal Processes*, Nauka, Moscow (in russian).
4. Fedorenko,R.P. (1978) *Approximate Solution of Optimal Control Problems*, Nauka, Moscow, (in russian).
5. Sagomonyan,A.J. (1974) *Penetration*, MGU, Moscow, (in russian).
6. Aptukov,V.N., Belousov,V.L. and Kanibolotski,M.A. (1986) "Optimization of the multilayer plate structure under penetration of rigid indenter", Mech.Comp.Mater., 2, 252-257 (in russian).

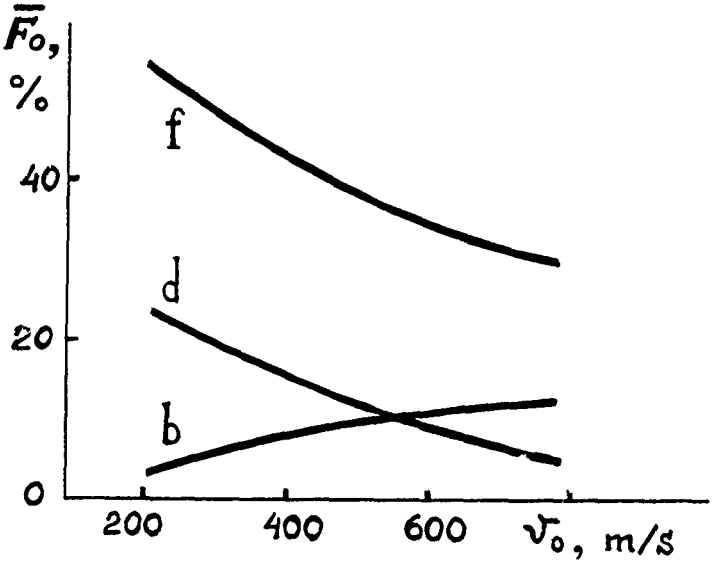


Fig. 1.

Third International Conference on Inverse Design Concepts and Optimization in Engineering Sciences (ICIDES-III), Editor: G.S. Dulikravich, Washington D.C., October 23-25, 1991.

INVERSE PROBLEMS IN THE DESIGN, MODELING AND TESTING OF ENGINEERING SYSTEMS

Dr. Oleg M. Alifanov, Professor and Chairman of Department of Space System Engineering and Design, Dean of the College of Cosmonautics, Moscow Aviation Institute, 4, Volokolamskoye Sh., Moscow, 125871, USSR

ABSTRACT

Formulations, classification, areas of application, and approaches to solving different inverse problems are considered for design of structures, modeling, and experimental data processing. Problems in the practical implementation of theoretical-experimental methods based on solving inverse problems are analyzed in application to identification of mathematical models of physical processes, input data preparation for design parameter optimization, design parameter optimization itself, model experiments, large-scale tests, and real tests of engineering systems. This methodology provides an opportunity to improve the quality of investigations and to accelerate realization of research achievement.

INTRODUCTION

The process of design and testing of a new complex technical object can be arbitrarily divided into a number of steps and sections (Fig. 1). Each of them is very important and essential. If the problems are posed correctly and their solutions are accurate at each step then the developed engineering system will be effective and reliable. Very often structures of today vehicles work in extreme modes, on the limit of structural materials capacity. That is why any mistake made on any of the stages of design and experimental development could result in a catastrophe comparable to those of Chernobyl or Challenger.

Operational conditions of technical equipment in many industries become more and more sophisticated and severe. At the same time, the requirements for reliability and service life as well as effective technological decisions also grow. Therefore, we need not only to improve old, traditional methods of research, design and testing of structures but also to develop altogether new, more perfect ones. To these new methods we can refer those based of solution of inverse problems. The latest 15-20 years witness permanent growth of interest to them. How can we explain it? First of all, this approach made it possible to consider real phenomena taking into account non-linearity and non-stationarity of physical processes characterising today engineering systems. This is a very important point, since the above mentioned phenomena become determinating when operational conditions of the vehicles approach criticality. Conventional classical methods can hardly cope with these difficulties.

The chief advantage of the inverse problems methods is that they enable us to conduct experimental studies under conditions as close as possible to real ones or to study the engineering systems directly. Also, such approach enhances the informative value of these studies, accelerating the experimental works as compared to the traditional methods, and reducing their cost. Besides

Third International Conference on Inverse Design Concepts and Optimization in Engineering Sciences (ICIDES-III), Editor: G.S. Dulikravich, Washington D.C., October 23-25, 1991.

taking into account non-stationarity and non-linearity, inverse problems methods provide an opportunity to analyse account multidimensionality and interdependency of physical processes, indirect measurements, and real scale of time.

All these advantages and possibilities of inverse problems are of special importance for aerospace and rocket technology. Therefore some of the first formulation and solution processes for the inverse problems, in particular, the inverse heat transfer problems, appeared in this area of application.

GENERAL FORMULATION OF INVERSE PROBLEMS AND THEIR CLASSIFICATION

All phenomena in nature are characterized by some cause-and-effect relationships, and it is possible in the construction of mathematical models of physical processes to designate quantities that are causal characteristics of the process and quantities that are resultant characteristics.

Accordingly, all problems can be classified into two types. In the first, they involve study of the effect on the basis of given causes. These are direct problems. In the second - study of the causes on the basis of specified effects. These are inverse problems. Inverse problems have one common attribute in contrast to the case of direct problems. Their formulations cannot be reproduced in a real experiment. It is not possible to reverse the cause-and-effect relation physically, instead of mathematically. For example, it is impossible to reverse the course of a heat transfer process or to change the course of time. Therefore, in mathematical formalization, this property is manifested in incorrect mathematical conditioning and must be taken into account in the development of solution methods and in applying them in practice. When formulating general statements of inverse problems and choosing the main classes of them, the statements of direct problems are supposed to be known. Each direct problem (within the framework of an accepted mathematical model) can be compared with a certain set of inverse problems. All inverse problems can be divided into three classes on the basis of the general objective: inverse problems that arise in the diagnostics and identification of physical processes; inverse problems that arise in the design of engineering products; inverse problems that arise in the control of processes and products.

Inverse problems of the first class usually involve experimental studies. In these cases it is necessary to reconstruct causal characteristics on the basis of certain measured "output" effect characteristics. These problems are primary, both with respect to direct problems and with respect to the other two classes of inverse problems, since they are connected with construction of mathematical models and determination of different characteristics of the models.

Inverse problems of design type consist in determining design characteristics of an engineering unit on the basis of given quality indices within certain limits. Required characteristics are causal with respect to these indices and limits.

In the case of the control, the role of causal characteristics is played by controlling influences the change in which creates the control action expressed by the system state, i.e. the effect.

It should be noted that there exists a fundamental difference between the two types of problems, between problems of diagnostics and identification and problems of design and control. In the case of design and control problems, the widening of the class of acceptable solutions usually simplifies things, since it is then necessary to find any practically feasible solution that would ensure the extremum of quality criterion with the given accuracy. At the same time, for identification and diagnostics problems the wider the class of possible solutions, the worse the situation. Specifically,

Third International Conference on Inverse Design Concepts and Optimization in Engineering Sciences (ICIDES-III), Editor: G.S. Dulikravich, Washington D.C., October 23-25, 1991.

the errors of causal characteristics determined can increase which will make obligatory the use of regular methods of solution.

It should be noted that the theory and methodology of solution of inverse problems (that appear with diagnostics and identification of physical processes) are less developed than those for the other two classes of problems.

According to causal characteristics required it is possible to divide inverse problems of each group into various kinds. Most often, MMs of physical processes are based on equations with partial derivatives. In a general case, four kinds of inverse problems are introduced for them, viz., boundary, coefficient problem, retrospective problems, and geometric problems [1,2]. Boundary problems consist in finding functions and parameters that form boundary conditions; coefficient problems involve determining of functions and parameters that form part of equation coefficients; retrospective problems, (i.e. time reversed ones) consist in finding initial conditions; geometric ones presuppose reconstructing geometric characteristics of a domain or some points, lines or surfaces within a domain (for examples, determining co-ordinates of a phase transfer boundary or of a contact line of materials with different physical properties).

Now, if we again look at the block-scheme of development and creation of an important engineering object (see Fig. 1) we can point out possible and expedient fields of application of new methodology based on the solution of inverse problems. They are marked by shading. Thus, we can see that the scope of application of inverse problems to design and testing is rather wide. It can also be added that there exist a lot of useful applications of these methods for investigation, optimization and development of different technological processes as well.

INVERSE HEAT TRANSFER PROBLEM

Among the most developed and widely used in practice there are inverse problems of heat transfer. Consider now their posing.

In correspondence with three main forms of heat transfer let's introduce three groups of inverse problems: inverse problems of heat conduction, inverse problems of convective heat transfer, and inverse problems of radiative heat transfer. If combined or complex heat transfer is considered, corresponding statements of inverse problems will appear.

Let us now, for example, dwell upon a more concrete formulation of the two groups of inverse heat transfer problems.

INVERSE HEAT CONDUCTION PROBLEMS (IHCP). Problems of this kind are the best investigated and the most widely used in practice [1-4].

As an example, let us consider a one-dimensional problem of heat conduction in a two-layer plate assuming that the layer materials have different thermal properties and that in one of them there occurs a phase transfer, e.g., melting. Layer boundaries $b_1(\tau)$, $b_2(\tau)$, $b_3(\tau)$ can move with time as a result of some physical processes (ablation, thermal expansion or shrinking, mechanical deformation). The internal front of phase transfer $\eta(\tau)$ is also moveable.

We'll assume that temperature field $T(x, \tau)$ in the plate is described by equation system for generalized heat conduction

$$C_j \frac{\partial T_j}{\partial \tau} = \frac{\partial}{\partial x}(\lambda_j \frac{\partial T_j}{\partial x}) + K_j \frac{\partial Tj}{\partial x} + S_j, \quad j = 1, 2, 3 \tag{1}$$

in domains $b_1(\tau) < x < \eta(\tau)$, $\eta(\tau) < x < b_2(\tau)$, $b_2(\tau) < x < b_3(\tau)$, respectively. Conjunction conditions on lines $\eta(\tau)$ and $b_2(\tau)$ have the form

Third International Conference on Inverse Design Concepts and Optimization in Engineering Sciences (ICIDES-III). Editor: G.S. Dulikravich. Washington D.C., October 23-25, 1991.

$$T_1(\eta(\tau)-0,\tau)=T_2(\eta(\tau)+0,\tau)$$

$$\lambda_1\frac{\partial T_1}{\partial x}\bigg|_{x=\eta(\tau)-0}-\lambda_2\frac{\partial T_2}{\partial x}\bigg|_{x=\eta(\tau)+0}=r\frac{\partial\eta}{\partial\tau}$$

$$T_2(b_2(\tau)-0,\tau)=T_3(b_2(\tau)+0,\tau)-R\,\lambda_2\frac{\partial T_2}{\partial x}\bigg|_{x=b_2(\tau)-0}$$

$$\lambda_2\frac{\partial T_2}{\partial x}\bigg|_{x=b_2(\tau)-0}=\lambda_3\frac{\partial T_3}{\partial x}\bigg|_{x=b_2(\tau)+0}$$

To the system (1) let us also add initial temperature distributions

$$T_j(x,0)=\xi_j(x),\quad j=1,2,3$$

at $b_1(0)\le x\le\eta(0)$, $\eta(0)\le b_2(0)$, $b_2(0)\le x\le b_3(0)$, respectively, and conditions on the plate boundaries. As boundary conditions we can regard temperatures

$$T_j(b_j(\tau),\tau)=t_j(\tau),\quad j=1,3;$$

or heat fluxes

$$-\lambda_j\frac{\partial T_j}{\partial x}\bigg|_{x=b_j(\tau)}=q_j(\tau),\quad j=1,3;$$

or Newton conditions of convective heat transfer

$$-\lambda_j\frac{\partial T_j}{\partial x}\bigg|_{x=b_j(\tau)}=\alpha_j[T_j(b_j(\tau),\tau)-T_j^*(\tau)],\quad j=1,3;$$

or conditions that take into account body heat transfer with the environment by means of convection and radiation, and also the heat source that is caused by other processes (melting, sublimation, atom recombination, etc.)

$$-\lambda_j\frac{\partial T_j}{\partial x}\bigg|_{x=b_j(\tau)}=\alpha_j[T_j(b_j(\tau),\tau)-T_j^*(\tau)]+A_j q_{r_j}-\varepsilon_j\sigma T_j^4(b_j(\tau),\tau)+g_j,\quad j=1,3.$$

Here q_r is an incident radiant flux; σ - is the Stephan-Boltzmann constant. Various combinations of the above-mentioned boundary conditions on lines $b_1(\tau)$ and $b_3(\tau)$ are also possible.

Third International Conference on Inverse Design Concepts and Optimization in Engineering Sciences (ICIDES-III). Editor: G.S. Dulikravich. Washington D.C., October 23-25, 1991.

Coefficients C_j, λ_j, K_j and the source S_j in the equations in the general case can be functions of co-ordinate x, time τ, and temperature T_j, or any combination of these variables; in the simplest case they will be constant. Values $r, R, \alpha_j, A_j, \varepsilon_j, g_j$ can be considered as functions of the time and the corresponding temperature.

In the given problem, the causal characteristics will be volumetric heat capacities C_j, thermal conductivities λ_j, convection coefficients K_j, sources S_j, movement of boundaries b_1, b_2, b_3, and phase transfer front η; volumetric heat of phase transfer r, contact thermal resistance R, boundary temperatures t_j, heat fluxes q_j, ambient temperatures T_j^*; absorption coefficients A_j, emissivities ε_j; and surface heat sources g_j. The inverse problem of any kind consists in determining certain values of the sum total of causal characteristics adduced above. Certain additional conditions should be given. In most cases they will be temperature measurements $T(d_i, \tau) = f_i(\tau)$, $i = \overline{1, N}$ in N stationary or moving points d_i of a body; it is seldom that spatially continuous temperatures are considered.

According to the above-introduced causal characteristics of heat transfer processes, the following kinds of inverse problems can be introduced.

The first kind is a *retrospective heat conduction problem*, or the problem with reverse time - the finding of temperature distributions in previous moments (in other words - the determining of the prehistory of the given heat state);

The second kind is *a boundary inverse problem* - the reconstruction of thermal conditions at the boundary of the body. A problem connected with the continuation of the solution of heat conduction equation an overdetermined boundary belongs to this type of problems;

The third kind is *a coefficient inverse problem of heat conduction* - the specification of coefficient of the heat conduction equation (the identification of heat conduction operator).

Finally, it is possible to introduce one more kind of inverse problem, *a geometric* one that consists in finding some geometric characteristics of a heated body, e.g. in reconstructing the movement of the heat transfer boundary of a body on the basis of the results of temperature measurements within the body.

Combined statements are possible when causal characteristics of different types are sought simultaneously. For example, we can simultaneously estimate boundary conditions and temperature field in the past moments of time in the problem without initial conditions. This problem is a combination of a boundary problem and a retrospective one. There can exist natural combinations of a boundary problem and a coefficient one as well as those of a boundary problem and a geometric inverse problem of heat conduction.

INVERSE PROBLEM OF CONDUCTIVE-AND-CONVECTIVE HEAT TRANSFER FOR A POROUS BODY [?]. One more typical problem is connected with the development and testing of porous cooling systems of various designs. In these cases it is necessary to have information on the following characteristics: heat fluxes on blown surfaces; thermal conductivity λ_s; internal heat transfer coefficient α_V of a porous body, heat transfer coefficient α_0 at a coolant inlet into a porous material. Determination of these values from transient temperature measurements in porous structure is reduced to the solution of an inverse problem of conductive-and-convective heat transfer. In the one-dimensional case for a flat layer of a porous material with gaseous coolant, the MM of heat and mass transfer has the form

$$C_s \frac{\partial T_s}{\partial \tau} = \frac{\partial}{\partial x}\left(\lambda_s \frac{\partial T_s}{\partial x}\right) - \frac{\alpha_V}{1-P}(T_s - T_g),\ x \in (0, b),\ \tau \in (0, \tau_m]; \tag{2}$$

$$(\rho c_p)_g \frac{\partial T_g}{\partial \tau} = \frac{\partial}{\partial x}\left(\lambda_g \frac{\partial T_g}{\partial x}\right) - (\rho\, v\, c_p)_g \frac{\partial T_g}{\partial x} + \frac{\alpha_V}{P}(T_s - T_g), \tag{3}$$

$$x \in (0, b),\ \tau \in (0, \tau_m];$$

$$T_s(x, 0) = \xi_s(x),\ T_g(x, 0) = \xi_g(x), \tag{4}$$

$$-\lambda_s \frac{\partial T_s(b, \tau)}{\partial x} = \alpha_0[T_s(b, \tau) - T_{g0}]; \tag{5}$$

$$(\rho\, v\, c_p)_g\, T_g(b, \tau) = (\rho\, v\, c_p)_g\, T_{g0} + \alpha_0[T_s(b, \tau) - T_{g0}]; \tag{6}$$

$$-\lambda_s \frac{\partial T_s(0, \tau)}{\partial x} = q(\tau); \tag{7}$$

$$\frac{\partial^2 T_g(b, \tau)}{\partial x^2} = 0; \tag{8}$$

$$-\frac{dp_g}{dx} = \alpha(\mu v)_g + \beta(\rho v)_g^2; \tag{9}$$

$$\rho_g = \frac{P_g M_g}{8314\, T_g}. \tag{10}$$

Here indices s and g mean solid and gaseous phases respectively; c_p is specific heat capacity at constant pressure; ρ is density; v is velocity; capital P is porosity of the solid; a small letter p means pressure; μ is viscosity; M is molecular weight; α and β are hydraulic coefficients; T_{g0} is initial temperature of the injected gas.

This model contains the energy equations for solid and gaseous phases both the corresponding initial (4) and boundary conditions (5)-(8), and a modified Darcy's law (9) and equation of state for the gas (10). The condition (8) is one of the variants of natural boundary condition. It provides for the uniqueness of the direct-problem solution and, simultaneously, gives results that agree well with those corresponding to the actual boundary conditions of the first and second kind.

The unknown causal characteristics include $q, \lambda_s, \alpha_V, \alpha_0$.

The measurement data are specified with the conditions:

$$T_s(d_n, \tau) = f_n(\tau),\ \tau \in [0, \tau_m],\ n = \overline{1, N},\ N \geq 1,\ 0 \leq d_1 < d_2 < \ldots\ d_N \leq b$$

EXPERIMENTAL-THEORETICAL INVERSE-PROBLEM METHOD

In an exact formulation, any inverse problem can be written in compact form using an operator equation of the first kind

$$Au = f,\ u \in U,\ f \in F. \tag{11}$$

Here an operator A and right side f are given data. Value u is an unknown. It may be vector, function, or vector-function. Let us assume that operator A is continuous, and spaces U and F are metric.

It is known, that the problem (11) is called well-posed if it meets the following requirements (the Hadamard conditions):

* solution of the problem exists for any right side;

* solution is unique;
* it depends continuously on f.

If at least one of the requirements is violated, this problem is called ill-posed. This is the very situation, which is observed in solving the inverse problems.

This requires not only the development of special mathematical methods, but also proper technical organization of the studies. Experience indicated that only with a rational combination of physical and mathematical fundamentals it will be possible to make effective and creative use of the methods considered.

We shall use the concept of *an experimental-theoretical inverse problem method*, by which we mean an aggregate of studies and developments that includes physical and mathematical statement of the inverse problem, methods and algorithms for its solution, the necessary technical systems, and organization of experimental studies.

ON THE HISTORY OF THE MATHEMATICAL SUBJECT-MATTER

A retrospective look at the matter of solving inverse heat transfer problems and utilization of corresponding methods justifies to the fact that a tendency for rapid development of the scientific trend observed to-day was of irregular nature before.

The interest and attention shown by investigators to this problem appeared incidentally. The first formulations and first attempts of solving inverse problems, perhaps, should be related to determination of historical climate and heat condition of earth's ground layer. These are works of Fourier, Poisson and Kelvin in the 19th century.

It should be noted that some methods used at present are based on solutions known long enough. The example of this - presentation of solutions of linear problems of heat conduction through Dugamel integral (1832) with further numerical inversion of it. However, the corresponding procedures for determining unsteady heat fluxes appeared much later in works by T.J. Mirsepassi, one of the first having been published in 1958 [5], in works by G. Stolz (1960) - [6], by J.V. Beck (1962 and later in [7,8]), by G.T. Aldoshin, A.S. Golosov, V.I. Zhuck (1968 and later in [9,10]) by O.M. Alifanov (1969 and later in [11-14]) and by other authors. Regularization of heat state of solid bodies in the form of exponential law of temperature change was discovered in 1901 by J. Boussinesq. At the same time the basics for the theory of regular heat state was developed by G.M. Kondratiev and later by A.V. Lyikov in the 40s and the 50s. In 1955 the principle of regular heat state was used by N.V. Shumakov to find non-stationary heat fluxes through a successive interval method [15]. Apparently, it is the first "promulgated" technique for solving boundary inverse problems of heat condition.

Note that for a particular case of so-called pseudo-inverse heat condition problem W.H. Giedt in 1955 [16] and O.N. Kastelin jointly with L.N. Bronsky in 1956 [17] published a procedure for its solution which still finds its application.

A solution of heat conduction problem in the Cauchy generalized formulation presented as an infinite power series was obtained by J. Stefan in 1890 [18]. This result can be considered as the first exact solution of a one-dimensional inverse problem with constant coefficients, although for this purpose it was not used until the studies of A.G. Tyomkin and O.R. Burggraf [19, 20] who in 1961 and 1964, respectively, got similar by form solutions for a series of other linear inverse problems of heat conduction.

Thus, despite the fact that necessary preconditions for constructing solution of inverse problems appeared already in the last century and at the very beginning of the current century, practical

conclusions, nevertheless, have been drawn quite recently. The most active and stable period for the development of solution methods and their application falls on the last 20 years.

Let us touch upon history of mathematical studying and solving ill-posed problems.The conditions for well-posed formulation of any problem of mathematical physics were introduced by J.Hadamard in 1902 [21]. Usually it was assumed that if the original mathematical formulation of a problem did not satisfy any of these conditions, it was then of no physical or practical sense, and, consequently, there was no reason of constructing its solution. Gradually, however, the attitude of mathematicians and physicists towards ill-posed problems began to change. Already in 1926 T. Carleman makes the first attempt to solve an ill-posed problem [22]. In the 3Os new investigations on determination of historical climate have been made by A.N. Tikhonov. In 1943 he formulated for the first time in a complete form the so-called *conditionally-ill-posed statement* of ill-posed problem of mathematical physics assuming a stable solution in the compact class of functions [23]. This fundamental result, beginning from 1953, is further developed in the works by M.M. Lavrentiev and by V.K. Ivanov (see bibliography in [24, 25]). To this trend we can refer an interesting study by F.John in which he presents a method of solving heat conduction equation with inverse time [26].

The most weightful mathematical result of general nature in the area of ill-posed problem opening a fruitful direction in the mathematical physics and computing mathematics was obtained in 1963 by A.N. Tikhonov [27]. It should be noted that very close idea was proposed for solving linear integral equations of the first kind by Phillips in 1962 [28]. But he did not give any strict substantiation of this approach. Tikhonov's method of *regularization* broadened considerably the bounds of effective practical use of ill-posed problems in various fields of science and technology. Since that time this method has got intensive development in the works by A.N.Tikhonov, V.K. Ivanov, V.Ya. Arsenin, V.A. Morozov, A.B. Bakushinsky, V.B. Glasko, V.N. Strakhov and many other mathematicians (see bibliography in [25, 29]).

At present we have quite a complete mathematical theory of solving ill-posed problems, the pivot of which being this very method.

The majority of works devoted to a development of the regularization method treat one of its forms which got the name of a *variational method.*

Other forms are also possible. Among the most universal is a so called *iterative regularization* which is most effectively realized with the help of non-linear gradient algorithms. This quite a general method has been proposed by O.M.Alifanov [30, 31] and mathematically grounded together with S.V.Rumyantsev [32, 33]. Important contribution to solving inverse heat conduction problems by the iterative regularization has been made by E.A. Artyukhin.

Also, it is necessary to mention a book of R. Latt'es and J.-L. Lions [34] in which they suggest the quasi-inversion method specially for the equations with partial derivatives. A close approach was suggested by O.M. Alifanov in 1971 for solving inverse heat conduction problem in the Cauchy statement [13]. It is called the *artifical hyperbolization* method. But these approaches haven't strict substantiation.

Simultaneously with the development of the general theory of ill-posed problems and construction of regular method for their solution a process is observed with respect to the elaboration of stable and effective in practice methods and algorithms for solving inverse problems of heat conduction. The initial phase of developing the computational procedures to solve these problems (till the time when a regularization method appeared in 1963 and, evidently, after another few years when the attention of practical workers was attracted by this method, i.e. somewhere in 1968-1970)

Third International Conference on Inverse Design Concepts and Optimization in Engineering Sciences (ICIDES-III). Editor: G.S. Dulikravich. Washington D.C., October 23-25, 1991.

can be named *a heuristic regularization* and the corresponding methods got a conventional term of *direct methods*. In other words the authors of corresponding algorithms achieved stability and acceptable accuracy of results basing mainly on the physical sense and, consequently, on the physical level of rigour. Apart from the above works to this trend in solution of inverse problems we can refer *a trial-and-error method* used by L.A. Kozdoba [35] and methods of *linear dynamic filtration* being developed by Yu.M. Matsevitiy, A.V. Multanovsky and D.F. Symbirsky [36, 37]. Rigorous mathematical conditions are not yet formulated in the approaches pointed above.

Alongside with heuristic methods, beginning from the end of the 60s and in early the 70s, there appeared mathematically rigorous methods of solving inverse heat conduction problems.

In their majority these methods are related to the linear problem formulation and constructed basing on a variational technique of regularization and, later on, on iterative regularization. Just to illustrate this, refer to some works both on the first [1, 38-41] and on the second [2, 4, 30, 42] directions. Both approaches, as computational experiments and actual physical tests show, turn out to be acceptable for solving various nonlinear problems as well [1, 2-4, 31, 43-46].

APPLICATIONS OF INVERSE-PROBLEM METHODS

Numerous scientific and practical results have now been obtained with the aid of the pertinent methods. Let us briefly dwell on some of them.

HEAT DIAGNOSTICS. Let us start with non-stationary heat diagnostics [2,41,47]. The method of boundary inverse heat conduction problems can be used in thermal diagnostics of both slow and fast heat transfer processes. Our investigations have demonstrated that it is possible to reconstruct heat-flux and heat transfer coefficients with accuracy comparable to that of temperature measurements in the solid body. We have developed different principles of one-, two- and three-dimensional thermal indirect measurements based on solution of boundary inverse problems, which have required dimensionality.

On the basis of these principles, sensing devices for heat diagnostics of high-temperature gas flows has now been designed, refined experimentally, and put to practical use in various branches of industry. In particular, these are different types of uncooled and cooled sensors. For example, similar sensors are used for experimental studies on plasmatrons and gasdynamic stands in which the gas jets are created by special aviation and rocket engines.

Similar sensors can be used successfully to measure not only convective, but also radiative heat fluxes. They are capable of much faster response rates than the Gardon-type sensors widely used in practice.

Experimental studies showed that heat-flux variations at frequencies up to 100 Hz can be registered by using uncooled sensors and processing their readings by solving a boundary IHCP.

One-dimensional sensors can be used to measure transient local heat fluxes and local heat transfer coefficients. To determine discrete fields of these values it is necessary to install a sufficient number of sensors at various space points, for example, at various points of streamlined surface of a solid body. However, if we go to solution of two-and three-dimensional inverse problems of heat conduction, we can reconstruct continuous spatial-time dependences of heat fluxes and heat transfer coefficients on a body surface. In these cases temperature measurements are usually made on part of a heat-insulated boundary of the body, namely on a line for a two-dimensional case and on a surface for a three-dimensional case. Sensors with such sensitive elements [2,47] can be mounted on a model or a mock-up of the object under study, or on a full-scale object, the thermal conditions

of which is determined under test or design operating conditions. Sometimes temperature measurements can be conducted within a solid body.

The above methods for indirect measurements are of special value in the diagnostics of heat-transfer processes under various conditions that do not admit of easy calculation, as in investigation of the laminar to turbulent flow transition, the interaction of shock waves with boundary layers, heat transfer in separation zones, streamlining by nonequilibrium flows of dissociated gas, in the case of heat exchange with boiling, injection of gas or liquids into boundary layers, and so forth.

It is important to note, that the procedures of *simultaneous determination* in experiment of the two or more functions (or parameters) in heat balance equation on body surface are developed [2,47]. For example, we can find simultaneously a local coefficient of convective heat transfer as a function of temperature factor α (Tw/T*) and an emissivity of the surface as a function of its temperature ε (Tw) for known environment characteristic temperature T*(τ). Basis of these procedures is special formulations and solution methods of boundary IHCPs.

The boundary inverse-problem method is one of basic for study of *non-stationary heat transfer* in the system: solid-gas (or liquid).

It is known, that a heat transfer coefficient, obtained for conditions when an influence of solid body on thermal state of boundary layer is taken into account can considerably differ from a heat transfer coefficient, which is determined for stationary conditions. The approach to study non-stationary heat exchange includes two parts. The first one consists in solution of joint heat transfer problems, when equations of heat-and-mass transfer both for solid and gas (or liquid) must be solved simultaneously.

The second is experimental investigations of non-stationary heat transfer and, in many cases, the experiment still remains the major technique of such studies [48,51]. Such experimental investigations are based on simulation of natural transient heat-and-mass transfer and determination of non-stationary heat transfer coefficients as functions of time. It is required not only to correctly conduct and successfully carry out experimental research, but also (and this is very important) to find effective ways of processing the obtained data. It was found that inverse problem forms an effective means of getting the necessary results in experimental information processing.

Use of the inverse-problem methods to process experimental data permits to develop *new approaches to the very formulation of the experiments* to investigate heat and mass transfer, making such experiments more efficient and informative. For example, a new universal procedure has been proposed for aerodynamic thermal tests to investigate heat transfer in a broad range of Reynolds numbers using working chambers of comparatively small sizes [52]. This technique is based on the use of the boundary inverse heat conduction problem, that has made it possible to conduct experiments under essentially nonsteady heat-transfer conditions with long models mounted in the working section of the wind tunnel before it is started (which had previously been impossible). Part of the model is situated directly in the supersonic nozzle. This makes it possible to investigate flows with uniform fields of the gasdynamic parameters over practically the entire characteristic rhombus, and this, in its turn, makes it possible to set up not only laminar but also transitional and turbulent boundary layers on the model.

Another area of application of those methods relates to investigation of *temperature fields, heat flux-fields and also thermal stresses* in structural materials, something that is very important for various types of flight vehicles, engines, and power-generating equipment [47]. It is often found that temperature sensors cannot be mounted inside of materials due to technological, structural and

methodical reasons (because of its violating the integrity, and strength properties of materials, introducing distortions into the temperature field and into the field of thermal stresses, and also due to the difficulties in providing good thermal contacts of sensors with the material, etc). It is then necessary to reconstruct the temperature field from temperature and heat-flux measurements made on part of the boundary of the body, i.e. to solve the corresponding inverse problem. This approach has been used, for example, in investigating the hot strength of graphite structures, and has produced good results.

New and important field of use of methods based on solution of the inverse problems is experimental-theoretical studies of heat-and-mass transfer in porous mediums, in particular, *porous cooling systems*. These systems are an effective means of heat protection. It is performed by the coolant supply through special inserts made of porous materials. Coolant here is gas or liquid. In the course of experimental studies of porous cooling systems it is necessary to determine non-stationary thermal boundary conditions on the surface of a porous body and to identify heat effect of coolant injection into a boundary layer. The direct measuring of values included into the boundary conditions of a heated surface is either very difficult or downright impossible, but the temperature on the opposite surface of a solid matrix can be measured. In this case we are faced with the necessity of solving a boundary inverse problem for an equation system for heat-and-mass transfer in a porous structure [2,53,55]. For a gaseous coolant appropriate formulation of inverse problem was considered above.

Of practical importance is the problem of studying the *heating and heat destruction of thermal protective materials*, including the investigation of reducing convective heat transfer due to injection of gaseous products from the ablated surface. The main types of measurements in experimental study of such materials are temperature measurements within the bodies (usually by means of thermocouples) and on the external surface (by optical methods) and measurements of the ablation rate. The processing of measurement data can be performed by methods based on the solution of inverse heat conduction problems.

The following example is referred to a determination of *thermal properties of different medium and materials*, in particular, heat-protective materials interacting with high-enthalpy gas flow. Thermophysical measurements, based on classical techniques, for many materials can be made only at temperatures and rates of heating much less than those in reality. To avoid the above discrepancy is possible simulating the required conditions of specimen heating on special test facilities (plasmatrons, in the jets of rocket engines and other) with a successive treatment of temperature measurements by coefficient inverse problem [56-64]. That is, using some mathematical model of heat transfer in the material (in the simplest case - a heat conduction equation) we are to find a required value (or values), for example a heat conductivity as function of temperature, "adjusting" the calculated temperatures to those thus measured. Thermal properties thus obtained correspond to the heating conditions brought near to real conditions in which the material operates. In many cases, if properties of decomposing materials are investigated, it is necessary to develop inverse problem procedure for mathematical model that takes account of the non-isothermal decomposition kinetics.

Another field is *the estimation of contact resistances* which characterize the heat transfer between the connected parts of structures as well as the prediction of their change in the course of time, in particular for structures, where there is a great number of bolted and riveted joints, hinges and so on. For thermal shields it is necessary to know *the resistance of adhesive film*, and this problem often can be interpreted as the problem of contact resistance specification. The method of

boundary inverse problem can be successfully applied to processing the results of specially conducted experiments in solving the problem of contact heat transfer, non-stationary conditions included.

The next field of application of inverse problems is *diagnostics of friction.* In mechanical engineering, the investigations of friction and wear of different movable joints are of great importance because machines reliability and overhaul period depend on them. Besides, these investigations permit to reduce friction losses and, consequently, increase machines efficiency. Today, bench tests is very often the only means to test experimentally a movable joint. But they can not substitute service tests which provide the most complete data on a joint performance in operating conditions. At the same time, service tests of friction units rarely give data on friction losses. Thus, for example, the existing methods of direct measuring of friction torque, characterizing work in friction, rest on the use of special elastic elements, i.e. torsion devices. Their lay out presents a problem even in bench tests. In operating conditions measuring of friction torque with these devices is often impossible. So, work in friction (friction torque) is defined through other measurements well correlated with the sought-for quantity. The most suitable are temperature measurements not requiring complex equipment. Using these data it is possible to reconstruct heat release in friction zone. Almost all friction energy (85-100%) goes into heat. Thus, it becomes possible to estimate work in friction, and, accordingly, friction torque, using the data on heat release. Heat release itself may be found by solving inverse heat transfer problem with known temperature measurements.

Using this approach and iterative regularization, appropriate procedure for tests of the sliding bearing was developed and used in practice [65]. Obtained results of 10-15% agree with the results of torsion measurements.

The above applications concern *diagnostic and identification problems.* General procedure for structural and parametric identification of physical processes, based on solving ill-posed inverse problems, is presented in [66].

With the help of inverse problem principle various *design problems* also may be solved. The problem of the optimal design of a multilayes heat shield is considered. It is required to determine the design characteristics (the number, materials and thicknesses of the layers) of such shield, one of whose boundaries as well as the corresponding layer is subjected to external transient heating and ablation, while the other is subjected to cooling by the circulating heat transfer agent. The total mass of the shield is the criterion for the quality of the heat protection. The optimization problem has a number of restrictions taken into account, which are dictated by the requirements of the admissible temperature conditions for the layers, the specific heat of the coolant, the thermal stresses, and so on. Therefore we have a combined coefficient - geometric inverse problem of thermal design type. This problem is solved by the iterative method [67,68].

At present methods based on solution of different inverse problems find their application not only for model thermal experiments and parameter optimization. They are also used for *full-scale tests*, in particular, for diagnostics of heat transfer boundary conditions and heat loads on different real structures and for identification of thermal properties of heat protection and heat insulation materials in real operating conditions.

One field of application of these methods is *thermal-vacuum test of spacecrafts.* Such approach permitted to create new effective procedure of testing. It includes the following three main parts: special preliminary testing of object for the purpose of identification and correction of mathematical

Third International Conference on Inverse Design Concepts and Optimization in Engineering Sciences (ICIDES-III). Editor: G.S. Dulikravich. Washington D.C., October 23-25, 1991.

models of heat transfer processes in test object; choice of thermal simulator mode with help of solution of the inverse problem of control type; regular testing itself.

Very important fields of applications of inverse problems are different *nature (real) experiments and tests*, for example, flight tests. In many of these cases, such approach is the only possible means for obtaining necessary quantitative information about heat conditions of vehicles under test, since other methods turn out to be unfit. Appropriate procedures and technical devices were created and used for study (in flight experimental conditions) of porous cooling system, reusable thermal protection, thermocontrol coating of space vehicles and strength of structures of flight vehicles.

For example, developed methods were applied to study of *thermal modes of reusable heat protection* of "Buran" aerospace vehicle. The flight tests were conducted on special automatic re-entry vehicles "Bor-4" series. In these cases heat diagnostics was carried out in the following ways:

- estimation of heat fluxes on the surface of the tiled thermal shield;
- quality analysis of the effects of physical-chemical reactions on the thermal shield surface with its catalytic properties being changed;
- evaluation of heat state of the thermal shield surface in the tiles gaps;
- estimation of the inner heat state of the tiled thermal shield material under the heating in flight conditions.

Unique results were obtained by means of these methods in the course of such tests.

The next important example has to do with diagnostics of *radiative characteristics of thermal control coatings* of spacecrafts. Of great interest is an experimental determination of the solar radiation integral absorption factor and integral semi-spherical emissivity of external surface in the conditions of actual operation of the coatings. In particular, such studies are conducted on vehicles of "Cosmos", "Meteor", "Meteor-Priroda" series. In the result it was possible to construct a mathematical model for varying the radiation characteristics of coatings in the course of time and predict these variations for longer time of operational use of the vehicle, as compared with duration of experiment.

Besides model experiments, design and testing of technical units inverse problems find their fruitful use in investigations, optimization and operating diagnostics of *various technological processes*. Just for example let us touch upon some of them.

Procedures for determination of heat loads by inverse-problem solution may be very helpful in experimental study of *liquid cooling* in continuous casting and heat-treatment of metals. Such cooling removes heat flows of rather high specific rate - up to 100 $^{mW}/_{m^2}$ with realization of high velocity non-stationary processes. Complex thermohydrodynamic processes occurring while spraying liquid over a high temperature surface cannot be described so far with the required accuracy by means of theoretical methods. So, such kind of investigations are still described through experiments. The experimental data are obtained and generalized by solving inverse problems of heat exchange.

The direct estimation of local rates of the removed heat flow during liquid cooling and with boiling is hindered by rather great change of surface temperature rate. Standard heat flux meters have time constant about 1 sec - two orders more than process characteristic time. Effective measuring means for these purposes may be obtained on the basis of boundary inverse problems principles [70].

Another example is the thermofretting of metals. This is a progressive trend in heat-treatment technology for critical steel products that operate under heavy mechanical loads, such as the disks

and rotors of large power-generating steam turbines. It is now impossible to investigate and optimize the thermofretting process without experimental testing, and this is a typical area in which inverse-problem methods can be used to good effect.

Inverse problems of structure mechanics. Problems of reconstruction of loads on the structure by its stress-deformed state parameters as well as problems of determination of the fields of stresses and shears in a given part of construction elements by stresses (shears) values on a part of its surface fall under the class of inverse problems of mechanics of deformated solid [69]. An analysis is made of corresponding methods and their practical application for investigation of strength of space vehicles during flight tests.

Of course, the range of possible practical uses of the inverse-problem methods is considerably broader than that indicated above.

To summarize, we observe that these experimental-theoretical methods not only have a broad spectrum of important applications, but they are distinguished of high information yield and enough high reliability. For more complete acquaintance with existing today methods and algorithms of solving ill-posed inverse problems and their different applications refer to the following books [1-4,25,29,34-37,41,48]. Also, it can be recommended to look through the numbers of Inzh.Fiz.Zh: vol.29, no.1, 1975; vol.33, no.6, 1977; vol.39, no.2, 1980; vol.45, no.5, 1983; vol.49, no.6, 1985; vol.56, no.3, 1989 (English translation in Journal of Engineering Physics - bibliography data is the same). The numbers were dedicated specially to those problems.

REFERENCES

1. O.M.Alifanov. Identification of Heat Transfer Processes of Flight Vehicles. - Moscow: Mashinostroenie, 1979, 216 p. (in Russian).

2. O.M.Alifanov. Inverse Heat Transfer Problems. - Moscow: Mashinostroenie, 1988, 280 p. (in Russian).

3. J.V.Beck, B.Blackwell, C.R.St.Clair, Jr. Inverse Heat Conduction. Ill-posed Problems. - A Wiley-Interscience Publication, New Jork, 1985, 308 p.

4. O.M.Alifanov, E.A.Artyukhin, S.V.Rumyantsev. Extreme Methods of Solving Ill-posed Problems and Their Application to Inverse Heat Transfer Problems. - Moscow: Nauka, 1988, 288 p. (in Russian).

5. T.J.Mirsepassi. Heat Transfer Charts for Time-Variable Boundary Condition. Part I - Semi-Infinite Solid. - ASME Paper 58-SA-7, 1958.

6. G.Stolz. Numerical Solutions to an Inverse Problem of Heat Conduction for Simple Shapes. - J.Heat Transfer, 1960, v.82, No. 1, pp.20-26.

7. J.V.Beck. Calculation of Surface Heat Flux from an Internal Temperature History. - ASME Paper 62-HT-46, 1962, 11 p.

8. J.V.Beck. Surface Heat Flux Determination Using an Integral Method. - Nucl.Eng.Des., 1968, v.7, No.2, pp.170-178.

9. G.T.Aldoshin, A.S.Golosov, V.I.Zhuk. Solution of an inverse problem of nonstationary heat conduction for a slab. Heat and mass transfer. Minsk, Naura i Teknika. v.8, 1968, pp.186-199 (in Russian).

10. V.I.Zhuk, A.S.Golosov. Inzh.Fiz.Zh., 1975, vol.29, No. 1, pp.45-50 (Engl. transl. in: J.Eng.Phys., 1975, vol.29, No.1).

11. O.M.Alifanov. Solution of a Non-Stationary Heat Conduction Problem for Investigation of Ablation of Heat Protection Materials. - In: Preprints to the All-Union Conference of Young Scientists on Heat-and-Mass Transfer (January 27-30, 1969), Minsk: 1969, 187 p. (in Russian).

12. O.M.Alifanov. Solution of the Problem of Nonstationary Heat Conduction and its Application for Studying the Heat Shield Materials. - In: Investigations of Nonstationary Convective Heat and Mass Transfer. - Minsk: Nauka i Tekhnika, 1971, pp.322-333 (in Russian).

13. O.M.Alifanov. Study of Direct and Inverse Heat Conduction Problems Conformably to Design of Thermal Protection of Flight Vehicles. Doctorate thesis, Moscow: Moscow Aviation Institute, 1971 (in Russian).

14. O.M.Alifanov. Inzh.Fiz.Zh., 1973, vol.24, No.6, pp.1129-1137. (Engl.transl. in: J.Eng.Phys., 1973, v.24, No.6).

15. N.V.Shumakov. Methods of Experimental Study of Solid Body Heating. Doctorate thesis, Moscow: Energy Institute named after G.M.Krzhizhanovsky, 1955 (in Russian).

16. W.H.Giedt. The Determination of Transient Temperatures and Heat Transfer at a Gas-Metal Interface Applied to a 40 mm Gun Burrel. - Jet Propulsion, 1955, v.25, No.4, pp.158-162.

17. O.N.Kastelin, L.N.Bronsky. Heating of a Blunt Body in the Supersonic Flow. - In: Physical Gasdynamics, Heat Transfer and High Temperature Gas Thermodynamics. Moscow: Publ.H. of USSR Acad. of Sciences, 1962, pp.233-238 (in Russian).

18. J.Stefan. On the Theory of Ice Formation, Especially on Ice Formation in Polar Seas (Uber die Theorie der Eisbildung, insbesondere uber die Eisbildung in Polarmeere). Sitzungsberichte der Kaiserlichen Akademic Wiss, Wien., Math. naturwiss. Kl., 1890, v.98(2a), pp.965-973 (in German).

19. A.G.Tyomkin. Determination of Variable Outside Heat Effects by Methods of Heat Conduction. - Izv. Vyssh. Uchebn. Zaved., Energetika, 1961, No. 5, pp.60-71 (in Russian).

20. O.R.Burggraf. An Exact Solution of the Inverse Problem in Heat Conduction Theory and Applications. - J.Heat Transfer, 1964, v.86c., p.373-382.

21. J.Hadamard. Lectures on Cauchy's Problem in Linear Partial Differential Equations. - Yale University Press, New Haven, CT, 1923.

22. T.Carleman. Les fonctions quasi analytiques. Paris (1926),

23. A.N.Tikhonov - Dokl. Akad. Nauk SSSR, 1943, v.39, No.5, pp.195-198 (Engl. transl. in: Soviet Math. Dokl., 1943, v.39, No.5).

24. M.M.Lavrentiev. On Some Ill-posed Problems of Mathematical Physics. - Novosibirsk: Izd. Sib. Otd. Akad. Nauk SSSR, 1962, 92 p. (in Russian).

25. A.N.Tikhonov, V.Ya.Arsenin. Methods of Solving Ill-Posed Problems. - Moscow: Nauka, 1986, 288 p. (in Russian).

26. F.John. Numerical Solution of the Heat Equation for Preceding Times. Ann. mat. pura ed. appl., 4, 40(1955), pp.129-142.

27. A.N.Tikhonov - Dokl. Akad. Nauk SSSR, 1963, v.151, No.3, pp.501-504 (Engl. transl. in: Soviet Math. Dokl., 1963, vol.151, No.3).

28. D.L.Phillips. A Technique for the Numerical Solution of Certain Integral Equations of the First Kind. - J.Assoc. Comput. Mach. 1962, v.9, No.1, pp.84-97.

29. V.A.Morozov. Regular Methods of Solving Ill-posed Problems. - Moscow: Izd. Mosc. State Univ., 1974, 359 p. (in Russian).

30. O.M.Alifanov. Inzh. Fiz. Zh., 1974, v.26, No.4, pp.682-689 (Engl. transl. in: J.Eng. Phys., 1974, v.26, No.4).

31. O.M.Alifanov. Teplofiz. Vys. Temp., 1977, v.15, No.3, pp.598-605 (Engl. transl. in: High Temperatures, 1977, v.15, No.3).

32. O.M.Alifanov, S.V.Rumyantsev. Dokl. Akad. Nauk SSSR, 1979, v.248, No.6, pp.1289-1291 (Engl. transl. in: Soviet Math. Dokl., 1979, v.248, No.6).

33. O.M.Alifanov, S.V.Rumyantsev. Inzh. Fiz. Zh., 1980, v.39, No.2, pp.253-258 (Engl. transl. in: J.Eng. Phys., 1980, v.39, No.2).

34. R.Lattes, J.-L. Lions. Methode de Qusi-Reversibilite et Applications. Dunod. Paris. 1967.

35. L.A.Kozdoba, P.G.Krukovsky. Methods of Solving Inverse Problems of Heat Transfer. - Kiev: Naukova Dumka, 1982, 359 p. (in Russian).

36. Yu.M.Matsevity, A.V.Multanovsky. Identification in the Problems of Heat Conduction. - Kiev: Naukova Dumka, 1982, 240 p. (in Russian).

37. D.F.Simbirsky. The temperature diagnostics of engines. Kiev: Tekhnika, 1976, 208 p. (in Russian).

38. A.N.Tikhonov, V.B.Glasko. - Zh. Vychisl. Mat. Mat. Phys., 1967, v.7, No.4, pp.910-914 (Engl. transl. in: USSR Comput. Math. and Math. Phys., 1967, v.7, No.4).

39. O.M.Alifanov. Regularization of Solutions of Inverse Heat Conduction Problems. - In: Heat and Mass Transfer. - Minsk: Nauka i Tekhnika, v.8, 1972, pp.89-98 (in Russian).

40. O.M.Alifanov, Inzh. Fiz. Zh., 1973, v.24, No.2, pp.324-333 (Engl. transl. in: J.Eng. Phys., 1973, v.24, No.2).

41. O.M.Alifanov, V.K.Zantsev, B.M.Pankratov, et al. Algorighms for Diagnostics of Heat Loads of Flight Vehicles. Under the editorship of Academician V.P.Mishin. - Moscow: Mashinostroenie, 1983, 168 p. (in Russian).

42. E.A.Artyukhin, S.V.Rumyantsev. Inzh. Fiz. J., 1980, v.39, No.2, pp.264-269 (Engl. transl. in: J. Eng. Phys., 1980, v.39, No.2).

43. E.A.Artyukhin. Inzh. Fiz. J., 1981, v.41, No.4, pp.587-592 (Engl. transl. in: J. Eng. Phys., 1981, v.41, No.4).

44. O.M.Alifanov, E.A.Artyukhin. Teplofiz. Vys. Temp., 1978, v.16, No.4, pp.819-825 (Engl. transl. in: High Temperatures, 1978, v.16, No.4).

45. O.M.Alifanov, V.V.Mikhailov. Inzh. Fiz. Zh., 1978, v.35, No.6, pp.1124-1129 (Engl. transl. in: J.Eng. Phys., 1978, v.35, No.6).

46. O.M.Alifanov, I.E.Balashova. Izv. Sib. Otd. Akad. Nauk SSSR, Tekhn. nauki, 1987, No.2, pp. 5-11 (in Russian).

47. V.P.Mishin, O.M.Alifanov. Mashinovedenie. Part 1: 1986, No.5, pp.19-29 (Engl. transl. in: Soviet Mashine Science, 1986, No.5, pp.16-25); Part 2: 1986, No.6, pp.11-21 (Engl. transl. in: Soviet Mashine Science, 1986, No.6, pp.8-16).

48. N.V.Shumakov. A Method of Successive Intervals in Thermometry of Transient Processes. - Moscow: Atomizdat, 1979, 216 p. (in Russian).

49. E.K.Kalinin, I.I.Berlin, V.V.Kostyuk, et al. Inzh. Fiz. Zh., 1972, v.22, No. 4, pp.610-613 (Engl. transl. in: J.Eng. Phys., 1972, v.22, No.4).

50. O.M.Alifanov, M.I.Gorshkov, V.K.Zantsev, B.M.Pankratov. Inzh. Fiz. Zh., 1975, v.29, No.1, pp.26-30 (Engl. transl. in: J.Eng. Phys., 1975, v.29, No.1).

51. V.L.Sergeyev, L.A.Sergeyeva. Study of Non-stationary Heat Transfer for Flat and Axially Symmetric Flows. Preprint No.5 - Minsk: Institute of Heat-and-Mass Transfer, 1985, 63 p. (in Russian).

52. O.M.Alifanov, N.T.Batura, A.M.Bespalov, et. al. Inzh. Fiz. Zh., 1977, v.33, No.6, pp.988-992 (Engl. transl. in: J. Eng. Phys., 1977, v.33, No.6).

53. O.M.Alifanov, E.A.Artyukhin, A.P.Tryanin. Teplofiz. Vys. Temp., 1983, v.21, No.6, pp.1160-1168 (Engl. transl. in: High Temperatures, 1983, v.21, No.6).

54. O.M.Alifanov, A.P.Tryanin. Inzh. Fiz. Zh., 1985, v.48, No.3, pp.472-483 (Engl. transl. in: J. Eng. Phys., 1985, v.48, No.3).

55. O.M.Alifanov, A.P.Tryanin, A.Lozhkin. Inzh. Fiz. Zh., 1987, v.52, No.3, pp.461-468 (Engl. transl. in: J. Eng. Phys., 1987, v.52, No.3).

56. Yu.V.Polezhaev, F.B.Yurevich. Heat Protection. Moscow: Energiya, 1976, 392 p. (in Russian).

57. K.G.Omelchenko, M.V.Savelov, V.P.Timoshenko. Teplofiz. Vys. Temp., 1974, v.12, No.4, pp.761-768 (Engl. transl. in: High Temperatures, 1974, v.12, No.4).

58. V.M.Yudin. Distribution of heat in glass-reinforced plastic. - Proceedings of TsAGI. No. 1267, - Moscow: Izd. TsAGI, 1970, 41 p. (in Russian).

59. O.M.Alifanov, M.V.Klibanov. Inzh. Fiz. Zh., 1985, v.48, No. 6, pp.998-1003 (Engl. transl. in: J.Eng. Phys., 1985, v.48, No.6).

60. E.A.Artyukhin. Teplofiz. visok. temp., 1981, v.19, No.5, pp.963-967 (Engl. transl. in: High Temperatures, 1981, v.19, No.5).

61. E.A.Artyukhin, V.E.Kullikh, A.S.Okhapkin. Inzh. Fiz. Zh., 1983, v.45, No.5, pp.788-794 (engl. transl. in: J. Eng. Phys., 1983, v.45, No.5).

62. A.S.Okhapkin. Inzh, Fiz. Zh., 1985, v.49, No.6, pp.989-994 (Engl. transl. in: J. Eng. Phys., 1985, v.49, No.6).

63. A.A.Goryachev, V.M.Yudin. Inzh. Fiz. Zh., 1982, v.43, No.4, pp.641-648 (Engl. transl. in: J. Eng. Phys., 1982, v.43, No.4).

64. P.V.Prosuntsov, S.V.Reznik, Inzh. Fiz. Zh., 1985, v.49, No.6, pp.977-982 (Engl. transl. in: J. Eng. Phys., 1985, v.49, No.6).

65. I.N.Chersky, O.B.Bogatin, N.P.Starostin. Inzh. Fiz. Zh., 1984, v.47, No.6, pp.1000-1006 (engl. transl. in: J. Eng. Phys., 1984, v.47, No.6).

66. O.M.Alifanov, Inzh. Fiz. Zh., 1985, v.49, No.6, pp.889-897 (Engl. transl. in: J. Eng. Phys., 1985, v.49, No.6).

67. O.M.Alifanov. Inzh. Fiz. Zh., 1977, v.33, No.6, pp.972-981 (Engl. transl. in: J. Eng. Phys., 1977, v.33, No.6).

68. V.V.Mikhailov. Inzh. Fiz. Zh., 1980, v.39, No.2, pp.286-291 (Engl. transl. in: J. Eng. Phys., 1980, v.39, No.2).

69. I.G.Kolker, A.Yu.Odinokov. Izv. Vyssh. Uchebn. Zaved., Aviatekhnika, 1988, No.2, pp.36-39 (in Russian).

70. V.G.Labeish. Liquid Cooling of High Temperature Metal. - Leningrad: Leningrad University, 1983, 172 p. (in Russian).

Third International Conference on Inverse Design Concepts and Optimization in Engineering Sciences (ICIDES-III), Editor: G.S. Dulikravich, Washington D.C., October 23-25, 1991.

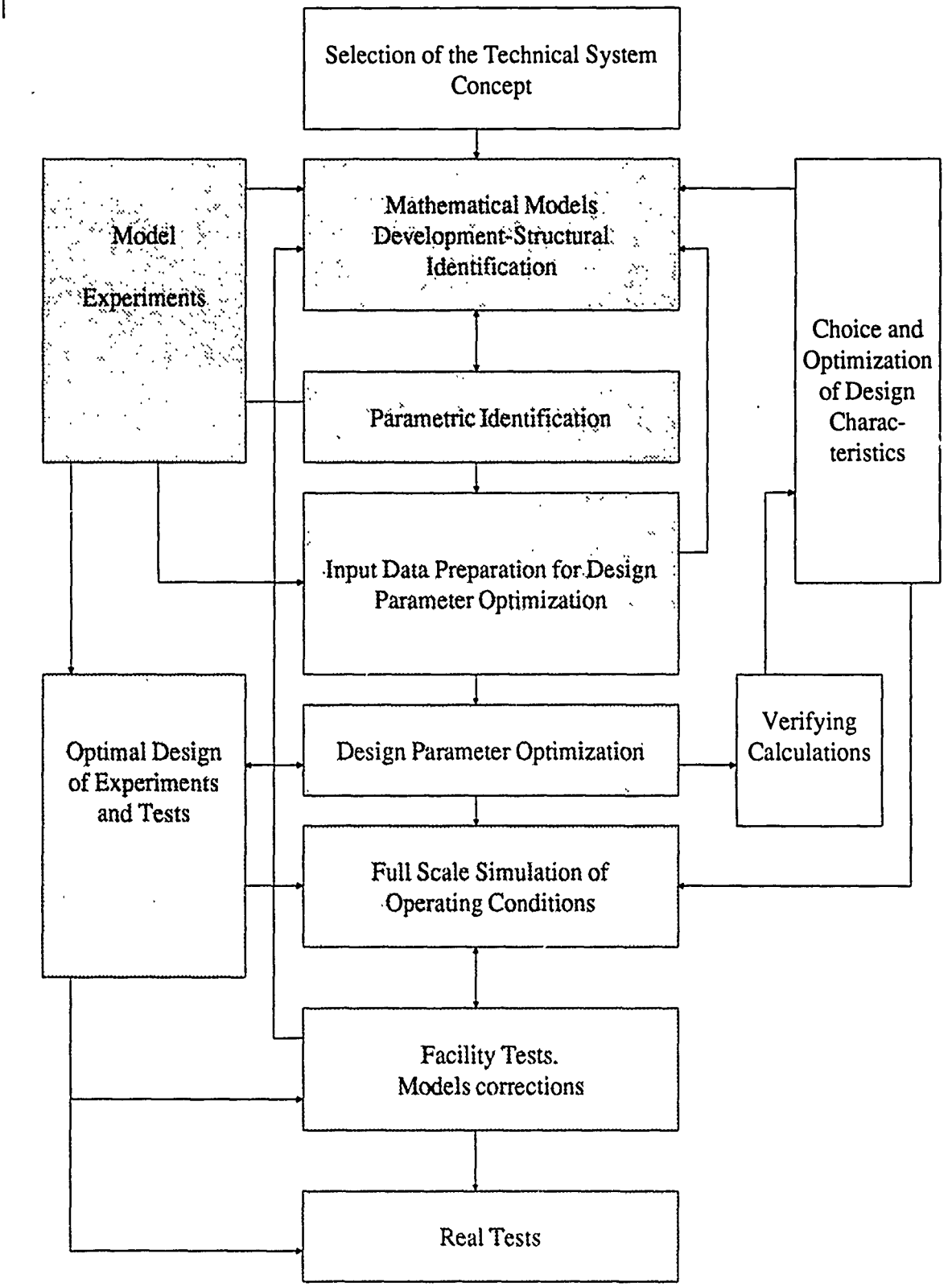


Fig. 1. Block Diagram of Design and Testing

Third International Conference on Inverse Design Concepts and Optimization in Engineering Sciences (ICIDES-III). Editor: G.S. Dulikravich. Washington D.C., October 23-25, 1991.

INVERSE PROBLEMS AND OPTIMAL EXPERIMENT DESIGN IN UNSTEADY HEAT TRANSFER PROCESSES IDENTIFICATION

Eugene A.Artyukhin

Department of Space System Engineering and Design
College of Cosmonautics
Moscow Aviation Institute
Volocolamskoye sh.,Moscow,125871
USSR

ABSTRACT

Experimental-computational methods for estimating characteristics of unsteady heat transfer processes are analysed. The methods are based on principles of distributed parameter system identification. Theoretical basis of such methods is numerical solutions of nonlinear ill-posed inverse heat transfer problems and optimal experiment design problems. Numerical techniqes for solving problems pointed out are breafly reviewed. The results of practical application of identification methods are demonstrated when estimating effective thermo-physical characteristics of composite materials and thermal contact resistance in two-layer systems.

INTRODUCTION

In creating different thermally stressed structures and systems, of wide importance are mathematical modelling and simulation of heat transfer processes occurring inside them. The use of mathematical simulation allows to predict a thermal state of the dynamical system under consideration in wide range of its operational conditions and to estimate the effect of different factors on the system behaviour. Accurate enough thermal state simulation for the system is one of the main procedure, when optimizing thermal conditions and design parameters.

The thermal mathematical model of a system or a process analysed is formed basing on the heat and mass exhange theory (see, e.g.[1]) and it contains a set of characteristics. Characteristics are usually determined by experimental way. By this, most of them can be determined only by means of indirect measurements. In this case a mathematical model is used which is of the given structure and usually contains unknown constant parameters.

It should be emphasized that in determining characteristics, methods of carring out experiments as well as methods of data processing should consider peculiarities of mathematical models used to simulate thermal conditions . But this factor is not taken into account in overwhelming majority of traditional methods for determining characteristics. Simple mathematical models and severely controlled heating conditions for specimen are used in these methods. Traditional methods for determining of thermophysical characteristics can serve as an example [2]. As the result, a desired accuracy of determining characteristics is not provided. In this case mathematical simulation of thermal conditions is also realized with the low accuracy.

Shortcomings of traditional methods for determining characteristics are displayed when analysing a wide enough range of thermal processes. In particular, one can refer to such processes heat transfer in composite heat shield and thermo-insulating materials, contact heat transfer in high-temperature power plants, heat and mass exchange when materials and structures interact with high-enthalpy homogeneous and heterogeneous flows and

Third International Conference on Inverse Design Concepts and Optimization in Engineering Sciences (ICIDES-III), Editor: G.S. Dulikravich, Washington D.C., October 23-25, 1991.

many others. That is why one must develop and implement new methods of study, providing trustworthy information on different characteristics of thermal processes analysed.

Since characteristics should correspond to the mathematical model used, their determination should be considered as a part of mathematical model building by using experimental data. This procedure is called identification problem [3]. When determining characteristics, the mathematical model structure is supposed to be known. In this case one can speak about parametric identification problem [4] or parameter estimation problem [5]. Unsteady thermal processes are referred, as a rule, to the category of dynamical distributed parameter systems. This allows to use experimental-computational methods for determining characteristics based on the main principles and approaches of distributed parameter system identification [6].

IDENTIFICATION OF HEAT TRANSFER CHARACTERISTICS

In identifying heat transfer processes, problems of determining characteristics in mathematical models with given structure are formulated as coefficient-type inverse heat transfer problems [7]. Methods and algorithms for solving these problems are the effective means for determining characteristics of different thermal processes and systems [8,9]. In spite of achievements available, the inculcation of methods based on solving coefficient inverse heat transfer problems was not very active, till recently, because of the following. The fact is that the solution of such problems strongly depends on the used scheme of temperature measurements [4,10,11]. It means that quite different results can be obtained for the same heating conditions of the system analysed but for different number of temperature sensors and their locations. That is why almost every experimental-computational study is followed by labour-intensive analysis of thrustworthyness of the rusults obtained on the basis of numerous parametric computations (See, e.g., [12]).Preliminary optimal design of temperature measurements and other experiment conditions allows to reduce considerably the volume of work. The combination of methods and algorithms for solving inverse problems and experiment design problems is the methodological foundation of identification procedure. This combination forms the new approach increasing essentially an efficiency of thermal studies and determination of heat transfer characteristics.

The voluminous literature is devoted to methods and algorithms for solving inverse heat transfer problems. One can point out, in particular, monographs [4,5,13-20] and bibliography inside them. Most of works available deal with the solution of boundary inverse heat conduction problems, in which thermal boundary conditions are determined by using unsteady temperature measurements inside the body analysed. The considerably lesser number of publications is devoted to solving coefficient inverse problem (see, e.g., bibliography inside [4,14,16,18,19]).

Algorithms suggested at present for solving coefficient inverse problems are based, in overwhelming majority, on minimizing the residual functional.The minimization procedure is built by using an exhaustive method [14,21],matching method [18], method of optimal dynamical filtration [19] and gradient methods. To compute a gradient of the residual functional, the following techniques are used: finite difference method [22], sensitivity functions [23] and a solution of boundary-value problems for conjugate variables, which are written down for linearized direct problems [24-26], as well as for finite difference analogues of direct problems [27]. Efficiency of these techniques is mainly analysed in application to coefficient inverse heat conduction problems to determine thermo-physical characteristics depending on

Third International Conference on Inverse Design Concepts and Optimization in Engineering Sciences (ICIDES-III), Editor: G.S. Dulikravich, Washington D.C., October 23-25, 1991.

temperature. The analysis of recent publications [28] says that the most "popular" techniques for solving coefficient inverse problems are based on iterative regularization principle [4].

In contrast to the number of publications on inverse heat transfer problems, works on optimal design of thermal experiments are not very numerous. One can see the bibliography on this topic in works [4,13].

Methods for solving experiment design problems are based on a finite-dimensional approximation of unknown functions. In this case the inverse problem is reduced to determining the vector of unknown parameters. Then, properties of Fisher's information matrix are analysed, elements of which are computed by using sensitivity functions. The elements depend on experiment conditions (see, e.g. [4]).

The determinant of the information matrix or the square root from the minimum eigenvalue of this matrix are used as the criterion of an experiment quality. Experiment conditions are chosen by exhaustion of a given set of possible conditions [29], by the parametric accuracy analysis of the inverse heat transfer problem solution [25] or by solving optimization problem [30,31].

At last, only several publications are available on analysing the complex procedure of heat transfer processes identification and on simultaneous usage of techniques for solving inverse problems and experiment design problems. There exist isolated works devoted to design, carring out and data processing of real experiments [32,33].

The main goal of this lecture is to demonstrate the efficiency of parametric identification methods through the examples of experimental-computational investigations of heat transfer processes.

INVERSE HEAT TRANSFER PROBLEMS

Many different particular inverse heat transfer problem statements are considered in practice. To describe general features of methods and algorithms for solving ill-posed inverse problems and to avoid details it is convenient to use the general inverse problem formulation in the operator form.

Let us consider an unsteady heat transfer process or thermal system, state model of which has the form of a boundary-value problem

$$L\left(x,\tau,T,\frac{\partial T}{\partial \tau},\frac{\partial T}{\partial x},\frac{\partial^2 T}{\partial x^2},u,v \right) = 0, \quad x \in Q, \quad \tau \in [\,0,\tau_m\,] \qquad (1)$$

$$T(x,0) = T_0(x), \quad x \in \bar{Q} = Q + \Gamma \qquad (2)$$

$$B\left(x,\tau,T,\frac{\partial T}{\partial x},u \right) = v(\tau), \quad x \in \Gamma \qquad (3)$$

where $L(\cdot)$ is a non-linear operator; $B(\cdot)$ is an operator of boundary conditions; T is the state variable (temperature); τ is time; x is space; u is vector of characteristics of the system analysed; $v(\tau)$ is an external action. In the model (1)-(3) the state variable T can be a scalar or vector function of space and time.

Third International Conference on Inverse Design Concepts and Optimization in Engineering Sciences (ICIDES-III), Editor: G.S. Dulikravich, Washington D.C., October 23-25, 1991.

The model (1)-(3) is a direct problem and under given values for external action $v(\tau)$ and vector of characteristics u permits to predict the system s thermal state. If vector u is unknown or given with low accuracy, but there is some additional information about the solution of the problem (1)-(3), then an inverse problem appears for determining vector of characteristics u. The additional information is formed on the basis of measuring the state variable in a subdomain of Q. When the state variable is temperature, measurements are usually carried out in some number N of separate points of the domain Q

$$T_{meas}(X_i,\tau) = f_i(\tau), \quad i = \overline{1,N} \qquad (4)$$

where X_i, $i = \overline{1,N}$ are coordinates of temperature sensor locations. The inverse problem is to determine u from conditions (1)-(4). By this, the form of operator B as well as the number of sensors N are chosen so that we can provide uniqueness of the inverse problem solution [4].

The state model (1)-(3) can be treated as the transformation Au of a space of characteristics into a space of the state variable in measurement points. As the result of measurements a vector-function $f = \{ f_1(\tau), f_2(\tau),\ldots,f_N(\tau)\}$ is formed. The inverse problem is to determine u so that computed state variable in measurement points is equal to measured values. In this case the inverse problem (1)-(4) can be presented as a non-linear operator equation of the first kind

$$Au = f, \quad u \in U, \quad f \in F, \quad A: U \to F \qquad (5)$$

where operator A is constructed on the basis of the model (1)-(3); U is the solution space; F is the space of vector-functions being measured.

The main distinction of inverse problems is ill-posedness. The inverse operator A^{-1} can be unlimited and small errors in the right part can lead to large deviation in the solution. So, to solve inverse problems it is necessary to use special, regulating methods [34].

It should be noted that the solution space U in the inverse problem (5) is constructed by taking into account constraints arising from physical point of view. For example unknown characteristics must be positive in many cases.

To solve coefficient inverse problems the iterative regularization method has displayed quite a high efficiency. This method is based on minimizing, by means of gradient methods of the first order, residual functional

$$J(u) = \| Au - f \|_F^2 \qquad (6)$$

The regularization parameter is the number of the last iteration, which is determined in the process of problem solving from a regularizing condition

Third International Conference on Inverse Design Concepts and Optimization in Engineering Sciences (ICIDES-III). Editor: G.S. Dulikravich. Washington D.C., October 23-25, 1991.

$$J(u) \cong \delta^2 \qquad (7)$$

where δ^2 is the error of input data, calculated in space F.

It should be noted that for linear ill-posed problems the iterative regularization method received severe mathematical substantiation. In a non-linear case such substantiation is not available. However, extensive computational experiments confirm high efficiency of this method for solving non-linear problems as well (see, e.g. [4,16]).

In constructing algorithms for solving coefficient inverse heat transfer problems, when the unknown characteristics depend on the state variable, a common approach is the parametrization of functions sought for, in particular by means of cubic B-splines [35]. The solution is sought for as

$$z(T) = \sum_{k=1}^{m} p_k \varphi_k(T) \qquad (8)$$

where $z(T)$ is an unknown characteristic; p_k, $k = \overline{1,m}$ are constant parameters; $\varphi_k(T)$, $k = \overline{1,m}$ is the given system of basis functions. The inverse problem is to determine a vector of parameters $u = [p_1, p_2, \ldots, p_m]^T$, the composition of which includes coefficients of approximation of all functions sought for. An iterative procedure of minimizing the residual functional (6) by using the method of conjugate gradient projection is built via formulas

$$p_k^{r+1} = P_v\left[p^r{}_k + \gamma_k g_k^r \right], \quad r = 0,1,\ldots,R, \qquad (9)$$

$$g_k^r = J_k^{(r)} + \beta_r g_k^{r-1},$$

$$\beta_0 = 0, \quad \beta_r = \sum_{k=1}^{m} (J_k^{(r)} - J_k^{(r-1)}) J_k^{(r)} \Big/ \sum_{k=1}^{m} (J_k^{(r-1)})^2,$$

where P_v is the operator of projecting on the multitude W of admissible solutions; R is the number of the last iteration. The calculation of gradient components J_k, $k = \overline{1,m}$ is accomplished through the solution of a boundary-value problem for conjugate variable [9]. An approximate method is used to realize the projection operation [38].

A descent parameter is determined from the condition

$$\gamma_r = \operatorname*{Arg\,min}_{\gamma > 0} J\left[P_v(u^r + \gamma g^r) \right] \qquad (10)$$

where $g = [g_1, g_2, \ldots, g_m]^T$. If one characteristic is unknown in the

Third International Conference on Inverse Design Concepts and Optimization in Engineering Sciences (ICIDES-III), Editor: G.S. Dulikravich, Washington D.C., October 23-25, 1991.

inverse problem, then to solve a problem of minimization (10) we can make use of known methods, such as a "golden section" method [36]. For multiparameter inverse problems, of much greater computational efficiency is the technique based on representation of a descent parameter γ as a vector value [37]. Various modifications of this technique are described in [4]. Parameter γ_r is determined for unconstraint minimization procedure and then projection operations are successively realized for all unknown functions [38]. It should be emphasized that in many cases good results have been obtained by using unconstraint methods for minimizing the residual functional. The high capacity for work of such iterative algorithms for solving coefficient inverse problems is demonstrated, for example, in [4,10,24,39,40].

OPTIMAL EXPERIMENT GESIGN

The input data for solving the inverse problem are formed basing on information obtained in the result of corresponding experiments and measurements. Under formation are two groups of values. The first group includes values displayed in model (1)- (3), determining the conditions of an experiment: a dimension of a specimen $\bar{Q}$ in study, duration of an experiment τ_m, initial distribution of a state variable $T_0(x)$, external action $v(\tau)$. Combine these conditions to vector

$$w = \{ Q, \tau_m, T_0(x), v(\tau) \} \qquad (11)$$

The second group of values characterizes the conditions for measuring a state variable and in the case under consideration includes the sensor number N and vector of their space positioning in the specimen $X = [X_1, X_2, \ldots, X_N]^T$. These values make up a scheme or a plan of measurements

$$\xi = \{ N, X \} \qquad (12)$$

In total, vectors w and ξ determine a plan of the experiment

$$\pi = \{ w, \xi \} \qquad (13)$$

The inverse problem (5) can be solved, generally speaking, with different plans of the experiment Π . But the results of studies have shown that quite an arbitrary selection of elements of the experiment plan (13) can lead to large errors in the inverse problem solution [4,10,31,41]. Hence, a problem arises on optimization or optimal design of experiments in identifying thermal processes with the aim of providing maximum accuracy for the unknown characteristics determination in the assumed mathematical model [42]. A search for optimal plans of experiments leads to the necessity of solving extreme problems

$$\pi_o = \text{Arg max } \Psi(\pi), \quad \pi \in \Pi \qquad (14)$$

where $\Psi(\pi)$ is the quality criterion of the experiment, characterizing the accuracy of solution of the inverse problem under analysis; Π is a set of admissible plans.

The accuracy of solution of the inverse problem (5) is determined by properties of the Freshe derivative A' of operator A, reflecting the nature of error transformation of the right part f into errors of solution u [43]. It is possible to show [4] that the above properties of A' are characterized by eigenvalues μ_k, $k = \overline{1,m}$ of matrix

$$M = \{ \Phi_{j,k}, \quad j,k = \overline{1,m} \} \qquad (15)$$

where $\Phi_{j,k} = \frac{1}{N} \sum_{i=1}^{N} \int_0^{\tau_m} \varkappa_i(\tau)\, \theta_j(X_i,\tau)\, \theta_k(X_i,\tau)\, d\tau$

$\varkappa_i(\tau)$, $i = \overline{1,N}$ are weight functions, giving a possibility to consider the presupposed errors in the measurements of a state variable, $\theta_k(x,\tau) = \partial T(x,\tau)/\partial p_k$, $k = \overline{1,m}$ are sensitivity functions. For the inverse problem (5) matrix (10) coincides with the Fisher's normalized information matrix, widely used in the theory of experiment design [44]. The following values can be used in particular as an optimization criterion: a square root from the minimum eigenvalue $\sqrt{\mu_{min}}$ and a determinant $\det M = \prod_{k=1}^{m} \mu_k$. The computational experiments carried out showed high capacity for work of the given criteria [4,32,33,41]. A set of admissible plans is formed with regards for the conditions of uniqueness of solution of the inverse problem and with constraints, characterizing the capacity of the experiment equipment used and that of measurements [4].

To determine the elements of matrix (15) it is necessary to calculate sensitivity functions $\theta_k(x,\tau)$, $k = \overline{1,m}$. These functions are calculated using a boundary-value problem obtained as the result of diferentiation of relations (1)-(3) through parameters p_k, $k = \overline{1,m}$. Here, due to non-linearity of operators L and B, sensitivity functions depend on the vector of unknown parameters u. Hence, it is possible to construct only approximate, locally optimal plans of experiments involving apriori information about vector u [44]. The studies carried out show that apriori information, usually available, gives a possibility to get local-optimal plans close enough to exact plans [4,41,46].

Using described methods for solving problems of optimal design of thermal experiments there have been developed corresponding computational algorithms based on the scanning method [45] and on the optimal control theory [31]. Their high efficiency is shown, for example, in [4,32].

Third International Conference on Inverse Design Concepts and Optimization in Engineering Sciences (ICIDES-III). Editor: G.S. Dulikravich. Washington D.C., October 23-25, 1991.

IDENTIFICATION OF EFFECTIVE THERMOPHYSICAL CHARACTERISTICS OF COMPOSITE MATERIALS

The latest two decades witness constant increase of publications devoted to methods and algorithms for solving coefficient inverse heat conduction problems and to their application. In fact, the first results of investigations in this field were published in 1963 [47,48]. The main part of subsequent works dealt with suggesting algorithms and analysing their computational efficiency. Experimental-computational studies are considered in considerably smaller part of publications.

One of the main goal of investigations is to create a reliable non-stationary method for determining effective thermophysical characteristics of composite thermal protective materials at high temperatures [39,49]. It is clear today that such methods should be built by using identification approaches icluding the solution of coefficient inverse heat conduction problems and experiment design.

To illustrate the practical application of identification methods let us consider determination of the effective thermal conductivity for glass-reinforced plastic on silicone binder, heated by a high-enthalpy gas flow [32].

To realize a complex procedure of identification there has been conducted a number of experiments with a one-side gas-dynamic heating of flat specimens of the material of 20 mm thickness. Temperature measurements at different depth from a heated surface were taken by means of thermocouples. The nominal heating conditions and duration of the experiments were given beforehand.For control of its reproduction in the experiments and for formation of a boundary condition of the first kind, measurements have been used by the thermocouple nearest to a heated surface. The location of these thermocouples in specimens was further considered as the origin of a solid axis x . The indications of thermocouples located at the biggest distance from a heated surface served as the second boundary condition of the first kind. The location of thermocouples was determined by means of X-ray radioscopy. All subsequentexperiments showed approximately the same results, heating conditions of all specimens being similar to each other.

The mathematical model of heat transfer process in the material looked like a boundary-value problem for the non-linear heat conduction equation

$$C(T)\frac{\partial T}{\partial \tau} = \frac{\partial}{\partial x}\left(\lambda(T)\frac{\partial T}{\partial x}\right), \quad 0<x<L, \quad 0<\tau\leq\tau_m \qquad (16)$$

$$T(x,0) = T_0(0), \quad 0 \leq x \leq L \qquad (17)$$

$$T(0,\tau) = v_1(\tau) \qquad (18)$$

$$T(1,\tau) = v_2(\tau) \qquad (19)$$

The results of temperature measurements of (4) type in the internal points of interval [0,L] served as input data for solving the inverse problem on determination of function $\lambda(T)$ The inverse problem analyzed has a

Third International Conference on Inverse Design Concepts and Optimization in Engineering Sciences (ICIDES-III), Editor: G.S. Dulikravich, Washington D.C., October 23-25, 1991.

unique solution at $N \geq 1$ [4].

Optimal planning of an experiment was made first. Since its heating conditions and time were given, the control over the experiment quality was carried out only by means of selecting an optimal plan of measurements (12). For this purpose an extreme problem of measurement planning has been solved

$$\xi_o = \text{Arg max } \Psi [M(\xi,\lambda(T))], \qquad \xi \in \Xi \qquad (20)$$

where $\Xi = \{(n,X): N \geq 1,\ 0 < X_i < 1,\ i=\overline{1,N}\}$.

To solve problem (20) there has been used a procedure of work [45]. The boundary conditions of the first kind (15),(16) are shown in Figure 1. The dependence $\lambda(T)$ obtained by traditional method served as apriori information about the unknown function. Function $\lambda(T)$ was approximated by a cubic B-spline of (8) type with "natural" boundary conditions [35] with the parameter number $m = 4$. So, vector $p = [\, p_k, k=\overline{1,4}\,]$ was unknown. Sensitivity functions $\vartheta_k(x,\tau)$, $k = \overline{1,m}$ were determined from a solution of boundary-value problems obtained by differentiating relations (16)-(19) through parameters p_k, $k = \overline{1,4}$.

The results of solving of a problem on selecting an optimal location of one/ and two thermocouples are given in Figure. 2, where a change of the experiment quality criterion is illustrated $\Psi [M(\xi,\lambda(T))] = \sqrt{\mu_{min}}$ depending on the sensors setting coordinates. For two sensors there are shown surface sections $\Psi(X_1,X_2)$ by planes drawn through the point of maximum value of criterion parallel to coordinate planes.

The results obtained show that in the analyzed experiment to provide high accuracy of solution of an inverse problem one sensor should be set in the narrow enough domain close to the origin of coordinates. Besides, in this experiment two sensors will be sufficient since at $N > 2$ the location coincidence of the second and successive sensors seems most optimal. The conclusions made are fully confirmed by data of computational experiments [32].

A solution of the inverse problem followed then using the procedure of work [24]. A thermogram of the corresponding experiment is shown in Figure. 1. To verify validity of the measurement plan and to estimate the authenticity of the inverse problem solution analysis was made of the effect of the initial guess about the unknown function on the solution [32]. The results of such an analysis are given in Figure. 3.

It is seen that the solution of the inverse problem does not depend on values of initial guess, thus proving high authenticity of identification results obtained. For comparison on Fig. 3 there is also given a temperature dependence of thermal conductivity obtained by the method of monotonic heating. It is seen that in the high-temperature region there is a considerable difference of this dependence from that obtained from the solution of the inverse problem. Here, the dependence $\lambda(T)$ obtained as a result of identification provides much better temperature correspondence, calculated from (16)-(19), with values measured experimentally, this confirming high authenticity of results as well.

Third International Conference on Inverse Design Concepts and Optimization in Engineering Sciences (ICIDES-III), Editor: G.S. Dulikravich, Washington D.C., October 23-25, 1991.

It should be noted as a conclusion of this section that effective thermophysical characteristics of high-temperature composite materials can atrongly depend on heating conditions. It is caused by thermal destruction of a binder [49], this process depending on heating rate [50]. The analogous dependence takes place for semi-transparent materials [51]. To avoid this factor, methods based on solution of inverse heat transfer problems have been developed for determining heat transfer characteristics in more complicated mathematical models taking into account effects of thermal decomposition [25,39,52,53] and heat transfer by radiation [40,54].

IDENTIFICATION OF CONTACT THERMAL RESISTANCES IN MULTILAYER STRUCTURES

Contact heat transfer is important in different technical systems. The main characteristic of this process is contact thermal resistance. At present stationary methods are widly used to determine contact thermal resistances in different joints [55,56]. Non-stationary methods based on solving inverse heat transfer problems are more effective (see, e.g. [7,17]) but in spite of the fact that the first works devoted to such methods were published about twenty years ago [57-59], only isolated investigations are known in this field especially experimental-computational studies. Works devoted to optimization of experiments for identifying contact thermal resistances are also isolated.

The application of identification method is considered in this section to determine thermal contact resistances between fuel and shel in fuel rods of a nuclear-power reactor.Transient processes between successive stationary states are analyzed when the reactor is started up for the first time.The results of experimental-computational studies presented in works [33,60-63] are breafly discussed.

The mathematical model of a non-stationary heat transfer process in a fuel rod is given by the following boundary-value problem

$$C_1(T)\frac{\partial T_1}{\partial \tau} = \frac{1}{x}\frac{\partial}{\partial x}\left(\lambda_1(T)\frac{\partial T_1}{\partial x}\right) + q_v(x,\tau),\ L_0<x<L_1,\ 0<\tau\le\tau_m \qquad (21)$$

$$C_2(T)\frac{\partial T_2}{\partial \tau} = \frac{1}{x}\frac{\partial}{\partial x}\left(\lambda_2(T)\frac{\partial T_2}{\partial x}\right),\ L_1<x<L_2,\ 0<\tau\le\tau_m \qquad (22)$$

$$T_1(x,0) = T_{0,1}(0),\quad L_0\le x\le L_1 \qquad (23)$$

$$T_2(x,0) = T_{0,2}(0),\quad L_1\le x\le L_2 \qquad (24)$$

$$\frac{\partial T_1(L_0,\tau)}{\partial x} = 0 \qquad (25)$$

$$\lambda_1(T_1(L_1,\tau))\frac{\partial T_1(L_1,\tau)}{\partial x} = \lambda_2(T_2(L_1,\tau))\frac{\partial T_1(L_1,\tau)}{\partial x} \qquad (26)$$

Third International Conference on Inverse Design Concepts and Opumization in Engineering Sciences (ICIDES-III). Editor: G.S. Dulikravich. Washington D.C., October 23-25, 1991.

$$-R\cdot\lambda_1(T_1(L_1,\tau))\frac{\partial T_1(L_1,\tau)}{\partial x} = T_1(L_1,\tau) - T_2(L_1,\tau) \qquad (27)$$

$$\lambda_2(T_2(L_2,\tau))\frac{\partial T_2(L_2,\tau)}{\partial x} = \alpha(\tau)[T_2(L,\tau)-T_e(L,\tau)] \qquad (28)$$

In the model (21)-(28) initial temperature distributions $T_{o,1}(x)$ and $T_{o,2}(x)$ are computed by solving the corresponding stationary problem. Energy release in fuel $q_v(x,\tau)$ was computed taking into account radial nonuniformity $\bar{q}(x)$ and integral heat release $q_l(\tau)$ measured by neutron detectors

$$q_v(x,\tau) = q(\tau)\bar{q}(x) \qquad (29)$$

where $$q(\tau) = \frac{q_l(\tau)}{2\pi\int_{L_0}^{L_1}\bar{q}(x)x\,dx}$$

The contact thermal resistance R is unknown but temperarures are avaible measured in some points of the structure analysed

$$T_{meas}(X_{j,i},\tau) = f_{j,i}(\tau), \quad i = \overline{1,N_j}, \quad j = 1,2 \qquad (30)$$

The inverse problem is to determine R from conditions (21)-(30).During each transient regime contact thermal resistance R was considered as a constant .The main goal of the investigation was to determine experimentally R depending on integral heat release q_l.

Iterative numerical algorithms were developed for solving inverse problems analysed [60,62], the residial functional being written down in the form

$$J = \sum_{j=1}^{2}\sum_{i=1}^{N_j}\left[\int_0^{\tau_m}\left(T_{j,i}(X_{j,i},\tau)-f_{j,i}(\tau)\right)^2 d\tau + \left(T_{j,i}(X_{j,i},0)-f_{j,i}(0)\right)^2\right] \qquad (31)$$

Algorithms for solving temperature measurements design were also developed.These algorithms were used in carring out experimental-computational studies of contact heat transfer processes in fuel rods.Some results are breafly discussed below.

General sequence of stages was similar to that for thermophysical

Third International Conference on Inverse Design Concepts and Optimization in Engineering Sciences (ICIDES-III), Editor: G.S. Dulikravich, Washington D.C., October 23-25, 1991.

characteristics identification.At the first stage parametric analysis of the accuracy of inverse problem solution as well as optimal temperature measurement design were made.Input data for solving this problems one can see in work [61].

The results of measurement design for one thermocouple are shown in Figure 4.One can see that the thermocouple installation into the fuel is much more effective.The conclusions made are fully confirmed by data of parametric accuracy analysis of the inverse problem solution (61).Computations show that it is quite enough to use one thermocouple.Basing on the results obtained.thermocouples were installed on the internal surfaceof fuel tablets which had the shape of hollow cylinders.

The results of experimental data processing are illustrated in Figure 5.One can see that a decrease takes place when q_l is approximately equal to 210W/cm.It testifys to the fact that the fuel gets in touch with the shell. For comparison the dependance analysed is shown here,which was obtained by using the method of work [64].The last one does not predict the moment of touch and so gives much more optimistic results of safety analysis.

CONCLUSION

The results presented demonstrate high efficiency of methods for thermal studies based on distributed parameter system identification.Such methods facilitate to obtain trustworthy data for heat transfer characteristics and increase the accuracy of mathematical simulation of thermal conditions.

REFERENCES

1. A.V. Lykov, "Heat-and-mass exchange (Nandbook)", Moscow, Energia, 1978 (in Russian).

2 . E.S. Platunov et al, " Thermophysical measurements and instruments", Leningrad, Mashinostroenie, 1986 (in Russian).

3. P. Eyknoff, "System Identification. Parameter and State Estimation", John Wiley and Sons Ltd., New York, 1974.

4. O.M. Alifanov, E.A. Artyukhin and S.V. Rumyantsev, "Extreme Methods for Solving Ill-posed Problems and Their Application to Inverse Heat Transfer Problems", Moscow, Nauka, 1988 (in Russian).

5. T.V. Beck, K.T.and Arnold, "Parameter Estimation in Engineering and Science", John Wiley and Sons, New York, 1977.

6. E.A. Artyukhin, "Identification of heat transfer processes in high-temperature structure by methods of inverse problems", Items of atomic science and engineering, in series: Atomic- gidrogen power and technology, Issue 3, pp. 71-73, 1988.

7. O.M. Alifanov, "Identification of Heat Transfer Processes of Flight Vehicles", Moscow, Mashinostroenie, 1979 (in Russian).

8. V.P. Mishin and O.M. Alifanov, "Quality Improvement in Final Design of Thermally Stressed Structures and Inverse Problems. General Questions of Theory", Mashine Design, No 5, pp. 19- 24, 1986.

9. V.P. Mishin and O.M. Alifanov, "Quality Improvement in Final Design of Thermally Stressed Structures and Inverse Problems. Practical Applications", Mashine Design, No 6, pp. 11-21, 1986.

10. E.A. Artyukhin and A.S. Okhapkin, "Parametric Accuracy Analysis in Solving a Non-linear Inverse Problem of the Composite Material Thermal Conductivity Recovery", J. Engineering Physics, Vol. 75, No 5, pp. 1275-12281, 1983.

11. Y. Sukahava, Sh. Aihava and F. Kojima, "A Method for Parameter Estimation of a Class of Non-linear Distributed Parameter Systems under Noisy Observation", Proc. of 6th IFAC Simp. on Identifi- cation and System Parameter Estimation, Arlington, Virginia, USA, June 7-11, 1982, Washington, Mc Gregor and Werner Inc., pp. 1144-1149, 1982.

12. E.A. Artyukhin, V.E. Killikh and A.S. Okhapkin, "Reconstruction of the Asbo-textolite Effective Thermal Conductivity from the Inverse Problem Solution", J. Engineering Physics, Vol. 45, No. 5, pp. 788-793, 1983.

13. D.F. Simbirsky, "The Temperature Diagnostics of Engines", Kiev, Tekhnika, 1976 (in Russian).

14. L.A. Kozdoba and P.G. Krukovsky, "Methods for Solving Inverse Heat Transfer Problems", Kiev, Naukova Dumka, 1982 (in Russian).

15. Yu.M. Matsevity and A.V. Multanovsky, "Identification in Heat Conduction Problems", Kiev, Naukova Dumka, 1982 (in Russian).

16. O.M. Alifanov, "Inverse Heat Transfer Problems", Moscow, Mashino-stroenie, 1988 (in Russian).

17. J.V. Beck, B. Blackwell, and C.R. St.Clair, "Inverse Heat Conduction - Ill-Posed Problems", John Wiley and Sons, New York, 1895.

18. N.I. Nikitenko, "Conjugate and Inverse Problems of Heat and Mass Transfer", Kiev, Naukova Dumka, 1988 (in Russian).

19. Yu.M. Matsevity, and C.O.Lupshenko, "Identification of Thermo-physical Properties of Solids", Kiev, Naukova Dumka, 1990 (in Russian).

20. E. Hensel, "Inverse Theory and Applications for Engineers", Prentice Hall, Englwood Cliffs, New Jersey, 1991.

21. L.F. Yankelev and L.I. Guseva, "Method for Simultanous Determination of Thermal Conductivity and Specific Heat per Unit Volume, Depending on Temperature", J. Engineering Physics, Vol.28, No. 4, pp. 652-656, 1975.

22. K.G. Omelchenko and V.G. Pchelkina, "Solution of the Non-linear Inverse Heat Conduction Problem to Determine Thermophysical Characteristics", J. Engineering Phusics, Vol. 29, No. 1, pp. 95-98, 1975.

23. E.A. Artyukhin, "Determination of Thermal Diffusivity from Experimental Data", J. Engineering Physics, Vol. 29, No. 1, pp. 878-881, 1975.

24. E.A. Artyukhin, "Temperature Dependence Reconstruction of the Thermal Conductivity from the Inverse Problem Solution", High Temperatures, Vol. 19, No 5, pp. 963-967, 1981.

25. E.A. Artyukhin and A.S. Okhapkin, "Temperature Depence Determination of the Composite Material Thermal Conductivity Trough Data of Unsteady Experiments", J. Engineering Physics, Vol. 44, No. 2, pp. 274-281, 1983.

26. E.A. Artyukhin and A.V. Nenarocomov, "Numerical Solution of the Coefficient Inverse Heat Conduction Problem", J. Engineering Physics, Vol. 53, No. 3, pp. 474-480, 1987.

27. A.A. Goryatchev and V.M. Yudin, "Solution of the Inverse Coefficient Heat Conduction Problem", J. Engineering Physics, Vol.43, No. 4, pp. 641-648, 1982.

28. Identification of Dynamical Systems and Inverse Problems, Theses of Int. Conf., Suzdal, USSR, October 1990, Suzdal, 1990.

29. D.F.Simbirsky and A.V.Guley, "Optimal Design of Experimental-Computational Determining the Thermal Conductivity of Solids Under Condition of Non-stationary Heating", J. Engineering Physics, Vol. 45, No.5, pp. 732-737,1983.

30. E.A.Artyukhin, "Measurement Design for Solving Coefficient Heat Conduction Problems", J. Engineering Physics, Vol. 48, No. 3, pp. 490-495, 1985.

31. E.A.Artyukhin and A.V.Nenarokomov, "Optimal Experiment Design when Determining the Total Emissivity of Materials", High Temperatures, Vol. 26, No. 5, pp. 971-977, 1988.

32. E.A.Artyukhin, L.I.Guseva, A.P.Tryanin, and A.G.Shibin, "Data Processing and Design of Transient Thermophysical Experiments", J. Engineering Physics, Vol. 56, No. 3, pp. 414-419, 1989.

33. E.A.Artyukhin, A.V.Nenarokomov, A.P.Tryanin, S.A.Utenkov and V.V.Yakovlev, "Investigation of Contact Heat Transfer in Fuel Rods", Int. Seminar "Thermophysics - 90", Obninsk, USSR,September 25-28 1990, Theses, Obninsk, pp. 126-132, 1990.

34. A.N.Tikhonov and V.Y.Arsenin, "Solution of IU-Posed Problems, V.H.Winston and Sons, Washington, D.C., 1977.

35. S.B.Stechkin and Yu.N.Subbotin, "Splines in Computational Mathematics", Moscow, Nauka, 1976 (in Russian).

36. F.P.Vasiliev, "Numerical Methods for Solving Extreme Problems", Moscow, Nauka, 1989 (in Russian).

37. E.A.Artyukhin and S.V.Rumyantsev, "Optimal Choice of Descent in Dradient Methods for Solving Inverse Heat Conduction Problems", J. Engineering Physics, Vol. 39, No. 2, pp. 865-869, 1980.

38. E.A.Artyukhin, A.G.Ivanov and A.V.Nenarokomov, "Solution of Coefficient Inverse Heat Conduction Problems Taking Into Account A priori Information about Values of Unknown Functions", J. Engineering Physics (to be published).

39. V.M.Yudin, "Heat Distribution in Glass-Rainforced Plastics". - Proc. of TsAGI, Issue 1267, Moscow, TsAGI, 1970.

40. P.V.Prosuntsov and S.V.Resnik, "Determination of Thermophysical Properties of Semi-Transparent Materials", J.Engineering Phvsics, Vol. 49, No. 6, pp. 977-982, 1985.

41. E.A.Artyukhin, S.A.Budnik, A.S.Okhapkin, "Numerical Solution of Coefficient Inverse Heat Conduction Problems and Optimization of Temperature Measurements", J. of Engineering Physics, Vol. 55, No. 2, pp. 292-299, 1988.

42. E.A.Artyukhin, "Optimal Experiment Design when Identifying Transient Heat Transfer Processes", J.Engineering Physics, Vol. 56, No. 3, pp. 378-382, 1989.

43. L.V.Kontorovich and G.P.Akilov, "Functional Analysis", Moscow, Nauka, 1984 (in Russian).

44. S.M.Ermakov (Editor), "Mathematical Theory of Experiment Design", Moscow, Nauka, 1984 (in Russian).

45. E.A.Artyukhin, "Measurements Design for Solution of Coefficient Inverse Heat Conduction Problems", J. of Engineering Physics, Vol. 48, No. 3, pp. 490-495, 1985.

46. E.A.Artyukhni, L.I.Guseva, A.P.Tryanin and A.G.Shibin, "The Inflience of Input Data Uncertainty on Results of Temperature Measurement Design", J. Engineering Physics, Vol. 58, No. 5, pp. 848-853, 1990.

47. Yu.V.Polezhaev, "On Using Experiment with Non-stationary Ablation to Determine Thermal Conductivity and Other Properties of Glassy Thermal Protective Matterials", High Temperature, Vol. 1, No. 1, pp.33-38, 1963.

48. J.V.Beck, "Calculation of Thermal Diffusivity from Temperature Measurements", J. Heat Transfer, Vol. 85, No. 2, pp. 181-182, 1963.

49. Yu.V.Polezhaev and F.B.Yurevich, "Thermal Propertion", Moscow, Energiya, 1976 (in Russian).

50. V.M.Yudin at el, "Study of Thermal Destruction of Polymeric Binders", Proc. of TsAGI, Issue 2065, Moscow, 1980.

51. P.V.Prosuntsov and S.V.Reznik, "Analysis of Thermal Conductivity Data of Translucent Dispersive Materials for Heat Calculations", "Gagarin Scientific Readings on Astronautics and Aeronautics, 1989", Moscow, Nauka, pp. 56-60, 1990.

52. E.A.Artyukhin, "Optimal Measurement Design in Identification of Heat Transfer processes in Decomposing Materials", Heat/Mass Transfer, Minsk Int. Forum, USSR, May 24-27 1988, Theses, Section 8, Minsk, pp. 22-24, 1988.

53. A.S.Okhapkin, "Investigation of Heat Transfer Characteristics in Composite Thermal Protective Material", J. Engineering Physics, Vol. 49, No. 6, pp. 989-984, 1985.

54. P.V.Prosuntsov and S.V.Reznik, "Mathematical Model Coefficient Inverse Problem of Radiative-Conductive Heat Transfer in Semi-Transparent Dispersive Medium", Proceeding of the Siberian Branch of the USSR Academy of Sciences, Vol. 10, Issue 2, pp.3-9,1986

55. V.M.Popov, "Contact Heat Transfer in Fixed and Detachable Connections', Moscow,Energia,1971 (in Russian).

56. Yu. P.Shlikov, E.A.Ganin, and S.N.Tsarevsky, "Contact Thermal Resistance", Moscw, Energia,1977 (inRussian).

57. J.V.Beck, "Transient Sensitivity Coefficients for the Thermal Contact Conductance", Int. J. Heat Mass Transfer, Vol. 12, No. 1, pp. 621-633, 1969.

58. J.V.Beck, "Determination of Transient Experiments forTermal Conductance", Int. J. Heat Mass Transfer, Vol. 12, No. 1, pp. 621-633, 1963.

59. S.V.Smishlyaeva, V.M.Yudin, "Experimental Study of Contact Resistance in Structural Joints", Transactions of TsAGI, Vol. 2, No. 2, pp. 66-72, 1971.

60. E.A.Artyukhin and A.V.Nenarokomov, "Reconstruction of the Contact Thermal Resistance from a Solution of the Inverse Heat Conduction Problem", J. Engineering Physics, Vol. 46, No. 4, pp.677-682, 1984.

61. E.A.Artyukhin, A.V.Nenarokomov, A.P.Tryanin, S.A.Utenkov, and V.V.Yakovlev, "Analysis of Measurement Schemes when Identifying Contact Thermal Resistances in Fuel Rods", Items of Atomic Science and Engineering, In Series: Atomic-Hidrogen Power and Technology, Issue 3, pp. 75-76, 1988.

62. E.A.Artyukhin, A.V.Nenarokomov, A.P.Tryanin, S.A.Utenkov, and V.V.Yakovlev, "Contact Thermal Resistantces Identification in Fuel Rods, Part 1. Development of Algorithms", J. Engineering Physics (to be published).

63 E.A.Artyukhin, A.V.Nenarokomov, A.P.Tryanin, S.A.Utenkov, and V.V.Yakovlev, "Contact Thermal Resistances Identification in Fuel Rods, Part II. Experiment", J. Engineering Physics (to be published).

64. P.N.Strijov, F.Pazdera and V.V.Yakovlev, "The Improved Version of the Fin Code and its Verification",Preston, G.B.,September 19-22, 1988. IAEA-TC-657/3.4.

Third International Conference on Inverse Design Concepts and Optimization in Engineering Sciences (ICIDES-III). Editor: G.S. Dulikravich, Washington D.C., October 23-25, 1991.

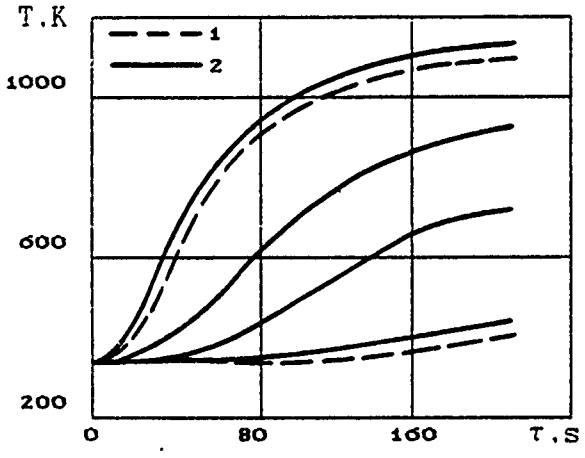


Fig.1 Results of temperature measurements:
1 - for solving the design problems;
2 - for solving the inverse problem.

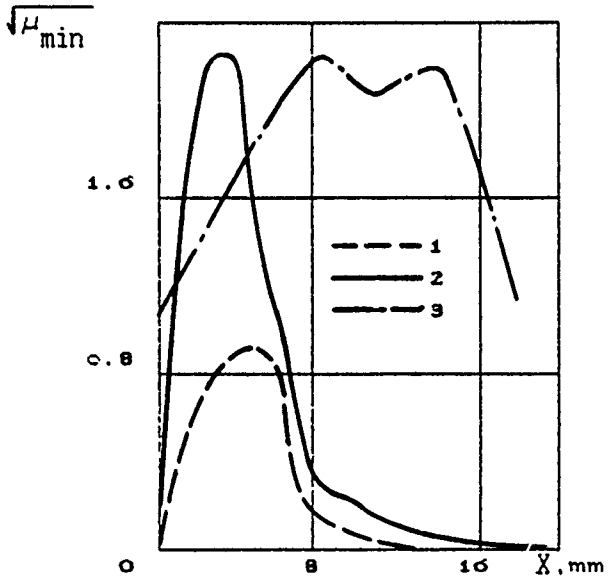


Fig.2 Dependance of the efficiency criterion on the coordinates of thermosensor locations:
1 - N=1; 2 - N=2,section 1;
3 - N=2,section 2.

Third International Conference on Inverse Design Concepts and Optimization in Engineering Sciences
(ICIDES-III), Editor: G.S. Dulikravich, Washington D.C., October 23-25, 1991.

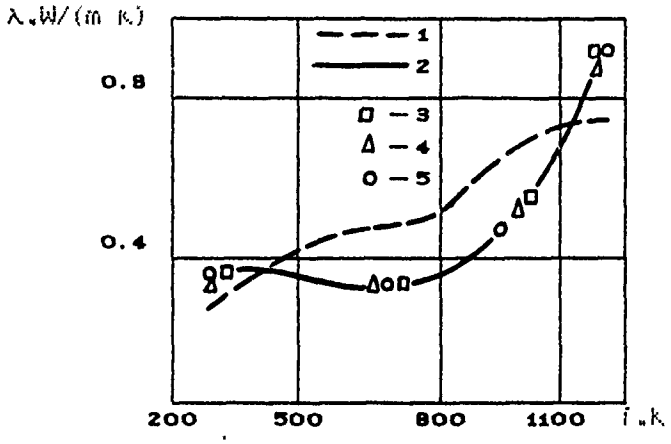


Fig.3 Dependence of thermal conductivity on temperature: 1 - traditional method, 2 - inverse problem solution; 3 - λ=0.2 W/(m k); 4 - λ=0.4; 5 - λ=0.

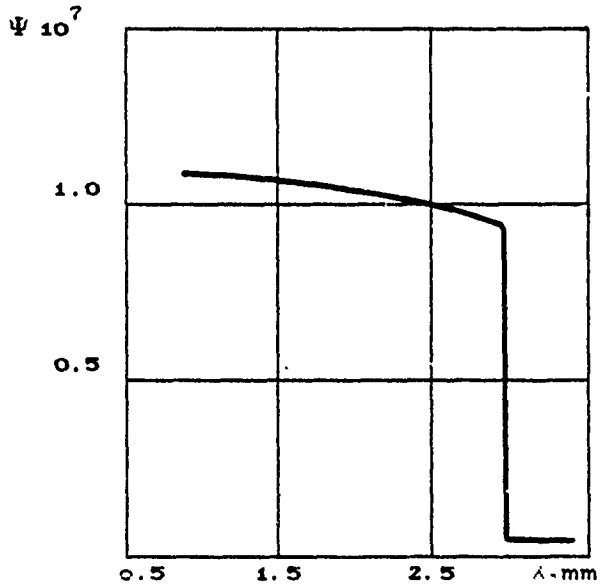


Fig.4 Change of design criteria Ψ depending on sensor coordinate x.

Third International Conference on Inverse Design Concepts and Optimization in Engineering Sciences (ICIDES-III), Editor: G.S. Dulikravich, Washington D.C., October 23-25, 1991.

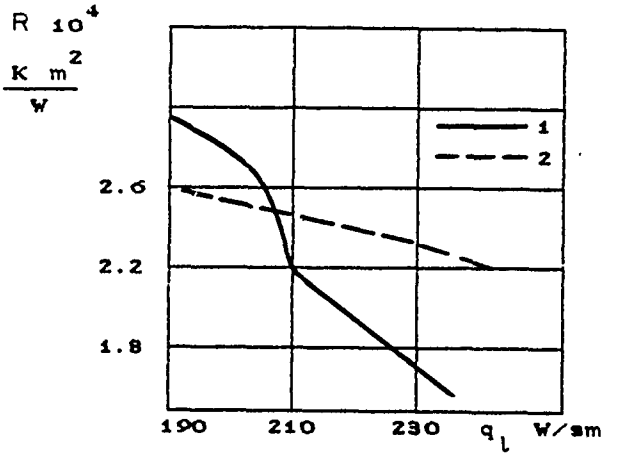


Fig.5 Dependence of contact thermal resistance on integral heat release:
1 - inverse problem solution;
2 - prediction.

Third International Conference on Inverse Design Concepts and Optimization in Engineering Sciences (ICIDES-III). Editor: G.S. Dulikravich. Washington D.C. October 23-25, 1991.

A NEW METHOD OF OPTIMAL DESIGN FOR A TWO-DIMENSIONAL DIFFUSER BY USING DYNAMIC PROGRAMMING

Chuangang Gu (Ph.D, Prof.)
Moujin Zhang (Doctor Degree Candidate)
Xi Chen (Ph.D)
Yongmiao Miao (Ph.D., Prof.)

Dept. of Power Mach. Eng.
Xi'an Jiaotong University P. R. China

ABSTRACT

A new method for predicting the optimal velocity distribution on the wall of a two-dimensional diffuser is presented in the paper. The method by Principle of Dynamic Programming solves the optimal control problem with inequality constraints of state variables. The physical model of optimization is to protect the separation of the boundary layer while getting to be maximum pressure ratio in a diffuser of a specified length (or getting to the shortest length in a specified pressure ratio). The calculation results are fairly in agreement with the experimental ones. It shows that optimal velocity distribution on a diffuser wall should be as: the flow decelerates first quickly and then smoothly, while the flow is near separation but always protects from it. The optimal velocity distribution can directly be used to design the contour of the diffuser.

INTRODUCTION

A diffuser is an important part of compressors, fans and other air ducts. More and more attentions have been paid to its design. In the past dozens of years, the popularization and development of the optimization technique make it possible to design a diffuser with optimal velocity distribution

The index of optimizing a diffuser is to obtain the highest pressure ratio under the condition of a minimum constructional length. Generally speaking, in order to get an optimal shape of a diffuser, it is necessary to know an optimal velocity distribution on its wall. With the distribution, the boundary layer can be avoided seperation and a maximum pressure ratio (or pressure recovery) can be obtained in a specified length.

Nowadays, most designs of diffusers, which are two-dimensional or axial-symmetrical, are still based on experience. Designers often use the criteria of the diffusing angle or the equivalent diffusing angle and one-dimensional calculational method to design it. Obviously, it is too simple to reach the index of the optimal design.

Stratford(1959) proposed that the loss in a diffuser with the minimum length is the minimum while the boundary layer inside it is close to but just before occurrence of separation, then the velocity distribution is the best and the shape of the diffuser is optimal. Some researchers, such as H. liebeck, H. Fernboly, have used this principle to make some optimal designs.

Many authors also investigated the flow field in a diffuser and study how to control the flow

Third International Conference on Inverse Design Concepts and Optimization in Engineering Sciences (ICIDES-III), Editor: G.S. Dulikravich, Washington D.C., October 23-25, 1991.

separaction.

Some authors attempt to use the optimal control theory to solve the optimal design of a diffuser, because the governing equations of the flow in it are differential ones.

Gu and Ji (1987) proposed an optimal design problem of a diffuser, using the optimal control theory and the boundary layer theory. The optimal velocity distribution on its wall was obtained by using Pontryangin's maximum principle.

In order to meet the demands of engineering application, the optimal problem has to satisfy some constraints in both aerodynamics and strength which can be divided into two parts: one is called as constraint of state variable and another constraint of control variable. Those constraints are often inequality and make it very difficult to solve the problem in mathematical treatment.

It is well known that Pontryagin's principle can only solve the optimal control problem with constraints of control variables. To overcome the difficulty, many authors have done some research work and modifications such as continuous transfer techique (Jocobson, 1969; Gu, 1987) and expanded penalty function method (Gu and Miao, 1987).

However, for a problem with more inequality constraints of state variables the treatment is not efficient which have been stated by Gu and Miao(1987). That is to say, The more the constraints, the more the difficulties. On the contrary, the principle of dynamic programming is quite good at treating of state and control constraints. The more the constrains, the faster the calculation, because the numer of considered states and decisions decreases in seeking optimal decision.

In the present work, a physical model and a mathematical expression for dynamic programming are established and calculated. The result yielded by the method is quite in agreement with not only the experimental ones but also the result by Pontryagin's maximum principle.

ESTABLISHMENT OF AN OPTIMAL DESIGN PROBLEM OF A DIFFUSER

It is well known that the flow losses in a diffuser mainly consist of separation loss and friction one. Obviously, the former is greater than the latter. The friction loss is always inevitable. However, it doesn't vary greatly because the friction coefficient is approximately a constant in the fully–developed turbulent flow. The total friction loss can be considered as increasing proportionally with the axial length of a diffuser. So the key to designing an efficient diffuser is to avoid the separation of boundary layer. Considering the two factors mentioned above, Stratford. (1959) proposed that the properties of a diffuser with the minimum length and without boundary layer separation is optimal.

Generally, the turbulence degree at the inlet of a diffuser in engineering is so high that we can assume for convenience that the boundary layer has become a turbulent one at the inlet edge. And incompressible flow is only considered in present work.

The typical expressions of a optimal problem for a diffuser are as follows:

A) Pressure rise coefficient is maximum (i.e. the discharge velocity is minimum) under the condition of a provided constructional length and without separation of the boundary layer.

B) The length of a diffuser is minimum under the condition of a provided discharge velocity (i.e. the pressure rise coefficient is known) and without separation of the boudnary layer.

It can be proved that the expressions A) and B) are correlative.

Third International Conference on Inverse Design Concepts and Optimization in Engineering Sciences (ICIDES-III), Editor: G.S. Dulikravich, Washington D.C., October 23-25, 1991.

The separation of the boundary layer is a very complex problem. According to the change of velocity in main flow, the separation of boundary layer can be predicted by some experimental formulas to some extent. The following equations are adopted as the basis of solving the optimal problem, (Ref. 1,3,4,5,6,7,8,9,10).

The velocity shape factor of boundary layer is introduced as follows:

$$\Gamma = \frac{\delta_2 du}{Udx} Re_{\delta_2}^{m} \qquad \begin{cases} m = 1/4 & \text{turbulent flow} \\ m = 1 & \text{laminar flow} \end{cases} \tag{1}$$

where

$$\delta_2 = \int_0^\infty \frac{u}{U}\left(1 - \frac{u}{U}\right)dy \quad Re_{\delta_2} = \frac{U\delta_2}{\nu}$$

U is the velocity of main flow.

$\Gamma > 0$ denotes acceleration flow, and $\Gamma < 0$ deceleration one. So Γ can be used to judge whether the separation happens or not.

For a deceleration flow, the relationship between $\delta_2$and U is as follows (Ref.1) :

$$\frac{d}{dx}\left[\delta_2\left(\frac{U\delta_2}{\nu}\right)^{1/4}\right] = 0.0175 - 4.15\frac{\delta_2}{U}\frac{dU}{dx}\left(\frac{U\delta_2}{\nu}\right)^{1/4} \tag{2}$$

For convenience, the length of a diffuser, L, is used as a characteristic length; the velocity at the inlet, C, as a characteristic velocity. Then Eq. (2) can be rewritten in a non–dimensional form. The non–dimensional length of a diffuser contour is $S = X/L$, the non–dimensional velocity $V = U/C$, the non–dimensional momentum thickness $\theta = \delta_2/L$. So the Re δ_2 is

$$Re_{\delta_2} = U \cdot \delta_2 / \nu = V \cdot \theta \cdot Re_0$$

where $Re_0 = C \cdot L/\nu$ at the inlet of the diffuser.

Then Eq. (2) becomes as:

$$\frac{d}{ds}\left[\theta(Re_0 \cdot V \cdot \theta)^{1/4}\right] = 0.0175 - 4.15 \cdot \frac{\theta}{V}\frac{dV}{ds}(Re_0 \cdot V \cdot \theta)^{1/4} \tag{3}$$

Substituting the non–dimensional form of Eq. (1) into Eq. (3), we yield

$$\frac{d\theta}{ds} = (0.014 - 3.52 \cdot \Gamma)(Re_o \cdot V \cdot \theta)^{-1/4} \tag{4}$$

According to the result of Nikuradse's experiments, Buri proposed that the boundary layer will separate when Γ is not greater than −0.06. As stated by Gu and Ji(1987) to ensure the flow in a diffuser to be far from separation, we utilize the limit of Γ as :

$$-0.04 \leqslant \Gamma \leqslant 0$$

MATHEMATICAL EXPRESSION OF THE OPTIMAL PROBLEM

The mathematical expression of the index of optimization A) is as follows:

Index function:

$$J(*) = V(*) \rightarrow min \tag{5}$$

s.t.

Third International Conference on Inverse Design Concepts and Optimization in Engineering Sciences (ICIDES-III), Editor: G.S. Dulikravich, Washington D.C., October 23-25, 1991.

$$\frac{dV}{ds} = \Gamma \cdot V^{3/4} \cdot \theta^{-5/4} \cdot Re_o^{-1/4} \tag{6-1}$$

$$\frac{d\theta}{ds} = (0.014 - 3.52 \cdot \Gamma)(Re_o \cdot V \cdot \theta)^{-1/4} \tag{6-2}$$

$$0 > \Gamma \geqslant -0.04 \tag{7}$$

$$V(o) = 1, \qquad \theta(o) = \theta_o \tag{8}$$

$$V(*), \qquad \vartheta(*), free \tag{9}$$

So the mathematical expression for dynamic programming solution is as follows:

Index function:

$$J(1) = \int_o^1 \Gamma V^{3/4} \theta^{-5/4} Re_o^{-1/4} ds \to min \tag{10}$$

s.t.

$$dV / ds = \Gamma V^{3/4} \theta^{-5/4} Re_o^{-1/4} \tag{6-1}$$

$$d\theta / ds = (0.014 - 3.52\Gamma)(Re_o V\theta)^{-1/4} \tag{6-2}$$

initial condition: $V(o) = 1 \qquad \theta(o) = \theta_o$ (11)

control constraint: $-0.04 \leqslant \Gamma < 0$ (12)

state constraint: $0 < V < 1 \qquad \theta_o \leqslant \theta$ (13)

Quantizing the equations listed above, we yield:

$$J = \min_{\Gamma(k)} \left\{ \sum_{k=0}^{N} \Delta S * \left[\Gamma(k) V(k)^{3/4} \theta(k)^{-5/4} Re_o^{-1/4} \right] \right\} \tag{14}$$

$$V(k+1) = V(k) + \Delta S * \left[\Gamma(k) V(k)^{3/4} \theta(k)^{-5/4} Re_o^{-1/4} \right] \tag{15}$$

$$\theta(k+1) = \theta(k) + \Delta S * \left\{ (0.014 - 3.52\Gamma(k)[Re_o V(k)\theta(k)]^{-1/4} \right\} \tag{16}$$

$$-0.04 \leqslant \Gamma(k) < 0 \tag{17}$$

$$0 < V(k) \leqslant 1 \tag{18}$$

$$\theta_o \leqslant \theta(k) \tag{19}$$

and the iterative relation becomes

$$\begin{cases} J(V,\theta,k) = \min_{\Gamma(k)} \left\{ \Delta S * [\Gamma(k) V(k)^{3/4} \theta(k)^{-5/4} Re_o^{-1/4}] + J(V,\theta,k+1) \right\} \\ J(V,\theta,N) = 0 \end{cases} \tag{20}$$

CALCULATION RESULT AND ANALYSIS

In calculation, Reo and N are taken as 10^6 and 10 respectively. The state variables and control variables are quantized respectively. The sets of admissible state variables are as follows:

V = {0.4, 0.45, 0.5, 0.55, 0.6, 0.65, 0.7, 0.75, 0.8, 0.85, 0.9, 0.95, 1.0}

θ = {0.00226, 0.00508, 0.00781, 0.01058, 0.01336, 0.01890, 0.02168, 0.02445, 0.02722, 0.03}

Then the allowed quantized states are:

{(0.4, 0.00226), (0.4, 0.00508), (0.4, 0.0078), ···,···,···,···,···,(1, 0.03)}

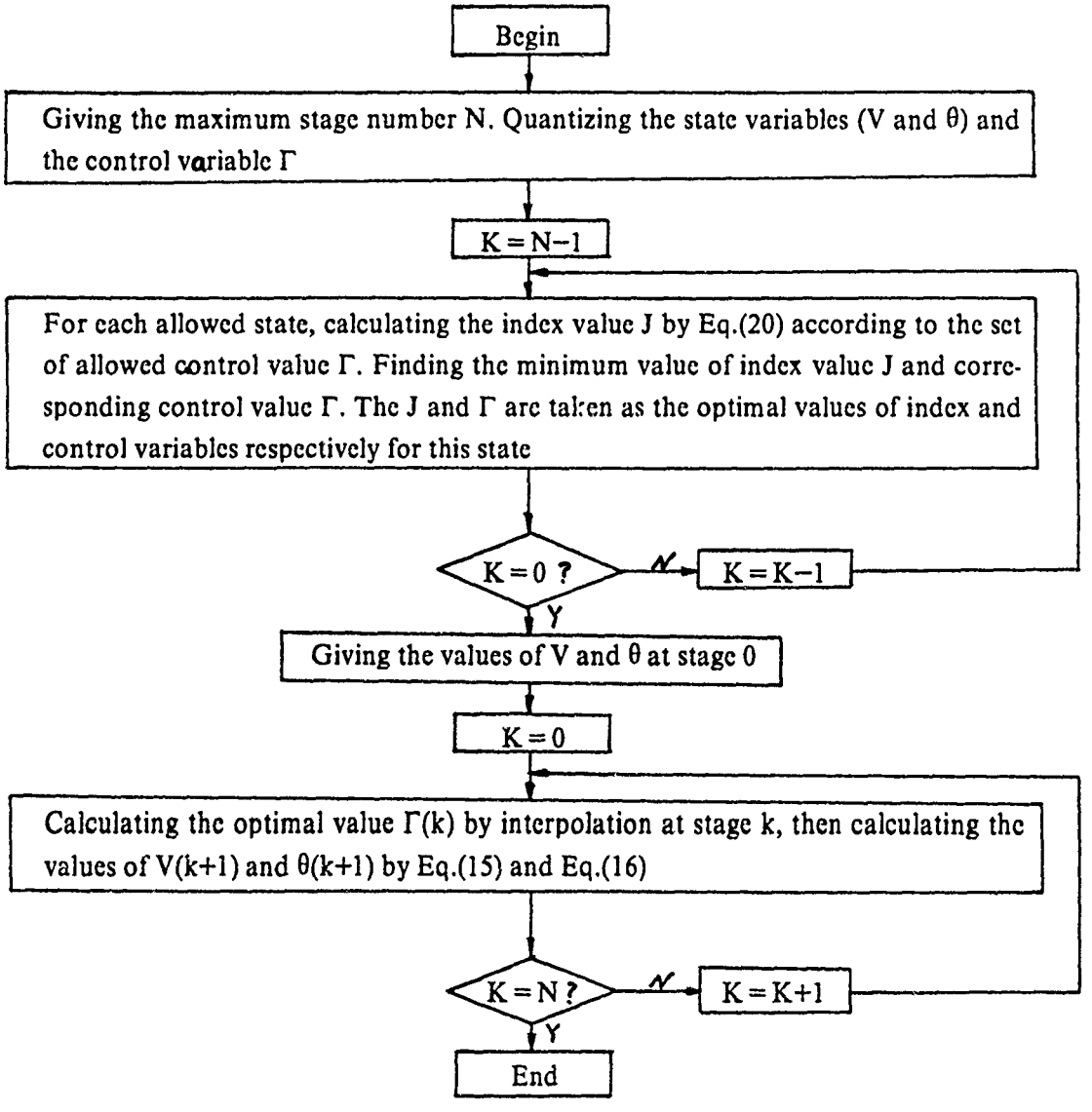
And the set of admissible control variable is as follows:

$\Gamma = \{-0.04, -0.035, -0.03, -0.025, -0.02, -0.015, -0.01, -0.005\}$

The two-dimensional dynamic Programming Computatinal procedure is used because there are two state variables, the calculation procedure is presented in the computer flow chart. The initial value of V and θ, that is , the values at stage o, are taken as 1 and 0.00226 respectively. The calculation results at stage 5 are presented in Table 1. There is only a part of all results because the results are too many to list them all. At each stage, a similar table can also be listed.

In the table 1, a grid point stands for a allowed quantized state, the value put to the right-up of a grid point is the optimal value of index J at this state, and the one put to the right-down of the grid point is the corresponding optimal value of control variable Γ.

Computer flow chart.



Third International Conference on Inverse Design Concepts and Optimization in Engineering Sciences (ICIDES-III), Editor: G.S. Dulikravich, Washington D.C., October 23-25, 1991.

As shown in Fig. 1, curve ABC is an optimal velocity distribution of the diffuser. The results are is quite in agreement with the experimental data and the results calculated by Pontryagin's maximum principle by Gu and Ji,(1987).

The optimal velocity distribution ABC is also called as an optimal deceleration curve for a diffuser. In the range above the curve, including the curve, there is no separation while Γ is not less than -0.04; on the contrary, in the range under the curve, separation will happen. So the curve ABC is a critical line ($\Gamma=-0.04$) between separation and non-separation.

Drawing a deceleration curve AB′C′ in the nonseparation range, we can find that for a diffuser with a specified length, the discharge velocity V^* is always less then V'. On the other hand, for a specified discharge velocity V' (which menas a specified pressue rise coefficient) the corresponding optimal length S^* is always less than S'. That means reducing velocity along the optimal deceleration curve ABC will yield the maximum pressure rise coefficient in a specified length or the minimum length of a diffuser in a specified pressure rise. In this case, the length is minimum and the loss is nearly minimum because there is no separation.

From the physical explanation of the optimal deceleration curve in Fig.1 It is also proved that the two expressions of index functions A) and B) of the optinal control problem are correlative. That is, the optimal velocity distribution obtained by one index function can satisfy another automatically.

THE CALCULATION OF THE DIFFUSER CONTOUR

The contour of the diffuser is calculated by means of the optimal velocity distribution on the surface, so that it is also called as optimal design problem or inverse problem. It is well known that solving the problem directly in X–Y plane will involve non-identifed of calculated region. So coordinate transformation is neccessary. It is the easiest way to transfer the X–Y plane to Φ–Ψ plane.

The governing Equations. in Φ–Ψ plane has been deduced strictly in the paper as:

Taking an element in X–Y plane and considering incompressible, potential flow, the continuity equation and non-rotation equation are as follows:

$$\frac{\partial V_x}{\partial x}+\frac{\partial V_y}{\partial y}=0 \tag{21}$$

$$\frac{\partial V_y}{\partial x}-\frac{\partial V_x}{\partial y}=0 \tag{22}$$

Velocity vector is

$$\bar{V}=|V|\cdot(\bar{i}\cdot\cos\beta+\bar{j}\cdot\sin\beta) \tag{23}$$

Where |V| is the amplitude of $\bar{V}$. β is the angle between $\bar{V}$ and coordinate line X.

The transform relation between X–Y plane and Φ–Ψ plane is:

$$\left.\begin{aligned} f_x&=(Y_\Psi\cdot f_\Phi-Y_\Phi\cdot f_\Psi)/J\\ f_y&=(-X_\Psi f_\Phi+X_\Phi\cdot f_\Psi)/J\end{aligned}\right\} \tag{24}$$

Where J is Jacobi matrix.

Substituting Eq. (23) and Eq. (24) into Eq.(21), because of $J\neq 0$, then we yield:

$$\frac{\partial V}{\partial\Phi}(Y_\Psi\cos\beta-X_\Psi\sin\beta\ )+\frac{\partial V}{\partial\Psi}(-Y_\Phi\cos\beta+X_\Phi\sin\beta\ )$$

Third International Conference on Inverse Design Concepts and Optimization in Engineering Sciences (ICIDES-III), Editor: G.S. Dulikravich, Washington D.C., October 23-25, 1991

$$+V\cdot(-X_{\Psi}\frac{\partial\sin\beta}{\partial\Phi}+Y_{\Psi}\frac{\partial\cos\beta}{\partial\Phi})+V(X_{\Phi}\frac{\partial\sin\beta}{\partial\Psi}-Y_{\Phi}\frac{\partial\cos\beta}{\partial\Psi})=0 \tag{25}$$

The four items on the left side of Eq. (25) are as follows respectively,

$$\frac{\partial V}{\partial\Phi}\cdot(Y_{\Psi}\cdot\cos\beta-X_{\Psi}\sin\beta)=\frac{\partial V}{\partial\Phi}\cdot\sqrt{X_{\Psi}^2+Y_{\Psi}^2}$$

$$\frac{\partial V}{\partial\Psi}\cdot(-Y_{\Phi}\cdot\cos\beta+X_{\Phi}\sin\beta=0$$

$$V\cdot\left(-X_{\Psi}\frac{\partial\sin\beta}{\partial\Phi}+Y_{\Psi}\frac{\partial\cos\beta}{\partial\Phi}\right)=0$$

$$V\cdot(X_{\Phi}\frac{\partial\sin\beta}{\partial\Psi}-Y_{\Phi}\frac{\partial\cos\beta}{\partial\Psi})=V\cdot\frac{\partial\beta}{\partial\Psi}\cdot\sqrt{X_{\Phi}^2+Y_{\Phi}^2}$$

In deducing the definations of normal and tangent unit vectors of equal Φ and equal Ψ lines, Eq. (25) can be rewritten as,

$$\frac{\partial V}{\partial\Phi}\cdot\sqrt{X_{\Psi}^2+Y_{\Psi}^2}+V\cdot\frac{\partial\beta}{\partial\Psi}\sqrt{X_{\Phi}^2+Y_{\Phi}^2}=0 \tag{26}$$

It can be easily proved that:

$$\sqrt{X_{\Psi}^2+Y_{\Psi}^2}=\sqrt{X_{\Phi}^2+Y_{\Phi}^2}=V/J$$

And substituting it into Eq.(26), finally, the continuity equation in $\Phi-\Psi$ plane can be given as:

$$\frac{\partial\ln V}{\partial\Phi}+\frac{\partial\beta}{\partial\Psi}=0 \tag{27}$$

In the similar way, the non-rotation equation in $\Phi-\Psi$ plane is:

$$\frac{\partial\ln V}{\partial\Psi}-\frac{\partial\beta}{\partial\Phi}=0 \tag{28}$$

Two Laplace's Eqs. can be obtained from Eq. (27) and Eq.(28):

$$\frac{\partial^2\ln V}{\partial^2\Psi}+\frac{\partial^2\ln V}{\partial\Phi^2}=0 \tag{29}$$

$$\frac{\partial\beta^2}{\partial\Phi^2}+\frac{\partial\beta^2}{\partial\Psi^2}=0 \tag{30}$$

The velocity distribution within the diffuser can be obtained by solving Eq. (29) with ADI method. Then from Eq.(28) the values of β on the top line ($\Psi=0$ or $\Psi=1$) of the potential flow region can also be yielded, so the shape of potential flow region can be defined. The diffuser contour can be modified by adding thickness of boundary layer. The calculation result is shown in Fig.4, the line of $Y/L=0$ is the central line of diffuser. The shape is quite similar to the real size of B. S. Stratford's diffuser. The equivalent diffusing angle of the diffuser is 19 ° (integral angle), and is much greater than ordinary recommended angle.

CONCLUSIONS

The optimal deceleration curve (i.e. optimal velocity distribution) on the wall of a diffuser is first obtained by using the principle of dynamic programming. In solving optimal control problem of fluid mechnics with inequality constraints of state and control variables, the dynamic programming method has many advantages over others. The physical model of optimization for a diffuser is to avoid the

Third International Conference on Inverse Design Concepts and Optimization in Engineering Sciences (ICIDES-III). Editor: G.S. Dulikravich, Washington D.C., October 23-25, 1991.

separation of boundary layer while getting to the maximum pressure rise in a diffuser of a specified length (or getting to the shortest length in a specified pressure rise). The calculation results are fairly in agreement with the experimental ones and the results calcaulated by Pontrayagin's maximum principle.

The optimal velocity distribution on a diffuser wall should be as: the flow decelerates first quickly and then smoothly, and the flow is near separation but always protects from it. The optimal velocity distribution can also be expanded to design an unsymmetric diffuser.

ACKNOWLEDGEMENTS

The research work is supported by The National Science Fund Committee of China (No.59076261) Application of Optimal Control Theory In Turbomachinery Design). The authors wish to express their sincere thanks for it.

REFFERENCES

1. Gu, Chuan Gang and Ji, Yong 1987, Theoretical Analysis of The Optimal Shape for A Two-dimensional diffuser with Incompressible Flow, Proc. of the 2nd China-Japan Joint Conference on Fluid Machinery, C1-3, pp416-422.
2. Larson, R. E. and Casti, J. L., 1982, Principles of Dynamic Programming, Marcel Dekker Inc.
3. Liu, G. L., The optimal aeronatical desing theory of plane cascades J. of Mechanics (chinese) 1981.
4. Stratford, B. S., 1959, The predication of Separation of the Turbulent boundary layer, J. of Fluid Machanics, Vol. 5, No.1.
5. Stratford, B. s., 1959, An experimental Flow with Zero Skin Friction Throughtout its region of pressure Rise, J. of Fluid Mechanics, Vol.5, No.1.
6. Schlichting, H., 1979, Boundary Layer Theory
7. Shuang, Huo, 1975, Optimization based on Boundary layer Concept for compressible Flow, Trans. ASME, J. of Eng. for Power, Vol. 97, No.2.
8. Senoo, Y. and Nishi, M., 1977, Prediction of Flow Separation in A Diffuser by A boundary Layer Calculation, Trans. ASME, J. of Fluid Eng., Vol.99, No.3.
9. Gu. Chuan Gang and Miao, Yong Miao 1987, Blade Design of Axial-Flow Compressors by the Method of Optimal control Theory —Physical Model and Mathematical Expression, Trans. ASME, J. of Turbomachinery, Vol.109, No.1, pp 99-102.
10. Gu, Chuan Gang and Miao, Yong Miao, 1987, Blade Design of Axial-Flow Compressors by the Method of Optimal control Theory — Application of Pontryagin's maximum principle, A Sample calculation and its results, Trans. ASME, J. of Turbomachinery, Vol.109, No.1, pp 103-107.
11. Jacobson, D. H. and Lele, M. M., 1969, A Tranformation Technique for optimal control Problem with a state Variable Inequality constraint,Trans. IEEE. J. of Automatic Control,

Third International Conference on Inverse Design Concepts and Optimization in Engineering Sciences (ICIDES-III), Editor: G.S. Dulikravich, Washington D.C., October 23-25, 1991.

Vol. AC-14, No.5.

	0.577	0.601	0.626	0.655	0.684	0.710	0.732	0.750	0.780
θ=.00226	-.040	-.040	-.040	-.040	-.040	-.040	-.040	-.040	-.040
	0.750	0.763	0.776	0.789	0.803	0.818	0.842	0.870	0.930
θ=.00503	-.040	-.040	-.040	-.040	-.040	-.040	-.040	-.040	-.040
	0.822	0.831	0.840	0.849	0.858	0.867	0.879	0.907	0.993
θ=.00781	-.040	-.040	-.040	-.040	-.040	-.040	-.040	-.040	-.040
	0.863	0.870	0.877	0.884	0.891	0.897	0.906	0.926	1.017
θ=.01058	-.040	-.040	-.040	-.040	-.040	-.040	-.040	-.040	-.040
	0.890	0.895	0.901	0.906	0.912	0.917	0.924	0.938	1.028
θ=.01336	-.040	-.040	-.040	-.040	-.040	-.040	-.040	-.040	-.040
	0.909	0.913	0.917	0.922	0.926	0.931	0.936	0.947	1.031
θ=.01613	-.040	-.040	-.040	-.040	-.040	-.040	-.040	-.040	-.040
	0.923	0.926	0.930	0.934	0.938	0.941	0.946	0.954	1.030
θ=.01890	-.040	-.040	-.040	-.040	-.040	-.040	-.040	-.040	-.040
	0.935	0.938	0.941	0.944	0.948	0.951	0.954	0.961	1.028
θ=.02168	-.040	-.040	-.040	-.040	-.040	-.040	-.040	-.040	-.040
	V=0.85	V=0.80	V=0.75	V=0.70	V=0.65	V=0.60	V=0.55	V=0.50	V=0.45

Table 1

Third International Conference on Inverse Design Concepts and Optimization in Engineering Sciences (ICIDES-III), Editor: G.S. Dulikravich, Washington D.C., October 23-25, 1991.

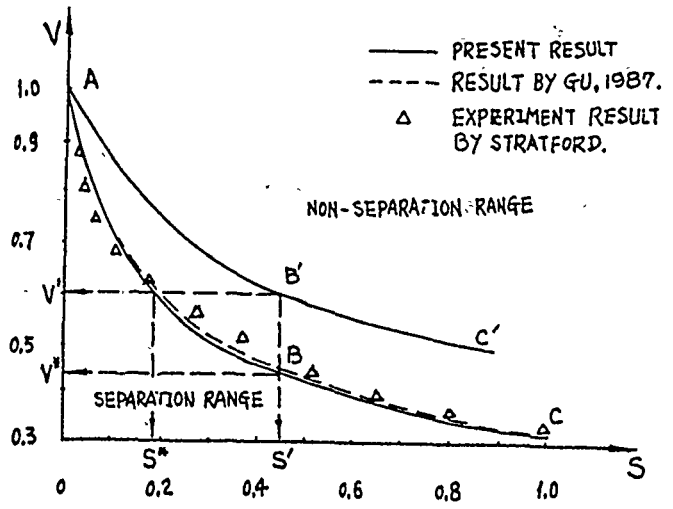


Fig.1 Optimal velocity distribution

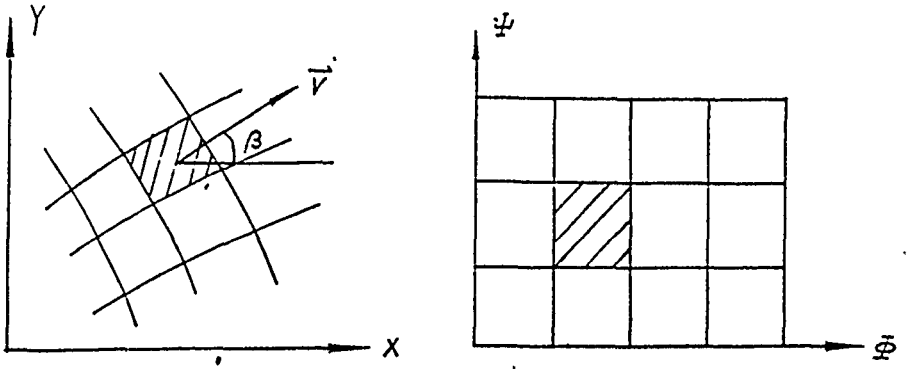


Fig.2. Coordinate tranformation

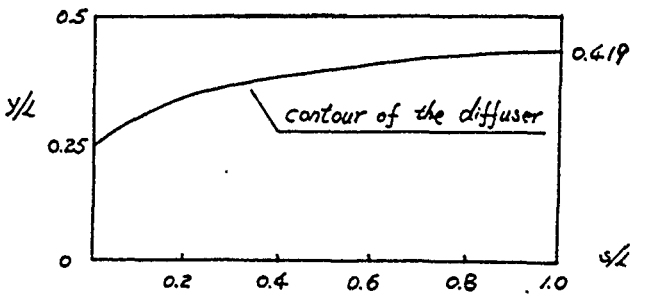


Fig.3 contour of the optimal diffuser

Third International Conference on Inverse Design Concepts and Optimization in Engineering Sciences (ICIDES-III). Editor: G.S. Dulikravich. Washington D.C., October 23-25, 1991.

AN INVERSE METHOD WITH REGULARITY CONDITION FOR TRANSONIC AIRFOIL DESIGN

Zhu Ziqiang, Xia Zhixun, and Wu Liyi
Inst. of Fluid Mechanics
Beijing Univ. of Aeronautics and Astronautics
Beijing 100083, China

ABSTRACT

It is known from the Lighthill's exact solution of the incompressible inverse problem that in the inverse design problem the surface pressure distribution and the free stream speed can not both be prescribed independently. This implies the existence of a constraint (regularity condition) on the prescribed pressure distribution. The same constraint exists at compressible speeds. In this paper, a well–posed inverse design method for transonic airfoil is presented. In the method, the target pressure distribution contains a free parameter that is adjusted during the computation to satisfy the regularity condition derived in this paper. A few design results are presented here in order to demonstrate the capability of the method.

INTRODUCTION

Recently, a number of design methods have been developed and used for the design of transonic airfoils and wings. Slooff[1] reviewed these methods and divided them into three major categories: indirect, inverse, and aerodynamic optimization. Indirect methods are characterized by the fact that the designer has no control over either the aerodynamic quantities or the geometry. The hodograph and fictitious gas methods are in this category. In inverse methods, the classical inverse problem of aerodynamics is solved. The designer specifies an arbitrary pressure distribution on an airfoil or wing, while the geometry of the airfoil or the wing that realizes the given pressure distribution is determined as the result of the solution. Aerodynamic optimization methods are those in which a nonlinear optimization algorithm is linked with a flow analysis code to minimize or maximize some aerodynamic object functions such as the lift–to–drag ratio.

The conventional inverse design methods are the most used in the industry application. The currently existing inverse methods for transonic airfoil design can be subdivided into two categories: (a) methods utilizing Dirichlet–type boundary conditions derived from the target pressure distribution; (b) methods utilizing Neumann–type boundary conditions in combination with some geometry correction procedure (residual– correction method).

In fact, in inverse problems, both a Dirichlet– and a Neumann–type boundary condition must be satisfied on the airfoil contour to be determined. This gives rise to a nonlinear problem with unknown boundary to be solved iteratively. In the first approach, the required target pressure distribution is imposed on an initial airfoil as a

Third International Conference on Inverse Design Concepts and Optimization in Engineering Sciences (ICIDES-III), Editor: G.S. Dulikravich, Washington D.C., October 23-25, 1991.

AN INVERSE METHOD WITH REGULARITY CONDITION FOR TRANSONIC AIRFOIL DESIGN

Zhu Ziqiang, Xia Zhixun, and Wu Liyi
Inst. of Fluid Mechanics
Beijing Univ. of Aeronautics and Astronautics
Beijing 100083, China

ABSTRACT

It is known from the Lighthill's exact solution of the incompressible inverse problem that in the inverse design problem the surface pressure distribution and the free stream speed can not both be prescribed independently. This implies the existence of a constraint (regularity condition) on the prescribed pressure distribution. The same constraint exists at compressible speeds. In this paper, a well–posed inverse design method for transonic airfoil is presented. In the method, the target pressure distribution contains a free parameter that is adjusted during the computation to satisfy the regularity condition derived in this paper. A few design results are presented here in order to demonstrate the capability of the method.

INTRODUCTION

Recently, a number of design methods have been developed and used for the design of transonic airfoils and wings. Slooff[1] reviewed these methods and divided them into three major categories: indirect, inverse, and aerodynamic optimization. Indirect methods are characterized by the fact that the designer has no control over either the aerodynamic quantities or the geometry. The hodograph and fictitious gas methods are in this category. In inverse methods, the classical inverse problem of aerodynamics is solved. The designer specifies an arbitrary pressure distribution on an airfoil or wing, while the geometry of the airfoil or the wing that realizes the given pressure distribution is determined as the result of the solution. Aerodynamic optimization methods are those in which a nonlinear optimization algorithm is linked with a flow analysis code to minimize or maximize some aerodynamic object functions such as the lift–to–drag ratio.

The conventional inverse design methods are the most used in the industry application. The currently existing inverse methods for transonic airfoil design can be subdivided into two categories: (a) methods utilizing Dirichlet–type boundary conditions derived from the target pressure distribution; (b) methods utilizing Neumann–type boundary conditions in combination with some geometry correction procedure (residual– correction method).

In fact, in inverse problems, both a Dirichlet– and a Neumann–type boundary condition must be satisfied on the airfoil contour to be determined. This gives rise to a nonlinear problem with unknown boundary to be solved iteratively. In the first approach, the required target pressure distribution is imposed on an initial airfoil as a

Third International Conference on Inverse Design Concepts and Optimization in Engineering Sciences (ICIDES-III), Editor: G.S. Dulikravich, Washington D.C., October 23-25, 1991.

FORMULATION OF THE INVERSE PROBLEM

The full potential equation can be written in terms of the perturbation velocity potential as

$$(1-M_\infty^2)\bar{\varphi}_{\bar{x}\bar{x}}+\bar{\varphi}_{\bar{z}\bar{z}}=K\frac{\partial}{\partial\bar{x}}\left(\frac{1}{2}\bar{\varphi}_{\bar{x}}^2\right)+\bar{H} \tag{1}$$

Where M_∞ is the free stream Mach number, $K(\gamma,M_\infty)$ is a transonic similarity parameter, γ is the ratio of specific heats, $(\bar{x},\bar{z})$ is a Cartesian coordinate system, and $\bar{H}$ represents all the higher order terms.

the tangency condition on the airfoil may be written as

$$\bar{\varphi}_{\bar{z}}(\bar{x},\pm 0)=\bar{f}'_{\pm}(\bar{x})+\bar{Q} \tag{2}$$

where $\bar{f}_{+}(\bar{x})$ and $\bar{f}_{-}(\bar{x})$ are the equations of the upper and lower airfoil surfaces respectively, and $\bar{Q}$ represents all the higher order terms.

the pressure coefficients on the airfoil surface are expressed as

$$C_{p\pm}(\bar{x})=-2\bar{\varphi}_{\bar{x}}(\bar{x},\pm 0)+\bar{S} \tag{3}$$

where $\bar{S}$ represents all the higher order terms.

In a residual–correction method, the solution $\bar{\varphi}(\bar{x},\bar{z})$ of Eq. (1) for an initial airfoil $\bar{f}_{\pm}(\bar{x})$ has been obtained by means of an existing analysis code, the objective here is to determine the amount of the geometry correction $\Delta\bar{f}_{\pm}(x)$ corresponding to the pressure difference $\Delta C_{p\pm}(x)$ between the specified and calculated pressure. If a small perturbation $\Delta\bar{\varphi}(\bar{x},\bar{z})$ is further introduced, we can obtain the potential equations for $\Delta\bar{\varphi}(\bar{x},\bar{z})$ according to the transonic small–disturbance theory

$$\Delta\varphi_{xx}+\Delta\varphi_{zz}=\frac{\partial}{\partial x}\left[\frac{1}{2}(\varphi_x+\Delta\varphi_x)^2-\frac{1}{2}\varphi_x^2\right] \tag{4}$$

$$\Delta\varphi_z(x,\pm 0)=\Delta f'_{\pm}(x) \tag{5}$$

$$\Delta C_{p\pm}(x)=-2\frac{\beta^2}{K}\Delta\varphi_x(x,\pm 0) \tag{6}$$

here $\beta=\sqrt{1-M_\infty^2}$, and the new variables have been introduced as

$$x=\bar{x},\quad z=\beta\bar{z},\quad \varphi(x,z)=(K/\beta^2)\bar{\varphi}(\bar{x},\bar{z}),\quad f_{\pm}(x)=(K/\beta^3)\bar{f}_{\pm}(\bar{x}) \tag{7}$$

By applying Green's theory to Eq.(4) and introducing a decay function similar to that used by Nørstrud[13], we can get the integral equations

$$\Delta u_s(x)=\frac{1}{\pi}\int_0^1\Psi_x(x,0;\xi,0)\Delta w_s(\xi)d\xi+G_s(x)$$
$$-\frac{1}{\pi}\int_0^1[I_s(x,\xi,+0)G(\xi,+0)+I_s(x,\xi,-0)G(x,-0)]d\xi \tag{8}$$

$$\Delta w_a(x)=\frac{1}{\pi}\int_0^1\frac{\Delta u_a(\xi)}{\xi-x}d\xi$$

Third International Conference on Inverse Design Concepts and Optimization in Engineering Sciences (ICIDES-III), Editor: G.S. Dulikravich, Washington D.C., October 23-25, 1991.

$$-\frac{1}{\pi}\int_0^1 [I_a(x,\xi,+0)G(\xi,+0)-I_a(x,\xi,-0)G(x,-0)]d\xi \tag{9}$$

here

$$\Delta u_s(x)=\Delta\varphi_x(x,+0)+\Delta\varphi_x(x,-0) \tag{10}$$

$$\Delta u_a(x)=\Delta\varphi_x(x,+0)-\Delta\varphi_x(x,-0) \tag{11}$$

$$\Delta w_s(x)=\Delta\varphi_z(x,+0)-\Delta\varphi_z(x,-0) \tag{12}$$

$$\Delta w_a(x)=\Delta\varphi_z(x,+0)+\Delta\varphi_z(x,-0) \tag{13}$$

$$\Psi(x,z;\xi,\zeta)=ln[(x-\xi)^2+(z-\zeta)^2]^{\frac{1}{2}} \tag{14}$$

$$G(x,z)=\frac{1}{2}\left[(\varphi_x+\Delta\varphi_x)^2-\varphi_x^2\right] \tag{15}$$

$$I_s(x,\xi,\pm)=\int_0^\infty \Psi_{\xi x}(x,0;\xi,\zeta)exp[-2R_{\pm}(\xi)\zeta]d\xi \tag{16}$$

$$I_a(x,\xi,\pm)=\int_0^\infty \Psi_{\zeta z}(x,0;\xi,\zeta)exp[-2R_{\pm}(\xi)\zeta]d\xi \tag{17}$$

$$R_{\pm}(x)=\left|f''_{\pm}(x)/\varphi_x(x,\pm 0)\right| \tag{18}$$

For convenience, the correction function $\Delta f_{\pm}(x)$ is split into symmetric $\Delta f_s(x)$ and antisymmetric $\Delta f_a(x)$ parts

$$\Delta f_s(x)=\Delta f_+(x)-\Delta f_-(x) \tag{19}$$

$$\Delta f_a(x)=\Delta f_+(x)+\Delta f_-(x)$$

Since $\Delta f'_a(x)=\Delta w_a(x)$, the antisymmetric part can be determined by direct evaluation of the right-hand side of Eq. (9). On the other hand, since $\Delta f'_s(x)=\Delta w_s(x)$, the symmetric part must be solved implicitly. Consequently, the correction $\Delta f_{\pm}(x)$ is obtained by integrating $\Delta w_s(x)$ and $\Delta w_a(x)$ with respect to x.

CONSTRAINTS FOR INVERSE PROBLEM

In the incompressible flow, it was demonstrated by Lighthill,[12] using conformal mapping method, that the geometry of an airfoil for a given speed distribution can be determined only if the prescribed speed distribution satisfied the following three integral constraints

$$\int_0^{2\pi} log\left|\frac{q_0}{q_\infty}\right| d\omega=0 \tag{20}$$

$$\int_0^{2\pi} log\left|\frac{q_0}{q_\infty}\right| cos\omega\ d\omega=0 \tag{21}$$

$$\int_0^{2\pi} log\left|\frac{q_0}{q_\infty}\right| sin\omega\ d\omega=0 \tag{22}$$

here q_0 is the prescribed speed distribution on the airfoil surface, q_∞ is the speed at infinity, ω is the polar angle in the transformed plane. The first constraint known as regularity condition is a consequence of the fact that the speed at infinity is q_∞. Eqs. (21) and

(22) together express that the airfoil is a closed contour and the angle of incidence is zero (or any other specified value):

In order to formulate the regularity condition for transonic flow, differentiating both sides of Eq(4) with respect to x, we have

$$\nabla^2 V(x,z) = \frac{\partial^2 G(x,z)}{\partial x^2} \tag{23}$$

here

$$V(x,z) = \Delta\varphi_x(x,z) \tag{24}$$

with a Dirichlet–type boundary condition

$$V_x(x,\pm 0) = V_0(x) = -\frac{K}{2\beta^2}\Delta C_{p\pm}(x) \tag{25}$$

and a constraint at infinity

$$\Delta\varphi_x(x,z) \to 0 \quad ; \quad (x^2 + \frac{z^2}{\beta^2} \to \infty) \tag{26}$$

Now we use the transformation

$$T(\chi) = x + iz = \frac{1}{4}\left(\chi + \frac{1}{\chi}\right) + \frac{1}{2} = \frac{1}{4}\left(re^{i\omega} + \frac{e^{-i\omega}}{r}\right) + \frac{1}{2} \tag{27}$$

where $\chi = re^{i\omega}$ is the complex variable in the transformed plane. The entire plane in the physical plane is mapped onto the outside of the unit circle, the chord of the airfoil (z=0, $0 \leqq x \leqq 1$) is corresponds to the unit circle (r=1, $0 \leqq \omega \leqq \pi$) on the transformed plane. Substituting Eq. (27) into Eq. (23) yields

$$\nabla^2 V(r,\omega) = L / |T'(\chi)|^2 \tag{28}$$

where

$$L(r,\omega) = \left(\frac{\partial\omega}{\partial x}\right)^2 \frac{\partial^2 G}{\partial\omega^2} + 2\left(\frac{\partial r}{\partial x}\frac{\partial\omega}{\partial x}\right)\frac{\partial^2 G}{\partial r\partial\omega} + \left(\frac{\partial r}{\partial x}\right)\frac{\partial^2 G}{\partial r^2} + \frac{\partial^2 r}{\partial x^2}\frac{\partial G}{\partial r} + \frac{\partial^2\omega}{\partial x^2}\frac{\partial G}{\partial\omega}$$

The boundary conditions in the transformed plane are

$$V(r,\omega)|_{r=1} = V_0(\omega) \tag{29}$$

$$V \to 0 \quad ; \quad (r \to \infty) \tag{30}$$

By applying Green's theory to Eq.(28), an integral expression can be obtained as

$$V(r_1,\omega_1) = \frac{r_1^2 - 1}{2\pi}\int_0^{2\pi} \frac{V_0(\omega)}{r_1 - 2r_1\cos(\omega-\omega_1) + 1} d\omega$$

$$+ \frac{1}{2\pi}\int_0^{2\pi}\int_1^{\infty} \log\left[\frac{r_1 - 2rr_1\cos(\omega-\omega_1) + r^2}{r_1^2 r - 2rr_1\cos(\omega-\omega_1) + 1}\right]\frac{L}{|T'(\chi)|^2} r\,dr\,d\omega \tag{31}$$

If $r_1 \to \infty$, the above equation becomes

$$\int_0^{2\pi} V_0(\omega)d\omega = \int_0^{2\pi}\int_1^{\infty} \frac{L\log r}{|T'(x)|^2} r\,dr\,d\omega \tag{32}$$

In physical plane, Eq. (32) can be written as

$$\int_0^1 [\Delta\varphi_x(x,+0) - \Delta\varphi_x(x,-0)]\omega_x\,dx = \iint_{-\infty}^{\infty} \log r \frac{\partial^2 G(x,z)}{\partial x^2} dx\,dz \tag{33}$$

Third International Conference on Inverse Design Concepts and Optimization in Engineering Sciences (ICIDES-III), Editor: G.S. Dulikravich, Washington D.C., October 23-25, 1991.

Using an integration by parts and introducing the decay function, we can obtain the final form of the regularity condition

$$\int_0^1 \Delta u_a(x)\omega_x dx = \int_0^1 [I_v(x,+0)G(x,+0) + I_v(x,-0)G(x,-0)]dx \tag{34}$$

here

$$I_v(x,\pm 0) = \int_0^\infty \frac{rr_{xx} - r_x^2}{r} exp[-2R_{\pm}(x)z]dz \tag{35}$$

The above discussion indicates that the prescribed pressure distribution should contain an adjustable parameter to guarantee that the regularity condition is satisfied. Thus the surface pressure distribution is to be prescribed in the form

$$C_{ps\pm}(x) = F_{\pm}(\sigma,x) \tag{36}$$

where σ is a parameter that is found as part of the solution. For convenience, the following form of C_{ps} is used in this paper:

$$C_{ps\pm}(x) = \sigma F_{\pm}(x) \tag{37}$$

In order to assure that the resulting airfoil has a specified trailing edge gap, the following closure condition must be satisfied:

$$\int_0^1 \Delta w_s(x)dx = 0 \tag{38}$$

This closure condition can assure that the trailing edge thickness of the current airfoil is always kept equal to that of the initial airfoil.

Although the regularity condition in closed form (34) is obtained from the simple transonic small disturbance theory with Nørstrud assumption, its practical utility will be shown by numerical examples in the following section.

NUMERICAL AND COMPUTATIONAL ASPECTS

In order to discrete the integrals appearing in Eqs. (16) and (17), the range of integration with respect to ζ is divided into subintervals. Assuming that $R_{\pm}(\xi)\zeta$ is constant on each subinterval, Eqs. (16) and (17) can be expressed as

$$I_s(x,\xi,\pm 0) = \sum_{n=0}^{N} exp[-2R_{\pm}(\xi)\zeta_n] \int_{\zeta_n - \frac{1}{2}\Delta\zeta_n}^{\zeta_n + \frac{1}{2}\Delta\zeta_n} \Psi_{\zeta x}(x,0;\ \xi,\zeta)d\zeta \tag{39}$$

$$I_a(x,\xi,\pm 0) = \sum_{n=0}^{N} exp[-2R_{\pm}(\xi)\zeta_n] \int_{\zeta_n - \frac{1}{2}\Delta\zeta_n}^{\zeta_n + \frac{1}{2}\Delta\zeta_n} \Psi_{\zeta z}(x,0;\ \xi,\zeta)d\zeta \tag{40}$$

The range of integration with respect to x is also divided into subintervals, and on each of subinterval $\Delta u_s(x)$, $\Delta u_a(x)$, $G(x,\pm 0)$, *and* $\Delta w_a(x)$ are assumed to be constants, while $\Delta w_s(x)$ is assumed to vary linearly, the final expressions of Eqs. (8) and (9) in discretized form are as follows:

$$\Delta u_s(x_i) = \sum_{k=1}^{I+1} \mu_{ik}^s \Delta w_s(x_{k-\frac{1}{2}}) + G_s(x_i) - \sum_{k=1}^{I} \left[v_{ik}^s G(x_k,+0) + \hat{v}_{ik}^s G(x_k,-0) \right] \tag{41}$$

Third International Conference on Inverse Design Concepts and Optimization in Engineering Sciences (ICIDES-III), Editor: G.S. Dulikravich, Washington D.C., October 23-25, 1991.

$$\Delta w_a(x_i) = \sum_{k=1}^{I} \mu_{ik}^a \Delta u_a(x_k) - \sum_{k=1}^{I} \left[\nu_{ik}^a G(x_k, +0) - \hat{\nu}_{ik}^a G(x_k, -0) \right] \tag{42}$$

The discretized form of Eq. (34) and (38) can be expressed as

$$\sum_{i=1}^{I} \Delta u_a(x_i)(\omega_{i+\frac{1}{2}} - \omega_{i-\frac{1}{2}}) = \sum_{i=1}^{I} \left[\nu_i^r G(x_i, +0) + \hat{\nu}_i^r G(x_i, -0) \right] \tag{43}$$

$$\sum_{i=1}^{I} [\Delta w_s(x_{i-\frac{1}{2}}) + \Delta w_s(x_{i+\frac{1}{2}})](x_{i+\frac{1}{2}} - x_{i-\frac{1}{2}}) = 0 \tag{44}$$

where the coefficients

$$\mu_{ik}^s,\ \mu_{ik}^a,\ \nu_{ik}^s,\ \hat{\nu}_{ik}^s,\ \nu_{ik}^a,\ \hat{\nu}_{ik}^a,\ \nu_i^r,\ \hat{\nu}_i^r$$

are the integral expressions on each of the subinterval. The full expressions are omitted here.

In order to improve the convergence, the following modifications have been taken in this paper:

1). A Riegels type of leading edge correction is taken in the method. The purpose of such correction is to remove the singularity at the leading edge of the round–nosed airfoil.

2). In order to increase the ability to deal with the shock, an artificial viscosity term is added to the integral equation method.

3). A Smoothing–relaxation procedure is proposed and used in this paper.

The inverse problem can be solved by the iteration process as follows:

1). The flowfield is solved for an initial airfoil $f_{\pm}(x)$ by a direct analysis code. From the calculated pressure distribution $C_{p\pm}(x)$, and the target pressure distribution $C_{ps\pm}(x)$, the residual $\Delta C_{p\pm}(x) = \sigma C_{ps\pm}(x) - C_{p\pm}(x)$ can be obtained.

2). The adjustable parameter σ is determined from the regularity condition (43).

3). The geometric correction $\Delta f_{\pm}(x)$ is determined by solving the equations (41)–(42). Thus a new geometry is obtained from the following Smoothing–relaxation procedure:

$$f_{\pm}^{n+1}(x_i) = f_{\pm}^{n}(x_i) + \delta \left[\Delta f_{\pm}^{n+1}(x_i) + 0.5 \left(\Delta f_{\pm}^{n+1}(x_{i-1}) + \Delta f_{\pm}^{n+1}(x_{i+1}) \right) \right] \tag{45}$$

where δ is a relaxation factor.

The same process is repeated until the calculated pressure distribution agrees with the prescribed one.

Several test cases are presented to show the validity and applicability of the procedure. A nonisentropic potential solver for 2–D transonic flow[14] is used as the analysis code.

In the first example, the target pressure distribution is taken from the result of RAE2822 airfoil, the free stream Mach number is 0.73, and the angle of attack is $\alpha = 2.05^\circ$. The initial airfoil is NACA0012 airfoil, the initial angle of attack is $\alpha = 0.0$. After 12 design cycles, the RAE2822 airfoil is already recovered. Indeed the designed airfoil is rotated in a clockwise direction by 2.05° with respect to the original airfoil. This is because the initial angle of attack is chosen to be 0°, the angle between the free stream and the X–Axi is always 0° during iterations. Fig.1 shows the target and initial

Third International Conference on Inverse Design Concepts and Optimization in Engineering Sciences (ICIDES-III), Editor: G.S. Dulikravich, Washington D.C., October 23-25, 1991.

pressure distribution. Fig.2 shows the convergence procedure of the pressure distribution.

The second example is chosen to show the function of the regularity condition. In Ref. [15], Strand gave a velocity distribution which did not satisfy the Lighthill's three integral constraints in incompressible flow, hence there is no airfoil corresponding to this velocity distribution. Strand modified this velocity distribution according to the Lighthill's constraints, and designed the airfoil corresponding to the modified velocity distribution, the results is showed in Fig. 3. Now, we calculate this example using the present method. For convenience, only the velocity distribution on the lower surface is multiplied by the free parameter σ. After 7 design cycles, the converged solution is obtained, the velocity distributions are given in Fig. 4. In this case, the output velocity distribution on the lower surface is not consistent with input velocity distribution, this is because the free parameter σ is not equal to 1, but equal to 1.07. The results show that the method can adjust the improperly input velocity distribution to the acceptable velocity distribution automatically, and design the airfoil corresponding to the modified velocity distribution. Comparing the figures the present result is closer with input data than Strand's one. On the other hand, if the regularity condition is not included in the method, the design procedure will not converge for this example.

CONCLUSIONS

A regularity condition in closed form for transonic flow is presented in this paper, and a well posed inverse design method for transonic airfoil is formulated. The results show that the method is a reliable and efficient method for the design of airfoil at transonic speeds. When the target pressure distribution is not properly given, the code can adjust the target pressure distribution automatically and design the airfoil corresponding to the modified pressure distribution.

REFERENCES

1. Slooff, J. W., "A survey of computational Methods for Subsonic and Transonic Aerodynamic Design", Paper at ICIDES– I , Austin, Tex., U.S.A., 1984.

2. Volpe, G. and Melnik, R.E., "The Role of Constraints in the Inverse Design Problem for Transonic Airfoils", AIAA Paper 81–1233, 1981.

3. Carlson, L. A., "Transonic Airfoil Design Using Cartesian Coordinates," NASA CR–2578, 1976.

4. Tranen, T. L., " A Rapid Computer Aided Transonic Airfoil Design Method", AIAA Paper 74–501, 1974.

5. Henne, P. A., "An Inverse Transonic Wing Design Method", AIAA Paper 80–0330, 1980.

6. Shankar, V., "A Full Potential Inverse Method Based on a Density Lineaerization Scheme for Wing Design", AIAA Paper 81–1234. 1981.

7. Davis Jr., W. H., "Technique for Developing Design Tools from the Analysis Methods of Computational Aerodynamics", AIAA Paper 79–1259, 1979.

8. McFadden, G. B., "An Artificial Viscosity Method for the Design of Supercritical Airfoils", Ph. D. Thesis, N. Y. University, 1979.

9. Fray, J. M. J., Slooff, J. W. *et al.*, "Inverse Method with Geometric Constraints for Transonic Airfoil Design", Int. J. for Numerical Methods in Engineering, Vol. 22, pp. 327–339, 1986.

10. Greff, E., Mantel, J., "An Engineering Approach to the Inverse Transonic Wing Design Problem", Comm. Appl. Num. Meth., Vol. 2, pp. 47–56,1986.

11. Takanashi, S., "Iterative Three–Dimensional Transonic Wing Design Using Integral Equations", J. Aircraft, NO.8 Vol.22, 1985.

12. Lighthill, M. J., "A New Method of Two–Dimensional Aerodynamic Design", ARC RM 2112, April. 1945.

13. Nϕrstrud, H., "High Speed Flow Past Wings", NASA CR–2246, 1973.

14. Zhu Z. Q., Bai Xue–song, "The Computation of Transonic Analysis and Design", Acta Mechanica, 78, pp 81–94, Springer Verlag, 1989.

15. Strand, T., "Exact Method of Designing Airfoils with Given Velocity Distribution in Incompressible Flow", J. Aircraft, Vol. 10, No. 11, 1973.

Third International Conference on Inverse Design Concepts and Optimization in Engineering Sciences (ICIDES-III), Editor: G.S. Dulikravich, Washington D.C., October 23-25, 1991.

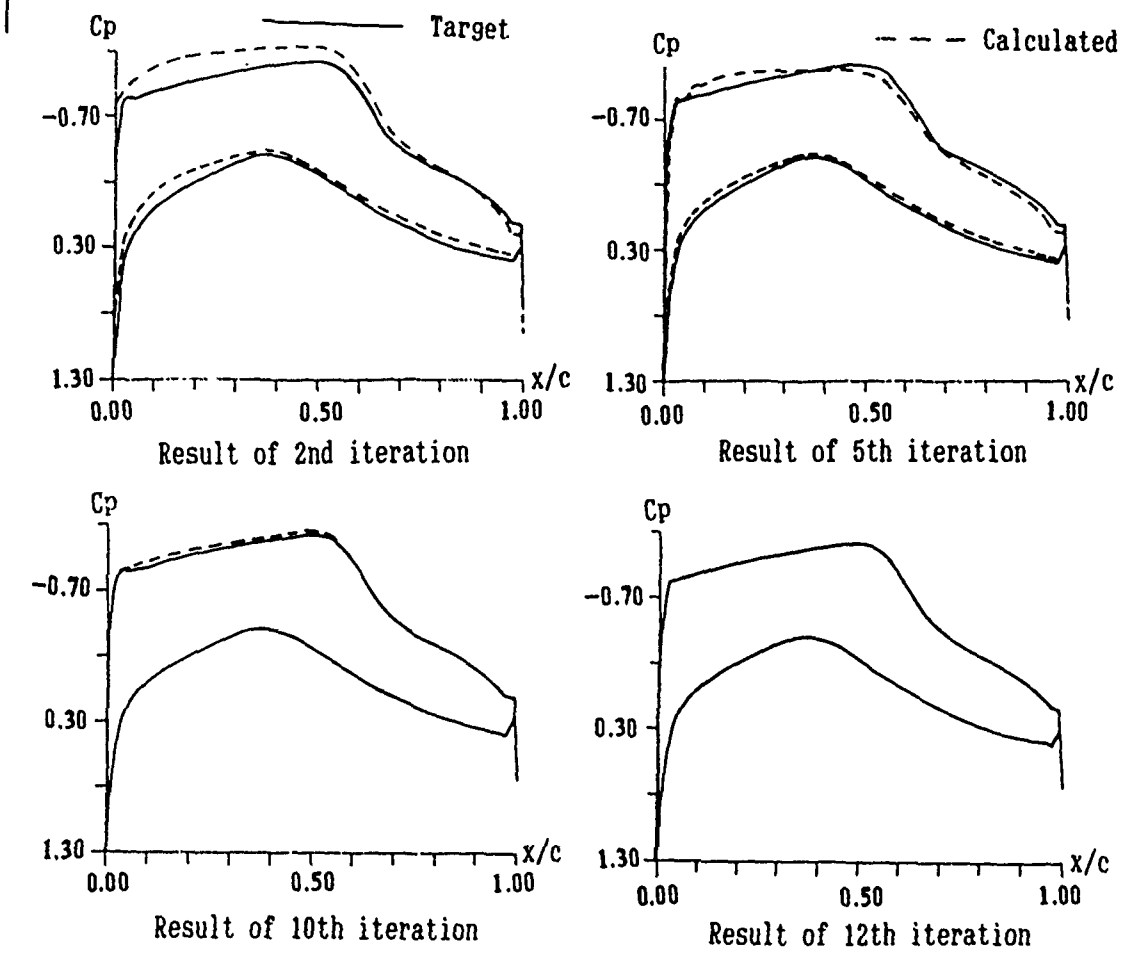


Fig. 2 Convergence history of the pressure distribution (example 1)

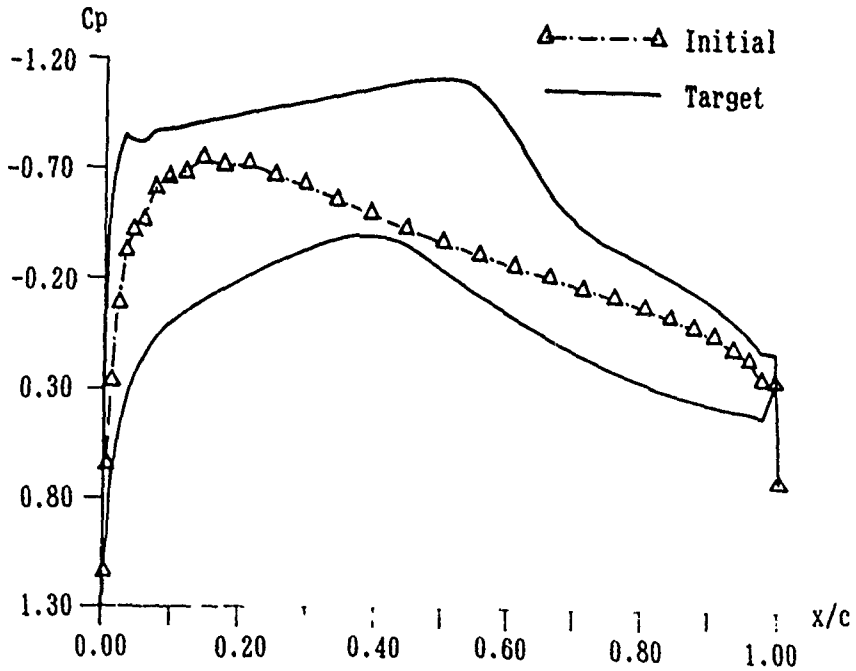


Fig. 1 Comparison of initial, target pressure distribution (example 1)

Third International Conference on Inverse Design Concepts and Optimization in Engineering Sciences (ICIDES-III), Editor: G.S. Dulikravich, Washington D.C., October 23-25, 1991.

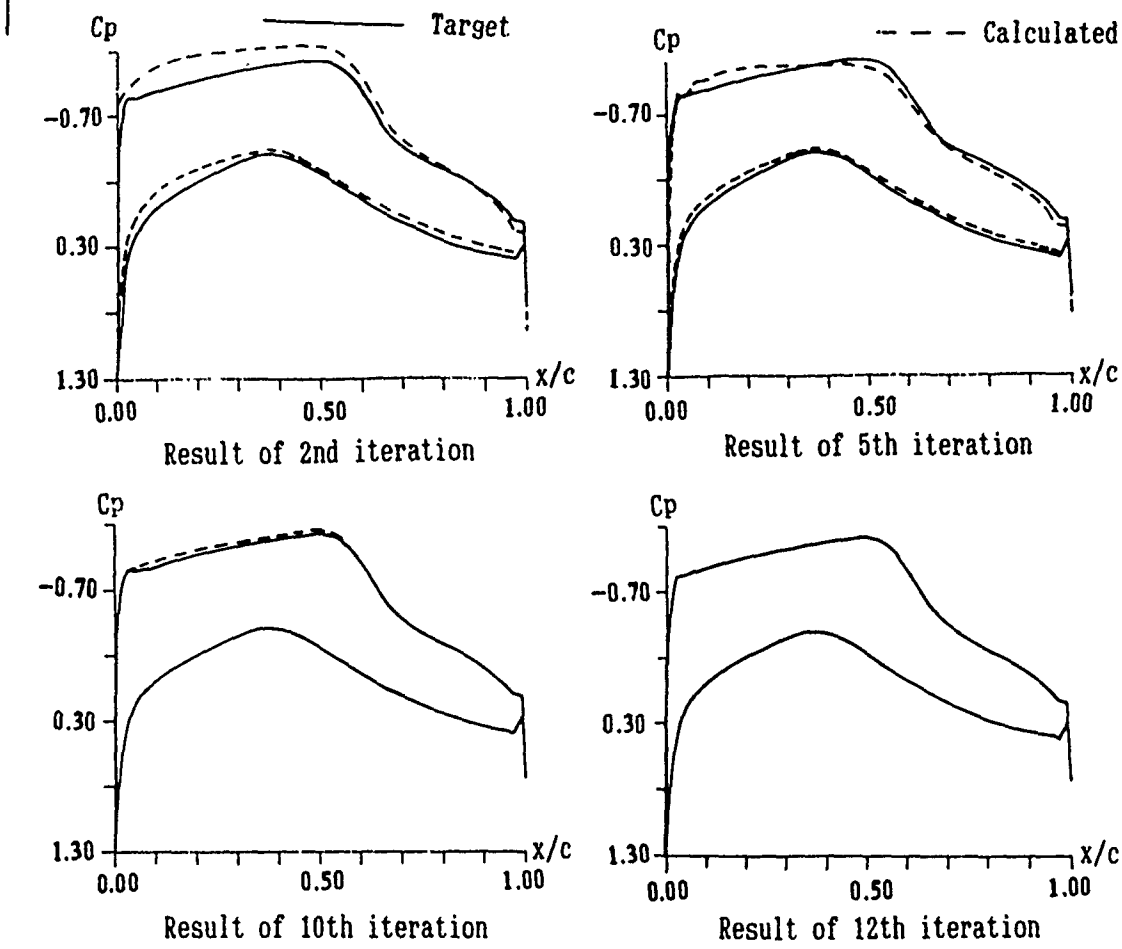


Fig. 2 Convergence history of the pressure distribution (example 1)

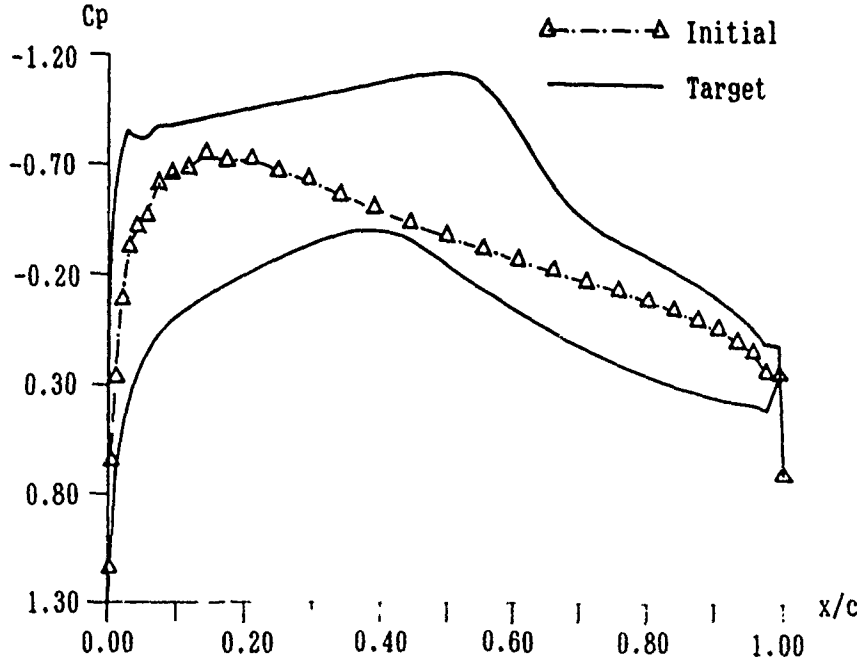


Fig. 1 Comparison of initial, target pressure distribution (example 1)

Third International Conference on Inverse Design Concepts and Optimization in Engineering Sciences (ICIDES-III), Editor: G.S. Dulikravich, Washington D.C., October 23-25, 1991.

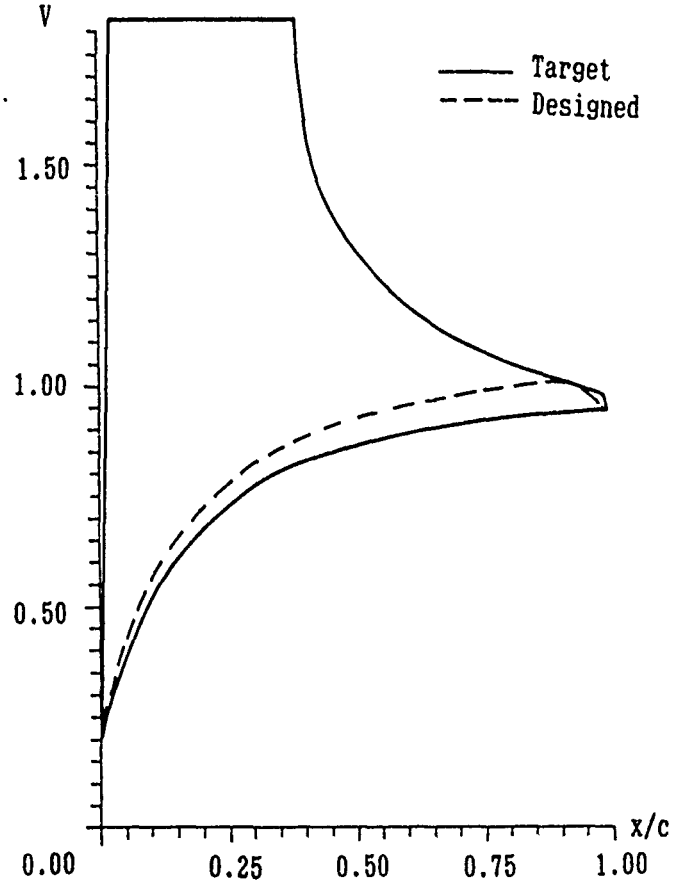


Fig. 4 The input and designed velocity distribution (example 2)

Third International Conference on Inverse Design Concepts and Optimization in Engineering Sciences (ICIDES-III), Editor: G.S. Dulikravich, Washington D.C., October 23-25, 1991.

Study of a New Airfoil Used in Reversible Axial Fans

Li Chaojun *Wei Baosuo* *Gu Chuangang*

Xi'an Jiaotong University
Xi'an, People's Republic of China

Abstract

The characteristics of reversal ventilation of axial flow fan is analysed in the paper. In according to the theory of flow around the airfoil, a new airfoil — "s" shaped airfoil with double circular arc is presented and experimented in the wind tunnel. the experimental results have shown that the characteristics of new airfoil in reversal ventilation is the same as that in normal ventilation and is better than that of existing airfoils of reversible axial fans.

Nomenclature

u	tangential velocity of impeller
c	absolute velocity
w	relative velocity
θ	enter angle of relative velocity of flow
θ_r	installation angle of blade
P_t	theoretical total pressure
$\overline{P_t}$	coefficient of theoretical pressure
ρ	dencity of flow
r	radius
τ	blade solidity
$\Phi = \frac{c_z}{u_t}$	coefficient of flow rate
c_y	lift coefficient
c_x	drag coefficient
α	attack angle
k	slope of characteristic line of pressure coefficient
b	blade chord
F	half of the maximum thickness of airfoil
$\bar{f}$	deflection of airfoil $\left(\bar{f} = \frac{F}{b}\right)$

Subscript

Third International Conference on Inverse Design Concepts and Optimization in Engineering Sciences (ICIDES-III), Editor: G.S. Dulikravich, Washington D.C., October 23-25, 1991.

1 before blade cascade
2 after blade cascade
u tangential direction
z axial direction
m for mean radius
o for $\overline{P}_t = 0$
t tip
h hub

Introduction

The reversible ventilation of a fan is a problm which often arises in many places, for example, in road and railway tunnels where it is required to drive the air in one or the other direction depending upon the condition that exists at the time. Though an axial fan whose impeller blades are formed with conventional airfoil can drive the air in opposite direction by simply reversing the rotor, it is found that the characteristics of reversal ventilation is much lower than that of the normal ventilation, the efficiency of fan decreasing sharply and the flow rate being about 40-50% of normal ventilation.

The characteristics of reversal ventilation of axial fan with single indepedent impeller is analysed in the paper. In accordance with the theory of flow around an airfoil, a new airfoil—"s" shaped airfoil with double circular arc is presented. If the impeller blades are formed with such airfoil, the axial fan can operate in each direction to provide a substantially equal but opposite flow with a higher efficiency than can be obtained by existing fan with conventional blades. The reversal ventilation can be achieved by simply reversing the rotor of fan. The "s" shaped airfoil presented in the paper provides a basis for constructing a new type reversible axial fan with simple construction, easy control and better characteristics.

The characteristics of fan impeller during normal and reversal rotation

According to the 2–D cascade theory, the velocity triangle of a blade cascade of the axial fan with single indepedent impeller is shown in Fig.1.

From the Eular equation

$$P_t = \rho u(c_{2u} - c_{1u}) = \rho u(w_{1u} - w_{2u}) \tag{1}$$

then the coefficient of theoretical pressure is

$$\overline{P_t} = P_t / \rho u_t^2 = u(w_{1u} - w_{2u}) / u_t^2 \tag{2}$$

where u_t is peripheral velocity of impeller.

Writting $$\bar{r} = \frac{r}{r_t} = \frac{u}{u_t} \tag{3}$$

Third International Conference on Inverse Design Concepts and Optimization in Engineering Sciences (ICIDES-III), Editor: G.S. Dulikravich, Washington D.C., October 23-25, 1991.

$$\Phi = \frac{c_z}{u_t} \tag{4}$$

thus the eq.(2) becomes

$$\overline{P_t} = \bar{r}\Phi(tg\theta_1 - tg\theta_2) \tag{5}$$

From fig.1

$$tg\theta_1 = \frac{w_{1u}}{c_z} = \frac{u - c_{1u}}{c_z} = \frac{\bar{r}}{\Phi} - tg\delta_1 \tag{6}$$

According to the cascade theory [4]

$$tg\theta_2 = A\,tg\theta_1 + B \tag{7}$$

Where

$$A = \frac{1 - \frac{\tau}{4}(dc_y / d\alpha)cos\beta}{1 + \frac{\tau}{4}(dc_y / d\alpha)cos\beta} \tag{8}$$

$$B = \frac{\frac{\tau}{2}(dc_y / d\alpha)sin\beta}{1 + \frac{\tau}{4}(dc_y / d\alpha)cos\beta} \tag{9}$$

β—the entry angle of relative velocity during $P_t = 0$, i.e. angle of zero lift line (Fig1)

From eq. (5), (6), (7) we get

$$p_t = (1 - A)\bar{r}^2 - \bar{r}\Phi[B + (1 - A)tg\delta_1] \tag{10}$$

The slope of characteristic line of $\overline{P_t}$ is

$$K = \frac{d\overline{P_t}}{d\Phi} = -\bar{r}[B + (1 - A)tg\delta_1] \tag{11}$$

When $\overline{P_t} = 0$, the coefficient of flow rate Φ would have the maximum value

$$\Phi_0 = \frac{(1 - A)\bar{r}}{B + (1 - A)tg\delta_1} \tag{12}$$

and the flow rate becomes maximum too

$$\theta_0 = u_t \int_{r_h}^{r_t} 2\pi r \Phi_0 dr \tag{13}$$

If representing with mean radius r_m

$$\bar{r}_m = \frac{r_m}{r_t}$$

thus

$$\Phi_{om} = (1 - A)\overline{r_m} / [B + (1 - A)tg\delta_1] \tag{12a}$$

$$\theta_{om} = u_t \Phi_{om} \pi(r_t^2 - r_h^2) \tag{13a}$$

It is noted, that the preceding equations are all suitable for both normal and reversal rotating of impeller.

For axial fan with single independent impeller no matter what the rotating direction may be, the air flow into the blade cascade always with axial direction, i.e the angle $\delta_1 = 0$. Making

Third International Conference on Inverse Design Concepts and Optimization in Engineering Sciences (ICIDES-III), Editor: G.S. Dulikravich, Washington D.C., October 23-25, 1991.

superscript " ′ " for condition of reversal ventilation, thus from the eq. (10), (11), (12a), (13a) the following equations are getten:

1) the theoretical pressure coefficient

$$\overline{P_t} = (1 - A)\bar{r}^2 - \bar{r}\Phi B \tag{14}$$

$$\overline{P'_t} = (1 - A')\bar{r}^2 - \bar{r}\Phi' B' \tag{15}$$

2) the ratio of K of reversal ventilation to that of normal ventilation

$$\bar{K} = \frac{K'}{K} = \frac{B'}{B} \tag{16}$$

3) the ratio of maximum theoretical reversal flow rate to maximum theoretical normal flow rate during $\overline{P_t} = 0$

$$J_0 = \frac{\theta'_{om}}{\theta_{om}} = \frac{\Phi'_{om}}{\Phi_{om}} = \frac{(1 - A')B}{(1 - A)B'} \tag{17}$$

Assum that $dc_y / d\ \alpha$ maintains constant during normal and reversal ventilation, and insert eq.(8), (9) into eq. (16), (17)

$$\bar{K} = \frac{\sin\beta'[1 + \frac{\tau}{4}(dc_y / d\alpha)\cos\beta]}{\sin\beta[1 + \frac{\tau}{4}(dc_y / d\alpha)\cos\beta']} \tag{18}$$

$$J_0 = \frac{ctg\beta'}{ctg\beta} \tag{19}$$

From fig 2

$$\beta = \beta_r - \alpha_0 \ , \beta' = \beta_r + \alpha'_0$$

then inserting into eq.(18).(19)

thus

$$\bar{K} = \frac{\sin(\beta_r + \alpha'_0)[1 + \frac{\tau}{4}(dc_y / d\alpha)\cos(\beta_r - \alpha_0)]}{\sin(\beta_r - \alpha_0)[1 + \frac{\tau}{4}(dc_y / d\alpha)\cos(\beta_r + \alpha'_0)]} \geqslant 1 \tag{18a}$$

$$J_0 = \frac{ctg(\beta_r + \alpha'_0)}{ctg(\beta_r - \alpha_0)} \leqslant 1 \tag{19a}$$

From preceding two equations, it is found that J_0 less than 1 and $\bar{K}$ larger than 1 except $\beta' = \beta$ (i.e. $\alpha_0 = -\alpha'_0$). It follows that if the impeller of fan rotates in opposite direction, the maximum flow rate of fan would decrease and the slope of characterstic line of $\overline{P_t}$ would become steep.

Because the α_0, α'_0 are relative with geometrical parameters of blade cascade, such as airfoil deflection $\bar{f}$, blade solidity τ, installation angle of blade θ_r and blade thickness c. therefore J_0 and $\bar{K}$ must be the function of such parameters

$$J_0 = f(\bar{f}, \tau, \theta_r, c)$$

$$\bar{K} = f(\bar{f}, \tau, \theta_r, c) \tag{20}$$

From eq. (18a), (19a) if $\beta = \beta'$ (i.e $\alpha_0 + \alpha'_0 = 0$)

Third International Conference on Inverse Design Concepts and Optimization in Engineering Sciences (ICIDES-III), Editor: G.S. Dulikravich, Washington D.C., October 23-25, 1991.

then

$$J_0 = 1, \bar{K} = 1 \tag{21}$$

It means that the characteristics of fan during contrary rotation is the same as that during normal rotation, therefore the best effect of reversal ventilation is obtained.

It is clean that only following two condition can satisfy the eq.(21)

(1) $\alpha_0 = \alpha'_0 = 0$

It can be obtained that if the airfoil deflection $\bar{f} = 0$, such as the flat plate airfoil, ellipse airfoil, the characteristics of such airfoils are lower and not satisfactory for uc.

(2) $\alpha_0 = -\alpha'_0 (\alpha_0 \neq 0, \alpha'_0 \neq 0, \bar{f} \neq 0)$

It can be obtained when the zero lift line of cascade in reversal ventilation is parallel to that in normal ventilation, i.e. the airfoil must posses the reversal symmeterical npofile.

"S" SHAPED AIRFOIL WITH DOUBLE CIRCULAR ARC

On the basis of analysis in preceding section we present a new airfoil—"s" shaped airpoil with double circular arc as shown in fig.3. It is a reversal symmeterical airfoil satisfying the condition $\alpha_0 = -\alpha'_0$.The centre line of the airfoil posses the shape of "s", which is connected by two circular–arc lines $\overset{\frown}{ABC}$ and $\overset{\frown}{CDE}$ tangential to each other. At the middle points of two arcs (B.D) the deflection of centre line is maximum.

$|y_{max}| = F$

Where F is the half of the maximum thickness of airfoil.

The equations of centre line of airfoil may be written as

arc $\overset{\frown}{ABC}$ $\quad \left(x - \frac{b}{4}\right)^2 + (y + a)^2 = R^2 \qquad x \in (0, \frac{b}{2})$

arc $\overset{\frown}{CDE}$ $\quad \left(x - \frac{3b}{4}\right)^2 + (y - a)^2 = R^2 \qquad x \in (\frac{b}{2}, b)$ (22)

where $a = (b^2 / 32F) - \frac{F}{2}$ (23)

R(radius of circular arc) $= \frac{1}{2}\sqrt{\frac{b^2}{4} + \left(\frac{b^2}{16} - \frac{F}{2}\right)}$ (24)

The formation of airfoil profile

Along the centre line BCD a number of circles with radius $r = F$ are drawn whose centre points are at the arc BCD,then a number of another circles are drawn along the arcs $\overset{\frown}{AB}$ and $\overset{\frown}{DE}$,whose centre are at these arcs and whose radiuses are identifed with the perpendiculars from center points to abscissa line x. Drawing envolope line around such circles, the profile of the new airfoil is formed.

If the chord of the airfoil b is constant, taking different value of F , a number of "s" shaped airfoil with different deflection $\bar{f}$ would be obtained.

Third International Conference on Inverse Design Concepts and Optimization in Engineering Sciences (ICIDES-III), Editor: G.S. Dulikravich, Washington D.C., October 23-25, 1991.

EXPERIMENTAL RESULT

Four "s" shaped airfoils with different $\bar{f}$ are experimented in wind tunnel in aerodynamic laboratory of Jiaotong University in october 1987. Their symbols are CS-3($\bar{f}$ =3%), C-3.5($\bar{f}$-3.5%) CS-4($\bar{f}$=4%) and CS-7(f-7%).

The experimental results of these airfoilsare shown in Fig 4. From fig 4a) It is seen that with the increaring of attack angle α the lift coefficients c_y increase and reach the maximum value then decrease gradually. In the range $\alpha = 0^\circ \sim 13^\circ$, the c_y of airfoil CS-4 is the highest among others ($c_{ymax} = 0.87$) and the c_y of airfoil CS-7 is lower than that of others. From Fig 4 b) it is seen that the drag coefficent c_x of all four airfoils are increased from $\alpha = 0^\circ$ and the c_x of airfoil CS-7 is much higher than that of others. In the range of attack angle α from 0° to 10° the $c_x$of airfoil CS-4 is lower than that of others. It is followed that the acrodynamic characteristic of airfoil CS-4 is better than that of others. Furthermore when the deflection of airfoil is too big ($\bar{f}$>7%), the drag coefficient c_x of airfoil would increase sharply. The acrodynamic characteristic of airfoil CS-4 is compared with the conventional airfoil (NACA-64, NACA-66). From Fig 5 a), 6 a) it is shown, though the c_y of airfoil CS-4 is lower than that of NACA airfoil in normal ventilation, it is much higher than that in reversal ventilation, expecialy at bigger attack angle. From Fig 5 b), 6 b) it is seen, in the range $\alpha = 0 \sim 10^\circ$ the drag coefficient c_x of airfoil CS-4 is lower than that of NACA airfoil in normal ventilation, while $\alpha > 10^\circ$ it is higher than that of NACA airfoil, but in reversal ventilation condition the c_x of airfoil CS-4 is much lower than that of NACA airfoil in all range of attack angles in experiment.

In order to analyse the flow around the "s" shaped airfoil , the pressure discribution along the surface of airfoil CS-3 at $\alpha = 4^\circ$ is measured as shown in Fig 7. There are two areas bounded by pressure coefficient c_p line of airfoil. The area on the preceding half of airfoil ($x / b = 0 \sim 0.5$) is positive, which indecates that the lift force on the airfoil is upward; The area on the rear half of airfoil ($x / b = 0.5 \sim 1.0$) is negative, which indecates the lift force on the airfoil is downward. Since the preceding area is bigger than the rear area, so the summary lift force on the airfoil is upward. Varying the attack angle α, the two areas and the summary lift force would be changed.

In the Fig 7. $c_p = (P_i - P_0) / \frac{1}{2} \rho c_\infty^2$, where P_i is the pressure at the surface of airfoil. P_0 is the ambient pressure, c_∞ is the flow velocity in the wind tunnel.

Conclusion

1) If the impeller of axial fan with conventional airfoil rotates in reversal direction, the maximum theoretical flow rate would decrease, the characteristic line of P_t become steep, the

Third International Conference on Inverse Design Concepts and Optimization in Engineering Sciences (ICIDES-III), Editor: G.S. Dulikravich, Washington D.C., October 23-25, 1991.

characteristics of fan would be worse.

2) The characteristic of impeller in reversal ventilation is identical with that in normal ventilation, when the deflection of airfoil $\bar{f}=0$ or $\bar{f}\neq 0$ but the profile of airfoil is reversal symmeterical.

3) The "s" shaped airfoil presented in the paper is a reversal symmeterical airfoil. When the impeller whose blade is formed with such airfoil rotates in opposite direction, its characteristic would be the same as that in normal ventilation.

4) The synthetical characteristic of axial fan whose impeller blade is formed with "s" shaped airfoil would be better than that formed with conventional airfoil, especially in reversal ventilation condition, therefore the new airfoil presented in the paper is more available for reversible axial fan.

Reference

1. Radha krishna, H.C. Aswa Thanarayana, P.A. and Ramachandran, Rm. "Some Flow Studies on "s" Cambered Acrofoils" Proceeding of Conference on Fluid Machinery, 1979 Budapest.
2. Ravindram, M. and Radha Krishna, H.C. "Influence of Blade Profiles on the Performance of a Fully Reversible Axial Pump–turbine" Proceeding of Conference of Fluid Machinery, 1979 Budapest.
3. Ravindram, M. and Radha Krishna, H. C. "Characteristics of a Fully Reversible Axial Pump–turbine for Application in Tidal Power Plants" Paper presented at the Conference on Future Energy Concept, Orgaized by IEE, London, Jab–Fab 1979.
4. Longhua Li "Feasibility study of inverse ventilation in Chinese coal–mines by simple reversing the axial fan" The 2nd China–Japan Conference on Fluid Machinery, 1989 Xi'an China.

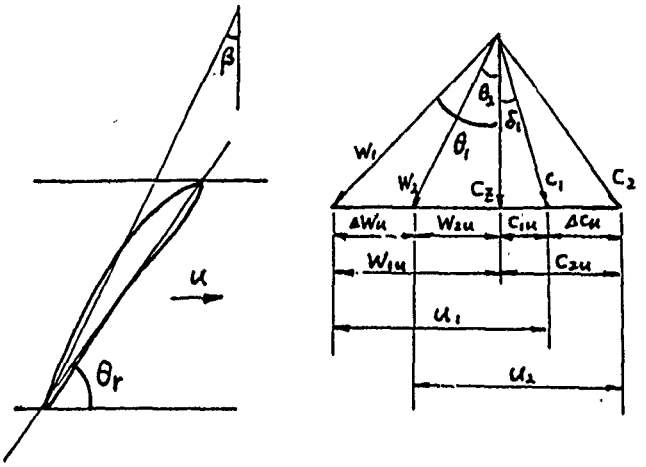


Fig.1. The velocity triangle of a blade cascade

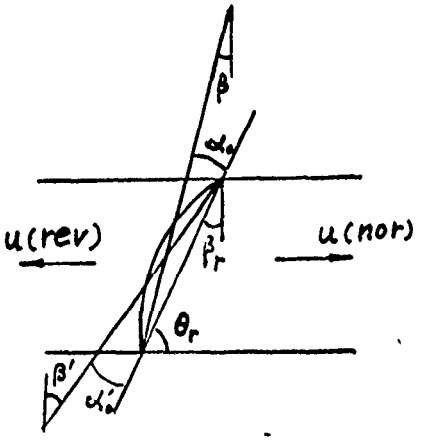


Fig.2. Normal and contrary flow around an airfoil

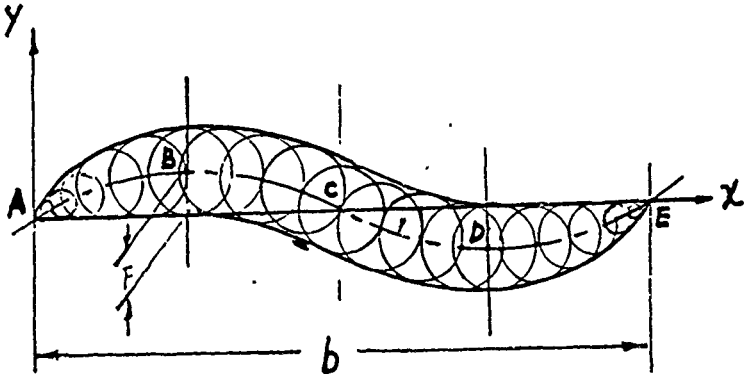


Fig.3. "S" shaped airfoil with double–circular arc

Third International Conference on Inverse Design Concepts and Optimization in Engineering Sciences (ICIDES-III), Editor: G.S. Dulikravich, Washington D.C., October 23-25, 1991.

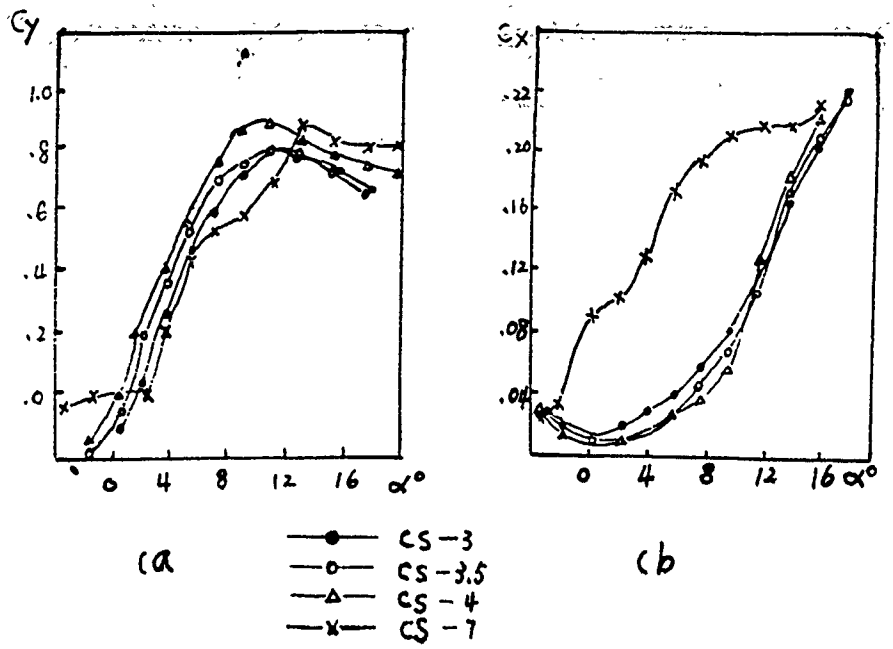


Fig.4. The experimental results of CS–4 airfoil series

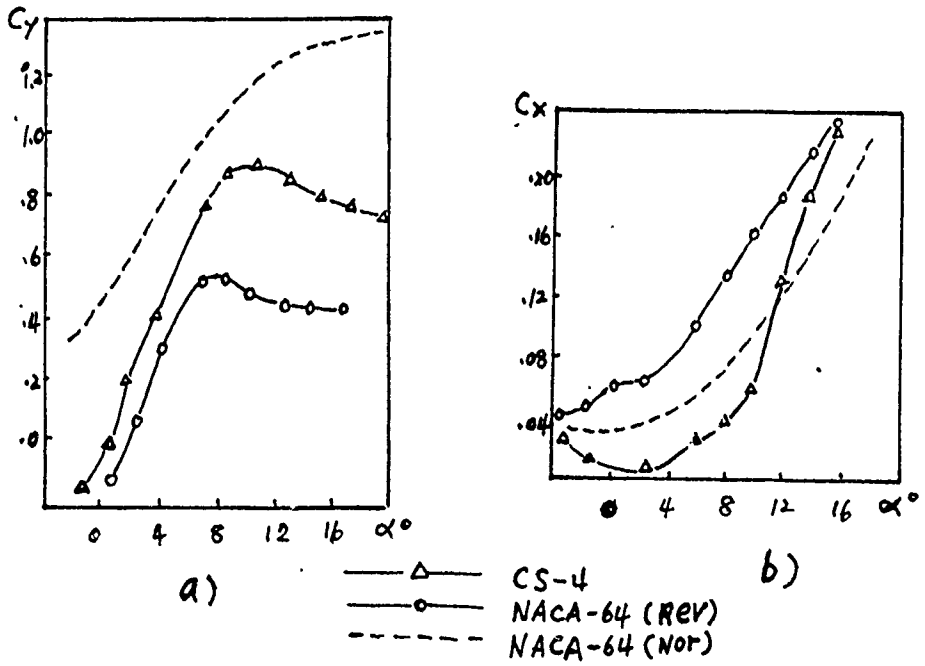


Fig.5. Comparision of airfoil CS–4 with conventional aisfoil NACA–64 in normal and reversal ventilation

Third International Conference on Inverse Design Concepts and Optimization in Engineering Sciences (ICIDES-III), Editor: G.S. Dulikravich, Washington D.C., October 23-25, 1991.

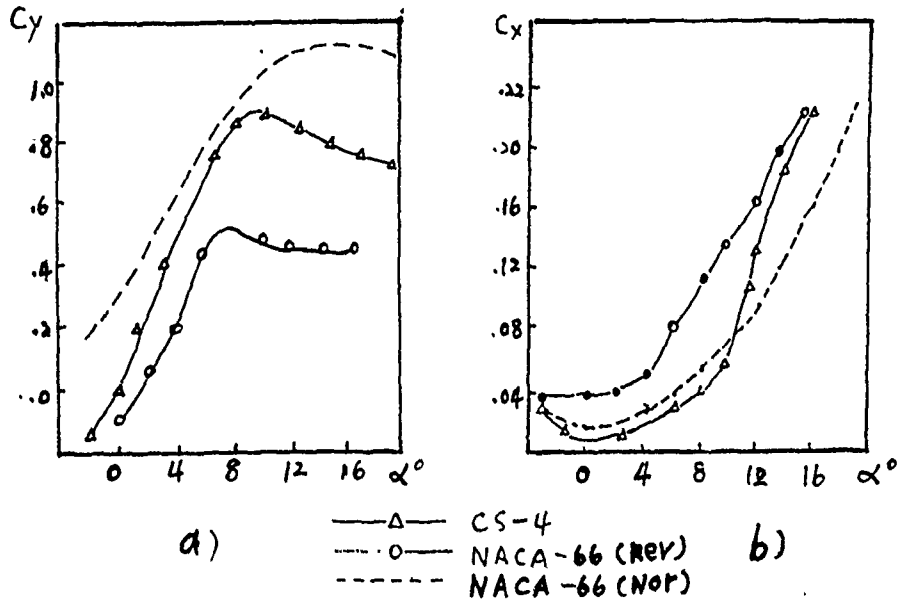


Fig.6. Aerodynamic characteristic comparision of CS–4 airfoil with airfoil NACA–66 in normal and reversal ventilation

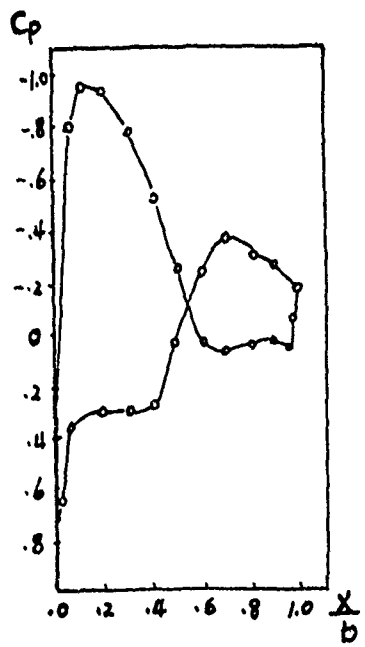


Fig.7. The pressure discribution along the surface of airfoil CS–3.

Third International Conference on Inverse Design Concepts and Optimization in Engineering Sciences (ICIDES-III). Editor: G.S. Dulikravich. Washington D.C., October 23-25, 1991.

INVERSE PROBLEMS IN DIFFRACTION

Andrew G.Mikheev and Aleksey S.Shamaev

Institute for Problems in Mechanics USSR Academy of Sciences
Pr. Vernadskogo 101. Moscow 117526, USSR.

ABSTRACT

A two-dimensional problem of diffraction of a plane electromagnetic wave on a smooth 2π-periodic surface is considered. Numerical algorithm, solving this problem is developed.

An inverse problem of determination of the shape of 2π-periodic surface using the performance data of reverse scattering is considered.

Inverse problem was solved by means of minimization of the residual functional with the help of gradient descent method. The initial data were calculated with the help of the numerical method. On each step of iterative method of minimization ,the residual functional was calculated approximately with the help of small slope method. The examples of the shape determination are considered.

INTRODUCTION

The new approximate methods, solving the problem of diffraction on a smooth two-dimensional infinite wave-like surface (for example [1],[2]) give us hope of solving the problem of the wavy shape determination using the performance data of reverse electromagnetic scattering.

The aim of this paper is to show the advance of the approximate method of small slope in connection with the inverse diffraction problem. For this purpose we consider only periodic surfaces because for such surfaces there may be developed numerical methods, solving the direct problem with the high accuracy, so the accuracy of the approximate method, solving the inverse problem, may be investigated.

In the first part of this paper the two-dimensional direct problem of diffraction of a plane electromagnetic wave on a smooth 2π-periodic surface is considered. the numerical method, solving the direct problem of diffraction is developed:
With the help of Green's function of Flocke canal the direct problem is reduced to the one-dimensional integral equation. The kernel of the integral equation contains logarithmic singularity, which is expressed in the explicit form. The well convergent series for calculating the kernel of the integral equation are developed. The integral equation is solved using the method of moments .

In the second part of this paper the small slope method is applied for the problem of diffraction on a periodic

Third International Conference on Inverse Design Concepts and Optimization in Engineering Sciences (ICIDES-III), Editor: G.S. Dulikravich, Washington D.C., October 23-25, 1991.

surface, the algorithm, solving the inverse problem, is developed, the examples of shape determination are presented:
The inverse problem of determination of the shape of 2π-periodic surface using the performance data of reverse scattering are considered. Inverse problem was solved by means of minimization of the residual functional with the help of gradient descent method. The initial data were calculated by means of multiple solving of the integral equation . On each step of iterative method of minimization ,the residual functional was calculated approximately with the help of small slope method. The formulas for approximate calculations of residual functional are presented.

1. Mathematical formulation of the direct problem.

The unknown function u satisfies the Helmholtz equation

$$\Delta u + k^2 \cdot u = 0 \qquad (1)$$

in the region $\Omega = \{ (x,y) \mid -\infty < x < f(y), \quad 0 \le y \le 2\pi \}$.
Here k is wave number, $k=\frac{\omega}{c}$, $f(y)$ is smooth 2π-periodic function.

The boundary condition for the function u is :

$$u(f(y),y) = 0 \qquad (2)$$

In the region $x < x_0 = \inf_{[0,2\pi]} f(y)$ the radiation condition

$$u = e^{ik(x\cdot\cos\alpha+y\cdot\sin\alpha)} + \sum_{n=-\infty}^{+\infty} T_n \cdot e^{-i\gamma_n x} e^{i\lambda_n y} \qquad (3)$$

is imposed on u . Here α is the angle between the wave vector of incident wave and x - axis, $\lambda_n = k\cdot\sin\alpha + n$, $\gamma_n=\sqrt{k^2 - \lambda_n^2}$, $\mathrm{Re}\ \gamma_n \ge 0$ $\mathrm{Im}\ \gamma_n \ge 0$. T_n are unknown amplitudes of scattered plane waves.

The function u is also assumed to satisfy the

Third International Conference on Inverse Design Concepts and Optimization in Engineering Sciences (ICIDES-III), Editor: G.S. Dulikravich, Washington D.C., October 23-25, 1991

Flocke conditions:

$$u(x,\ 2\pi) = u(x,\ 0)\cdot e^{it} \tag{4}$$

$$\frac{\partial u}{\partial y}(x,\ 2\pi) = \frac{\partial u}{\partial y}(x,\ 0)\cdot e^{it} \tag{5}$$

where $t = 2\pi k\cdot\sin\alpha$.

2. Mathematical formulation of the inverse problem.

Let us consider the set of direct problems (1) - (5) for resonance values of parameters k and α ($\alpha \in (-\frac{\pi}{2},0)\cup(0,\frac{\pi}{2})$,

$$k = = k(\alpha) = \frac{1}{2|\sin\alpha|} \ ). \tag{6}$$

Problem:

For the given function $T_{-sign\alpha} = T_{-sign\alpha}(\alpha)$ (T_n are determined in (3)) where $\alpha \in (-\frac{\pi}{2},0)\cup(0,\frac{\pi}{2})$ determine 2π-periodic function $f(y)$.

ANALYSIS

1. Numerical algorithm, solving the direct problem.

With the help of Green's function of Flocke canal

$$G(M,P) = \frac{i\pi}{2}\sum_{m=-\infty}^{+\infty} H_c^{(1)}\left(k\cdot\sqrt{\delta x^2 + (\delta y+2\pi m)^2} \right)\cdot e^{-imt} \tag{7}$$

(here $\delta x = x_M - x_P$, $\delta y = y_M - y_P$, $H_c^{(1)}(x)$ - is the Hankel function of the first kind of order 0) the problem is reduced to the one-dimensional integral equation for the $\frac{\partial u}{\partial n}(f(y),y)$:

$$-\frac{1}{2\pi}\cdot\int_{0}^{2\pi} G\left[f(y_M),y_M,f(y_p),y_p\right]\cdot I(y_p)\cdot\frac{\partial u}{\partial n}(f(y_p),y_p)dy_p =$$

$$= e^{ik(f(y_M)\cdot\cos\alpha+y_M\cdot\sin\alpha)} \qquad (8)$$

Here $I(y) = \sqrt{1+[f'(y)]^2}$.

The integral equation (8) was solved with the help of method-of-moments :

Let us divide the segment $[0,2\pi]$ into N equal length segments, using points y_i ($y_0=0$, $y_N=2\pi$). Consider functions :

$$\phi_i(y) = \begin{cases} 1, & y \in [\,y_{i-1},y_i\,] \\ 0, & y \notin [\,y_{i-1},y_i\,] \end{cases}$$

Let us seek an approximate solution of equation (8) in the following form :

$$\Psi^N(y) = \sum_{i=1}^{N} D_i^N\cdot\phi_i(y) \qquad (9)$$

where coefficients D_i^N are to be determine.

Function $\Psi^N(y)$ assume to satisfy equation (8) in points $y_{i-\frac{1}{2}} = \frac{1}{2}\cdot(y_{i-1}+y_i)$. It gives following equations for D_i^N coefficients determine :

$$\sum_{i=1}^{N} D_j^N\cdot\int_{y_{j-1}}^{y_j} G\left[f(y_{i-\frac{1}{2}}),y_{i-\frac{1}{2}},f(y_p),y_p\right]\cdot I(y_p)dy_p =$$

Third International Conference on Inverse Design Concepts and Optimization in Engineering Sciences (ICIDES-III). Editor: G.S. Dulikravich, Washington D.C., October 23-25, 1991.

$$= \exp\left[i\tilde{R}\left(f(y_{i-\frac{1}{2}})\cdot\cos\alpha + y_{i-\frac{1}{2}}\cdot\sin\alpha\right)\right] \qquad (10)$$

The expression (11) gives the well convergent series, which gives us the method for calculating the kernel of the integral equation (8).

$$G(M,P) = \frac{i\cdot e^{i\lambda_o\delta y}\cdot e^{i\gamma_o|\delta x|}}{2\gamma_o} +$$

$$+ \sum_{n=1}^{\infty}\left[e^{i\frac{t}{b}\delta y}\cdot\left(ch(\tfrac{t}{b}|\delta x|)\cdot\Phi_1(n,\delta x,\delta y) - \right.\right.$$

$$\left.\left. - i\cdot sh(\tfrac{t}{b}|\delta x|)\cdot\Phi_2(n,\delta x,\delta y)\right) + R(n,\delta x,\delta y)\right] \qquad (11)$$

Here $M = (x_M, y_M)$, $P = (x_P, y_P)$, $b=2\pi$,

$$\Phi_1(n,\delta x,\delta y) = \frac{\cos(n\delta y)}{n}\cdot e^{-n|\delta x|} \qquad (12)$$

$$\Phi_2(n,\delta x,\delta y) = \frac{\sin(n\delta y)}{n}\cdot e^{-n|\delta x|} \qquad (13)$$

$$R(n,\delta x,\delta y) = \frac{i}{2}\cdot\left(\frac{e^{i\lambda_n\delta y}\cdot e^{i\gamma_n|\delta x|}}{\gamma_n} + \frac{e^{i\lambda_{-n}\delta y}\cdot e^{i\gamma_{-n}|\delta x|}}{\gamma_{-n}}\right) -$$

$$- \frac{e^{i\frac{t}{b}\delta y}\cdot e^{-n|\delta x|}}{n}\cdot\left(ch(\tfrac{t}{b}|\delta x|)\cdot\cos(n\delta y) - \right.$$

$$\left. i\cdot sh(\tfrac{t}{b}|\delta x|)\cdot\sin(n\delta y)\right) \qquad (14)$$

R satisfy the expression (15)

Third International Conference on Inverse Design Concepts and Optimization in Engineering Sciences (ICIDES-III), Editor: G.S. Dulikravich, Washington D.C., October 23-25, 1991.

$$| R(n,\delta x,\delta y) | < \frac{C}{n^2} \qquad (15)$$

Rows (12), (13) can be summed:

$$\sum_{n=1}^{\infty} \Phi_1(n,\delta x,\delta y) = -\ln 2 + \frac{|\delta x|}{2} - \frac{1}{2}\cdot \ln\left[\mathrm{sh}^2\left(\frac{\delta x}{2} \right) + \right.$$

$$\left. + \sin^2\left(\frac{\delta y}{2} \right) \right] \qquad (16)$$

$$\sum_{n=1}^{\infty} \Phi_2(n,\delta x,\delta y) = \mathrm{arctg}\left[\frac{\sin(\delta y)}{e^{|\delta x|} - \cos(\delta y)} \right] \qquad (17)$$

The kernel of the integral equation contains logarithmic singularity, which is expressed in the explicit form in (16).

2. Approximate method, solving direct problem

The well known small perturbation method gives following formulas for amplitudes T_n :

$$T_n^{S.P.} = A\cdot\delta_{on} + B_n f_n + \sum_m C_{mn}\cdot f_m\, f_{n-m} \qquad (18)$$

Here $f_n = \frac{1}{2\pi}\int_0^{2\pi} e^{-iny} f(y)\, dy$, $\delta_{on} = \begin{cases} 1 & n = 0 \\ 0 & n \neq 0 \end{cases}$

$$A = -1, \quad B_n = -2i\gamma_o, \quad C_{mn} = 2\gamma_o\gamma_m,$$

The small slope method solving the problem of diffraction on a smooth two-dimensional infinite wave-like surface was presented in [1]. In the case of periodic surface amplitudes T_n were sought in the following form:

$$T_n^{S.S.} = \frac{1}{2\pi}\int_0^{2\pi} e^{-iny}\, e^{i(\gamma_o+\gamma_n)f(y)} .$$

$$\cdot (a_n + \sum_m b_{mn} \cdot f_m \cdot e^{imy}) dy \qquad (19)$$

where a_n, b_{mn} were constants to be determined. Let the values $T_n^{S.S.}$ satisfy the following conditions:

a) $$|T_n^{S.S.} - T_n^{S.P.}| < \text{const} \cdot \varepsilon^3 \ , \ \varepsilon \to 0 \qquad (20)$$

where $\varepsilon = \max_{0 \le y \le 2\pi} |f(y)|$

b) Shift surface along x - axis condition:

$$T_n^{S.S.}[f(y)+x_o] = e^{i(\gamma_o+\gamma_n)x_o} \cdot T_n^{S.S.}[f(y)] \qquad (21)$$

c) shift surface along y - axis condition:

$$T_n^{S.S.}[f(y+y_o)] = e^{iny_o} \cdot T_n^{S.S.}[f(y)] \qquad (22)$$

Condition (20) will be valid for (18) if

$$a_o = A \qquad (23)$$

$$i(\gamma_o + \gamma_n) \cdot a_n + b_{nn} = B_n \qquad (24)$$

$$Q_{mn} = - Q_{n-m,n} \qquad (25)$$

where $Q_{mn} = C_{mn} -$

$$- \frac{\gamma_o + \gamma_n}{2} (2i \cdot b_{mn} - (\gamma_0 + \gamma_n) \cdot a_n), \text{ and the}$$

conditions (12) and (13) will in turn be satisfied if

$$b_{on} \equiv 0 \qquad (26)$$

In the article [1] the following expressions were proposed,

Third International Conference on Inverse Design Concepts and Optimization in Engineering Sciences (ICIDES-III). Editor: G.S. Dulikravich. Washington D.C., October 23-25, 1991.

which satisfy (23) ÷ (26):

$$a_n = \frac{1}{(\gamma_n+\gamma_o)^2}\left(C_{on} + C_{nn} - 2i(\gamma_n + \gamma_o)B_n\right)$$

$$b_{mn} = \frac{-i}{2(\gamma_n+\gamma_o)}\left(C_{n-m,n} + C_{mn} + C_{nn} + C_{on}\right) - B_n$$

3. Algorithm, solving the inverse problem.

Let

$$\vec{d} = (d_1, \cdots, d_M, \cdots, d_{2M+1})$$

Consider the set of surfaces, which are determined with the help of functions:

$$f(y) = \sum_{n=1}^{m} d_n \cdot \sin ny + d_{M+1} + \sum_{n=1}^{m} d_{n+M+1} \cdot \cos ny$$

Let us suppose that we know values of the inverse scattering function for surface, corresponding to vector $\vec{d}^{\,o}$:

$$T_1^o = T(\alpha_1), \quad T_2^o = T(\alpha_2), \quad \cdots$$

$$\cdots, \quad T_N^o = T(\alpha_N)$$

for angles $\alpha_1, \alpha_2, \cdots, \alpha_N$.

The numerical algorithm for vector $\vec{d}^{\,o}$ reconstruction on values $T_i^o, \cdots T_N^o$ was constructed. This algorithm is based on minimization of the residual functional with the help of gradient descent method. Direct problem on each iteration step is solved with the help of small slope approximate method. On each step of iterative method of minimization ,the residual functional was calculated approximately with the help of small slope method.

Residual functional is determined by following expression:

Third International Conference on Inverse Design Concepts and Optimization in Engineering Sciences (ICIDES-III). Editor: G.S. Dulikravich. Washington D.C., October 23-25, 1991.

$$\Phi(\vec{\alpha},\vec{d}) = \sum_{m=1}^{N} \left| T_m^o - R(\alpha_m,\vec{d}) \right|^2 \qquad (27)$$

Here $\vec{\alpha} = (\alpha_1, \cdots \alpha_N)$,

$R(\vec{\alpha},\vec{d})$ is the inverse scattering functional, corresponding to small slope method:

$$R(\vec{\alpha},\vec{d}) = \sum_m \frac{1}{2\pi} \cdot \left[-\delta_{om} + i f_m \cdot \left(\frac{|ctg\ \alpha|}{2} - \gamma_m \right) \right] \cdot$$

$$\cdot \int_0^{2\pi} e^{i(m+sign\alpha)y} \cdot e^{i|ctg\alpha| f(y)} dy$$

$$f_m = \frac{1}{2\pi} \cdot \int_0^{2\pi} f(y) \cdot e^{-imy}\, dy \quad ,$$

Coefficients T_m^o were calculated with the help of numerical method (7) - (17).

RESULTS

Consider the example of solving the direct problem with the help of IBM PC AT 386-387 computer. The values of parameters are : $k = 1.4$, $\alpha = 30^o$, $f(y) = 0.3 \cdot \sin y$; in numerical algorithm $N = 50$.

	Numerical algorithm	Small slope method
energy error	$0.3 \cdot 10^{-4}$	$0.16 \cdot 10^{-2}$
CPU time	3 min 54 sec	1 sec
T_{-2}	-0.072	-0.073
T_{-1}	0.349 - 0.010i	0.347 - 0.005i
T_o	-0.926 + 0.052i	-0.926 + 0.049i

Third International Conference on Inverse Design Concepts and Optimization in Engineering Sciences (ICIDES-III), Editor: G.S. Dulikravich, Washington D.C., October 23-25, 1991.

Consider examples of Furie coefficients reconstruction of surface determine function:

First simulation was carried out for N=10 , M=1 , $\vec{d}^{o}$ = (0, -0.3, 0.51) . After 7 iterations vector $\vec{d}^{*}$: (0.000, -0.300 , 0.503) was obtained as the minimum of the functional (27).

Second simulation was carried out for N=6 , M=2 , $\vec{d}^{o}$ = (0, 0, -0.1, 0.2 0.2) . After 44 iterations vector $\vec{d}^{*}$: (0.000, 0.000, -0.092, 0.195, 0.190) was obtained as the minimum of the functional (27).

REFERENCES

1. A.G.VORONOVICH, Small slope approximation in the theory of scattering of waves at rough surfaces, Journal experim. and theor. Phys., V. 89(1985), issue 1(7), pp. 116-125(In Russian.)

2. Ishimary A., Winebrenner D. Investigation of a surface field phase perturbation technique for scattering from rough surfaces.//Radio science -1985.- V. 20. -N. 2. pp. 161 - 170.

Third International Conference on Inverse Design Concepts and Optimization in Engineering Sciences (ICIDES-III), Editor: G.S. Dulikravich, Washington D.C., October 23-25, 1991.

OPTIMIZATION OF TRANSISTOR DESIGN INCLUDING LARGE SIGNAL DEVICE/CIRCUIT INTERACTIONS AT EXTREMELY HIGH FREQUENCIES (20-100$^+$ GHz)

Ralph Levy and H. L. Grubin
Scientific Research Associates, Inc.
50 Nye Road, P. O. Box 1058
Glastonbury, CT 06033

ABSTRACT

Transistor design for extremely high frequency applications requires consideration of the interaction between the device and the circuit to which it is connected. Traditional analytical transistor models are too approximate at some of these frequencies and may not account for variations of dopants and semiconductor materials (especially some of the newer materials) within the device. Physically based models of device performance are required. These are based on coupled systems of partial differential equations and typically require 20 minutes of Cray computer time for a single AC operating point. A technique is presented to extract parameters from a few partial differential equation solutions for the device to create a nonlinear equivalent circuit model which runs in approximately 1 second of personal computer time. This nonlinear equivalent circuit model accurately replicates the contact current properties of the device as computed by the partial differential solver on which it is based. Using the nonlinear equivalent circuit model of the device, optimization of system design can be performed based on device/circuit interactions.

INTRODUCTION

The evaluation of the potential performance of semiconductor devices for analog applications is usually performed in two ways. First, the device may be characterized through small signal admittance or scattering parameters which may be obtained by experiment for existing devices or by numerical simulation for a new device structure prior to fabrication. From these results, the devices can be characterized in terms of small signal parameters such as the unity gain cutoff frequency, f_t, and f_{max}. While these parameters provide a valid estimation of the limits of the device operation under linear, small signal conditions, such estimate will typically be in error under large signal conditions. Under large signal, high power conditions, nonlinear effects within the device become important. At low frequency, the nonlinear effects manifest themselves primarily as bias dependent parameters such as bias dependent transconductance and capacitance. At high frequency these parameters will also exhibit hysteresis effects due to the nonequilibrium nature of transport within the device.

As a result of these nonlinearities it is imperative that the performance of the device be evaluated while embedded in its operational circuit. It is the device-circuit interaction and resulting performance that is of interest and not simply the device characterization. Since it is obviously too costly and time consuming to design, fabricate and test a new device and then design, test, and redesign a circuit around the device in hope of achieving the desired performance, an alternative must be found. This alternative is numerical modeling. Funda-

Third International Conference on Inverse Design Concepts and Optimization in Engineering Sciences (ICIDES-III), Editor: G.S. Dulikravich, Washington D.C., October 23-25, 1991.

mentally, device-circuit interaction can be modeled using, equations to represent the device and coupling the external circuit to it through boundary conditions. While this has been and will continue to be done, it is presently too costly, even on the supercomputers available today, for all but the simplest of circuits. As a result, devices are approximated by nonlinear equivalent circuit elements in the large circuit simulation procedures. The adequacy of these equivalent circuit models has a direct impact on the predicted results.

In an effort to improve these device models Madjar and Rosenbaum [1] and Khatibzadeh and Trew [2] have developed procedures in which the FET is modeled by a system of nonlinear ordinary differential equations relating the gate and drain currents to the time dependent gate and drain voltages. The coefficients of these ODE's are determined **analytically**, using highly approximate models of the device. The present work is a significant generalization of the approach of [1] and [2]. Here the coefficients of the ODE's representing the device are determined **numerically**, through a physically based model; in this case the drift and diffusion equations and the moments of the Boltzmann transport equation. The resulting ODE representation is then executed, and the validity of the results are verified at select operating points. With such an agreement established, the equivalent circuit model can then be used with a higher degree of confidence in a complex circuit simulation and device/circuit optimization.

This study is based on three concepts. First the entire program is based on large signal concepts. Most large signal predictions of device performance are based upon small signal concepts; the assumption being that a 'good' small signal device is also a 'good' large signal device. Thus quantities such as the cutoff frequency, f_{max}, etc., have been used to assess device performance. However, this is not appropriate since the power requirements for MIMIC applications preclude small signal operation. MIMIC devices will be operated under large signal conditions, and large signal assessment of device performance is required.

Second, the computational device physics model is based on the drift and diffusion equations (DDE) for the 20-40 GHz range and on the nonequilibrium balance equations obtained from the first three moments of the Boltzmann transport equations (MBTE) for the 40-100$^+$ GHz range. The MBTE equations include the effects of carrier acceleration and velocity overshoot that are increasingly important as the frequency of interest increases and feature size decreases. Both analyses include the effects of processing parameters on device performance.

Third CAD compatibility was achieved by linking the DDE and MBTE analyses to nonlinear equivalent circuit analysis developed under a study sponsored by the National Science Foundation [3]. The nonlinear equivalent circuit model based on DDE or MBTE computed characteristics permitted very rapid (less than 1 second of Cray computer time) calculations of large signal AC performance of a device that accurately reproduced the more costly full calculations.

Coupling the nonlinear equivalent circuit model with the DDE and MBTE permits, for the first time a capability of performing fast and accurate calculations that describe device/circuit interactions. The nonlinear equivalent circuit model is compatible with commercially available CAD software and would run on a workstation. The nonlinear

Third International Conference on Inverse Design Concepts and Optimization in Engineering Sciences (ICIDES-III), Editor: G.S. Dulikravich, Washington D.C., October 23-25, 1991.

equivalent circuit model has been coupled to a numerical optimization program and used to determine realistic goals for device/circuit performance.

Physical Modeling

The key element of the simulation is the system of partial differential equations used to describe the transient transport of electrons and holes in the devices. Drift and diffusion equations (DDE) are commonly used to describe transport in unipolar and bipolar devices. While these equations are valid at the low end of the frequency scale, they are incorrectly applied at higher frequency scales, typically those in the range of 40^+ GHz or when structural feature sizes are reduced. For GaAs based devices this is in the sub-2500 Å region. When DDE procedures are inadequate the procedures of choice involve either the moments of the Boltzmann transport equation (MBTE), or Monte Carlo (MC) methods. Both MBTE and MC procedures are computationally more intensive that DDE simulations. Unfortunately, Monte Carlo algorithms require the most intensive computational resources, and are not presently practical for a CAD environment.

A brief description is now presented of the DDE and MBTE analyses and how SRA's nonlinear equivalent circuit analysis is based on the results of the MBTE calculations.

Semiconductor Drift and Diffusion Equations

The governing drift and diffusion equations are the continuity equations for electrons and holes and Poisson's equation:

$$\frac{\partial N}{\partial t} = \nabla \cdot \left[-N\mu_n \nabla(\psi+\psi_n) + D_n \nabla N \right] + G - R \qquad (1)$$

$$\frac{\partial P}{\partial t} = \nabla \cdot \left[P\mu_p \nabla(\psi+\psi_p) + D_p \nabla P \right] + G - R \qquad (2)$$

$$\nabla \cdot \epsilon \nabla \psi = e(N - N_D - P + N_A) \qquad (3)$$

where N and P are the electron and hole concentrations, respectively, and e is the electron charge. The quantity within the square brackets represents the electron and hole currents densities, $-J_n/e$ and J_p/e, respectively, G represents generation, R recombination, ψ is the potential, ϵ the permittivity, and N_D and N_A are the concentrations of donors and acceptor ions, respectively. The terms ψ_n and ψ_p are introduced to account for variations in the conduction and valence band energy levels. Through ψ_n and ψ_p such effects as band gap narrowing and heterojunctions may be accounted for.

Within the context of equations (1) through (3) materials such as gallium arsenide are represented by field dependent mobilities with a region of negative differential conductivity (NDC). While NDC is included in the subject analysis we point out that it is a feature never included in the analytical representations of nonlinear devices.

Moments of the Boltzmann Transport Equations

It is now commonly accepted that the major inadequacy of the drift and diffusion equations is the use of equilibrium field dependent velocity relationships. Its usage is a statement that acceleration is to be ignored. The MBTE overcomes this inadequacy.

The nonequilibrium MBTE are obtained by taking the moments of the Boltzmann transport equation with respect to carrier density, momentum and energy. This yields a set of governing equations which are similar in form to the equations utilized for multi-phase flow in fluid dynamics. The governing equations reflect the conservation, or balance laws of carrier density, carrier momentum and carrier energy and are written down for two species of electrons namely, the central (small effective mass) and satellite (large effective mass) valley carriers and one type of hole. Incorporation of holes is both for breakdown consideration as well as for the possibility of buried 'p' layers in the design of FETS. The balance equations follow.

Carrier Balance (or equations of continuity):

$$\partial n_1/\partial t = -\nabla\cdot(n_1 V_1) - n_1\Gamma_1 + n_2\Gamma_2 - R \tag{4}$$

$$\partial n_2/\partial t = -\nabla\cdot(n_2 V_2) + n_1\Gamma_1 - n_2\Gamma_2 \tag{5}$$

$$\partial n_3/\partial t = -\nabla\cdot(n_3 V_3) - R \tag{6}$$

where n_1 and n_2 are the central valley and satellite valley carrier number densities respectively while $\mathbf{V}_1$ and $\mathbf{V}_2$ are the corresponding velocities. Γ_1 and Γ_2 are the corresponding scattering rates for particle conservation. Γ_1 represents scattering of carriers from the Γ valley to the L valley in GaAs. Γ_2 is the return rate. R represents the net recombination of electrons and holes, assumed to occur only through the Γ valley electrons. n_3 and $\mathbf{V}_3$ are the number density and velocity of holes.

Momentum Balance (Newton's Law) for the Central Valley:

$$\partial(n_1\mathbf{P}_1)/\partial t + \nabla\cdot(n_1\mathbf{V}_1\mathbf{P}_1) + n_1\mathbf{P}_1\Gamma_3 = -n_1 e\mathbf{F}_n - \nabla\wp_1 - \nabla\cdot\sigma_1 + n_1[\mathbf{V}_1\cdot\mathbf{V}_1/2 + T_1/m_1]\nabla m_1 \tag{7}$$

where there is a force contribution due to spatial variations in the effective mass. In the above the momentum, $\mathbf{P}_1$, and the field, $\mathbf{F}_n$, are defined by

$$\mathbf{P}_1 \equiv m_1\mathbf{V}_1 \tag{8}$$

$$\mathbf{F}_n = -(\nabla\psi + \nabla\chi/e) \tag{9}$$

m_1 is the mass of the central valley carrier, e is the electronic charge, ψ is the electric potential and χ is the electron affinity. $\mathbf{F}$ is the field due to potential differences and conduction band discontinuity arising from material variations. The partial pressure, $\wp_1$, is

related to the central valley carrier temperature, T_1, and number density by the perfect gas relationship, which results from the assumption of Boltzmann statistics,

$$p = n_1 k T_1 \tag{10}$$

where k is Boltzmann's constant. Γ_3 is the scattering rate for the central valley carrier momentum. Contributions to Γ_3 include impurity, acoustic phonon, polar phonon, nonpolar intervalley scattering. The effects of electron-hole scattering is accounted for through an enhancement of the impurity scattering. The term $\nabla:\sigma_1$ represents the stress forces. In this study, the stress tensor, σ_1, is approximated by the relationship

$$\sigma_1 = \eta_1 \nabla V_1 \tag{11}$$

where η_1 is the viscosity associated with the central valley carriers. Similar momentum conservation equations can be written for the satellite valley and for holes.

Energy Balance for the Central Valley Carriers:

There are various forms in which the central and satellite valley carrier energy equations can be described. We choose to cast the energy equations in terms of the central and satellite valley temperatures, T_1 and T_2.

$$\begin{aligned} &\partial(n_1 T_1)/\partial t + \nabla\cdot(n_1 V_1 T_1) + (n_1 T_1 \Gamma_5 - n_2 T_2 \Gamma_6) = \\ &\quad -2/3[n_1 T_1 \nabla\cdot V_1 + \sigma_1:\nabla V_1/k - \nabla\cdot(\kappa \nabla T_1)/k] \\ &+ 3V_1\cdot V_1 m_1[n_1(2\Gamma_3 - \Gamma_1) + n_2\Gamma_2] - n_1 V_1 T_1/m_1\cdot\nabla_{m1} \end{aligned} \tag{12}$$

In equation (12) Γ_5 denotes energy relaxation within the central valley **plus** energy exchange with the satellite valley; Γ_6 denotes energy exchange between the satellite and central valley. All energy exchange between electrons and holes is ignored. A similar energy conservation equations can be written for the satellite valley electrons and for holes. In the energy balance equation for electrons and holes equations the contribution of the recombination have not been included.

The potential is related to the total number density through Poisson's equation

$$\nabla\cdot\epsilon\nabla\psi = e[(n_1 + n_2 - n_0) - (n_3 - p_0)] \tag{13}$$

where n_0 is the donor density, p_0 is the acceptor density and ϵ is the permitivity.

In two dimensions, the complete problem description requires 13 equations consisting of 3 continuity equations, 6 momentum equations, 3 energy equations and a Poisson's equation. The boundary conditions for potential are the same as used for the drift and diffusion equations. At ohmic contacts, the boundary condition is given by the sum of the applied bias and an appropriate built-in potential. The temperature of all carriers are assumed to be at 300K at the ohmic contacts. The carrier densities at the contacts are fixed at the value of local doping. For velocities, the normal gradient is taken to be zero.

Consideration of the External Circuit

Typically, in device simulations the voltage at the contacts are either fixed at a constant value or a time dependence is specified. When an external circuit is introduced, the voltage on the contact is determined by solving the device equations along with the circuit equation. The external circuit thus represents a boundary condition as far as the device simulation is concerned.

Transition of the Device/Circuit Results to Systems and Circuit Engineers.

The present study was predicated in two facts: (1) While the ideal way to transition the technology of device physics and device-circuit interactions is to deliver to the systems engineer a time dependent code that incorporates all of the partial differential equations describing the device, and the ordinary differential equations describing the circuit, the long run times generally associated with solving both the DDE and MBTE algorithms, rendered this approach impractical for engineers. (2) The approach favored by engineers to allow practical device-circuit interfacing is to obtain analytical representations of the dc current voltage characteristics of a given three terminal device, as well as analytical approximations for the relevant capacitances of the device, and then lump these parameters into a large signal simulator that solves the following set of coupled ordinary differential equations [3]:

$$I_g(t) = I_{g_o}[V_g(t),V_d(t-t_1)] + C_{gg}\, dV_g(t-t_2)/dt + C_{dg}\, dV_d(t)/dt \qquad (14)$$

$$I_d(t) = I_{do}[V_g(t-t_0),V_d(t)] + C_{gd}\, dV_g(t)/dt + C_{dd}\, dV_d(t-t_2)/dt \qquad (15)$$

In the above the terms t_0, t_1, t_2, represent time delays associate with transit of carriers between the gate and drain, drain and gate, and source and gate, respectively. The capacitive contributions are functions of the gate and drain voltage, with the time delays appropriate to the equation in which they appear. Equations of the type represented by equations (14) and (15), which are "SPICE"-like equations, are then typically coupled to harmonic balance programs.

Application of standard numerical optimization techniques with two-dimensional systems of partial differential equations (DDE or MBTE) is conceptually straightforward. However, implementation requires large computer resources, making it of limited interest to device designers at this time. Use of the equivalent circuit analysis, equations (14) and (15), results in very fast calculations that could be performed rapidly on a personal computer. The issue then becomes the accuracy of the equivalent circuit model. Other researchers [1] and [2] determine the coefficients and time delays from analytical considerations. This is a useful approach for device designs and materials in operating regimes that are well understood. The intent of the present work is to extend the utility of the equivalent circuit model to materials, designs and operating conditions that are not well understood. To achieve this goal the coefficients and time delays for equations (14) and (15) are derived from solution of two-dimensional systems of partial differential equations. This procedure obviates the need to make approximations that permit analytical expressions to be written for the coefficients and time delays in (14) and (15). It also permits extension of the analysis to other device designs and complex doping distributions.

The procedures for obtaining the terms relevant to equations (14) and (15);

$$C_{gg}, C_{dg}, C_{gd}, C_{dd}, t_0, t_1, t_2$$

involves five broad steps. These are identified below.

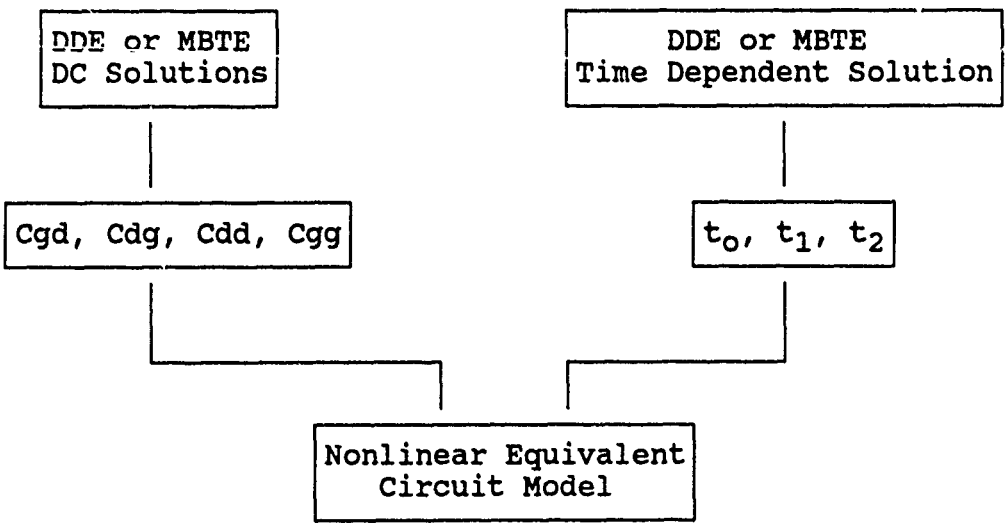
(1) From the DDE or MBTE algorithm the dc characteristics of the device are obtained.

(2) Perturbations of the dc characteristics are obtained as a function of gate and drain voltage. Small changes in the net charge on the drain and gate contacts are computed as a function of changes in gate voltage on the gate contact; leading to values for C_{gg} and C_{gd}. A similar procedure yields involving changes in drain voltage lead to values of C_{gd} and C_{dd}.

(3) Time dependent calculations demonstrate that there are transit time delays associated with the imposition of a signal on the gate contact and its observation on the drain contact. Similarly a change in voltage on the drain contact will have its effect on the gate contact delayed. Time dependent DDE or MBTE calculations are performed and the time delays associated with this are represented by the terms t_0 and t_1. Time delay associated with the source-gate loop is represented by t_2.

(4) The above parameters are incorporated onto the ODE solvers of equations (14) and (15).

A flow chart describing the above is shown below.



The advantage of the ODE solver over that which incorporates solutions to the partial differential equations is **engineering time**. A system of ODE solvers that can be used to replicate the output of the two-dimensional physically based models could be effectively used by circuit engineers to represent the device in circuit codes. It is worthwhile noting

that alternative formulations for fast calculations can be considered; e.g., quasi two-dimensional analysis of Snowden and Pantoja [4]. To use such an analysis, the predictions would be calibrated against an MBTE solution for the operating conditions of interest.

RESULTS

The above equivalent circuit model was compared to the drift and diffusion calculation of the FET of figure 1 in AC operation at 20, 40 and 60 GHz with a resistive load on the drain. Lissajous of these calculations are presented in figures 2 and 3. Comparisons of three power gain calculations at the same frequencies are shown in table 1. The lissajous, after the initial transient, and the AC power calculations are well represented by the equivalent circuit analysis.

Large Signal Circuit Dependent Results at 94 GHz

Large signal circuit dependent operation at 94 GHz was studied by connecting a 0.25 micron gate FET to a resistive load as shown in Figure 4. The drain battery voltage was set at 3 volts. Since the computed current levels in the device were dependent on the analysis used, the resistor was sized to have a one volt drop under DC conditions for a gate width of 300 microns. A sinusoidal voltage was applied to the gate at an amplitude of 0.5 volts and a frequency of 94 GHz. The gate and drain voltages and currents are presented in figure 8 as a function of time. The computed contact currents become periodic in time (steady AC) in less than one cycle and show sinusoidal periodic behavior at all contacts. Nonlinear effects which manifest themselves in gain compression, were not apparent at this gate bias level.

Nonlinear Equivalent Circuit Analysis at 94 GHz

The nonlinear equivalent circuit analysis of the recessed gate FET was implemented based on the MBTE calculations. Curve fits were obtained for I_d (Vg, Vd) and for the capacitive coefficients in equations 14 and 15. Figure 5 and 6 show the equivalent circuit results in the same form as the MBTE calculations. The lissajous are seen to have the same shape and similar harmonic content. It should be noted that while the MBTE calculation required twenty-five minutes of Cray Supercomputer time the Nonlinear Equivalent Circuit Analysis required less than one second of time on a personal computer.

Load Pull Calculations at 94 GHz

To demonstrate the ability to perform load pull simulations, such a calculation was performed by applying a sinusoidal signal at the gate with a magnitude of 0.5 volts. A sinusoidal voltage was applied to the drain with a magnitude of 0.6 volts and a phase lag of 200° behind the gate signal. This calculation was performed using the DDE, MBTE and the SRANEC analysis based upon the MBTE parameters. Figure 7 shows the Vg-Vd lissajous figure for these three calculations. Figure 8 compares the computed output for the load pull for each analysis. Note again the significant differences between the DDE and the MBTE calculations.

To demonstrate the utility of the equivalent circuit model an optimization program was mated to the **equivalent** circuit model. The optimization program drove the gate and drain voltages sinusoidally with an imposed phase delay:

$$V_g = V_g^o + \Delta V_g \sin(\omega t) \qquad (16a)$$

$$V_d = V_d^o + \Delta V_d \sin(\omega t - \phi) \qquad (16b)$$

The following optimization problem was posed: For fixed V_g^o = -2 volts, V_d^o = 4 volts and ΔV_d = 1 volt what values of ΔV_g and ϕ will provide a power gain of 8 db at an input power of 10^{-2} watts. ΔV_g was constrained to be in the range $0 \le \Delta V_g \le 1.5$ volts. This problem was solved at a series of frequencies from 10 GHz to 50 GHz using a Quasi-Newton optimization procedure with BFGS updating. For frequencies from 10 to 20 GHz the desired power gain of 8 db was achieved. Above 20 GHz the power gain decreased as a function of frequency as shown in figure 9. Solution of the above problem at each frequency required 30 to 90 AC device calculations. This would be unreasonably time consuming and expensive for a drift and diffusion analysis even on modern supercomputers. Using the equivalent circuit model each optimization requiring 30-90 AC steady state device calculations took approximately 1 minute of time on an IBM PC.

CONCLUSIONS

Using physically based research algorithms a nonlinear equivalent circuit analysis of a transistor operating at extremely high frequencies (20-100+ GHz) can be generated. The nonlinear equivalent circuit model reproduces transistor contact current in less than one second of computer time that required approximately 20 minutes of Cray supercomputer time suing the full physically based models. With this accuracy and concurrent run time advantage, tranditional optimizatiton techniques can be brought to bear on the device/circuit interaction problem.

ACKNOWLEDGEMENTS

The authors are grateful for many discussions with F. Rosenbaum, C. Bozler, M. Hollis, R.A. Murphy and G. Mathews. Portions of this work were supported by DARPA and NSF.

REFERENCES

1. A. Madjar and F. J. Rosenbaum, IEEE Trans. Micro. Th. and Tech., MTT-28, 781 (1981).

2. M. A. Khatibzadeh and R. J. Trew, IEEE Trans. Micro. Th. and Tech., MTT-36, 231 (1988).

3. H. L. Grubin, J. P. Kreskovsky and R. Levy, Modeling of Large Signal Device/Circuit Interactions, IEEE/Cornell Conference on Advanced Concepts in High Speed Semiconductor Devices and Circuits, Cornell University, August 1989; National Science Foundation Contract ISI-8861316.

4. C. M. Snowden and R. R. Pantajo, "Quasi-Two-Dimensional MESFET Simulations for CAD", IEEE Transactions on Electron Devices, vol. 36, No. 9, 1989.

5. C. M. Snowden, M. S. Howes and D. V. Morgan, IEEE Trans. of Electron Devices, ED-30, 1817 (1983).

Third International Conference on Inverse Design Concepts and Optimization in Engineering Sciences (ICIDES-III), Editor: G.S. Dulikravich, Washington D.C., October 23-25, 1991.

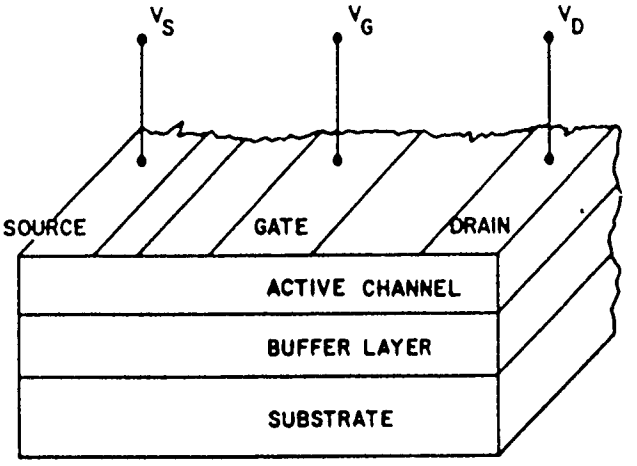


Figure 1. FET Schematic from Reference 5.

PHYSICAL PARAMETERS FOR THE 0.5 μm GATE LENGTH GaAs MESFET USED IN THE SIMULATION	
GATE LENGTH	0.55 μm
GATE WIDTH	300 μm
CHANNEL THICKNESS	0.15 μm
SOURCE TO GATE SPACING	0.5 μm
DRAIN TO GATE SPACING	0.6 μm
BUFFER LAYER THICKNESS	0.2 μm
GATE METALLIZATION	ALUMINUM
SCHOTTKY BARRIER HEIGHT	0.80 V
TEMPERATURE	350 K
DOPING OF ACTIVE LAYER	1.5×10^{23} m^{-3}
DOPING AT CONTACTS	3.7×10^{23} m^{-3}
SUBSTRATE IMPURITY LEVEL	1.0×10^{23} m^{-3}

Table 1.

Third International Conference on Inverse Design Concepts and Optimization in Engineering Sciences (ICIDES-III), Editor: G.S. Dulikravich, Washington D.C., October 23-25, 1991.

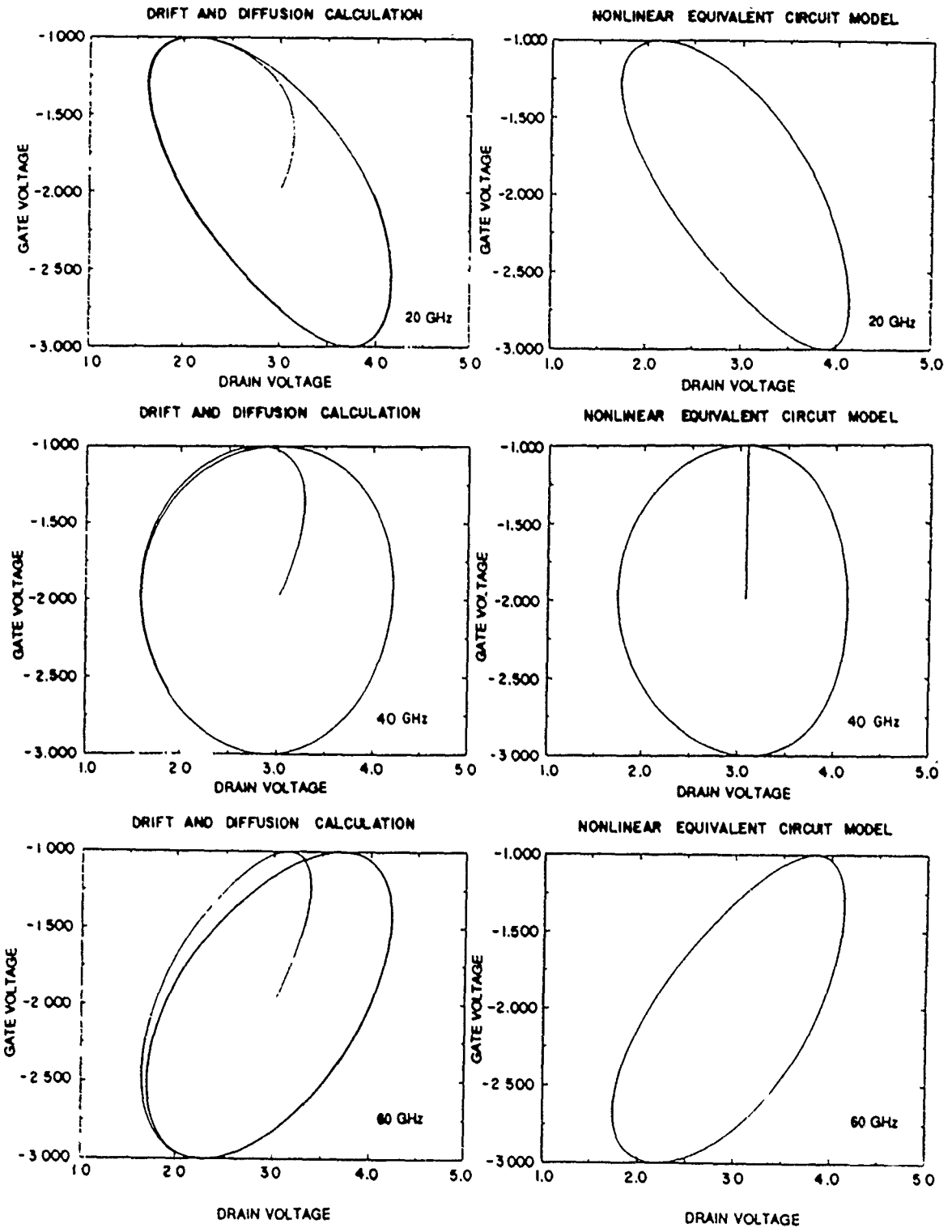


Figure 2. V_g - V_d Lissajous Comparison.

Third International Conference on Inverse Design Concepts and Optimization in Engineering Sciences (ICIDES-III), Editor: G.S. Dulikravich, Washington D.C., October 23-25, 1991.

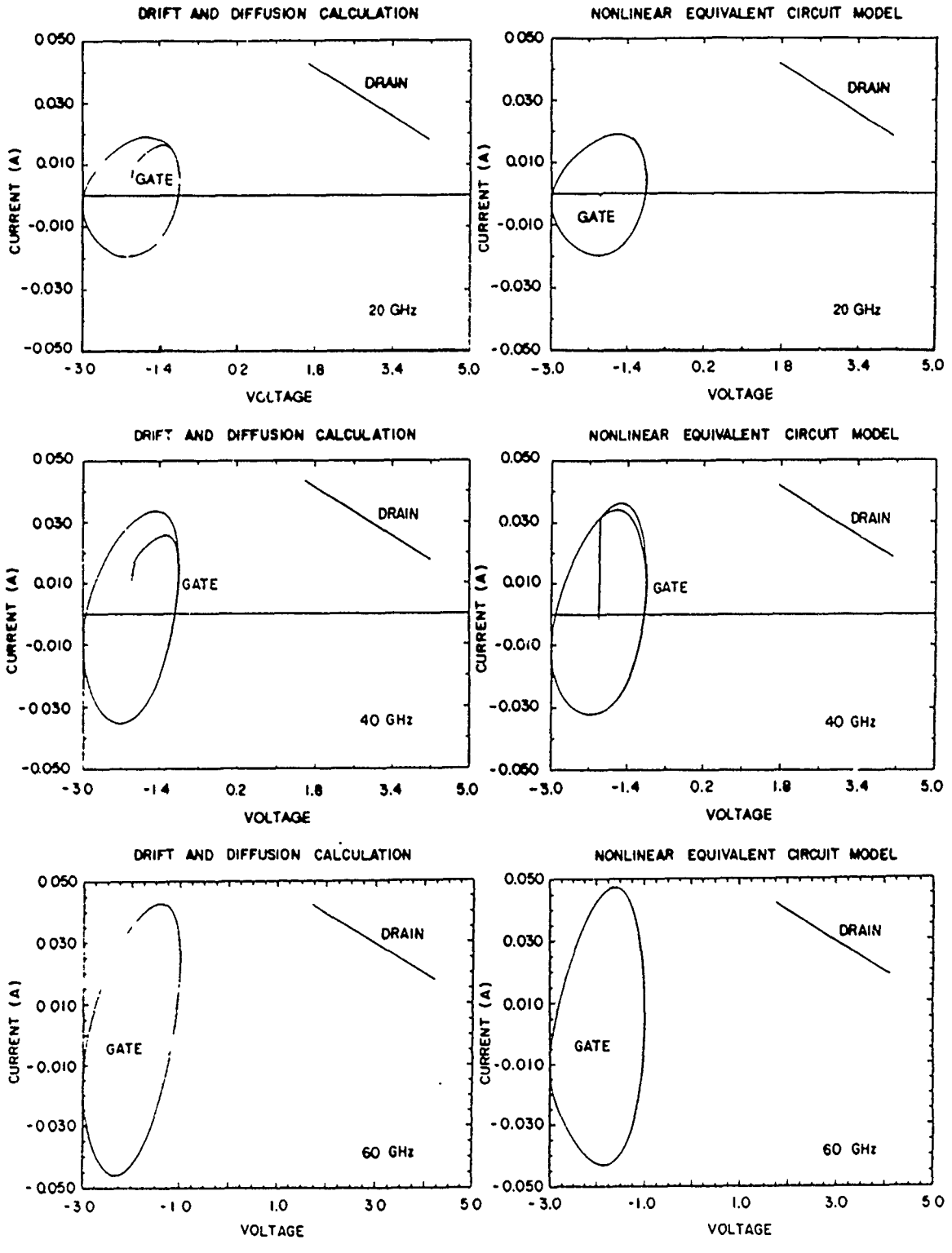


Figure 3. I-V Lissajous Comparison.

Third International Conference on Inverse Design Concepts and Optimization in Engineering Sciences (ICIDES-III), Editor: G.S. Dulikravich, Washington D.C., October 23-25, 1991.

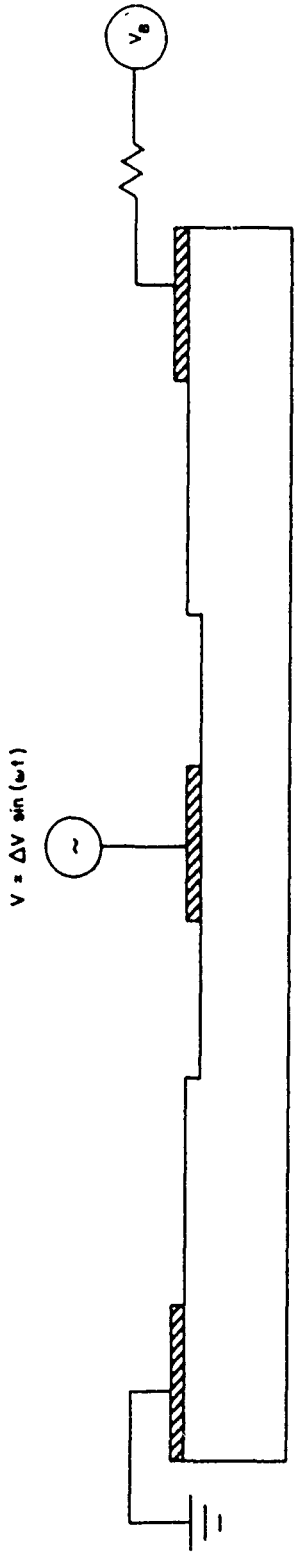


Figure 4. Schematic of FET with Resistive External Load.

Third International Conference on Inverse Design Concepts and Optimization in Engineering Sciences (ICIDES-III), Editor: G.S. Dulikravich, Washington D.C., October 23-25, 1991.

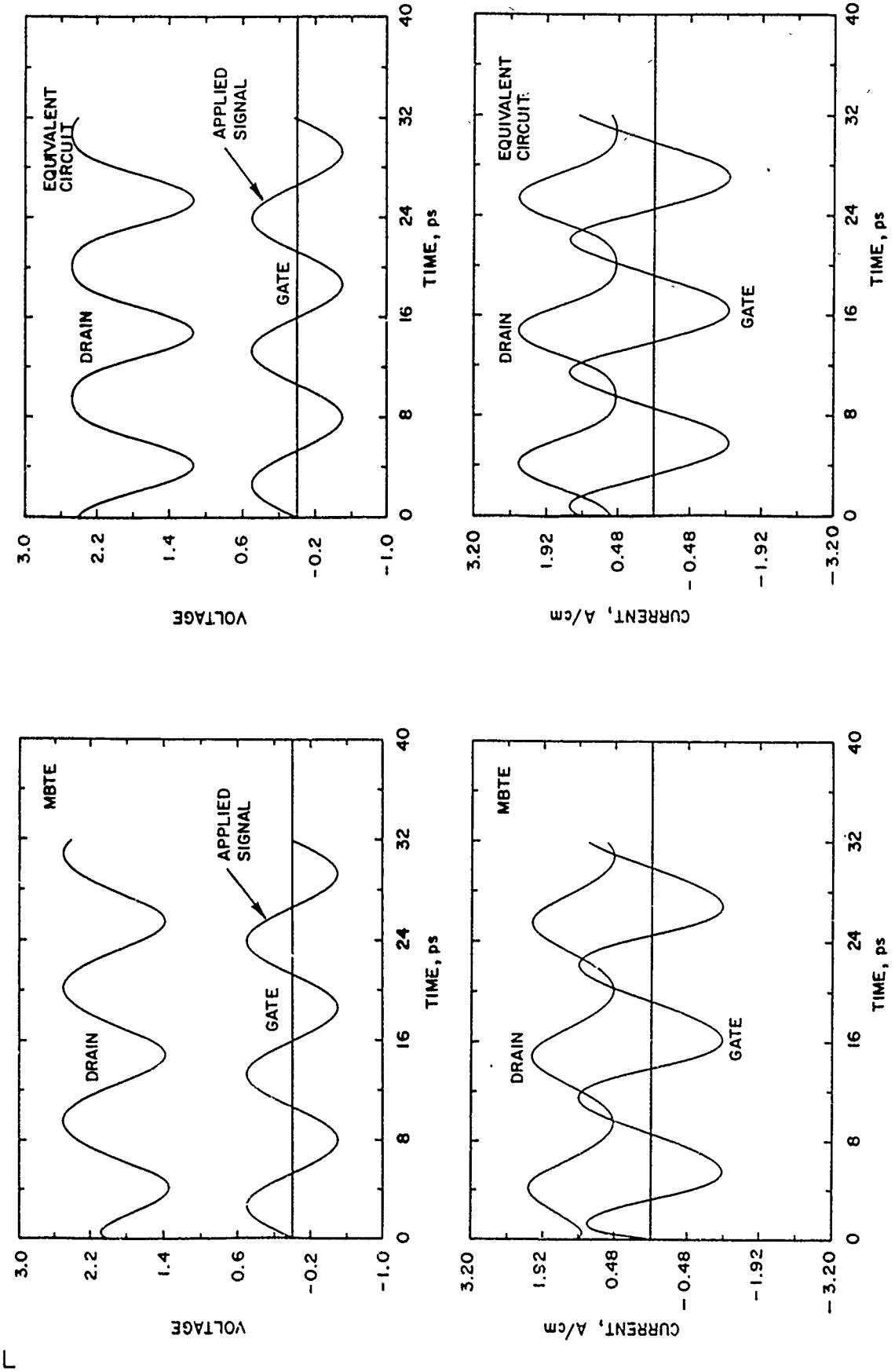


Figure 5. MBTE and Nonlinear Equivalent Circuit Gate and Drain Contact Large Signal Voltage and Current as a Function of Time at 94 GHz.

Third International Conference on Inverse Design Concepts and Optimization in Engineering Sciences (ICIDES-III), Editor: G.S. Dulikravich, Washington D.C., October 23-25, 1991

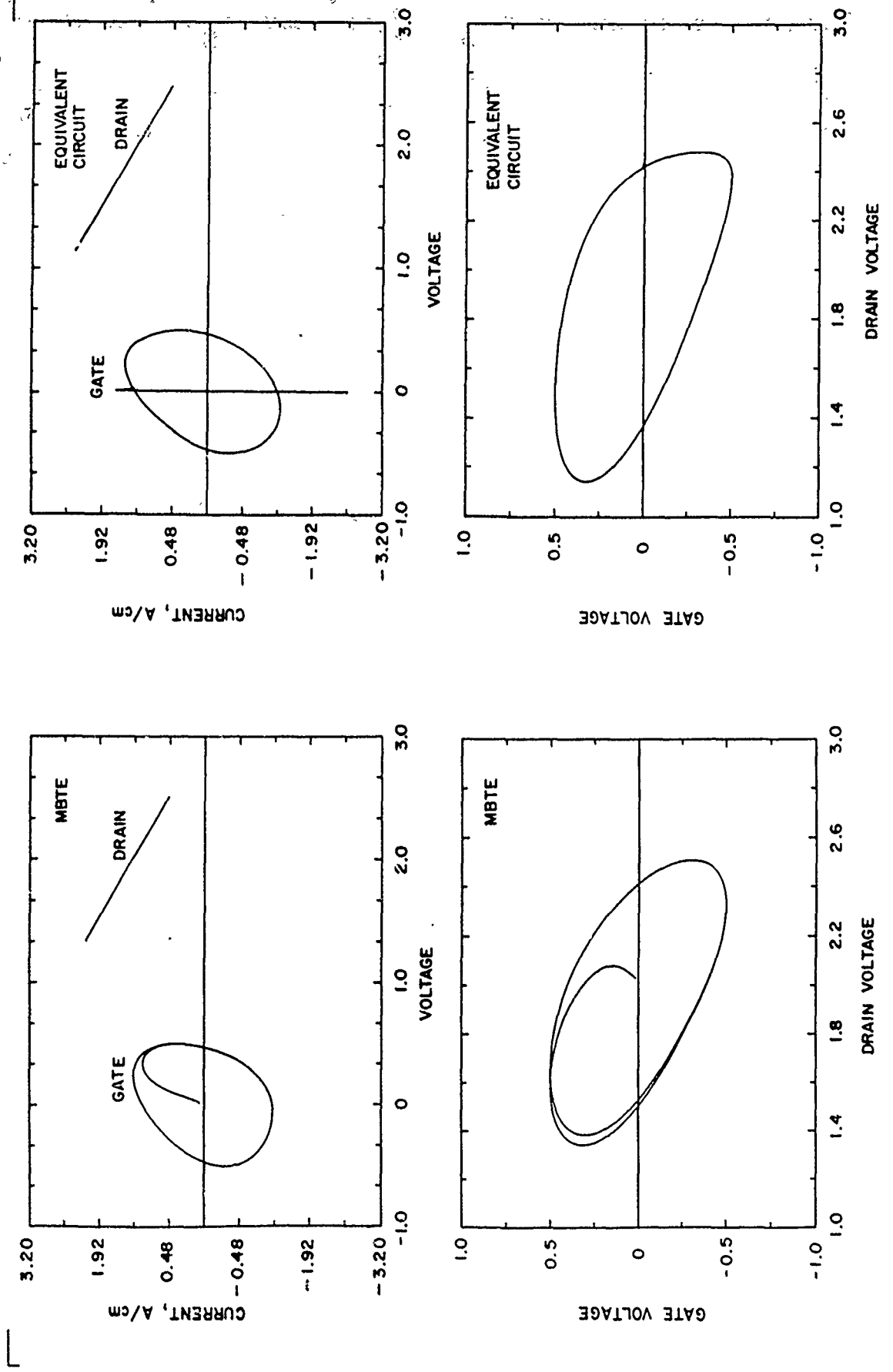


Figure 6. Large Signal Lissajous (MBTE and Nonlinear Equivalent Circuit) at 94 GHz.

Third International Conference on Inverse Design Concepts and Optimization in Engineering Sciences (ICIDES-III), Editor: G.S. Dulikravich, Washington D.C., October 23-25, 1991.

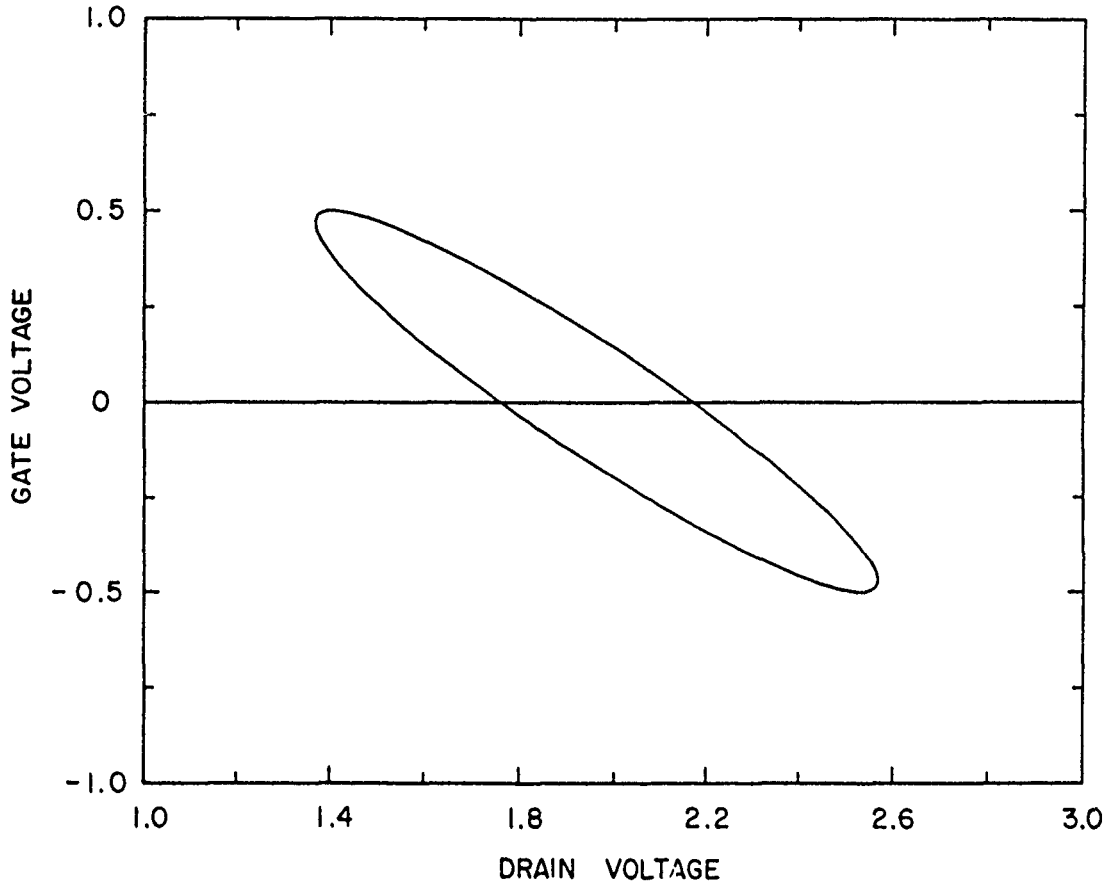


Figure 7. V_g - V_d Lissajous of Applied Signal in Load Pull Calculations at 94 GHz.

Third International Conference on Inverse Design Concepts and Optimization in Engineering Sciences (ICIDES-III). Editor: G.S. Dulikravich. Washington D.C., October 23-25, 1991.

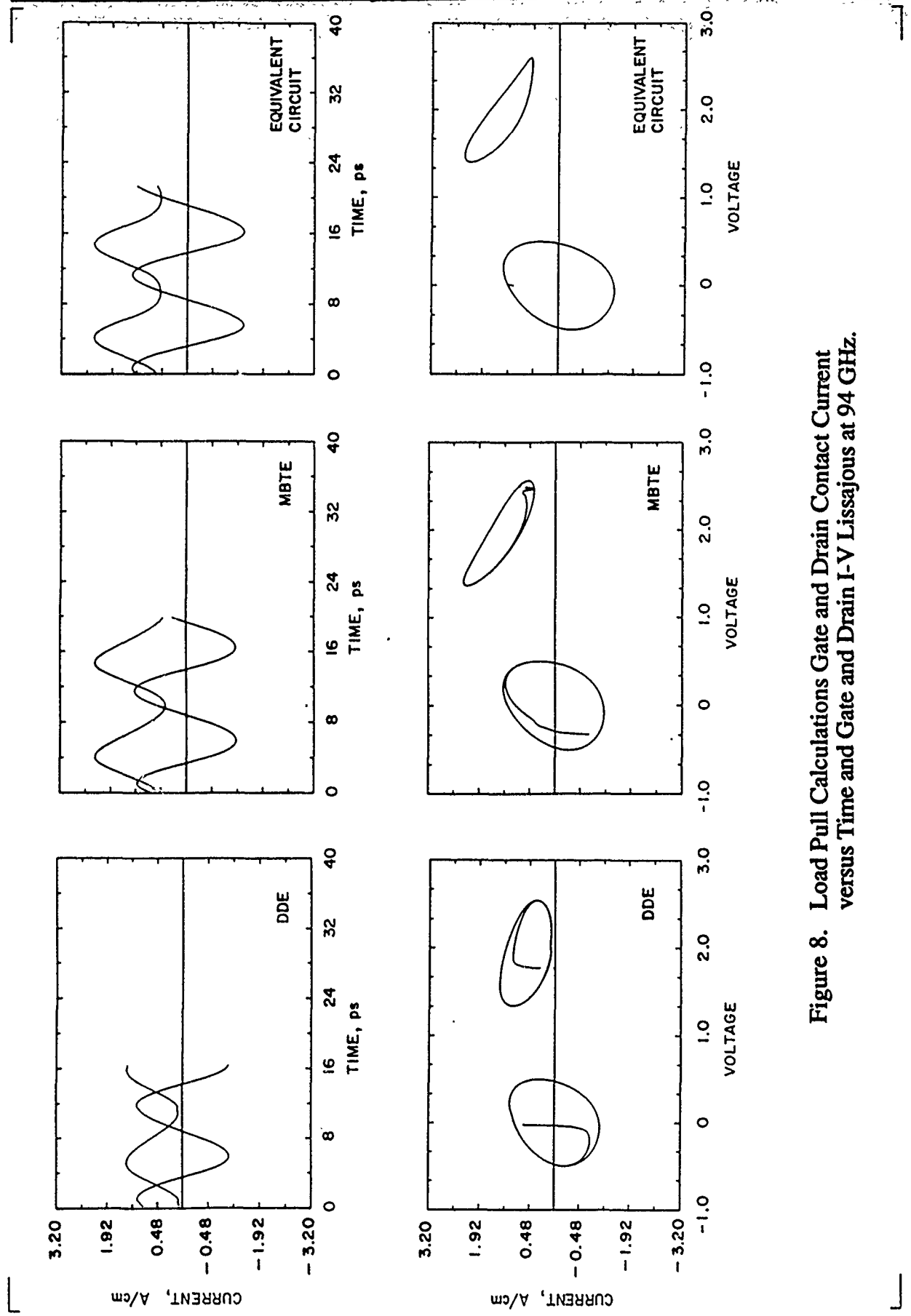


Figure 8. Load Pull Calculations Gate and Drain Contact Current versus Time and Gate and Drain I-V Lissajous at 94 GHz.

Third International Conference on Inverse Design Concepts and Optimization in Engineering Sciences (ICIDES-III), Editor: G.S. Dulikravich, Washington D.C., October 23-25, 1991.

	DRIFT AND DIFFUSION CALCULATION	NONLINEAR EQUIVALENT CIRCUIT MODEL
20 GHz	3.92	4.03
40 GHz	1.32	1.25
60 GHz	0.78	0.80

Table 2. Ratio of Output Power to Input Power - Comparison of Drift and Diffusion Calculation and Nonlinear Equivalent Circuit.

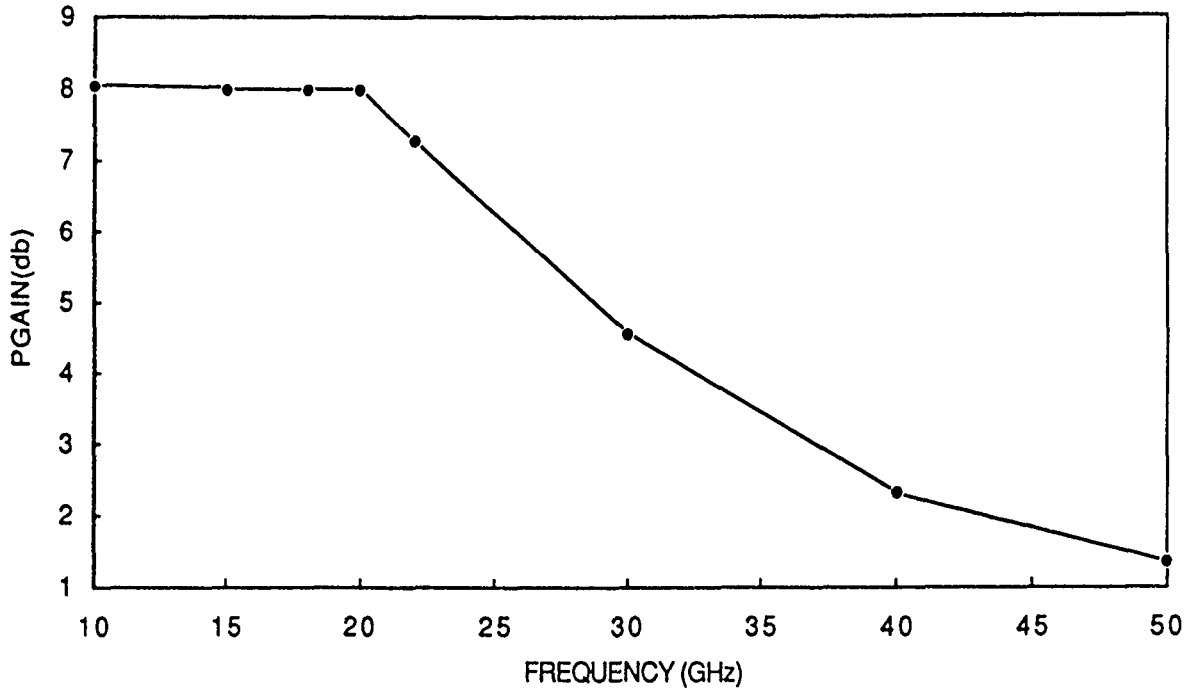


Figure 9. AC Power Gain versus Frequency at Fixed Input AC Power.

Third International Conference on Inverse Design Concepts and Optimization in Engineering Sciences (ICIDES-III). Editor: G.S. Dulikravich. Washington D.C., October 23-25, 1991.

Design of Transonic Compressor Cascades Using Hodograph Method

Chen Zuoyi Guo Jingrong
(Dept. of Thermal Engineering, Tsinghua University)
(Beijing, China)

1. Introduction

The design of transonic turbine cascade using Hodograph Mathod is presented in Ref.1, 2, 3, etc. But up to now, there are no published papers about the design of transonic compressor cascade using Hodograph Mathod. It is given in this article.

The design of flow mode in the transonic compressor cascade must be as follows: (1) the flow in nozzle part should be uniform and smooth. (2) the location of sonic line should be resonable, and (3) aerodynamic character of the flow canal in subsonic region should be met. The rate through cascade may be determined by velocity distribution in subsonic region. (i.e. by the numerical solution of Chaplygin equation). The supersonic sections A′C′ and AD are determined by the analystical solution of Mixed–Type Hodograph equation. If the shock wave exist that we should consider the flow turn by the shock wave. (The "shock wave–Mean Stream Line Turn Method" has been used).

2. The compressor canal design using the analytical solution of Mixed–Type Hodograph equation

In general, the analytical solution of Mixed–Type Hodograph equation (i.e. the nozzle solution) is used in the design of transonic turbine cascade. Can it be used in the design of compressor? Our research shows that it is sure.

For example, if we use the generalization Tricomi approximation, the approximate compressible function is:

$$K_a(\sigma) = b^6(\sigma) / (1 - cb\sigma)^5 \tag{1}$$

For this approximation, comparing the approximate compressible function $K_a(\sigma)$ to the true compressible function $K(\sigma)$, the difference is very small in supersonic region but not in subsonic region. This is suitable for the design of transonic turbine cascade because the analytical solution only apply in the supersonic region. But for the design of compressor cascade, the analytical solution must be used in subsonic region. In order to decrease the difference, we should used the other boundary condition to determine the coefficients b and c, this is:

$$K_a(\sigma)\big|_{M\sigma^*=0.3} = K(\sigma)\big|_{M\sigma^*=0.3} \tag{2}$$

$$\left.\frac{dK_a(\sigma)}{d\sigma}\right|_{\sigma=0} = \left.\frac{dK(\sigma)}{d\sigma}\right|_{\sigma=0} \tag{3}$$

Third International Conference on Inverse Design Concepts and Optimization in Engineering Sciences (ICIDES-III). Editor: G.S. Dulikravich, Washington D.C., October 23-25, 1991.

and we obtain the c, b as follows:

If $\gamma = 1.4$ $c = -0.28236$

$b = 1.15709$

The comparision between $K(\sigma)$ and $Ka(\sigma)$ is shown in Fig.2.

3. To determine the leading edge shock wave and coming flow parameters of transonic compressor cascade

On the basis of the sonicline location which has been given in design and according to the application of analytical solution in compressor canal, we may obtain the profile C′A′ and DA, along with the velocity distribution in C′A′ and DA. (i.e. obtain the geometry of leading edge and the Ma_A, Ma_A (see Fig.3)). If the computation model in Fig.3 is used, we can consider that the flow turn proceeded from coming flow Ma_{100} at the leading edge of suction and pressure surface respectively. If the turn angles are δ and δ',

thus $\delta + \delta' = \Phi$

here Φ is geometric angle of leading edge.

Two shock waves are produced when the flow turn suddenly. The shock wave angles are β_1, β_2, β'_1 and β'_2 respectively. Thus, from the relationship of oblique shock wave, we obtain:

$$tg(\beta_1 - \beta_2) = 2ctg\beta_1 \left[Ma_1^2 sin^2\beta_1 - 1 \right] / \left[Ma_1^2(\gamma + cos2\beta_1) + 2 \right] \tag{4}$$

$$tg(\beta'_1 - \beta'_2) = 2ctg\beta'_1 \left[Ma_1^2 sin^2\beta'_1 - 1 \right] / \left[Ma_1^2(\gamma + cos2\beta'_1) + 2 \right] \tag{5}$$

$$\beta'_1 - \beta'_2 = \Phi - (\beta_1 - \beta_2) \tag{6}$$

$$Ma_2^2 = \frac{Ma_1^2 + \frac{2}{\gamma - 1}}{\frac{2\gamma}{\gamma - 1} Ma_1^2 sin^2\beta_1 - 1} + \frac{Ma_1^2 cos^2\beta_1}{\frac{\gamma - 1}{2} Ma_1^2 sin^2\beta_1 + 1} \tag{7}$$

$$Ma_2^{'2} = \frac{Ma_1^2 + \frac{2}{\gamma - 1}}{\frac{2\gamma}{\gamma - 1} Ma_1^2 sin^2\beta'_1 - 1} + \frac{Ma_1^2 cos^2\beta'_1}{\frac{\gamma - 1}{2} Ma_1^2 sin^2\beta'_1 + 1} \tag{8}$$

in previous five equations, the known parameters are Ma_2, Ma_2' and Φ, and unknown parameters are β_1, β_2, β'_1, β'_2, Ma_1, so the solutions are completely dertermined by the five equations.

Third International Conference on Inverse Design Concepts and Optimization in Engineering Sciences (ICIDES-III), Editor: G.S. Dulikravich, Washington D.C., October 23-25, 1991.

If the shock wave is strong, the flow turn passing the shock wave should be considered. The model of design is shown in Fig.4.

We consider that the shock wave strength is determined by the flow turn on the meanstreamline, i.e. the shock wave angles β_1^* and β_2^* are determined by the flow turn angle δ^*, thus the follwoing relations may be obtained:

$$M_{a_{B1}}^2 = \frac{2ctg\beta_1^* + 2tg(\beta_1^* - \beta_2^*)}{2ctg\beta_1^* sin^2\beta_1^* - tg(\beta_1^* - \beta_2^*)(\gamma + cos2\beta_1^*)} \tag{9}$$

$$M_{a_{B2}}^2 = \frac{Ma_{B1}^2 + \frac{2}{\gamma-1}}{\frac{2\gamma}{\gamma-1}Ma_{B1}^2 sin^2\beta_1^* - 1} + \frac{Ma_{B1}^2 cos^2\beta_1}{\frac{\gamma-1}{2}Ma_{B1}^2 sin^2\beta_1^* + 1} \tag{10}$$

Now, the flow field can be divided into two parts, the region before the shock wave and after the shock wave. In the region A′BA, applied the Hodograph Mixed–Type Equation to determine the profile and velocity distribution of the C′A′ and DB. There are four parameters Ma_{B1}, Ma_{B2}, β_1^*, and β_2^* in the Eq.9 and Eq.10. If the Ma_{B2} is determined, thus the relation between β_1^* and β_2^* can also be determined, and the design of Hodograph Method that consider the sudden change proceeded from the shock wave may be solved with the alternative method. For example, we assume the β_2^* and therefore the location of shock wave can be determined, i.e. the location of point B is determined, and the Ma_{B2} can also be determined. From the Eq.9 and Eq.10, the Ma_{B1} and β_1^* may be obtained, and the δ^* may also be obtained. After this, we can obtain the turn–meanline EF. On the basis of the EF we can solve the velocity distribution on the BA, and the Ma_2 can be obtained. So that from the Eq.4~ Eg.8 the new β_2' can be determined. Put the new β_2^* in previous calculation and till it is satisfied.

In the subsonic region, the numerical solution of Chaplygin Eguation can be used. i.e.

$$\frac{\partial}{\partial\theta}\left(P\frac{\partial\psi}{\partial\theta}\right) + \frac{\partial}{\partial M_a^*}\left(Q\frac{\partial\psi}{\partial M_a^*}\right) = -\frac{Q}{M_a^*}L(\psi_\infty) \tag{11}$$

4. Design example

Using previous theory and mathod, two compressor cascade have been designed. The one is called J–3–Type cascade, and the other is called Ma–Type cascade which is designed on the basis of velocity distribution of the compressor cascade which is provided by Ref.4.

The designed parameters of transonic compressor–3 profil are: Mach number at outlet is 0.62, flow angle at outlet is 45 ° , cascade pitch is 50mm, the Mach number and flow angle

Third International Conference on Inverse Design Concepts and Optimization in Engineering Sciences (ICIDES-III). Editor: G.S. Dulikravich, Washington D.C., October 23-25, 1991.

at inlet are 50 ° and 1.22 respectively. The designed cascade profile is shown in Fig 5. The profile coordinates and its velocity distribution are shown in Table 1.

Comparing the velocity distribution of J–3–Type cascade with the calculating of the Time Marching method, we find the results are in agreement (see Fig.6).

The profile of Ma–Type cascade comparing with the cascade in Ref.4 is also in agreement (see Fig.7).

5. Conclusion

1. The Hodograph Method may be used to the design of transonic compressor cascade.
2. The flow field may be divided into two parts for using Hodograph method design, to solve the Hodograph Mixed–Teyp Equation in supersonic region and the Chaplygin Equation in subsonic region.
3. If the strength of shock wave is large, the flow turn by shock wave, the "Shock wave–Meanstreamline turn Method" is suitable for this design.

Reference

1. Chen Zuoyi, Journal of Tsinghua Univ., Vol.21, No.4, 1981.
2. Chen Zuoyi, Journal of Tsinghua Univ., Vol.22, No.4, 1982.
3. G.Karadimas, Institute for Fluid Dynamics lecture Series 59.
4. William. T. Thompkins, Jr, GT and PDL Report, No.162, Sept. 1981, MIT.

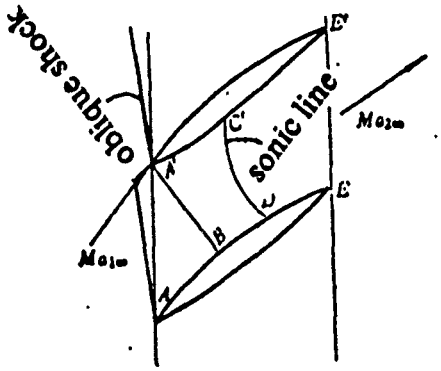


Fig.1 The flow model of transonic compressor cascade

Third International Conference on Inverse Design Concepts and Optimization in Engineering Sciences
(ICIDES-III), Editor: G.S. Dulikravich, Washington D.C., October 23-25, 1991.

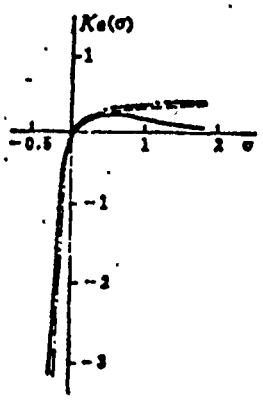


Fig.2 Comparision between Ka(σ) and K(σ) respecting to various coefficients a and b

true K(σ)
Ka(σ): b=0.024 c=−0.78 / b
Ka(σ): b=1.15609 c=−0.28236

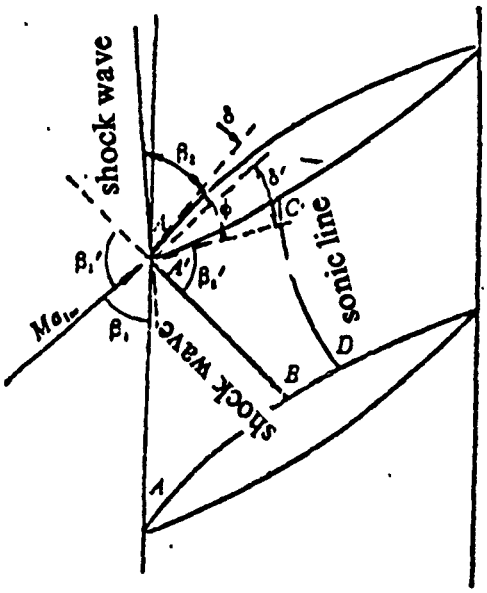


Fig.3 The relation between the leading edge shock wave and coming flow parameters

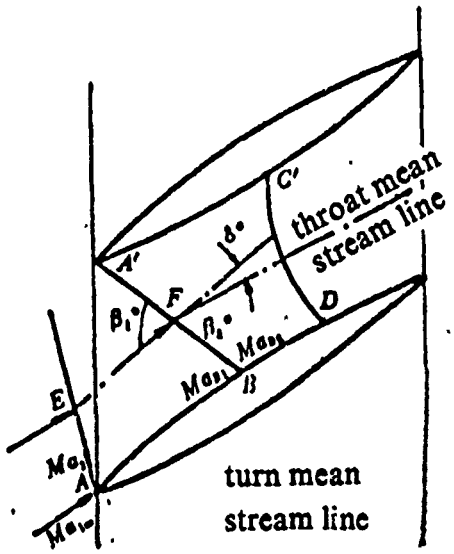


Fig.4 Calculation model in compressor cascade

Third International Conference on Inverse Design Concepts and Optimization in Engineering Sciences (ICIDES-III), Editor: G.S. Dulikravich, Washington D.C., October 23-25, 1991.

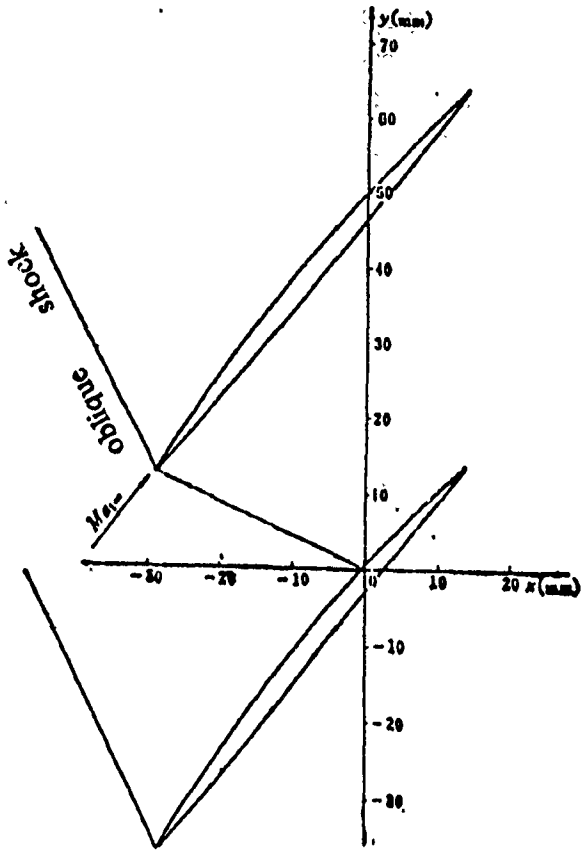


Fig.5 Transonic compressor cascade J–3–Type with Hodograph Method oblique shock

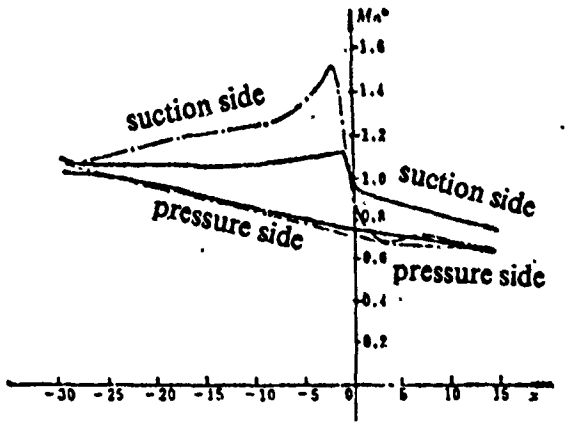


Fig.6 Velocity distribution comparison between Hodograph Method and Time Marching method

——— Hodograph Method
—·— Time Marching Method

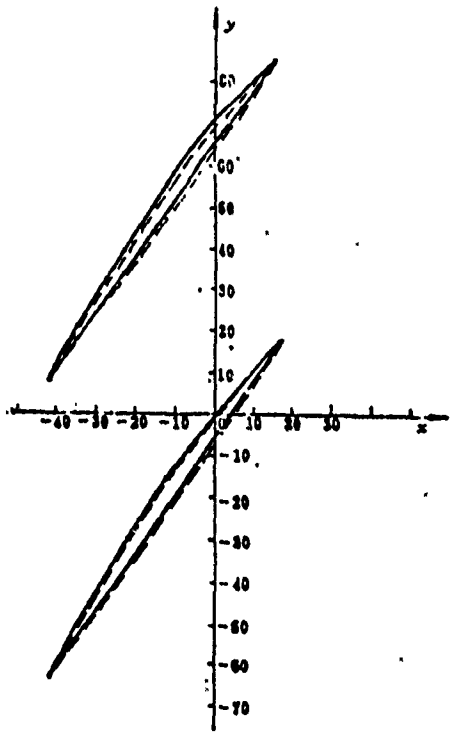


Fig.7 Comparison between the transonic compressor cascade (Ma–Type) pro ceeded from inverted calculation with Hodograph Method and Ref.4

——— Profile in Ref.4
– – – – Profile by Hodograph Method

Third International Conference on Inverse Design Concepts and Optimization in Engineering Sciences (ICIDES-III), Editor: G.S. Dulikravich, Washington D.C., October 23-25, 1991.

The Research Progress on Hodograph Method of Aerodynamic Design at Tsinghua University

Chen Zuoyi Guo Jingrong
(Tsinghua University)

1. Introduction

The Hodograph Method is a classical method in fluid dynamics. Because it can transform the nonlinear equation to the linear. So it is always used to resolve the fluid dynamic equation in the early time. For example, the well known Karmen–Jein formula is obtained from Hodograph equation. Then the Hodograph method is widely applicated in the research of transonic flow. Due to the Mixed–Type character of transonic flow equation, the Hodograph method may be the only accurate method to solve the transonic flow equation. In the 1970's, the Hodograph method start to be used in the inverse problem of fluid dynamics. (i.e. design problem, such as the work by Hobsen and karadimas (Ref.1) In the 1980's., we have done systematic reserch work on Hodograph method in Tsinghua University, and have taken much progress as the follows.

1. Research progress on the analytical solution of Hodograph Mixed–Type equation

The various analytical solutions of Hodograph Mixed–Type equation are presented in Ref.3. If we use these solutions to solve the inverse problem, especially design the cascade profile, there are limits on various boundary condition. We can't always find right solution under any boundary condition. So that the application scope may be restricted. The differences among various analytical solution of Hodograph Mixed–Type equations and their application conditions have been presented. It shows the differences are obvious (see Fig.1).

The application scope of the four nozzle–solution of Hodograph is shown in Table.1.

All the nozzle–solutions of Hodograph were straight line corresponding with the mean stream line before. If we use them in the inverse probiem of cascade, the best one is prefered to be curve mean streamline. The nozzle–solution of Hodograph corresponding with the curve mean streamline is presented. We get the analytical solution of Mixed–Type Hodograph equation that is corresponding with the parabolic coordinates, as shown in Fig.2.

The relationship between the parabolic and rectangular coordinates is:

$$x=\frac{1}{2}(\xi^2-\eta^2) \tag{1}$$

$$y=\xi\eta \tag{2}$$

Thus the vorticity of V may be represented by:

Third International Conference on Inverse Design Concepts and Optimization in Engineering Sciences (ICIDES-III), Editor: G.S. Dulikravich, Washington D.C., October 23-25, 1991.

$$\nabla \times \vec{V} = \frac{1}{\xi^2 + \eta^2}\left(\frac{\partial(V_\eta\sqrt{\xi^2+\eta^2})}{\partial\zeta} - \frac{\partial(V_\xi\sqrt{\xi^2+\eta^2})}{\partial\eta}\right) \tag{3}$$

It satisfies:

$$\frac{\partial\psi}{\partial\xi} = \sqrt{\xi^2+\eta^2}\,\rho V_\eta \tag{4}$$

$$\frac{\partial\psi}{\partial\eta} = \sqrt{\xi^2+\eta^2}\,\rho V_\xi \tag{5}$$

If the equivalent velocity is introduced:

$$\hat{V}_\eta = \sqrt{\xi^2+\eta^2}\,V_\eta \tag{6}$$

$$\hat{V}_\xi = \sqrt{\xi^2+\eta^2}\,V_\xi \tag{7}$$

the similar Mixed–Type Hodograph equation can be obtained:

$$\frac{\partial^2\psi}{\partial\hat{\sigma}^2} + K(\sigma)\frac{\partial^2\psi}{\partial\theta^2} = 0 \tag{8}$$

2. Design of the transonic turbine and compressor cascade using Hodograph method

we have presented the new method to design the transonic turbine and compressor cascade using Hodograph. This method is that applicated the Chaplygin equation numerical solution to solve the subsonic area and applicated the analytical solution of Mixed–Type Hodograph equation to solve the supersonic area.

The differential equation for numerical solution of Chaplygin equation is:

$$\psi_{r_{i,k}} = \left[B_{i,k} + \frac{p_{a,k}}{S_{i,k}}\psi_{r_{i+i,k}} + \left(\frac{Q_{i,k}}{l_{i,k}^2} + \frac{T_{i,k}}{2l_{i,k}}\right)\psi_{r_{i,k+1}} + \frac{P_{i,k}}{S_{i,k}^2}\psi_{r_{i-1,k}} + \left(\frac{Q_{i,k}}{l_{i,k}^2} - \frac{T_{i,k}}{2l_{i,k}}\right)\psi_{r_{i,k-1}}\right] / [2P_{i,k}/S_{i,k}^2 + 2Q_{i,k}/l_{i,k}^2] \tag{9}$$

The profile coordinates equations are:

$$x - x_0 = \int_1^{M_a^*} -h\frac{\rho_\infty}{\rho^*}\frac{Ma_\infty^*}{Ma^*}\cos\theta_\infty\left[P + Q\left(\frac{d\theta}{dMa^*}\right)^2\right]\frac{\partial p}{\partial\theta}\cos\theta dMa^* \tag{10}$$

Third International Conference on Inverse Design Concepts and Optimization in Engineering Sciences (ICIDES-III), Editor: G.S. Dulikravich, Washington D.C., October 23-25, 1991.

$$y-y_0=\int_1^{Ma^*}-h\frac{\rho_\infty}{\rho^*}\frac{Ma^*_\infty}{Ma^*}cos\theta_\infty\left[P+Q\left(\frac{d\theta}{dMa^*}\right)^2\right]\frac{\partial\psi}{\partial\theta}sin\theta dMa^* \tag{11}$$

The profile coordinates equations which are obtained by the analytical solution of Mixed–Type Hodograph equation are:

$$x-x_0=\left[\int -l^*\frac{cos\theta}{Ma^*}\left(\frac{\partial\psi}{\partial\sigma}+K_a(\sigma)\frac{\left(\frac{\partial\psi}{\partial\theta}\right)^2}{\frac{\partial\psi}{\partial\sigma}}\right)d\theta\right]_{\psi=1} \tag{12}$$

$$y-y_0=\left[\int_{\theta_*}^{\theta} -l^*\frac{sin\theta}{Ma^*}\left(\frac{\partial\psi}{\partial\sigma}+K_a(\sigma)\frac{\left(\frac{\partial\psi}{\partial\theta}\right)^2}{\frac{\partial\psi}{\partial\sigma}}\right)d\theta\right]_{\psi=1} \tag{13}$$

The location of shock wave is the importantance in design. The method of profile design by the given location of shock wave is also presented. The comparision between the design shock wave locatgion and the experiment is shown in Fig.3.

3. The basic equation of three dimensional Hodograph method

On the basis of the general theory in three dimensional flow and the correspondence between the physical surface and Hodograph, the basic equations of three dimensional Hodograph method have been obtained.

Using the concept of equivalent physical surface and equivalent Hodograph, we obtain the different equation of streamfunction with Hodograph coordinates and integral equation for returning from the Hodograph to the physical surface.

The correspondence between S1 flow surface and equivalent physical surface is shown in Fig.4.

The streamfunction equation of Hodograph corresponding to the S1 flow surface is

$$A_1\frac{\partial^2\psi}{\partial\hat{\omega}^2}+A_2\frac{\partial\psi}{\partial\hat{\omega}}+A_3\frac{\partial^2\psi}{\partial\hat{\omega}\partial\hat{\theta}}+A_4\frac{\partial\psi}{\partial\hat{\theta}}+A_5\frac{\partial^2\psi}{\partial\hat{\theta}^2}=0 \tag{14}$$

here $\hat{\omega}$ is equivalent velocity. $\hat{\theta}$ is the equivalent flow angle.

The relationship between the equivalent velocity and true velocity is

$$\hat{\omega}e^{i\hat{\theta}}=A+Bi$$

$$B=\frac{1}{K_3}(r\omega_o+r^2\omega-r\omega_r\frac{n_\theta}{n_r}) \tag{15}$$

Third International Conference on Inverse Design Concepts and Optimization in Engineering Sciences (ICIDES-III), Editor: G.S. Dulikravich, Washington D.C., October 23-25, 1991.

$$A = \frac{1}{K_2}(\varepsilon\omega_z + \beta\omega_\theta)$$

Similarly, we can obtain the streamfunction equation of Hodograph corresponding to the S2 flow surface, that is:

$$\tilde{A}_1\frac{\partial^2\psi}{\partial\tilde{\omega}^2} + \tilde{A}_2\frac{\partial\psi}{\partial\tilde{\omega}} + \tilde{A}_3\frac{\partial^2\psi}{\partial\tilde{\omega}\partial\tilde{\theta}} + \tilde{A}_4\frac{\partial\psi}{\partial\tilde{\theta}} + \tilde{A}_5\frac{\partial^2\psi}{\partial\tilde{\theta}^2} = 0 \tag{16}$$

The correspondence between S2 flow surface and equivalent physical surface is shown in Fig.5.

The relationship between the equivalent velocity and actual velocity is:

$$\tilde{A}K_6 = \omega_z - \frac{n_z}{n_\theta}(\omega_\theta + \omega r) \tag{17}$$

$$\tilde{B}K_5 = \omega_r - \frac{n_r}{n_\theta}(\omega_\theta + \omega r) \tag{18}$$

The integral equations for returning from the Hodograph to the S1 surface are:

$$z - z_o = \int_{\hat{\theta}_o}^{\hat{\theta}} \left\{ \frac{1}{\sqrt{\varepsilon}\hat{\omega}} cos\hat{\theta} \left[\frac{\partial(\frac{\sqrt{\varepsilon}}{\rho b})}{\partial\hat{\theta}}\frac{\partial\psi}{\partial\hat{\theta}} + \frac{\sqrt{\varepsilon}}{b\rho\hat{\omega}}\frac{(\frac{\partial\psi}{\partial\theta})^2}{(\frac{\partial\psi}{\partial\hat{\omega}})} - \frac{\partial(\frac{\sqrt{\varepsilon}}{b\rho})}{\partial\hat{\omega}}\frac{(\frac{\partial\psi}{\partial\hat{\theta}})^2}{(\frac{\partial\psi}{\partial\hat{\omega}})} + \frac{\sqrt{\varepsilon}}{b\rho}\hat{\omega}\frac{\partial\psi}{\partial\hat{\omega}} \right] \right\} d\hat{\theta} \tag{19}$$

$$\theta - \theta_o = \int_{\hat{\theta}_o}^{\hat{\theta}} \left\{ \frac{1}{r\hat{\omega}} sin\hat{\theta} \left[\frac{\partial(\frac{\sqrt{\varepsilon}}{\rho b})}{\partial\hat{\theta}}\frac{\partial\psi}{\partial\hat{\theta}} + \frac{\sqrt{\varepsilon}}{b\rho\hat{\omega}}\frac{(\frac{\partial\psi}{\partial\theta})^2}{(\frac{\partial\psi}{\partial\hat{\omega}})} - \frac{\partial(\frac{\sqrt{\varepsilon}}{b\rho})}{\partial\hat{\omega}}\frac{(\frac{\partial\psi}{\partial\hat{\theta}})^2}{(\frac{\partial\psi}{\partial\hat{\omega}})} + \frac{\sqrt{\varepsilon}}{b\rho}\hat{\omega}\frac{\partial\psi}{\partial\hat{\omega}} \right] \right\} d\hat{\theta} \tag{20}$$

The integral equation for returning from the Hodograph to the S2 surface is:

$$z - z_o = \int_{\tilde{\theta}_o}^{\tilde{\theta}} \frac{cos\tilde{\theta}}{\tilde{\omega}K_6} \left[\frac{\partial K_4}{\partial\tilde{\theta}} - \frac{\partial\psi}{\partial\tilde{\theta}} + \frac{K_4}{\tilde{\omega}}\frac{(\frac{\partial\psi}{\partial\tilde{\theta}})^2}{(\frac{\partial\psi}{\partial\tilde{\omega}})} - \frac{\partial K_4}{\partial\tilde{\omega}}\frac{(\frac{\partial\psi}{\partial\tilde{\theta}})^2}{(\frac{\partial\psi}{\partial\tilde{\omega}})} + \tilde{\omega}K_4\frac{\partial\psi}{\partial\tilde{\omega}} \right] d\tilde{\theta} \tag{22}$$

$$r-r_o=\int_{\bar{\theta}_o}^{\bar{\theta}}\frac{sin\tilde{\theta}}{\tilde{\omega}K_5}\left[\frac{\partial K_4}{\partial\tilde{\theta}}\frac{\partial\psi}{\partial\tilde{\theta}}+\frac{K_4}{\tilde{\omega}}\frac{(\frac{\partial\psi}{\partial\tilde{\theta}})^2}{(\frac{\partial\psi}{\partial\tilde{\omega}})}-\frac{\partial K_4}{\partial\tilde{\omega}}\frac{(\frac{\partial\psi}{\partial\tilde{\theta}})^2}{(\frac{\partial\psi}{\partial\tilde{\omega}})}+\tilde{\omega}K_4\frac{\partial\psi}{\partial\tilde{\omega}}\right]d\tilde{\theta} \tag{23}$$

4. The aerodynamic design of Hodograph is revolutionary surface

On the basis of the three dimensional flow Hodograph method, the aerodynamic design of Hodograph in revolutionary surface is presented.

The Hodograph equation corresponding to the revolutionary surface can be obtained from Hodograph equation corresponding to the S1 flow surface.

$$M_a^*\frac{\partial^2\psi}{\partial Ma^{*2}}+\left[1-\frac{M_a^*}{\bar{b}}\frac{\partial\bar{b}}{\partial M_a^*}-\frac{M_a^*}{\bar{\rho}}\frac{\partial\bar{\rho}}{\partial M_a^*}+\frac{2}{\bar{b}^2}(\frac{\partial b}{\partial\theta})^2-\frac{1}{\bar{b}}\frac{\partial^2 b}{\partial\theta^2}\right]\frac{\partial\psi}{\partial M_a^*}$$
$$-\frac{1}{\bar{b}}\frac{\partial\bar{b}}{\partial\theta}\frac{\partial^2\psi}{\partial M_a^*\partial\theta}-\left[\frac{1}{\bar{b}M_a^*}\frac{\partial\bar{b}}{\partial\theta}+\frac{2}{\bar{b}^2\bar{\rho}}+\frac{\partial\bar{b}}{\partial M_a^*}\frac{\partial\bar{b}}{\partial\theta}+\frac{\partial\bar{b}}{\partial\theta}\frac{\partial\bar{\rho}}{\partial M_a^*}\frac{1}{\bar{b}\bar{\rho}^2}+\frac{1}{\bar{b}}\frac{\partial^2\bar{b}}{\partial M_a^*\partial\theta}\right]\frac{\partial\psi}{\partial\theta}$$
$$+\left[\frac{1}{M_a^*}+\frac{1}{\bar{b}}\frac{\partial\bar{b}}{\partial M_a^*}+\frac{1}{\bar{\rho}}\frac{\partial\bar{\rho}}{\partial Ma^*}\right]\frac{\partial^2\psi}{\partial\theta^2}=0 \tag{23}$$

The integral equations for returning from the Hodograph to revolutionary surface are

$$z-z_0=\int_{\hat{\theta}}^{\hat{\theta}}\frac{h\rho_\infty Ma_\infty^* cos\hat{\theta}_\infty cos\hat{\theta}}{Ma^*\rho^*}\left[\frac{\partial(\frac{1}{\bar{\rho}\bar{b}})}{\partial\hat{\theta}}\frac{\partial\psi}{\partial\hat{\theta}}+\frac{1}{\bar{b}\bar{\rho}Ma^*}\frac{(\frac{\partial\psi}{\partial\hat{\theta}})^2}{\frac{\partial\psi}{\partial Ma^*}}-\frac{(\frac{\partial\psi}{\partial\hat{\theta}})^2}{\frac{\partial\psi}{\partial Ma^*}}\frac{\partial(\frac{1}{\bar{\rho}\bar{b}})}{\partial Ma^*}\right.$$
$$\left.+\frac{Ma^*}{\bar{b}\bar{\rho}}\frac{\partial\psi}{\partial Ma^*}\right]d\hat{\theta} \tag{24}$$

$$\theta-\theta_0=\int_{\hat{\theta}}^{\hat{\theta}}\frac{h\rho_\infty Ma_\infty^* cos\hat{\theta}_\infty sin\hat{\theta}}{(r_0+ztg\alpha_1)Ma^*\rho^*}\left[\frac{\partial(\frac{1}{\bar{\rho}\bar{b}})}{\partial\hat{\theta}}\frac{\partial\psi}{\partial\hat{\theta}}+\frac{1}{\bar{b}\bar{\rho}Ma^*}\frac{(\frac{\partial\psi}{\partial\hat{\theta}})^2}{\frac{\partial\psi}{\partial Ma^*}}-\frac{(\frac{\partial\psi}{\partial\hat{\theta}})^2}{\frac{\partial\psi}{\partial Ma^*}}\frac{\partial(\frac{1}{\bar{\rho}\bar{b}})}{\partial Ma^*}\right.$$
$$\left.+\frac{Ma^*}{\bar{b}\bar{\rho}}\frac{\partial\psi}{\partial Ma^*}\right]d\hat{\theta} \tag{25}$$

In order to determine the supersonic region, the analytical solution of Hodograph Mixed–Type equation corresponding to revolutionary surface is presented.

From the streamfunction equation:

Third International Conference on Inverse Design Concepts and Optimization in Engineering Sciences (ICIDES-III), Editor: G.S. Dulikravich, Washington D.C., October 23-25, 1991.

$$Ma^{*}\left[\frac{\partial^{2}\psi}{\partial\sigma^{2}}K^{2}-\frac{\partial\psi}{\partial\sigma}\frac{dK}{dMa^{*}}\right]+\frac{Ma^{*}}{\bar{\rho}}\frac{\partial\bar{\rho}}{\partial Ma^{*}}K\frac{\partial\psi}{\partial\sigma}+\left[\frac{2}{Ma^{*}}+\frac{1}{\bar{\rho}}\frac{\partial\bar{\rho}}{\partial Ma^{*}}\right]\frac{\partial^{2}\psi}{\partial\hat{\theta}^{2}}=0 \quad (26)$$

If put the

$$F(\sigma)=\left[\frac{2}{Ma^{*}}+\frac{1}{\bar{\rho}}\frac{\partial\bar{\rho}}{\partial Ma^{*}}\right]/(Ma^{*}K^{2}) \quad (27)$$

thus the streamfunction equation can be transformed to the analytical solution equation which is similarly the plane flow

$$F(\sigma)\frac{\partial^{2}\psi}{\partial\hat{\theta}^{2}}+\frac{\partial^{2}\psi}{\partial\sigma^{2}}=0$$

Design example:

Design parameters: $r=1.29$ $M_{\infty}=0.2238$ $\hat{\theta}_{\infty}=0$

$T_{\infty}=1490$ k $\theta_{2}=73$ $M_{2}=1.15$

$R_{0}=300$mm $\alpha_{1}=26.56$ $H_{0}=50.05$mm

The profile in the revoluitonary surface with the Hodograph Method is shown in Fig.6.

5. Summary

The research progress of Hodograph method on aerodynamic design in Tsinghua University has summrized in this article. i.e. (1) There are some restricted conditions in application with Hodograph method to design the transonic turbine and compressor cascades. (2) The Hodograph method design is suitable not only to the transonic turbine cascade but also to the transonic compressor cascade (3) The three dimensional Hodograph method will be developed after obtaining the basic equation in three dimensional of Hodograph method, as the example the transonic turbine cascade design of Hodograph in revolutionary surface is presented.

Reference

1. D.E.Hobson. CUED / A–Turbo / TR 40. NOV.1972.
2. Karadimas Von–Karman Institute for Fluid Dynamics Lecture Series 59.
3. C. FERRARI and F.G.TRICOMI. Transonic Aerodynamics Academic press York and Landon.
4. Chen Zuoyi, papers of ISABE. 1983, Paris.
5. Chen Zuoyi. Journal of Engineering Thermophysics, Vol.4. No.4. 1983.
6. Chen Zuoyi, Journal of Tsinghua Univ., Vol.22, No.1, 1982.
7. Chen Zuoyi, Journal of Tsinghua Univ., Vol.21, No.4, 1981.

Third International Conference on Inverse Design Concepts and Optimization in Engineering Sciences (ICIDES-III), Editor: G.S. Dulikravich, Washington D.C., October 23-25, 1991.

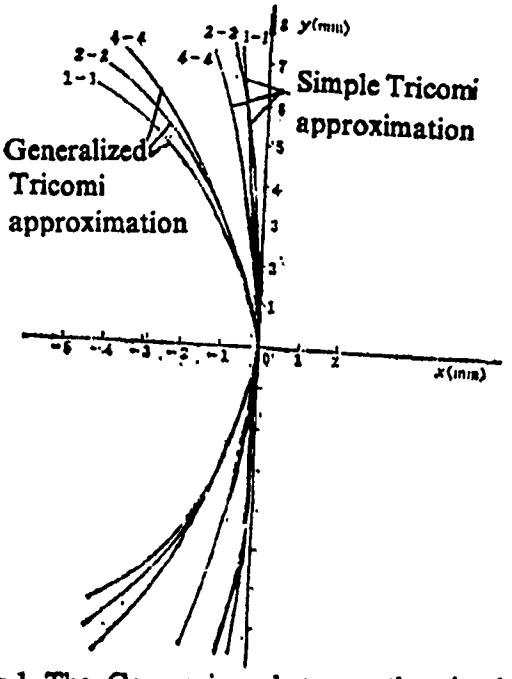


Fig.1 The Comparison between the simple Tricomi approximation and generalized Tricomi approximation under various condition

Table 1 The Comparison of application scope under various nozzle solution

$\frac{\partial M_{t1}}{\partial x^*}$ \ θ_{t1}	-0.043	-0.08	-0.08	-0.10	-0.12	-0.14	-0.16
0.2	◇ ○ □ ☆	○ ☆					
0.26	◇ ○ □ ☆	◇ ○ □ ☆	◇ ○ ☆				
0.32		◇ ☆ □	◇ ○ □ ☆	◇ ○ □ ☆	◇ ○ □ ☆		
0.39					◇ ☆ □	□ ☆	□ ☆
0.45							□

Note: approximation
normal solution
- Generalized
- Homographic
- Tomotika–Tamada
- Generalized Tomotika–Tamade

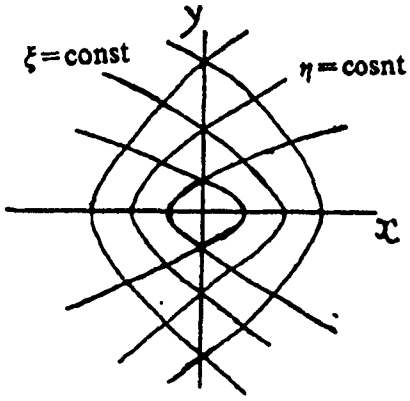


Fig.2 The parabolic coordinates in physic plane

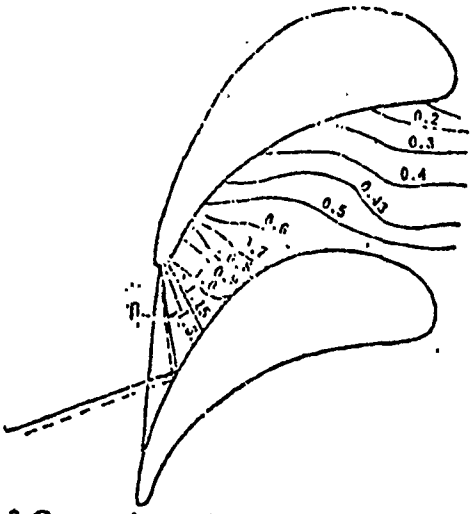
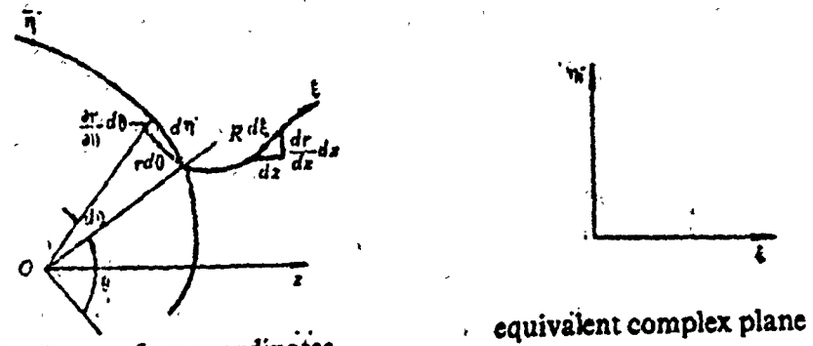


Fig.3 Comparison of shock wave Location Between Design and Experiment Q9 cascade profile

——experimental shock wave
——design shock wave

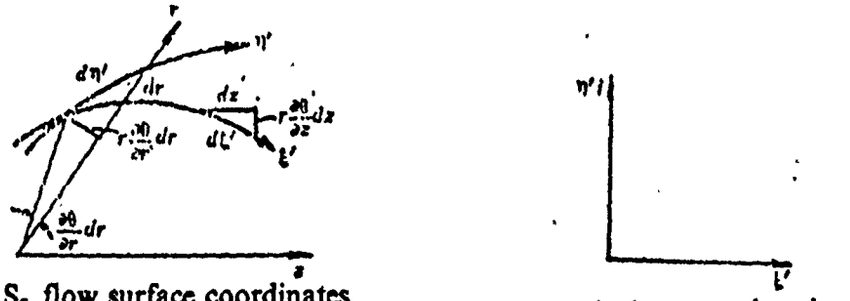
Third International Conference on Inverse Design Concepts and Optimization in Engineering Sciences
(ICIDES-III), Editor: G.S. Dulikravich, Washington D.C., October 23-25, 1991.



S_1 flow surface coordinates

equivalent complex plane

Fig.4 S_1 flow surface and equivalent complex plane



S_2 flow surface coordinates

equivalent complex plane

Fig.5 S_2 flow surface and equivalent complex plane

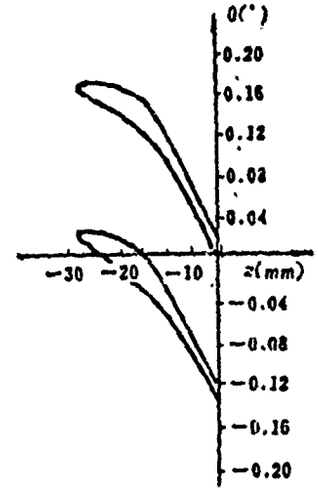


Fig.6 The transonic cascade profile in revolutionary surface using Hodograph method.

NUMERICAL OPTIMIZATION IN GERMANY:

A NON EXHAUSTIVE SURVEY ON CURRENT ACTIVITIES WITH EMPHASIS ON AERONAUTICS

Luciano Fornasier

DASA - MESSERSCHMITT-BÖLKOW-BLOHM GmbH
Military Aircraft Division - CFD Aerodynamics
Postfach 80 11 60 - D 8000 München 80
Federal Republic of Germany

ABSTRACT

Without claim to completeness, some recent progresses achieved in development and application of numerical optimization methods are presented. With emphasis lying on aeronautical problems, the activities in the field of aerodynamic design by CFD methods, structural optimization and determination of optimal flight trajectories are surveyed. As the reviewed methods show different levels of mathematical background, capability, maturity and applicability, the need for a stronger exchange of information and experiences between the different disciplines emerges as a key factor for increasing the impact of numerical optimization strategies in the design process.

INTRODUCTION

As a combined result of strives for improving the quality of new designs while reducing associated production costs and of recent progresses in computing power and numerical methodology, development and application of numerical strategies dealing with the optimization problem are drawing considerable attention at universities, research institutes and industries in Germany.

The objective of this paper is to report about some of the most recent activities considered to be representative of the current status and not that of reviewing all new contributions in this field. Due to this author's affiliation to the aeronautical community, the selection has been purposely restricted to applications pertinent to the aerospace field. Furthermore, optimization related activities which are object of individual papers presented at this conference has been not considered herein, [1],[2] and [3]. Hence, it would be misleading to argue from this review that numerical optimization is not being pursued in other scientifical disciplines or industrial branches or that no other methods than those presented here are presently in development in this country.

In the presentation of the selected methods the main aim is to provide rather general information covering the type of problem considered, the

motivation and the goal(s) of the used approach, together with a short description of the algorithm employed and a brief review of the results achieved. A more technical description of the methods themselves should be found in the referenced sources.

The reminder of this paper is organized as follows. In Section I optimization of aerodynamic shaping is considered. An optimization method for structural problems is presented in Section II. Application of different methods for the determination of optimal flight paths is discussed in Section III. Finally some author's comments are given in the concluding remarks section.

SECTION I: AERODYNAMIC DESIGN BY CFD METHODOLOGY

The whole process of aerodynamic design can be divided into two phases. In the first phase - that of preliminary design - the major design variables, such as configuration arrangement, general dimensions, wing planform and loading, are determined by parametrical studies involving interdisciplinary optimization of overall system efficiency against the mission requirements. It is during the following phase - that of detailed design - that the external contour of the configuration is worked out in details aiming at maximising the aerodynamic efficiency. Traditionally, aerodynamic designers used analysis of wind tunnel model testing for improving the design in an heuristic cut-and-try process. As a result of increasingly stringent performance requirements and of growing complexity of modern aircraft systems, wind tunnel testing time and associated costs increased almost exponentially with succeding generations of aircraft. This cost escalation has provided considerable incentive for the development and application of numerical simulation techniques. Relying on computer solution of mathematical representation of flow phenomena, the new discipline known as Computational Fluid Dynamics (CFD) is becoming one of the basic engineering tools in configuration design. Computers used as digital simulators of flow physics are well suited to analysing a wide range of candidate configurations, thus increasing the prospect that an optimum design will be identified. A systematic investigation of all possible geometrical variants is, however, still too time consuming and expensive for the present computing resources. Therefore, the greatest potential of CFD methodology should be individuated in the possibility of defining the configuration shaping capable of producing the desired aerodynamic characteristics. Of course, such possibility does not exist in wind tunnel experiments or flight tests. While the importance of such design procedures is generally well understood, difficulties connected with the solution of a nonlinear and, in the general case, ill-posed mathematical problem have sofar prevented the establishment of a single 'ideal' approach capable of solving any arbitrary design problem. Instead, several different approaches have been proposed for solving particular problems.

The Inverse Approach.

In the inverse formulation, a surface geometry is sought for which some flow variable distribution is prescribed, as for example the classical inverse methods which provide the airfoil geometry required to generate a

given pressure distribution. Following this approach, de Mattos and Wagner at the University of the Army, Munich, developed an efficient technique for the aerodynamic design of transonic wing sections with prescribed pressure distribution, [4]. The method belongs to the class of the iterative direct-inverse methods, in which the difference between the target and the pressure distribution computed by an analysis code is fed into an inverse algorithm capable of driving it to zero by successive relofting of an initial geometry. The basic ingredients of the present method are a finite difference code solving the full potential equation for the inviscid analysis of transonic flows about airfoils and an inverse algorithm based on the surface blowing technique. The analysis code developed by de Mattos in [5] is utilized to solve the transonic, full potential equation. Its formulation is written in steady, conservation-law form for a twodimensional body conforming curvilinear system. The Holst and Balhaus artificial density scheme is employed for the spatial discretization of the governing equation. Convergence to steady state is achieved through iteration in pseudo-time using the AF2 approximate factorization algorithm. The potential values on the profile during a design cycle are updated from an expression derived in the curvilinear coordinate system to satisfy the prescribed pressure distribution. This produces a blowing contravariant velocity distribution that is used to reloft the section geometry in order to recover the zero normal contravariant velocity used as boundary condition in the analysis loop. The blowing contravariant velocity is calculated using a second-order accurate residual expression. Essentially, this method can be considered a refinement of the procedure of Gally and Carlson [6], whereby the application of the more efficient AF2 approximate factorization scheme instead of the SLOR procedure in the analysis method and the more accurate computation of the normal velocity in the blowing algorithm are to be regarded as significant improvements.

As most of the 'pure' inverse algorithms, the procedure just described does not guarantee that the new airfoil shape will be practical or physically meaningful. In particular, in generating the airfoil modifications for arbitrary pressure distributions the procedure can yield open trailing edges or contour cross-overs with unphysically negative trailing edge thickness. To suppress insurgence of such undesirable features, the contour lines are rotated about the leading edge. Moreover, in order to avoid convergence problems, the contour displacement is underrelaxed. The whole procedure is then applied to the new airfoil geometry and the design loop design iterated until a convergence criterion has been reached.

Assuming as initial geometry the NACA 0012 profile three design exercises have been presented in [4] for validating the proposed design method. In the first case the design of a laminar profile is considered. Aiming at maintaining laminar flow for as much extent as possible along the cord, a pressure distribution exhibiting a plateau over a vast portion of the chord has been prescribed as design target, attempting to avoid the unfavourable pressure gradient of the original airfoil, figure 1. The result after the 12th iteration can be considered convereged for all engineering purposes. Figure 2 compares the profile designed by the present method with the original profile: the airfoli maximum thickness was increased from 12% to approximately 14%, while its location is moved further downstream at about 35% of the chord. The second case considers the elimination of the shock that existed in the original airfoil for a transonic freestream condition. This procedure represents a typical concern in the design of modern commercial airplane. Figure 3 presents the converged pressure distribution obtained with the present method as compared with the original distribution for the NACA 0012 and with the target pressure.

The authors report that this case required 22 iterations to converge, and that a large underrelaxation was necessary to stabilize the relofting procedure. An expanded view of the generated profile as compared with the original one is shown in figure 4. Also in this case the designed profile is about 2% thicker than the original one, so that a wing with the new profile would benefit from increased fuel capacity and decreased structural weight. In the third case, the program ability to recover a known geometry was checked. The target profile was obtained as a derivation of a NLF-0415 profile by scaling the maximum profile thickness to 12% and buiding a symmetric profile with this thickness distribution. Using the analysis code, the pressure distribution was calculated over the modified profile, and this was specified as target for the redesign exercise. The pressure distribution on the NACA 0012 - which was again taken as starting geometry - the target one and that obtained for the designed profile are compared in figure 5. A comparison of the corresponding geometries is shown in figure 6. It is completely evident that method reproduced exactly the target geometry, despite having started from a very different profile.

All these three cases demonstrate the program ability to solve efficiently the proposed problems. The scheme exhibits good convergence characteristics which the authors credit to the fact that the inverse algorithm used here deals directly with the flow physics rather than employing mathematical optimization. Improvements aimed at reducing computational costs by using replacing the onset flow condition presently used at the beginning of each design cycle with the perturbated flowfield computed at the previous are planned. Incorporation of a boundary layer routine for taking into account viscous effects is currently under way. An extension to the three-dimensional case for covering both the cases of rotary and fixed wings is envisaged.

The numerical optimization approach.

For practical design purposes, however, the inverse formulation suffers from the lack of a mechanism to control the geometry of the resulting contour, so that it cannot be used for constrained design purposes. To overcome these drawbacks, many researchers sorted out of using optimization strategies. Here, in principle, any available analysis code can be used as 'black-box' to provide the data required to approach the target function iteratively. One of the biggest advantages of the optimization approach is the possibility to take into account the geometrical constraints into the iterative process, either by selection of proper variables or by inclusion of some penalty terms into the object function that should be minimized (constrained optimization). Of all acceptable geometries, the optimization algorithm will then determine the one that minimizes the object function. In general, the optimization approach is well adaptable to complicate cases where it is difficult to determine the dependance between target function and design variables, i.e. in the aerodynamic problem, the dependance between desired flow characteristics and geometry. Hence numerical optimization can and in fact has been applied to three dimensional problems with consideration of geometrical constraints but its application can require very large computational power, since it involves the analysis of the candidate design at each iteration step. The total amount of computing time depends essentially on: a) the method used as analysis tool; b) the number of optimization steps to convergence; c)

the quantity of information required by the optimization algorithm at each iteration step. When using time-consuming analysis code, i.e. Euler or Navier-Stokes solvers, the number of analysis computations should be kept as low as possible. As the random search requires only one analysis computation at each iteration, while multiple analysis computations are required to define the gradient of the object function with respect to the design variables, there is a trade-off between the number of iterations and their computational costs.

To find out the best strategy for aerodynamic applications, Bock at Dornier compared a random search method based on evolution theory to an universal gradient search method [7]. By application of the multi-level evolution theory GRUP [8] and of the COPES code of Vanderplaats [9] to the relatively simple problem of wave minimization for a two-dimensional profile, Bock found that the evolution theory requires a much larger number of iterations than the gradient code. Basing on this experience, Bock proceeded then to couple the COPES code to three different analysis codes in use at the aero design department at Dornier. For body shape optimization at supersonic speeds, the COPES code was combined with the Euler space-marching method of Rieger [10]. This is a finite volume method solving the inviscid equations in conservative form. By restriction to purely supersonic flows, the problem becomes hyperbolic, so that when balancing the flux across the surfaces of each finite volume the flux of the volume layer normal to the stream direction can be deduced from the values of the upstream layers. A Runge-Kutta integration method is used to define the flux values in downstream direction. Although the Euler method is capable of treating arbitrary bodies, the optimization procedure was first restricted to bodies of revolution for sake of comparison with results obtained using linearized potential equatial and slender body theory. In order to convert the problem into one of variable optimization, the body contour is approximated by superimposition of Legendre polynomials and a triangular function, the latter taking into account that optimum shapes for given thickness might have a kinked contour. To demonstrate the efficiency of the combined code, the classical Sears-Haack problem to determine the body of minimum drag having a given volume was examined. Starting from a parabolic arc contour and a smaller volume than the target one, the optimization progress of the design objective (drag) and of the constraint (body volume) computed by the code are presented in figure 7. In order to save the computer time the analysis code was run using a coarser grid at the beginning and switching to a finer one after the step N=30. The steps N=1 to N=9 are small contour variations prescribed by input to establish the initial gradient; after step N=10 the COPES determines automatically the design variable variations. Examination of the drag and volume histories reveals how the COPES proceeds to the find the optimum. In the first steps the code increases the body volume for recovering a feasible design condition (the starting body violates the volume constraint). Then the wave drag is decreased, while the volume is maintained constant. In figure 8 the optimum shapes computed for Mach numbers equal to 1.5 and 3.0 are compared to the Sears-Haack body, which is the analytical optimum under the assumption of linearized theory and slender body simplification. Unlike slender body theory results, which are independent of the freestream Mach number, the present method show a definite Mach number dependancy. Interestingly the Euler/COPES optimum shape for the smaller Mach number is closer to the Sears-Haack body, whilst the wave drag value of Mach number 3.0 are nearer to the slender-body value. According to Bock, these discrepancies can be explained bearing in mind that the Sears-Haacks body has a vertical tangent and therefore a small subsonic flow region at the two pointed ends, which cannot be calculated by the present space-marching

Euler method.

For the design of efficient transonic wing sections Sobieczky developed a method [11] which allows to modify the geometry of an existing airfoil so that, for a given flow condition, a shockfree flow is obtained. Bock has coupled this method to COPES to build an optimization procedure where some of the Sobieczky's input variables can be used as design parameters to find a profile which is not only shockless but also represents an optimum with respect to a certain objective and fulfils given constraints.
A full potential analysis code and a boundary layer method for the evaluation of the viscous displacement thickness are part of the optimization procedure. The practical capabilities of the method are illustrated by the following redesign exercise. Starting from the Dornier A-7 profile, Bock was able to improve the aerodynamic efficiency of about 12% (lift-to-drag ratio from 39.7 to 445.) while maintaining the same maximum thickness (t/c = 14.4%) and the same trailing edge thickness. The figure 9 shows the comparison of the contour (displacement and wall), the characteristics in the supersonic region, and the pressure distribution for the initial airfoil (already shock free) and the optimized airfoil. As a large number of additional test calculations not shown here proved, it is very easy to redesign existing profiles for improving transonic performance. Off-design behaviour can be easily considered by inclusion of a multiple-point optimization strategy.

Finally Bock coupled the COPES code with a subsonic multielement airfoil code package, which is able to calculate high lift characteristics of flapped airfoils in presence of trailing edge separation. The combined procedure has been used for finding the relative position of flap and main airfoil capable of yielding the maximum lift, figure 10. As the design objective depends on only two variables (horizontal and vertical translation of the flap with the regard to the main airfoil), the optimization history can be graphycally displayed, figure 11. It can be seen that the reference point is moved very close to the main profile, where the clearance constraint (minimum channel gap) becomes active. As it turned out the analysis code looses accuracy when the slot width become smaller. Nevertheless, the optimization procedure has been successfully applied to optimization of translation and deflection of three-element systems.

At the DLR Institute for Design Aerodynamics different inverse and analysis tools are in intensive use for the aerodynamic design of airfoils, wings and nacelles. In order to adapt these methods for the requirements of the design tasks, several improvement have been incorporated [12]. On the other hand, first steps toward an approach based on a numerical optimization technique coupled with an analysis tool have been performed [13] and [14]. Figure 12 shows a block diagram of an iterative procedure for the design of a supersonic wing. Here, the wing is described by a set of design variables which are weight coefficients of Legendre polynomials. For this wing, the flow field is calculated using a method solving the Euler equations. The calculated flow field is used to define the object function. With the object function and the informations from the previuos steps, the numerical optimization technique calculates a new set of design variables. If a given convergence criterion is not reached, the next iteration cycle is performed. The use of Legendre polynomials leads to a suitable description of the wing surface and allows incorporation of geometrical equality constraints like leading edge radius and wing volume by a reduction of the number of design variables. Figure 13 shows the optimiaztion history for a conical delta wing with a leading edge sweep of 75

degrees, an onflow Mach number equal to 4.5 and a design lift coefficient equal to 0.15. Here a Legendre polynomial of order N=5 is used which leads to a total of 9 design variables. The object function is the lift-to-drag ratio L/D. The optimization starts on a coarse mesh with 24 x 10 cells and continues on a medium and a fine mesh. The figure shows that most of the variation of the design variables is done on the coarsest grid while only small changes occur for the medium and fine meshes. Figure 14 shows the effect of an increasing order of the Legendre polynomial (i.e. increasing the number of design variables) on the optimal lift-to-drag ratio. Isomach lines in a cross-section for the starting configuration and for the result of the configuration for an order of N=3 and N=5 of the legendre polynomial are plotted in figure 15. It can be seen that for increasing number of design variables the strength of the crossflow shock decreases and the optimal L/D is increased. The procedure described above can also be used in an inverse mode where the object function is now an integral over the difference of the prescribed and the calculated pressure distribution. Figure 16 shows the pressure distribution as function of the arc length. In order to validate this approach the target pressure distribution was calculated for a given wing with the same analysis method used in the optimization loop. The result of the design procedure shows very small discrepancies to the given pressure distribution while the pressure as well as the geomtry of the initial configuration are far away from the result. A fisrt step for an aerodynamic design by an approach based on an inverse tool coupled with an optimization technique has been performed. Here, the input of the inverse method for the design of transonic airfoil is changed by an optimization. Figure 17 shows an application of this procedure. The starting airfoil has a lift-to-drag ratio equal to L/D=48.7 corresponding to a lift coefficient of CL = 1.1 at a Reynolds number of 2.5 millions and an onflow Mach number of Ma = 0.60. After 114 iterations cycles a new airfoil shape exhibiting an efficiency of L/D = 102.3 is obtained.

SECTION II: AN OPTIMIZATION SYSTEM FOR SPACE AND AIRCRAFT STRUCTURES

Methods solving structural optimization problems have since many years a widespread use in aerospace industries. Especially for complex design problems, their application leads to definition of optimal layouts which fulfill all constructive requirements. So far, the structural weight has been the objective function most commonly used. Design of space and aircraft structures, however, requires consideration of additional parameters which have to taken into account during the optimization process. In the design of modern airplane, for example, structural weight savings may introduce unacceptable limitations on aerodynamic performance by static and dynamic aeroelastic phenomena. For spacecraft structures different requirements have to be fulfilled during the launch phase and the operation in orbit. Optimization methods are the most rationale way to determine unique and optimal compromise solutions. To solve these problems, the optimization system LAGRANGE is being developed at MBB with the technical cooperation from the universities of Bayreuth, Munich and Siegen, [15] - [17] . The system is applicable to the design of high performance structures involving large scale optimization problems with multidisciplinary objectives and constraints to be solved simultaneously. The development is focused on three main topics: optimization models, structural analysis with sensitivity analysis and optimization algorithms. The optimization models are based on the general nonlinear programming problem. The design

variables are cross sectional areas of trusses and beams, wall thicknesses cf membrane and shell elements, laminate thicknesses of layers in composite elements or nodal coordinates for geometry optimization problems. The constraints in form of inequalities may be any limitation of displacements, stresses, strains, buckling loads, dynamic response, heat loads, etc. A variety of different optimiaztion algorithms (such as inverse barrier function, method of multipliers, sequential linear programming, recursive quadratic programming, generalized reduced gradients, etc) are available which can chosen depending on the actual design problem. The structural and sensitivity analysis are based on finite element methods. Static, stability dynamic, aeroelastic and flutter modules have been implemented. The finite element package is MSC-NASTRAN compatible as far as possible. Special features include the handling of laminated composites, which allows the optimization of each layer. Important for parctical applications is the integration into the existing CAE-environment by use of standard interfaces.

A variety of structural optimization problems has already been successfully performed with LAGRANGE. Present development efforts are focused on the improvement of the analysis and sensitivity modules for dynamic response, structural stability and heat transfer. Furthermore the optimization models have to be extended especially in order to improve the capability of geometry optimization. The following examples have been chosen for illustrating the current capabilities of the LAGRANGE system. The first example refers to the sizing of an alluminium frame located at the engine inlet of a combat aircraft. For the formulation of optimization problem it is important to know that a milling machine will be used to realize a variable thickness distribution. So a large number of design variables can be defined in order to calculate the optimal thickness of the frame. The finite element model is shown in figure 18. It involves 975 degrees of freedom, 930 elemnts and 97 loads cases. The objective function is the weight. The constraints are used to ensure static requirements. Stability constraints are taken into account to prevent buckling and lateral instability of webs. Since the constraints has to be satisfied for each single load case a very large number of constraints (NG=92 829) is obtained. Together with the thickness design variables (N=187) it makes up a large scale problem. The initial design has infeasible buckling loads and stresses. The optimization algorithm needs 20 iterations to achieve convergence. Figure 19 shows the optimization history for the buckling constraints, where the most critical constraint at each iteration is monitorized. The optimal design fulfills all static requirements and achieves a weight reduction of about 25% over the initial (unfeasible) design.

To illustrate the interdisciplinary simultaneous optimization a study for a composite fin of an advanced supersonic aircraft is presented.The two objectives considered in the application of the multicriterion approach are the minimum weight and the maximum aerolastic efficiency. Since these two objectives cannot be met simultaneously, an objective conflict arises leading to a typical vector optimization problem. The finite element model of the fin is presented in figure 20 together with the panel model of the aircraft used to calculate the fin aerodynamic characteristics. The functional efficient solutions are illustrated in figure 21 where the aerodynamic efficiency η is plotted against the normalized structural weight W/Wo. The lower and upeer limits of the effieciency $.85 < \eta < .95$ represent the range of practical importance. In this case the design with $\eta = .89$ and $W/Wo = 2.83$ is chosen as as optimal compromise solution. For designs with $\eta > .89$ the increase of the structural weight is too large in

comparison to the relatively small improvements of the aerodynamic efficiency. On the other hand, the designs with $\eta < .89$ deliver no essential reductions in weight. This example demonstrates the utility of representing in graphic form the functional efficient boundary as an effective help in selecting the most appropriate design.

SECTION IV: NUMERICAL OPTIMIZATION OF FLIGHT TRAJECTORIES

Historically, the optimization of ascent trajectory of rockets has been one of the driving applications for developing new optimization methods, more efficient algorithms and related software in the last thirty years. This can be explained with the stringent necessity of accurate determination of the best ascent profile in terms of fuel consumption, since the payload transferable to a given orbit is only a small fraction of the total lift-off mass of the rocket. Mathematically, the problem is casted into a set of ordinary differential equations describing the motion of the center of mass from lift-off to burn-out of the last stage subject to aerodynamic, gravitational and thrust forces. The purpose of the optimization is to determine the time history of the pitch and yaw angles, which are considered as the control variables, suitable to maximize the payload for the desired orbit while fulfilling all vehicle and mission constraints. In the last years, appearance of non-ballistic, manouverable reentry vehicles have fostered application of optimization methods to the descent problem, where the aerodynamic lift is used to change the flight path for maximizing the cross range and/or minimizing the total head load accumulated during the reentry. Finally, new space transportation projects based on two-stage concepts like the German Sänger Study have stimulated interest in the optimization of high altitude separation conditions of rocket-type upper stages from airbreathing lower stages.

All these optimization problems are optimal control problems which cannot be solved analytically unless using severe simplifying assumptions. These approximate solutions can be usefully employed for preliminary system design purposes but must be checked making use of numerical solutions obtained using more complete dynamic models. To promote and coordinate the developmental efforts in this field, the German Research Association (DFG) started a multiyear programme called 'Application-oriented Optimization and Control (Methods)'. Within the frame of this programme, scientists from several institutes of the German Aerospace Research Establishment (DLR) and from various technical universities are working in close contact on mathematical foundations of new optimization methods and development, implementation and application of numerical methods on practical problems.

At the Technical University of Munich the problem of ascent optimization for a rocket type upper stage of a space transportation system with an air breathing first stage has been recently investigated, [18]. Since the separation of these systems takes places at a hypersonic speed at high altitude with a small flight path angle inclination, an ascent may not be possible without a lifting capability. However, an upper stage consisting of a fuselage type body can produce a limited amount of lift even if it is not equipped with wing. The investigation shows that with the use of efficient optimization techniques this limited lift capability can be exploited for achieving an ascent to orbit even for a horizontal flight condition at separation. In addition to the usual point mass dynamics modelling, the investigation included pitching moment balance and rotary dyna-

mics effects. It was found that the results based on point mass modeling are valid also for the model including rotary dynamics when the thrust vector angle is fixed. However, differences exist between the results for both models when thrust vector angle is considered as control variable. This is because an effective use of thrust vector angle would require too large aerodynamic balancing moment. Thus, thrust vectoring must be restricted so that its potential for improving the ascent performance can be only utilized to a small extent.

At the Institute for Flight Systems Dynamics of the DLR two new methods are under development with the primary goal of having efficient software for trajectory optimization of aerospace vehicles, [19]. The algorithm presented under the name PROMIS is based on parametrizing the control function and using the multiple shooting for integrating the systems equations numerically. The other method called TROPIC is based on direct collocation for solving the differential equations. Both methods share the advantage of not relying on adjoint differential equations for gradient generation. This feature makes the methods flexible as far as changes in problem formulation are concerned. The methods have been successfully applied to the optimization of the ARIANE V ascent trajectories and HERMES reentry trajectories. Further developement currently under way will enable apllication to trajectory optimization of winged launchers with airbreathing engines, for instance HOTOL or SÄNGER.

A numerical optimization method based on the multiple shooting technique has been used to investigate the possibility of extracting energy from wind shear and transferring it to the airplane, [20]. The possibility of extracting energy from non-uniform, horizontal air stream (wind shear) was first observed with the flight of birds and considered as a means for use in the flight of sailplanes. In this study the determination of the trajectories for maximum energy extraction has been formulated as an optimal control problem. Basic characteristics of optimal trajectories has been obtained together with details about the geometric properties of the flight path and the corresponding speeds histories. The wind shear level necessary for maintaining continuous flight has been evaluated as function of the aerodynamic efficiency and wing loading. As expected, aerodynamic efficiency is a factor having a great effect. By contrast, wing loading is found to be of minor importance for the wind shear problem considered.

CONCLUDING REMARKS

Without claim to completeness, some recent progresses achieved in development and application of numerical optimization methods are presented. With emphasis lying on aeronautical problems, the activities in the field of aerodynamic design by CFD methods, structural optimization and determination of optimal flight trajectories are surveyed. While the capabilities in structural and flight control optimization appear to be adequate to the current demand in these fields, the potential of the CFD analysis codes seems to have not be completely transferred to the design methodology. In particular, the application of time-consuming flow solvers solving the Euler and Navier-Stokes equations to optimization of complete three-dimensional airplane configurations and of the aerothermodynamic characteristics of hypersonic configurations is currently hampered by the lack of efficient optimization strategies. Current practice of coupling flow analysis codes to optimization algorithms in a 'black-box mode' results in

computing time levels unaffordable for three-dimensional problems. On the contrary, as the survey of the optimal flight control methods revealed, efficiency can at best be obtained by tailoring the optimization algorithms on the specific problems. Based on this experience, future efforts for improving the CFD design capabilities will require a tighter cooperation between mathematicians and engineers for development of strongly coupled analysis/optimization algorithm. Adaption of existing optimal control techniques to CFD problems deserves careful consideration.

ACKNOWLEDGMENTS

The author wishes to thanks Dr. Bock from Dornier, Dr. Schöne from DLR - Braunschweig, Prof. Sachs and his coworkers from the Technical University of Munich , Prof. Wagner and Mr. de Mattos from the University of Stuttgart for their kind assistance in the preparation of this paper.

REFERENCES

[1] Sobieczky, H., and Quian, Y.J., "Inverse method of Characteristics for Aerodynamic Design", in International Conference on Inverse Design and Optimization in Engineering Sciences, 1991.

[2] Schmidt. E., and Grein, H.D., "Supercritical Blade Design on Stream Surfaces of Revolution with an Inverse Method", in International Conference on Inverse Design and Optimization in Engineering Sciences, 1991.

[3] Greff, E., Forbrich, D., and Schwarten, H., "Applications of the Direct Inverse Analogy Method (DIVA) and Viscous Design Optimization Techniques", in International Conference on Inverse Design and Optimization in Engineering Sciences, 1991.

[4] de Mattos, B.S., Wagner, S., and Azevedo, J.L.F., "Transonic profile Design in Curvilinear Coordinates Using an Approximate Factorization Algorithm", Institut für Luftfahrtechnik und Leichtbau, Universität der Bundeswehr München, to be published.

[5] de Mattos, B.S., "Calculation of Three-Dimensional Transonic Potential Flow Using an Implicit Approximate Factorization Algorithm", Master Thesis, Instituto Tecnologico de Aeronautica, São Josè dos campos, SP, Brazil, 1990.

[6] Gally, T.A., and Carlson, L.A., "Transonic Wing Design Using Inverse Methods in Curvilinear Coordinates", J. Aircraft, Vol. 22, No. 8, Aug. 1985, pp. 665-660.

[7] Bock, K.W., "Aerodynamic Design by Optimization", in Computational Methods for Aerodynamic Design (Inverse) and Optimization, Agard Conference Proc. No. 463, May 1989, pp. 20 1-12.

[8] Rechenberg, I., "Evolutionsstrategien", in Medizinische Informatik und Statistik (Series), Simulationsmethoden in der Medizin und Biologie (Volume), Springer Verlag, Berlin/Heidelberg/New York, 1978

[9] Vanderplaats, G.N., "CONMIN - FORTRAN Program for Constrained Function Minimization", NASA TMX-62 282, 1973.

[10] Rieger, H., "Aerodynamics of Hypersonic Lifting Vehicles", AGARD Conference Proceedings No. 428, 1988

[11] Sobieczky, H., "Design of Advanced Technology Transonic Airfoils and Wings", in Subsonic/transonic Configuration Aerodynamics, AGARD Conference Proceedings No. 285, 1981.

[12] Köster, H., Rohardt, C.H., Horstmann, K.H., and Radespiel, R., "Aerodynamic Design Techniques at the DLR Institute for Design Aerodynamics", in Computational Methods for Aerodynamic Design (Inverse) and Optimization, Agard Conference Proc. No. 463, May 1989, pp. 3 1-15.

[13] Schöne, J., "Design of Supersonic Wings Using an Optimization Strategy Coupled with a Solution Scheme for the Euler Equations", AIAA Paper 90-3060, 1990.

[14] Schöne, J., and Rohardt, C.H., "CFD Application: Aerodynamic Design Using Numerical Optimization Technique", Space Course on Low Earth Orbit Transportation and Orbital Systems, Aachen, 1991.

[15] Kneppe, G., Hartzheim, W., and Zimmermann, G., "Development and Application of an Optimization Procedure for Space and Aircraft Structures", in GAMM-Seminar on Discretization Methods and Structural Optimization, University of Siegen, Germany, 1988.

[16] Kneppe, G., "MBB-LAGRANGE: Structural Optimization System for Space and Aircraft Structures", in COMMET Seminar on Computer Aided Optimal Design, University of Bayreuth, Germany, 1990.

[17] Schneider, G., Krammer, H., and Gödel, H., "Integrated Design Analysis and Optimization - Preliminary Results Fin Optimization", AGARD 70th SMP Meeting on Integrated Design Analysis and Optimization, April 1990.

[18] Sachs, G., Drexler, J., and Stich, R., "Ascent Optimization and Control Problems of Wingless Upper Stages", presented at the 41th Congress of the International Astronautical Federation, Paper IAF 90-296, 1990.

[19] Jänsch,C., Schnepper, K., Well, K.H., "Ascent and Descent Trajectory Optimization of ARIANE V / HERMES", Report No. 197 from the Schwerpunktprogramm der Deutschen Forschungsgemeinschaft ANWENDUNGSBEZOGENE OPTIMIERUNG UND STEUERUNG, 1990.

[20] Sachs, G., Knoll, A., and Lesh, K., "Optimal Control for Maximum Energy Extraction from Wind Shear", Report No. 125 from the Schwerpunktprogramm der Deutschen Forschungsgemeinschaft ANWENDUNGSBEZOGENE OPTIMIERUNG UND STEUERUNG, 1989.

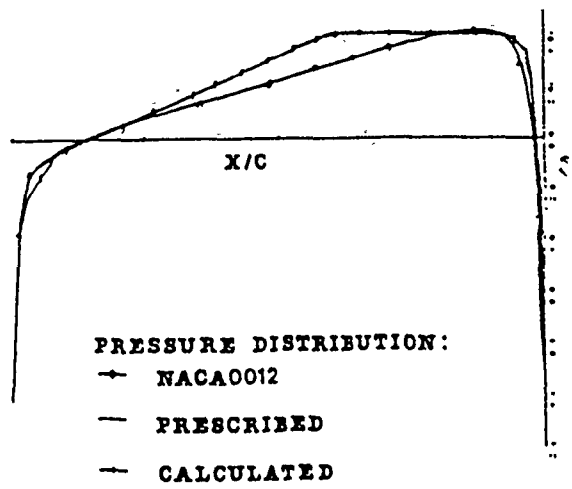


Fig. 1 Case I from [4]: Comparison of pressures

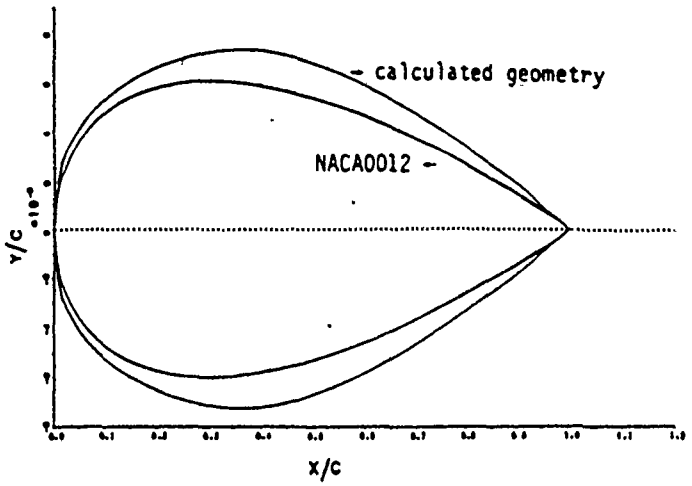


Fig. 2 Case I From [4]: Comparison of contours

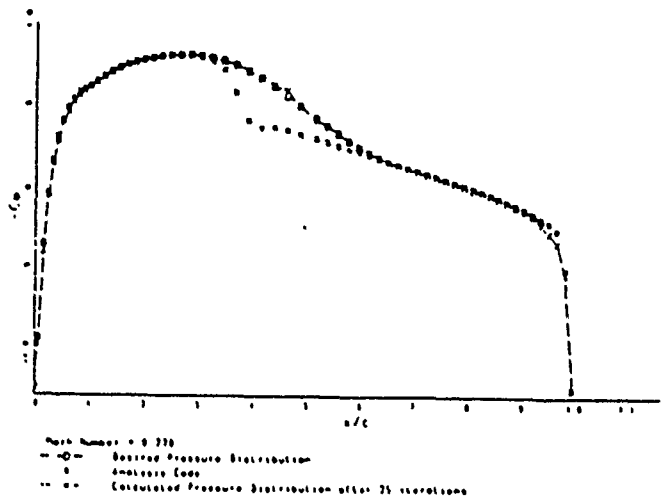


Fig. 3 Case II from [4]: Comparison of pressures

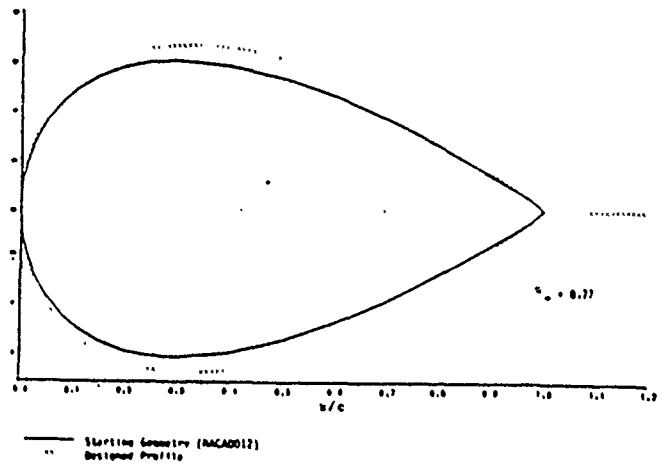


Fig. 4 Case II From [4]: Comparison of contours

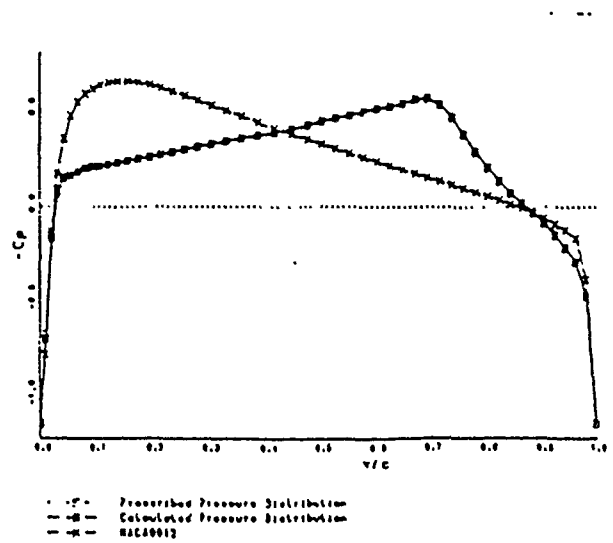


Fig. 5 Case III from [4]: Comparison of pressures

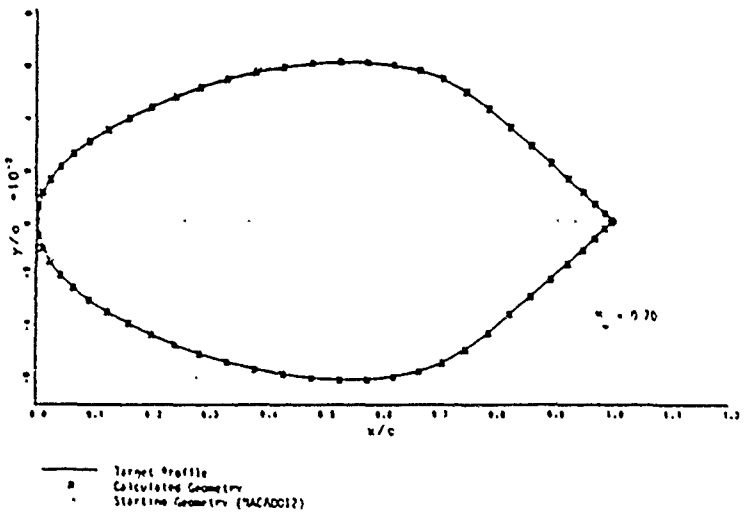


Fig. 6 Case III From [4]: Comparison of contours

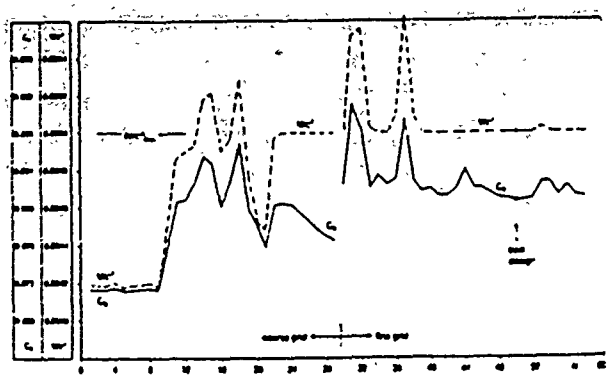


Fig. 7 Optimization Progress of Minimum Wave Drag Body of Revolution, from [7]

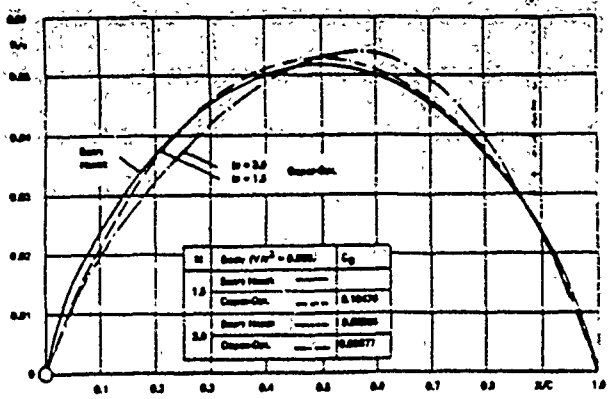


Fig. 8 Minimum Wave Drag Bodies Compared to Sears-Haack Body, from [7]

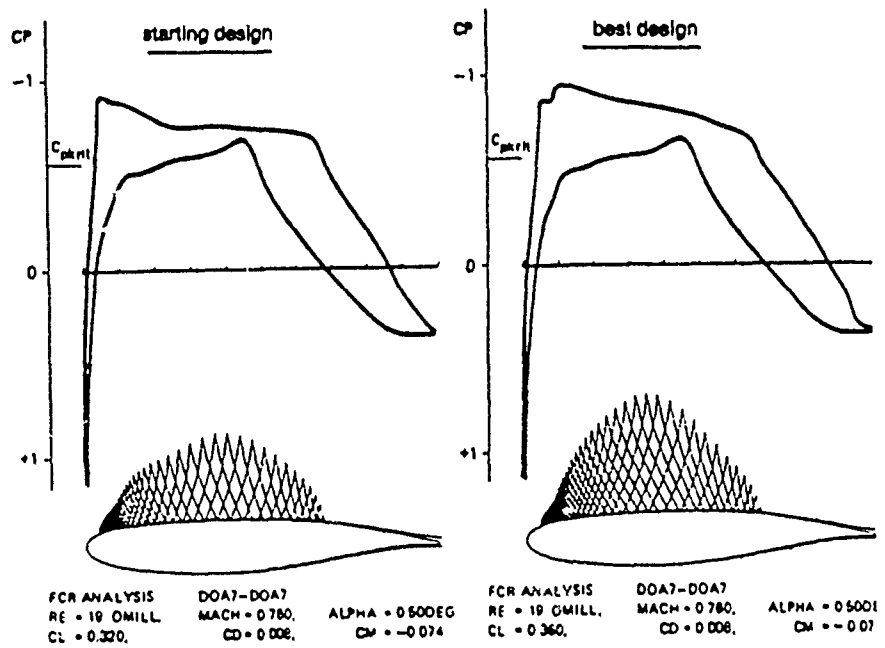


Fig. 9 Starting and Best Design of Transonic Airfoil Optimization, from [7]

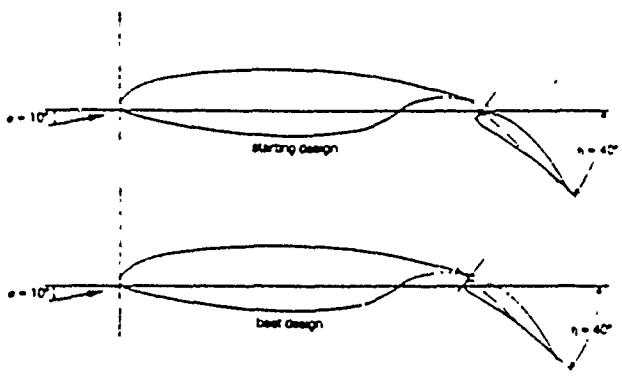


Fig. 10 Starting and Best Design of Flap Position Optimization, from [7]

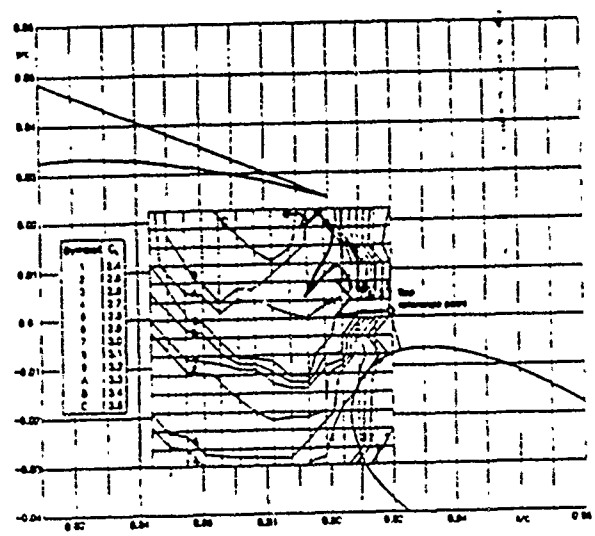


Fig. 11 Optimization Progress of Flap Position Optimization, from [7]

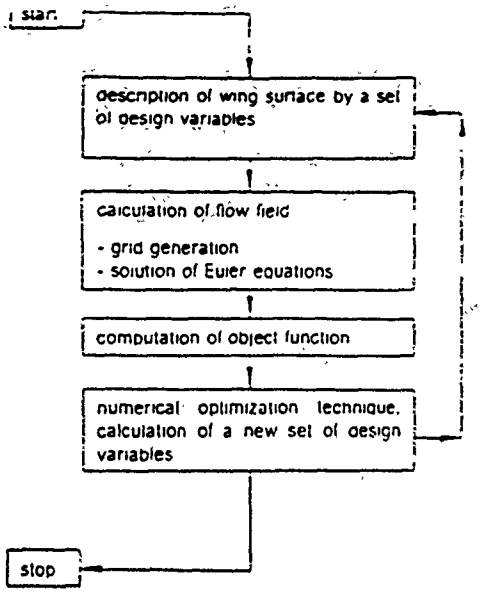


Fig.12 Iterative design procedure based on analysis tool coupled with optimization method

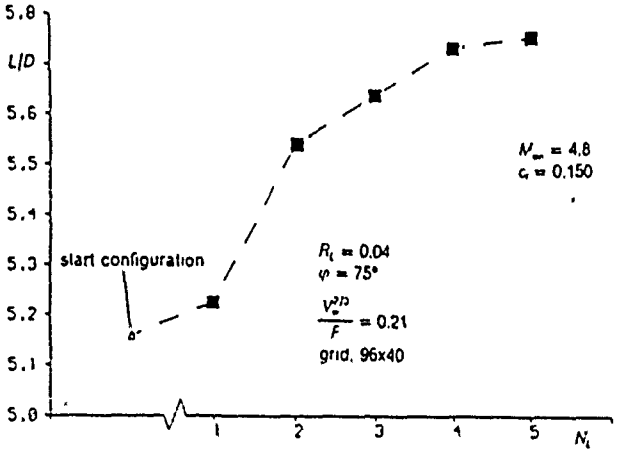


Fig.14 Influence of order of Legendre polynominal on result of optimization

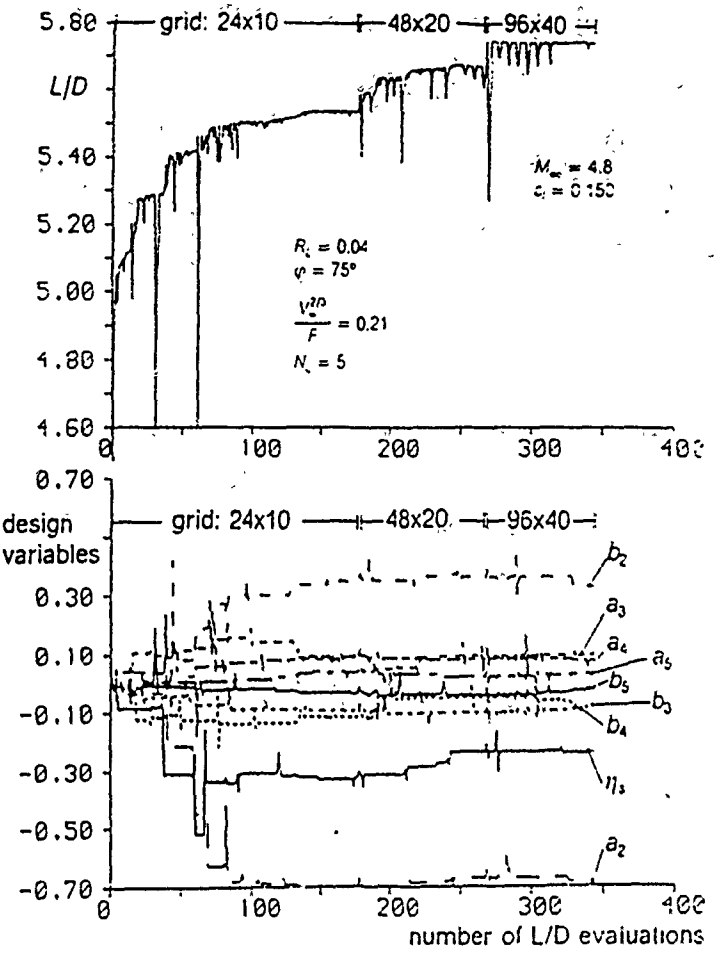


Fig.13 Optimization history for conical delta wing

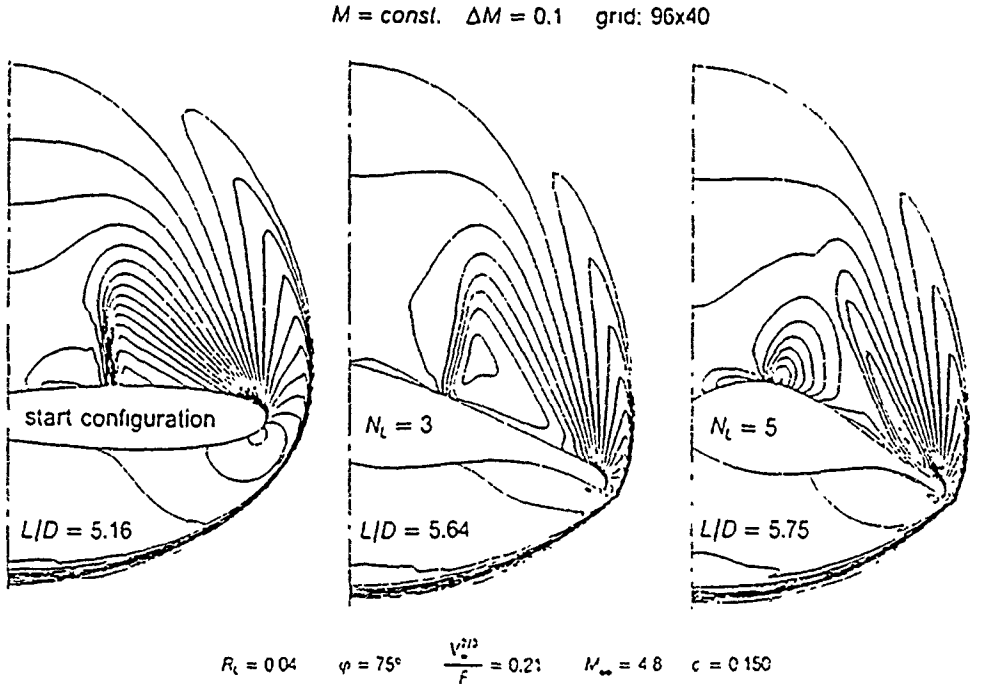


Fig.15 Iso-Mach lines for start configuration and optimized delta wings

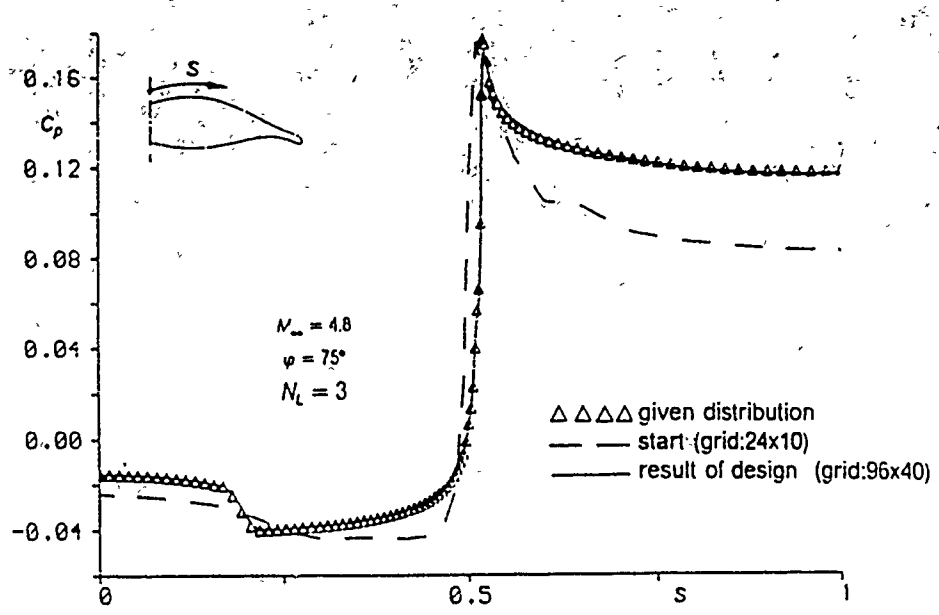


Fig. 16 Result of inverse design based on a coupling of analysis method and optimization technique

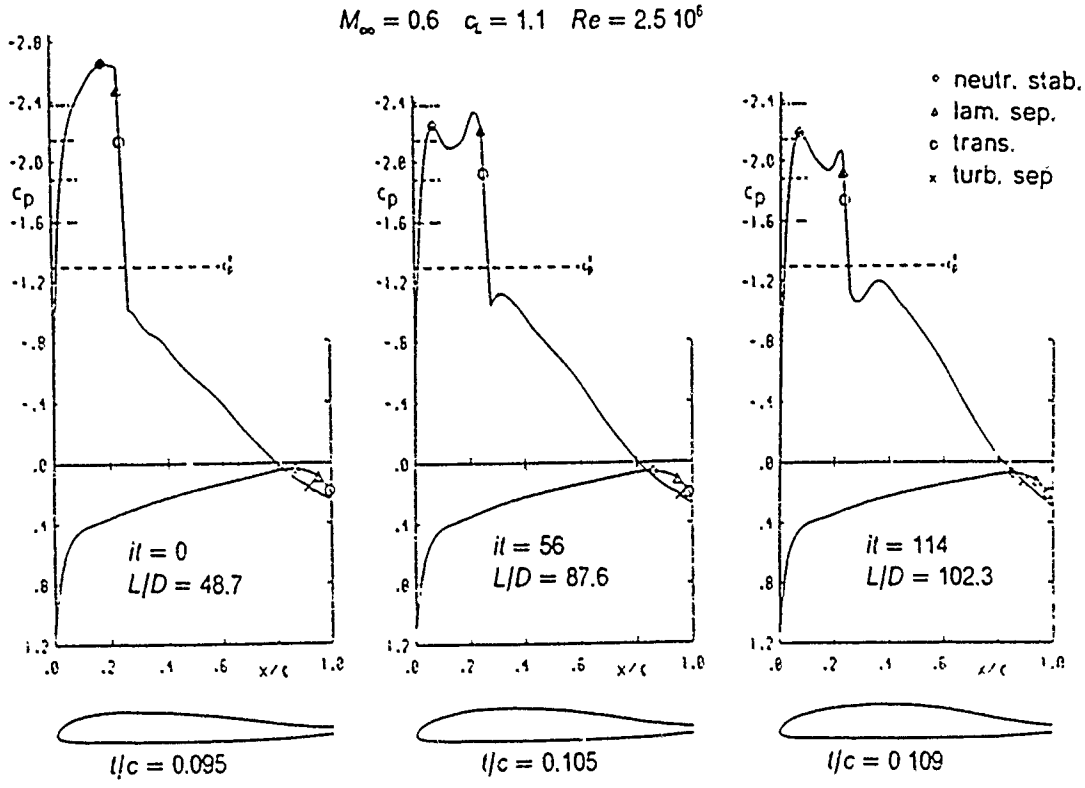


Fig. 17 Pressure distribution for transonic airfoil during optimization; here, the inverse design tool is coupled with the optimization technique

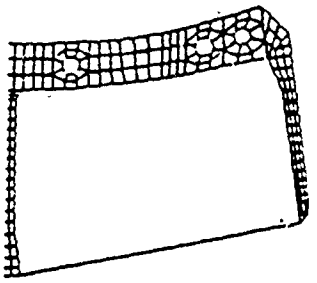


Fig. 18 FEM of Inlet Frame (half model), from [16]

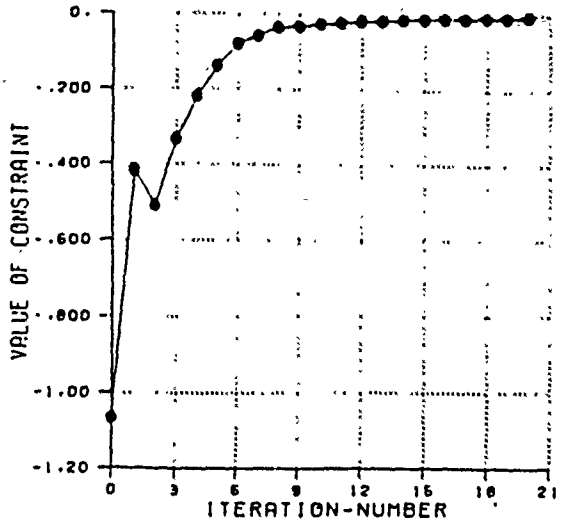


Fig. 19 History of most critical buckling constraint for frame optimisation, from [16]

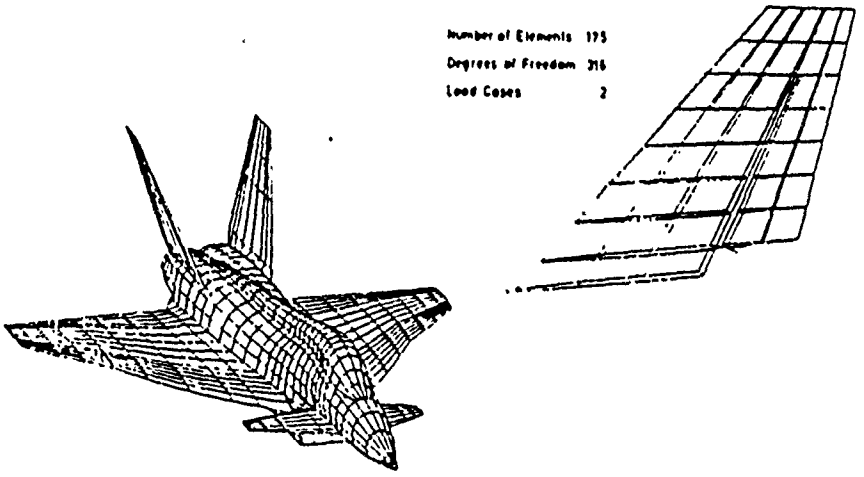


Fig. 21 Functional Efficient Boundary for Composite Fin, from [16]

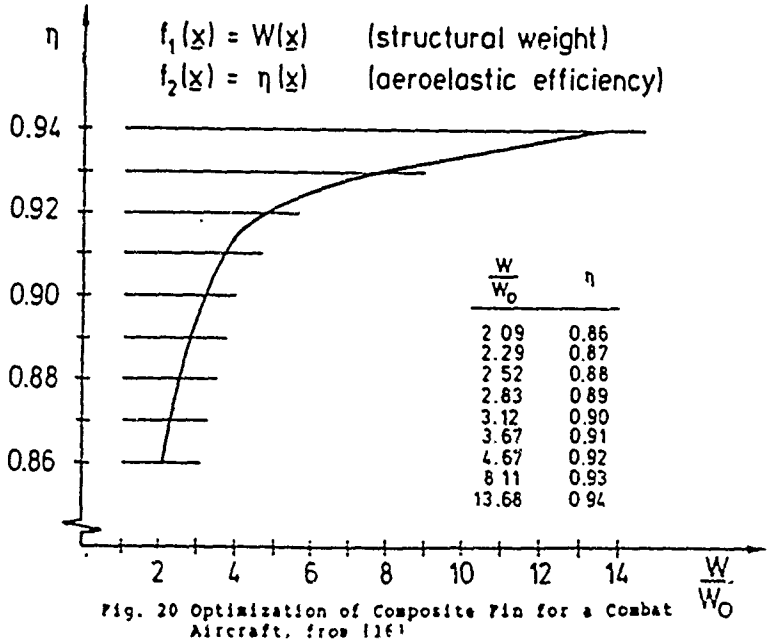


Fig. 20 Optimization of Composite Fin for a Combat Aircraft, from [16]